

# ASF'E'21

## Proceedings of the International Conference in Ljubljana, 10-11 June, 2021

in edition of Applications of Structural Fire Engineering



### Editors

Robert PEČENKO

Sabina HUČ

Cvetanka CHIFLIGANEC

Tomaž HOZJAN



University of Ljubljana  
Faculty of *Civil and  
Geodetic Engineering*

in edition of Applications of Structural Fire Engineering

# **Proceedings of the International Conference in Ljubljana, 10-11 June, 2021**

University of *Ljubljana*  
Faculty of *Civil and Geodetic Engineering*



**Proceedings of the International Conference in Ljubljana, 10-11 June 2021  
in edition of Applications of Structural Fire Engineering**

Ed. Pečenko R., Huč S., Chifliganec C., Hozjan T.

ISBN 978-961-6884-72-3 (PDF)

ISSN 2570-8074

Publisher: University of Ljubljana, Faculty of Civil and Geodetic Engineering  
June 2021

457 pages

Cataloging in publication record (CIP) was prepared in National and  
University Library in Ljubljana/Kataložni zapis o publikaciji (CIP) pripravili v  
Narodni in univerzitetni knjižnici v Ljubljani

COBISS.SI-ID 65513219

ISBN 978-961-6884-72-3 (PDF)

**Publisher's note:** this Proceedings has been produced from PDF files provided by the individual contributors. The publisher makes no representation, express or implied, with regard to the accuracy of the information contained in this book and cannot accept any legal responsibility or liability for any errors or omissions that had be made.

## LIST OF CONTENTS

<b>Preface</b>	9
<i>Ian Burgess, František Wald</i>	
<b>Acknowledgement</b>	10
<b>Keynote lectures</b>	
How passive the passive fire protection layers actually are? <i>Simo Hostikka</i>	12
Towards an advanced, time-dependent analysis of fire exposed steel structures <i>Neno Torić</i>	13
<b>Session: Steel structures I</b>	
Numerical analysis on post-fire residual capacity of the restrained high strength structural steel columns under axial compression <i>Lin-Xin Song, Guo-Qiang Li</i>	19
Experimental study on pull-out test of hot-cast anchors exposed to ISO-834 fire <i>Yong Du, Jian Zhu</i>	25
Cold-formed stainless steel lipped-channel and sigma sections beams at elevated temperatures <i>Flávio Arrais, Nuno Lopes, Paulo Vila Real</i>	31
Evaluation of steel structures fire vulnerability through fragility curves <i>Enrico Cardellino, Donatella De Silva, Emidio Nigro</i>	37
Performance of ductile connections in 3-D composite frames under fire conditions <i>Yu Liu, Shan-Shan Huang and Ian Burgess</i>	43
The design of moment connections for improved post-fire seismic performance <i>Chrysanthos Maraveas, Daphne Pantousa, Theodore L. Karavasilis</i>	49
The impact strength of selected steel types after fire – Experimental tests related to simulated fire conditions <i>Mariusz Maslak, Michal Pazdanowski, Marek Stankiewicz, Paulina Zajdel</i>	55
Predicting the capacity of slender steel columns at elevated temperature with finite element method and machine learning <i>Qi Tong, Carlos Couto, Thomas Gernay</i>	61
<b>Session: Concrete structures I</b>	
Evaluation of curing age effect on the fire spalling behavior and bending load capacity of prestressed concrete beam <i>Michika Hashida, Hiroyuki Ikeya, Kentaro Fujimoto, Mitsuo Ozawa</i>	68

Proposal for a preliminary fire calculation method to determine acceptable cover depths of concrete slabs <i>Wenxuan Wu, Cristian Maluk</i>	74
Effects of thermal elongation in multi-level industrial production facilities and warehouses in case of fire <i>Iselle De Beuckeleer, Tom Molken, Martin Classen</i>	80
Experimental investigation of the elastic modulus of high strength concrete at elevated temperatures <i>Tulio A. P. Coelho, Sofia M. C. Diniz, Francisco C. Rodrigues, Ruben Van Coile</i>	86
Application of advanced load and structural analysis in case of fire for the assessment of existing structures <i>Shana Van Hout, Martin Classen, Tom Molken</i>	92
Structural performance of reinforced concrete walls under ISO fire exposure <i>Mohsen Roosefid, Marie H�el�ene Bonhomme, Pierre Pimienta</i>	98
Post-cooling compressive behaviour of high-strength self-compacting concrete – Influence of binder materials <i>Marija Jel�ci� Rukavina, Ivan Gabrijel, Ivanka Netinger Grube�a</i>	104
Structural fire design of one-way reinforced concrete ribbed slabs using different assessment methods <i>Omid Pouran, Ulrich Montag</i>	110
<b>Session: Composite and other structures I</b>	
Performance of CFS stud-to-sheathing screw connections at elevated temperatures <i>Tharindu Abeysiriwardena, Mahen Mahendran</i>	119
The influence of coping on long-span continuous beam under fire loading <i>Priya Natesh, Anil Agarwal</i>	125
The interfacial bond slip behavior of I-section steel and reactive powder concrete at high temperatures <i>Yuzhuo Wang, Tiangui Xu, Bingjie Zhang</i>	131
Wall deformation during fire resistance tests – A comparative study between hollow-brick walls and gypsum-sheathed stud walls <i>Rene Prieler, Benjamin Ortner, Stefan Thumser, G�unther Schwabegger, Christoph Hochenauer</i>	137
Load-bearing composite timber - glass wall prototype in fire conditions <i>Nikola Perkovi�, Vlatka Raj�ci�, Chiara Bedon, Jure Barbali�</i>	143
Behaviour of innovative concrete-filled built-up cold-formed steel columns in fire <i>H�elder D. Craveiro, Rohola Rahnvard, Rui Sim�es, Aldina Santiago, Lu�s La�m</i>	149
Fire endurance analysis of ordinary structural glass elements <i>Chiara Bedon, Christian Louter</i>	155

## **Session: Modelling and application of structural fire engineering I**

- Transient temperature distribution in hot-cast anchors by 3D heat transfer 162  
*Jingzhi Chen, Yong Du, Jian Zhu*
- A case study of structural fire safety design of unprotected composite beams with fin-plate joints 168  
*Naoya Yotsumoto, Takeo Hirashima, Koji Toyoda*
- Pressure increase in enclosures of steel doors and its effect on the deformation process during fire resistance tests – A numerical study 174  
*Rene Prieler, Bernhard Klemm, Simon Pletzer, Stefan Thumser, Günther Schwabegger, Christoph Hochenauer*
- Extension of the zone method for the design of circular concrete columns subjected to a standard fire 180  
*David Krybus, Marcus Achenbach, Livia Prifti*
- GoZone: A numerical model for travelling fires 186  
*Antonio Gamba, Jean-Marc Franssen*
- FE analysis of fasteners exposed to fire: evaluation of concrete cone capacity 192  
*Hitesh Lakhani, Jan Hofmann, Azime Bal*
- Exemplar performance-based structural fire design of a high-rise building 198  
*Ali Ashrafi, Jenny Sideri, Pierre Ghisbain, Reyhaneh Abbasi, Zhi Zhang*

## **Session: Steel structures II**

- Fire resistance of stainless steel elliptical hollow section beam-columns with out-of-plane buckling 205  
*Flávio Arrais, Nuno Lopes, Paulo Vila Real*
- Temperature of galvanized steel specimens heated in electrical furnace 211  
*Margherita Autiero, Antonio Bilotta, Donatella de Silva, Emidio Nigro, Lello Pernice*
- Temperature distribution in the coatback of a partially fire-protected member 217  
*Patrik Dobrovolny, Jakub Sejna, Frantisek Wald*
- Development of a hybrid semi-rigid connection for steel structures 223  
*Ying Hu, Hui Lin, Shan-Shan Huang, Ian Burgess, Miles Owarish*

## **Session: Timber structures I**

- A calculation method for flame extension from partially exposed mass timber enclosures 230  
*Danny Hopkin, Michael Spearpoint*
- Effect of wood mineralisation on ignition time and burning dynamics parameters 236  
*Nataša Knez, Andreja Pondelak, Andrijana Škapin, Friderik Knez, Rožle Repič*
- Methodology for the assessment of timber structures exposed to fire through NDT 242  
*Dante Marranzini, Giacomo Iovane, Beatrice Faggiano*

Simplified smouldering test development for the test of wooden structural materials <i>Peter Harsányi, Martin Schneider, Sebastian Reiter, Peter Anderwald</i>	248
 <b>Session: Concrete structures II</b>	
Residual mechanical properties of 120 MPa HFRC post fire 120 MPa-grade hybrid fiber-reinforced concrete exposed to temperatures up to 800 °C <i>Honghui Qi, Yong Du, J.Y. Richard Liew</i>	257
Finite element analysis of reinforced concrete flat slabs tested with different configurations at elevated temperature <i>Norlizan Wahid, Tim Stratford</i>	263
Fire-protection with alkali-activated cement binder <i>Jakub Šejna, Vít Šmilauer, Stanislav Šulc, Pavel Reiterman, František Wald</i>	269
Fire resistance analysis of reinforced concrete two-way slabs <i>Fidan Salihu, Fatos Pllana, Meri Cvetkovska</i>	275
Measurement of strains and crack propagation by digital image correlation method in fire exposed concrete slab <i>Katarzyna Mróz, Marcin Tekieli, Izabela Hager</i>	281
Effect of tension lap splice on the behaviour of reinforced concrete beam during fire <i>Andreas Grübel, Hitesh Lakhani, Jan Hofmann</i>	287
Performance criteria for performance based fire design of concrete and composite structures <i>Ruben Van Coile, Thomas Gernay, Danny Hopkin, Negar Elhami-Khorasani</i>	293
 <b>Session: Other topics I</b>	
Diatomaceous earth for improving the bushfire resistance of cement blocks <i>Indunil Erandi Ariyaratne, Anthony Deloge Ariyanayagam</i>	300
Full-scale experiment of a bushfire safe room <i>Sahani Hendawitharana, Anthony Deloge Ariyanayagam</i>	306
WUIFIRESAFE – structural fire resistance of buildings in the wildland-urban interface <i>Cesare Fiorini, Hélder Craveiro, Luís Simões da Silva, Aldina Santiago, Luís Laím</i>	312
Wind driven (forced draught) impact on enclosure fires <i>Jan Smolka, Kamila Kempná, Pavel Danihelka, Eleni Asimakopoulou, Tomaz Hozjan, Petr Kučera, Paul Grimwood</i>	318
Numerical validation of firefoam for narrow facade cavity fire <i>Benjamin Khoo, Wolfram Jahn, Panagiotis Kotsovinos, Guillermo Rein</i>	324
Background and limitations of the Eurocode parametric fire curves, including the fire decay phase <i>Andrea Lucherini, Balsa Jovanovic, Ruben Van Coile, Bart Merci</i>	330

Effects of the fire decay phase on the bending capacity of a fire-exposed reinforced concrete slab <i>Balša Jovanović, Andrea Lucherini, Ruben Van Coile, Bart Merci, Robby Caspeepe, Edwin Reynders, Geert Lombaert</i>	336
<b>Session: Composite and other structures II</b>	
Small-scale fire tests of LSF floor-ceiling systems <i>Edward Steau, Mahen Mahendran</i>	343
Experimental study on bond behavior between steel and concrete at elevated temperatures <i>Ira Banoth, Anil Agarwal</i>	349
Cement mortar as passive fire protection in steel columns <i>Hugo Caetano, Aldina Santiago, Luís Laím, Askan Shahbazian</i>	355
Experimental and numerical investigation on temperature profile in timber-concrete composite beam type floor slab in fire <i>Cvetanka Chifliganec, Meri Cvetkovska, Robert Pečenko, Tomaž Hozjan</i>	361
Modelling of steel to timber joint exposed to fire <i>Kristyna Vopatova, Jaroslav Zeman, Kamila Cábová</i>	367
<b>Session: Modelling and application of structural fire engineering II</b>	
Early-warning methods for collapse of steel portal frames under fire <i>Wei Ji, Guoqiang Li, Chengyuan Feng, Yao Wang, Xinjie Li</i>	374
Numerical simulation of a fire resistance test and prediction of the flue gas leakage using CFD/FEM coupling <i>Rene Prieler, Simon Pletzer, Stefan Thumser, Günther Schwabegger, Christoph Hochenauer</i>	382
A two-scale FE model to address connections in coupled fire-structure simulations <i>Qingfeng Xu, Hèrm Hofmeyer, Johan Maljaars</i>	388
Benchmark study for fire design of steel beam <i>Batuhan Der, František Wald, Martin Vild</i>	394
Numerical modelling of steel members protected with intumescent coating <i>Igor Džolev, Sofija Kekez, Andrija Rašeta</i>	400
<b>Session: Other topics II</b>	
Reliability evaluation of concrete beams exposed to fire <i>Tulio A. P. Coelho, Sofia M. C. Diniz, Francisco C. Rodrigues, Ruben Van Coile</i>	407
An improved reliability-based approach to specifying fire resistance periods for buildings in England <i>Ian Fu, Ieuan Rickard, Danny Hopkin</i>	413

A simplified model for predicting the deformed shape of natural stone masonry walls subjected to fire loading <i>Elodie Donval, Duc Toan Pham, Ghazi Hassen, Patrick de Buhan, Didier Pallix</i>	419
Towards a safety concept for natural fires – the need of code calibration <i>Marcus Achenbach</i>	425
<b>Session: Timber structures II</b>	
Experimental characterisation of the fire behaviour of CLT ceiling elements from different leading suppliers <i>Danny Hopkin, Carmen Gorska, Michael Spearpoint, Ian Fu, Harald Krenn, Tim Sleik, Gordian Stapf</i>	432
Sensitivity analysis of a PYCIF model <i>Robert Pecenko, Tomaz Hozjan</i>	438
A sensitivity analysis applied to the reduced cross-section method of a timber beam under parametric fire <i>Sabina Huč, Tomaz Hozjan</i>	445
Prediction of temperature of individual parts of cladding systems during fire <i>Nikola Lišková, Kamila Cábová, František Wald, Kristo Mela, Mikko Malaska</i>	451
<b>Committees</b>	457

## **Preface**

Fire-resistant design and analysis has moved significantly over the last three decades, from a long-term reliance on prescriptive rules, design tables and simple analytical models, towards recognizing the benefits of performance-based approaches. This applies to all areas of fire engineering, including prediction of the behaviour of fires, transfer of heat to structural elements, and structural response at elevated temperature.

The pandemic in 2020 and 2021 has caused the Conference Applications of Structural Fire Engineering, held in Ljubljana, Slovenia on 10-11 June 2021, to transfer to a virtual platform, which brings both advantages and disadvantages. As has been the case with previous ASFE conferences, the papers selected for this volume of Proceedings present a distillation of the current state of the art in research, development and applications of advanced performance-based design methods for concrete, steel and timber structures. The great disadvantage of an online conference is that researchers and practitioners do not actually meet, get to know each other or discuss issues in depth. We all know that the Gala Dinner, in some respects an unnecessary addition to a technical conference, can act as a powerful catalyst to future research collaborations. We all hope that future conferences can return mainly to the face-to-face model.

The first three ASFE conferences were organised in Prague, on 19-20 February 2009, 28-29 April 2011 and 19-20 April 2013, with support from the COST TU0904 network “Integrated Fire Engineering and Response” (<http://fire.fsv.cvut.cz>). An important step for researchers was the inclusion in 2015 of the conference proceedings into the arena of international scientific metrics by indexation in the Scopus database. Subsequent Conferences took place in Dubrovnik 15-16 October 2015, Manchester 14-16 September 2017 and Singapore 13-16 June 2019. The next Conference is tentatively scheduled to take place in Guayaquil on 14-16 September 2023.

Ian Burgess and František Wald

## Acknowledgment

The organising committee would like to thank the authors for submitting and presenting very interesting papers on diverse research topics of structural fire engineering. Special thanks also go to all participants of the 7<sup>th</sup> ASFE conference for their interest. We wish to thank the reviewers for their response in a short time. We are grateful to the ASFE Steering Committee for their support and guidance. We would like to extend our gratitude to the sponsors and donors for their generous support of the conference, despite the unpleasant circumstances that prevented the exchange of opinions and knowledge in person.

## Organizing committee

University of Ljubljana  
Faculty of *Civil and Geodetic Engineering*



University of Maribor

Faculty of Electrical Engineering  
and Computer Science



## Sponsors and donors



**KOLEKTOR**

**VG5**  
GRADNJA & INŽENIRING

*Elea* **iC**

**KNAUF**



**DRI**

**HC**  
HARCO



**biroUDOVČ**  
projektiranje, nadzor, svetovanje  
STANISLAV UDOVČ s.p.



**xella**

**IRGO**



**POMGRAD**

Proceedings of the International Conference in Ljubljana, 10-11 June 2021  
in edition of Applications of Structural Fire Engineering

**Session**

**Keynote lectures**

## **HOW PASSIVE THE PASSIVE FIRE PROTECTION LAYERS ACTUALLY ARE?**

Simo Hostikka<sup>a</sup>, Deepak Paudel<sup>a</sup>

<sup>a</sup>Aalto University, Department of Civil Engineering, Espoo, Finland

Passive fire protection products are commonly based on mineral materials with porous structure for low thermal conductivity. Although the mineral materials can often be considered inert in fire temperatures, many products contain additional binder materials that decompose at temperatures much lower than the typical criteria for product acceptance. This is especially important for mineral wools, such as stone wool. In this presentation we demonstrate the influence of exothermic binder reactions on the cold side -temperatures during fire resistance tests. By multi-physics simulation, we investigate the effects of the stone wool properties, such as binder content and density, and boundary conditions (permeable or non-permeable). We show that the binder oxidation reactions can reduce the product's fire resistance time and pose a threat to protected materials with low critical temperature. The efficiency of thermal protection greatly improves when the stone wool core is closed between non-permeable surface layers. In such products, however, two- and three-dimensional transport effects may start to play a role, indicating the need for future research.

# TOWARDS AN ADVANCED, TIME-DEPENDENT ANALYSIS OF FIRE EXPOSED STEEL STRUCTURES

Neno Torić<sup>a</sup>, Ian W. Burgess<sup>b</sup>

<sup>a</sup> University of Split, Faculty of Civil Engineering, Architecture and Geodesy, Split, Croatia

<sup>b</sup> University of Sheffield, Department of Civil and Structural Engineering, Sheffield, United Kingdom

## Abstract

The paper presents new research developments regarding the application of a unified rheological model capable of taking into account the influence of creep at both fast and slow strain-rates on the total strain development of steel structures and their components exposed to fire. This type of advanced material model is necessary in order to enable simulation of material behaviour when a structure is exposed to transient heating regimes, including stationary heating. The aim of developing this type of material model is to provide a reliable time-dependent representation of material behaviour so that numerical simulations of structure response to fire attack are enabled to follow the linked progress of heating and straining, regardless the type of heating curve to which the structural members are exposed. The paper presents further verification of the unified rheological model in modelling a series of stationary creep tests conducted on European Grade S355 steel.

**Keywords:** time-dependent behaviour, creep, steel, fire

## 1 INTRODUCTION

It is well known that development of fire in a compartment is associated with three distinctive heating phases: growth, fully-developed and decay phase. The length of the time interval and the temperature intensity in all three phases of the fire depend on the geometry of the fire compartment in terms of the area of ventilation openings, the amount of fuel per floor area and its distribution in the compartment. All three phases influence the value of incident heat flux imposed on steel members in the vicinity of the fire source. Since variation of compartment temperature represents a governing factor for the generated value of heat flux and the corresponding member heating rate, there is a direct link between the heating rate of the compartment temperature and the heating rates of members. In order to illustrate possible outcomes of the member heating rate in a compartment a plot of temperature vs time curves (Torić *et al.*, 2011) is presented in Figure 1 for a range of different compartment parameters in an industrial hall (60x40x7.5 m).

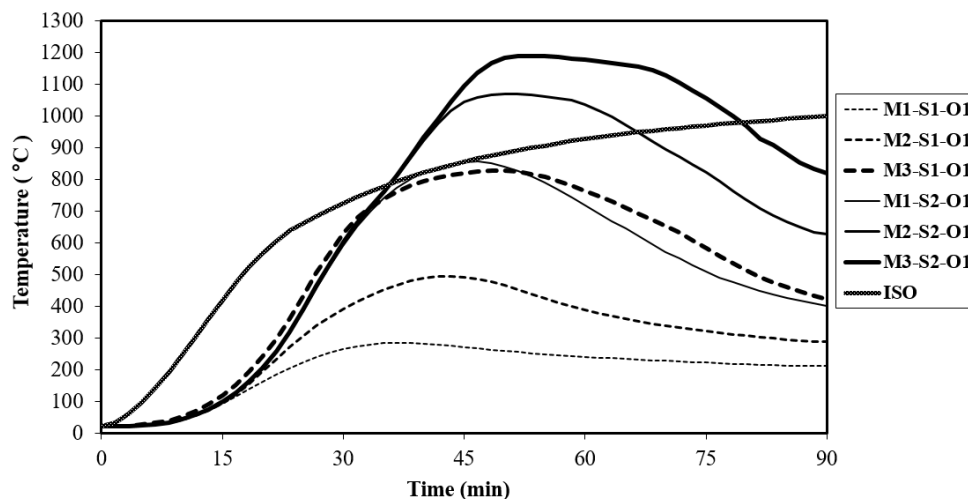


Fig. 1 Temperature-time history of a steel member in an industrial hall (Torić *et al.*, 2011)

Figure 1 presents temperature-time history of a load-bearing steel member for a varying fuel mass: 35-70-105 kg/m<sup>2</sup>, floor surface covered with fuel: 5-10% and surface of the openings: 1-5-10%. It can be seen that, by varying the compartment and fuel parameters, a wide range of heating-rates can be generated in a steel member. It can be seen that steel members generally experience three heating phases similar to the compartment heating phases. Lower heating rates are generally expected in fire-protected steel members. An example is presented in Figure 2 where a section HE240M is exposed on all four sides to a parametric fire which has a heating phase similar to ISO fire (ISO 834-1, 1999). The section is fire-protected with passive protection of thickness within the range 0.5-2 cm.

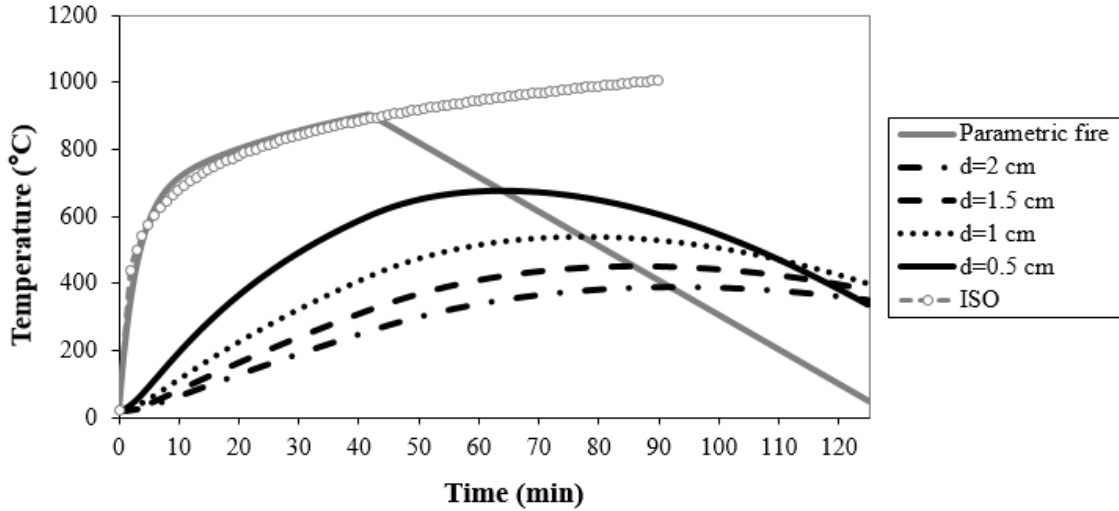


Fig. 2 Temperature-time history of a protected I section (HE240M) exposed to parametric fire

Graphs presented in Figure 1 and 2 indicate that there is a wide range of possible heating scenarios (rates) that may occur in a general fire event, starting from very low heating rates (an example of protected steel members in Figure 2) to very high heating rates (case of higher value of fire load in an industrial steel hall presented in Figure 1). This represents the main motivation for considering time-dependent analysis in fire related structural behaviour due to complex strain development in steel which is heating- and strain-rate-dependent.

## 2 FRAMEWORK FOR ADVANCED TIME-DEPENDENT ANALYSIS

The strain components for steel in case of fire (Anderberg, 1988) can be defined as:

$$\varepsilon_{tot} = \varepsilon_{th}(T) + \varepsilon_{\sigma}(\sigma, T) + \varepsilon_{cr}(\sigma, T, t) \quad (1)$$

in which:  $\varepsilon_{tot}$  is the total strain,  $\varepsilon_{th}(T)$  is the temperature-dependent thermal strain,  $\varepsilon_{\sigma}(\sigma, T)$  is the stress-related strain (stress and temperature dependent) and  $\varepsilon_{cr}(\sigma, T, t)$  is the creep strain (stress, temperature and time-dependent strain).

In general, advanced time-dependent analysis covers material behaviour in different heating scenarios and different strain rate exposures. With respect to heating scenarios, to the generation of high temperature in a fire can be divided into three heating-rate categories: high, medium and low. There is no scientific consensus on the boundaries between these heating rate categories. However, since the development of time-dependent strain (creep) depends on the time of exposure to each heating rate, the boundaries can be provisionally divided with respect to the influence of creep on the overall structural response: high heating rates (>20°C/min), intermediate heating rates (10-20°C/min) and low heating rates (<10°C/min). In general, high heating rates are generated if the fire is located in the vicinity of a member. Fire testing with the ISO834 standard fire curve is a good example of a situation which generates very high heating rates in tested members. Low heating rates are generated in members where fire-protection is applied, or where the member is far from the fire source.

With respect to strain-rate exposure and its influence, response of the structure in case of fire can also be provisionally divided into three categories of strain rates: high ( $>0.1/\text{min}$ ), medium ( $0.02\text{-}0.1/\text{min}$ ) and low ( $<0.02/\text{min}$ ) (Torić and Burgess, 2016). Low strain-rates are present in cases when creep is initially activated and in normal service load conditions. High strain rates are present at the onset of a structure's collapse mechanism. An increase of strain-rate leads to an apparent increase of the yield strength of steel, which may be considered as positive material effect. Due to variation of heating-rate conditions, as well as the inevitable change of strain-rate during exposure to fire, it is necessary to use a material model with the ability to take account of these effects on the overall strain output.

Since material models are generally obtained either by stationary or transient test methods, there is no unified material model covering these aspects of fire-related response. The proposed unified rheological model aims to take into account the two main variables that govern structure response during fire: heating-rate and strain-rate sensitivity.

### 3 DESCRIPTION OF THE UNIFIED RHEOLOGICAL MODEL

As stated in the previous section, the unified rheological model takes into account the effects of heating- and strain- rate on the material response, and therefore provides an adequate strain model during exposure to high temperature. The model is composed of two components (Figure 3), each representing strain output of steel at low and high strain rates. KV1 is a Kelvin-Voight element representing strain output at high strain rates, where due to inertial effects an apparent yield strength increase occurs. At normal strain rates this strain component represents stress-related (mechanical) strain. KV2 is an element which represents strain output where low (creep) strain rates are imposed.

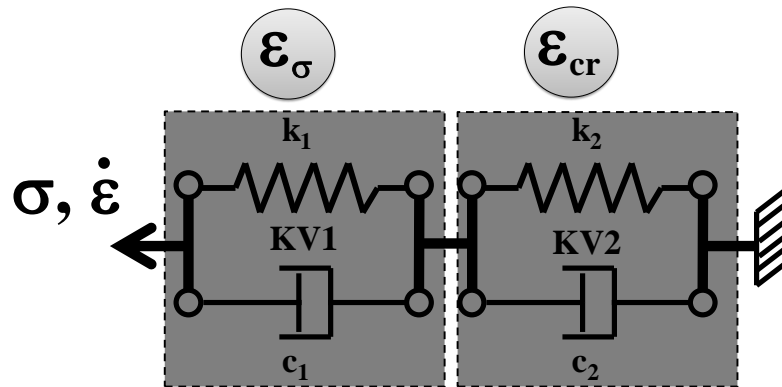


Fig. 3 Constitutive components of a unified rheological model

A parallel connection between the elements of each KV element divides the total stress into the two components (Figure 4):

$$\sigma = \sigma_1 + \sigma_2 ; \sigma_1 = k_1(\sigma, T)\varepsilon ; \sigma_2 = c_1(\dot{\varepsilon}, T)\dot{\varepsilon} \quad (2)$$

Where  $\sigma_1$  represents the stress in the spring and  $\sigma_2$  represents the stress in the damper.

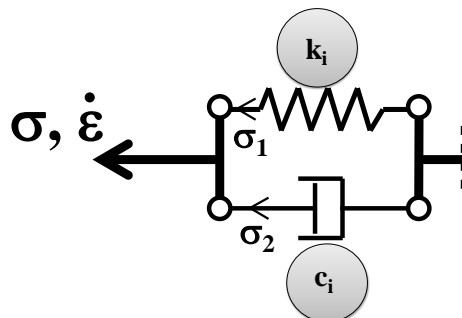


Fig. 4 Stress distribution and the components of a single KV

The damper values for  $c_1$  and  $c_2$  of the unified rheological model are determined with the following relationship:

$$c_i = \frac{\sigma_{di}}{\dot{\varepsilon}_i}; i = 1,2 \quad (3)$$

Where  $\sigma_d$  represents damper stress and  $\dot{\varepsilon}$  represents the strain rate. A set of temperature and strain-rate dependent curves used to determine the damper values  $c_1$  and  $c_2$  as well as spring values  $k_1$  and  $k_2$  can be found in references (Torić and Burgess, 2016, Torić *et al.* 2016a, 2016b). These curves are generally based on elevated-temperature test data from various researchers on European steel grades S275 and S355, as well as other grades.

The differential equation describing the strain evolution for each KV element can be written as:

$$\frac{\sigma}{c_i} = \frac{k_i}{c_i} \varepsilon_i + \dot{\varepsilon}_i \quad (i = 1,2) \quad (4)$$

In Equation (4)  $\dot{\varepsilon}_i$  represents the first strain derivative of the  $i$ -th KV, and  $k_i$  and  $c_i$  represent the spring and damper functions of the corresponding KV element. There are two ways in which Equation (4) can be solved, and they are based on whether the stress is constant or there is varying strain-rate introduced in the unified rheological model.

#### 4 PERFORMANCE OF THE UNIFIED MODEL ON ANALYSIS OF STATIONARY CREEP TESTS

Performance of the unified rheological model is tested by comparing the output of the unified model to the results of stationary creep tests conducted on grade S355JO steel. The test data is adopted from a research paper by Brnic *et al.* (2010). A stationary creep test, at constant stress and temperature, is generally used to determine creep strain of a particular alloy. The general output from this kind of test is a time-dependent strain curve, which is an S-shaped curve if all three creep phases occur, which contains elastic and time-dependent creep strain. Since the objective of the paper is to test the performance of the rheological model within the scope of prolonged exposure to a constant load, such stationary creep tests are used as a base for comparison. Figure 5 presents a performance comparison between the rheological model and creep tests conducted at 400°C. Two creep tests, conducted at 188 MPa and 94 MPa stress-levels, are presented. The stress level mentioned are relative to the 0.2% stress at normal temperature at the ratios  $0.8\sigma_{0.2}$  and  $0.4\sigma_{0.2}$ . The input data for the rheological model are the normal-temperature data  $\sigma_{0.2}=388.0$  MPa,  $E_{20}=210.0$  GPa. The reduction factor for 0.2% stress at 400°C obtained by test was used as a reference strength reduction factor, while the reduction factor from Eurocode 3 (EN1993-1-2, 2005) for modulus of elasticity at 400°C was adopted.

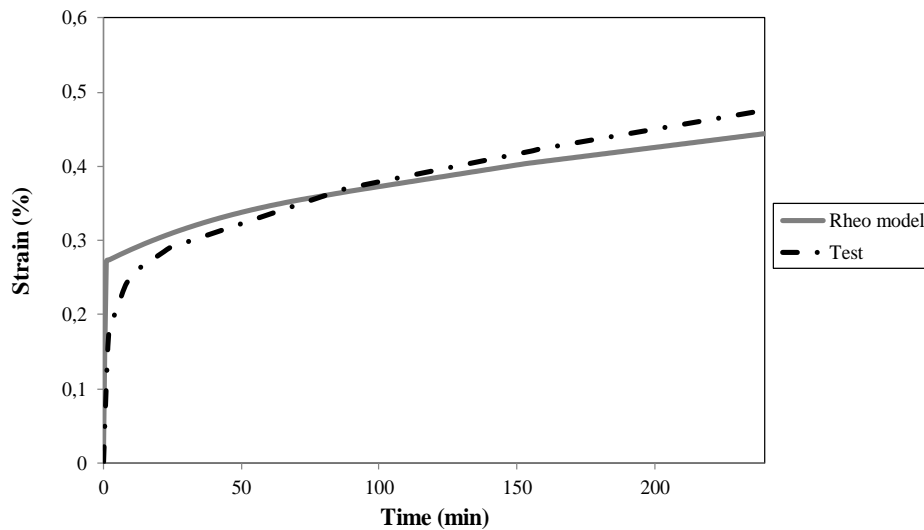


Fig. 5 Comparison between the rheological model and a creep test at 400°C,  $\sigma=0.8\sigma_{0.2}$  (Brnic *et al.*, 2010).

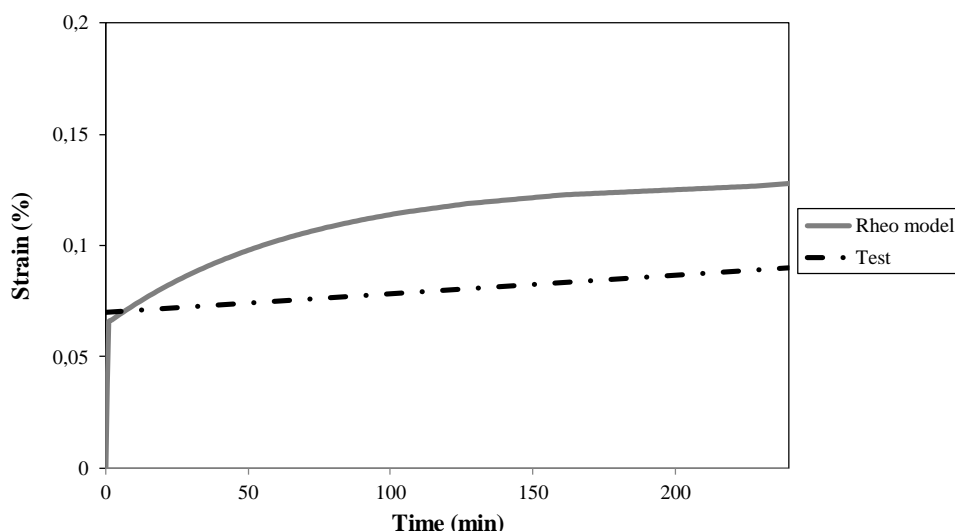


Fig. 6 Comparison between the rheological model and a creep test at 400°C,  $\sigma=0.4\sigma_{0.2}$  (Brnic *et al.*, 2010).

It can be seen from Figures 5 and 6 that the rheological model provides a reasonable strain output in comparison to test data, thus providing a good estimate of the creep strain development within the time interval generally considered relevant in structural fire design (240 minutes).

## 5 CONCLUSIONS

A preliminary analysis of the performance of a unified rheological model in modelling the stationary creep tests of steel grade S355JO is presented. Considering the results presented it can be concluded that the unified model provides creep output comparable to the selected creep study of grade S355JO at 400°C. Further comparisons are planned in order to fully validate the model's capabilities for the mentioned creep scenario.

## ACKNOWLEDGMENT

This work was partially supported through project KK.01.1.1.02.0027, a project co-financed by the Croatian Government and the European Union through the European Regional Development Fund - the Competitiveness and Cohesion Operational Programme.

## REFERENCES

- Anderberg Y., 1988. *Modelling Steel Behaviour*, *Fire Safety Journal*, 13(1), p. 17-26.
- Brnic, J., Canadija, M., Turkalj, G., Lanc, D., 2010. *Behaviour of S 355JO steel subjected to uniaxial stress at lowered and elevated temperatures and creep*, *Bulletin of materials science*, 33 (4), p. 475-481.
- EN1993-1-2, 2005. *Eurocode 3 - Design of Steel Structures - Part 1-2: General Rules - Structural Fire Design*, European Committee for Standardization, Brussels, Belgium
- ISO 834-1, 1999. *Fire Resistance Tests – Elements of Buildings Construction, Part-1 General Requirements*, International Organization for Standardization, Switzerland
- Torić, N., Peroš, B., Boko, I., 2011. *Reliability of steel structures under fire conditions*, in *Proceedings of the Sixth International Seminar on Fire and Explosion Hazards*, 11-16 April 2011, Leeds, UK, p. 891-901.
- Torić N., Burgess I.W., 2016. *A unified rheological model for modelling steel behavior in fire conditions*, *Journal of constructional steel research*, 127, p. 221-230.
- Torić, N., Sun R.-R., Burgess, I.W., 2016a. *Development of a creep-free stress-strain law for fire analysis of steel structures*, *Fire and Materials*, 40(7), p. 896-912.
- Torić, N., Sun R.R. and Burgess, I.W., 2016b. *Creep-free fire analysis of steel structures with Eurocode 3 material model*, *Journal of Structural Fire Engineering*, 7(3), p. 234-248.

Proceedings of the International Conference in Ljubljana, 10-11 June 2021  
in edition of Applications of Structural Fire Engineering

**Session**

**Steel structures I**

# NUMERICAL ANALYSIS ON POST-FIRE RESIDUAL CAPACITY OF THE RESTRAINED HIGH STRENGTH STRUCTURAL STEEL COLUMNS UNDER AXIAL COMPRESSION

Lin-Xin Song<sup>a</sup>, Guo-Qiang Li<sup>a,b</sup>

<sup>a</sup> College of Civil Engineering, Tongji University, Shanghai 200092, China

<sup>b</sup> State Key Laboratory for Disaster Prevention in Civil Engineering, Tongji University, Shanghai 200092, China

## Abstract

In practice, steel columns are the critical load-bearing components of steel structures and they are usually restrained by adjacent components. At and after fire, the restraint will induce additional deflection in the restrained columns and the mechanical properties of high strength structural steel (HSS) may reduce significantly, both of which will further reduce the post-fire residual capacity of the restrained columns. Therefore, identifying the post-fire residual capacity of the restrained HSS columns is important for evaluating the safety of continuing use of the HSS structures after fire. This paper presents the numerical analysis on post-fire residual capacity of the restrained HSS columns under axial compression, based on a verified model built in ABAQUS. It can be concluded that the maximum temperature experienced during the fire, restraint stiffness ratio and load ratio have significant effects on the post-fire residual capacity of the restrained HSS columns.

**Keywords:** restrained steel column; high strength structural steel; post-fire; residual capacity; numerical analysis

## 1 INTRODUCTION

The application of high strength structural steel (HSS) in construction industry has more advantages than conventional mild structural steel in terms of safety, reliability, economy and environmental benefits (Bjorhovde, 2010; Wang *et al.*, 2016). In practice, steel columns are the critical load-bearing components of steel structures and they are usually restrained by adjacent components connected to them. When exposed to elevated temperatures, the restraint will induce additional deflection in the restrained columns. Moreover, the mechanical properties of steel may reduce significantly at and after fire, especially for HSS. The develop of deflection and reduction of mechanical properties will further reduce the post-fire residual capacity of the restrained columns. Therefore, identifying the post-fire residual capacity of the restrained HSS columns is important for evaluating the safety of continuing use of the HSS structures after fire.

The existing research mainly focused on the behaviour of restrained steel columns under fire and it can be found that after restrained steel columns buckled at elevated temperature, the post-buckling performance can still be used (Wang *et al.*, 1994; Lennon *et al.*, 2003; Huang *et al.*, 2003; Li *et al.*, 2010). For the residual capacity of steel columns after fire, Liu (2003) conducted experimental studies on non-restrained Q460 HSS columns to investigate the post-fire axial residual capacity and proposed a simplified method based on parameter analysis considering cross-sectional shape, cooling method, maximum temperature experienced during the fire and slenderness ratio to calculate the stability coefficient of axial compression columns after fire. Wang *et al.* (2012) conducted experimental studies on symmetrically restrained, asymmetrically restrained and non-restrained Q345 steel columns to investigate the post-fire behaviour and found that distinct restraint resulted in columns with distinct strain after fire and distinct overall stiffness before failure. Li *et al.* (2020) conducted experimental studies on axially restrained Q550 HSS columns to investigate the post-fire axial residual capacity and proposed a simplified method based on parameter analysis considering maximum temperature, load ratio, axial restrained stiffness ratio, slenderness ratio and steel grade to calculate the post-fire residual capacity of restrained HSS columns.

Up to now, few studies have been made on the post-fire residual capacity of the restrained HSSS columns and Li *et al.* (2020) only considered the axial restraint for restrained columns. In general, columns in HSSS structures are restrained by adjacent components not only axially but also rotationally. Wang *et al.* (1994) have found that columns with axial and rotational restraint can experience higher temperature before failure than the corresponding ones with only axial restraint. Therefore, it is necessary to consider the rotational restraint. This paper presents the numerical analysis on post-fire residual capacity of the restrained HSSS columns under axial compression, based on a verified model built in ABAQUS, considering the effect of maximum temperature experienced during the fire, axial and rotational restrained stiffness ratio and load ratio.

**2 NUMERICAL MODEL**

A numerical model is built in ABAQUS to investigate the post-fire residual capacity of the restrained HSSS columns under axial compression.

**2.1 Basic information of the numerical model**

The cross section of HSSS column is H80×80×8×8(mm) and the longitudinal length of the column is 1560mm corresponding to the slenderness ratio of 80. The initial geometric imperfection is considered to be 1/1000 of the column length and the welding residual stress is introduced based on the model proposed by Ban *et al.* (2014).

The mechanical properties are based on QT Q690 HSSS. At ambient temperature, the yield strength is 803MPa and the elastic modulus is 206000MPa by measurement. The mechanical properties at elevated temperatures are calculated according to the predictive formulas proposed by Huang *et al.* (2018), while the post-fire mechanical properties are calculated according to the predictive formulas proposed by Li *et al.* (2017).

Shell elements S4R are assigned to the column. The column is divided into 50 units in the length direction, 20 units in the cross section of the web and 10 units in the cross section of each side of the flange. The boundary conditions of the column are set as hinge. Spring elements SPRING2 are set to simulate the axial and rotational restraints. During the whole analysis process, the restraints remain the same as the pre-designed state.

Buckling analysis is conducted first and its result of first-order buckling mode is used as the initial geometric imperfection shape in the following analysis. The main four analysis steps are set up to simulate the process of applying dead load, heating, cooling and static load until failure.

**2.2 Validation of the numerical model**

A numerical model is established in accordance with the experiment conducted by Li *et al.* (2020) using the above method. In the experiment, the column HC1 was loaded until failure at ambient temperatures without being heated, while the columns HC2 and HC3 were loaded until failure after being heated to pre-selected temperatures and then cooling down to ambient temperature. The experimental and numerical results on axial displacement-temperature curve and mid-height lateral displacement-temperature curve are presented in Fig.1 and Fig.2 respectively. The experimental and numerical results on buckling temperature and ultimate bearing capacity are listed in Table 1.

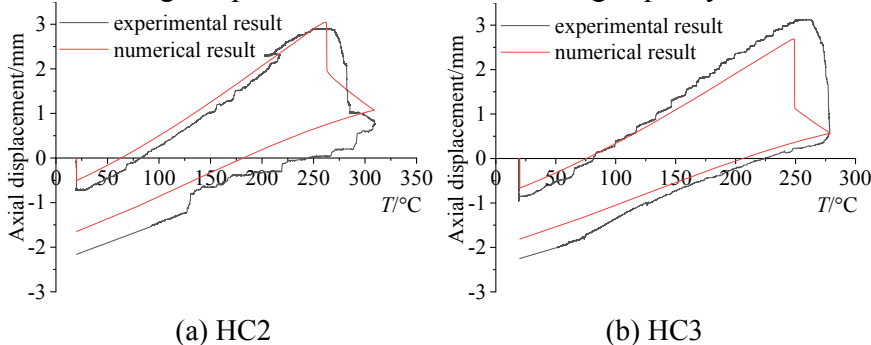


Fig. 1 The experimental and numerical results on axial displacement-temperature curve

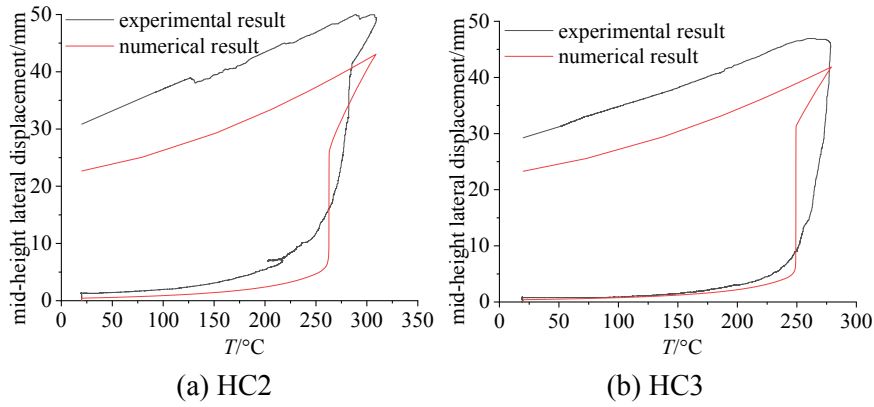


Fig. 2 The experimental and numerical results on mid-height lateral displacement-temperature curve

Table 1 The experimental and numerical results on buckling temperature and ultimate bearing capacity

Specimen no.	buckling temperature /°C			ultimate bearing capacity/kN		
	Experimental	Numerical	Error	Experimental	Numerical	Error
HC1	-	-	-	723	719	-0.56%
HC2	268	261	-2.61%	385	381	-1.12%
HC3	252	248	-1.59%	398	412	3.51%

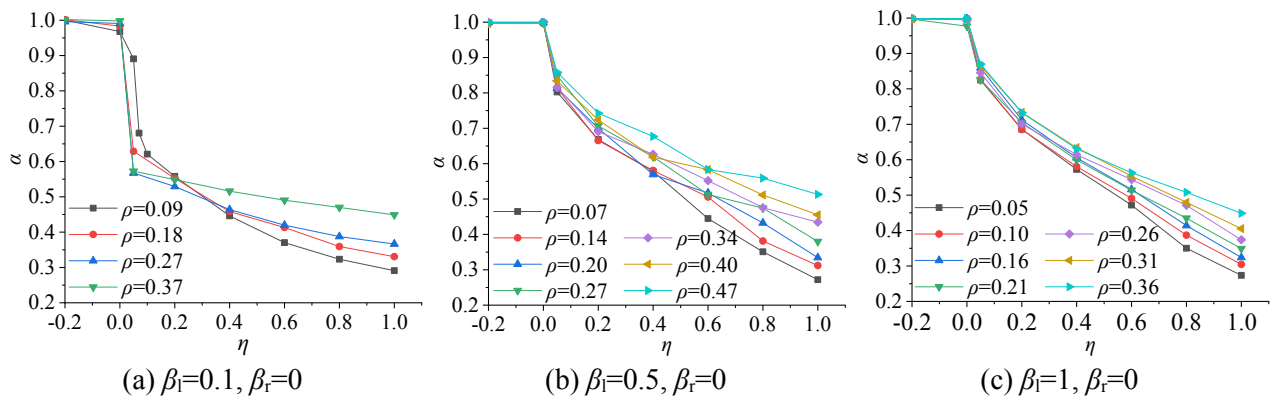
It can be found that the curves obtained from the numerical model accurately reflects the displacement changes of the columns during the experimental process. The errors of the buckling temperature and ultimate bearing capacity of the columns without being heated and after fire obtained from the numerical model are within 5%. Therefore, the numerical model is validated.

### 3 PARAMETRIC ANALYSIS

Parametric analysis is conducted to investigate the effect of maximum temperature experienced during the fire, the restraint stiffness ratio and load ratio on the post-fire residual capacity of the restrained HSSS columns under axial compression based on the validated numerical model.

Some key definitions are provided in this study: (1) Buckling temperature,  $T_{bu}$ , is the temperature at which restrained columns reach the maximum axial force in the heating phase. Critical temperature,  $T_{cr}$ , is the temperature at which the axial force in the heating phase restored to the initial value,  $P_0$ , at ambient temperature. (2) Residual capacity factor,  $\alpha$ :  $\alpha = N_{crT}/N_{cr}$ .  $N_{crT}$  is the post-fire ultimate bearing capacity named post-fire residual capacity, while  $N_{cr}$  is the ultimate bearing capacity at ambient temperature without being heated. (3) Relative temperature factor,  $\eta$ :  $\eta = (T - T_{bu}) / (T_{cr} - T_{bu})$ . (4) Axial stiffness ratio,  $\beta_l$ :  $\beta_l = k_l / k_{cl}$ . Rotational stiffness ratio,  $\beta_r$ :  $\beta_r = k_r / k_{cr}$ .  $k_l$  and  $k_r$  are the axial and rotational stiffness of the restraint respectively.  $k_{cl}$  and  $k_{cr}$  are the axial and rotational stiffness of columns at ambient temperature without being heated respectively. (5) Load ratio,  $\rho$ :  $\rho = P_0 / N_{cr}$ .

#### 3.1 Effect of maximum temperature



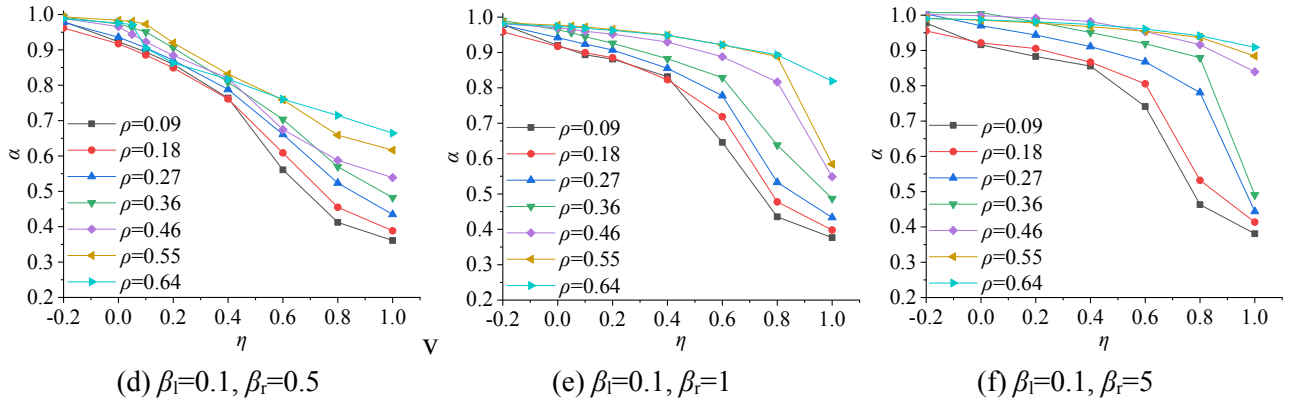


Fig. 3  $\alpha$ - $\eta$  curves with different stiffness ratio and load ratio

The  $\alpha$ - $\eta$  curves with different stiffness ratio and load ratio are shown in Fig. 3.

It can be found that when  $\eta < 0$  ( $T < T_{bu}$ ),  $\alpha$  is close to 1, i.e., fire process has little effect on the residual capacity when the maximum temperature experienced during the fire is below the buckling temperature. The reason is that during the heating and cooling process, columns experience elastic deflection before buckling, which will recover after cooling down to ambient temperature. In addition, the buckling temperature of the restrained column is generally less than  $600^{\circ}\text{C}$ , thereby when the maximum temperature is lower than the buckling temperature the mechanical properties of HSSS after fire can almost recover to the original values without being heated.

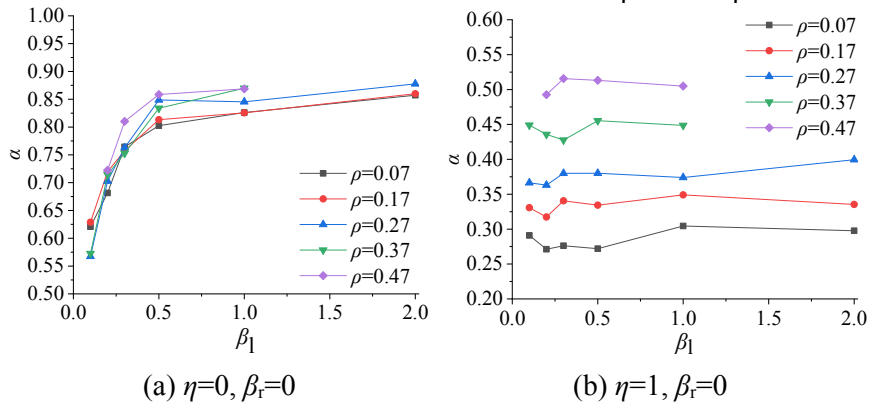
When  $\eta=0$  ( $T=T_{bu}$ ), columns reach the buckling state.  $\alpha$  reduces significantly when columns with only axial restraint, while  $\alpha$  decreases slightly if columns with axial and rotational restraint. This is because columns buckle when exposed to the buckling temperature, thereby the plastic deflection will develop rapidly without rotational restraint and cannot fully recover after fire, resulting in the significant decrease of residual capacity. If columns are rotationally restrained, the plastic deflection will not develop so rapidly that the residual capacity will reduce less prominently.

When  $0 < \eta < 1$  ( $T_{bu} < T < T_{cr}$ ),  $\alpha$  decreases as the maximum temperature rises. This is because when the maximum temperature rises, the plastic deflection develops and mechanical properties of HSSS reduce, thereby the residual capacity reduces. In addition,  $\alpha$  has an approximately negative linear correlation with the maximum temperature for the axially restrained columns. As for the axially and rotationally restrained columns, as the maximum temperature increases,  $\alpha$  decreases slightly before significantly when the maximum temperature exceeds a certain value, which is different under different load ratio.

When  $\eta=1$  ( $T=T_{cr}$ ), columns reach the critical failure state. The critical temperature is the maximum temperature considered in this study. Since  $\eta=0$  ( $T=T_{bu}$ ) and  $\eta=1$  ( $T=T_{cr}$ ) correspond to the buckling state and critical failure state respectively, the following analysis will focus on the influence of restraint stiffness ratio and load ratio for the case of  $\eta=0$  and  $\eta=1$ .

### 3.2 Effect of stiffness ratio

The  $\alpha$ - $\beta_i$  and  $\alpha$ - $\beta_r$  curves with different load ratio for the case of  $\eta=0$  and  $\eta=1$  are shown in Fig. 4.



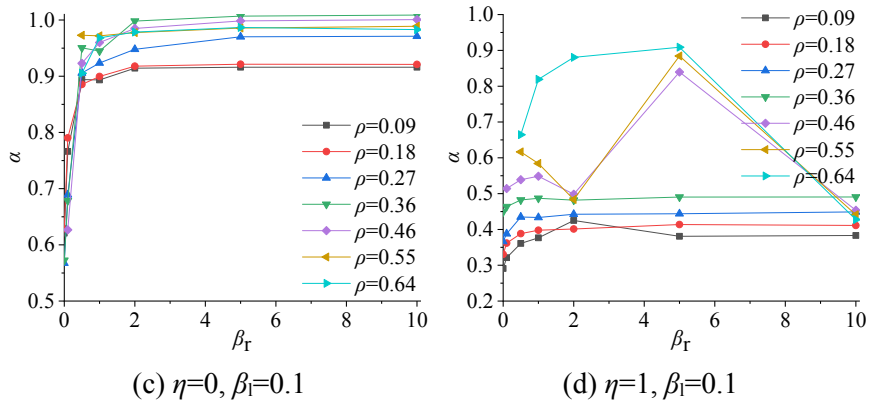


Fig. 4  $\alpha$ - $\beta_i$  and  $\alpha$ - $\beta_r$  curves with different load ratio for the case of  $\eta=0$  and  $\eta=1$

When  $\eta=0$  ( $T=T_{bu}$ ),  $\alpha$  increases as the axial restraint stiffness ratio increases. The reason is that when the axial restraint stiffness increases, the thermal stress induced by unfree thermal expansion in the column will also increase, thereby the buckling state occurs earlier in the heating process, i.e., buckling temperature will be smaller. Therefore, the plastic deflection and reduction of mechanical properties of HSSS becomes less, leading to less reduction on residual capacity. In addition, the rotational restraint prominently increases  $\alpha$  because the rotational restraint can decrease the calculated length of columns. And the rotational restraint stiffness ratio has an upper limit, above which the increase of rotational restraint stiffness ratio has little effect on the residual capacity. When  $\eta=1$  ( $T=T_{cr}$ ), the axial restraint stiffness ratio has little effect on  $\alpha$ , while the rotational restraint stiffness ratio can affect  $\alpha$  especially when the load ratio is greater than 0.4.

### 3.2 Effect of load ratio

The  $\alpha$ - $\rho$  curves with different stiffness ratio for the case of  $\eta=0$  and  $\eta=1$  are shown in Fig. 5.

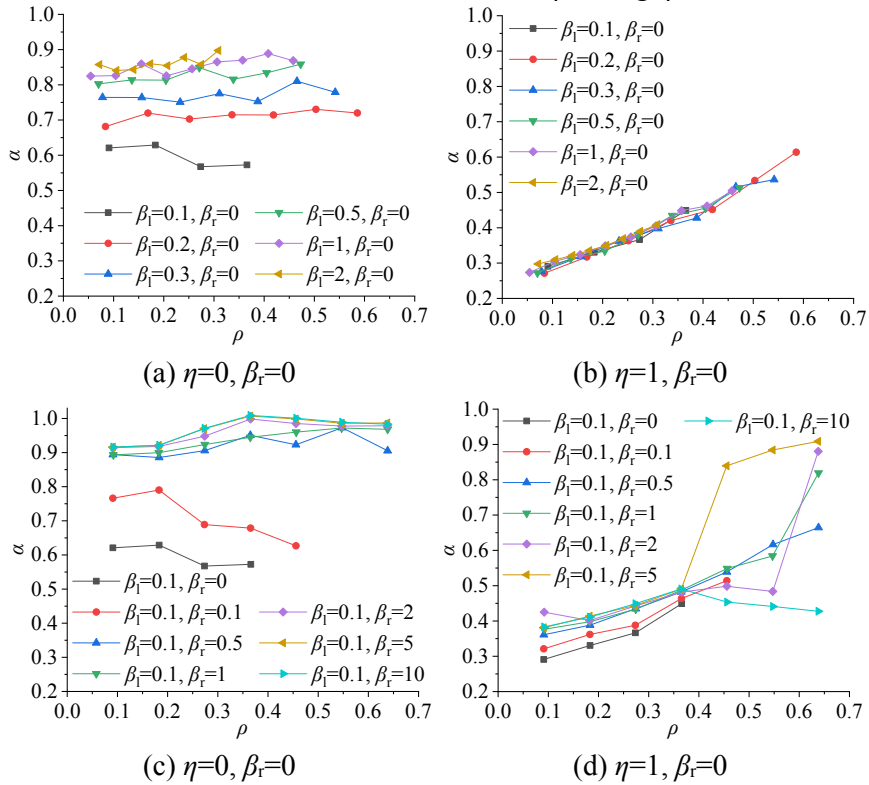


Fig. 5  $\alpha$ - $\rho$  curves with different stiffness ratio for the case of  $\eta=0$  and  $\eta=1$

When  $\eta=0$  ( $T=T_{bu}$ ) the load ratio has little effect on  $\alpha$ , while when  $\eta=1$  ( $T=T_{cr}$ )  $\alpha$  increases as the load ratio increases in most cases. This is because when the load ratio increases, the critical failure state that the axial force of the restrained column restores to the initial value will occur earlier

during the heating process, i.e., critical temperature will be smaller. Therefore, the plastic deflection and reduction of mechanical properties of HSSS becomes less, leading to less reduction on residual capacity. In addition, for the case of  $\eta=1$ , when columns with only axial restraint,  $\alpha$  has an approximately positive linear correlation with load ratio.

#### 4 CONCLUSIONS

The numerical analysis on post-fire residual capacity of the restrained HSSS columns under axial compression is presented in this paper. The following concluding remarks can be summarized.

- When  $T < T_{bu}$ , the fire has little effect on the residual capacity of the restrained HSSS columns.
- When  $T=T_{bu}$ , the columns reach the buckling state. The residual capacity increases as the axial restrained stiffness ratio increases or with the rotational restraint. But there is an upper limit for the rotational restraint stiffness ratio, above which the increase of the rotational restraint stiffness ratio has little effect on the residual capacity. As for the load ratio, it has little effect on the residual capacity.
- When  $T_{bu} < T < T_{cr}$ , the residual capacity decreases as the maximum temperature rises. The reduction law of residual capacity with the increase of maximum temperature is different between the columns with and without rotational restraint.
- When  $T=T_{cr}$ , the columns reach the critical failure state. The residual capacity generally increases as the load ratio increases. As for the stiffness ratio, the axial stiffness ratio has little effect on the residual capacity, while the rotational stiffness ratio can affect the residual capacity especially under load ratio above 0.4.

#### ACKNOWLEDGMENTS

The research work presented in this paper is supported by the National Natural Science Foundation of China through the contract 51878506. The support is gratefully acknowledged.

#### REFERENCES

- Ban H.Y., Shi G., Shi Y.J. 2014. *Experimental and unified model investigations on residual stress within high strength steel welded I-sections. Engineering Mechanics*, 31(8), p. 83-91.
- Bjorhovde R. 2010. *Performance and design issues for high strength steel in structures. Advances in Structural Engineering*, 13(3), p. 403-411.
- Huang L., Li G.Q., Wang X.X., Zhang C., Choe L., Engelhardt, M. 2018. *High temperature mechanical properties of high strength structural steels Q550, Q690 and Q890. Fire Technology*, 54, p. 1609-1628.
- Huang Z.F., Tan K.H. 2003. *Rankine approach for fire resistance of axially-and-flexurally restrained steel columns. Journal of Constructional Steel Research*, 59(12), p. 1553-1571.
- Lennon T., Moore D. 2003. *The natural fire safety concept—full-scale tests at Cardington. Fire Safety Journal*, 38(7), p. 623-643.
- Li G.Q., Lyu H.B., Zhang C. 2017. *Post-fire mechanical properties of high strength Q690 structural steel. Journal of Constructional Steel Research*, 132, p. 108-116.
- Li G.Q., Miao J.R., Song L.X., Cai W.Y., Jiang J. 2020. *Investigation on Postfire Residual Capacity of High-Strength Steel Columns with Axial Restraint. Journal of Structural Engineering*, 146(9), p. 04020182.
- Li G.Q., Wang P.J., Wang Y.C. 2010. *Behaviour and design of restrained steel column in fire, Part 1: Fire test. Journal of Constructional Steel Research*, 66(8-9), p. 1138-1147.
- Liu T.Z. 2015. *Study on post-fire mechanical behaviour of high strength Q460 steel columns. Master Thesis, Chongqing University (in China).*
- Wang W.Y., Li G.Q. 2016. *Research progress of fire resistance design theory of high strength steel structures. Industrial Construction*, 46(7), p. 61-67.
- Wang X.T., Zhou M., Wang W.Z. 2012. *Experimental study of fire response and post-fire mechanical behaviour of restrained H-steel columns after exposure to fire. Journal of Building Structures*, 33(2), p. 18-25.
- Wang Y.C., Moore D. B. 1994. *Effect of Thermal Restraint on Column Behaviour in a Frame. Fire Safety Science*, 4, p. 1055-1066.

## EXPERIMENTAL STUDY ON PULL-OUT TEST OF Hot-cast Anchors exposed to ISO-834 Fire

Yong Du<sup>a</sup>, and Jian Zhu<sup>a</sup>

<sup>a</sup> Nanjing Tech University, College of Engineering, Nanjing, China

### Abstract

In order to investigate the bond strength of hot-cast anchors under subject to ISO-834 fire, a series of pull-out test were conducted, including of 19 sets under transient temperature, 4 sets under steady temperature. It indicated that the slipping history of mounted steel cables could be divided into three stages, i.e. constant, accelerated and sharply accelerated slipping rate. The bond strength approximately kept constant before slipping sharply accelerated. When the hot-cast anchors were under lower tensile force ratio subject to transient temperature, the filler material can achieve melting temperature (420°C) and failed. With the increase of temperature and tensile force ratio, the wires wrapped filler material while slipping. Test resulted that the filler in hot-cast anchors can provide enough bond force within 1 hour exposed to ISO834 fire. Hot-cast anchors would be failed under fires as the slipping achieved the value of 8.5% diameter of the steel cable.

**Keywords:** bond strength, elevated temperature, failure mode, hot-cast anchor

## 1 INTRODUCTION

Anchors are key components in pre-tension structures as well as an important support to provide the fire safety for global structures. Large space building fire and bridge fire cases indicated that fires not only caused damage to the pre-stressed cables, but also decreased loading capacity of anchor under fire (Du et al. 2019). However, there are a few research results on quantitative evaluation of anchor capacity at high temperature. In this paper, a series of pull-out tests of hot-cast anchor at elevated temperature were conducted to investigate the slipping history and bonding force history. The effect of tension force ratio, wrapped area of filler to steel wires and temperature history on the mechanical response were also included into the test plan. The critical time and failure mode of hot-cast anchors will be also investigated by pull-out tests at elevated temperature. Finally, the failure criterion would be proposed.

## 2 EXPERIMENTAL PLAN

### 2.1 Specimens

The ratio of zinc to copper is shown in Table 1.

Table 1 Component of zinc copper alloy filler

Component	Content/%	m.p. /°C
Zinc	98±0.2	419.53
Copper	2±0.2	1083.4

The test information of each specimen was listed in Table 2 and table 3 respectively, and the geometric shape was shown in Figs. 2 and 3.

The small scale internal thread hot-cast anchor with a bearing ring welded at one end of the steel cable was clamped by upper connector as shown in Figs. 3 and 4(a). Herein, the tension force ratio is defined as the ratio of the tension force to the ultimate strength of a steel cable.



Fig. 2 Full-scale hot-cast anchors

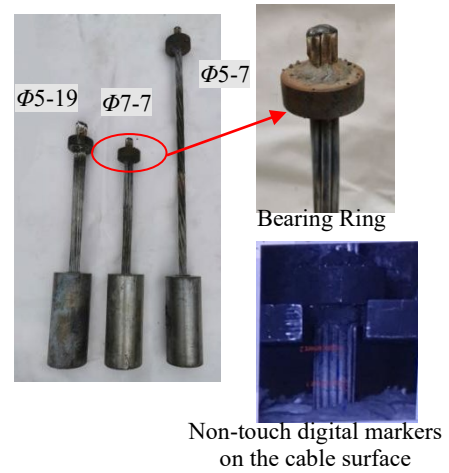


Fig. 3 Small scale hot-cast anchors

Table 2 Summary of test information for small scale hot-cast anchors

Group	ID	Tension force ratio (Temp/°C)	Wrapped area/cm <sup>2</sup>	Socket cup external radius (internal)/mm	Cable Nominal Diameter/mm	Temperature
A	A1	0.1	379.03	85 (50)	25 (Φ5-19 Parallel Wire)	Transient
	A2	0.2				
	A3	0.3				
	A4	0.4				
	A5	0.5				
	A6	0.6				
B	B1	0.2	195.50	85 (50)	21 (Φ7-7 Parallel Wire)	Transient
	B2	0.3				
	B3	0.6				
C	C1	0.2	123.15	70 (50)	15.2 (Φ5-7 Steel Strand)	Transient
	C2	0.3				
	C3	0.6				
D	D400	0.3 (400°C)	379.03	85 (50)	25 (Φ5-19 Steel Strand)	Constant
	D500	0.3 (500°C)				
	D600	0.3 (600°C)				
	D700	0.3 (700°C)				

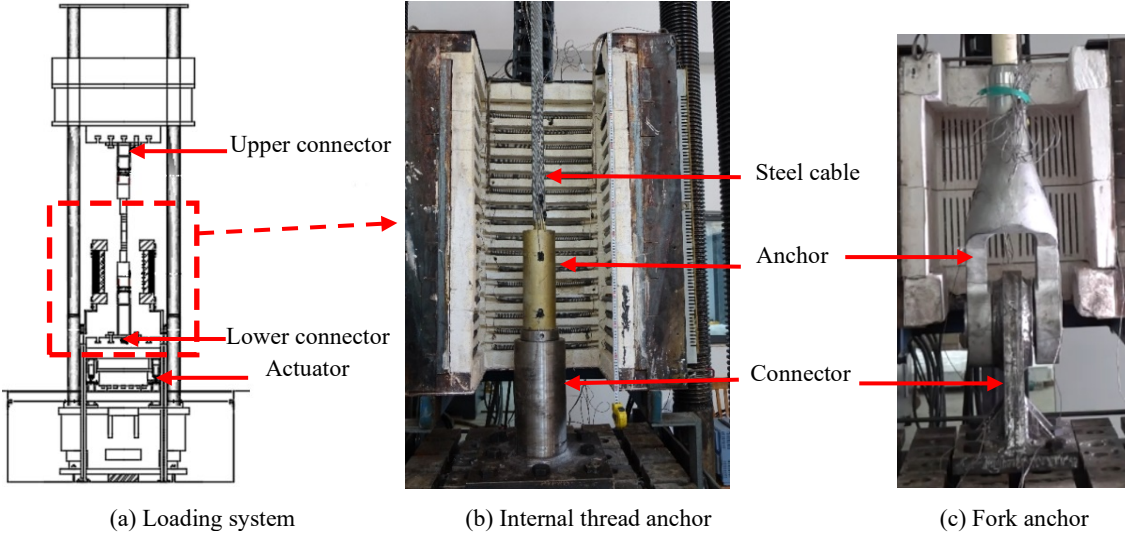
Table 3 Summary of information for full-scale hot-cast anchors

ID	Wire	Socket Cup External Radius (Internal)/mm	Wrapped Area /mm <sup>2</sup>	Connector	Tension force ratio	Temperature
LW-19A	Φ5-19 Parallel Wire	88 (65)	686.44	Internal Thread	0.3	Constant
LW-19B	Φ5-19 Parallel Wire	88 (65)	686.44			
LW-127B	Φ5-127 Parallel Wire	200 (150)	6184.23	Internal Thread	0.4	
LW-48B	Φ48 Vanadium- coated steel cable	129 (90)	2245.50			
CE-121B	Φ5-121 Parallel Wire	115~279 (94~152)	5987.09	Fork	0.4	
CE-127B	Φ5-127 Parallel Wire	125~298 (106~155)	6084.48			

## 2.2 Test Setup and Loading program

As shown in Fig. 4, the test loading system was YAW-10000F microcomputer controlled electro-hydraulic servo tension test machine, and the heating system was a multifunctional gas-assisted electric heating furnace. The non-contact video strain / displacement monitoring system was used to test the slipping process of the steel cable mounted in hot-cast anchor.

Two kinds of temperature loading program were followed. One program is that loading at a constant rate (0.3kN/s) up to the target tensile force, and then exposed to ISO-834 fire till failed. The other is that heating to a target temperature following ISO-834 fire and holding constantly after the target tensile force achieved.



(a) Loading system (b) Internal thread anchor (c) Fork anchor  
 Fig. 4 Pull-out test set-up for hot-cast anchor at elevated temperature

**3 TEST OBSERVATION**

**3.1 Failure Mode of Small Scale Hot-cast Anchors at Elevated Temperature**

The pull-out test of Groups A~C exposed to transient temperature was conducted as shown in Fig. 5. Under different tensile force ratios in a range of 0.1 to 0.6 interval of 0.1, the failure modes were different subject to ISO-834 fire. As shown in Fig. 5(a), when the tensile force ratio was not higher than 0.3 (A1~A3 list in Table 2), the filler material fully melted and flew out of socket cup when failed. As shown in Fig. 5(a), when the tensile force ratio was higher than 0.3 (A4~A6 list in Table 2), the filler material wrapped wires was pull out with partly melted when failed. The test observation of Group B and Group C was the same as that of Group A as shown in Fig. 5 (b) and Fig. 5 (c).



(a) Anchors A1~A6 (from left to right) (b) Anchors B1~B3 (from left to right) (c) Anchors C1~C3 (from left to right)  
 Fig.5 Failure modes of the pull-out test for small scale hot-cast anchors exposed to transient temperature

The pull-out test of Group D exposed to constant temperature was conducted as shown in Fig. 6. Under the same tensile force ratio of 0.3, the failure modes were different subject to different target temperature, as shown in Fig. 6(a). When the target temperature was not higher than 400 °C, the filler material wrapped wires was pull out as shown in Fig. 6(b). At 500 °C and 600 °C, the filler material wrapped wires was pull out with partly melted when failed as shown in Fig. 6(c). At 700 °C, the filler material fully melted and flew out of socket cup as shown in Fig. 6 (d). Generally, the failure modes of hot-cast anchors at elevated temperature can be divided into three types dependent on the tension force level and target temperature, i.e. filler fully melting, filler wrapped wires with partly melting and filler fully wrapped wires.

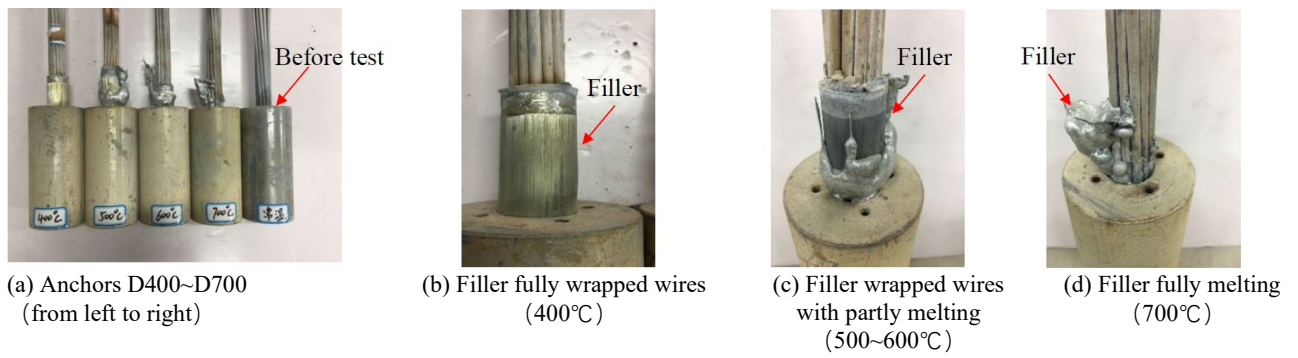


Fig.6 Failure modes of the pull-out test for small scale hot-cast anchors exposed to constant temperature

### 3.2 Failure Modes of Full Scale Hot-cast Anchors at Elevated Temperature

As shown in Fig. 7, the full scale hot-cast anchors displayed the similar slipping history during the pull-out test at elevated temperature. Comparison of the failure mode between small scale hot-cast anchors and full scale anchors, it indicated that filler fully melting, filler wrapped wires with partly melting and filler fully wrapped wires were included in both categories.

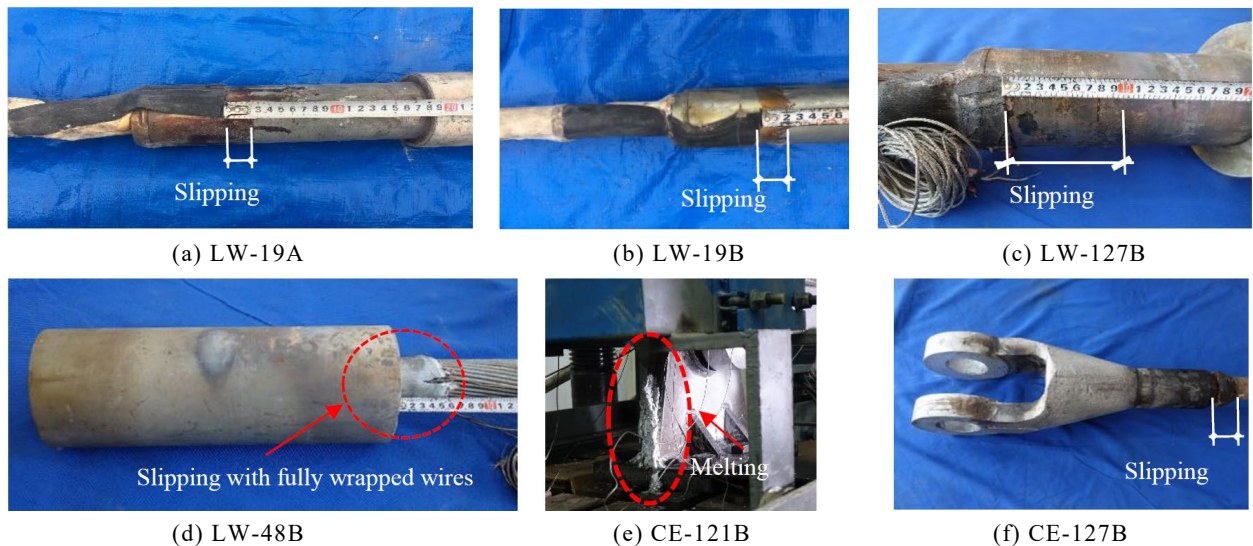


Fig.7 Failure modes of full scale hot casting anchors

## 4 TEST RESULTS AND ANALYSIS

### 4.1 Bond Action of Small Scale Hot-cast Anchor at Elevated Temperature

Fig. 8 shows the pull-out test results of Group A subject to ISO834 fire. It indicated that the tensile force experienced a long constant stage, and then sharply decreased as shown in Fig. 8(a). Group B and Group C were the similar as those of Group A, but the tensile force holding constant stage was shorter than that of Group A. It indicated that with the increase of tensile force ratio and area of wires wrapped, the bond strength of hot-cast anchors decreased.

As shown in Fig. 8(b), the slipping history of Group A experienced three stages, i.e. constant, accelerated and sharply accelerated slipping rate. Herein, the interval point between accelerated and sharply accelerated slipping rate was defined as the value of 8.5% of the nominal diameter of steel cables. As shown in Fig. 8(b), all interval points of slipping curve were before those of tensile force against heating time. The same as those of Groups B and C.

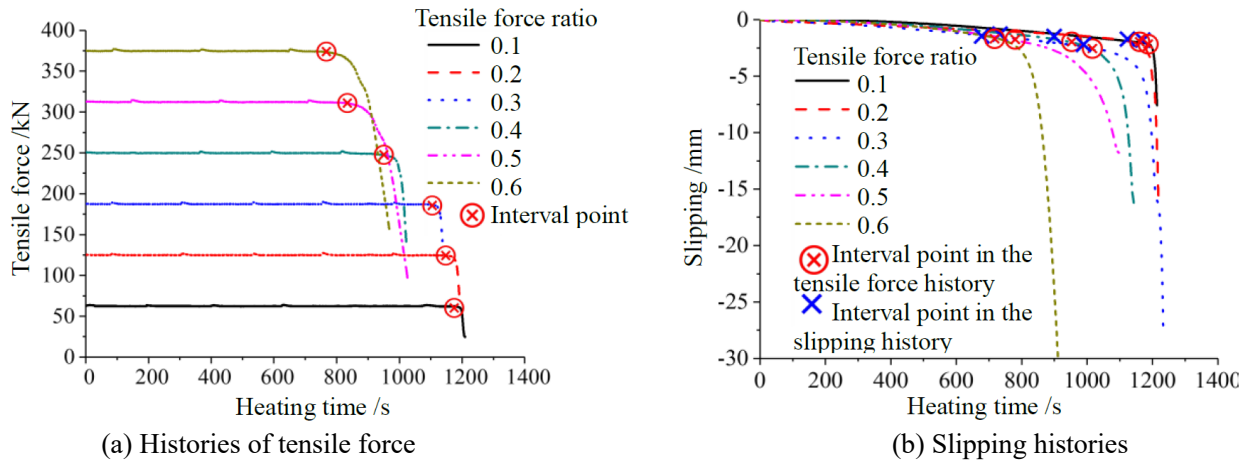


Fig. 8 Pull-out test results of small scale anchors subject to transient temperature

Fig. 9 shows the pull-out test results of Group D subject to constant heating temperature. The tensile force and slipping experienced the similar histories as those of Groups A~C. Generally, with the increase of target heating temperature, the bond strength of hot-cast anchors decreased.

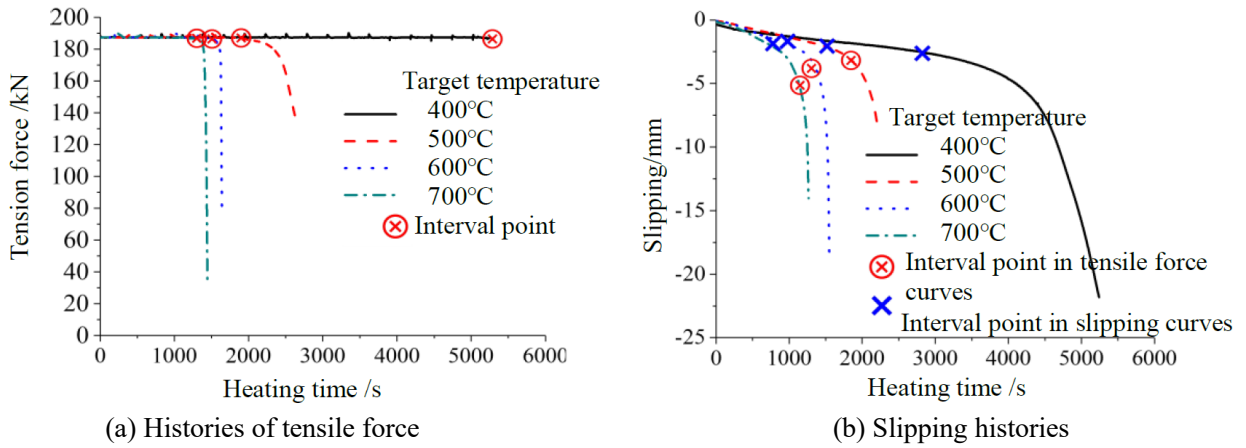


Fig. 9 Pull-out test results of small scale anchors subject to constant temperature

#### 4.2 Bond Action of Full Scale Hot-cast Anchor at Elevated Temperature

As shown in Fig. 10, three thermocouples were embedded in the full-scale hot-cast anchor filler to test the transient temperature distribution for checking 3D heat transfer numerical analysis and critical temperature in the corresponding paper (Chen et al. 2021).

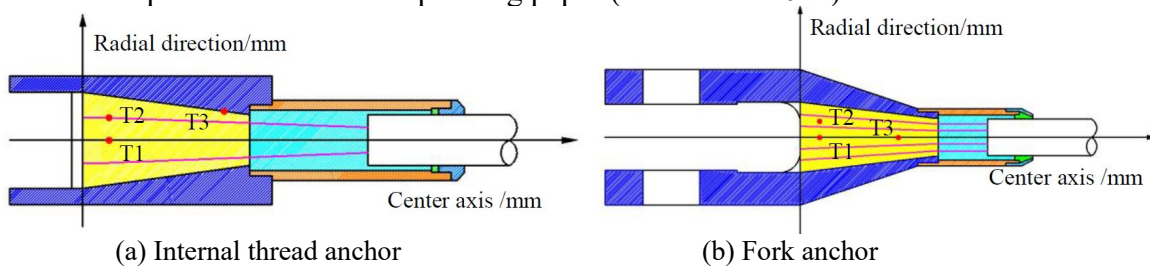


Fig. 10 Thermocouple location in hot-cast anchors

Table 4 Slipping data of full scale hot-cast anchors

ID	Tensile force ratio	Interval point in slipping curves		Interval point of tensile force against slipping curve	
		Slipping/mm	Heating time/s	Slipping/mm	Heating time/s
LW-19A	0.3	2.975	735	5.495	1067
LW-19B	0.4	2.975	867	3.494	909
LW-127B	0.4	6.715	1657	6.415	1657
LW-48B	0.4	4.080	1002	6.101	1058
CE-121B	0.4	6.800	2833	7.673	2869
CE-127B	0.4	6.885	2175	11.492	2254

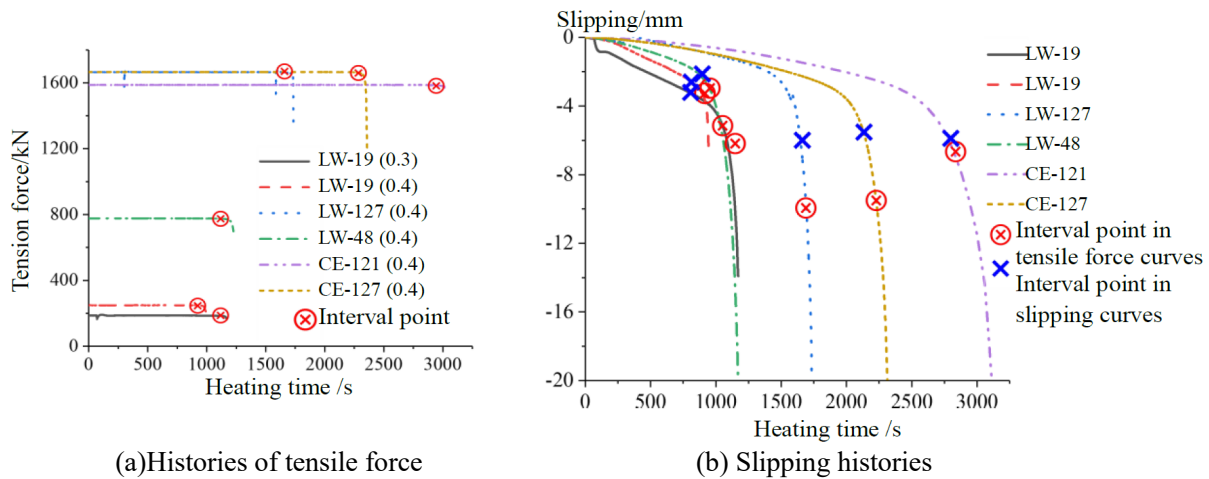


Fig. 11 Pull-out test results of full scale anchors subject to transient temperature  
 In general, the tension force history and slipping process of full-scale hot-cast anchors were similar to those of small scale hot-cast anchor as shown in Fig. 11. The tension process was characterized by tensile force holding stage and dropping stage as shown in Fig. 11(a). The slipping process shows stable growth, accelerated growth and sharply dropping as shown in Fig. 11(b). All interval points of slipping curve were before those of tensile force against heating time as list in Table 4.

### 4.3 Failure Criterion of Hot-cast Anchors at elevated temperature

As listed in Table 4, although the interval points of tensile force against heating time were longer than those of slipping, they were close together in some cases. If the interval point of tensile force against heating time was taken as failure time, it would not be safe and difficult to monitor the decrease of pre-tension force for steel cables. Considering of fire protect for hot-cast anchors, the heat transfer in anchors would be slow down and the gap between two interval points would be extended.

Therefore, it is suggested that when the slipping reached the value of 8.5% of the nominal diameter of the steel cable, hot-cast anchors subject to fire would be failed.

## 5 CONCLUSIONS

The fire resistance limit and failure mode of hot-cast anchor at elevated temperature were studied by a series of pull-out tests exposed to transient temperature and target constant temperature respectively. The conclusions are as follows:

- The failure mode of hot-cast anchors is dependent on the tensile force ratio wrapped wires area and target heating temperature, including of filler fully melting, filler slipping with partly melting and filler slipping. It is less than 1 hour that hot-cast anchors will be failed as exposed to ISO834 fire.
- The sliding process of filler experienced linear growth stage, accelerated growth stage and sharply accelerated stage. The process of tension force experienced the constant stage and sharply dropping stage. The interval points at sharp change of slipping were before those of tensile force.
- It is suggested that the hot-cast anchors will be failed when the slipping at the end of steel cable achieved the value of 8.5% of its nominal diameter.

## REFERENCES

Du Y., Zhu Y., Jiang J., Li G. 2019. *Transient temperature distribution in pre-tensioned anchors of cable-supported structures under ISO834 fire*, Thin-Walled Structures, England, 138, p. 231-242.  
 Chen J, Du Y., Zhu J., 2021. Transient temperature distribution in hot-cast anchors by 3D heat transfer, in *Applications of Structural Fire Engineering*, 10-11 June 2021, Ljubljana, Slovenia.

## COLD-FORMED STAINLESS STEEL LIPPED-CHANNEL AND SIGMA SECTIONS BEAMS AT ELEVATED TEMPERATURES

Flávio Arrais<sup>a</sup>, Nuno Lopes<sup>a</sup>, Paulo Vila Real<sup>a</sup>

<sup>a</sup> RISCO, Department of Civil Engineering, University of Aveiro, Portugal

### Abstract

The use of stainless steel as a structural material has been increasing in construction due to its different advantages when compared to conventional carbon steel, such as its better behaviour under elevated temperatures, which is important in buildings design. This research presents a numerical parametric study on the behaviour of stainless steel laterally unrestrained beams with cold-formed lipped-channel and sigma sections in case of fire, considering different dimensions, stainless steel grades, member slenderness, temperatures and bending moment diagrams. Beams fire resistances are obtained with geometrically and materially non-linear analysis including imperfections, with the software SAFIR, and compared to the load bearing capacities obtained from recently proposed design formulae for EN 1993-1-2. It is concluded that improvements to these simple design rules can be proposed aiming at the development of more precise prescriptions for cold-formed stainless steel beams in case of fire.

**Keywords:** cold-formed, stainless steel, beams, temperature, finite element modelling

### 1 INTRODUCTION

Stainless steel applications as a structural material have increased due to different characteristics, such as durability, corrosion resistance and aesthetic appearance (Gardner, 2005). However, its higher fire resistance, when compared to carbon steel, is also an important property that can be decisive for the structural elements material choice. In addition, structural elements composed of cold-formed thin-walled steel sections are becoming increasingly common in buildings due to their lightness, ability to support large spans and easy fabrication (Dubina *et al.*, 2012). The most common types of open cross-sections beams and purlins elements are the lipped-channel (C), the sigma ( $\Sigma$ ) and also the zed (Z) shapes (Liu and Yang, 2012). Combining the material characteristics of stainless steel and the efficiency of thin-walled cold-formed open sections may become an interesting solution in terms of structural application.

However, cold-formed open section profiles are more susceptible to the occurrence of local buckling phenomena due to the high slenderness of their components. In these members, local, distortional and global instabilities such as lateral-torsional buckling are common failure modes. Elevated temperatures impose significant loss of strength and stiffness on steel structural members, where the fire behaviour of cold-formed stainless steel members is still not completely understood. Currently, there is already several research on cold-formed open profiles at elevated temperatures, but on carbon steel (Kankanamge and Mahendran, 2012; Laím *et al.*, 2015; Arrais *et. al.*, 2016 and 2021b). However, for stainless steel members the research begins to develop at normal temperatures (Fan *et al.*, 2019). This paper presents a numerical analysis of the behaviour of simply supported members with cold-formed stainless steel lipped-channel (C) and sigma ( $\Sigma$ ) sections in case of fire when subjected to simple bending. A parametric study, considering different stainless steel grades, cross-section slendernesses and bending diagrams is performed for different elevated temperatures and the obtained numerical results are compared with the design prescriptions of Eurocode 3.

The fire resistance of cold-formed stainless steel lipped-channel and sigma beams is obtained using the software SAFIR (Gernay and Franssen, 2017). This software applies the finite element method (FEM) for geometrically and materially nonlinear analysis with imperfections included (GMNIA). Especially developed for the study of structures under fire, SAFIR has been applied in several studies,

such as on lipped-channel carbon steel columns at elevated temperatures including validation with experimental tests (Arrais *et al.*, 2021a).

With the purpose of better understanding the behaviour of these profiles, the different instability modes and corresponding critical loads for these elements are analysed using finite strip CUFSM software (Schafer and Ádány, 2006) and CAST3M (CEA, 2012). Moreover, the local, distortional and global instability modes obtained in CAST3M are used to define the geometrical imperfection shapes by applying the interface with SAFIR, the RUBY software (Couto *et al.*, 2013).

## 2 FIRE DESIGN RULES

prEN 1993-1-2 (CEN, 2020) design formulae are analysed to better understand the accuracy of these new generation design rules for cold-formed stainless steel at elevated temperatures.

Thin-walled cold-formed cross-sections are generally slender and, in these cases, the effective cross-section properties should be considered instead of the gross cross-section properties. prEN 1993-1-2 (CEN, 2020) includes in its Annex C the stainless steel mechanical properties reductions at elevated temperatures.

Following the prescriptions of the prEN 1993-1-2, the lateral-torsional buckling resistance moment of a laterally unrestrained beam with slender cross-sections and uniform temperature is:

$$M_{b,fi,t,Rd} = \chi_{LT,fi} W_{eff,y} k_{2,\theta,com} f_y / \gamma_{M,fi} \quad (1)$$

where  $\chi_{LT,fi}$  is the reduction factor for lateral-torsional buckling in the fire design situation and  $k_{2,\theta,com}$  the reduction factor to the strength at 2% total strain.  $\chi_{LT,fi}$  should be determined by:

$$\chi_{LT,fi} = \frac{1}{\phi_{LT,\theta,com} + \sqrt{\phi_{LT,\theta,com}^2 - \bar{\lambda}_{LT,\theta,com}^2}} \leq 1 \quad (2)$$

with

$$\phi_{LT,\theta,com} = 0,5 \left[ 1 + \alpha_{LT} \bar{\lambda}_{LT,\theta,com} + \bar{\lambda}_{LT,\theta,com}^2 \right] \quad (3)$$

$\alpha_{LT}$  is the elevated temperature imperfection factor for lateral-torsional buckling obtained by:

$$\alpha_{LT} = \alpha_{LT,0} / \xi_{\theta,com} \quad (4)$$

with  $\alpha_{LT,0} = 0,76$  obtained from Table C.4 of Annex C, for other section types and for any stainless steel grade, and  $\xi_{\theta,com} = \sqrt{k_{2,\theta}/k_{E,\theta}}$  the temperature dependent factor where  $k_{E,\theta}$  is the reduction factor for the slope of the linear elastic range at temperature  $\theta_a$  given in Annex C for stainless steels. The relative slenderness  $\bar{\lambda}_{LT,\theta,com}$  at the steel temperature  $\theta_a$  is given by:

$$\bar{\lambda}_{LT,\theta,com} = \xi_{\theta,com} \bar{\lambda}_{LT} \quad (5)$$

and the relative slenderness  $\bar{\lambda}_{LT}$  for slender sections given by:

$$\bar{\lambda}_{LT} = \sqrt{\frac{W_{eff,y} f_y}{M_{cr}}} \quad (6)$$

where  $M_{cr}$  is the elastic critical moment for lateral torsional-buckling buckling, obtained with CAST3M and RUBY software, based on gross cross-sectional properties, considering the loading conditions, the moment distribution and the lateral restraints. The bending moment resistances of each considered cross-section are obtained with SAFIR.

The effect of the bending moment distribution between the lateral restraints of a member may be considered by modifying the reduction factor  $\chi_{LT,fi}$  as:

$$\chi_{LT,fi,mod} = \frac{\chi_{LT,fi}}{f} \leq 1.0 \text{ and } \chi_{LT,fi,mod} \leq \frac{1}{\bar{\lambda}_{LT,\theta,com}^2} \quad (7)$$

For the factor  $f$ , the following expressions should be used for:

$$\text{- Austenitic: } f = 1 - 0.83(1 - k_c) \geq 0.67 \quad (8)$$

- Ferritic:  $f = 1 - 0.60(1 - k_c) \geq 0.76$  (9)
- Duplex:  $f = 1 - 0.67(1 - k_c) \geq 0.73$  (10)

According to the prEN 1993-1-1 (CEN, 2020), for  $-1 \leq \psi \leq 1$ , the correction factor  $k_c$  is:

$$k_c = \frac{1}{1.33 - 0.33\psi} \quad (11)$$

### 3 NUMERICAL MODELLING

To determine the ultimate load bearing capacity, the finite element SAFIR software is applied, considering shell elements, with three layers, and four nodes with six degrees of freedom (three translations and three rotations). Loads in the parallel directions to the beam axis are applied, distributed along the whole cross-section at the ends according to the bending moment diagram. Restraints are imposed to reproduce end pinned supports, one of which is a roller support. The numerical models with restraints and loads are presented in Figures 1 and 2.

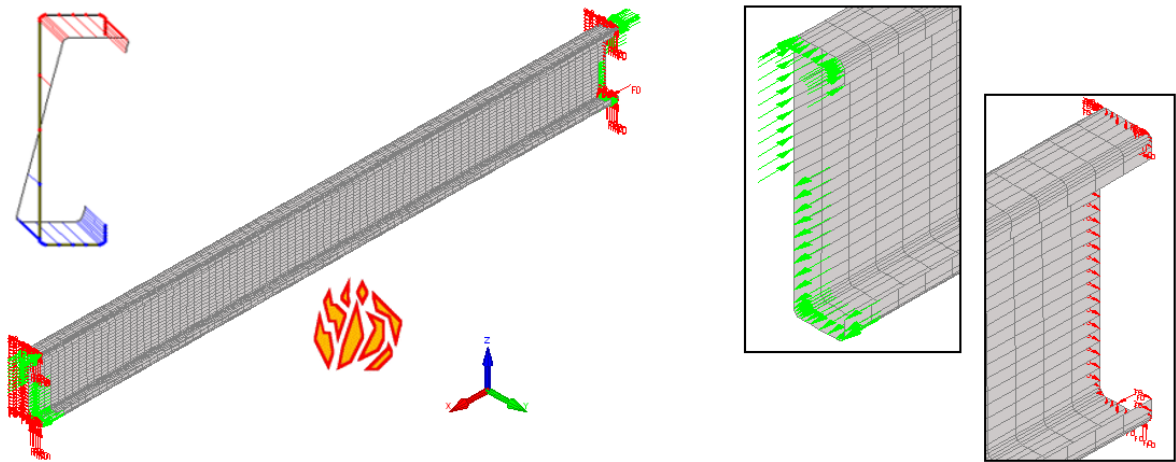


Fig. 1 Adopted numerical model for lipped-channel cross-section beams

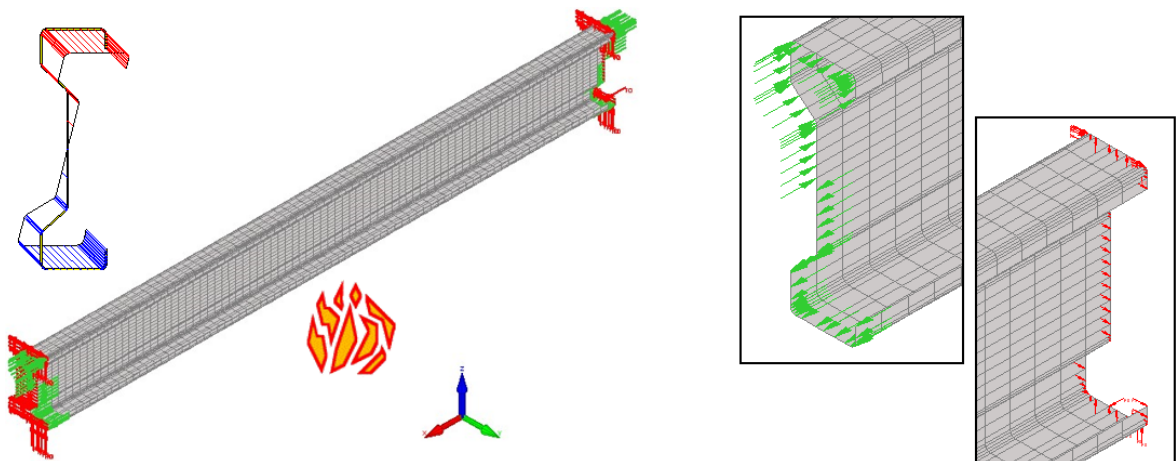


Fig. 2 Adopted numerical model for sigma cross-section beams

The corners enhanced strength due to the cold-formed fabrication process is not considered, as it is also not considered in EC3 design procedure when buckling is likely to occur. Membrane residual stresses are neglected, considering only flexural residual stresses on lipped-channel sections (Schafer and Peköz, 1998). Due to observed low influence at high temperatures, residual stresses are not considered on sigma sections.

Geometric initial imperfections are considered in the numerical model analysis. These imperfections were generated with different shapes based on the local (L), distortional (D) and global buckling (G) modes. For that purpose, the CAST3M and RUBY interface for SAFIR were applied, where the lowest eigenvalue for each instability mode is considered. Following EN 1993-1-5 (CEN, 2006), geometric imperfections may be based on the shape of critical buckling modes (Figure 3).

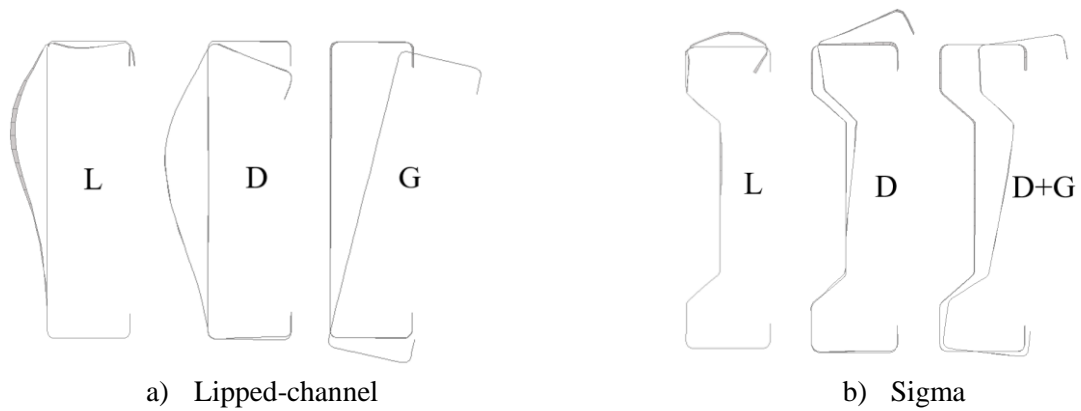


Fig. 3 Cross-section geometric imperfections for a) lipped-channel and b) sigma beam numerical models

For the imperfections amplitude, 80% of  $b/100$  is considered for local and distortional imperfections and 80% of  $L/750$  for global imperfections, following the recommendations of Annex C of Part 1-5 of EC3 and the geometric fabrication tolerances from EN 1090-4 (CEN, 2018), where  $b$  is the height of the web or the width of the flange (whichever presents the larger deflection) and  $L$  is the element length. The initial imperfections are combined, also bearing in mind the EN 1993-1-5 recommendations. This EC3 part states that in combining imperfections, a leading imperfection should be chosen, and the accompanying imperfections may have their value reduced to 70%. With the purpose of only analysing the member buckling curve and not the cross-section resistance, the latter is made equal to the numerically obtained resistant bending moment for a laterally restrained beam, MSafir, res, and the critical bending moment is also determined numerically with CAST3M and RUBY software. In numerical modelling, the constitutive law applied followed the model proposed in EN 1993-1-2:2005 (CEN, 2005b).

## 4 PARAMETRIC STUDY AND COMPARISON WITH FIRE DESIGN RULES

### 4.1 Case study

The main parameters considered in the numerical models are presented herein. Double hinged beams with different lipped-channels and sigma cross-sections are analysed (see Table 1). The sections dimensions are referenced by  $C/\Sigma_h \times b \times c \times (t)$  [mm] in Figure 4 and Table 1. Member lengths vary from 0.5 m to 10 m, to cover a range of standard slenderness (from 0.1 to 2.0). For this research, temperatures of 350, 500, 600 and 700 °C are adopted, with 350 °C being the EC3 proposed critical temperature for Class 4 cross-sections when no calculation is made, while the remaining temperatures are the most common critical temperature ranges in stainless steel elements. These temperatures are considered uniform throughout the cross-section to easily compare the design formulations proposed in EC3 and due to the reduced thickness of the walls' cross-section. The stainless steel grades used were 1.4301 (Austenitic grade also known as 304), 1.4401 (Austenitic grade also known as 316), 1.4003 (Ferritic grade), and 1.4462 (Duplex). Different bending moment diagrams (non-uniform,  $\psi = -1$  and 0, and uniform,  $\psi = 1$ ) are studied.

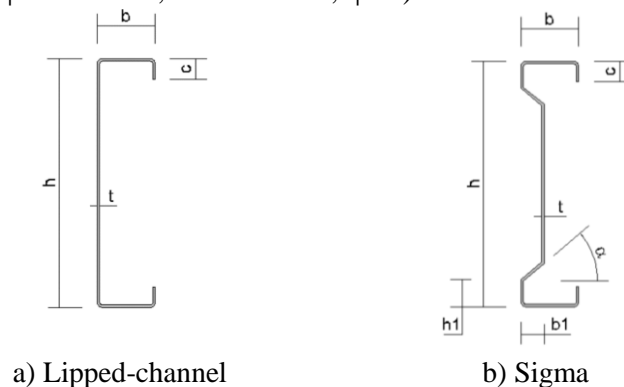


Fig. 4 a) Lipped-channel and b) Sigma cross-section shape representative dimensions

Table 1 Cross-sections analysed and respective dimensions

Designation	h [mm]	b [mm]	c [mm]	t [mm]	h1 [mm]	b1 [mm]	$\alpha$ [°]
C 229x64x20x(1.5)	229	64	20	1.5	-	-	-
C 170x64x20x(1.5)	170	64	20	1.5	-	-	-
C 229x48x20x(1.5)	229	48	20	1.5	-	-	-
C 229x64x15x(1.5)	229	64	15	1.5	-	-	-
C 100x50x10x(1.6)	100	50	10	1.6	-	-	-
C 150x51x20x(1.5)	150	51	20	1.5	-	-	-
C 155x77x31x(2.0)	155	77	31	2.0	-	-	-
$\Sigma$ 150x43x20x(2.0)	150	43	20	2.0	20	20	30
$\Sigma$ 229x64x20x(1.5)	229	64	20	1.5	30	30	30
$\Sigma$ 250x70x25x(2.5)	255	70	25	2.5	30	30	30

## 4.2 Numerical results and fire design rules

This research is based on more than 4000 numerical simulations. Figures 5 and 6 present the results of the numerical models C\_229x64x20x(1.5) and  $\Sigma$ \_229x64x20x(1.5), considering uniform (Figure 5) and non-uniform (Figure 6) bending moments, at the different temperatures, for the austenitic stainless steel. Due to the page limitation, not all the results are displayed here. In the following charts,  $M_{Safir, res}$  represents the cross-section resistance obtained by the SAFIR software considering the initial imperfections. Table 2 presents a brief statistical analysis. The results obtained for non-uniform bending ( $\psi = 0, -1$ ) with low member slenderness are affected by shear buckling phenomenon. Therefore, those values are not considered since it is not in the scope of this work.

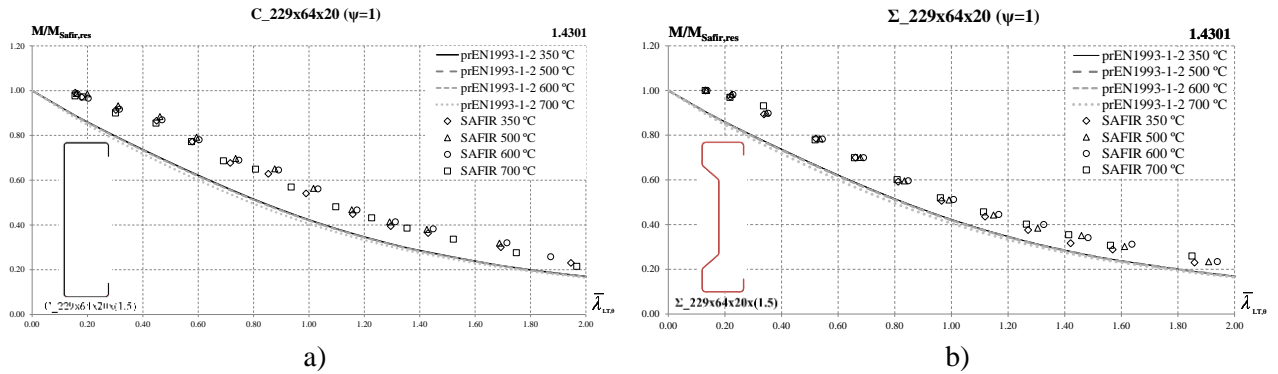


Fig. 5 a) Lipped-channel and b) Sigma cross-section beams  $\psi=1$

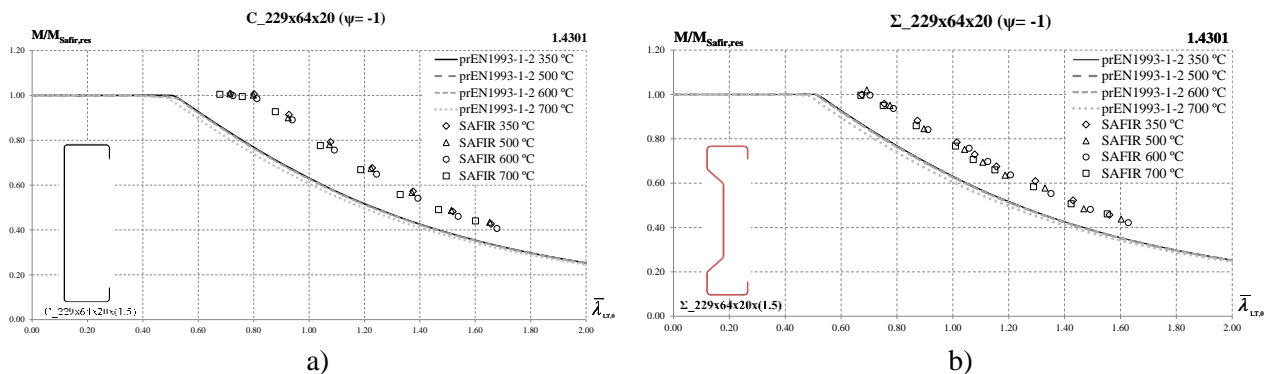


Fig. 6 a) Lipped-channel and b) Sigma cross-section beams  $\psi = -1$

Table 2 Statistical evaluation of prEN 1993-1-2 for the different sections analysed and stainless steel grades

Cross-section type	Austenitic				Ferritic				Duplex			
	$\mu$	s	Max.	% uns.	$\mu$	s	Max.	% uns.	$\mu$	s	Max.	% uns.
Lipped-channel	0.82	0.09	1.01	0	0.86	0.18	1.02	0	0.85	0.08	1.01	0
Sigma	0.84	0.11	1.03	0	0.87	0.21	1.03	0	0.86	0.11	1.01	0

In general, the numerical results are on the safe side, however the prEN1993-1-2 buckling curve is still over-conservative specifically for non-uniform bending (see Figure 6 for  $\psi = -1$  and Table 2).

## 5 CONCLUSIONS

A numerical study on the behaviour of unrestrained cold-formed stainless steel beams was presented. The accuracy of the new generation of the Eurocode 3 was evaluated against numerically obtained bending resistances. The performed parametric study considered simply supported beams with cold-formed lipped-channel and sigma sections in case of fire, when subjected to simple bending. The influence of the different stainless steel grades, cross-section slendernesses and loading types was also considered. A comparison between the ultimate loads and the formulae prescribed in the new generation of the Eurocode 3 was performed, concluding that the calculation rules are on the safe side but being sometimes too conservative for the tested cold-formed stainless steel beams.

## ACKNOWLEDGMENTS

This research work was performed within the framework of the project “StaSteFi - Fire design of stainless steel members”, PTDC/ECI-EGC/30655/2017, supported by the Portuguese Operational Programme “Competitividade e Internacionalização”, in its FEDER/FNR component, and the Portuguese Foundation for Science and Technology (FCT), in its State Budget component (OE).

## REFERENCES

- Arrais, F., Lopes, N., Vila-Real, P. 2016. *Behaviour and resistance of cold-formed steel beams with lipped channel sections under fire conditions*. *Journal of Structural Fire Engineering*, Vol. 7 (4), p. 365–387.
- Arrais, F., Lopes, N., Vila-Real, P. 2021a. *Fire design of slender cold-formed lipped channel and sigma section members with uniform temperature under compression*. *Fire Safety Journal*, Vol. 122, 103340.
- Arrais, F., Lopes, N., Vila-Real, P. 2021b. *Fire behaviour and resistance of cold-formed steel beams with sigma cross-sections*. *Journal of Structural Fire Engineering*, (in press).
- CAST3M. 2012, Development sponsored by French Atomic Energy Commission; <http://www-cast3m.cea.fr/>
- CEN European Committee for Standardisation. EN 1993-1-1:2005a. *Eurocode 3, Design of steel Structures – Part 1–1: General rules - General rules and rules for buildings*, Belgium.
- CEN European Committee for Standardisation. EN 1993-1-2:2005b. *Eurocode 3, Design of steel Structures – Part 1–2: General rules - Structural fire design*, Belgium.
- CEN European Committee for Standardisation. prEN 1993-1-2:2020. *Eurocode 3, Design of steel Structures – Part 1–2: General rules - Structural fire design*, Belgium.
- CEN European Committee for Standardisation. EN 1993-1-5:2006. *Eurocode 3, Design of steel Structures – Part 1–5: Plated structural elements*, Belgium.
- CEN European Committee for Standardisation. EN 1090-4:2018. *Execution of steel structures and aluminium structures - Part 4: Technical requirements for cold-formed structural steel elements and cold-formed structures for roof, ceiling, floor and wall applications*, Belgium.
- Couto, C., Vila Real, P., Lopes, N. 2013. *RUBY – an interface software for running a buckling analysis of SAFIR models using Cast3M*, University of Aveiro.
- Dubina, D., Ungureanu, V., Landolfo, R. 2012. *Design of cold-formed steel structures*, ECCS – European Convention for Constructional Steelwork, Ernst & Sohn.
- Fan, S., Chen, M., Li, S., Ding, Z., Shu, G., Zheng, B. 2019. *Stainless steel lipped C-section beams: Numerical modelling and development of design rules*. *J. Constr. Steel Res.*, Vol. 152, p. 29–41
- Gardner, L. 2005. *The use of stainless steel in structures*, *Progress in Struct. Eng. and Mat.*, Vol. 7, p. 45-55.
- Gernay, T., Franssen, J.M. 2017. *Modelling structures in fire with SAFIR®: Theoretical background and capabilities*. *Journal of Structural Fire Engineering*, Vol. 8 (3), p. 300–323.
- Kankanamge, N., Mahendran, M. 2012. *Behaviour and design of cold-formed steel beams subject to lateral torsional buckling*. *Thin-Walled Structures*, Vol. 51, p. 25–38.
- Laím, L., Rodrigues, J. P. C., Craveiro, H. 2015. *Flexural behaviour of beams made of cold-formed steel sigma-shaped sections at ambient and fire conditions*, *Thin-Walled Structures*, Vol. 87, p. 53–65
- Liu, Q., Yang, J. 2012. *An experimental study into flexural behaviour of sigma purlins attached with roof sheets*. *Engineering Structures*, Vol. 45, p. 481–495.
- Schafer, B.W., Ádány, S. 2006. Buckling analysis of cold-formed steel members using CUFSM: conventional and constrained finite strip methods, *18th Int. Conference on Cold-Formed Steel Structures*, Florida.
- Schafer, B.W., Peköz, T. 1998. *Computational modelling of cold-formed steel: characterizing geometric imperfections and residual stresses*, *Journal of Constructional Steel Research*, No. 47, p. 193–210.

## EVALUATION OF STEEL STRUCTURES FIRE VULNERABILITY THROUGH FRAGILITY CURVES

Enrico Cardellino<sup>a</sup>, Donatella de Silva<sup>a</sup> and Emidio Nigro<sup>a</sup>  
enrico.cardellino@unina.it, donatella.desilva@unina.it and emidio.nigro@unina.it

<sup>a</sup> Department of Structures for Engineering and Architecture, University of Naples Federico II, Via Claudio, 21, Napoli, 80125, Italy

### Abstract

In the fire engineering field, probabilistic and semi-probabilistic approaches to evaluate the fragility or the robustness of structures is still little used. Therefore, based on results of many advanced thermomechanical analyses conducted on steel structures, fire fragility curves have been constructed using the Cloud Analysis method. The original idea of this work is to obtain fragility curves useful both for the fire designers to assess the vulnerability of steel structures and for the fire protection manufacturers to optimize the design of the protective materials. The results show that seismically designed steel structures have a more performing behaviour than non-seismically designed ones. The fragility curves are a probability-based procedure to evaluate the fire structural vulnerability and to guide the fire protection design of steel structures considering the main uncertain parameters characterizing the structural fire behaviour.

**Keywords:** Fire; Fragility Curves; Steel structures; Vulnerability.

## 1 INTRODUCTION

Areas with high seismic risk need structures characterized by a material that is light, ductile and resistant at the same time. Having a high ductility and high mechanical efficiency understood as the resistance weight ratio, structural steel has a good compromise between these characteristics. Therefore, it is possible to obtain better seismic performance with the use of elements with a smaller quantity of material than, for example, reinforced concrete structures. This is seismically positive, but it is negative from fire resistance point of view, because reducing the volume of material increases the section factor. Therefore, the assessment of the fire vulnerability of steel structures should go hand in hand with the design and the fragility curves could be a simple and quick tool to do this. Generally, in the literature the use of probabilistic models is more used to describe the fire action rather than the behaviour of the structure subject to it (Khorasani et al., 2014); indeed, the probabilistic approach is used for selecting the fire scenarios (Nigro et al., 2014). However, lately, (Miano et. al., 2020) implemented a probabilistic approach to assess performance-based structural behaviour in case of fire. Applying the Cloud method (Jalayer et al., 2014), the fragility of reinforced concrete structures subjected to earthquake and fire was assessed. Based on what has been mentioned, fire fragility curves for steel structures have been constructed.

## 2 FRAGILITY FUNCTION

In this work the fragility curves are developed for the seismically and non-seismically designed steel structures before and after the application of fire protection. To evaluate the fragility curves, the Cloud Method has been used. This method distributes the advanced thermomechanical analysis results in the logarithmic space versus first the fire intensity and then the protective thickness. Based on previous distribution it is possible to implement the linear regression-based probabilistic model. Assuming that

$$Y = \{Y_i, i = 1 : N\} \quad (1)$$

$$Y_i = \left[ \max \frac{D_j}{C_j} \right]_i \quad (2)$$

is the critical demand capacity ratio by N advanced structural analyses performed varying fire intensity in function of several fire loads

$$q_{fd,i} = \{q_{fd,i}, i = 1:N\} \quad (3)$$

the probabilistic model can be described as following:

$$E[\log Y | q_{fd}] = \log \eta_{Y|q_{fd}} = \log a + b \log q_{fd} \quad (4)$$

$$\sigma_{\log Y|q_{fd}} = \sqrt{\frac{\sum_{i=1}^n (\log Y_i - \log \eta_{Y|q_{fd,i}})^2}{n-2}} \quad (5)$$

Where:

- $\eta_{Y|q_{fd}}$  is the median for Y given  $q_{fd}$ ;
- $\sigma_{\log Y|q_{fd}}$  is the logarithmic standard deviation for Y given  $q_{fd}$ .

The fragility function from cloud method is a three-parameter function

$$\psi = \{ \log a, b, \sigma_{\log Y|q_{fd}} \} \quad (6)$$

and can be expressed as shown below:

$$P(Y \geq 1 | q_{fd}) = P(\log Y > 0 | q_{fd}) = 1 - \Phi \left( \frac{-\log \eta_{Y|q_{fd}}}{\sigma_{\log Y|q_{fd}}} \right) = \Phi \left( \frac{\log \eta_{Y|q_{fd}}}{\sigma_{\log Y|q_{fd}}} \right) \quad (7)$$

As mentioned, these results are in terms of demand-capacity ratios, which, in this work, are function of the level of performance (LoP) IV (The Ministerial Decree 2015). Thanks to level of performance the limit of deformation ( $f_{lim} = L/100$ ) has been set. The fulfilment of this limitation guarantee contained damage during the fire otherwise failure occurred.

$$Y_i = \frac{D_j}{C_j} = \frac{f_{\max j}}{f_{\lim j}} \geq 1 \Rightarrow \text{Failure occurred.} \quad (8)$$

### 3 THERMOMECHANICAL ANALYSIS

#### 3.1 The structures

To assess deformative behaviour of steel structures during the fire, numerous thermomechanical analysis have been carried out. But, to reduce the computational burden and to satisfactorily assess the demand, the substructures criteria (EN1991) was used, characterizing the structural fire response of the entire structure through the modelling of significant parts of it. Therefore, non-seismically designed (NSD) steel frames and seismically designed (SD) steel frames were analysed. The NSD frame is distinguished from SD one having no bending continuity in the beam nodes column and having a low lateral stiffness. The analysed frames are characterized by 5 floors and 5 bays, with a beams' length of 6.0 m and columns' height of 4.0 m for the first floor and 3.5 m for the other ones (Figure 1).

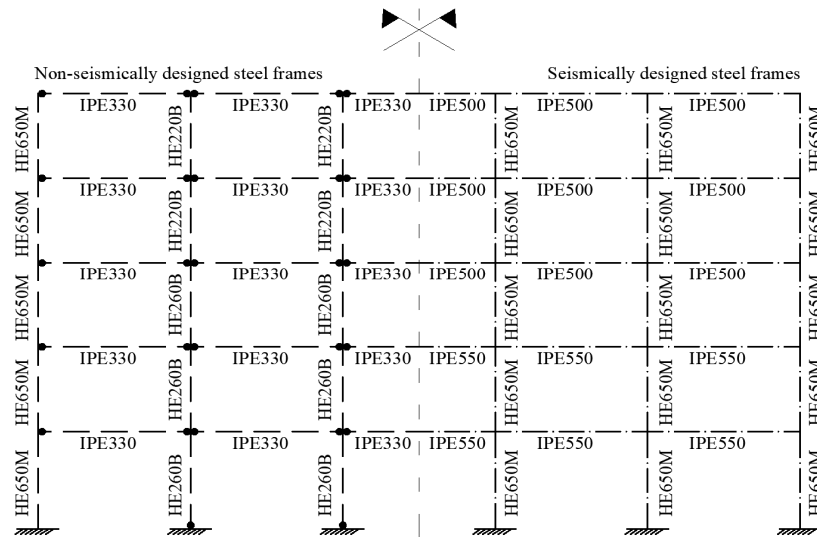


Fig. 1 NSD and SD steel frames.

### 3.2 The fire

The fire inside a compartment produces a temperature variation which is characterized by multiple random parameters. Furthermore, the behaviour of a structure during a fire is also a function of where it develops. Therefore, advanced thermomechanical analyses under numerous fire curves and the generalised fire to the entire ground floor with an area  $A = 360 \text{ m}^2$ , were considered. Then, in accordance with EN1991, the different heat release rate curves (HRR) were evaluated as a function of a time  $t_\alpha = 300 \text{ s}$ , while the fire loads  $q_d$  were considered variable from  $100 \text{ MJ/m}^2$  to  $1900 \text{ MJ/m}^2$ . The ventilation factor "O" is chosen equal to  $0.2 \text{ m}^{-1}$ , to have a fire governed by fuel for each fire load. Using the software O-ZONE, 36 fluid dynamics analyses were carried out obtaining the fire curves shown in figure 2.

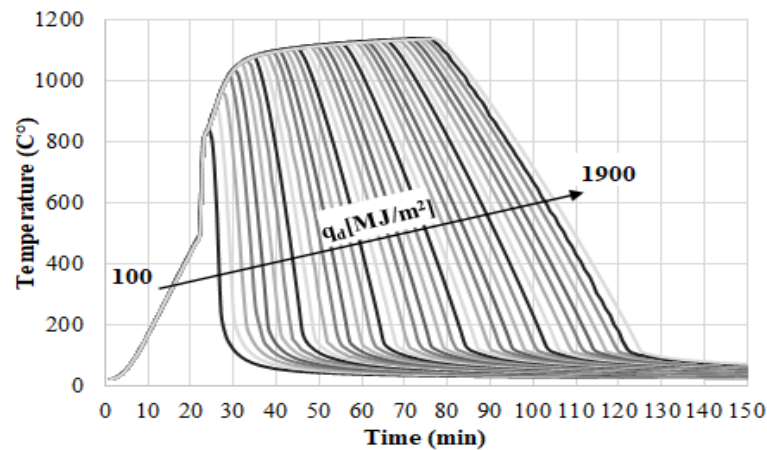


Fig. 2 Fire curves from natural fire models.

### 3.3 The Analysis

Using the set of fire curves, various thermomechanical analysis were performed. SAFIR software was used both for the thermal analysis of the single protected and non-protected sections and for the advanced mechanical analysis. As the fire progresses, the deformations increase, and the maximum deflection is the control parameter related to the LoP IV. In the applied semi-probabilistic approach, the "Demand" is the maximum deformation resulting from analysis and the "Capacity" is fixed by the performance limit.

## 4 FIRE FRAGILITY CURVES

### 4.1 Varying the fire load

Thanks to the analyses carried out on steel structures with and without passive fire protection (PFP) it was possible to have the data family in terms of DCR varying the fire load. The analyses showed that in order to obtain an acceptable reduction in fragility, NSD structures require a much greater thickness of fire protection than SD ones.

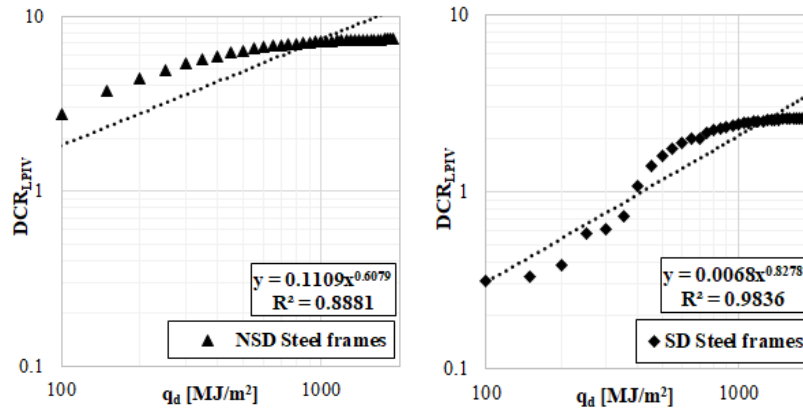


Fig. 3 Distribution of DCR for NSD and SD unprotected steel frames in logarithmic scale.

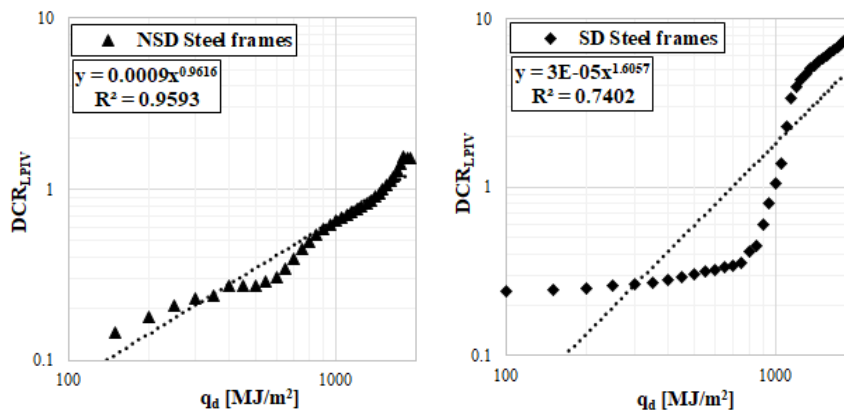


Fig. 4 Distribution of DCR for NSD and SD protected steel frames in logarithmic scale.

The distributions of data are shown in figures 3 and 4 for NSD and SD unprotected and protected steel frames in the logarithmic scale. The linear interpolation allows to calculate the statistical properties of distributions which are essentially to evaluate the cumulative distribution function (CDF). The CDF expresses the probability of failure representing the probability of exceeding the performance target (figure 5).

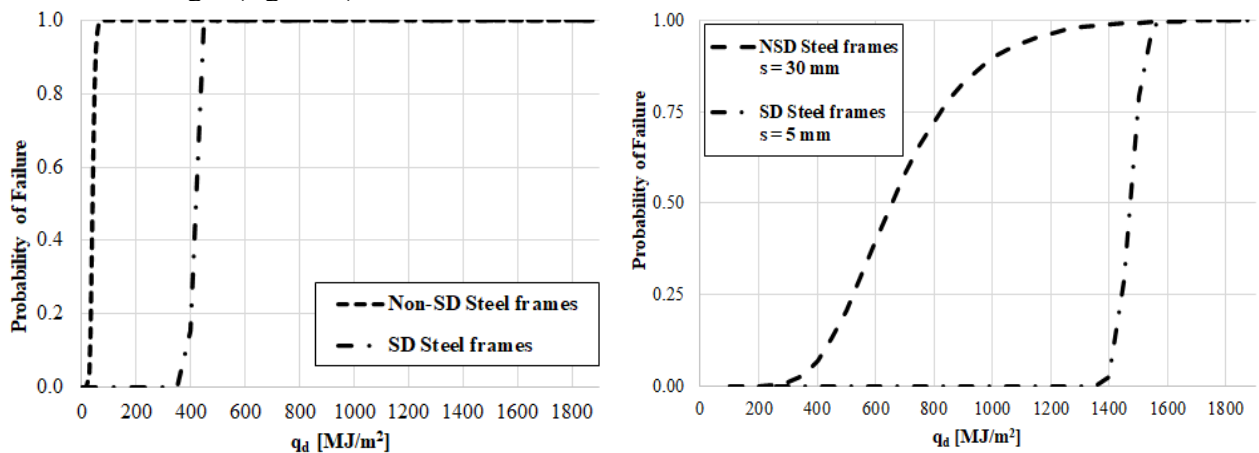


Fig. 5 Fragility curves NSD and SD steel frames, without and with PFP.

From the trend of fragility curves it can be observed the less performing behaviour of the NSD steel frames than the SD ones. All this is remarked in the presence of protective because increase the gap between the two fragility curves.

### 4.2 Varying the thickness of PFP

With the same geometry, structural type, loads and intensity of the fire, in the previous paragraph it emerged that the fire fragility is significantly influenced by application of PFP to protect the structural elements. In this regard, to see how much the thickness of the fireproof plaster can vary this influence, further thermomechanical analysis were carried out considering fireproof plaster with a thickness ranging between 6 mm and 44 mm.

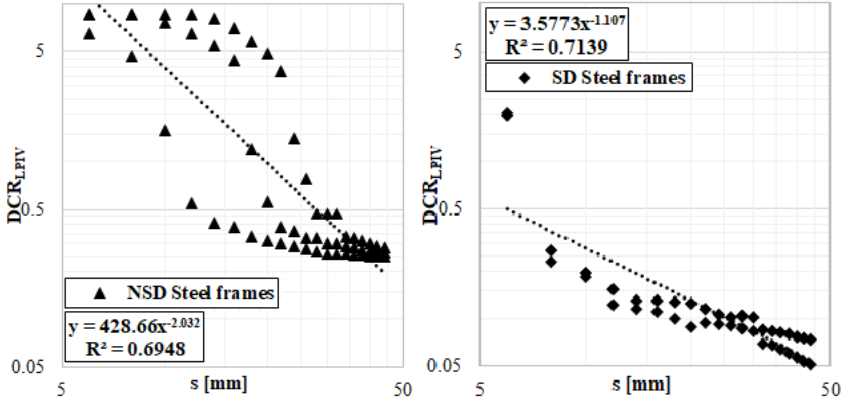


Fig. 6 Distribution of DCR for NSD and SD protected steel frames in logarithmic scale.

Furthermore, considering the fire loads characteristic of the most common intended use (as in table S.2-10 of EN1991) and that their average is between 500-600 MJ/m<sup>2</sup>, for fire loads between 250-750 MJ/m<sup>2</sup> the thermomechanical analyses were carried out. Downstream of the analysis, new families of DCRs were obtained (figure 6) for which it was possible to calculate the statistical properties and to define the fire fragility curves (figure 7).

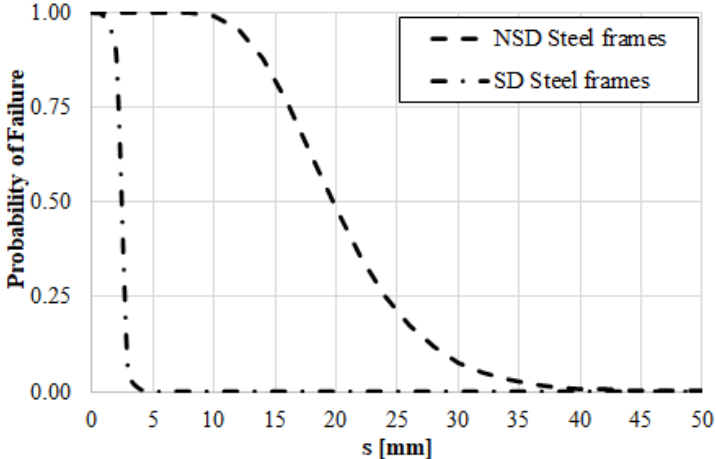


Fig. 7 Fragility curves NSD and SD steel frames varying the thickness of fireproof plaster.

## 4 CONCLUSIONS

In this paper the probability-based methodology to assess the fragility of steel structure subjected to fire action was used. The procedure was carried out with reference to substructures of seismically and non-seismically designed steel structures. The final results shown:

- Steel structures designed to support vertical loads alone (NSD) are extremely vulnerable to fire when they do not have a PFP system. In fact, observing the respective fragility curve

there is a high probability of exceeding the performance target even for relatively low fire load values, about  $100 \text{ MJ} / \text{m}^2$  (Figure 5).

- Steel structures designed to support seismic loads (SD) through MRF systems have a more efficient fire behaviour than the previous ones. An almost unacceptable probability of exceeding the performance target begins to be observed for fires characterized by a fire load greater than  $400 \text{ MJ} / \text{m}^2$  (Figure 5).
- The use of protective fire-retardant plaster for both NSD and SD steel structures causes a significant fragility reduction (Figure 5). In SD steel structures, double the reduction of fragility is obtained by applying only 1/6 of the thickness of the protective layer used for NSD steel structures.
- To assess the fire vulnerability of existing steel structures characterized by a structural typology such as those analysed the fragility curves in function of fire loads could be used. Indeed, knowing the intended use, the associated fire load can be estimated and the probability of exceeding the performance target can be obtained from the fragility curves in figure 5 (with or without PFP).
- The fragility curves that express the overcoming of the performance target as a function of the protective thickness (figure 7) could be a valid tool both for designers and for PFP producers. For existing steel structures or to be built, it is possible to orient the choice of fire protection and estimate the consequent reduction of fragility.

## REFERENCES

- A. Miano, D. de Silva, A. Compagnone and G. Chiumiento, “Probabilistic seismic and fire assessment of an existing reinforced concrete building and retrofit design”, *Structural Engineering and Mechanics*, Vol. 74, No. 4 (2020) 1- <https://doi.org/10.12989/sem.2020.74.4.001>.
- E. Nigro, A. Bilotta, D. Asprone, F. Jalayer, A. Prota and G. Manfredi, “Probabilistic approach for failure assessment of steel structures in fire by means of plastic limit analysis”, *Fire Safety J.*, 68, 16-29. <https://doi.org/10.1016/j.firesaf.2014.05.020>.
- EN1991 Eurocode 1: Actions on structures - Part 1-2: General actions - Actions on structures exposed to fire.
- F. Jalayer, L. Elefante, R. De Risi, G. Manfredi, “Cloud analysis revisited: efficient fragility calculation and uncertainty propagation using simple linear regression”, Tenth U.S. National Conference on Earthquake Engineering, *Frontiers of Earthquake Engineering* July 21-25, 2014.
- N. E. Khorasani N, M. Garlock, P. Gardoni. Fire load: survey data, recent standards, and probabilistic models for office buildings. *Eng Struct* 2014;58:152–65.
- T. Gernay, N. Elhami Khorasani, M. Garlock, “Fire fragility curves for steel buildings in a community context: A methodology”, *Engineering Structures* 113 (2016) 259–276 <https://doi.org/10.1016/j.engstruct.2016.01.043>.
- The Ministerial Decree 3 August 2015 as emended by the Ministerial Decree 18 October 2019, “Technical fire prevention standards”.

## PERFORMANCE OF DUCTILE CONNECTIONS IN 3-D COMPOSITE FRAMES UNDER FIRE CONDITIONS

Yu Liu<sup>a</sup>, Shan-Shan Huang<sup>a</sup>, Ian Burgess<sup>a</sup>

<sup>a</sup> University of Sheffield, Department of Civil and Structural Engineering, Sheffield, United Kingdom

### Abstract

A novel axially and rotationally ductile connection has previously been proposed by the authors to prevent brittle failures of connections in fire. The study is now extended to investigation of the fire performance of the ductile connection in composite structures, particularly using a 3-dimensional model to consider the contribution of out-of-plane structural elements to the behaviour of the connection and the behaviour of the frame as a whole. In this paper, the design and the component-based model of the ductile connection have been briefly introduced. A composite frame has been designed according to the typical frame used in the Cardington full-scale fire tests. Three 3-dimensional composite frame models with different types of connections have been built using the software Vulcan to compare the performance of the ductile connection in fire with ideally rigid and pinned connections. Finally, 2-D models have been built to simulate the central and edge secondary beams of the composite frame to make a comparison between 2-D modelling and 3-D modelling.

**Keywords:** Composite connection, Ductility, Component-based model, Fire, 3-D modelling

### 1 INTRODUCTION

Connections are potentially the weakest parts of a structure in fire. Connection failures may lead to the detachment of connected beams, the collapse of slabs, the buckling of columns and even the progressive collapse of the entire building. In order to enhance the robustness of structures in fire and prevent brittle failures of connections, a novel axially ductile connection has been proposed by the authors (Liu *et al.*, 2019a, 2019b, 2020a, 2020b, 2020c, 2021). The performance of the ductile connection within bare-steel frames in fire has already been well studied by the authors. It can be concluded that in steel-framed structures, compared with commonly-used connection types, the ductile connection can provide additional ductility to accommodate the axial deformations of connected beams at elevated temperatures, thus greatly reducing the axial forces generated in the beams and their connections.

The connection behaviour in composite structures in fire is quite different from that in bare-steel structures, due to the shear connection between the beams and the composite slab. During a fire event, a composite slab can act as shielding to the top part of the connection, reducing its temperature and enhancing its performance. In addition, the thermal bowing phenomenon, caused by the composite slabs restraining the thermal expansion of steel beams, affects the connection performance and generates higher early-stage rotations. AI-Jabri (1999) carried out a series of tests on flexible end-plate composite connections at elevated temperatures and proposed a component-based model to predict the high-temperature response of the composite end-plate connections. Li *et al.* (2012) proposed a simplified method to calculate the non-linear characteristics of composite connection in the analysis of beam catenary action at elevated temperatures based on the results of their three tests on flush end-plate composite joints. Fischer *et al.* (2017) investigated the effect of connection type and slab reinforcement type on the performance of composite beams in fire using 3-D FE models of composite beams with simple connections. Suwondo *et al.* (2019) built a 3-D Abaqus composite building model to simulate the progressive collapse of composite steel frames exposed to fire following earthquake. In the latter model, all the connections were simplified as ideally rigid or pinned connection and connection failures were not considered. The component-based model of the composite ductile connection has been previously proposed by the authors and incorporated into the

software Vulcan (Liu *et al.*, 2021). Parametric studies have been carried out on three parameters, including connection thickness, diameter of semi-cylindrical section and number of longitudinal rebars within the effective width of slab, using 2-D single composite beam models. However, structural members within a composite frame always interact with each other and work as a whole. The influence of out-of-plane structural elements, particularly slabs, on the connection performance should be taken into consideration when modelling connections within composite structures. Therefore, it is decided to build 3-D composite frame models to further investigate the fire performance of the ductile connection in composite structures.

In this paper, the design of the ductile connection and its composite component-based model have been introduced first. 3-D composite frame models with different types of connections have been built using Vulcan to compare the performance of the ductile connection in fire with other connection types, including ideally rigid and pinned connections. Finally, the central and edge secondary beams of the composite frame have been modelled using 2-D single composite beam models, and the simulation results have been compared with the results of the 3-D integrated model.

**2 DESIGN AND COMPONENT-BASED MODEL OF THE DUCTILE CONNECTION**

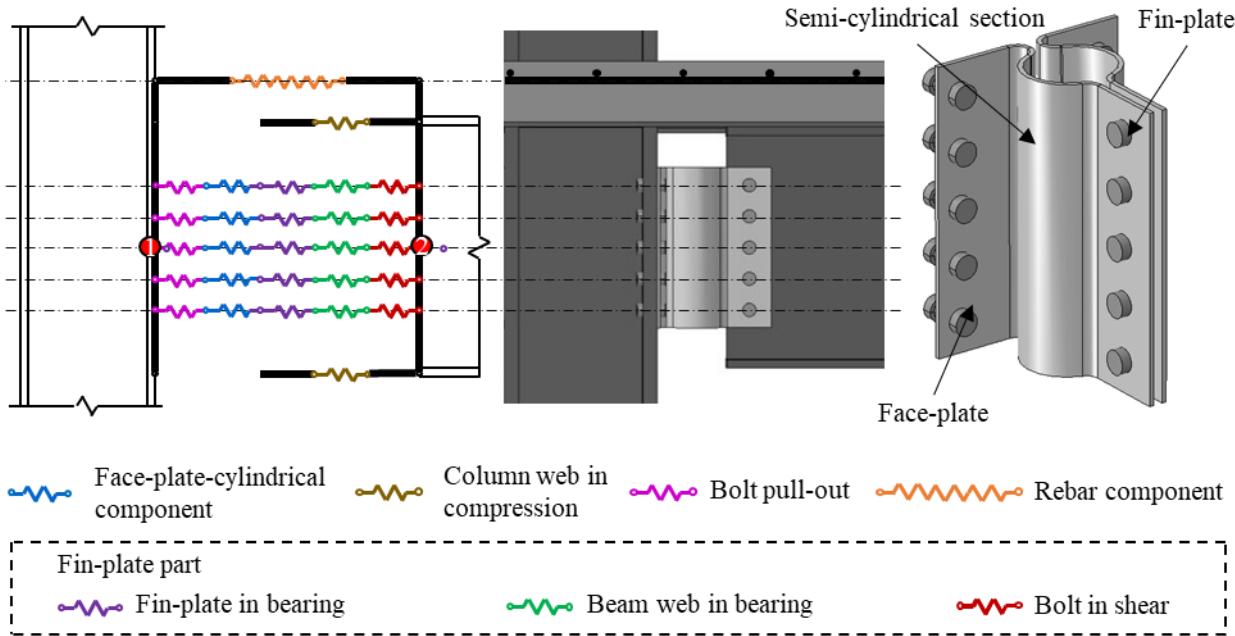


Fig. 1 The proposed ductile connection and its component-based model

The proposed ductile connection and its composite component-based model are shown in Fig. 1. This figure shows that the ductile connection consists of two identical parts, and each part takes the form of a fin-plate bolted to beam web, a face-plate bolted to column flange or column web, and a semi-cylindrical section between the fin-plate and the face-plate. The function of the semi-cylindrical section is to provide additional ductility by allowing the face-plate to move towards and away from the face-plate. Therefore, the diameter of the semi-cylindrical section is the most critical parameter when designing the ductile connection, and should be determined according to the ductility demands of connected beam. Several equations have been previously proposed by the authors to calculate the ductility demands of steel beam (Liu *et al.*, 2019b) and composite beam (Liu *et al.*, 2021) under fire conditions. Apart from the semi-cylindrical section, all the other parameters, such as plate thickness, plate height and the number of bolt rows, can be designed according to the Eurocode (CEN, 2005). It can be seen from Fig. 1 that the component-based model of the composite ductile connection includes components representing face-plate-cylindrical component, column web in compression, bolt pull-out, rebar component, fin-plate in bearing, beam web in bearing and bolt in shear. The mechanical properties of all components have been described in detail in the author's previous papers, and so they are not repeated here. The composite component-based model of the ductile connection has been

converted into a connection element following the principles of the finite element method, and incorporated into Vulcan to facilitate global frame analysis.

### 3 3-D COMPOSITE FRAME MODEL

The composite frame used in this paper to investigate the connection performance is based on the typical frame used in the Cardington full-scale fire tests (Lennon *et al.*, 1999, Wald *et al.*, 2004). The section sizes for the primary beams, secondary beams, columns and slab are shown in Fig. 2, and the dimensions of the ductile connections are shown in Fig. 3. A uniformly distributed load of 5.4 kN/m<sup>2</sup> is applied on to the slab. Several assumptions are made here:

- Full shear connection is assumed between the beam and slab;
- Fire occurs only on the lower floor;
- The central secondary beam is unprotected and its temperature is set equal to fire temperature;
- All the edge secondary beams, primary beams and lower columns have the same level of protection, and their temperatures are set to be 70% of the fire temperature;
- The upper columns remain at ambient temperature;
- The connection temperature is set to be equal to the temperature of the beam to which it is connected.

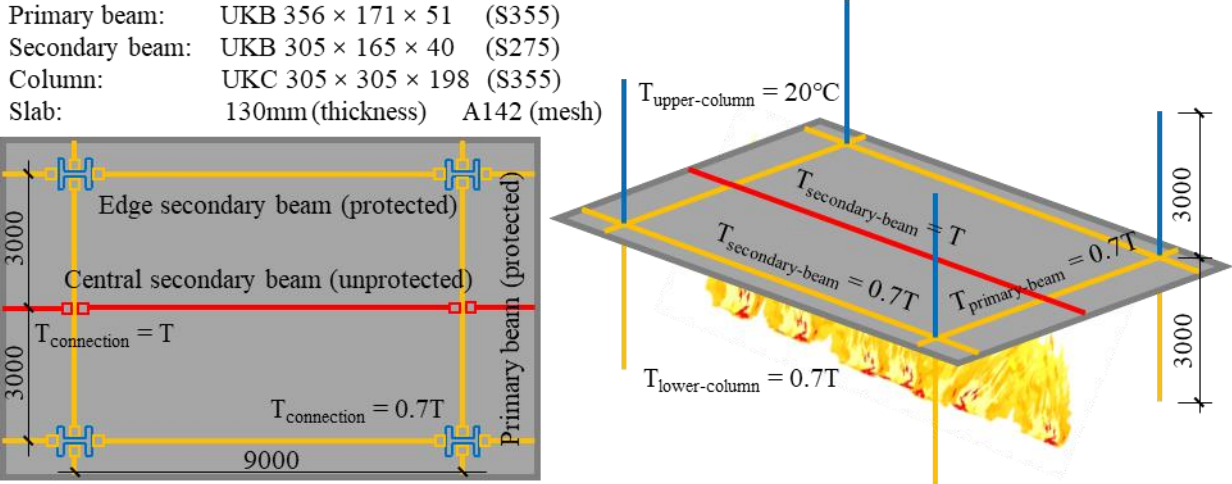


Fig. 2 Design of the composite frame

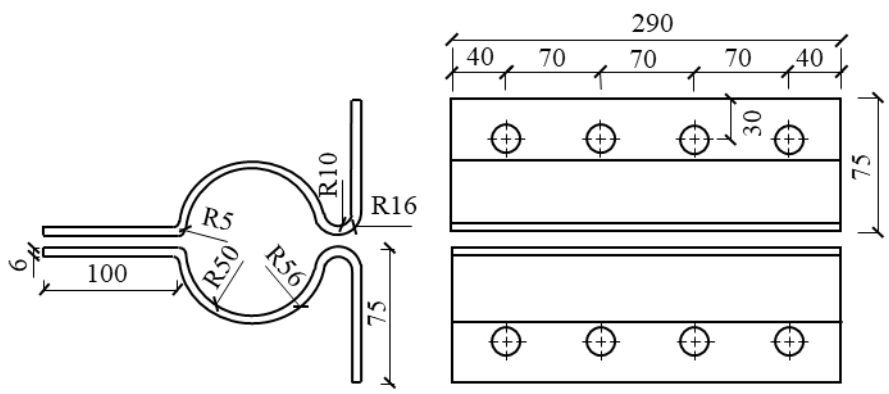
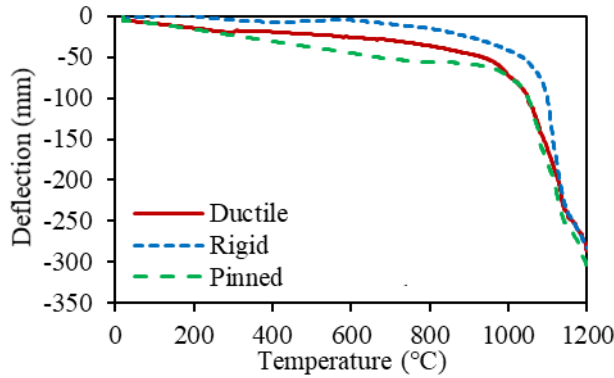


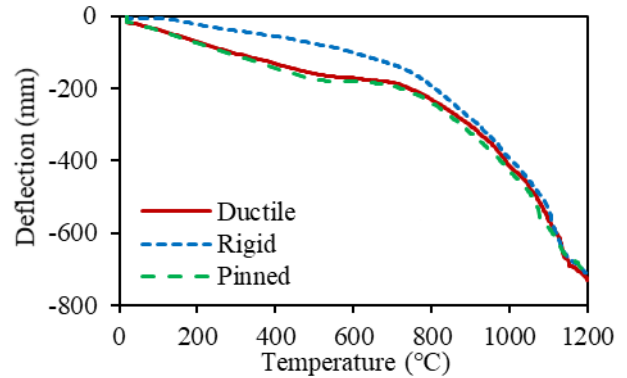
Fig. 3 Dimensions of the ductile connection

Three composite frames with different types of connection, including ductile connections, ideally rigid and pinned connections, were modelled using Vulcan. The comparison results are shown in Fig. 4, where the horizontal axes plot the temperature of the central secondary beam. Fig. 4 (a) – (c) show that the change of connection types has little effect on beam deflection. The deflection of the beam

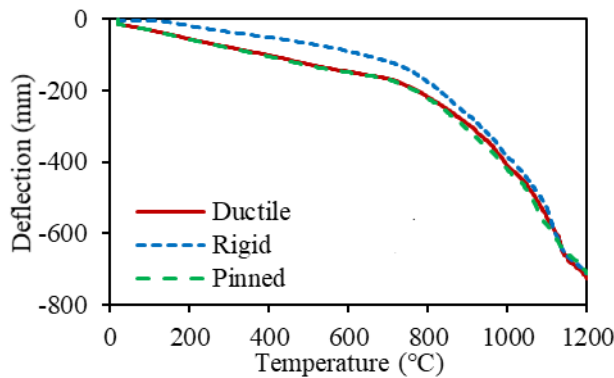
with rigid connection is generally less than that of the beam with ductile connection or pinned connection. Compared with other connection types, the axial force generated in the beam with ductile connections is significantly reduced, as shown in Fig. 4 (d) – (f). This indicates that the ductile connection has considerable axial deformability to accommodate both the net expansion of the beams during early heating and their net contraction during the high-temperature catenary stage, thus potentially preventing the premature brittle failure of the connection. Comparing the temperature at which the connection force becomes tensile, it is found that the central secondary beam enters the catenary action stage first, since it is unprotected. The primary beam enters the catenary action stage last, at nearly 1200°C. This is due to the fact that the primary beam has a larger cross section and shorter span compared with the secondary beams.



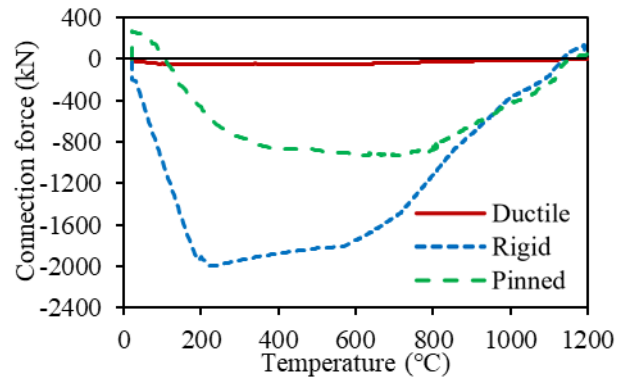
(a) Mid-span deflection of primary beam



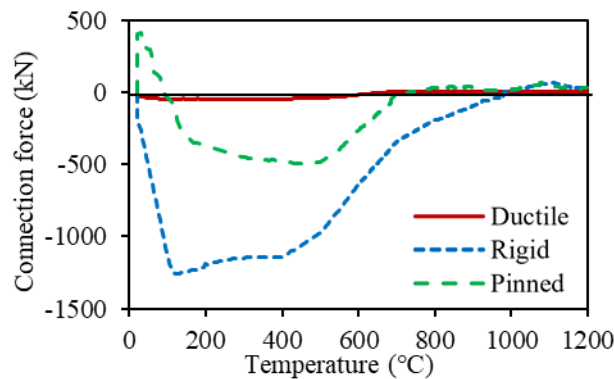
(b) Mid-span deflection of central secondary beam



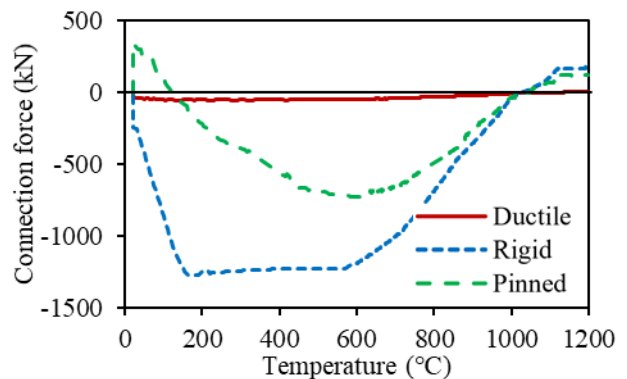
(c) Mid-span deflection of edge secondary beam



(d) Primary beam to column connection



(e) Central secondary beam to primary beam connection



(f) Edge secondary beam to column connection

Fig. 4 Comparison results (central secondary beam temperature)

## 4 COMPARISON BETWEEN 2-D AND 3-D MODELS

In this section, the central and edge secondary beams of the composite frame with ductile connections (Fig. 2) are modelled separately using 2-D Vulcan composite beam models. The width of the slab used in the single beam model is the effective width of the concrete flange of the composite beam, which is  $b_{eff} = l/4 + b_0$ , where  $b_0$  represents the width of the steel flange occupied by shear studs. The comparison results between the 2-D single beam models and 3-D integrated composite frame model are shown in Fig. 5. It is reasonable that the mid-span deflections of beams obtained from the 2-D models are greater than those of the 3-D model, as shown in Fig. 5 (a) and (b). This is because in the 3-D model, structural elements outside the plane, such as primary beam and slab, can provide support to the secondary beams and share the external loading, which cannot be simulated in a 2-D model. These two kinds of models result in similar connection forces, as shown in Fig. 5 (c) and (d). This is due to the inherent mechanical properties of the ductile connection. The maximum strength of the compressive force-displacement curve of the ductile connection can be quickly reached at a very small compressive displacement, and then the curve remains nearly horizontal, which means that the increase of the compressive displacement will lead to very little increase of the compressive force of the ductile connection (Liu *et al.*, 2020a). However, if the ductile connection is replaced by other types of connections, 2-D and 3-D models result in significant differences in the calculated connection forces. In general, the comparison between the 2-D and 3-D models confirms the importance of using 3-D modelling and considering the interactions between the structural elements of a composite steel-framed structures when investigating their fire performance.

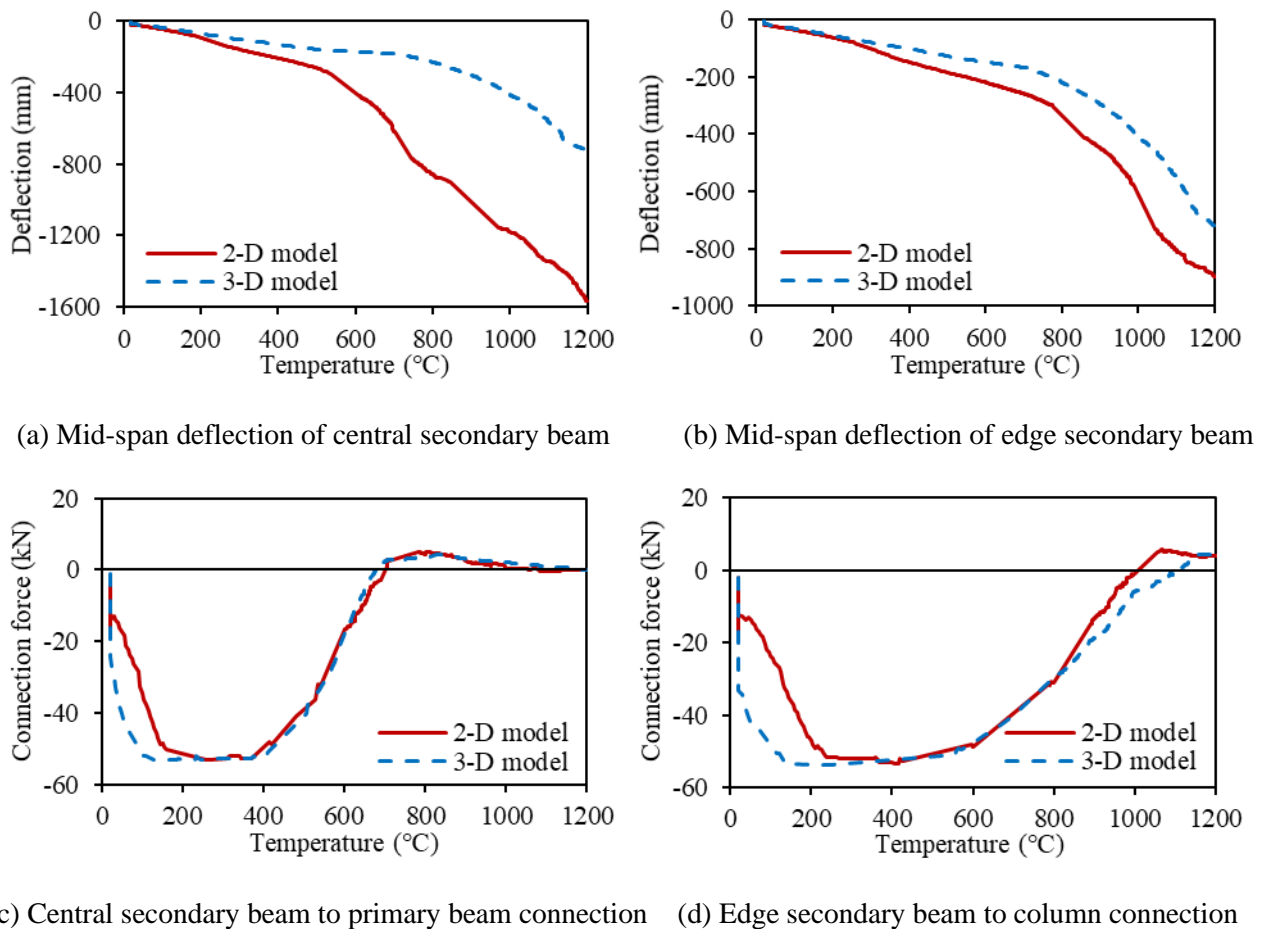


Fig. 5 Comparison between 2-D single composite beam models and 3-D integrated composite frame model

## 5 CONCLUSIONS

This paper presents an investigation of the fire performance of a novel ductile connection in composite structures, using 3-D modelling. The design and the composite component-based model of the ductile connection have been introduced first. A composite frame has been designed as similar

to the frame used in the Cardington fire tests. Three 3-D composite frame models with different connections, including the ductile connection and ideally rigid and pinned connections have been built using Vulcan to compare their performance. Results show that the ductile connection can provide additional axial ductility to accommodate the deformation of connected beam in fire, thus significantly reducing the axial force generated in the connection. This excellent deformability gives the ductile connection the ability to prevent brittle failures of connections and enhance the robustness of structures in fire. 2-D single composite beam models have also been built to simulate the central and edge secondary beams of the composite frame, separately. The mid-span beam deflection of 2-D model is larger than that of the 3-D integrated model. The comparison between 2-D and 3-D modelling shows that the influence of out-of-plane structural elements should be taken into consideration when studying the performance of connections in composite structures and therefore, 3-D modelling is recommended.

## REFERENCES

- Al-Jabri, K. S. 1999. The behaviour of steel and composite beam-to-column connections in fire. University of Sheffield.
- CEN 2005. Eurocode 3: Design of steel structures—Part 1-8: Design of joints.
- Fischer, E. C. & Varma, A. H. 2017. Fire resilience of composite beams with simple connections: Parametric studies and design. *Journal of Constructional Steel Research*, 128, 119-135.
- Lennon, T., Moore, D. & Bailey, C. 1999. The behaviour of full-scale steel-framed buildings subjected to compartment fires. *The Structural Engineer*, 77, 15-21.
- Li, J.-T., Li, G.-Q., Lou, G.-B. & Chen, L.-Z. 2012. Experimental investigation on flush end-plate bolted composite connection in fire. *Journal of Constructional Steel Research*, 76, 121-132.
- Liu, Y., Huang, S.-S. & Burgess, I. 2019a. Ductile connections to improve structural robustness in fire. *Proceedings of the 6th Applications of Structural Fire Engineering Conference (ASFE'19)*, 2019a Singapore. Nanyang University of Technology
- Liu, Y., Huang, S.-S. & Burgess, I. 2019b. Investigation of a steel connection to accommodate ductility demand of beams in fire. *Journal of Constructional Steel Research*, 157, 182-197.
- Liu, Y., Huang, S.-S. & Burgess, I. 2020a. Component-based modelling of a novel ductile steel connection. *Engineering Structures*, 208, 110320.
- Liu, Y., Huang, S.-S. & Burgess, I. Investigation of the performance of a novel ductile connection within bare-steel and composite frames in fire. *Proceedings of the 11th International Conference on Structures in Fire (SiF2020)*, 2020b Australia, Queensland. The University of Queensland, 662-672.
- Liu, Y., Huang, S.-S. & Burgess, I. 2020c. Performance of a novel ductile connection in steel-framed structures under fire conditions. *Journal of Constructional Steel Research*, 169, 106034.
- Liu, Y., Huang, S.-S. & Burgess, I. 2021. Fire performance of axially ductile connections in composite construction *Fire Safety Journal*, 103311.
- Suwondo, R., Cunningham, L., Gillie, M. & Bailey, C. 2019. Progressive collapse analysis of composite steel frames subject to fire following earthquake. *Fire safety journal*, 103, 49-58.
- Wald, F., Silva, S., Moore, D. & Lennon, T. Structural integrity fire test. *Proceedings Nordic Steel Conference*, 2004.

# THE DESIGN OF MOMENT CONNECTIONS FOR IMPROVED POST-FIRE SEISMIC PERFORMANCE

C. Maraveas, D. Pantousa, T.L. Karavasilis

Steel Structures Lab, Department of Civil Engineering, University of Patras, Patra, Greece

## Abstract

The criteria for selecting steel structures for post-fire reuse are simplified. A key consideration is the impact of elevated temperatures (fire) on the material properties and steel geometry. Another concern relates to poor understanding of the post-fire performance of steel under seismic loading, when cyclic loading, plastic-hinge formation and other similar effects are developed. The research explored the post-fire cyclic performance of unprotected beam-column connections. The steel connections are exposed to different fire scenarios based on standard and natural fire curves, resulting in modification of material properties and deformations. The deformations are limited to code defined limits for reinstatement. The post-fire performance under monotonic and cyclic loading was reviewed and compared with pre-fire performance using numerical simulations. The outcomes yielded useful insights about the design of moment connections for improved post-fire performance.

**Keywords:** Post-fire, Steel Structures, Moment Connections, Cyclic performance, Reinstatement

## 1 INTRODUCTION

The investigation of the seismic performance of steel structures has gained traction in the last decade through technology-driven numerical and experimental investigations of steel structures. The approach translated to the development of earthquake-resistant steel structures that exhibit limited structural and non-structural damage after seismic loading and potential application after earthquakes. The seismic performance has been augmented by extensive research on the performance of steel structures under fire attack, resulting in improved design methods for fire resistance of steel structures. However, post-fire reinstatement has not been widely studied, especially when the structure is built in earthquake-prone areas, resulting in exhaustive loading and plastic deformations. The safe post-fire reuse is important for the building owner/user (business continuation and repair cost.) as well as for estimating the insurance company compensations and premiums.

A majority of steel structures exposed to fire do not collapse and suffer limited structural damage; this increases the potential for reuse after exposure to fire. The One Meridian Plaza, Philadelphia, USA (1990) (USFA-TR-049, 1991), Churchill Plaza at Basingstoke (2005) (Wang, 2002), and Broadgate, London (1990) (P113, 1991) are cases in point. Following the Broadgate fire, investigations were undertaken, and it was confirmed that structural elements were not fireproofed and the active firefighting systems were not active during construction. Even though the fire lasted for nearly five hours under extreme temperatures (1000 °C), the performance of the steel structures was less impacted. Since the structural damage was minimal, the repairs were completed within a short period of time.

The reinstatement of steel structures after the fire event has key implications for post-fire deformations and the residual mechanical properties. According to previous studies, although the mechanical properties of steel are reduced at elevated temperatures, they can be recovered after cooling down to room temperature (Outinen *et al.*, 2004; Lee *et al.*, 2004; Tao *et al.*, 2013; BS5950-8, 2003; Cooke, 1998; Li *et al.*, 2003). The recovery level is a function of several parameters, including maximum temperature during heating, rate of cooling, the chemical composition of steel, thermal treatment of steel during production (Maraveas *et al.*, 2017a). Upon cooling, the residual mechanical properties of high strength steel and bolts show higher degradation than ordinary steel

due to thermal treatment of steel during production (Maraveas *et al.*, 2017a; Maraveas *et al.*, 2017b).

The reinstatement of steel structures is grounded on simplified criteria guided by literature (Tide, 1998; Kirby *et al.*, 1986; Smith *et al.*, 1986; Maraveas *et al.*, 2017a) and design codes (BS5950-8, 2003), which propose the reuse of steel structures after a fire. The proposal is only applicable in cases when the deformations are low. In addition, the specific limits of displacements and rotations are delineated. A fundamental question is whether the reuse of steel structures according to the simplified criteria is safe for accidental load combinations, like earthquake loading combinations.

The steel structures designed for high earthquake loads can survive a fire attack without considerable damage. Due to design against extreme seismic loads, the cross-sections are thick for better critical temperature and fire resistance. Furthermore, their load ratio is low. Based on the simplified criteria, these steel structures can be repaired and reused, even if the post-fire performance to earthquake loading has not been studied. The seismic performance is affected by the following parameters; mechanical properties of steel after exposure to elevated temperatures and cooling down, and post-fire residual deformations.

Critical structural elements for the performance of steel structures under seismic loading are moment beam-column connections, which are severally affected by post-fire degradation of mechanical properties of bolts (Maraveas *et al.*, 2017a; Maraveas *et al.*, 2017b; Maraveas *et al.*, 2021a; Maraveas *et al.*, 2021b) investigated the seismic post-fire performance of a number of moment beam-column connection. The connections with the critical design component of the bolts (according to EN1998-1-8, 2005) were severely affected by fire in terms of moment resistance, stiffness and energy dissipation. This paper investigates proper methods for improved post-fire performance of such moment connections—especially the effect of over-design of connections on bolts' steel grade and diameter.

## **2 NUMERICAL SIMULATIONS' METHODOLOGY AND VALIDATION**

### **2.1 Simulation methodology and analysis parameters**

In order to predict the post-fire cyclic performance of moment beam-column connections and the fire effect to cycle loading performance, the seven steps were chosen:

1. Development of the numerical connection model, including local imperfections ( $b/100$  according to Maraveas *et al.*, 2017c) and residual stresses (according to BSK 99 (Abambres *et al.*, 2016).
2. Monotonic/cyclic loading of the connection following a specific applied displacement history for comparison reasons.
3. Perform coupled thermal – structural analysis. Three sides exposure of beam considered. During thermal analysis, a firing curve (standard fire curve or extreme parametric fires according to EN1991-1-2, 2015) is applied. The fire curve is cooling down when the post-fire displacements and rotations are near the limits per BS 5950-8, 2003. In order to approach the displacement or rotation limit, trial and correct rounds of analysis are repeated.
4. For the post-fire analysis, the maximum temperature developed in each node is set up as the initial temperature. The post-fire residual geometry from the coupled thermal-structural is used.
5. The post-fire residual mechanical model for structural steel and bolts is implemented according to Maraveas *et al.*, 2017a.
6. The thermal expansion coefficient is given as zero.
7. Monotonic /Cyclic analysis is performed for the post-fire connection is performed and compared with the pre-fire performance of the connection. The used methodology is shown as a flowchart in Figure 1.

### **2.2 Validation against experimental results**

The validation of numerical models against experimental results from the literature. The validation against experimental results presented by ElSabbagh *et al.*, 2019 were specific to simulation

connections under cyclic loading. The validation against experimental results presented by Santiago, 2008 and Santiago et al., 2010 focused on thermal and structural analysis of connections under fire. Detailed information is presented in Maraveas et al., 2021b.

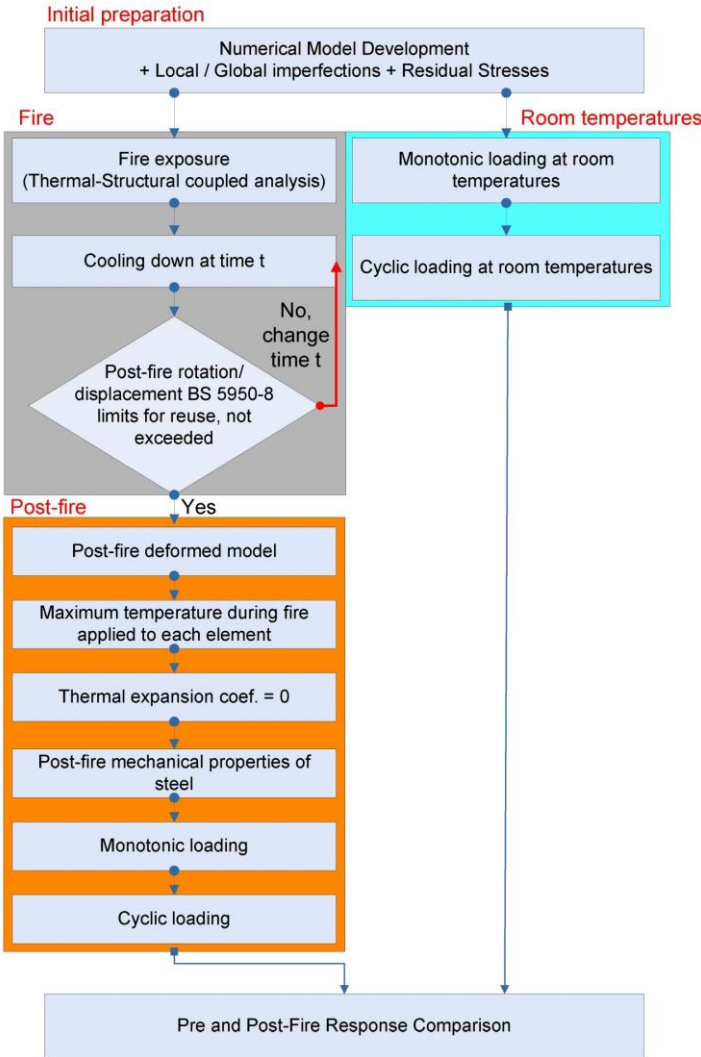


Fig. 1 Flowchart of applied methodology (Maraveas et al., 2021b)

### 2.3 Geometry of studied connection and proposed modifications

The studied connection is presented in Fig. 2. Two modifications examined in order to assess their post-fire performance. First, the bolts steel grade modified to 10.9 and second, the diameter of bolts changed to M22.

## 3 SIMULATION RESULTS

### 3.1 Temperatures during fire exposure

The developed temperatures on steel members and bolts are shown in Fig. 3. For standard fire exposure, the temperatures of bolts exceed 500 °C while steel approached 700 °C. For fast fire exposure, the maximum temperatures were similar. For slow fire exposure, the developed temperatures were lower than standard and their effect on the post-fire performance of the connections limited.

### 3.2 Post-fire monotonic performance

The analysis of the examined steel connection for (a) increased bolt grade and (b) increased bolt diameter is shown in Fig. 4. From these graphs, it can be seen that when the steel grade is increased,

the post-fire moment capacity increased too, but stiffness does not considerable change. Similarly, when the bolt diameter increased, similar performance obtained.

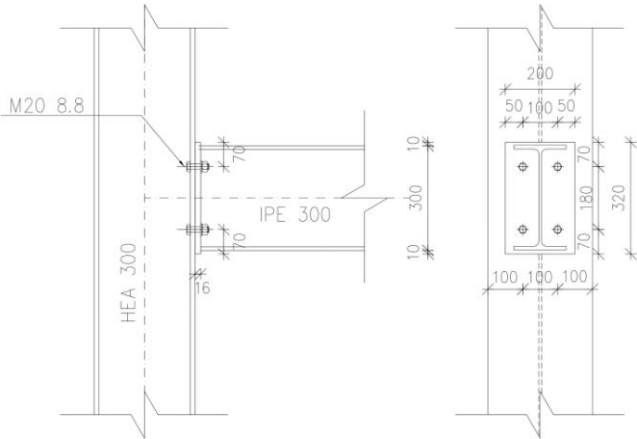


Fig. 2 Studied connection (Maraveas et al., 2021b)

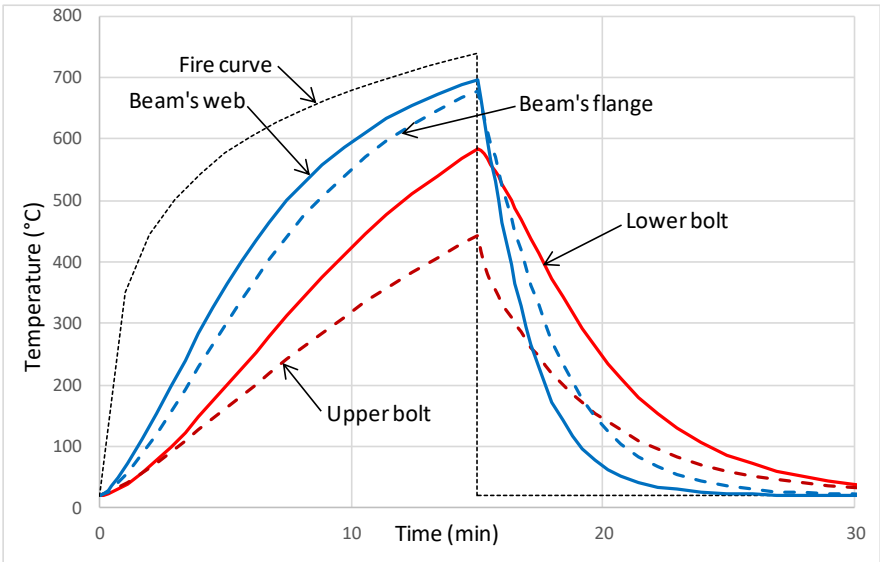


Fig. 3 Temperatures on steel and bolts for Standard fire exposure (Maraveas et al., 2021b)

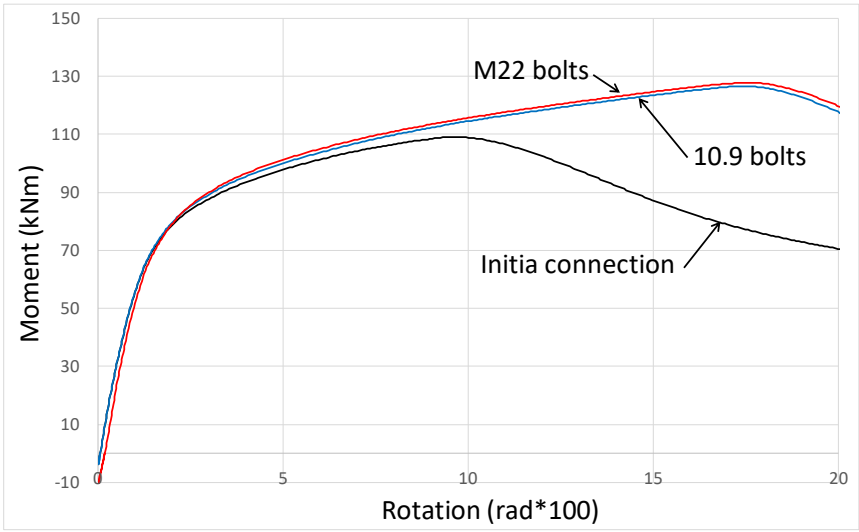


Fig. 4 Post-fire moment-rotation monotonic diagrams of connection as in Fig. 2 compared with same connection with steel bolts' grade 10.9 and with bolts' diameter M22

### 3.3 Post-fire cyclic performance

The post-fire cyclic loaded performance of the studied connections with proposed modifications are presented in Fig. 5. The performance for increased bolt diameter does not have any change, but the performance for increased bolt grade is improved in terms of energy dissipation.

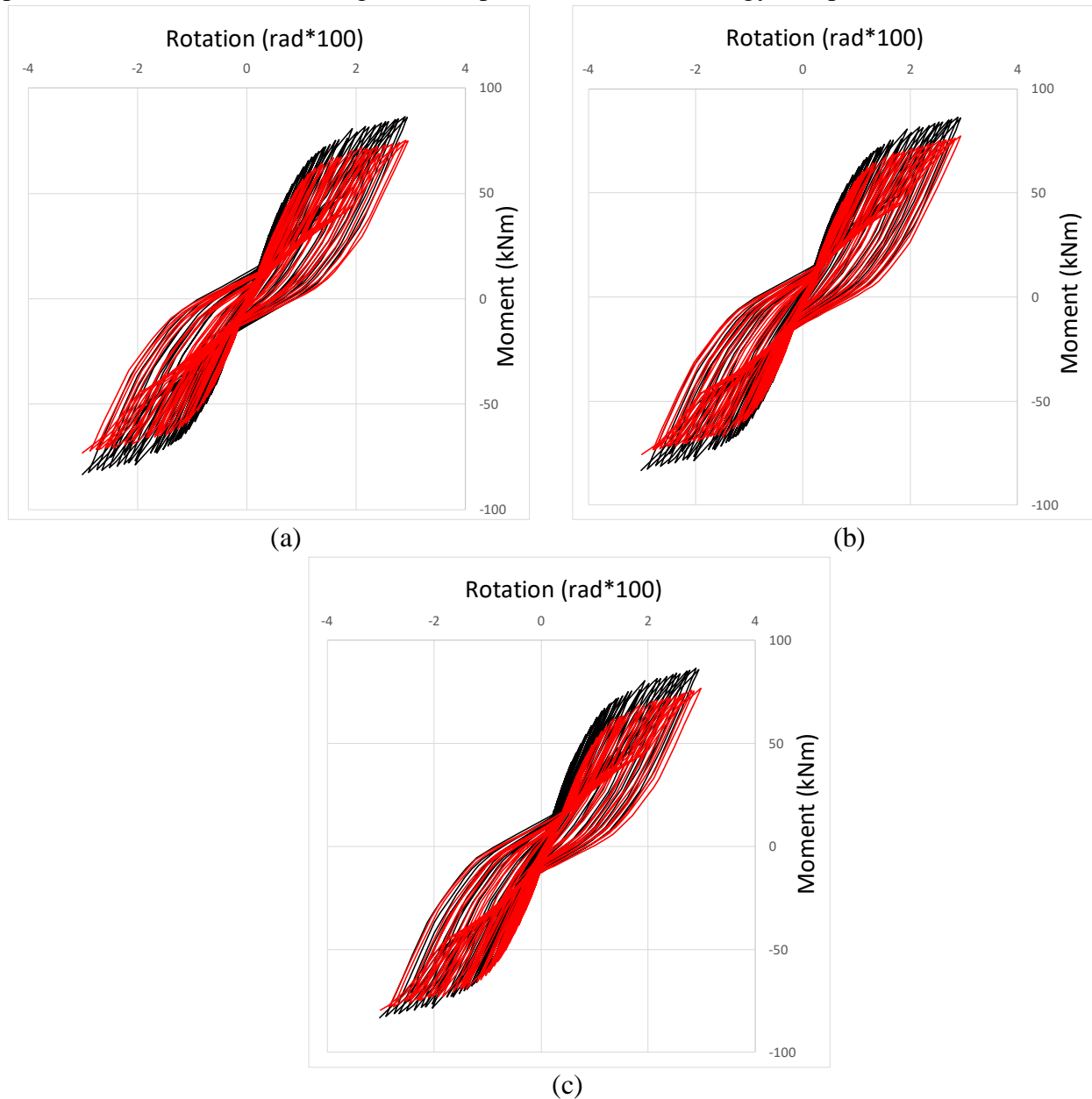


Fig. 5 Post-fire moment-rotation cyclic diagrams of connection (a) as in Fig. 2, (b) with bolts' grade 10.9 and (c) with bolts' diameter M22 vs the pre-fire response of the connection (black lines) of Fig. 2

## 4 CONCLUSIONS

This paper presents initial research on possible design improvements of steel moment connections for post-fire reinstatement without replacing the bolts. Extensive numerical simulations performed with the use of the novel methodology. The over-design of bolts to reduce the fire effects on the connection and achieve improved moment capacity, stiffness and energy dissipation during an earthquake was noted. The bolts changed to 10.9 - a grade higher than the initial design- and the post-fire moment capacity was increased, but in terms of stiffness, there was limited improvement. The increase in bolts' diameter from M20 to M22, improved the post-fire moment capacity but the stiffness improvement and energy dissipation under cyclic loading was limited. Given the limitations of this research (only one connection was analysed), there is a need for further investigations.

## ACKNOWLEDGMENTS

This research was funded in the context of the project “(S-S-F-Reuse) Post-fire seismic performance of steel structures and reuse criteria” (MIS 5047150) under the call for proposals “Support to researchers with emphasis to young researchers – Part B” (EDBM103). The project is co-financed by Greece and the European Union (European Social Fund- ESF) and the Operational Programme Human Resources Development, Education and Lifelong Learning 2014-2020.

## REFERENCES

- Abambres M., Quach W.-M., 2016. *Residual stresses in steel members: a review of available analytical expressions*, International Journal of Structural Integrity, 7(1), p. 70-94.
- BS 5950-8, 2003. *Structural use of steelwork in building, Part 8: Code of Practice for Fire Resistant Design*, London: B.S. Institution.
- Cooke G.M.E., 1998. *An introduction to the mechanical properties of structural steel at elevated temperatures*, Fire Safety Journal, 13(1), p. 45-54.
- Sabbagh A., Sharaf T., Nagy S., ElGhandour M., 2019. The behaviour of extended end-plate bolted connections subjected to monotonic and cyclic loads, Engineering Structures, 190, p. 142-159.
- EN 1993-1-2, 2005. *Eurocode 3: Design of steel structures, Part 1-2: General rules - structural fire design*, Brussels: European Committee of Standardization (CEN).
- EN 1993-1-8, 2005. *Eurocode 3: Design of steel structures - Part 1-8: Design of joints*, Brussels: European Committee for Standardization (CEN).
- Kirby B. R., Lapwood D., Thompson G., 1986. *The reinstatement of fire damaged steel and iron-framed structures*, British Steel Corporation, Swindon Laboratories, Swindon, U.K.
- Lee J., Engelhardt M., Taleff E., 2012. *Mechanical properties of ASTM A992 steel after the fire*, Engineering Journal, 49(1), p. 33-44.
- Li Q.-G., Jiang S.-C., Yin Y.-Z., Chen A., Li M.-F., 2003. *Experimental Studies on the Properties of Constructional Steel at Elevated Temperatures*, Journal of Structural Engineering, 129(12), p. 1717-1721.
- Maraveas C., Fasoulakis Z., Tsavdaridis K. D., 2017a. *Post-fire assessment and reinstatement of steel structures*, Journal of Structural Fire Engineering, 8(2), p. 181-201.
- Maraveas C., Fasoulakis Z., Tsavdaridis K. D., 2017b. *Mechanical properties of high strength and very high strength steel at elevated temperatures and after cooling down*, Fire Science Reviews, 6(3).
- Maraveas C., Gernay T., Franssen J.M., 2017c. *Sensitivity of elevated temperature load-carrying capacity of thin-walled steel members to local imperfections*, in Applications of Fire Engineering, Proceedings of the International Conference of Applications of Structural Fire Engineering (ASFE 2017), Manchester, U.K.
- Maraveas C., Sofianopoulos D.S., 2021a. *The behaviour of steel beam-to-column connections in fire*, 10<sup>th</sup> Hellenic National Conference of Steel Structures, Athens, Greece.
- Maraveas C., Pantousa D., Karavasilis T.L., 2021b. *Post-fire cyclic loading performance of unprotected beam-column moment connections*, Journal of Building Engineering (Under Review)
- Outinen J., Makelainen P., 2004. *Mechanical properties of steel at elevated temperatures and after cooling down*, Fire and Materials, 28, p. 237-251.
- P 113, 1991. *Investigation of Broadgate Phase 8 fire*, Ascot: The Steel Construction Institute.
- Santiago AMC, 2008. *The behaviour of beam-column steel joints under natural fire*, PhD Thesis, Universidade de Coimbra, Portugal.
- Santiago, A., Simões da Silva, L., Vila Real, P., 2010. *Numerical Modelling of the Influence of Joint Typologies on the 3D Behaviour of a Steel Sub-Frame Under a Natural Fire*, Fire Technology, 46, p. 49-65.
- Smith C.I., Kirby B.R., Lapwood D.G, Cole K.J., Cunningham A.P., Preston R.R., 1981. *The reinstatement of fire damaged steel-framed structures*, Fire Safety Journal, 4(1), p. 21-62.
- Tao Z., Wang X., Uy B., 2013. *Stress-strain curves of structural and reinforcing steel after exposure to elevated temperatures*, Journal of Materials in Civil Engineering, 25(9), p. 1306-1316.
- Tide RHR, 1998. *The integrity of structural steel after exposure to fire*, Engineering Journal, 35(1), p. 26-38.
- USFA-TR-049, 1991. *Highrise Office Building Fire One Meridian Plaza*, Philadelphia, Pennsylvania: U.S. Fire Administration, FEMA.
- Wang Y.C., 2002. *Steel and Composite Structures: Behaviour and Design for Fire Safety*, CRC Press.

## THE IMPACT STRENGTH OF SELECTED STEEL TYPES AFTER FIRE Experimental tests related to simulated fire conditions

Mariusz Maslak<sup>a</sup>, Michal Pazdanowski<sup>a</sup>, Marek Stankiewicz<sup>a</sup>, Paulina Zajdel<sup>a</sup>

<sup>a</sup> Cracow University of Technology, Faculty of Civil Engineering, Cracow, Poland

### Abstract

The results of the research on the change in the value of the breaking energy KV, conducted for selected steel grades used in building structures on the basis of the Charpy impact test, are presented. These changes were recorded in relation to the initial state, after the samples were subjected to a simulated fire exposure in the steady-state heating regime and then cooled down. The S355J2+N, 1H18N9T steels and also X2CrNiMoN22-5-3 duplex steel were selected for detailed analysis. The fire conditions were simulated by heating the samples and then keeping them for a specified time at a constant temperature of: 600°C (first series) and 800°C (second series), respectively. Two alternative cooling variants were investigated in the experiment: slow open air cooling of the samples, simulating the natural fire progress, without any external extinguishing action, and cooling in water mist simulating an extinguishing action by a fire brigade.

**Keywords:** fire, structural steel, steady-state heating regime, impact test, breaking energy.

## 1 INTRODUCTION

The suitability assessment of structural steel for further use after a fire will be reliable only when the analysis would take into account the potential permanent changes which may have occurred in its microstructure as a result of high temperature fire plume acting on it [Maslak, Zwirski, 2017]. Those changes should be associated in general with significant increase in brittleness observed after cooling down of the material, and this is related with a risk of unconstrained initiation and subsequent violent propagation of brittle fractures [Kharchenko et al., 2006]. This in turn may result in sudden and unexpected, and thus very dangerous to the user, failure of the bearing structure. In our research the susceptibility of steel to the occurrence of brittle cracks after fire has been verified by Charpy impact test [Alar et al., 2015]. The action of fully developed fire has been simulated by appropriate conditioning of the samples. Prior to testing the samples have been subjected to thermal treatment of formalized course. At the first stage of this process the samples have been heated with constant speed until they have reached the temperature of 600°C (first series) or 800°C (second series), then kept in this temperature for 60 minutes, according to the conventional steady state heating regime (Fig. 1).

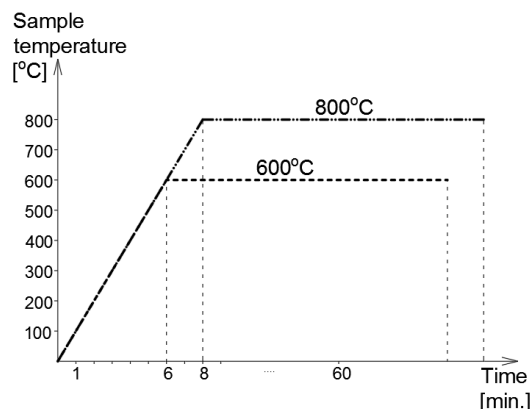


Fig. 1 Fire action simulated during research

After heating the samples have been cooled until they reached room temperature. During this research, for comparative reasons two alternative cooling regimens have been considered: free cooling of the samples in the open air, simulating self-extinguishing of a fire, and cooling in the water mist, corresponding to the intervention of fire brigade. The following steels, frequently used in the construction industry have been selected for detailed analysis:

- **S355J2+N** steel – low alloy, two phase, ferritic-perlitic, subjected to normalization,
- **1H18N9T** steel – high alloyed Ni-Cr, single phase, acid-resistant, supersaturated with a temperature of approximately 1100°C,
- **X2CrNiMoN22-5-3** steel – high alloyed, two phase, austenitic-ferritic, of duplex type, supersaturated with a temperature of approximately 1050°C in water.

These steels have been considered as representative for the whole groups of steels used in the construction industry with respect to the expected results of research conducted by us.

## 2 THE CONDUCT AND INTERPRETATION OF THE IMPACT STRENGTH EXPERIMENT

The impact strength tests on the prepared samples have been conducted according to the recommendations of the code EN ISO 14556 on an instrumented JB-W450E-L Charpy pendulum, having the potential energy of 450 J. The R8 (American type) pendulum hammer has been selected for the tests, as it is understood that in construction industry an impact by a flat surfaced object is more probable (with respect to the classical R2 pendulum hammer of European type). The destructive tests have been conducted in the temperature of +20°C (simulating summer conditions) and alternatively in the temperature of -20°C (to simulate winter conditions). Each time the curve depicting the relation between force  $F$  [kN] acting on the broken sample and displacement  $s$  [mm] of this force application point was registered. This curve unequivocally corresponds to the relation between the breaking work  $W_t$  [J] (usually interpreted as the energy dissipated during breaking of the sample) and such the displacement. In addition, the lateral expansion  $LE$  [mm] of broken samples has been measured as well. Due to the high number and random character of obtained results in each measurement station, these results have been averaged and subsequent analyses have been conducted on averaged graphs  $F=F(s)$  and  $W_t=W_t(s)$  and also on the lateral expansion  $LE$  value averaged over measurements taken. The obtained results have been archived, using three digit notation scheme, with consecutive digits interpreted as shown in table 1. The sample denoted with single digit 1, 2 or 3 in this notation denotes the initial state of the analyzed steel (a sample which did not undergo the preliminary heat treatment).

Table 1 Description mode of the samples subjected to impact testing

First digit of the description – steel grade	Second digit of the description – heating temperature	Third digit of the description – cooling mode	Additional information – test temperature
<b>1</b> – S355 <b>2</b> – 1H18N9T <b>3</b> – X2CrNiMoN22-5-3	<b>6</b> – 600°C <b>8</b> – 800°C	<b>0</b> – free cooling in the open air <b>1</b> – cooling in water mist	+20°C -20°C

Six full size ISO Charpy V-10 impact test samples have been conducted on steels S355J2+N and 1H18N9T. In the case of X2CrNiMoN22-5-3 duplex steel the samples had to be reduced in size to ISO Charpy V-7.5, as the potential energy of the 450 J pendulum proved to be insufficient to break these samples both in the initial state, as well as after heating simulation conducted in the temperature of 600°C during one hour, with rapid cooling in water mist. Examination of the notch profile of samples in the initial state on a notch profile projector XT-50, has shown that the notches made were located just below the upper tolerance limit specified in the standard EN-ISO 148-1. Subsequent analysis of the notches in the same samples after heat treatment and removal of the scale formed as a result of oxidation of steel surface has shown increase in the size of notches, so in

several cases their size exceeded the allowed tolerance. According to the provisions of the standard ASTM E23-92, changes of this type may result in an increase in the breaking energy by at most 2÷3 J in brittle samples and by a negligible value in ductile samples. The scale observed on samples made of S355J2+N steel was loosely bonded to the substrate, while on the samples made of 1H18N9T and also of X2CrNiMoN22-5-3 steels it formed a tight top layer.

### 3 DISCUSSION OF OBTAINED RESULTS

#### 3.1 S355J2+N steel

The averaged results obtained for this steel in the temperature of +20°C are depicted in Fig. 2a, while those obtained in the temperature of -20°C are depicted in Fig. 2b, correspondingly. The first of these results correspond to the F type curve (according to EN ISO 14556), denoting plastic zone devoid of unstable crack growth zone, while the second correspond to the D type curve, unequivocally revealing zone of this type and cracking followed by plastic self-restraint.

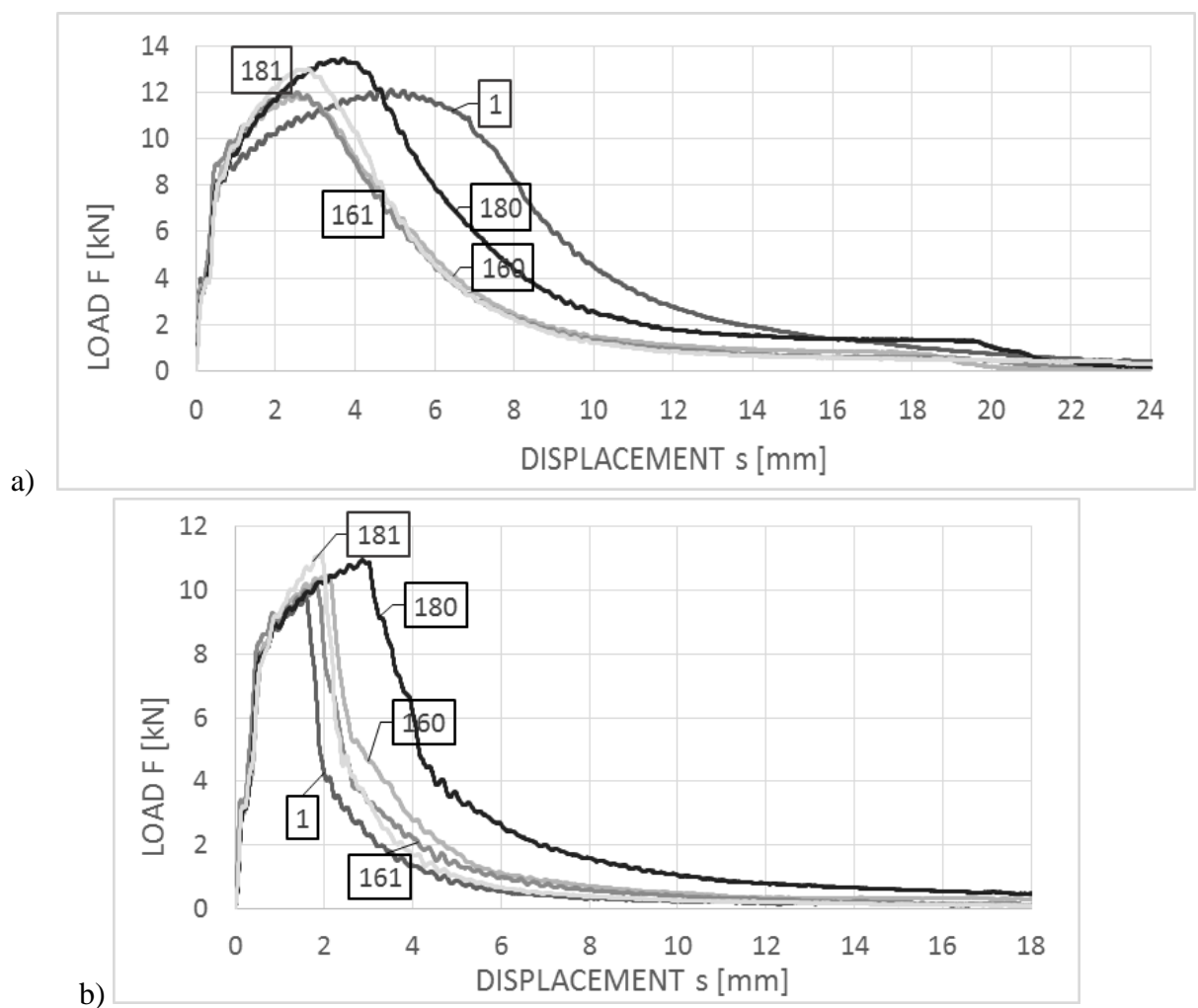


Fig. 2 Averaged F-s curves obtained on samples made of S355J2+N steel: a) tests conducted in +20°C, b) tests conducted in -20°C.

The analyzed steel in the initial state and in the temperature +20°C (Fig. 2a – specimen 1) exhibited higher values of breaking energy (117 J) and lateral expansion LE (1,94 mm) with respect to the remaining samples made of the same steel and subjected to preliminary heat treatment. In the case of experiments conducted in the temperature of -20°C the opposite proved to be true. Both breaking energy (26 J) and lateral expansion LE (0,56 mm) in the initial state (Fig. 2b – specimen 1) proved to be smaller than those obtained on the samples subjected to heat treatment. The cooling mode significantly differentiated the behaviour of analyzed samples subjected to heat treatment in the

temperature of 800°C, with respect to impact strength tests conducted both in the temperature of +20°C as well as in the temperature of -20°C. The heating of this type usually results in partial austenitic change in the steel structure. The following slow cooling in the open air (sample 180) leads under those circumstances to the development of structure containing spheroidal carbides uniformly distributed in the ferritic lattice, and this results in increased plasticity and impact strength. Fast cooling with water (sample 181) resulted in carbon oversaturation of a part of ferrite formed from austenite and hardening of steel, and thus decreased plasticity and impact strength. This phenomenon has not been observed on samples heated to 600°C only. The shapes of curves associated with samples 160 and 161 were very close, as can be observed on both Fig. 2a and Fig. 2b. For the reasons listed above the results obtained for the specimens denoted with 180, regardless of the temperature at which the impact test has been made, definitely stood out from all other simulations conducted for this steel. The remaining scenarios, both those associated with the heating temperature of 600°C (regardless of the cooling mode), and the heating temperature of 800°C followed by cooling with water yielded similar results expressed by similar shape of the  $F=F(s)$  curves and thus estimated values of the breaking work ( $60\div 74$  J at +20°C and  $31\div 35$  J at -20°C, respectively) and lateral extension LE ( $1.05\div 1.37$  mm at +20°C and  $0.73\div 0.89$  mm at -20°C, respectively).

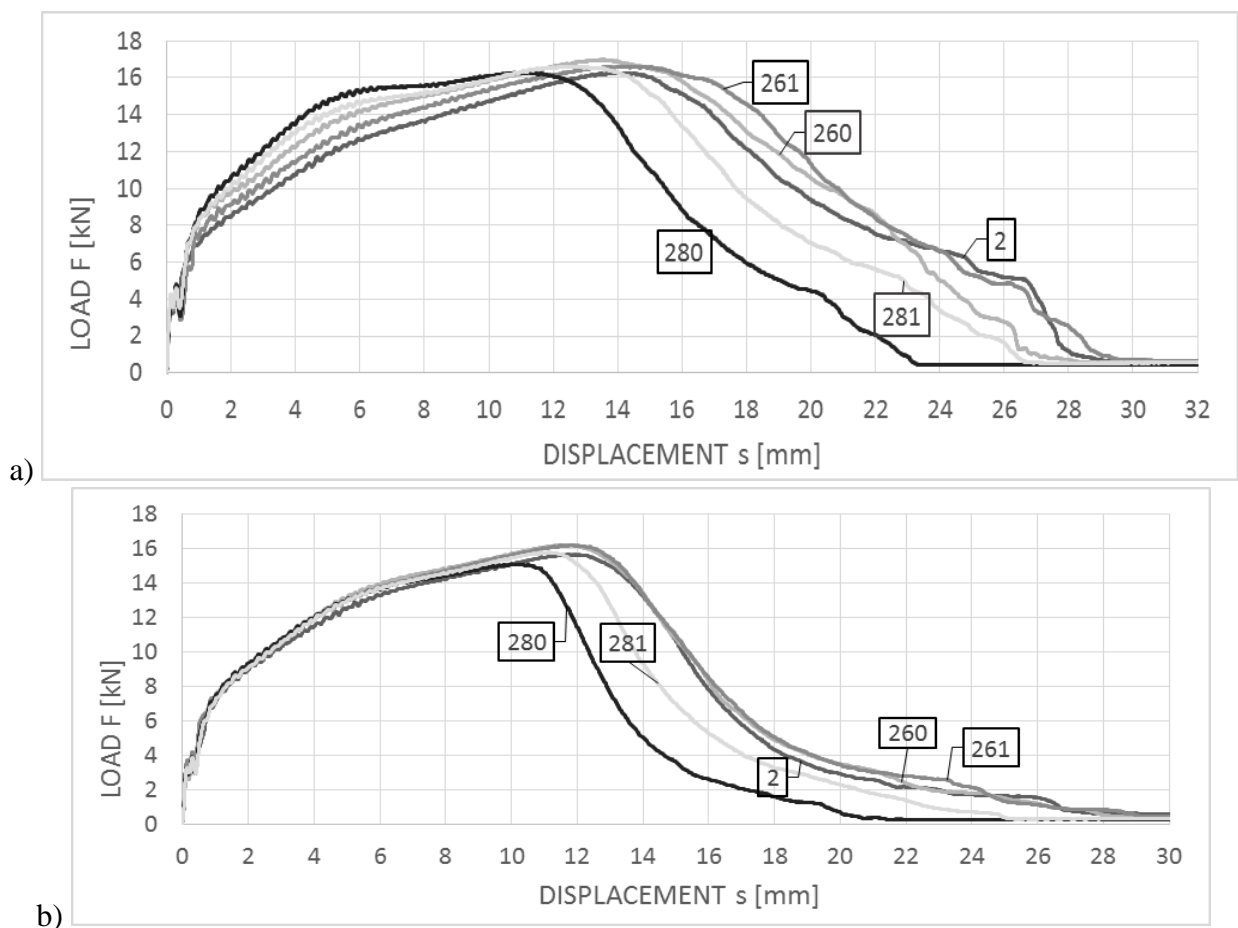


Fig. 3 Averaged  $F-s$  curves obtained for samples made of 1H18N9T steel: a) tests conducted in +20°C, b) tests conducted in -20°C.

### 3.2 1H18N9T steel

Averaged results obtained for this steel are depicted in Fig. 3a with respect to the impact strength tests conducted in the temperature of +20°C, and Fig. 3b – with respect to the analogous tests conducted in the temperature of -20°C. The curves depicted in both figures this time correspond to the F type curves (according to EN ISO 14556), with plastic zone devoid of unstable crack growth area. All the samples made of this steel regardless of the testing temperature are characterized by a

fully plastic fracture. The breaking work value obtained during the tests conducted in +20°C remained within the span of 251÷330 J, while the same work obtained during tests conducted in -20°C remained within the span of 171÷240 J. The obtained values of lateral extension LE remained within 1.51÷1.94 mm (obtained at the temperature of +20°C) and 1.77÷2.00 mm (obtained at the temperature of -20°C). The largest decrease in the breaking work with respect to the untreated material has been observed for this specimen (sample 2) in heating scenarios assuming heating up to 800°C. This temperature is located in the upper limit of the harmful  $\sigma$  phase precipitation range in the 18/9 class austenitic steels. Slow cooling from this level (sample 280) results in a relatively long transfer time of this steel through the zone associated with precipitation of the harmful phase. Fast cooling with water (sample 281) results in freezing of the microstructure with lower content of the phase  $\sigma$ , and thus lower reduction of the breaking work.

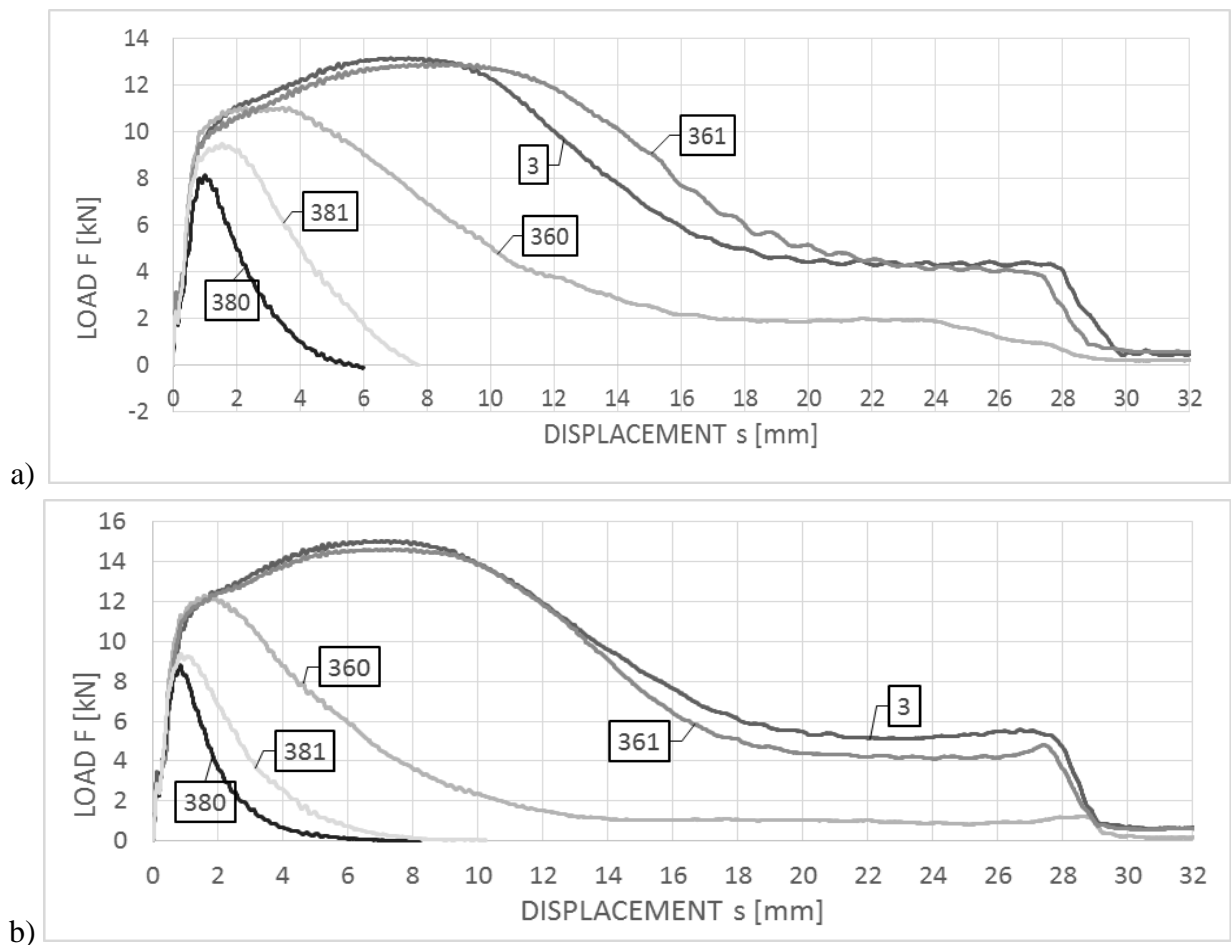


Fig. 4 Averaged F-s curves obtained for samples made of X2CrNiMoN22-5-3 steel: a) tests conducted in +20°C, b) tests conducted in -20°C.

### 3.3 X2CrNiMoN22-5-3 steel

The averaged impact strength tests authoritative for this steel are juxtaposed in Fig. 4a with respect to the tests conducted in +20°C, and Fig. 4b with respect to the tests conducted in -20°C. Both sets of curves may be classified as belonging to the type F (according to EN ISO 14556), in spite of substantial differences obtained for breaking work in the considered simulated fire scenarios. All the curves are devoid of unstable crack growth zone. For the samples made of steel remaining in the initial state (specimen 3), and samples subjected to the simulated fire restricted to 600°C during one hour followed by fast cooling with water (sample 361), no significant differences may be observed between the shapes of compared curves depicted in both Fig. 4a and 4b. For this scenario in both cases similar values of breaking work (230 J and 260 J) as well as lateral extension (2.10 mm and 2.44 mm) are obtained. Additionally, the curves characterizing this impact test exhibit a plateau in the final stage of the experiment indicating incomplete break in the specimen. The slow cooling of

the sample in the open air resulted in slow transition through the critical brittle zone at 475°C, as a consequence a disadvantageous precipitation of secondary brittle phases occurred accompanied by a change in the  $\delta$  ferrite precipitation form to the acicular secondary ferrite  $\alpha'$ . This resulted in, with respect to the sample 361, significant decrease in impact strength. This scenario of simulated fire seems to be the most susceptible to changes in the impact testing temperature for this steel, as during the impact test in temperature of +20°C the breaking work of 127 J and lateral expansion LE at the level of 2.04 mm have been obtained. During the test conducted at the temperature of -20°C the respective values of 90 J and 1.44 mm have been obtained. The fire scenarios related to the heating temperature of 800°C during one hour result in intensive precipitation of numerous carbides, nitrides and intermetallic phases from supersaturated ferrite and austenite. Under such circumstances fast cooling with water (sample 381) prevents the occurrence of brittleness 475°C. Unrestricted and slow cooling of the sample on open air (sample 380) results in successive occurrence of additional harmful brittle phases, thus implicating further decrease in impact strength. In this scenario, in both analyzed cases, low values of the breaking work (in the range of 15÷35 J) have been obtained.

#### 4 CONCLUDING REMARKS

The results presented above indicate different behaviour of the tested steel grades during the impact strength tests. Thus they may constitute a basis for drawing relatively reliable conclusions regarding post-fire susceptibility of a given material to the initiation and propagation of brittle cracks, and this seems to be crucial for the assessment of its suitability for further use. Of the steels covered in this research, especially the steels similar in behaviour to the S355J2+N grade seem to be remarkably prone to the destruction of this type. This statement refers in particular to the winter conditions, as under those conditions a zone of unstable crack growth manifests itself in a pronounced manner. Let us note, however, that the simulated fire scenario, which proved itself to affect the impact strength of steel S355J2+N in a least adverse manner, at the same time affected the impact strength of steel 1H18N9T in the most adverse manner. The steel X2CrNiMoN22-5-3 exhibited during tests very high sensitivity to the heating temperature. Its susceptibility to brittle fracture after heating to 800°C during one hour proved to be substantially higher than the one obtained after heating to only 600°C during the same time. At the lower heating temperature the cooling regimen substantially affects the final impact strength, as the slow cooling in the open air results in substantial decrease in breaking work measured in experiment, especially in the simulated winter conditions.

#### REFERENCES

- ASTM E 23-92. Standard Test Methods for notched bar impact testing of metallic materials.
- Alar Ž., Mandić D., Dugorepec A., Sakoman M., 2015. Application of instrumented Charpy method in characterisation of materials. *Interdisciplinary Description of Complex Systems* 13 (3), p. 479-487.
- EN-ISO 148-1, 2006. Metallic materials – Charpy pendulum impact test. Part 1: Test method.
- EN-ISO 14556, 2015. Metallic materials – Charpy V-notch pendulum impact test. Instrumented test method.
- Kharchenko V.V., Kondryakov E.A., Zhamaka V.N., Babutskii A.A., Babutskii A.I., 2006. The effect of temperature and loading rate on the crack initiation and propagation energy in carbon steel Charpy specimens, *Strength of Materials*, 38 (5), p. 535-541.
- Maslak M., Zwirski G., 2017. Changes in structural steel microstructures following heating and cooling episodes in fires, *Safety & Fire Technique*, 48, p. 34-52.

# **PREDICTING THE CAPACITY OF SLENDER STEEL COLUMNS AT ELEVATED TEMPERATURE WITH FINITE ELEMENT METHOD AND MACHINE LEARNING**

Qi Tong<sup>a</sup>, Carlos Couto<sup>b</sup>, Thomas Gernay<sup>a</sup>

<sup>a</sup> Department of Civil and Systems Engineering, Johns Hopkins University, Baltimore, USA

<sup>b</sup> RISCO, Civil Engineering Department, University of Aveiro, Campus Universitário de Santiago, Aveiro, Portugal

## **Abstract**

This work applies finite element (FE) modeling and machine learning (ML) techniques to investigate the resistance of slender steel columns at elevated temperatures. First, a numerical study is performed with the FE software SAFIR to evaluate the columns' response for a range of cross-sections and boundary conditions. The FE model is used to generate a large dataset for training and testing three types of ML models: support vector regression (SVR), artificial neural network (ANN), and polynomial regression (PR). The trained models are compared against experimental data and an analytical model. The results show that the ML models provide more accurate predictions in the training and testing datasets compared with the analytical model. The predictions from the ANN and SVR also reasonably agree with the experimental data. These results suggest that ML techniques can be used to derive efficient surrogate models for capacity prediction of such members in fire.

**Keywords:** Finite element method, Machine learning, Slender steel column, Fire

## **1 INTRODUCTION**

The fire behavior of slender steel columns is influenced by the complex interaction between local, global, and distortional instability modes at elevated temperatures. This behavior has been investigated in the literature using high-fidelity FE models, but the computational cost limits the ability to conduct parametric analyses needed to derive robust design methods. An alternative is the use of analytical methods derived from mechanics-based principles and experimental observations. For predicting the resistance of slender steel members at elevated temperature, a simple analytical method is provided in the Eurocode 3 part 1.2 (CEN 2005). Couto et al. (Couto et al. 2015) recently proposed an improvement to this method based on the effective cross-section and the yield strength at 2% total strain for Class 3 and Class 4 cross-sections. While analytical methods are very useful for design, they are necessarily based on simplifying assumptions.

Machine learning (ML) techniques, increasingly used in many engineering fields, provide an opportunity to derive efficient surrogate models and identify prevailing parameters for capacity prediction (Salehi and Burgueño 2018). The adoption of ML techniques in structural fire engineering could provide a way to derive low-cost models for predicting the behavior of complex members and structural assemblies subject to fire (Naser 2019, Chaudary et al. 2020, Naser 2021). This work studies the application of three types of ML techniques to determine the resistance of I-shaped cross-section slender steel columns at elevated temperature. To build the dataset required for training of the ML models, high-fidelity FE simulations with shell elements are carried out using the software SAFIR. The trained ML models are compared with Couto et al.'s analytical model and with experimental data not included in the training dataset.

## **2 FINITE ELEMENT MODELING**

The FE software SAFIR (Franssen and Gernay 2017) is applied to predict the resistance of slender steel columns at elevated temperature and generate the datasets to construct the ML models. The ability of the FE models to capture the behavior of slender steel columns subjected to uniform heating is validated against eight experimental tests on Class 3 and 4 I-shaped cross-section columns as described in (Franssen et al. 2016). The critical temperature and failure mode observed in the tests are well captured by SAFIR. For critical temperature, the average ratio of SAFIR/Test is 1.007 with

a standard deviation of 0.03. Therefore, the SAFIR numerical models can be used to generate the datasets for ML.

An extensive FE study is conducted to obtain the load capacity of columns at elevated temperature. Considered cross-sections range from IPE300 to IPE600. Ambient temperature steel grade include S235, S355 and S460. Temperature at which the capacity is evaluated is assumed uniform in the section and ranges from 300-800°C with a 100°C increment. The length of the columns is 4.5 meters, while different boundary conditions are studied. A total of 1728 data points are generated.

To build the numerical models, geometric imperfections are obtained for local and global modes through buckling analyses with the software Abaqus to obtain the eigenmodes. For global imperfection, the amplitude follows the design recommendation, i.e.  $L/1000$ , where  $L$  is the length of the column. For local imperfection, the amplitude is calculated as 80% of the geometric fabrication tolerances as recommended in (CEN 2008; Couto and Real 2021). In this study, the amplitudes of local imperfections are calculated following Table 1 in (Couto and Real 2021). The global imperfection and local imperfection are combined following the recommendation of Annex C in Part 1-5 of Eurocode 3 (CEN 2006). The lowest eigenmode is the leading imperfection and the amplitude of the other eigenmode is reduced to 70%.

The coordinates of the nodes with geometric imperfections are then exported to SAFIR. The members are discretized using 4-noded shell elements. A sensitivity analysis on the mesh size is conducted showing convergence of the results with 120 elements on the length, 6 elements on the flange, and 10 elements on the web. Two rigid 100 mm thick end plates are added at both ends of the column, as shown on Figure 1. The size of the horizontal plate equals the web height and flange width. The width of the vertical plate equals the web height and its length is 150 mm. The load is axially applied on the edge of the vertical plate on the top with no eccentricity such that the load can be distributed evenly on the web and flange. The rotations of the shell edge of the vertical plate are either fixed or pinned in  $M_x$ ,  $M_y$ , and  $M_z$  directions. The pattern of residual stresses follows the one for hot-rolled columns (Couto and Real 2021) as shown in Figure 1(b). The residual stress is added to the integration points of the shell element and transformed into residual strains by SAFIR; the detailed procedure can be found in (Lopes 2009). The ultimate load-bearing capacity of the columns is calculated by SAFIR by first uniformly increasing the temperature in the section up to the target value and then progressively loading the column until failure.

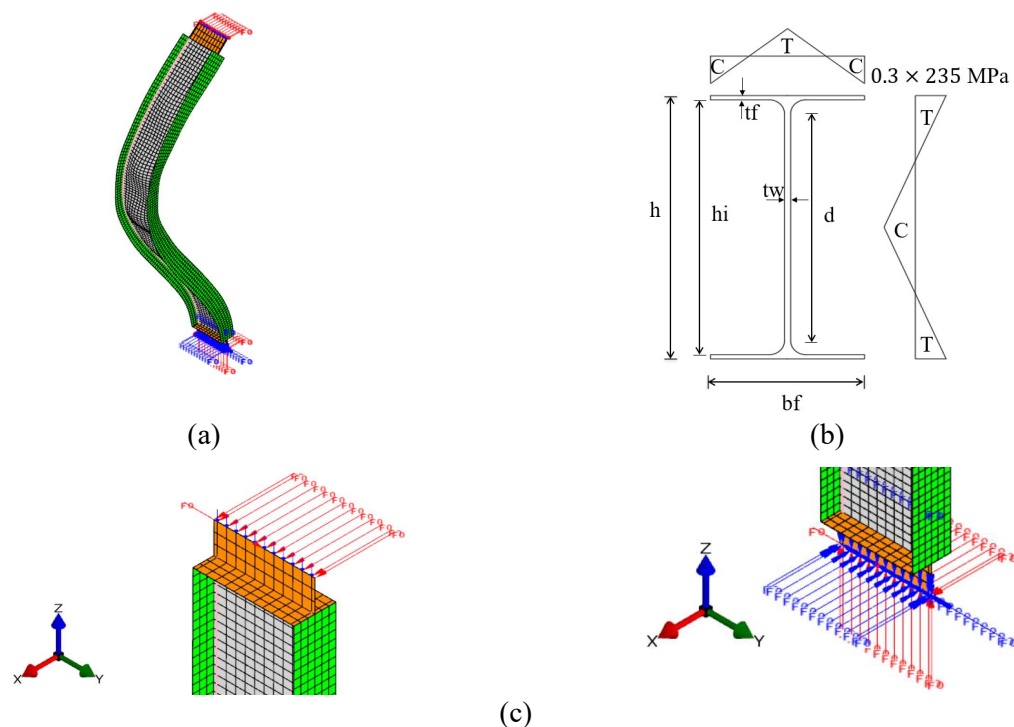


Fig. 1 The numerical model in SAFIR: (a) shell model for IPE500 column at 300 °C; (b) cross-section dimensions and residual stresses; (c) boundary conditions with end plates and pinned-fixed supports

### 3 MACHINE LEARNING MODELS

The 1728 data points obtained from the FE analysis are randomly divided into two groups for training and testing the ML models, with a ratio of 9:1. The trained ML models are also validated against experimental data published in (Kucukler et al. 2020) and in (Wang et al. 2014). Cross-validation is applied to tune the parameters in the ML models. The input parameters and output are summarized in Table 1, in which  $N_{u,T}$  is the load capacity at elevated temperature,  $N_{u,20}$  is the load capacity at 20 °C,  $h_w/t_w$  and  $b_f/2t_f$  are the adimensional web and flange dimensions,  $F_{y\_web}/E$  and  $F_{y\_flange}/E$  are the adimensional web and flange yield strengths, and top and bottom are the boundary conditions at the two ends (either fixed or pinned). The  $h_w/t_w$  of the cross-sections ranges from 31.1 to 52.5 while  $b_f/2t_f$  ranges from 4.7 to 8.2. Three ML methods are considered herein, namely SVR, ANN and PR as described in the next sections. The Python package Scikit-learn (Pedregosa et al. 2011) is used for the implementation.

Table 1 Parameters for the ML models

input parameters							output
$h_w/t_w$	$b_f/2t_f$	$F_{y\_web}/E$	$F_{y\_flange}/E$	$temperature(^{\circ}C)$	$top$	$bottom$	$N_{u,T}/N_{u,20}$

#### 3.1 Support Vector Machine Regression (SVR)

SVR is developed as an extension of the support vector machine (SVM), which aims to find a hyperplane in an n-dimensional space (n is the number of features, i.e. input parameters) that classifies the training datasets in different classes. While the objective of SVM is to find a hyperplane that has the maximum margins ( $\pm\varepsilon$ ), the extension SVR aims to find a flat hyperplane with margins ( $\pm\varepsilon$ ) that accept the data points within or on the margins while rejecting the data points outside the margins. The hyperplane can be written in Equation (1) for linear SVR:

$$y_i = w^T x_i + b \quad (1)$$

in which  $x_i$  and  $y_i$  are the  $i$ th input and output in the training dataset,  $w$  is the weight matrix and  $b$  is the bias.

For nonlinear SVR, the hyperplane can be written as:

$$y_i = w^T \varphi(x_i) + b \quad (2)$$

in which  $\varphi(x_i)$  is the nonlinear kernel function that maps the input vectors to a higher dimension space. The deviation of points within the margins ( $\pm\varepsilon$ ) is zero. The deviation of points outside the margins ( $\pm\varepsilon$ ) is the distance of these points to the margins ( $\xi_i$  and  $\xi_i^*$ ). The loss function of SVR is written as:

$$\text{minimize: } \frac{1}{2} \|w\|^2 + C \sum_{i=1}^n (\xi_i + \xi_i^*) \quad (3)$$

Constraints:

$$\begin{aligned} y_i - wx_i - b &\leq \varepsilon + \xi_i \\ wx_i + b - y_i &\leq \varepsilon + \xi_i^* \\ \xi_i, \xi_i^* &\geq 0 \end{aligned}$$

in which  $\frac{1}{2} \|w\|^2$  is the regularization term added to seek the flattest hyperplane with a small weight.  $C$  is a trade-off between the accepted tolerance of deviation  $\varepsilon$  and the flatness of the solution.

#### 3.2 Artificial Neural Network (ANN)

The ANN consists of several neurons arranged in multiple layers (input layer, hidden layer, and output layer) and the connections between them. The neurons are the main process unit which is a linear or

nonlinear function describing the relationship of input and output of the neuron. In this work, a feed-forward and backpropagation algorithm is used to build the ANN. The feed-forward means the information is transmitted from the input layers to the output layers. Once the ANN model is built, the training process starts to assign random values to the weights connecting the neurons in the input, hidden, and output layers. The input parameters are fed in the neurons in the input layers and multiplied by the weighted values. The sums of the multiplication and bias are put through a transfer function or activation function to generate the output of the neurons in the hidden layers or the output layers. Typical activation functions include linear, logistic sigmoid, hyperbolic tan function and rectified linear unit function. The output of neurons can be written as:

$$output_j = f(\sum_{i=1}^n w_{ij}x_i + bias_j) \quad (4)$$

in which  $output_j$  is the output of  $j$ th neuro and  $x_i$  is the input from  $i$ th neuron in the last layer.  $f$  is the transfer function.  $bias_j$  is the bias for  $j$ th neuro. The predicted values in the output layer are compared to the known observations. The difference of predicted and known values are used to adapt the weights through the backpropagation algorithm. The forward feed and backpropagation algorithm is repeated to adjust the weights iteratively until the error between known and predicted value reaches an accepted tolerance. The optimal hidden layer in this work is 6.

### 3.3 Polynomial Regression (PR)

The general form for polynomial regression is written as:

$$Y = X\omega + \varepsilon \quad (5)$$

in which  $Y$  is the vector of responses,  $X$  is the feature matrix,  $\omega$  is the coefficient and  $\varepsilon$  is the bias. The polynomial regression extends the inputs of the linear model, which is obtained by raising the initial inputs to a power. The new inputs are created with degrees less than or equal to the specific order. The new feature matrix includes 1) bias; 2) converting the initial inputs to their higher-order terms for each degree; 3) combination of all pairs of initial inputs. For instance, if there are two inputs,  $[x_1, x_2]$ , a degree-2 polynomial expansion would produce a new feature matrix  $[1, x_1, x_2, x_1^2, x_1x_2, x_2^2]$ . Models with higher degrees may closely fit most of the data in the training dataset, however, it may also capture the noises in the data, resulting in a larger error on the testing dataset (i.e. over-fitting). To prevent over-fitting in polynomial regression, ridge regression is applied to fit the polynomial feature matrix. The ridge regression adds a regularization term to the sum of squares of residuals. The loss function of ridge regression is written as:

$$minimize: \sum_{i=1}^n \|y_i - \sum_{j=0}^m x_{ij}w_j\|^2 + \lambda \sum_{j=0}^m \|w_j\|^2 \quad (\lambda > 0) \quad (6)$$

in which the  $y_i$  is the known observation,  $\sum_{j=0}^m x_{ij}w_j$  is the predicted value, and  $\lambda$  is the tuning parameter which controls the complexity of the model. As  $\lambda$  grows larger, the ridge regression effectively shrinks coefficient  $w_j$  to be 0 and selects a small subset of features to build the model, which prevents training a more complex model and thus avoid over-fitting.

## 4 RESULTS

To quantify the performance of the different models, the  $R^2$  value is evaluated for the models against the training and testing dataset and the experimental data. Table 2 gives the results for the SVR, ANN, and PR (degree 2) models. Predictions by the analytical model by (Couto et al. 2015) with  $\chi_{fi}$  from Eurocode 3 Part 1.2 (CEN 2005) are also included. The three ML models provide better agreement with the training and testing dataset than the analytical model. For the validation against experimental data, 16 data points obtained from (Kucukler et al. 2020) and (Wang et al. 2014) are used. The predicted capacity from the ANN agrees best with the experimental data with  $R^2$  of 0.945, followed by PR and the analytical model. The SVR model does not agree well with the experimental data.

Table 2 Performance of ML and analytical models

regressor ( $R^2$ )	train	test	experiment
SVR	0.999	0.998	0.087
ANN	0.999	0.999	0.945
PR (degree 2)	0.976	0.980	0.864
Analytical (Couto et al. 2015)	0.948	0.943	0.838

Figure 2 (a)-(d) plot the predicted capacity  $N_{u,T}/N_{u,20}$  using SVR, ANN, PR, and analytical models against the numerical estimations from SAFIR. For training and testing datasets, the predicted capacities are scattered in six groups, corresponding to the elevated temperature levels. The results from SVR, ANN, and PR agree well with the capacity evaluated by SAFIR. The ANN and PR models are also able to predict the capacity in the experimental datasets with good agreement. Overall, the trained ANN and PR models, which are built on extensive validated FE analysis data, can predict the resistance of the slender steel columns at elevated temperature with high accuracy. The performance of the ML models can be further improved by considering a larger dataset including a greater range of inputs. For instance, different column lengths can be included in the training dataset to improve prediction of capacity when global buckling occurs.

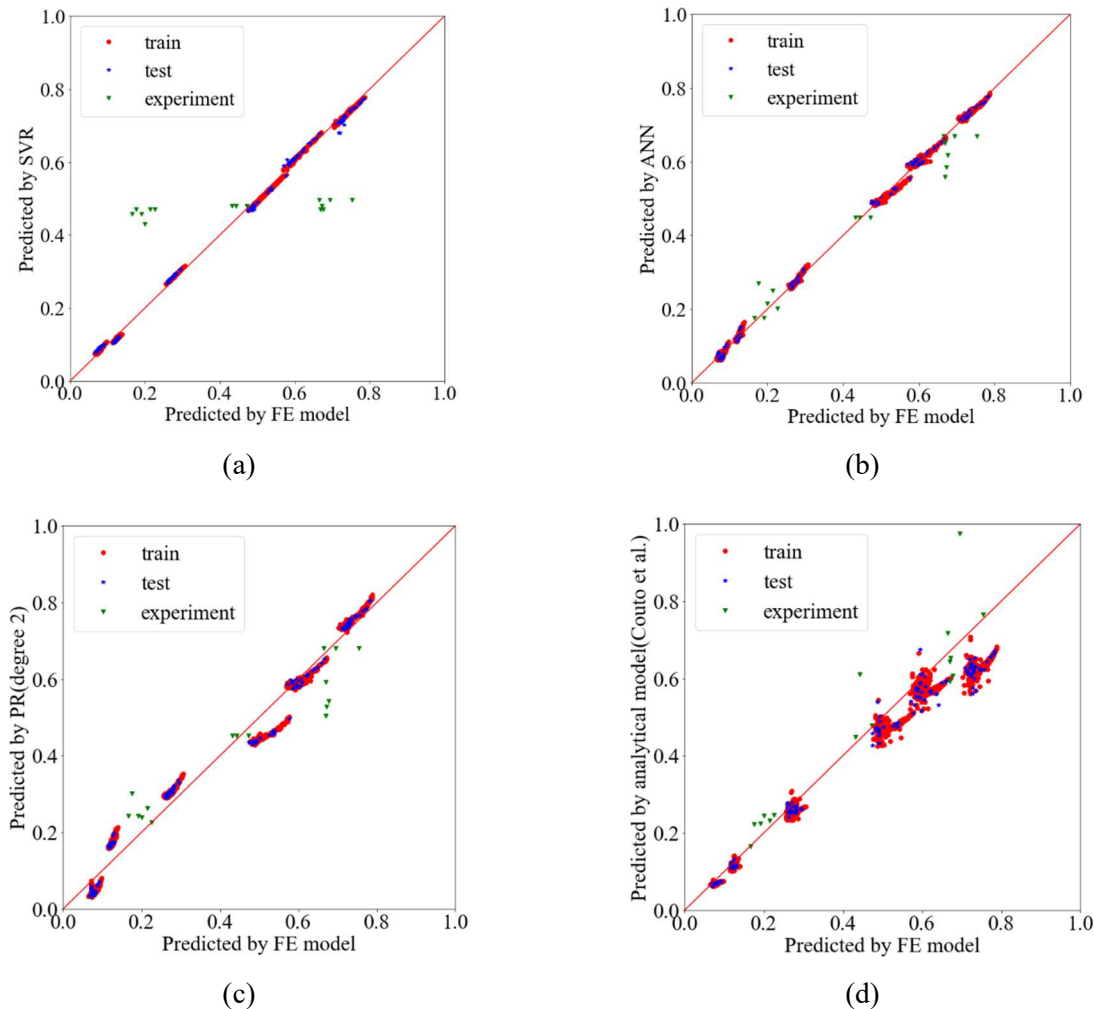


Fig. 2 Predicted capacity  $N_{u,T}/N_{u,20}$  for slender steel columns at elevated temperature: Comparison between SAFIR finite element model and (a) SVR; (b) ANN; (c) PR; (d) Analytical model (Couto et al.)

## 5 CONCLUSIONS

This study investigated the potential of Machine Learning (ML) models to capture the capacity at elevated temperature of slender steel columns. A numerical study based on validated nonlinear finite element modeling with shell elements was conducted to build a dataset of 1728 data points for columns with a range of cross-sections, temperature, yield strength and boundary conditions. The columns exhibited failure by local, global, and distortional buckling. The dataset was used to train and test three ML models, namely based on support vector regression (SVR), artificial neural network (ANN), and polynomial regression (PR).

The results indicate that the three tested ML models are able to predict the resistance of the columns in the training and testing dataset with an excellent accuracy ( $R^2$  greater than 0.998 for SVR and ANN, and greater than 0.976 for PR). The ML models agreed better with the FE data than a state-of-the-art analytical model. The ANN and PR models were also able to capture experimental data not used to train the model with a  $R^2$  of 0.945 and 0.864, respectively. It is expected that the accuracy against test data could be further improved by increasing the training dataset and including other inputs in the ML models. This work shows that the ML models are able to accurately predict the resistance of columns under uniform heating while also being computationally efficient. In future works, more complex configurations such as structural assemblies or localized fire exposures will be explored.

## REFERENCES

- CEN, EN., 2008, *1090-2: execution of steel structures and aluminium structures—part 2: technical requirements for steel structures*, European Committee for Standardisation, Brussels.
- CEN. EN.,2005,1993-1-2, *Eurocode 3: design of steel structures — part 1–2: general rules —structural fire design*. Brussels: European Committee for Standardisation.
- CEN. EN.,2006, 1993-1-5, *Eurocode 3 — design of steel structures — part 1-5: plated structural elements*. Brussels: European Committee for Standardisation.
- Chaudhary R.K., Jovanović B., Gernay T., Van Coile R., 2020. Generalized fragility curves for concrete columns exposed to fire through surrogate modelling. In *Proceedings of the 11th International Conference on Structures in Fire (SiF2020)*. 1-2 December 2020, online, p. 322-332.
- Couto C, Real P.V., 2021. *The influence of imperfections in the critical temperature of I-section steel members*, *Journal of Constructional Steel Research*, 179, p.106540.
- Couto C, Real P.V., Lopes N, Zhao B., 2015. 'Resistance of steel cross-sections with local buckling at elevated temperatures', *Journal of Constructional Steel Research*, 109, p.101-114.
- Franssen J.M, Gernay T., 2017. *Modeling structures in fire with SAFIR®: Theoretical background and capabilities*, *Journal of Structural Fire Engineering* ,8(3), p. 300-323.
- Franssen J.M, Zhao B, Gernay T., 2016. *Experimental tests and numerical modelling on slender steel columns at high temperatures*, *Journal of Structural Fire Engineering*, 7(1), p.30-40.
- Kucukler M, Xing Z, Gardner L., 2020. *Behaviour and design of stainless steel I-section columns in fire*, *Journal of Constructional Steel Research*, 165, p.105890.
- Lopes N., 2009. *Behaviour of Stainless Steel Structures in Case of Fire*, Ph.D. thesis, Universidade de Aveiro, Portugal.
- Naser M.Z., 2019. *Fire resistance evaluation through artificial intelligence-A case for timber structures*. *Fire safety journal*, 105, p.1-18.
- Naser M.Z., 2021. *Mechanistically Informed Machine Learning and Artificial Intelligence in Fire Engineering and Sciences*. *Fire Technology*, p.1-44.
- Pedregosa F, Varoquaux G, Gramfort A, Michel V, Thirion B, Grisel O, Blondel M, Prettenhofer P, Weiss R, Dubourg V., 2011. *Scikit-learn: Machine learning in Python, the Journal of machine Learning research*, 12, p.2825-2830.
- Salehi H, Burgueño R., 2018. *Emerging artificial intelligence methods in structural engineering*, *Engineering structures*, 171, p.170-189.
- Wang W, Kodur V, Yang X, Li G., 2014. *Experimental study on local buckling of axially compressed steel stub columns at elevated temperatures*, *Thin-Walled Structures*, 82, p.33-45.

Proceedings of the International Conference in Ljubljana, 10-11 June 2021  
in edition of Applications of Structural Fire Engineering

**Session**

**Concrete structures I**

# EVALUATION OF CURING AGE EFFECT ON THE FIRE SPALLING BEHAVIOR AND BENDING LOAD CAPACITY OF PRESTRESSED CONCRETE BEAM

Michika Hashida<sup>a</sup>, Hiroyuki Ikeya<sup>a</sup>, Kentaro Fujimoto<sup>b</sup>, Mitsuo Ozawa<sup>a</sup>

<sup>a</sup> Gunma University, Faculty of Science and Engineering, 1-5-1, Tenji-cho, Kiryu, Gunma, 376-8515, Japan

<sup>b</sup> PS Mitsubishi Construction Co., Ltd., 2-4-24, Harumi, Cyuou-ku, Tokyo, 104-8572, Japan

Contact person: Mitsuo Ozawa, ozawa@gunma-u.ac.jp

## Abstract

In this study, we investigated the effect of curing age on the fire spalling and bending load bearing capacity of Prestressed concrete (PC) beams. A heating test based on the RABT 30 rapid heating curve was conducted on PC beams. The curing ages considered in this study were 3 and 24 months. The water content of PC beam at 3 and 24 months are 5.1% mass and 3.3% mass, respectively. The PC beams were subjected to bending load tests to evaluate the residual bending load capacity. The results suggested that the maximum fire spalling depth and area of PC beam at the curing age of 3 months was greater than that of 24 months. The ultrasonic pulse velocity test showed that the concrete deteriorated due to heating and the occurrence of fire spalling. Additionally, in the bending load test, the initial stiffness and ultimate bending load capacity of the PC beam at the curing age of 3 months was smaller than that of 24 months.

**Keywords:** prestressed concrete, fire spalling, curing age, residual bending load capacity, heating test

## 1 INTRODUCTION

Reinforced concrete (RC) structures suffer from fire spalling in high temperature environments. Recent studies reported two major theories of fire spalling: thermal stress theory (Andergerg, 1997), vapor pressure theory (Bazant, 1997), and their combination. Compressive strength and water content ratio are also major factors on fire spalling of concrete. Recent paper investigated affected by water content and curing age on the fire spalling of concrete (Ozawa et al., 2016). On the other hand, PC structures are more prone to fire spalling compared to RC structures because of the prestressing force introduced in PC beams (Gales et al., 2011, Na-Hyun et al., 2015, Fujimoto et al., 2018). However, only a few studies analyzed the effect of curing age on the fire spalling behavior in PC beams exposed to fire.

In this study, we conducted heating tests on PC beams cured for 3 and 24 months. Additionally, the PC beams were subjected to bending load tests after the fire tests to investigate the effect of curing age on the fire spalling and bending load capacity of PC beams.

## 2 EXPERIMENT

### 2.1 Properties of concrete

Table 1 and 2 shows the mix proportion and properties of concrete, which had a water-to-cement ratio of 33.5%. High early strength Portland cement (density: 3.13 g/cm<sup>3</sup>) was used to prepare the specimens. For fine aggregates-1 and fine aggregates-2, river sand (density: 2.57 g/cm<sup>3</sup>) and crushed stone sand (density: 2.52 g/cm<sup>3</sup>) were used, respectively. For coarse aggregate, granite stone was used (density: 2.52 g/cm<sup>3</sup>).

Table 1 Mixture proportion of concrete

Water cement ratio (%)	Fine aggregate ratio (%)	Unit weight (kg/m <sup>3</sup> )					
		Water	Cement	Fine aggregates-1	Fine aggregates-2	Coarse aggregates	Admixture
33.5	38.9	165	493	454	192	1045	394

Table 2 Properties of fresh concrete

Air content (%)	Slump (cm)	Temperature (°C)
3.4	14.5	23.7

Table 3 Type of specimens, compressive strengths and water content

Type	Curing age (months)		Compressive strength (N/mm <sup>2</sup> )	Water content (%)
	Heating test	Bending load test		
PC-con	-	5	86.3	5.1
PC-3	3	5	86.3	5.1
PC-24	24	28	85.5	3.3

Table 3 shows the compressive strengths and water content for various specimens. PC-con is non-heating specimen. PC-3 and PC-24 were subjected to the heating test at a curing age of 3 and 24 months, respectively. After the heating test, PC-3 and PC-24 were subjected to bending load tests. The compressive strength of the mixture was approximately 86 MPa for all specimens. The water content was 5.1% in PC-con and PC-3, and 3.3% in PC-24.

## 2.2 PC beam

Fig. 1 shows the shape and dimensions of the PC beam specimen. The width, height, and length of PC beam specimens were 200 mm, 200 mm, and 1500 mm, respectively. The width and height of the heated area at the center of the PC beam were 200 mm and 160 mm, respectively. The prestressing steel bar used was 17 mm in diameter (SBPR930/1080). The reinforcing bars of D10 (SD345) were placed inside the specimen in the axial direction, and D6 (SD295) was used for stirrups.

Type K thermocouples were placed at 5 mm, 10 mm, 20 mm, 40 mm, 60 mm, and 125 mm from the heated surface to measure the internal temperature of the specimen. On the second day after casting, the specimens were subjected to the prestressing force.

The prestressing force was applied using a hydraulic jack system. The initial prestressing force was 113.5 kN, which was designed to produce a compressive stress of 5 N/mm<sup>2</sup> at the center bottom edge of the specimen. The specimen was wet-cured for three days and cured in air in the laboratory until the heating test was started on the fourth day.

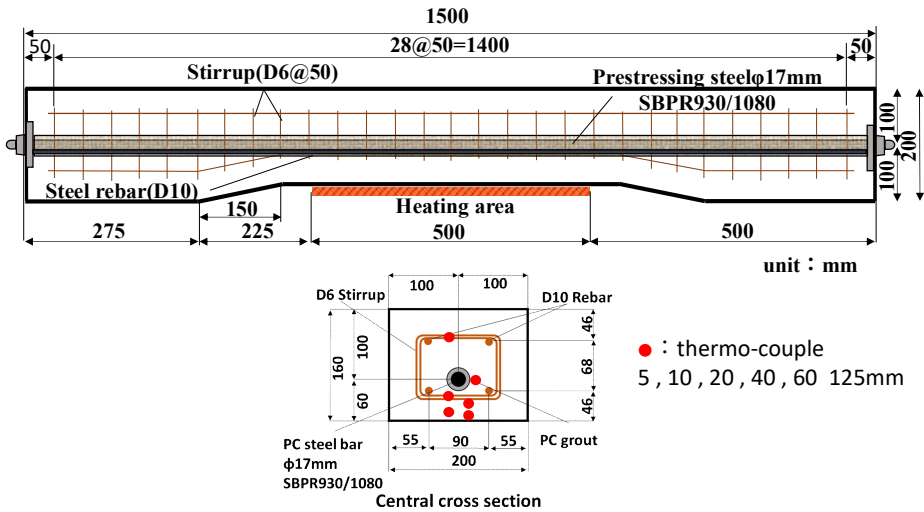


Fig. 1 Shape and dimensions of the PC beam specimen.

**2.3 Heating test**

The heating test was conducted using a high-performance horizontal gas furnace. The heating condition was based on the RABT 30 rapid heating curve. The entire 500 mm long bottom side area at the center of the specimen was heated. The specimens were covered with insulation blankets to control the temperature rise in the non-heating area. Fire spalling was observed based on spalling and peeling sounds of concrete pieces from the scuttle of the gas furnace. After the fire test, the extent and depth of the spalling were measured using a thickness meter.

**2.4 Bending load test**

Fig. 2 shows the outline of the bending load test. The distance between the fulcrums was 1200 mm, and the load was concentrated at two points with an equal moment section of 200 mm. The load was measured by the load cell, which had a capacity of 300 kN.

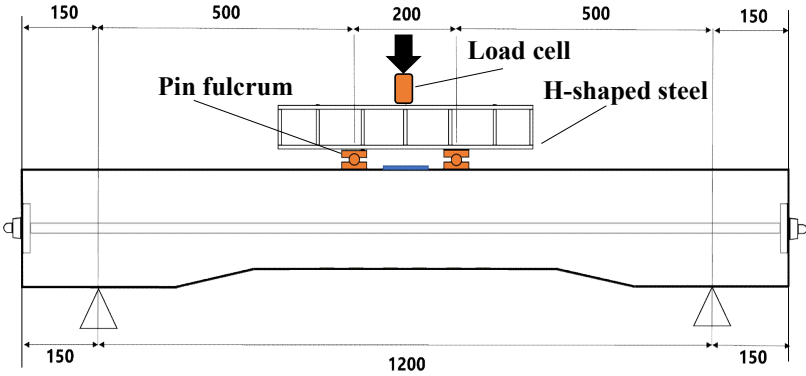


Fig. 2 Outline of bending load test (Unit:mm)

### 3 RESULTS AND DISCUSSION

#### 3.1 Fire spalling condition

Fig. 3 shows the condition of the heated surface and the spalling depth contours. The maximum spalling depths in PC-3 and PC-24 were 32.9 mm and 19.9 mm, respectively. In PC-3, there was an area where the internal stirrup was exposed. The maximum spalling depth and area of PC-3 was larger than that observed in PC-24. The water content in PC-24 was lower than that of PC-3 owing to the curing age. It was assumed that the water vapor pressure had been reduced. Resent paper reported that moisture content leads to vapor pressures and spalling behavior (Ozawa et al 2016). Therefore, the degree of damage caused by fire spalling was smaller in PC-24 than that observed in PC-3.

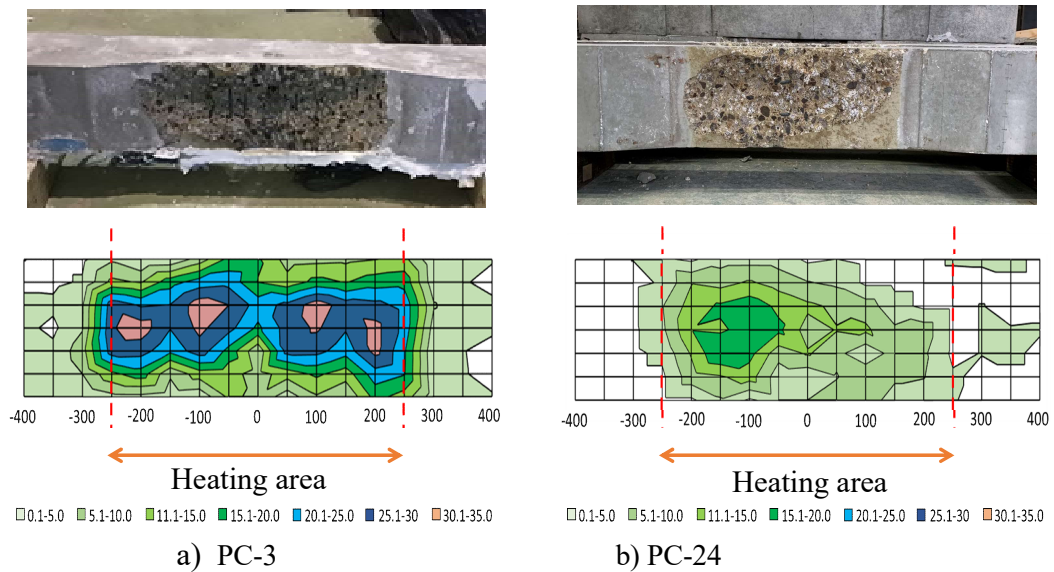


Fig. 3 Condition of the heated surface and the spalling depth contours (Unit:mm)

#### 3.2 Internal temperature

Fig. 4 shows the temporal changes in the internal temperature of each PC beam. In PC-3, a rapid temperature rise was observed at 5 mm approximately 4 minutes after the heating process started. Thereafter, the temperature at the 10 mm and 20 mm positions increased rapidly and in that order. In PC-24, a rapid temperature rise was observed at 5 mm, approximately 5 minutes after the heating process started. Similarly, the temperature of the 10 mm position increased rapidly. The rapid increase in internal temperature was probably due to fire spalling because concrete was damaged by fire spalling and the thermocouple that was placed inside was exposed to the gas furnace.

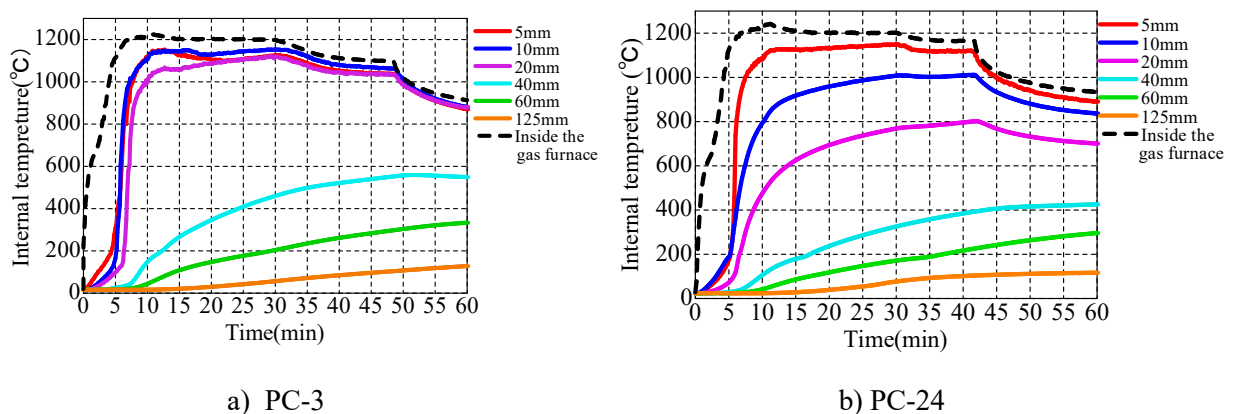


Fig. 4 Temporal changes in the internal temperature of PC beams

### 3.3 Degradation of PC beam due to high temperature

Fig. 5 and 6 shows the distribution of internal temperature and the ultrasonic pulse velocity (US) in the center part in the depth direction from the heated surface. The internal temperature of PC-3 and PC-24 was approximately 1120 °C at 5 mm. The maximum spalling depth of PC-3 was 32.9 mm and that of PC-24 was 19.9 mm. The temperature at maximum spalling depth of PC-3 and PC-24 was 800 °C. The US of PC-con without heating was 4500 m/s. PC-3 has a maximum fire spalling depth of 32.9 mm, and the US value drops to 2000 m/s near the heating surface. The maximum fire spalling depth of PC-24 is approximately 19.9 mm, but the US value is 1500 m/s. It can be observed that the US value is smaller for PC-3 compared to PC-24 because the fire spalling depth is larger. Even when compared with PC-con, it can be confirmed that the US of PC-3 and PC-24 damaged by heating is lower.

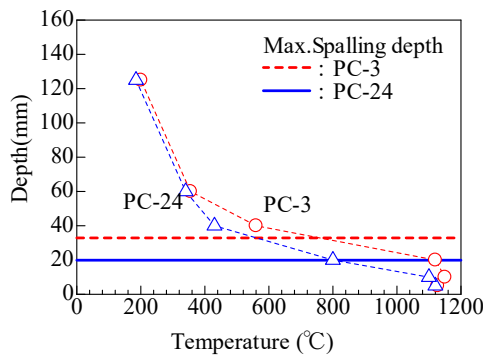


Fig. 5 Distribution of maximum temperature

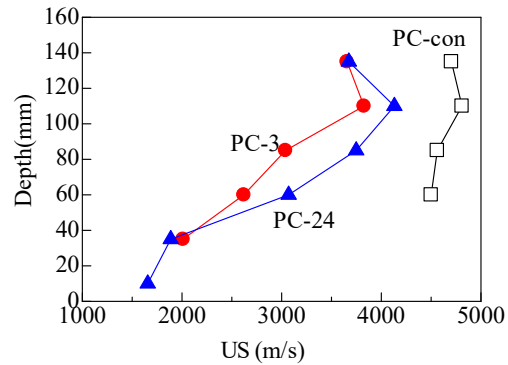


Fig. 6 Distribution of US in PC beam

### 3.4 Relationship between load and displacement

Fig. 7 shows the relationship between load and displacement in the bending load test. PC-con was unloaded when the load reached approximately 90 kN to confirm the effect of prestress. At the time of unloading, it was confirmed that the bending cracks were closed in all the specimens. Bending fracture indicates that the concrete at the upper edge has reached a compressive failure occurred in all PC beams (Fig.8). This indicates that PC-3 and PC-24 were damaged by heating. However, as PC bars did not yield, the prestress was applied continuously. The initial rigidity of PC-3 and PC-24 subjected to the heating test was lower than that of the PC-con, which was not subjected to the heating test. The PC-con cracked at approximately 40 kN, and the displacement at the center of the specimen was 0.7 mm at that time. On the other hand, the displacements of PC-3 and PC-24 at that time were 3.1 mm and 4.8 mm, respectively. The US values show that concrete matrix deteriorated due to heating in (Fig. 6).

Previous studies (M.B.S. Sollero et al., 2020) have shown that the mechanical properties, such as compressive strength and elastic modulus of heated concrete decreases. Therefore, the deterioration of concrete due to heating may have affected the initial rigidity of the load-displacement relationship.

Moreover, cracks and cross-sectional defects were also observed in the specimens due to heating. The reduction of prestress and cracking due to sectional defects has a significant effect on the rigidity of concrete. Therefore, the initial rigidity of PC-3, which was significantly damaged by the fire spalling, was smaller than that of other specimens.

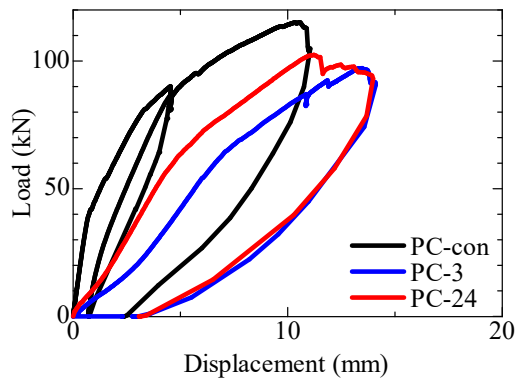


Fig. 7 Relationship between load and displacement Fig. 8 Compressive failure of Upper part in PC beam

#### 4 Conclusions

The results of this study can be summarized as follows:

- As the curing age increases, the water content decreases, thereby decreasing the fire spalling depth and scale.
- In the ultrasonic pulse velocity (US) test, it was found that the US declined, and the concrete strength decreased. The cracking of concrete due to heating may have affected the results.
- In the bending load tests of PC beams, the initial rigidity of PC-3 and PC-24, which were subjected to heating tests, decreased significantly without heating compared to PC-con. It is considered that the decrease in initial rigidity of PC-3 and PC-24 was affected by the section loss due to fire spalling and reduction in compressive strength and modulus of elasticity of the concrete.

#### REFERENCES

- Y. Anderberg, 1997. Spalling phenomena of HPC and OC, in *Proceedings of the International Workshop on Fire Performance of High-strength Concrete*, NIST, Gaithersburg, Maryland, p. 69–73.
- Z.P. Bazant, 1997. Analysis of pore pressure, thermal stress, and fracture in rapidly heated concrete, in *Proceedings of the International Workshop on Fire Performance of High-strength Concrete*, NIST, Gaithersburg, Maryland, p. 155–164.
- M. Ozawa, K. Akashi, and R. Kamata, T. Tanibe, S.P. Sirjana, 2016. Effects of curing ages on spalling failure under ring restraint test of high strength concrete during fire, in *Proceedings of the 7<sup>th</sup> International Conference of Asian Concrete Federation “Sustainable Concrete for now and the Future”*, 30 Oct – 02 Nov, Hanoi, Vietnam.
- Gales J., Bisby L.A., and Gillie M., 2011. *Unbonded post tensioned concrete in fire: A review of data from furnace tests and real fires*. *Fire Saf. J.*, Vol.46, Issue.4, p. 151–163.
- Na-Hyun Y., Seung-Jai C., Sang-Won L., and Jang-Ho J.K., 2015, *Failure behavior of unbonded bi-directional prestressed concrete panels under RABT fire loading*, *Fire Saf. J.*, 71, p. 123–133.
- Fujimoto K., Ozawa M., Yamamoto S., and Izutsu K., 2018, Explosive spalling behavior and load capacity of prestressed concrete members exposed to fire, in *The International Federation for Structural Concrete 5<sup>th</sup> International fib Congress 2018*, October 2018, Melbourne, Australia.
- Sollero M.B.S., Moreno Junior A.L., Costa C.N., 2020, *Residual mechanical strength of concrete exposed to high temperatures – international standardization and influence of coarse aggregates*, *Construction and Building Materials*, 234(20), p. 117371.

# PROPOSAL FOR A PRELIMINARY FIRE CALCULATION METHOD TO DETERMINE ACCEPTABLE COVER DEPTHS OF CONCRETE SLABS

Wenxuan Wu<sup>a</sup>, Cristian Maluk Zedan<sup>a</sup>

<sup>a</sup> The University of Queensland, School of Civil Engineering, Brisbane, Australia

## Abstract

Structural fire engineering solutions vary in complexity and require building dimensions as inputs; therefore, design choices for fire safety are sometimes relegated to latter design stages, resulting in diminished options. The research proposed a new method that allows for the preliminary design of the concrete cover required for slabs as a function of the compartment size and ventilation condition (i.e., opening factor). The modified parametric fire analysis and finite-difference heat transfer model are adopted to calculate the different cover depths resulting in time-to-failure. The equivalent time of fire severity is defined by a summation of movable fuel's burnout time and the period of reinforcement's temperature increment during the cooling phase (i.e., effective time). A case study of a simply supported reinforced concrete slab demonstrates the method further. This proposed method also allows engineers to add or reduce complexity at either stage to give a quick decision in early-stage design. To date, this method is limited to a ventilation-controlled compartment.

**Keywords:** Numerical study, reinforced concrete slab, ventilation-controlled, parametric fire

## 1 INTRODUCTION

In the early stage of fire engineering design, engineers are often asked for minimum dimensions of structural elements design in accordance with the required fire resistance level (FRL), before performing more detailed computations and validation. The initial design feasibility decides the engineer hours and costs significantly, as the larger deviation leads to a more time-consuming correction and repetition.

Published papers and codes often examine the prescriptive requirements that aid engineers to choose structural elements based on standard fire exposure. Codes from different regions provide a prescriptive solution for selecting the minimum dimensions and axis distances for reinforced concrete walls, slabs, columns and beams according to the required fire-resistance level and design load ratio (CEN, 2004, AS, 2001, SNZ, 2007). Codes helped structural engineers develop a more refined initial design, especially for those who have limited fire backgrounds. However, the issue is that the prescriptive design only applies to the standard fire curve used in furnace testing, not for the real fire scenarios, for example, a compartment fire under ventilation-controlled condition.

The "Parametric Fire" proposed by Eurocode 1 (CEN, 1991) has considered the effect on maximum fire temperature and burning duration due to the ventilation conditions, allowing to produce a more realistic time-temperature relationship for any combination of fuel load in consideration of firefighting measures, construction of lining materials and the effect caused by ventilation dimension. Thus, a more applicable method based on modified Parametric fire to discover the general pattern between minimum requirements and fire intensity for the structural member is addressed in this paper, and a worked example is addressed to further demonstrate the theory.

## 2 THEORY AND CONCEPTS

The overall objective of structural fire engineering design is to ensure the equivalent fire severity (the sums of effective time and burnout time) is no longer than the time-to-failure:

$$t_{fail} \geq t_{bo} + t_{eff} \quad (1)$$

Where  $t_{fail}$  is the time a load-bearing structural member would experience failure

$t_{bo}$  is the time of movable fuel has completely consumed

$t_{eff}$  is the time of element to reach maximum temperature in the decay phase after burnout

A flow chart (see Fig. 1) demonstrates the procedure of the methodology. The procedure can be divided into two separate paths:

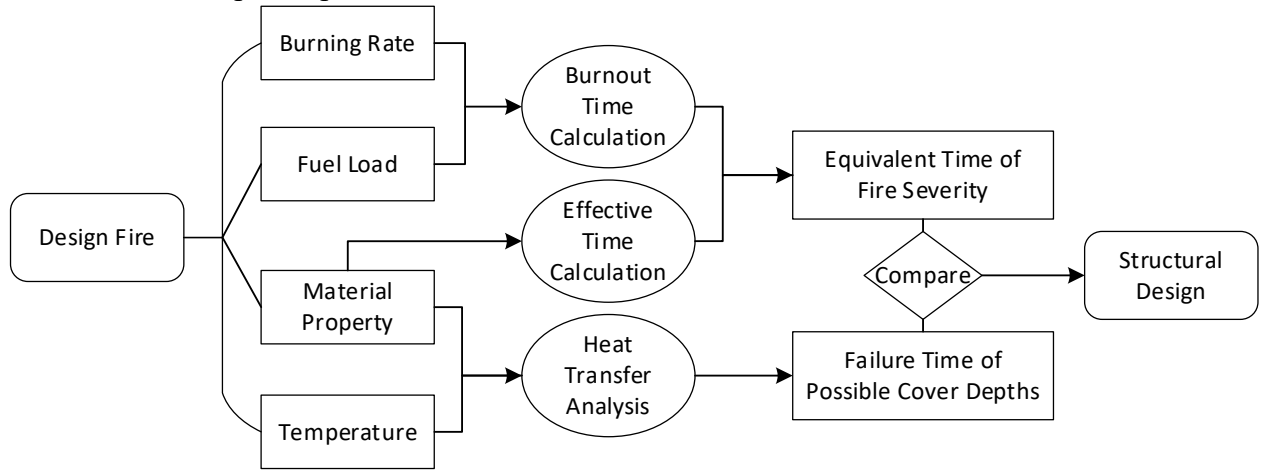


Fig. 1 Flow chart demonstrating the methodology

- The methodology starts from a design fire in a compartment, where fire-safety relevant characteristics (e.g., fuel load, material thermal properties and the ventilation conditions) can be obtained, followed by fire design parameters (e.g., maximum temperature, burnout time) can be determined by empirical equations. These equations can be either adopted from previous experimental data or published papers. By this means, fire severity can be found, which is essentially how long the fire could effectively harm the structural member.
- In the meantime, find the failure time of all possible bottom cover depths by conducting heat transfer analysis with known material thermal properties; maximum allowable temperature or bending capacity loss determined by load ratio could be used as the failure threshold. By comparison between the equivalent fire severity and different failure time for all possible depths, an acceptable design range is subsequently obtained.

## 2.1 Modified Parametric fire and Maximum Temperature

In this paper, to assess the failure time for all possible cover depths, a modified parametric fire with an unlimited burning duration has been used. The highest temperature in the steady-state is limited by the ventilation condition of the compartment. Fig. 2(a) shows a typical curve of parametric fire and an unlimited curve.

The CIB (Thomas and Heselden, 1972) first established a plot that correlates the maximum temperature to certain ventilation conditions (opening factor  $A_T/A_0H^{1/2}$ ) from numerous experimental data based on the wood fire. For design purposes, a more explicit equation developed by Law (1983), summarized by Walton and Thomas (Walton et al., 2016) has been adopted in the later section instead of the original plot from Thomas. The maximum temperature is given either by Fig. 2(b) or equation:

$$T_{\max} = 6000(1 - e^{-0.1\Omega})/\sqrt{\Omega} \quad (2)$$

Where

$$\Omega = \frac{A_t - A_0}{A_0\sqrt{H_0}} \quad (3)$$

Where  $A_0$  is the area of the opening

$H_0$  is the height of the opening

$A_t$  is total enclosure area of the compartment

An opening factor 10 is generally considered as the transition boundary from Regime-II to Regime-I fire, and maximum resultant temperature can be observed in opening factor 10.

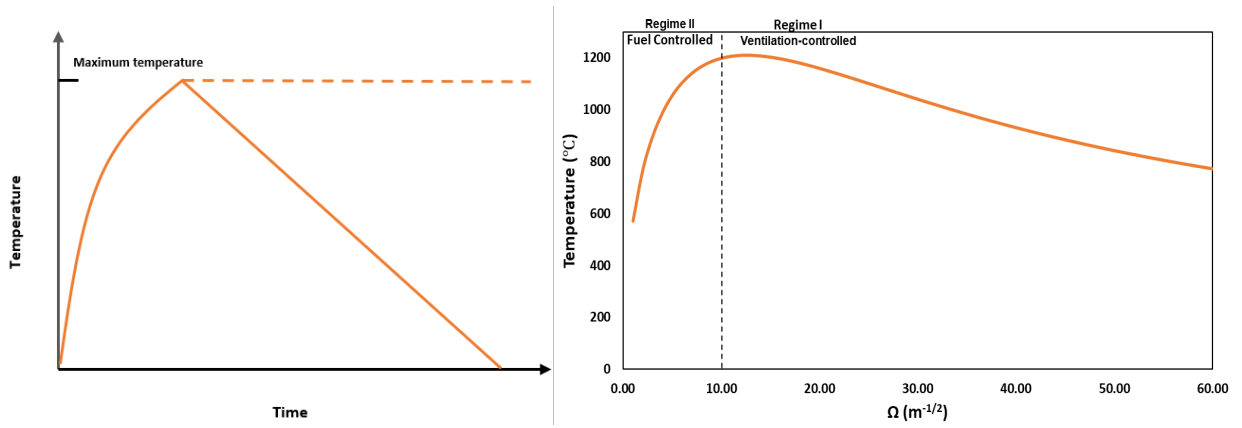


Fig. 2 (a) Typical parametric fire with a limited duration (solid line) and unlimited duration (dash line); (b) maximum temperature in a ventilation-controlled compartment

## 2.2 Burnout Time and Effective Time

In the parametric fire,  $O$  is the ventilation factor ( $m^{0.5}$ ) given by:

$$O = A_0 \sqrt{H_0} / A_t \quad (4)$$

For ventilation-controlled fires, as the burning rate is constant and depending on the ventilation condition (Kawagoe, 1958), the duration of the burning period can be simplified to:

$$t_{bo} = 0.0002 q_{f,d} / O = \frac{0.0002 E}{A_0 \sqrt{H_0}} \quad (5)$$

Where  $q_{f,d}$  is the design fuel load density

Any fire will experience a decay phase due to its limited fire load, but the temperature of the structural member would have a delayed increase until it reaches a peak value, shown in Fig. 3(a). This period is referred to as an effective duration in the decay phase, which also has an impact on a structural member. The effective duration was firstly proposed by Wickström (Wickström, 1985) for parametric fire, and recently studied by Gernay (Gernay, 2019) for the burnout resistance in standard fire curve.  $\Delta t$  depends on the depth of the point considered, which is essentially an application of Fourier number.

$$\Delta t = \mu x^2 / a \quad (6)$$

Where  $a$  is the actual thermal diffusivity ( $m^2 s^{-1}$ ) of the passive fire protection, considering  $5.7 \times 10^{-7}$  for concrete bottom cover (Drysdale, 2011).

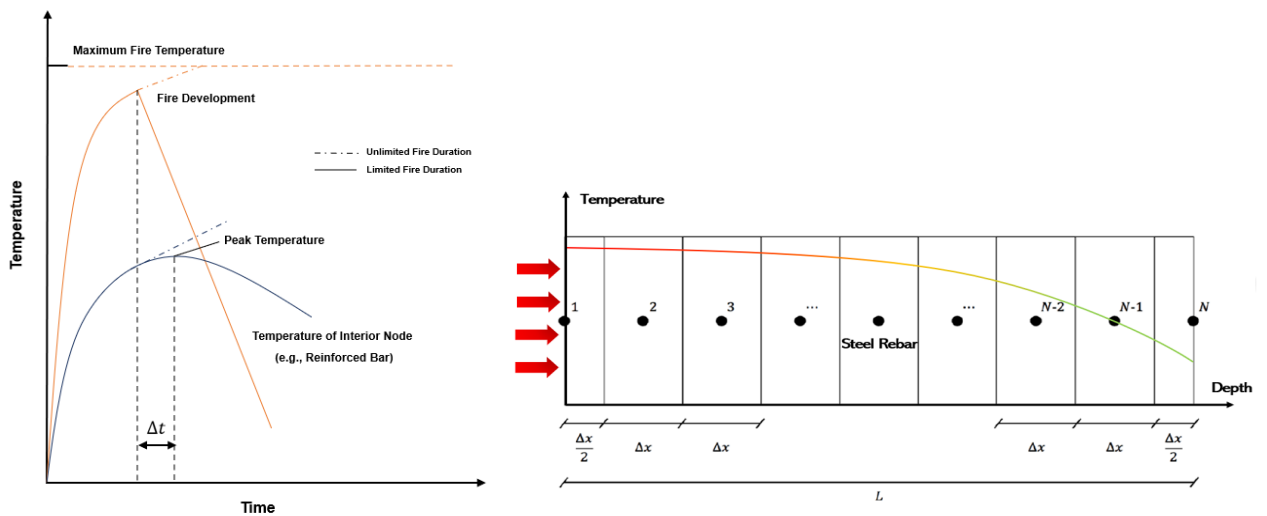


Fig. 3 (a) Original plot by Thomas from experimental data; (b) Plot proposed by Law for design purpose.

### 2.3 Heat Transfer Analysis

The discretization of the one-dimensional finite-difference heat transfer model has been conducted to find the failure time, originally described by Dusinberre (Dusinberre, 1961). The concrete slab along thickness can be divided into numerous interior nodes (from 2,3...to N-1) with a  $\Delta x$  thickness, nodes located at the edge with a  $\Delta x/2$  thickness (nodes labelled with 1 and N). The steel bar located inside the reinforced slab at a certain distance from the edge. The lining surface (Node=1) receives the heat flux from radiation and convection of the hot upper layer, where the source of radiation depending on the fire scenario. The heat penetrated from the fire node exposed to the fire and transferred to the next interior node via conduction. The last node (node=N) is exposed to the ambient temperature, where gives a low heat transfer coefficient, experienced heat losses to the ambient environment through radiation, shown in Fig. 3(b). The numerical solution of temperature-time step is given:

$$\begin{aligned}
 T_1^{j+1} &= T_1^j + \frac{2\Delta t}{\Delta x \rho c_p} \left( h_{T,x=0} (T_g - T_1^j) - k \frac{T_1^j - T_2^j}{\Delta x} \right), x = 0 \\
 T_i^{j+1} &= T_i^j + \frac{\Delta t}{\Delta x^2 \rho c_p} \left( k (T_{i-1}^j - 2T_i^j + T_{i+1}^j) + \frac{\partial k}{\partial T} \cdot \left( \frac{T_{i+1}^j - T_{i-1}^j}{2\Delta x} \right)^2 \right), 0 < x < L \\
 T_N^{j+1} &= T_N^j + \frac{2\Delta t}{\Delta x \rho c_p} \left( k \frac{T_{N-1}^j - T_N^j}{\Delta x} - h_{T,x=L} (T_N - T_0^j) \right), x = L
 \end{aligned} \quad (7)$$

Where  $j - 1$  represents the last time step, and  $j + 1$  represents the next step,  $i - 1$  refers to the last node, and  $j + 1$  refers to the next node.

### 3 WORKED EXAMPLE

A simply-supported concrete slab is used as case study, inputs are listed in Table 1.

Table 1 Inputs parameters for compartment and concrete slab

Parameters	Reference Case	Comments
Type	Office	A square compartment ( $W=D$ ) is taken for diminishing the effect from geometry and considering a characteristics fuel load density of 511 MJ/m <sup>2</sup> for an office building (CEN, 2002).
Lining Material	Plaster	Common lining material of office, gives the density = 1250 kg/m <sup>3</sup> , specific heat capacity = 1088 J/kgK and conductivity = 0.43 W/mK.
Ceiling Height	2.4 m	Standard height of an office in Australia.
Opening Height	2 m	Standard height of the door in Australia, which enables to calculate the different opening area reversing from a certain opening factor (multiple openings are possible).
Opening Factor $\Omega$	10	Regardless of the variation of compartment size, a certain opening factor defines the maximum temperature within the compartment, which also enables to assess of variable dimensions (5-100m <sup>2</sup> ). 1/O = 10.7 due to slightly different equations
Fuel	Cellulosic	Cellulosic fuel is taken for general fuel type in an office building, leads to a net calorific value of 20 MJ/kg (CEN, 2002).
Design Fuel Load	613.2 MJ/m <sup>2</sup>	According to $q_{f,d} = q_{f,k} \cdot m \cdot \delta_{q1} \cdot \delta_{q2} \cdot \delta_n$ (CEN, 2002)
Maximum Temperature	1199 °C	The maximum temperature for different opening factors within the compartment, according to Eq. 2.
Material Type	Reinforced Concrete Slab	All the thermal properties are temperature-dependent and referenced from Eurocode 2 (CEN, 2004)
Bottom Cover Depth	15-75 mm	Referenced from AS 3600 (AS, 2001)
Load Ratio	0.5	Most buildings have a load ratio of 0.5 or less (Buchanan and Abu, 2017)
Limiting Temperature	485 °C	Limiting temperature corresponding to the load ratio, according to the equation from AS 3600 (AS, 2001) or NZS 3404 (SNZ, 2007): $T_{lim} = 720 - 470r_{load}$

Different failure time for each cover depth is extracted from heat transfer analysis, according to regression analysis, an equation to express the correlation between failure time and bottom cover depth can be obtained, as shown in Fig. 4(a). Different effective time can be calculated for different depths of concrete cover via Eq. (5). By adding the effective time to burnout time, the correlation between different equivalent fire severity and floor area (ranging from 5m<sup>2</sup> to 100m<sup>2</sup>) can be obtained by regression analysis (Fig. 4(b)). By establishing simultaneous equations, the correlation between cover depth and floor area under the critical duration can be solved, as shown in Fig. 5(a).

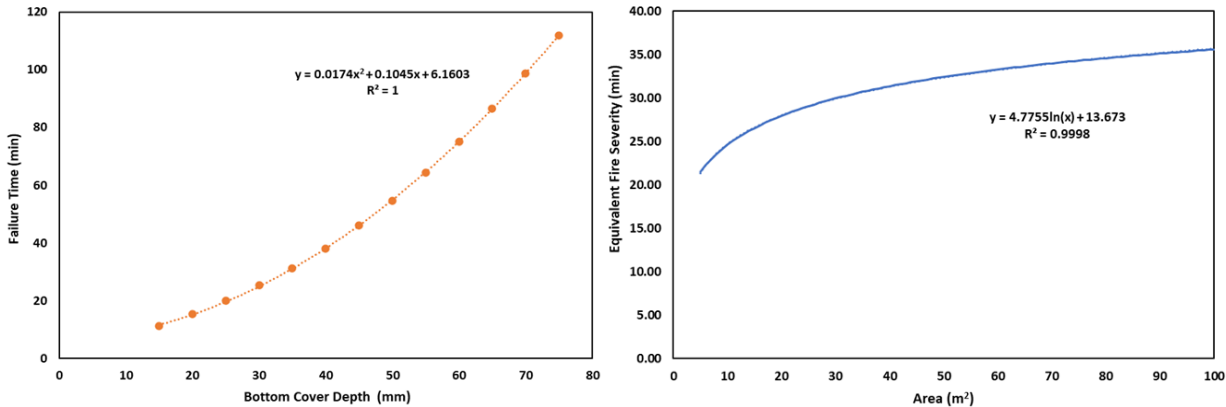


Fig. 4 (a) Failure time versus bottom cover depth; (b) Equivalent fire severity versus floor area

The equation has a high degree of accuracy from the regression analysis where  $R^2=0.9981$ ; only 5m<sup>2</sup> – 50m<sup>2</sup> is shown in the graph due to the equation for 50m<sup>2</sup> – 100m<sup>2</sup> is relatively flat which is easy to estimate from the existed curve. The curve essentially divides the graph into two areas, the area above the curve is defined as an “Acceptable Area” where the failure time is larger than the equivalent fire severity. Contrarily, the area below the curve is defined as an “Unacceptable Area” where the failure time is shorter than the equivalent fire severity.

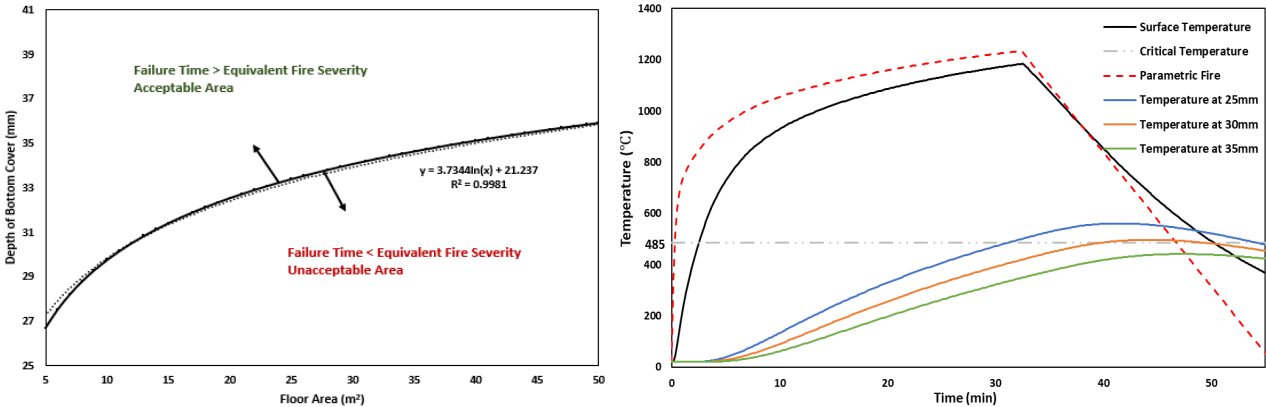


Fig. 5 (a) Relationship between cover depth and floor area in parametric fire under 1/O=10.7. (b) Example parametric fire with a floor area of 50m<sup>2</sup> under 1/O=10.7.

In order to validate the results, a 50 m<sup>2</sup> floor area compartment has been used to generate a typical parametric fire curve (with a complete cooling stage), as shown in Fig. 5(b). In this case, the concrete cover of 30mm depth just reaches the critical condition under the limited parametric fire (the middle curve), where more than 35mm depth of bottom cover would never reach the failure condition (the bottom curve) during the whole fire.

The 50m<sup>2</sup> (x-axis) corresponds to 35.8mm (y-axis) in Fig. 5(a), which means only when the concrete bottom cover is deeper than 35.8mm, the fire safety design in this certain fire scenario is met. Even with a tiny discrepancy between the results, they still show consistency and feasibility to conduct a preliminary fire safe calculation using this proposed methodology.

## 4 CONCLUSIONS

This paper used modified parametric fire, adopted empirical formulas and numerical heat transfer analysis to establish a methodology that includes the comparison between fire severity and failure time to give a safety design range for the concrete slab, the case study discovers multiple advantages:

- Divide the problem into two separate paths (i.e., time-to-failure and equivalent fire severity) allows us to explore the advantages of various levels of complexity or simplification in either part. For example, more complicated and refined structural analysis can be done to find a more accurate failure time. Additionally, empirical equations (e.g., burning rate and time-to-flashover) could be replaced to adapt to the real fire situation; criteria could be justified to comply with the codes in different regions (e.g., the limiting temperature and factored load); simplifications (e.g., constant thermal properties) can be assumed to reduce the degree of difficulties in assessing the heat transfer, especially for estimating the cooling phase behaviour.
- Establish the concept of “unacceptable area” and “acceptable area,” which enables engineers to have a quick response to the design requirements based on simple information such as ventilation and type of building. For the case study, a “Rules of Thumb” for choosing the depth of concrete cover to satisfy the fire safety design is obtained, by both plot (visually) and equations (numerically) for a standard office with floor area ranging from 5-100m<sup>2</sup> and an opening factor 10.
- The principle also can be expanded towards other conditions of ventilation-controlled fire within the compartment and other load-bearing construction materials or structural systems by following the same procedures to produce more design region. As for other concrete members with three or four sides of fire exposure, the problem can be solved by a more refined heat transfer model to carry out the analysis.

However, the methodology in the current stage also has its limitations:

- The work is based on a ventilation-controlled compartment, which means it has limited applications to other types of space such as opening area and tunnel. Additionally, this work is not including the compartment area exceeds 100m<sup>2</sup>; the feasibility for larger space is to be verified.
- The design fire is more suitable for cellulose-typed burning, such as a wood fire. Since the liquid fire would have a sharper cooling stage when it has burned out, where the heat release rate turns to zero immediately, and temperature decreases drastically, which leads to a shorter effective time than the calculation, however, more conservative.

## REFERENCES

- AS 2001. AS 3600 Concrete structures. *Standards Australia, Sydney*.
- BUCHANAN, A. H. & ABU, A. K. 2017. *Structural design for fire safety*, John Wiley & Sons.
- CEN 1991. 1-2: 2002 Eurocode 1: Actions on structures—Part 1-2: General actions—Actions on structures exposed to fire.
- CEN 2002. 1-2: Eurocode 1: Actions on structures—Part 1-2: General actions—Actions on structures exposed to fire.
- CEN 2004. *BS EN 1991-1-2:2002 – Eurocode 2: Design of concrete structures — Part 1-2: General rules — Structural fire design*, European Committee for Standardization, Brussels.
- DRYSDALE, D. 2011. *An introduction to fire dynamics*, John Wiley & Sons.
- DUSINBERRE, G. M. 1961. *Heat-transfer calculations by finite differences*, International Textbook Company.
- GERNAY, T. J. 2019. Fire resistance and burnout resistance of reinforced concrete columns. 104, 67-78.
- KAWAGOE, K. J. B. R. 1958. Fire behaviour in room. 27.
- SNZ 2007. NZS 3404: 1997 Steel Structures Standard. *Standards New Zealand, Wellington*.
- THOMAS, P. & HESELDEN, A. 1972. *Fully-developed fires in single compartments*, Fire Research Station.
- WALTON, W. D., THOMAS, P. H. & OHMIYA, Y. 2016. Estimating temperatures in compartment fires. *SFPE handbook of fire protection engineering*. Springer.
- WICKSTRÖM, U. 1985. Application of the standard fire curve for expressing natural fires for design purposes. *Fire safety: science and engineering*. ASTM International.

## EFFECTS OF THERMAL ELONGATION IN MULTI-LEVEL PRODUCTION FACILITIES AND WAREHOUSES

### In case of fire

Iselle De Beuckeleer<sup>a</sup>, Tom Molken<sup>a,b</sup>, Martin Classen<sup>a</sup>

<sup>a</sup> KU Leuven, Department of Civil Engineering, Materials and Construction Division, Campus De Nayer, Belgium

<sup>b</sup> Sweco Belgium bv, Buildings Division, Hasselt, Belgium

#### Abstract

Expansion joints are generally provided in large spans to relieve thermally induced stresses. In some particular cases, functional requirements of a building restrict the installation of these joints. For a case study of a multi-level cleanroom facility, a thermo-plastic and mechanical analysis was performed with the finite element software SAFIR<sup>®</sup>. This preliminary study with simplified material models of a jointless hollow core floor was conducted to assess thermal elongation effects on the bearing columns and secondary staircase cores during an ISO834 fire. This paper also investigates if concrete-filled cores of a hollow core slab favourably influence the temperature-time relation. The outcomes of this research demonstrate that thermal expansion is limited to 10 cm in case of a fire. After a push-over analysis, it can be concluded that this structure requires a minimum of expansion joints and well-designed details of starter bar reinforcement.

**Keywords:** thermal elongation, hollow core floors, concrete-filled cores, large compartment fires, push-over analysis

## 1 INTRODUCTION

In the design of buildings, the consequences of deformations in ambient conditions due to thermal effects, creep, and shrinkage should be considered in the service limit states (EN 1992-1-1, 2005). Only when their effects are significant and influence the ultimate limit state of stability, they should be considered in this limit state. However, a simplification is possible because these effects may be omitted in the global analysis as expansion joints are incorporated at every distance  $d_{joint}$  to accommodate resulting deformations. The American report (ACI 224.3R-95, 2013) proposes recommended values for the joint distance in buildings due to contraction (shrinkage) and expansion (thermal effects). Depending on the design temperature change, distances with a lower and upper bound of 60 and even 200 m are set. There is a tendency to enlarge the distance between joints as the related details are difficult to engineer for water- and airtightness.

Besides the advantages of jointless structures, the designer should be aware of the effect of thermal expansion in case of fire. This was already recognized in the earliest work, for example, by (Langdon-Thomas, 1972). Nevertheless, more recent publications (Bulletin 74, 2014) deal with this topic for precast structures. It should be recognized that in the simplified methods based on nominal fire exposure, the allowance to neglect thermal effects (EN 1992-1-2, 2004) does not always lead to safe results, as can be seen in the overview of historical failures later on. Considerable axial and horizontal forces are induced in the horizontal (beams and slabs) and vertical bearing elements (columns), resulting in earthquake-like damage.

Further on, it is already shown that concrete elements can suffer a delayed failure (Dimia, et al., 2011; Gernay, 2019). Therefore, the risk of failure due to thermal elongation is not always present during the fire but perhaps after the fire brigade or even other people enter the building again. At least it can be mentioned that this risk is not only apparent during or after a compartment fire, but it can also be expected during a so-called travelling fire (Stern-Gottfried & Rein, 2012).

After a literature review of historical failures, a case study will be presented, and some possible fire scenarios are discussed. A thermal analysis of the slab and mechanical response of the major bearing elements is proposed. Finally, some conclusions and needs for further research are formulated.

## 2 HISTORICAL FAILURES

Neglecting the effects of thermal elongation can lead to severe damage and even building failure. In general, vertical members are not sufficiently reinforced with stirrups to withstand forces generated under fire conditions (Taerwe, 2007). Some historical collapses are briefly described hereafter.

### 2.1 Military Personnel Records Center (NPRC-MPR) in Overland, United States (1973)

In 1973, an extensive fire in the Military Personnel Records Center was reported (Mostafaei, et al., 2009). The uncontrollable fire was ignited on the top floor of this six-storey reinforced concrete building, where a large amount of fuel - 21,7 million military record files - were stored. Twelve hours later, thermal expansion caused a collapse of the 18 cm thick roof slab and a subsequent shear failure of the 41 cm square-tied columns. A lack of expansion joints in the roof slab, and thermal elongation effects led to lateral deformations up to 60 cm at the top of the corner columns. The severity of the structural damage to the columns is shown in Fig. 1(a).

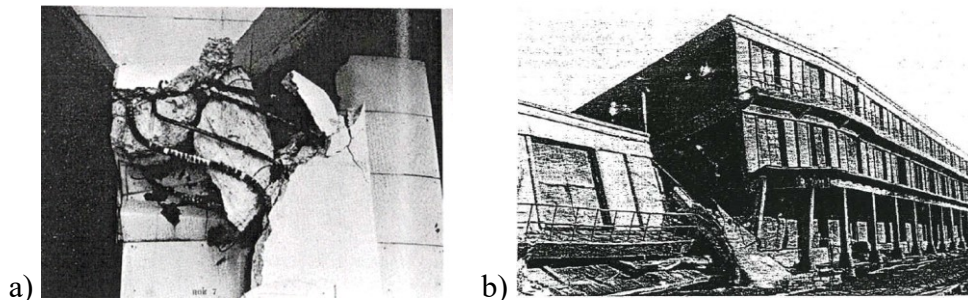


Fig. 1 (a) Shear failure of a column in the NPRC-MPR in Overland, United States (Mostafaei, et al., 2009) and (b) Partial collapse of a warehouse in the harbour of Ghent, Belgium (Taerwe, 2007).

### 2.2 Warehouse in the harbour of Ghent, Belgium (1974)

In 1974, a three-storey warehouse in the harbour of Ghent (Belgium) caught fire (Taerwe, 2007). The reinforced concrete structural parts met all minimum requirements with regard to the geometrical dimensions and concrete cover. Approximately one hour and twenty minutes after ignition, the construction partially collapsed, Fig. 1(b). Three-sided heating of the beams caused major thermal elongations, which were hindered by the unheated adjacent elements on one side. Thermal expansion of the beams in one direction eventually initiated a shear failure of several critical columns. Later, fire simulations demonstrated that the construction lost its structural integrity at a mean temperature increase of 150-200°C.

### 2.3 Katrantzos Department building in Athens, Greece (1980)

At the end of 1980, a suspected arson fire started on the 7<sup>th</sup> floor of this eight-storey reinforced concrete building (Beitel & Iwankiw, 2002). A quick fire spread was inevitable since compartmentation and sprinkler systems were lacking. A post-fire structural analysis indicated that large parts of the 5<sup>th</sup> to the 8<sup>th</sup> floor had collapsed due to restrained thermal forces exceeding the structural capacity of the bearing elements or connections.

### 2.4 Library of Linköping, Sweden (1996)

In 1996, a fire-induced collapse of the city library in Linköping (Sweden) occurred (Taerwe, 2007). The large opening (52 m x 3.6 m) on the first floor interrupts fire compartmentation between the ground floor and first floor. During this rapidly spread fire, the surrounding beams along the floor opening and the adjacent parts on the first floor were heated up on two or more sides. Thermal restrained elongation of the floor slabs triggered an unexpected shear failure in the stabilizing walls and critical columns 30 minutes after flashover, even though a fire resistance of 60 minutes was attributed to this library building.

### 3 CASE-STUDY

In 2020, the Sweco company was consulted for the design of a pharmaceutical production facility in Belgium. The fire design of the construction became challenging as this is a jointless building (cleanroom environment). At that time, some practical issues were encountered related to the typology of this type of buildings. For this reason, this jointless building is the subject of the elaborated case study.

The half part of the floor plan and a cross-section of the building are presented in Fig. 2. It consists of a 12 m wide central core with technical equipment and two equal square shape wings of 47 by 47 m<sup>2</sup>. The total jointless length of this air-conditioned building equals 106 m. An evacuation staircase (concrete core) of 5 by 6 m<sup>2</sup> is situated at the end of each wing. The live load of the floors is 15 kN/m<sup>2</sup>, and steel truss beams support them (at the 12.15 and 24.15 m level) or precast concrete beams for small spans below the 4.45 and 16.45 m level. The height of the truss beams is used for the technical supplies of the production process; the false ceiling is suspended on the lower girder.

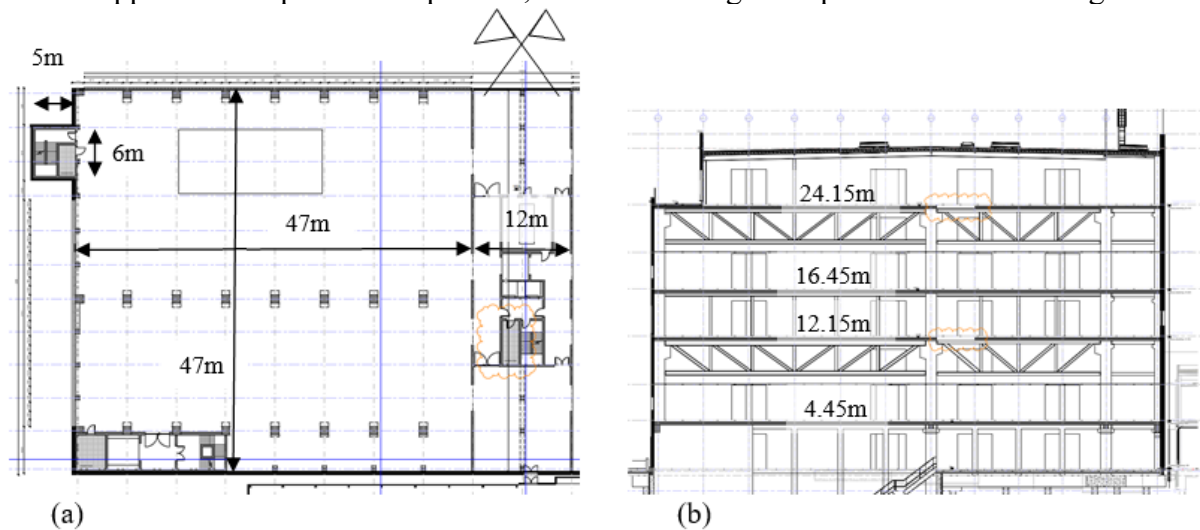


Fig. 2 (a) Floor lay-out, half-part of the building and (b) cross-section.

Uniaxial thermal elongation of a 47 m concrete slab made out of 6 m span hollow core slabs submitted to fire, can lead to unexpected failure patterns. It should be mentioned that this verification becomes mandatory to comply with the (EN 1992-1-1, 2005) standard by exceeding the  $d_{joint}$  of 30 m. Questions arise about the influence of the partial concrete core filling (at the supports), action on the columns (1x1 m<sup>2</sup>) and how the connection with the secondary staircases can be executed in the most simple and suitable way.

### 4 FIRE SCENARIOS

The envisaged compartments are relatively large, which reduces the risk of a compartment fire. Local fires or travelling fires are much more likely to occur in such cases. Even smouldering fires do have a higher probability of occurrence due to the expected lack of oxygen in this airtight building. Nevertheless, a compartment fire was used for its simplicity, and as the elongation effect is merely discussed, only the heating phase of the ISO834 fire will be regarded in this study.

### 5 THERMAL ACTION

Thermal simulations are executed with the aid of the well-known thermo-plastic finite element software SAFIR<sup>®</sup> (Franssen & Gernay, 2017). This tool allows for a combination of thermal analysis which is performed in a 2D environment (cross-section analysis), and mechanical analysis, including material and geometrical nonlinearities. The thermal and mechanical properties used in the modelling can be found in Table 1 and correspond to those used in combination with an ISO834 heating load of the material. In this preliminary study, differences between the concrete and reinforcement grades of the topping and hollow core material are not taken into account. The floor slab is heated at the bottom,

is kept at a temperature of 20°C at the top level, and adiabatic boundary conditions are used on the sides of the hollow core element. A gravity load of 18980 N/m from the self weight, dead load and fixed part of the live load was applied. The prestressing effect is neglected so far.

Table 1 Thermal and mechanical properties.

Material	Concrete	Prestressing strand
Aggregate	Limestone/calcareous	-
$\alpha_{c,hot}$ [W/m <sup>2</sup> K]	25	25
$\alpha_{c,cold}$ [W/m <sup>2</sup> K]	4	4
$\epsilon$	0.7	0.7
$\rho$ [kg/m <sup>3</sup> ]	2400	7850
$f_c$ and $f_y$ [MPa]	50	1200
$f_t$ [MPa]	4.5	-
$E$ [N/mm <sup>2</sup> ]	37000	200000
$\nu$	0.3	0.3

As this is an industrial building, a fire rating of 2 hours or 120 minutes is obligatory in Belgium. The temperature distribution of the 200 mm thick hollow core slabs with 50 mm of compression layer (including a reinforcement mesh) is given in Fig. 3. The temperature-time relations for a slab without filled cores (6 cores – solid lines) and with (4 cores – dashed lines) at the same location are given. The HC indication in the notations stands for the hollow-core position (or the equivalent level with the filling). Differences become more distinct at higher levels in the cross-section, which is logically also the case for the average temperature.

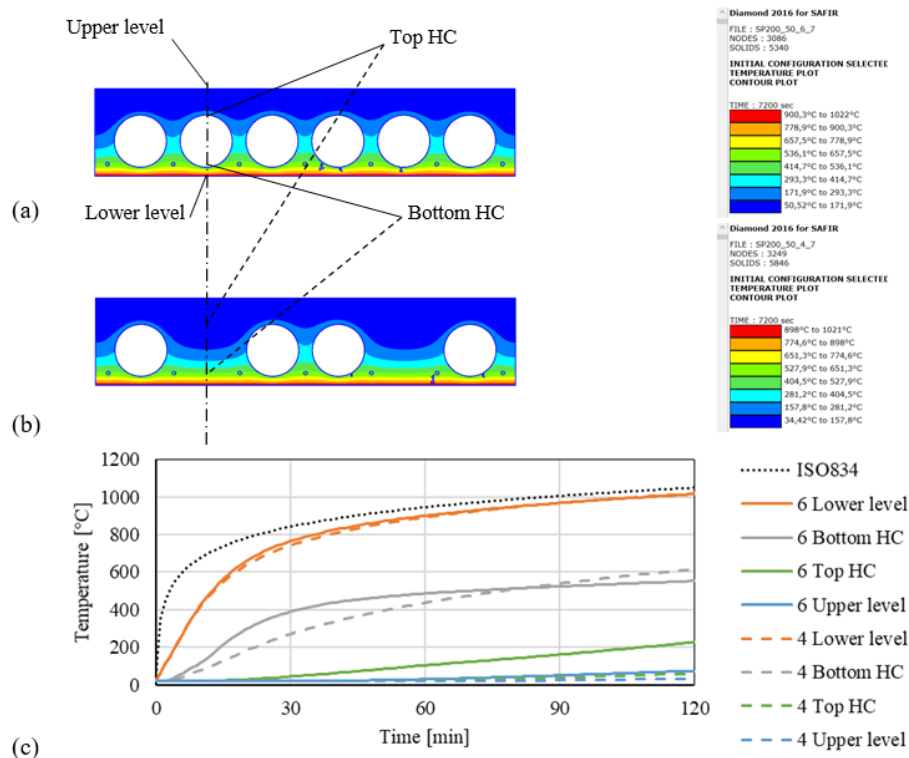


Fig. 3 Typical section without (a), with (b) concrete-filled cores and calculated temperature-time relation at specific locations of the cross-section.

Note that by definition the most unfavourable situation for the elongation does not occur in the heating phase, although building requirements only ask for this verification.

## 6 MECHANICAL RESPONSE

After performing the thermal analysis for a 2D cross-section of the slab with adiabatic boundary conditions, the temperature profiles are transferred to a beam model in the same finite element software SAFIR® (Franssen & Gernay, 2017). For steel reinforcement, the Eurocode 2 (EN 1992-1-2, 2004) material model is applied with the properties out of Table 1, whereas an adapted concrete material model is used with an explicit formulation of the transient creep (Gernay, et al., 2013).

### 6.1 Thermal elongation of floor slab

Several simulations are performed to show the differences between the approach used for the analysis. With fixed ends and a member analysis of a hollow core slab with topping (6m-6HC) like prescribed in section 5, tremendous forces up to more than 20 MN are developed per hollow core slab, see Fig. 4(a). Differences caused by the filled concrete cores (6m-4HC) at the support are neglectable. It makes a remarkable difference once the stiffness of the structure is entered in the simulation.

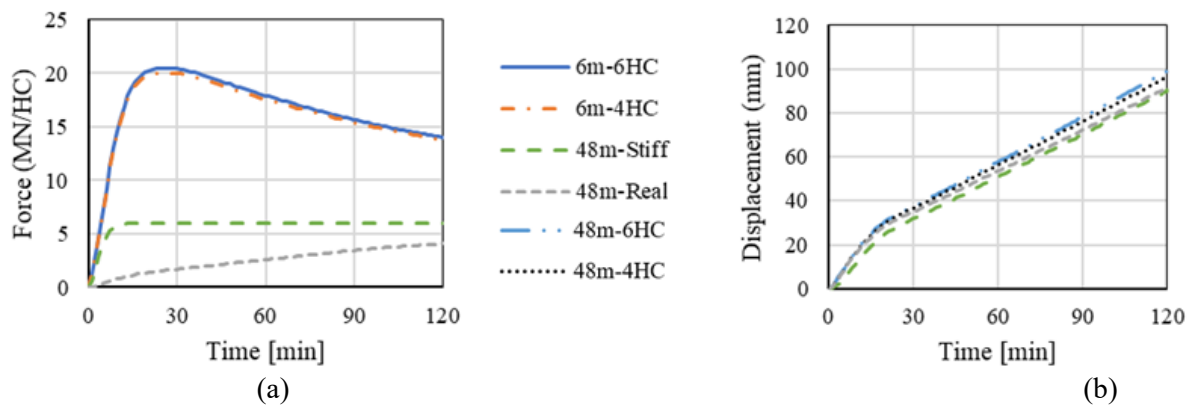


Fig. 4 (a) Developed forces and (b) elongation.

Looking at the floor plan of Fig. 2(a), it can be seen that over the width of the floor (47 m), only 3 columns (=  $n$ , beside the secondary staircase) will resist a horizontal displacement. With C35/45 concrete, a cross-section of 1 by 1 m<sup>2</sup>, a 4.45 m (H) height and an estimated cracked second moment of area of one-third of the uncracked one, a spring constant  $k$  expressed by Eq. (1) is valid. This spring constant is entered in the software by a 40.7 m HEA100 steel beam with an equivalent horizontal stiffness ( $k = EA/L$ ) and indicated as 48m-Real. To highlight the difference between fixed and extremely stiff, the results of a 37 times stiffer spring are shown and labelled as 48m-Stiff. It can be noticed that by entering a "reasonable" spring, forces decrease with a factor 3.4 and the time of appearance is different, see Fig. 4(a).

$$k = \frac{P}{\Delta l} = n \frac{3EI_{cracked}}{H^2} \left( \frac{1.2}{w} \right) = 3 \frac{3 \cdot 34 \cdot 10^9 \cdot 1.1^3}{4.45^2} \left( \frac{1.2}{47} \right) = 11 \text{ MN/m} \quad (1)$$

Despite the significant differences in the developed force, the difference in the displacement is relatively low. Obviously, the elongation of the 6 m elements with fixed ends is zero and not shown, but this time in Fig. 4(b) the free expansion of a 48 m hollow core floor without (48m-6HC) and with (48m-4HC) two filled concrete cores at the supports is given. By applying thermal elongation formulas out of (EN 1992-1-2, 2004), the generated thermal strains correspond with a uniform temperature increase of respectively 210 and 310°C in case of a 60 and 120 minutes fire exposure.

### 6.2 Secondary concrete staircase cores

In the design of this production facility, the emergency staircases are executed as a concrete core. A strategy is proposed where a rigid body motion of secondary staircases is used as a push-over analysis, Fig. 5. The 10 cm elongation at 4.15 m would cause a rotation of  $0.10/4.15 = 0.024$  rad or even 12 cm vertical displacement at the toe of the 5 m wide staircase. This means an elongation of 12% for 1 m long well-anchored starter bars, which is way too far for class B or C reinforcement.

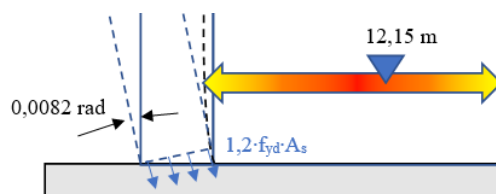


Fig. 5 Deformation scheme.

No other solution than an (expensive) joint can be offered at the 4.15 m floor location, which can compensate for a 10 cm elongation in case of fire. However, at the next floor level of 12.15 m, the rotation is limited to  $0.10/12.15 = 0.0082$  rad or the vertical displacement is limited to 4.1 cm. The corresponding strain is only 4.1% with the same boundary conditions, which is suitable for the applied class B reinforcement (5% characteristic strain) and avoids the application of unnecessary complicated joints. For the design of the foundation and the concrete core, it is recommended to account for the effects of overstrength. A factor of 1.2 is proposed to avoid non-expected failure mechanisms. Also, a verification of the equilibrium is needed with the calculated eccentricity.

## 7 CONCLUSIONS

A proposal is formulated for a uniform heating verification with a uniform temperature increase of at least  $200^{\circ}\text{C}$  looking to the findings out of the literature (Taerwe, 2007) and own investigations for R60. In the case of R120 requirements, this uniform heating should be increased up to  $300^{\circ}\text{C}$ .

A reasonable estimation of the spring constant is needed to limit the influence on the developed forces in the design. However, to estimate the elongations, even a free elongation delivers accurate results. It is also found that the filling of concrete cores at the support does not have a significant influence. Some provisions are given for the design of stiff secondary concrete staircases which might be pushed outwards by the elongation of large concrete structures.

A time delay in the developed forces is observed, which proves that a study including the cooling phase is needed. Also, the effect of prestressing is still disregarded and should be investigated.

## REFERENCES

- ACI 224.3R-95, 2013. *Joints in concrete structures*, Farmington Hills: ACI.
- Beitel, J. & Iwankiw, N., 2002. *Analysis of needs and existing capabilities for full-scale fire resistance testing*, Gaithersburg: NIST, National institute of standards and technology.
- Bulletin 74, 2014. *Planning and design handbook on precast building structures*. Lausanne: Fédération internationale du béton (fib).
- Dimia, M. S., Guenfoud, M., Gernay, T. & Franssen, J.-M., 2011. Collapse of concrete during and after the cooling phase of a fire. *Journal of fire protection engineering*, Volume 21, pp. 245-263.
- EN 1992-1-1, 2005. *Design of concrete structures - Part 1-1: General rules and rules for buildings (+AC 2008)*. Brussels: European Committee for Standardization.
- EN 1992-1-2, 2004. *Design of concrete structures - Part 1-2: General rules - Structural fire design*. Brussels: CEN.
- Franssen, J. & Gernay, T., 2017. Modelling structures in fire with SAFIR. *Journal of Structural Fire Engineering*, vol. 8, nr. (3), pp. 300-323.
- Gernay, T., 2019. Fire resistance and burnout resistance of reinforced concrete columns. *Fire Safety Journal*, pp. 67-78.
- Gernay, T., Millard, A. & Franssen, J., 2013. A multiaxial constitutive model for concrete in the fire situation: Theoretical formulation. *International Journal of Solids and Structures*, 50(22-23), pp. 3659-3673.
- Langdon-Thomas, G., 1972. *Fire Safety in Buildings*. London: Adam & Charles Black.
- Mostafaei, H., Sultan, M. & Bénichou, N., 2009. *Recent developments on structural fire performance engineering - A state-of-the-art report*, Ottawa: National research council of Canada. Institute for research in construction. N° RR-275.
- Stern-Gottfried, J. & Rein, G., 2012. Travelling fires for structural design-Part II: Design methodology. *Fire safety journal*, pp. 96-112.
- Taerwe, L., 2007. *From member design to global structural behaviour*. Coimbra, Fire design of concrete structures - from materials modelling to structural performance.

## EXPERIMENTAL INVESTIGATION OF THE ELASTIC MODULUS OF HIGH STRENGTH CONCRETE AT ELEVATED TEMPERATURES

Túlio A. P. Coelho<sup>a</sup>, Sofia M. C. Diniz<sup>a</sup>, Francisco C. Rodrigues<sup>a</sup>, Ruben Van Coile<sup>b</sup>

<sup>a</sup> Federal University of Minas Gerais, Department of Structural Engineering, Minas Gerais, Brazil

<sup>b</sup> Ghent University, Department of Structural Engineering and Building Materials, Ghent, Belgium

### Abstract

Concrete is susceptible to damage caused by physical-chemical processes during heating, resulting in the reduction of the elasticity modulus, which decays monotonically. After cooling, the elastic modulus is lower than for the heated concrete. After fire concrete heated above 300°C is commonly removed, but cooler concrete is often maintained in the rehabilitated structure. Therefore, the temperature-dependency of the elasticity modulus of a high strength concrete after exposure to elevated temperatures (in casu heating up to 225°C) is studied through the non-destructive technique of excitement impulse. In this method, the elastic modulus is measured by obtaining a natural vibration frequency from a mechanical impulse received by an acoustic sensor. The results indicate a considerable reduction of elastic modulus, in the range of 30%-35% after heating to 225°C.

**Keywords:** elevated temperatures, concrete, elastic modulus, non-destructive testing.

### 1 INTRODUCTION

Concrete has advantages when exposed to high temperatures in comparison to other building materials such as wood and steel, including the non-emission of toxic gases and the characteristic of being an incombustible material. According to Wendt (2006), citing Mehta & Monteiro (1994), concrete is also capable of maintaining its strength over a period long enough for fire rescue operations. However, concrete is susceptible to permanent damage caused by physical-chemical processes during heating, including: loss of compressive strength, reduction of the elasticity modulus, cracking due to thermal stresses, destruction of the adhesion between the cement paste and the aggregates, and the loss of adhesion between the concrete and the steel (Wendt, 2006).

The modulus of elasticity, or Young's modulus, is a measure of the stiffness of a material. The greater the modulus of elasticity, the less deformable the material is. Subject to high temperatures, the modulus of elasticity behaves similarly to most of the mechanical properties of concrete. In general, the resistance, modulus of elasticity and tensile strength decrease considerably, in addition, its decay is monotonic, and after cooling, its value is lower than that of heated concrete (Xiao and König, 2004). Also according to these authors, the type of aggregate has a great influence on the elasticity module. Young's modulus values decrease more significantly for cured concrete submerged in water and it does not correlate with heating and cooling cycles, but with the maximum temperature reached during heating.

After fire, concrete heated above 300°C is commonly removed (Ni and Gernay, 2021). The permanent damage after exposure to lower elevated temperatures is, however, not yet fully understood. Therefore, an experimental investigation is made into the elastic modulus of concrete during heating up to 225°C and subsequent cooling. This investigation is intended to highlight the need for further investigations into the possibility of continued use post-fire of concrete heated to relatively low temperatures (i.e. lower than 300°C).

The non-destructive technique of impulse excitation coupled to an instrumented oven is implemented in this work to determine the variation of the modulus of elasticity as a function of the increase in temperature. In this method, the modulus of elasticity of the material is measured by obtaining its natural frequency of vibration from a mechanical impulse, captured by an acoustic response sensor (ATCP - Physical Engineering). According to PEREIRA et al (2015), non-destructive tests allow

obtaining information regarding the defect content of a given product, the technological characteristics of a material, or even, the monitoring degradation in service of components, equipment and structures.

## 2 MATERIALS AND METHODS

### 2.1 Materials

With the aid of the Experimental Structure Analysis Laboratory (LAEES) of the Federal University of Minas Gerais (UFMG), a 90 cm long, water-cured concrete beam, with a 30x15 cm cross-section was made for this test. For the production of concrete, CP V ARI PLUS cement was used with a characteristic resistance at 28 days ( $f_{ck}$ ) equal to 30 MPa. Table 1 shows the concrete composition used to make the concrete.

Table 1: Concrete composition used to make the tested beam

CP V ARI PLUS (Kg)	Coarse Natural Sand (m <sup>3</sup> )	Pebble (Kg)	Water (L)	Muraplast FK 118 (Additive) (mL)	Factor Water / Cement	Density (Kg /m <sup>3</sup> )	Mortar content (%)
1,47	3,42	3,41	1	11,71	0,68	2281	0,589

The specimens were extracted from the concrete beam. The specimens were made in rectangular formats with dimensions of approximately 15,0 x 3,0 x 1,0 cm, in three cutting planes: XY, XZ, YZ, according to Fig. 1.

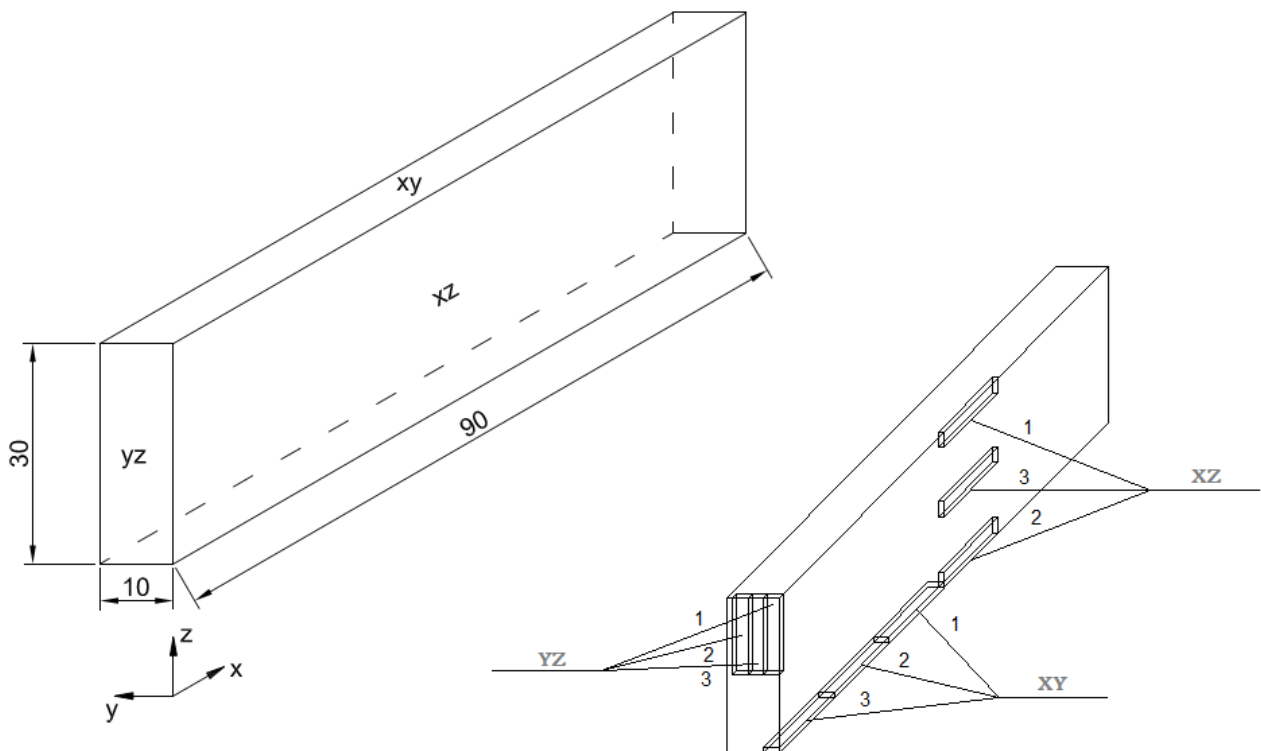


Fig. 1 Concrete beam (30x10x90cm) with the cutting planes: XY, XZ, YZ.

These planes represent the two directions that contain the largest surface area of the specimen, as can be seen. It is important to note that the specimens extracted from the XZ plane were purposely selected at different heights of the beam, in order to evaluate the effect of compaction on the elasticity module.

## 2.2 Equipment

To characterize the elastic modulus as a function of temperature, the instrumented oven HT1150 of the Sonelastic line was used, developed by ATCP - Physical Engineering and by the group of Physical Engineering and Materials Microstructure (GEMM). The oven works in conjunction with an automatic pulsator and a directional microphone for high temperatures.

In addition, the oven allows continuous use of temperature up to 1150 °C, having a derivative integral proportional controller (PID) with 3 ramps and 3 levels, with internal dimensions of 100x150x200 mm, hence the need to extract the specimens in the above measures.

From its use, the modes of flexural vibration (where the modulus of elasticity was obtained) and torsional (from which the modulus of shear) were obtained as a function of the temperature of the samples. In this case, the work in question was concerned with the study of the modulus of elasticity.

## 3 METHODOLOGY

The non-destructive tests were performed at the Laboratory of Experimental Analysis of Structure (LAEES) of the Federal University of Minas Gerais (UFMG). The method of impulse excitation, used in the data acquisition equipment used in this test, is based on the ASTM E1876 (2006) standard, which addresses the evaluation of the modulus of elasticity and damping of materials from the natural frequencies of vibration of the test specimens.

The basic principle of operation of the Sonelastic equipment is the application of a mechanical pulse of short duration, through the pulsator, in the specimen that responds with vibrations in its natural frequencies, according to the imposed conditions, which are obtained by the acoustic capturer (both located outside the specimen). The Sonelastic software identifies what these frequencies are and their respective damping and, thus, analyzes the transient vibrations, from which it extracts the frequencies for the calculation of the elastic modulus and the respective attenuation rates for the calculation of the damping (PEREIRA, et al. , 2015).

Performing this procedure at different temperatures, dynamic elastic modulus for different temperatures are calculated. In the case of the test performed, the maximum temperature reached was 225 °C due to technical limitations of the specific equipment used.

Before starting the test, the nodal lines of the specimens located at  $0.224L$  (where  $L$  is the specimen length) of each end are delimited. These nodal lines are defined for the vibration mode equal to 1 which defines the maximum amplitude in the center of the specimen and at its ends (COSSOLINO & PEREIRA, 2010). In this way, the specimens are positioned with the modal lines on the supports and the point of impact in its center. Thus, transversal and flexional vibrations are obtained.

The modulus of elasticity ( $E$ ) is then determined by the frequency of flexural vibration, while the transverse strain modulus ( $G$ ) is determined by the frequency of torsional vibration (ASTM E1876).

For this purpose, the processing unit was programmed to acquire data per minute, the oven temperature being increased by 5 °C at each time interval (per minute). The initial temperature of all tests was at room temperature and the maximum temperature reached by the oven was set at 225 °C, as already mentioned, for 1 hour. Note that the procedure does not ensure that a uniform temperature is reached within the specimen. This was done to obtain assess the relevance of more elaborate and costly testing whereby slower heating will be used to ensure more uniform temperatures.

In addition to the configuration of the processing unit, the Sonelastic software was also programmed for measurements at continuous high temperature, taking readings regarding the flexional and torsional vibration mode with estimated Poisson coefficient.

#### 4 RESULTS ANALYSIS

The obtained variation of the modulus of elasticity as a function of temperature for the three tests in each of the three planes can be seen in Fig. 2 to 4.

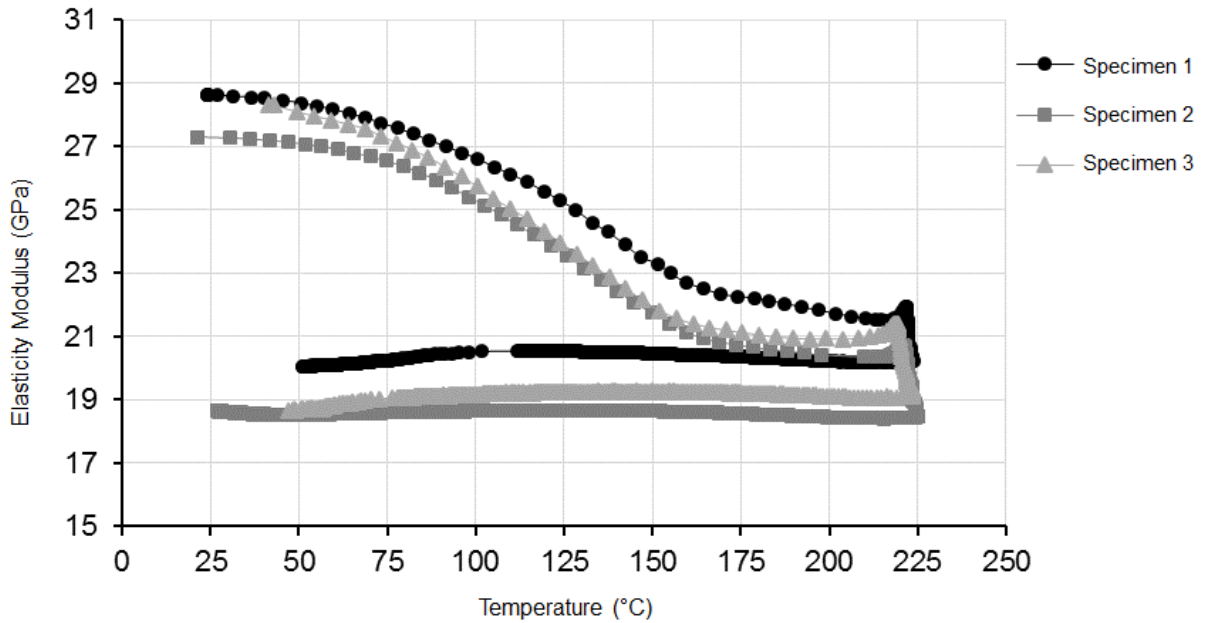


Fig. 2 Variation of the modulus of elasticity for the specimens in the XY plane.

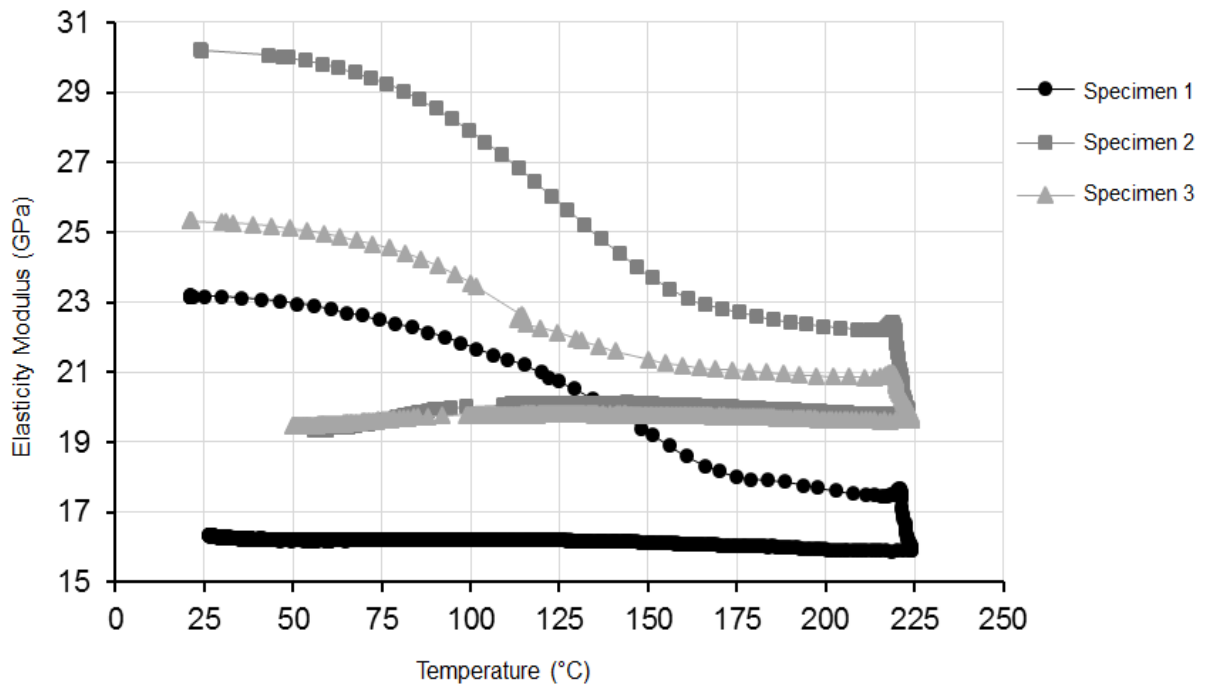


Fig. 3 Variation of the modulus of elasticity for the specimens in the XZ plane.

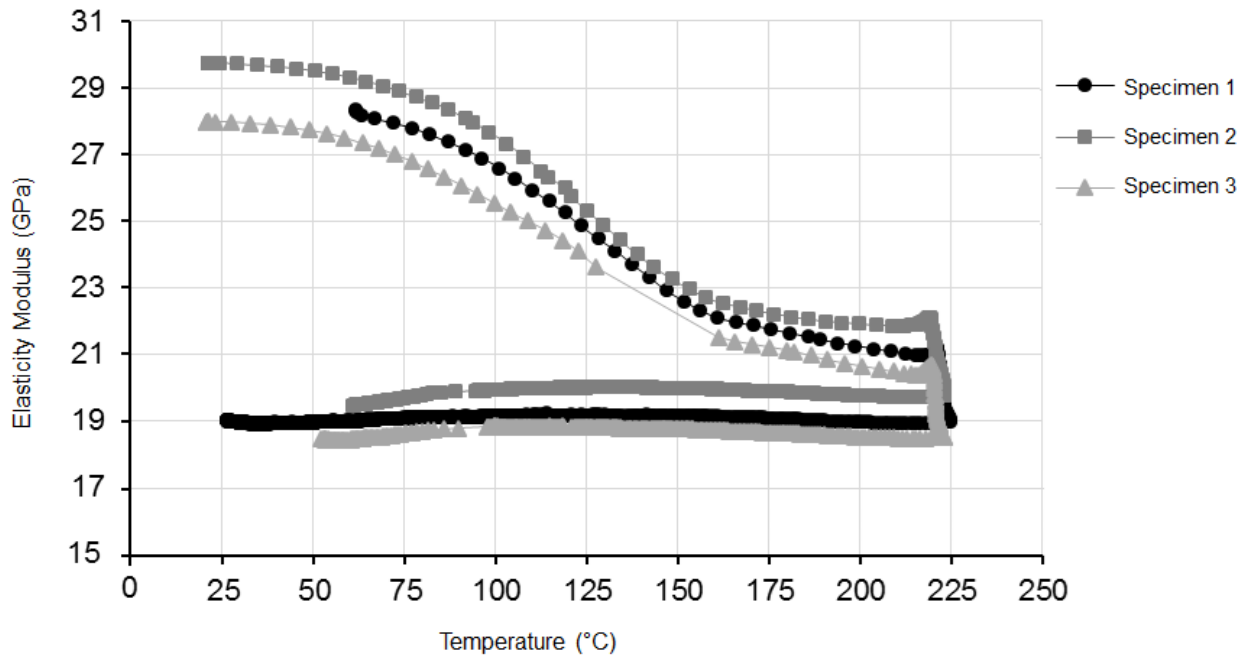


Fig. 4 Variation of the modulus of elasticity for the specimens in the YZ plane.

It is observed that with the increase in temperature there is a sharp drop in the elasticity modulus and when decreasing the temperature the specimen does not recover its modulus of elasticity, this fact occurs in all cases.

It is observed, in all the graphs presented here, that there is considerable scatter for the elastic modulus at the start of the test. It can be seen that with the increase in temperature, all specimens showed the same loss of rigidity behavior. In percentage, the losses were very similar, presenting, at the end of the test, a loss of approximately 33% (Fig. 5).

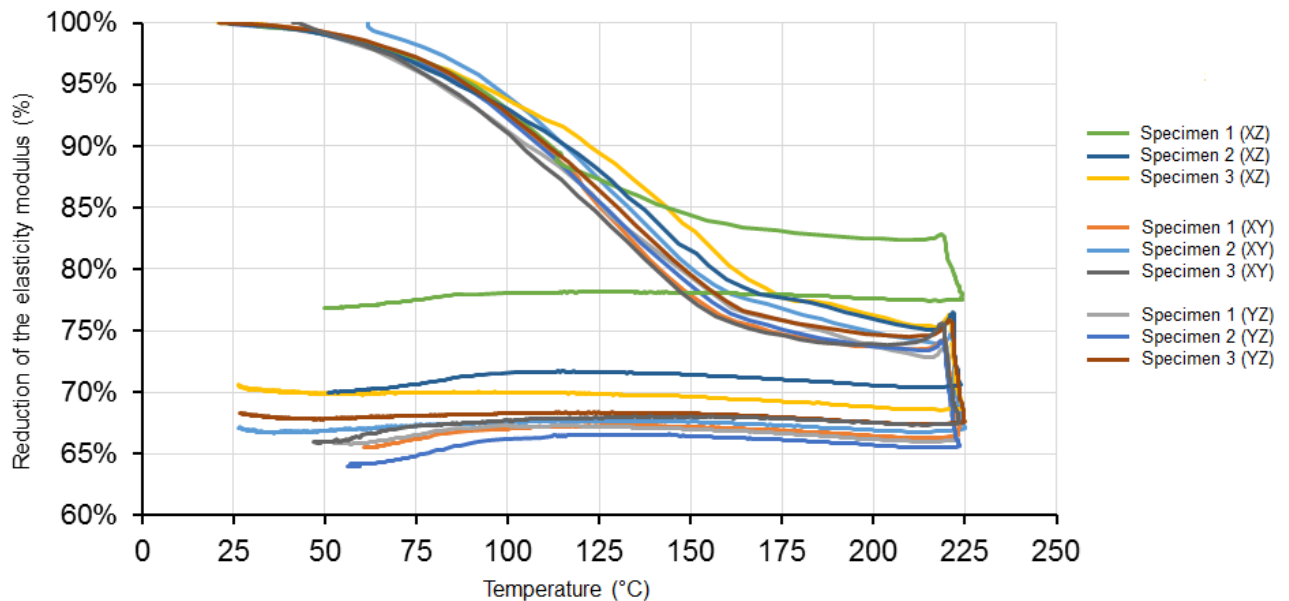


Fig. 5 General comparison of the elasticity modulus decay curves due to temperature.

Considering the above figures, different regions for the loss in the modulus of elasticity can be observed. There appears to be first region between room temperature and 160°C with a fast decrease of in the elastic modulus. In this region, the evaporation of all free water occurs, as well as the start of the loss of the chemically bonded water. According to Wendt (2006), this corresponds with an increase in permeability and total degradation of ettringite, a component responsible for the initial grip and resistance, as well as an increase in the concentration of calcite.

A second region between 160 and 220°C is observed where the decrease in elastic modulus is markedly slower. Note, however, that the transient nature of the tests (no uniform temperature) makes definite conclusions difficult. While maintaining the temperature at approximately 225°C for 1 hour a further reduction in the elastic modulus is recorded. During cooling, the modulus of elasticity is approximately constant. It should be noted that it does not recover with the reduction in temperature, and that for some specimens a further reduction in elastic modulus is recorded.

The figures highlight that the XY and YZ planes have less variability in the elastic modulus when compared to the XZ plane. This issue can be explained by the fact that it is precisely this plane where the extraction of the specimens took place at different heights of the beam. In other words, it is perceived that different heights refer to different levels of compaction and, consequently, different elasticity modulus values. Thus, these results suggest that the better the compaction, the greater the modulus of elasticity and vice versa. Some effect on the percentage reduction of the modulus of elasticity at elevated temperatures is observed. This issue further emphasizes the importance of compaction control when making concrete

The results can be compared with those obtained by Bilow & Kamara (2008). Considering the aggregates used and the initial modulus of elasticity of approximately 28 GPa, the results of Bilow and Kamara referring to the siliceous aggregates are considered. From (Bilow & Kamara, 2008) it can be seen that for the temperature at which the test was performed, 235 °C or 437 °F, a reduction of the elasticity modulus to a residual value of approximately 60% is expected. In the current study, a residual value of approximately 67% has been observed, a slightly higher retention than expected, probably due to the characteristics of the concrete composition and the heating regime.

## 5 CONCLUSIONS

An exploratory experimental study was conducted into the elastic modulus of concrete during heating to 225°C and subsequent cooling. Even for these small temperature increases, significant permanent reduction in the elastic modulus was observed (approximately 33%). The decrease in elastic modulus already starts at very low temperatures (below 100°C). This may have important implications for the continued use of concrete after heating.

The applied non-destructive test method, i.e. continuous acoustic test during heating and cooling, was found very promising. The obtained results were furthermore in line with selected results published in literature. The preliminary investigation has shown both the relevance and the importance of this type of study. Follow up studies using an adjusted heating regime are recommended.

## REFERENCES

- American Society For Testing Materials, 2006. *Standard test method for dynamics Young's modulus, shear modulus, and Poisson's ratio by impulse excitation of vibration*. ASTM designation E1876 – 09.
- Bilow, D. N., Kamara, M. E., 2008. *Fire and concrete structures*. Structures 2008 conference – ASCE.
- Cossolino, L. C ., Pereira, A. H. A., 2010. *Elastics module: overview and characterization methods*. Technical and Scientific Information ITC-ME: ATCP - Physical Engineering.
- Mehta, P.K .; Monteiro, P.M., 1994. *Concrete: structure, properties and materials*. São Paulo: Pini.
- Ni, S., Gernay, T. (2021). *A framework for probabilistic fire loss estimation in concrete building structures*. Structural Safety, 88, 102029.
- Pereira, L. R. S ., Maldonado, T. T., Alves, R. C ., Carrasco, E. V. M., 2015. *Estimated modulus of elasticity as a function of temperature using excitation waves*. XV EBRAMEM - Brazilian Meeting on Wood and Wooden Structures.
- Wendt, S. C., 2006. *Analysis of color change in concretes subjected to high temperatures as an indication of reached temperatures and thermal degradation*. Dissertation (Master's) - Graduate Program in Civil Engineering at the Federal University of Rio Grande do Sul. Porto Alegre.
- Xiao, J.; König, G., 2004. *Study on concrete at high temperature in China – An overview*. Journal Fire Safety, 39(1):89-103.

# APPLICATION OF ADVANCED LOAD AND STRUCTURAL ANALYSIS IN CASE OF FIRE for the assessment of existing structures

Shana Van Hout<sup>a</sup>, Martin Classen<sup>b</sup>, Tom Molkens<sup>a,b</sup>

<sup>a</sup> Sweco Belgium bv, Buildings Division, Brussels, Belgium

<sup>b</sup> KU Leuven, Campus De Nayer, Department of Civil Engineering, Materials and Construction Division, Belgium

## Abstract

Due to the refurbishment, extension or execution and design errors, it happens that a reassessment of structures is needed. This is to satisfy the legal requirements of fire resistance, and sometimes even those in ambient conditions. In practice, primarily simplified design models are used in combination with the well-known partial factor method. Consequently, an expensive upgrade of the bearing capacity of the structure besides even more expensive fire protection will be needed. In the current paper, an assessment procedure is proposed that starts with a more refined load analysis. This directly impacts all limit state conditions (service, ultimate and fire). The proposed analysis uses the changing behaviour of a structure during the fire situation, called structural interaction. Besides the economic impact, the ecologic, social and safety aspects (in case of fire) will also be treated.

**Keywords:** load analysis, load arrangement, structural interaction, resilient structures, membrane action

## 1 INTRODUCTION

Once fire resistance is involved, it becomes common practice to apply more advanced methods of analysis, including material and geometrical non-linearities (Franssen & Gernay, 2017), mostly applied by the meaning of finite element analysis (FEM). At that moment, the potential of advanced analysis methods becomes available like the one following from catenary action at a beam level, tensile membrane action (TMA) for slabs or compression membrane action (CMA) (Gouverneur, 2014). However, the applications stay limited towards member analysis. Nowadays, the practice is shifting to more probabilistic structural fire engineering, where also the modelling of the permanent and live load is reviewed (Balsa, et al., 2021).

Despite the features of those advanced analysis methods, one important step is neglected and has not been treated in a profound scientific way: the load analysis and his (changing) behaviour during the fire event. The load arrangement is seen as a fixed property, primarily based on a simplified analysis (one-way bearing, for example) and only valid in combination with small deformations that will not create an interaction between the load-carrying element and the one that should be supported. Due to higher deformations of a slab subjected to fire, the load analysis will change, which mostly leads to (completely) different load arrangements.

Nevertheless, actual codes specifically demand a limit state design that should be based on structural and load models appropriate for the relevant limit state (EN 1990, 2002). In case of fire, but in some extend already applicable in the ultimate limit state verification and certainly, for accidental actions, both models can or even should be adapted according to the envisaged limit state. The combination of modified load and structural analysis can result in essential savings (economic, ecological and social).

To show the issue and the possibilities which can be created a more academic example at a system level is presented in Chapter 2 based on a simple square model of a one-way or two-way bearing slab with a masonry wall in the middle and that in ambient conditions. Once fire is involved, the stiffness of a slab is changing due to the temperature increase. How this can be treated is explained

in Chapter 3. Here an analytical way is compared to the outcomes of finite element method (FEM) analysis. Chapter 4 deals with a real case study, where a comparison is made between the outcomes of a classic approach and the one proposed. Finally, conclusions can be found in the last Chapter 5. Even with multiplication in cost for the study, the benefit of a more refined load analysis is still significant. In this case study, the firstly proposed additional reinforcement was not anymore needed in ambient conditions. However, a (strongly) reduced and modified fire protection was still needed in case of a fire.

**2 STRUCTURAL INTERACTION**

Two simple more academic examples illustrate the influence of structural behaviour in the load analysis. Each time a part of a continuous beam-shape structure is analysed; a three-story high building (system) with a square floor plan of 6 by 6 m<sup>2</sup> with at two ends symmetrical boundary conditions. Attention will be given to the floor above ground floor level, the level that will be submitted to fire in the next chapter. Material properties are listed in Table 1.

Table 1. Material properties.

Material	Density	Strength	Young modulus	Poisson's ratio	Material model
	kN/m <sup>3</sup>	[N/mm <sup>2</sup> ]	[N/mm <sup>2</sup> ]	[-]	
Concrete	25	f <sub>ck</sub> = 30	32000	0.2; cracked 0	EC2
Reinforcement	78.5	f <sub>yk</sub> = 500	200000	0.3	EC2
Masonry	17.8	f <sub>k</sub> = 10	10000	0.25	EC6

In the first example, a one-way bearing slab (OWS, Fig. 1 (a)) is showed with a bearing wall (0.15 m) in the middle, parallel to the span, which is not present at the lowest ground level. This is a typical layout for an apartment building with an open space at the lower level (the one submitted to fire). The investigated transfer slab is a thick one-way slab of 0.42 m. All levels above do have a thickness of 0.20 m (minimum for acoustic performance) and have a square floorplan (half part modelled). Secondly, a relatively thin (0.22 m) two-way bearing slab (TWS, Fig 1 (c)) above the ground floor is analysed with one-way slabs for the upper levels (rooms of 3x6 m<sup>2</sup>), again with a thickness of 0.20 m. Besides the own weight, a dead load of 2 kN/m<sup>2</sup> was added, and a live load of 2 kN/m<sup>2</sup> (dwelling) was also applied on the upper level (habitable attic). The story height is set equal to 3 m. For each example, two different thicknesses of the transfer-slab will be investigated, see Fig. 1. This difference in thickness or the relaxation factor is set equal to 3<sup>-1/3</sup> = 0.69.

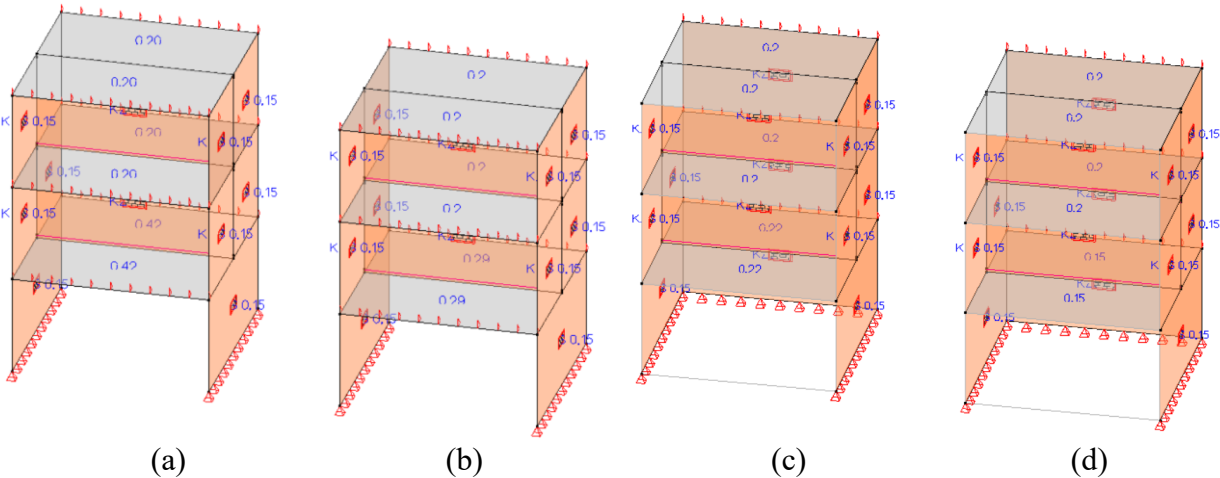


Fig. 1 Figures of both models (a) + (b) OWS and (c) + (d) TWS with two different thicknesses of the transfert-slab, stiff (a) + (c) or relaxed (b) + (d).

## 2.1 Analytical load analysis versus FEM.

A classic load arrangement is used in a first approach where gravity loads just descent vertically to the transfer slab without any load redistribution. Based on the yield line theory, the loads for OWS and TWS can be found by *Eqs. (1) and (2)*, respectively. It is seen that the total load on each wall for both cases at the level of the transfer-slab is equal. The load distance  $s$  (perpendicular to the wall direction) in *Eq. (1)* varies from 0 in the corners to 6 m (2 times  $6/2$ ) at half span of the slab.

$$\text{Wall load}_{\text{OWS}} = 2 \cdot (s \cdot (0.2 \cdot 25 + 2 + 2) + 3 \cdot 0.15 \cdot 17.8) = 16 \rightarrow 124 \text{ kN/m} \quad (\sum L = 420 \text{ kN}) \quad (1)$$

$$\text{Wall load}_{\text{TWS}} = 2 \cdot (3 \cdot (0.2 \cdot 25 + 2 + 2) + 3 \cdot 0.15 \cdot 17.8) = 70 \text{ kN/m} \quad (\sum L = 420 \text{ kN}) \quad (2)$$

In modern design procedures, a building or at least part of it will be analysed by means of a finite element method (FEM) model. Many commercially easy-to-use tools are available; however, limited to linear elastic material behaviour. As long as compression forces mainly load the masonry wall, the validity of such models is more or less standing. Therefore, a first reference model is made with a continuous wall till the ground floor level, making the stiffness of the transfer-slab less critical. Loads are compared at the upper level of the first level wall to avoid discrepancies caused by the misbehaviour of the shell elements (in bending), see Table 2 (total loads of the analytical solution becomes  $420 - 3 \cdot 0,15 \cdot 17,8 \cdot 6 = 372 \text{ kN}$ ).

Table 2. Loads on upper part of the wall following different stiffnesses and typology of the transfer-slab.

Model	Analytical	FEM, reference	FEM, stiff	FEM, relaxed	Fire
$(\sum L)_{\text{OWS}}$	-372 kN	-365 kN	-298 kN	-131 kN	-131 kN <sup>†</sup>
$(\sum L/L)_{\text{OWS}}$	-62 kN/m	-61 kN/m	-50 kN/m	-22 kN/m	-22 kN/m <sup>‡</sup>
$(\sum L)_{\text{TWS}}$	-372 kN	-242 kN	-44 kN	+23 kN	0 kN <sup>†</sup>
$(\sum L/L)_{\text{TWS}}$	-62 kN/m	-40 kN/m	-7 kN/m	+4 kN/m	0 kN/m <sup>‡</sup>

<sup>†</sup> at the toe of the wall a value of  $-8 \cdot 6 = -48 \text{ kN}$  must be added or for <sup>‡</sup> a linear distributed load of  $-8 \text{ kN/m}$ .

The first two columns (light grey shaded) show that the summed values of the OWS system are very close to each other. The shape of the load distribution is, however, different but is not shown and discussed here. For the TWS-system, load distribution towards the parallel walls of the bearing direction at the upper stories plays a significant role. Out of the FEM model the simplification of the one-way bearing direction is questionable.

## 2.2 Small displacements of the bearing structure

In a next step, a stiff transfer slab is foreseen above the ground floor, like shown in Fig. 1 (a) + (c). The thickness of 0.42 m is determined by a maximum final deflection of  $L/500$  in ambient conditions, accounting for the cracked stiffness based on practical reinforcement; upper mesh #150/8 + lower mesh #150/10 +  $7\text{Ø}12/\text{m}$  in the bearing direction and creep (creep-factor  $\varphi_{(t,t_0)} = 2$  (EN 1992-1-1, 2005)). Even with this rather stiff slab compared to the number of levels and span, the load descends towards about 80 % (Table 2) of what can be presumed based on infinite stiffness for the OWS-slab. Due to the relatively stiff upper floors in the TWS-slab system, the decrease is even more pronounced; only 12% of the analytical load is left. This in the understanding that the stiff floors do have the capacity at the load resistance level to carry the loads at each level.

## 2.3 Medium to large displacements of the bearing structure

The same structure can be analysed as a first estimation, only accounting for the creep by reducing the stiffness by a factor  $(1 + \varphi_{(t,t_0)}) = 3$ . The second moment of area is defined by the third power of the total slab height, so a reduction of this thickness is needed by a factor  $3^{-1/3} = 0.69$ , see Fig 1 (b) and (d). Compression forces on top of the wall are now reduced to 35% in the OWS system and become even tensile forces for the TWS-system, leading to cracking (see Table 2).

### 3 STRUCTURAL INTERACTION IN CASE OF FIRE

Due to a fire situation, the lower part of the slab of the previous academic example will be heated. Due to the influence on the Young modulus of the steel, the stiffness is decreasing significantly. For continuous slabs also the compression zone will be infected at the location of the hogging moment; here the well-known 500°C isotherm method is proposed. The following iteration process, Fig. 2, will be used to facilitate the load analysis and verification of the obtained results.

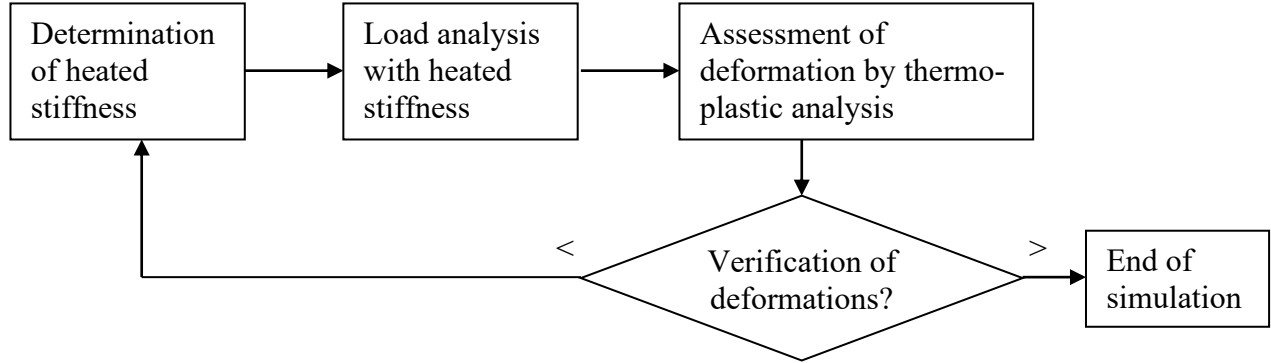


Fig. 2. Flow chart proposed iteration process.

In the previous chapter descending loads are shown once the stiffness of a transfer-slab is decreasing. Besides cracking and creep, the heating effect makes the stiffness further decrease during the fire. So, a first estimation is needed of the heated stiffness, subsequently, a load analysis can be performed by the 3D-model used for the ambient design. This load arrangement can then be used as input for a more time-costly thermo-plastic analysis. Two situations can be imagined; '>' out of Fig. 2 indicates that the required fire rating is reached and that the obtained deformation of the thermo-plastic analysis is at least equal or more prominent as the one out of the 3D-model. This is the end of the simulation. In the opposite case ('<') a new iteration is needed.

#### 3.1 Heated stiffness

Depending on the required fire rating, temperature profiles can be determined by thermal section analysis or out of Annex A (EN 1992-1-2, 2004). An independency of the load arrangement history is assumed, and the bending stiffness at the fire rating time  $R$  is presumed to be representative. As a simplification, the whole span length will be verified with the cracked stiffness. Further on for a continuous beam a smeared approach can be used with a length-weighted average stiffness for the parts that are subjected to negative or positive bending moments. The purely analytical Eqs. (3) and (4) do give estimations that can be used as a lower bound of the heated stiffness ( $I_{R,est}$ ).

$$I_{pos,R,est} = b \frac{\left(\frac{A_{sl} k_{y,\theta} f_{y,k}}{0.8 \cdot f_{ck}}\right)^3}{12} + b \left(\frac{A_{sl} k_{y,\theta} f_{y,k}}{0.8 \cdot f_{ck}}\right) \left(h - \frac{A_{sl} k_{y,\theta} f_{y,k}}{2 \cdot 0.8 \cdot f_{ck}}\right)^2 + \alpha_e \cdot k_{E,\theta} \cdot A_{sl} \cdot \left(h - c - \frac{\emptyset}{2}\right)^2 \quad (3)$$

$$I_{neg,R,est} = b \frac{\left(\frac{A_{su} f_{y,k}}{0.8 \cdot f_{ck}} - x_{500^\circ C}\right)^3}{12} + b \left(\frac{A_{su} f_{y,k}}{0.8 \cdot f_{ck}} - x_{500^\circ C}\right) \left(h - x_{500^\circ C} - \frac{A_{su} f_{y,k}}{2 \cdot 0.8 \cdot f_{ck}}\right)^2 + \alpha_e \cdot A_{su} \cdot \left(h - x_{500^\circ C} - c - \frac{\emptyset}{2}\right)^2 \quad (4)$$

where  $I_{R,est}$  Second moment of area estimation (subscript *est*), at a fire rating time  $R$  valid for area subjected to a positive (*pos*) or negative (*neg*) bending moment.

$A_s$  Longitudinal upper (*u*) or lower (*l*) cross-section of the reinforcement area.

$k_{y,\theta}$  Reduction factor of the yield strength of the reinforcement steel at a temperature  $\theta$  corresponding with the fire rating time  $R$  in the section.

$f_{y,k}$  Characteristic yield strength of the reinforcement.

$f_{c,k}$  Characteristic compression strength of the concrete (cylinder).

$h$  Total height of the section or slab.

- $\alpha_e$  Ratio between the Young modulus of steel  $E_s$  and secant modulus of concrete  $E_{cm}$ .
- $k_{E,\theta}$  Reduction factor of the Young modulus of the reinforcement steel at a temperature  $\theta$  corresponding with the fire rating time  $R$  in the section.
- $c$  Concrete cover on the reinforcement.
- $\emptyset$  Equivalent diameter of the reinforcement bars (area weighted).
- $x_{500^\circ C}$  level of the 500°C isotherm corresponding with the fire rating time  $R$  in the section.

### 3.2 Load analysis

Once the heated stiffness is estimated ( $I_{R,est}$ ) the thickness of the slab subjected to fire ( $h_{eq}$ ) can be adapted to obtain the exact second moment of area. A new calculation will result in a load arrangement and vertical displacement different as the one used in the ambient conditions. It is this data that will be transferred to a thermo-plastic FEM-model by a one-way coupling.

### 3.3 Thermo-plastic assessment

For the worked example of section 2 the assessment procedure is done by the well-known FEM tool SAFIR® (Franssen & Gernay, 2017), which includes geometrical and material non-linearity. A two-step procedure is followed, firstly a thermal analysis of the involved plates and secondly a mechanical analysis. The same slab and reinforcement of the example are used and heated up by using an ISO834 smoke gas temperature curve. Material properties can be found in Table 3.

Table 3. Thermal and mechanical properties.

Material	Siliceous concrete	Reinforcement
$\alpha_{c,hot}$ [W/m <sup>2</sup> K]	25	25
$\alpha_{c,cold}$ [W/m <sup>2</sup> K]	4	4
$\varepsilon$	0.7	0.7
$\rho$ [kg/m <sup>3</sup> ]	2400 (46kg/m <sup>3</sup> H <sub>2</sub> O)	7850
$f_c$ and $f_y$ [MPa]	30	500
$E$ [N/mm <sup>2</sup> ]	33000	200000

### 3.4 Example

Based on Eqs. (3) and (4) an additional reduction of the cracked stiffness with a factor 3.6 for OWS and 3.3 for TWS can be expected in case of fire. For the sake of simplicity, the determined values out of Table 2, column ‘FEM-relaxed’ are adapted to the ones of the ‘Fire’ column and used in the thermo-plastic analysis. In the case of a fire event, the importance of the boundary conditions (BC) increases as they can allow for bending, compression (CMA), and tensile membrane action (TMA). For each investigated system, two simulations have been executed; displacement in the bearing direction are allowed (free) or prohibited (fix). Table 4 lists the results of these analysis based on analytical fire loads (ana) and those coming out of the last column of Table 2.

Table 4. Displacements and resistance time of both systems with two boundary conditions and loads.

Model	OWS				TWS			
	Free/fire	Fix/fire	Free/Ana	Fix/Ana	Free/fire	Fix/fire	Free/Ana	Fix/Ana
Displacement	-155mm	-61mm	-177mm	-82mm	-40mm	-250mm	-180mm	-281mm
Rating	168min	161min	142mn	125min	>8h	>8h	>8h	>8h

When rigid horizontal support can be expected, it is clear that the expected deformations stay low due to an arch-effect in the slab (Molkens, et al., 2017). However, when no horizontal stiffness in the building system and its surroundings is available, the slab reacts with tensile membrane action and a compression ring, resulting in deformations comparable to the one based on  $I_{R,est}$ .



# STRUCTURAL PERFORMANCE OF REINFORCED CONCRETE WALLS UNDER ISO FIRE EXPOSURE

Mohsen Roosefid<sup>a</sup>, Marie-Hélène Bonhomme<sup>a</sup>, Pierre Pimienta<sup>b</sup>

<sup>a</sup> IRSN (Institut de Radioprotection et de Sécurité Nucléaire), Fontenay-aux-Roses, France

<sup>b</sup> Université Paris-Est, CSTB (Scientific and Technical Center for Building), Champs-sur-Marne, France

## Abstract

The phenomenon of transient thermal strain of concrete at elevated temperatures has been clearly demonstrated through various experiments. However, little evidence is established for fire performance of the reinforced concrete bearing walls. This paper presents a numerical investigation of the thermomechanical behaviour of such walls exposed on one side to a two-hour ISO fire exposure in the framework of the international benchmark “Vulcain tests on 3 Walls”. The concrete behaviour was modelled by a damageable elastic constitutive law. The identification of the evolution of the model parameters with temperature has been performed using the energetic-regularization technique on the basis of experimental results of the tested concrete. It is illustrated through this numerical investigation that the proposed model can be relevant for predicting the global behaviour of reinforced concrete structures exposed to ISO fire.

**Keywords:** reinforced concrete wall, thermomechanical model, Finite Element method, damage modelling, transient thermal strain

## 1 INTRODUCTION

The reinforced concrete bearing walls in the nuclear facilities must be designed for minimum two hours of fire resistance according to the regulations of the French “Autorité de Sécurité Nucléaire” (Nuclear Safety Authority). Indeed, the nuclear requirements e.g. the confinement of radioactivity impose additional constraints on the fire safety provisions in order to limit the concrete cracking or spalling risk. However, more evidence is still necessary to confirm such fire performance of concrete structures because there are limited data available, especially regarding to the degradation of concrete structures due to ageing related phenomena.

In the framework of the International benchmark “Vulcain tests on 3 Walls”, three full-scale tests on a reinforced concrete wall exposed to ISO fire with 3 different levels of uniaxial mechanical loading were carried out in CSTB (Jihad *et al.*, 2019). The experimental test results have shown that the deflections of the walls decreased with the increased applied mechanical loading. Indeed, the external mechanical loading influences the phenomenon of transient thermal strain which develops in fire-exposed concrete and has implications on the structural behaviour. In order to assess the capability of available concrete models to take into account this phenomenon in reinforced concrete bearing walls mechanical behaviour under fire exposure, a numerical model developed on the basis of a finite element (FE) computer code using a damage model has been applied to these tests. The comparison of calculated results and experimental ones gives an accurate idea of the precision of the numerical model and leads to an assessment of the advanced modelling of such type of structure system.

## 2 VULCAIN TESTS ON 3 WALLS

These full-scale tests are with the objective to provide the experimental results on the structural behaviour of load bearing concrete walls in a fire situation. The test specimen was designed to analyse the thermo-mechanical experimental response of the ordinary concrete ( $f_c$  28 days = 32 MPa) walls tested at the age of 2 years. Three full-scale reinforced concrete walls of section 1.2 m width, 0.2 m thick and 3.0 m height were exposed on one side to ISO 834-1 fire with 3 different

levels of uniaxial mechanical loading (0, 100 and 1100 kN). Each wall involved was reinforced by a steel mesh (rebar  $\varnothing$  5.5 mm, mesh 11.9 x 11.9 mm<sup>2</sup>) positioned at 5 cm from the shuttered surface. The wall specimens were loaded before the fire test and then the load was maintained constant throughout the fire test. The boundary conditions at the top and the bottom of the walls were pivot connections centred on the thickness allowing only rotation along the horizontal axis. Thermomechanical properties of the tested concrete were determined on the basis of tests results carried out within the framework of Mindeguia's thesis (Mindeguia, 2009). Various compression tests were carried out on cylindrical samples (104 mm in diameter and 300 mm long) at room and high temperatures under thermal loads of 120, 250, 400 and 600 °C reached with a slow heating rate of 1 °C/min. Thermal strains under load were measured for two load levels 0.2 and 0.4 of initial compressive strength (20%  $f_c$  and 40%  $f_c$ ). Besides, the fracture energy ( $G_f$ ) was derived from 3-point bending tests. The thermomechanical properties of the tested concrete are shown in Fig. 1.

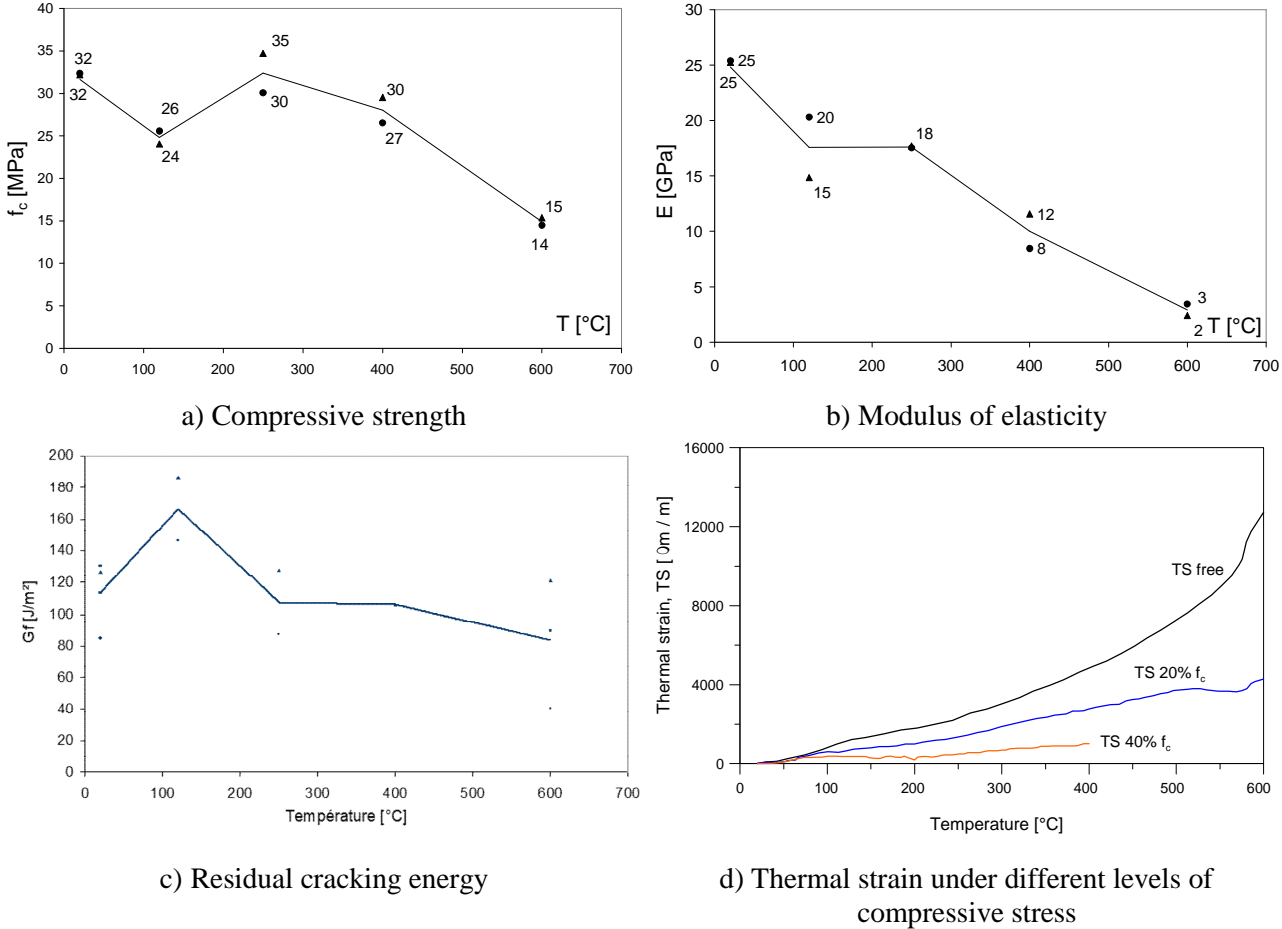


Fig. 1 Thermomechanical properties of the tested concrete

### 3 NUMERICAL INVESTIGATION OF THE FIRE TESTS

#### 3.1 Modelling

The present analysis is based on the constitutive model of elasticity coupled with damage, proposed by Mazars (Mazars, 1984). In this regard, a number of comments need to be made. One important choice is that the model must allow the finite element calculation of concrete structures in fire. Moreover, its final industrial use imposes robustness and easy implementing. In general, the finer the description of the material behaviour, the bigger the problems of numerical convergence are in concrete structures simulation, thus in practice limiting utility of the modelling. All these considerations brought the authors to model the concrete behaviour thanks to Mazars's model, which is implemented in CAST3M finite element code (Verpeaux *et al.*, 1988). In this model, the concrete is supposed to behave elastically and to remain isotropic, and it is assumed that only the elastic properties of the concrete are affected by damage. The coupling of

elasticity and damage processes is achieved by substituting the nominal stress tensor,  $\sigma$ , by the effective stress tensor,  $\tilde{\sigma}$ , in accordance with the strain equivalence principle. This leads to:

$$\sigma = (\mathbf{1} - D) \cdot \tilde{\sigma} \quad (1)$$

where  $D$  is the damage parameter.

The damage parameter  $D$  is defined as a combination of two damaging modes defined by  $D_t$  and  $D_c$ , for tensile and compressive states of stress, respectively, and ranges between 0 and 1 ( $0 \leq D \leq 1$ ).

When  $D$  is 0, the concrete is undamaged, whereas a value close to 1 indicates a rupture of the concrete.

The damage is controlled by the equivalent deformation,  $\tilde{\varepsilon}$ , who takes into account only the positive value of the principal strain:

$$\tilde{\varepsilon} = \sqrt{\langle \varepsilon_1 \rangle_+^2 + \langle \varepsilon_2 \rangle_+^2 + \langle \varepsilon_3 \rangle_+^2} \quad (2)$$

where  $\langle \varepsilon_i \rangle_+$  are defined as follows:

$$\langle \varepsilon_i \rangle_+ = \varepsilon_i \quad \varepsilon_i \geq 0 \quad (3)$$

$$\langle \varepsilon_i \rangle_+ = 0 \quad \varepsilon_i < 0$$

According to the damage model, damage occurs when the state of tension in the material reaches a certain threshold  $K$ . The damage occurrence criterion is expressed as follows:

$$f(\varepsilon, D) = \tilde{\varepsilon} - K(D) = 0 \quad (4)$$

with  $K(D) = \varepsilon_{D0}$  if  $D = 0$  in which  $\varepsilon_{D0}$  is the strain threshold.

The parameters  $D_t$  and  $D_c$  are explicitly related to the equivalent strain,  $\tilde{\varepsilon}$ , and the strain threshold,  $\varepsilon_{D0}$ . The associated equations are, respectively, for tension and compression:

$$D_t = 1 - \frac{\varepsilon_{D0}(1-A_t)}{\tilde{\varepsilon}} - \frac{A_t}{\exp[B_t(\tilde{\varepsilon}_M - \varepsilon_{D0})]} \quad (5)$$

$$D_c = 1 - \frac{\varepsilon_{D0}(1-A_c)}{\tilde{\varepsilon}} - \frac{A_c}{\exp[B_c(\tilde{\varepsilon}_M - \varepsilon_{D0})]} \quad (6)$$

The parameters  $A_t$ ,  $A_c$ ,  $B_t$  and  $B_c$  describe the shape of the stress-strain curve and can be identified on the basis of the uniaxial monotonic loading in tension and compression tests.

The identification of the evolution of the damage parameters of the Mazars model has been performed based on tests results presented in paragraph 2. For concrete thermomechanical properties evolution beyond 600°C, the trend of those given in Eurocode 2 Part 1-2 was taken as an input data. The procedure of identification of the Mazars' model parameters using the energetic-regularization technique based on the so-called Hillerborg method is reported in (Roosefid *et al.*, 2020).

### 3.2 Thermomechanical behaviour of the walls

Here the results obtained with a numerical model developed under the computer code CAST3M are explained and discussed. This 3D structural model represents the concrete wall and the reinforcing steel meshes with different types of finite elements (see Fig. 2). In this structural model, the reinforcing steel bars are represented by elastic-perfectly plastic bar element and a perfect bond between concrete and steel is assumed.

In order to perform whole fire analysis, the developed numerical model is divided into two different steps, one for heat transfer analysis and another one for structural analysis. The heat transfer analysis is conducted on the basis of a 2D model, which means that the temperature is calculated only on one horizontal concrete cross section. The cross-section temperature field obtained in such a way is then imposed uniformly to the whole height of the concrete walls.

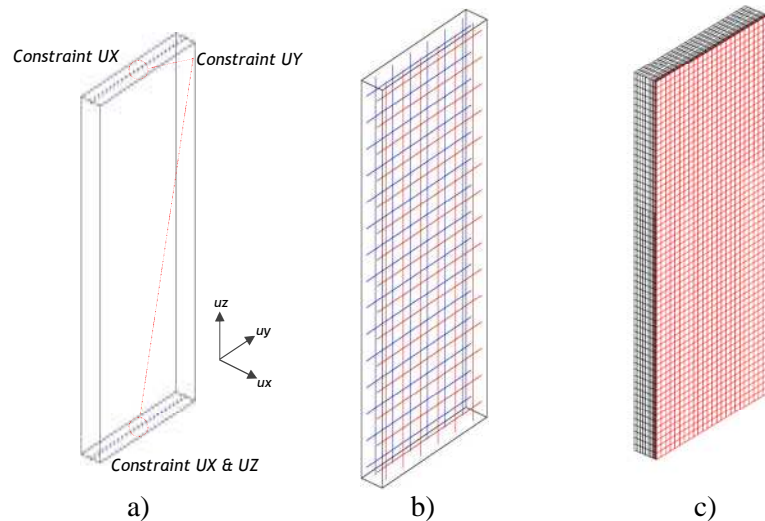


Fig. 2 (a) Boundary conditions, (b) reinforcement model and (c) concrete model

In the heat transfer analysis, the thermal properties of concrete and reinforcing steel are those given in EN 1992-1-2. The heat transfers are assumed to be unidirectional in the direction perpendicular to the exposed face of the walls. The net heat flux is based on heat transfer by convection and radiation. The coefficient of heat transfer by convection on the exposed and unexposed faces are equal, respectively, to 25 and 4 W/m<sup>2</sup>K according to EN 1991-1-2. The emissivity of the concrete surface is also taken equal to 0.7. A comparison of calculated and test temperatures for different distances from exposed face in cross section through the walls is illustrated in Fig. 3.

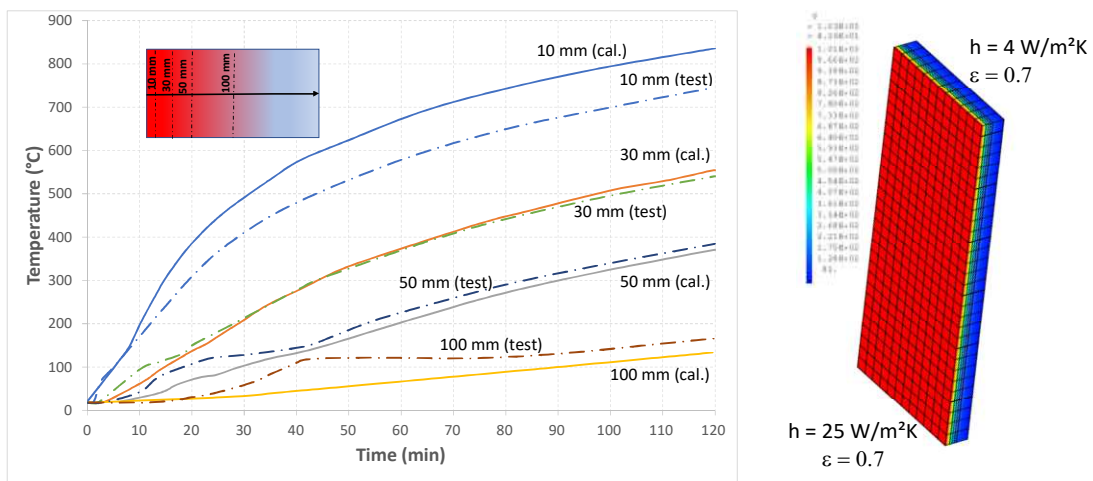


Fig. 3 Comparison between numerical and experimental temperatures of the studied walls

The global structural behaviour of the walls is analysed on the basis of previously calculated temperature field. The results of the numerical analyses of the walls are compared to the experimentally measured values through the ratio of the calculated deflection ( $w$ ) to the maximal experimentally measured deflection of the walls ( $w_{max, test}$ ), versus time, as shown in Fig. 4. It can be observed that globally the numerical simulations using free thermal strain follow quite closely the experimental results, except for the wall loaded at 1100 kN in which the difference between predicted and measured displacement appears significant. The authors think that the wall loaded at 1100 kN induces more transient thermal strain, which leads to lower thermal expansion than the other walls, thus creating a lower thermal curvature. As a consequence, a relatively high design load level in the fire situation ( $\mu_{fi} = 0.44$  for concrete wall loaded at 1100 kN using simplified design method for walls according to the section 12 of EN 1992-1-1) can lead to a deflection more than two times lower than the one measured on the walls loaded at 0 et 100 kN during the fire test. By taking into account the effect of the transient thermal strain, a good agreement between the

measured and the predicted displacement in the case of the wall loaded at 1100 kN can be noticed in Fig. 4c.

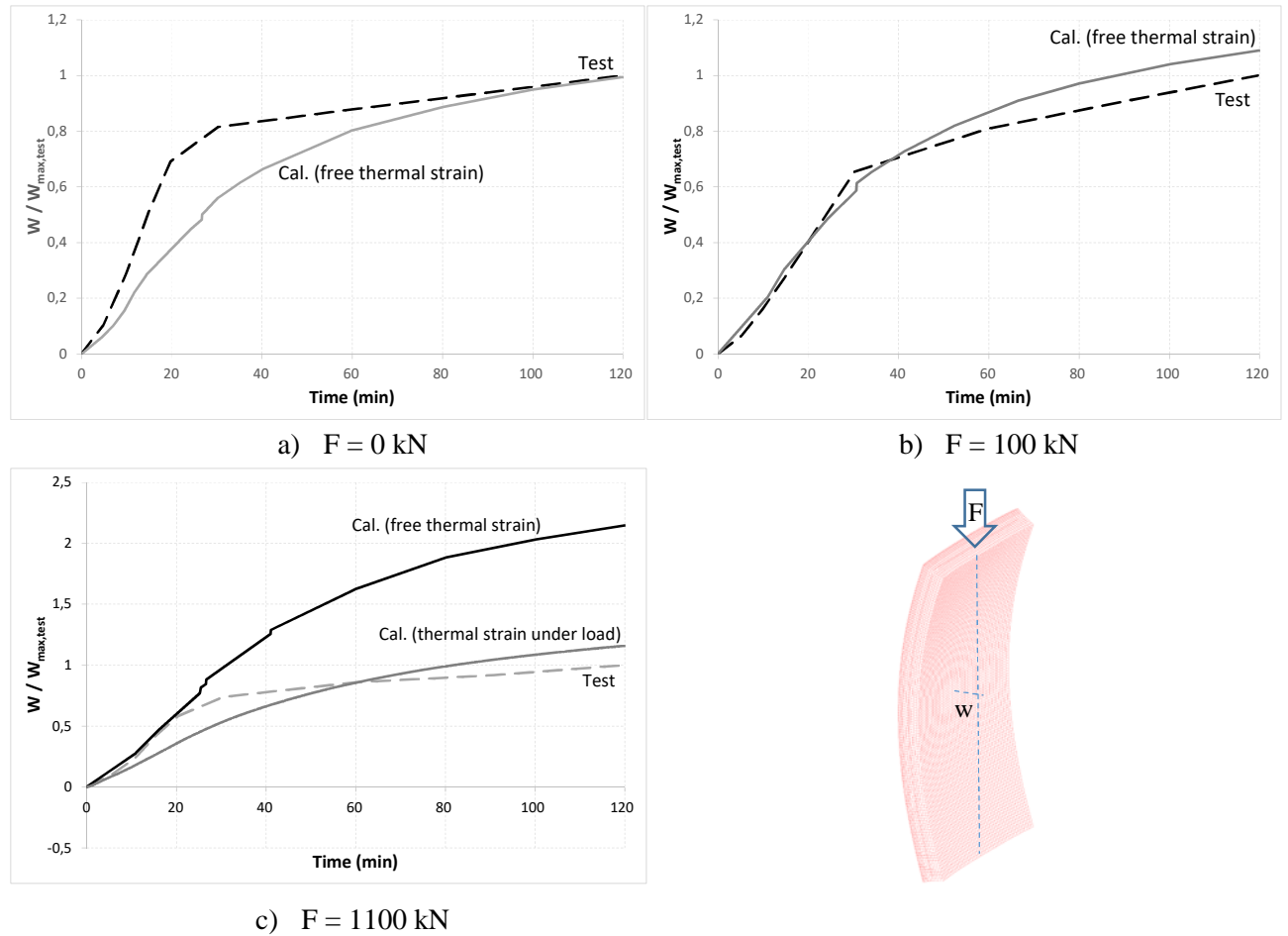


Fig. 4 Comparison between predicted and measured deflections of the 3 walls loaded at 0, 100 and 1100 kN

### 3.3 Explicit transient thermal strain formulation

In order to capture transient thermal strain with the numerical model, the solution of taking it into account by an explicit term in the strain decomposition has been proposed by most researchers in the literature. As a consequence, the concrete macroscopically measurable strains at elevated temperatures can be divided into individual strain components according to Eq. (7):

$$\varepsilon_{tot} = \varepsilon_e + \varepsilon_{th} + \varepsilon_{tr} \quad (7)$$

where  $\varepsilon_{tot}$  is the total strain,  $\varepsilon_e$  the elastic strain,  $\varepsilon_{th}$  the free thermal strain and  $\varepsilon_{tr}$  the transient thermal strain. The transient thermal strain rate  $\dot{\varepsilon}_{tr}$  is supposed to be proportional to the free thermal strain rate  $\dot{\varepsilon}_{th}$  until temperatures of about 500°C, according to Anderberg and Thelandersson's model (Anderberg *et al.*, 1976). Beyond 500°C, this model proposes the relationship of Eq. (9):

$$\dot{\varepsilon}_{tr} = k_2 \frac{\sigma}{f_{c,20}} \dot{\varepsilon}_{th}; T \leq 500^\circ\text{C} \quad (8)$$

$$\dot{\varepsilon}_{tr} = 0.1 \times 10^{-3} \frac{\sigma}{f_{c,20}} \dot{T}; 500^\circ\text{C} \leq T \leq 800^\circ\text{C} \quad (9)$$

where  $k_2$  is a constant depending on the kind of aggregate and concrete mix,  $\sigma$  the applied stress and  $f_{c,20}$  the compressive strength at ambient temperature. For modelling a structural element, the stress evolution across the section during the fire is different depending on the position in the section which leads to a number of configurations in the stress-temperature space, due to the development of thermal stresses in the section (Gernay *et al.*, 2012). The  $k_2$  variation with temperature on the basis of the experimental results of the tested concrete is presented in Fig. 5.a. In Fig. 5.b., the curves related to Anderberg and Thelandersson's model obtained using the value 2.1

for the constant  $k_2$  are compared with experimental data; the predictions of this model agree with the test results up to 500°C.

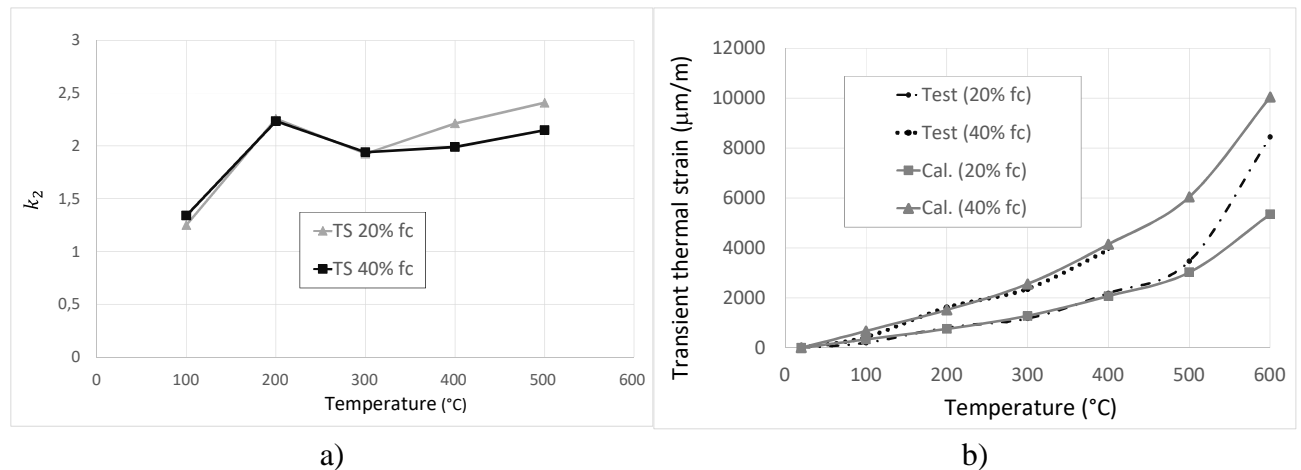


Fig. 5 (a) Variation of  $k_2$  with temperature on the basis of the experimental results of the tested concrete  
(b) Comparison of the transient thermal strain model with experimental data

## 4 CONCLUSIONS

Three important full-scale fire tests have been conducted within the scope of the international benchmark “Vulcain tests on 3 Walls” on reinforced concrete bearing walls. The numerical analysis of those tests has shown the need of introducing transient thermal strain in the concrete models of the structural elements. Therefore, the authors carried out numerical simulations taking into account an explicit term for transient thermal strain. In conclusion, the authors think that the Mazars’ elastic damageable model can be relevant for predicting the global structural behaviour of reinforced concrete structures exposed to fire, when it integrates explicitly a term for transient thermal strain.

## REFERENCES

- Jihad, M., M., Pinoteau N. and Pimienta P., 2016. A thermomechanical experimental investigation on 3 loaded concrete walls exposed to ISO 834-1 fire, in *9th International Conference on Structures in Fire*.
- Mindeguia, J.-C., 2009. *Contribution Expérimental a la Compréhension des risqué d’Instabilité Thermiques des Béton*, PhD Thesis, Université de Pau et des Pays de l’Adour (in French).
- Mazars, J., 1984. *Application de la mécanique de l’endommagement au comportement non linéaire et à la rupture du béton de structure*, PhD Thesis. Univ. Paris 6, ENS Cachan (in French).
- Verpeaux P., Charras T. and Millard A., 1988. *CASTEM 2000 : une approche moderne du calcul des structures*, *Calcul des Structures et Intelligence Artificielle*, ed. par Fouet J-M., Ladevèze P. et Ohayon R, *Pluralis*, p. 261–271.
- Roosefid M., Bonhomme M.-H., Pimienta P., 2020. Modeling the structural behavior of reinforced concrete walls under ISO fire exposure, in *11th International Conference on Structures in Fire*, p. 262-270.
- Anderberg, Y. and Thelandersson, S., 1976. *Stress and deformation characteristics of concrete at high temperatures: 2 experimental investigation and material behavior model*, Bulletin 54, Lund Institute of Technology, Sweden.
- Gernay, T. and Franssen J.-M., 2012. A formulation of the Eurocode 2 concrete model at elevated temperature that includes an explicit term for transient creep, *Fire safety journal*, 51, pp. 1-9.
- CEN, EN 1991-1-2, 2003. *Eurocode 1: Actions on structures - Part 1-2: General actions - Actions on structures exposed to fire*, European Committee for Standardisation.
- CEN, EN 1991-1-1, 2005. *Eurocode 2: Design of concrete structures - Part 1-1: General rules and rules for buildings*, European Committee for Standardisation.
- CEN, EN 1992-1-2, 2005. *Eurocode 2: Design of concrete structures - Part 1-2: General rules - structural fire design*, European Committee for Standardisation.

# POST-COOLING COMPRESSIVE BEHAVIOUR OF HIGH-STRENGTH SELF-COMPACTING CONCRETE

## Influence of binder materials

Marija Jelčić Rukavina<sup>a</sup>, Ivan Gabrijel<sup>a</sup>, Ivanka Netinger Grubeša<sup>b</sup>

<sup>a</sup> University of Zagreb, Faculty of Civil Engineering, Zagreb, Croatia

<sup>b</sup> Josip Juraj Strossmayer University of Osijek, Faculty of Civil Engineering and Architecture Osijek, Osijek, Croatia

### Abstract

Decades of research have shown that concrete structures can be severely damaged depending on the fire exposure temperature and duration, but in most cases can retain the essential part of their load-bearing capacity after fire exposure. To assess the damage to structures and propose repair measures, it is essential to evaluate the residual properties of the material composing the structural element. This paper presents the experimental investigation of the compressive stress-strain relationship for self-compacting concrete mixes with different binders before and after heating to high temperatures up to 800°C. Specimens were tested in uniaxial compression both under ambient conditions and after exposure to a predefined elevated temperature. The mechanical properties in terms of compressive strength, modulus of elasticity and strain at peak strength were calculated from stress-strain curves and compared with the values in the unheated condition. The results showed that for the tested mixes, the difference in residual mechanical properties can significantly vary depending on the type of binder used.

**Keywords:** self-compacting concrete, high temperatures, stress-strain curves, mechanical properties

## 1 INTRODUCTION

The advantages of self-compacting concrete at room temperature over conventional concrete are the improved internal structure, which is achieved by more effective particle packing due to the higher percentage of fines. A high percentage of fines in SCC is usually achieved by using mineral additives (both pozzolanic and non-pozzolanic), since increasing the cement content in the concrete mix leads to a significant increase in material cost and can sometimes have negative effects on concrete properties (Güneyisi and Gesoğlu, 2011).

The dense microstructure of the self-compacting concrete provides good strength and low permeability properties, which implies good durability of the concrete under aggressive exposure conditions, but the better durability properties generally have a negative effect on the behaviour of the concrete during and after exposure to high temperatures (RILEM Committee, 2007). Since the self-compacting concretes have received insufficient attention in the literature concerning fire-related properties (Abed and de Brito, 2020), the main objective of this work was to perform a study on the residual stress-strain behaviour of concrete produced with different binders (involving different mineral additives) in order to evaluate their influence on mechanical behaviour after cooling.

## 2 EXPERIMENTAL PROGRAM

### 2.1 Mix design

The details of the concrete mixes studied are given in Table 1. In all the mixes, CEM I 42.5 R and dolomite powder were used as binders. In addition, both pozzolanic (metakaolin and fly ash) and non-pozzolanic (limestone powder) mineral additives were used as partial replacement of cement in usual weight percentages for particular additives in the mixes designated M2-M7. A constant powder quantity (670 kg/m<sup>3</sup>) and water-to-powder ratio ( $w/p = 0.27$ ) were selected for all mixes. The aggregates were of dolomitic origin and had a maximum nominal size of 16 mm. The 150-mm cube compressive strength (mean and absolute deviation) of the concrete at the age of 365 days,

when the heating of the specimens took place, is presented in Table 1 and shows the positive influence of the pozzolanic mineral additives on the compressive strength.

Table 1 Concrete mix proportioning for 1 m<sup>3</sup>

Component /Mix ID		M1 (REF)	M2 (MK5)	M3 (MK15)	M4 (FA20)	M5 (FA30)	M6 (LF5)	M8 (LF15)
Cement	kg	450	427,5	382,5	360	315	427,5	382,5
Metakaolin	*%	-	5	15	-	-	-	-
	kg	-	22,5	67,5	-	-	-	-
Fly ash	*%	-	-	-	20	30	-	-
	kg	-	-	-	90	135	-	-
Limestone	*%	-	-	-			5	15
	kg	-	-	-			22,5	67,5
Dolomite filler	kg	220						
Water	l	180						
w/c		0,40	0,42	0,47	0,5	0,67	0,42	0,47
Fine aggr.	kg	862						
Coarse aggr.	kg	696						
SP	l	5,6	4,5	6,3	4,1	3,4	5,0	3,9
VMA	l	0,7						
**f <sub>c</sub> , 365 days	MPa	104.2±1.7	107.3±0.8	118.3±1.3	108.1±2.3	109.6±0.6	95.8±2.2	91.2±0.3

\* % by cement weight; \*\* compressive strength obtained on 150-mm cubes

## 2.2 Specimens – curing, dimensions and heat treatment

The prepared test specimens for the experimental programme were cylinders with dimensions Ø/L = 75/225 mm. All specimens were demoulded one day after casting and stored in a curing room for another 27 days at a temperature of 20±2°C and a relative humidity of 95%. Then the specimens were placed in the normal laboratory conditions until high-temperature exposure. The specimens were heated approximately one year after casting when they had a low moisture content to avoid explosive spalling. The first part of the temperature cycle consisted of a heating rate  $\Delta T/\Delta t$  of 2°C/min (inside the furnace) up to the target temperatures (200°C, 400°C, 600°C and 800°C). Thereafter, the temperature was kept constant until uniform thermal conditions were ensured in the specimens, while the last part of the cycle consisted of a slow cooling to ambient temperature inside the closed furnace to avoid thermal shock of specimens. Eight cylindrical specimens were used for each temperature cycle, with one specimen equipped with NiCr thermocouples that monitored the temperature evolution across the specimens (both surface and in the centre) according to RILEM recommendations (RILEM Technical Committee, 2007) for high temperature testing. After cooling, the specimens were stored in a standard laboratory environment until testing.

## 2.3 Mechanical testing

The stress-strain relationship tests in compression were carried out on universal testing machine with a capacity of 3000 kN, Figure 1. Strain was measured with two LVDT displacement gauges having reference length of 10 cm, attached to the central part of the specimen. The tests were performed at a constant piston-controlled displacement rate of 0.02 %/s. The compressive strength, f<sub>c</sub>, corresponded to the peak stress reached in the material during the test, while the static Youngs modulus was calculated as the slope of the secant connecting the points of the stress-strain curve corresponding to stresses of cca 5 MPa and 1/3 of the obtained peak stress. Mechanical testing was carried 7 days after the cooling of specimens to ambient temperatures since in this period the largest decrease in mechanical properties is expected (Hertz, 2005). Three specimens of each concrete type per set temperature were tested. To obtain influence of temperature on studied properties, non-heated specimens were tested as well and normalised values are reported. Beside the mechanical properties, the morphology and microstructure of the concrete mixes were analysed on polished

specimens in the transverse direction in a JEOL 5500 LV SEM coupled with an Oxford energy dispersion spectrometer using backscattered electrons and a low vacuum.



Fig. 1 Experimental setup – test machine and electronic equipment for compressive stress-strain monitoring

## 2 RESULTS AND DISCUSSION

### 2.1 Behaviour after heating to temperature of 800°C

Testing of specimens after heating to the maximum temperature of 800°C could not be performed after 7 days due to excessive degradation of specimens (Figure 1(a)).



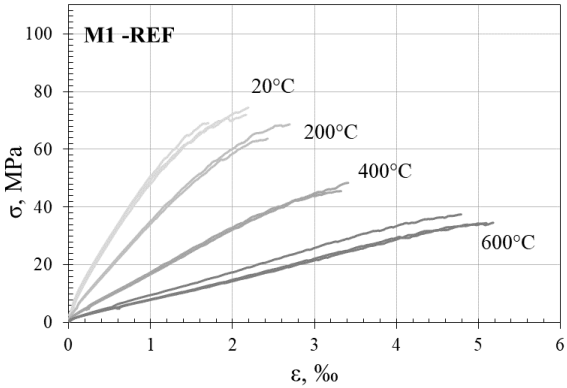
Fig. 1 The post-cooling appearance of reference concrete specimens heated to 800°C

Figures 1(b) and (c) show the damages to the concrete specimens at the later time points. During heating, lime (CaO) is formed from the dehydration of portlandite at temperatures between 400-600°C (Khoury et al, 2008) or from the thermal decomposition of the dolomite aggregate and filler at a temperature higher than 700°C (Engler et al, 1988). Under laboratory conditions, the absorption of atmospheric moisture led to rehydration of lime accompanied by a 44 percent increase in volume (Lin, Lin and Powers-Couche, 1996). This resulted in flaking of the surface and crumbling of the test specimens. The extensive damages of specimens were the reason to choose the maximum treatment temperature of 600°C for further testing.

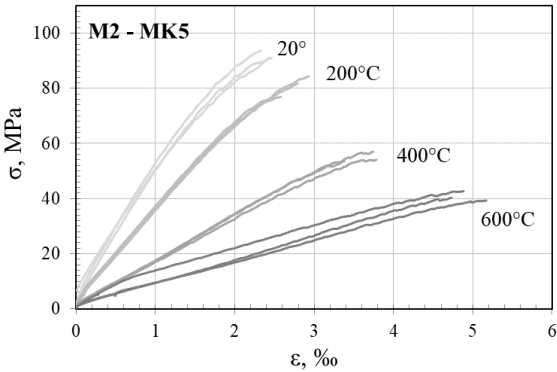
### 2.1 Mechanical properties

Figure 2 (a)-(e) shows the compressive residual stress-strain curves of concrete specimens subjected to predefined temperature cycles. The stress-strain curves include the ascending branch of the curves up to the peak stress. Descending part of the  $\sigma$ - $\epsilon$  graph was not captured during the test since the rate of displacement was piston controlled. A good reproducibility of the results was obtained after exposure to each target temperature. The shape of the curves is strongly influenced by temperature. The ductility of the concrete is higher with increasing temperature, i.e. with increasing temperature the curve becomes smoother with lower maximum stress reached and higher

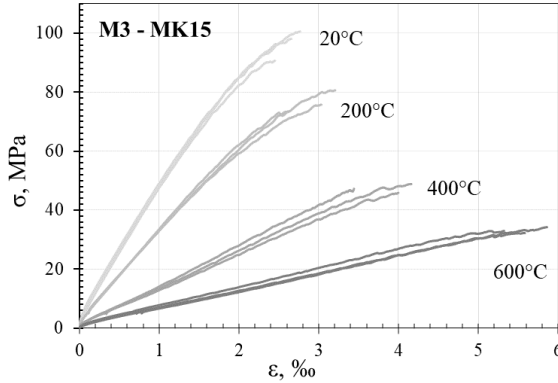
deformation at peak stress. This applies to all mixes except fly ash containing mixes after exposure to 200°C, where the curves of unheated and heated concrete are very similar, Figures 2 (d) and (e).



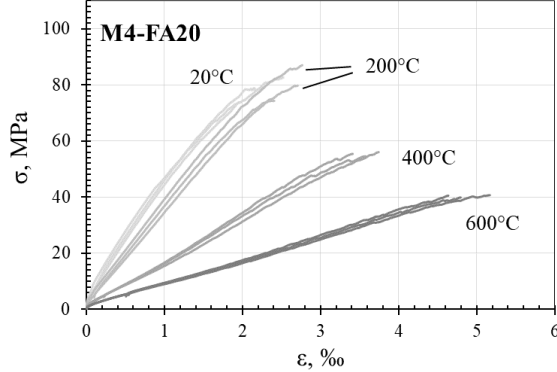
a)



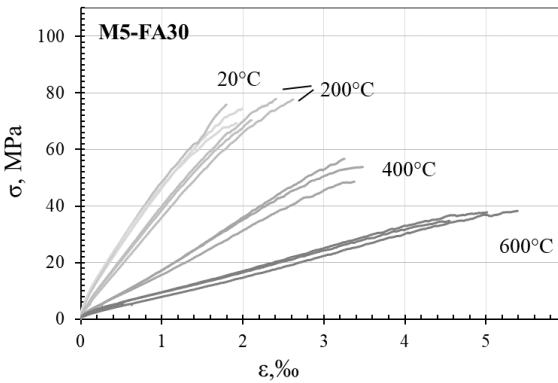
b)



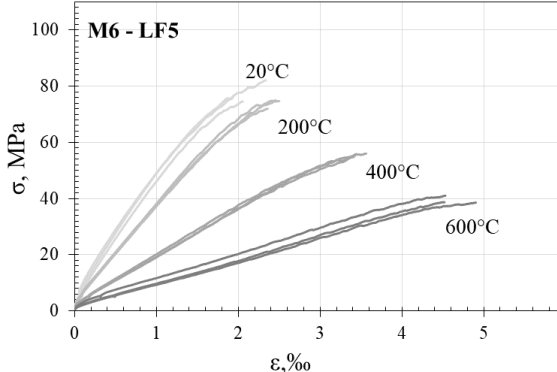
c)



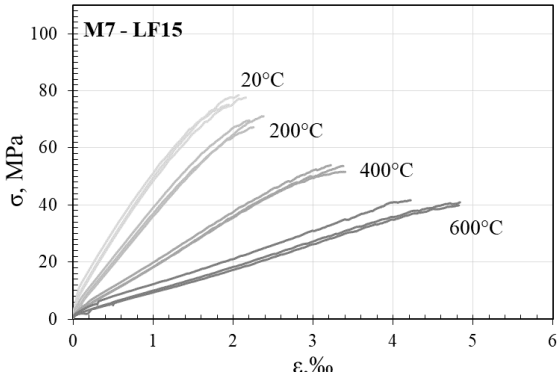
d)



e)



f)



g)

Fig. 2 Post-cooling stress-strain curves of tested concretes

Figure 3 (a)-(c) shows the effect of high temperatures on the peak stress (compressive strength), modulus of elasticity and strain at peak stress of the tested concrete mixes in terms of normalised values (ratio of the particular property of the heated and unheated specimens). Compared to the reference mix, the replacement of cement by metakaolin had a negative effect on the compressive strength in the whole temperature range, as opposed to the replacement with fly ash, which increased the relative compressive strength, especially after a temperature treatment at 200°C. The obtained results agree well with studies carried out by previous research on fly ash concretes where the positive influence on compressive strength was explained by formation of tobermorite, but contrast with the results obtained on concretes with metakaolin where positive influence was also observed (Fu et al., 2005).

Mixes with limestone (as non-pozzolanic material) showed comparable behaviour (difference  $\leq 5\%$ ) to the reference mix.

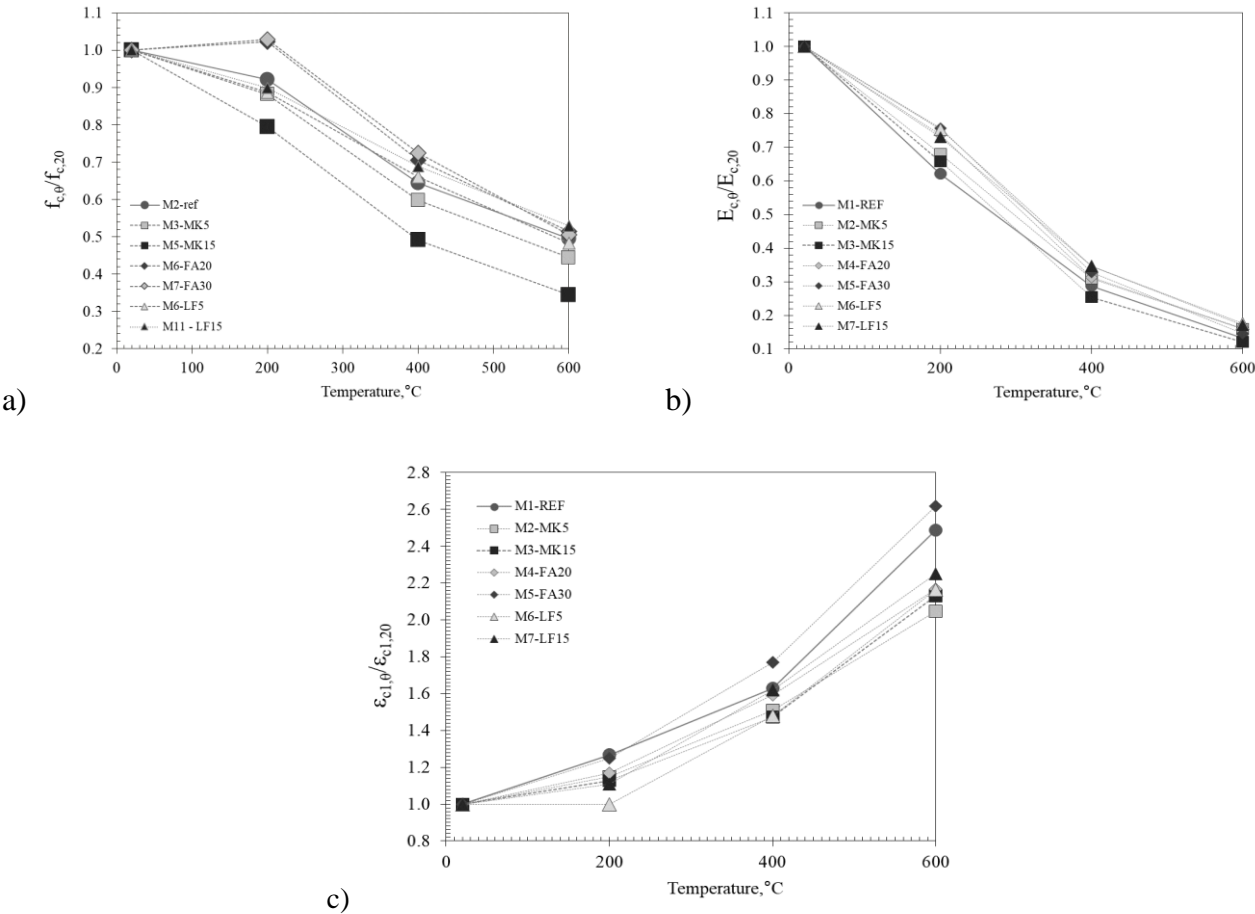


Fig. 3 Normalised values of a) peak stress b) modulus of elasticity c) strain at peak stress

High temperature negatively influences the elastic properties of concrete primarily because of the disintegration of hydrated cement products and breakage of bonds in the microstructure (Khoury *et al.*, 2007). As expected, higher influence of elevated temperatures on modulus of elasticity was observed compared to compressive strength, but in this case lower differences between studied mixes (at higher temperatures) can be noticed (Figure 3 (b)). After cooling from 200°C, the difference in modulus of elasticity between the studied mixes is 14% and continues to decrease at higher temperature.

From Figure 3 (c) it can be seen that the differences in relative strain at peak stress between studied mixes increase with the increasing temperature of exposure, i.e. after 200°C, 400°C and 600°C differences are 14%, 26% and 57%, respectively.

## 2.2 Microstructural observation

Figure 4 shows SEM images of the specimens heated to 400°C, which clearly show different damage at the interface depending on the mineral additive used, which in turn, affected mechanical properties after cooling, as shown in the previous section. Wider interface cracks observed when blended with metakaolin, Figure 4 (a), are the result of the stronger initial interface as metakaolin has finer grains compared to another mineral additive used (Siddique and Khan, 2011).

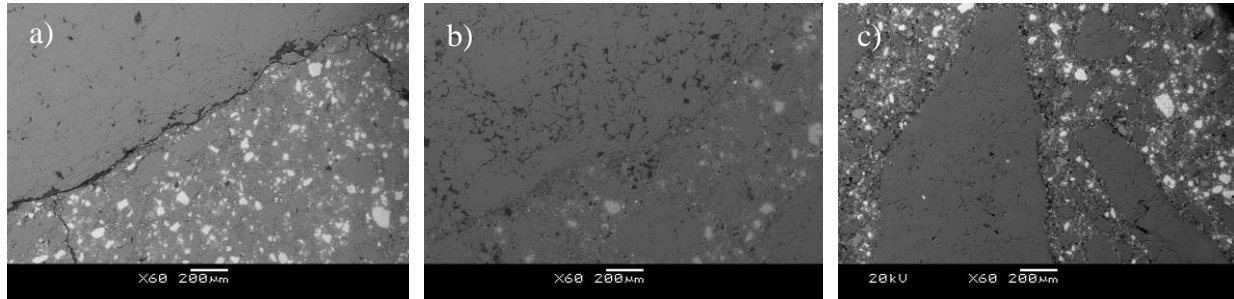


Fig. 4 SEM images of mixes a) with metakaolin b) fly ash c) limestone after heating to 400°C

## 4 CONCLUSIONS

As mentioned previously, the advantages of self-compacting concrete at room temperature over conventional concrete is its improved internal structure achieved by more effective particle packing due to the higher percentage of fines.

Based on the obtained results, this study proved that different mineral additives used to produce self-compacting concrete can significantly influence its behaviour after high temperature exposure. It is obvious that compressive strength class, as given in EN 1992-1-2 for HSC, is not the only criterion for by which the changes in mechanical properties of self-compacting concrete exposed to high temperatures can be judged. The different microstructure caused by the presence of different mineral additives in concrete affects the mechanical properties that remain after exposure to high temperatures.

## REFERENCES

- Abed, M. and de Brito, J., 2020. Evaluation of high-performance self-compacting concrete using alternative materials and exposed to elevated temperatures by non-destructive testing, *Journal of Building Engineering*, 32, p. 101720. doi: 10.1016/j.jobte.2020.101720.
- De Schutter, G. and Audenaert, K. 2007. Final report of RILEM TC 205-DSC: durability of self-compacting concrete, *Materials and Structures*, 41(2), pp. 225–233. doi: 10.1617/s11527-007-9319-9.
- Güneyisi, E. and Gesoğlu, M., 2011. Properties of self-compacting portland pozzolana and limestone blended cement concretes containing different replacement levels of slag, *Materials and Structures*, 44(8), pp. 1399–1410. doi: 10.1617/s11527-011-9706-0.
- Fu, Y. F. et al., 2005. Stress-strain behaviour of high-strength concrete at elevated temperatures, *Magazine of Concrete Research*, 57(9), pp. 535–544. doi: 10.1680/macr.2005.57.9.535.
- Khoury, G. A. et al., 2007. Fire design of concrete structures – materials, structures and modelling - State of art report. fib Bulletin No. 38
- Lin, W., Lin, T. and Powers-Couche, L. J., 1996. Microstructures of fire-damaged concrete, *ACI Materials Journal*, (93), pp. 199–205.
- RILEM Technical Committee, 2007. Recommendation of RILEM TC 200-HTC: Mechanical concrete properties at high temperatures—modelling and application, Part 1: Introduction - General presentation', *Materials and Structures*, pp. 841–853. doi: 10.1617/s11527-006-9203-z.
- Siddique, R. and Khan, M. I. 2011. *Supplementary Cementing Materials*, Springer Berlin Heidelberg.
- EN 1992-1-2: 2013/A1:2019 Eurocode 2: Design of concrete structures -- Part 1-2: General rules -- Structural fire design (EN 1992-1-2:2004+AC:2008)

## **STRUCTURAL FIRE DESIGN OF ONE-WAY REINFORCED CONCRETE RIBBED SLABS USING DIFFERENT ASSESSMENT METHODS**

Omid Pouran<sup>ab</sup>, Ulrich Montag<sup>ab</sup>

<sup>a</sup> Kraetzig & Partner Engineering Consultants, Bochum, Germany

<sup>b</sup> Bergische Universität Wuppertal, Wuppertal, Germany

### **Abstract**

Structural fire design of one-way reinforced concrete ribbed slabs can be performed using different methods. In this regard, EN 1992-1-2 proposes tabular prescriptive data and simplified methods to estimate load bearing classes. These tools and methods can be used provided that the corresponding prescribed requirements are fulfilled. EN 1992-1-2, further, gives some general recommendations to use advanced calculation methods. In Germany, there are old buildings with reinforced ribbed slabs that have to be fire protected according to the current normative rules. Some of these slabs may not fulfil the mentioned requirements for the both methods in the fire situation. In addition, using prescriptive or simplified methods to assess load bearing capacity may result in an uneconomical results. In reality, there might exist more resistance in the considered ribbed slabs dependent on the boundary conditions of supports and existing reinforcement ratio of the cross-sections.

To understand the real behaviour of one-way reinforced ribbed slabs exposed to fire, advanced structural analysis has to be performed using a realistic model that takes account of mechanically and thermally induced effects in the structure simultaneously. The stiffness of the structure exposed to fire might be highly affected, thus only nonlinear (physical) thermo-mechanical analysis of the structure using Finite Element method is applicable.

In this study, the results of nonlinear thermo-mechanical analyses of one-way reinforced concrete ribbed slabs with various boundary conditions along with the results based on the existed normative methods are explained and discussed. The nonlinear analyses performed using software package (SOFiSTiK, 2020) take into account the reinforcement ratio of the cross-sections. These results are scopes of a project in the practice and may provide complementary explanations, comparisons and conclusions to the existing design methods and rules.

**Keywords:** concrete, ribbed slabs, nonlinear, fire.

### **INTRODUCTION**

In general, the new normative regulations such as Eurocodes demand higher standards and requirements for fire design compared to the older regulations. The designer has a wide choice of methods for verifying the fire resistance based on the acceptability to regularity authorities. In case of reinforced concrete structures, there are number of old buildings in Germany which have to be re-designed or re-verified for fire situation due to retrofitting or new developed fire safety concept. In this regard, assuming nominal ISO-fire curve as thermal actions for fire design, EN 1992-1-2:2004 proposes three assessment methods:

- **Tabulated data (Level 1).** The tabulated values of minimum required cross-section dimensions and axis distances of reinforcements for different types of members (member analysis) are given. The latter is for various fire exposure periods corresponding to the test results. In this analysis, thermally induced restraint forces caused by thermal axial or in-plane thermal expansions are neglected. The minimum allowable given values in the tables

are conservative. The critical temperature of reinforcement  $\theta_{cr}$  for the stress level of less or equal 70% of maximum allowable reinforcement stress at normal situation is assumed 500°C and is the limit criterion of the tests (Narayanan & Beeby, 2005), (Hosser, 2012);

- **Simplified calculation models (Level 2).** By using temperature profiles of concrete members after specified duration of ISO fire with predefined given thermal boundary properties, the strength and stiffness of the cross-section are reduced. Using the zone-method, the reduced cross-section is designed for the design mechanical actions in fire situation. The latter does not take into account the indirect thermal actions;
- **Advanced calculation models (Level 3).** Members, part of structure or the whole structure can be designed for fire situation by global advanced calculation methods. For coupling the thermally induced effects with the mechanical-induced effects, nonlinear-iterative computation may be carried out taking into account temperature dependent material properties. The indirect-induced-thermal effects are incorporated stepwise in the model. This process requires separate thermal analyses of concrete elements and importing the effects of elevated temperatures within cross-section into the mechanical model by using multi-layered strain model (Harte, et al., 2000). Physical-stepwise-nonlinear analysis can now be performed by taking into account the spontaneous loss of strength and stiffness of the cross-section as well as considering the rising thermally induced stresses within the structure or member. This procedure is shown in Fig. 1. Considering global bending response of reinforced concrete structures from physical nonlinear analysis, different parameters might affect the bending moments. They can be related to the used material model, modelling the spalling phenomena and other various considerations in the analysis. These parameters have been discussed in (Pouran & Harte , 2015), (Pouran, et al., 2017) and (Pouran, et al., 2019).

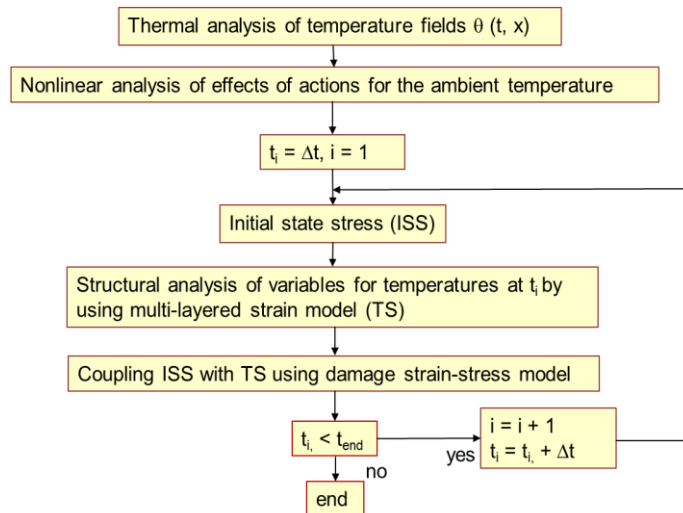


Fig. 1 The procedure of sequential-thermo-mechanical analysis

In case of ribbed slabs, EN 1992-1-2 proposes prescriptive tabulated data (level 1) for minimum required height of slabs,  $h_{s,min} \geq 80$  mm and minimum required width of ribs,  $b_{rib,min} \geq 80$  mm. The use of simplified calculation methods (level 2) are not directly or accurately applicable as the code does not include the temperature profiles for the ribbed cross-sections. Further, there is not much data, accordingly, on how to perform the advanced calculation methods (level 3).

In fact, there might be cases that the minimum requirements for the considered ribbed slabs or the axis distance of reinforcement do not fit into prescribed requirements (given in the tables) or the structural fire engineer should apply methods which give more economic and environment-friendly solutions.

As a scope of a project in the practice, an old building with large area of ribbed slabs should be re-designed for fire situation due to a newly developed fire safety concept. The focus of this paper is to investigate and compare the application and results of different fire design assessments proposed by EN 1992-1-2. A simply supported single-span beam (case 1: statically determinate) and a continuous beam (case 2: statically indeterminate) are selected for the current study. The latter systems are representative of strips of one-way ribbed slab with an effective width of flange of 0.5 m with two reinforcement arrangements as shown in Fig. 2. Further, the geometry and dimensions of the cross-sections are tabulated in Table 1. In the following sections, different methods are applied to determine the fire resistance of these both cases. The results are compared and summarized eventually.

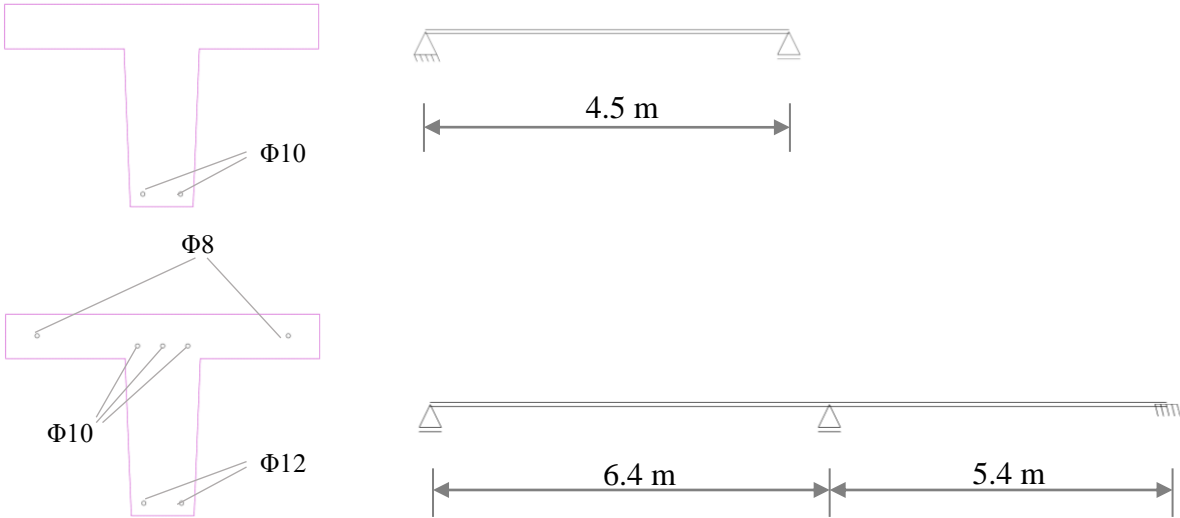


Fig. 2 Geometry and reinforcement arrangements for two beams used for the study

Table 1 Dimensions of ribbed slabs

Slab thickness $h_s$ (cm)	Height of rib $h_{rib}$ (cm)	Total height $h_{tot}$ (cm)	Top width of rib $b_{rib,top}$ (cm)	Bottom width of rib $b_{rib,bot}$ (cm)	Axis distance of bottom bars in the rib from the nearest exposed surfaces $a_{rib,bot}$ (mm)
7	25	32	12	10	20

**LEVEL 1: VERIFICATION OF FIRE RESISTANCE USING PRESCRIBED TABULAR DATA IN EN 1992-1-2 FOR BOTH STATICALLY DETERMINATE (CASE 1) AND STATICALLY INDETERMINATE (CASE 2) SYSTEMS**

For the assessment of fire resistance for ribs and flanges of one-way reinforced ribbed slabs, EN 1992-1-2 recommends use of Table 5.5 for the rib and Table 5.8 for the flange. It can be simply verified that minimum requirement of axis distance for the lower reinforcement in the rib  $a_{min} = 22.5$  mm for the considered lower width of  $b_{rib,bot} = 100$  mm is not fulfilled (see Table 2). Consequently, the ribbed slab cannot meet the requirements for R30.

Table 2 Part of Table 5.5 of EN 1992-1-2 for simply supported beams corresponding to rib (left)  
Part of Table 5.8 of EN 1992-1-2 for simply supported solid slabs corresponding to flange (right)

Standard fire resistance	Minimum dimensions (mm)					Standard fire resistance	Minimum dimensions (mm)					
	slab thickness $h_s$ (mm)	axis-distance $a$					Possible combinations of $a$ and $b_{min}$ where $a$ is the average axis distance and $b_{min}$ is the width of beam					
		one way	two way:				Web thickness $b_w$			Class WA	Class WB	Class WC
1	2	3	$l_x/l_y \leq 1,5$	$1,5 < l_x/l_y \leq 2$	4	5	6	7	8			
REI 30	60	10*	10*	10*		$b_{min} = 80$ $a = 25$	120	160	200	80	80	80
REI 60	80	20	10*	15*		$b_{min} = 120$ $a = 40$	160	200	300	100	80	100

$l_x$  and  $l_y$  are the spans of a two-way slab (two directions at right angles) where  $l_y$  is the longer span.  
For prestressed slabs the increase of axis distance according to 5.2(5) should be noted.  
The axis distance  $a$  in Column 4 and 5 for two way slabs relate to slabs supported at all four edges. Otherwise, they should be treated as one-way spanning slab.  
\* Normally the cover required by EN 1992-1-1 will control.

$a_{sid} = a + 10\text{mm}$  (see note below)  
For prestressed beams the increase of axis distance according to 5.2(5) should be noted.  
 $a_{sid}$  is the axis distance to the side of beam for the corner bars (or tendon or wire) of beams with only one layer of reinforcement. For values of  $b_{min}$  greater than that given in Column 4 no increase of  $a_{sid}$  is required.  
\* Normally the cover required by EN 1992-1-1 will control.

### LEVEL 1: VERIFICATION OF FIRE RESISTANCE DURATION BASED ON THE CRITICAL TEMPERATURE OF REINFORCING STEEL FOR BOTH STATICALLY DETERMINATE (CASE 1) AND STATICALLY INDETERMINATE (CASE 2) SYSTEMS

The critical steel temperature ( $\theta_{cr}$ ) for reinforcing bars defined in EN 1992-1-2 for design of beams and slabs is 500°C. This is under the assumption that the cross-section design has been carried out for a degree of utilization factor of  $\beta_{fi} = 0.7$  in fire situation.

With  $\beta_{fi}$  in the range of 0.6 to 0.8, it can be assumed that the critical reinforcing steel temperature varies between 550°C and 450°C respectively. Assuming  $\beta_{fi} < 0.6$ ,  $\theta_{cr}$  can be increased accordingly and the cross-section may represent more resistance.

For the considered strips of the ribbed slabs, temperatures reached in the centre of reinforcing bars are determined up to 90 minutes. The transient thermal analyses were performed assuming an upper ( $\alpha_u$ ) and lower ( $\alpha_l$ ) values of thermal conductivity for concrete according to EN 1992-1-2. The thermal parameters and properties are listed in Table 3.

Table 3 Thermal parameters and properties

Heat transfer coefficient (W/K/m <sup>2</sup> )	25
Fire curve	ISO – fire curve
Emission coefficient	0.7
Density (kg/m <sup>3</sup> )	2400
Thermal conductivity acc. to EN 1992-1-2	
Upper boundary	$\alpha_u$ (temperature-dependent)
Lower boundary	$\alpha_l$ (temperature-dependent)
Specific heat	Variable acc. to EN 1992-1-2
Initial temperature (°C)	20

To estimate the resistance class of the cross-section in fire situation based on the critical reinforcing steel temperatures, the time elapsed until the temperature in the centre of reinforcement reaches critical temperatures of 450°C and 550°C are evaluated (see Table 4). Further, the temperatures for the upper reinforcement in the ribs at 90 minutes for case 2 are given in this table.

It can be observed that the steel temperatures for the upper reinforcement in the ribs do not reach the critical value of  $\theta_{cr} = 450^\circ\text{C}$  even at 90 minutes. The considered slab can be classified into fire

resistance according to the evaluated times for the critical steel temperatures in the bottom of rib (see Table 4). These critical temperatures vary between 25 and 33 minutes. The latter lower and upper values can be related to  $\beta_{fi} = 0.8$  and  $0.6$  respectively. This is valid for all the ribbed slabs with the considered geometry and axis distance of reinforcements without considering the support conditions. It can be concluded that using the average values in the table for  $\beta_{fi} \leq 0.65$ , the considered ribbed slab can be classified in R30 without considering the boundary conditions.

Table 4 Range of fire resistance durations for the considered critical reinforcement temperatures and temperatures at  $t = 90$  minutes at upper reinforcements

Temperature in the centre of the reinforcement	$t$ (min), bottom of rib $a_{rib,bot} = 2$ cm	
	Upper boundary of thermal conductivity $\alpha_u$	Lower boundary of thermal conductivity $\alpha_l$
$\theta_{cr} = 450^\circ\text{C}$	25	25
$\theta_{cr} = 550^\circ\text{C}$	30	33
	$t$ (min) for top bars in rib with $a_{rib,top} = 2$ cm	$t$ (min) for bars in slab with $a_s = 3.4$ cm
$\theta_{t=90min}(^\circ\text{C})$ for $\alpha_u$	425	550

### LEVEL 2: VERIFICATION OF THE FIRE RESISTANCE BASED ON THE SIMPLIFIED CALCULATION METHOD PROPOSED BY EN 1992-1-2: ANNEX E.2 FOR STATICALLY DETERMINATE SYSTEM (CASE 1)

The proposed simplified method in Annex E of EN 1992-1-2 (here section E.2) provides an extension to the use of tabular data for beams where the axis distance,  $a_{rib,bot}$ , is less than the proposed prescribed tables in this code. The latter procedure can be formulated as (without explanations for the designations):

- (1) Fire load  $\rightarrow$  standard fire exposure curve
- (2)  $M_{Ed,fi} = W_{Ed,fi} l_{eff}^2 / 8 \rightarrow 3.1 \cdot 4.5^2 / 8 \approx 7.85$  kNm
- (3)  $M_{Rd,fi} = \gamma_s / \gamma_{s,fi} \cdot k_s(\theta) \cdot M_{Ed} (A_{s,prov} / A_{s,req}), A_{s,prov} / A_{s,req} \leq 1.3$   
 $\gamma_s = 1.15, \gamma_{s,fi} = 1.0, k_s(\theta=540^\circ\text{C}, \text{ at } t = 30 \text{ min}) \approx 0,46$  (for  $\epsilon_{s1,fi} < 2,0 \%$ )  
 $\approx 0,66$  (for  $\epsilon_{s2,fi} > 2,0 \%$ )  
 $M_{Ed} = 12.13$  kNm  
 $A_{s,prov} = 1.57 \text{ cm}^2, A_{s,req} = 1.1 \text{ cm}^2 \rightarrow A_{s,prov} / A_{s,req} = 1.3$
- (4)  $M_{Ed,fi} \leq M_{Rd,fi}$   
For  $\beta_{fi} \leq 0.65$ :  
 $M_{Rd1,fi} = 8.34$  kNm  $> M_{Ed,fi} \approx 7.85$  kNm  
 $M_{Rd2,fi} = 11.97$  kNm  $> M_{Ed,fi} \approx 7.85$  kNm

It can be concluded that for  $\beta_{fi} \leq 0.65$ , the considered ribbed slab can be classified in R30.

### LEVEL 2: VERIFICATION OF FIRE RESISTANCE BASED ON SIMPLIFIED CALCULATION METHOD PROPOSED BY EN 1992-1-2:ANNEX E.3 FOR STATICALLY INDETERMINATE SYSTEM (CASE 2)

The method in this section is proposed to evaluate the moment of resistance at supports and in the mid-span for fire design. It is a simplified calculation with reference to a case of statically

determinate beam. It simply states that the moment of resistance can be evaluated from design moment for the ambient temperature based on three modification factors.

This method should be used in accordance with Table 5.5 for beams (corresponding to rib) and Table 5.8 for slabs (corresponding to flange) of EN 1992-1-2. Further, the application is valid provided that the temperature of the top reinforcement does not exceed 350°C for the aimed resistance class.

Using the latter tables, the minimum requirements for the beam cross-sections have to be fulfilled:

- For rib,  $b_{\text{rib,bot}} = 100 \text{ mm} > b_{\text{min}} = 80 \text{ mm}$ ,  $a_{\text{rib,bot}} = 20 \text{ mm}$  is not larger than  $a_{\text{min}} = 22.5 \text{ mm}$ ;
- For slab,  $h_s = 70 \text{ mm} > h_{s,\text{min}} = 60 \text{ mm}$ ,  $a_{\text{slab}} = 34 \text{ mm} > a_{\text{min}} = 10 \text{ mm}$

It can be concluded that the considered ribbed slab cannot be classified in R30.

### **LEVEL 3: VERIFICATION OF FIRE RESISTANCE BASED ON ADVANCED CALCULATION METHODS FOR STATICALLY DETERMINATE SYSTEM (CASE 1)**

Using the zone method in a more accurate way the moment of resistance at 30 minutes can be estimated in fire situation. For case 1, the reinforcement in the rib is under tension and may yield as exposure time increases. The further check here is control of maximum compressive strain governed over the the top compressive part of beam cross-section.

$$M_{\text{Rd,fi}} = 12.06 \text{ kNm}, t = 30 \text{ min}, \theta_s = 540^\circ\text{C}$$

$$\varepsilon_{\text{cc,fi}} = 0.26 (\text{‰}) < 3.5 (\text{‰})$$

The considered beam can be classified in R30.

### **LEVEL 3: VERIFICATION OF THE FIRE RESISTANCE DURATIONS BASED ON ADVANCED CALCULATION METHODS FOR STATICALLY INDETERMINATE SYSTEMS (CASE 2)**

Nonlinear thermo-mechanical analysis has been performed for the considered continuous beam (case 2). The latter is carried out for the sake of comparison and study for two boundary conditions assumed at the right end support (see Fig. 3): simply supported (case I) and support with rotational restraint (case II). The first case is a simplified case and the second case is the closer to the reality model.

Due to thermal gradients, bending moments are induced and the moment increases over the mid-support (B) on the unexposed face. In fire situation, the latter may lead to yielding of the top reinforcement as the temperature increases and failure of structure. This is in fact the case for the considered beams. As shown in Fig. 3, the value of fire design moment  $M_{\text{Ed,fi,t}}$  increases at the mid-support and reaches its maximum values (illustrated in green) at  $t = 25$  and  $27.5$  minutes for the both considered cases. The latter is due to the fact that the cross-section has reached its allowable temperature-dependent moment of resistance. For the case II, there exists more reserve after the cross-section has reached its full resistance capacity due to higher degree of statically indeterminacy and moment redistribution. Further the main important check for the considered cross-section at the mid-support is to control the maximum compressive strain prior to the point of failure. It has to remain under the limited temperature dependent values given in Eurocode 2. The design bending moments from the both cases as well as maximum compressive strains in the farthest fibre (close to the fire exposed side) are illustrated in Fig. 4. In addition, the moment of resistance and accordingly the maximum compressive strain in the farthest fibre are given for the cases I and II and for a system without considering the thermal restraint forces and thermally induced strains. The latter is similar to the case of statically determinate systems. Two main apparent results from these curves are:

- The fire resistance of the case II (42:30 minutes) is approximately 40% larger than case I and therefore R30 can be easily achieved;
- The maximum applicable compressive strains for the cross-section without considering thermal induced effects are much smaller than the cases I and II from approximately 15 minutes to the point of failure.

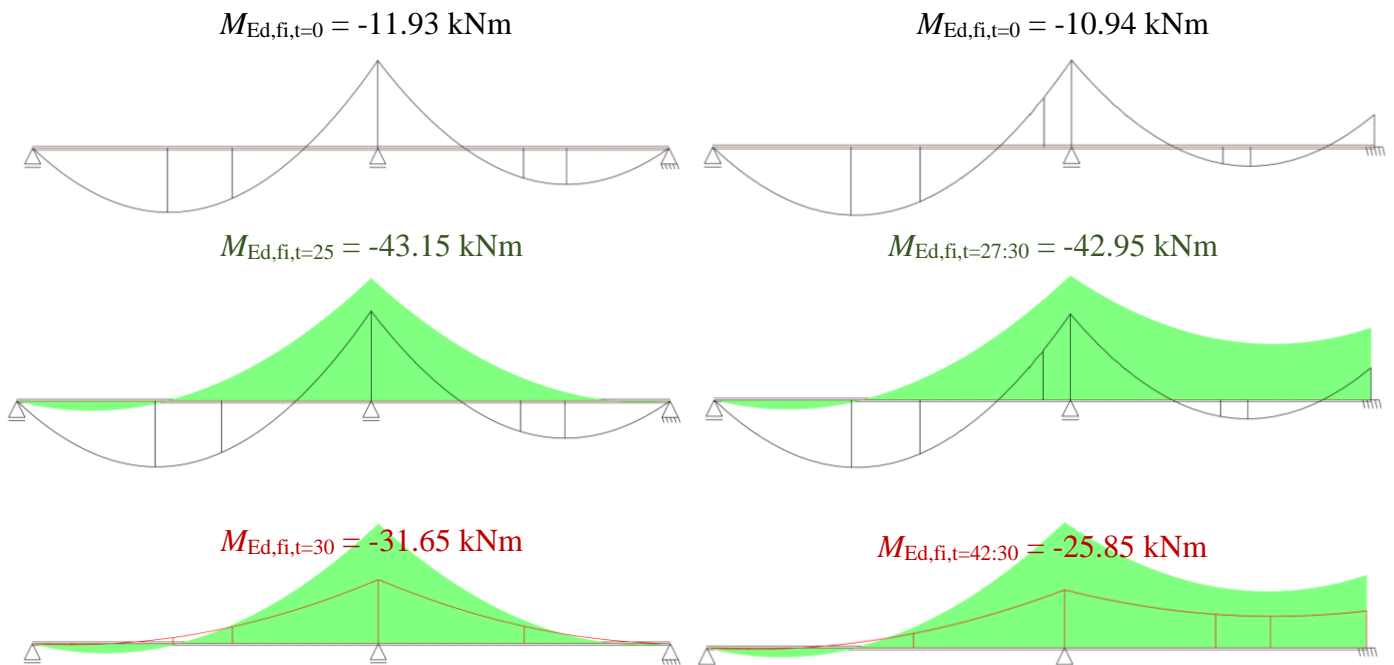


Fig. 3 Design moment in fire situation at different time intervals for cases I and II

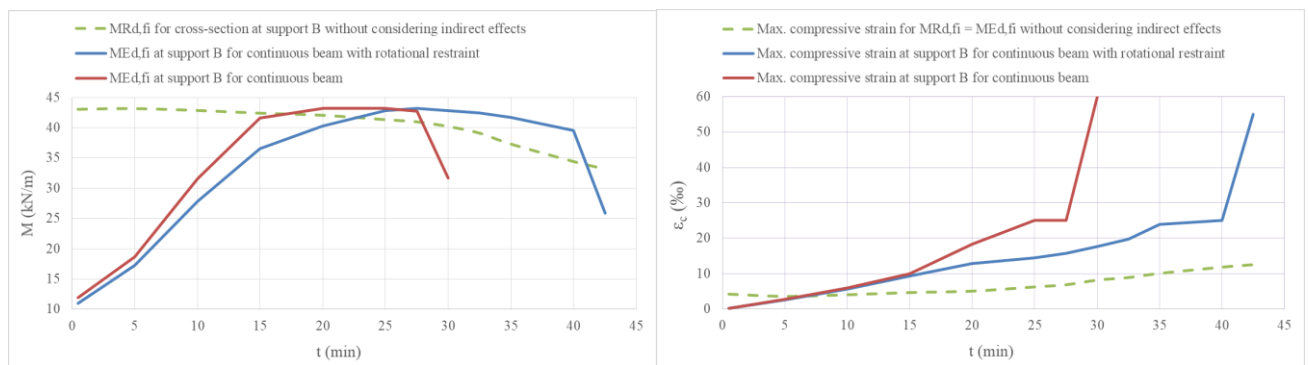


Fig. 4 Design moment in fire (left) and maximum value of compressive strains in the farthest fibers (right) up to the point of failure for a cross-section at the mid-support

## CONCLUSIONS

From the results evaluated based on different assessment methods (summarized in Table 5), it can be concluded that:

- For case 1, the considered statically determinate ribbed slab: the direct applicable method to verify R30 is the simplified method proposed in Annex E.2 of EN 1992-1-2. The level 1 and level 3 assessments are further applicable and can be used to verify R30 provided that the thermal analysis is performed for the considered ribbed cross-section.
- For case 2, the statically indeterminate ribbed slab: there is no direct method to verify R30 from EN 1992-1-2. Level 1 can be applied using temperatures from thermal analysis and by controlling the degree of utilisation. Further using nonlinear thermo-mechanical

analysis (level 3) the considered continuous beam has shown about 40% reserve after reaching R30. In this regard, complementary recommendations can be implemented in EN 1992-1-2 for the statically indeterminate ribbed slabs systems with axis distance of reinforcement close to the exposed side  $a_{rib,bot} = 2$  cm with the considered cross-section dimensions.

Table 5 Summary of results based on different assessment methods

	Level 1: prescribed values in EN 1992-1-2	Level 1: using temperatures from thermal analysis	Level 2: using Annex E.2 in EN 1992-1-2	Level 2: using Annex E.3 in EN 1992-1-2	Level 3: without considering the thermal indirect effects	Level 3: without considering the thermal indirect effects
Case 1	R30 ✘	R30 ✔	R30 ✔	Not applicable	R30 ✔	R30 ✔
Case 2	R30 ✘	R30 ✔	Not applicable	R30 ✘	---	R30 ✔ (with 40% additional reserve)

## REFERENCES

SOFiSTiK. Service Pack 2020-2 Build 131.

Harte, R., Krätzig, W. B., Noh, S. Y. & Petryana, Y. S., 2000. On progressive damage phenomena of structures. *Computational Mechanics*, Volume 25, pp. 404-412.

Hosser, D., 2012. *Brandschutz in Europa–Bemessung nach Eurocodes. Erläuterungen und Anwendungen zu den Brandschutzteilen der Eurocodes*. 2 ed. s.l.:s.n.

Narayanan, R. S. & Beeby, A. W., 2005. *Designers' Guide to EN 1992-1-1 and EN 1992-1-2. Eurocode 2: Design of Concrete Structures: General Rules and Rules for Buildings and Structural Fire Design (Vol. 17)*. s.l.:s.n.

Pouran, O., Anders, S., Harte, R. & Montag, U., 2019. *Influence of variation of concrete compressive strength on the bending response of a cut-and-cover tunnel structure considering results of small-scale tests at elevated temperatures*. Singapore, ASFE'19.

Pouran, O. & Harte, R., 2015. *Nonlinear Structural Analysis of Cut-And-Cover Tunnels Exposed to Fire*. Dubrovnik, s.n., pp. 43-48.

Pouran, O. & Harte, R., 2017. *Influence of heating rate and thermal incompatibilities on the test results of concrete cylinder specimens with polypropylene fibres under heating*. Manchester, CRC Press, pp. 63-72.

Pouran, O., Harte, R. & Peter, C., 2017. PARAMETERS AFFECTING THE STRUCTURAL ANALYSIS OF A TUNNEL STRUCTURE EXPOSED TO FIRE. *Acta Polytechnica CTU Proceedings*, Volume 7, pp. 47-51.

Proceedings of the International Conference in Ljubljana, 10-11 June 2021  
in edition of Applications of Structural Fire Engineering

**Session**

**Composite and other structures I**

# PERFORMANCE OF CFS STUD-TO-SHEATHING SCREW CONNECTIONS AT ELEVATED TEMPERATURES

Tharindu Abeywardena<sup>a</sup> and Mahen Mahendran<sup>b</sup>

<sup>a</sup> PhD researcher, Queensland University of Technology (QUT), Australia

<sup>b</sup> Professor, Queensland University of Technology (QUT), Australia

## Abstract

Gypsum plasterboard sheathed light gauge steel framed (LSF) walls are commonly utilized in residential and commercial low- and mid-rise buildings due to their numerous advantages. It is well known that the stability provided by the gypsum plasterboards to these walls through their screw connections can significantly enhance the load-bearing capacity of LSF walls. The local behaviour of screw connections can be divided into two components, in-plane and pull-through. However, when LSF walls are exposed to fire conditions, the performance of screw connections is significantly affected by the rapid changes in mechanical properties of gypsum plasterboards and cold-formed steel studs, which could lead to premature in-plane shear or pull-through failures at the screw connections. In this study, a series of experiments was conducted to determine the in-plane and pull-through responses of stud-to-gypsum plasterboard sheathing screw connections at elevated temperatures. Using the experimental results, suitable capacity and stiffness reduction factors were proposed, representing both in-plane and pull-through behavioural characteristics, for use in analytical and advanced numerical simulations.

**Keywords:** LSF walls; Stud-to-gypsum plasterboard sheathing screw connections; Elevated temperatures; In-plane shear failures; Pull-through failures.

## 1 INTRODUCTION

The use of light gauge steel studs made of cold-formed steels (CFS) has become increasingly popular due to their superior benefits over other construction materials. LSF walls are typically lined with sheathing boards such as gypsum plasterboard, magnesium oxide board, oriented strand board and calcium silicate board. Among them, gypsum plasterboard is preferred due to its enhanced thermal performance. CFS studs and sheathing boards are connected using self-drilling screws. Therefore, in addition to the fire protection, stud-to-sheathing screw connections provide significant stability to the studs by reducing the global slenderness and significantly enhancing the load-bearing capacity (Telue and Mahendran 2001, Vieira et al., 2013, Dias et al., 2019). Many studies have been conducted to investigate the thermal performances of LSF walls (Ariyanagam and Mahendran, 2017, 2018, 2019, Dodangoda, 2019, Steau and Mahendran, 2020, 2021), however, little study has been done on the behaviour of screws at elevated temperature. The restraints given by the screw connections can be primarily categorised as local in-plane and pull-through. In-plane and pull-through restraints are engaged when the relative displacement between stud and sheathing occurs in the plane and perpendicular to the plane of the sheathing, respectively.

During fire exposure, the performance of stud-to-sheathing connections declines due to the reduction of mechanical properties of the sheathing boards and CFS. If the reduction of strength and stiffness of connections is known, the load-bearing behaviour of LSF walls under fire conditions can be analysed more accurately using advanced finite element techniques. There is limited research conducted to investigate the behaviour of these connections at elevated temperatures. Therefore, plasterboard restraints are often ignored in design due to lack of experimental data.

In this study, a series of experiments was conducted to investigate the elevated temperature in-plane and pull-through behaviour of stud-to-sheathing connections, from which appropriate analytical reduction factor equations are proposed for use in the design of LSF walls.

## 2 GYPSUM PLASTERBOARDS

Gypsum plasterboards have become one of the most popular sheathing material due to their advanced thermal performance. The core of the gypsum plasterboard consists of  $CaSO_4 \cdot 2H_2O$  and a small

quantity of additives such as glass fibre and vermiculite. The gypsum core is covered by a heavy paper layer, as shown in Fig. 1. Mechanical property reduction of gypsum plasterboards at elevated temperatures is significantly higher compared to that of cold-formed steel. Therefore, the performance reduction of screw connections is expected to be mostly governed by the mechanical property reduction of gypsum plasterboards.

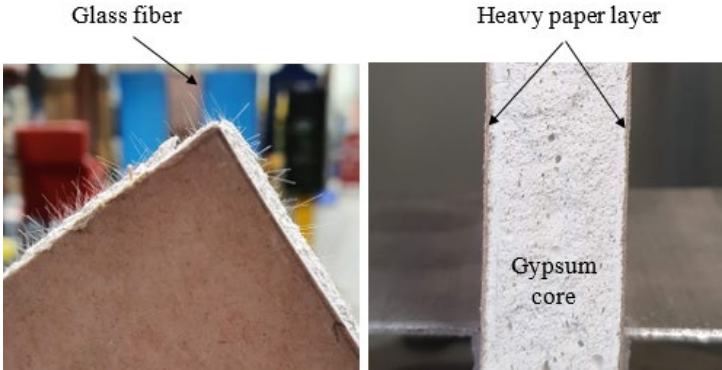


Fig. 1 Gypsum plasterboard sheathing

**2.1 Behaviour at ambient temperature**

The mechanical properties of 16, 13 and 10 mm gypsum plasterboards were investigated at ambient temperature in accordance with AS 2588 (2018). The width of the plasterboard samples was chosen as 100 mm. Using an Instron testing machine, a uniform displacement rate of 25 mm/min was applied until a bending failure occurred.

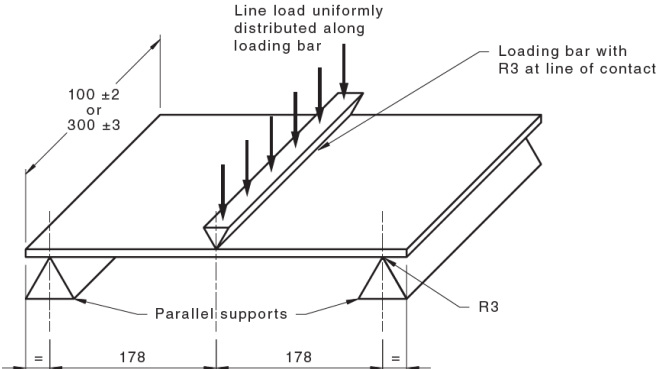


Fig. 2 Three-point bending setup

Table 1 Elastic modulus and bending strength of 16, 13 and 10 mm plasterboards

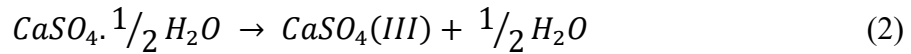
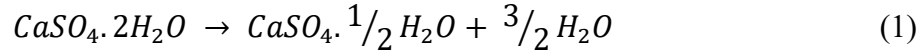
Plasterboard thickness	Plasterboard orientation	Elastic modulus (MPa)			Bending strength per unit width (N/mm)		
		Front	Back	Avg.	Front	Back	Avg.
16 mm	Transverse	2829	2916	3150	1.36	1.34	2.06
	Longitudinal	3447	3407		2.75	2.79	
13 mm	Transverse	2531	1933	2439	0.60	0.64	1.07
	Longitudinal	2634	2660		1.58	1.48	
10 mm	Transverse	1747	1655	1999	0.43	0.41	0.70
	Longitudinal	2307	2285		0.94	1.01	

It was observed that, in terms of bending behaviour, plasterboards show anisotropic behaviour. This is due to the machine direction of the outside cardboard layer. Therefore, four bending tests were conducted for face-up, face-down, transverse and longitudinal orientations. Table 1 summarises the average elastic modulus and bending strength in each case. Even though the load-displacement curves

showed a significant anisotropic behaviour, the elastic modulus values for each orientation were reasonably close.

## 2.2 Behaviour at elevated temperatures

When exposed to elevated temperatures, gypsum plasterboards undergo a series of chemical reactions (Dodangoda, 2019). At 150 and 172 °C, chemically bound water is being released where reactions 1 and 2 take place, respectively. When the temperature is further increased, reaction 3 and 4 takes place at 380 and 1100 °C, respectively.



Using a series of three-point bending tests, Cramer et al. (2003) and Rahmanian (2011) investigated the mechanical properties of gypsum plasterboard at elevated temperatures. Strength and stiffness variation at elevated temperatures can be categorised into three temperature regions: ambient temperature to 100 °C, 100 °C to 200 °C and temperatures higher than 200 °C. The average elastic modulus and bending strength variation can be derived from Eqs. 5-6, respectively, and by using the parameters given in Table 2.

$$\frac{E_T}{E_{AT}} = aT + b \quad (5)$$

$$\frac{F_T}{F_{AT}} = cT + d \quad (6)$$

Table 2 Elevated temperature mechanical property reduction parameters for gypsum plasterboards

Temperature	a	b	c	d
23-100 °C	1.37E-03	9.69E-01	2.48E-04	9.94E-01
100-200 °C	-7.55E-03	1.86	-5.12E-03	1.53
200-400 °C,	-6.21E-04	4.74E-01	-1.73E-03	8.53E-01

## 3 IN-PLANE BEHAVIOUR

In order to investigate the local in-plane response, a symmetrical test setup similar to Winter (1958) was utilized, as shown in Fig. 3. This test setup represents the actual in-plane behaviour of stud-to sheathing connections and the output of a single test consists of the average behaviour of eight stud-to-sheathing screw connections. High strength G500 and 550 CFS studs with thicknesses of 1.2 and 0.75 mm, respectively, were used in the test series. A uniform displacement of 0.05 mm/s was applied from a hydraulic pump and the load and displacements were measured using a load cell and two digital displacement measuring devices. The temperatures were monitored using four K-type thermocouples placed on the four faces of the plasterboards. Two tests were conducted at each elevated temperature.

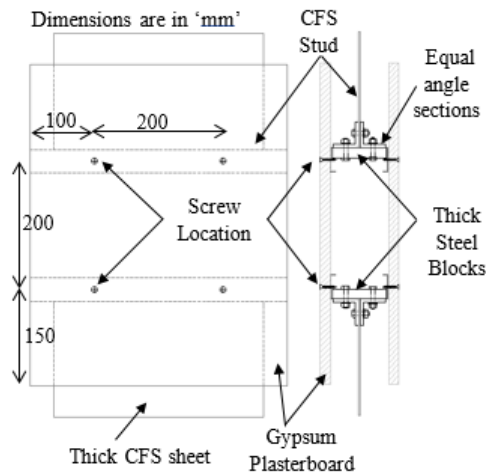


Fig. 3 In-plane test setup

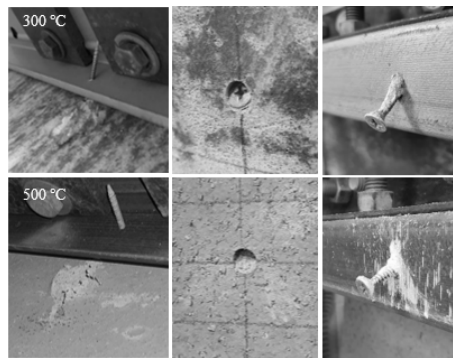


Fig. 4 Failure modes at elevated temperatures

Fig. 4 illustrates the in-plane shear failure modes at elevated temperatures. It could be observed that both stiffness and capacity are reducing at temperatures above 100 °C and the reduction is more severe from 100 °C to 200 °C. Similar to strength and stiffness variation of gypsum plasterboards, the reduction behaviour can be categorized into three different regions: ambient to 100 °C, 100 °C to 200 °C and temperatures above 200 °C. In-plane stiffness and capacity at elevated temperatures can be calculated using Eqs. 7-8 and Table 3.

$$\frac{k_T}{k_{AT}} = eT + f \quad (7)$$

$$\frac{P_T}{P_{AT}} = gT + h \quad (8)$$

Table 3 In-plane stiffness and capacity reduction parameters

Temperature	e	f	g	h
23-100 °C	2.48E-04	9.94E-01	1.16E-03	9.73E-01
100-200 °C	-6.08E-03	1.63E+00	-5.15E-03	1.60E+00
200-500 °C,	-9.93E-04	6.10E-01	-9.90E-04	7.73E-01

#### 4 PULL-THROUGH BEHAVIOUR

In order to investigate the pull-through behaviour, a test setup similar to Kesti (2000) was employed, as shown in Fig. 5. A uniform displacement of 0.05 mm/s was applied from a hydraulic pump and the load and displacements were measured using a load cell and two digital displacement measuring devices. The temperatures were monitored using two K-type thermocouples placed on the top and bottom faces of the plasterboard. Two tests were conducted at each elevated temperature.

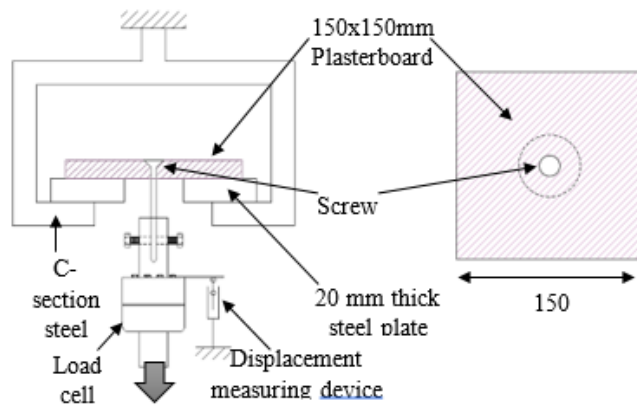


Fig. 5 Pull-through test setup

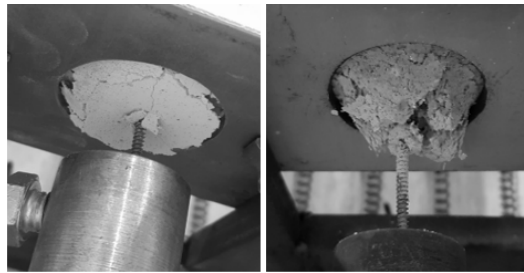


Fig. 6 Pull-through failure at elevated temperature

Pull-through failures observed during the elevated temperature tests are shown in Fig. 6. Similar to in-plane response, pull-through stiffness and capacity reduction factors can be derived using Eqs. 7-8 and the parameters given in Table 4.

Table 4 Pull-through stiffness and capacity reduction parameters

Temperature	e	f	g	h
23-100 °C	4.42E-03	8.98E-01	6.76E-04	9.84E-01
100-200 °C	-6.67E-03	2.01E+00	-5.98E-03	1.65E+00
200-700 °C,	-1.59E-03	9.91E-01	-7.06E-04	5.96E-01

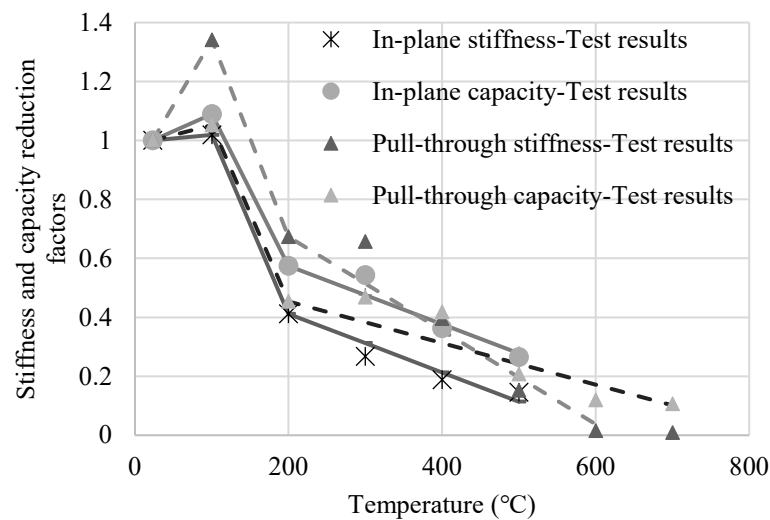


Fig. 7 Comparison of in-plane and pull-through reduction factors

## 6 CONCLUSIONS

In-plane and pull-through behavioural parameters are required to accurately analyse the load-bearing capacities of LSF walls. Often in design, the support provided by the sheathing boards is ignored due

to lack of experimental data on screw connection behaviour. In a fire event, gypsum plasterboard sheathing provides protection to the LSF walls from flame, smoke and heat penetration for a considerable amount of time. However, the mechanical properties of gypsum plasterboards decline with increasing temperature and hence also the performance of screw connections. It was observed that when the temperature is increased to 100 °C the stiffness and capacity increase slightly, but when the temperature is further increased to 200 °C, a significant reduction (40-60%) of both stiffness and capacity occurs. Suitable equations are proposed to determine both in-plane and pull-through strength and stiffness variations at elevated temperatures for an economical and safe design of LSF walls subject to fire conditions.

## ACKNOWLEDGMENTS

The authors wish to thank Australian Research Council (Grant Number LP170100952) and National Association of Steel Framed Housing (NASH) for providing financial support and QUT for providing the required research facilities. They appreciate the valuable technical guidance and support provided by Mr Ken Watson and his NASH staff. They also extend their appreciation to the technical staff at Banyo Laboratory (QUT) for their support to the experimental study. Finally, the authors acknowledge the generous contributions of Bluescope Steel, Enduroframe and USG Boral in providing the required CFS studs and plasterboards.

## REFERENCES

- Telue, Y., & Mahendran, M. (2001). Behaviour of cold-formed steel wall frames lined with plasterboard. *Journal of Constructional Steel Research*, 57(4), 435-452.
- Vieira Jr, L. C. M., & Schafer, B. W. (2013). Behavior and design of sheathed cold-formed steel stud walls under compression. *Journal of Structural Engineering*, 139(5), 772-786.
- Dias, Y., Mahendran, M., & Poologanathan, K. (2019). Axial compression strength of gypsum plasterboard and steel sheathed web-stiffened stud walls. *Thin-Walled Structures*, 134, 203-219.
- Ariyanayagam, A. D., & Mahendran, M. (2017). Fire tests of non-load bearing light gauge steel frame walls lined with calcium silicate boards and gypsum plasterboards. *Thin-Walled Structures*, 115, 86-99.
- Ariyanayagam, A. D., & Mahendran, M. (2018). Experimental study of non-load bearing light gauge steel framed walls in fire. *Journal of Constructional Steel Research*, 145, 529-551.
- Ariyanayagam, A. D., & Mahendran, M. (2019). Influence of cavity insulation on the fire resistance of light gauge steel framed walls. *Construction and Building Materials*, 203, 687-710.
- Dodangoda, M. T., Mahendran, M., Keerthan, P. & Frost, R. L. (2019). Developing a performance factor for fire rated boards used in LSF wall systems. *Fire Safety Journal*, 109, 102872.
- Steau, E., Mahendran, M., & Poologanathan, K. (2020). Experimental study of fire resistant board configurations under standard fire conditions. *Fire Safety Journal*, 116, 103153.
- Steau, E., & Mahendran, M. (2021). Elevated Temperature Thermal Properties of Fire Protective Boards and Insulation Materials for Light Steel Frame Systems. *Journal of Building Engineering*, 102571.
- Cramer, S. M., Friday, O. M., White, R. H., & Sriprutkiat, G. (2003). Mechanical properties of gypsum board at elevated temperatures. In *Fire and materials 2003: 8th International Conference, January 2003, San Francisco, CA, USA*. 33-42.
- Rahmanian, I. (2011). Thermal and mechanical properties of gypsum boards and their influences on fire resistance of gypsum board based systems, PhD Thesis, The University of Manchester, Manchester, UK.
- Winter, G. (1958). Lateral bracing of columns and beams. *Journal of the Structural Division*, 84(2), 1561-1.
- Standards Australia. (2018). Gypsum plasterboard. AS/NZS 2588. Sydney, Australia
- Kesti, J., (2000). Local and distortional buckling of perforated steel wall studs, PhD Thesis, Helsinki University of Technology, Espoo, Finland.

## THE INFLUENCE OF COPING ON LONG-SPAN CONTINUOUS BEAM UNDER FIRE LOADING

Priya S Natesh<sup>a</sup>, Anil Agarwal<sup>b</sup>

<sup>a</sup> Assistant Professor, Faculty of Science and Technology, ICFAI Foundation for Higher Education  
(Declared as Deemed to be University u/s 3 of the UGC Act 1956), Hyderabad- 501 203, India  
e-mail: priyas@ifheindia.org

<sup>b</sup> Assistant Professor, Department of Civil Engineering, Indian Institute of Technology, Hyderabad - 502 285, India  
e-mail: anil@iith.ac.in

### Abstract

The requirement of large column-free spaces demands long-span beams. Very few studies have been conducted on the behaviour of long-span composite beams subjected to fire loading. In this paper, the behaviour of a long span beam of 13m span and double angle connection with 2 hours of fire protection is subjected to 3 hours of fire loading is studied numerically. The influence of coping on the ends of the beam was studied in detail. The presence of coping affects the location of buckling and the amount of lateral force acting on the column. If the beam is provided with coping at the bottom end, the steel beam web near angle connection undergoes local buckling near the connection, and it causes buckling of the angles in the connection and thereby induces high tensile force demand in the associated welded connection. This force demand on the welded connection is highly localised and may even cause the fracture of the connection. If the beams are without any coping, the welded connection will only be subjected to a negligible tensile force under fire loading. If the beams are coped at the bottom, the runout failure can be prevented by providing additional rebars at the support.

**Keywords:** long span, composite beam, fire loading, coping, rebar

### 1 INTRODUCTION

There is an increase in the need for significant space demands for long-span beams and slabs, especially in steel structures. Most of the research work happened in composite steel-concrete beams with short span composite beams under fire loading spanning up to 5-7m. Wainman & Kirby, 1987 studied the behaviour of the simply-supported composite beam of effective span 4.58m under fire loading. Zhao & Kruppa, 1995 performed an experimental investigation on the composite beam with a span around 5m under fire loading. They investigated the effect of varying the concrete slab width and influence of protection for steel beam. Huang et al., 1999 developed the 3D composite beam using the VULCAN computer program to understand the influence of shear stud connectors in the simply-supported steel-concrete composite beam. Ranzi and Zona (2007) formulated an analytical model of the steel-concrete composite beam to predict partial shear interaction, including the shear deformability of the steel component under elevated temperature. Anil et al., 2011(a, b), 2014(a, b), studied the impact of shear tab connection in the stability of 10 storey office building subjected to a corner compartment fire. Kodur et al., 2013 conducted a numerical investigation on the behaviour of steel-concrete bridge girders under fire loading. Selden et al., 2014, 2015 conducted a full-scale experimental investigation on the behaviour of steel-concrete composite beam system under fire loading. 3.80 m long beams with lightweight flat slabs of 89mm depth and 914mm width connected to the supporting column through shear tab connections. Jiang et al., 2015 extended Opensees- an open resource object-oriented software to predict the behaviour of composite beams under fire loading. Fischer et al., 2015, 2016, 2017 studied the behaviour of different types of beam to column connections such as shear tab connection, single angle connection, double angle connection under fire loading. Choe et al. 2018 performed an experimental investigation on the long span continuous steel-concrete composite beam with various beam-column connections. There is very little research work on the behaviour of long-span composite beams under fire loading. The design of a robust connection for a long span beam is yet to achieve, as the recent research in NIST observed long-span composite beam collapse

with double angle connection. This paper attempt to study the influence of coping in the behaviour of long-span continuous beams under fire loading.

## 2 MODELLING AND VALIDATION

Eurocode specified data were used for modelling material properties. Abaqus software was used for modelling purpose. The steel beam, concrete slab, angles used in the connections, bolts, rebars, wire mesh, and shear studs were modelled with solid elements. Three-dimensional heat transfer analysis was carried out to capture the temperature-time history at every node in the model. A sequentially coupled stress analysis was conducted to predict the mechanical behaviour under fire loading. Modelling various material properties and analysis procedures is discussed in detail in Natesh and Agarwal, 2020, so not being discussed here for brevity. The results were validated with experimental data from literature Zhao et al., 1995; Wainman and Kirby, 1987; and Choe et al., 2018. The validation of temperature at various point and midspan deflection of the beams with various literature are shown in figure1-3. All beams were connected to the column using a double angle connection. The angles were bolted to the beam and welded to the column. The welded connections were modelled using connector elements. At the time of fire loading, the beam was subjected to a gravity load of 45% of its ultimate capacity.

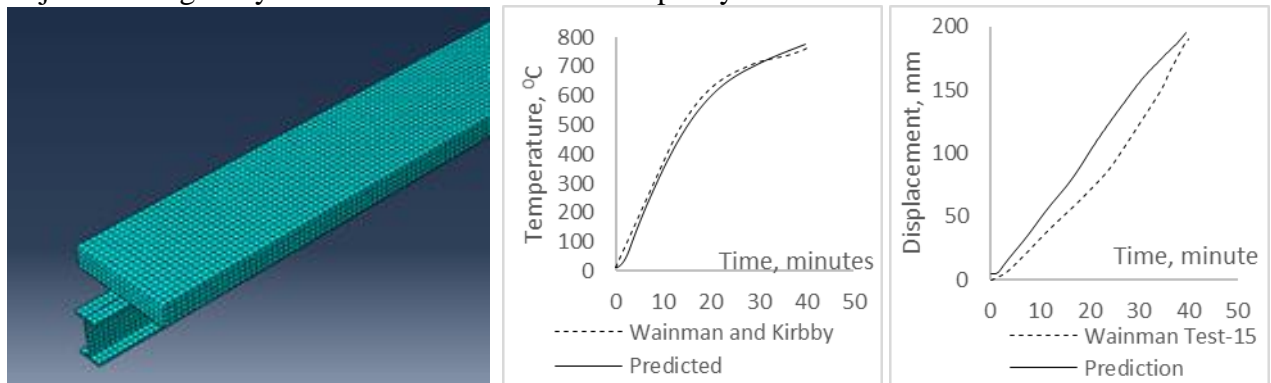


**Fig. 1** Validation of analysis procedure– Wainman, 1987, T15 (a) Isometric view of the model (b) Mid span deflection (c) Steel bottom flange temperature

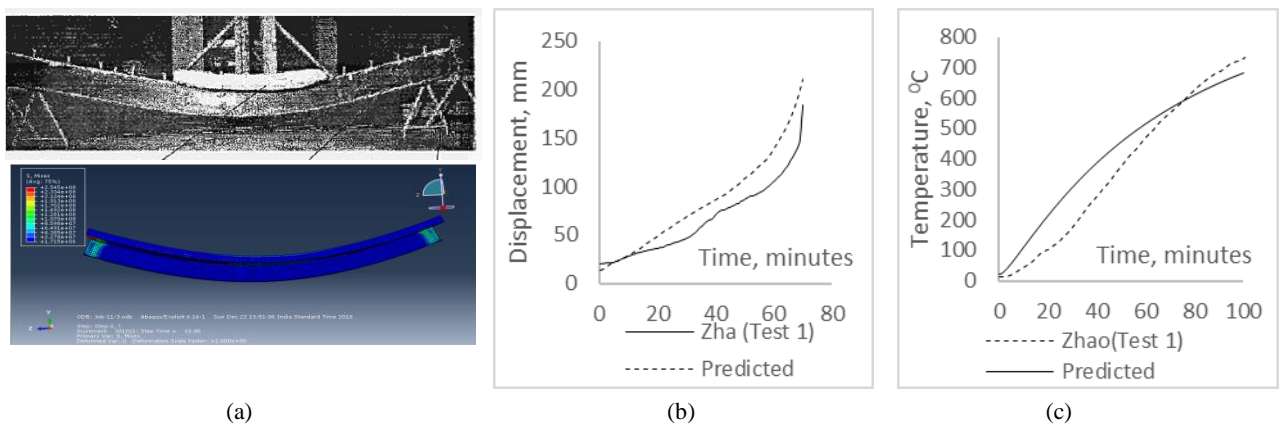


**Fig. 2** Validation of analysis procedure– Zhao, 1995, Test 1 (a) Comparison of the deflected shape with Experiment (b) Mid span deflection (c) Steel bottom flange temperature

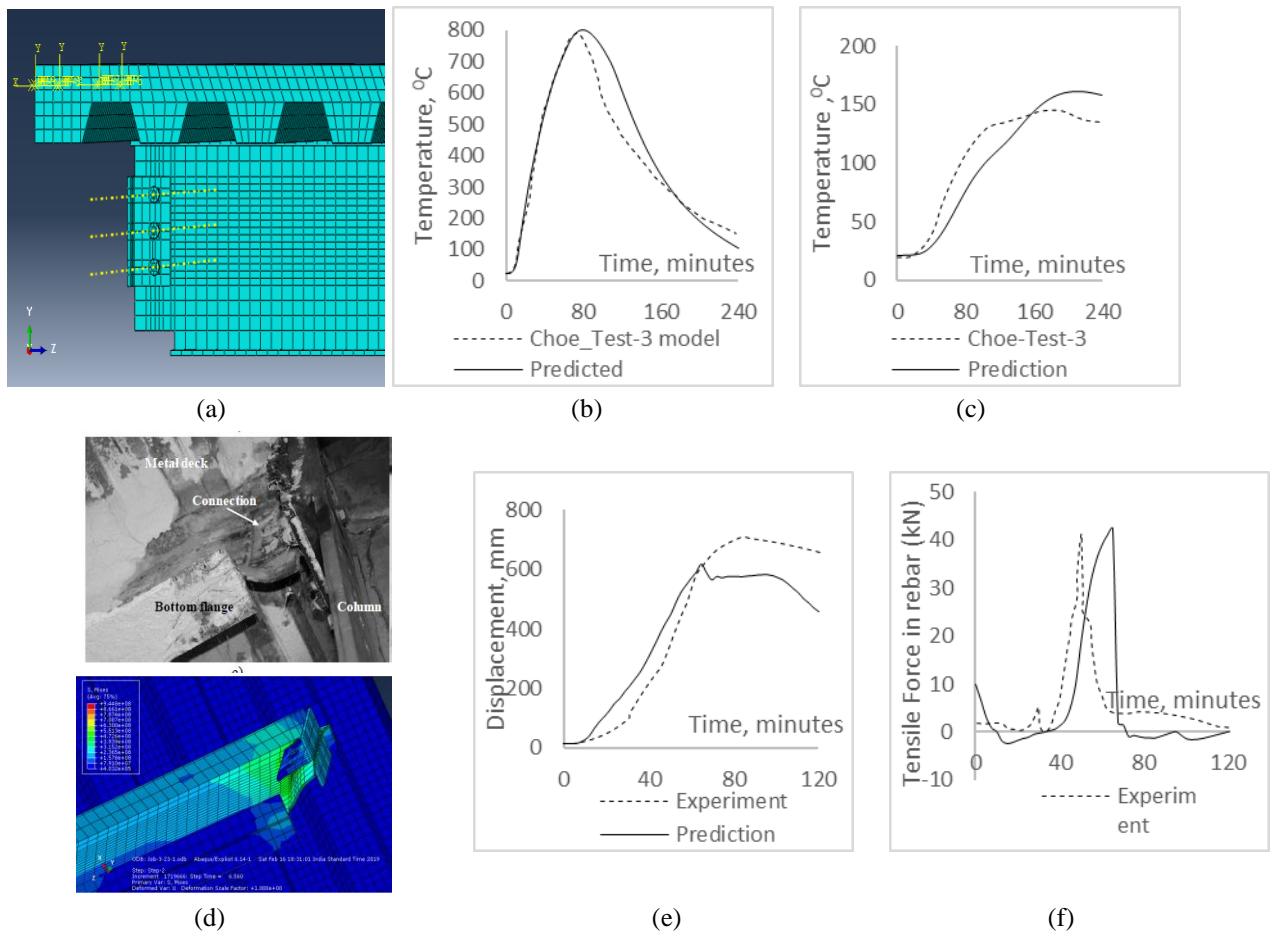


**Fig. 3** Validation of analysis procedure– Choe et al., 2018, Test 3 (a) Beam model (b) Steel bottom flange temperature (c) Concrete top Temperature (d) Comparison of the buckled shape of the beam with Experimental picture (e) Mid span deflection (f) Axial restraint force Vs time at the connection

## 2 PARAMETRIC STUDY

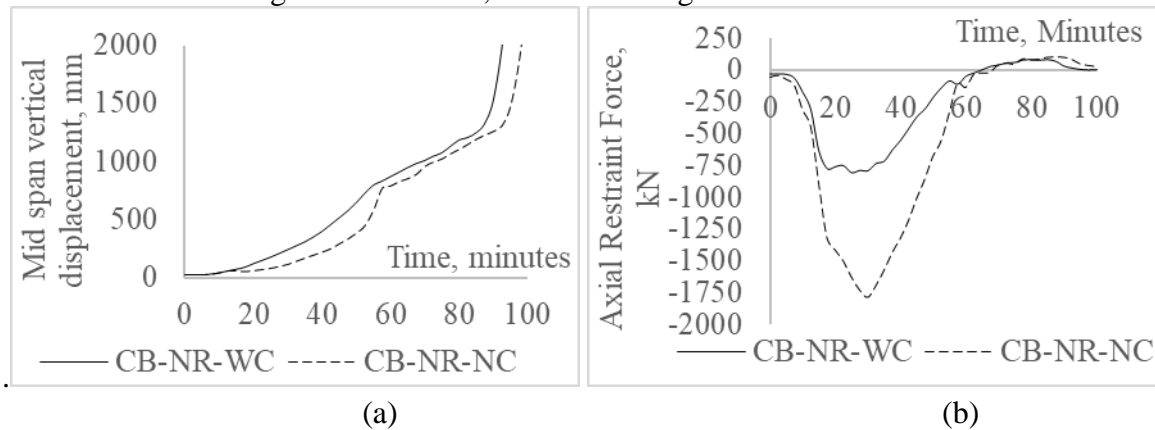
A detailed parametric study was conducted to understand the effect of coping in composite beams under fire loading. Five models, as listed in table 1, were modelled and run the analysis. The long span composite beam from the literature Choe et al., 2018 with a span of 13m was used for all parametric studies. All models were having 2-hour fire protection for the beams and 3-hour fire protection for the connections. Furthermore, they were exposed to a fire loading for 3 hours. All beams were provided with wire mesh to take care of shrinkage effects. Two beams with serial number 1 and 2 were without any additional reinforcement at the support, and three beams with serial numbers 3-4 were with rebars at the support. Four rebars with a diameter of 12.7 mm were provided in the hogging zone of the beam ends as additional reinforcements.

Table 1: Summary of the parametric analysis

Sl. No.	Model Name	Provision of additional rebars	Coping location
1	CB-NR-BC	Not provided	Bottom ends
2	CB-NR-NC	Not provided	No coping
3	CB-WR-BC	Provided	Bottom ends
4	CB-WR-NC	Provided	No coping
5	CB-WR-TC	Provided	Top ends

### 3.1 Presence of Coping

Two beams were considered; one beam was modelled with the coping at the bottom and another without any coping. Both the models were not having any rebars. The wire mesh was provided to avoid shrinkage effects in the beam. The midspan deflection and axial restraint force in the column are shown in figure 4. Until 17 minutes, both the beams behaved in similar ways. Around 17 minutes, the steel beam touched the column. Further heating caused the buckling of the beam. The localised buckling near coping was observed in the beam with coping at the bottom, which causes the buckling of the double angle connection, and it induced higher tensile force in the weld. Whereas in the beam without coping, the buckling was observed away from the connection. Moreover, such localised force demand was not there in the connection. Until the first 55 minutes of heating, the beam without coping had less very midspan deflection compared to the beam with coping. The difference in midspan deflection was around 280 mm at 55 minutes. It is due to the alternate load transfer through the column. In beams without coping, the axial restraint force developed at the column was 1000 kN more than that of the beam with coping. Runout failure was observed at around 80 minutes and 83 minutes for the beam with and without coping, respectively. The excessive bearing near bolt holes, as shown in figure.



**Fig.4** Comparison of (a)Midspan vertical displacement Vs time (b)Axial restraint force

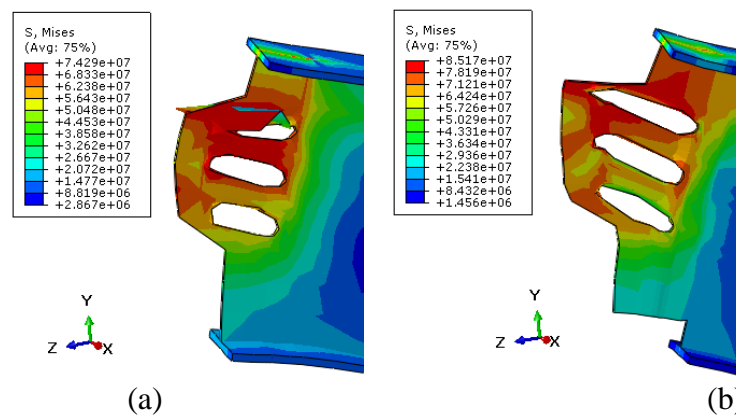


**Fig. 5** Bolt holes at the time of failure for (a) CB-NR-WC (b) CB-NR-NC

### 3.2 Location of coping

Three beams were modelled by changing the location of the coping. CB-WR-BC and CB-WR-TC were with coping at the bottom and top, respectively, as shown in figure 6. Whereas CB-WR-NC without any coping. In addition to wire mesh, all three beams were having four additional rebars of diameter 12.7 mm provided at the hogging zone of the beam near support. The behaviour of beam without coping and with top coping was comparable. The axial restraint force induced in the column by the beam without coping and beam with top coping was 1000kN more than the beam with bottom coping. It reduced the midspan vertical deflection in the beam. When the deflection exceeds 250mm, the rebars start taking the load in all the beam members, preventing the beam's

failure. In the beam with bottom coping, the web and bottom flange undergone local buckling once the beam expands and touches the column. The local buckling was near coping. It induced the twisting of the connection angles and tensile force demand in the welded connection. The global buckling was observed in the beams with coping at the top and no coping conditions, and the location of buckling was far away from the connection. So, such localised tensile force demand was not observed in the connection. The tensile force demand in the weld starts reducing once the reinforcement started taking the load.

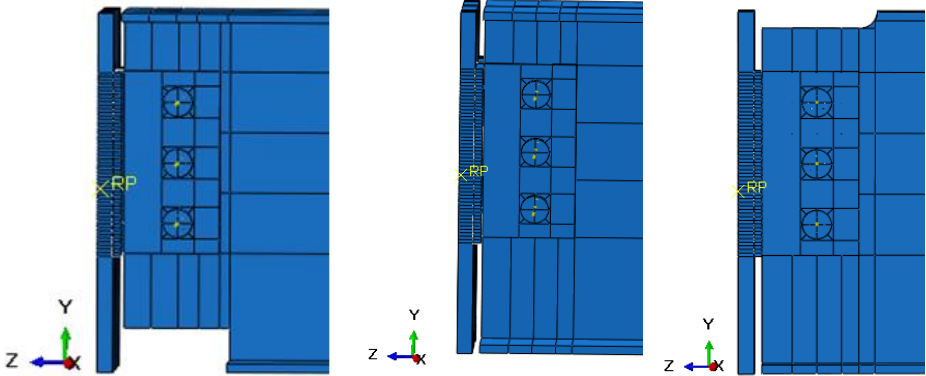


Fig. 6 Connection details of (a) CB-WR-BC (b) CB-WR-NC (c) CB-WR-TC

All beams were able to survive the fire loading of 3 hours due to the presence of rebar at the support. The midspan deflection and axial restraint force in the column are shown in figure 7.

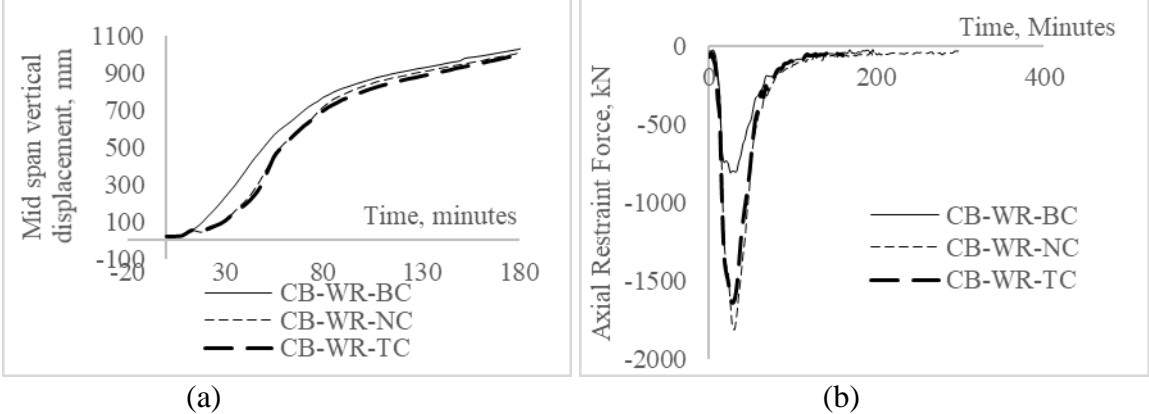


Fig.7 Comparison of (a)Midspan vertical displacement Vs time (b)Axial restraint force

### 3 CONCLUSIONS

A three-dimensional beam was modelled and validated using Abaqus. A parametric study was conducted to understand the behaviour of composite beams with additional rebars at the support and location of coping at the edges.

**Influence of coping without any reinforcement:** Both beams were modelled without any rebar. Until 55 minutes after heating, the flexural strength of beams without coping was much better than the beam with coping. At 55 minutes, the midspan deflection in the beam with coping was around 280 mm more than the beam without coping. This is due to the full contact of the beam end with the column during expansion and associated high restraint force offered by the column. The runout failure was observed around 80-83 minutes in both beams irrespective of coping.

**Influence of coping with reinforcement:** The provision of rebars at the support prevents early runout failure of the beam during heating. The rebar provides an alternative load path during the heating phase once the deflection reaches around 250mm. The location and presence of coping and rebars in the concrete slab influence the tensile force demand in the welded connection.

## REFERENCES

- ABAQUS (2012), ABAQUS/Standard Version 6.12 User's Manuals, ABAQUS, Providence, RI.
- Agarwal, A., Selden, K. L., and Varma, A. H. (2014b), Stability behaviour of steel building structures in fire conditions: Role of composite floor system with shear-tab connections, *J. Struct. Fire Eng.*, 5(2), 77–96. doi:10.1260/2040-2317.5.2.77
- Agarwal, A., and Varma, A. H. (2014a), Fire induced progressive collapse of steel building structures: The role of interior gravity columns. *Engineering Structures*, 58, 129-140. doi: 10.1016/j.engstruct.2013.09.020
- Agarwal A. (2011a), Stability of steel building structures under fire loading. PhD dissertation. School of Civil Engineering, Purdue Univ.; 2011.
- Agarwal, A., Varma, A. H. (2011b), Design of steel columns at elevated temperatures due to fire: effects of rotational restraints, *Eng J*, AISC.
- Cedeno, G., Varma, A.H. and Agarwal, A. (2009), Behaviour of floor systems under realistic fire loading, Proceedings on CD-ROM of the ASCE Structures Congress, ASCE, Reston, VA, pp. 1-10. doi: 10.1061/41031(341)224
- Choe, L., Ramesh, S., Seif, M., Hoehler, M., Grosshandler, W., Gross, J., Bundy, M. (2018), Fire Performance of Long-Span Composite Beams with Gravity Connections, Proc. of the 10th International Conference on Structures in Fire SERT, Ulster University, Belfast, UK, June 6-8, 2018.
- Choe, L. , Ramesh, S. , Hoehler, M. , Seif, M. , Bundy, M. , J. and Glisic, B. (2019), Compartment Fire Experiments on Long-Span Composite-Beams with Simple Shear Connections, Part 2: Test Results, Technical Note (NIST TN), National Institute of Standards and Technology, Gaithersburg, MD, [online], <https://doi.org/10.6028/NIST.TN.2055>
- European Committee for Standardization (CEN) (2005), Eurocode 4: Design of Composite Steel and Concrete Structures, Part 1-2: General Rules – Structural Fire Design, European Committee for Standardization, Brussels.
- European Committee for Standardization (CEN) (2002), Eurocode 1: Actions on Structures, Part 1.2: General Actions – Actions on Structures Exposed to Fire. European Committee for Standardization.
- Fischer, E.C., Varma, A.H., Agarwal, A. (2019), Performance-Based Structural Fire Engineering of Steel Building Structures: Design-Basis Compartment Fires, *Journal of Structural Engineering (United States)*, 2019, 145(9)
- Fischer, E. C., Selden, K. L., & Varma, A. H. (2017), Experimental Evaluation of the Fire Performance of Simple Connections,” *Journal of Structural Engineering*. 143(2), 04016181. doi: 10.1061/(ASCE)ST.1943-541X.0001664
- Fischer, E. C., and Varma, A. H. (2016), Fire resilience of composite beams with simple connections: Parametric studies and design, *J. Constr. Steel Res.*, 119–135. doi: 10.1016/j.jcsr.2016.08.004
- Fischer, E. C., and Varma, A. H. (2015), Fire behaviour of composite beams with simple connections: Benchmarking of numerical models, *J. Constr. Steel Res.*, 111, 112–125. doi: 10.1016/j.jcsr.2015.03.013
- Natesh P.S., Agarwal A. 2020. *Numerical Modelling of Continuous Composite Beam Under Fire Loading*. In: Subramaniam K., Khan M. (eds) *Advances in Structural Engineering*. Lecture Notes in Civil Engineering, vol 74. Springer, Singapore. [https://doi.org/10.1007/978-981-15-4079-0\\_7](https://doi.org/10.1007/978-981-15-4079-0_7).
- Selden, K. L., Fischer, E. C., & Varma, A. H. (2015), Experimental investigation of composite beams with shear connections subjected to fire loading. *Journal of Structural Engineering*, 142(2), 04015118. doi: 10.1061/(ASCE)ST.1943-541X.0001381
- Selden, K. L., Fischer, E. C., & Varma, A. H. (2014) Advanced Fire Testing of a Composite Beam with Shear Tab Connections, *Structures Congress*
- Wainman, D.E. and Kirby, B.R. (1987), Compendium of UK standard fire test data, unprotected structural steel – 1, Reference Number RS/RSC/S10328/1/98/B, British Steel Corporation (now Corus), Swinden Laboratories, Rotherham.
- Zhao, B., and Kruppa, J. (1997), Fire Resistance of Composite Slabs with Profiled Steel Sheet and of Composite Steel Concrete Beams, Part 2: Composite Beams. ECSC – agreement No. 7210 SA 509, CTICM, France.

# The interfacial bond slip behavior of I-section steel and reactive powder concrete at high temperatures

Yuzhuo Wang<sup>a</sup>, Tiangui Xu<sup>a</sup>, Bingjie Zhang<sup>a</sup>

<sup>a</sup> College of Civil Engineering, Shandong Jianzhu University, Jinan, Shandong Province 250101, PR China

## Abstract

The paper presents the interfacial bond slip behavior between I-section steel and reactive powder concrete at high temperature. Push-out tests were conducted on 10 specimens at high temperature by considering the impact of experiencing the maximum temperature. The test results show that the ultimate bond load of the specimen decreases with the increase of temperature and the ultimate bond load of the specimen at 600 °C is only 7.8% of that at room temperature (20 °C). The ultimate bond load of the specimens decreases greatly before 250 °C and the descend rate of the bond load reduces obviously when the temperature exceeds 250 °C. Based on the analysis of the test data, the bond-slip calculation formula of I-section steel and reactive powder concrete at high temperature is proposed.

**Keywords:** I-section steel; reactive powder concrete; push-out test; bond-slip calculation formula; high temperature

## 1 INTRODUCTION

Reactive powder concrete (RPC) is a new type of cement-based composite material with ultra-high mechanical properties and excellent durability. RPC is used to replace ordinary concrete in steel reinforced concrete structure, which not only perfectly inherits the advantages of high bearing capacity, high stiffness and good seismic performance of the structure, but also further reduces the section size of components. Therefore, steel encased reactive powder concrete (SRRPC) has a good application and development prospect. In SRRPC structure, the interfacial bond slip behavior between steel and reactive powder concrete is the key to ensure structural safety. The bond slip behavior will directly affect the bearing capacity, resulting in the collapse of buildings and serious losses. Therefore, it is of great significance to study the bond slip behavior of steel and reactive powder concrete at high temperature.

At present, some research has been contributed to the interfacial bond slip behavior of I-section steel and reactive powder concrete at room temperatures. (Bae *et al.*, 2016) studied the influence of compressive strength of the concrete, concrete cover, and inclusion ratio of steel fiber on the bond performance between steel and RPC. (Bu *et al.*, 2018) carried out the push out test on six SRRPC specimens. The process of interface fracture and interfacial bond mechanism were analyzed, and the distribution mode of bond stress along the embedment length of shape steel and RPC interface were obtained. However, no research on the interfacial bond slip behavior of I-section steel and reactive powder concrete at high temperatures has been reported by far. High temperature has a significant effect on the bond slip behavior between concrete and steel (Tao *et al.*, 2012, Li *et al.*, 2015, Wang *et al.*, 2020, and Wang *et al.*, 2021). Therefore, it is necessary to study the interfacial bond slip behavior of I-section steel and reactive powder concrete at high temperatures.

In this paper, the push out tests of 10 SPPRC specimens were carried out at high temperature. The

research in this paper can provide a reference for the structural performance safety of SRRPC at high temperature.

## 2 EXPERIMENTAL PROGRAMS

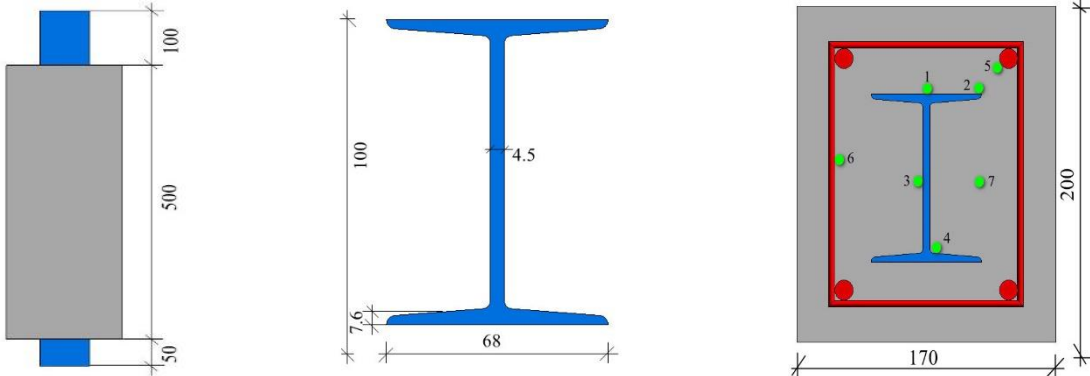
### 2.1 Test specimens

A total of 10 SRRPC specimens were designed and tested, including 1 baseline specimen at room temperature and 9 specimens experiencing high temperatures. A schematic presentation of specimens is shown in Figure 1. For all the specimens, the size of the concrete block was 200 mm × 170 mm × 500 mm. The section size of I-shaped steel was 100 mm × 68 mm × 4.5 mm × 7.6 mm and the total length of I-shaped steel was 650 mm, including 500 mm of embedded length, 100 mm long left outside of the concrete at the top of the column, and 50 mm long left outside of the concrete at the bottom of the column. The specimens were heated to various temperatures which were 20 °C, 100 °C, 150 °C, 200 °C, 250 °C, 300 °C, 350 °C, 400°C, 500°C, and 600 °C. They were named as SRRPC-01 (20 °C), SRRPC-02 (100 °C), SRRPC-03 (150 °C), SRRPC-04 (200 °C), SRRPC-05 (250 °C), SRRPC-06 (300 °C), SRRPC-07 (350 °C), SRRPC-08 (400 °C) SRRPC-09 (500 °C), CES-10 (600 °C), respectively. The details of specimens are summarized in Table 1.

A number of concrete cubic blocks, with size 100 mm × 100 mm × 100 mm, were cast at the same time of pouring SRRPC specimens. They were allowed to cure under the same conditions as the SRRPC specimens for at least 28 days and strength tests were carried out. The compressive strength of reactive powder concrete was 123.7 MPa and the elastic modulus was 49.2 GPa. In addition, the mechanical properties of rebar and steel were tested, as shown in Table 2.

Table 1 SRRPC specimen details

Specimen	Anchorage length of steel (mm)	Steel ratio (%)	Heating temperature (°C)	Section size (mm×mm)
SRRPC-01	500	4.2	20	170×200
SRRPC-02	500	4.2	100	170×200
SRRPC-03	500	4.2	150	170×200
SRRPC-04	500	4.2	200	170×200
SRRPC-05	500	4.2	250	170×200
SRRPC-06	500	4.2	300	170×200
SRRPC-07	500	4.2	350	170×200
SRRPC-08	500	4.2	400	170×200
SRRPC-09	500	4.2	500	170×200
SRRPC-10	500	4.2	600	170×200



(a) specimen shape                      (b) I-shaped steel                      (c) section size and thermocouple layout

Fig. 1 Diagram of SRRPC specimen (Unit: mm).

Table 2 Steel and reinforcement properties

Type	Elastic modulus (GPa)	Yield strength (MPa)	Tensile strength (MPa)
Steel	208.7	783	851
Reinforcement (6mm)	200.3	473	615
Reinforcement (12mm)	200.5	468	624

## 2.2 Measurement of temperature field

The temperatures of specimens were measured by built-in thermocouples. The thermocouples (TC) were only arranged on the midsection of specimen, due to the temperature was uniformly distributed along the axial direction of specimen. There were seven measuring points, named as TC-1 to TC-7, provided on the midsection as shown in Figure 1(c). TC-1 was installed to measure the temperature at the middle of the flange, TC-2 was installed to measure the temperature at the flange tip, TC-3 was used to measure the temperature at the web, TC-4 was used to measure the temperature at the inside of the flange, TC-5 was used to measure the temperature of steel reinforcing bar, TC-6 was used to measure the temperature at the stirrup, TC-7 was to record the temperature of the reactive powder concrete.

## 2.3 Test procedure and loading scheme

Before the test, the specimen was installed on the cushion block. The upper end of specimen was taken as loading end. The concrete at the lower end of specimen was supported by U-shaped cushion block, and the steel at the lower end remained free. The center of the specimen and the loading point were always maintained in a vertical position to avoid eccentric loading during the test, as shown in Fig. 2. The thermocouples in the specimen were connected with the data acquisition instrument, and heating furnace had been fixed. A piece of rock wool and a steel plate were placed between the specimen and the pressure sensor to protect the pressure sensor from high temperature and make sure the loading be evenly applied.

During the test, the furnace was heated with heating rate of 4 °C/min. The furnace temperature was measured by thermocouple automatically. The temperature would be kept in constant once the furnace temperature reached the preset value. Then, the loading was applied when the temperature of all measuring points reached the required temperature. During this test, the displacement and load of specimen were obtained by a computer control pressure testing machine. The SRRPC specimens were loaded at a rate of 5 kN/min until the end of test. The test would be finished when the steel was pushed out by approximately 40 mm. After the test, the apparent characteristics and crack patterns of the specimen were observed and recorded.

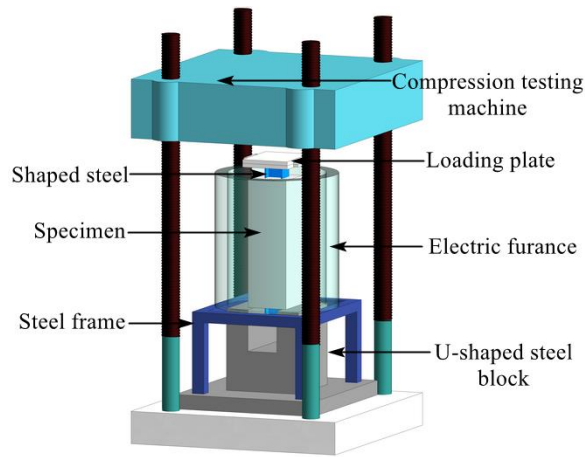


Fig. 2 Test set-ups

### 3 TEST RESULTS

#### 3.1 Temperature time histories

The temperature distribution in the column is helpful to understand the behavior of columns under fire. The temperature time histories of the part of specimens are shown in Figure 3. The results showed that the rising speed of temperature slowed down with the increase of measuring point depth. However, the temperatures of all the measuring points would be finally reached the same value. In this stage, all curves of temperature time history tended to be horizontal.

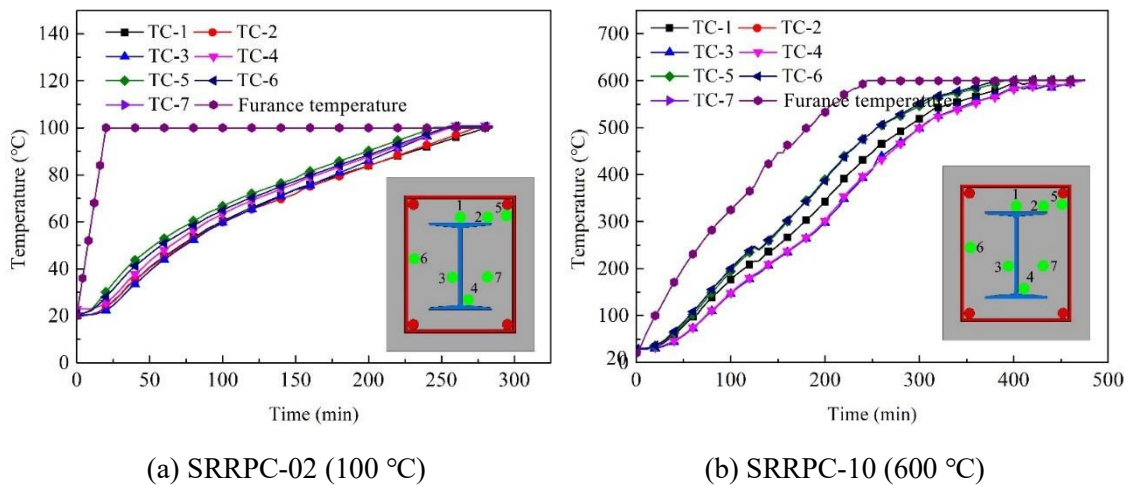


Fig. 3 Variation of temperature time histories of the specimens

#### 3.2 Failure modes

The failure mode of the specimen was recorded in detail, as shown in Fig. 4. All the phenomena of the specimens were classified into three categories according to the form of crack: no crack, 45° diagonal crack and horizontal crack. Due to the obvious stress concentration phenomenon at the tip of the steel flange limb, cracks appear at the tip of the flange and are distributed along 45°, horizontal direction, or both types of cracks occur simultaneously. The form of cracks gradually changed from horizontal cracks to 45° diagonal crack due to the different deterioration of the concrete on the outside of steel. In addition, cracks in some specimens only appear on one side due to the uneven quality of concrete itself.

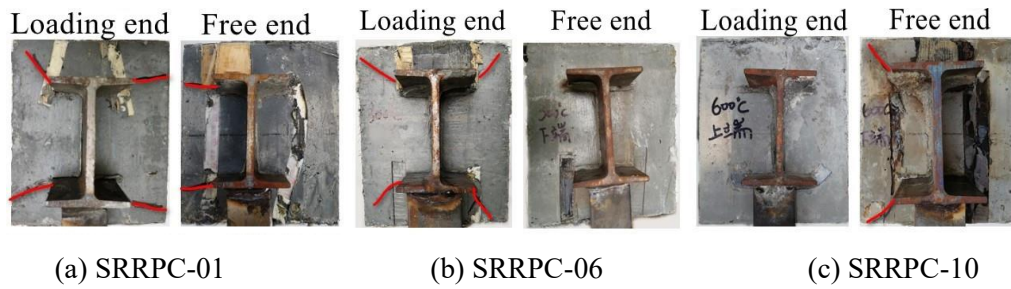


Fig. 4 Failure mode of specimen

### 3.3 The load-slip (P-S) curves

The test data are plotted in Figure 5, which clearly shows the load-slip curve of the specimen. It could be seen that: (1) the variation trends of the P-S curves of SRRPC at high temperatures were much similar to that at room temperature, which could be roughly divided into three stages: the ascending stage, the descending stage, and the residual stage. (2) The ultimate bond load of the specimens decreases greatly before 250 °C and the descend rate of the bond load reduces obviously when the temperature exceeds 250 °C. (3) Compared with room temperature specimen (20 °C), the ultimate bond load of the specimens SRRPC-02 to SRRPC-10 decreased by 81.4%, 73.7%, 64%, 48.1%, 30.4%, 25%, 18.8%, 15.4% and 7.8%, respectively.

Figure 6 shows the relation between the experiencing maximum temperature and ultimate bond load. It can be seen that the ultimate load decreased when the temperature varied between 20 °C and 600 °C. Based on the test data, the formula to calculate the relation between different high temperatures and ultimate bond loads was obtained by regression fitting [see Eq. (1)].

$$P_u = 0.0015T^2 - 1.99T + 690.18 \quad 20 \text{ } ^\circ\text{C} \leq T \leq 600 \text{ } ^\circ\text{C} \quad (1)$$

where  $P_u$  is the ultimate bond load of the specimen, kN;  $T$  is the experiencing maximum temperature of specimen, °C.

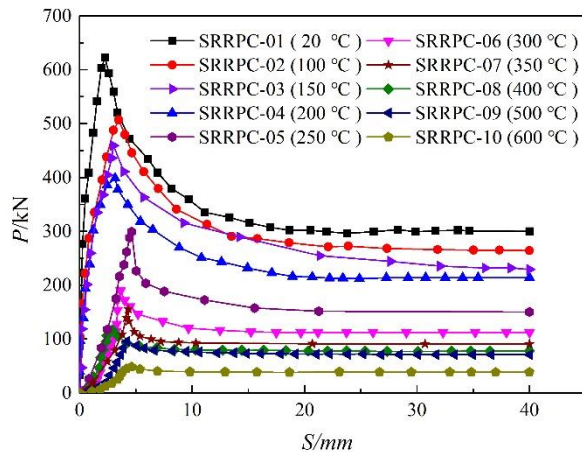


Fig. 5 The P-S curves of specimens at different high temperatures

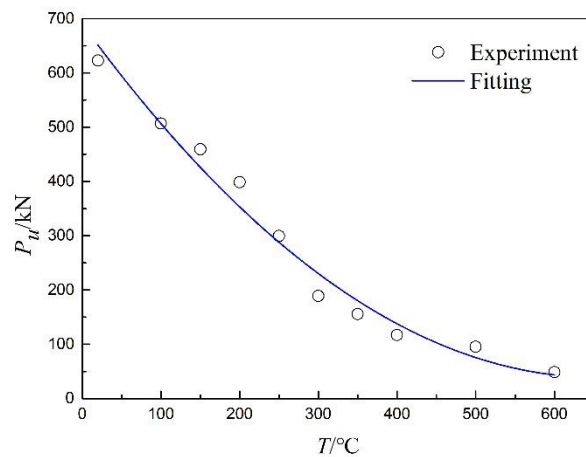


Fig. 6 Relation between ultimate bond load and maximum temperature

#### 4 CONCLUSIONS

This paper experimentally studied the bond-slip properties of I-section steel and reactive powder concrete at high temperatures. Major conclusions can be drawn:

- The cracks of specimens can be divided into three types: no crack, 45° diagonal crack and horizontal crack. With the increase of temperature, the crack patterns gradually changed from horizontal crack to 45° diagonal crack.
- The bond load of the specimen decreases with the increase of temperature and the ultimate bond load of the specimen at 600 °C is only 7.8% of that at room temperature.
- The ultimate bond load of the specimens decreases greatly before 250 °C and the descend rate of the bond load reduces obviously when the temperature exceeds 250 °C
- Based on the test data, the formula to calculate the relation between different high temperatures and ultimate bond loads was obtained.

#### ACKNOWLEDGMENTS

The authors gratefully acknowledge the financial support provided by National Natural Science Foundation of China (Grant Number: 51878397, 51378302).

#### REFERENCES

- Bae B., Choi H.K., Choi C.S. 2016. *Bond stress between conventional reinforcement and steel fiber reinforced reactive powder concrete*. *Construction and Building Materials*, 112, p. 825-835.
- Bu L.T., Luo K.Y. 2018. Interface bonding performance between shape steel and reactive power concrete (RPC) in steel reinforced RPC structures. *Science Technology and Engineering*, 18(3), p. 307-312(in Chinese).
- Li J.H., Qiu D.L., Yu K., et al. 2015. Bond-slip behavior between shaped steel and concrete in SRC structures at elevated temperature. *Journal of Basic Science and Engineering*, 23(5), p. 914-931(in Chinese).
- Tao Z., Yu Q. 2012. Residual bond strength in steel reinforced concrete columns after fire exposure. *Fire Safety Journal*, 53, p. 19-27.
- Wang Y.Z., Liu Z.Q., Li G.Q., et al. 2020. Factors influencing bond properties in concrete encased steel columns at high temperatures. *International Journal of Steel Structures*, 20(3), p. 1040-1051.
- Wang Y.Z., Zhang B.J., Liu Z.Q., et al. 2021. Effect of temperature on the bond-slip between I-shaped steel and concrete. *Advances in Structural Engineering*, 3, p. 136943322199355.

## **WALL DEFORMATION DURING FIRE RESISTANCE TESTS**

### **A comparative study between hollow-brick walls and gypsum-sheathed stud walls**

Rene Prieler<sup>a</sup>, Benjamin Ortner<sup>a</sup>, Stefan Thumser<sup>b</sup>, Günther Schwabegger<sup>b</sup>, Christoph Hochenauer<sup>a</sup>

<sup>a</sup> Graz University of Technology, Institute of Thermal Engineering, Inffeldgasse 25/B, 8010 Graz, Austria

<sup>b</sup> IBS-Institut für Brandschutztechnik und Sicherheitsforschung GmbH, Petzoldstraße 45, 4020 Linz, Austria

#### **Abstract**

The present study investigates the wall deformation in conjunction with a steel door as test specimen. The relative displacement of the adjacent wall and the test specimen is of main interest regarding gap formation and flue gas leakage. For this purpose, fire resistance tests were carried out using hollow-brick and gypsum-sheathed stud walls. It was found that the deformation of the brick wall is highly affected by the steel door. The highest deformation of 20 mm to the fire side was recorded at half the height of the door. When the door was in an off-centre position, the maximum wall deformation as well as the flue gas leakage were increasing. In contrast, when gypsum-sheathed stud walls were used, the maximum wall deformation was near the centre of the stud wall construction instead of the door's half height. Thus, it can be concluded that the wall deformation is more affected by the mechanical load of the door when hollow-bricks are used instead of stud walls.

**Keywords:** Wall deformation, Hollow-bricks, Gypsum-sheathed stud wall, Fire resistance test

## **1 INTRODUCTION**

Fire resistivity is crucial for the selection of modern building materials or constructions, such as doors, windows etc. The resistance against a fire is commonly determined by standardized fire resistance tests using a pre-defined thermal exposure to a heat source. To fulfil a certain fire resistance level three main issues are essential: (a) limited thermal heat transfer through the test specimen, (b) mechanical stability of the test specimen and (c) prevention of flue gas leakage. Focused on issue (c), the present study investigates the wall deformation in conjunction with the position of a steel door as test specimen. In addition, the intumescent material between the door (test specimen) and its frame, the relative displacement of the adjacent wall and the door is of main interest regarding gap formation and flue gas leakage during the experiment.

In the past, the deformation process of different wall types was already investigated, when they were exposed to fire or a thermal load. This is commonly done by standardized fire resistance tests (see European Standard EN 1363-1 / Fire Resistance Test—Part 1: General Requirements) using a testing furnace. The tested wall construction is placed in the front wall of the furnace. The furnace is operated with natural gas or oil-fired burners to ensure that the average temperature can be achieved according to the standard.

### **1.1 Hollow-brick walls**

The temperature distribution and deformation of masonry brick walls exposed to standard fire conditions were experimentally analysed by Nguyen and Meftah (Nguyen and Meftah, 2012). A wall made of hollow-bricks was tested in two configurations: Non-load-bearing wall and load-bearing wall (load at the top of the wall). For both cases the temperature distribution and deformation was considered. It was found that the maximum deformation occurs in the middle of the wall. Based on the experimental results, numerical simulations were carried out to predict the deformation as well as the spalling behaviour of the bricks (Nguyen et al., 2009; Nguyen and Meftah, 2014). Further numerical studies to predict the thermo-mechanical response of brick walls exposed to fire were published by Nadjai et al. (Nadjai et al., 2003) and Prakash et al. (Prakash et al., 2020).

## 1.2 Gypsum-sheathed stud walls

Compared to the limited number of experimental and numerical studies on the behaviour of brick walls in fire resistance tests, fire-related research of stud walls has been significantly more extensive. In a recent study, Dias et al. (Dias et al., 2019) investigated stud walls sheathed with steel and plasterboards. It was found that the steel sheathing did not affect the stud temperature significantly compared to the plasterboards. Ariyanayagam and Mahendran (Ariyanayagam and Mahendran, 2018) tested the usage of low strength steel for the studs in the walls, which reduced the fire resistance level by about 25%. Park et al. (Park et al., 2011) tested a load-bearing stud wall exposed to a real fire scenario instead of the standard fire conditions, which are generally used to determine the fire resistance level. Further experimental studies regarding the fire response of stud walls were published by Chen et al. (Chen et al., 2020; Chen et al., 2020). Despite the high number of studies, which took different constructions of stud walls into account, numerical studies are still limited to the temperature and deformation of the steel studs instead of an entire wall (e.g. Nassif et al., 2014; Ye and Chen, 2020).

## 1.3 Objectives of the present study

However, for both wall types only studies with a “homogeneous” construction of the walls without a test specimen were carried out (see sections 1.1 and 1.2). To determine and certify the fire resistance level of a fire safety product (e.g. steel door), the test specimen (fire safety product) is embedded in the wall. The entire assembly (test specimen + wall) is exposed to the fire during the testing phase. Therefore, both parts will affect each other with regard to the thermal response to the fire and the deformation. Furthermore, the different thermo-mechanical response of the wall and the test specimen results in the formation of gaps, and, thus, flue gas leakage. The present study investigates the wall deformation during fire resistance tests, when a fire safety steel door is embedded in the wall. The following materials and configurations were taken into account:

- Two wall types: (i) Hollow-brick walls and (ii) gypsum-sheathed stud walls
- Three different installation positions of the steel door within the wall are considered

Thus, six fire resistance tests were carried out in the course of the study.

## 2 EXPERIMENTAL SETUP

The fire resistance testing furnace used for the experimental investigation as well as the testing procedure was described in detail in Prieler et al. (Prieler et al., 2019). The dimension of the furnace is 4.5 m (width), 1.25 m (depth) and 4 m (height). Under operating conditions, four natural gas burners were active to ensure that the time-dependent temperature in the furnace, according to the standard, can be achieved. The testing time was 30 minutes for each experiment.

### 2.1 Test specimen – Steel door

A fire safety steel door was placed in the tested wall to identify the effect of a test specimen on the wall deformation during a fire resistance tests. The steel door is shown in Fig. 1.



Fig. 1 Tested steel door embedded in the stud wall (temperature measurement positions are marked)

The temperature measurement positions are marked with black dots and are also placed according to the standard. In section 3, the average temperature of the steel door will be determined in five measurement points, which were indicated by black circles in Fig. 1. The same steel door type was used in all six experiments with its dimension of 1.375 m (width), 2.5 m (height) and 64 mm (thickness). During the experiments it was found that the measured temperatures at the fire unexposed side of the steel door were similar for each test case. Thus, the thermal expansion and, subsequently, the mechanical load to the adjacent wall was comparable.

**2.2 Wall types and positions of the test specimen**

With respect to the position of the door, three fire resistance tests were carried out with the wall made of hollow-bricks (4 m in height and 4.5 m in width). As an example, the configuration with the steel door in the left position is depicted in Fig. 2. Above the door a lintel was placed. The wall around the steel door was equipped with dots to optically observe the displacement of the wall during the experiment.

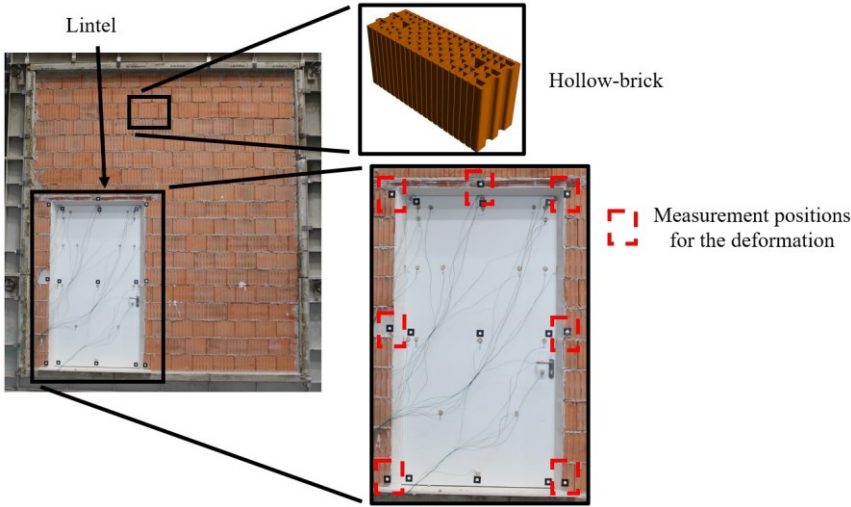


Fig. 2 Test configuration where the test specimen is placed in the left position in the brick wall

In addition to the brick walls, three fire resistance tests with gypsum-sheathed stud walls were carried out. Steel profiles (CW-shaped – 50x50x0.6 mm) were arranged from the left to the right with a distance of 625 mm in between. Around the door’s position UA-shaped steel profiles were used (50x40x2 mm). The steel studs were covered by gypsum plasterboards with a thickness of 12.5 mm (fire and ambient side). Furthermore, the space between the gypsum boards was filled with stone wool. For the experiments with the stud walls, the deformation was observed at the same positions as presented in Fig. 2. In Fig. 3, the wall construction (left) as well as the three different door positions (same for the brick walls) are shown. When the door was in the left or right position, the distance to the left and right edge of the wall was 20 cm.



Fig. 3 Construction of the stud wall and test configurations (door placed at the left, middle and right position in the wall)

### 3 RESULTS AND DISCUSSION

In this section, the temperature of the steel door (fire unexposed side) will be presented to ensure that the thermal expansion of the door is comparable between the tests (see section 3.1). However, the temperature of the walls was not observed during the tests. In section 3.2 and 3.3, the wall deformation of the brick and stud walls are compared and the effect of the test specimen will be analysed.

#### 3.1 Temperature at the steel door

In Fig. 4, the measured temperature increase above ambient temperature at the fire unexposed side of the steel door for all six experiments are shown. The displayed data represents the average values from the five measurement positions marked in Fig. 1. It can be seen that the temperature trend of the steel door is very close for all fire resistance tests, and as a result, the thermal expansion and mechanical load on the walls are similar as well. Thus, the deformation of the walls can be compared.

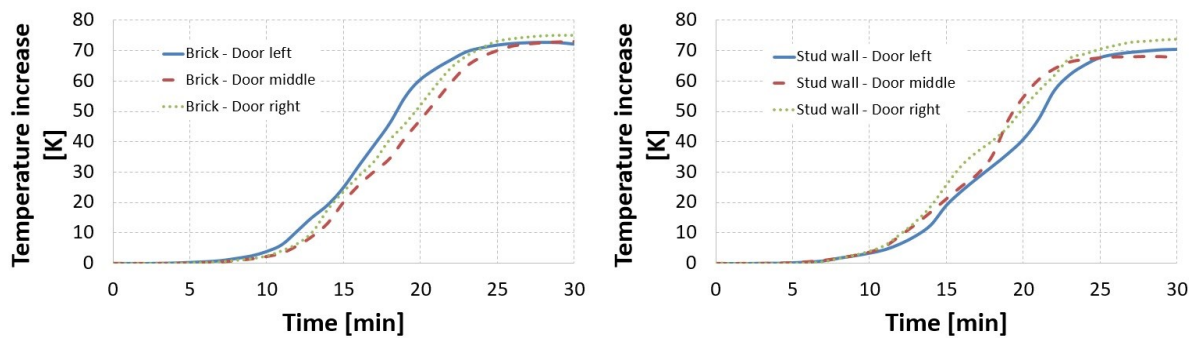


Fig. 4 Measured average temperature increase compared to ambient temperature at the fire unexposed side of the steel doors

#### 3.2 Deformation – Hollow-brick walls

The deformation of the brick wall in the vicinity of the test specimen is displayed in Fig. 5. It can be seen that highest deformation of the wall was observed when the construction was asymmetric (door in left or right position). The highest deformation in both cases occurred at the door’s half height with -41 mm (left – position “K”) and -50 mm (right – position “G”). The negative value represents the deformation to the fire side. At the upper edge of the door, the deformation was slightly lower with -36 mm (left – position “F”) and -46 mm (right – position “A”). However, the maximum deformation of -20 mm was recorded when the door was placed in the centre position, which is significantly lower compared to the asymmetric positions.

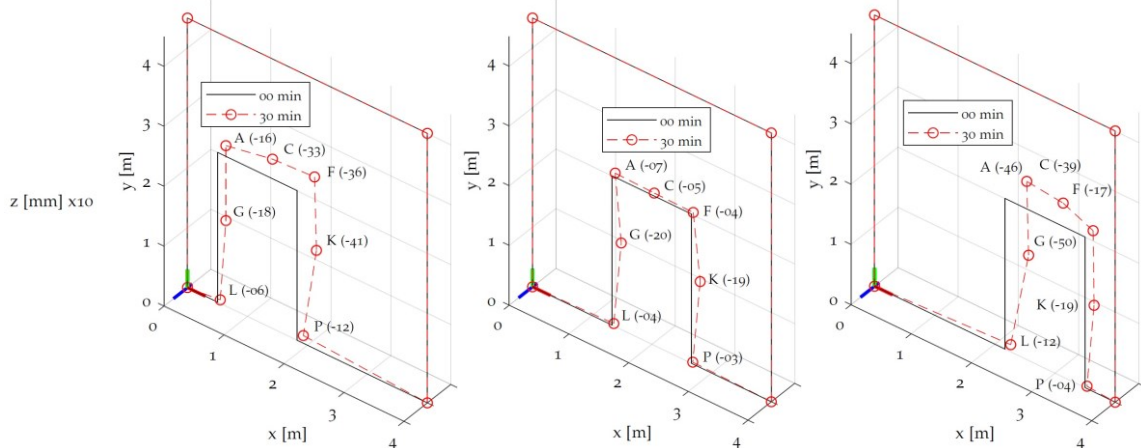


Fig. 5 Deformation of the hollow-brick walls after 30 minutes testing time for the door in the left, middle and right position

Without test specimen the maximum deformation of the wall would be expected in the middle of the entire construction, which is approx. at the upper edge of the door. Due to the test specimen, the position of the maximum deformation was shifted downwards to the door’s half height. Thus, it can be concluded that the mechanical load of the expanding/deforming door has a significant effect on the deformation of the brick wall. This effect is more obvious when the door is in central position. Although the deformation of the wall can be high with approx. -50 mm in asymmetric arrangement, only a slight gap formation was observed between the door and the adjacent wall, leading to minor flue gas leakage (see Fig. 6).



Fig. 6 Door deformation after 30 minutes: Door in the brick wall left position (left), in the right position (centre) and in the middle of the stud wall (right)

**3.3 Deformation – Gypsum-sheathed stud walls**

The deformation of the stud walls after 30 minutes testing time is displayed in Fig. 7. In asymmetric positions of the door the maximum deformation was lower with values around -20 mm (left – position “I” and “P”; right – position “A” and “I”). It can be seen that the position of the maximum deformation was not limited to the region near the door’s half height. The same effect was observed when the door was in the centre position. Here, the maximum deformation was at the upper edge of the door near the centre of the entire wall construction. This was expected also without a test specimen in the wall. Thus, the door does not significantly change the position of the maximum wall deformation.

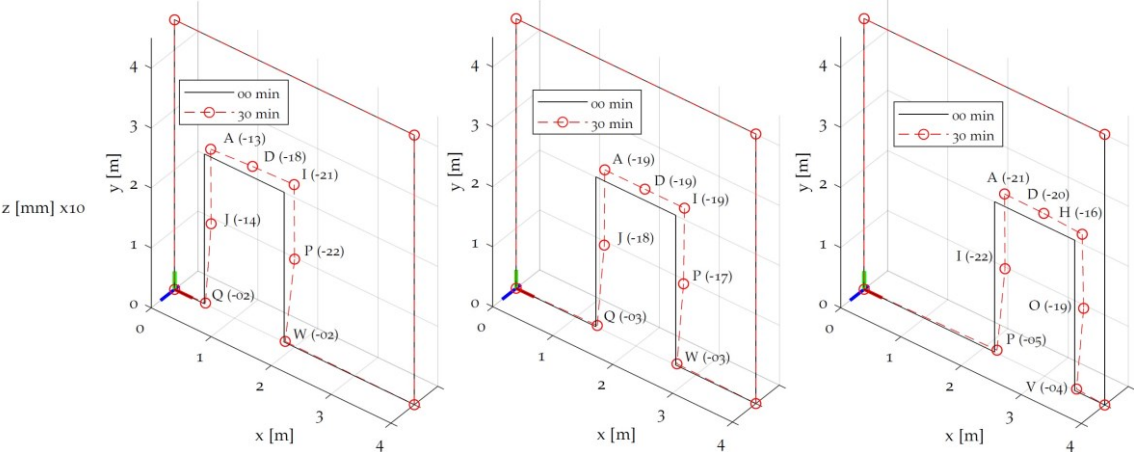


Fig. 7 Deformation of the gypsum-sheathed stud wall after 30 minutes testing time for the door in the left, middle and right position

Since the wall deformation showed a lower dependence on the mechanical load of the door, the overall wall deformation was lower compared to the brick wall. However, the deformation of the door is mainly related to the thermal expansion of the steel, which is the same in all six experiments. Due to the different behaviour of wall and door deformations, a higher gap formation was observed for asymmetric positions of the door as well as the centre position (see Fig. 6 right).

## 4 CONCLUSION

In the present study, the effect of a test specimen on the deformation of a wall made of hollow-bricks and gypsum-sheathed stud walls was examined. The following conclusion can be made:

- Overall the brick wall showed a higher maximum deformation of approx. -40 mm to -50 mm compared to -20 mm when the stud wall was tested.
- The asymmetric arrangement of the test specimen showed the highest deformation of the brick wall. In the stud wall, the asymmetric positioning of the door showed no effect on the maximum deformation.
- The maximum deformation of the brick wall was observed at the door's half height instead of the middle of the entire wall construction. Thus, it was concluded that the wall deformation was highly affected by the mechanical load of the test specimen.
- In contrast, the maximum deformation of the stud wall was observed near the middle of the wall construction (at the upper edge of the door), proving a lower effect of the door's mechanical load on the wall deformation compared to the brick wall.

## ACKNOWLEDGMENTS

This work was financially supported by the Austrian Research Promotion Agency (FFG), "Virtuelle Bauteilprüfung mittels gekoppelter CFD/FEM-Brandsimulation" (project 857075, eCall 6846234) and "Entwicklung von CFD/FEM Brandsimulationsmodellen mit Fokus auf Holz- und Gipsbauteile sowie komplexen Konstruktionen" (project 876469, eCall 28585806).

## REFERENCES

- Ariyanayagam A.D., Mahendran M. 2018. *Fire performance of load bearing LSF wall systems made of low strength steel studs. Thin-Walled Structures*, 130, p. 487-504.
- Chen W., Ye J., Zhao Q., Jiang J. 2020. *Full-scale experiments of gypsum-sheathed cavity-insulated cold-formed steel walls under different fire conditions. Constructional Steel Research*, 164, p. 105809.
- Chen W., Jiang J., Ye J., Zhao Q., Liu K., Xu C. 2020. *Thermal behavior of external-insulated cold-formed steel non-load-bearing walls exposed to different fire conditions. Structures*, 25, p. 631-645.
- Dias Y., Mahendran M., Poologanathan K. 2019. *Full-scale fire resistance tests of steel and plasterboard sheathed web-stiffened stud walls. Thin-Walled Structures*, 137, p. 81-93.
- Nadjai A., O'Garra M., Ali F. 2003. *Finite element modelling of compartment masonry walls in fire. Computers and Structures*, 81, p. 1923-1930.
- Nassif A.Y., Yoshitake I., Allam A. 2014. *Full-scale fire testing and numerical modelling of the transient thermo-mechanical behaviour of steel-stud gypsum board partition walls. Construction and Building Materials*, 59, p. 51-61.
- Nguyen T.-D., Meftah F., Chammas R., Mebarki A. 2009. *The behaviour of masonry walls subjected to fire: Modelling and parametrical studies in the case of hollow burnt-clay bricks. Fire Safety Journal*, 44, p. 629-641.
- Nguyen T.-D., Meftah F. 2012. *Behavior of clay hollow-brick masonry walls during fire. Part 1: Experimental analysis. Fire Safety Journal*, 52, p. 55-64.
- Nguyen T.-D., Meftah F. 2014. *Behavior of clay hollow-brick masonry walls during fire. Part 2: 3D finite element modelling and spalling assessment. Fire Safety Journal*, 66, p. 35-45.
- Park S.-H., Manzello S.L., Bundy M.F., Mizukami T. 2011. *Experimental study on the performance of a load-bearing steel stud gypsum board wall assembly exposed to a real fire. Fire Safety Journal*, 46, p. 497-505.
- Prakash P.R., Azenha M., Pereira J.M., Lourenco P.B. 2020. *Finite element based micro modelling of masonry walls subjected to fire exposure: Framework validation and structural implications. Engineering Structures*, 213, p. 110545.
- Prieler R., Mayrhofer M., Eichhorn-Gruber M., Schwabegger G., Hochenauer C. 2019. *Development of a numerical approach based on coupled CFD/FEM analysis for virtual fire resistance tests—Part A: Thermal analysis of the gas phase combustion and different test specimens. Fire and Materials*, 43, p. 34-50.
- Ye J., Chen W. 2020. *Simplified calculation of fire resistant temperature for cold-formed steel load-bearing composite walls. Structures*, 28, p. 1661-1674.

# LOAD-BEARING COMPOSITE TIMBER - GLASS WALL PROTOTYPE IN FIRE CONDITIONS

Nikola Perković<sup>a</sup>, Vlatka Rajčić<sup>a</sup>, Chiara Bedon<sup>b</sup>, Jure Barbalic<sup>a</sup>

<sup>a</sup> University of Zagreb, Faculty of Civil Engineering, Zagreb, Croatia

<sup>b</sup> University of Trieste, Department of Engineering and Architecture, Trieste, Italy

## Abstract

The use of structural glass for load-bearing composite systems in building is increasing. Typical solutions can take the form of hybrid systems in which glass interacts with steel, aluminum or timber, under a multitude of boundary and loading conditions of technical interest. Among others, fire accidents represent a critical design condition for glass and glass composites, and require dedicated performance indicators and validation methods. In this paper, the load-bearing performance of a composite timber-glass panel for load-bearing applications is explored under the effects of sustained mechanical loads (25 kN/m) and fire exposure (standard furnace test). A pilot test is carried out on a full-scale prototype of timber-glass prefabricated module, based on conventional recommendations for the experimental assessment of constructional members in fire. As shown, its overall load-bearing performance is governed by the intrinsic properties of timber (for the perimetral frame) and glass (for the insulated (IGU) panel), that is used to cover up to 3.2×2.7 square meters of facade, with a relatively small thickness (63.52 mm IGU thickness). The fire endurance is thus addressed towards reference performance indicators for vertical load-bearing members (i.e., walls) and towards the observations of the pilot experiment.

**Keywords:** Timber, glass, fire, fire endurance, composite timber-glass facade element

## 1 INTRODUCTION

In recent decades, wood and glass materials for constructions attracted special attention by designers, and the development of specific recommendations for design. Among others, the however, the performance of load-bearing systems in fire conditions is still challenging. This is the case of both timber and glass, and evenly of composite timber-glass structural members.

In this paper, the attention is given to the fire performance assessment of a composite load-bearing timber-glass wall prototype derived from the “VETROLIGNUM” design concept. The modular system can be recognized as efficient structural prefabricated systems for buildings and capable to contribute to the seismic resisting mechanism (Rajčić & Žarnić, 2012; Žarnić *et al.*, 2020), as well as to the thermal and energy balance (Rajčić *et al.*, 2020). On the other side, the prototype itself should be able to act as active and efficient barrier for the protection of building occupants under extreme actions such as fire.

In this regard, the paper presents an original furnace test for a full-scale composite wall prototype under fire and sustained mechanical loading. The combined thermo-mechanical performance of the system is explored as a preliminary stage of ongoing research studies. The analysis of load-bearing systems composed of glass and asked to sustain mechanical loads even in presence of fire events is rather challenging and not properly addressed in the literature. Exploratory studies in this direction can be found for simple glass members (Kozłowski & Bedon, 2021, Louter *et al.*, 2021). Both intrinsic material properties and their degradation with temperature (Bedon, 2017), as well as the interaction of sustained loads with fire exposure effects can result in fire endurance parameters that can be hardly predicted for glass composites. The fire performance and endurance of the hybrid specimen prototype is addressed in this paper towards conventional parameters and performance indicators in use for load-bearing walls and constructional members composed of traditional materials for buildings. Potentials and limits of conventional experimental procedures for novel structural systems are hence discussed on the base of pilot experimental observations.

## 2 LABORATORY TEST

### 2.1 Specimen

The load-bearing prototype consisted of a frame made of wooden members and an insulated (IGU) glass infill to create the composite system in Fig. 1. Transom and mullions were characterized by wood sections with 160×100 mm nominal dimension. Angle interconnections were also realized with wood screws ( $\Phi$  10×280 mm, type Assy 3.0 SK). The IGU panel (double laminated elements with 4×10 mm thick float layers in total, and 13 mm of interposed cavity) was kept in place by wooden frame slats introduced along the edges of glass, on both sides, and located on the entire frame perimeter. The slats were profiled in such a way that grooves were made to prevent glass falling out, but also to avoid possible penetration of air and water. The wooden frame was then coated with two layers of reactive coating (type Pyroplast Wood T and Pyroplast Wood Top) manufactured by Sika. The sample was attached to the foundation system of the furnace as in Fig. 2, through 10 point fixings consisting of L-shaped steel (285 mm their distance). The vertical edges of the sample remained free. Any space between the vertical edges of the specimen and the furnace was thus filled with ceramic wool.

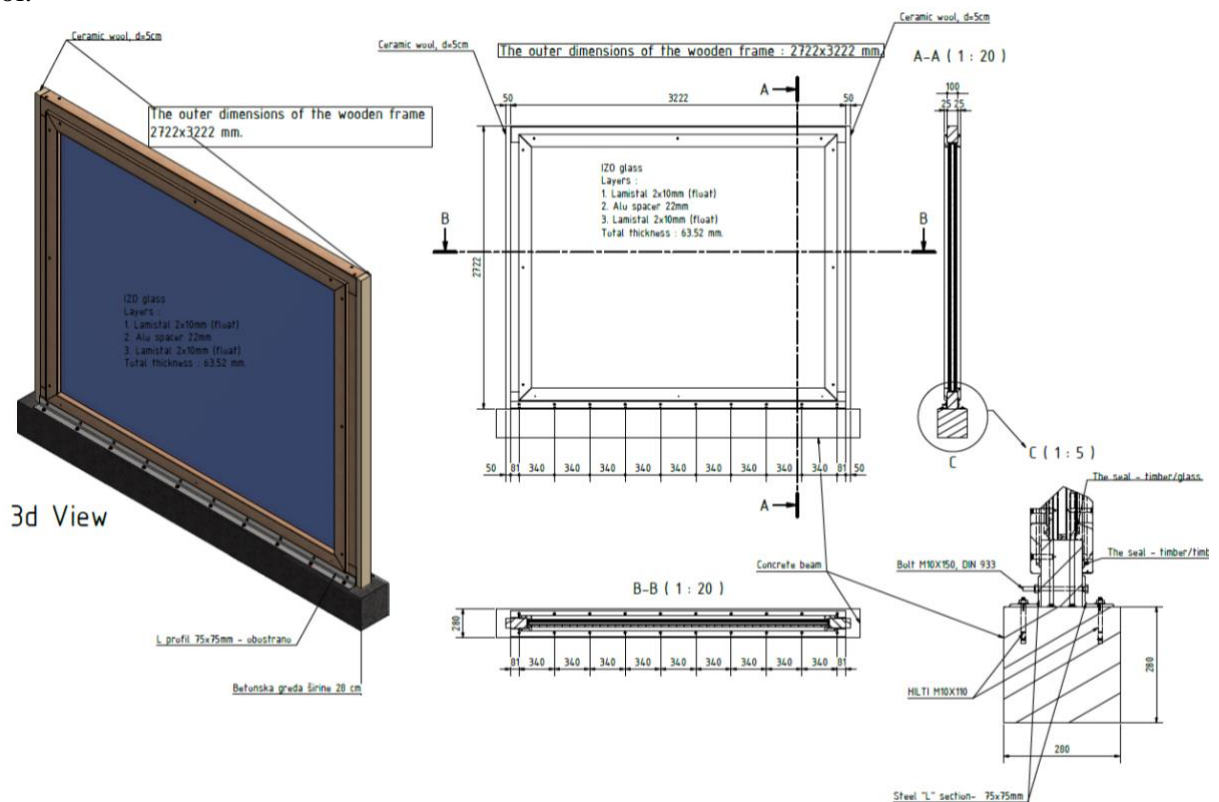


Fig. 1 Test specimen: overview and details



Fig. 2 Specimen preparation in the test furnace

## 2.2 Experimental procedure

The fire furnace experiment was carried out at LTM – Laboratory for thermal measurements in Oroslavje (Croatia), as schematized in Fig. 3. More precisely, the specimen was placed in the furnace as in Fig. 3. The facade element was preliminary subjected to a constant vertical load of 25 kN / m (Fig. 3a). Fire loading was described with six blowpipes on liquid fuel (HRN EN 1363-1: 2020), see Figs. 3b-3c. The air temperature in the test room was maintained at 20°C ( $\pm 5$ ) for 24 hours before testing. Heating was then determined by standard temperature curve (HRN EN 1353-1: 2020), while measuring the furnace temperature with 6 evenly distributed thermocouples (type K, see P1-P6 in Fig. 3). Direct contact of thermocouples and open flame was avoided, and a distance of 100 mm from the fire-exposed side of the sample was also ensured. Static pre-pressure in the fire area was maintained in the range of 15 Pa ( $\pm 2$ ) during the test. The dedicated sensor was placed at a height of 2.3 m from the floor.

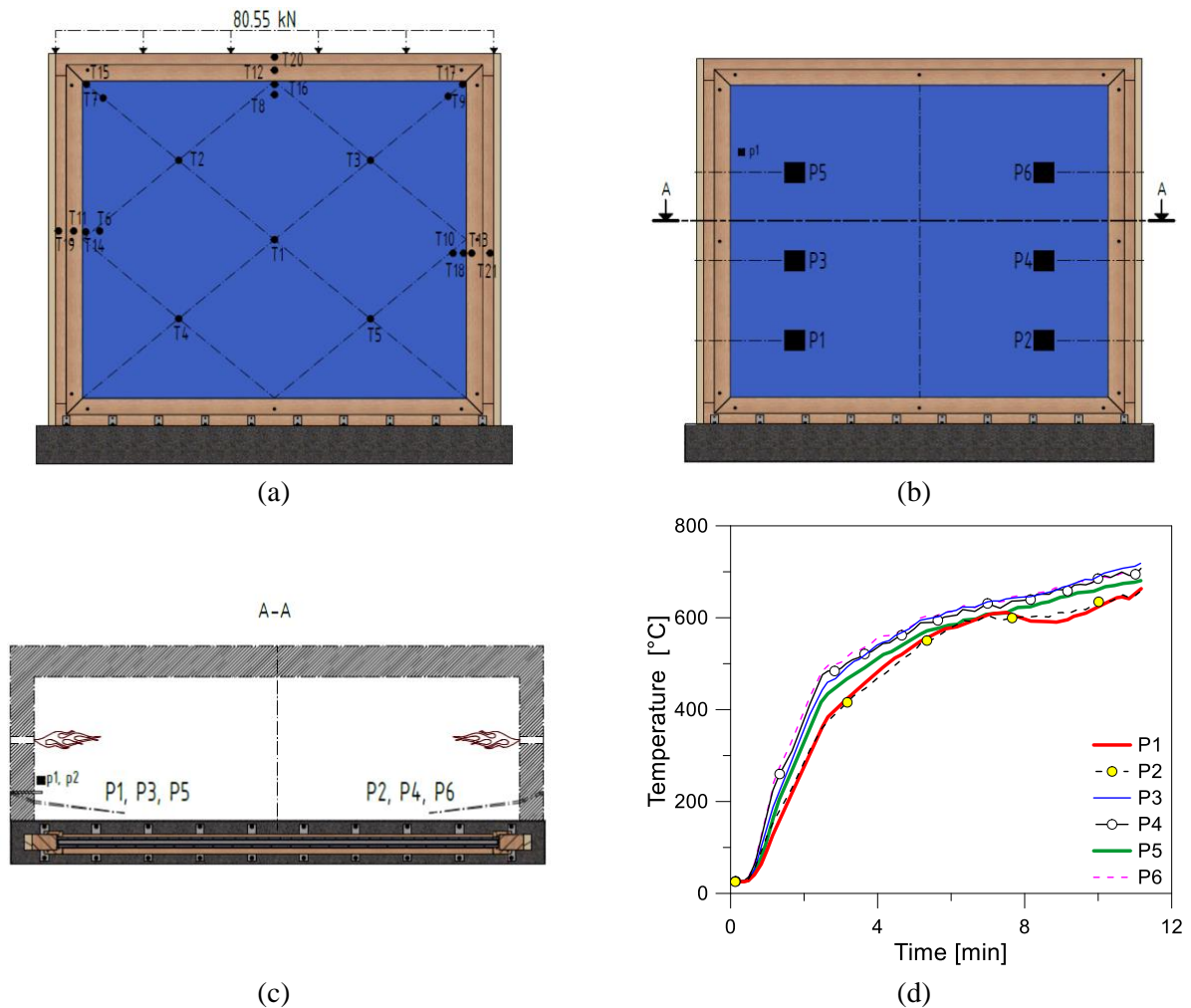


Fig. 3 (a)-(c) Measuring temperature points in the furnace and (d) internal temperature during the test

## 3 TEST RESULTS

### 3.1 Temperature analysis

A set of 21 thermocouples was used to measure the specimen temperature under fire. More specifically, the measure of average temperature increase on the unexposed side (criterion 140 K) was carried out at 5 control points (T1-T5), as in Fig. 3a. One of them was set in the centre of the specimen, while the remaining 4 in the centre of each quarter of the wall. Furthermore, the measure of maximum temperature increase on the unexposed side (criterion 180 K) was carried out with attention for:

- T6-T10: glass (50 mm from wooden slats);

- T11-T13: wooden slats (mid-span sections);
- T14-T18: glass –next to the wooden slats;
- T19-T21: wooden transoms (external edges).

Typical trends can be seen in Fig. 4.

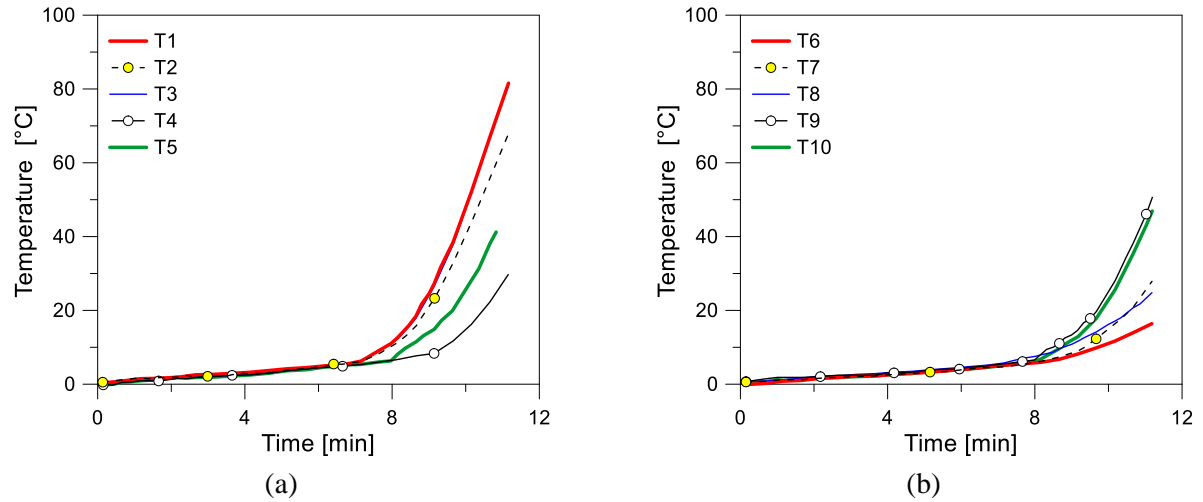


Fig. 4 Temperature evolution on the unexposed side of the specimen: (a) maximum and (b) average values

### 3.2 Deformation analysis

During the test, vertical deformations were measured at two points next to its free edges (VD1 and VD2). The performance of the wall prototype was carried out towards the reference criteria for vertical load-bearing systems, that is:

- maximum deformation (contraction):

$$C = \frac{h}{100} = \frac{2722}{100} = 27,2 \text{ mm} \quad (1)$$

- maximum contraction deformation rate :

$$\frac{dC}{dt} = \frac{3h}{1000} = 8,2 \text{ mm/min} \quad (2)$$

Typical experimental measurements are shown in Fig. 5. Worth to be noted that the failure time for the specimen (less than 12 min) is associated to both deformation ( $C$ ) and deformation rate ( $dC/dt$ ) values that are significantly lower than reference limits. The contraction is estimated in a 25% part compared to Eq. (1), while the maximum deformation rate is measured in approximately the 50% part of Eq. (2).

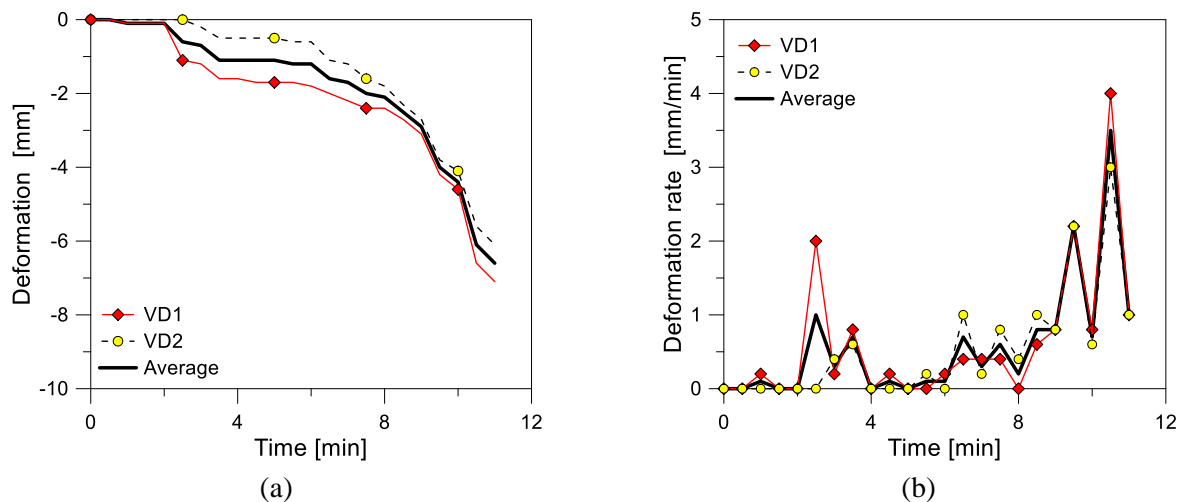


Fig. 5 Measured (a) deformation and (b) deformation rate of the specimen

### 3.3 Criteria

For the classification of the elements not meeting the R criteria, it is automatically sufficient that the E and I criteria are met. The final classification (based on testing as in Table 1) is set by verifying the time value obtained for mechanical resistance in fire under a standard time-temperature exposure (Fig. 6).

Table 1 Experimental observations. Key: E= exposed; U= unexposed

Time [min:s]	Side	Observation
0:00		Start
2:21	E	Cracks the first layer of glass
6:53	E	Fall-out of laminated glass
7:49	E	Cracks the glass layer
9:40	U	The cracked outer layer of glass
10:55	U	Shattering of laminated glass + Fire break (specimen centre)
11:05		End of test



Fig. 6 Time criteria for the tested prototype

### 3.4 Failure mechanism

Fig. 7a shows the time instant when the first layer of glass crack, while Fig. 7b is taken at the end of the experiment. No damage was observed in the exterior side of the of the timber joint. On the other side, Fig. 8 shows typical charring effects for the frame on both the unexposed and exposed sides.



Fig. 7 (a) Cracking of the first layer of glass panel and (b) view of the specimen at the end of experiment



Fig. 8 Timber frame at the end of experiment: (a) unexposed or (b) exposed sides

#### 4 CONCLUSIONS

Both structural glass and timber are largely used in buildings to realize a multitude of load-bearing solutions. As such, a special care is required to address the performance capacities under ordinary and extreme design loads. In this paper, the attention was focused on the fire endurance assessment of a novel composite timber-glass wall that was designed to act as efficient prefabricated modular unit in buildings. A pilot furnace experiment was carried out on a full-scale prototype able to cover up to  $3.2 \times 2.7$  square meters of facades with a relatively small thickness (63.52 mm).

#### 5 ACKNOWLEDGMENTS

This research was funded by The Croatian Science Foundation (Project no. IP-2016-06-3811 VETROLIGNUM—“Prototype of multipurpose composite timber-load bearing glass panel”, coordinator Prof. Vlatka Rajcic, University of Zagreb, Croatia).

#### 6 REFERENCES

- Bedon C. 2017. *Structural Glass Systems under Fire: Overview of Design Issues, Experimental Research, and Developments*. *Advances in Civil Engineering*, Article ID 2120570, doi: 10.1155/2017/2120570.
- Kozlowski M., Bedon C. 2021. *Sensitivity to Input Parameters of Failure Detection Methods for Out-of-Plane Loaded Glass Panels in Fire*. *Fire*, 4(1): 5, doi: 10.3390/fire4010005.
- Louter C., Bedon C., Kozlowski M., Nussbaumer A. 2021. *Structural Response of Fire-Exposed Laminated Glass Beams under Sustained Loads; Exploratory Experiments and FE-Simulations*. *Fire Safety Journal*, in press, available online, doi: 10.1016/j.firesaf.2021.103353.
- Rajčić V., Perkovic N., Bedon C., Barbalic J., Žarnić R. 2020. *Thermal and Energy-Efficiency Assessment of Hybrid CLT-glass Façade Elements*. *Applied Sciences*, 10(9), 3071.
- Rajčić V., Žarnić R. 2012. Seismic response of timber frames with laminated glass infill. Proceedings of the 45th CIB-W18 Meeting, Växjö, Sweden, 27–30 August 2012; pp. 333–344.
- Žarnić R., Rajčić V., Kržan M. 2020. *Response of laminated glass-CLT structural components to reverse-cyclic lateral loading*. *Constr. Build. Mater.*, 235, 117509.

## BEHAVIOUR OF INNOVATIVE CONCRETE-FILLED BUILT-UP COLD-FORMED STEEL COLUMNS IN FIRE

Hélder D. Craveiro<sup>a</sup>, Rohola Rahnavard<sup>a</sup>, Rui A. Simões<sup>a</sup>, Aldina Santiago<sup>a</sup>, Luís Laím<sup>a</sup>

<sup>a</sup> ISE, Department of Civil Engineering, University of Coimbra, Coimbra, Portugal

### Abstract

Aiming to expand the applicability of cold-formed steel solutions it's crucial to promote synergies between different structural materials. In this research innovative composite columns combining cold-formed steel profiles and concrete are investigated through experimental testing and numerical modelling. The closed built-up cold-formed steel columns comprised several commercially available cross-sections, such as lipped channels and plain channels fastened using self-drilling screws. Experimental fire resistance tests on concrete-filled and bare steel columns were conducted considering the influence of axial restraint to thermal elongation. Finite element models were developed to reproduce the observed behaviour. Comparisons were established between bare steel and composite solutions assessing in detail the observed enhancements. The concrete infill increased the fire resistance of the columns contributing to mitigate local buckling phenomena.

**Keywords:** Composite, cold-formed steel, closed built-up, finite element model

### 1 INTRODUCTION

Cold-formed steel sections are highly versatile and present several advantages that ensure high competitiveness in the construction sector (Yu et al., 2010, Dubina et al., 2012). The high versatility ensures that single sections with multiple configurations may be combined in effective ways ensuring higher load-bearing capacity and torsional stiffness, maintaining the existing manufacturing process. Relevant research has been conducted on built-up cold-formed steel members at both ambient temperature and fire conditions (Craveiro, H. et al., 2014, Craveiro, H. et al. 2016 and Yang, J., et al., 2020). However, as it is well known the fire resistance of unprotected cold-formed steel elements is reduced due to high section factors and high thermal conductivity of steel. Hence, new solutions can be tested to mitigate this issue and also to try to expand the field of applicability of cold-formed steel products, for instance for prefabricated composite CFS-concrete elements. When dealing with closed built-up cold-formed steel sections the easiest solution is to use concrete as an infill to increase the load-bearing capacity of such members and their fire resistance. Some studies were already reported on composite CFS-Concrete members, but this type of solutions still require further investigation, assessing in detail the effects of confinement in mitigating local buckling phenomena and the enhancements in terms of structural fire resistance that the use of concrete provides to the solution. Such members may be further developed to create an innovative structural framing skeleton or to create individual solutions for strengthening or fire resistance purposes.

In this paper an experimental research is detailed on closed built-up bare steel and concrete-filled closed built-up cold-formed steel columns. Two different cross-sections were tested (R and 2R). The R built-up cross-section consisted of one lipped channel and a plain channel fastened on the flanges, along the length of the profiles, whereas the 2R closed built-up cross-section comprised 2 lipped channels fastened back-to-back on the web (I section) and two plain channels fastened to the flanges of the I section. Then the built-up tubes were filled with concrete. Also, the mechanical properties of the cold-formed steel S280GD+Z were evaluated at both ambient and elevated temperatures, providing relevant input data to the numerical models.

Based on the obtained results numerical models were developed to reproduce the observed behaviour using Abaqus. The developed models are detailed presenting all strategies and assumptions considered.

## 2 EXPERIMENTAL TESTS

The experimental campaign comprised tensile coupon tests at elevated temperature to characterize the degradation of mechanical properties of steel and fire resistance tests on closed built-up cold-formed steel columns and concrete-filled composite cold-formed steel columns.

The mechanical properties were assessed using steady-state tensile tests on coupon specimens at elevated temperatures ranging from 20 to 800 °C. In Fig. 1 the experimental stress vs strain curves are plotted for the tested temperature range. This data was used in the numerical modelling as input.

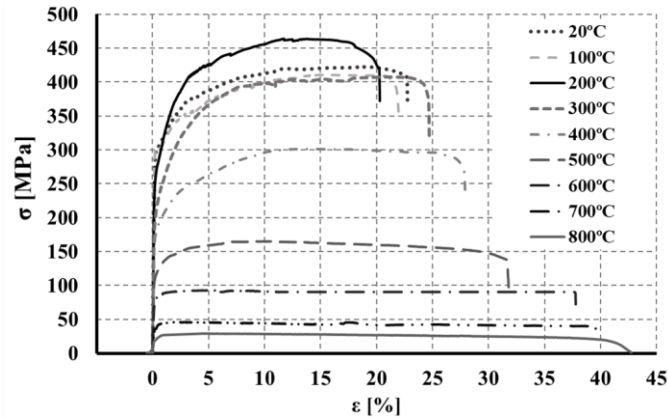


Fig. 1 Stress-strain curves of the S280GD+Z steel; temperatures ranging from 20 to 800°C.

The experimental set-up comprised a two-dimensional (2D) reaction steel frame ((1) in Fig. 2 a) and b)) and a 3D restraining steel frame adaptable for different levels of stiffness ((2) in Fig. 2 a) and b)) capable of providing different restraining levels to the column in fire. Also, different boundary conditions were considered in these tests. The 2D reaction frame was composed of two HEB 500 and one HEB 600 beam. For the fire resistance tests, a low value of restraint to thermal elongation was adopted. The axial restraint imposed to the CFS column was 3 kN/mm, considering a 3D frame composed by four HEA 200 columns and four HEB 200 beams (2 on top and 2 on bottom) arranged orthogonally. This restraining system intends to reproduce the actual boundary conditions of a CFS column inserted in a real building structure. Hence, the system allowed the application of the serviceability load selected. After reaching the desired load level the rigid body movement of the top beams of the restraining frame was blocked. Then the electric furnace was turned on and from this moment the restraint to thermal elongation was active. During the fire tests axial forces increased, due to thermal expansion, up to a certain maximum, and then reduced again when the column was no longer able to withstand the applied load. A global view of the experimental system is presented in Fig. 2.

The serviceability load was applied using a hydraulic jack, placed in the 2D reaction frame (3) in Fig. 2. The thermal action was applied by a vertical modular electric furnace ((4) in Fig. 2 programmed to reproduce the standard fire curve ISO 834.

The test specimens were fabricated using lipped channels (C-section) and plain channels (U-section) fastened together with self-drilling screws with different arrangements (Fig. 3).

The length of all profiles was 2950 mm and the spacing of the fasteners along the length of the column was 725 mm. The spacing adopted for the self-drilling screws was based on the observation of designed CFS structures.

In the fire resistance tests, a service load was initially applied. The magnitude of that service load was a percentage of the design buckling load determined at ambient temperature for the bare CFS columns. Hence, even for the case of concrete-filled CFS columns (concrete acting only as fire protection material), the service load adopted in the experimental tests was only based on the design buckling load for the bare steel column. In this investigation a 50%  $N_{b,Rd}$  load level was adopted ( $P_0$ ) for the fire resistance tests. In Table 1 the determined design buckling loads and the initial load values applied in the fire resistance tests are presented for both cross-section shapes and solutions tested, namely the bare steel and the composite one.

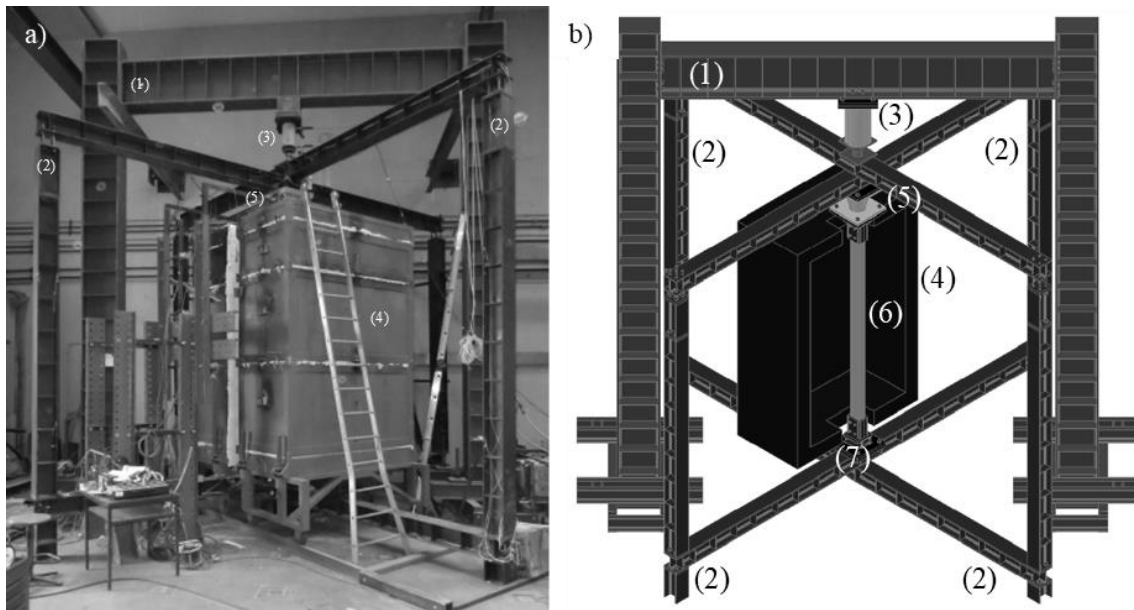


Fig. 2 Global view of the experimental set-up. b) Schematic view.

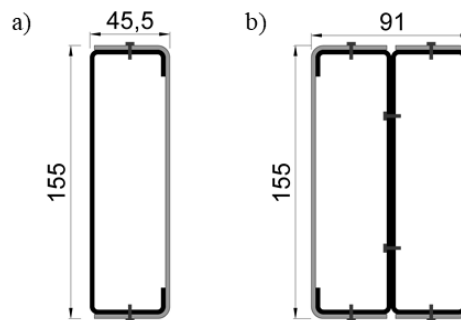


Fig. 3 Dimensions of the closed built-up cross-sections (with and without concrete infill) tested in the scope of this investigation, with 1.5 mm (concrete-filled) and 2.5 mm (bare steel). a) R section. b) 2R section.

Table 1 Predicted values for CFS columns and initial load values.

	R				2R			
	$t_{\text{composite}}=1.5 \text{ mm}$		$t_{\text{bare}}=2.5 \text{ mm}$		$t_{\text{composite}}=1.5 \text{ mm}$		$t_{\text{bare}}=2.5 \text{ mm}$	
	Pinned	Fixed	Pinned	Fixed	Pinned	Fixed	Pinned	Fixed
$N_{b,rd}$ [kN]	45.35	81.58	76.55	168.27	159.06	203.82	305.57	443.42
$P_0$ [kN]	22.68	40.79	38.27	84.13	79.53	101.91	152.78	221.71

### 3 NUMERICAL MODELLING

The FEM models were developed in the commercial finite element analysis (FEA) software Abaqus. The developed models are used to assess the suitability of the combination of thin-walled CFS profiles with concrete in an innovative composite solution (CFS+CON), tailored for prefabrication. The validation of the finite element model developed to reproduce the behaviour of CFS columns under fire conditions with restrained thermal elongation consisted of comparing the evolution of the non-dimensional ratio between the generated restraining forces during fire tests with the initial applied service load ( $P/P_0$ ) as a function of the mean temperature of the CFS column ( $\theta_{cr}$ ). Cold-formed steel profiles were modelled using the S4R shell finite element whereas the concrete infill was modelled using the C3D8R finite element. To simulate the fire resistance tests it was necessary to perform heat transfer analysis, buckling analysis and finally mechanical analysis at elevated temperatures considering the degradation of mechanical properties. In the finite element model, the fire action was

modelled using two types of surface, namely film condition and radiant to ambient. These two types of surface correspond to heat transfer by convection and heat transfer by radiation, respectively. For calibration purposes, the thermal action was the one recorded in the chamber of the furnace (gas furnace temperature). A 2D numerical model was developed to estimate temperature distribution in each cross-section tested, adopting a 4-node linear heat transfer or mass diffusion quadrilateral element, DC2D4. For all tested cross-sections the adopted convective heat transfer coefficient ( $\alpha_c$ ) was 12 W/m<sup>2</sup>K (lower than 25 W/m<sup>2</sup>K used for ISO 834 fire curve) for the fire test curves and the radiative heat flux was calculated using a steel (cold-formed steel with a zinc coating) emissivity of 0.21 and 0.7 for the furnace electrical resistances ( $\epsilon=0.14$ ). The Stefan-Boltzmann constant was  $5.67 \times 10^{-8}$  W/m<sup>2</sup>K<sup>4</sup>. Mechanical properties for steel were defined using the data extracted from the experimental tensile coupon tests (Fig. 1) (Eq. 1 and Eq. 2), whereas for concrete the was modelled considering the Concrete Damage Plasticity model which is defined by a uniaxial compression and tension response.

$$\sigma_{true} = \sigma_{nom}(1 + \epsilon_{nom}) \quad (1)$$

$$\epsilon_{ln}^{pl} = \ln(1 + \epsilon_{nom}) - \frac{\sigma_{true}}{E} \quad (2)$$

The non-linear stress-strain relation is assumed for compression and defined according to the EN 1994-1-2. Finally, for the five constitutive parameters ( $\psi$  – dilatation angle;  $\epsilon$  – flow potential eccentricity;  $f_{b0}/f_{c0}$  – ratio of initial equibiaxial compressive yield stress to initial compressive yield stress;  $k$  – the ratio of second stress invariant on the tensile meridian;  $\mu$  – viscosity parameter) required to complete the definition of the constitutive model, no information was available from the experimental tests and therefore the software default values were applied.

Elastic buckling analysis was performed. The computed buckling modes were used as input. For the definition of the initial geometric imperfections, the first global buckling mode, a distortional and local buckling modes were considered. The amplitude of the initial geometric imperfections was  $L/1000$  for global imperfections,  $t$  for distortional and  $h/200$  for local imperfections. To reproduce the behaviour of CFS columns under simulated fire conditions with restrained thermal elongation the surrounding structure used in the experimental tests was replaced by a linear spring (3 kN/mm) connected to the centroid of the column to be simulated.

Finally, the structural analysis was performed using as input the temperature distribution calculated in the heat transfer and the initial deformed configuration obtained from the elastic buckling analysis. In the mechanical analysis, a Dynamic Explicit procedure was considered.

## 4 RESULTS

The tested columns failed mainly due to global flexural buckling about the minor axis for both monosymmetric (R-section) and doubly symmetric sections (2R-section). Local buckling only was visible to large lateral displacements. This can indicate that the concrete infill may mitigate effectively local buckling phenomena of individual cold-formed steel profiles, as well as the overlapping of steel plates.

In the fire resistance tests, the temperature of the specimens was monitored at several locations along the length of the column and at the cross-section level, collecting relevant data to define critical temperatures of the tested columns and to validate the developed numerical models. In Fig. 4 the temperature evolution for the R cross-section is depicted, as well as the comparison with the obtained results from the heat transfer analysis using Abaqus. Overall a very good agreement is observed between experimental and numerical results. In Table 2 and Table 3 some results, namely temperature at the peak load  $\theta_{peak}$ , the maximum load attained due to restraint to thermal elongation  $P_{max}$  (service load + generated axial forces), critical temperature  $\theta_{cr}$  and critical time  $t_{cr}$ , are presented for the tested cross-sections considering pinned boundary conditions.

In Fig. 5 and Fig. 6 the experimental results obtained in the fire resistance tests of cold-formed steel columns and composite cold-formed steel columns (concrete acting mainly as a protection material) are depicted and compared. The enhancements in terms of fire resistance provided by the concrete infill are clear. As it can be observed in Fig. 5 and Fig. 6 the fire resistance time increases from

approximately 10 minutes (cold-formed steel profiles with 2.5 mm) to about 30 minutes (concrete-filled columns with CFS profiles with 1.5 mm).

In Fig. 5 a) a comparison between the experimental and numerical results is also established for the concrete-filled R-section in fire with restrained thermal elongation. It was observed that the finite element prediction is slightly conservative in terms of the fire resistance time.

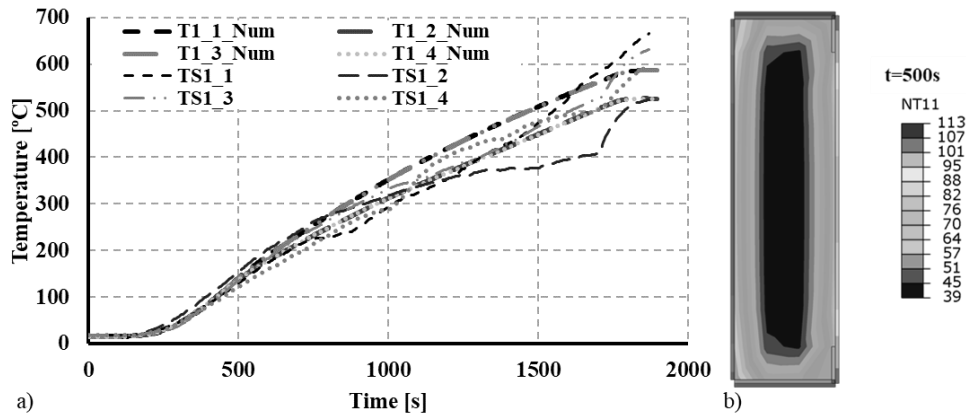


Fig. 4 Temperature evolution for the R cross-section and comparison with the predicted evolution using heat transfer analysis.

Table 2 Experimental results for R columns.

Test Reference	$\theta_{peak}$ [°C]	$P_{max}$ [kN]	$P_{max}/P_0$	$\theta_{cr}$ [°C]	$t_{cr}$ [min]
R_PP_50LL_K1-1	316	35	1.61	359	25.1
R_PP_50LL_K1-2	274	32	1.58	346	26
R_FF_50LL_K1-1	344	57	1.40	375	28.5
R_FF_50LL_K1-2	295	60	1.49	336	29

Table 3 Experimental results for 2R columns.

Test Reference	$\theta_{peak}$ [°C]	$P_{max}$ [kN]	$P_{max}/P_0$	$\theta_{cr}$ [°C]	$t_{cr}$ [min]
2R_PP_50LL_K1-1	441	94	1.22	500	31.5
2R_PP_50LL_K1-2	406	93	1.18	423	29
2R_FF_50LL_K1-1	404	117	1.15	504	32.3
2R_FF_50LL_K1-2	387	116	1.14	485	32.1

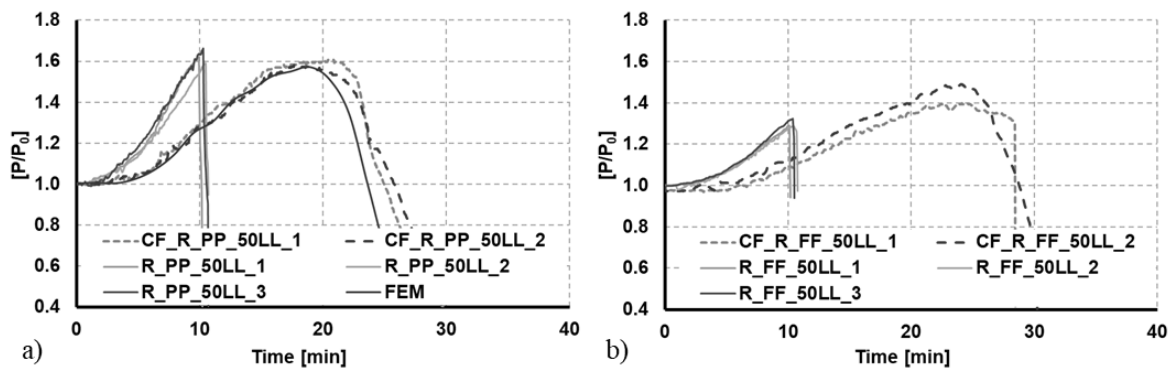


Fig. 5 Experimental results obtained for bare steel and composite columns for the R cross-section considering pinned and fixed boundary conditions and FEM calibration (a).

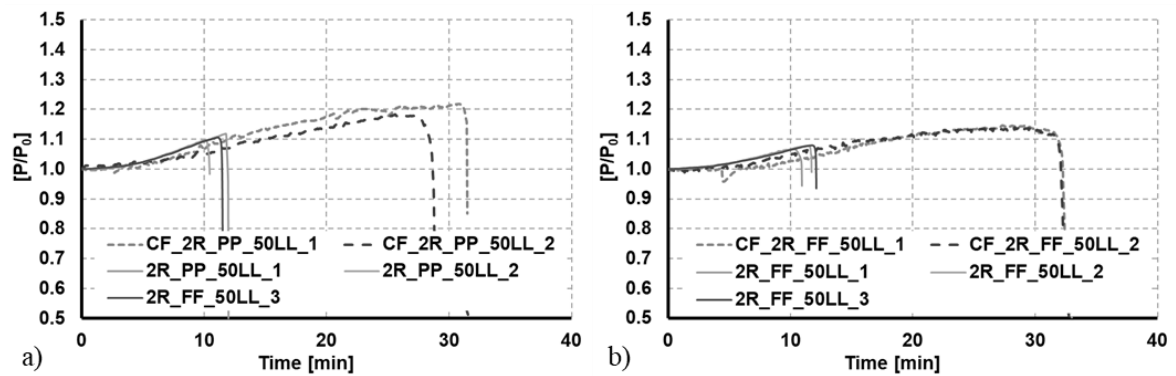


Fig. 6 Experimental results obtained for bare steel and composite columns for the 2R cross-section considering pinned and fixed boundary conditions.

## 5 CONCLUSIONS

This paper reported an exploratory research on the use of closed built-up CFS-Concrete composite columns under compression in fire, considering the effect of restraint to thermal elongation. The concrete-filled closed built-up CFS-Concrete columns presented an enhanced structural fire behaviour and the achieved confinement contributed to preventing local buckling phenomena in the thin-walled profiles. Additional studies are still required to further calibrate the developed numerical models and to conduct additional parametric studies. Moreover, comparisons with design predictions according to the EN 1994-1-2 are still necessary considering the general method for the design of composite columns in fire.

## ACKNOWLEDGMENTS

The authors gratefully acknowledge the Portuguese Foundation for Science and Technology (FCT) for its support under the framework of the research project POCI-01-0145-FEDER-031858 - INNOCFSCONC financed by FEDER funds through the Competitvity Factors Operational Programme-COMPETE and the research project PCIF/AGT/0062/2018 – INTERFACESEGURA, financed by FCT through National funds. This work was partly financed by FCT / MCTES through national funds (PIDDAC) under the R&D Unit Institute for Sustainability and Innovation in Structural Engineering (ISISE), under reference UIDB / 04029/2020.

## REFERENCES

- Craveiro, HD, Rodrigues, JPCR, Laím, L., 2016, Buckling resistance of axially loaded cold-formed steel columns. *Thin-Walled Structures*, **106**, pp. 358-375.
- Craveiro, HD, Rodrigues, JPCR, Laím, Luís, 2016, Experimental analysis of built-up closed cold-formed steel columns with restrained thermal elongation under fire conditions. *Thin-Walled Structures*, **107**, pp. 564-579.
- Dubina, D., Ungureanu, V., Landolfo, R., 2012, Design of cold-formed steel structures. Eurocode 3: Design of steel structures. Part 1-3: Design of cold-formed steel structures, ECCS – European Convention for Constructional Steelwork, Wiley-Blackwell.
- Hegyi, P., Dunai, L., 2016, Experimental study on ultra-lightweight-concrete encased cold-formed steel structures Part I: Stability behaviour of elements subjected to bending. *Thin-Walled Structures*, **101**, 75-84.
- Hegyi, P., Dunai, L., 2016, Experimental investigations on ultra-lightweight-concrete encased cold-formed steel structures Part II: Stability behaviour of elements subjected to compression. *Thin-Walled Structures*, **101**, 100-108.
- J. M. Irwan, A. H. Hanizah, I. Azmi, and H. B. Koh, 2011, Large-scale Test of Symmetric Cold-formed Steel (CFS)-concrete Composite Beams with BTTST Enhancement. *Journal of Constructional Steel Research*, **67**, 720-726.
- Uy. B. and Bradford, M. A., 1995, Local buckling of cold-formed steel in composite structural elements at elevated temperatures, *Journal of Constructional Steel Research*, **34** (1), 53-73.
- Yang, Jingjie, Wang, Weiyong, Shi, Yu, Xu, Lei, 2020, Experimental study on fire resistance of cold-formed steel built-up box columns, *Thin-Walled Structures*, Volume 147, 106564.
- Yu, W.-W. and Laboube, R., 2010, *Cold-Formed Steel Design – Fourth Edition*, John Wiley & Sons, Inc.

# FIRE ENDURANCE ANALYSIS OF ORDINARY STRUCTURAL GLASS ELEMENTS

Chiara Bedon<sup>a</sup>, Christian Louter<sup>b</sup>

<sup>a</sup> University of Trieste, Department of Engineering and Architecture, Trieste, Italy

<sup>b</sup> Institute of Building Construction, Faculty of Civil Engineering, Technische Universität Dresden, Germany

## Abstract

Glass material is largely used for load-bearing components in buildings. For this reason, standardized calculation methods can be used in support of safe structural design in common loading and boundary conditions. The mechanical performance of structural glass elements in fire, however, still represents an open challenge. Often, special fire-resisting glass solutions are used for limited practical applications only, and ordinary soda-lime silica glass prevails in design. Moreover, conventional recommendations and testing protocols in use for load-bearing members composed of traditional constructional materials are not already addressed for glass members. This paper elaborates on the fire endurance and failure detection methods for structural glass beams that are subjected to standard ISO time-temperature for fire exposure and in-plane bending mechanical loads. Fire endurance assessment methods are discussed with the support of Finite Element (FE) numerical analyses.

**Keywords:** structural glass, laminated glass, fire, material properties, modelling

## 1 INTRODUCTION

Ordinary soda-lime silica glass is frequently used in buildings as load-bearing material for floors, roofs, walls, columns. For this reason, design recommendations, guidelines and codes for (structural) glass applications are under continuous development. Several practical applications are in fact characterized by a multitude of loading combinations, restraints, etc. In this context, relatively little is recognized about the mechanical performance in fire conditions. Most of fire-related studies for glass are focused on the investigation of the thermal performance and fracture (failure time and “fallout” collapse mechanism) for glass infill panels for doors, windows and facades. Limited attention is currently given to the mechanical performance under fire exposure of structural glass components (i.e., self-weight and additional sustained mechanical loads), as for example in Fig. 1.

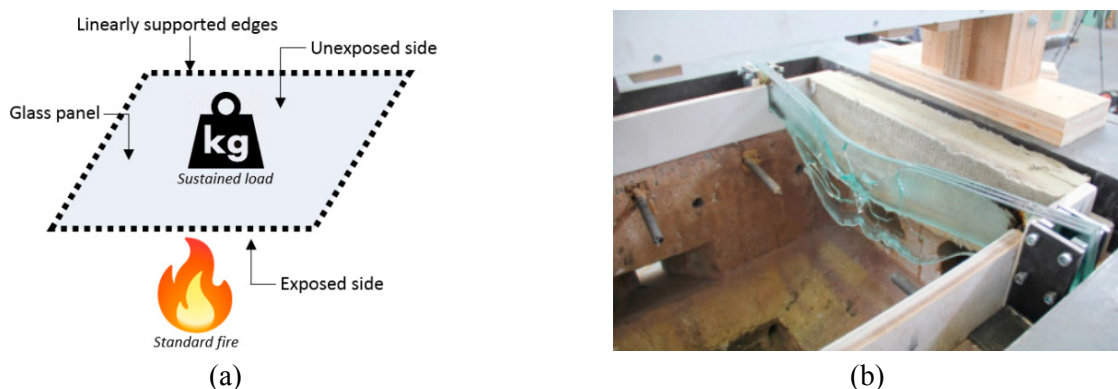


Fig. 1 Thermo-mechanical analysis of glass members under fire exposure and sustained loads: (a) out-of-plane (reproduced from (Kozłowski & Bedon, 2021) under the terms and permission of a CC-BY license) or (b) in-plane bending (Louter *et al.*, 2021)

The present paper explores the structural performance of ordinary glass members under in-plane bending setup and fire. Based on simple case-study configurations, Finite Element (FE) numerical simulations are presented to address the combined effect of thermal and mechanical aspects, as well

as the validity / applicability of conventional fire endurance approaches that are in use for load-bearing structural members composed of traditional materials.

## 2 REFERENCE SYSTEM

The current investigation takes inspiration from past literature efforts (Kozłowski & Bedon, 2021; Louter *et al.*, 2021). More precisely, a monolithic glass element in agreement with the nominal geometry discussed in (Bedon & Louter, 2018) is firstly considered ( $L= 1.36\text{m}$ ,  $H= 0.3\text{m}$ ,  $t= 10\text{mm}$  for glass, with  $L_p= 125\text{mm}$  and  $H_p=50\text{mm}$  for the protection layer). According to (Louter *et al.*, 2021) and Fig. 2, its in-plane bending response is explored under a sustained load  $F$  and a standard ISO time-temperature curve.

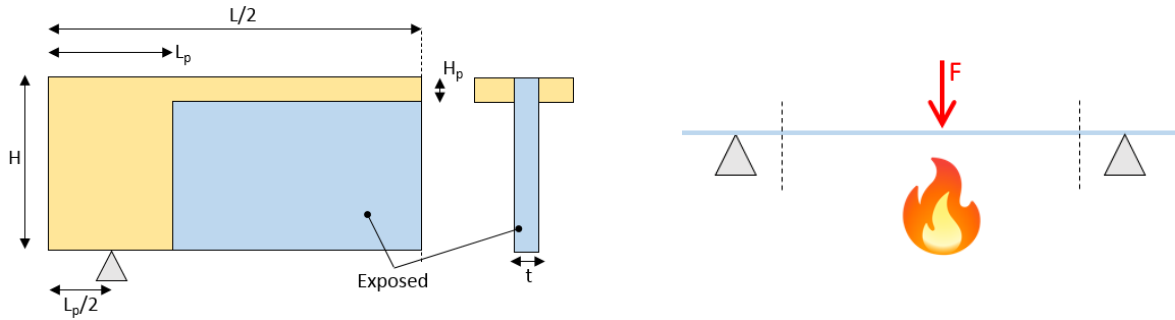


Fig. 2 Schematic representation of the reference setup

## 3 NUMERICAL MODELLING

### 3.1 Strategy and material properties

The overall numerical analysis is carried out in ABAQUS (Simulia, 2019) and takes advantage from earlier research studies. More precisely, a thermal analysis is first carried out on a full 3D solid model reproducing the geometry of glass beam. The thermal distribution in time is hence considered as input configuration in time for the mechanic analysis of the in-plane bending setup as in Fig. 2. In doing so, a special attention is paid for the thermal and mechanical characterization of glass material, as a function of temperature, so as to capture the typical degradation of modulus of elasticity with hot temperatures, as well as the progressive modification of specific heat, conductivity, etc. To this aim, the input parameters are taken from (Bedon & Louter, 2018; Louter *et al.*, 2021), where the FE numerical approach is validate to experimental (furnace) results on simple monolithic glass panels or laminated glass beams (Fig. 1b). Under the imposed standard time-temperature curve from ISO 834-1, the bending analysis is focused on the effects of sustained mechanical loads as in Fig. 2. To this aim, the collapse load ( $F_{20}$ , in the following) is first calculated for the monolithic glass beam in cold condition. Successively, the thermo-mechanical analysis is carried out to explore the interaction of fire exposure with  $F_{fire}$  mid-span load of variable magnitude, as a function of  $F_{20}$ .

### 3.2 Fire endurance analysis

The fire endurance of the case-study system is carried out by local and global analysis of principal stress peaks over the time of analysis (with 45MPa, 70MPa or 120MPa the reference strength value for annealed (AN), heat-strengthened (HS) and fully tempered (FT) glass types, respectively). In this regard, possible decrease in the resistance in cold conditions is disregarded. Furthermore, special care is spent for the analysis of deformations. For flexural loaded members, the EN1363-1 recommends the deformation and deformation rate limits given in *Eqs. (1)-(2)*:

$$D_{lim} = \frac{L^2}{400d} \quad [mm] \quad (1)$$

$$DR_{lim} = \frac{L^2}{9000d} \quad [mm/min] \quad (2)$$

where  $L$  is the bending span (in millimetres) and  $d$  the distance between the extreme fibre of the cold design compression zone and the extreme fibre of the cold design tension zone (in millimetres).

## 4 RESULTS

### 4.1 Stress and temperature

Differing from the bending analysis in cold conditions, the first remarkable effect of combined fire exposure is represented by the migration of stress peaks in the glass beam, from the typical tensile (bottom) edge towards the coldest regions of the member. A typical example is shown in Fig. 3 for selected time intervals of analysis. Worth to be noted, as also discussed in (Louter *et al.*, 2021), is the bridge effect due to the presence of a protection layer as in Fig. 2, to preserve a minimum stiff thickness for the glass member object of study.

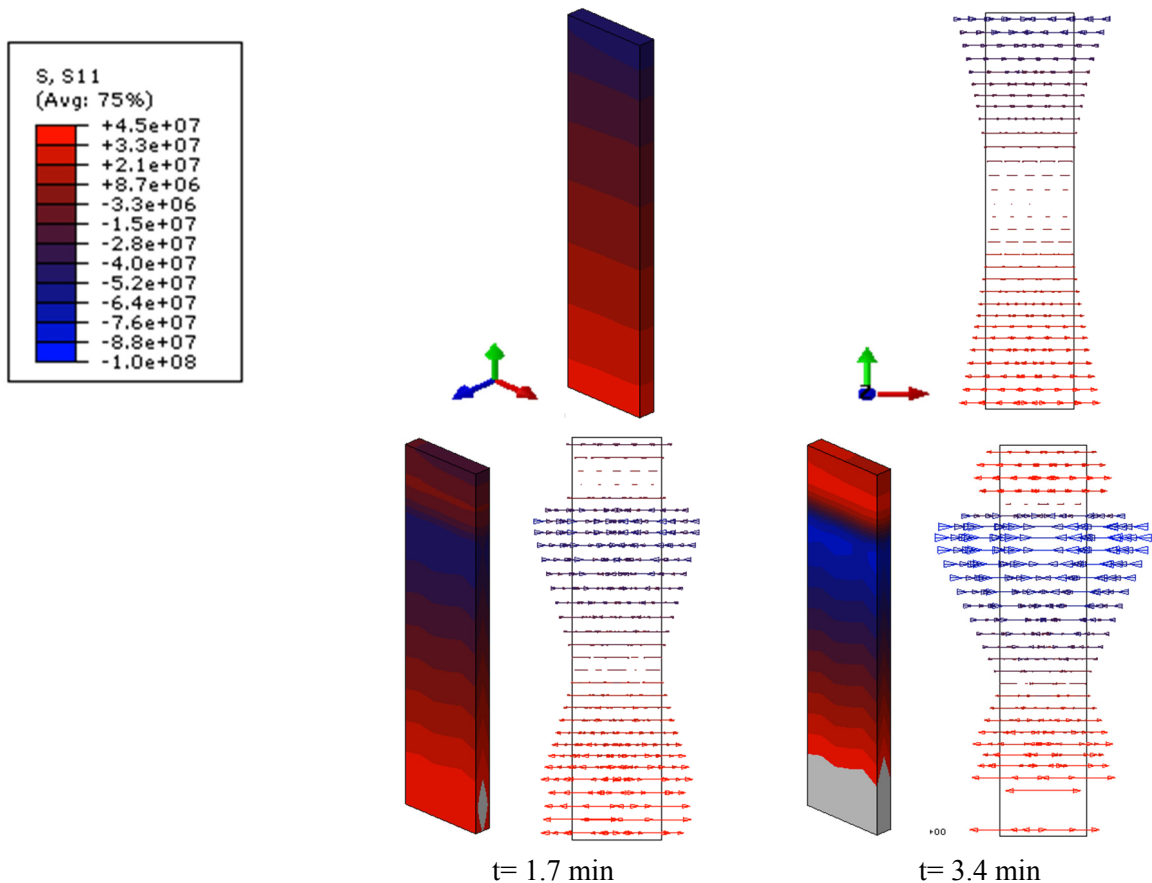


Fig. 3 Stress distribution at the mid-span region for a monolithic beam, as a function of time exposure (ABAQUS). Stress values in Pa (example for M-F75% model)

A more detailed stress analysis of the glass member should necessarily consider key control points for the beam, as well as the maximum envelope of stress peaks in the span and in the thickness of glass. Fig. 4, in this regard, can support the analysis of stress peaks in the mid-span control point P1, which is expected to carry on most of the sustained mechanical loads. Worth to be noted in Fig. 4b is the initial decrease of measured stress values, as a function of the increasing temperature due to fire and thus the progressive relaxation of glass modulus of elasticity. After  $\approx 2$  minutes of fire exposure, the case-study member is subjected to a further increase of stress peaks in P1, but also in the coldest regions (i.e., P3). The typical result is a “stress failure condition” that is frequently governed by the coldest regions in the top of the beam, rather than at its mid-span bottom region. This condition necessarily requires a careful analysis of stress distributions in time, both in the span of the beam but also in the thickness of monolithic or laminated glass layers.

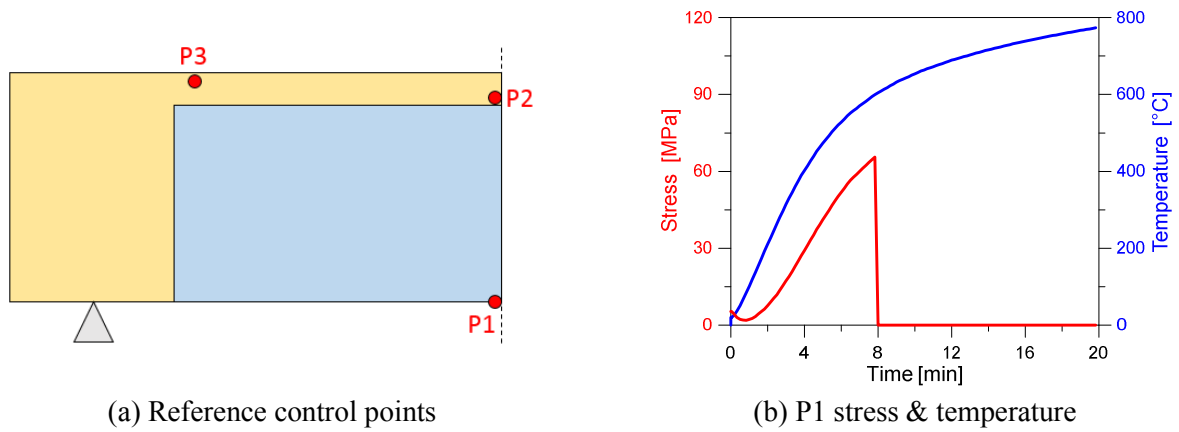


Fig. 4 Stress and temperature evolution at P1 control point (ABAQUS, example for M-F10% model)

#### 4.2 Fire endurance analysis

As discussed in Section 3.2, the fire endurance analysis is carried out in this study in terms of stress failure detection (i.e., tensile strength limit for glass), but also typical deformation limit values in use for traditional constructional materials in beams.

To this aim, Fig. 5 shows a typical variation of stress peaks in P1 for the monolithic beam under variable magnitudes of sustained loads, where M-FX% denotes the numerical model with a X% part of failure load in cold conditions ( $F_{20}$ ). Given that the stress analysis in P1 is not sufficient, the maximum envelope calculation reveals that most of the configurations are characterized by fracture of glass that theoretically propagated from the mid-span region, as in cold conditions, but also to the top edge region (P3). The final result can take the form of the resisting domain reported in Fig. 5b, where the effect of different glass types is also emphasized. Worth to be noted is that as far as  $(F_{fire} / F_{20})$  decreases from the unitary value, the expected failure time progressively increases for all the examined conditions. On the other side, the failure time starts to decrease for sustained loads of limited amplitude ( $F_{fire} / F_{20} < \approx 0.5$ ). This effect depends on the critical role of the cold / protected top region of glass, in combination with the progressive relaxation of tensile region and migration of stress peaks in the beam (i.e., from P1 towards P3) due to fire.

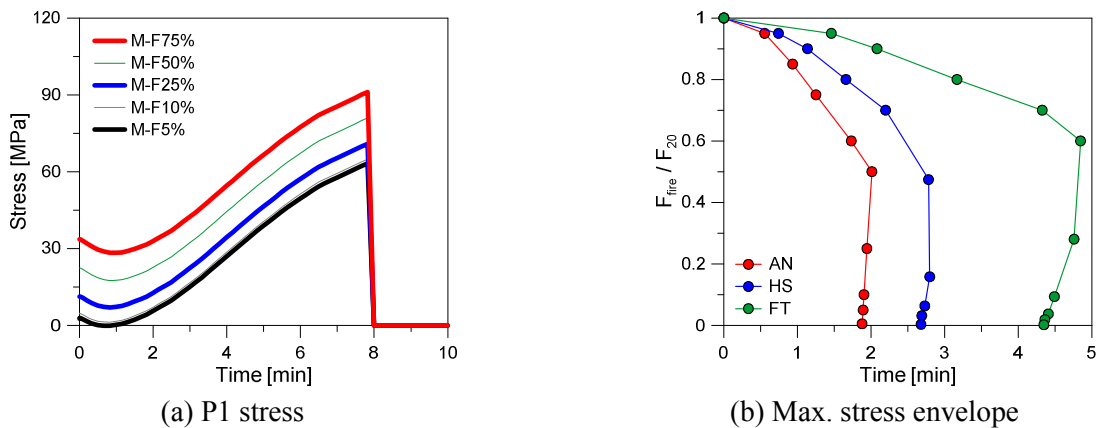


Fig. 5 Failure time for monolithic glass beams, based on stress analysis (ABAQUS)

When the deflection limits from Eqs. (1) and (2) are taken into account for the same configurations, typical results as in Fig. 6 are obtained. In this case, it is possible to notice that both the deformation trend (Fig. 6a) and the deformation rate trend (Fig. 6c) are slightly sensitive to the magnitude of sustained load. This suggests, differing from the stress failure analysis, a prevailing role of thermal load on the mechanical one. A direct effect can be quantified in the limited variation of the predicted failure time in terms of deformation limit, see Fig. 6b, as well as in a negligible modification of deformation rate parameters.

Most importantly, however, is to highlight that both  $D_{lim}$  and  $DR_{lim}$  overestimate (for the examined system) the actual fire endurance. In terms of deformation rate, for example, numerical results in Fig.

6d show that the stress failure is detected for  $DR$  values that are in the range of  $\approx 0.6$  mm/min and lower than the standard value from *Eq. (2)*, thus suggesting a specific calibration for glass material.

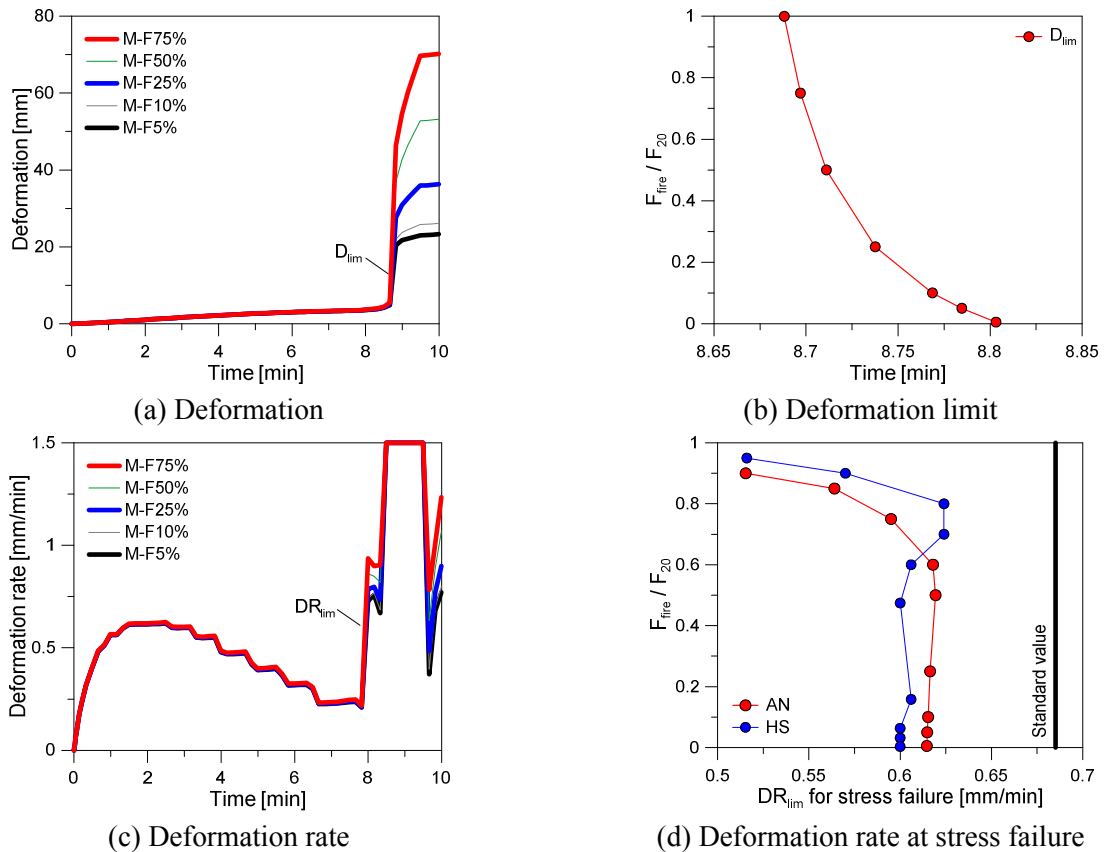


Fig. 6 Failure time for monolithic glass beams, based on deformation analysis (ABAQUS)

Another relevant aspect is represented by the distribution of sustained loads, and the corresponding bending response of the examined beams. A comparative example is shown in Fig. 7 for members under mid-span concentrated load  $F$  or distributed load  $q$ . Worth to be noted in Fig. 7b that the effect in terms of stress failure detection can be perceived for high mechanical load magnitudes only (i.e.,  $F_{fire} / F_{20} > \approx 0.5$ ).

Similarly, no remarkable modifications can be noticed in terms of deformation limit and corresponding failure time, compared to Fig. 5c. Again, the deformation rate value leading to stress failure is calculated in the order of  $\approx 0.6$  mm/min, that is lower than the standard value from *Eq. (2)*. This finding confirms a rather stable response of the beam under mid-span or distributed sustained loads, but the current overestimation of failure time based on deformation parameters rather than stress peaks analysis.

In conclusion, the analysis is focused on the performance of glass members still in agreement with Fig. 2, but characterized by a laminated glass section as in Fig. 8a, in place of the monolithic one. The number of glass layers is set in  $N_{LG} = 2, 4$  or  $6$  respectively, and thus the in-plane bending resistance of laminated members in cold conditions is in the order of  $R_B = 2, 4$  or  $6$  times higher compared to the monolithic solution.

The thermo-mechanical analysis of laminated sections in fire can be summarized as in Fig. 8b. Worth to be noted that the stress failure detection for laminated members is characterized by relatively higher failure time, that increases with  $N_{LG}$ . This failure time increase, however, is less pronounced than  $R_B$  with  $N_{LG}$  in cold conditions, and follows a non-linear trend towards the mechanical loading parameter ( $F_{fire} / F_{20}$ ). The parametric analysis on laminated glass members shows also that the predicted deformation rate (at stress failure), compared to the value in *Eq. (2)*, further decreases to  $\approx 0.35$  mm/min, and this finding can be seen as a direct effect of local stress distributions that are non-uniform in the span but also in the thickness of multiple glass layers.

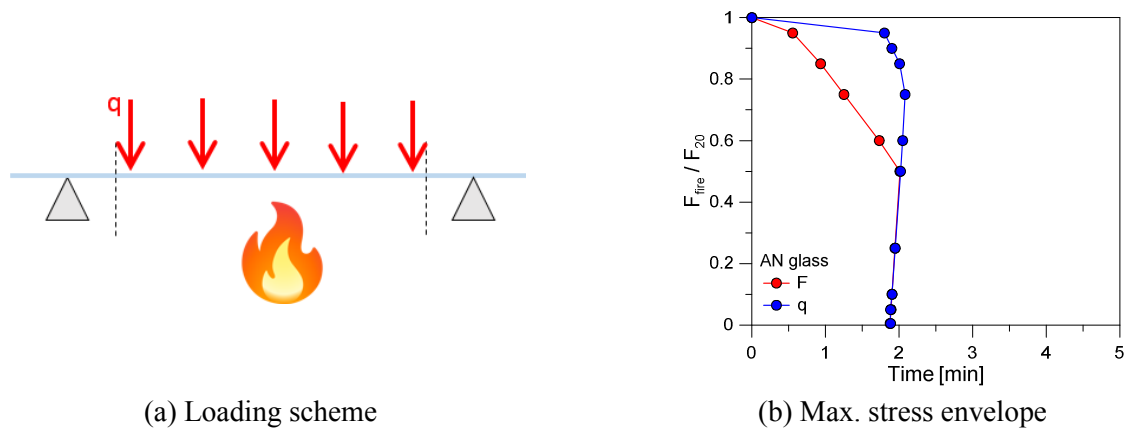


Fig. 7 Failure time for monolithic or LG beams under mid-span or distributed sustained load (ABAQUS).

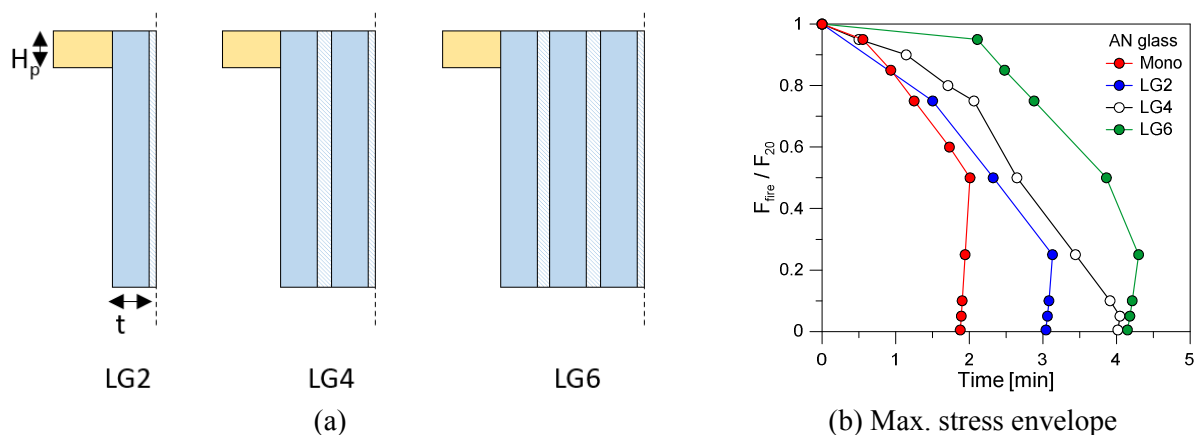


Fig. 8 Failure time for monolithic or LG beams under mid-span sustained load (ABAQUS)

## 5 CONCLUSIONS

Ordinary glass is largely used in buildings, but limited attention is given to its mechanical performance under extreme design loads such as fire. This paper explored the in-plane bending response of glass beams under fire, giving evidence of current issues in their fire endurance analysis. As shown, the attention should be focused on stress peaks and deformation parameters, which are sensitive to various mechanical and geometrical properties. Compared to cold conditions, however, several modifications can be observed in the bending analysis and capacity, due to fire effects. In this regard, it is expected that the theoretical predictions could be further generalized to cover several configurations of technical interest, as well as validated with the support of experimental analyses.

## ACKNOWLEDGMENTS

The presentation of this paper in ASFE 21 is funded by MULTIWALL project (FRA-2020 UniTS).

## REFERENCES

- Bedon C. 2017. *Structural Glass Systems under Fire: Overview of Design Issues, Experimental Research, and Developments*. *Advances in Civil Engineering*, Article ID 2120570, doi: 10.1155/2017/2120570.
- Bedon C., Louter C. 2018. *Thermo-mechanical Numerical Modelling of Structural Glass under Fire - Preliminary Considerations and Comparisons*. *Challenging Glass Conference Proceedings*, v. 6, p. 513-524, ISSN 2589-8019, doi: 10.7480/cgc.6.2173
- Kozłowski M., Bedon C. 2021. *Sensitivity to Input Parameters of Failure Detection Methods for Out-of-Plane Loaded Glass Panels in Fire*. *Fire*, 4(1): 5, doi: 10.3390/fire4010005
- Louter C., Bedon C., Kozłowski M., Nussbaumer A. 2021. *Structural Response of Fire-Exposed Laminated Glass Beams under Sustained Loads; Exploratory Experiments and FE-Simulations*. *Fire Safety Journal*, in press, available online, doi: 10.1016/j.firesaf.2021.103353.
- Simulia 2019. ABAQUS v.6.14 computer software and online documentation, Dassault Systems, RI, USA.

Proceedings of the International Conference in Ljubljana, 10-11 June 2021  
in edition of Applications of Structural Fire Engineering

**Session**

**Modelling and application of structural fire engineering I**

## TRANSIENT TEMPERATURE DISTRIBUTION In Hot-Cast Anchors by 3D Heat Transfer

Jingzhi Chen<sup>a</sup>, Yong Du<sup>a</sup> and Jian Zhu<sup>a</sup>

<sup>a</sup> Nanjing Tech University, College of Engineering, Nanjing, China

### Abstract

Hot-cast anchors are key components which are always used in pre-tension steel structures and suspension bridges. In order to assess the fire safety of hot-cast anchors, the transient temperature distribution in them should be investigated. A numerical heat transfer model in 3D was developed by ABAQUS software and checked by fire test results. It indicated that the temperature distribution along the longitudinal centre axis of anchors was non-uniform as well as it on cross-section. An analytic formula was derived from the basic principle of heat transfer theory in 2D. The coordinate of cross-section against centre axis was also determined where the deviation between 3D heat transfer simulation and analytic formula was small enough to conservatively take the temperature history as the same one. Finally, the advanced method and simple method were proposed to determine the transient temperature distribution and critical temperature for fire safety of hot-cast anchors.

**Keywords:** hot-cast anchor, numerical analysis, analytical method, temperature distribution

## 1 INTRODUCTION

Pre-tension steel structures are benefit from high strength of material, economic and structural efficiency, which are widely used in large-span roof structures or suspension bridges. Anchors always play the important role to transfer pre-tension force between supports and steel cables. During structural full service period, fire scenario should be taken into account. However, pre-tension anchors tend to be damaged in fire, and the fire safety should be designed correctly.

In recent years, the thermal properties of the filler material (zinc copper alloy) of hot-cast anchors have been tested at high temperature, and heat transfer numerical simulation in 2D has also been investigated by (Du et.al, 2019). A series of pull-out test of hot-cast anchors exposed to ISO-834 fire also were reported in the corresponding paper (Du and Zhu, 2021). In the present paper, the heat transfer numerical analysis in 3D by using ABAQUS software was operated to study the transient temperature distribution subject to ISO834 fire and checked by the test data. The aim of this study is to proposed the method to determine the critical temperature for fire safety design of hot-cast anchors.

## 2 2D HEAT TRANSFER ANALYSIS OF HOT-CAST ANCHORS

### 2.1 Theoretical method

Fig. 1 shows a hot-cast anchor exposed to fire and the profile helps to understand its geometric shape. In fire scenario heat is transferred to the outer surface of anchor cup by thermal radiation and convection. Then, thermal conduction in cup wall and filler will come on the cross-section and along longitudinal direction, i.e. 3D heat transfer.

Fig. 2 shows the thermal resistance system for understanding heat transfer in hot-cast anchors. Thermal radiative resistance,  $R_{\text{radi}}$ , and thermal convection resistance,  $R_{\text{conv}}$ , are parallel to constitute the fire environment resistance  $R_{\text{air}}$  as well as the thermal conductivity resistance  $R_{\text{cond}}$  of zinc-copper alloy filler and steel wires to form  $R_{\text{cond}}$  as below:

$$R_{air} = \frac{1}{\frac{1}{R_{radi}} + \frac{1}{R_{conv}}} = \frac{1}{Ah_r + Aa_c} \quad (1)$$

$$R_{cond} = \frac{1}{\frac{1}{R_{s2}} + \frac{1}{R_r}} = \frac{1}{\frac{2\pi\lambda_s}{\ln r_s} + \frac{2\pi\lambda_r}{\ln r_r}} = \frac{1}{2\pi(\lambda_s + \lambda_r)} \quad (2)$$

Fig. 3(a) shows the geometric shape of the cross-section of hot-cast anchor.

The total thermal resistance  $R_m$  of a hot-cast anchor is the serial of the environmental thermal resistance  $R_{air}$ , the thermal resistance  $R_s$  of the steel socket wall as below:

$$R_m = R_{air} + R_s + R_{cond} = \frac{1}{Ah_r + Aa_c} + \frac{1}{2\pi\lambda_r} + \frac{1}{2\pi(\lambda_s + \lambda_r)} \quad (3)$$

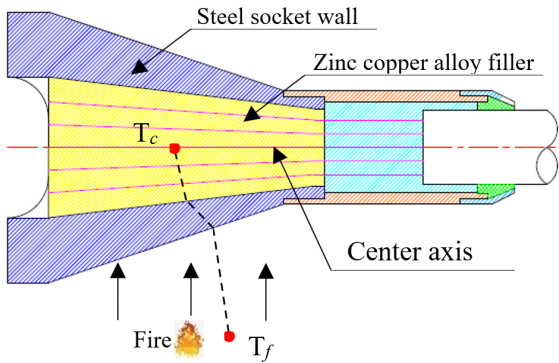


Fig.1 Hot-cast anchor exposed to fire

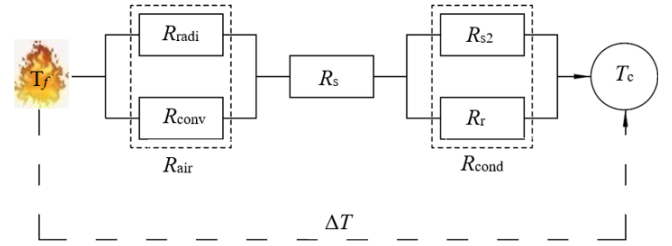


Fig.2 Thermal resistance system of heat transfer for hot-cast anchors

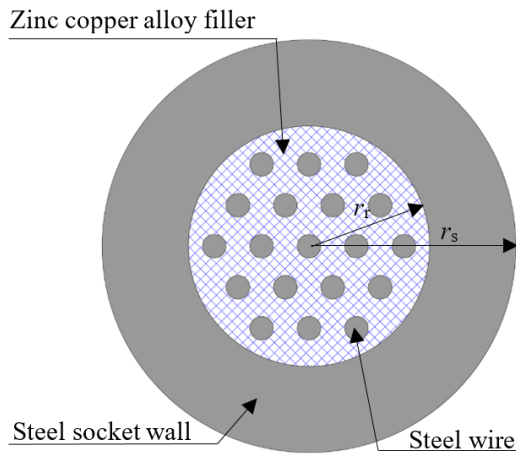


Fig. 3 Cross-section of a hot-cast anchor



Fig. 4 Fire test specimens (Du et al. 2021)

Finally, according to Fourier's law and the transient temperature of steel members with non-light fire protection exposed to fire, the transient temperature at the centre point on the cross-section of a hot-cast anchor can be obtained as below:

$$\begin{aligned} T_s(t + \Delta t) &= \frac{1}{R_i} \cdot \frac{1}{\rho_s c_s V + \frac{\rho_i c_i F_i d_i}{2}} \cdot [T_f(t) - T_s(t)] \cdot \Delta t + T_s(t) \\ &= \frac{1}{R_m} \cdot \frac{1}{\rho_s c_s V + \frac{\rho_m c_m F_i d_i}{2}} \cdot [T_f(t) - T_s(t)] \cdot \Delta t + T_s(t) \end{aligned} \quad (4)$$

where  $\rho_s$ , density of steel, in  $\text{kg/m}^3$ ;

$c_s$ , specific heat capacity of steel, in  $\text{J/kg}\cdot^\circ\text{C}$ ;

$d_i$ , thickness of fire protection layer or outer member, in m;

$F_i$ , inner surface area per meter of fire protection layer or surface of member, in  $\text{m}^2/\text{m}$ ;

$V = \pi r_s^2$ , component volume per unit length, in  $\text{m}^3/\text{m}$ ;

$\rho_m = \frac{\rho_s v_s + \rho_r v_r}{v_s + v_r}$ , mixed density of zinc copper alloy filler and steel socket cup, in  $\text{kg/m}^3$ ;

$c_m = \frac{c_s m_s + c_r m_r}{m_s + m_r}$ , specific heat capacity of zinc copper alloy filler and steel socket cup, in  $\text{J/kg}\cdot^\circ\text{C}$ .

## 2.2 Comparison of heat transfer between theoretical method and 2D numerical analysis

A series of fire tests have been conducted to investigate the transient temperature distribution for hot-cast anchors which are shown in Fig. 4 and temperature measure points are shown in Fig. 5 (Du et.al, 2021). The 2D heat transfer numerical model of hot-cast anchors was established by ABAQUS software (Du et.al, 2019).

Fig.6 shows the temperature history of point T1 in LW-127 anchor as well as point T1 and T3 in CE-127 anchor respectively. Comparison of temperature histories at each point between the results from Eq. (4) and 2D simulation, the maximum deviation is in the range of 8.4%, 3.8% and 7.3% respectively. It indicates that Eq. (4) is suitable to predict the transient temperature due to 2D heat transfer at the centre point on the cross-section of hot-cast anchors.

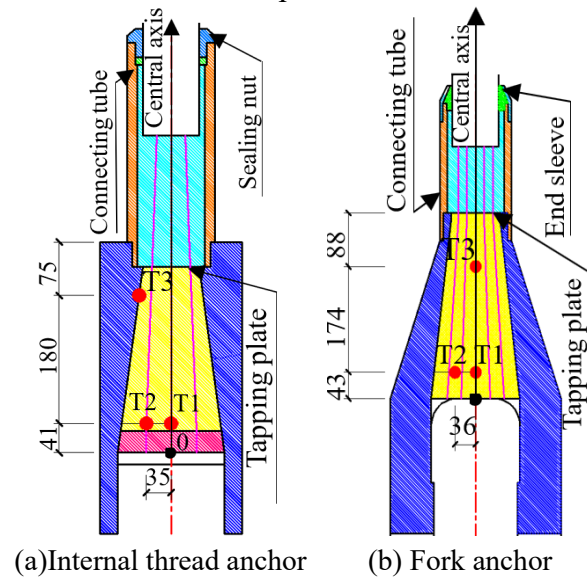


Fig. 5 Geometric size and temperature measure points for anchors (Du et al. 2021)

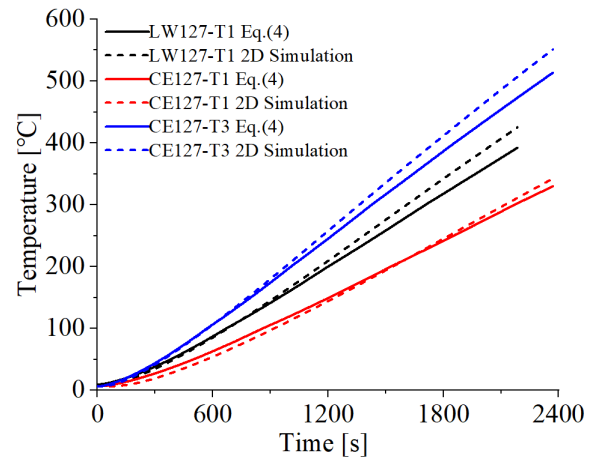


Fig. 6 Comparative analysis of heat transfer theory and 2D heat transfer model of hot-cast anchor

## 3 HEAT TRANSFER ANALYSIS IN 3D OF HOT-CAST ANCHOR

### 3.1 3D heat transfer numerical model

In this paper, the 3D heat transfer analysis numerical model was developed as shown in Fig.7. The transient temperature distribution of typical internal thread hot-cast anchor and fork hot-cast anchor subject to ISO834 fire were studied respectively, such as specimens LW-127 and CE-127.

The material of steel socket wall is ZG35Cr1Mo structural steel, the tapping plate is 40Cr alloy structural steel, the connecting tube used hot-rolled seamless steel pipe and the sealing nut and end

sleeve used Q235-A structural steel; The strength steel cable is 1670 MPa. The thermal properties of material mentioned above corresponded to EN1992-1-2 and Du et.al, 2017 respectively. The ten node tetrahedral element (DC3D10) is used to simulate filler, and eight node linear hexahedral element (DC3D8) is used for other components of anchor. The convective conductivity was taken as  $25\text{W}/(\text{m}^2\cdot\text{K})$ , the radiation coefficient as 0.4, the absolute zero as  $-273\text{ }^\circ\text{C}$ , and the Stefan-Boltzmann constant as  $5.67\times 10^{-8}\text{W}/(\text{m}^2\cdot\text{K}^4)$ . Each component of the hot-cast anchor was bound with tie command.

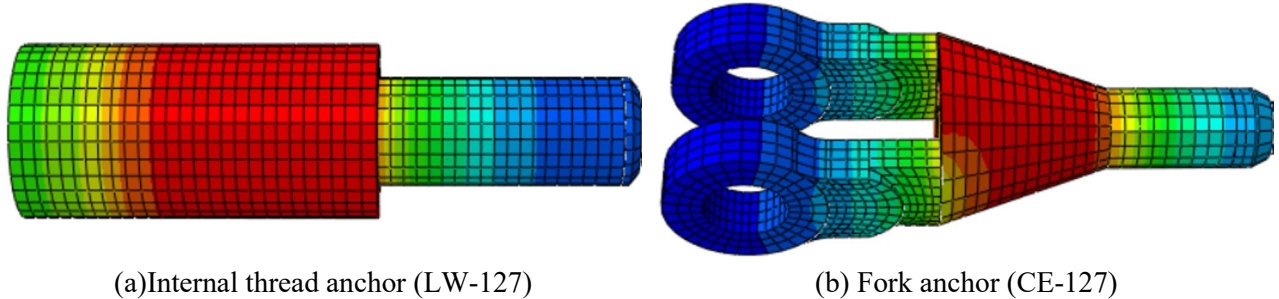


Fig.7 3D heat transfer numerical model of hot-cast anchors

### 3.2 Transient temperature distribution along longitudinal central axis of hot-cast anchor

Figs. 8 shows the transient temperature distribution along the longitudinal central axis of the internal thread hot-cast anchor (LW-127) and fork hot-cast anchor (CE-127) subject to ISO834 fire. The 3D numerical analysis resulted that the transient temperature distribution along the central axis of anchors was non-uniform in the fire time range of 600s, 1200s, 1800s and 2185s. From the original point, the temperature increased to the maximum value corresponding to the centre axis at 140 mm and 180 mm, and decreased towards the end of LW-127 or CE-127 due to heat transfer along the longitudinal direction, as shown in Fig. 8 respectively. As the heat transfer in 2D, the temperature distributed monotonically along the centre axis resulted from Eq. (4). Especially, the temperature increased significantly as the cross-section size of fork anchor CE-127 decreased along the centre axis as shown in Fig. 8(b). It should be noted that the minimum deviation of temperature between the results from Eq. (4) and 3D simulation of LW-127 or CE-127 was against the centre axis at 140 mm and 60 mm. It was suggested that Eq.4 can be used to determine the temperature history at especial cross-section to represent of the heating process of hot-cast anchors for fire safety design.

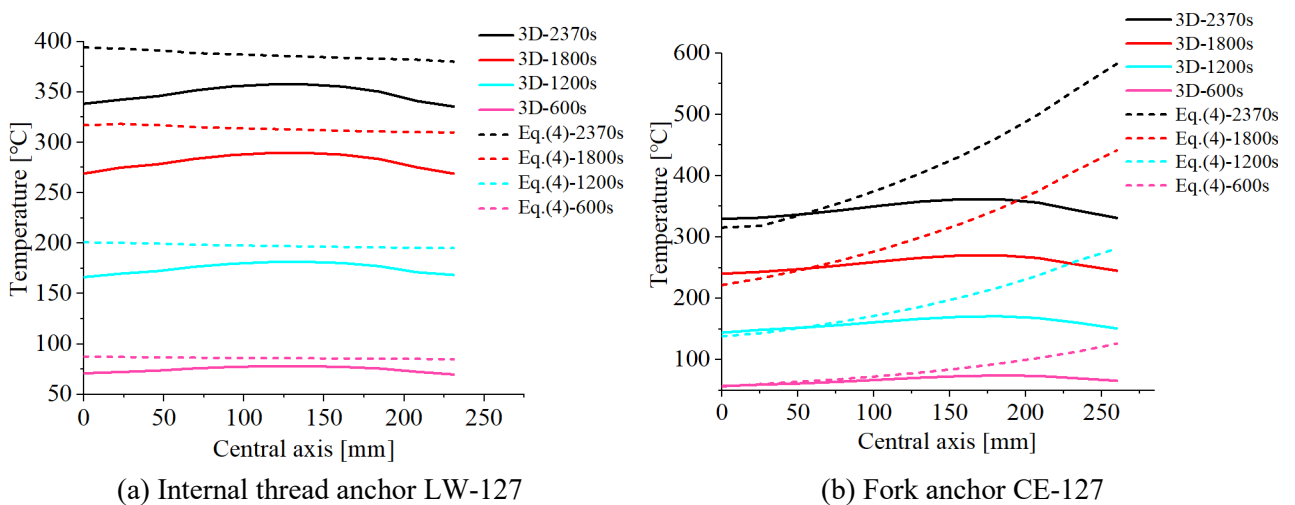
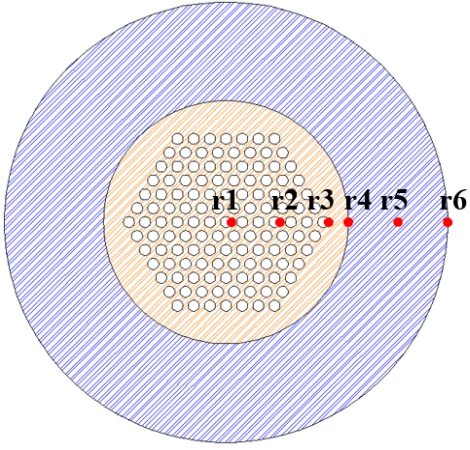
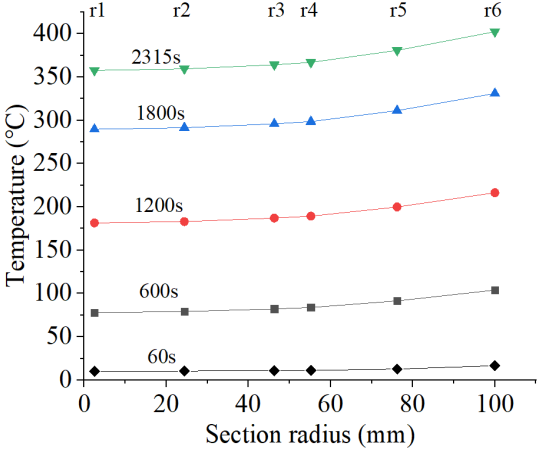


Fig.8 Transient temperature distribution along central axis of hot-cast anchors

### 3.3 Transient temperature distribution on the cross section of hot-cast anchors

As the geometric shape of the cross-section of anchors is circular, the temperature measure points are marked along the radius shown in Figs. 9(b) and 10(b) respectively. According to the coordinate

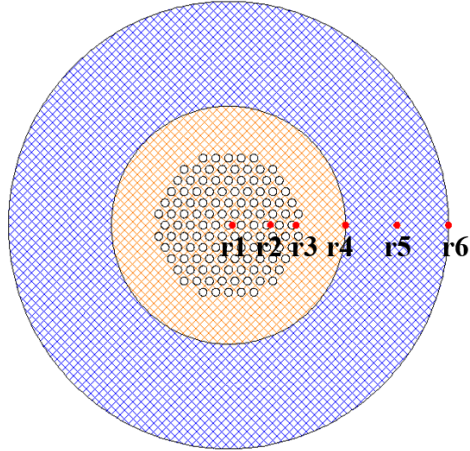
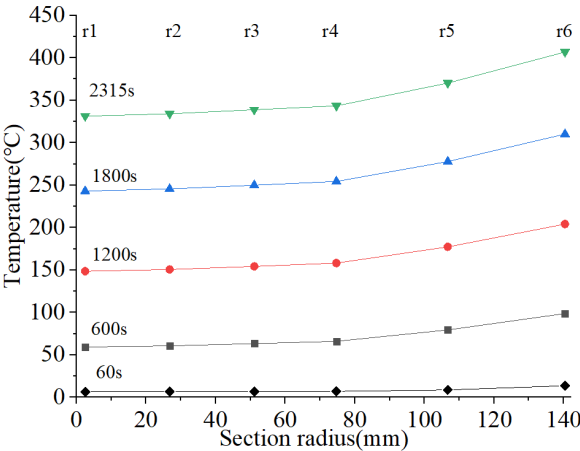
of the maximum temperature shown in Fig. 8, the cross-section of hot-cast anchor LW-127 was taken in the middle of the length in the longitudinal direction, and that of hot-cast anchor CE-127 at 4/5 length from the origin. Points r4 and r6 are on the internal and external surface of socket cup respectively and r5 in the middle of thickness. Point r1 is the centre point of the cross-section and point r3 is the edge of steel wire. Point r2 is at the middle from the centre point to edge in the radius. A series of temperature distribution on the cross-section in the time range of 600s, 1200s, 1800s and 2185s were shown in Figs. 9(a) and 10(a) respectively. It indicated that the temperature distribution linearly increased from the centre to the turning point r4, and then, to the external surface of socket cup.



(a) Temperature rise at different measuring points

(b) Location of different measuring points

Fig.9 Temperature distribution on the cross-section of internal thread anchor LW-127



(a) Temperature rise at different measuring points

(b) Location of different measuring points

Fig.10 Temperature distribution on the cross-section of fork anchor CE-127

**3.4 Comparison of temperature histories between 3D numerical analysis and test**

Fig. 11 shows the temperature histories at measuring points T1~T3 in anchors. Comparison of the temperature histories between 3D simulation and test results, both of anchor LW-127 and anchor CE-127 agreed well. The maximum deviations were 4.5% and 14.3% respectively. It indicated that 3D heat transfer numerical analysis can estimated the temperature history accurately.

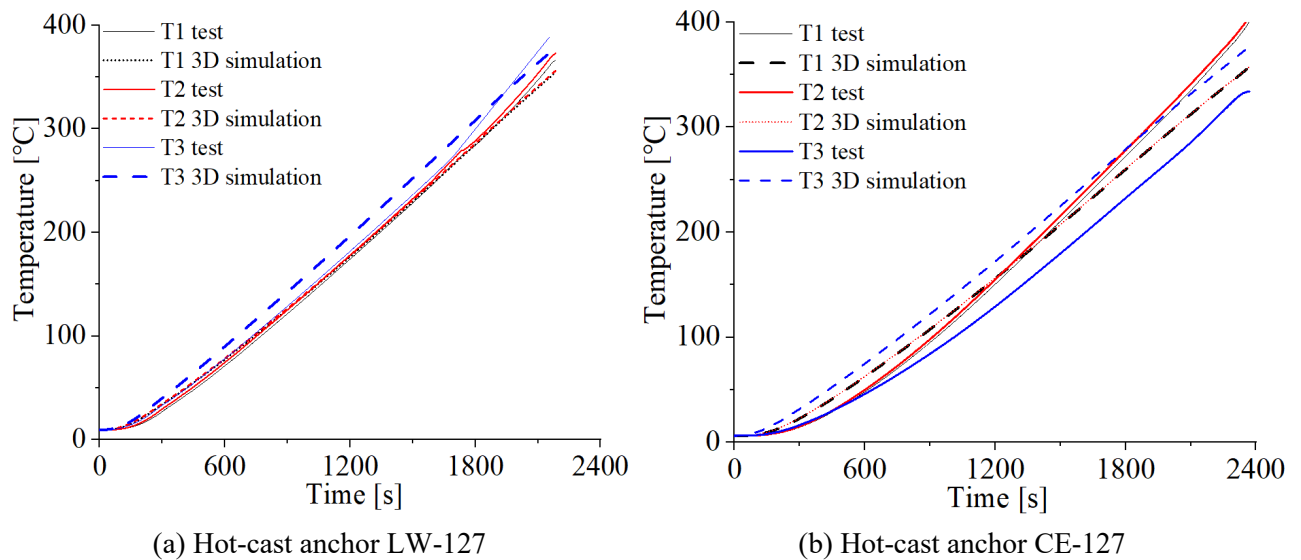


Fig.11 Comparison of temperature histories between 3D numerical analysis and test

### 3.4 Strategies on estimating temperature history for hot-cast anchors

The heat transfer procedure of other hot-cast anchors shown in Fig. 4 was investigated by Eq. (4), 3D simulation and fire test. It indicated that there was the similar heat transfer procedure for all hot-cast anchors shown in Fig. 4. Herein, both of the advanced analysis method and simple method, i.e. 3D heat transfer numerical analysis and theoretical formula, Eq. (4) are proposed to estimate the transient temperature distribution for hot-cast anchors subject to fire. Corresponding to the failure time from a series of tension test of hot-anchors subject to ISO-834 fire (Du and Zhu 2021), the methods proposed in the present paper can be used to determine the critical temperature of hot-cast anchors.

## 4 Conclusions

This paper investigated the transient temperature distribution of hot-cast anchors by the basic principle of heat transfer theory and numerical analysis by using ABAQUS software. The conclusions were drawn as follows:

- The theoretical formula can estimate the history of temperature on cross-section accurately comparing with 2D heat transfer numerical analysis. 3D heat transfer numerical analysis is more precise than that of 2D numerical analysis and agrees well with the fire test results.
- The temperature distribution along the longitudinal centre axis is non-monotonic. A peak point of temperature is always at 1/2 and 4/5 length from original against the centre axis for internal thread anchors and fork anchors respectively. On the circular cross-section of hot-cast anchors, the temperature increases linearly in the filler and socket wall respectively.
- The advanced analysis method and simple method are proposed to estimate the transient temperature distribution and critical temperature for hot-cast anchors subject to fire.

## REFERENCES

- Du Y., Zhu Y., Jiang J., Li G. 2019. *Transient temperature distribution in pre-tensioned anchors of cable-supported structures under ISO834 fire*, Thin-Walled Structures, England, 138, p. 231-242.
- BSI. 2007. *Eurocode 3, Design of steel structures. Part 1-2. General rules. Structural fire design*, BSI publications.
- BSI. 2005. *Eurocode 4, Design of Composite Steel and Concrete Structures, Part 1.2: General Rules - Structural Fire Design*. BSI publications.
- China Planning Press. 2017. *GB51249-2017, Code for fire safety of steel structures in buildings*. China Planning Press,
- Du Y., Zhu J., 2021. Experimental study on bound strength of hot-cast anchors exposed to ISO834 fire, in *Applications of Structural Fire Engineering*, 10-11 June 2021, Ljubljana, Slovenia.

## A CASE STUDY OF STRUCTURAL FIRE SAFETY DESIGN OF UNPROTECTED COMPOSITE BEAMS WITH FIN-PLATE JOINTS

Naoya Yotsumoto<sup>a</sup>, Takeo Hirashima<sup>b</sup>, Koji Toyoda<sup>a</sup>

<sup>a</sup> General Building Research Corporation of Japan, Fire Safety Department, Osaka, Japan

<sup>b</sup> Chiba University, Graduate School of Engineering, Chiba, Japan

### Abstract

A case study of structural fire safety design of composite beams protected only at the ends when a simple evaluation method proposed by the authors is applied to secondary beams in an office building is introduced. The result showed that the beam would collapse in about 35 min when only the fin-plate joints at the beam ends are fire-protected. However, the fire resistance time can be improved to 1 hour when the number of bolts is doubled and the range of fire-protection at the beam end is extended to 10 % of the total beam length. This is due to the improvement of load-bearing capacity in the joint by increasing bolt amount and the reduction of bending moment and shear force at the fire-protection boundary, which is the structural weak point, by the extension of the protection range. Thus, it is possible to determine the optimum specification for the joint and fire-protection range by applying this evaluation method.

**Keywords:** Fire safety design, Composite beam, Fin-plate joint, Bending moment resistance, Fire protection

### 1 INTRODUCTION

The authors have previously proposed an evaluation method of bending moment resistance of unprotected composite beams with fin-plate beam-to-girder joints based on load-bearing fire tests (Yotsumoto *et al.*, 2020). In the method, it is possible to consider the hogging moment resistance of the fin-plate joint considering the effect of reinforcement continuity and the temperature distribution of the composite beam and the joint when only the beam ends are fire-protected. Recent studies have proposed large deformation analysis methods using FEM that can be used for fire-resistant design of beams including joints, but these cannot always be applicable in practice due to the cost and complexity of the analysis. The advantage of our method is that the hogging moment resistance of the joint and the temperature distribution in the axial direction can be considered using a simple method that does not require FEM analysis.

This paper presents a case study of the fire safety design of composite beams protected only at the ends when the evaluation method is applied to secondary beams in an office building. In addition, based on the case study, a specification with one-hour fire resistance is presented in which the number of bolts in the joints and the fire protection range at the beam ends are optimized.

### 2 SUBJECT OF THE CASE STUDY

The model building is a nine-story office building covered in the "Fire resistant Design Examples" section of the Recommendations for Fire Resistant Design of Steel Structures (AIJ, 2017). The beam in the office room (see Fig. 1), where a fully-developed compartment fire is expected to occur, is the subject of the study. The design load on the beam is an equally distributed load  $w=19.6$  kN/m, taking into account the live load in the office area and the dead load of the floor slab. The bending moment  $wl^2/8$  is 297 kN m and the maximum shear force  $wl/2$  is 108 kN, where the support span of the beam  $l$  is 11 m.

The details of the composite beam are shown in Figure 2. The cross-section of the beam is I-600 x 200 x 12 x 22, and the steel grade adopted is SN400 (JIS G 3136). The lower-limit yield point of the SN400B is 235 N/mm<sup>2</sup>, and the lower-limit tensile strength is 400 N/mm<sup>2</sup>. The floor slab on the

beam is a 150 mm thick flat RC slab in which double layered reinforcements are arranged. The compressive design strength of the concrete shall be 21 N/mm<sup>2</sup>. Deformed steel bars (nominal diameter 10 mm) are applied for the RC slab, and arranged at 200 mm- and 300 mm-intervals in the short and long side direction respectively for both the upper- and lower-side reinforcements. Headed studs used to tie the floor slab to the beam are placed at 200 mm intervals (two studs per location), determined to exceed the minimum number of studs required for fully composite beams. The yield moment of this composite beam is 704 kN m, and the long-term allowable bending moment is 469 kN m. Regarding the load level of the beam, the ratio of the bending moment to the long-term allowable bending moment is 63%, and that of the maximum shear force to the long-term allowable shear force is 18%.

The detail of the fin-plate joint is shown in Figure 2(c). In the fin-plate joints, the 16 mm thick gusset plate welded to the girder and the web at the beam ends are connected by friction type using high strength bolts F10T-M20 (JIS B 1186). The bolts are placed in a single row of 6 bolts, which is general for the beam depth of 600mm. The beams shall be unprotected. However, the joints at the beam ends and the girders shall be fire-protected so that the hogging moment resistance of the joints is not significantly reduced. To protect the beam ends and girders, a 12.5-mm alkaline-earth silicate wool blanket (AES blanket) offering an equivalent fire resistance of 1 hour is used. Protection materials shall be attached to the girders in a boxed-shape and to the beam ends in a profiled-shape. The range of fire-protection at the beam ends shall be from the gusset plate ends to 30 mm in the mid-span.

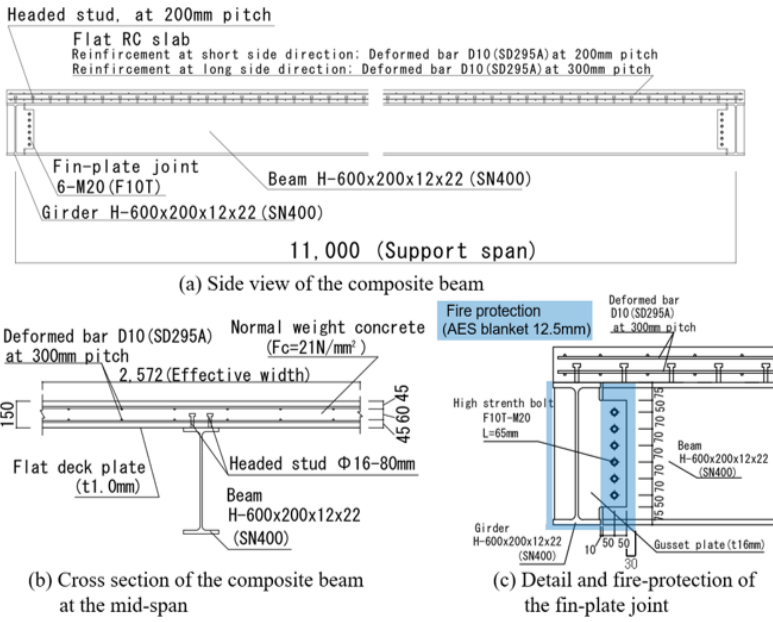
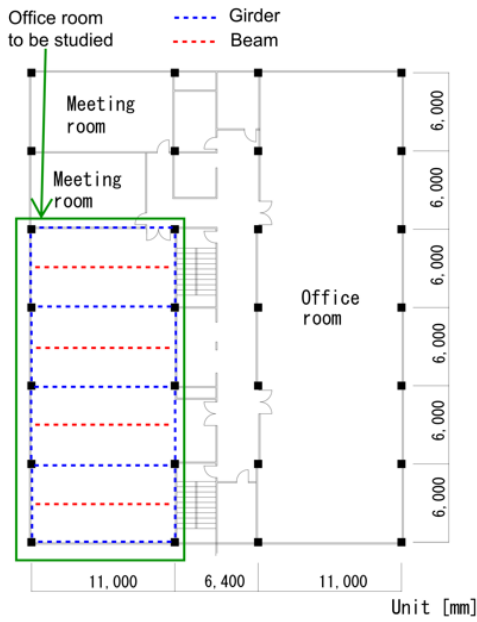


Fig.1 Office room to be studied

Fig.2 Details of composite beam and joint

**3 EVALUATION METHOD OF THE FIRE RESISTANCE**

**3.1 Assumed failure modes and evaluation model of fire resistance**

In this case study, both bending failure based on simple plastic theory (three-hinge mechanism) and shear failure are assumed as the failure modes of the beam (see Figure 3). Regarding the bending failure, when the total moment resistance (sum of the sagging moment resistance at the mid-span and the hogging moment resistance at the beam end) is reduced to the bending moment, a three-hinge state is created and the beam collapses. Two bending failure modes shall be assumed: a case in which plastic hinges are formed at the fin-plate joints and the mid-span (Bending failure mode I), and a case in which plastic hinges are formed at the fire-protection boundary and the mid-span (Bending failure mode II). For the mode I, the total moment resistance  $TIM_u$  is the sum of the sagging moment resistance  $BM_u^+$  at the mid-span and the hogging moment

resistance  $JRM_u^-$  at the fin-plate joint, and the bending moment is the sum of the bending moment  $cM$  at the mid-span and that  $JM$  at the fin-plate joint. For the mode II, the total moment resistance  $T_2M_u$  is the sum of  $BM_u^+$  and the hogging moment resistance  $BM_u^-$  at the fire-protection boundary, and the bending moment is the sum of  $cM$  and the bending moment  $eM$  at the fire-protection boundary. The sagging and hogging moment resistance of the composite beam are calculated based on EC4, while the hogging moment resistance of the fin-plate joint considering the effect of reinforcement continuity is calculated using the model proposed by the authors.

Regarding the shear failure, when a uniformly distributed load is applied, the shear force increases toward the beam ends. Since the hogging moment occurs and the concrete slab at the beam ends is cracked due to tensile forces, the slab is expected to resist little shear force. Therefore, the shear resistance shall be determined only at the web of the steel beam. Considering these factors, the shear resistance shall be evaluated at the fire-protection boundary where the highest shear force occurs in the unprotected area. In this study, shear failure of the joint is not assumed because temperature of the joint is relatively low by the effect of the fire-protection.

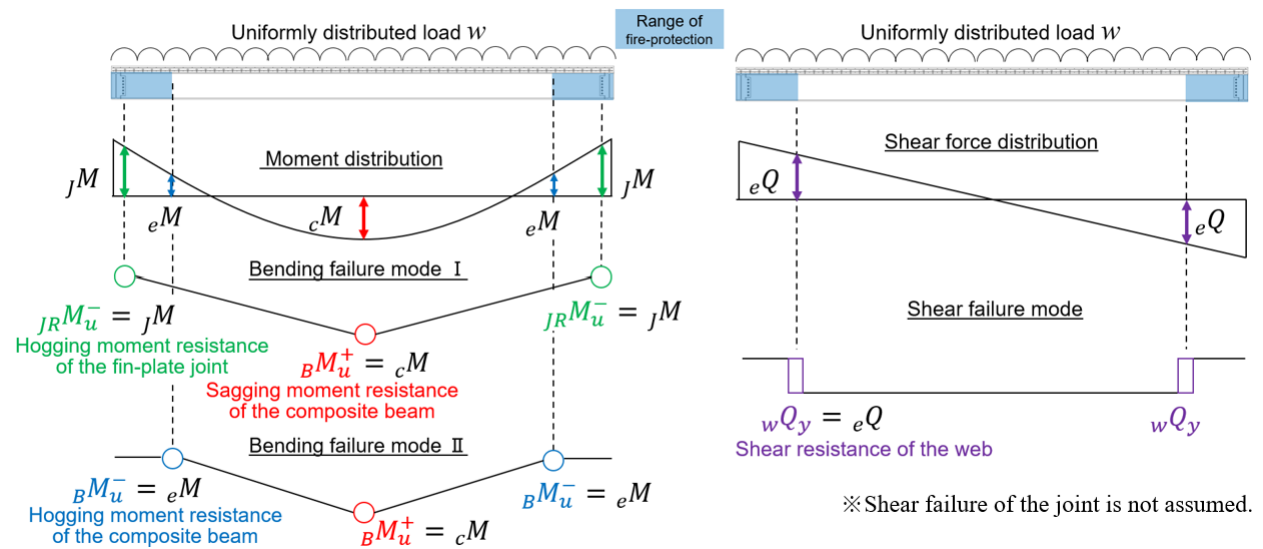


Fig.3 Assumed failure modes of the beam

### 3.2 Safety factor of moment resistance to prevent joint failure during cooling phase

It has been pointed out that there is a risk of fracture of the beam end joints due to thermal stress caused by shrinkage of the beam during the cooling phase after the fire (British Steel plc, 1999). The authors previously conducted load-bearing fire tests of unprotected composite beams connected with steel girders to examine the influence of the axial force by restraining the axial deformation (Dwiputra *et al.*, 2018). As a result, the beams continued to retain their load-bearing capacity without any fractures of joints even in the cooling phase after reaching the limiting deflection in accordance with ISO 834. Therefore, it is possible that the load-bearing capacity of the beam can be maintained during the cooling phase without fracture of the joint by ensuring that the deflection of the beam does not reach the ISO limiting deflection. According to the analysis of the test results, when the beam deflection reached the ISO limit deflection, the ratio of the bending moment to the total moment resistance at elevated temperature ranged from 0.73 to 0.92 (Yotsumoto *et al.*, 2020). For these reasons, in the present evaluation, the total moment resistance shall be reduced to 2/3 as a safety factor against the risk of fracture of the joints during the cooling phase. On the other hand, from the discussion of the shear resistance in the authors' experiments, it was confirmed that the beams did not immediately lose their load-bearing capacity even when the shear yield resistance of the beam web using the actual strength was reached. Therefore, the shear resistance shall be evaluated without considering the safety factor.

### 3.3 Strength of the materials at elevated temperature

For the strength models of the materials at elevated temperatures, the average values of the coupon test data in Japan (e.g., AIJ, 2017) shown in Figure 4 are used. Since the tensile strength data for headed studs in Japan was available only up to 800°C, the tensile strength after 800°C was extrapolated to be zero at 1200°C, referring to EC4. The compressive strength of the concrete at elevated temperature was determined by using the design compressive strength and the strength reduction factor depended on the water-binder ratio (AIJ, 2017).

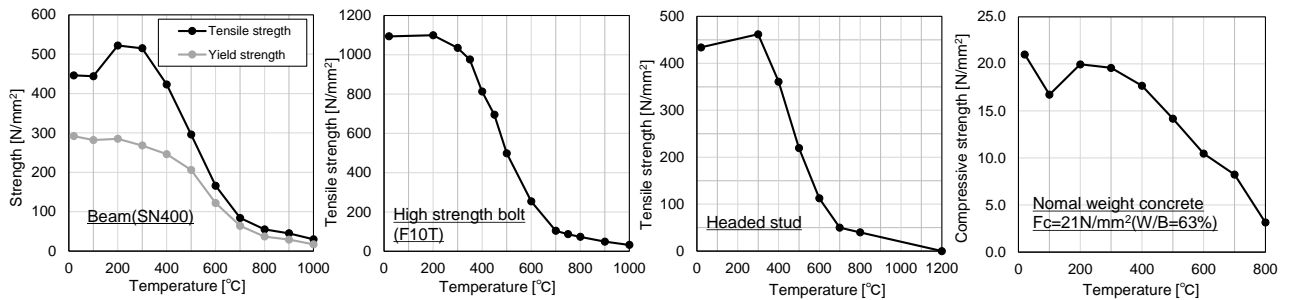


Fig.4 Strength models of the materials at elevated temperatures

## 4 RESULTS OF THE CASE STUDY

Figure 5 shows the calculated temperatures of the unprotected composite beam at the mid-span and the bolt at the fin-plate joint when a three-dimensional heat transfer model (Yotsumoto, 2020) is applied to the beam shown in Chapter 2. The temperatures in the cross-section are used to evaluate the sagging moment resistance  ${}_B M_u^+$  of the composite beam at the mid-span, the hogging moment resistance  ${}_B M_u^-$  of the composite beam and the shear yield resistance  ${}_w Q_y$  of the web at the fire-protection boundary. The bolt temperature is used to evaluate the hogging moment resistance of the fin-plate joint. Since the temperatures of the reinforcements are less than 350°C at 120 minutes and there is slight decrease in their strength, the nominal value at ambient temperature (295 N/mm<sup>2</sup>) shall be used for the yield stress of the reinforcements.

The calculated results of the shear yield resistance and the moment resistance are shown in Figures 6 and 7, and the relationship between support span (load level) and fire resistance time is shown in Figure 8. The fire resistance time is the time at which the resistance is reduced to equal the working load. The fire resistance time due to bending failure is the time when the total moment resistance multiplied by 2/3 equals the bending moment, as explained above.

As shown in Figure 8, in the case of an 11-m span (load level 63%), the fire resistance time is determined to be 36 min in bending failure mode I. The fire resistance for 60 min is satisfied for a span of 8 m (load level 33%). In the case of a 9-m span, the fire resistance time exceeded 60 min except for bending failure mode I. Although the beam depth of 600 mm is a little excessive for a span of 9 m, the fire-protection of beams may be omitted by increasing the number of bolts or otherwise improving the hogging moment resistance of the fin-plate joints.

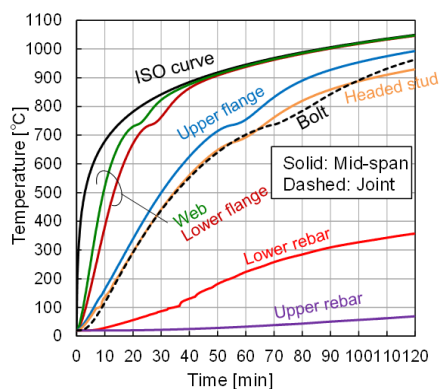


Fig.5 Temperature calculation results

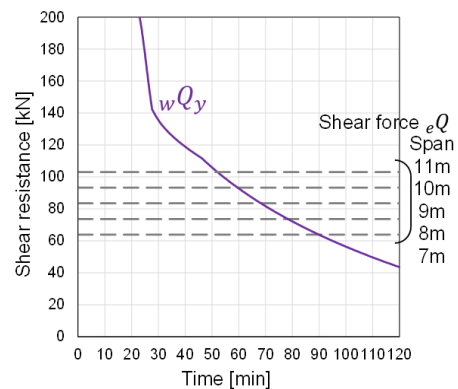
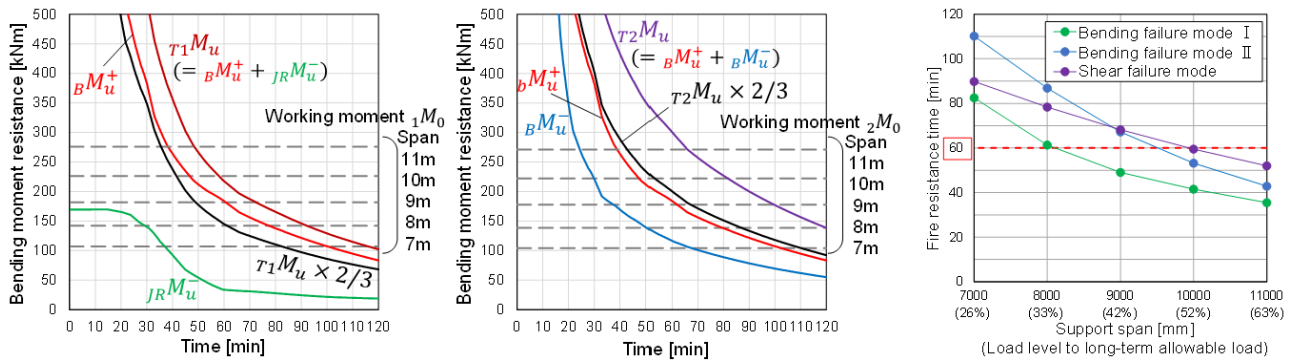


Fig.6 Shear resistance



(a) Bending failure mode I

(b) Bending failure mode II

Fig.8 Relation between span and fire resistance time

Fig.7 Bending moment resistance

Finally, the specification satisfying the 60-minute fire resistance for a span of 11 m is examined. As shown in Figure 8, the fire resistance time for any failure mode is less than 60 min for a span of 11 m. The following strategies are considered for satisfying a 60-minute fire resistance time for a span of 11 m;

- 1) improve the resistance of the fin-plate joints,
- 2) prevent the formation of plastic hinges of the composite beam at the protection boundary,
- 3) prevent the shear failure of the web at the protection boundary.

For 1), increasing the number of bolts in the fin-plate joint and suppressing the increase in bolt temperature are considered to be effective. For 2) and 3), it is effective to reduce the hogging moment and shear force working at the unprotected area by extending the range of fire-protection at the beam ends and moving the protection boundary to the mid-span. The extension of the range of fire-protection also reduces the temperature rise of the joints.

The detail near the fin-plate joint of the improved specification applying the above strategies is shown in Figure 9. The number of bolts is doubled to 6 x 2 rows, and the range of fire-protection at the beam ends is extended to 10% of the support span. This results in an 80% reduction in the amount of fire-protection compared to protecting the entire length of the beam.

The temperature of the bolts in the improved specification is shown in Figure 10. The temperature of the bolts at 60 min is about 520°C. Compared to the case of protecting only at the joints, the temperature is about 180°C lower. In addition to the effect of extending the protection range, the effect of increasing the volume (heat capacity) of the bolts and gusset plate also contributes to the suppression of the temperature rise of bolts.

The calculated results of the shear yield resistance and the moment resistance in the improved specification are shown in Figures 11 and 12, and the relationship between support span and fire resistance time is shown in Figure 13. As shown in Figure 12(a), the hogging moment resistance  $JRM_u^-$  of the joint at 60 min is improved to more than the sagging moment resistance  $BM_u^+$  at the mid-span due to the increase in the number of bolts and the suppression of temperature rise. The reason why  $JRM_u^-$  in Figure 12(a) increases from around 20 min is that the maximum strength of the joints is determined not by the shear strength of the bolts but by shear-out of the web reflecting the strength increase at 100-200°C in the tensile strength of the beam steel shown in Figure 4. Compared to the case of protecting only at the joints, for a span of 11 m, the shear force and bending moment working at the protection boundary are reduced by 16% and 30%, respectively. As a result of these improvements, the fire resistance time of the improved specification for a span of 11 m is determined to be 61 min by the bending failure mode I, as shown in Figure 13.

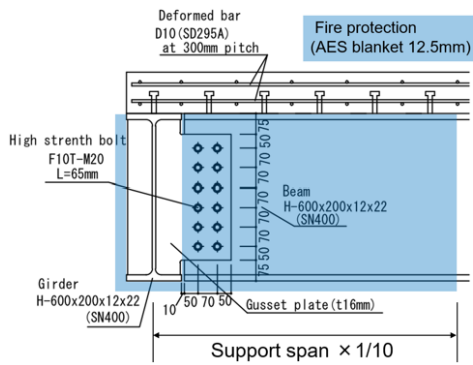


Fig.9 Detail of fin-plate joint (Improved specification)

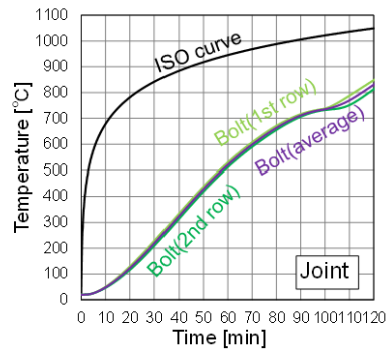


Fig.10 Temperature calculation results (Improved specification)

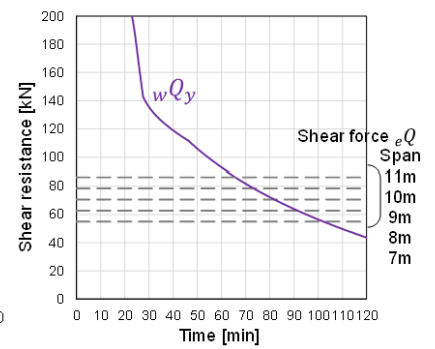
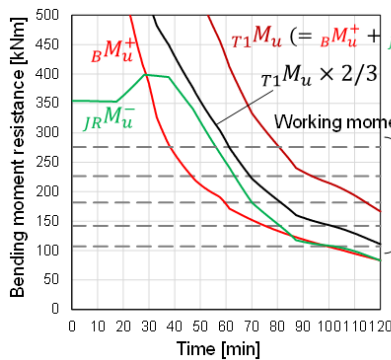
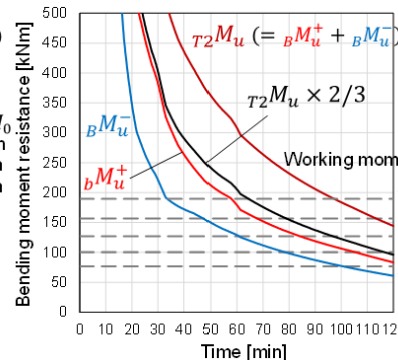


Fig.11 Shear resistance (Improved specification)



(a) Bending failure mode I



(b) Bending failure mode II

Fig.12 Bending moment resistance (Improved specification)

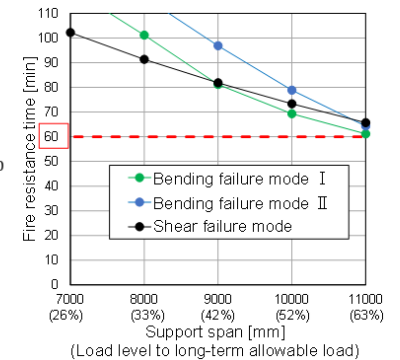


Fig.13 Relation between span and fire resistance time (Improved specification)

## 5 CONCLUSIONS

This paper presented a case study of the fire safety design of a secondary beam in an office building when applying the evaluation method for bending moment resistance of composite beams with fin-plate joints in fire proposed by the authors. As a result, the fire resistance time was evaluated to be 36 minutes for the basic specification in which the number of bolts in the joint was 6 x 1 row and only the beam end joint was protected. The case study indicated that it is necessary to improve the hogging moment resistance of the joints and to prevent shear failure and plastic hinging at the fire-protection boundary in order to achieve one-hour fire resistance. As a countermeasure to those, by doubling the number of bolts in the joints and extending the range of fire-protection at the beam ends to 10% of the span, it was shown that beams could potentially have a fire resistance for one hour.

## REFERENCES

- N. Yotsumoto, T. Hirashima, K. Toyoda, 2020. *Evaluation of the fire performance of unprotected composite beams with fin-plate joints*, *The 11<sup>th</sup> International Conference on Structures in Fire*, November 30–December 2, Brisbane, Australia, p. 101–112.
- Architectural Institute of Japan, 2017. *AIJ recommendations for Fire Resistant Design of Steel Structures* (in Japanese)
- British Steel plc, Swinden Technology Centre, 1999. *The behaviour of multi-storey steel framed buildings in fire*, A European joint research programme
- R. Dwiputra, N. Yotsumoto, T. Hirashima, F. Ozaki, Y. Murakami, K. Kimura, 2018. *Load-bearing fire tests of unprotected composite beams panned with steel girders*, *The 10<sup>th</sup> International Conference on Structures in Fire*, June 6–8, Belfast, UK, p.561–568.
- Architectural Institute of Japan, 2017. *Guide Book for Fire-Resistive Performance of Structural Materials* (in Japanese)

# **PRESSURE INCREASE IN ENCLOSURES OF STEEL DOORS AND ITS EFFECT ON THE DEFORMATION PROCESS DURING FIRE RESISTANCE TESTS**

## **A NUMERICAL STUDY**

Rene Prieler<sup>a</sup>, Bernhard Klemm<sup>a</sup>, Simon Pletzer<sup>a</sup>, Stefan Thumser<sup>b</sup>, Günther Schwabegger<sup>b</sup>,  
Christoph Hochenauer<sup>a</sup>

<sup>a</sup> Graz University of Technology, Institute of Thermal Engineering, Inffeldgasse 25/B, 8010 Graz, Austria

<sup>b</sup> IBS-Institut für Brandschutztechnik und Sicherheitsforschung GmbH, Petzoldstraße 45, 4020 Linz, Austria

### **Abstract**

Steel doors are often equipped with gypsum boards in its inner structure to enhance the thermal resistivity against a fire. This is mainly characterized by the chemically bound water in  $\text{CaSO}_4 \cdot 2 \text{H}_2\text{O}$ , which separates from gypsum due to endothermic reactions. Water is released in its gaseous form leading to an elevated pressure within the door. In the present study the effect of the pressure within the steel door's enclosure on the deformation process was numerically investigated. Besides the thermal expansion of the steel a pressure load inside was virtually applied in the simulation to address the pressure increase due to the water vapour release. In the experiment a deformation of the steel door to the fire unexposed side was detected (28 mm). However, the simulation without pressure in the enclosure showed a deformation in the other direction (fire exposed side) with about -25 mm. With increasing pressure inside the door, the predicted deformation showed a close accordance with the experimental data (30 mm in the simulation).

**Keywords:** Fire resistance test, Computation fluid dynamics, Finite element method, Steel door, Deformation

## **1 INTRODUCTION**

Fire protective elements are commonly tested and certified for a certain fire resistance level according to the standard (e.g. EN 1363-1:2012-07). For this purpose, standardized fire resistance tests are carried out, exposing the test specimen to a pre-defined fire source (time-dependent temperature trend). During such fire resistance tests, the (i) gas phase combustion in the furnace, the (ii) heat transfer through the test specimen and its (iii) deformation are in close interaction. Thus, it is clear that the simulation of all mentioned issues and interactions is leading to a computational expensive simulation approach (see Tondini et al., 2016). Nevertheless, due to the increasing computer power several authors used numerical approaches for the prediction of single issues of a fire resistance test (combustion, heat transfer or deformation) as well as some basic coupling approaches to investigate their interactions. The number of publications regarding the effect of fires in fire resistance tests on the thermal resistance and mechanical stability of test specimen by coupled CFD/FEM simulations (Computational Fluid Dynamics/Finite Element Method) is limited. The simplest coupling approach considers the gas phase combustion and the heat transfer in a coupled CFD/FEM simulation (e.g. Livkiss et al., 2017; Sandström et al., 2009). The gas phase combustion (fire) is simulated using CFD and heat fluxes to the solid structure exposed to the fire are predicted. In the following FEM simulation, the heat transfer through the test specimen is calculated. For steel structures a close accordance to measured data were found in the aforementioned studies. However, the release of volatile components from building materials, such as gypsum (water vapour) or wood (pyrolysis), can affect the heat transfer process, but were not covered by these studies. Prieler et al. (Prieler et al., 2018) proposed a methodology to cover the gas phase combustion, heat transfer in the test specimen (gypsum) and release of water vapour from gypsum into the gas phase in one CFD simulation. Further studies are not limited to the thermal

heat transfer in the test specimen, but also carried out the structural analysis using FEM simulation (e.g. Silva et al., 2016; Malendowski and Glema, 2017).

In the present study a fire safety steel door, as test specimen with gypsum boards inside, will be experimentally and numerically tested in a fire resistance test. Due to the heating process, the gypsum boards are releasing water vapour, which increases the pressure inside the steel enclosure. The numerical methodology proposed by Prieler et al. (Prieler et al., 2019; Prieler et al., 2020) will be used to predict thermal and mechanical response of a fire safety steel door exposed to the fire. In the simulation different pressures will be numerically applied within the steel enclosure to reveal the effect on the deformation of the steel door. The predicted deformation will be compared to measured data during the test. In section 4.2 the reference simulation will be presented without pressure within the steel enclosure of the door. In addition, the simulation results with over-pressure within the door will be shown and discussed in section 4.3.

## 2 EXPERIMENTAL SETUP

The fire resistance test was carried out using the testing furnace shown in Fig. 1, where the variable ceiling was fixed at a height of 4 m. Furthermore, the width of the furnace was 4.5 m and the depth was 1.25 m. During the furnace operation, which was 40 minutes in the present study, four natural gas burners are activated. The control system of the burner adapted the fuel input to achieve a pre-defined time-dependent temperature trend in the gas phase of the furnace, simulating a fire scenario. The pre-defined temperature trend as well as the standardized testing procedure of the fire resistance test can be found in EN 1363-1:2012-07. In the furnace, 12 plate thermocouples (see Fig. 1) are arranged, and the average furnace temperature was calculated based on these measurement data. The average temperature was in close accordance to the pre-defined temperature trend from EN 1363-1:2012-07. It can be seen in Fig. 1 that the deformation of the door was also observed at 9 positions marked by the black dots (“A” to “I”).

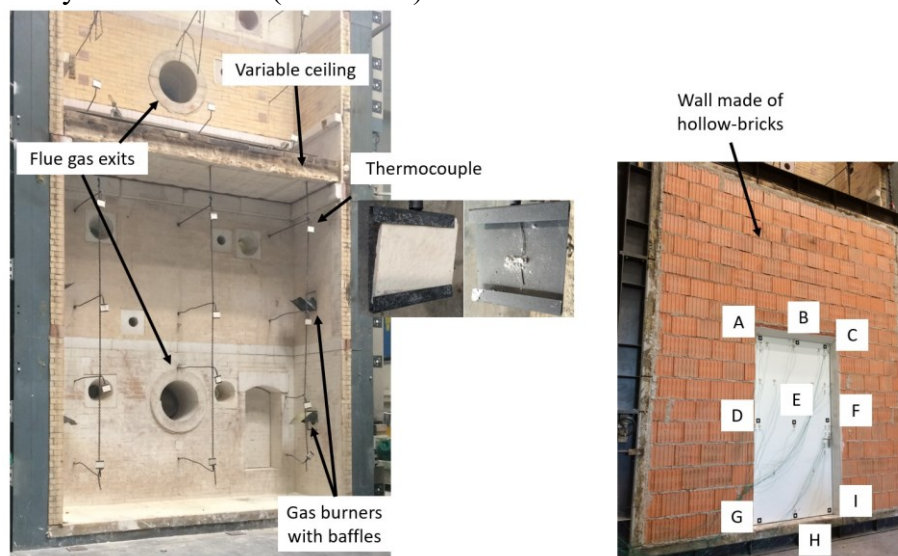


Fig. 1 Fire resistance test furnace (left) and the test specimen embedded in a wall made of bricks (right)

The fire safety steel door used in this study was also equipped with several thermocouples at the fire unexposed side. However, for the validation in the present study only the marked positions will be displayed in section 4.1 (see Fig. 2 – marked with dots). The positions “P1” and “P6” have a distance of 25 mm from the door’s edge/corner and “P2” and “P5” are arranged 100 mm from the edge/corner. Measurement position “P3” is placed in the centre of the door. The door was equipped with a gypsum board and mineral wool inside the steel casing with a total thickness of 64 mm. The other dimension of the door was 1.375 m (width) and 2.5 m (height).

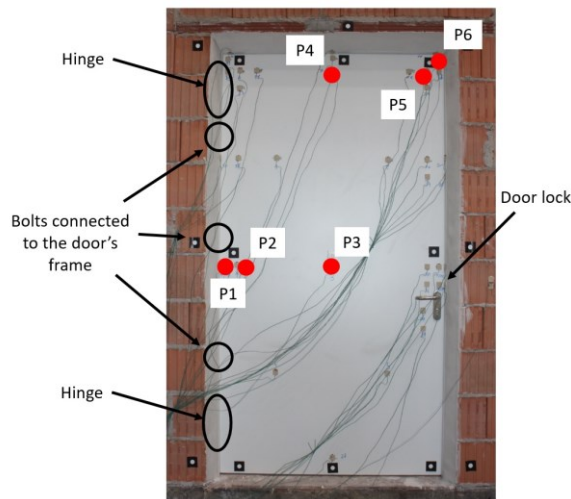


Fig. 2 Position of the thermocouples at the steel door for the comparison with the predicted data as well as the position of the hinges, bolts and door lock

### 3 NUMERICAL METHODOLOGY

The numerical methodology used to predict the fire behaviour of the door with an over-pressure inside the steel enclosure was proposed in (Prieler et al., 2019; Prieler et al., 2020) and is shown in Fig. 3. Detailed information about the combustion and radiation models in the CFD simulation, the material properties of the steel door and contact treatment between the door and the wall in the FEM simulation can be also found in these publications.

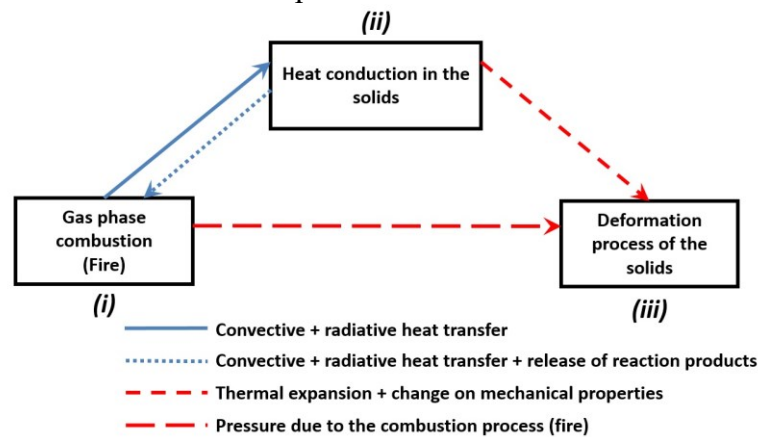


Fig. 3 Methodology for the CFD/FEM coupling

#### 3.1 Gas phase combustion and heat transfer in the test specimen (CFD)

In this methodology the CFD simulation considers the gas phase combustion in the furnace and the heat transfer in the test specimen (door), which is described in (Prieler et al., 2019). The advantage of this approach is that also the release of volatile components from the test specimen (e.g. water vapour from gypsum or combustibles from wood) and its effect on the gas phase combustion (e.g. water vapour from gypsum is cooling down the gas phase) can be simulated. This was successfully shown in Prieler et al. (Prieler et al., 2018).

#### 3.2 CFD/FEM coupling

The CFD simulation calculated the temperatures in the test specimen with high spatial and temporal resolution, thus, the thermal behaviour of the door is available for the structural analysis. Temperature data were exported from CFD for each time step and position using a developed script. The extracted data were further mapped on the numerical grid for the FEM simulation using the “profile preserving method” to ensure that the temperature profile in the door is still the same as predicted in CFD. In (Prieler et al., 2020) the entire methodology is shown in detail.

### 3.3 Structural analysis (FEM)

Since the temperature in the test specimen is available for each time step and numerical grid point due to the mapping procedure, the thermal expansion as well as the deformation during the fire resistance test can be calculated. For the FEM simulation only the steel casing was considered, caused by the assumption that the steel has the highest thermal expansion coefficient compared to the gypsum and the mineral wool inside the door. The contact between the door and the adjacent wall by the bolts, hinges and the door lock was defined as bonded contact using a Multi-Point Constraint (MPC) formulation. The other contact faces were treated as frictional contacts (augmented Lagrange method). Thus, gap formation between the door and the wall can be predicted. More details as well as the temperature-dependent material properties of steel can be found in (Prieler et al., 2020). In addition, an over-pressure up to 0.15 bar was defined inside the door to address the increasing and expanding mass of water vapour from gypsum partially trapped in the steel enclosure. In the FEM simulation the wall was assumed as rigid body.

## 4 RESULT AND DISCUSSION

### 4.1 Temperatures in the furnace and at the test specimen

The average temperature observed at all 12 plate thermocouples in the furnace is shown in Fig. 4 (left). It can be seen that the CFD model of the gas phase combustion showed a good agreement with the experimental data for the entire testing time. Furthermore, the heat transfer to the test specimen is calculated. In Fig. 4 (right) the simulated temperatures at the fire unexposed side are compared at the measurement positions. Here, a slight under-prediction at all positions can be detected. Nevertheless, the overall accordance is sufficient for the further FEM simulation.

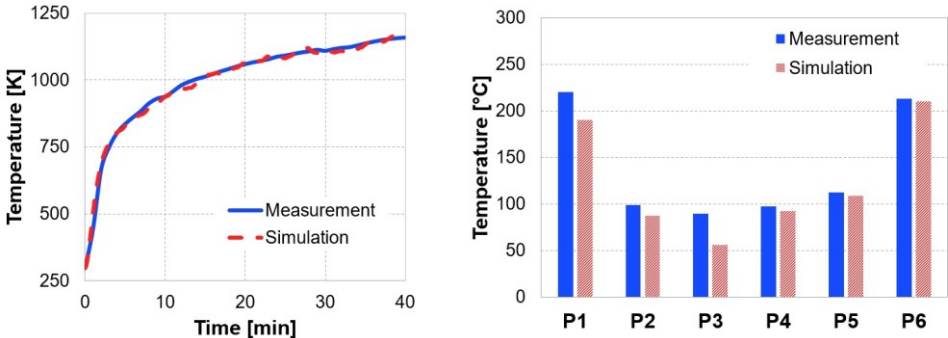


Fig. 4 Measured and simulated average furnace temperature during the fire resistance test (left) and temperatures at the fire unexposed side of the door after 40 minutes (right)

### 4.1 Deformation without in the steel enclosure of the door

In Fig. 5 the measured deformation in the middle of the upper part of the door “B” and the centre of the door “E” is shown by the blue solid line as well as the simulation result without pressure (red).

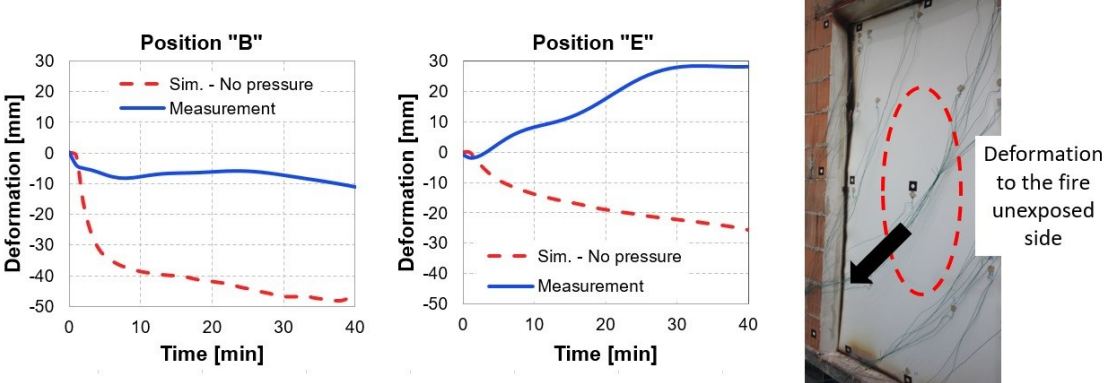


Fig. 5 Measured and simulated deformation at “B” and “E” during the fire resistance test (left, middle) and the door after 40 minutes (right)

In the charts of Fig. 5, negative values represent a deformation to the fire side. At the upper part of the door (“B”) the experiment showed a deformation of the door to the fire side with approx. -10 mm. However, the FEM simulation predicted a much higher deformation to the fire exposed side. A rapid increase was simulated up to 10 minutes leading to a final deformation of approx. -50 mm. The same results were found at the bottom of the door at “H”. In the door’s centre (position “E”) the measurement revealed that the door is deforming to the fire unexposed side due to the increase of the pressure within the steel enclosure (28 mm). In contrast, the simulation without consideration of this pressure showed a deformation to the fire exposed side with a value of -25 mm. It can be concluded that the over-pressure within the door is essential for the prediction of the test specimen’s deformation.

**4.2 Deformation with pressure in the steel enclosure of the door**

Based on the conclusion from section 4.1, an over-pressure inside the steel enclosure of 0.1 and 0.15 bar was defined. The pressure increase is constant between the beginning of the fire resistance test and 20 minutes (end of the dehydration process in the gypsum when the door was heated up). After 20 minutes the pressure was constant with the aforementioned values.

Fig. 6 displays the predicted deformation at “B” and “E” with and without pressure. At the top of the door the increasing pressure is leading to a lower deformation of the door. However, the displacement of the measurement position is still too high. This can be also observed at the corners of the door (e.g. “A”, “C”, “G” and “I”). It has to be mentioned that the wall was assumed to be rigid in the simulation and the effect of the wall deformation on the behaviour of the door could be a reason for the deviations near the wall. Although the results in the vicinity of the wall need improvement, the calculated deformation in the door’s centre (“E”) was in close accordance to the measurement. Due to the pressure inside the steel enclosure of the door, the door deforms to the fire unexposed side instead of the fire exposed side (without pressure). Best results were achieved for the door deformation with an over-pressure of 1.5 bar with a deformation of 30 mm.

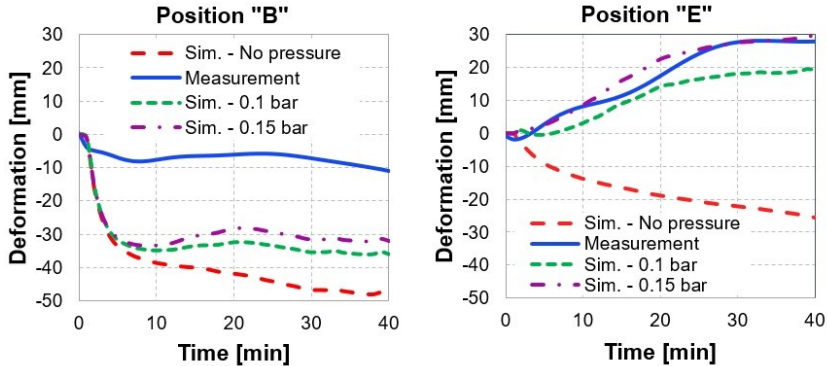


Fig. 6 Measured and simulated deformation at “B” and “E” during the fire resistance test without pressure and with a pressure of 0.1 and 0.15 bar inside the door

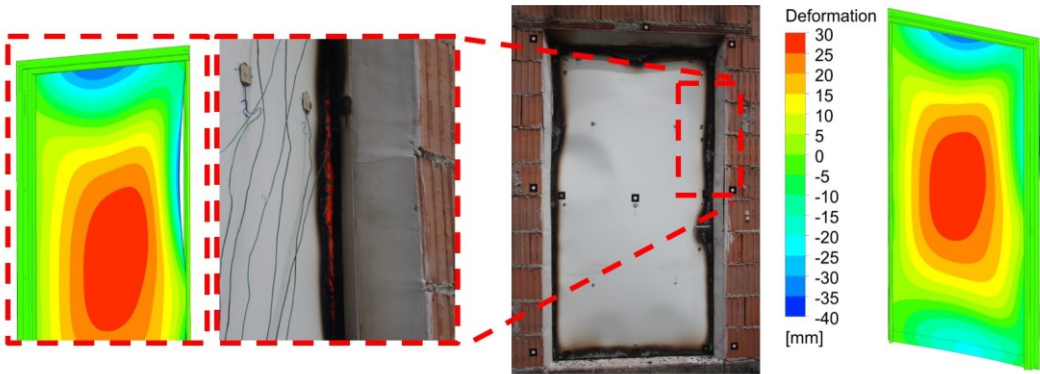


Fig. 7 Deformation of the steel door (right) and gap formation at the right hand side of the door (left) after 40 minutes testing time

The contour plot of the deformation and the deformed door after the fire resistance test is shown in Fig. 7. It can be seen that the predicted deformation of the door to the fire unexposed side is located at the door's centre, which is in close agreement to the measurement. However, the FEM simulation predicted that the deformation at the corners and upper part of the door was too high (direction to the fire exposed side). Eventually, the FEM simulation showed that gap formation between the door and the wall/door frame occurs above the door lock. This effect was also covered by the simulation as it can be seen in Fig. 7.

## 5 CONCLUSION

In the present study the effect of the pressure increase within the enclosure of a fire safety steel on its deformation was numerically investigated. The simulation results were compared to the measurement data of a fire resistance test of the same door. Based on the results the following concluding remarks can be made:

- Without pressure inside the steel enclosure, the steel door was deforming to the fire exposed side, however, the deformation of the door was in the opposite direction in the real test scenario (fire unexposed side).
- When a virtual pressure inside the steel enclosure was applied, the centre of the steel door was deforming in close accordance to the observations (to the fire unexposed side) with a maximum value of 30 mm (FEM) and 28 mm (experiment).
- The simulation was also capable to predict the gap formation between the door and the wall.
- At the corners and the upper part of the door the FEM simulation still calculated a higher deformation to the fire exposed side. This can be explained by the fact that the wall was assumed to be rigid in the simulation. For a better prediction the interaction with the wall deformation has to be considered in future studies.

## ACKNOWLEDGMENTS

This work was financially supported by the Austrian Research Promotion Agency (FFG), "Virtuelle Bauteilprüfung mittels gekoppelter CFD/FEM-Brandsimulation" (project 857075, eCall 6846234) and "Entwicklung von CFD/FEM Brandsimulationsmodellen mit Fokus auf Holz- und Gipsbauteile sowie komplexen Konstruktionen" (project 876469, eCall 28585806).

## REFERENCES

- Livkiss K., Andres B., Johansson N., van Hees P. 2017. *Uncertainties in modelling heat transfer in fire resistance tests: A case study of stone wool sandwich panels*. *Fire and Materials*, 41, p. 799-807.
- Malendowski M., Glema A. 2017. *Development and Implementation of Coupling Method for CFD-FEM Analyses of Steel Structures in Natural Fire*. *Procedia Engineering*, 172, p. 692-700.
- Prieler R., Mayrhofer M., Eichhorn-Gruber M., Schwabegger G., Hochenauer C., 2018. A numerical methodology to predict the gas/solid interaction in fire resistance tests, in *10th International Conference on Structures in Fire*, 6-8 June 2018, Belfast, UK, p. 383-390.
- Prieler R., Mayrhofer M., Eichhorn-Gruber M., Schwabegger G., Hochenauer C. 2019. *Development of a numerical approach based on coupled CFD/FEM analysis for virtual fire resistance tests—Part A: Thermal analysis of the gas phase combustion and different test specimens*. *Fire and Materials*, 43, p. 34-50.
- Prieler R., Gerhardter H., Landfahner M., Gaber C., Schluckner C., Eichhorn-Gruber M., Schwabegger G., Hochenauer C. 2019. *Development of a numerically efficient approach based on coupled CFD/FEM analysis for virtual fire resistance tests— Part B: Deformation process of a steel structure*. *Fire and Materials*, 44, p. 704-723.
- Sandström J., Wickström U., Veljkovic M., 2009. Adiabatic surface temperature – A sufficient input data for a thermal model, in *Application of Structural Fire Engineering*, 19-20 February 2009, Prague, Czech Republic, p. 102-107.
- Silva J.C.G., Landesmann A., Ribeiro F.L.B. 2016. *Fire-thermomechanical interface model for performance-based analysis of structures exposed to fire*. *Fire Safety Journal*, 83, p. 66-78.
- Tondini N., Vassart O., Lechene S., Franssen J.-M. 2016. *An integrated modelling strategy between a CFD and an FE software*. *Journal Structural Fire Engineering*, 7(3), p. 217-233.

## EXTENSION OF THE ZONE METHOD FOR THE DESIGN OF CIRCULAR CONCRETE COLUMNS SUBJECTED TO A STANDARD FIRE

David Krybus<sup>a</sup>, Marcus Achenbach<sup>b</sup>, Livia Prifti<sup>a</sup>

<sup>a</sup> RIB Engineering GmbH, Stuttgart, Germany

<sup>b</sup> LGA KdöR, Department of Design Review, Nürnberg, Germany

### Abstract

The Zone Method has been developed by Hertz as a simplified method for the design of rectangular concrete cross-sections subjected to fire suitable for a manual calculation. The cross-section is reduced by a “damaged” zone. The remaining area is modelled with the constant, temperature-dependent strength of concrete and reinforcing steel. Thermal strains are disregarded. Achenbach extends the Zone Method for the use as a nonlinear method. The temperature-dependent stress-strain curves for concrete and reinforcing steel of the Advanced Method are applied, which allows the determination of the state of strain and the calculation of deflections and inner forces of the considered member. The effect of hindered thermal strains of the compressed reinforcing steel is modelled by a reduced area of reinforcement. This proposed Extended Zone Method is verified by checking the theoretical background and is successfully validated by the recalculation of laboratory tests. In this paper, the application of the Extended Zone Method is enhanced towards circular cross-sections. The equations for the calculation of the damaged zone to model the loss of cross-section resistance or stiffness are derived. The proposed equations are validated by the recalculation of laboratory test and compared to the results of the Advanced Method. It can be shown, that the Extended Zone Method is suitable for the check of the fire resistance of circular concrete columns and leads to a safe and economic design.

**Keywords:** concrete columns, circular columns, simplified methods, zone method

## 1 INTRODUCTION

The check of the fire resistance is an essential part of the design of concrete columns and can control the area of required reinforcement. According to Eurocode 2 (EN 1992-1-2, 2004), this check can be performed by three levels of assessment:

1. tabulated values, which are restricted regarding the parameters of the column (dimensions, area of reinforcement, structural system,...),
2. simplified methods, intended for the use as a manual calculation scheme,
3. advanced methods, which can be solved by numerical methods only.

Advanced methods (AM) using the stress-strain curves and thermal properties of concrete given in Eurocode 2 are implemented in an increasing number of commercial design codes and are used by professional engineers. But the interpretation of results can be difficult and requires deep knowledge in thermal analysis, numerical methods and limits of the numerical analysis of concrete structures at elevated temperatures. A common way to validate results commonly applied by professional engineers is a cross-check using a second design code. But this can be limited, if the second code uses also the same method, in the case of fire safety engineering the Advanced Method (AM). Hence an alternative method is necessary to allow an independent check of the calculated results.

This is the motivation for Achenbach to extend the Zone Method by Hertz (1981) from a manual calculation scheme towards a nonlinear method suitable for the implementation in design software. The Extended Zone Method (EZM) by Achenbach (2018) is limited to walls or rectangular cross-sections and examinations for circular cross-sections are not yet published. Hence it is necessary to develop the theory by Hertz further and to validate the proposed equations.

## 2 EXTENDED ZONE METHOD FOR RECTANGULAR COLUMNS

### 2.1 Zone Method by Hertz

The basic idea of the Zone Method proposed by Hertz (1981) is to model the effect of the deterioration of the cross-section by means of a so-called “damaged” zone. It is assumed that the reduced cross-section can be modelled with constant material properties, which are related to the centroid  $M$ , as shown in Figure 1. Hertz assumes that thermal strains can be disregarded because they are partly recovered by transient thermal strains. He also assumes that isotherms are parallel to the surface. This allows to express the temperature dependant axial resistance of the concrete cross-section  $n_{RC,\theta}$  by a section through the centroid parallel to  $y$  for  $b < h$ :

$$n_{RC,\theta} = \int_{-\frac{b}{2}}^{\frac{b}{2}} f_{c,\theta} dy = \int_{-\frac{b}{2}}^{\frac{b}{2}} k_c(\theta) \cdot f_{ck} dy = f_{ck} \cdot k_{c,m} \cdot b. \quad (1)$$

The nonuniformly distributed concrete strength  $f_{c,\theta} = k_c(\theta) \cdot f_{ck}$  is expressed by a mean strength  $k_{c,m} \cdot f_{ck}$  with  $k_{c,m} = \int_{-\frac{b}{2}}^{\frac{b}{2}} k_c(\theta) dy / b$ . The mean strength of the cross-section is redistributed as a stress block, as indicated in Figure 1 by the introduction of a “damaged” zone:

$$n_{RC,\theta} = f_{ck} \cdot k_{c,m} \cdot b = f_{ck} \cdot k_c(\theta_M) \cdot (b - 2 \cdot a_{z,f}), \quad (2)$$

with  $a_{z,f} = b/2 \cdot (1 - k_{c,m}/k_c(\theta_M))$ .

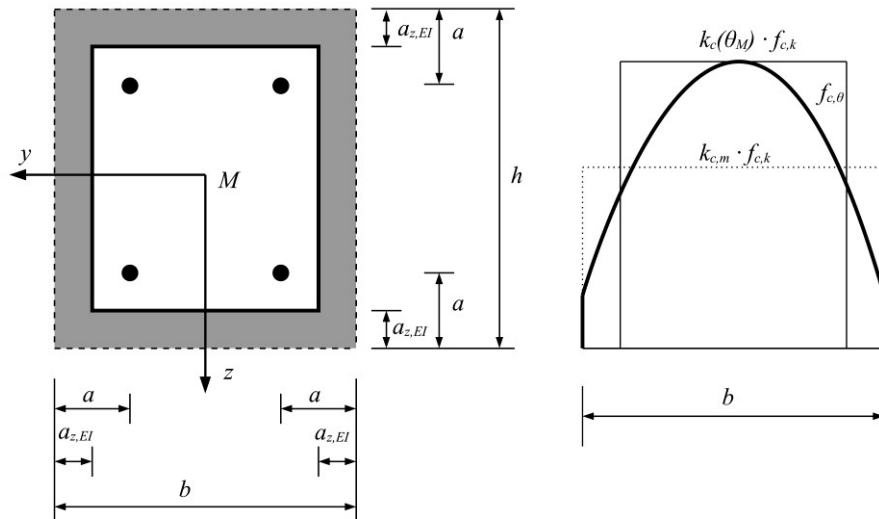


Fig. 1 Left: cross section for the Extended Zone Method, right: distributions of concrete strength at  $z = 0$

Hertz derives also formulas to model the mean loss of stiffness of the concrete cross-section and recommends using a damaged zone  $a_{z,EI}$  for compression members. To allow a calculation by hand the empiric equation

$$a_{z,EI} = \frac{b}{2} \cdot \left( 1 - \left( k_{c,m} / k_c(\theta_M) \right)^{4/3} \right) \quad (3)$$

is proposed by Hertz. The strength of the reinforcement is modelled with the strength obtained at 0.2 % proof stress. The resistance of the cross-section is described by temperature-dependent material properties and it is assumed, that every fibre can reach the necessary strain. Hence the Zone Method is a plastic design method.

## 2.2 Extended Zone Method by Achenbach

Achenbach examines the assumptions of the Zone Method by Hertz (Achenbach and Morgenthal, 2016, Achenbach, 2018) and can prove the basic idea of a reduced cross-section by comparison to the results of advanced material laws. A further development towards a nonlinear method (EN 1992-1-1, 2004) suitable for the implementation in commercial design software is proposed (Achenbach and Morgenthal, 2016). The proposal comprises the use of the temperature-dependent stress-strain curves given in Eurocode 2 (EN 1992-1-2, 2004) and the introduction of a reduction factor  $\eta_s$  for the area of the compressed reinforcement. This reduction factor is introduced to model the effect of the hindered thermal strains. The proposed Extended Zone Method (EZM) is described by the assumptions:

1. thermal strains and stresses can be disregarded,
2. the concrete cross-section is reduced by  $a_{z,EI}$ ,
3. the concrete is represented with a constant temperature  $\theta_M$  using the stress-strain curves of the Advanced Method,
4. the peak strain of the concrete  $|\varepsilon_{c1,\theta}|$  is at least 3.5 ‰,
5. the stress-strain curves of the Advanced Calculation Method are used for the reinforcement,
6. the strength of the compressed reinforcement is reduced by  $\eta_s(\theta)$ .

A value of  $\eta_s = 1$  (no reduction) is proposed for  $20\text{ °C} \leq \theta < 100\text{ °C}$  whereas  $\eta_s = 0.5$  is recommended for  $400\text{ °C} \leq \theta < 1200\text{ °C}$ . Other values can be interpolated linearly. For reinforcement under tension, the reduction factor is defined by  $\eta_s = 1.0$ . The proposed EZM is validated by the recalculation of laboratory tests (Achenbach, 2018, Achenbach et. al, 2019) and it can be shown, that the results are comparable to the results of the Advanced Method given in Eurocode 2 (EN 1992-1-2, 2004).

## 3 EXTENSION FOR CIRCULAR COLUMNS

### 3.1 Damaged zone calculation

The axial resistance of a circular cross-section displayed in Figure 2 can be obtained similarly to a rectangular cross-section:

$$n_{RC,\theta} = \int_0^{2\pi} \int_0^r f_{c,\theta} \cdot r \, dr \, d\varphi = \int_0^{2\pi} \int_0^r k_c(\theta) \cdot f_{ck} \cdot r \, dr \, d\varphi. \quad (4)$$

By the introduction of the mean strength reduction factor  $k_{c,m}$  the axial resistance writes to

$$n_{RC,\theta} = 2 \cdot \pi \cdot f_{ck} \int_0^r k_c(\theta) \cdot r \, dr = \pi \cdot r^2 \cdot k_{c,m} \cdot f_{ck}, \quad (5)$$

where

$$k_{c,m} = \frac{2 \int_0^r k_c(\theta) \cdot r \, dr}{r^2}. \quad (6)$$

The resistance of the reduced cross-section with a constant strength expressed for the temperature at the mid-point  $M$  is assumed to be equal to the resistance of the full cross-section with distributed strength:

$$n_{RC,\theta} = \pi \cdot r^2 \cdot k_{c,m} \cdot f_{ck} = \pi \cdot (\eta_f \cdot r)^2 \cdot k_c(\theta_M) \cdot f_{ck}. \quad (7)$$

The reduction factor  $\eta_f = \sqrt{k_{c,m}/k_c(\theta_M)}$  can be used for the expression of the width of a damaged zone

$$a_{z,f} = r \cdot \left( 1 - \sqrt{\frac{k_{c,m}}{k_c(\theta_M)}} \right). \quad (8)$$

The recommendation for the stiffness reduction factor given by Hertz to  $\eta_{EI} \approx \eta_f^{4/3}$  can be proved by numerical integration of the bending stiffness formula of the circular cross-section with a distributed temperature-dependent Young's modulus  $E_{c,\theta} \approx (k_c(\theta))^2 \cdot E_c$  and its comparison with the stiffness of the reduced cross-section with a constant mid-point modulus. As this applies for circular cross-sections as well, we can assume the damaged zone width for columns to model the loss of stiffness can be approximated by:

$$a_{z,EI} = r \cdot \left( 1 - \left( \frac{k_{c,m}}{k_c(\theta_M)} \right)^{2/3} \right). \quad (9)$$

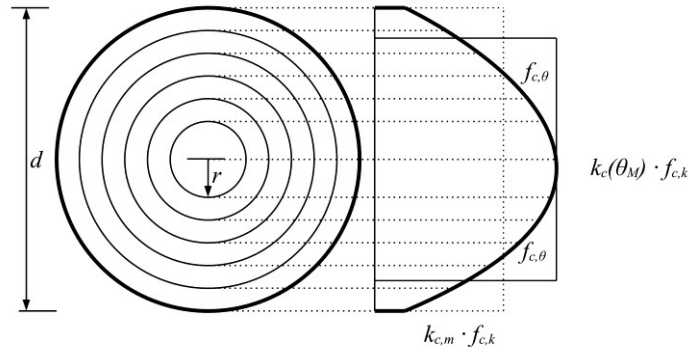


Fig. 2 Cross section of a circular column and section through the centre

### 3.2 Zone distribution

The calculation of the mean reduction coefficient  $k_{c,m}$  for a wall or a rectangular cross-section is done by the division into  $n$  parallel zones of equal thickness or into elements of equal size, according to EN 1992-1-2 (2004). For each zone or element, the mean temperature  $\theta_i$  and the corresponding strength reduction factor  $k_{c,i}(\theta_i)$  are determined. The mean reduction may be calculated by

$$k_{c,m} = \frac{1 - 0,2/n}{n} \sum_{i=1}^n k_{c,i}(\theta_i). \quad (10)$$

For the circular cross-section, two different divisions are adopted and compared. In both, the circle is divided into a set of annuli as can be seen in Figure 3.

In the first one, the width of each annulus in radial direction  $\Delta r$  is constant, similar to the constant width of a rectangular zone. For the series of  $1 \cdots n$  zones, the outer radius of an annulus  $i$  writes to

$$r_i = \frac{i}{n} \cdot r. \quad (11)$$

The second approach is based on constant area of each annulus with the outer radius of

$$r_i = \sqrt{\frac{i}{n}} \cdot r. \quad (12)$$

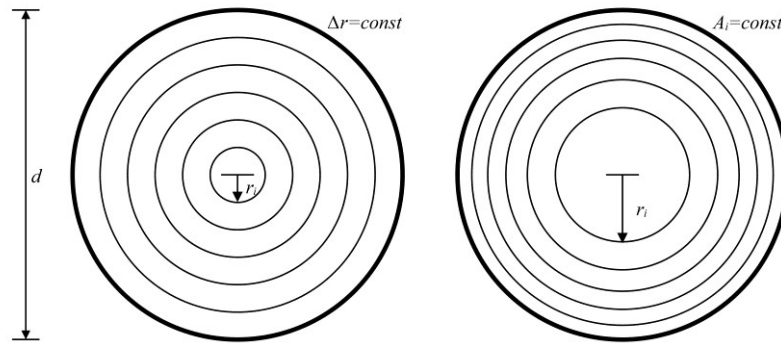


Fig. 3 Left: cross section division with constant  $\Delta r$ , right: division with constant area  $A_i$

The calculation of the damaged zone width stands on the equality of the axial strength or the stiffness of the reduced cross-section and the original one. The axial strength of the original cross-section can be approximated by the sum of strengths of particular annuli. The comparison of these approaches for several cross-section diameters and various temperatures shows a smaller difference for the method of constant area. This approach is preferred for further calculations.

#### 4 RECALCULATION OF LABORATORY TESTS

Compared to columns with a rectangular cross-section, experimental investigations of circular columns are rather rare. There are only few laboratory test results available. A small test series is carried by Franssen and Dotreppe (2003) for the comparison of the experimental results and the fire resistances calculated by simplified methods.

The test assessment is illustrated in Fig. 4. Four columns with the same diameter of 30 cm and the length of 210 cm are divided into two subsets with different reinforcement ratios. Each column is pinned, but different axial loads are imposed before subjected to the standard fire.

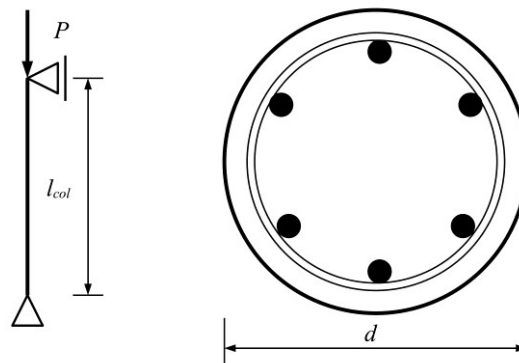


Fig. 4 Structural system and cross section of the considered laboratory tests

Experimental tests are recalculated by two different methods, namely by the Advanced Method implemented in InfoCAD (2020) and by the Extended Zone Method implemented in BEST (2021). As no measured values of material parameters are referenced, the nominal properties of the concrete, classified as C60, and the reinforcement S 500 are used. Thus, the recalculation can be regarded as a check of the safety of both methods. In both applications, a minimal load imperfection of  $l/2000$  is regarded to take uncertainties of the axial load into account.

In the temperature analysis, all columns are subjected to fire heated by the standard temperature-time curve according to EN 1991-1-2 (2004) assuming the surface emissivity of the columns  $\varepsilon_{res} = 0,7$ . The density of the concrete is considered of  $\rho = 2300 \text{ kg} \cdot \text{m}^{-3}$  and the moisture content of 3 %, as no information is given. The thermal conductivity is assumed with the lower limit function according to EN 1992-1-2 (2004). The calculated temperature distribution is the basis for the structural analysis at elevated temperatures.

Table 1 gives an overview of the input parameters of every specimen of the test series with appropriate results. The measured time of the collapse is denoted  $t_{exp}$ . The fire resistances calculated by the Advanced Method are given by  $t_{cal,AM}$  and by the Extended Zone Method by  $t_{cal,EZM}$  accordingly.

Table 1 Input parameters and results of the considered circular columns

#	$l_{col}$ [cm]	$d$ [cm]	$c_{nom}$ [mm]	$d_w$ [mm]	$f_{ck}$ [MPa]	$A_s$	$f_{yk}$ [MPa]	$P$ [kN]	$t_{exp}$ [min]	$t_{cal,AM}$ [min]	$t_{cal,EZM}$ [min]
C1	210	30	30	8	60	6Ø12	500	1260	156	143	126
C2	210	30	30	8	60	6Ø12	500	1770	131	112	97
C3	210	30	30	8	60	6Ø20	500	1450	187	144	109
C4	210	30	30	8	60	6Ø20	500	1900	163	120	91

## 5 CONCLUSIONS

It is shown that the calculated fire resistances of the 4 specimens by the Advanced Method as well as by the Extended Zone Method are shorter than the measured times, proving the safety of both methods. The Extended Zone Method is classified as a simplified method, so as expected it is slightly more conservative compared to the Advanced Method.

The enhancement of the Extended Zone Method towards circular cross-section seems to be suitable for a safe and economic fire design of circular columns. However, recalculations of further laboratory tests are necessary to validate the Extended Zone Method, as it is already done for rectangular columns. The number of presented results is not sufficient for a statistical analysis. Another option would be the verification of a set of results obtained by the Advanced Method, as it can be considered as a numerical laboratory test.

The Extended Zone Method can be easily implemented in available software programs for design at normal temperature by some relatively simple extensions. This method represents a reasonable alternative to the more complex Advanced Method for the fire design of columns at elevated temperatures and may allow a cross-check of calculated results.

## REFERENCES

- Achenbach, M., Morgenthal, G., 2016. *Extension of the Zone Method of Eurocode 2 for Reinforced Concrete Columns Subjected to Standard Fire*, Journal of Structural Fire Engineering 7: 82-96.
- Achenbach, M., 2018. *Weiterentwicklung der Zonenmethode für den Nachweis der Feuerwiderstandsdauer von rechteckigen Stahlbetondruckgliedern*, PhD Thesis, Bauhaus-Universität Weimar.
- Achenbach, M., Gernay, T., Morgenthal, G., 2019. *Quantification of model uncertainties for reinforced concrete columns subjected to fire*, Fire Safety Journal, 108.
- Baehr, H. D., Stephan, K., 1998. *Wärme- und Stoffübertragung*, 3. Auflage. Berlin: Springer.
- BEST 21.0, 2021. *Hochbaustütze*, RIB Software SE, Stuttgart
- EN 1991-1-2, 2002. *Eurocode 1: Actions on structures – Part 1-2: General actions – Actions on structures exposed to fire*.
- EN 1992-1-1, 2004. *Eurocode 2: Design of concrete structures – Part 1-1: General rules and rules for buildings*.
- EN 1992-1-2, 2004. *Eurocode 2: Design of concrete structures – Part 1-2: General rules - Structural fire design*.
- Franssen, J.-M. and Dotreppe, J.-C., 2003. *Fire Tests and Calculation Methods for Circular Concrete Columns*, Fire Technology, 39, pp. 89–97.
- Hertz, K., 1981. *Design of fire exposed concrete structures*. Report 160, Technical University of Denmark, Institute of Building Design, Lyngby.
- InfoCAD 20a, 2020. *Tragwerksanalyse für den Brandfall*, InfoGraph GmbH, Aachen

## GOZONE: A NUMERICAL MODEL FOR TRAVELLING FIRES

Antonio Gamba<sup>a</sup>, Jean-Marc Franssen<sup>b</sup>

<sup>a</sup> Liege University, UEE Department, antonio.gamba@uliege.be

<sup>b</sup> Liege University, UEE Department, jm.franssen@uliege.be

### Abstract

It has been shown that fire in large compartments tend to burn locally and to move across the floor over a period of time generating a non-uniform temperature distribution. These fires are widely known as “travelling fires” (Rein *et al.*, 2007). In this work, the framework of a new numerical model for travelling fires is briefly presented, followed by a practical case of comparison with an experimental large-scale fire test. The model is based on a zone model combined with a cellular automata model. GoZone, the software in which the model has been implemented is aimed to describe for any shape of compartment the complex dynamics of the fire from ignition, to a phase of growing localised fire that eventually may travel in the compartment, possibly followed by a flashover.

**Keywords:** Travelling Fire, Numerical Model, Fire Dynamics, GOZone

### 1 INTRODUCTION

Several studies have shown that significantly non-uniform temperature distributions are likely to appear in compartments of large size, challenging the assumption of a uniform gas temperature (B.R. Kirby, D.E. Wainman, L.N. Tomlinson, 1999). Fire in large compartments tends to burn locally and to move across the floor over a period of time, which leads to the now widely known concept of “travelling fires” (Rein *et al.*, 2007). In the last two decades, “travelling fires” have been observed in several tragic events (Dai, Welch and Usmani, 2017): in the WTC fire (U.S.A. , 2001), in Windsor Tower (Spain, 2005) and at TU Delft Architecture Faculty (Netherlands 2008). This generated a renewed interest toward the study of fire dynamics that led several researchers to propose solutions to address the travelling fire problem. Although several models have been developed for travelling fires during the past years (Clifton, 1996; Stern-Gottfried and Rein, 2012; Dai, Welch and Usmani, 2017; Rackauskaite, Hamel and Rein, 2017), limitations related to the fire dynamics and geometry of the compartment are a constant among the proposed solutions. These limitations are linked: to the strong assumption of an imposed constant fire spread velocity, to the fact that the fire is assumed to travel a priori (irrespective of fuel configuration) and to a fixed one-dimensional fire propagation. Therefore, the geometry of the compartment is limited to rectangle-based shapes. The fuel load must be uniformly distributed and the rate of heat release density  $RHR_f$  uniform, limiting the range of applicability of these solutions to very simple problems. In addition to that, the fire is considered to be in fuel-controlled conditions, which is a strong assumptions according to Dai (Dai *et al.*, 2019), considering that there are evidences of travelling fires in air-controlled conditions (B.R. Kirby, D.E. Wainman, L.N. Tomlinson, 1999). A new model for travelling fire, aimed to overcome these drawbacks, is presented in this paper as well as an application example of a travelling fire in air-controlled scenario.

### 2 GOZONE FRAMEWORK

GoZone, the software in which the model has been implemented, is aimed to describe for any shape of compartment the complex dynamics of the fire from ignition, to a phase of growing localised fire that eventually may travel in the compartment, possibly followed by a flashover. For this purpose, several sub-models were implemented and are presented in the following sections.

## 2.1 Cellular Automata and Zone model

GoZone is based on OZone, the well-known zone model developed at the university of Liege by Cadorin (Cadorin and Franssen, 2003). In zone models, the situation in the fire compartment is commonly described by the balance of mass and balance of heat in the compartment described through four or two (two-zone or one-zone) Ordinary Differential Equations (ODEs). By solving these equations each discrete time step, the zone model gets important parameters such as the smoke temperature, its evolution over time, the clear layer temperature... The code of OZone is embedded in GoZone for the evaluation of the hot smoke temperature, its evolution as a time function and the evolution of other quantities such as the temperature of the clear layer and the mass of Oxygen in the compartment.

The geometrical limitations found in the travelling fire models proposed so far in literature are overcome in the context of this work by a cellular automata concept, with a discretisation of the floor of the compartment in cells. Cellular Automata (CA) are models used to solve a wide range of problems, they have recently found application to simulate fire spreading in forest and wildland fires (Quartieri *et al.*, 2010). CA models are characterised by:

- *A physical environment*, generally made of a discrete lattice of cells, called grid in two-dimensional problems. The lattice defines the domain in which the CA is applied. In GoZone, the physical environment is represented by the fire compartment, the floor of the compartment is meshed with triangular or quadrilateral cells in a structured or unstructured manner identifying the lattice; the same discretisation is mirrored up and assigned to the lower plane of the smoke layer.
- *The cell's states*: each cell has a proper state that can change in time. The cell state is here: burning or not. Moreover, cells are characterised with properties such as fuel load density, fire growth rate, rate of heat release density and height of fuel. While cell state can be seen as an “ON or OFF” state, a cell property is a given input of the model.
- *A local transition rule*, which acts upon a cell to generate a change in state from one discrete time step to the next one. The transition rule is based on an ignition strategy, while a change in state of a cell or a group of cells from fuel-controlled (predefined) to air –controlled is governed by the combustion strategy.
- *The cells' neighbourhoods*, for each cell in the lattice there is a neighbourhood that locally influences the evolution of the cell via the transition rule. The cells neighbourhoods are all the burning cells and smoke cells provided that radiation heat transfer to the cell is not obstructed by walls (eventual internal walls or core and also external walls in non-convex compartments).

Practically speaking, the model and its input file are created through a graphical user interface coupled with GMSH, an open source 3D finite element mesh generator with a built-in CAD engine and post-processor (Geuzaine, C.; Remacle, 2009).

## 2.2 Ignition Strategy

Contrarily to what has been proposed so far in literature, the fire dynamics in GoZone is not evaluated by assigning a predefined fire velocity or fire path. Instead, it is regulated by an ignition strategy. This strategy of ignition has been developed from a material characterisation in terms of ignitability accounting for several typologies of time-varying heat flux exposures. The model is based on a critical energy of ignition, evaluated according to *Eq. (1)*. This quantity represents the minimum energy needed to be accumulated by a specific material to be ignited.

$$E_{cr} = \int_0^{t_{ign}} (q'(t) - q_{cr}) dt \quad (1)$$

where  $t_{ign}$                       time of ignition [s]  
 $q_{cr}$                                 critical heat flux [W/m<sup>2</sup>]  
 $q'$                                     heat flux contribution from smoke and burning cell [W/m<sup>2</sup>]

The term in the integral is considered only when it is positive and disregarded otherwise. The critical heat flux is assumed equal to 12.5 [kW/m<sup>2</sup>] (Spearpoint and Quintiere, 2001).

Thermal radiation is assumed to be the main mechanism governing the fire spreading (Drysdale, 2011). In GoZone, the ignition strategy is fed by two main contributions: the radiation from the hot smoke layer and the radiation from burning cells towards the unburning cells.

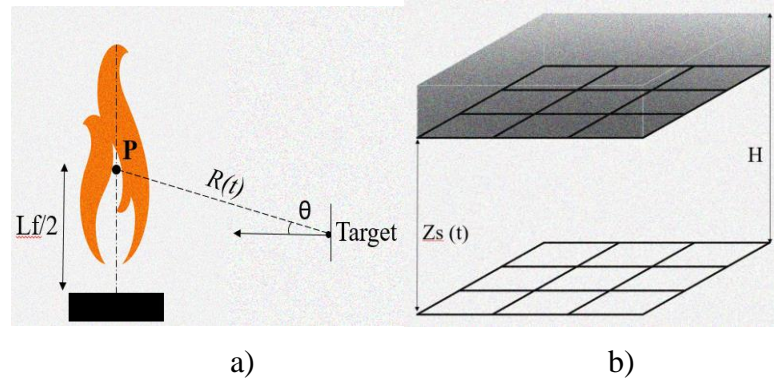


Fig. 1 Fire and Smoke to fuel radiation concept: a) Point Source Model ; b) smoke layer discretisation

Radiation from a burning cell toward a non-burning one is evaluated by using a Point Source Model (PSM) (Fig.1a). Although this is a simple model, PSM has been tested and compared with other analytical models by Fleury resulting to be an appropriate means for the evaluation of fire radiation toward a target (Fleury, Spearpoint and Fleischmann, 2011). The impinging heat flux from the fire to a target cell is evaluated according to Eq. (2):

$$q'(t) = \frac{\chi_r RHR(t)}{4\pi R(t)^2} \cos \theta(t) \left[ \frac{W}{m^2} \right] \quad (2)$$

where  $\chi_r$  radiative fraction coefficient set as 0.3 [/] (Drysdale, 2011)  
 $RHR(t)$  rate of heat released by the burning cell [W]  
 $R(t)$  distance between the point at half of the flame length and the target [m]  
 $\theta(t)$  angle between the normal of the receiving surface and the line of sight

Radiation from hot smoke toward a non-burning cell is treated assuming the smoke layer as an isothermal surface with temperature and elevation provided by the zone model (OZone). The smoke surface at its elevation is discretised by mirroring the discretisation of the floor surface (Fig.1b). The smoke cell is considered as a blackbody emitting surface ( $\epsilon_s=1$ ) and its emissive power is evaluated according to Stephan Boltzmann's law (Incropera *et al.*, 2007) Eq. (2).

$$E_s = T_s^4 \epsilon_s \sigma \left[ \frac{W}{m^2} \right] \quad (2)$$

The flux received by a fuel cell j from a smoke cell k is evaluated accounting for the view factor ( $\phi_{k,j}$ ) between the two cells (CEN- European Committee for Standardization, 2002) Eq. (3):

$$q'_{k-j} = \phi_{k,j} E_s \left[ \frac{W}{m^2} \right] \quad (3)$$

where  $E_s$  Emitting power of the smoke cell [W/m<sup>2</sup>]  
 $T_s^4$  Temperature of the smoke [K]  
 $\sigma$  Stephan Boltzmann constant [W/m<sup>2</sup>K<sup>4</sup>]

### 2.3 Combustion Strategy

When the fire starts, it is assumed to be in fuel-controlled conditions. The rate of heat released (RHR) in the burning cells within this condition follow the indication described in EN1993-1-2. Fig. (2)

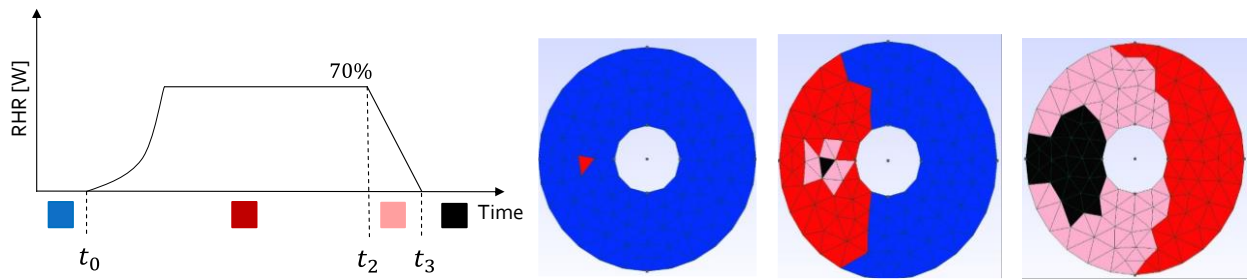


Fig. 2 Rate of heat released in fuel controlled fire scenario and colour palette

In Fig. 2, the first burning cell is an input of the problem, the RHR follows a t-square behaviour in its growing phase, until it reaches a plateau and enters in a descending phase when 70% of the fuel is burnt. During these phases the cell from red becomes pink to turn in black thereafter when it is completely burnt. In the meanwhile, GoZone with the ignition strategy, checks whether the critical energy criteria is met in the unburned cells (blue); if it is the case, they are going to be ignited (from blue to red).

Air-controlled fire strategy is linked with the mass of oxygen in the compartment evaluated according to Eq. (4):

$$m_{ox}' = m_{ox,in}' + m_{ox,out}' - 1.27m_{fi}' \quad (4)$$

where  $m_{ox}'$  mass of oxygen [kg], in /out = entering/leaving the compartment  
 $m_{fi}'$  pyrolysis rate [kg/s]

A stoichiometric combustion factor of wood equal to 1.27 has been considered for the combustion process (Drysdale, 2011).

The oxygen distribution in the compartment is assumed to be uniform according to the hypothesis of a well-steered reactor and the fire is assumed to be in fuel controlled regime as long as the oxygen content obtained by time integration of Eq. (4) is positive. When the oxygen content drops to zero, the strategy in an air-controlled regime is inspired from an extended fire duration concept, in the sense that the pyrolysis rate and the power released in the compartment are proportional to the mass of oxygen mass entering from the openings in the compartment Eq. (5):

$$RHR_{air} = \sum_i^{nb \text{ openings}} m_{fi}'(i) H_{c,e} = \frac{m_{ox,in}'(i)}{1.27} H_{c,e} \quad (5)$$

where  $m_{ox,in}'(i)$  mass of oxygen entering from i-opening [kg]  
with  $H_{c,e}$  the effective heat of combustion taken as 14 MJ/kg (CEN- European Committee for Standardization, 2002).

The fire dynamics with this solution is addressed by distributing the total power available to the cells which are closest to the opening location among those that were burning before the switch to the air-controlled regime. Ignitions of new cells and propagation of the fire during the air-controlled regime are still possible provided that the critical energy criteria is met in some cells and if the limit in terms of power given by Eq. (5) is not exceeded. This will happen typically when either breakage of new openings is detected (according to the different strategies implemented in the zone model) or if some burning cells enter in the decreasing phase. In this case, the cell among the non-burning cells which is the closest to an active opening will ignite or re-ignite first.

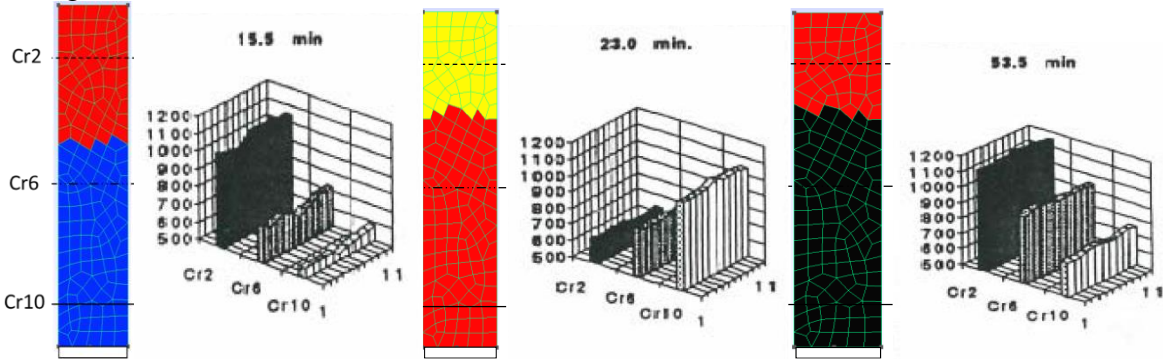
### 3 BST/STR 1993: TEST 3

The BST/FSR test series performed in 1993, better known as Gordon Cooke's fire tests, consists of nine different compartment fire tests performed in one compartment, varying fuel load, opening size and ignition methodology (B.R. Kirby, D.E. Wainman, L.N. Tomlinson, 1999). Authors observed consistently in the nine tests performed that the fire travelled from the back of the compartment toward the opening, seeking air, then once all the fuel was consumed near the opening region, the fire

travelled back again toward the ignition region. This test series is emblematic because it may be regarded as an early example of what is now termed “travelling fires” where the position of the burning zones moved and was severely influenced by the ventilation. The compartment has been modelled in GoZone with 160 unstructured quadrilateral cells of area approximately equal to 1 m<sup>2</sup>. The materials properties have been assigned according to the indication provided by the author of the test in their paper (B.R. Kirby, D.E. Wainman, L.N. Tomlinson, 1999), as well as the fuel load density to characterise the fire. However to characterise the fuel cell, GoZone needs as well the rate of heat release density and fire growth rate. These input parameters have been chosen according to the suggestion provided by Eurocode 1 part 2 where a fuel load density of 380 MJ/m<sup>2</sup> can be associated to an Hotel Room compartment according to table E.4. Therefore, rate of heat release density and fire growth rate have been chosen consistently according to table E.5. The comparison with the tests is thus made in a situation that is as close as possible to a design situation in which the fire action is not known a priori.

**3.1 Fire Dynamics comparison**

Fig. (6) shows the results in terms of fire evolution obtained in GoZone compared with the gas temperature measured during the test from left to right. The fire initially propagates slowly toward the opening (void white box), then the increasing temperature in the hot gases and the associated radiation help the fire to spread faster toward the opening. The compartment at the time of 19 minutes is completely engulfed in flames. After a few minutes, a transition to an air-controlled situation due to a lack of oxygen takes place. Cells on the opposite side of the opening depicted in yellow cannot burn due to a lack of oxygen. The air entering from the opening feeds the burning cells (red) and the fire travels from the opening to the opposite side. At time 64 minutes the fire is completely extinguished.



**3.2 Gas Temperature Comparison**

Comparisons in terms of the evolution of gas temperature, in the centre line of the compartment just above crib lines 2, 6 and 10 are shown in Fig. (7). The solid line represents the measured test gas temperature, whereas the dashed line represents the GoZone prediction.

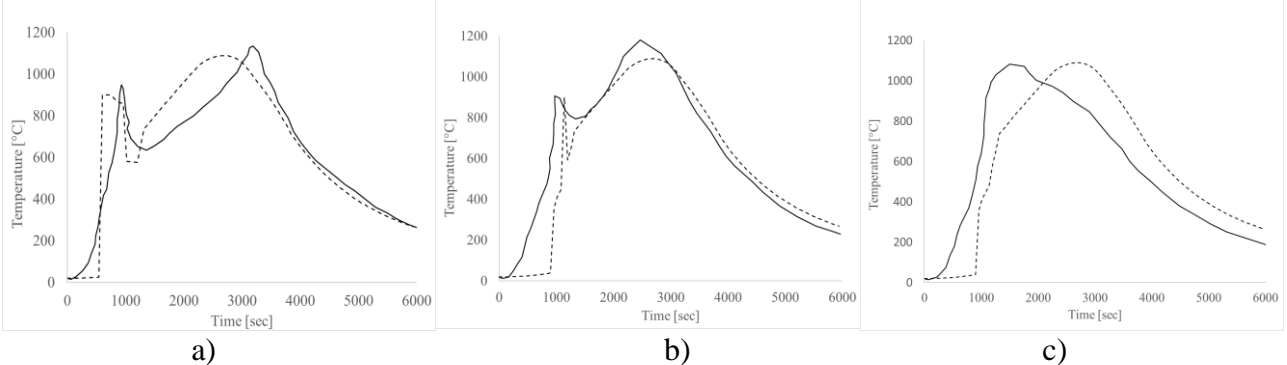


Fig. 7 Gas Temperature comparison: a) crib line 2; b) crib line 6; c) crib line 10

Figure 7a shows that the two separate peaks of temperature when the fire travels forth and back can be reproduced by GoZone a priori prediction. Furthermore GoZone correctly predicts the maximum temperature in crib line 10 that is close to the opening, see 7c. Moreover also the total duration of the fire seems to be well predicted by GoZone.

#### 4 CONCLUSIONS

A numerical model has been presented to predict the fire development in compartments. The basic idea is to combine an existing two zone model with a discretisation of the floor by mesh of triangular or quadrilateral cells of finite size, with each cell possibly having its own characteristics with regard to fire load and its own status with regard to combustion. Fire propagation is driven by radiation from burning cells as well as from the hot smoke layer. While being based on simplifying assumptions, this model proved to have the capability to predict several of the important features of the development of a fire in a compartment from ignition to flashover such as fire propagation and temperature development. GoZone has the capability to represent several features of the compartment (real shape of the plan view of the floor, real position and surface of any opening) and of the fire load characteristics (density, rate of heat release density, time constant for fire propagation, elevation above ground level, all possibly varying across the compartment, plus any position possible for the fire origin). Moreover, the run time of current problems on a laptop is in the order of a minute. This model has the ambition to occupy an empty niche between the geometry constrained analytical models presented so far for travelling fires and the more sophisticated CFD models.

#### REFERENCES

- B.R. Kirby, D.E. Wainman, L.N. Tomlinson, T. R. K. and B. N. P. (1999) 'NATURAL FIRES IN LARGE SCALE COMPARTMENTS', *International Journal on Engineering Performance-Based Fire Codes*, 1(2), pp. 43–58.
- Cadorin, J. F. and Franssen, J. M. (2003) 'A tool to design steel elements submitted to compartment fires - OZone V2. Part 1: Pre- and post-flashover compartment fire model', *Fire Safety Journal*. doi: 10.1016/S0379-7112(03)00014-6.
- CEN- European Committee for Standardization (2002) *EN 1991-1-2, Eurocode 1: Actions on structures – Part 1-2: General actions – Actions on structures exposed to fire*, CEN- European Committee for Standardization. doi: 10.1017/CBO9781107415324.004.
- Clifton, G. (1996) *Fire Models for Large Firecells*.
- Dai, X. *et al.* (2019) 'Characterising natural fires in large compartments – revisiting an early travelling fire test (BST/FRS 1993) with CFD', in: London: 15th International Interflam Conference, p. 12.
- Dai, X., Welch, S. and Usmani, A. (2017) 'A critical review of “travelling fire” scenarios for performance-based structural engineering', *Fire Safety Journal*, 91, pp. 568–578. doi: 10.1016/j.firesaf.2017.04.001.
- Drysdale, D. (2011) *An Introduction to Fire Dynamics: Third Edition, An Introduction to Fire Dynamics: Third Edition*. doi: 10.1002/9781119975465.
- Fleury, R., Spearpoint, M. and Fleischmann, C. (2011) 'EVALUATION OF THERMAL RADIATION MODELS FOR FIRE SPREAD BETWEEN OBJECTS', *PROCEEDINGS*.
- Geuzaine, C.; Remacle, J. F. (2009) 'Gmsh: a Three-Dimensional Finite Element Mesh Generator with Built-in Pre- and Post-Processing', *Facilities. Int. J. Numer. Meth. Eng.*
- Incropera, F. P. *et al.* (2007) *Fundamentals of Heat and Mass Transfer 6th Edition, Fundamentals of Heat and Mass Transfer 6th Edition*. doi: 10.1016/j.applthermaleng.2011.03.022.
- Quartieri, J. *et al.* (2010) 'A Cellular Automata model for fire spreading prediction', in *International Conference on Urban Planning and Transportation - Proceedings*.
- Rackauskaite, E., Hamel, C. and Rein, G. (2017) 'Improved travelling fires methodology - iTFM', in *Applications of Structural Fire Engineering*. Czech Technical University in Prague. doi: 10.14311/asfe.2015.063.
- Rein, G. *et al.* (2007) 'Multi-Storey Fire Analysis for High-Rise Buildings', *11th Interflam*.
- Spearpoint, M. J. and Quintiere, J. G. (2001) 'Predicting the piloted ignition of wood in the cone calorimeter using an integral model - Effect of species, grain orientation and heat flux', *Fire Safety Journal*. doi: 10.1016/S0379-7112(00)00055-2.
- Stern-Gottfried, J. and Rein, G. (2012) 'Travelling fires for structural design-Part I: Literature review', in *Fire Safety Journal*. doi: 10.1016/j.firesaf.2012.06.003.

## FE ANALYSIS OF FASTENERS EXPOSED TO FIRE: Evaluation of concrete cone capacity

Hitesh Lakhani<sup>a</sup>, Jan Hofmann<sup>a</sup>, Azime Bal<sup>a</sup>

<sup>a</sup> University of Stuttgart, Institute of Construction Materials, Stuttgart, Germany

### Abstract

The paper presents results of numerical study conducted to investigate the concrete cone capacity of single headed stud anchor ( $h_{ef} = 50$  mm), exposed to standard fire. A 3D sequentially coupled thermo-mechanical finite element analysis is performed using commercially available FE software Ansys®. The thermal properties, mechanical properties, and thermal strain, of concrete as function of temperature are taken from EN1992-1-2. Since, the investigation primarily focussed on concrete cone failure, the anchor (steel) was assumed to be linear elastic. Nevertheless, the thermal properties and thermal strains of steel are considered as per EN1993-1-2. The temperature dependent nonlinear behaviour of concrete is modelled using Menetrey-Willam plasticity model with exponential softening. One of the salient features of the model is that it uses higher order elements. Moreover, a comparison is also made between the numerical & experimental results and current design guidelines.

**Keywords:** Fasteners, Concrete cone capacity, Fire resistance, Headed stud, Thermo-mechanical analysis

### 1 INTRODUCTION

In recent years, the use of fasteners has significantly increased in construction industry. And so has the interest of researchers, in fire resistance of fasteners (Eligehausen and Fuchs, 2007). The fasteners used for structural applications should have a fire resistance equal or greater than the elements being connected. Generally, in most cases, for unprotected fasteners loaded in tension during fire, steel failure mode is decisive. But, due to the steep thermal gradients induced in concrete during fire and degradation of mechanical properties with increase in temperature, the capacities of failure modes of fasteners associated with concrete is also reduced significantly. Hence, for fasteners made of stainless steel and/or larger (bolt) sizes, concrete cone failure may be the decisive failure mode for small anchorage depths. It should also be acknowledged that there is also an increase in application of chemical fastening systems such as bonded anchors and post installed rebars in construction industry. But for such fasteners pull-out failure mode would be decisive (Lakhani and Hofmann, 2017, 2018) and should be designed accordingly (Hofmann et al., 2019a; Lakhani et al., 2020).

The fire resistance of fasteners can be estimated by using simplified design method given in informative annex of EN1992-4:2018, for cases when the fire resistance values are not given in corresponding European Technical Approvals (ETAs). The current design procedure is prescriptive in nature and is applicable only for standard fire exposures (Hofmann et al., 2019b). The EN1992-4 design guideline gives a linear reduction factor for concrete cone capacity. The reduction factor is a function of anchor embedment depth ( $h_{ef}$ ). For fire exposure up to 90 minutes the reduction factor is given by  $h_{ef}/200$ , which is further reduced in a step to  $0.8 \times h_{ef}/200$  for fire exposure between 90 to 120 minutes. Therefore, for fasteners with  $h_{ef} = 200$  mm, not influenced by edge, the concrete cone capacity is unaffected up to 90 minutes of standard fire exposure. The basis for these guidelines is the extensive numerical study conducted by Periskic (2009) on headed studs.

Simulating the behaviour of fasteners loaded in tension is very challenging, even under ambient conditions. Since it relies on the tensile capacity of concrete and the material model should be able to correctly simulate the complex mix mode fracture of concrete. The problem gets more complicated at elevated temperature due to various well know complexities associated with modelling concrete behaviour at elevated temperature. Hence, simulating the behaviour of fasteners has always been a challenging numerical problem.

The present paper discusses a 3D sequentially coupled thermo-mechanical model which can successfully solve this numerical challenge and can be used to further investigate concrete related failure modes of fasteners during fire.

## 2 NUMERICAL INVESTIGATION

To numerically analyse the behaviour of fastener under fire a sequentially coupled 3D thermomechanical analysis is performed using commercially available FE software Ansys® (Version: 2020R1). To keep the geometry simple, a headed stud with embedment depth ( $h_{ef}$ ) of 50mm, was assumed to be set in concrete with edge distance of  $4 \times h_{ef}$  in both directions. Furthermore, to optimise the problem, only one-fourth of the geometry was modelled using symmetry boundary conditions. Figure 1 shows the geometric details of the concrete volume and headed stud.

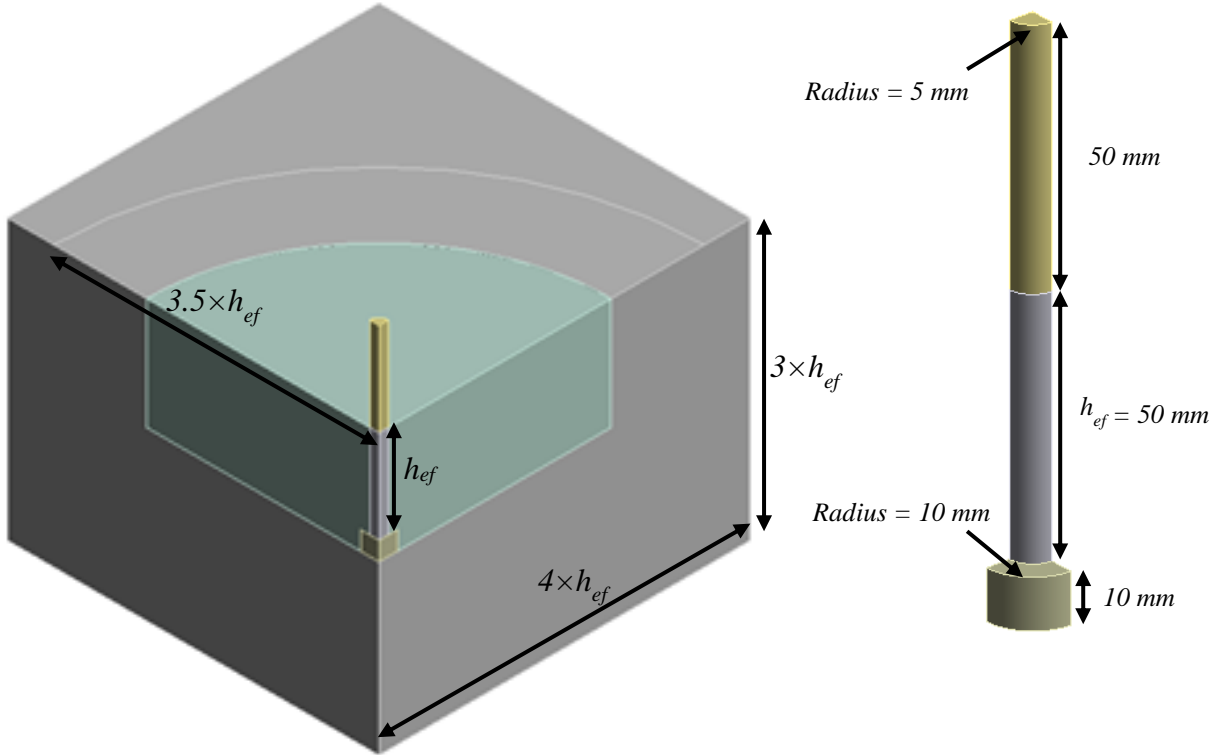


Fig. 1 Geometric details of the headed stud and the concrete volume

### 2.1 Thermal analysis

The concrete slab and headed stud were exposed to fire only from one side i.e., the side on which it was set. The fire exposure was modelled using ISO834 (ISO 834-1:1999) standard temperature time curve. The heat transfer from the surrounding hot gases to the exposed surface was modelled using radiation (emissivity=0.8) and convection (convective heat transfer coefficient = 25 W/m<sup>2</sup> K) boundary conditions. The temperature dependent density, specific heat and conductivity of concrete were taken from Eurocode2 (EN1992-1-2, 2004). Specific heat for dry concrete and lower limit conductivity were used for the simulations. The choice of thermal properties for concrete was based on the validation performed by Lakhani et. al., (2013). The temperature dependent thermal properties of steel were taken from Eurocode3 (EN1993-1-2, 2005). The contact between headed stud surface and concrete surfaces were taken as bonded for the thermal analysis. Both concrete and steel (headed stud) geometries were discretised using Solid70 element, which is a linear element with a single degree of freedom, temperature at each node.

In case of uniform fire exposure on concrete slab the heat transfer may be idealised as 1-D, thus, thermal gradients would occur only along the slab thickness. But, due to the presence of (steel) headed stud which has higher conductivity in comparison to concrete, there also exist a relatively gradual

radial thermal gradient (radiating out from the headed stud). The calculated temperature gradients along the headed stud and the depth of concrete slab away from the headed stud, are shown in fig. 2. Since, the anchor acts as a thermal bridge, it leads to reduction in temperature (of concrete) near the surface and increase the temperature at deeper points along the embedment depth.

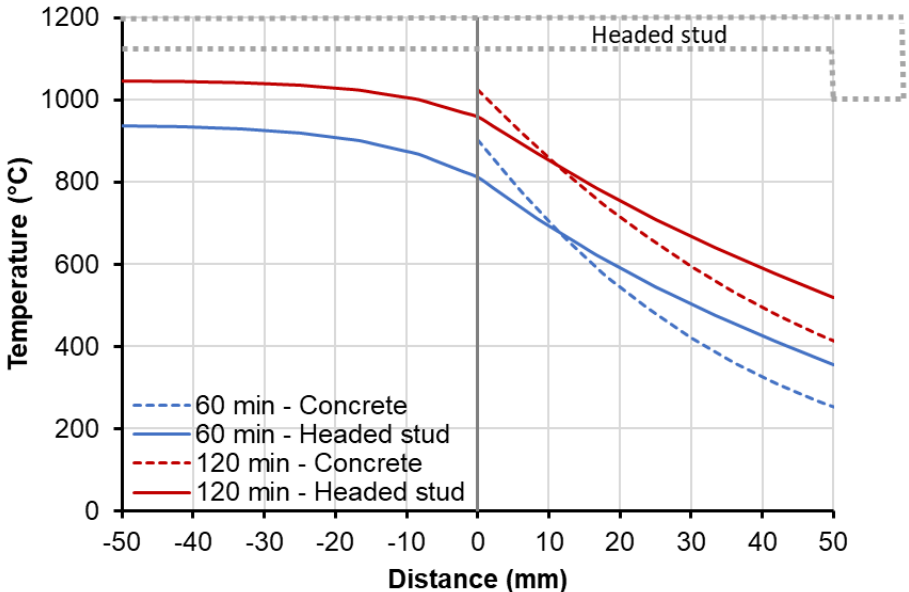


Fig. 2 Temperature variation along headed stud and concrete thickness

**2.2 Mechanical analysis**

To compute the load-deformation behaviour of headed stud at different duration of fire exposure, namely, 30, 60, 90 & 120 minutes, the nodal temperature from the thermal analysis were imported into the mechanical analysis. The headed stud is allowed to expand freely during the targeted exposure duration and there after is loaded by applying incremental displacement on the top face of the anchor. The boundary conditions applied during the mechanical analysis are shown in fig 3.

- A → symmetry along Z-axis
- B → Restrained displacements along Y-axis
- C → symmetry along X-axis
- D → Incremental displacement (loading after the 30/60/90/120 minutes of fire exposure)

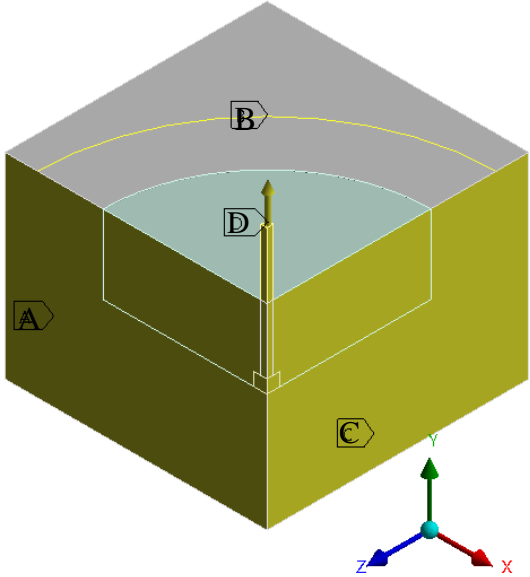


Fig. 3 Applied boundary conditions for mechanical analysis

The geometry was discretised using higher-order 3-D 10-node elements (tetrahedral elements with mid side nodes-CPT217) & 20-node (hexahedral elements with mid side nodes-CPT217) for concrete & steel, respectively. Since, in the presented study only concrete cone failure was investigated, the

steel was assumed to be linear elastic with 200000 MPa Young's modulus and 0.33 Poisson's ratio. The thermal strain for steel were taken from Eurocode3 (EN1993-1-2, 2005).

The concrete was assumed to be made of calcareous aggregates, hence, the corresponding compressive strength degradation and thermal strain from Eurocode2 (EN1992-1-2,2004) were used. The degradation in tensile strength was also taken from Eurocode2 but with slight modification for numerical reasons. Thus, the tensile strength at and above 600°C is kept constant at a value corresponding to 10% of ambient value. The following material properties were used for concrete: uniaxial compressive strength = 25 MPa, uniaxial tensile strength = 2.0 MPa, Poisson's ratio = 0.18, biaxial compressive strength = 28.75 MPa and fracture energy = 0.07 N/mm. The Menetrey-Willam plasticity model with exponential softening, available in Ansys® is used for modelling the nonlinear behaviour of concrete. The dilation angle, 28° and fracture energy were assumed to be independent of temperature. In other words, they were assumed to be same for all temperature. The uniaxial stress-strain constitute law was defined using power law until a stress level corresponding to 85% of the peak stress in the descending branch, followed by exponential softening. The concrete is assumed to be linear up to 30% of the peak stress at each temperature. The residual stress level at each temperature, beyond ultimate strain is assumed to be 20% (of correspond compressive strength) under compression and 10% (of corresponding tensile strength) under tension.

Figure 4 shows the predicted load-displacement behaviour of headed stud at 30, 60, 90 & 120 minutes of standard fire exposure. As expected, the initial displacement of the anchor before being loaded increases with increasing exposure duration but the percentage increase decreases with increasing fire duration. It can also be observed that the reduction in concrete cone capacity is significant during early phase of fire exposure. In the presented case the concrete cone capacity reduces to 53% (with reference to its capacity at ambient temperature) in 30 minutes and to 26% in 120 minutes.

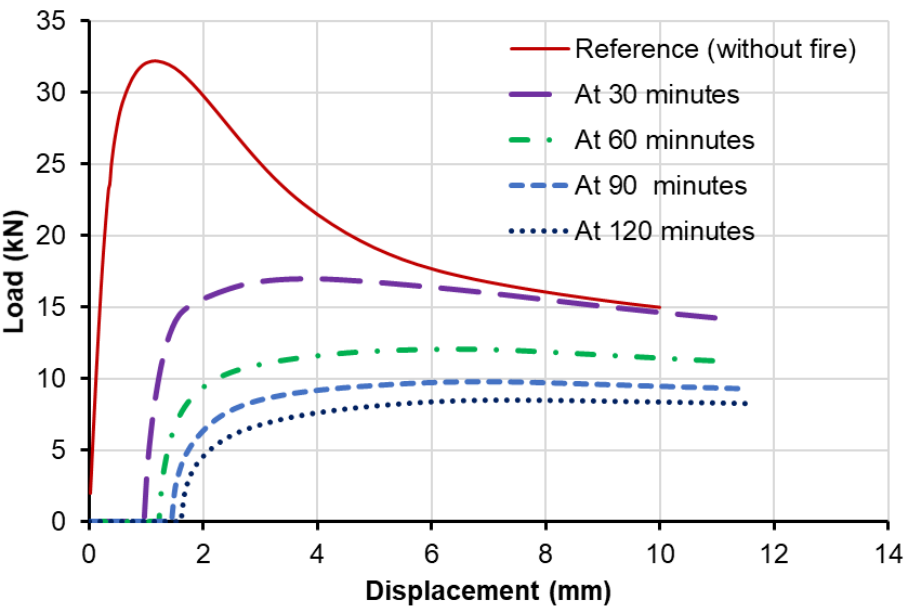


Fig. 4 Load displacement response of headed stud at different fire exposure durations

The crack pattern corresponding to the peak load at 60 minutes and 120 minutes are shown in fig. 5 (a) and (b), respectively. The principal strain contour indicted by red colour in fig 5, corresponds to a crack width greater than 0.3mm. The main crack is due to the formation of concrete cone and the secondary vertical cracks are formed due to the thermal stresses. The inclined crack near the edge of the concrete slab is due to the combined effect of the specimen geometry and thermal stresses induced due to steep thermal gradients in concrete.

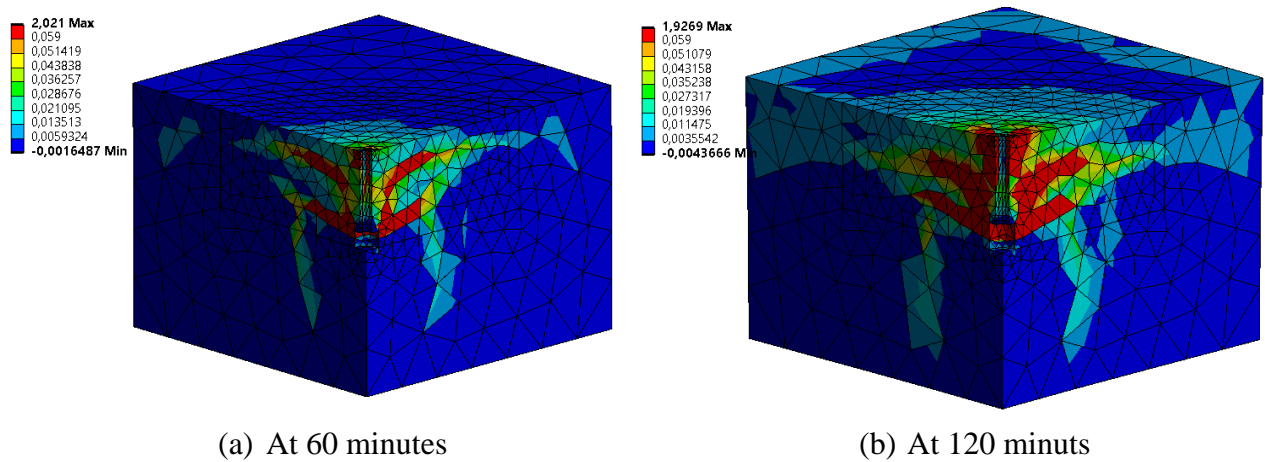


Fig. 5 Crack pattern at peak load

Furthermore, a comparison between the results obtained in the current study, experimental results from Reick, (2001) and the current design recommendations in EN1992-4, is shown in fig 6. The results predicted using the model discussing in this paper and EN1992-4 recommendations are on the conservative side but the safety margins in the design recommendations are high for fire durations less than 60 minutes.

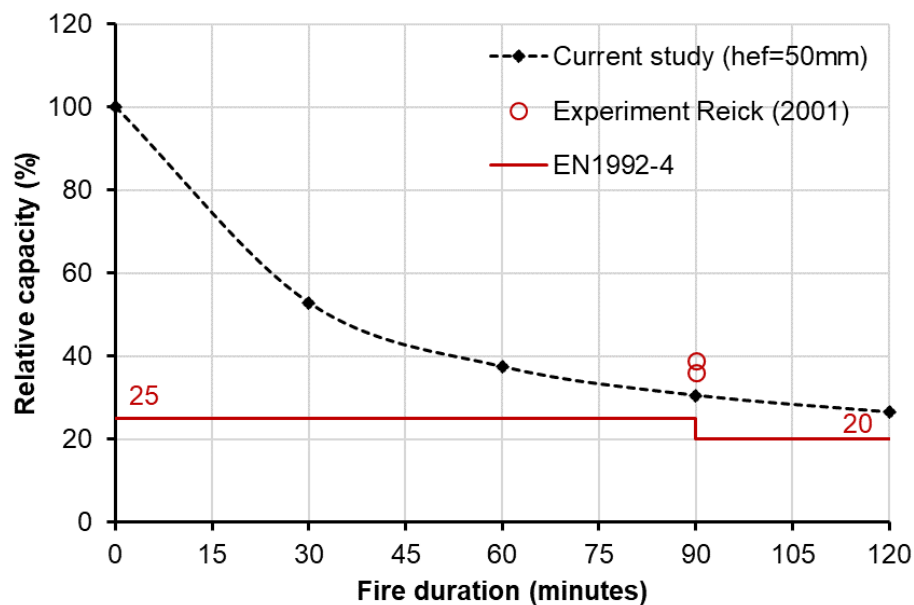


Fig. 6 Comparison between predicted, experimental and EN1992-4 concrete cone capacity

#### 4 CONCLUDING REMARKS

The paper presented a numerical study based on a 3D sequentially coupled thermo-mechanical model developed in Ansys® to investigate the concrete cone failure capacity of mechanical fasteners under fire. On the bases of the results obtained within the scope of this study the following conclusions can be drawn:

- A good comparison is obtained between the presented numerical results and (very) limited experimental results. Thus, the model can be used for further investigating the concrete related failure modes of mechanical fasteners. But, at the same time, it should be acknowledged that more experimental results are needed to further validate the numerical model.
- The recommendations of the current design guidelines are on the conservative side, but the safety margins are high for fire duration smaller than 60 minutes. Moreover, the results show that further steps at 30 & 60 minutes could be a more realistic representation of the concrete

cone capacity under fire. But once again experimental results are needed to back such recommendations.

## REFERENCES

- Ansys® Academic Research Mechanical, Release 2020 R1.
- Eligehausen, R., Fuchs, W., 2007. Recent developments and open problems in fastening technique, in: *Proceedings of the 2nd International Symposium on Connections between Steel and Concrete*. Stuttgart, Germany.
- EN1992-1-2:2004, Eurocode 2: Design of concrete structures - Part 1-2: General rules - Structural fire design. European Committee for standardization, Brussels.
- EN1992-4:2018, Eurocode 2 - Design of concrete structures - Part 4: Design of fastenings for use in concrete. European Committee for standardization, Brussels.
- EN1993-1-2:2005, Eurocode 3: design of steel structures - Part 1-2: General rules — Structural fire design. European Committee for standardization, Brussels.
- Hofmann, J., Lakhani, H., Aggarwal, J., 2019a. *Post installed rebars - Pull-out capacity during fire*. *Otto-Graf-Journal* 18.
- Hofmann, J., Lakhani, H., Periškić, G., 2019b. *Design concept for the behaviour of fasteners under fire*, in: *Commentary to EN1992-4: Design of Fastenings for Use in Concrete*. DAfStb, Berlin.
- ISO 834-1:1999, Fire-resistance tests - Elements of building construction - Part 1: General requirements. International Organization for Standardization.
- Lakhani, H., Aggarwal, J., Hofmann, J., 2020. Predicting the fire rating of cantilever slab-wall connection with post installed rebar, in: *Proceedings of the 11th International Conference on Structures in Fire (SiF2020)*. The University of Queensland, Australia, <https://doi.org/10.14264/17f73ed>
- Lakhani, H., Hofmann, J., 2018. On the pull-out capacity of post-installed bonded anchors and rebars during fire, in: *Proceedings of 10th International Conference on Structures in Fire, SiF'2018*, Belfast, United Kingdom, pp. 165–171.
- Lakhani, H., Hofmann, J., 2017. A numerical method to evaluate the pull-out strength of bonded anchors under fire, in: *Proceedings of 3rd International Symposium on Connections between Steel and Concrete*, University of Stuttgart, Stuttgart, Germany.
- Lakhani, H., Kamath, P., Bhargava, P., Sharma, U.K., Reddy, G.R., 2013. *Thermal analysis of reinforced concrete structural elements*. *Journal of Structural Fire Engineering*, 4, 227–244. <https://doi.org/10.1260/2040-2317.4.4.227>
- Periskic, G., 2009. *Entwicklung eines 3D thermo-hygro-mechanischen Modells für Beton unter Brandbeanspruchung und Anwendung auf Befestigungen unter Zuglasten*. PhD Thesis, Universität Stuttgart. (in German)
- Reick, M., 2001. *Brandverhalten von Befestigungen mit großem Randabstand in Beton bei zentrischer Zugbeanspruchung*. PhD Thesis, Universität Stuttgart. (in German)

## EXEMPLAR PERFORMANCE-BASED STRUCTURAL FIRE DESIGN OF A HIGH-RISE BUILDING

Ali Ashrafi, Ph.D., P.E.<sup>a</sup>, Jenny Sideri, Ph.D., P.E.<sup>a</sup>, Pierre Ghisbain, Ph.D., P.E.<sup>a</sup>, Reyhaneh Abbasi, Ph.D.<sup>a</sup>, Zhi Zhang, Ph.D.<sup>a</sup>

<sup>a</sup> Thornton Tomasetti, 120 Broadway, New York, NY 10271, USA

### Abstract

Performance-based structural fire design (PBSFD), as an innovative alternative to traditional prescriptive methods for structural fire protection, has been explicitly addressed in a recent publication by the American Society of Civil Engineers (ASCE, 2020), which showcases proper application and potential benefits of PBSFE through four exemplar building designs. This paper provides an overview of one of the four exemplar designs, which was a mixed-use high-rise building designed by Thornton Tomasetti (TT), and peer reviewed by four academic advisors. The exemplar high-rise design identified that a prescriptive code-compliant design might not provide the level of safety presumed by the code. By contrast, by employing PBSFD and incorporating modifications not only to fireproofing but more importantly to structural design, the design achieved improved safety, economy, and environmental impact.

**Keywords:** tall buildings, structural fire engineering, performance-based design, finite-element analysis, computational fluid dynamics

## 1 INTRODUCTION

Performance-based structural fire design (PBSFD), is an innovative alternative to traditional prescriptive methods for structural fire protection. PBSFD, when properly implemented, provides building designs that have equivalent or superior fire performance to that obtained by current prescriptive provisions. PBSFD has been explicitly addressed in two recent publications in the United States: *ASCE 7-16 Appendix E Performance-Based Design Procedures for Fire Effects on Structures* (ASCE 2016), and *Structural Fire Engineering, Manual of Practice No. 138* (ASCE 2018). A third publication: *Performance-Based Structural Fire Engineering, Exemplar Designs of Four Regionally Diverse Buildings using ASCE 7-16, Appendix E* (ASCE 2020), which was released in 2020 by ASCE's Structural Engineering Institute and sponsored by the Charles Pankow Foundation, showcases proper application and potential benefits of PBSFD through four exemplar building designs. These were steel buildings of different occupancies, heights, and locations within the US. Each design was developed by leading structural engineering firms and all designs were peer reviewed by a panel of four academic advisors.

This paper provides an overview of the mixed-use high-rise exemplar building located in the Midwest of USA and designed by Thornton Tomasetti (TT). The exemplar high-rise design identified that a prescriptive code-compliant design might not provide the level of safety presumed by the code. By contrast, by employing PBSFE and incorporating modifications to structural design in addition to fireproofing, the design achieved improved safety, economy, and environmental impact. Furthermore, it was shown that such benefits were not achievable in this case by only modifying the fireproofing without structural modifications.

## 2 BUILDING DESCRIPTION

The building is a previously completed Risk Category III real project, type I-A, mixed-use, 50-story-tall building (Fig. 1), which was built in the mid-2010s and located in the Midwest of USA. The building design is generic and representative of a common type of modern high-rise building design in the United States. The building is comprised of two distinct structural systems; the 20 upper floors are residential floors with concrete columns and two separate concrete cores to resist lateral loads. The 30 lower floors are office floors with steel perimeter columns, steel

beams, and a single larger concrete core to resist lateral loads. The transition between the upper and lower structural systems is achieved by several interconnected steel transfer trusses located at the 30th floor. The trusses transfer loads from a denser column spacing in the upper residential floors to a wider column spacing in the lower office floors. The construction type of the building per the applicable building code prescriptively requires the primary and secondary members to have a 3 h and 2 h fire resistance rating, respectively, except the roof is permitted to have a 1-1/2 h fire resistance rating. Two features of the building are considered for PBSFD: a typical bay of the steel frame of the 30 lower floors, and the transfer trusses as a unique structural feature of the building.

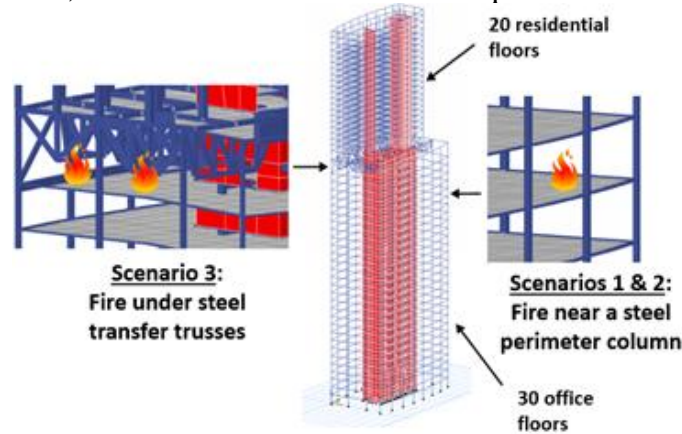


Fig. 1 Building geometry and fire scenario locations considered for PBSFD

### 3 DESIGN STRATEGY

A series of design scenarios were developed, ranging from minimal to highest impact implementation of PBSFD on the building's structural design.

- Design 0 corresponds to prescriptive requirements for fireproofing (indeterminate performance).
- Design 1 corresponds to applying the amount of fireproofing needed to ensure safe occupant evacuation outside the building or refuge areas, while the structure is able to support refuge areas without collapse until fire burnout (minimum performance). This design is not applicable to the high-rise building described herein, as the entire structure must not collapse in order to meet this evacuation requirement.
- Design 2 corresponds to applying the amount of fireproofing needed to ensure the structure can withstand fire burnout without any collapse. This is an engineered PBSFD approach with the ability to modify fireproofing but not the structural system (optimum performance). For the building design described in this paper, Design 2 was not possible to achieve because, for the typical bay of the steel frame at the lower 30 office floors, the connection demands could not be accommodated by only adjusting fireproofing without modifying the connections. This demonstrates that a prescriptive code-compliant design might not provide the level of safety presumed by the code.
- Design 3 corresponds to applying the amount of fireproofing needed and performing structural modifications to ensure the structure can withstand fire burnout without any collapse. This is an engineered PBSFD approach with the ability to modify both the fireproofing and the structural system (optimum performance). In this case, the structural fire engineer can influence the structural design to achieve the desired level of performance, while maximizing the benefits of PBSFD including improved safety, economy, and environmental impact. For this particular building, Design 3 was developed for the typical bay and Designs 2 and 3 were similar for the transfer trusses.

### 4 STRUCTURAL DESIGN FIRE SCENARIOS

The choice of design fuel load has a significant impact on the structural responds in fire, and the designer should consider several factors such AHJ requirements, likelihood and intensity of a

severe fire and space compartmentalization. This building was designed with both characteristic fuel loads of 511 MJ/m<sup>2</sup> and 656 MJ/m<sup>2</sup>, corresponding to 80% and 95% fractile for office occupancy as given in Eurocode 1, Annex E. No reduction was considered for any of the fire detection or suppression methods, except that the sprinkler reduction factor was considered for the 80% fractile scenario. The area under transfer trusses is a mechanical space, with a tightly defined description of its content. For this building study, a conservative fuel load similar to the office load was considered.

The structural design fire scenarios were defined in the context of effective temperature time histories acting on the structure. Both localized and compartment fires were considered. Compartment fires were modeled using the parametric temperature–time curve methodology of Annex A in Eurocode 1. Since opening factor significantly affects the duration, shape and peak temperature of compartment fires, several fire scenarios were explored by varying the opening size (and hence the opening factor) to obtain critical but realistic fire scenarios. **Figure 2a** illustrates an intense localized fire (Fire Scenario 1) originating from a workstation near a perimeter steel column of the typical bay, simulated in the Fire Dynamics Simulator (FDS). **Figure 2b** illustrates the compartment fire scenarios for typical bay (2A and 3B), and for the transfer trusses (3A and 3B). Fire scenarios 2A and 3A correspond to the 95% fractile design fuel load, without reduction due to sprinklers, and the lowest realistic opening factor, resulting in more intense fires consistent with a building with minimal openings in a more conservative regulatory environment. Fire scenarios 2B and 3B correspond to the 85% fractile design load, with reduction due to sprinklers, and a higher opening factor, resulting in less intense fires consistent with a more modern building with more openings in a less conservative regulatory environment. More detailed information on the design fire scenarios can be found in ASCE, 2020.

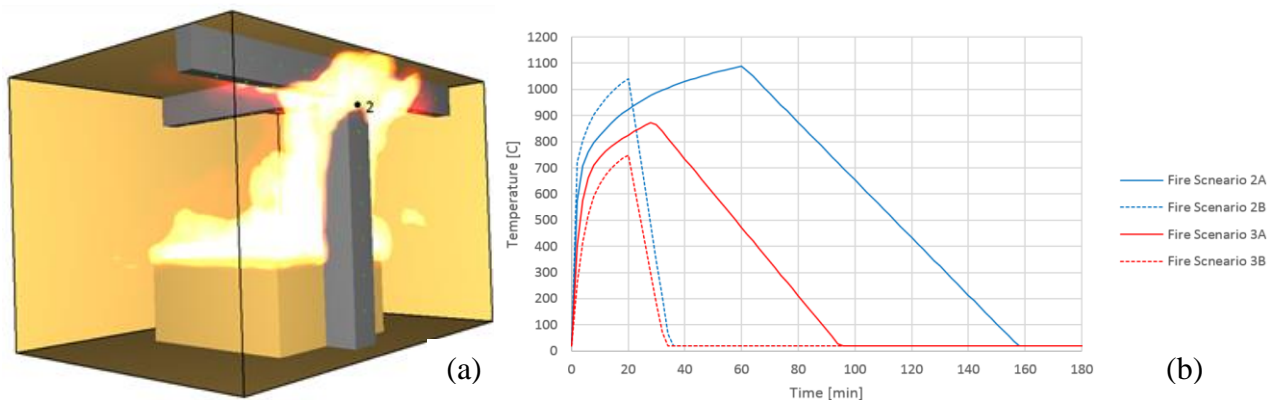


Fig. 2 a) FDS model for localized Fire Scenario 1 at typical bay, and b) compartment fires for typical bay (Fire Scenarios 2A and 2B) and transfer trusses (Fire Scenarios 3A and 3B)

## 5 ANALYSIS & DESIGN ITERATIONS

### 5.1 Typical Bay

The general purpose finite element software Abaqus was used to simulate a 3D model of a typical beam-slab-column subassembly, in which the impact of connections on the complex structural behavior was considered (**Figure 3a**). The model includes three wide-flange primary steel beams with equivalent concrete slab strips to account for their composite action, a wide-flange exterior steel column and shear tab plates representing the connections between beams and column. All members were modeled with 4-node composite layer shell elements that can model local failure modes (e.g. web or flange local buckling) and can be easily modified to change the fireproofing thickness. Temperature-dependent thermal and mechanical properties for steel and concrete material were defined according to Eurocode 3. More details about the model, including information on how the connections were considered, and the model's limitations, can be found in ASCE, 2020. Heat transfer and structural analysis were performed in Abaqus to capture the

response of the structural system under Fire Scenarios 1, 2A, and 2B. Spatial variability of heating was considered in the 3D space for Fire Scenario 1, where adiabatic surface temperatures were mapped from the FDS model, while uniform temperature time-histories were applied on the members as convection and radiation interactions for Fire Scenarios 2A and 2B. The model was first subjected to gravity loads per the extreme event load combination of ASCE 7-16, 2016, and subsequently subjected to temperature time histories mapped from the previous heat transfer analysis.

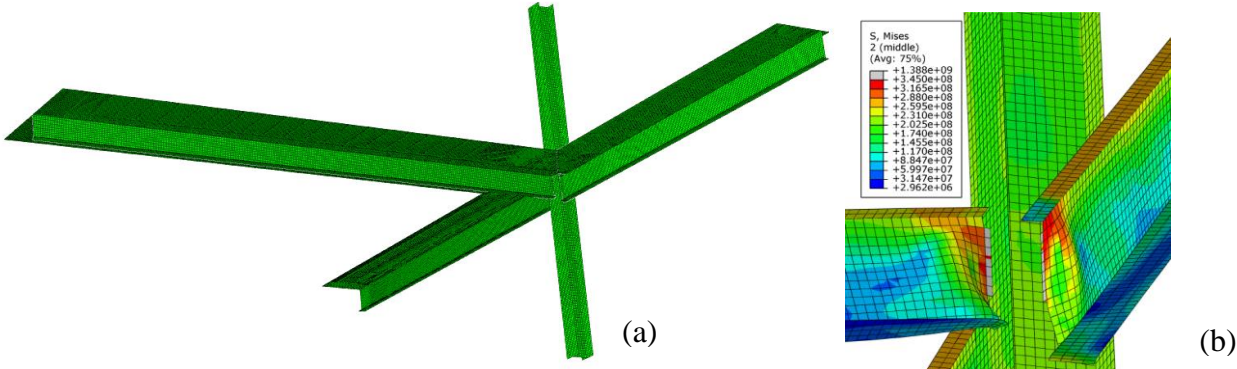


Fig. 3 a) Abaqus 3D model at typical bay, and b) contact between beam bottom flange and lower web with column flange, for Fire Scenario 2A and 2-h fire rated members

Design iterations were performed for all fire scenarios and with beams’ and column’s fireproofing corresponding to 1-hr, 2-hr and 3-hr fire rating. Analysis results were presented as time-histories in terms of section cut forces of slabs at interior beam midspan plotted against concrete capacity (reduced per elevated temperatures), interior beam sag (vertical displacement), and steel temperature at interior beam’s web column’s flange. ASCE, 2020, also describes in detail the complex behavior of the connections, including the evolution in time of contact forces between the interior beam’s bottom flange/lower web and column, contact forces between the concrete slab and column, and section cut forces at the shear tab locations. An example contact scenario is depicted in **Figure 3b** from two different angles, which occurs at  $t = 6,900$  s for Fire Scenario 2A and 2-h rated members, along with Von Mises stress contours on the steel. In this figure, the bottom flange and the lower web of both beams are in full contact with the adjacent column, whereas local buckling is observed at the beams’ ends.

**5.2 Transfer Trusses**

The finite element software SAFIR, which specializes in structural analysis in fire, was used to simulate a 3D model of the upper 20 concrete stories of the building as well as the steel transfer trusses (**Figure 4a**). The two-way flat slab system was approximated by equivalent slab strips defined according to the ACI 318 provisions. At the transfer level, in which the top chords of the trusses are encased in the slab, the slab system was approximated by T-beams defined according to the ACI 318 provisions. The steel members and the slab strips were modeled as beam elements. For the transfer trusses, only Design 2 was considered, when fireproofing can be adjusted, as long as the structural frame does not collapse after burnout. Design 3 is considered similar to Design 2 because structural modifications do not provide a more efficient way of achieving the performance goals. For each of the Fire scenarios 3A and 3B, several heat transfer and structural analyses were performed with different fireproofing thicknesses applied to the transfer truss members. After each analysis, any member or system failure and the demand-to-capacity ratios of the still-intact steel and concrete members were reviewed to analyze the impact of the selected fireproofing. Member or system failure typically included global buckling of perimeter truss members, followed by load redistribution that prevented collapse or multiple truss member buckling followed by collapse, depending on the fire scenario and fireproofing thicknesses applied. Example 2D heat transfer analysis results are illustrated in **Figure 4b**.

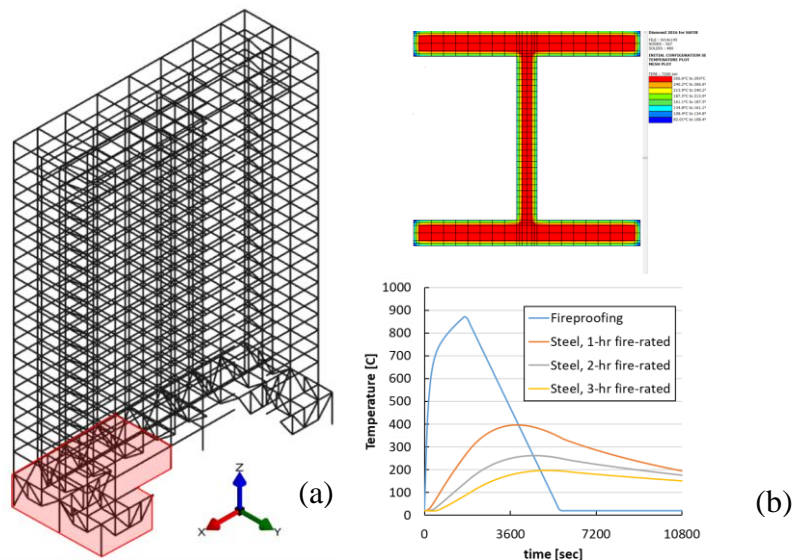


Fig. 4 a) SAFIR 3D model of 20 upper floors and transfer trusses (fire scenarios applied in compartment shown in red) and b) SAFID 2D model of a transfer truss member at  $t = 7,200$  s, protected with a 1-h fire rating, and section web temperature time histories for different fire ratings.

## 6 DESIGN SUMMARY

### 6.1 Typical Bay

For the typical floor framing, Design 2 was considered including the maximum fireproofing thickness for beams according to the applicable UL design, regardless of how a beam is classified. Nonetheless, connection demands were large enough to require that connections be changed to provide more strength or deformation capacity. Hence, Design 2 was not achievable. For Design 3, connections were changed by providing slots that can accommodate the movements resulting from the structural response to fire. The primary beam connections were designed as slip-critical so that in ambient conditions the bolts do not slip and the connections can provide adequate bracing to the columns, while in fire conditions the bolts can slide to relieve thermal forces and also adequately sustain gravity and column bracing loads. The option of providing increased connection capacity was not selected as it required substantial strengthening of the connections and sometimes the columns. The secondary beam connections were designed with slots and finger-tight bolts to accommodate the movement because of structural response to fire and to prevent imposition of large weak axis bending and torsional loads on spandrels. For all connections, additional fireproofing was provided locally to limit the reduction of their capacities, particularly the bolts during fire. Beam behavior was checked through capturing steel plasticity and buckling explicitly in the model and checking concrete forces against capacity, accounting for thermal changes in properties of steel and concrete. The beams remained capable of carrying the loads with fireproofing reduced to 2-h rating for Fire Scenario 2A, and 1-h rating for Fire Scenario 2B. Additional fireproofing at connections offset some of these reductions, resulting in a total fireproofing change in the beams of +7% in Fire Scenario 2A and -41% in Fire Scenario 2B. The columns (gravity only) were checked for their ability to carry their loads when deformed as a result of the thermal expansion. Columns showed adequate reserve capacity to survive with lower fireproofing by 38%. Additional bending demand on the columns owing to thermal push was acceptable, as a plastic hinge did not compromise the load carrying capacity. The adequacy of the column to carry the loads at the offset due to thermal expansion was verified. The typical slab is a lightweight concrete slab on top of a metal deck with wire mesh reinforcement. The metal deck was unprotected in Design 0 and remained unprotected in Design 3. The wire mesh was relied on to develop catenary action in the direction of the metal deck during a fire, as the exposed metal deck would rapidly lose capacity during a fire. The strength of the wire mesh was limited by the partial lap typically used, which could only transfer 50% of the tensile capacity of the mesh. It was found

that slab deflections resulting from catenary action (11.1” for Fire Scenario 2A and 9.2” for Fire Scenario 2B, which were acceptable given the other large deflections of the steel framing during fire) could be significantly lowered (5.2” for Fire Scenario 2A and 4.7” for Fire Scenario 2B) by doubling the wire mesh laps and mobilizing 100% of the mesh in tension.

## 6.2 Transfer Trusses

For the transfer trusses, Design 2 involves changes to the fireproofing to achieve burnout capacity. Because the response of the transfer trusses to fire can affect all the upper supported floors, Design 2 was provided with several options, all of which satisfy the performance criteria, but with different extent of impacts on the upper floors (ASCE, 2020). The design team would select one of these designs based on the building owner’s preferences. For Design 3, the design team has the option of modifying the structure to achieve the same performance. The failure mode in the trusses was buckling of structural members, and the solution could be a combination of providing additional strength, or additional fireproofing. Providing additional fireproofing locally has limited additional cost and is the most straightforward solution. Unlike typical areas in a structure, the alternative solution of creating alternative load paths is not reasonable for the transfer trusses, which are main structural features of the building. Hence, Design 3 is the same as Design 2.

## 7 CONCLUSIONS

The large range of building performances obtained when considering the full design space for the same building highlights the limitations of a prescriptive approach in providing a solution that is specific to a project and meets the appropriate performance goals. The presented design example has identified deficiencies of the prescriptive code when a code compliant design might not perform adequately for structural safety or adequately limit the extent of damage. Many circumstances in which PBSFD can reduce the fireproofing needs of a structure while achieving the required safety goals have also been identified. Being a rational design approach that explicitly studies the parameters of the design space and adjusts them based on their impact, PBSFD allows for achieving better safety and performance for the same cost, or better economy for the same performance and safety. In addition, PBSFD helps quantify the expected behavior of buildings during fire, allowing for informed decisions and reliable performance. Within the context of PBSFD, this analysis also showed that just being able to adjust the fireproofing has its limitations and cannot always result in a satisfactory outcome, even when it can improve performance in comparison with the prescriptive design. Only the incorporation of modifications to structural design in addition to fireproofing provides the designer with all the tools required to achieve performance goals for the buildings considering their specific features.

## REFERENCES

- American Society of Civil Engineers, ASCE 7-16, 2016. *Appendix E, Performance-Based Design Procedures for Fire Effects on Structures*.
- American Society of Civil Engineers, 2018. *Structural Fire Engineering, Manual of Practice No. 138*.
- American Society of Civil Engineers, 2020. *Performance-Based Structural Fire Engineering, Exemplar Designs of Four Regionally Diverse Buildings using ASCE 7-16, Appendix E*.
- ACI 318-19, 2019. *Building Code Requirements for Structural Concrete and Commentary*. American Concrete Institute.
- Dassault Systèmes Simulia Corp. 2011. Abaqus software. Johnston, RI: Dassault Systèmes Simulia Corp.
- EN 1991-1-2, 2002. *Eurocode 1: Actions on Structures—Part 1–2: General Actions—Actions on Structures Exposed to Fire*. British Standards Institute.
- EN 1993-1-2, 2005. *Eurocode 3: Design of steel structures—Part 1-2: General rules—Structural fire design*. British Standards Institute.
- Franssen J.-M., T. Gernay T, 2017. *Modeling structures in fire with SAFIR®: Theoretical back-ground and capabilities*. J. Struct. Fire Eng. 8 (3), 300–323.
- McGrattan K., Hostikka S., McDermott R., Floyd J., Weinschenk C., Overholt K., 2013. *Fire dynamics simulator user’s guide*. NIST special publication, 1019(6).

Proceedings of the International Conference in Ljubljana, 10-11 June 2021  
in edition of Applications of Structural Fire Engineering

**Session**

**Steel structures II**

# FIRE RESISTANCE OF STAINLESS STEEL ELLIPTICAL HOLLOW SECTION BEAM-COLUMNS WITH OUT-OF-PLANE BUCKLING

Flávio Arrais<sup>a</sup>, Nuno Lopes<sup>a</sup>, Paulo Vila Real<sup>a</sup>

<sup>a</sup> RISCO, Department of Civil Engineering, University of Aveiro, Portugal

## Abstract

Stainless steel has different advantages when compared to conventional carbon steel. The corrosion resistance and aesthetic appearance are the most known, but its higher fire resistance can also be a decisive factor. Members with elliptical hollow sections integrate the architectural attributes of the circular hollow sections and the structural advantages of the rectangular hollow sections. Hence, the application of stainless steel material combined with these elliptical hollow profiles stands as an interesting design option. This work presents a numerical study on the behaviour of stainless steel members with elliptical hollow sections, subjected to axial compression and bending about the strong axis at elevated temperatures. With the ultimate bearing capacities obtained from material and geometric non-linear analysis with imperfections, using the finite element software SAFIR, the safety and accuracy of different design procedures, such as the Eurocode 3 rules, are analysed.

**Keywords:** stainless steel, elliptical hollow section, beam-columns, elevated temperature, finite element modelling

## 1 INTRODUCTION

The application of stainless steel as a structural material has been increasing due to a variety of desirable qualities such as its durability, resistance to corrosion and aesthetic appearance (Gardner, 2005). Despite having a high initial value, stainless steel may be a competitive material if life cycle cost is taken into account, due to its low maintenance needs. Moreover, it has a higher fire resistance when compared to carbon steel (CEN, 2005b).

The most common group for structural applications is the austenitic stainless steel, but due to specific advantages, some interest has been recently shown for increasing the use of different stainless steel groups, also for structural purposes, such as the ferritic and austenitic-ferritic (Duplex) steels. Some of the advantages are the very good resistance to wear and stress corrosion cracking of the duplex grade and the lower percentage of Nickel of the ferritic grade, reducing its price. The application of these stainless steel groups can vary from buildings, to towers, domes and bridges (footbridges and road bridges) (Baddoo, 2008; Gardner, 2008 and 2019).

Elliptical hollow sections (EHS) compile the circular hollow sections (CHS) architectural attributes and the rectangular hollow sections (RHS) structural benefits. They present better torsional behaviour when compared to open sections and higher bending strength than CHS profiles. Thus, the application of stainless steel combined with EHS stands an interesting design choice. Recent studies on stainless steel beam-columns under fire conditions have been focusing on members with I-sections (Lopes *et al.*, 2012; Kucukler *et al.*, 2021) or square and circular hollow sections (Lopes and Vila Real, 2014; Lopes *et al.*, 2019), and only recently these stainless steel members with EHS at elevated temperatures have begun to be studied (Arrais *et al.*, 2020). Current design standards, such as the Eurocode 3 (EC3), fire calculation guidelines have been developed mainly for I-profiles without any reference to this type of cross-sections, which may not be applicable to members composed of EHS. This research investigates the behaviour of stainless steel EHS members subjected to combined axial compression and bending at elevated temperatures with numerical analysis, taking into account the out-of-plane buckling. A parametric study is performed considering different stainless steel grades, member lengths, cross-section slenderness, bending moment diagrams about the strong axis and elevated temperatures.

The safety and accuracy of the EC3 design methodology for these members are analysed applying material and geometric non-linear analysis considering imperfections using the SAFIR finite element software (Gernay and Franssen, 2017). For this purpose, the numerically obtained ultimate members' capacities are compared with the EC3 prescriptions. Also, a new methodology presented by Kucukler *et al.* (2021) for stainless steel I-section beam-columns at elevated temperatures, which will be part of the future generation of the EN 1993-1-2, is here presented and analysed.

## 2 FIRE DESIGN RULES FOR STAINLESS STEEL BEAM-COLUMNS

According to the EN 1993-1-2 (CEN, 2005b), the fire resistance of stainless steel members is calculated in the same way as for carbon steel, changing only the material mechanical properties. Regarding the cross-section classification, equation (1) is used to determine the parameter  $\varepsilon$ , needed for the determination of the EC3 classification limits. Since the current EN 1993-1-2 does not present classification limits specific for EHS, the limits from the reference Gardner *et al.* (2012) are considered. The corresponding classification limits are given in Table 1.

$$\varepsilon_{fi} = 0.85 \left[ \frac{235}{f_y} \frac{E}{210000} \right]^{0.5} \quad (1)$$

Table 1 EC3 recommended classification limits for EHS (Gardner *et al.*, 2012)

Cross-section classification	$D_e/t \varepsilon_{\theta}^2$
	Compression and bending
Class 1	50
Class 2	70
Class 3	$\frac{2520}{5\psi + 23}$

The interaction formulae for beam-columns in case of fire of EN 1993-1-2 were developed based on carbon steel members with I-sections of Class 1 and 2 (Talamona, 1995). In fire situation, higher strains are acceptable when compared to normal temperature design. Therefore, instead of 0.2% proof strength usually considered at normal temperature, for cross-sections of Class 1, 2 and 3, at elevated temperatures the stress corresponding to 2% total strain should be adopted for the yield strength. Nevertheless, for Class 4, according to EN 1993-1-2 Annex E, the 0.2% proof strength should be used, with the yield strength reduction factors for stainless steel presented in Annex C of the same standard. Despite this, the cross-section resistance was obtained numerically. The formulae for Class 4 cross-section members subjected to combined axial compression and bending about the major axis in fire situation, considering the out-of-plane buckling, are used.

$$\frac{N_{fi,Ed}}{\chi_{z,fi} A_{eff} k_{0.2p,\theta} \frac{f_y}{\gamma_{M,fi}}} + k_y \frac{M_{y,fi,Ed}}{W_{eff,y} k_{0.2p,\theta} \frac{f_y}{\gamma_{M,fi}}} \leq 1 \quad (2)$$

$A_{eff}$  (effective area) and  $W_{eff}$  (effective section modulus) are the cross-section effective properties, determined at normal temperatures. The effective area ( $A_{eff}$ ) was calculated according to Chan and Gardner (2008b) proposal for EHS:

$$A_{eff} = A \left[ \frac{90}{D_e/t} \frac{235}{f_y} \right]^{0.5} \quad (3)$$

Considering the equivalent diameter  $D_e = H^2/B$ , whose variables are represented in Figure 1, and the effective section modulus ( $W_{eff}$ ) calculated according to Chan and Gardner (2008a) proposal:

$$W_{eff} = W_{el} \left[ \frac{140}{D_e/t} \frac{235}{f_y} \right]^{0.25} \quad (4)$$

with the equivalent diameter in bending about the strong axis, for  $H/B > 1.36$ ,  $D_e = 0.4H^2/B$ .

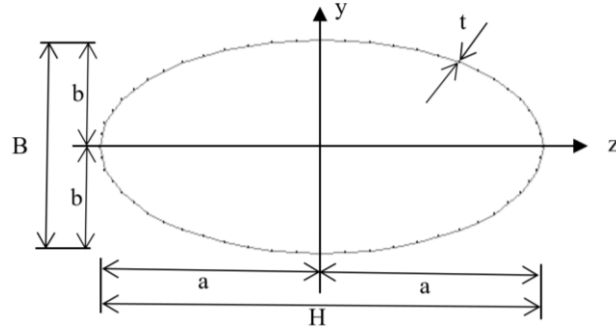


Fig. 1 EHS dimensions

The reduction factor  $\chi_{z,fi}$  can be obtained according to equation (5):

$$\chi_{fi} = \frac{1}{\phi_{\theta} + \sqrt{\phi_{\theta}^2 - \bar{\lambda}_{\theta}^2}} \quad (5)$$

with

$$\phi_{\theta} = \frac{1}{2} \left[ 1 + \alpha \bar{\lambda}_{\theta} + \bar{\lambda}_{\theta}^2 \right] \quad (6)$$

and  $\alpha$  an imperfection factor determined by:

$$\alpha = 0,65 \sqrt{235/f_y} \quad (7)$$

The recommended interaction factor  $k_y$ , for Class 4 cross-sections, is:

$$k_y = 1 - \frac{\mu_y N_{fi,Ed}}{\chi_{y,fi} A_{eff} k_{0.2p,\theta} \frac{f_y}{\gamma_{M,fi}}} \leq 3 \quad (8)$$

$\mu_y$  is given by:

$$\mu_y = (2\beta_{M,y} - 5)\bar{\lambda}_{y,\theta} + 0,44\beta_{M,y} + 0,29 \leq 0,8 \text{ with } \bar{\lambda}_{y,20^\circ\text{C}} \leq 1,1 \quad (9)$$

and  $\beta_M$ , which is in function of the bending diagram shape, for end moments obtained with:

$$\beta_M = 1,8 - 0,7\psi \quad (10)$$

where  $\psi$  is the ratio between the end moments ( $-1 \leq \psi \leq 1$ ).

Kucukler *et al.* (2020) presents a different approach based on the future generation of normal temperature structural steel design EN 1993-1-1 (CEN, 2006a) to be consistent with the different EC3 parts. For all cross-section Classes, the stress corresponding to 2% total strain is adopted for the yield strength. Therefore, the formula for slender cross-section members subjected to combined axial compression and bending about the major axis in fire situation, with out-of-plane buckling is:

$$\frac{N_{fi,Ed}}{\chi_{z,fi} A_{eff} k_{2,\theta} \frac{f_y}{\gamma_{M,fi}}} + k_{zy} \frac{M_{y,fi,Ed}}{\chi_{LT,fi} W_{eff,y} k_{2,\theta} \frac{f_y}{\gamma_{M,fi}}} \leq 1 \quad (11)$$

with  $k_{zy} = 0,8k_{yy}$  for the design of members with doubly symmetric cross-sections and:

$$k_{yy} = C_{my} \left[ 1 + D_{1,y} (\bar{\lambda}_{y,\theta} - D_{2,y}) n_y \right], \text{ for } \bar{\lambda}_{y,\theta} < D_{3,y} \quad (12)$$

$$k_{yy} = C_{my} \left[ 1 + D_{1,y} (D_{3,y} - D_{2,y}) n_y \right], \text{ for } \bar{\lambda}_{y,\theta} \geq D_{3,y} \quad (13)$$

where  $C_{my} = 0,6 + 0,4\psi \geq 0,4$ ,  $D_y$  have the values of Table 2 and  $n_y$  for slender sections is:

$$n_y = \frac{N_{fi,Ed}}{\chi_{y,fi} A_{eff} k_{2,\theta} \frac{f_y}{\gamma_{M,fi}}} \quad (14)$$

Table 2 Values of auxiliary coefficient  $D_y$

Coefficient	Austenitic	Ferritic and Duplex
$D_{1,y}$	2,5	2,0
$D_{2,y}$	0,2	0,3
$D_{3,y}$	1,4	1,6

### 3 NUMERICAL MODEL DEVELOPMENT AND PARAMETRIC ANALYSIS

Slender EHS members under compression and bending, with the cross-section's dimensions and H/B ratios from Table 3, are analysed. The lengths of 1, 3, 7 and 10 m, corresponded to different slenderness from 0.15 to 2.00, are considered. The stainless steel grades studied are 1.4301 (Austenitic also known as 304), 1.4401 (Austenitic also known as 316), 1.4003 (Ferritic), and 1.4462 (Austenitic-ferritic also known as Duplex). Different bending moment diagrams (uniform  $\psi=1$  and non-uniform  $\psi=-1$  and 0) are taken into account. The uniform elevated temperatures of 350 °C (being the EC3 proposed critical temperature for slender sections when no calculation is made), 600 °C and 700 °C (common critical temperatures in this type of structural elements) are also considered.

Table 3 Elliptical hollow sections analysed and respective dimensions

Designation	H [mm]	B [mm]	T [mm]	H/B [-]
EHS 140x85x2.0	140	85	2.0	1.65
EHS 150x75x2.0	150	75	2.0	2.00
EHS 200x100x2.5	200	100	2.5	2.00
EHS 200x100x4.0	200	100	4.0	2.00
EHS 300x150x4.0	300	150	4.0	2.00
EHS 150x50x3.0	150	50	3.0	3.00

The finite element software SAFIR, considering shell elements with four nodes with each six degrees of freedom (three translations and three rotations) is applied with the constitutive law proposed in EN 1993-1-2 (CEN, 2005b). Doubled hinged conditions are applied at both ends being longitudinal (x-x axis) displacement prevented at mid-span, to ensure the element and load symmetry. The loads are applied at the member extremities parallel to x-x axis, distributed over the cross-section surface to avoid local instability phenomena (Figure 2). The end-plates are considered at normal temperature with 10 times the thickness of the element's wall. Geometric imperfections are introduced into the numerical model by changing the nodal coordinates affine to the buckling mode shapes obtained with the software CAST3M (CEA, 2012), applying the interface RUBY (Couto *et al.*, 2013).

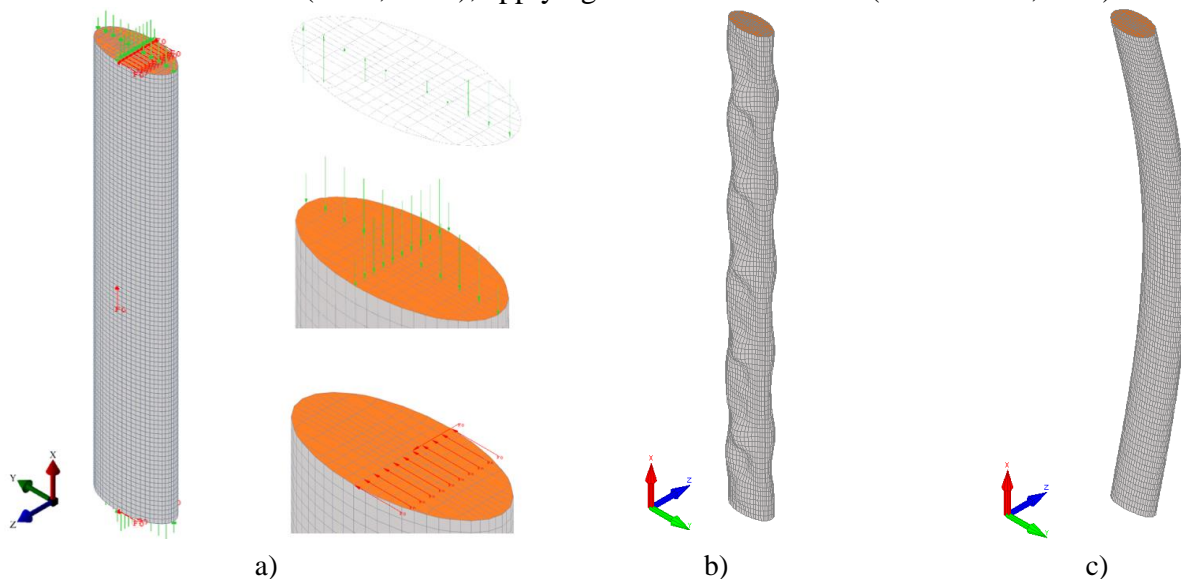
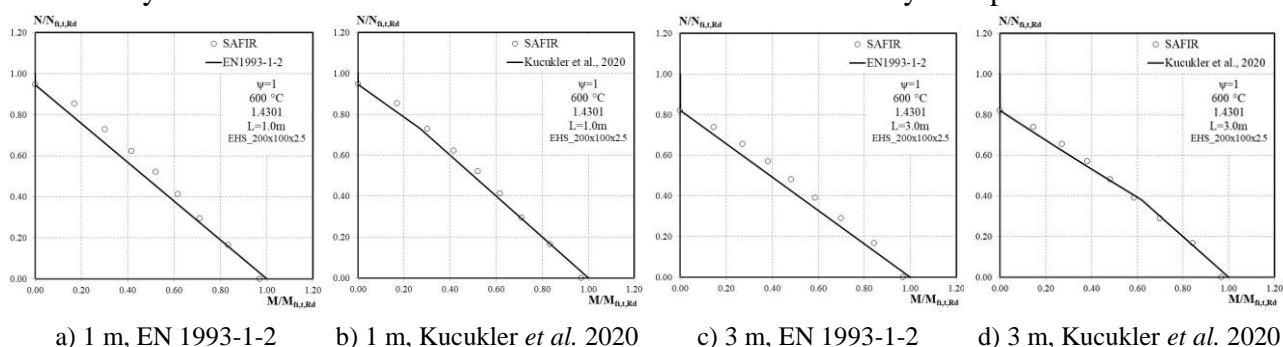


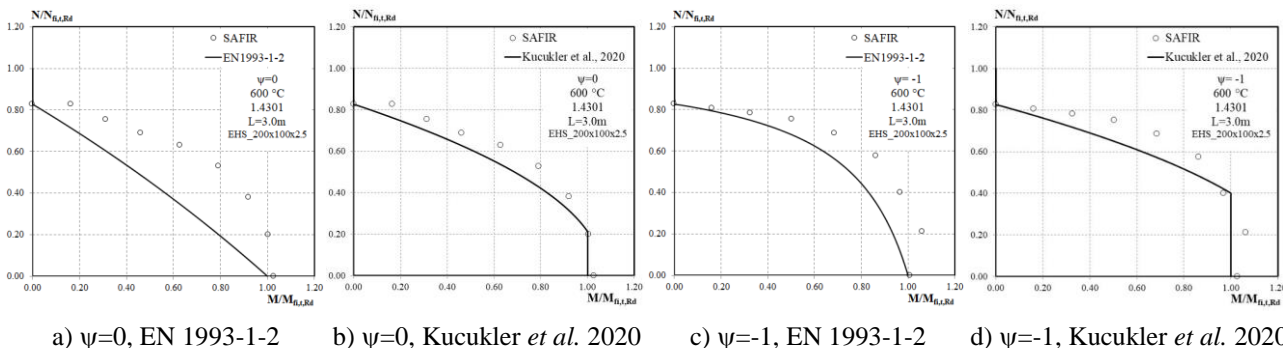
Fig. 2 a) Numerical model for a beam-column with b) local and c) global imperfections amplified

For the imperfections' amplitude, 80% of (H or B)/100 is considered for local imperfections and 80% of L/750 for global imperfections, following the recommendations of Annex C of EN 1993-1-5 (CEN, 2006) and the geometric fabrication tolerances from D.1 of Annex D of EN 1090-2+A1 (CEN, 2008) and EN 10219-2 (CEN, 2019), where H and B represent the dimensions in both directions y and z from elliptical sections (Figure 1) and L the element length. According to EN 1993-1-5, the geometric imperfection's combination is introduced in the numerical model. This part of EC3 states that, in combining imperfections, a leading imperfection should be chosen, and the accompanying imperfections may have their value reduced to 70%. The leading imperfection is chosen based on the achieved lower resistances from each individual imperfection resistance obtained.

With the purpose of better understanding the behaviour of EHS stainless steel beam-columns in case of fire, with out-of-plane buckling, Figures 3 and 4 illustrate the influence of some parameters on the interaction curves, analysing also the accuracy of the different design formulations. Since there is a page limitation for the paper, not all the results are presented here. The cross-section resistance is numerically obtained with the SAFIR software. A brief statistical analysis is presented at Table 4.



a) 1 m, EN 1993-1-2      b) 1 m, Kucukler *et al.* 2020      c) 3 m, EN 1993-1-2      d) 3 m, Kucukler *et al.* 2020  
 Fig. 3 Comparison of the interaction curves with the numerical results of different lengths members subjected to compression and uniform bending at 600 °C, for the stainless steel grade 1.4301



a)  $\psi=0$ , EN 1993-1-2      b)  $\psi=0$ , Kucukler *et al.* 2020      c)  $\psi=-1$ , EN 1993-1-2      d)  $\psi=-1$ , Kucukler *et al.* 2020  
 Fig. 4 Comparison of the interaction curves with the numerical results of 3 m beam-columns subjected to compression and non-uniform bending at 600 °C, for the stainless steel grade 1.4301

Table 4 Statistical evaluation of the different fire design rules for the different stainless steel grades

Design Rules	Austenitic				Ferritic				Duplex			
	$\mu$	s	Max.	% uns.	$\mu$	s	Max.	% uns.	$\mu$	s	Max.	% uns.
EN 1993-1-2	0.88	0.16	1.02	1.14	0.89	0.11	1.02	1.31	0.84	0.14	1.01	1.08
Kucukler <i>et al.</i> 2020	0.92	0.11	1.05	4.13	0.93	0.08	1.04	3.46	0.87	0.09	1.04	2.33

Considering 1458 numerical simulations, the results are in general on the safe side, where the current design rules are too conservative, specially when considering the non-uniform bending. The Kucukler *et al.* (2020) methodology presents a better approximation to the numerical results.

#### 4 CONCLUSIONS

A numerical parametric study on the fire behaviour of beam-columns with stainless steel elliptical hollow sections, with out-of-plane buckling, was presented. The accuracy of the current Part 1-2 of

Eurocode 3 prescriptions and Kucukler *et al.* (2020) new methodology to be incorporated at the prEN 1993-1-2 was evaluated against numerically obtained ultimate bearing capacities. The influence of different cross-section slenderness, member lengths, stainless steel grades, loading types and temperatures, was considered and analysed. The current EN 1993-1-2 design rules provide generally safe approximations, however too conservative for non-uniform bending.

The main conclusions were that the existing calculation rules from the EC3 do not provide accurate approximations for stainless steel beam-columns with elliptical hollow section and the new methodology proposed by Kucukler *et al.* (2020) provides closer and safe approximations for this type of cross-sectional members.

## ACKNOWLEDGMENTS

This research work was performed within the framework of the project “StaSteFi - Fire design of stainless steel members”, PTDC/ECI-EGC/30655/2017, supported by the Portuguese Operational Programme “Competitividade e Internacionalização”, in its FEDER/FNR component, and the Portuguese Foundation for Science and Technology (FCT), in its State Budget component (OE).

## REFERENCES

- Arrais, F., Lopes, N., Vila Real, P. 2020. Fire resistance of stainless steel slender elliptical hollow section beam-columns, *11<sup>th</sup> International Conference on SiF*, Brisbane, Australia.
- Baddoo, N. R. “Stainless steel in construction: A review of research, applications, challenges and opportunities”, *Journal of Constructional Steel Research*, vol. 64, no. 11, 2008, pp 1199–1206.
- CAST3M. 2012, Development sponsored by French Atomic Energy Commission; <http://www-cast3m.cea.fr/>
- CEN European Committee for Standardisation. EN 1993-1-1:2005a. *Eurocode 3, Design of steel Structures – Part 1–1: General rules - General rules and rules for buildings*, Belgium.
- CEN European Committee for Standardisation. EN 1993-1-2:2005b. *Eurocode 3: Design of Steel Structures - Part 1–2: General rules - Structural fire design*, Belgium.
- CEN European Committee for Standardisation. EN 1993-1-5:2006. *Eurocode 3, Design of steel Structures – Part 1–5: Plated structural elements*, Belgium.
- CEN, European Committee for Standardisation. EN 1090-2+A1:2008. *Execution of steel structures and aluminium structures - Part 2: Technical requirements for steel structures*, Belgium.
- CEN European Committee for Standardisation, EN 10219-2:2019. *Cold Formed Welded Steel Structural Hollow Sections - Part 2: Tolerances, Dimensions and Sectional Properties*, Belgium.
- Chan, T. M., Gardner, L. 2008a. *Bending strength of hot-rolled elliptical hollow sections*, *Journal of Constructional Steel Research*, Vol. 64, p. 971–986.
- Chan, T. M., Gardner, L. 2008b. *Compressive resistance of hot-rolled elliptical hollow sections*, *Engineering Structures*, Vol. 30 (2), p. 522–532.
- Couto, C., Vila Real, P., Lopes, N. 2013. *RUBY – an interface software for running a buckling analysis of SAFIR models using Cast3M*, University of Aveiro.
- Gardner, L. 2005. *The use of stainless steel in structures*, *Progress in Struct. Eng. and Mat.*, Vol. 7, p. 45–55.
- Gardner, L. 2008. *Aesthetics, economics and design of stainless steel structures*, *Ad Steel Const*,4, p. 113–122.
- Gardner, L. 2019. *Stability and design of stainless steel structures – Review and outlook*, *Thin-Walled Structures*, Vol. 141, p. 208–216.
- Gardner, L., Chan, T.M., Abela, J. M. 2011. *Structural behaviour of elliptical hollow sections under combined compression and uniaxial bending*. *Advanced Steel Construction*, Vol. 7 (1), p. 86–112
- Gernay, T., Franssen, J.M. 2017. *Modelling structures in fire with SAFIR®: Theoretical background and capabilities*. *Journal of Structural Fire Engineering*, Vol. 8 (3), p. 300–323.
- Kucukler, M., Xing, Z., Gardner, L. 2021. Stability of stainless steel I-section beam-columns at elevated temperatures. *International Journal of Structural Stability and Dynamics*. Vol. 21 (3), 2150037.
- Lopes, N., Vila Real, P., Simões da Silva, L., Franssen, J.M. 2012. *Numerical analysis of stainless steel beam-columns in case of fire*, *Fire Safety Journal*, Vol. 50, p. 35–50.
- Lopes, N., Vila Real, P. 2014. Fire resistance of stainless steel structural elements with class 4 square hollow sections subject to combined bending and axial compression, *8th Int. Conference on SiF*, Shanghai, China.
- Lopes, N., Manuel, M., Sousa, A. R., Vila Real, P. 2019. Parametric study on austenitic stainless steel beam-columns with hollow sections under fire, *Journal of Constructional Steel Research*, Vol. 152, p. 274–283.
- Talamona, D. 1995. *Flambement de Poteaux Métalliques Sous Charge Excentrée, à Haute Température* (in French), *PhD Thesis University Blaise Pascal, Clermont–Ferrand, France, 1995.*

## TEMPERATURE OF GALVANIZED STEEL SPECIMENS heated in electrical furnace

Margherita Autiero<sup>a</sup>, Antonio Bilotta<sup>a</sup>, Donatella de Silva<sup>a</sup>, Emidio Nigro<sup>a</sup>, Lello Pernice<sup>b</sup>

<sup>a</sup> University of Naples Federico II, DiSt-Department of Structures for Engineering and Architecture, Naples, Italy

<sup>b</sup> AIZ - Associazione Italiana Zincatura, Rome, Italy

### Abstract

Hot dip galvanization is economic and efficient to protect steel members from corrosion. Recent studies showed that galvanization can also reduce the surface emissivity with a beneficial effect on the temperature of steel elements exposed to fire. Background documents for structural Eurocodes suggest considering this positive effect by a two-stages emissivity relationship. To analyze the effect of galvanization on the heating of steel elements, forty-four 50x50mm steel plates were exposed on one face in electrical furnace. A variable thickness of the plates allowed obtaining equivalent section factor ( $A_m/V$ ) ranging between 20 and 200m<sup>-1</sup>. Both galvanized and blank steel specimens were tested to have a direct comparison between the temperatures. The test results showed that the heating in galvanized samples was slower than the blank ones till the galvanization layer was effective (i.e. about 500°C).

**Keywords:** steel members, galvanization, emissivity, fire test, electrical furnace

### 1 INTRODUCTION

Galvanization is a surface coating process to protect steel members from corrosion, in which the steel is coated with zinc to prevent it from rusting. The most common galvanization method is hot-dip galvanizing. During this process the protective zinc coating is obtained by dipping the steel element into a bath of molten zinc usually at about 450°C. The zinc coating is formed by a metallurgic reaction during which several zinc-iron alloy layers are formed. Therefore the coating is bound to steel beneath and not only laid on top of it. The formation of the zinc coating depends on several factors. On the one hand it depends on the galvanizing conditions as melting temperature, dipping time, and chemical composition of zinc bath. On the other hand, it depends on the surface condition and on the chemical composition of the steel (silicon and phosphorous content). Silicon concentration in quantities between 0.04 and 0.12% (Sandelin steel) or above 0.25% (hyper-Sandelin steels) can accelerate the iron-zinc reaction to form thicker zinc coating with a different alloy layer structure (Pernice, 2021). The categories of steel composition according to EN ISO 14713-2 are: Category A - Low silicon content steel ( $Si \leq 0.04\%$ ), Category B: Non-Sandelin intermediate composition steels ( $14\% < Si \leq 0.22\%$ ), Category C: Sandelin steel ( $0.04\% < Si \leq 0.14\%$ ) and Category D: hyper-Sandelin steels ( $Si > 0.22\%$ ).

The surface coating can modify the emissivity surface that is the ratio of the energy radiated from a surface of a material to the energy radiated from a black body, under the same conditions, at the same temperature and wavelength. The emissivity ranges between zero and one.

The radiative component of the net heat flux depends on the emissivity of flame,  $\varepsilon_f$ , and member surface,  $\varepsilon_m$ . The lower the emissivity of a surface, the slower the heating.

The radiation depends on the chemical composition in a layer with a thickness of about 0 a 10<sup>-10</sup>m (Sala, 1986). The radiation of galvanized surfaces should hence be provided exclusively by the alloy layer 45·10<sup>-6</sup> to 250·10<sup>-6</sup> m or from the upper pure zinc layer alone, which is only a few micrometres thick. Therefore, the emissivity of hot dip galvanized steel elements is influenced by the character of the layer formation, the oxidation of zinc and, since the melting point of zinc is at only 419°C, the melting of the outer zinc layer. As a result, the emissivity of the galvanized surface is variable depending on the temperature.

Jirku and Wald (2013) obtained a constant value of emissivity for galvanized steel elements equal to 0.32 by a fire test in an experimental building and two furnace tests in a horizontal furnace on steel members with IPE200 cross sections and hollow tube sections.

Mensinger and Gaigl (2019) assessed an emissivity curves as a function of temperature for hot-dip galvanized steel elements by small-scale and full-scale tests. The temperature-dependent emissivity was determined for various hot-dip galvanized surfaces; therefore, category A, B and D were tested, combined with all possible surface conditions. The results showed an emissivity dependent on temperature, as well as the influence of weathering with the negative influence of an outdoor storage. Moreover, the results highlighted that the zinc-iron alloy layers have a big influence on the emissivity value. Indeed only for steel belonging to category A and B emissivity lower than 0.7 was obtained, for steel temperatures up to 530 °C. As the temperature rises, the emissivity increases due to chemical reactions thus a new layer structure is formed with a higher roughness and an increasing emissivity. Therefore, EN1993-1-2 suggests a simplified surface-independent constant emissivity,  $\varepsilon_m = 0,70$  for blank steel, whereas the results experimental showed a temperature-dependent emissivity for hot-dip galvanized steel, with values lower than 0.7. Since the studies showed a positive effect of galvanization on the temperature development of steel elements and this effect could be significant for steel structural elements not far from reaching a required fire resistance time in a prescriptive approach, a two-stages emissivity relationship ( $\varepsilon_m = 0,35$  for  $\theta_{a,t} \leq 500$  °C;  $\varepsilon_m = 0,70$  for  $\theta_{a,t} > 500$  °C) is suggested in Mensinger and Gaigl (2019). This two-stage emissivity approach enables a simple application in design methods of the Eurocodes for steel element exposed to fire. It is already proposed for the new drafts of the next generation of structural Eurocodes. The results of experimental tests on small-scale galvanized and ungalvanized steel elements are discussed below.

## 2 EXPERIMENTAL TESTS

The tests were performed in an electrical furnace by exposing to heat only the upper face of specimens and using protective materials that reduce heat exchange on the remaining faces.

The test samples were forty-four 50x50mm steel plates. To have section factor ( $A_m/V$ ) ranging between 20 and 200m<sup>-1</sup>, the thickness of the samples was considered variable. For each section factor, both galvanized and blank steel specimens were tested. The label of the specimen is X-Y-Z: where X is the section factor of the specimen, Y indicates if the samples is galvanized (G) or ungalvanized (NG) and Z indicates the number of the specimen. The thickness of the specimens and their section factors are listed in Table 1. The results obtained for three representative section factors are discussed ( $A_m/V= 40, 80, 200$  m<sup>-1</sup>). For each section factor three galvanised and one ungalvanized specimens are considered.

Table 1 Test matrix

Blank steel	Galvanized steel			$A_m/V$ [m <sup>-1</sup> ]	s [mm]
20_NG_1	20_G_1	20_G_2	20_G_3	20	50
30_NG_1	30_G_1	30_G_2	30_G_3	30	35
40_NG_1	40_G_1	40_G_2	40_G_3	40	25
50_NG_1	50_G_1	50_G_2	50_G_3	50	20
60_NG_1	60_G_1	60_G_2	60_G_3	60	17
70_NG_1	70_G_1	70_G_2	70_G_3	70	14
80_NG_1	80_G_1	80_G_2	80_G_3	80	12.5
90_NG_1	90_G_1	90_G_2	90_G_3	90	11
100_NG_1	100_G_1	100_G_2	100_G_3	100	10
125_NG_1	125_G_1	125_G_2	125_G_3	125	8
200_NG_1	200_G_1	200_G_2	200_G_3	200	5

The specimens were placed inside a sequence of five Fireguard13 silicate - calcium panels 12.7 mm thick. Four panels were carved in the middle. The box was placed on a thickness of rock wool and finally on refractory bricks. To ensure that the specimen is always aligned to the upper face of the box, rock wool is placed below it (Fig. 1a). To measure the temperature in the steel samples two Chromel/Alumel K thermocouples were placed into each element, on the face directly exposed (2) and the face not exposed (1). Another Chromel/Alumel K thermocouple (3) and the furnace own thermocouple (4) were used to measure the temperature in the furnace (Fig. 1b).

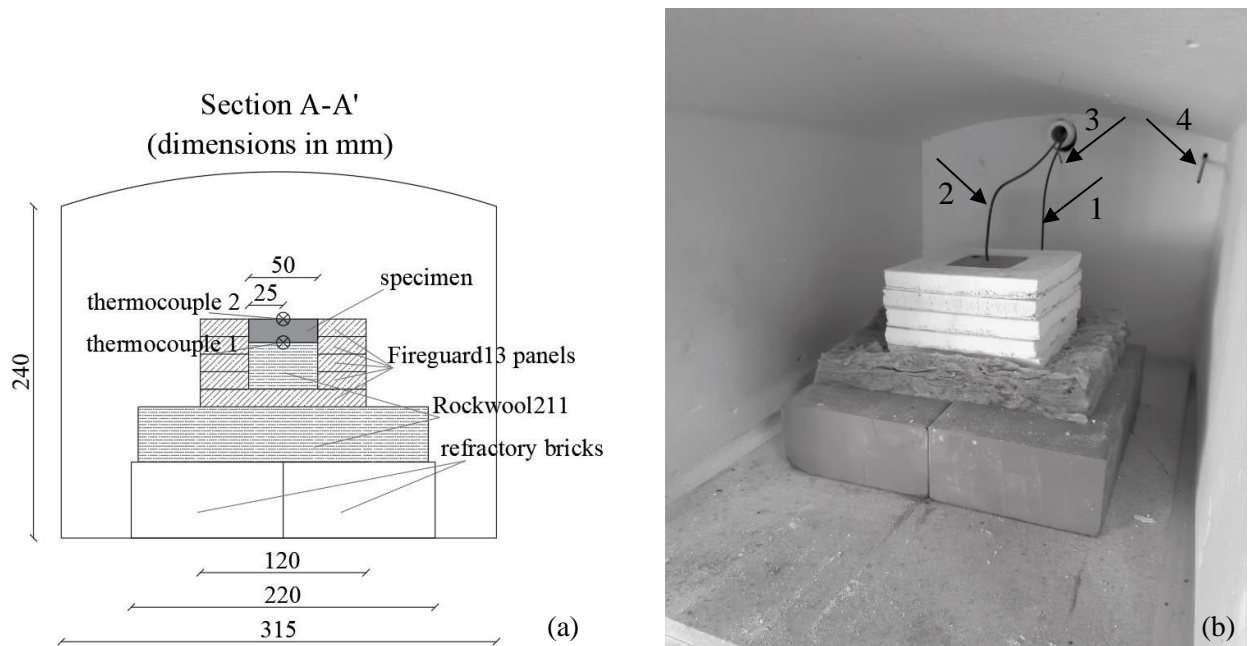


Fig. 1 Test setup: (a) setup cross section, (b) setup in the furnace

Fig. 2a shows that the heating curves for the two galvanized specimens were sufficiently similar. Hence, for a direct comparison between the heating curves of the galvanized and blank specimens, the mean value (indicated as G\_M) of the temperature of the two galvanized specimens was considered for each section factor.

Fig. 2b shows the results for ungalvanized (NG) and galvanized (G) specimens (NG), with dashed and continuous curves respectively.

The galvanized samples show slower heating than the corresponding blank one. For example, at 1800 seconds the blank specimen attain a temperature  $\theta_{80\_NG} = 400$  °C while the same galvanized specimens  $\theta_{80\_G} = 315$  °C. This difference of 86°C changes during the heating with a maximum value of 168 °C at 2700 seconds. The temperatures are  $\theta_{80\_NG} = 625$  °C for the blank specimen and  $\theta_{80\_G} = 456$  °C for the galvanized specimen.

Fig. 3 shows the direct comparison of the experimental results of galvanised and ungalvanized specimens obtained for the three different section factors  $A_m/V = 40 - 80 - 200$  m<sup>-1</sup>.

Due to different values of  $A_m/V$  the heating curves are clearly different, but for same  $A_m/V$  the maximum temperature difference between galvanised and blank samples occurs when the temperatures in galvanised specimens are about 500 °C. Clearly this temperature occurs at different heating times.

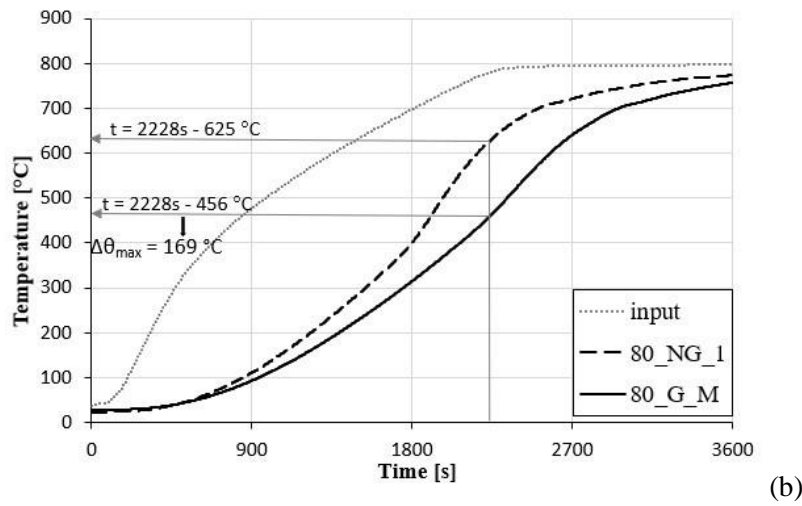
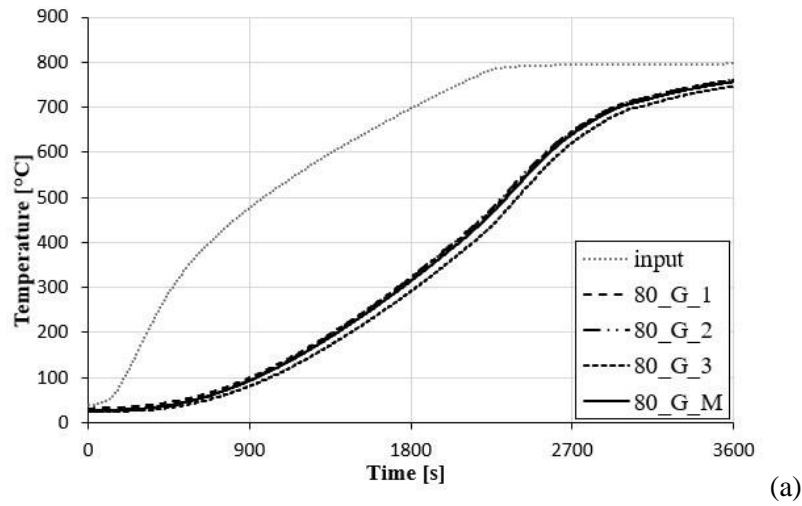


Fig. 2 Comparison of measured temperature of galvanized specimens (a) and comparison of measured temperature of the blank sample and the mean value of the galvanized ones (b).

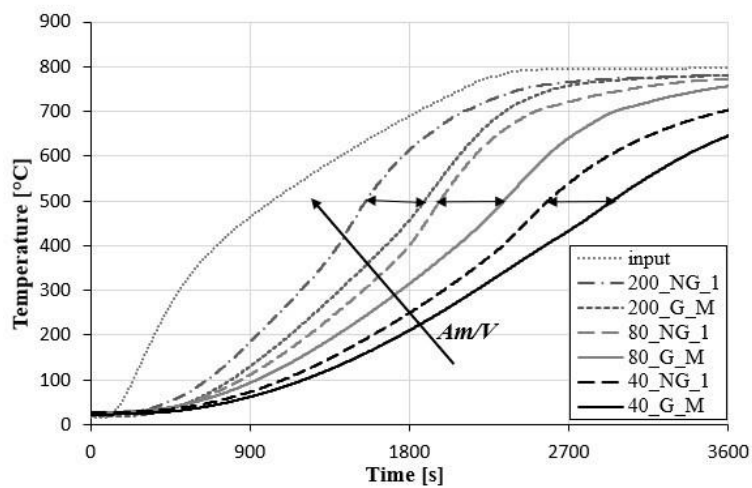


Fig. 3 Comparison between experimental results of the different galvanized (G) and blank (NG) specimens.

A simulation of the tests on galvanized samples was carried out by implementing the analytical method suggested by Eurocode EN1993-1-2. The effect of galvanizing was modelled according to the two-stages emissivity relationship ( $\epsilon_m = 0,35$  for  $\theta_{a,t} \leq 500$  °C;  $\epsilon_m = 0,70$  for  $\theta_{a,t} > 500$  °C).

As thermal action the thermal input curves obtained from each test was considered. The convective thermal flux was defined with a convection coefficient,  $\alpha_c$ , lower than the one used for the standard fire curve. This value of  $\alpha_c$  was determined for three different section factors based on the mean of the temperatures read by the lower and the upper thermocouple. By considering the specimen as a grey emitter and the furnace walls area bigger than the sample surface, a mean value  $\alpha_c = 6.4 \text{ W/m}^2\text{K}$  was calculated. Fig. 4 compares the temperatures recorded by thermocouples and calculated by the analytical method for galvanised specimens. A good agreement is attained for  $A_m/V= 40 \text{ m}^{-1}$ , excellent for  $A_m/V= 80 \text{ m}^{-1}$  and acceptable, for  $A_m/V= 200 \text{ m}^{-1}$ .

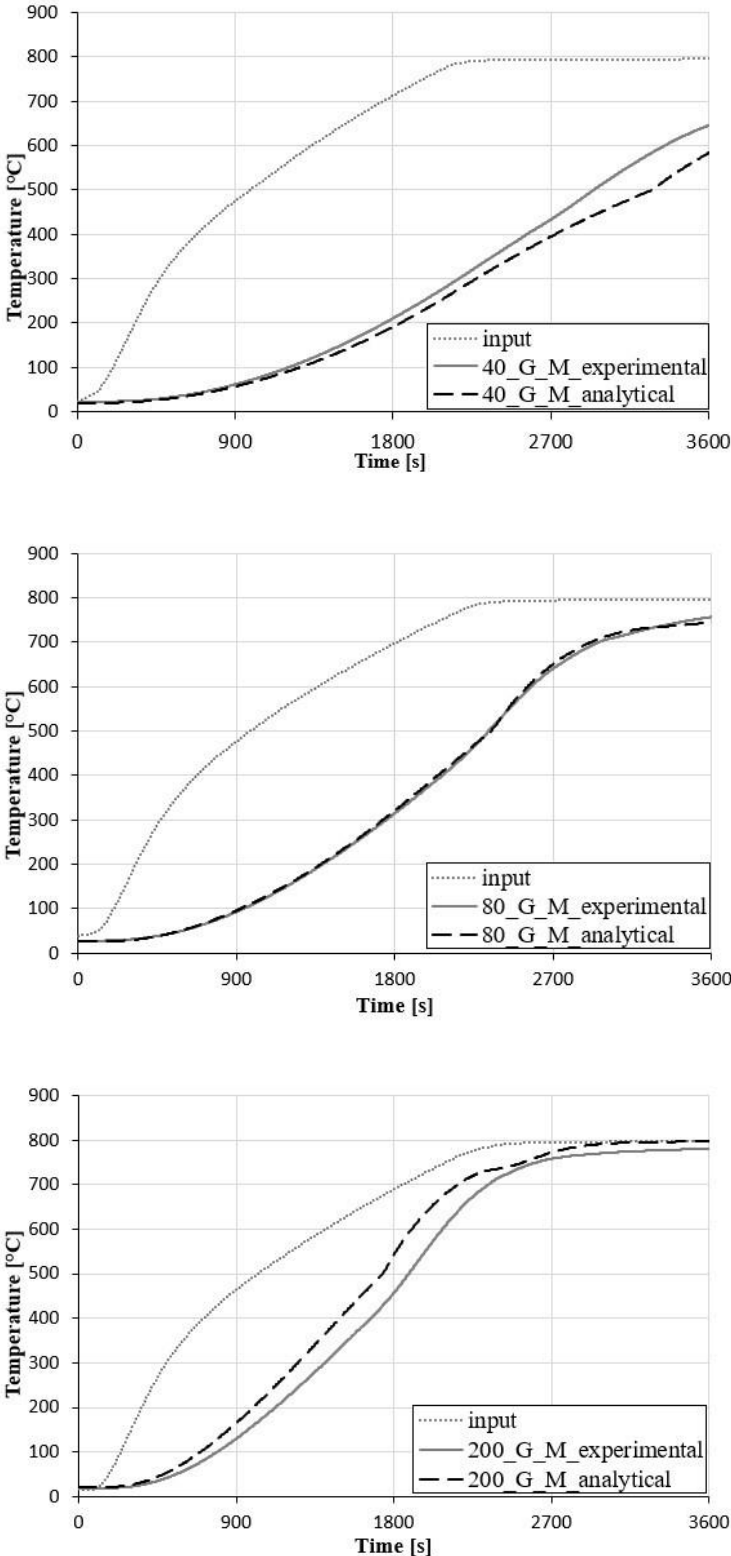


Fig. 4 Comparison between experimental and analytical results obtained for galvanized samples.

Based on the experimental results the analytical expression in Eq. (1):

$$\varepsilon = 0.5 \cdot (\varepsilon_{max} - \varepsilon_{min}) \cdot \tanh \left[ \left( \frac{1}{\beta} \right) \cdot (\theta_{a,t} - \gamma) \right] + 0.5 \cdot (\varepsilon_{max} + \varepsilon_{min}) \quad (1)$$

has been calibrated by varying the parameter  $\varepsilon_{max}$ ,  $\varepsilon_{min}$ ,  $\beta$  and  $\gamma$  for each single section factor. These values are, on average,  $\varepsilon_{min} = 0.36$  (Dev.st = 0.09),  $\varepsilon_{max} = 0.66$  (Dev.st = 0.05),  $\beta = 77$  (Dev.st = 15.31) and  $\gamma = 480$  (Dev.st = 28.31). A further calibration carried out considering all the test results, provided  $\varepsilon_{min} = 0.38$ ,  $\varepsilon_{max} = 0.53$ ,  $\beta = 1$  and  $\gamma = 500$ .

The Fig.5 shows the two curves obtained from the Eq. (1) with these values. Both curves confirmed that the emissivity depends on steel temperature with smaller value till a temperature of about 500 °C. The calibration carried out for each section factor shows a results variety, but in any case, the mean value is not very different from the calibration carried out for all the  $A_m/V$ , which confirm the two stages approach proposed in Mensinger and Gaigl (2019).

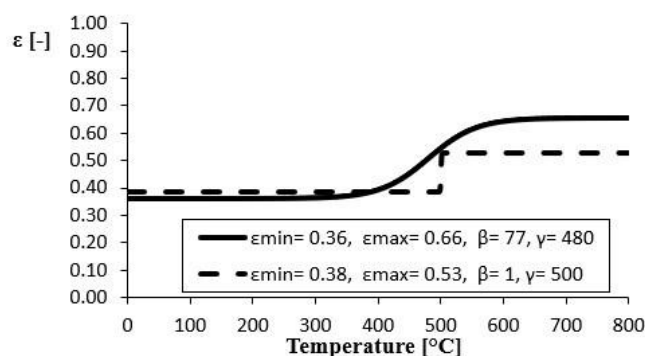


Fig. 5 Emissivity curves obtained for the two different calibrations.

### 3 CONCLUSIONS

The paper shows the effect of galvanization on the heating of steel elements. High temperature tests were performed in an electrical furnace by exposing only the upper face of specimens and using protective materials that reduce heat change on the remaining faces. The results showed that galvanized samples have a slower heating than the blank samples, therefore the beneficial effect of the galvanization on the heating was observed. A specific value of the convection coefficient,  $\alpha_c$ , was evaluated to compare experimental results with analytical predictions. The setup can be used to carry out further high temperature tests, to investigate the effect of different surface conditions.

### ACKNOWLEDGMENTS

The authors would like to thank Emanuele Scaiella and all the technicians of the DiSt Laboratory for assistance in carrying out the fire tests.

### REFERENCES

- EN 1991-1-2, Eurocode 1: Actions on structures - Part 1-2: General actions - Actions on structures exposed to fire, 2002.
- EN 1993-1-2, Eurocode 3: Design of steel structures - Part 1-2: General rules -Structural fire design, 2005.
- Gaigl C., Mensinger M., 2017. Hot dip galvanized steel constructions under fire exposure, in *FireSS 2017 - 2nd International Fire Safety Symposium*, 7-9 June 2017, Naples, Italy. p. 557-564.
- Gaigl C., 2019. *Fire resistance of hot-dip galvanized steel structures*, PhD Thesis, Technical Univ. of Munich.
- Jirku J., Wald F., 2013. Influence of zinc coating to a temperature of steel members in fire, in *ASFE'13 - Application of Structural Fire Engineering*, 19-20 April 2013, Prague, Czech Republic.
- Nigro E., Pustorino S., Cefarelli G., Princi P. 2010. *Progettazione di strutture in acciaio e composte acciaio-calcestruzzo in caso di incendio*. U. Hoepli Editore.
- Pernice L. 2021. *Zincatura a caldo*. Mirapromotion Srl. (in Italian)
- Sala A. 1986. *Radiant properties of materials: Tables of radiant values for black bodies and real materials*, Elsevier Science Ltd.

## TEMPERATURE DISTRIBUTION IN THE COATBACK OF A PARTIALLY FIRE-PROTECTED MEMBER

Patrik Dobrovolny<sup>a</sup>, Jakub Sejna<sup>a</sup>, Frantisek Wald<sup>a</sup>

<sup>a</sup> Czech Technical University in Prague, Faculty of Civil Engineering, Prague, Czech Republic

### Abstract

Whenever fire unprotected steel members are attached to a fire-protected steel member and penetrate its passive fire protection, additional heat will be conducted to this member during a fire. This can result in a local hot spot in the primary member that may reduce the actual fire resistance. The wide variation in loss of fire resistance is because geometries can vary, and in particular because of the influence of the section factors of the attachments. The influence of the partial protection was experimentally and numerically studied at the Czech Technical University in Prague. Four partially fire-protected plates were heated according to the nominal standard fire curves in a small horizontal furnace. A Finite Element Analysis (FEA) was validated and was applied to a numerical study of an unprotected steel beam under fire separation sealing, which was connected to a steel column. A description was prepared of the development of heat for various fire exposures under fire protection of different lengths and nonlinear thermal conductivity with different section factors.

**Keywords:** steel structures, fire design, fire protection, beam, coatback.

### 1 INTRODUCTION

For extended exposure to fire, structural members may require thermal protection to restrict their temperature to levels at which sufficient member residual strength is retained. This protection often takes the form of interposing thermal insulation between the heating environment and the structural members. Fire protection for structural steel sections can be provided by a wide variety of passive fire protection systems, including suitable board systems, which generally form a boxed enclosure of the steel beams and columns, and by sprayed mineral cementitious systems, or by sprayed reactive coatings, which generally follow the profiled shape of the steel section. The primary heat transfer mechanisms are convection and radiation onto the exposed surface of the protected structural members. Heat also flows into the protected member by conduction from the (hotter) unprotected members connected to them. Part of the length of these unprotected members is insulated to reduce the temperature of the member and hence to reduce the heat conducted into the protected member. This protection of attached secondary members is referred to as coatback. The coatback length is set to control the flow of heat into the protected members and thus to delay strength and stiffness degradation.

A closed-form solution of the 1D heat conduction equation for determining the coatback length in offshore structures was developed by Yasserli (2002). The coatback length is a function of the size of the member, the intensity of the heating, the thickness and the properties of the fire coating, and the specified survival time. Parlor (2010) published recommendations for UK good practice confirmed by experience for protecting the adjoining 500 mm of unprotected structural steel to limit unwanted heat transfer. Ways in which different applications of passive fire protection influence the collapse time of Floating production storage and of the Offloading vessel module structure are presented in (Friebe et al, 2014). A series of heat analyses and thermal elasto-plastic FEA were prepared for various passive fire protection coatings, together with the resultant collapse time. The numbers of coatings are compared with each other. In a simplified example of a main girder to which secondary members are attached perpendicular, the use of a conventional coatback length of 450 mm for the secondary members was found to be adequate. A coatback length greater than 450 mm does not result in any substantial delay of an increase in temperature or of deflection growth.

Podolski (2017) confirms, when tensile membrane action is used in composite floor slabs, that the elimination of fire protection to the internal secondary beams can be justified. Podolski investigated how the coatback distance is influenced by various parameters, including the intumescent coating thickness, the steel section factor, the steel section depth, the thermal conductivity of the intumescent coating, and the limiting temperature. A fire protection length on the unprotected steel section is designed that gives a temperature at the end of the protection not more than 2 % higher than the temperature of the protected steel section. A simplified numerical method powered by a software tool that enables the required coat back length to be determined has been developed by (Breunese 2019). The method was verified by comparing the calculated steel temperatures with full three-dimensional simulations. The studies show that omitting coat backs significantly reduces the time to reach the critical steel temperature.

**2 EXPERIMENT**

The experiment consisted of four steel samples, which were loaded according to the standard temperature-time curve for 60 mins. The test took place in a small horizontal furnace at the University Center for Energy Efficient Buildings in Buštěhrad, Czech Republic. The dimensions of the samples were 300 x 60 x 8 mm. Half of the length of the sample was treated on three sides by fire spraying (Promat. 2021), the temperature parameters of which at elevated temperatures were tested in detail experimentally and numerically (Dobrovolny, 2021). The thickness of the fire protection was 10 mm for two of the samples and 20 mm for the other two samples. The walls inside the furnace were treated by spraying. The untreated side was attached to the ceiling of the furnace. Thermocouples were located on the protected and unprotected parts of the samples. The geometry of a sample is shown in Figure 1.

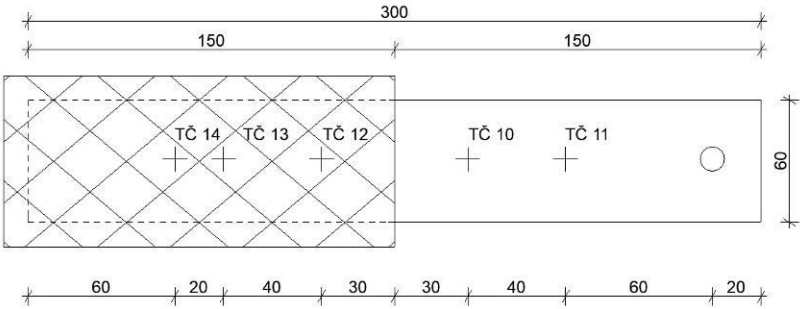


Fig. 1 The geometry of a sample and the position of the thermocouples



Fig. 2 The samples before and after the test

Five jacketed thermocouples 2.5 mm were designed for two of the samples and two jacketed thermocouples were designed for the other two samples. The samples before and after the test are shown in Figure 2. The measured temperature profile is shown in Figure 3, and the values for significant points are presented in Table 1.

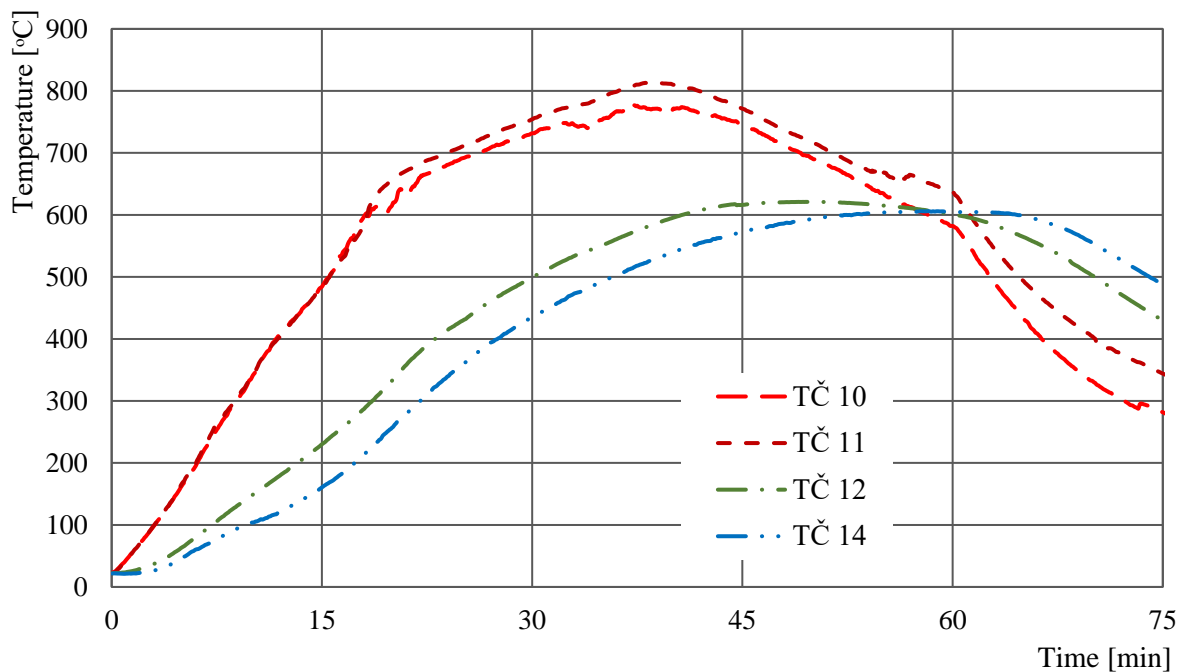


Fig. 3 Temperature distribution in sample 4 with protection thickness of 10 mm

Tab. 1 Temperature development in sample 4 with the protection thickness of 10 mm

$t$ , min	TČ1	TČ2	TČ3	TČ10	TČ 11	TČ 12	TČ13	TČ14
15	483.2	213.4	645.3	484.1	483.8	230	312.4	160.5
30	676.8	480.2	796.7	731.6	754.4	499.7	543.9	436.2
45	714.7	600.3	737.1	745.8	771.2	616.2	573.8	572.7
60	608.0	613.1	540.7	582.1	636.8	601.1	359.9	605.3

### 3 NUMERICAL SIMULATION

The numerical model is processed in the ANSYS Mechanical program (Lawrence, 2020). A partially protected connection of the beam to the column is proposed. When modelling, the column is considered to be perfectly insulated. Heat is supplied to the column from the beam. Heating of the protected and unprotected parts of the beam are considered to be from three sides. The structure of the ceiling is assumed to be perfectly insulated from the upper side. The column is protected at the connection point of the beam by fire protection of the same thickness as the beam. The model is shown in Figure 4. Loading by heat transfer and radiation takes place according to the standard nominal temperature curve. The SOLID 70 element, which has eight nodes and one degree of freedom, is used for the numerical solution. The thermal properties of the steel were considered according to EN 1993-1-2:2005. The fire protection material was simulated as multilinear, see Table 2.

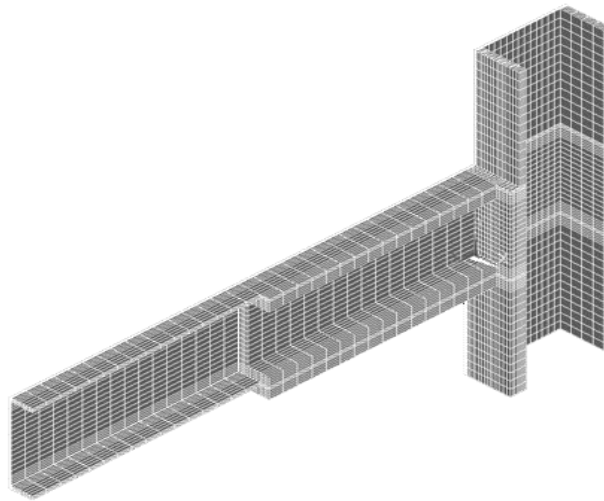


Fig. 4 Column and beam in the FEA model

Tab. 2 The multilinear characteristics of the fire protection material (Protocol, 2004)

Temperature [°C]	20	200	400	600	800	1000
Specific heat capacity [J/kg×K]	924	968	1032	1112	1208	1320
Thermal conductivity [W/m×K]	0.079	0.096	0.137	0.212	0.330	0.500
Density [kg/m <sup>3</sup> ]	440					

A mesh sensitivity study and subsequent validation approved thirty-two thousand nodes as appropriate for prediction. The model was validated on the results of a fire test until one hour after the start of loading. The results are shown in Figure 5. The differences are due to heating of the samples during the experiment from the top edges, which was not fully prevented, while the numerical model does not assume heating from these edges. The level of accuracy is mainly dependent on the accuracy with which the thermal properties of the fire protection material can be defined (Wang et al, 2012).

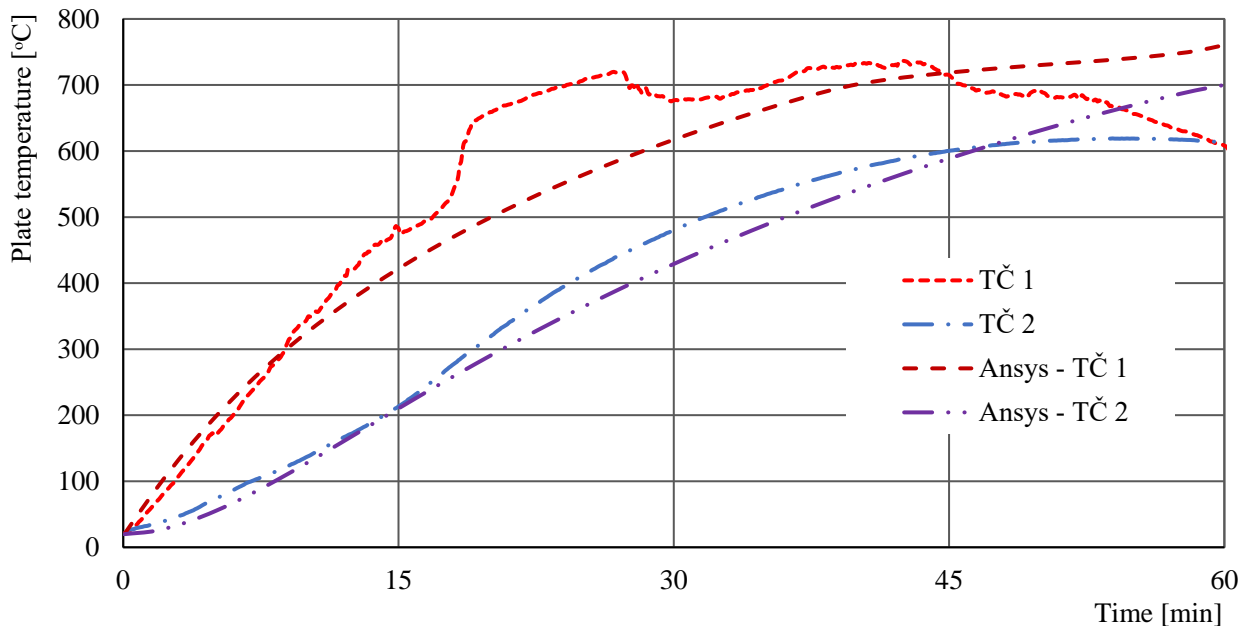


Fig. 5 A comparison between the temperature course of the numerical model and the temperature course of the experiment, protection thickness 20 mm

The sensitivity study focused on the influence of the cross-sectional coefficient of the column, the beam, and the fire protection of the beam on the length of fire protection. The temperature distribution under fire protection is presented in Figure 6 for beam IPE220, column HEB300, coatback 500 mm, 15 min fire exposure. Figure 7 presents the temperature development under fire protection when changing the cross-section of the beam, column HEB300, length of fire protection 500 mm and thickness 20 mm, exposure to fire for 90 min. The graphs show the rapid decrease in temperatures under fire protection confirmed by experiments and by accidents described in the literature. The table shows that the generally-used fire protection length of 500 mm can be considered sufficient. When 500 mm protection length is used for various cross-sections, the temperatures in the numerical model are shown in Table 3.

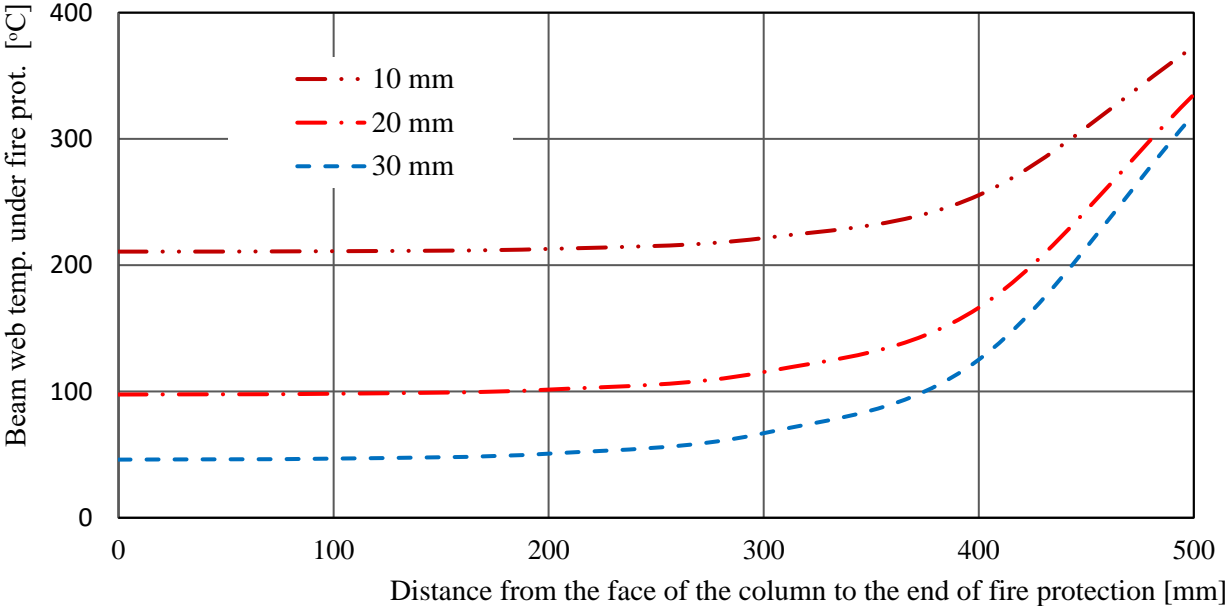


Fig. 6 Temperature development under fire protection for different thicknesses of fire protection, beam IPE220, column HEB300, coatback 500 mm, fire exposure for 15 min

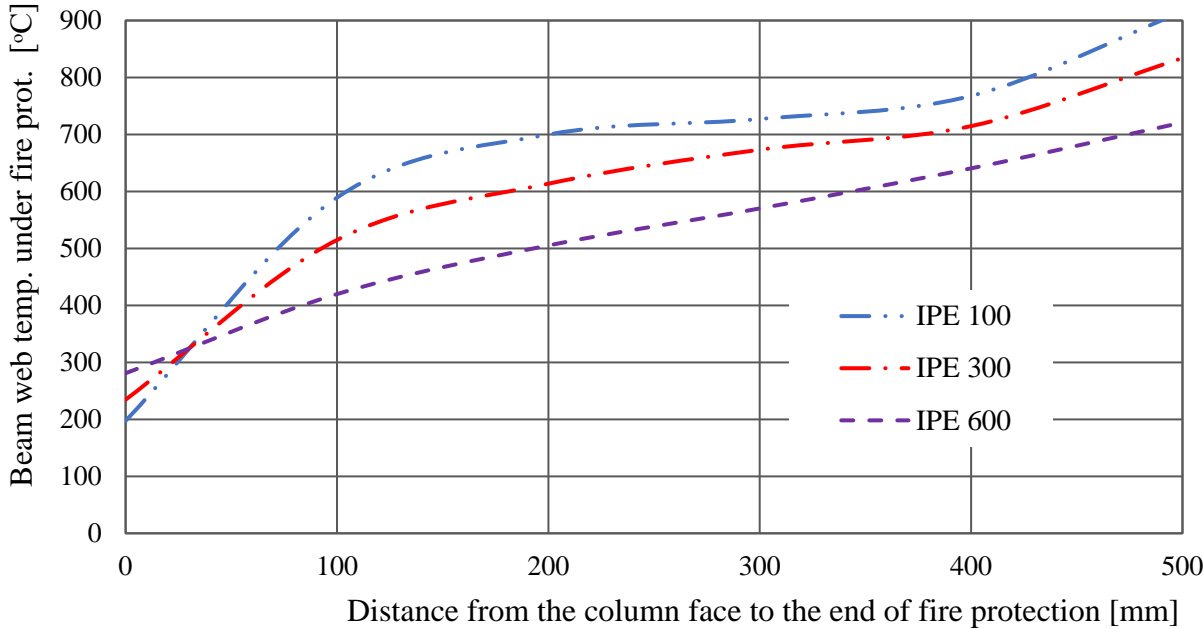


Fig. 7 Temperature development under fire protection when changing the cross-section of the beam, column HEB300, length of fire protection 500 mm and thickness 20 mm, exposure to fire for 90 min

Tab. 3 Beam temperatures in the connection to the column  
for various fire time exposures and coatback lengths

Beam	Section factor $A_m/V$	Protection length / Profile height	Time exposure/coatback length The temperature at a connection to the column [°C]			
			15 min/ 100 mm	30 min/ 200 mm	60 min/ 200 mm	120 min/ 500 mm
IPE 160	269	3.13	246	365	398	275
IPE 220	221	2.27	226	337	416	331
IPE 300	188	1.67	209	312	421	351
IPE 330	175	1.52	203	304	421	377
IPE 500	116	1.00	173	260	425	415

#### 4 CONCLUSIONS

The potential for heat transfer from unprotected structural steel into protected structural steel should be taken into consideration. A sensitivity study (Dobrovolný, 2021) has shown that there is no simple direct relationship between the height of the cross-section, the section factor of the members, or the thickness of the fire protection and the necessary coatback length.

The study showed a rapid decrease in the temperature under fire protection. For fire protection designed for a certain temperature of the column, the predicted temperature is observed to be about 250 mm from the beginning of the fire protection.

The results of our study confirm that a good estimate of the coatback length based on European best practice is 450 mm or 500 mm up to 120 mins for members that are fire protected for expected fire resistance. For short time exposure, up to 30 mins, the length is conservative and may be shortened (Breunese, 2019).

The work was supported by CVUT in Prague grant SGS19/150/OHK1/3T/11.

#### REFERENCES

- Breunese A. 2019. *A simple method for calculation of coat back lengths*, Promat. <https://www.promat.com>.
- Dobrovolný P. 2021. *Partially fire-protected steel members*, Master's thesis, in Czech, CVUT in Prague, <https://dspace.cvut.cz/handle/10467/93442>.
- EN 1993-1-2:2005 Eurocode 3, *Design of steel structures - Part 1-2, General rules, Structural fire design*, Brussels, 2004.
- Friebe M., Jang B.S., Jim A. Y., 2014. *A parametric study on the use of passive fire protection in FPSO topside module*. *International Journal of Naval Architecture and Ocean Engineering*. 6(4), p. 826–839. doi:10.2478/IJNAOE-2013-0216
- Lawrence K. L. 2020, *Structural & Thermal Analysis Using the ANSYS Mechanical APDL Release 2020 Environment*, ANSYS Tutorial Release 2020, Schroff.
- Odolski D., Wang Y.Ch., Yuan J. 2017. *Numerical investigation of intumescent coatback on unprotected secondary beams*, *Applications of Fire Engineering*, Manchester. DOI<https://doi.org/10.1201/9781315107202>
- Parlor B. 2010. *Code of practice for junctions between different Fire protection systems when applied to load bearing structural steel elements*, Technical Guidance Document 008, Association for Specialist Fire Protection, <https://asfp.org.uk>.
- Promat, 2021. *PROMASPRAY® P300*, <https://www.promat-see.com>
- Protocol, 2004. *TERFIX test protocol*, FIRES FR 057/04CPTERFIX, Batizovce.
- Thompson, M. K., Thompson J. M. 2017. *ANSYS mechanical APDL for finite element analysis*, Elsevier.
- Wang Y.C., Burgess I.W., Wald F., Gillie, M. 2012. *Performance-Based Fire Engineering of Structures*, Boca Raton, Florida, USA: CRC Press.
- Yasseri S. 2002. Coat-back length in passive fire protection. in *Offshore Mechanics and Arctic Engineering Conference*. p. 621–627.

# DEVELOPMENT OF A HYBRID SEMI-RIGID CONNECTION FOR STEEL STRUCTURES

Ying Hu<sup>a,b</sup>, Hui Lin<sup>a,b</sup>, Shan-Shan Huang<sup>c</sup>, Ian Burgess<sup>c</sup>, Miles Owarish<sup>d</sup>

<sup>a</sup> Chongqing University, School of Civil Engineering, Chongqing, P.R. China

<sup>b</sup> Key Laboratory of New Technology for Construction of Cities in Mountain Areas (Chongqing University), Ministry of Education, Chongqing 400045, PR China

<sup>c</sup> University of Sheffield, Department of Civil and Structural Engineering, Sheffield, UK

<sup>d</sup> M10 Fire Consultancy Ltd, Arguen House, 4-6 Spicer Street, St. Albans, Hertfordshire, UK

## Abstract

Simple steel connections commonly comprise shear-tab and web-angle joints based on connection classification. The shear-tab connection has excellent stiffness in resisting shear forces, whereas the web-angle joint exhibits the highest ductility of all steel joints. This paper describes development of a novel type of steel joint, which adds a single web angle to a shear-tab joint. The structural behavior of this hybrid joint has been experimentally investigated, and the results are described in this paper. Moreover, shear-tab and web-angle joints have also been tested as a benchmark for direct comparison of different joint types. All these steel joints were made of carbon steel of Grade Q345B. Grade 8.8 high-strength bolts and ER50-6 welding wire were employed for fabrication. Ductile and non-ductile failure modes were observed in the tested steel joints. Steel joints may also fail by bolt fracture in shear. This failure mechanism may result in a reduction of connection ductility. In addition, the moment-rotation curves of steel joints were extracted from the test results, with consideration of effects of different vertical lines of bolts. It should be noted that the hybrid connection has a potential to replace the present shear-tab connection due to its increased ductility and strength.

**Keywords:** Connection, Bolts, Shear-tab, Web-angle, Connection ductility

## 1 INTRODUCTION

Connection of steel members is a complicated issue for a steel-framed building when subjected to a fire. Maintaining the structural integrity of a building requires steel connections with sufficient fire resistance and the ability to avoid connection failure in a fire situation. However, the published research work on the Cardington full-scale fire tests (Lamont, 2001; Liu et al., 2019) reveals the vulnerability of steel connections in fire. Connection failures were described in the report on the collapse of the World Trade Center buildings of New York (Shyam-Sunder, 2005). It should be highlighted that connections are a vital component in a steel-framed structure, being responsible for tying all other steel members together. The connection behavior becomes complicated due to the effects of material deterioration and thermal expansion at high temperatures. The first generation of fire tests on steel connections aimed to study the rotational characteristics of common connections at elevated temperatures and the fire performance of high-strength bolts (Kruppa, 1976). The fire tests completed by Al-Jabri (1999) revealed that isolated joints could not describe the performance of joints within a structural frame, especially in a fire situation, where a large axial force was generated simultaneously in steel beams due to thermal expansion and thermal bowing effects. In addition, the component-based approach simplifies a steel connection into an array of components within which each component has its own non-linear force-displacement characteristics. This method provides a computationally cost-effective procedure for simulation of connection behavior in fire (Liu et al., 2019). The simulations and tests on connections performed by Yu et al. (2009) and Hu et al. (2009) showed that connection ductility in fire may be limited by fracturing of key (brittle) components. It should be highlighted that connection failure may increase the buckling

length of a detached supporting column, as well as damage the floor slabs and allow fire to spread into adjacent compartments. So an ideal connection should have sufficient strength and ductility to retain the structural integrity of a building when exposed to a fire.

This article aims to develop a novel shear-tab hybrid connection with the potential to provide both strength and ductility when exposed to fire. This connection typology is characterized by adding a single web angle into a shear-tab connection for achieving connection ductility (Hu et al., 2017). For comparison, shear-tab and web-angle connections have also been added to the test plan for exploring their moment-rotation characteristics at ambient temperature.

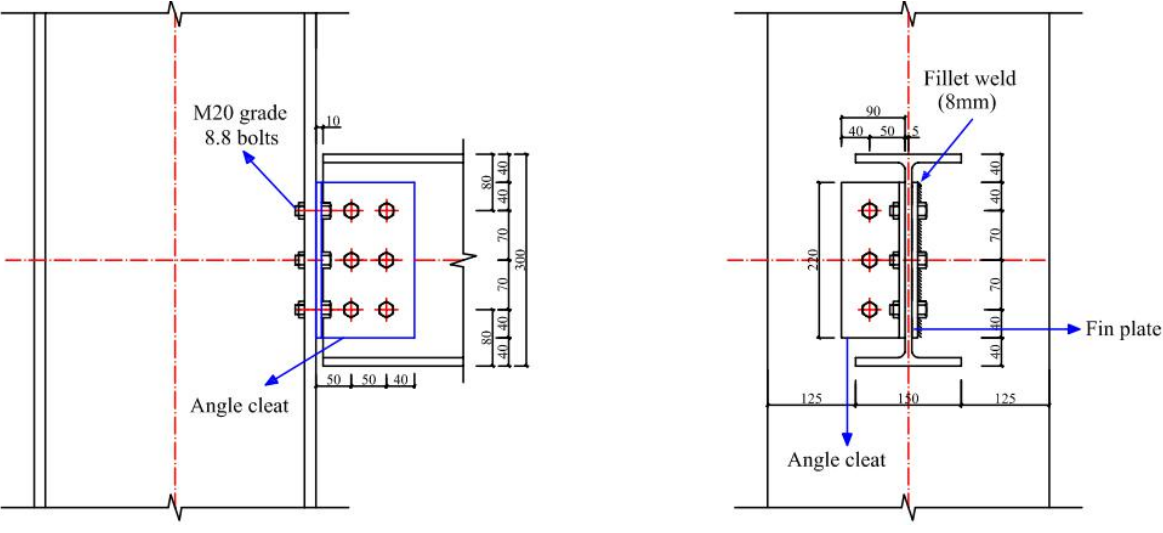
## 2 EXPERIMENTAL PROGRAM

### 2.1 Test specimens

The test program mainly consisted of six connection tests on the three connection types in accordance with GB50017, as shown in Table 1. Each connection typology was represented by two steel connections of the dimensional details shown in Fig. 1. The reason for having two tests per connection typology was to discover the effects of different vertical lines of bolts on connection performance when subjected to external forces. All connection specimens adopted the same column section (H400x400x12x16 mm) and the same beam section (H300x150x10x12 mm). As described previously, the hybrid connection employed a fin plate (shear tab) and a single web angle to connect beams to columns, while the shear-tab connection only used a single shear tab. High-strength bolts (Grade 8.8) and fillet welds were employed in fabrication. The gas shielded welding technique was used for shear tab welding to the column face with ER50-6 welding wire. The yield and peak strengths of fillet welds should meet the nominal values of 430 and 550 MPa respectively, as stipulated by GB50017. However, the double-web-angle connection was characterized by using only high-strength bolts for connection (no welding was needed). In addition, all H-shape steel sections were made of Q355 steels, with the measured yield strength of 363 MPa.

Table 1 Test program for steel connections

	Beam	Column	Angle steel	Fin plate	Fillet weld	Vertical lines of bolts
FWJ-1	H300x150x10x12	H400x400x12x16	L140x90x8	-140x8	8 mm	Double vertical lines
FWJ-2	H300x150x10x12	H400x400x12x16	L100x100x8	-100x8	8 mm	Single vertical line
FPJ-1	H300x150x10x12	H400x400x12x16	/	-140x8	8 mm	Double vertical lines
FPJ-2	H300x150x10x12	H400x400x12x16	/	-100x8	8 mm	Single vertical line
WAJ-1	H300x150x10x12	H400x400x12x16	L140x90x8	/	/	Double vertical lines
WAJ-2	H300x150x10x12	H400x400x12x16	L100x100x8	/	/	Single vertical line



(a)

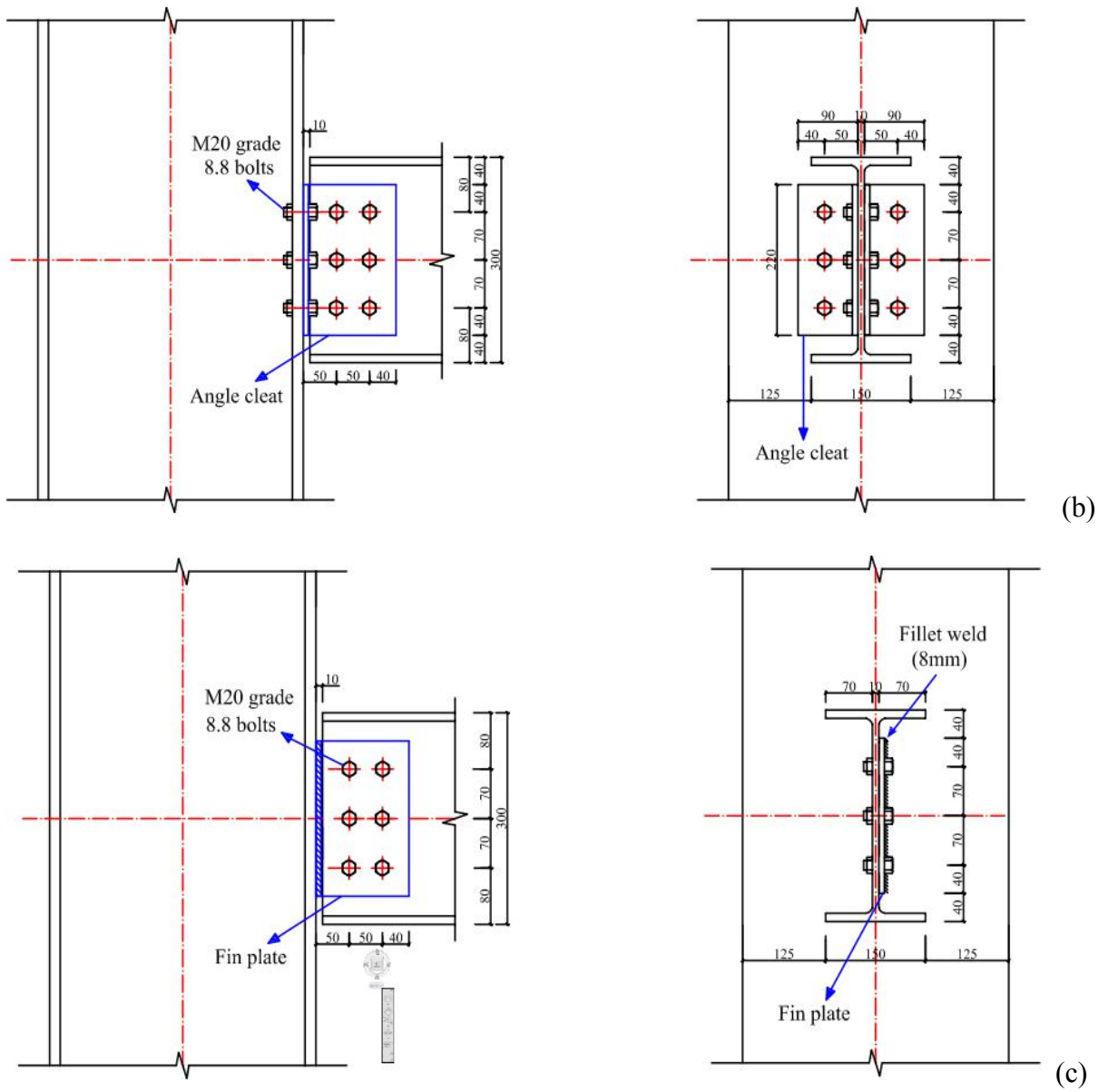


Fig. 1 Connection types: (a) Hybrid connection; (b) Double angle web cleats; (c) Fin plates

## 2.2 Test setup and instrumentation

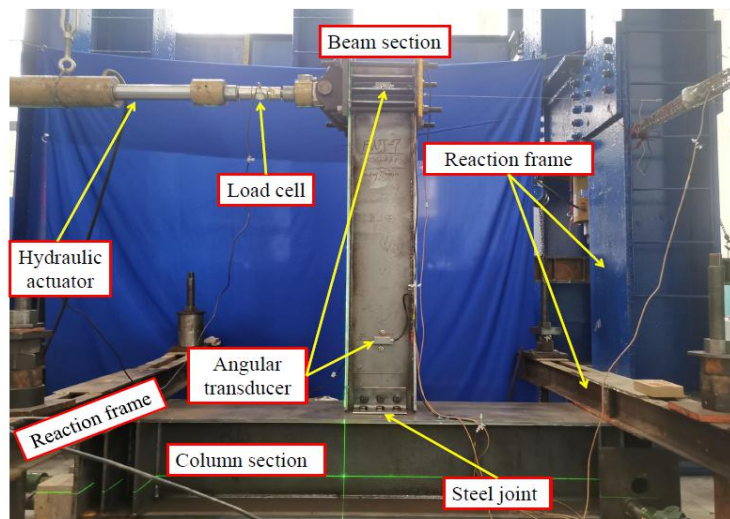


Fig. 2 Experimental setup for connection tests

These connections were tested in the Structural Research Laboratory of Chongqing University. The test setup was designed to accommodate the specimens with beams in a vertical alignment, as illustrated in Fig. 2. The column section was mounted onto the strong floor using a reaction frame as shown. Both ends of the column were attached to the vertical reaction frame using short extended segments to achieve fully-rigid boundary conditions. Two angular transducers were attached onto the beam section during testing: one close to the connection and the other placed at the far end of the beam section as shown. The tensile force was applied to the beam end through a hydraulic actuator. The force measurement was recorded using a data-logging system through the load cell. The readings from the angular transducers were recorded simultaneously by this system.

### 3 EXPERIMENTAL RESULTS

#### 3.1 Moment-rotation curves with connection failures

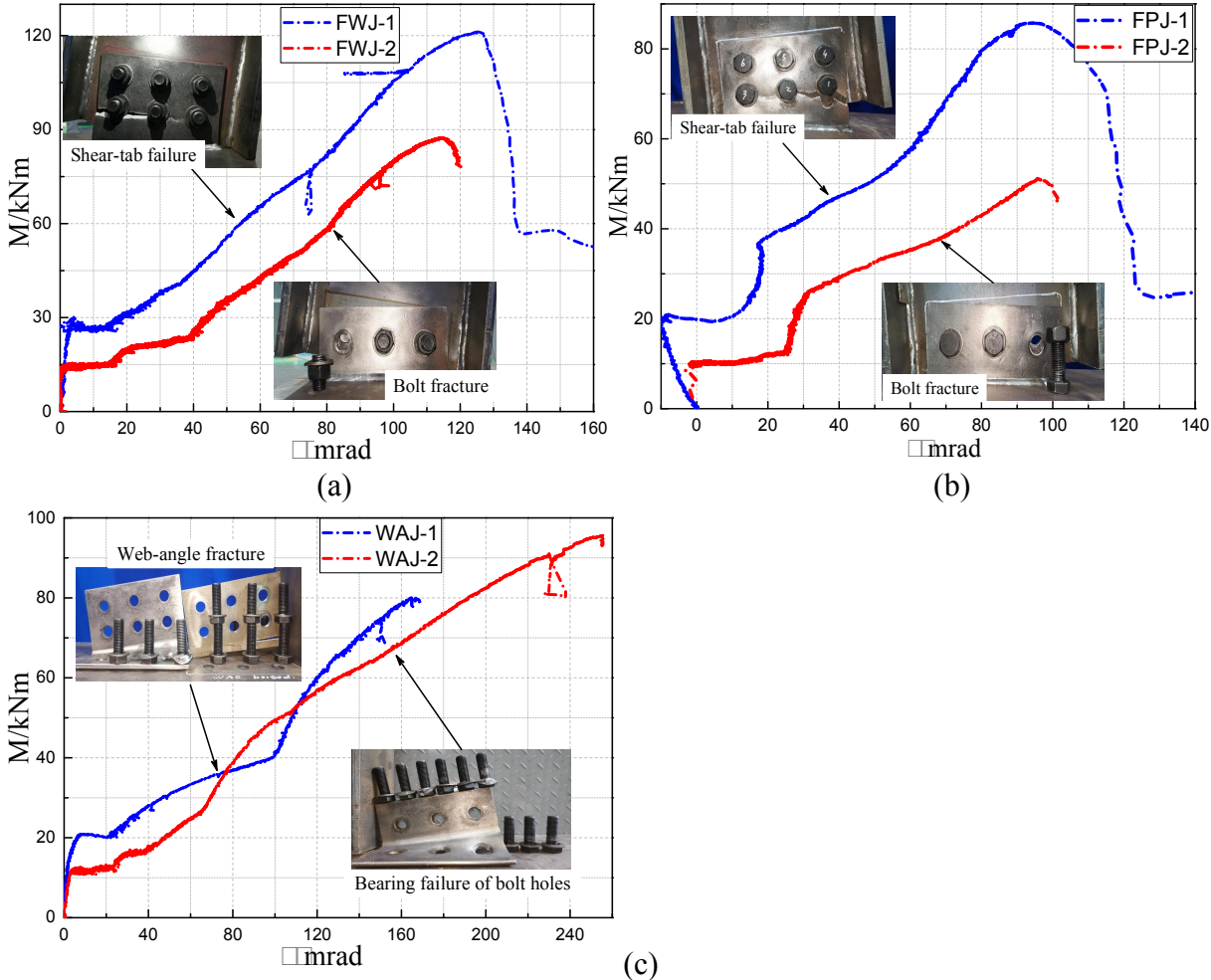


Fig. 3 Moment-rotation curves: (a) hybrid connection; (b) fin-plate connection; (e) web-angle connection

The connection specimens were tested at ambient temperature, with their failure modes and moment-rotation curves being displayed in Fig. 3. Both bolt fracture and shear-tab failure were observed in the hybrid and shear-tab connections. This observation reveals that these two connection failure modes are associated with the number of vertical lines of high-strength bolts employed. Using two vertical lines of bolts can obviously increase the moment resistance for shear-tab and hybrid connections (see Fig 3a and 3b), because using two vertical lines of bolts in joints is capable of mobilizing the full strength of steel shear-tabs, while avoiding bolt fracture. However, bolt fracture was observed in the connections with a single vertical line of bolts; Grade

8.8 high-strength bolts were for the critical components of these steel joints when subjected to external moment. In addition, it is clear that about 33-58% increase of moment resistance was observed in the tested moment-rotation curves when using two vertical lines of bolts. The connection ductility was determined as the rotation corresponding to the peak moment in the curves. It is obvious that preventing bolt fracture can increase the connection ductility as shown in Fig. 4a. The web-angle connections exhibited the most ductile failure mechanism among these connections (see Fig. 4c). The tested web-angle connections showed two types of failure: web-angle fracture and bearing failure of bolt holes. These failure modes were reported in the research work of Yu et al. (2009). However, it should be noted that the web-angle connections in this study only considered a single vertical line of bolts during testing. This suggests that the failure modes reported in bolted web-angle connections are not really associated with the vertical lines of bolts, which might be attributed to material differences between the steel angles used.

### 3.2 Effects of connection typology

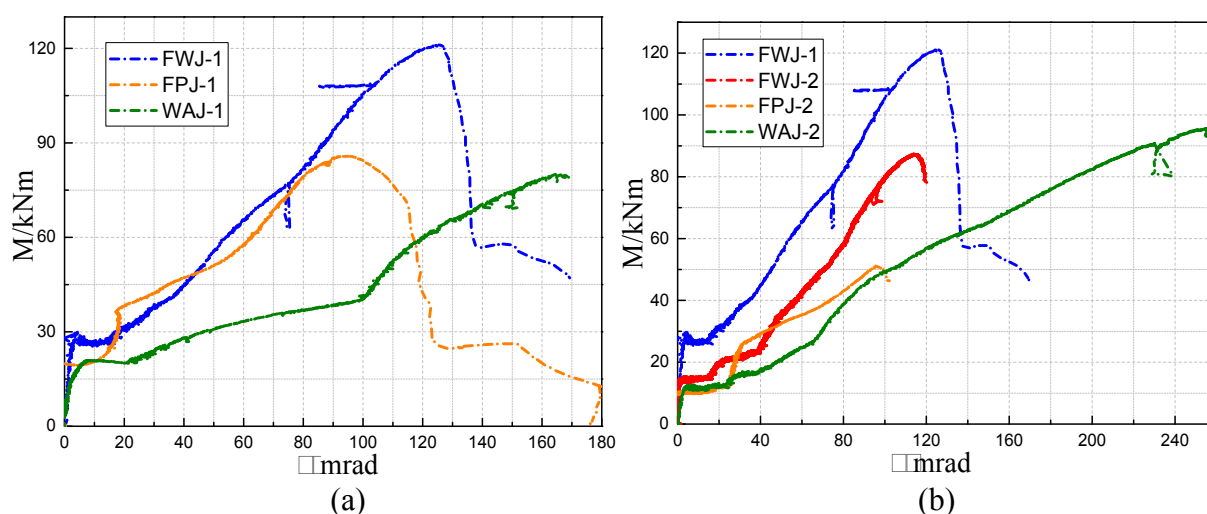


Fig. 4 Effects of connection types: (a) two vertical lines of bolts; (b) single vertical line of bolts

Fig. 4 shows the moment-rotation curves from the perspective of connection typology. The hybrid joint has higher initial stiffness and moment resistance than the shear-tab and web-angle joints. Its initial stiffness and moment resistance can be enhanced by using two vertical lines of bolts. The connection ductility was assessed by the rotational capacity corresponding to the maximum bending moment. Obviously, although the ductility of the hybrid joint was not the highest of the three, it was not the lowest. The failure of the hybrid connection was governed by the fracture of shear-tabs or bolt fracture, which implies that further stretching the web angle may be seen as a reserve of strength and ductility for this joint type.

## 4 CONCLUSIONS

The present study completed a number of tests on the moment-rotation characteristics of these connection types. From the test results, a number of findings can be drawn as follows. It should be noted that Grade 8.8 high-strength bolts may fracture in both the shear-tab and hybrid connections at ambient temperature. The connection moment resistance and initial stiffness can be significantly improved by using two vertical lines of bolts, except in the web-angle connections. Moreover, the hybrid connection's ductility can also be enhanced by using two vertical lines of bolts. The web-angle connection is the most ductile connection typology due to fully stretching two web angles. However, it should be highlighted that connection failures may be varied owing to changing connection configuration or typology.

## ACKNOWLEDGMENTS

The authors would like to acknowledge the financial support from National Natural Science Foundation of China (NSFC Project No. 51578092). My undergraduate mentor, Prof. Jia Cui, should be also acknowledged for his faithful support and effective comments on this project.

## REFERENCES

- Al-Jabri, K. S. (1999). *The behaviour of steel and composite beam-to-column connections in fire*. PhD Thesis, The University of Sheffield.
- Hu Y., Davison J.B., Burgess I.W., Plank R.J. (2009). *Component modelling of flexible end-plate connections in fire*. *International journal of steel structures*, 9(1), p.1-15.
- Hu Y., Xu T., Cui J. & Chongqing University 2017. *A flexible hybrid steel connection*, CN201710570476.2
- Kruppa, J. (1976). *Resistance au feu des Assemblages par boulons haute Resistance*. Puteaux, CTICM.
- Lamont, S. (2001). *The behavior of Multi-storey Composite Steel Framed Structures in response to Compartment Fires*. PhD Thesis, The University of Edinburgh.
- Liu Y., Huang, S.S., Burgess I.W. (2019). *Investigation of a steel connection to accommodate ductility demand of beams in fire*. *Journal of Constructional Steel Research*, 157 (1), p. 182-197.
- Shyam-Sunder, S. (2005), *Federal Building and Fire Safety Investigation of the World Trade Center Disaster: Final report on the collapse of World Trade Center Building 7*. Tech. rep., NIST NCSTAR 1A.
- Yu H., Burgess, I.W., Davison, J.B., Plank, R.J. (2009). *Experimental investigation of the behaviour of fin plate connections in fire*. *Journal of Constructional Steel Research*, 65 (3), p. 723-736.
- Yu H., Burgess, I.W., Davison, J.B., Plank, R.J. (2009). *Tying capacity of web cleat connections in fire, Part 1: Test and finite element simulation*. *Engineering Structures*, 31 (3), p. 651-663.

Proceedings of the International Conference in Ljubljana, 10-11 June 2021  
in edition of Applications of Structural Fire Engineering

**Session**

**Timber structures I**

## A CALCULATION METHOD FOR FLAME EXTENSION FROM PARTIALLY EXPOSED MASS TIMBER ENCLOSURES

Danny Hopkin<sup>a</sup> & Michael Spearpoint<sup>b</sup>

<sup>a</sup> OFR Consultants, Commerce House, Telford Road, Bicester, OX26 4LD

<sup>b</sup> OFR Consultants, Sevensdale House, Lever Street, Manchester, M1 1JA

### Abstract

Mass timber buildings present fire hazards that are often not addressed by design codes and guidance documents, if the structure is permitted to contribute as a source of fuel. One such hazard is increased external flaming as excess fuel burns outside of openings.

This may have implications for a building's fire strategy, be that in terms of storey-to-storey fire spread, or fire spread to adjacent buildings. This paper explores the development of a correlation between global equivalence ratio (GER) and external heat release rate (HRR), in function of the amount of internally exposed combustible surface area to a mass timber enclosure. The correlation is empirically calibrated against existing experimental data and is shown to give an adequate estimation of external HRR where the exposed surface area does not exceed c. 55% of the total enclosure surface area. A separate flame length correlation is developed and is shown to conservatively estimate the flame height from openings when benchmarked against an independent CLT enclosure fire test. However, further benchmarking is required against a larger range of experimental sources to establish the broad scope of applicability.

**Keywords:** mass timber, external flaming, vertical fire spread, global equivalence ratio

### 1 INTRODUCTION

The use of mass timber for the construction of buildings has gained in popularity in jurisdictions around the world where, in the past, it has not been the primary building material. Although this change is partly due to the aesthetic appeal of timber when expressed, it is predominantly due to its environmental credentials. Architects, developers, engineers and local authorities are keen to promote the benefits of using timber and given the declaration of a climate emergency by various jurisdictions, the wider adoption of timber will be a significant part of construction solutions that seek to reduce the built environment's impact on climate change. However, as a combustible structural solution, mass timber introduces fire hazards that are often not present in non-combustible buildings, particularly in terms of the ability of the structure to have a reasonable likelihood of surviving the full duration of a fire (burn-out) (Hopkin et al., 2020) and external fire spread (Law and Hadden, 2020).

External fire spread is one of the key hazards that engineers and authorities attempt to adequately address during the design of buildings. There are typically two objectives with respect to external fire spread, to: 1) inhibit the vertical spread on the surface external envelope of a building or between compartment floors; 2) inhibit the fire spread to or from adjacent buildings (Bartlett and Law, 2020). The external fire spread hazard can be exacerbated where the structure is a source of fuel or linings are combustible, as excess fuel can burn outside of openings, leading to increased flame lengths that have implications for 1) and 2) above.

This paper outlines a potential method of quantifying the external flaming (in terms of external HRR and flame height) associated with mass timber enclosures, such that appropriate design measures to mitigate external fire spread can be developed for future mass timber buildings.

## 2 EXTERNAL FLAMING FROM ENCLOSURE FIRES – GLOBAL EQUIVALENCE RATIO & EXTERNAL HEAT RELEASE RATE

### 2.1 The global equivalence ratio (GER)

In a ventilation-controlled fire, there is insufficient oxygen within the enclosure to burn all the combustible gases that result from the pyrolysis of the fuel. Consequently, some of the fuel is burned outside of the enclosure – resulting in external flaming (Bartlett and Law, 2020). The amount of fuel burned outside is typically quantified through the global equivalence ratio ( $\phi$ ), which is defined as:

$$\phi = \frac{\dot{m}_p r}{\dot{m}_a} \quad (1)$$

where  $\dot{m}_p$  is the maximum pyrolysis rate of the fuel inside the enclosure [kg/s],  $r$  is the stoichiometric ratio of air-to-fuel, which for wood is c. 5.7 (Bartlett and Law, 2020) and  $\dot{m}_a$  is the mass flow rate of air entering the enclosure [kg/s].

A global equivalence ratio (GER) of unity would imply perfect stoichiometry and thus no unburnt fuel exiting the enclosure. A GER > 1 will result in some of the combustible gases that result from the pyrolysis of the fuel burning outside of the enclosure.

The pyrolysis rate inside an inert cuboidal enclosure, with fuel on the floor, has been studied extensively, with both Kawagoe and Sekine (1963) and Delichatsios, et al. (2004) converging upon Equation (2) for ventilation controlled fires:

$$\dot{m}_p = C_v A_0 \sqrt{H_0} = 0.1 A_0 \sqrt{H_0} \quad (2)$$

where  $C_v$  [ $\text{m}^{2/5} \cdot \text{kg/s}$ ] is a constant describing the relationship between the opening factor  $A_0 \sqrt{H_0}$  [ $\text{m}^{5/2}$ ] and the pyrolysis rate of the fuel inside the enclosure,  $A_0$  is the ventilation area [ $\text{m}^2$ ] and  $H_0$  is the height of the ventilation opening(s) [m]. In the study of Delichatsios, et al. it is said that Equation (2) holds irrespective of fuel properties, leading to:

$$\dot{m}_p = 0.22 \dot{m}_a \quad (3)$$

with  $\dot{m}_a$  given by:

$$\dot{m}_a = 0.5 A_0 \sqrt{H_0} \quad (4)$$

### 2.2 Pyrolysis rate and combustible enclosures

Whilst the study of Delichatsios, et al. (2004) was limited to cuboidal enclosures with inert boundaries, it is postulated by the authors of this paper that the presence of combustible surfaces within an enclosure would lead to an increase in pyrolysis rate as additional flaming surfaces heat the overall fuel surface area. In a study of GER and CLT enclosures, Bartlett and Law (2020), postulate a similar concept, whereby the burning rate of the fuel inside the enclosure area is said to be some function / proportional to the ratio of combustible enclosure surface area ( $A_c$ ) to total enclosure surface area ( $A_t$ ).

To consider such an enhancement in pyrolysis rate due to the proportion of enclosure combustible surface area ( $A_c/A_t$ ), a scaled pyrolysis rate ( $\dot{m}_p^*$ ) is introduced herein via Equation (5). To ensure that as  $A_c/A_t$  increases the scaled pyrolysis rate ( $\dot{m}_p^*$ ) increases, the function ( $fn$ ) describing dependency on  $A_c/A_t$  is taken to be of the form  $1 - (A_c/A_t)$ :

$$\dot{m}_p^* \sim \frac{\dot{m}_p}{A_0 \sqrt{H_0} \cdot fn\left(\frac{A_c}{A_t}\right)} \sim \frac{\dot{m}_p}{A_0 \sqrt{H_0} \cdot \left(1 - \left(\frac{A_c}{A_t}\right)\right)} \quad (5)$$

### 2.3 Application to experimental data

Numerous recent experiments have been undertaken in combustible enclosures where the total HRR of the enclosure, i.e., inclusive of variable (room contents, etc.) and permanent fire load (timber linings, exposed timber structure, etc.) has been measured. For the purpose of evaluating Equation (5), data is taken from various experimental sources, including Gorska, et al. (2020), the University of Edinburgh (Hadden et al., 2017), Carleton University (X. Li et al., 2016), the National Fire Protection Association (NFPA) Foundation experiments (Su et al., 2018), and those by Li, et al. (2016) on medium density fibreboard (MDF) enclosures. An estimate of the maximum pyrolysis rate (as a result of the peak HRR) is made for each experimental series assuming 100% combustion efficiency and a net heat of combustion ( $\Delta H_c$ ) of 15,000 kJ/kg reflective of wood (Gorska, 2019). A resulting plot is given in Figure 1, where the scaled pyrolysis rate is plotted against  $A_c/A_t$ . For  $A_c/A_t$  in the range of 0 to 0.55, multiple experimental data sources collapse to a single curve, described by an exponential trend line (as shown). Whilst data is limited for  $A_c/A_t > 0.55$ , extrapolating the trend-line results in reasonable fit up to  $A_c/A_t \approx 0.80$ . The full trend and proposed scope of fit are shown in Figure 1.

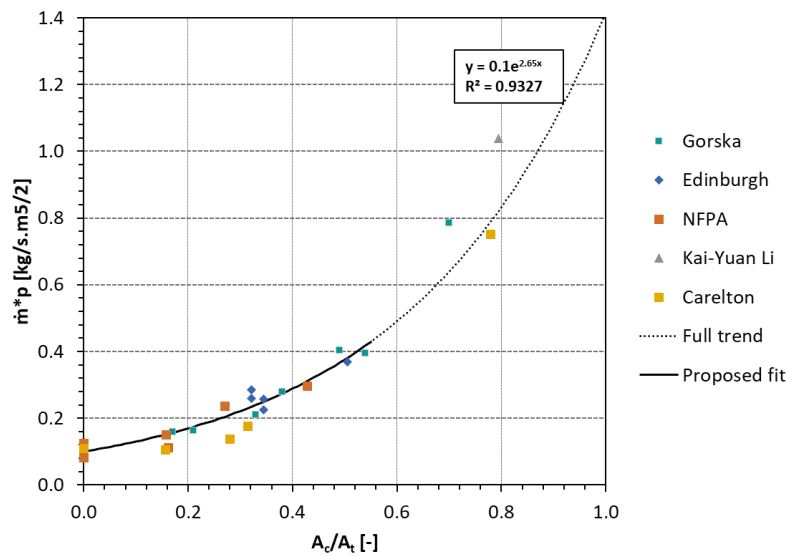


**Figure 1 – Ratio of combustibles to total enclosure surface area vs. scaled pyrolysis rate – comparison of experimental data and trend-line.**

From Figure 1, the scaled pyrolysis rate is described in function of  $A_c/A_t$  (via the trend line) as:

$$\dot{m}_p^* \sim 0.1e^{(8/3)(A_c/A_t)} \quad (6)$$

Correspondingly, the pyrolysis rate in function of  $A_c/A_t$  is resolved through combining Equations (5) and (6) to become Equation (7). When  $A_c/A_t = 0$ , Equation (7) simplifies to Equation (2):

$$\dot{m}_p \sim 0.1 \left(1 - \frac{A_c}{A_t}\right) e^{(8/3)(A_c/A_t)} A_0 \sqrt{H_0} \quad (7)$$

For wood as the fuel ( $r = 5.7$ ), combining Equation (7) with (1) and (4) describes the GER in function of  $A_c/A_t$ , i.e.

$$\phi = \frac{0.1 \left(1 - \frac{A_c}{A_t}\right) e^{(8/3)(A_c/A_t)} A_0 \sqrt{H_0} \cdot r}{0.5 A_0 \sqrt{H_0}} = 1.14 \left(1 - \frac{A_c}{A_t}\right) e^{(8/3)(A_c/A_t)} \quad (8)$$

For the purposes of exploring the external flaming hazard from a combustible enclosure, it is more useful to describe the GER in terms of the excess of fuel factor ( $f$ ), which gives the fraction of fuel burned outside of the compartment (relative to the total pyrolysis rate), as in Equation (9).

$$f = 1 - \frac{1}{\phi} = \frac{\dot{m}_{b,e}}{\dot{m}_p} \quad (9)$$

Where  $\dot{m}_{b,e}$  is the mass burning rate outside of the compartment [kg/s]. By inspection of Equations (8) and (9), it is seen that as  $A_c/A_t$  increases, so does the excess fuel factor ( $f$ ), e.g., for a GER of c. 2, the excess fuel factor is c. 0.5, corresponding to  $A_c/A_t \approx 0.42$ .

### 3 FLAME HEIGHTS FROM OPENINGS

#### 3.1 Experiments by Goble

Goble (2007) reports a systematic experimental study on flame heights from openings by varying parameters that include the opening size (ranging from 200 to 500 mm in width and height) and maximum heat release rate (from 26 to 305 kW) with a bench-scale enclosure (of internal dimensions c. (w) 1 m × (d) 1.5 m × (h) 1 m). Flame heights were estimated based upon digital image correlation, with the mean flame height relative to the neutral plane estimated based upon 50% intermittency / frequency. A plot of mean flame height versus total HRR ( $\dot{Q}_{tot}$  in kW) is given Figure 2 (left), covering a range of different opening sizes and aspect ratios.

#### 3.1 Correlating flame height

Lee, et al., (2007) describe two non-dimensional parameters relating to the convective flow at an opening and the characteristic exit velocity and the mass flow. The most relevant to this study is given below:

$$\ell_1 = (A_0 \sqrt{H_0})^{2/5} \quad (10)$$

Lee, et al., propose that the length scale  $\ell_1$  is a governing parameter in the height of flames emanating from an opening, and include this within a non-dimensional HRR ( $\dot{Q}^*$ ) as follows:

$$\dot{Q}^* = \frac{\dot{Q}_{ext}}{\rho_\infty C_p T_\infty \sqrt{g} \ell_1^{5/2}} = \frac{\dot{Q}_{tot} - 1500 A_0 \sqrt{H_0}}{\rho_\infty C_p T_\infty \sqrt{g} \ell_1^{5/2}} = \frac{\dot{m}_{b,e} \Delta H_c}{\rho_\infty C_p T_\infty \sqrt{g} \ell_1^{5/2}} \quad (11)$$

With  $\dot{Q}_{ext}$  the external HRR [kW],  $1500 A_0 \sqrt{H_0}$  defines the ventilation controlled HRR ( $\dot{Q}_v$  in kW),  $\rho_\infty$  the free stream density of air [kg/m<sup>3</sup>],  $C_p$  the specific heat of air [kJ/kg.K], and  $T_\infty$  the ambient temperature [K]. Subsequently, the flame height above the neutral plane can be considered as some function of the non-dimensional HRR ( $\dot{Q}^*$ ), adopting a scaled flame height ( $Z^*$ ) in lieu of true flame height, i.e.

$$Z^* = \frac{Z_f}{\ell_1} = fn(\dot{Q}^*) = fn \left[ \frac{\dot{Q}_{ext}}{\rho_\infty C_p T_\infty \sqrt{g} \ell_1^{5/2}} \right] = fn \left[ \frac{\dot{Q}_{tot} - \dot{Q}_v}{\rho_\infty C_p T_\infty \sqrt{g} \ell_1^{5/2}} \right] \quad (12)$$

Plotting  $\dot{Q}^*$  (as defined by Equation (11)) against  $Z^*$  for the experimental data reported by Goble, results in Figure 2 (right), leading to the trendline in Equation (13). From this, the flame height can be directly computed in function of the opening dimensions and the external HRR.

$$Z^* = \frac{Z_f}{\ell_1} = 2.0(\dot{Q}^*)^{3/5} = 2.0 \left[ \frac{\dot{Q}_{ext}}{\rho_\infty C_p T_\infty \sqrt{g} \ell_1^{5/2}} \right]^{3/5} \quad (13)$$

### 4 APPLICATION TO A PARTIALLY EXPOSED CLT COMPARTMENT

Gorska (2019) and Emberley, et al. (2017) report on a large-scale CLT experiment that was not used in the development of previous correlations describing the relationship between  $A_c/A_t$ , GER and excess fuel factor ( $f$ ). The experimental enclosure had internal dimensions of 3,500 × 3,500 × 2,700 mm, with a single door opening of 850 × 2,100 mm. The ceiling and a single wall were exposed

cross laminated timber (CLT), resulting in a combustible enclosure surface area of c. 21.7 m<sup>2</sup>. This represents c. 35% of the total enclosure surface area. Based upon the given geometrical parameters for the large-scale CLT experiment, Table 1 estimates the flame height from the opening using the correlations presented in Section 2 and 3.

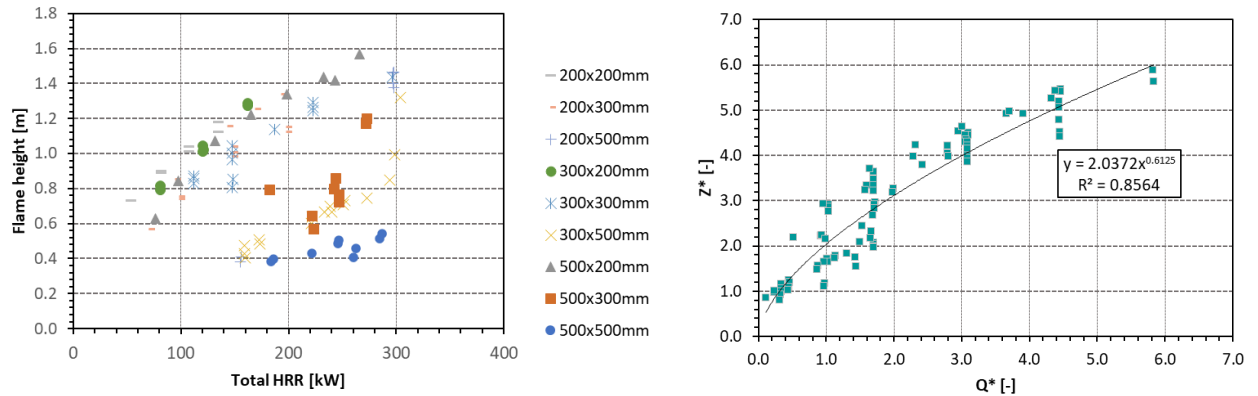


**Figure 2 – (left) Mean flame height (above neutral plane) versus total HRR for different opening sizes per Goble; (right)  $Q^*$  vs  $Z^*$  for experimental data by Goble (with trend-line).**

The flame height as calculated in Table 1 is expressed both relative to the neutral plane ( $Z_f$ ) and relative to the top of the opening ( $Z_{op}$ ). In the latter case, the neutral plane is taken as the half-height of the opening (in consistency with Equation (4)). From the peak pyrolysis rate, the peak total HRR is estimated as c. 6,400 kW (for a net heat of combustion ( $\Delta H_c$ ) of 15,000 kJ/kg) using Equation (7). Emberley, et al., estimated the HRR contribution from cribs to be c. 4,000 kW, i.e., c. 2,400 kW is estimated as being attributable to the CLT combustion. This would correspond with a CLT mass loss rate of c. 7.4 g/m<sup>2</sup>/s, when averaged across the 21.7 m<sup>2</sup> exposed CLT area.

**Table 1 – Computation of flame height from openings for experiment by Emberley, et al. and Gorska**

Parameter	Unit	Output	Parameter	Unit	Output
$A_c/A_t$	-	0.35	$A_0\sqrt{H_0}$	m <sup>5/2</sup>	2.59
$\phi$	-	1.88	$f$	-	0.47
$\dot{m}_p$	kg/s	0.43	$\dot{m}_{b,e}$	kg/s	0.20
$\dot{Q}_{ext} = \dot{m}_{b,e}\Delta H_c$	kW	3,010	$\ell_1$	-	1.46
$\dot{Q}^*$	-	1.06	$Z^*$	m	2.07
$Z_f$	m	3.02	$Z_{op}$	m	1.97

Figure 3 is taken from Emberley, et al. and Gorska, indicating the flame height above the opening at different intermittencies, also derived from digital image correlation. Taking the mean flame height as 50% intermittency (as indicated by the dashed line in Figure 3), the experimental figure is c. 1.55 m above the opening, in contrast with 1.97 m as derived in Table 1 (from the correlations presented).

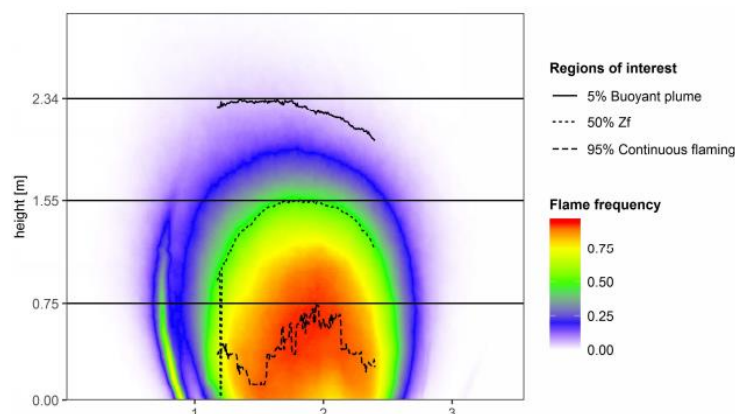


**Figure 3 – Flame height above opening at different frequencies, from Gorska (2019).**

## 5 CONCLUSIONS

Mass timber buildings present fire hazards that are often not addressed by design codes and guidance documents, if the structure is permitted to contribute as a source of fuel. One such hazard is increased external flaming as excess fuel burns outside of openings under ventilation-controlled fire conditions.

This paper has developed an empirical correlation that permits the estimation of the external HRR in function of the exposed combustible surface area in an enclosure, based upon the GER. This is supplemented with the derivation of an empirical flame height correlation based upon experiments by Goble. Both derived correlations are applied to a large-scale experiment by Emberley, et al., and Gorska where conservative agreement is shown in terms of the estimated and measured mean flame heights above an opening to a partially exposed CLT enclosure (with the calculated flame height above the opening approximately corresponding with a measured flame frequency of c. 25%).

Further work is required to benchmark the correlations against other experimental sources to establish the general field of applicability.

## REFERENCES

- Bartlett, A., Law, A., 2020. Influence of excess fuel from timber lined compartments. *Constr. Build. Mater.* 235, 117355. <https://doi.org/10.1016/j.conbuildmat.2019.117355>
- Delichatsios, M.A., Silcock, G.W.H., Liu, X., Delichatsios, M., Lee, Y.-P., 2004. Mass pyrolysis rates and excess pyrolysate in fully developed enclosure fires. *Fire Saf. J.* 39, 1–21. <https://doi.org/10.1016/j.firesaf.2003.07.006>
- Emberley, R., Gorska, C., Bolanos, A., Lucherini, A., Solarte, A., Soriguer, D., Gonzalez, M.G., Humphreys, K., Hidalgo, J.P., Maluk, C., Law, A., Torero, J.L., 2017. Description of small and large-scale cross laminated timber fire tests. *Fire Saf. J.* 91, 327–335. <https://doi.org/10.1016/j.firesaf.2017.03.024>
- Goble, K., 2007. Height of flames projecting from compartment openings (Master's thesis). University of Canterbury.
- Gorska, C., 2019. Fire dynamics in multi-scale timber compartments (PhD Thesis). The University of Queensland, Brisbane.
- Gorska, C., Hidalgo, J.P., Torero, J.L., 2020. Fire dynamics in mass timber compartments. *Fire Saf. J.* 103098. <https://doi.org/10.1016/j.firesaf.2020.103098>
- Hadden, R.M., Bartlett, A.I., Hidalgo, J.P., Santamaria, S., Wiesner, F., Bisby, L.A., Deeny, S., Lane, B., 2017. Effects of exposed cross laminated timber on compartment fire dynamics. *Fire Saf. J., Fire Safety Science: Proceedings of the 12th International Symposium* 91, 480–489. <https://doi.org/10.1016/j.firesaf.2017.03.074>
- Hopkin, D., Spearpoint, M., Gorska, C., Krenn, H., Sleik, T., Milner, M., 2020. Compliance road-map for the structural fire safety design of mass timber buildings in England. *SFPE Eur.* Q4.
- Kawagoe, K., Sekine, T., 1963. Estimation of Fire Temperature Rise Curves in Concrete Buildings and its Application. *Bull. Jpn. Assoc. Fire Sci. Eng.* 13, 1–12. <https://doi.org/10.11196/kasai.13.1>
- Law, A., Hadden, R.M., 2020. We need to talk about timber: fire safety design in tall buildings. *Struct. Eng. J. Inst. Struct. Eng.* 98, 10–15.
- Lee, Y.-P., Delichatsios, M.A., Silcock, G.W.H., 2007. Heat fluxes and flame heights in façades from fires in enclosures of varying geometry. *Proc. Combust. Inst.* 31, 2521–2528. <https://doi.org/10.1016/j.proci.2006.08.033>
- Li, K.-Y., Wang, J., Ji, J., 2016. An experimental investigation on char pattern and depth at postflashover compartments using medium-density fibreboard (MDF). *Fire Mater.* 40, 368–384. <https://doi.org/10.1002/fam.2291>
- Li, X., McGregor, C., Medina, A., Sun, X., Barber, D., Hadjisophocleous, G., 2016. Real-scale fire tests on timber constructions. *WCTE 2016 - World Conf. Timber Eng.*
- Su, J., Lafrance, P.-S., Hoehler, M., Bundy, M., 2018. Fire safety challenges of tall wood buildings – Phase 2: Task 2 & 3 – Cross laminated timber compartment fire tests (No. FPRF-2018-01). Fire Protection Research Foundation, Quincy.

## EFFECT OF WOOD MINERALISATION ON IGNITION TIME AND BURNING DYNAMICS PARAMETERS

Nataša Knez<sup>a</sup>, Andreja Pondelak<sup>a</sup>, Andrijana Škapin<sup>a</sup>, Friderik Knez<sup>a</sup>, Rožle Repič<sup>a</sup>

<sup>a</sup> Slovenian Building and Civil Engineering Institute, Ljubljana, Slovenia

### Abstract

Due to its manifold favourable properties wood is a desirable material in construction. Unfortunately, it burns quite easily, so a significant effort is made to improve the fire properties of the wood. A promising method of improving fire properties of wood is its mineralization. Several wood types, wood treating solutions, and wood treating protocols have been tested using cone calorimeter. The wood treatments were based on the incorporation of magnesium, calcium and strontium carbonate in the wood, using different treatment strategies and combinations.

For comparison of fire-related properties of differently treated wood, the ignition time under a variety of testing conditions was selected as an appropriate measure when testing using a standard cone calorimeter according to ISO 5660-1. Additionally, the heat release rate from burning wood sample in the experiment has been observed to better understand the dynamics of combustion.

The results show postponed ignition of mineralized wood and lower heat release rate values compared to untreated wood. Burning time in treated samples was also found to be longer. Finally, the results have been used to simulate an approximate reaction to fire class determination if the treated wood was used on facades and some other applications. The predicted reaction to fire class was used as the final criterion for the assessment of the treated wood compared to untreated wood. It was shown that in some cases, there was one step in classification difference (i.e. Euroclass D improved to Euroclass C reaction to fire).

**Keywords:** wood mineralisation, time of ignition, heat release rate in mineralised wood

## 1 INTRODUCTION

Wood is a sustainable construction material that has good mechanical and physical properties as well as pleasant effect on living conditions. Use of wood in construction, for façade or indoor linings brings up concerns about fire safety since wood can relatively easily burn. Suppression of fire with a help of fire retardants is most common approach but due to possible toxic effect in combustion it can be problematic when human lives are endangered. Many efforts have been made to find a nontoxic way of fire suppression.

Mineralisation of wood with inorganic fire retardants is a promising approach (Popescu, 2020, Lowden, 2013). Different impregnation procedures and chemical solutions have been proposed.

In presented study effect of different chemical solutions for wood mineralisation process on fire properties has been discussed involving untreated as well as thermally modified wood.

## 2 WOOD MINERALISATION

Wood mineralisation is a process of adding inorganic minerals to organic molecules of wood. Mineralisation is often performed by submerging a wood into a certain solution. Usually the process is improved when using an under pressure and/or overpressure conditions. With a help of different pressure levels a solution can protrude deeper into a wood structure.

For purpose of the study a procedure proposed by Pondelak et al (2019) was used. The wood was impregnated by a solution of acetoacetate which in further processing transforms into carbonate. Procedure of further processing takes 80 hours and consists of alternating cycles of soaking and drying at 80°C and 40 % to 80 % of relative humidity. After mineralisation procedure wood was

conditioned at 20°C and 65% of relative humidity for three weeks. In 10 mm thick testing samples the dry carbonate integration in wood was (12 ± 4) %.

For wood mineralisation many different solutions were used for forming different carbonates including calcium carbonate, magnesium carbonate, strontium carbonate and some mixtures of them as well. Sometimes the procedure has been repeated to increase the deposition of carbonate and consequently improve the fire characteristics.

### 2.1 Thermal modification

For comparison a thermally modified spruce and beech wood was also mineralised. Thermal modification was made according to commercial procedure Silvapro® (Rep et al, 2002, Rep et al, 2012) at 220°C. Mass loss of wood after thermal modification was between 11 % and 15%. The procedure including the cooling process took around 24 hours. Before mineralisation process the modified wood was conditioned for three weeks at 20°C and 65% of relative humidity.

## 3 MEASURING PRINCIPLE

For the purpose of the study reaction to fire has been observed. Reaction to fire is a property of material or product where contribution of material in case of fire is observed. It includes many aspects including observing heat release rate from the burning sample, fire growth rate, smoke release, presence of burning droplets or particles. A small scale testing was performed using cone calorimeter according to ISO 5660-1. Smoke produced during testing was analysed with FTIR analyser according to ISO 19702 and emissions of untreated and mineralised wood were compared. Cone calorimeter testing device includes an electrical heater for provision of constant, pre-set irradiated heat flux density. In our study the specimens were exposed to a constant heat flux of 50 kW/m<sup>2</sup>.

Testing of fire properties was performed on untreated and mineralised spruce and beech wood. For testing specimens of dimensions 100 mm × 100 mm of 10 mm thickness were used.

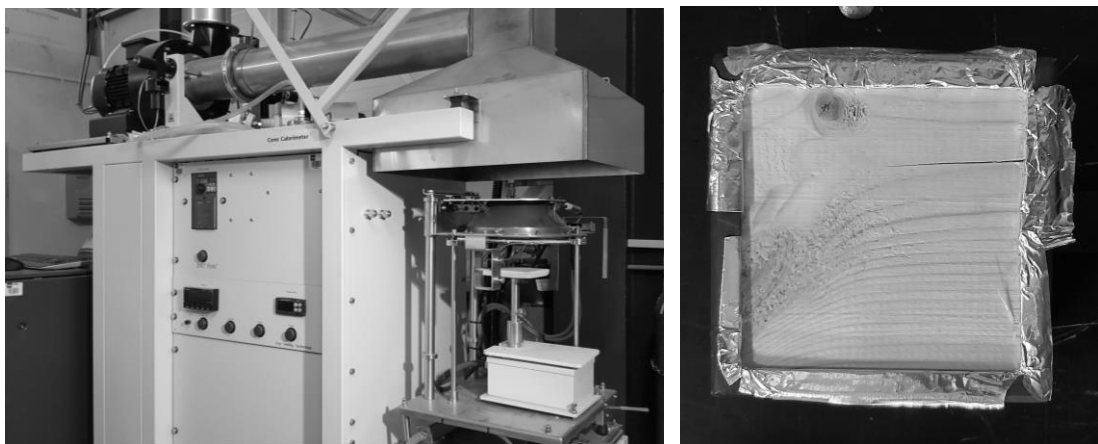


Fig. 1 Cone calorimeter (ISO 5660-1) testing device (left) and prepared specimen before testing (right).

## 4 RESULTS

Reaction to fire classification according to European standard EN 13501-1 is based on results of different tests. Untreated wood and wood based products usually fulfil requirements for Euroclass D based on two testing methods: small flame (EN ISO 11925-2) and SBI testing method (EN 13823). The latter is an intermediate scale testing method which requires relatively large testing specimens. For the purpose of this study a small scale testing method ISO 5660-1 was used instead, and the SBI parameters were determined by numerical simulation using ConeTool (RISE, Sweden). Numerical simulation is based on measured heat release rate (HRR) and time of ignition.

Mineralisation of wood with carbonates seems to delay ignition and prolong time to HRR's second peak. The time between the first and the second peak is related to the thickness of the tested specimen which for the purpose of this study was the same for all tested specimens.

Different types of carbonates or their mixtures have different effect on HRR. The effect is more pronounced in beech wood as it is in spruce wood. When comparing thermally modified wood with thermally modified and mineralised wood, a delay and reduction of HRR in mineralised wood for both species is significant.

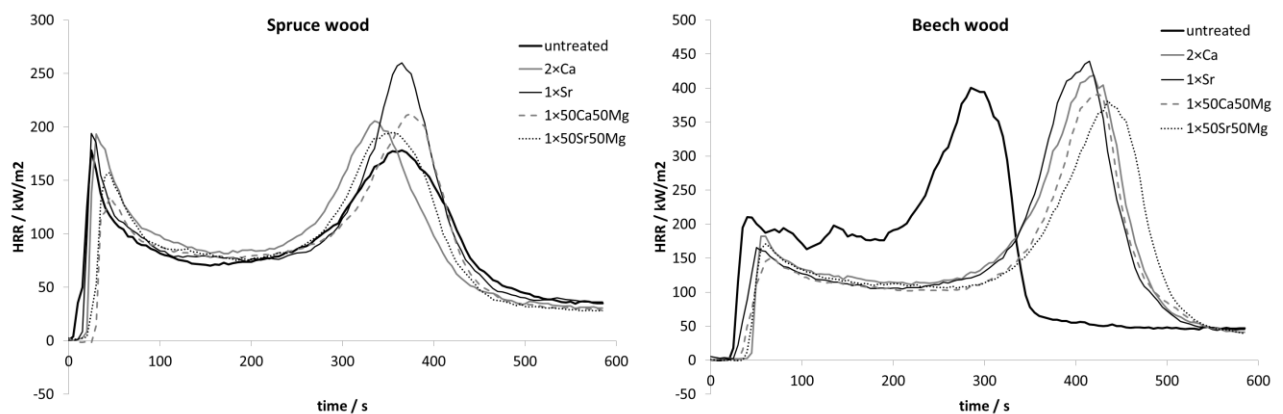


Fig. 2: Heat release rate for untreated and mineralised spruce (left) and beech (right) wood.

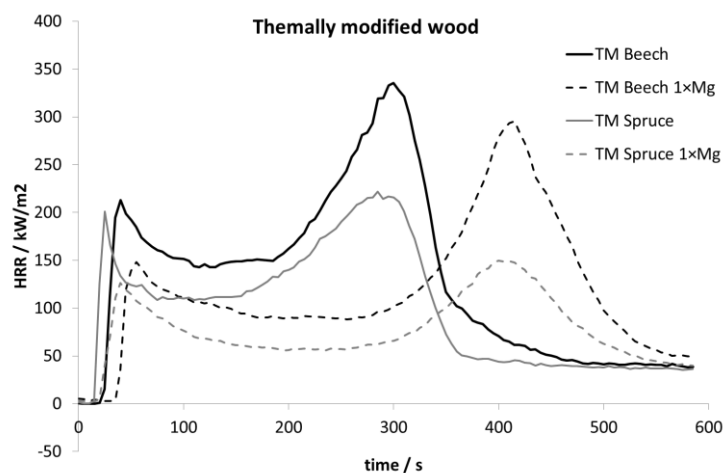


Fig. 3: Heat release rate for thermally modified (solid line) and thermally modified and mineralised (scattered line) spruce and beech wood.

#### 4.1 Results of numerical simulation

Improvement of reaction to fire properties of mineralised wood compared to untreated wood was evaluated by comparison of simulated SBI parameters THR (total heat release) and FIGRA (fire growth rate index). In both, treated spruce and beech wood a decrease of THR and FIGRA values was observed; which indicates better fire characteristics. In treated spruce and in beech wood large decrease of FIGRA parameter was observed for all proposed mineralisation treatments. In treated beech wood similarly a decrease was observed also in THR parameter. Thermally modified wood has typically worse reaction to fire characteristics as non-modified wood, but in the case modified wood is treated with mineralisation procedure, the effect on observed parameters suggests better fire behaviour.

Another observed parameter was ignition time which is defined as the time from exposure to occurrence of the sustained flaming. Mineralised wood typically ignited later as untreated wood. For both thermally modified spruce and beech wood the time of ignition was shorter as for untreated wood, but after mineralisation of modified wood the ignition time increased for about 30% in both wood species. Increased ignition time, which indicates postponed ignition, is suggesting improvement of fire characteristics.

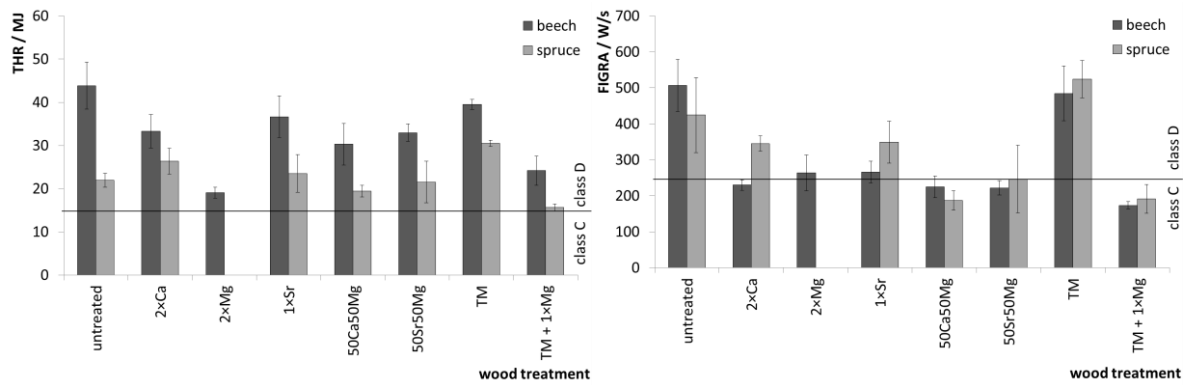


Fig. 4: Simulated values of THR (Total Heat release) and FIGRA (Fire growth rate index) for untreated, treated and thermally modified as well as both thermally modified and treated spruce and beech wood. The line indicates the limit value for Euroclass C (both THR and FIGRA criteria should be fulfilled).

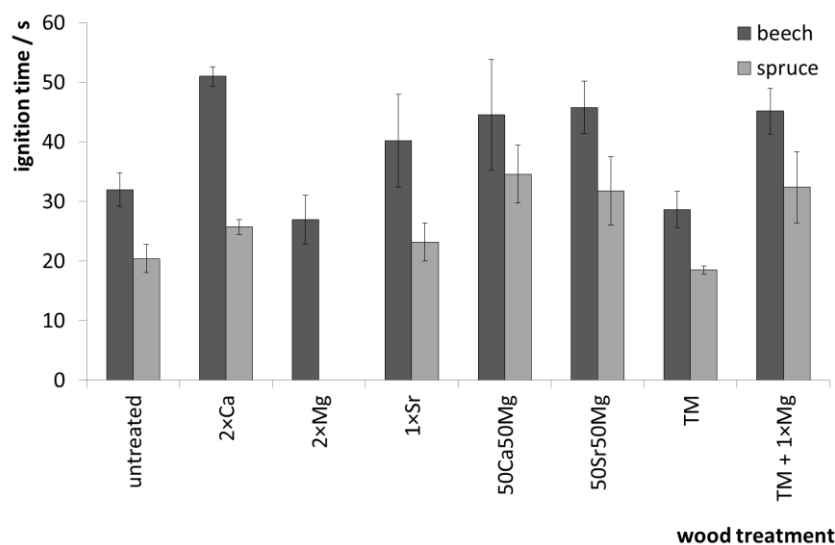


Fig. 5: Measured ignition time for untreated, treated and thermally modified as well as both thermally modified and treated spruce and beech wood.

Table 1 Average value of simulated parameters THR and FIGRA and measured time of ignition for untreated, impregnated and thermally modified (TM) spruce and beech wood. Treated: 2xCa: twice with calcium solution; 2xMg: twice with magnesium solution, 1xSr: once with strontium solution; 50Ca50Mg mixture of 50% of calcium and 50% of magnesium solution; 50Sr50Mg: mixture of 50% of strontium and 50% of magnesium solution; TM + 1xMg: thermally modified and mineralised with magnesium solution.

	spruce				beech			
	No.	average			No.	average		
		THR	FIGRA	time of ignition		THR	FIGRA	time of ignition
untreated	4	22,0±1,7	425±104	20,4±2,4	2	43,9±5,4	507±72	32,0±2,8
2xCa	4	26,4±3,0	345±21	25,8±1,3	4	33,3±3,9	230±14	51,0±1,6
2xMg					5	19,1±1,3	264±50	27,0±4,1
1xSr	5	23,5±4,4	349±58	23,2±3,2	5	36,7±4,8	266±30	40,2±7,8
50Ca50Mg	5	19,4±1,4	187±27	34,6±4,8	5	30,3±4,8	225±30	44,6±9,7
50Sr50Mg	5	21,5±4,8	246±94	31,8±25,8	5	33,0±2,1	222±20	45,8±4,4
TM	2	30,5±0,7	525±52	18,5±0,7	3	39,5±1,2	485±76	28,7±3,1
TM + 1xMg	5	15,6±0,9	191±40	32,4±5,9	5	24,2±3,4	174±10	45,2±3,8

## 4.2 Results of FTIR analyses

When testing with cone calorimeter some specimens' combustion gases were also analysed for presence of toxic gases using FTIR analysis. The analysis provides continuous measurement of several toxic gases. In treated spruce wood the most significant decrease compared to untreated wood was observed in formaldehyde concentration. In Figure 6 results of five measurements on untreated spruce wood and spruce wood treated with calcium solution are shown. Also CO/CO<sub>2</sub> ratio was calculated and more constant and generally lower values were observed for mineralised wood samples. In Figure 7 progression of CO/CO<sub>2</sub> ratio for five untreated spruce specimens and five spruce specimens mineralised with calcium carbonate is shown.

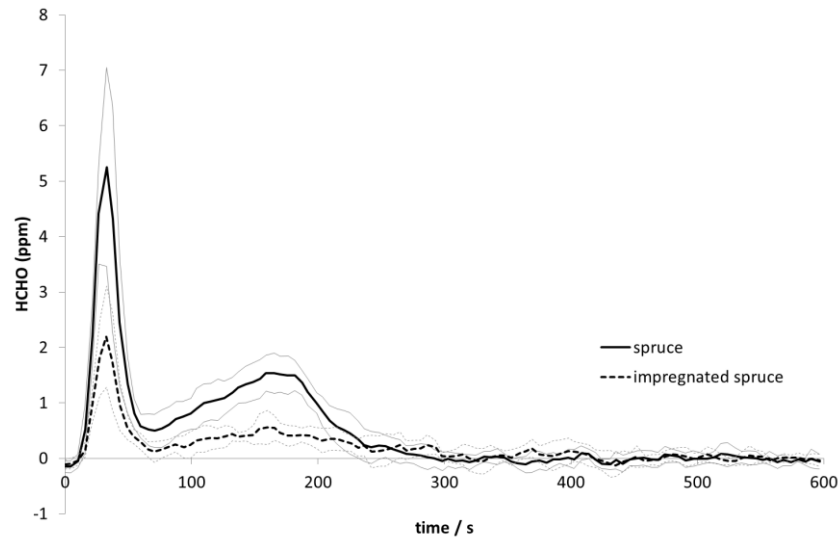


Fig. 6: Concentration of formaldehyde during cone calorimeter test for untreated spruce wood and spruce treated with calcium carbonate: Average value (thick line) with standard deviation (thin line) of five measurements.

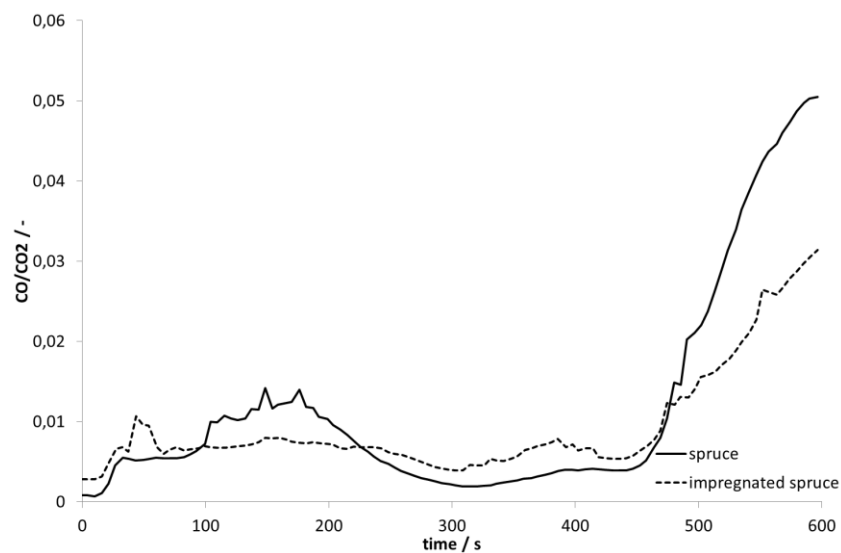


Fig. 7: CO/CO<sub>2</sub> ratio for five specimens measured with cone calorimeter for untreated spruce wood (solid line) and spruce treated with calcium carbonate (scattered line).

## 5 CONCLUSIONS

An extensive study of different impregnation technics for wood mineralisation was verified for reaction to fire properties. It was shown that different solutions and processes used for mineralisation have different effect on fire properties of treated wood. Furthermore the effect is not the same for different wood species. In beech wood the effect of mineralisation was more pronounced as in spruce wood.

Fire properties of wood typically worsen if the wood is subjected to thermal modification, However after mineralisation the fire properties treated thermally modified wood are typically better as in untreated wood. This was observed for both: spruce wood and beech wood. Some samples of thermally modified and mineralised spruce wood fulfilled criteria for both THR and FIGRA parameter for proposed Euroclass C.

Positive effect of wood mineralisation was observed also for release of formaldehyde when testing untreated spruce and spruce mineralised with calcium carbonate. CO/CO<sub>2</sub> ratio also shows generally lower values for impregnated spruce wood compared to untreated wood, indicating cleaner burning.

## ACKNOWLEDGMENTS

Part of the research was financed by Ministry of Education, Science and Sport of Republic of Slovenia and European Union – European Regional Development Fund (project WOOLF).

## REFERENCES

- Lowden L. A., Hull T. R. 2013. *Flammability behaviour of wood and a review of the methods for its reduction*. *Fire Science Reviews* 2(1), p. 1-19.
- Pondelak A., Sever Škapin A., Knez N., Škrlep L., Knez F., Pazlar T., Legat A. 2019. The process of wood mineralization by using acetoacetate solutions for improved essential properties. Patent application no. P 201900260. Ljubljana The Slovenian Intellectual Property Office.
- Popescu C. M., Pfriend A. 2020. *Treatments and modification to improve the reaction to fire of wood and wood based products – An overview*. *Fire and Materials*, 44(1), p. 100-111.
- Rep G., Pohleven F. 2002. *Wood modification—A promising method for wood preservation = Modifikacija lesa – obečavajuća metoda za zaštitu drva*. *Drvna industrija* 52(2). p. 71-76.
- Rep G., Pohleven F., Košmerl S. 2012. Development of the industrial kiln for thermal wood modification by a procedure with an initial vacuum and commercialisation of modified Silvapro wood, in: *Proceedings of the 6th European Conference on Wood Modification, University of Ljubljana, Slovenia*, p. 11–17.

## METHODOLOGY FOR THE ASSESSMENT OF TIMBER STRUCTURES EXPOSED TO FIRE THROUGH NDT

Dante Marranzini, Giacomo Iovane, Beatrice Faggiano

University of Naples “Federico II”, Department of Structures for Engineering and Architecture, Naples, Italy

### Abstract

The paper illustrates a methodology set up for the assessment of the fire damage on timber members, based on the application of in situ non-destructive (NDT) tests. The methodology proposed consists in the identification of the extent of damage by measuring the residual cross section and the charred depth of each structural member through the application of the drilling resistance method. Therefore, visual decay categories are defined. The fire exposure duration is evaluated. On these bases, the calculation of the residual strength is possible, so that recoverable members, which are still able to satisfy the design requirements, can be identified, together with the elements that require strengthening or substitution due to lack of bearing capability of the reduced cross section. The methodology has been applied and validated on the roofing timber structures of Palazzo Carafa di Maddaloni, in Naples (Italy) that was involved in a great fire on June 2018.

**Keywords:** Timber structures in fire, in-situ assessment of fire damage on timber, non-destructive test for fire damage identification, fire resistance of timber members, drilling technique.

### 1 INTRODUCTION

Timber is one of the most sustainable resources available. It is among the oldest materials used in construction for a variety of structural forms. Currently, timber use is increasing thanks to the improvement of the derivative products as glued laminated timber, cross laminated timber and laminated veneer timber. Although great progress has been done in the realization of innovative products that elevate the timber properties, the combustibility is still a weakness.

Frequently historical buildings with timber structures are involved in fires. After fire, even though timber members are partially burnt, generally designers provide for the removal aiming at improving safety condition and fire performance. When these alterations are done, the heritage value of the building is compromised. In this case the possibility to maintain historical structures in place should be firstly evaluated once the fire performance of timber is understood (Chorlton and Gales, 2019).

Wood is mainly composed by cellulose and lignin, substances characterized by a high carbon concentration, that is one of the principal combustion components. When timber is exposed to high temperature these substances undergo a thermal degradation called pyrolysis (White and Dietenberger, 2010; Bartlett et al., 2019). The pyrolysis starts with hemicellulose decomposition (Paoletto et al., 2012; Bartlett et al., 2019), which is announced by a typically crack pattern of timber, so called “alligatoring effect” (Piazza, 2005; Baroudi et al., 2017; Babrauskas, 2005). This propriety originates the capacity of wood to increase and propagate fire. However, from a more in-depth knowledge of the wood burning behaviour, it can be stated that timber has a predictable and reliable behaviour, in fact the rate of charring is approximately constant over time, it being described by the “charring rate” (Babrauskas, 2005; Friquin, 2010). Thanks to timber thermal properties, in a member exposed to fire the temperature gradient shows high variation (Frangi and Fontana, 2003; White and Dietenberger, 2010), so that the cross section is formed by a charring outer layer, a thin layer exposed to an elevated temperature and a cool interior zone. Given the relationship between mechanical properties and temperature of timber (Kretschmann, 2010; Hopkin, 2011) it can be stated that the cooler zone retains its structural integrity. Thus, a timber member showing damage confined to a specific location or partially burnt may be able to preserve a residual bearing capacity.

Nowadays there is not any regulations that provide standard methods to carry out these evaluations, furthermore regarding the state of art, few works showing the operative methodology are recognized. Therefore, a methodology for the assessment of fire damage can be inspired by the biological decay assessment, which is based on visual inspection and non-destructive techniques. The latter should be

opportunistically adapted, in order to evaluate the parameters that regulate the residual bearing capacity of the members damaged by fire.

In this paper the estimation of fire damage of timber structures is illustrated. The method used is based on the combination of visual inspection and instrumental diagnosis through the drilling resistance method. The proposed method was applied on the glue laminated timber structures of Palazzo Carafa di Maddaloni, an historical building in the centre of Naples, which was struck by a great fire involving a large extent of the roof in 2018. The actual structural safety-conditions and the recoverable members were identified, at the same time the method has been validated.

## 2 DESCRIPTION OF THE PROPOSED METHOD

### 2.1 The definition of visual fire damage maps

In the field of post fire assessment, visual inspection has the purpose of identifying the safety condition of the elements, strengthening strategies and the elements to be replaced, through the analysis of different parameters, such as the appearance of the element surface, the extension of damage and the external size of the cross section.

Given the lack of regulations, a method to conduct a visual inspection of structure damaged by fire is proposed. It is based on the following three steps: 1) *Photographic survey*: it is a preliminary study of the visual inspection, it allows to detect structure members most damaged, the intact ones and to assess the global damage conditions of the structure. Photographic survey can be useful to identify the parts of structure having different level of damage, so it is possible to define the instrumental survey strategy.

2) *Member size measurement*: it aims at evaluating the length of the members and the size of the cross section. The analysis can be lead with simple tools or advanced one, as laser scanning, in such a way to implement a 3D model (Cabalerio *et al.*, 2018). The analysis can be summarized in three phases, such as labelling of structural members, size measurement and data analysis. The size measurements of the cross section should be carried out in different point of each member, since this can be affected by either uniform or localized damage. It is then possible to identify the most damaged members and to determine the residual size of the members. This phase is supportive of the instrumental survey.

3) *Visual mapping*: it consists in the visual inspection of timber members, from which it is possible to assign the visual damage levels. The latter correspond to an increasing scale of damage, based on qualitative criteria, related to the geometrical and visual appearance of the member. A damage scale is proposed, with increasing damage from “levels 0” to “levels 4”. It is shown in Table 1. Thus, a member showing an heterogeneous damage can be characterized by different levels of damage.

Table 1 Definition of visual levels of damage

j=0	j=1	j=2	j=3	j=4
				
VISUAL APPEARANCE				
Original colours of wood	Black surface	Black surface slightly cracked	Black and cracked surface	Black and deeply cracked surface
GEOMETRICAL APPEARANCE				
Original shape	Original shape	Original shape	Section with slightly rounded corners. Reduction of cross section	Changing in shape of cross section. Reduction of cross section

For an immediate evaluation of the damage status of the whole member, the “Member coefficient of fire visual damage, FVD”,  $I_{m,j}$ , can be defined through the following Eq. (1):

$$I_{m,j} = \frac{S_{m,j}}{S_m} \quad (1)$$

where  $I_{m,j}$  ranges between 0 to 100 (%),  $S_{m,j}$  is the extent of the damage belonging to of the j-th level of damage in the m-th member ( $m^2$ ),  $S_m$  is the whole surface of the m-th member ( $m^2$ ). A value of  $I_{m,j}$  close to 100 indicates that the whole m-th member is characterized by the j-th damage level, conversely when  $I_{m,j}$  is close to 0 only a small part of the member shows the j-th level of damage. In addition, the FVD coefficient has been calculated with reference to the whole structure, as the ‘‘Global coefficient of fire visual damage’’  $I_{G,j}$ , ranging between 0 to 100 (%), as it follows (Eq. (2)):

$$I_{G,j} = \frac{\sum_{m=1}^n S_{m,j}}{\sum_{m=1}^n S_m} \quad (2)$$

The FVD coefficients are useful to understand the extent of damage on the structure. The main challenge of the visual mapping consists in defining a dimensionless parameter for quantifying the level of damage of timber members as a tool for planning the subsequent non-destructive tests.

## 2.2 The determination of residual cross sections through the drilling resistance method

The drilling resistance technique is a non-destructive method for the timber inspection. It is based on the resistance offered by the material to the advance of a small diameter drill bit. A detailed review on the current state of the art about the drilling resistance method is reported by Nowak et al. (2015). There are several experimental researches that involved the use of the drilling resistance method with the aim to estimate the biological decay and timber mechanical properties of timber, in some cases they consist in combined methods (Faggiano *et al.*, 2011; Lechner et al., 2014).

With regards to the post fire assessment, White and Woeste (2013), as well as Moller (2016) evaluated residual cross sections without NDT devices. Besides, few works about the application of the drilling method are available. Kasal, *et al.* (2006) determined a loss of resistance in drilling profile and a drop corresponding to the beginning of the charred layer, while Kukay et al. (2016) underlined the potential of the drilling resistance method in fire application. Recently Cabaleiro *et al.* (2021) evaluated the residual cross section and the apparent section of a timber member damaged in fire by using of the combination of drilling method and laser scanner.

The main purpose of the post fire assessment is to establish the safety condition of a wooden structure damaged by fire and to evaluate the residual bearing capabilities of members in order to decide if members can remain in place or need to be repaired or replaced. The determination of the residual cross section, retaining unchanged mechanical properties plays, a fundamental role. Given the density difference between char and timber, the residual cross section can be easily detected through the drilling resistance test. In the proposed method the limit area between the charred layers and the undamaged one is identified through drilling profile areas where the changing in resistance drilling value (amplitude) are greater than 5%. Accordingly, the residual cross section of a member having rectangular shape can be defined thanks to Equations (3) and (4) with reference to Figure 1a:

$$B_{res} = B^* - (d_{char,e} + d_{char,u}) \quad (3)$$

$$H_{res} = H^* - (d_{char,e} + d_{char,u}) \quad (4)$$

where  $B_{res}$  and  $B^*$ ,  $H_{res}$  and  $H^*$  (mm) are base and height of the residual cross section and of the overall cross section, included the charred layers, respectively;  $d_{char,e}$  and  $d_{char,u}$  (mm) are the depths of the charred layers, measured on the entry side and on the exit side of the drilling pin, respectively. The size variation of the cross section is evaluated as it follows (Eq. (5)):

$$\Delta A = \frac{B_{res} \cdot H_{res}}{B^* \cdot H^*} \quad (5)$$

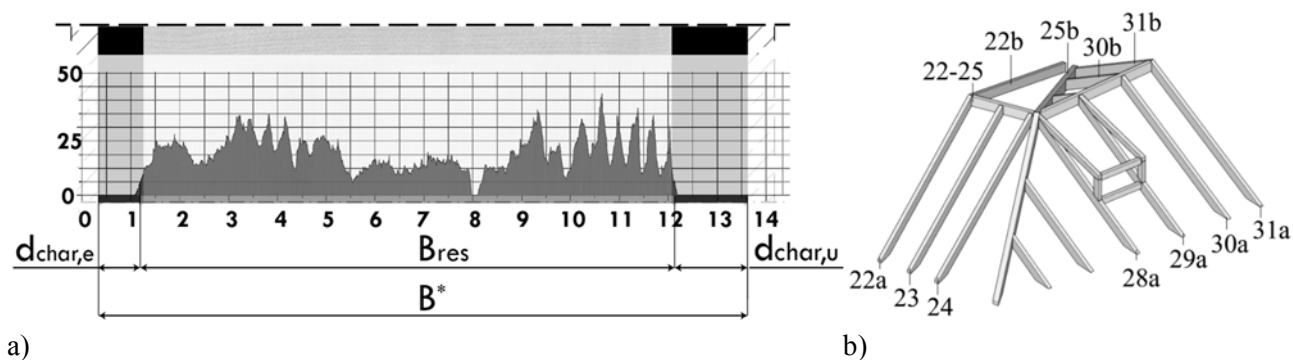


Fig. 1: a) Geometrical parameters derived from drilling resistance graph; b) 3D scheme of the case study.

A further analysis has defined the relationship between the levels of damage determined through the visual inspection and the depth of the char layers detected through the drilling resistance test. Therefore, a criterion that allows to approximately quantify the char depth also for the structural members that cannot be investigated with non-destructive devices is established.

### 3 APPLICATION OF THE METHOD TO THE CASE STUDY

#### 3.1 The visual fire damage maps

First of all, the geometrical survey of the roofing structures made of glue laminated timber GL28h was carried out (Fig. 1b). During the photographic survey three structure areas corresponding to different damage levels were roughly identified: a more damaged area including members 22a, 22-25, 23, 24, 25, 22; a less damaged area including members 26, 27, 28a, 29a, 30a, 30b, 31a, 31b; a third area with an extremely variable level of damage including members 22b, 25b, 29b.

For each member external sizes, height and base were measured in three different sections corresponding to the lower, upper and middle points of the member (respectively named A, B and M; Fig. 2a). Thus, each section was approximated to a rectangular shape. The visual damage map was drawn for each member, through the determination of the member FVD coefficient  $I_{m,j}$ . In Figure 2b results are exemplified for the member 24. Therefore the Global FVD coefficient ( $I_{G,j}$ ) was calculated (Fig. 2b). It is apparent that fire damage is heterogeneous and diffuse at the same time. It is also interesting to note that only the 38% of the investigated surfaces show a reduction in the cross section ( $I_{G,3} + I_{G,4}$ ), while the 49% of them is characterized by surface damage ( $I_{G,1}+I_{G,2}$ ).

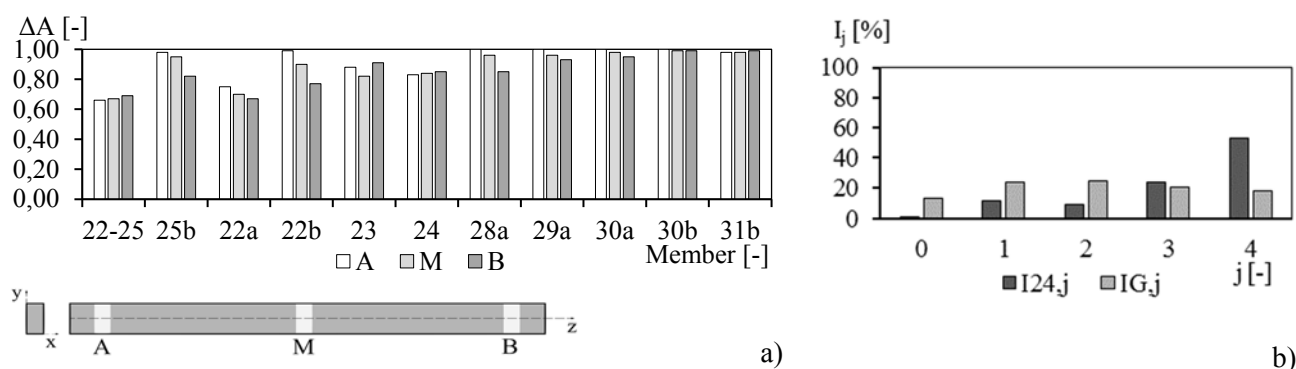


Fig. 2.: a) Size variation of member cross sections (A=lower; M=middle; B=upper); b) FVD coefficient ( $I_{m,j}$ ) distribution for member 24 and Global FVD coefficient distribution ( $I_{G,j}$ );

#### 3.2 The drilling resistance method

In the area under study only 11 out 23 members of the structures were tested, because the remaining 12 were not accessible for drilling. A total number of 83 measurements was carried out. The Resistograph IMLRESI F400 device (Rinn et al., 1996) was used. Velocity and sensitivity of the tool were respectively set on 400 rpm and “1”, as indicated for softwood (IML-RESI F-Series Manual,

<http://imlcanada.com>).

For each member the size variation of the cross-section was determined, assuming that it is constant over the member length and equal to minimum values obtained through the instrumental test. The results are shown in Figure 2a.

For the evaluation of the actual safety condition of the structure, loads were defined considering only the roof covering present at the moment of the analysis. The residual bearing capacity was determined according to the “reduced cross section method” (UNI EN 1995-1-2). Results are shown in terms of demand capacity ratio ( $DCR_{as}$ ; Fig. 3a). It is found that 2 elements are potentially unsafe, whereas 9 members are far from failure. Same procedure was followed for the bearing capability assessment for reuse in service conditions, so that reference is made to the corresponding load analysis. The results are shown in terms of  $DCR_{rs}$  (Fig. 3a). In this case it is found that most of the members have a residual capacity to carry the design load and thus they could be reused.

Finally, a relationship between the visual mapping data and the charred layers recorded with drilling device was found. The analysis was carried out comparing the charred thickness ( $d_{char,e}$  and  $d_{char,u}$ ) with the level of visual damage. In Figure 2b for each FVD levels the distribution of the charred thickness values is shown. From the results review it is found that:

- Increasing levels of visual damage correspond to increasing values of the charred thickness;
- The most severe FVD level ( $j=4$ ) is characterized by a large dispersion of the charred thickness;
- FVD levels 2 and 3 ( $j=2, j=3$ ) are characterized by small dispersion of the charred thickness;
- Blackened members showed insignificant reduction in cross section, since the values of charred thickness for the FVD level 1 ( $j=1$ ) are less than 3 mm.

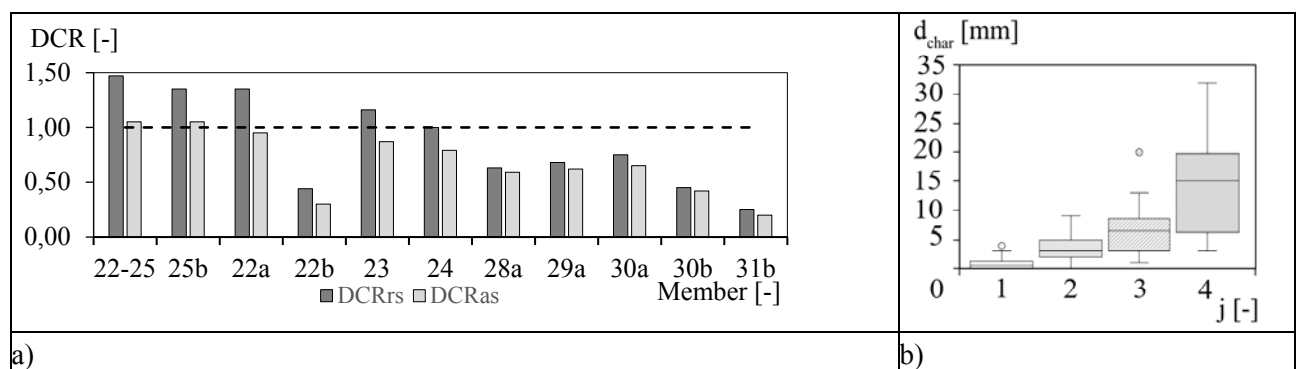


Fig. 2: a) Demand capacity ratio of the tested members ( $DCR_{rs}$ : reuse assessment;  $DCR_{as}$ : safety condition assessment; b) Relationship between the visual levels of damage ( $j$ ) and the charred depth ( $d_{char}$ )

#### 4 CONCLUSIVE REMARKS

This paper presents a methodological proposal for the post fire assessment of a timber structure. The approach is based on the visual inspection and the application of the drilling resistance method. The methodology was applied and validated on a case study. With regards to the method proposed, it has been possible to state that the application of the method to the case study efficiently led to the estimation of fire damage. The structural elements to be consolidated and the safe ones were identified. The visual mapping plays a fundamental role, allowing the definition of a relationship between the levels of damage and the charred layer. It is a fast and effective way to provide a preliminary estimation of the fire damage of the timber structure. In order to improve the relationship between visual mapping and the drilling resistance method future works are required for increasing the number of data, so that visual mapping predictions can be more realistic.

#### ACKNOWLEDGEMENT

Authors very much thanks prof. Roberto Castelluccio for allowing the application of the proposed method to the case study of Palazzo Carafa di Maddaloni in Naples. Devices and materials were provided by the Department of Structure for Engineering and Architecture of the University of Naples

“Federico II”. Eng. Emanuele Scaiella support for the in situ experimental campaign is also acknowledged.

## REFERENCES

- Babrauskas V. 2015. Charring rate of wood as a tool for fire investigations. *Fire Safety Journal*, 40(6), p. 528–554.
- Baroudi D., Ferrantelli A., Kai Yuan Li, Hostikka S. 2017. Thermomechanical explanation for the topology of crack patterns observed on the surface of charred wood and particle fibreboard. *Combustion and flame*, 182(8), p. 206-215.
- Bartlett A.I., Hadden R.M., Bisby L.A., 2019. A Review of Factors Affecting the Burning Behaviour of Wood for Application to Tall Timber Construction. *Fire Technology*, 55(1), p. 1-49.
- Cabaleiro M., Branco J. M., Sousa H. S., Conde H. 2018. First results on the combination of laser scanner and drilling resistance tests for the assessment of the geometrical condition of irregular cross-sections of timber beams. *Mater Struct*, 51(4), p. 99.
- Cabaleiro M., Suñer C., Sousa H. S., Branco J. M. 2021. Combination of laser scanner and drilling resistance tests to measure geometry change for structural assessment of timber beams exposed to fire, *Journal of Building Engineering*, 40(2021) p. 102365.
- Chorlton B. and Gales J., 2019. Fire performance of cultural heritage and contemporary timbers. *Eng. Struct.*, 201 (2019), p. 109739.
- Faggiano B., Grippa M.R., Marzo A., Mazzolani F.M. 2011. Experimental study for non-destructive mechanical evaluation of ancient chestnut timber. *J. Civil Struct. Health Monit.*, 1 (3–4), p. 103-112.
- Frangi A., Fontana M. 2003. Charring rates and temperature profiles of wood sections. *Fire and Materials*, 27(2), p. 91–102.
- Friquin K.L. 2011. Material properties and external factors influencing the charring rate of solid wood and glue - laminated. *Fire and materials*, 35(5) p. 303-327.
- Hopkin D.J., 2011. *The Fire Performance of Engineered Timber Products and Systems*, PhD Thesis Loughborough University (in England).
- Kasal B., Anthony R. 2004. Advances in in situ evaluation of timber structures. *Prog Struct Eng Mater*, 6 p. 94–103.
- Kretschmann D.E. 2010. *Mechanical properties of wood. Wood handbook: wood as an engineering material (Centennial ed.)*, U.S. Dept. of Agriculture, Forest Service, Forest Products Laboratory, Madison, WI, USA, p. 5-46.
- Kukay B., Todd C., Jahn T., Sannon J., Dunlap L., White R.H., Dietenberger M. 2016. Evaluating Fire-Damaged Components of Historic Covered Bridges. General Technical Report FPL-GTR-243, U.S. Department of Agriculture, Forest Service, Forest Products Laboratory, Madison, WI, USA.
- Lechner T., Nowak T., Kliger R. In situ assessment of the timber floor structure of the Skansen Lejonet fortification, Sweden. *Construction and Building Materials*, 58(2014) p. 85–93
- Moller C., 2016. *Restoring capacity in compromised glued laminated beams*. PhD Thesis, Montana Technological University (in Montana, USA).
- Nowak T.P., Jasienko J., Hamrol-Bielecka K., 2016. In situ assessment of structural timber using the resistance drilling method – Evaluation of usefulness. *Construction and building*, 102(2016) p. 403-415.
- Poletto M., Zattera A.J., Forte M.M.C., Santana R.M.C. 2012. Thermal decomposition of wood: Influence of wood components and cellulose crystallite size. *Bioresource Technology*, 109(April 2012) p. 148–153.
- Piazza M., Tommasi R., Modena R. 2005. *Strutture in legno*, Milan, Italy: Hoepli.
- Rinn F., Schweingruber F.H., Schär E. 1996. Resistograph and X-ray density charts of wood. Comparative evaluation of drill resistance profiles and X-ray density charts of different wood species, *Holzforschung-International Journal of the Biology, Chemistry, Physics and Technology of Wood*, 50(4) p. 303-311.
- UNI EN 1993-1-2:2005 Eurocodice 3 - Progettazione delle strutture di acciaio - Parte 1-2: Regole generali - Progettazione strutturale contro l'incendio.
- White R.H., Dietenberger M.A. 2010. *Fire safety of wood construction. In: Wood handbook: wood as an engineering material (Centennial ed.)*, U.S. Dept. of Agriculture, Forest Service, Forest Products Laboratory, Madison, WI, USA, p. 18-46.
- White R.H., Woeste F.E. 2013. Post-fire analysis of solid sawn heavy timber beams. *Structure magazine*, November 2013, p. 38-40.

## **SIMPLIFIED SMOULDERING TEST DEVELOPMENT For the test of wooden structural materials**

Peter Harsányi <sup>a</sup>, Martin Schneider <sup>a</sup>, Sebastian Reiter <sup>a</sup>, Peter Anderwald <sup>b</sup>

<sup>a</sup> Carinthia University of Applied Sciences, Department of Civil Engineering and Architecture, Austria

<sup>b</sup> AH Safety Engineering GmbH, Villach-Drobollach, Austria

### **Abstract**

The spread of smouldering fires in timber constructions is a common cause of fire events. Flammable insulation materials and ignition sources within the construction can induce a smouldering fire with a long and unnoticed initial fire formation. Charring rates are set as constant values in dimensioning standards. These values are based on the results of numerous studies on the burning behaviour of timber, carried out with standard fire exposure. The ISO-fire represents a steadily increasing temperature profile, which in most cases does not correspond to natural fire exposure. In smouldering fires, the lower combustion temperature and insufficient air supply can result in a significantly slower burning rate. For this purpose, a prototype testing method was developed to simulate the prevailing conditions in a smouldering fire and to identify possible weak points in the simplified prototype. The results show that the smouldering fire leads to a burning rate significantly lower than with a fully-developed fire according to the standard ISO fire curve conditions.

**Keywords:** smouldering fire, charring rate, fire test development, wood fire test

## **1 INTRODUCTION**

Wood is not only irreplaceable as a construction material for buildings and material for everyday objects, but also as an important source of energy. In the recent past, however, ecological aspects, in particular, have again led to increased use of wood in buildings. The attractive CO<sub>2</sub> balance of this building material (e.g. (Buchanan, 2007)) will also contribute to its further usage in the future. Due to the flammability of timber components, fire protection in timber construction is of great importance. The increased fire load due to the use of combustible building materials is offset by the fact that wood behaves more favourably in the event of fire than other non-combustible building materials (Lowden & Hull, 2013; Khoury, 2000). During the evenly progressive burning of a timber component, the interior of the cross-section is protected from high temperatures by the high insulating effect of the carbon layer that forms on the surface of the wood, and the mechanical properties of the remaining cross-section are largely retained (Lowden & Hull, 2013). As a result, the load-bearing capacity of timber structures in the event of a fire is easy to design and predict. The time of failure can be well estimated based on the usually uniform charring. The charring rate of the wood is decisive for the assessment of the load-bearing capacity of wooden components in case of fire. Experimental investigations of the burning behaviour of wood under different conditions are the basis for determining this value (see e.g. (Babrauskas, 2005)). The specific investigation of the charring rate of wood in the special case of a smouldering fire is the subject of the present work.

The determination of the burning behaviour of wood is usually carried out under compliance with standard fire curves, as described in the (ÖNORM EN 1363-1, 2020). Charring rates can be found in the standard required for the design (ÖNORM B 1995-1-2, 2011) as well as exemplarily compiled in (Tsai, 2010) and (Bobacz, 2008). Even though the fire behaviour of wood under normative fire exposure has already been extensively investigated, research showed that studies on the influence of long-lasting smouldering fires on the charring rate of wood have hardly been considered to date. The following work was therefore intended to create the first foundations for investigations of prolonged smouldering fires on wood and to clarify open questions about a potential test set-up.

## 2 EXPERIMENTAL PROGRAMM – SPECIMEN PREPARATION AND SETUP

The following experimental investigations are intended to show to what extent the lower temperatures and an insufficient air supply affect the burning behaviour of wood in a smouldering fire. The following variables were recorded and determined in the course of the fire tests:

Before the fire test:

- Bulk density of the test specimens,
- Moisture content of the wooden test specimens

During the fire test:

- Temperature profile of the heat source
- Temperature profile in the wood
- Weight loss of the wood samples

After the fire test:

- Charring depth

Now the determination of the charring rate can be carried out.

In order to enable an initial development of the test set-up, the parameters influencing the test result were reduced to a minimum. For this purpose, the wood species spruce was chosen for the test specimens. In the building industry, this type of wood is most commonly used for load-bearing components in middle Europe and can be considered representative. The dimensions of the planed spruce squared timber were  $W \times H \times L = 15.5 \times 9.5 \times 15.5$  cm. During production, care was taken to exclude specimens with defects such as knots or cracks.

To exclude the influence of the wood moisture on the tests, the samples were dried. The drying was carried out at a temperature of 85° C to a wood moisture content of 3 %. The wood moisture was measured using an electrical resistance measuring device with impact electrodes. Before the tests, the bulk density was determined by measuring and weighing the test specimens. An overview of the sample measurement can be found in Table 1. The specimens were then stored under laboratory conditions until the day of testing.

**Table 1 Specimen dimensions, wood moisture, weight and density**

speci- men	length [mm]	width [mm]	height [mm]	wood moisture %	weight (dried) [g]	density (dried) [kg/m <sup>3</sup> ]	weight (after lab cond.) [g]	wood moisture (at test) [kg/m <sup>3</sup> ]	density (at test) [kg/m <sup>3</sup> ]
V1	155,2	151,4	89,8	2,6	789,4	374,1	842,8	6,8	399,4
V2	155,1	151,5	91,9	2,3	784,1	363,1	836,6	6,7	387,4
V3	155,2	145,2	90,3	2,6	684	336,1	726,5	6,2	357,0
V4	154,7	151,3	90,9	2,1	701,6	329,8	746,2	6,4	350,7

In the development of the prototypical set-up, particular importance was given to the simplicity of the test device in the first step. It allows the air supply to be controlled via a regulated compressed air connection and the temperature of the test specimen to be recorded by temperature sensors. In order to achieve the most homogeneous temperature distribution possible in the test chamber, two gas burners with a burner output of 4,2 kW each were arranged under the test device in a first development step, which in turn heated a layer of quartz sand. The temperature of the sand was

measured by an embedded temperature sensor. The heat was transferred directly to the test specimen utilizing a 1 mm thick steel plate placed on the quartz sand. For the actual combustion chamber, a steel box with a length of 53 cm, a height of 29 cm and a width of 37 cm was used. The steel box was lockable but not completely airtight. The lid of the box had a 10 mm opening for the temperature sensor's specimen holder to pass through. Air was supplied via a compressed air hose with an inner diameter of 9 mm, which was connected to the compressed air regulator of the combustion chamber via a commercially available pneumatic connection with a plug nipple and quick-connect coupling. The regulator had a pressure gauge and allowed the air pressure to be adjusted in the range from 0 to 12 bar. The airflow was introduced into the interior of the combustion chamber via a nozzle. A commercially available hose nozzle for compressed air hoses with an inner diameter of 9 mm was used as the nozzle, which was inserted into a 10 mm hole in the wall of the combustion chamber. The outlet opening of the nozzle had an inner diameter of approximately 5 mm. A layout of the experimental setup can be found in Figure 1.

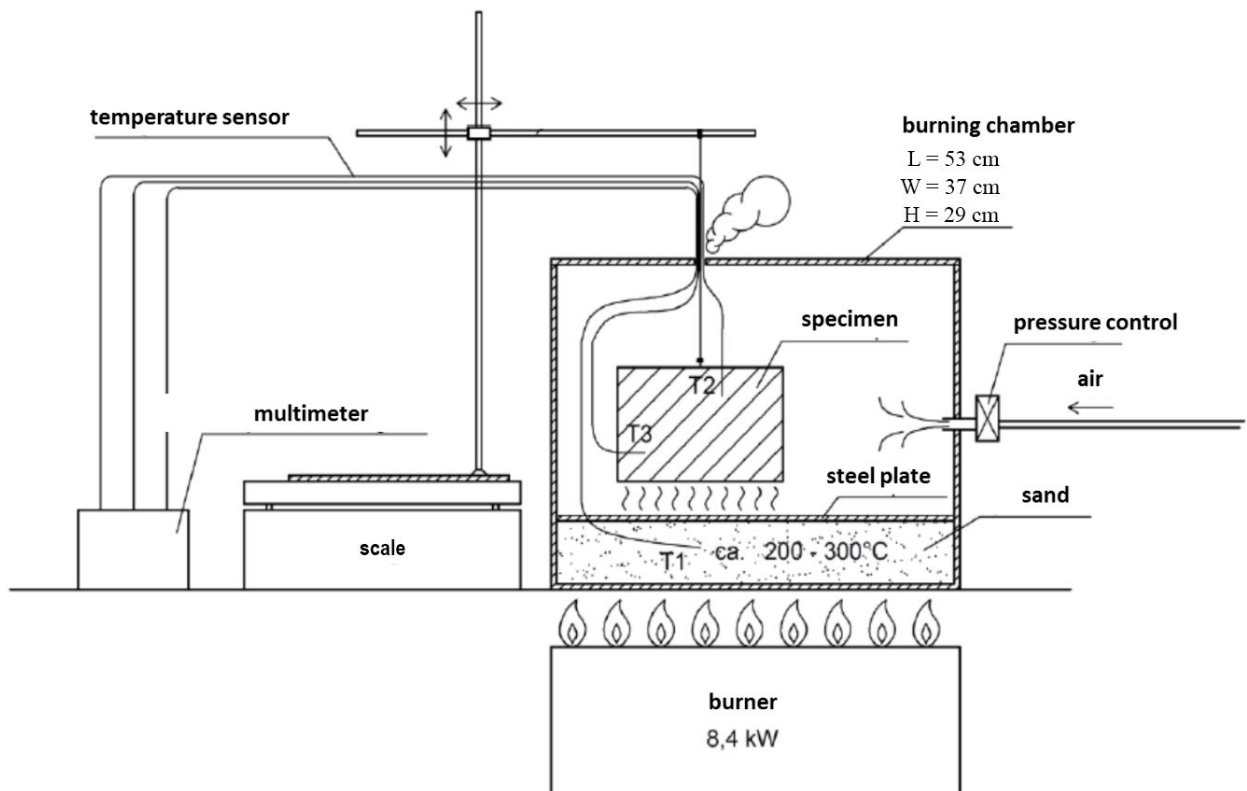


Figure 1 Experimental Setup, dimensions and measurement equipment

The holding device was connected to a precision scale that allows continuous measurement of the weight during the test period. Two temperature sensors were applied to the test specimens. Two holes with a diameter of 1.5 cm and a depth of 2.5 cm were made for this experiment. The test specimen was positioned hanging in the test room. For this purpose, a wood screw was screwed in on the side facing away from the fire load and held in position with the help of a wire and a holding device. Figure 2 shows the exact positions of the temperature sensors and the dimensions of the test specimens.

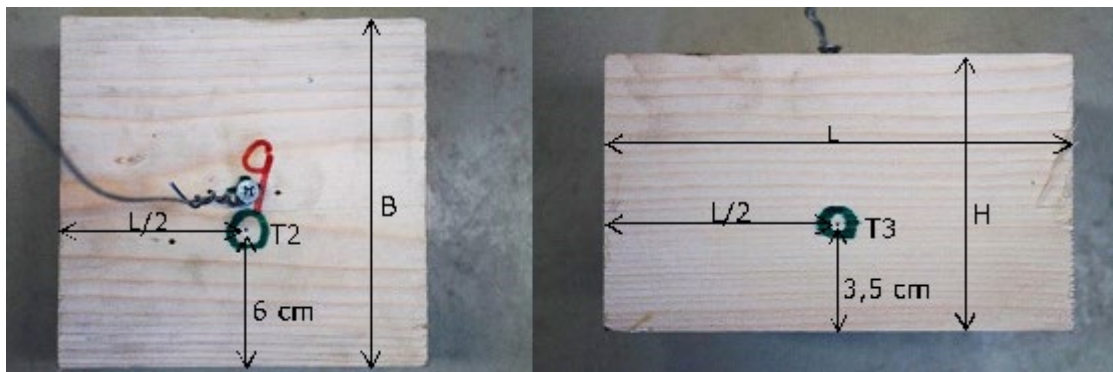


Figure 2 Specimen dimensions and positioning of the thermal couplers and fixing screw; with  $L \times B \times H = 15,5 \times 15,5 \times 9,5$  cm

### 3 EXPERIMENTAL PROCEDURE AND RESULTS

To initiate the combustion process, the test specimen must be ignited on its underside with a pilot flame. The initial attempt at ignition by means of a blowtorch (small gas burner) proved to be insufficient and disadvantageous since after ignition has taken place, the already burnt test specimen must first be placed in the combustion chamber of the test setup. In the meantime, the fire extinguished due to a lack of energy supply. This interruption of the combustion process would falsify the results of the fire tests. A practicable solution turned out to be ignition with commercially available chimney lighters (petroleum-soaked wood wool) under the test specimen. The ignition is carried out with the lid of the combustion chamber open to ensure the necessary ventilation for the complete ignition of the test specimen. In order to achieve an even flaming of the entire wood surface, three igniters were placed next to each other under the test specimen. After burning the igniters and igniting the test specimen, the lid of the combustion chamber was closed and the air supply was reduced to initiate the smouldering process. This approach can also be seen as a practical simulation of a developing fire due to an ignition source with an open flame and subsequent transition to a ventilation-controlled smouldering fire due to insufficient air supply in closed rooms. The duration of the ignition and heating phase until the start of the smouldering fire was 30 minutes.

A preheating period of about 90 to 120 minutes was required until the quartz sand reached the required operating temperature. A temperature between 250 and 300 °C should be reached before the start of the tests. In general, controlling the temperature and heating up the combustion chamber proved to be challenging. This can be explained, among other things, by the limited power of the gas burner and the heat losses to the ambient air. In addition, changes to the burner setting have a very delayed effect on the temperature in the combustion chamber due to the very long heating and cooling time of the quartz sand. It was therefore attempted to keep the temperature as constant as possible during the test. Nevertheless, the necessary heat energy to maintain the smouldering process was generated with the existing experimental equipment.

As the main influence on combustion, special attention was paid to a constant air supply, which precluded a complete smothering of the flames and at the same time allowed the smouldering fire process to be maintained. A pressure setting of approx. 1 bar was chosen as realistic as possible.

Based on a first calibration test with the prototypical measuring device, the following procedure was chosen for further testing (see Table 2).

**Table 2 Experimental procedure for each test**

phase	step	process	minute
preparation	1	preheating the combustion chamber to operating temperature	
	2	measuring and weighing the specimen	
	3	positioning of the specimen in the burning chamber	
	4	recording of the output temperatures	
ignition	5	Ignition of the test specimen with 3 chimney igniters each with an open lid	0
smouldering fire	6	Covering the combustion chamber	30
	7	Restriction of the air supply	
	8	Continuous recording of the measurement data	90
	9	End of the fire test	
follow-up	10	Extinguish the specimen with water	
	11	Weighing the charred, cooled test specimen	
	12	Determination of the charring depth	

An overview of the test results is shown in Figure 3. An increased mass loss can be observed especially in the first minutes after ignition and then flattens out further with the onset of the smouldering process.

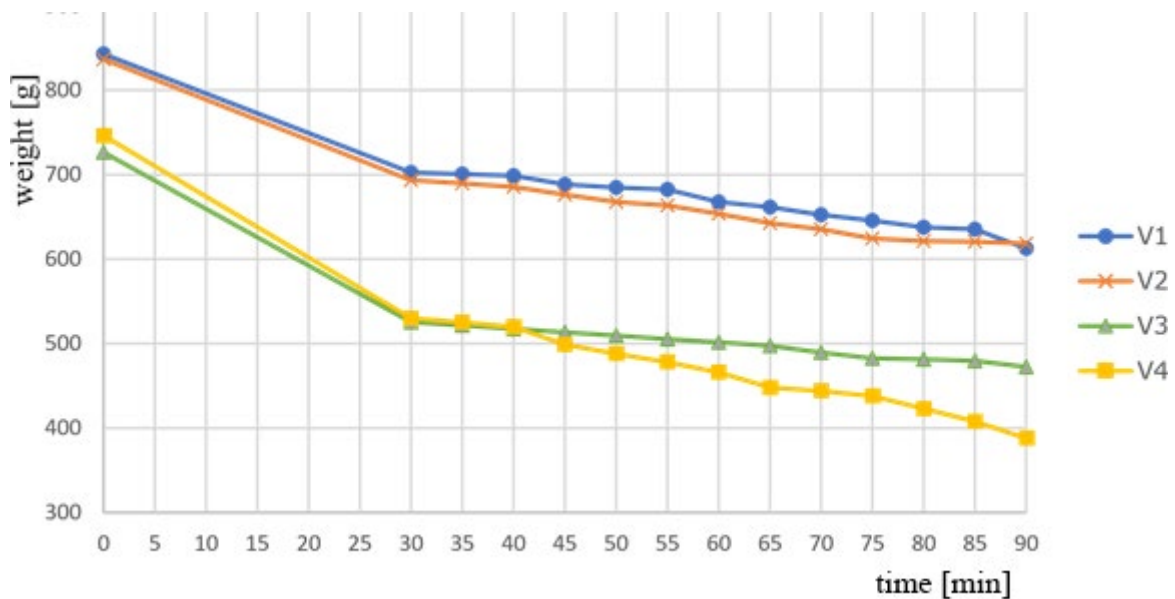


Figure 3 Experimental results over time

## DISCUSSION

Although the entire test set-up is kept simple and the mentioned interfering factors undoubtedly influence the test, the burn rates achieved show good consistency. Except for test 4 with an average of 4.0 g/min, the burn rates were between 2.4 and 2.8 g/min. (see Table 3).

**Table 3 Average charring rate after 90 minutes**

test	$m_1$ [g]	$m_2$ [g]	$\Delta m$ [g]	time [min]	$\dot{m}$ [g/min]
V1	842,8	612,6	230,2	90	2,6
V2	836,6	618,5	218,1	90	2,4
V3	726,5	472,5	254,0	90	2,8
V4	746,2	387,9	358,3	90	4,0

The following improvement for a future optimization of the test setup were identified:

- The targeted controlling of these parameters was limited by the adjustment options of the experimental setup during the execution of the tests and should be optimised in a further step.
- An additional measuring device for determining the air volume flow and the oxygen content of the combustion chamber atmosphere is recommended.
- Preheating the combustion chamber was very time-consuming and energy-intensive. The control of the fire chamber temperature is limited by the ambient conditions outdoors and the maximum power of the gas burner. Insulation of the combustion chamber is recommended in further development.
- A pilot flame is required to ignite the test specimens in the combustion chamber.

A cut through the test specimens shows that test specimens 1 to 3 have largely uniform charring down to the core area. Test specimen 4, however, shows considerably more severe burns than the other test specimens. A closer look reveals a drying crack in the centre of the test specimen, which may be partly responsible for the unfavourable burn rate (see Figure 4).

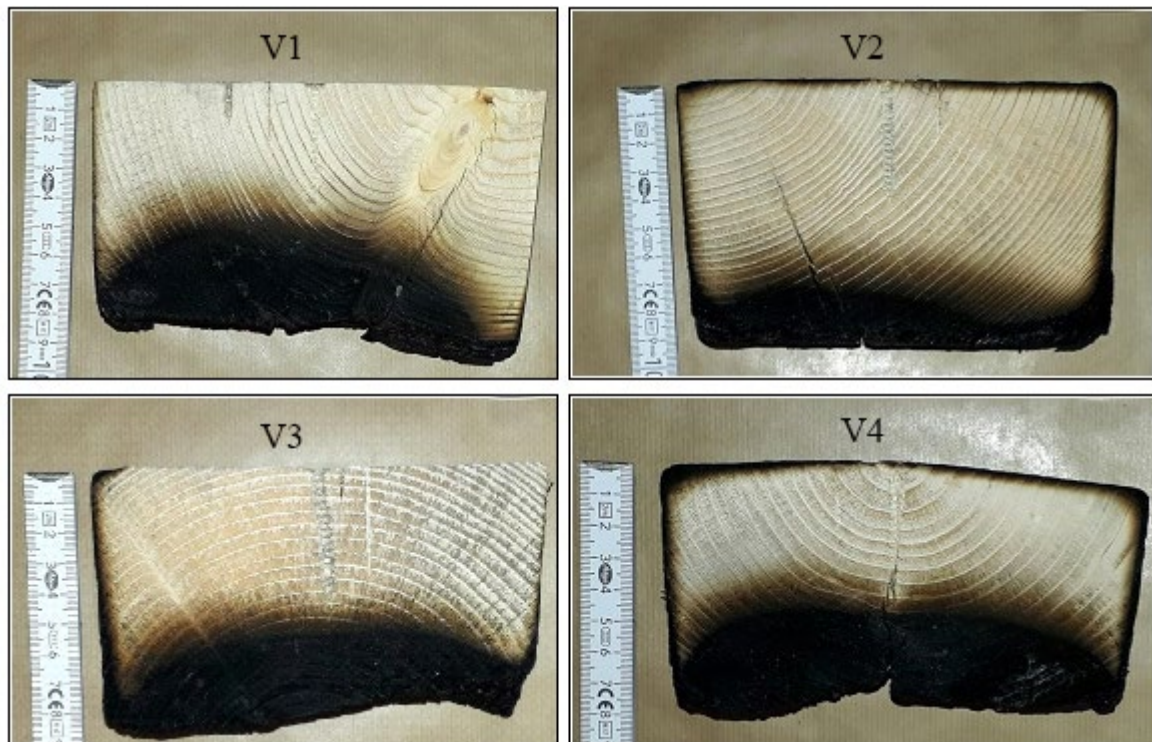


Figure 4 Specimen after the smouldering test

As expected, the charring rate in the ignition phase was higher than in the smouldering phase (see Figure 3). The very simplified test set-up, with its external influencing variables, low insulation of the test room and very basic air supply, led to satisfactory but fluctuating test results. An overview of the burn rate after 90 minutes of testing can be found in Table 4. The charring depth was determined according to (Lache, Topf & Wegener, 1992), whereby the distance between the original test specimen surface and the layer that was discoloured brown by burning but not transformed into charcoal was determined.

**Table 4 Overview of the charring rates**

test	time [min]	d <sub>0</sub> [mm]	d <sub>rest</sub> [mm]	d <sub>char</sub> [mm]	β [mm/min]
V1	90	92,0	55,3	36,7	0,41
V2	90	93,0	65,2	27,8	0,31
V3	90	93,0	55,3	37,7	0,42
V4	90	94,0	48,2	45,8	0,51
Mean value				37,0	0,41

To put the test results in perspective, they can be compared with fire tests by (Werther, 2016) and (Fornather, 2003). Similarities in the charring rate become clear in this context and show similar charring rates (see Table 5). (Werther, 2016) and (Fornather, 2003) conducted tests on spruce wood including cooling phases. Even if the temperature-time stress in these tests was different from that in the present investigations, their results can still be used as a reference point for the size of the charring rate at low thermal stress to verify the plausibility of their results. Compared to the normative burn rate of spruce of 0.65 [mm/min] under standard fire exposure (ÖNORM B 1995-1-2, 2011), there was a significant reduction of about 35 %.

**Table 5 Comparison of burning speeds to other researchers**

researcher	maximal temp.	time	charring depth	charring rate
(Werther, 2016)	ca. 600 °C	60 [min]	27 [mm]	0,44 [mm/min]
(Fornather, 2003)	ca. 700 °C	90 [min]	38 [mm]	0,42 [mm/min]
Own research	-	90 [min]	37 [mm]	0,41 [mm/min]

## 4 CONCLUSIONS

The following findings can be derived from the fire tests carried out:

- In a first step, the developed test setup succeeded in generating a smouldering fire of wood and in maintaining the smouldering process for the duration of the fire test. Weak points of the setup were identified for further optimization.
- In all tests, there was a uniform loss of weight in the smouldering phase and thus a constant charring rate.
- In the ignition phase, the burn-off was higher than in the smouldering phase.
- The experimental setup provided sufficient experimental data for the burn rate of spruce under smouldering fire conditions. A comparison of the measured data with similar experiments by

other researchers confirmed their plausibility. The average charring rate of the smouldering fires considered is clearly below the standard charring rate of spruce wood.

## ACKNOWLEDGMENTS

This work was supported by Interreg Slovenia as part of the cross-border cooperation program Interreg Slovenia - Austria [<http://www.si-at.eu/en2/fireexpert/>].

## REFERENCES

- Babrauskas, V. (2005) Charring rate of wood as a tool for fire investigations. *Fire Safety Journal*. [Online] 40 (6), 528–554. Available from: doi:10.1016/j.firesaf.2005.05.006.
- Bobacz, D. (2008) *Behavior of Wood in Case of Fire Proposal for a Stochastic Dimensioning of Structural Elements*. [Online]. Available from: <https://nbn-resolving.org/urn:nbn:de:101:1-200911247157> [Accessed: 6 May 2021].
- Buchanan, A. (2007) *Energy and CO2 Advantages of Wood for Sustainable Buildings*. (Institute of Professional Engineers Convention), 9.
- Fornather, J. (2003) *Brandverhalten von Holz unter besonderer Berücksichtigung stiftförmiger Verbindungsmittel - experimentelle und numerische Untersuchungen*. Wien, Universität für Bodenkultur Wien.
- Khoury, G.A. (2000) Effect of fire on concrete and concrete structures. *Progress in Structural Engineering and Materials*. [Online] 2 (4), 429–447. Available from: doi:<https://doi.org/10.1002/pse.51>.
- Lache, M., Topf, P. & Wegener, G. (1992) *Abbrandgeschwindigkeit von Vollholz, Brettschichtholz und Holzwerkstoffen*.
- Lowden, L.A. & Hull, T.R. (2013) Flammability behaviour of wood and a review of the methods for its reduction. *Fire Science Reviews*. [Online] 2 (1), 4. Available from: doi:10.1186/2193-0414-2-4.
- ÖNORM B 1995-1-2 (2011) *ÖNORM B 1995-1-2: 2011 09 01 - Eurocode 5: Entwurf, Berechnung und Bemessung von Holzbauten - Teil 1-2: Allgemeine Regeln - Bemessung für den Brandfall - Nationale Festlegungen zu ÖNORM EN 1995-1-2, nationale Erläuterungen und nationale Ergänzungen*. [Online]. Available from: [https://shop.austrian-standards.at/action/de/public/details/400068/OENORM\\_B\\_1995-1-2\\_2011\\_09\\_01](https://shop.austrian-standards.at/action/de/public/details/400068/OENORM_B_1995-1-2_2011_09_01) [Accessed: 6 May 2021].
- ÖNORM EN 1363-1 (2020) *ÖNORM EN 1363-1: 2020 04 15 - Feuerwiderstandsprüfungen - Teil 1: Allgemeine Anforderungen*. [Online]. Available from: [https://shop.austrian-standards.at/action/de/public/details/674485/OENORM\\_EN\\_1363-1\\_2020\\_04\\_15;jsessionid=C5DD2F8F675FD20AB4841C98778F77B0](https://shop.austrian-standards.at/action/de/public/details/674485/OENORM_EN_1363-1_2020_04_15;jsessionid=C5DD2F8F675FD20AB4841C98778F77B0) [Accessed: 6 May 2021].
- Tsai, W. (2010) *Charring Rates for Different Cross Sections of Laminated Veneer Lumber (LVL)*. [Online]. Christchurch, New Zealand, University of Canterbury. Available from: <https://core.ac.uk/download/pdf/35464613.pdf> [Accessed: 6 May 2021].
- Werther, N. (2016) *Einflussgrößen auf das Abbrandverhalten von Holzbauteilen und deren Berücksichtigung in empirischen und numerischen Beurteilungsverfahren*. [Online]. München, TU München. Available from: <https://mediatum.ub.tum.de/doc/1307126/document.pdf> [Accessed: 6 May 2021].

Proceedings of the International Conference in Ljubljana, 10-11 June 2021  
in edition of Applications of Structural Fire Engineering

**Session**

**Concrete structures II**

# RESIDUAL MECHANICAL PROPERTIES OF 120 MPa HFRC POST FIRE 120 MPa-grade Hybrid Fiber-Reinforced Concrete Exposed to Temperatures up to 800 °C

Honghui Qi<sup>a</sup>, Yong Du<sup>a</sup>, and J.Y. Richard Liew<sup>b</sup>

<sup>a</sup> Nanjing Tech University, College of Engineering, Nanjing, China

<sup>b</sup> National University of Singapore, Department of Civil and Environmental Engineering, Singapore

## Abstract

This paper reports the results of a series of experimental investigations on the residual mechanical properties of 120 MPa hybrid fiber-reinforced concrete (HFRC) exposed to temperatures up to 800 °C. A total of 120 specimens with different dimensions and steel fiber dosages were tested after exposed to different target temperatures. The test results show that there was no change in the compressive stiffness after heating temperature up to 200 °C, but lead to an improvement in the compressive strength and splitting tensile strength of HFRCs. More than 200 °C, with the target heating temperature increasing, the residual compressive, splitting tensile and flexural strength reduced after cooling down to ambient temperature. The residual mechanical properties of 120 MPa hybrid fiber-reinforced concrete was governed by the target heating temperature, and improved by the increasing dosage of the steel fiber.

**Keywords:** post fire, ultra-high strength concrete, steel fiber, residual mechanical properties

## 1 INTRODUCTION

The development of high-rise buildings and large-span bridges promotes the use of ultra-high strength concrete (UHSC) (Liew & Xiong, 2015). However, increasing the compressive strength of concrete leads to reduce its ductility (Wille et al., 2012). Experimental investigations have been reported on the ductility of UHSC improved by steel fibers (Wu et al., 2019).

Fire is an accidental scenarios occurring in buildings, which would threaten the life safety and property security. However, limited experimental results can be used to evaluate the high temperature-induced residual mechanical properties of UHSC with the strength class over 120 MPa. This paper investigated the residual mechanical properties of 120 MPa-class hybrid fiber-reinforced concrete (HFRC) exposed to temperatures up to 800 °C. The residual mechanical properties of 120 specimens with different steel fiber contents were tested at different elevated temperatures.

## 2 EXPERIMENTAL PROGRAM

### 2.1 Materials and mix proportions

P-II Type 52.5 cement with 28-day compressive strength of 63.2 MPa, basalt coarse aggregates with a particle size range of 5 - 20 mm, river sand, silica fume, superplasticizer and tap water were used in this study. Steel fiber and polypropylene (PP) fiber, were incorporated into the concrete mixture and their physical and mechanical properties are listed in Table 1. The target compressive strength of HFRC was 120 MPa. Four sets of 120 MPa-class HFRC with different fiber contents were fabricated. The mix proportions of HFRC are given in Table 2.

Table 1 Physical and mechanical properties of fibers

Series	Density [g/cm <sup>3</sup> ]	Melting point [°C]	Diameter [μm]	Length [mm]	Tensile strength [MPa]	Sectional shape
Steel fiber	7.85	1535	230	14	2900	Circular
PP fiber	0.92	170	18	19	560	Circular

Table 2: Mix proportions and properties of HFRC

Concrete ID	Cement [kg/m <sup>3</sup> ]	Silica fume [kg/m <sup>3</sup> ]	Sand [kg/m <sup>3</sup> ]	Coarse aggregate [kg/m <sup>3</sup> ]	Water [kg/m <sup>3</sup> ]	PP fiber [% by volume]	Steel fiber [% by volume]	SP* [L/m <sup>3</sup> ]	w/cm*
HFRC1	810	90	598	898	135	0.15	0	16.36	0.15
HFRC2	810	90	598	898	135	0.15	0.5	16.36	0.15
HFRC3	810	90	598	898	135	0.15	1.0	16.36	0.15
HFRC4	810	90	598	898	135	0.15	1.5	16.36	0.15

\* SP: Superplasticizer; w/cm: water to cementitious materials ratio

## 2.2 Specimen preparation and heating procedure

A total of 120 specimens, including 48 cubes, 24 prisms and 48 cylinders, were cast for the tests of compression, flexure and tension (see Table 3). Fresh HFRC were cast into the specific moulds and cured in the laboratory site for 24 hours; and then, the specimens were moved to the standard curing room with a temperature of 20±2 °C and relative humidity of 98% for 27 days.

Table 3 Geometry of specimens used for various tests and the curing condition

Residual strength index	Size of specimen	Sample number	Curing condition
Cubic compressive strength	100mm × 100mm × 100mm	24	All specimens subjected to 28-day moist curing
Cubic splitting tensile strength	100mm × 100mm × 100mm	24	
Cylindrical splitting tensile strength	Ø100mm × 200mm	24	
Flexural strength	100mm × 100mm × 400mm	24	
Cylindrical compressive strength	Ø100mm × 200mm	24	

An electric-gas hybrid furnace was used to heat the specimens at the rate of 10 °C/min up to different target temperatures, i.e., 100 °C, 200 °C, 400 °C, 600 °C and 800 °C. In addition to the ambient temperature of 20 °C, each target temperature was steadied for 4 hours to obtain the uniform temperature distribution in both furnace and specimens. Fig. 1 shows the temperature-time history curves. After the heating process, the furnace was automatically turned off and the specimens were cooled naturally to the ambient temperature.

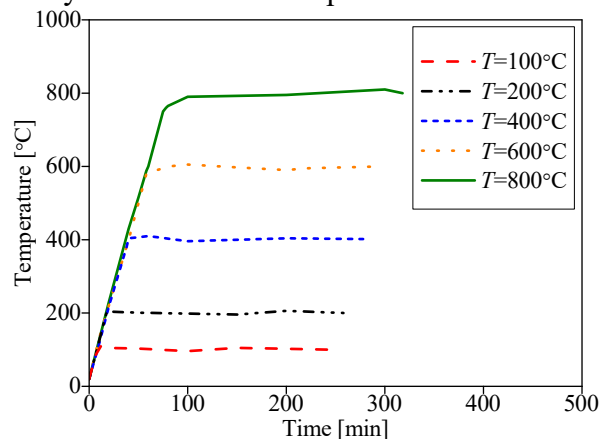


Fig. 1 Temperature-time history curves

## 2.3 Static loading tests

SANS servo-hydraulic testing machine was employed to conduct the uniaxial compression test, splitting tensile strength test and flexural strength test. In the compression test, The compressive load increased at a constant rate of 0.8 MPa/s. The maximum compressive load at failure was obtained by the testing machine and the test process was captured by a digital video recorder.

Fig. 2(a) and 2(b) show the setups for testing the cubic and cylindrical splitting tensile strength. The compressive load increased at a constant rate of 0.1 MPa/s. The loading process and the maximum splitting load at failure were recorded.

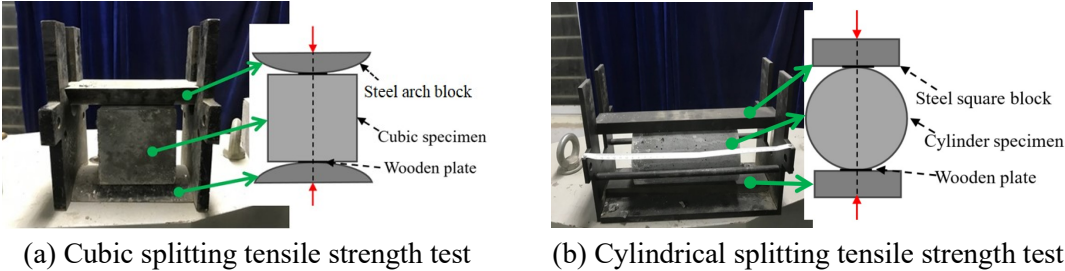


Fig. 2 Splitting tensile strength test setups

Fig. 3 shows the test setup and the schematic picture for flexural strength test. The load increased at a rate of 0.06 MPa/s until the specimen failed. The tested maximum flexural load and the failure process of the specimen were recorded during the test.

The multi-functional testing machine with load capacity of 10,000 kN shown in Fig. 4 was employed to perform the uniaxial compression test for 120 MPa-class HFRC cylinders. A constant displacement rate of 0.05 mm/min was adopted in the test. The strain of the specimen surface was measured by the strain gauge placed at mid-height of the specimen and along its longitudinal direction. The axial loads and displacements were automatically recorded by the testing machine.

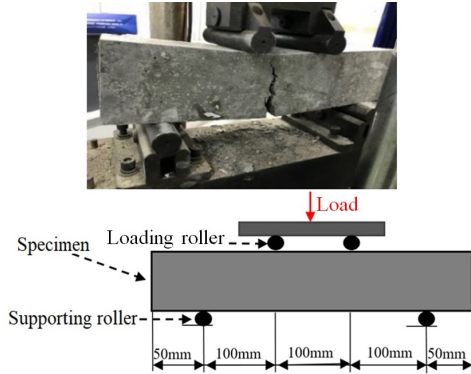


Fig. 3 Flexural strength test setup



Fig. 4 Multi-functional testing machine

**3 EXPERIMENTAL RESULTS AND DISCUSSIONS**

**3.1 Test observations and failure modes**

Figs. 5 to 7 show the failure modes of representative HFRC specimens with different geometrical shapes after exposed to the target temperature. The existing investigations (Xiong & Liew, 2015) have reported that PP fibers can prevent spalling in ultra-high strength concrete, and the test observations in this study confirm this conclusion, that is: after 4-hour exposure to the target temperature, no spalling occurred in 120 MPa-class HFRC specimens with 0.15% PP fiber by volume.

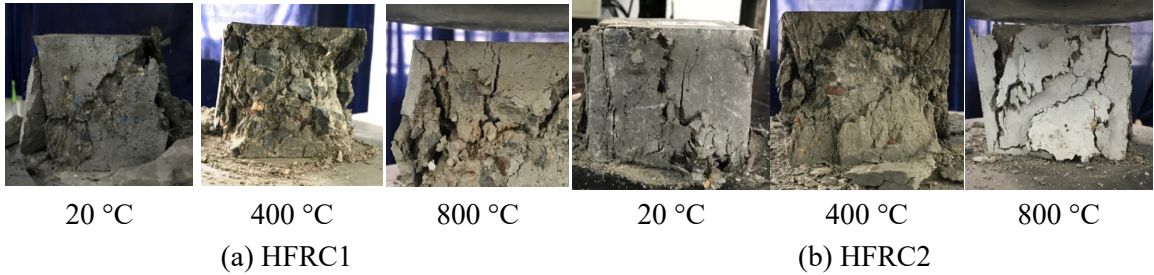


Fig. 5 Compressive failure in HFRCs (HFRC1 and HFRC2 as representative)



Fig. 6 Splitting tensile failure in HFRCs (HFRC2 as representative)

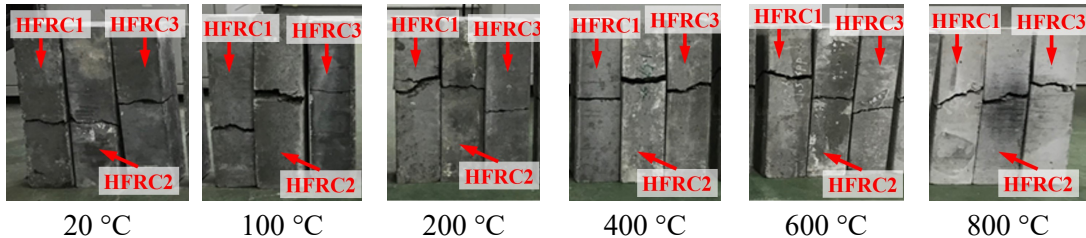


Fig. 7 Flexural failure in 120 MPa-class HFRC (HFRC1, HFRC2 and HFRC3 as representative)

Figs. 5 present the failure modes of 120 MPa-class HFRC specimens under compression loading test after exposed to elevated temperatures. The specimens under uniaxial compressive loading had a failure plane approximately parallel to the applied load direction following some cracks formed with an angle to the load direction. As shown in Fig. 6, the splitting failure plane of both cubic and cylinder specimens occurred along the loading direction and each specimen was split into two blocks. It is worth noting that the steel fibers were pulled out as the splitting failure occurred in the specimen HFRC2 after exposed to 400 °C. At the case of 800 °C, the steel fibers ruptured in the splitting failure plane of the specimen HFRC2. In the flexural test, specimens fractured at the middle of the span as shown in Fig. 7.

### 3.2 Stress-strain relationship

Fig. 8 shows the stress-strain curves of the 120 MPa-class HFRC specimens obtained from uniaxial compression test. In terms of the close slope in the elastic stage, those 120 MPa-class HFRC at the elevated temperatures of 100 °C and 200 °C had the same axial stiffness, as well as the case of 120 MPa-class HFRC at ambient temperature. Increasing the target temperature results in decreasing the axial stiffness in the elastic stage. Dissipated energy is used to evaluate the resistance ability of the concrete when subjected to the loads, which can be calculated by the area between the stress-strain curve and the strain axis until the stress reaches the peak. The results are discussed in Section 3.4.

### 3.3 Residual strength characteristics

Figs. 9 to 11 show the influence of elevated temperature on the residual strength characteristics of 120 MPa-class HFRC. It can be seen that i) within 200 °C, increasing the elevated temperature results in improving the compressive strengths of 120 MPa-class HFRC; however, these strength characteristics reduce at the case of temperature over 200°C; ii) within 100 °C, increasing the elevated temperature results in improving the splitting tensile strengths of 120 MPa-class HFRC; however, these strengths reduce at the temperature over 100 °C; iii) in the flexural loading test, no strength growth can be found at any elevated temperature with respect to the case at ambient temperature. The reason of increase of both compressive and splitting tensile strength after exposure to the temperatures of 100 °C and 200 °C can be deduced that the force between the gel particles (i.e., Van der Waals forces) increases due to the moisture evaporation and the consequent shrinkage in cement mortar, which leads to stimulate the secondary hydration reaction in curing the concrete (i.e., like steam curing).

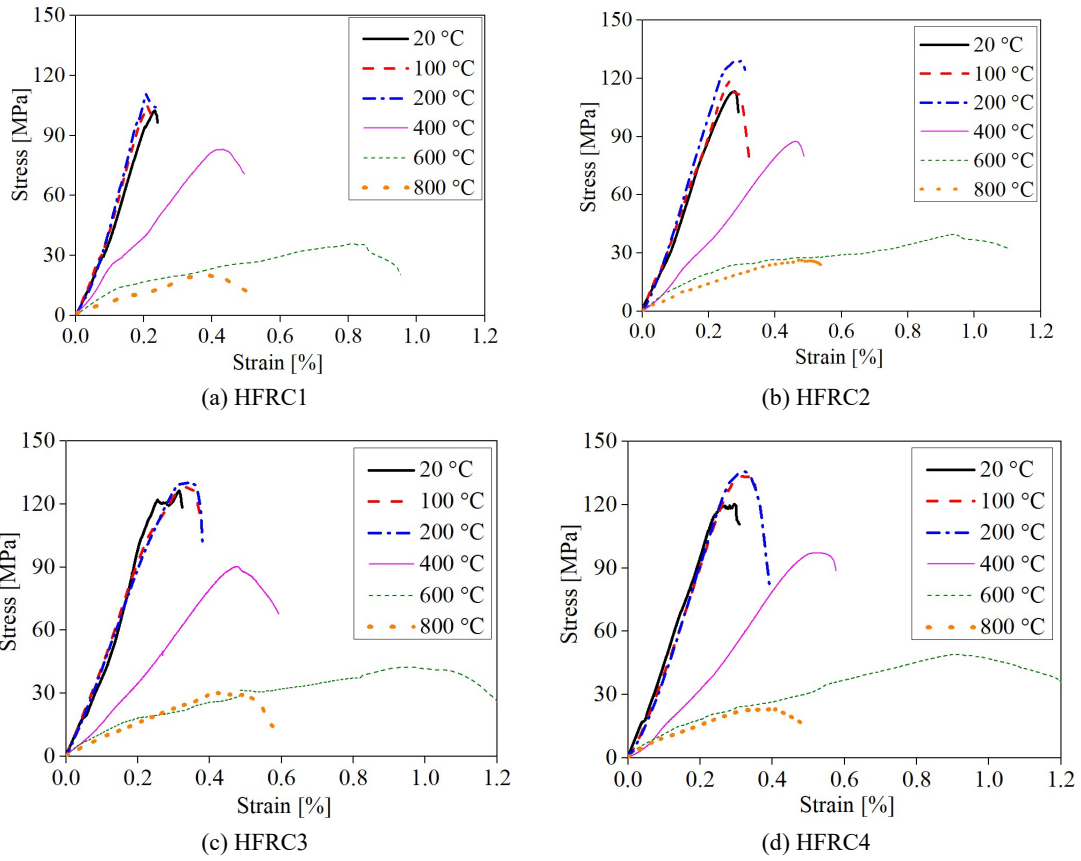


Fig. 8 Stress-strain curves of cylindrical specimens

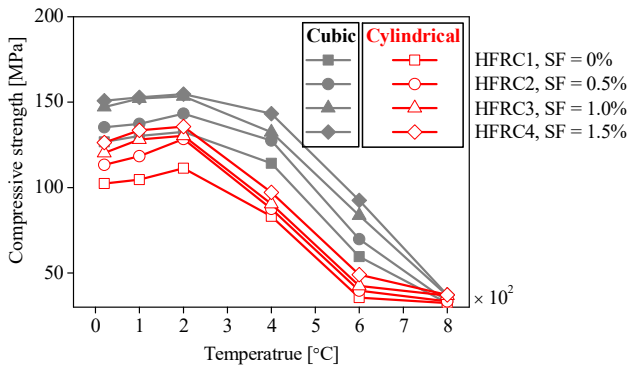


Fig. 9 Residual compressive strength

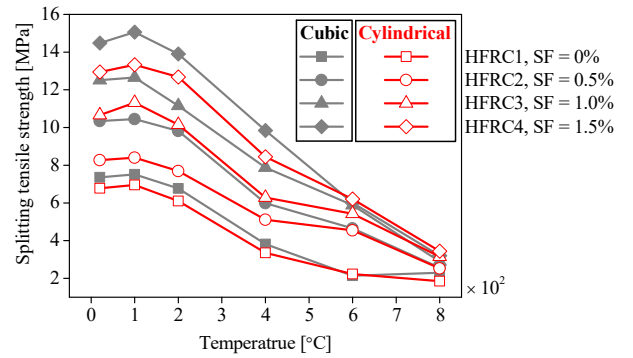


Fig. 10 Residual splitting tensile strength

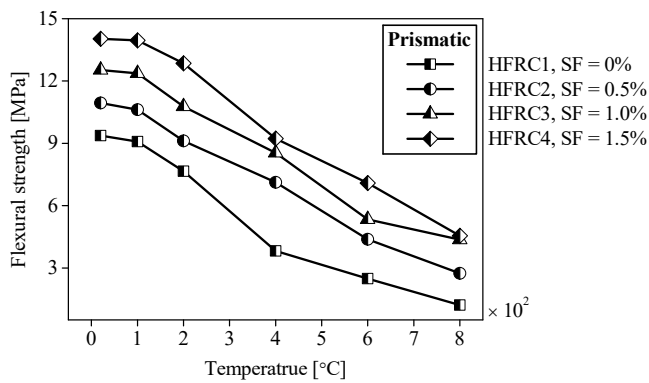


Fig. 11 Residual flexural strength

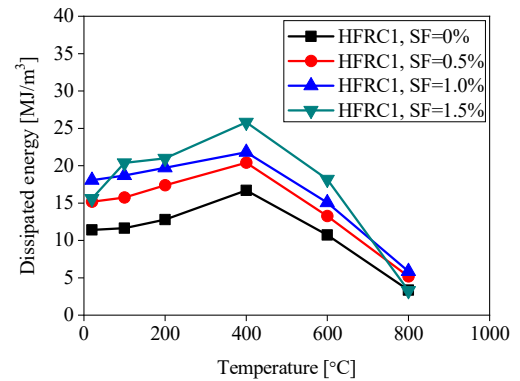


Fig. 12 Dissipated energy

A comparison of test results between cubic and cylindrical loading tests shown in Figs. 9 and 10 indicates that the residual cubic compressive strength is larger than the cylinder compressive

strength, and the similar rule can be found in the residual splitting strength. It is attributed to the reduced transverse restraint action when increasing the distance between the top and bottom platen surfaces.

Figs. 9 to 11 also show the influence of dosage of steel fiber on the residual strength characteristics of 120 MPa-class HFRC. The overall trend can be found that increasing the dosage of steel fiber improves the residual strengths (i.e., compression, splitting tension and flexure) of 120 MPa-class HFRC. This is due to the fact that i) the steel fibers can improve the tensile resistance of concrete and ii) the dosage of steel fiber can delay the crack rate of concrete.

### 3.4 Dissipated energy

Fig. 12 shows the energy dissipation of 120 MPa-class HFRC affected by elevated temperature. Before 400 °C, the dissipated energy increases with increasing of target temperature; however, the dissipated energy decreases when varying the target temperature from 400 °C to 800 °C. More research efforts need to be concentrated on the energy dissipation of 120 MPa-class HFRC to check if 400 °C is the temperature-induced performance transition point. The influence of dosage of steel fiber on the energy dissipation of 120 MPa-class HFRC can also be found in Fig. 12. Improving the dosage of steel fiber increases the dissipated energy of HFRC, which is due to the favorable energy dissipation of steel material.

## 4 CONCLUSIONS

This paper investigates the residual mechanical properties of 120 MPa-class HFRC exposed to temperatures up to 800 °C by performing a series of tests on cubic, prism and cylinder specimens with different dosages of steel fiber. The following conclusions can be drawn based on the test results and observations:

- No explosive spalling occurred in the heating procedure due to the contribution of mixing PP fibers in HFRC.
- Increasing the target temperature up to 200 °C has no remarkable change in the stiffness but leads to an improvement in the compressive strength and splitting tensile strength, which is caused by the moisture evaporation and the consequent shrinkage in cement mortar. The compressive strength, splitting tensile strength, and flexural strength of 120 MPa-class HFRC decrease when varying target temperature from 200 °C to 800 °C.
- Before 400 °C, the dissipated energy increases with increasing of the target temperature; however, the dissipated energy decreases when varying the target temperature from 400 °C to 800 °C. More research efforts need to be concentrated on this phenomenon.
- Regardless of the temperature, increasing the dosage of steel fiber improves the residual mechanical properties of 120 MPa-class HFRC. The effect of the steel fiber on the residual mechanical properties at 800 °C can be neglected, and this is due to the softening of steel fiber without providing the tensile resistance at this temperature.

## REFERENCES

- Liew J.Y.R., Xiong M. 2015. *Design guide for concrete filled tubular members with high strength materials - an extension of eurocode 4 method to C90/105 concrete and S550 steel*, Research Publishing Services, Singapore.
- Wille K., Naaman A.E., El-Tawil S., Parra-Montesinos G.J. 2012. *Ultra-high performance concrete and fiber reinforced concrete: achieving strength and ductility without heat curing*. *Materials and structures*, 45(3), p. 309-324.
- Wu K., Chen F., Chen C., Zheng H., Xu J. 2019. *Load-transfer mechanism and bond-stress components in steel and steel fiber - reinforced concrete structure*. *Journal of Structural Engineering*, 145(12), 04019160.
- Xiong M.X., Liew J.Y.R. 2015. *Spalling behavior and residual resistance of fibre reinforced ultra-high performance concrete after exposure to high temperatures*. *Materiales De Construcción*, 2015, 65(320), e071.

# FINITE ELEMENT ANALYSIS OF REINFORCED CONCRETE FLAT SLABS TESTED WITH DIFFERENT CONFIGURATIONS AT ELEVATED TEMPERATURE

Norlizan Wahid<sup>a</sup>, Tim Stratford<sup>b</sup>

<sup>a</sup> Faculty of Civil Engineering, Universiti Teknologi MARA, Cawangan Pulau Pinang, Malaysia

<sup>b</sup> School of Engineering, The University of Edinburgh, Edinburgh, Scotland

## Abstract

This paper examines the effect of different test configurations on the deflection response of reinforced concrete flat slab samples tested at elevated temperature. The configuration is varying in different support conditions and sample arrangements. The samples were modelled using finite element software (Abaqus) along with a prototype model of an actual flat slab system. The results show that different test configurations could affect the magnitude of the slab deflection. However, all models behave similarly to the prototype model, bending towards the heat source when exposed to high temperature. The test configuration that could produce comparable results with the actual flat slab system is the one with an unrestrained slab edge, where the sample arranged in an inverted position. The unrestrained edge model, however, produced a significant difference in deflection response and could lead to the misinterpretation of the flat slab behaviour at elevated temperature.

**Keywords:** Flat slab, elevated temperature, test configuration, deflection, finite element

## 1 INTRODUCTION

A study on the behaviour of reinforced concrete (RC) flat slabs at high temperature is usually conducted on an isolated sample of a slab-column connection. There are two different methods of sample arrangements applied in the previous test. First is the inverted position from the actual arrangement of the real flat slab system, as shown in Figure 1(a). The samples were heated from above where the compression side situated to avoid damage to the heating panel caused by a broken sample (Smith, Stratford and Bisby, 2014). The other one shows in Figure 1(b) is the upright position as an actual flat slab condition. As conducted by Annerel, Lu and Taerwe, (2013), the load was applied by hydraulic jack to the high strength bar that was anchored through the central slab opening on the column stub. The load is transferred to the slab surface, distributed symmetrically over eight loading points.

Heat transferred from heat source to slab surface create a thermal gradient throughout the slab thickness. The thermal gradient could cause a thermal bowing towards the heat source, which also be the direction of the slab deflection. This response was observed in the previous tests of RC flat slabs exposed to high temperature at the compression side (Kordina, 1997; Annerel, Lu and Taerwe, 2013; Wang *et al.*, 2020), which samples were arranged in the upright position (Figure 1(b)). However, Smith, Stratford and Bisby, (2014) had highlighted an opposite deflection direction of their samples that arranged in an inverted position (Figure 1(a)). Observation from the other study by Ghoreishi, Bagchi and Sultan, (2015) with the same arrangement was also deflected away from the heat source. This raised question of whether different test position could affect the deflection response of RC flat slab samples tested at high temperature.

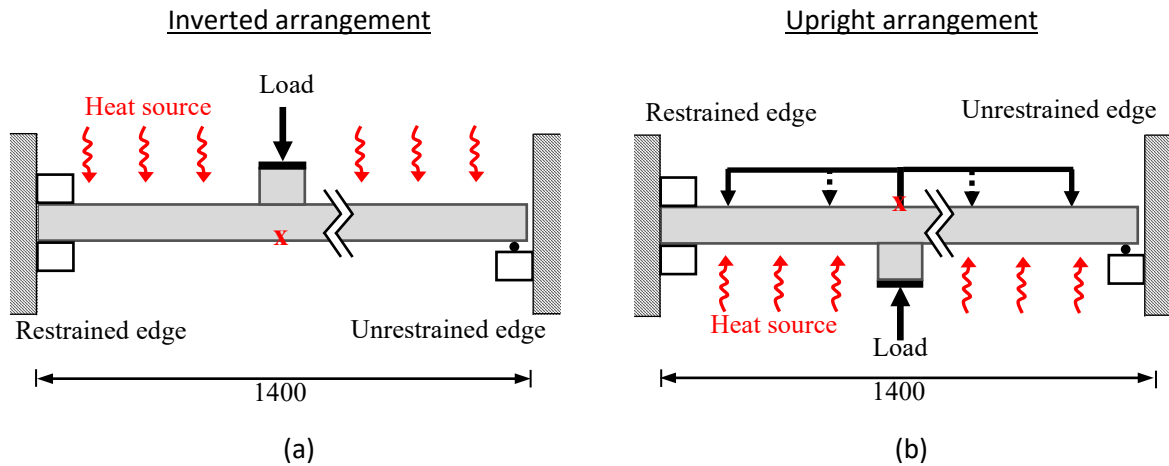


Figure 1 – Sample arrangements of elevated temperature test for RC flat slabs in (a) inverted and (b) upright positions. All units are in mm.

To date, all conducted tests in the literature had the same test arrangements, and the effect of different test configurations on the flat slab deflection behaviour at elevated temperature has yet to be studied. So, this study was carried out to examine these differences and determine the best test configurations that could imitate the actual flat slab behaviour at elevated temperature. The finding helps reviewers decide whether it is fair to directly compare the available test results in the literature of the RC flat slab with different configurations. It could also contribute to a better understanding of the behaviour of RC flat slab tested at elevated temperature.

## 2 FINITE ELEMENT MODELS

Two RC flat slab samples, HU75-08 and HR75-08, tested by Smith, Stratford and Bisby, (2014) in an inverted position as in Figure 1(a) were referred. The letter ‘H’ in the name indicates the slabs were heated, and ‘U’ and ‘R’ indicate the unrestrained and restrained support condition. The slabs were 1400 x 1400 mm wide and 75 mm thick, with a 120 x 120 x 100 mm column stub at the centre. All slabs were reinforced with a 0.8% flexural reinforcement ratio. The yield strength and Young’s modulus of the steel bars are 550 MPa and 200 GPa, respectively, while shear reinforcement was not provided. From the test, mean concrete compressive strength and tensile strength measured at ambient was 51 MPa and 4 MPa, respectively, with a moisture content of 4%. The slabs were preloaded with around 81% of its ultimate load, 82kN, and held constant while exposed to the high temperature for 120 minutes on its compression side.

There are five FE models build for this study as listed in Table 1, considering four different test configurations used in the previous research and one prototype model of an actual flat slab system. Two FE models were build based on the previous test of HU75-08 and HR75-08 (Smith, Stratford and Bisby, 2014), named **U75-I** and **R75-I**. Then, the same models with the same support conditions of unrestrained and restrained edge, **U75-U** and **R75-U**, were analysed in the upright position as in Figure 1(b) following the test arrangement by Annerel, Lu and Taerwe, (2013).

Table 1 Details of the finite element models.

	FE Models	Support conditions	Testing arrangement
Test configuration 1	U75-I	Unrestrained	Inverted
Test configuration 2	U75-U	Unrestrained	Upright
Test configuration 3	R75-I	Restrained	Inverted
Test configuration 4	R75-U	Restrained	Upright
Prototype model	PR75-U	Partially restrained	Upright

The fifth FE model, **PR75-U**, was built based on the prototype of a full flat slab system shown in Figure 2 to replicate the actual flat slab system behaviour at elevated temperature. The design and dimensions were inspired by the test slab of HR75-08 (Smith, Stratford and Bisby, 2014). The prototype was modelled as an isolated slab-column connection, arranged in an upright position and applied with a uniformly distributed load over the slab surface. The model was assigned with a symmetrical boundary condition on its edge, which is considered partially restrained in this study.

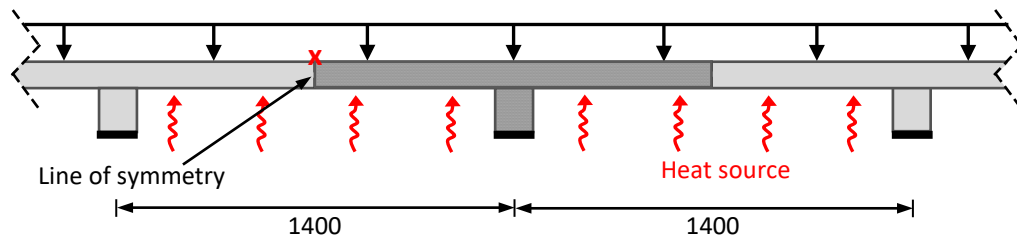


Figure 2 Prototype of a full flat slab system

The FE models were analysed using a *sequentially thermo-mechanical* method of analysis in Abaqus. The concrete material properties were expressed using the Concrete Damaged Plasticity model in Abaqus, where the Concrete Plasticity Parameters, constitutive models for Compressive Behaviour and Tensile Behaviour had been calibrated in the previous study (Wahid, Stratford and Bisby, 2019a). The temperature profile for test slab HU75-08 and HR75-08 had been predicted well in the previous analysis (Wahid, Stratford and Bisby, 2019b), with a maximum temperature of 537°C and 628°C, respectively. The temperature data of slab HU75-08 was applied to the unrestrained slab models of U75-I and U75-U, while the temperature data of test slab HR75-08 was used to the restrained slab models of R75-I, R75-U and PR75-U.

The FE prediction of deflection response of slab HU75-08 and HR75-08 had been calibrated with the test results (Smith, Stratford and Bisby, 2014), reported by Wahid, Stratford, & Bisby, (2019b). For calibration, spring stiffness was applied to the reaction support of the FE model since the actual supporting frame was reported moving during the experimental test (Smith, Stratford and Bisby, 2014). For this study, the same FE models were used for slab **U75-I** and **R75-I** but without the effect of spring stiffness. The supporting reaction frame was assumed to be perfectly rigid for a fair comparison with the other FE models.

### 3 RESULTS AND ANALYSIS

Figure 3 shows the prediction of the deflection response with respect to the heat exposure time. The preloading phase at ambient temperature is indicated by the exposure time of  $t < 0$ , and  $t > 0$  is the heated phase of the models under constant load. The deflection was measured at the maximum point that moved, responding to load application and heat exposure indicated by 'x' in Figure 1 and Figure 2. Unlike the other models for different test configurations, the movement of the actual flat slab system is at its midspan and thus explain the reversed deflection response of the prototype model **PR75-U** in Figure 3. For comparison purpose, the deflection was converted to 'relative difference of the midspan movement to the column height', presented as **PR75-U\***.

During the preloading phase, the model of all test configurations was deflected towards the direction of the applied load with almost the same magnitude, except for model **U75-I**. The unrestrained edge of model **U75-I** resulting in a more significant rotation angle,  $\Psi$  thus contribute to the vast difference of deflection compared to others. Although the upright model **U75-U** has similar unrestrained edge condition, the nature of its loading arrangement, which distributed over 8 points on the slab surface, had prevented the model from rotating as big as **U75-I**. It shows that an unrestrained edge slab tested in an inverted position could significantly affect the slabs' deflection response even at ambient temperature.

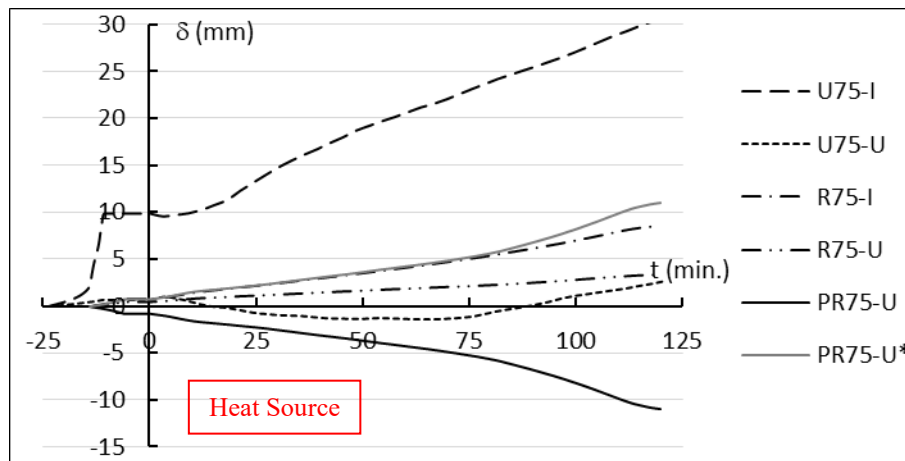


Figure 3 – Deflection response.

As been calibrated with test (Wahid, Stratford and Bisby, 2019b), deflection at high temperature of both unrestrained and restrained *inverted models* of **U75-I** and **R75-I** in Figure 3 were increased with time, moving away from the heat source. The unrestrained model **U75-I** continuously exhibits the most significant deflection response throughout the exposure time. While for model **R75-I**, the expansion was blocked by the restrained condition, developing an axial thrust that contributes to its strength capacity (Buchanan and Abu, 2017). Thus, it prevented the slab from making a bigger rotation angle,  $\Psi$  as in Figure 4 and resulting in a smaller deflection response of slab **R75-I**.

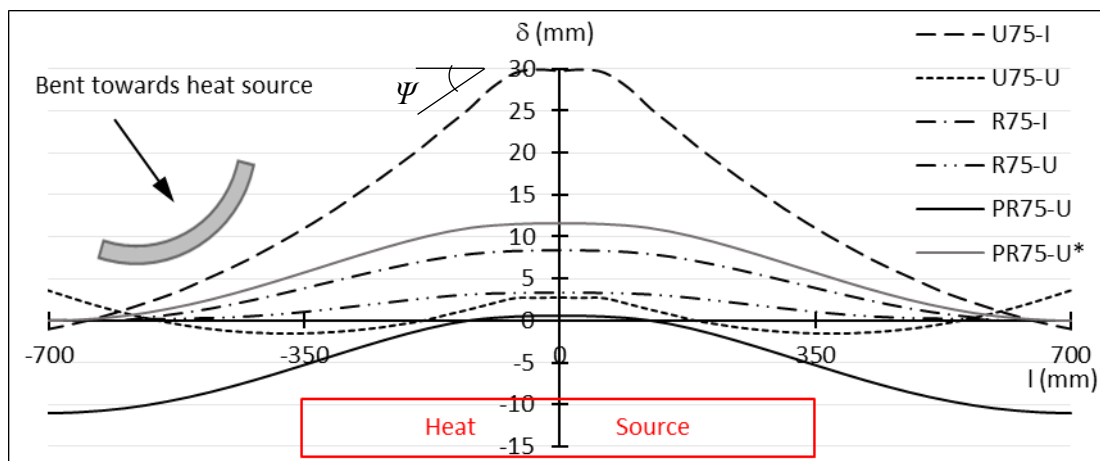


Figure 4 Deflection profile at  $t = 120$  minutes.

The models in the *upright position* were not responded as expected, where deflection moves towards the heat source as observed during the test by Annerel, Lu and Taerwe, (2013). The model **R75-U** experience the opposite response, where deflection moves away from the heat source. From Figure 3, only model **U75-U**, which have a similar configuration with the test (Annerel, Lu and Taerwe, 2013), had responded as expected for about 80 minutes. But then it deflected away from the heat source until the end of the exposure period.

Although all the models exhibit a deflection response that moves away from the heat source, the truth is these models were bowed towards the heat source. If carefully observed in Figure 4, apart from the excessive deflection profile of model **U75-I**, the deflection curve of the other models was close to the edited deflection profile of the prototype model **PR75-U\***, taken as the ‘relative difference of the slab profile to the point of maximum deflection’.

The bowing curve can be confirmed from the slab curvature,  $\kappa$  profile in Figure 5. Positive curvature indicates that the deflection profile is concave upwards, showing that it bends towards the heat source. Generally, all the models experience this response in the region between column and slab edge, in agreement with the curvature response of prototype model **PR75-U**. Model **R75-I** had

the closest curvature profile to the prototype model **PR75-U**. In contrast, model **U75-I** and **U75-U** experienced high curvature on their unrestrained edge, which shows that the slabs' edge curls up when exposed to high temperature.

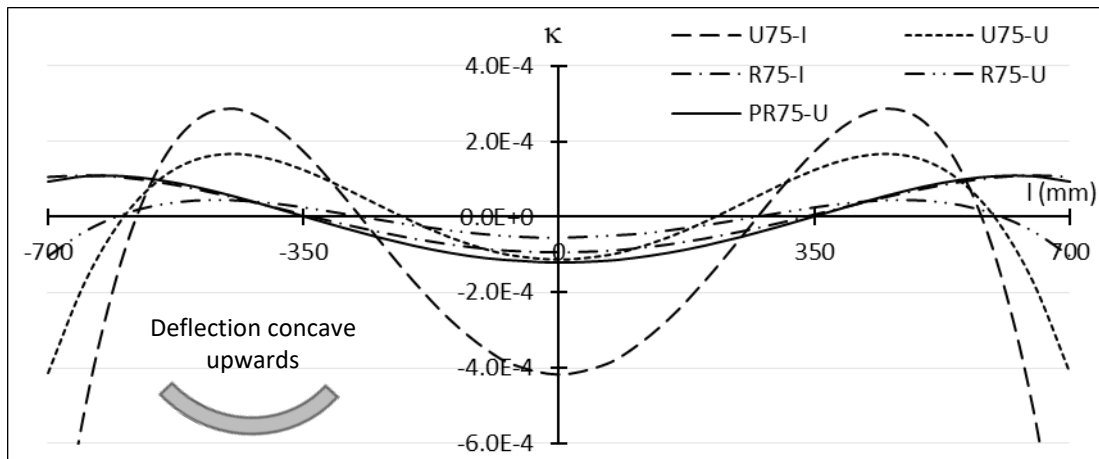


Figure 5 Slab curvature at  $t = 120$  minutes.

Overall, by comparing the results with the prototype model of an actual full flat slab system, the test configuration that could best imitate the behaviour of an RC flat slab structure at elevated temperature is the one with *restrained edge* and tested in an *inverted position* as in model **R75-I**. The other restrained edge model tested in an upright position, **R75-U**, could also produce similar behaviour but slightly underestimated the deflection response. In contrast, the test configuration with an unrestrained edge had made a deflection response significantly different from the other models.

It is proven that all models were behaving as expected regardless of the test configuration type when exposed to high temperature. All were deflected towards the heat source, or in a more precise statement, 'bend towards' the heat source. However, the response was misinterpreted to moved away from the heat source when focusing on the movement of the loading point, which is at the column location. Whereas in the actual flat slab system, the column does not move, the deflection point is considered at the midspan that moves when applied with load or exposed to a heat source.

#### 4 CONCLUSIONS

Different test configurations could affect the magnitude of deflection response of a flat slab model tested at elevated temperature. The effect is significant, especially from the model with an unrestrained edge. However, all models were behaving similarly with the prototype model of an actual flat slab system where it bends towards the heat source, although the deflection movement shows an opposite direction. It is because the deflection points of the different test configuration models were taken at the column area, while the actual deflection point that moves in the actual flat slab system is at its' mid-span. A fair comparison had been made with the prototype model by converting its deflection to the 'relative difference of the midspan to the column height' denoted by **PR75-U\***.

The recommended test configuration for studying the flat slab behaviour at elevated temperature is the one with restrained edge and test in an inverted position. This configuration had proven could produce a comparable result with the full flat slab system. In contrast, it is not advisable to test a flat slab sample without restraining its edge since it could cause discrepancies in the interpretation of flat slab behaviour at elevated temperature. The edge sample should at least restrain in the horizontal direction that acts as the adjacent slab panel on the actual flat slab system preventing the thermal expansion.

## ACKNOWLEDGMENTS

The authors would like to express their profound appreciation to the University of Edinburgh for providing the facilities for finite element analysis using Abaqus software and to the Universiti Teknologi MARA, Cawangan Pulau Pinang, for financially supporting this conference paper.

## REFERENCES

- Annerel, E., Lu, L. and Taerwe, L. (2013) ‘Punching shear tests on flat concrete slabs exposed to fire’, *Fire Safety Journal*, 57(November 2004), pp. 83–95. doi: 10.1016/j.firesaf.2012.10.013.
- Buchanan, A. H. and Abu, A. K. (2017) *Structural Design for Fire Safety*. 2nd Editio. New York, United States: John Wiley & Sons In.
- Ghoreishi, M., Bagchi, A. and Sultan, M. A. (2015) ‘Punching Shear Behavior of Concrete Flat Slabs in Elevated Temperature and Fire’, *Advances in Structural Engineering*, 18(5), pp. 659–674.
- Kordina, K. (1997) ‘Über das Brandverhalten Punktgestützter Stahlbetonplatten’ (On the Fire Behaviour of Reinforced Concrete Flat Slabs’. Berlin (Germany): Deutscher Ausschuss für Stahlbeton (DAfStb).
- Smith, H. K. M., Stratford, T. J. and Bisby, L. A. (2014) ‘Punching shear of restrained reinforced concrete slabs under fire conditions’, in *8th International Conference on Structures in Fire*. Shanghai: Tongji University Press, pp. 443–450.
- Wahid, N., Stratford, T. and Bisby, L. (2019a) ‘Calibration of concrete damage plasticity model parameters for high temperature modelling of reinforced concrete flat slabs in fire’, in *Applications of Structural Fire Engineering 2019, Singapore*.
- Wahid, N., Stratford, T. and Bisby, L. (2019b) ‘Modelling the deflection response of reinforced concrete flat slabs during heating’, in *Proceedings of the Interflam 2019 Conference*. London, pp. 1403–1414.
- Wang, D. ye *et al.* (2020) ‘Punching shear performance of concrete slabs under fire’, *Engineering Structures*. Elsevier, 225(July), p. 111094. doi: 10.1016/j.engstruct.2020.111094.

## FIRE-PROTECTION WITH ALKALI-ACTIVATED CEMENT BINDER

Jakub Šejna<sup>a</sup>, Vít Šmilauer<sup>a</sup>, Stanislav Šulc<sup>a</sup>, Pavel Reiterman<sup>a</sup>, František Wald<sup>a</sup>

<sup>a</sup> Czech Technical University in Prague, Faculty of Civil Engineering, Prague, Czech Republic

### Abstract

Fire resistance of unprotected steel structures is very low and steel elements must be protected from fire. One possibility is to create a protective layer of a cement-based material. Most types of cement have a low resistance to high temperatures, reducing mechanical properties. In flammability tests, cement activated with alkaline compounds showed better properties compared to conventional types of cement. This paper represents the determination of the properties of two H-Cement mortars with experlite or fireclay sand. Experiments carried out in a small kiln simulating a 1D load showed differences between elements in terms of heat transfer to the tested elements. The calculation model created to predict the course of the experiments has been validated and the unknown properties of the material have been calculated based on the data collected. The samples were tested in a small fire furnace. Finally, the thermal conductivity pattern was determined depending on the temperature.

**Keywords:** fire safety, alkali-activated cement, fire-protection, modelling, material properties

## 1 INTRODUCTION

Protection of the steel members by a layer of the thermal insulation material is traditional solution of passive fire safety. Most materials in cement bases do not behave well exposed to high temperatures, due to the formation of cracks in the protective layer. It offers the use of a new alternative alkaline-activated hybrid cement, H-Cement, which has better properties at higher temperatures than conventional types of cement.

The composition of H-Cement, as opposed to conventional cement, consists of the use of metallurgical slag along with an alkaline-activated inorganic geopolymer with a base of precipitated sewage in the production of bauxite. Portland cement's share of the H-Cement mix is 20 %. The production of H-Cement reduces CO<sub>2</sub> emissions by 80 % compared to the production of OPC (Martauz, 2016).

H-Cement exhibits properties like ceramic material at high temperatures, i.e. when H-Cement is heated to high temperatures due to the transformation of crystalline aluminosilicate phases to high melting points, and at temperatures above 800 °C there is a transformation into a ceramic form, so there is no significant development of cracks (Panias, 2014). Transformation and geopolymer water contained is an endothermic material that is very resistant to the effects of fire. When designing the protective layer of an H-Cement-based steel element, it is possible to use the heat transfer prevention property due to the thermal conductivity of hybrid cement, which ranges from 0,1-0,3 W/m/K when using experlite as a filler (Šmilauer, 2011).

Preliminary results (Daxner, 2016) demonstrated the excellent resistance of H-cement lightweight mortars to those of gypsum or alumina cement equivalents. Pilot tests for the larger experiment were performed (Šulc, 2021) on a laboratory burner and baseline values for thermal conductivity were determined.

This contribution aims to determine the thermal characteristics of the H-Cement layer at 20 mm thick on the steel sheet. The adhesion of H-Cement to steel has not yet been studied.

## 2 EXPERIMENTS

Two types of mortar were considered to verify the properties of the H-Cement coating for fire purposes, namely, a mortar not lightweight with fireclay sand and PVA fibres and a lightweight mortar of H-Cement with experlite and plating. The formulation used to make the mortar is given in

Table 1. The thickness of the 20 mm protective layer of H-Cement is chosen to ensure a fire resistance of at least 45 min.

Table 1 Composition of H-Cement mortar for 1 m<sup>3</sup>

Mortal	H-Cement [kg]	Fireclay [kg]		water [kg]	Experlite [kg]		Plasticizer [kg]	PVA fibres [kg]
		0-1 mm	1-2 mm		0-1 mm	1-2 mm		
Regular	119,62	119,62	239,24	44,21	-		-	0,31
Light weight	72,10	-			9,17	12,13	1,11	-

The experiment was carried out for both a non-lightweight mortar and a lightweight mortar. For one test, four samples measuring a steel sheet 180 × 100 × 12 mm were produced with a protective layer of 20 mm with the additional protection of the sides from mineral wool to ensure heat is applied to the sample from one side at a time. The protective layer was also applied from the sides of the steel element to simulate part of the bottom of the strip of the steel profile. Thermocouples for measuring steel temperature were placed on the non-heated side of the sample. The geometry of the sample is shown in Figure 1.

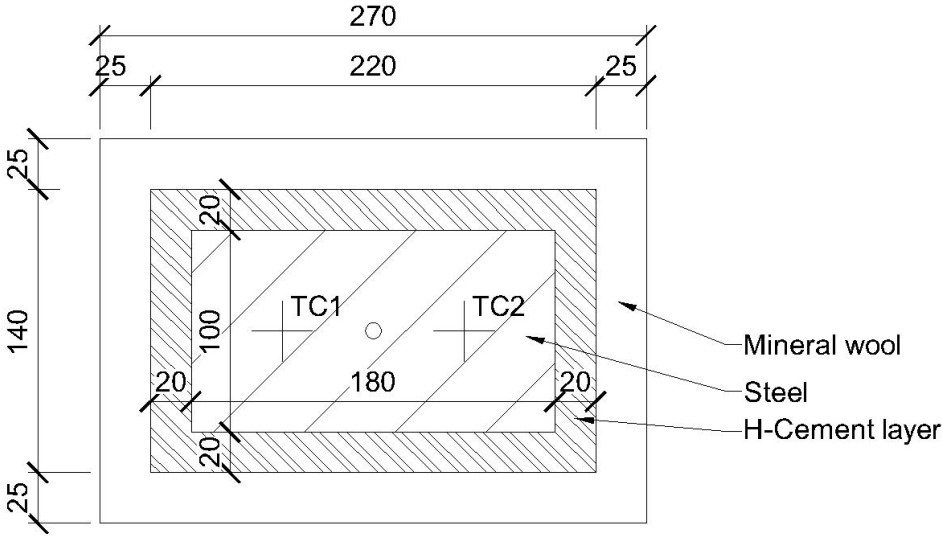


Fig. 1 The geometry of a sample and the position of the thermocouples

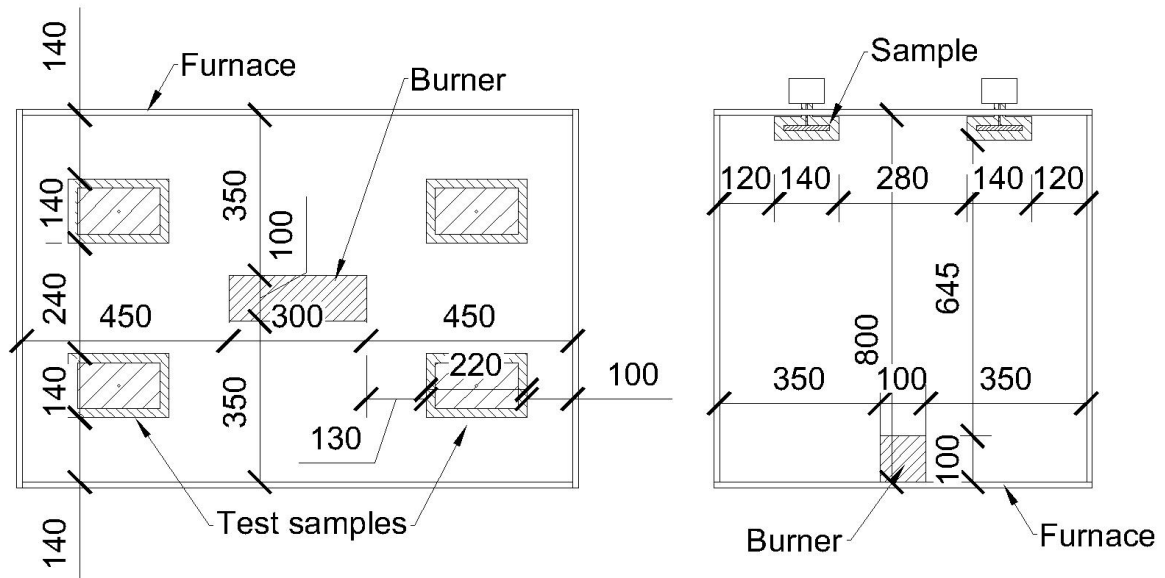


Fig. 2 Distribution of samples in furnace floor plan, and section of furnace

The experiment took 60 min, 45 min of faze heating, and 15 min of faze cooling. No significant cracks in the protective layer were evident when the samples were removed from the test furnace after the experiment. By the influence of cooling, these fissures were advancing in-depth and widening. All variants of H-cement-based lightweight mortars withstood exposure to high temperatures without causing visible cracks. For the lightweight variant of H-cement, cooling caused the edges of the test samples to fall off. Samples protected by a layer of H-cement, chamotte sand, and PVA fibres resisted waste even after cooling. Compared to the lightweight variants, however, there was a partial separation of the protective layer from the steel sheet due to the different cooling of steel and concrete.

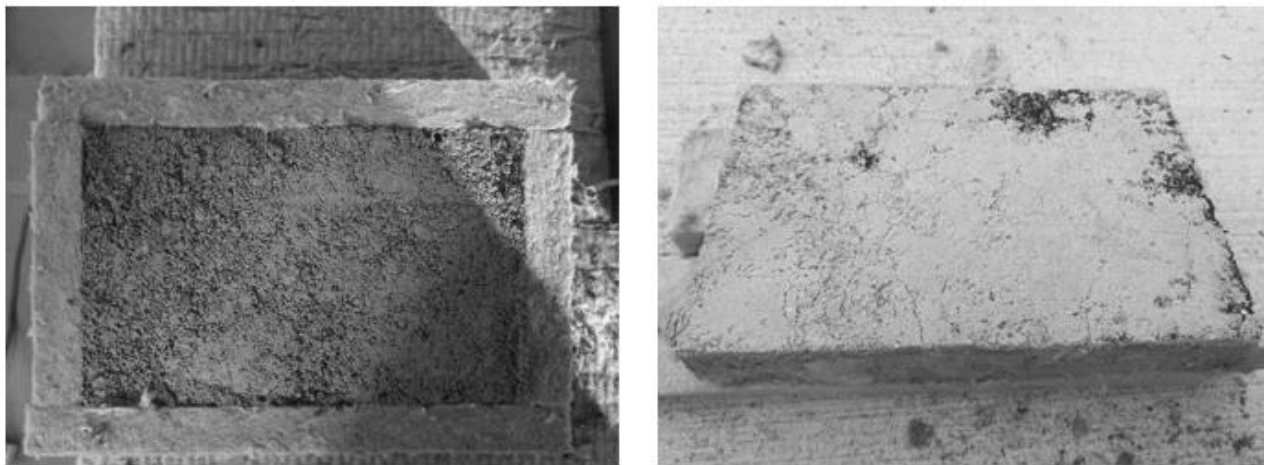


Fig.3 The samples before and after the test

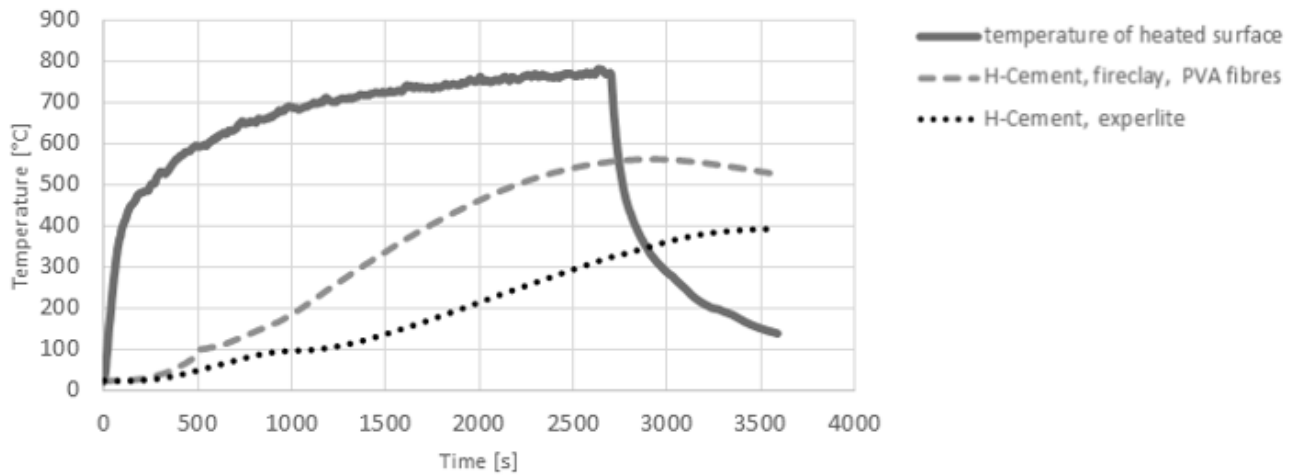


Fig.4 Test furnace temperature compared to steel temperature

Tab. 2: Comparing the predictions of the evolution of temperature and temperature achieved in the experiment on unprotected steel (H-Cement with experlite)

Time [min]	Temperature forecast [°C]	Experimental temperature [°C]
15	44,43	40,1
30	162,39	130,9
45	330,59	262,3



Fig.5 Destroyed sample after cooling

### 3 MORTAL CHARACTERISTICS

Model (Wang et al., 2013) was used to predict the material properties of H-cement with experlite. In many cases, however, there are no values available to describe the material. A prediction equation has therefore been used to describe the thermal conductivity of the porous material of H-cement with experlite, which can be applied in these very cases.

$$\lambda^* = C_1 + C_2 T^3 \quad (1)$$

The determination of the coefficients  $C_1$  and  $C_2$  was considered to be for vermiculite. Thus, the coefficient  $C_1$  can be replaced by the thermal conductivity at 20°C and the coefficient  $C_2$  by a formula considering the influence of volume weight.

$$C_1 = \lambda_0^* = A \frac{\rho}{1000} = 0,27 \frac{\rho}{1000} \quad (2)$$

$$C_2 = B \frac{(1000-\rho)}{1000} = 0,18 \frac{(1000-\rho)}{1000} \quad (3)$$

A lower value was achieved than the original assumption, where a thermal conductivity of 0,12 W/K/m was predicted for mortar at 20 °C. The improved thermal conductivity can be attributed to the effect of drying the sample and its low volume weight. The thermal conductivity is calculated using the data measured in the experiment. By the method of least squares, the values of coefficients A and B were determined for H-cement with experlite.

$$y = 0,09221 + 1,586E^{-11}x \quad (4)$$

$$\lambda_0^* = A \frac{\rho}{1000} \rightarrow A = \lambda_0^* \frac{1000}{\rho} = 0,09221 \frac{1000}{406} = 0,22712 \quad (5)$$

$$C = B \frac{(1000-\rho)}{1000} \rightarrow B = C_2 \frac{1000}{(1000-\rho)} 1000^3 = +1,586 \times 10^{-11} \frac{1000}{(1000-406)} 1000^3 = 0,0267 \quad (6)$$

Resulting H-cement thermal conductivity equation with experlite:

$$\lambda^* = 0,22712 \frac{\rho}{1000} + 0,0499T^3 \quad (7)$$

The effect of temperature on the change in volume weight and specific heat capacity was neglected for small samples. The change in the density of protective materials is due to the evaporation of the moisture content in the test samples. The samples were dried in a drying furnace when weight loss due to evaporation of the bound water in the samples was measured. Constant values were taken for basic models for concrete with a perlite filler that corresponds to the bulk weight of H-cement concrete with experlite. Values for basic modelling are given in Tab. 3.

Tab. 3: Material properties H-Cement with experlit

Material characteristics		H-Cement with chamotte	H-Cement with experlit
Density		1930 kg/m <sup>3</sup>	406 kg/m <sup>3</sup>
Specific thermal capacity		1050 J/kg/K	1150 J/kg/K
Thermal conductivity (W/m/K)	20°C	1,1000	0,097425
	100°C	0,9697	0,098100
	200°C	0,8508	0,099312
	300°C	0,7433	0,101686
	400°C	0,6472	0,104763
	500°C	0,5625	0,109002
	600°C	0,4892	0,114456
	700°C	0,4273	0,121282
	800°C	0,3768	0,129738
	900°C	0,3377	0,139827

Resulting H-cement thermal conductivity equation with fireclay:

$$\lambda_p = \left[ d_p \frac{V}{A_p} C_s \rho_s (1 + \phi/3) \frac{1}{(T_{fi} - T_s) \Delta t} \right] [\Delta T_s + (e^{\phi/10} - 1) \Delta T_{fi}] \quad (8)$$

$$\lambda_p = 1,1 - 0,136 \times 10^{-2}T + 0,0057 \times 10^{-4}T^2 \quad (9)$$

## 4 CONCLUSIONS

H-cement is an excellent bonding agent for fire-fighting materials, whether in compact or lightweight variants. Compared to the reference alumina cement, H-cement exhibits lower weight loss in temperatures above 300 °C in thermal insulation mortars. This is explained by the mild reaction of H-cement to experlite. This property is positively created by less mortar shrinkage and higher resistance to crack formation due to postburn cooling (whether shock by rapid cooling or gradual

cooling). At temperatures above 750 °C, the surface lightens, most likely by burning off residual black carbon, a feature that could be used for a quick colour indication of the temperature load history.

Heat-insulating H-cement mortar with experlite has created an effective fire suppression layer, preventing heat from entering the structure. The mortars have excellent adhesion to the steel element, dispensing with the need for any treatment of the steel by the underlying layers or coatings against corrosion.

Thermal conductivity of 0,093 W/m/K has been established for H-Cement with experlite mortar, with a specific heat capacity of 1150 J/kg/K at a dried weight of about 400 kg/m<sup>3</sup> and 20 °C. The thermal conductivity increases slightly with temperature.

## REFERENCES

- Daxner, J., 2016. Use of hybrid cement in fire resistant plasters. *88KHI/2016,2016*
- Hlaváček, P., et al., 2015. *Inorganic foams made from alkali-activated fly ash: Mechanical, chemical and physical properties. Journal of the European Ceramic Society*, 35.2: 703-709
- Martauz, P., et al. 2016. *Fundamental properties of industrial hybrid cement: utilization in ready-mixed concretes and shrinkage-reducing applications. Materiales de Construcción*, 66.322: 084.
- Panias, D.; Balomenos, E.; Sakkas, K. 2015. *The fire resistance of alkali-activated cement-based concrete binders. Handbook of alkali-activated cements, mortars and concretes. Woodhead Publishing*. p. 423-461.
- Šmilauer, V., et al. 2011. *Micromechanical multiscale model for alkali activation of fly ash and metakaolin. Journal of Materials Science*. 46(20), 6545-6555.
- Šulc, Stanislav, et al. 2021. *Fire protection of steel elements using lightweight hybrid cement mortar. Acta Polytechnica CTU Proceedings*. 2021(2), 1-6.

# FIRE RESISTANCE ANALYSIS OF REINFORCED CONCRETE TWO-WAY SLABS

Fidan Salihu<sup>a</sup>, Fatos Pllana<sup>a</sup>, Meri Cvetkovska<sup>b</sup>

<sup>a</sup> University of Pristina “Hasan Prishtina”, Faculty of Civil Engineering, Pristina, Kosovo

<sup>b</sup> University “Ss. Cyril and Methodius”, Faculty of Civil Engineering, Skopje, North Macedonia

## Abstract

The behavior of two-way reinforced concrete slabs in fire conditions and the influence of certain parameters on their fire resistance is presented in this paper. The influence of the concrete cover thickness, the span and the support conditions on the fire resistance of the slabs are analyzed. All analyzed slabs are exposed to Standard fire ISO 834. The numerical 3D analyses were conducted by using the software SAFIR2016. The numerically achieved results are compared with experimental results given in the literature. A satisfactory agreement during the entire fire test is noticed. It should be noted that in order to verify the numerically achieved results, there should be compliance of all parameters relevant for the testing with those of the numerical simulation. For comparison, the fire resistance is also calculated by applying the Yield Line Theory for slabs, by taking into account the reduced tensile strength of steel due to high temperatures.

**Keywords:** RC two-way slabs, fire resistance, 3D analysis, SAFIR

## 1 INTRODUCTION

In order to define the impact of different parameters on the fire resistance of two-way reinforced concrete slabs, numerical 3D analyzes were conducted using the SAFIR2016 software. The influence of the concrete cover thickness, the span and the support conditions on the fire resistance of the slabs is analyzed.

In order to draw a conclusion how a certain parameter affects the fire resistance of the reinforced concrete two-way slabs, the surface of the adopted reinforcement is equal to the surface of the required reinforcement EN1992-1-2 (EN, 2004).

The reinforced concrete two-way single span slabs exposed to fire from the bottom side are analyzed. The slabs are exposed to standard fire ISO 834, to the failure moment. For comparison, the fire resistance is also calculated by applying the Yield Line Theory for slabs (Johansen, 1972), by taking into account the reduced tensile strength of steel due to high temperatures. The temperatures in the reinforcement are obtained by using the SAFIR2016 program (Franssen & Gernay, 2017), while the strength and deformation properties of reinforcing steel at elevated temperatures is adopted according to the reduction coefficients given in EN1992-1-2 (EN, 2004).

## 2 VERIFICATION OF THE SOFTWARE SAFIR2016 ON EXPERIMENTAL EXAMPLES

### 2.1 Verification of the software SAFIR2016 for thermal analysis of fire exposed slabs

Figure 1 shows the temperature distribution in the slab cross section with a thickness of 100 mm, over time. The temperatures calculated with SAFIR2016 are compared with experimentally obtained temperatures during fire test of the slab (Lim L. , 2002). The temperature rise over time is shown for three surfaces: for the exposed side ( $x = 0$  mm), for the middle of the slab ( $x = 50$  mm) and for the unexposed side ( $x = 100$  mm). For the exposed side, the SAFIR2016 version gives higher temperatures than the experimentally obtained values. However, the calculated temperatures show similar trends. The slight discrepancy of the results could be related due to the fact that

physical and mechanical properties of materials as well as their temperature dependence are not exactly known.

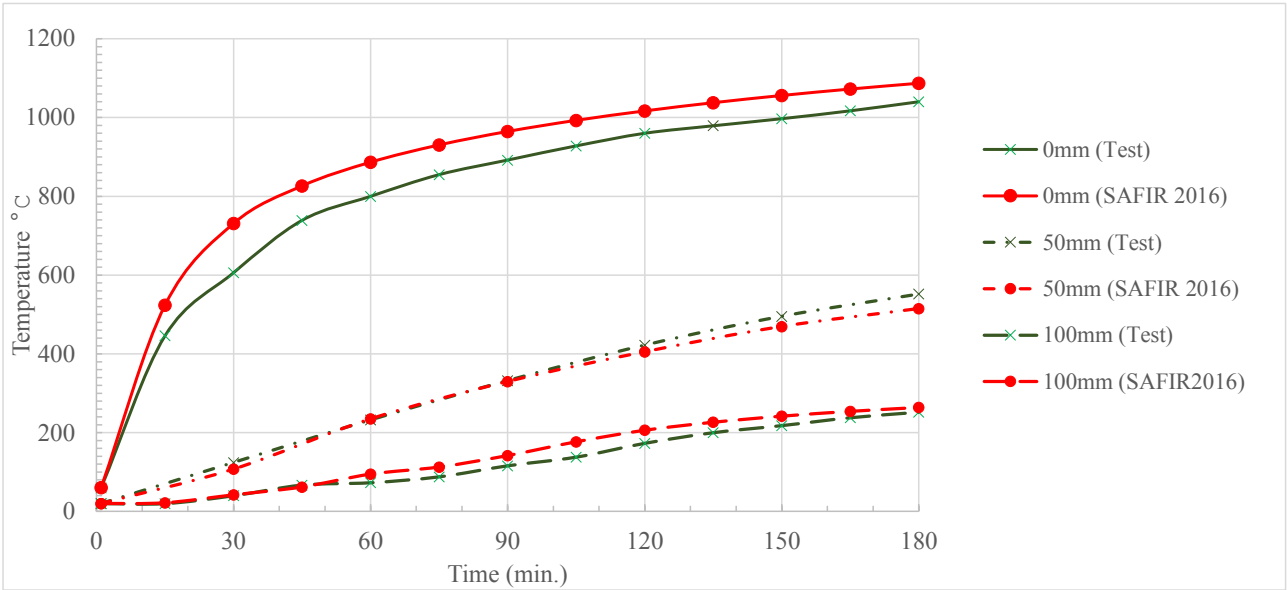


Fig. 1 Comparison of temperatures calculated with SAFIR2016 with the experimentally obtained temperatures for a 100 mm thick slab exposed to ISO fire

**2.1 Verification of the software SAFIR2016 for structural analysis of RC slabs exposed to fire**

This example verifies the SAFIR2016 program by comparing the numerically obtained results with the results of already conducted experimental investigations by Lim (Lim L. , 2002). A detailed description of the experiment can be found in the report (Lim L. , 2002).

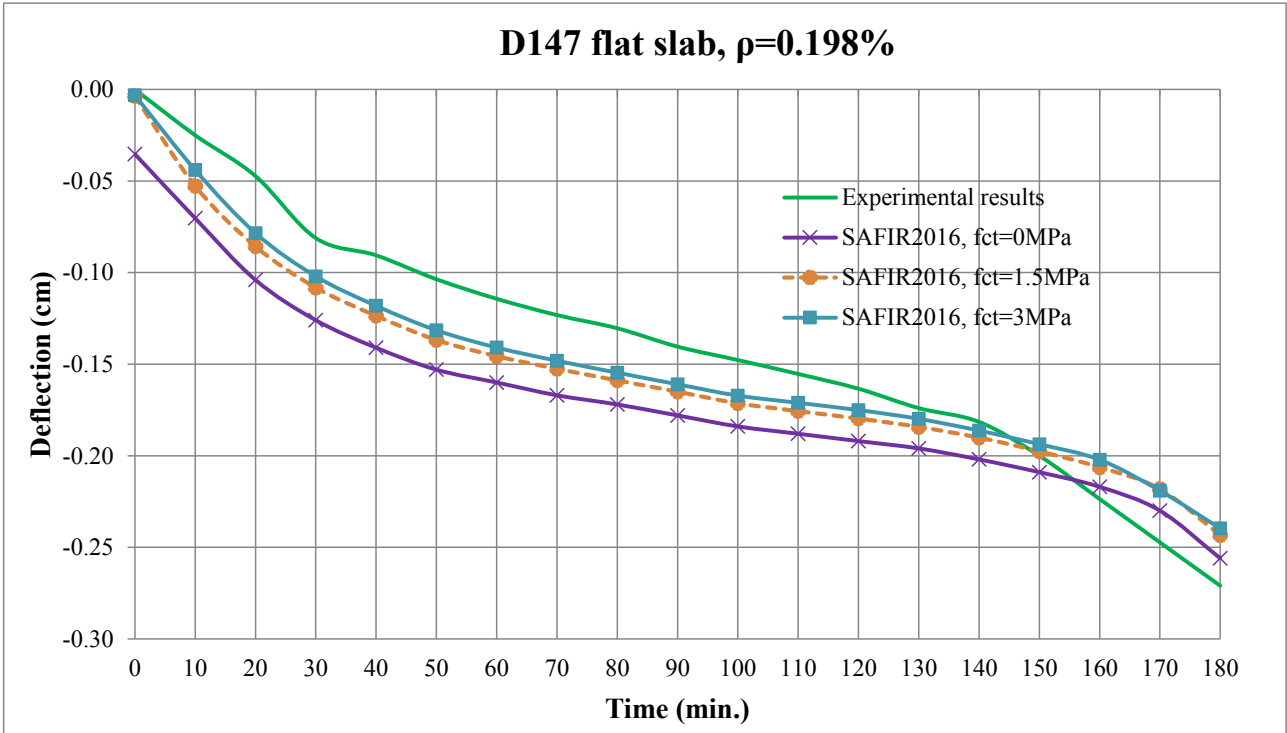


Fig. 2 Comparison of experimentally obtained slab displacements with displacements calculated with SAFIR2016, for different values of concrete tensile strength

Figure 2 compares the vertical slab displacements obtained with SAFIR2016 and the experimentally obtained displacements given in the literature (Lim L., 2002). Series of numerical

analysis were performed for different tensile strengths of concrete. The diagrams show that the numerical simulations give good results compared to the experimental results, where the higher values for the vertical displacements are due to the higher temperatures obtained with SAFIR2016 (Figure 1). For better matching of the results it is necessary to know the physical properties of the materials and the corresponding temperature dependence.

From the performed analysis it can be concluded that the increase in the concrete tensile strength causes a decrease in displacements.

**3 SIMPLY SUPPORTED SLABS**

The thickness of all analyzed slabs is  $h = 16 \text{ cm}$ . The design actions for fire situation are defined according to recommendations given in EN 1991-1-2 (EN, 2002). The temperature dependent physical and mechanical properties of the siliceous aggregate concrete (compressive strength  $f_{ck}=30\text{Mpa}$ ) and the reinforcement (yield strength  $f_{yk}=500\text{Mpa}$ ) are assumed according to EN 1992-1-2 (EN, 2004).

The dead load intensity is  $g=5.5 \text{ kN/m}^2$  including self weight of the slab, while live load intensity is  $q=4.0 \text{ kN/m}^2$ . The load intensity in fire condition is  $g+0.6q=7.9 \text{ kN/m}^2$ .

Table 1 Main reinforcement area as function of different concrete cover thickness ( $c_0$ ) and slab span

Span (m)	$c_0=2\text{cm}$		$c_0=2.5\text{cm}$		$c_0=3\text{cm}$	
	Asl,x (cm <sup>2</sup> /m)	Asl,y (cm <sup>2</sup> /m)	Asl,x (cm <sup>2</sup> /m)	Asl,y (cm <sup>2</sup> /m)	Asl,x (cm <sup>2</sup> /m)	Asl,y (cm <sup>2</sup> /m)
4	1.65	1.65	1.72	1.72	1.80	1.80
5	2.50	2.50	-	-	-	-
6	3.78	3.78	-	-	-	-

**3.1 Analysis of fire resistance according to SAFIR2016 software and simplified method**

Figure 3 shows the maximal vertical displacements of the slabs for different values of the concrete cover thickness, when they are exposed to fire from the bottom side. The results are obtained by 3D analysis using SAFIR2016 software. Additionally, the fire resistance obtained according to the simplified method which is based on the yield line theory for slabs (Johansen, 1972) is presented in Figure 3. It can be concluded that the fire resistance defined with the 3D analysis using the software SAFIR2016 is much higher than that obtained by the simplified method. This is due to the fact that the simplified method does not take into account the effect of tensile membrane forces which occur in case of large displacements and increase the fire resistance of two-way slabs (Bailey, 2004).

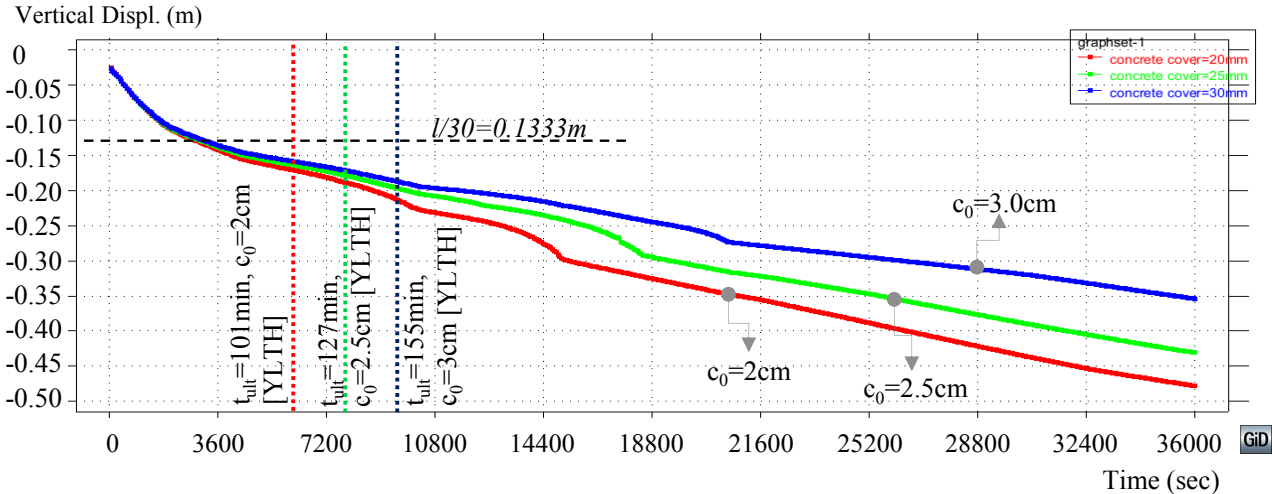


Fig. 3 Influence of the concrete cover thickness on the fire resistance of the simply supported slab with span  $l = 4 \text{ m}$ , according to the 3D analysis with the SAFIR2016 and according to YLTH

Figure 4 shows the vertical displacements of two-way slabs with different spans, and concrete cover 20 mm. From Figure 4 it can be seen that with the increase of span, the vertical displacements also increase, therefore according to the criterion of acceptable displacements  $l/30$ , the fire resistance decreases. According to the ultimate state criterion, all slabs have shown fire resistance higher than 10 hours. According to the simplified method, all the slabs have lost the resistance at the same time, because the initial stresses in the reinforcement for all the slabs have been the same, as well as the reduction in the tensile strength of the reinforcement is the same for the same concrete cover.

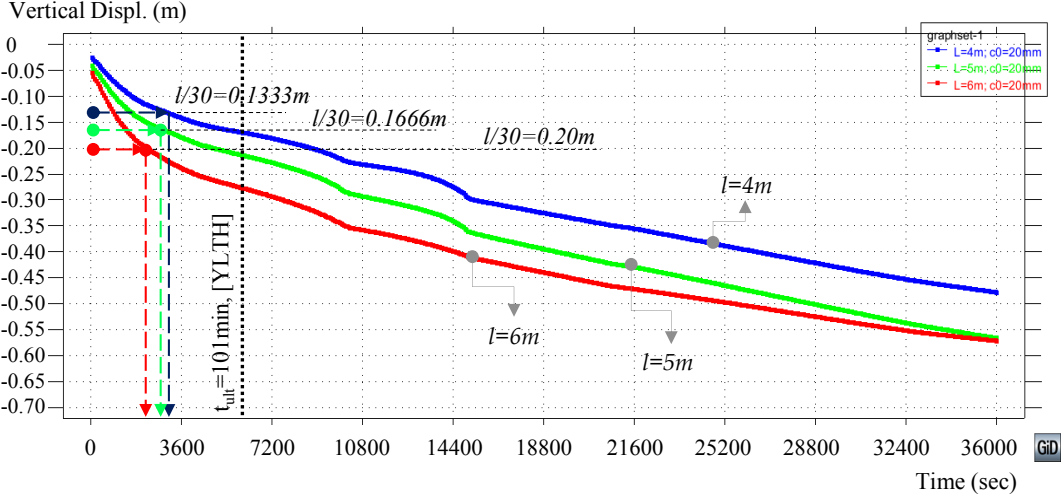


Fig. 4 Influence of the slab span on fire resistance of simply supported slab according to 3D analysis with SAFIR2016 and according to YLTH

**4 FIRE RESISTANCE OF TWO WAY SLABS WITH VARIOUS SUPPORT CONDITIONS**

Figure 5 shows the vertical displacements of the slabs with various support conditions. In terms of bearing capacity, all slabs have shown fire resistance higher than 10 hours. In terms of deformations, the supporting conditions of the slabs have a great influence on their behavior.

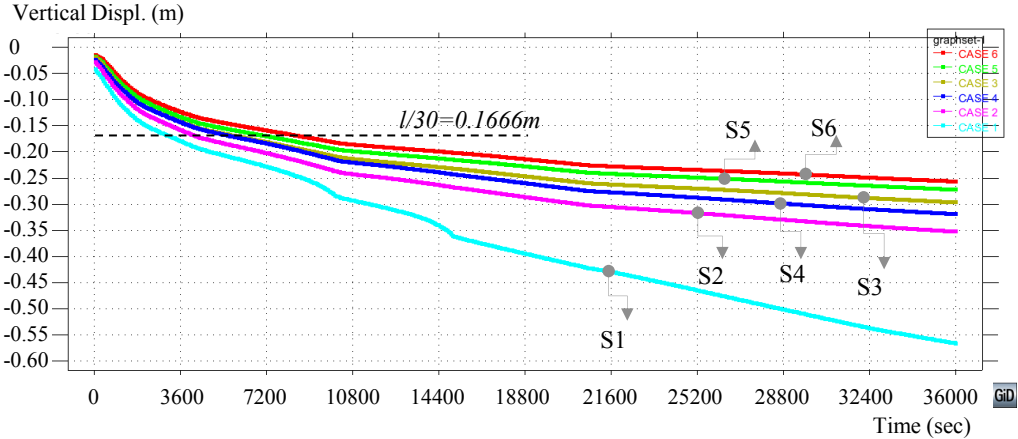


Fig. 5 Vertical displacements in two-way slabs, for different support conditions and fire from the bottom side

Figure 6 shows the support conditions for two-way slabs, analyzed by using SAFIR2016 software. All slabs have a span of  $l_x=l_y=5m$  and a concrete cover of 20mm. The provided area of the main reinforcement in top and bottom zone for all slabs is equal to the required area of reinforcement and is given in Table 2. The length of the main top reinforcement has been adopted according to the recommendations given in Eurocode2, part 1.2 (EN, 2002). The length of the anchorage must be added to the reinforcement length of the top zone, as shown in Figure 6.

Table 2 Main reinforcement area as function of support conditions

Slab	S1	S2	S3	S4	S5	S6
$Asl_x$ (cm <sup>2</sup> /m)	2.59	2.3	1.87	1.80	1.57	1.25
$Asl_y$ (cm <sup>2</sup> /m)	2.59	1.90	1.25	1.80	1.31	1.25
$Asl'_x$ (cm <sup>2</sup> /m)	-	3.75	3.00	3.00	2.57	2.15
$Asl'_y$ (cm <sup>2</sup> /m)	-	-	-	3.00	2.28	2.15

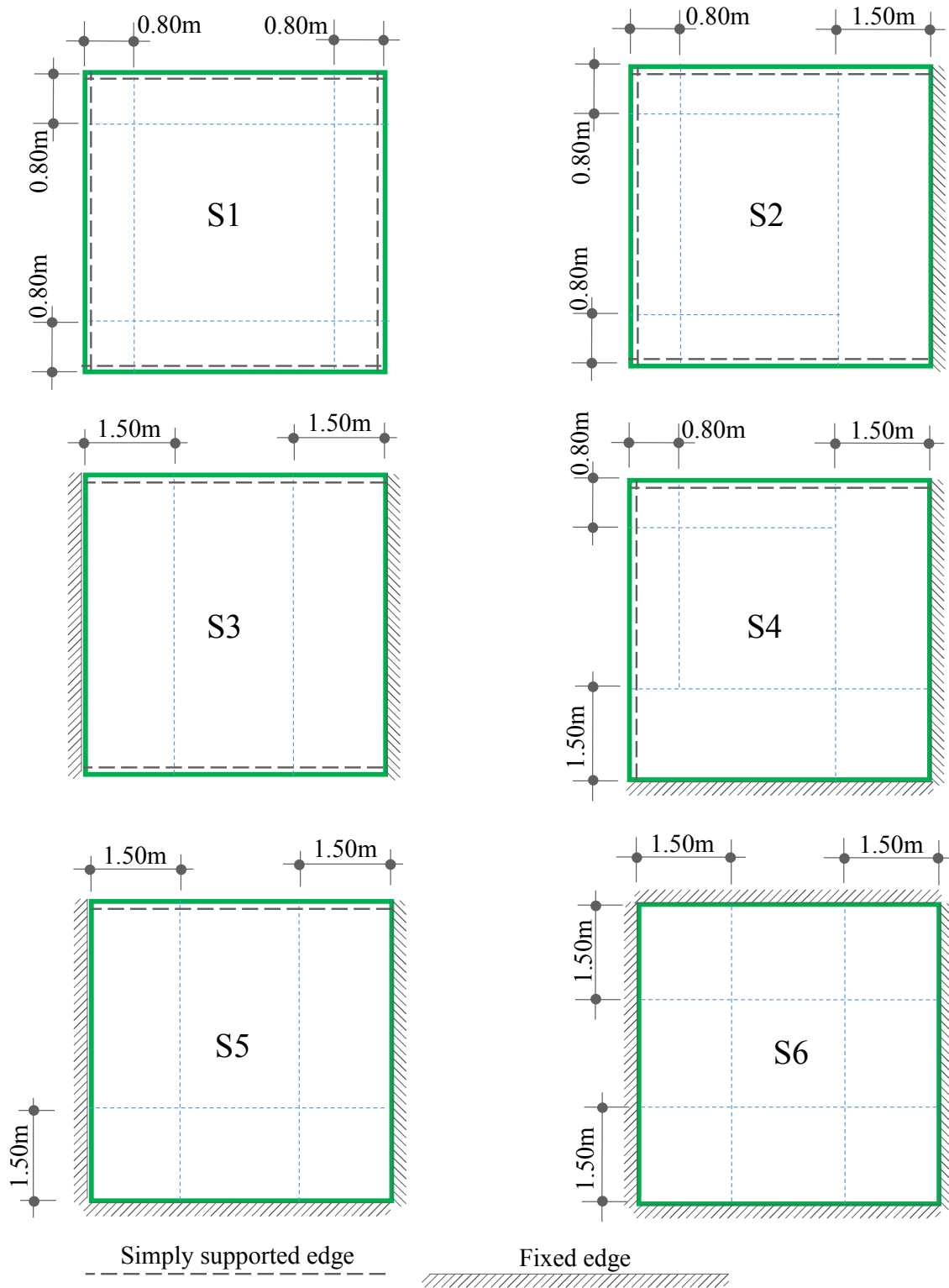


Fig. 6 Support conditions of analysed two way slabs with span  $l=5m$  and concrete cover 2.0 cm

## 5 CONCLUSIONS

Based on the conducted analyzes on the impact of certain parameters on the fire resistance of reinforced concrete two way slabs, conclusions were drawn. The application of these conclusions in the design of RC slabs, can significantly increase the fire safety of buildings.

- In case of two way slabs exposed to fire from the bottom side, by increasing the span, the vertical displacements increase too, but according to the load-bearing criteria, the two way slabs have high fire resistance, much higher than prescribed in the national fire safety regulations. The reason for the high load-bearing capacity in fire conditions are the initiated membrane tensile forces which are more pronounced at larger vertical displacements and increase the load-bearing capacity of the slabs.
- In two-way slabs, by increasing the span, the vertical displacements also increase, so according to the criterion for acceptable displacements  $l/30$ , the fire resistance is reduced.
- In two-way slabs, by increasing the concrete cover thickness, the fire resistance of the slabs increases.
- If simply supported two way slabs are analyzed according to the simplified method based on Yield Line Theory of slabs, the span does not affect the fire resistance, and the concrete cover thickness linearly increases the fire resistance of the slab. The reason for this phenomenon is that the simplified method does not include the influence of membrane tensile forces which are more pronounced at larger vertical displacements and increase the load-bearing capacity of the slab.
- Two-way slabs exposed to fire from the bottom side have better fire performance when they are fixed on all four sides, while reducing the number of fixed sides increases the vertical displacements in the span and reduces the fire resistance in terms of bearing capacity and in terms of deformations. In the case where the slab is fixed on two sides, better behavior is achieved when the fixation is on two opposite sides than on two adjacent sides.

## REFERENCES

- Bailey, C. G. (2004). Membrane action of slab/beam composite floor systems in fire. 1691-1703.
- Buchanan, A. (2004). *Structural design for fire safety*. New York, USA: Wiley.
- EN. (2002). *Eurocode 1: Actions on structures - Part 1-2: General actions - Actions on structures exposed to fire*. Brussels: European Comitee For Standardization.
- EN. (2004). *Eurocode 2: Design of concrete structures - Part 1-1: General rules and rules for buildings*. Brussels: European Committee For Standardization.
- EN. (2004). *Eurocode 2: Design of concrete structures - Part 1-2: General rules - Structural Fire Design*. Brussels: European Committee For Standardization.
- Franssen, J. M., & Gernay, T. (2017). *User's manual for SAFIR 2016c - A computer program for analysis of structures subjected to fire*. Liege: University of Liege.
- Johansen, K. W. (1972). *Yield-Line formulae for slabs*. CRC Press.
- Lim, L. (2002). *Experimental Fire Tests of Two-Way Concrete Slabs*. Christchurch, New Zealand: School of Engineering, University of Canterbury.
- Lim, L. C. (2003). *Membrane Action in Fire Exposed Concrete Floor Systems*. University of Canterbury, School of Engineering, Christchurch, New Zealand.

# MEASUREMENT OF STRAINS AND CRACK PROPAGATION BY DIGITAL IMAGE CORRELATION METHOD IN FIRE EXPOSED CONCRETE SLAB

Katarzyna Mróz<sup>a</sup>, Marcin Tekieli<sup>a</sup>, Izabela Hager<sup>a</sup>

<sup>a</sup> Cracow University of Technology, Faculty of Civil Engineering, Cracow, Poland

## Abstract

The Digital Image Correlation (DIC) method is applied to track the strains of the unheated top surface of the concrete slab exposed to fire from the bottom. Having acquired the pictures of unheated surface throughout the entire fire test, the images are pre-processed and results are converted from pixel coordination system to object coordination system. The strain field is calculated and presented for each picture taken during the test. Therefore, the changes in strains can be easily tracked. The DIC method enables also us to see the time when the central part of the top surface works in tension or compression and what is the strain of each point of the surface under analysis at any specified time. During the test, the time of the creation of local micro-cracks that predict crack development can also be assessed. The paper presents the results acquired for tests on unloaded and loaded slabs.

**Keywords:** concrete, fire, strains, crack, DIC

## 1 INTRODUCTION

Concrete examinations toward its susceptibility to fire spalling are developing with new testing methods and experimental approached. The aims of such are to gather new information on spalling mechanisms and spalling-influencing factors but also to provide more accurate data for analytical and numerical models. Within different issues relating to the prediction and modelling of concrete under severe conditions, like fire, the one of interest is the deformation of a concrete element determined during the tests. The Linear Voltage Displacement Transducers (LVDTs) are commonly used for the determination of vertical deflection (sagging and hogging effect) of the concrete slab during fire load (Miah, 2017). However, they require direct contact with the test element and allow only the measurement of vertical deformations at isolated points. Similarly, the strain gauges, even the temperature-resistant ones (up to 1000 °C) are highly sensitive to changes in humidity and air move, which are inherent problems during fire tests. As a result, their reliable application in case of a fire test is limited.

The exclusion of the above limitations can be achieved with the use of rapidly developing methods of remote structure monitoring. Contactless motion and deformation measurement are computer vision methods assuming optical flow-based algorithms. One such is digital image correlation (DIC) for which numerous way of applications were previously described (Khoo *et al.*, 2016, Pan, 2018), including measuring deformation and stress state under static and dynamic load, in the elastic and plastic state. DIC successfully examines both brittle and flexible materials (Zdanowicz *et al.*, 2020). In the present paper, the authors propose the use of DIC to measure changes in deformation of the unheated concrete surface during a fire test. The authors used the CivEng Vision, the DIC measurement system developed at CUT by (Tekieli *et al.*, 2015), to compare the strain state of a concrete element under unloaded and loaded conditions. The authors performed the preliminary studies (Mróz *et al.*, 2020) that have shown the reliable results obtained with the use of the Digital Image Correlation (DIC) method for monitoring the deformation field under elevated temperatures. To determine the deformation with an accuracy higher than one pixel without increasing the resolution of a picture, the sub-pixel measurement method was proposed by (Xiong *et al.*, 2011). By using sub-pixel measurement it is possible to increase the measurement resolution to 1/50 or even 1/100 of the total pixel size (integer pixel unit). Optical measurement with such measurement resolution can be used to study deformations of masonry and concrete structures. By using the

appropriate resolution of the optical sensor and high-quality lens it is possible to obtain a measurement resolution similar to that offered by traditional load cells (extensometers). To present the determined displacement and deformation fields, the most commonly used colour scale is jet scale, Fig. 1. Additionally, at the post-processing stage, virtual extensometers are installed on the surface of the concrete slab, making it possible to generate and analyse a deformation development in any direction and at any point, but also to track the cracks creations at the opening and closing phase.



Fig. 1 A jet colour scale

## 2 MATERIAL AND METHOD

### 2.1 Material and specimens

One concrete mix is selected to manufacture all the specimens tested in this campaign, Table 1. For determining the initial properties of concrete, standard specimens are manufactured. For fire spalling tests in the DRAGON furnace, the slab specimens of different geometries are produced. The summary of tested elements along with their dimensions and assigned purposes is presented in Table 2.

Table 1 Mix component for tested concrete

Component	Origin	Unit	Amount
CEM III A 42.5 N LH/HSR/NA	Góraźdze	kg/m <sup>3</sup>	400
Sand 0/2	Borzęcin	kg/m <sup>3</sup>	640
Riverbed gravel 2/8	Tar-Krusz	kg/m <sup>3</sup>	460
Riverbed gravel 8/16	Tar-Krusz	kg/m <sup>3</sup>	690
Water	-	kg/m <sup>3</sup>	150
Admixture Primo LM-131	Atlas	%mc	0.7
Admixture AddiCRET PT20	Hufgard	%mc	0.6

After moulding, the specimens are covered with geotextile and watered every day for 14 days. After 14 days, the specimens are demoulded but in case of each element to be tested in a fire test, the bottom (fire exposed) side is demoulded 14 days before running the particular fire test to prevent from air drying. The specimens are kept in the storage chamber with a relative humidity of 50±5 % until the day of the test. The age of concrete specimen at the time of fire test is between 300 and 330 days. Each test configuration consisted of 2 specimens. The concrete compressive strength at 28-days was 61 MPa and moisture content determined by drying of the reference sealed cylinders was ca. 4%.

Table 2 Summary of manufactured elements.

Assigned purpose	Dimensions (mm)		
unloaded (no restraint / no cold rim)	600	600	150
uniaxial compression, biaxial compression	785	785	150

### 2.2 Testing procedure

The rebuilt Dragon furnace has the furnace opening 600 x 600 mm in size and is equipped with a 140kW capacity gas burner. The temperature development in the furnace chamber refers to a standard fire scenario ISO 834-1. During the test, the specimen is hung on the top of the furnace with the suspension system to ensure the exact position in the opening and the axis of loading (in case of loaded tests). The Dragon furnace is equipped with a new loading frame. The external loading is provided with the use of four – (in case of biaxial loading) or two (in case of uniaxial loading) flat jacks with the capacity of 750 kN each. The load is distributed in one or two directions by the loading shoes fitted with steel Hilsdorf's brushes to reduce friction between loading shoes and concrete surface and to obtain pure compression. Three types of test were carried out i) unloaded element, entirely heated from the bottom in the area 600 x 600 mm, ii) uniaxial compression of 15 MPa, and

ii) biaxial compression of 15 MPa. In the case of a loaded test, the elements are enlarged with an unheated rim of 10 cm, to provide the distance from the direct heating and loading system.

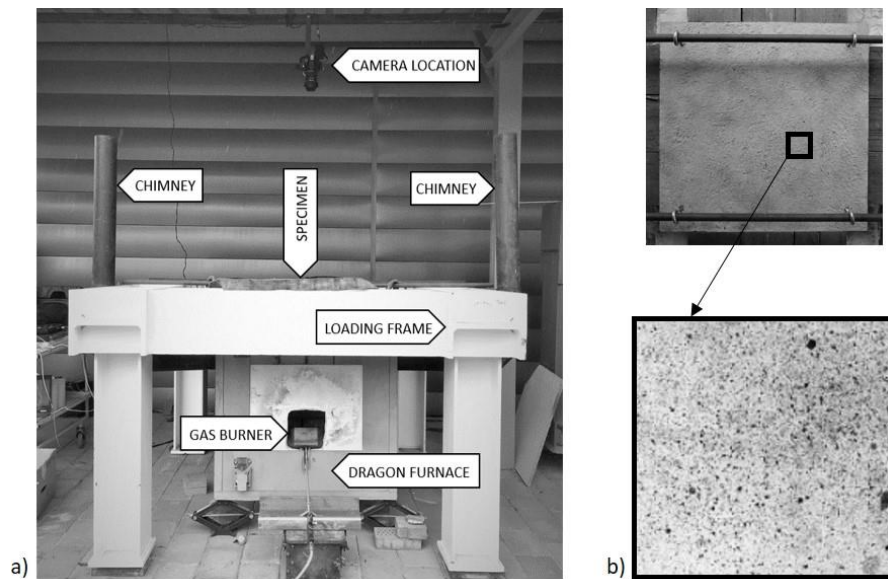


Fig. 2 a) Complete experimental setup, b) black dots pattern for reference set

To take pictures of the unheated side for the DIC method, the camera was installed 1.5 meters above the furnace on the steel substructure. During the fire load, the pictures were taken every 10 seconds during the fire test by a DSLR camera Nikon D5300 with a matrix resolution of 24 Mpx (6000 x 4000 px) equipped with low distortion zoom-lens Sigma 17-50 f/2.8 EX DC OS HMS. To create a subset of point to be tracked, the randomly black dots were distributed over the concrete surface, Fig. 2b. Having acquired the pictures of unheated surface throughout the entire test, the images are pre-processed to e.g. exclude noised pictures or equalize the colour space. Next, the DIC method is applied for pre-processed images and results are converted from pixel coordination system to object coordination system. Finally, the strain field in X and Y directions can be visualized in the form of a coloured map with the jet colour scale. The strain field is calculated for each picture taken during the test. Additionally, to present the strain development in a time of fire exposure, the virtual extensometer is used. The reference distance between ends of extensometers is equal to 50 mm. In the central zone, the virtual extensometers are distributed in the middle points of each side of the square rosette of size 20 cm x 20 cm. The rosette is placed centrally in the middle of the examined specimen. In the case of placing the extensometers in the external zone, the same procedure is used. The size of the rosette equals 55 cm x 55 cm and is applied only in the case of the unloaded slab. In Figure 2a, the complex setup with the Dragon furnace and camera location for DIC measurements is presented, while Figure 2b presents the pattern of black dots to be tracked by the DIC method.

### 3 RESULTS AND DISCUSSION

#### 3.1 DIC results – unloaded slab

When the slab is exposed to fire in the entire bottom surface, the concrete does not experience the restraint to thermal dilation due to the cold rim or the external load. As a result, in the very first minutes of fire exposure (up to ca. 2 minutes), before the first spalling event, the top surface does not present a significant strains distribution. It is observed that concrete works in both direction and only local random higher strains can be indicated. From the time when the spalling starts to occur (in the 2<sup>nd</sup> minute of fire exposure), the top surface starts to present compression (in blue) in the central part. While spalling events take place, not other significant observations are done. The strains of the top surface increase in time, but do not change the way of distribution. The cracking of the top surface is not observed. Spalling is terminated when the water starts to escape from the slab in liquid form through the anchors used to hang the slab over the furnace. Figure 3 presents the strain field

determined before the first spalling event and the maximum values of strains calculated during the test. The strain development in the central zone of the unheated surface in X and Y directions are examined by the virtual extensometers that are indicated in numbers from 5 to 8 in the central zone and A to B in the external part, Fig. 4. The direction of measurement is designated with an arrow. Firstly, the strain development indicates that the unloaded slab works in symmetric condition during the fire exposure time. It can be also observed, that spalling occurrence does not influence the development of strain. During the spalling period, the strains change from -0.045 % to -0.103 % in the central compression zone and from 0.032 % to 0.068 % in the perimeter. It confirms that if concrete thermal dilations are not restrained, the stress state does not change significantly and locally occurred spalling events are caused more due to the thermal gradient in the layer directly exposed to fire than due to the stress state. Finally, the strains start to increase exactly when the spalling is terminated. It is probably directly linked to the extensive shrinkage of drying concrete, as the water starts to flow out in liquid form contributing to the acceleration of concrete drying.

The DIC measurements are limited when the water spreads over the concrete surface and provide changes in the reference subset. Fortunately, such regions can be omitted in the analysis by cutting the wet area out of the region under analysis (reference subset), Fig 3 (the cut area from strain field).

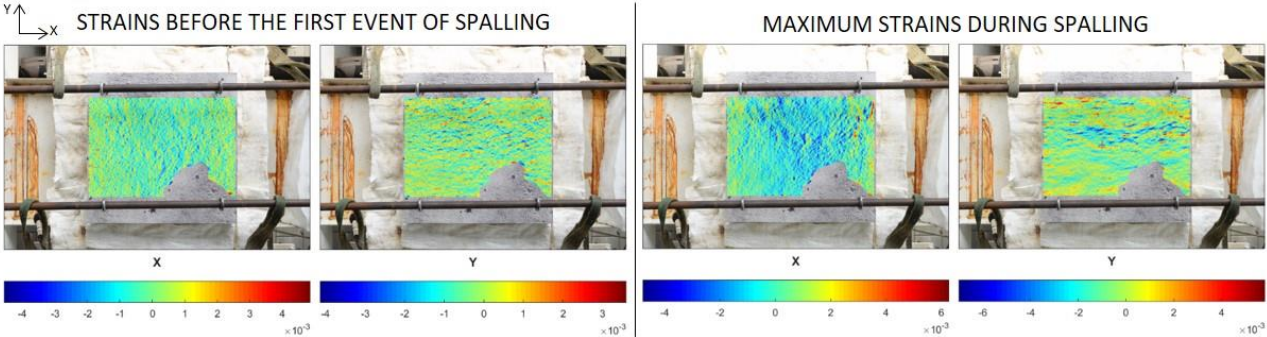


Fig. 3 Maps of strains before the first event of spalling in the unloaded test

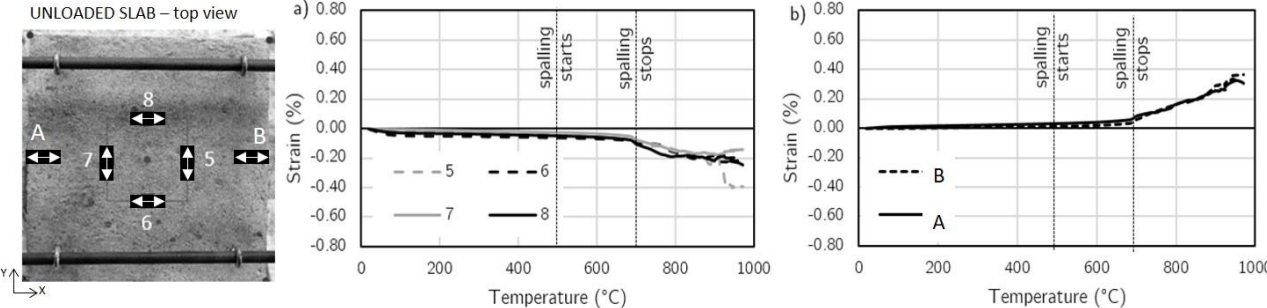


Fig. 4 Strain development at fire unexposed surface of the unloaded slab by DIC virtual extensometers

**3.2 DIC results – slab under uniaxial and biaxial compression**

In the case of slabs tested under external load, the strains on digital maps can be tracked until the first crack is created, Fig 5. It is due to the fact, that width of cracks that are measured are much greater than strains taking place in the top surface. Therefore the scale used to measure strains does not include such small values. It may be possible that after the first calculations of strains the cracked regions are cut out from the reference subset and strains can be recalculated. However, in this paper, the surface is considered as the entire area.

To provide information about the strain state in the loaded specimens, eight virtual extensometers are installed in the central part of the unheated surface (four in the X and four in the Y direction) in the post-processing stage. In Fig. 6 the location of virtual extensometers is indicated along with the diagrams of strain development in the temperature domain. The effect of thermal deformation of concrete is observed when the spalling is triggered (at ca. 600 °C).

In the case of uniaxial load, the top, unexposed to fire surface experiences additional compression with a strain value up to -0.205 % due to expansion of concrete that increases the load pressure.

Moreover, in the unloaded direction, the specimen expand to a great extent ( $> 0.6\%$ ), this is due to the extensive cracking observed during heating (which is well seen in Fig.5). The strain in expanding direction (X) reaches the value of 1.307 % while the spalling is active and increase up to 3.610 % after spalling termination due to shrinkage of drying concrete. While carrying out the uniaxial compression test, the first main crack is created in 2<sup>nd</sup> minute of fire exposure and it goes parallel to the applied load. The strains in the main cracks exceed 0.7 %. In the later phase of fire exposure, the development of another crack is tracked. Finally, the maximum strain which reflects the crack propagation is more than 0.23 %. The calculation of strain maps is not interrupted by any events limiting the usage of the DIC method. In the 22<sup>nd</sup> minute of fire exposure, the liquid water starts to escape from cracks but its amount does not affect the DIC calculations.

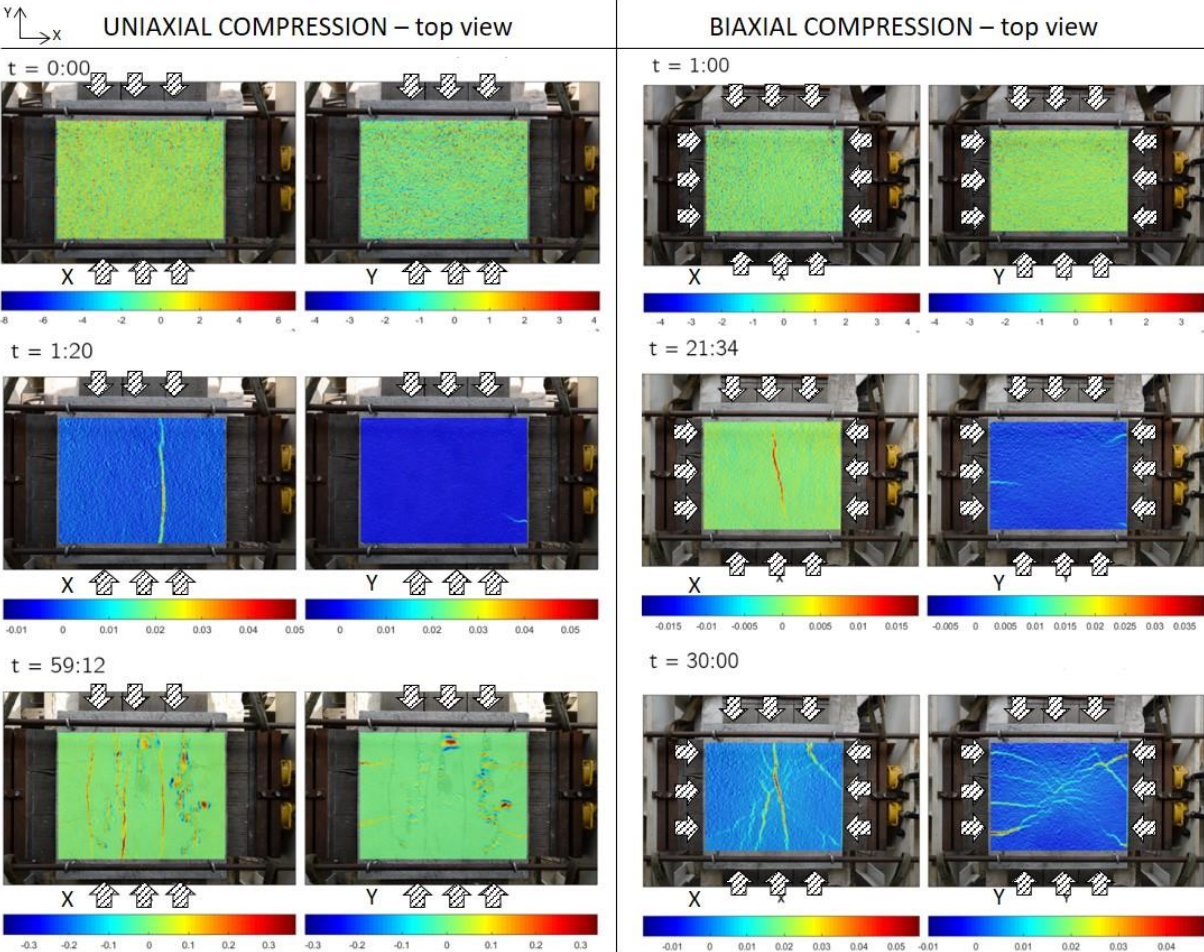


Fig. 5 Strain maps and crack development - uniaxial and biaxial compression

The biaxial compression provides the stress state that contributes to closing cracks and the first cracks are created after 20 minutes of fire exposure (Fig 5,  $t = 21:34$  min). The strain fields (Fig. 5) and strain plots (Fig. 6) let us observe that load acting from two sides result in minor strains of the top surface. The strains in compression measured between the beginning of the test and the first spalling event change from  $-0.023\%$  to  $-0.091\%$ . When spalling starts to occur, the strain increase and the unheated surface experience increased compression. However, when the temperature in the furnace exceeds  $750\text{ }^{\circ}\text{C}$ , the strains start to increase rapidly in other direction and the top surface experience intensive tension. It is also linked to enhanced cracking of the central part that is hardly visible by naked eyes but well defined by the DIC strain field, Fig. 5. Such sudden change of strain direction may be caused by such high spalling depth that the load start to act in the eccentricity. The distribution of strain over the surface is very uniform, which is impossible to present by another standard measurement method. The final pattern of crack that is measured, present the web of cracks (Fig. 5,  $t = 30$  min). It is worth emphasizing that such cracking developed in 9 minutes between the 21<sup>st</sup> and 30<sup>th</sup> minute of fire exposure. In the biaxial compression test, the spalling continued until the termination of the fire exposure.

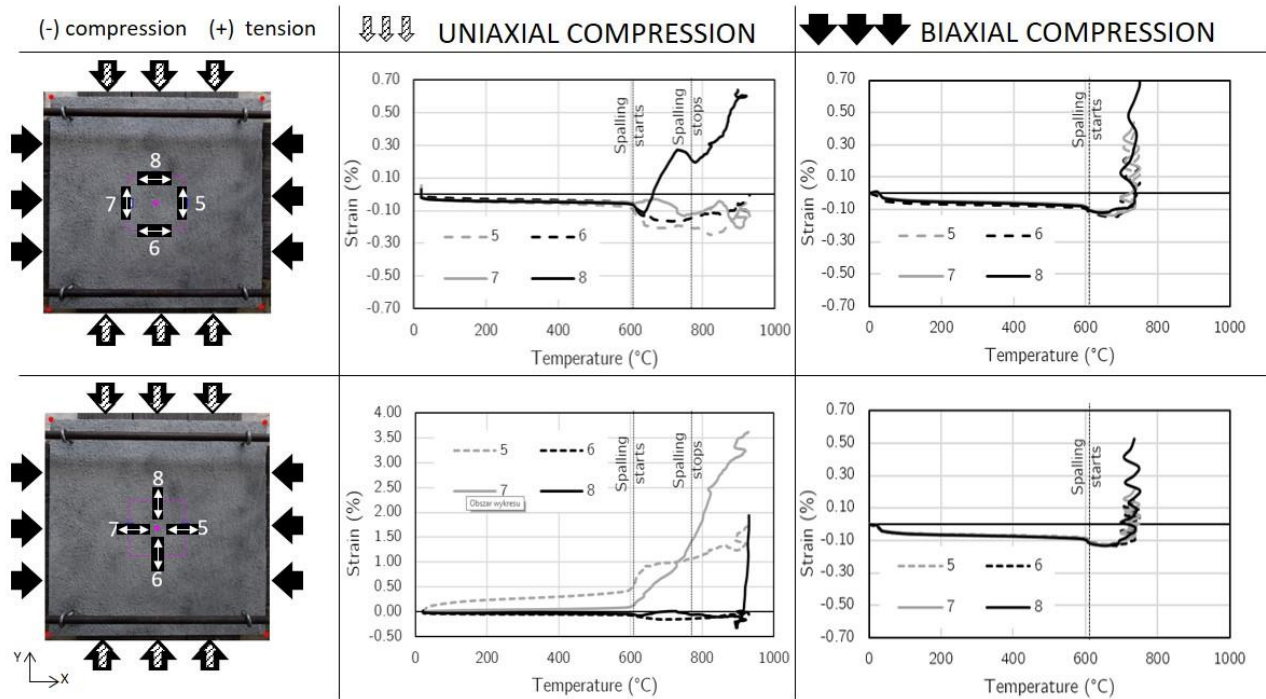


Fig. 6 Strain development in X and Y directions tracked by virtual extensometers for loaded tests

### 3 CONCLUSIONS AND PERSPECTIVES

DIC method provides a reliable device to determine the continuous strain field on an unheated part of an element exposed to fire. Its application let us conclude that the free thermal dilations of unloaded concrete slab provide an unlikely changing stress state which causes local spalling events resulted mainly from the thermal gradient in the layer directly exposed to fire. DIC shows that the strains start to increase exactly when the spalling is terminated and the liquid water starts to flow out. The increase in strains is linked to the extensive shrinkage of drying concrete. In the case of loaded slabs, it was directly proved that cracking of concrete is more likely to occur in the direction free from loading. It was also proven that cracking of concrete element does not terminate spalling. The cracking of the element is hardly visible by naked eyes but well defined by the DIC strain field. Hence, the DIC method provides highly desirable results for defining the mechanisms of spalling occurrence.

### ACKNOWLEDGMENTS

Financial support: the National Science Centre, Poland (grant number: 2016/23/N/ST8/01155), and a doctoral scholarship (K. Mróz) - the National Science Centre, Poland (NCN 2018/28/T/ST8/00352).

### REFERENCES

- Khoo S.W., Karuppanan S., Tan C.S., 2016. *A review of surface deformation and strain measurement using two-dimensional digital image correlation. Metrology and Measurement Systems*, 23, p. 461–480.
- Miah M.J., 2017. *The Effect of Compressive Loading and Cement Type on the Fire Spalling Behaviour of Concrete*, PhD Thesis, University of Pau and Pays de l'Adour, Pau, France, p. 87–89.
- Mróz K., Tekieli M., Hager I., 2020. *Feasibility study of digital image correlation in determining strains in concrete exposed to fire. Materials*, 13(11), 2516.
- Pan B., 2018, *Digital image correlation for surface deformation measurement: historical developments, recent advances and future goals. Measurement Science and Technology*, 29, 082001.
- Tekieli M., Słoński M., 2015. *Digital image correlation and Bayesian filtering in inverse analysis of structures, in Recent Advances in Civil Engineering: Computational Methods*, Poland: Wydawnictwo PK, p. 111–124.
- Xiong L., Liu X., Liu G., Liu J., Yang X., Tan Q., 2011, Evaluation of sub-pixel displacement measurement algorithms in digital image correlation, in *Int. Conf. MEC*, p. 1066–1069.
- Zdanowicz Ł., Seręga Sz., Tekieli M., Kwiecień A., 2020, *Polymer flexible joint as a repair method of concrete elements: flexural testing and numerical analysis. Materials*, 13(24), 5732.

## **EFFECT OF TENSION LAP SPLICE ON THE BEHAVIOUR OF REINFORCED CONCRETE BEAMS DURING FIRE**

Andreas Grübel<sup>a</sup>, Hitesh Lakhani<sup>a</sup>, Jan Hofmann<sup>a</sup>

<sup>a</sup> University of Stuttgart, Institute of Construction Materials, Stuttgart, Germany

### **Abstract**

The extensive numerical and experimental studies, on Reinforced Concrete (RC) beams, available in literature are limited to beams without lap splices. The fire resistance of beams with lap splices have seldom being investigated. The paper presents the results of numerical study to compare the fire resistance of simply supported beams without and with lap splice. The 3D coupled thermo-mechanical model used for the investigation also accounted for the reduction of bond strength with increase in temperature, to account for the possible bond failure. The effect of number of rebars spliced at a section was also investigated by choosing two different combinations of rebars for same (total) area of tension reinforcement. The beams with lap splice were found to have slightly better fire resistance as compared to beams without splice. This is due to the lower average temperature of the tension reinforcement because of the increased side cover to the spliced rebar.

**Keywords:** Lap-splice, Fire rating, Bond behaviour, Reinforced concrete

### **1 INTRODUCTION**

Over the years the behaviour of reinforced concrete beams exposed to fire have been extensively studied by large number of researchers. But the existing research is limited to beams without lap splices. Moreover, the widely used prescriptive design guidelines given in various design standards (EN1992-1-2, 2004; ACI/TMS 216.1-14, 2014), are based on studies on beams with continuous tension reinforcement i.e., without tension lap splices. Hence, there is a need to ascertain the applicability of these design guidelines to beams with tension lap splices.

Moreover, the bond behaviour between rebar and concrete changes (decreases) with increase in temperature during fire (Lakhani and Hofmann, 2018). Although the effect of bond on the fire resistance was found to be insignificant by Gao et al., (2013) and Kodur & Agrawal, (2017). But once again these studies were performed on beams without tension lap-splices.

Hence, to understand and investigate the behaviour of RC beams with tension lap splices under fire, the presented numerical study was conducted. Moreover, the current study augments the preliminary set of results from Lakhani et al., (2020) comparing the fire resistance of a beam without and with tension lap splice.

### **2 NUMERICAL MODEL**

The 3D coupled thermo-mechanical model used for the presented study has previously been used for simulating the behaviour of RC columns during fire (Lakhani et al., 2019; Lakhani and Ožbolt, 2019a, 2019b). Hence, is discussed very briefly in this section.

In the first step transient heat transfer analysis is conducted and the temperature distribution over a given solid volume is calculated. The heat transfer from the hot gases to exposed surfaces are modelled by radiation (surface emissivity = 0.8) and convection (heat transfer coefficient = 25 W/m<sup>2</sup> K) boundary condition. The thermal properties of concrete are taken as the lower bound thermal conductivity and specific heat for dry concrete, as per EN1992-1-2:2004. The selection of these thermal properties is based on the sensitivity/validation studies conducted by Lakhani et al., (2013). The thermal properties for steel were taken from EN1993-1-2:2005.

For the mechanical analysis concrete is modelled using isothermal microplane model (Ožbolt et al. 2001, 2005). The total strain tensor for concrete, has three components: mechanical strain, free

thermal strain and load induced thermal strain. The mechanical strain component is further composed of elastic, plastic, and damage part. Steel is modelled using von Mises plasticity model. Figure 1 (a) & (b) shows the used temperature dependencies of various mechanical properties of concrete and steel, respectively.

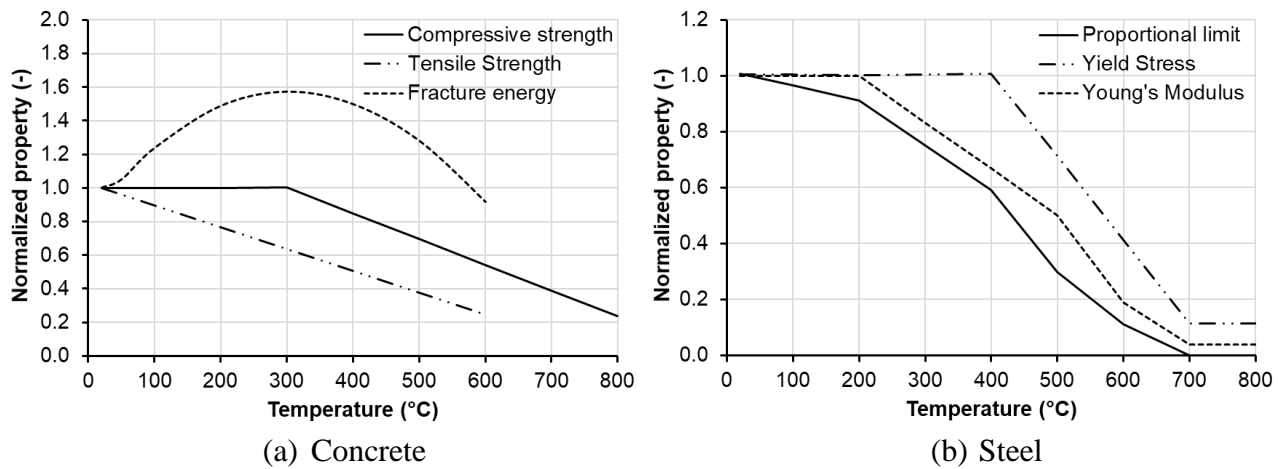


Fig. 1 Variation of mechanical properties with temperature

## 2.1 Bond at elevated temperature

Based on the extensive literature review of bond between ribbed rebars and concrete at elevated temperature, done by Lakhani and Hofmann, (2018), the degradation of pull-out bond resistance with temperature is assumed to be same as that for compressive strength. For the results presented in this paper concrete was assumed to be made of siliceous aggregates and the corresponding compressive strength degradation from EN1992-1-2 was used, as shown in fig. 2(a). To keep the bond-slip relationship relatively simple, the bond-slip relationship at elevated temperature is obtained by scaling the relationship at ambient condition proportional to the normalised bond strength shown in fig. 2 (a). Figure 2(b) shows the bond-slip relationship used for the presented numerical study. Since a 3D model is used for the present study, the splitting failure would be automatically accounted by the reduction in concrete mechanical properties with increase in temperature.

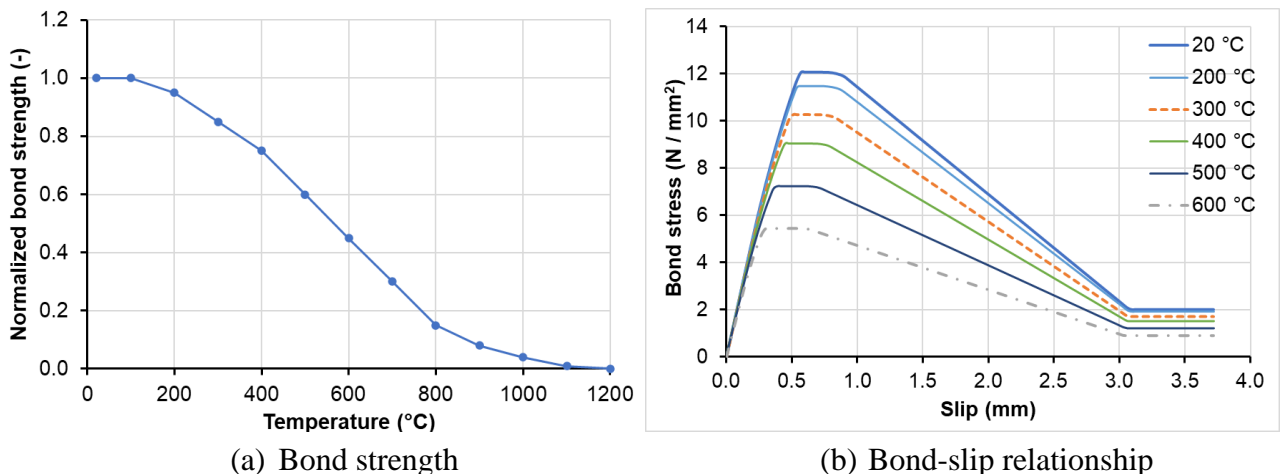


Fig. 2 Bond variation with temperature

## 3 NUMERICAL INVESTIGATION

The geometry of the beam selected for the investigation had a fire rating of 90 minutes as per EN1992-1-2:2004 for beam without tension lap splice. The beam had a cross-section of 300 mm × 380 mm and a total length of 3900 mm with clear span of 3825 mm. The bottom and side clear cover to tension reinforcement was 40 mm. Two combination of tension reinforcement, 2×20Ø & 4×14Ø, were

selected for the same total area of tension reinforcement to investigate the effect of number of rebars on the fire resistance of the beam. The shear reinforcement of the beam consisted of stirrups of 8 mm diameter at spacing of 150 mm.

The beam was exposed to ISO 834 standard fire from 3 sides and the top face of the beam was assumed to be insulated. The beam is simply supported and loaded with two-point loads as shown in fig. 3. The selection of the position of application of point load was based on the lap length calculated as per EN1992-1-1:2004. The required lap length was calculated to be 695 mm & 492 mm, respectively for 20 Ø & 14 Ø rebars. But for ease of modelling a splice length of 750 mm was taken for both the rebar diameters chosen for the investigation.

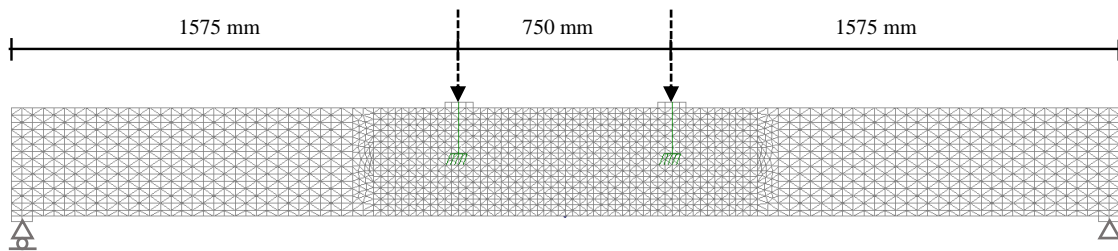


Fig. 3 Loading condition and geometric discretization of the beam

The concrete had a compressive strength of 48 MPa. The Young's modulus, tensile strength & fracture energy of concrete at ambient temperature were taken as 33000 N/mm<sup>2</sup>, 3.40 N/mm<sup>2</sup> & 0.08 N/mm, respectively. The reinforcing steel had a yield strength of 470 MPa and an ultimate strength of 555 MPa.

To save computational time only half of the beam along the width was modelled using symmetry boundary conditions. The concrete was discretized using 4-noded tetrahedron elements and the reinforcement with 8-noded hexahedral elements. Linear steel plates were modelled at the supports and the loading points to avoid localisation and stress concentrations at these locations. The bond between concrete and rebar was modelled using unit length bond elements as shown in fig. 4. The shear behaviour of these bond elements was defined by temperature dependent bond-slip relationship discussed in Section 2.1. The bond strength at ambient temperature was taken as 12 N/mm<sup>2</sup>.

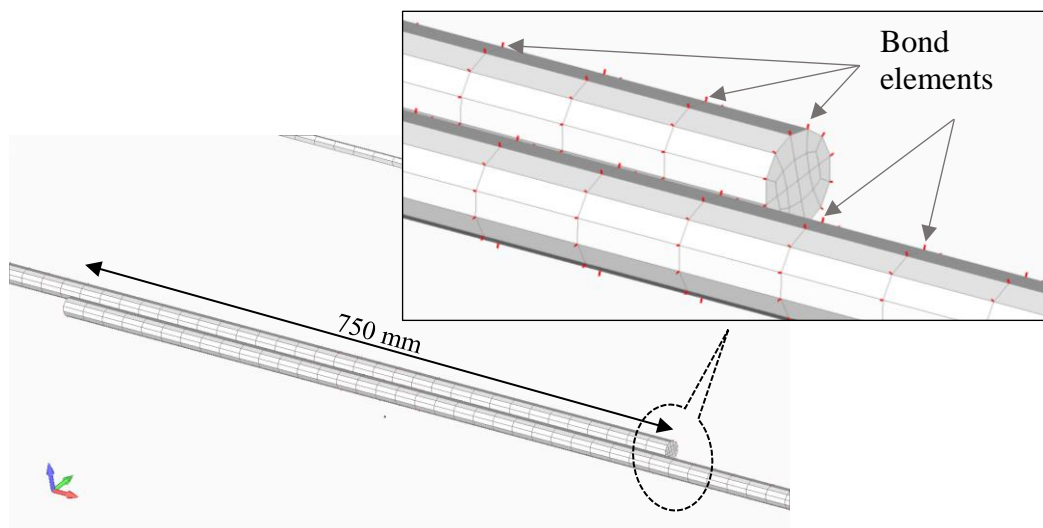


Fig. 4 Geometric discretization of reinforcement and the bond elements

Before analysing the behaviour of the beams under fire, the reference cases without fire were analysed for all the beams. All the beams failed due to yielding of reinforcement, which means that the splice length of 750 mm is sufficient at ambient conditions. Moreover, for all beams, the hinges were formed below the point of loading. Since, at this yielding section the amount of total reinforcement (area) is same, all the beams (with & without splice) had same maximum failure load. The load-displacement

diagrams for the reference beams are shown in fig. 5. The response of beam with lap splice is stiffer than the beam without lap splice, due to increased tension reinforcement due to lapping of reinforcement in the constant moment zone.

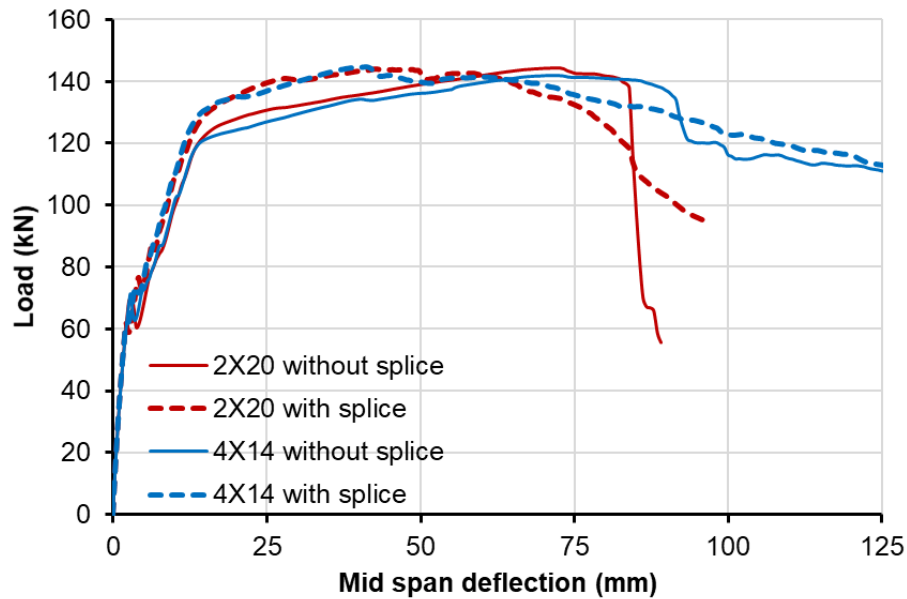


Fig. 5 Load displacement response of the beams at ambient conditions

Fig. 6 shows the crack pattern and hinge formations at maximum load, for all the 4 beams analysed. It is seen that for beams without splice, the flexural cracks are distributed in the constant moment zone between the point loads. Whereas, for beams with splice lesser flexural cracks are formed and the hinge is formed below the point of application of loads.

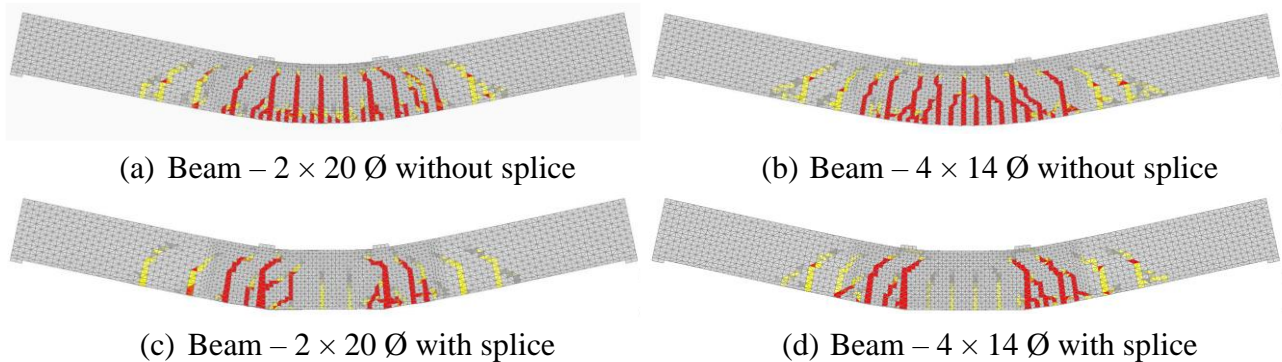


Fig. 6 Crack profile corresponding to maximum load for beams without and with splice at ambient conditions.

To compare the fire resistance of the beams without and with tension lap splice. The beams were loaded with three different load levels. The loaded levels, 96% (LL1), 68% (LL2) and 42% (LL3) are defined with reference to the ultimate load capacity of beam at ambient conditions. Hence, total 12 simulations with fire exposure were performed. The failure time for each beam was taken as the minimum of the time at last converged step or time at which the limiting deflection,  $D = L^2 / (400 \times d)$  (110 mm for the beam investigated) was reached.

The failure time for all 4 beams for three different load levels is plotted in fig 7. The beam with higher number of tension rebars (for a given total area of tension reinforcement) performed better in comparison to the beam with lesser number of tension rebars. This is because, in case of 4 tension rebars, the distance of middle two rebars from the side face is increased. Thus, the temperature of these rebars is lower than the rebars located in corners, Therefore, the average temperature of tension

reinforcement is reduced in comparison to case when only two rebars are present i.e., one in each corner.

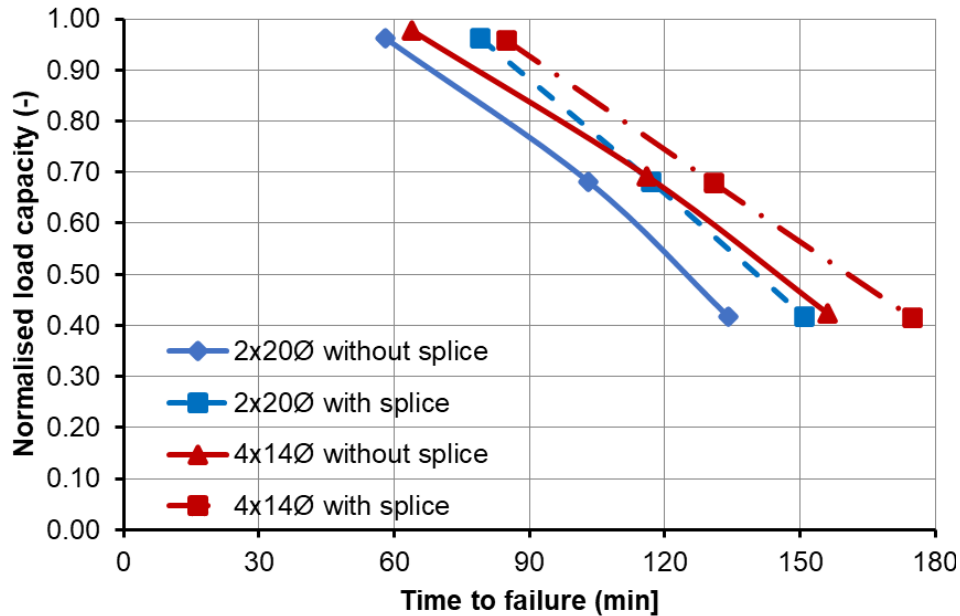


Fig. 7 Comparison of fire resistance of beams without and with tension splice

The beams with tension lap splices failed at a latter time as compared to beams without splices. The observed higher fire resistance is due to the lower temperature of the spliced rebar, which was a result of the increased side cover due to splicing. To further understand this point, one must understand that in beams the tension rebars are normally spliced in horizontal plane to keep the same effective depths. This means one of the spliced rebar is moved away from the exposed face thus leads to increased time to reach the same temperature.

#### 4 CONCLUDING REMARKS

The paper presented a comparison between the fire resistance of simply supported RC beams without and with tension splice. Based on the numerical results presented the following conclusions may be drawn:

- The beams with tension splices, performed slightly better under fire as compared to beams without splices,
- No failure mode associated with bond (pull-out / splitting) was observed for the case investigated in the presented study,
- Further investigations are needed to understand the effect of various parameters like cover thickness, rebar diameters, concrete strengths etc., on the response of RC beams with tension splices under fire,
- There is also a need of experimental results to validate the numerical results/model.

#### REFERENCES

ACI/TMS 216.1-14, 2014. Code requirements for determining fire resistance of concrete and masonry construction assemblies. American Concrete Institute.

EN1992-1-1, 2004. Eurocode 2: Design of concrete structures - Part 1-1: General rules and rules for buildings. European Committee for standardization, Brussels.

EN1992-1-2, 2004. Eurocode 2: Design of concrete structures - Part 1-2: General rules - Structural fire design. European Committee for standardization, Brussels.

EN1993-1-2, 2005. Eurocode 3: design of steel structures - Part 1-2: General rules — Structural fire design. European Committee for standardization, Brussels.

Gao, W.Y., Dai, J.-G., Teng, J.G., Chen, G.M., 2013. *Finite element modelling of reinforced concrete beams exposed to fire. Engineering Structures* 52, 488–501. <https://doi.org/10.1016/j.engstruct.2013.03.017>

- ISO 834-1, 1999. Fire-resistance tests - Elements of building construction - Part 1: General requirements. International Organization for Standardization.
- Kodur, V.K.R., Agrawal, A., 2017. *Effect of temperature induced bond degradation on fire response of reinforced concrete beams*. *Engineering Structures* 142, 98–109. <https://doi.org/10.1016/j.engstruct.2017.03.022>
- Lakhani, H., Hofmann, J., 2018. Effect of high temperature on the bond behaviour between reinforcement and concrete, in: *Fib Bulletin on “Advances on Bond in Concrete.”*
- Lakhani, H., Hofmann, J., Grübel, A., 2020. *Fire resistance of simply supported reinforced concrete beams with tension lap splices*, *Otto-Graf Journal* 19, 91–102.
- Lakhani, H., Kamath, P., Bhargava, P., Sharma, U.K., Reddy, G.R., 2013. *Thermal analysis of reinforced concrete structural elements*. *Journal of Structural Fire Engineering* 4, 227–244. <https://doi.org/10.1260/2040-2317.4.4.227>
- Lakhani, H., Ožbolt, J., 2019a. *Numerical investigations on the behaviour of reinforced concrete columns exposed to fire*. *Otto-Graf-Journal* 18.
- Lakhani, H., Ožbolt, J., 2019b. *Structural behaviour of Reinforced Concrete (RC) columns under fire*. *IOP Conference Series: Materials Science and Engineering* 615. <https://doi.org/10.1088/1757-899X/615/1/012088>
- Lakhani, H., Vučko, H., Ožbolt, J., Harapin, A., 2019. Behavior of concentrically loaded reinforced concrete columns under design fire, in: *Proceedings of the Fib Symposium 2019, Concrete - Innovations in Materials, Design and Structures*. Krakow, Poland.
- Ožbolt, J., Kožar, I., 2001. *Microplane model for concrete with relaxed kinematic constraint*, *Int Journal of Solids and Structures* 38, 2683-2711.
- Ožbolt, J., Kožar, I., Eligehausen, R., Periskic, G. 2005. *Three-dimensional FE analysis of headed stud anchors exposed to fire*, *Computers and Concrete*, 2(4), 249-266.

# PERFORMANCE CRITERIA FOR PERFORMANCE BASED FIRE DESIGN OF CONCRETE AND COMPOSITE STRUCTURES

Ruben Van Coile<sup>a</sup>, Thomas Gernay<sup>b</sup>, Danny Hopkin<sup>c</sup>, Negar Elhami Khorasani<sup>d</sup>

<sup>a</sup> Ghent University, Department of Structural Engineering and Building Materials, Ghent, Belgium

<sup>b</sup> Johns Hopkins University, Department of Civil and Systems Engineering, Baltimore, USA

<sup>c</sup> OFR Consultants, Oxford, UK

<sup>d</sup> University at Buffalo, Department of Civil, Structural and Environmental Engineering, Buffalo, USA

## Abstract

Performance based design (PBD) approaches allow for the definition of a custom structural fire protection strategy for a building. The acceptance of a trial design then relies on that design meeting predefined performance criteria, commonly assessed using numerical methods, testing, or a combination of both. The current paper provides the early-stage results of a literature overview of performance criteria for performance based fire design of concrete structures. The review indicates that a wide range of performance criteria are applied in the published literature. Recommendations for further investigations are formulated based upon the current state of knowledge on this issue.

**Keywords:** concrete; PBD; performance criteria; literature review

## 1 INTRODUCTION

Performance based design (PBD) for fire performance is a rational approach to design a new structure or evaluate an existing structure based on clear objectives and specified structural performance criteria (PC). ISO 24679-1:2019, *Fire safety engineering – Performance of structures in fire* provides a methodology to assess performance of structures when exposed to fire, including guidance on practical design processes for fire safety of structures, quantification of performance of structures in fire, and the use of different quantification methods. While this document provides a clear framework for PBD, limited guidance is available on the definition of PC for the structural fire analysis. In the following, the PBD framework of ISO 24679-1:2019 is summarily introduced, with a focus on clarifying the use and implied meaning of PC. Subsequently, the early-stage results of a literature review of PC for concrete and composite structures are presented.

## 2 THE PBD FRAMEWORK OF ISO 24679-1:2019

The PBD framework of ISO 24679-1:2019 highlights the need to identify the fire safety objectives (FSO), and from them to derive the functional requirements (FR). Subsequently the risk analysis approach must be chosen. This allows the engineer to define performance criteria (PC) which are calculable proxies for meeting the FR. In other words, if the PC are met, then it is assumed that the FR are fulfilled as well. These concepts and their relationship are clarified in the following, as insight in the overall framework is necessary for interpreting the meaning of PC.

### 2.1 Step 1: Identification of the Fire Safety Objectives

The design objectives relate to the stakeholder needs, including the need to fulfil mandatory (governmental) requirements. A successful design is then a solution to these needs, within the constraints imposed on the design by e.g., physics, time and money (Law et al., 2015). ISO 23932-1:2018 provides a non-exhaustive list of FSO: safety of life; property protection; continuity of operations; protection of the environment; preservation of heritage. Mandatory objectives may be listed in codes or regulations, or may be implicit in prescriptive guidance. The building owner, in consultation with the stakeholders, can add voluntary objectives. To support the identification of objectives for a design, it is recommended to start from the overarching goal of (structural) fire engineering: *Controlling fire risks to socio-economically acceptable levels*, as part of the overall

fire safety strategy, in analogy to the overarching goal in earthquake engineering (Bertero and Bozorgnia, 2004). The objectives applicable to a given design are then derived by qualitatively considering the potential consequences of a fire, and evaluating, in consultation with the stakeholders, whether such consequences need to be avoided.

## 2.2 Step 2: Derivation of Functional Requirements

ISO 23932-1:2018 defines FR as qualitative statements of the means to achieve specified FSO, considering the features of a built environment. Mandatory functional requirements may be listed in national legislations or building codes. Additional voluntary functional requirements can be derived from the FSO by the stakeholders. A typical FR related to the FSO of life safety is “*The building shall be designed and constructed so that, in the event of fire, its stability will be maintained for a reasonable period*”. This specific FR is listed in the 2010 English Building Regulations (The Stationery Office, 2010) and counts as a mandatory FR within the corresponding jurisdiction. In requiring stability “for a reasonable period”, the underlying idea is that the implementation of this FR will allow evacuation of people from the building in case of fire and fire brigade intervention, hence achieving the FSO of life safety. It is commonly up to the private stakeholders to define (additional) requirements with respect to for example property protection and continuity of operations. Examples of possible FR are:

- *The building shall be designed and constructed so that, in the event of fire, its stability will be maintained up to and including burnout.*
- *The building shall be designed and constructed so that, in the event of a fire, the usability of other floors will not be affected.*
- *The building shall be designed and constructed so that, following a fire, it can be repaired and reinstated within a reasonable period.*

## 2.3 Step 3: Select Risk Analysis Approach

The evaluation of structural fire performance is associated with many uncertainties. These uncertainties relate to the loading on the structure, the structure’s characteristics (material strength, thermal properties), the fire exposure, simplifications in the computational tools, the consequences of failure, etc. This implies that each design corresponds with a risk profile, i.e., combinations of unwanted events and associated occurrence probabilities. Meeting a FR is therefore rarely a yes/no question. The design should demonstrate sufficient confidence of meeting the FRs, i.e., the design should demonstrate an adequate safety level. For performance-based structural fire design, two routes are open to demonstrate adequate safety: (i) a deterministic credible worst case (CWC) approach; and (ii) a probabilistic approach. The chosen approach then translates into the applicable performance criteria (see the discussion on PC below).

In a CWC approach, uncertainty is partially addressed by assuming worse than average exposure and material characteristics (ISO 23932-1:2018). Where it is unclear which situation is more onerous, multiple scenarios are evaluated. What combination of parameter values constitutes a CWC approach can be specified in guidance documents. Importantly, the safety level eventually attained by the accepted design is not quantified and remains unknown. Considering the onerous design evaluations, the safety level is assumed to be sufficiently high. When design alternatives are each acceptable, no immediate comparison of their relative safety performance is possible.

In probabilistic analysis the full range of representative scenarios are identified and evaluated (ISO 23932-1:2018). The performance criteria are specified accordingly and refer to the frequency (probability) of unwanted events, or to a risk metric whereby also the consequences of the scenarios are evaluated. The acceptance of the design is done in comparative or absolute terms. In a comparative evaluation, the safety level is compared to the safety level of a design which is ‘deemed to satisfy’, while in an absolute evaluation a limiting probability or risk value is considered, or a direct ALARP (As Low As Reasonably Practicable) evaluation is performed (Van Coile et al., 2019). Within the probabilistic analysis, the safety level is explicitly evaluated and direct comparison of the design alternatives is possible – albeit within the modelling assumptions.

An important further clarification relates to a semi-probabilistic approach. In a semi-probabilistic approach, characteristic material properties, prescribed load conditions and safety factors are considered for the evaluation. This is the design methodology most applied in design standards around the world for normal design conditions. Crucially, in a semi-probabilistic approach the combination of material properties, load conditions and safety factors has been calibrated to obtain a predetermined safety level. From the authors' perspective, current guidance documents for structural fire design (such as the fire parts of the Eurocodes) are not sufficiently calibrated to be classified as semi-probabilistic. For example, the target safety levels for structures during (and after) fire are not clearly defined, and the safety factors for fire design appear not to be calibrated on a material level. Considering the current state-of-the-art, only the CWC approach and the full probabilistic approach are thus considered feasible for the PBD of structures exposed to fire.

#### **2.4 Step 4: Definition of Performance Criteria**

ISO 23932-1:2018 defines a PC as a threshold of performance that forms an agreed basis for assessing the safety of a built environment design. Multiple PC can be associated with a given FR, i.e., a set of PC. When the design meets the set of quantitative performance criteria (PC), it is considered to meet the corresponding qualitative FR. As such, the PC are considered a sufficient requirement for fulfilment of the FR, but not a necessary requirement. It is generally possible to specify other PC (possibly very similar ones) which can also be considered to fulfil the FR. The PC are deterministic or probabilistic, depending on the chosen risk analysis approach. When considering a deterministic CWC, the PC should ensure a conservative evaluation to account for the low level of treatment of uncertainty in the analysis (ISO 23932-1:2018).

When considering multiple FR, and in extension multiple FSO, different PC can apply. There is no reason why these PC would need to be mutually exclusive. For example, it is possible that the same PC apply both for the FSOs of life safety and property protection. Also, when evaluating the design's compliance with a PC, the performance evaluation should not be done mechanically and requires judgment in interpreting analytical results and an openness to (re-)assessing uncertainties.

### **3 REVIEW OF SFE PERFORMANCE CRITERIA FOR CONCRETE STRUCTURES**

#### **3.1 Introduction**

In accordance with ISO 24679-1:2019, the PC are sufficient conditions for demonstrating that the FR are met. Unfortunately, literature studies are not always clear in the FR addressed by a specific (set of) PC. In the review below, judgement has been applied to categorise PC. The fact that a set of PC can be defined to demonstrate meeting a single FR implies that the PC should not be seen in isolation. Thus, (i) the effectiveness of the PC in demonstrating compliance with a FR must be evaluated from the perspective of a set of PC; and (ii) the individual relevance of a PC relates to its relative importance as part of a set of PC.

#### **3.2 Performance criteria used in standard furnace testing**

Before reviewing the PC for PBD, it is useful to discuss the criteria used in standard furnace testing, which underlies the prescriptive design approach to fire design. The criteria used in furnace testing were selected to achieve a combination of objectives including: (i) allow standardization, (ii) protect the equipment, and (iii) be a proxy for the fire resistance requirements of load bearing capacity, insulation, and integrity. As these objectives fundamentally differ from the FR targeted in a PBD, the direct transposition of furnace testing criteria to performance criteria has little foundation, except for ensuring the compatibility with tested conditions.

In Europe, the fire resistance test standard EN 1363-1:2012 defines the fire resistance as the time in completed minutes for which a test specimen continues to maintain its ability to support the test load. Two criteria are used to assess this ability: one is based on the amount of deflection (in mm), while the second is based on the rate of deflection (in mm/min) (Dumont et al., 2016). Thresholds are defined as a function of the typology of the element. For example, the deflection threshold for

flexural loaded elements is  $L^2/(4000 d)$ , where  $L$  is the clear span of the test specimen and  $d$  is the distance from the extreme fiber of the cold design compression zone to the extreme fiber of the cold design tension zone of the structural section, both in millimetres. The British Standard BS 476-20:1987 considered a limiting deflection of  $L/20$  (Law et al., 2011). For the thermal insulation requirement, criteria are defined in terms of average and point-maximum temperature increases on the unexposed face. For the integrity requirement, criteria are based on visible flame-through, gap measurement, and ignition of a cotton-pad.

These criteria are well-defined and well-suited to the furnace testing environment. They fulfil the objective to provide a clear, standardized framework to enable comparison between tests conducted in different laboratories, classification, and certification. However, these criteria are of limited applicability to PBD, for mainly two reasons: (1) The correlation with meaningful FR is questionable. For example, exceedance of the deflection threshold of an isolated element is not indicative of global loss of load bearing capacity of a structural system (e.g., tensile membrane action). (2) In some cases, the criteria are easy to measure in a test environment but not adapted to engineering models and analysis. For example, assessment of the integrity criteria through numerical models is currently out of reach.

### 3.3 Performance criteria considering a credible worst-case approach

As part of the review, the applied set of PC and associated FR were extracted from selected published SFE studies. Often the FR were not explicitly listed; in those cases an interpretation was made. A great variety of PC-sets was obtained, see Table 1. Some PC can be evaluated in the temperature domain, e.g., (RWS, 2017), but most require a thermal-structural assessment. Due to the great variety in applied PC, grouping references was possible only to a limited extent.

Table 1 Set of performance criteria deemed to fulfil a functional requirement, credible worst case approach

Reference	Set of performance criteria (PC)	Functional requirement (FR)
ISO/TR 24679-6:2017	No overall loss of stability; Shear capacity check; Deflection limit; Rotation limit	Stability up to burnout; Maintain compartmentation
RWS (2017)	Reinforcement critical temperature; Concrete critical temperature	Repairability post-fire
(Law et al., 2011)	Reinforcement critical temperature; Deflection limit; Strain limit	Stability for a reasonable time*
(Franssen and Bruls, 1997); (Lilliu and Meda, 2013); (Green et al., 2014)	Achieve fire resistance time (no loss of stability for nominal fire exposure)	Stability for a reasonable time*
(Naser et al., 2014)	Stress limit	Stability for a reasonable time*
(Lelli et al., 2018)	No overall loss of stability	Stability up to burnout
(Hopkin et al., 2018)	No overall loss of stability; Utilisation limit; Deflection limit; Connection ductility	Stability up to / beyond burnout

\* not explicitly mentioned in the reference, interpretation in current study

Table 1 refers to evaluations whereby the PC is the achievement of a set fire resistance time. In such situations the actual engineering analysis relies on underlying evaluation criteria, such as overall stability of a numerical model or a deflection limit. The capabilities of the modelling tool define whether evaluating overall stability within the model is sufficient, or whether additional checks are required. Franssen and Bruls (1997) for example combine an overall numerical (non-linear beam

finite element) stability check with an analytical check of the shear capacity. This consideration naturally also applies to the PC *no overall loss of stability*.

The deflection limits adopted in ISO/TR 24679-6:2017 and (Law et al., 2011) apply a deflection limit of L/20. As noted above, this criterion is adopted from furnace test criteria.

### 3.4 Performance criteria considering a risk assessment approach

Results for selected studies classified as following a risk assessment approach are listed in Table 2. As is common in structural engineering, most of the performance criteria relate to probabilities of exceedance of a limit state, e.g. the probability of an overall loss of stability. A comprehensive risk-based approach whereby also the consequences (i.e. fatalities or costs) are included is more rare.

Table 2 Set of performance criteria deemed to fulfil a functional requirement, risk assessment approach

Reference	Set of performance criteria (PC)	Functional requirement (FR)
(Ellingwood and Shaver, 1974); ISO/CD TR 24679-8:2020	Achieve fire resistance time with specified reliability	Achieve fire resistance time
(Phan et al., 2010)	Capacity check; Deflection limit (as an alternative)	To be defined by stakeholders
(Lange et al., 2014)	Annualized repair cost and downtime	To be defined by stakeholders*

\* not explicitly mentioned in the reference, interpretation in current study

The studies whereby both the FR and PC refer to the achievement of a fire resistance time should be interpreted as follows. The FR of a nominal fire resistance time has been accepted as a proxy for fulfilling the FSO. Considering the uncertainty in structural response, however, the achievement of this fire resistance time cannot be guaranteed, i.e., there is a (small) probability of the fire resistance time being smaller than the target value. The PC makes this explicit by unambiguously listing a threshold probability of not achieving the required resistance time.

The report by Phan et al. (2010) listed in Table 2 provides general guidance on the application of PBD for structural fire design. It specifies that the FR should be defined in consultation with the stakeholders. Phan et al. further state that deflection limits can be used as a substitute to strength (capacity) assessments, and that a risk analysis can underlie the evaluation. The latter clarifies its inclusion in cases adopting a risk assessment approach.

The repair cost and downtime assessment by Lange et al. (2014) builds upon deflection evaluations, whereby different assumed deflection thresholds are applied for the damage classification. Lange et al. do not specify a threshold of the annualized repair cost and downtime for the design acceptance, but more generally state that this information can be of interest in the decision making.

## 4 EVALUATION AND RECOMMENDATIONS

The limited literature review shows that a wide range of PC and combinations of PC are being used in the performance-based fire safety assessment of concrete and composite structures. With respect to the credible worst case (deterministic) design approach, there appears to be a core set of individual PC which are used across studies, but no consensus emerged from the investigated works. This observation suggests that PC are commonly defined ad-hoc and that an in-depth review on this topic is in order.

To be usable, PC need to be formulated in terms of quantitative outputs of engineering models. Elucidating the relationship between these model outputs and qualitative functional requirements requires a high level of knowledge in the specific engineering field, which is built over time as the community embraces the PBD approach. For example, to assess a FR of “repairability within a reasonable period”, a PC could be formulated as a threshold on residual deflections. Yet, contrary to seismic engineering, there is very little data available in the structural fire engineering field linking repairs operations to deflection thresholds (Ni and Gernay, 2021).

Considering the actual state of knowledge for SFE, it is currently considered not feasible to state generally applicable meaningful PC. The PC need to be set case by case and expert judgment is

required and can be affirmed by stakeholders. For larger projects, the concurrence of a peer review panel with respect to the selection of relevant PC is recommended, as is common in earthquake engineering. This process of agreeing on PC with stakeholders and reviewers is particularly difficult due to the absence of guidance on the specification of PC.

## 5 CONCLUSIONS

Satisfying a set of quantitative performance criteria (PC) is considered to demonstrate achievement of the qualitative functional requirements (FR). In turn, achieving the FR acts as a proxy for achieving the project's fire safety objectives (FSO). Thus, satisfying the PC has far reaching implications, and the definition of the PC must be based on solid technical considerations.

Early-stage results of a review of PC and combinations of PC being used in current performance-based fire safety assessment of concrete and composite structures indicates a wide variation. Importantly, no consensus emerged from the reviewed works, suggesting that PC are commonly defined ad-hoc. To support the further adoption of performance-based structural fire engineering, in-depth studies on the definition of PC are recommended.

## REFERENCES

- Bertero, V. V., Bozorgnia, Y., 2004. The early years of earthquake engineering and its modern goal. In: Earthquake Engineering: From Engineering Seismology to Performance-Based Engineering, CRC Press, London, UK.
- BS 476-20:1987. *Fire tests on buildings materials and structures — part 20: method for determination of the fire resistance of elements of construction*. British Standards Institution, London, UK.
- Dumont, F., Wellens, E., Gernay, T., & Franssen, J. M. (2016). Loadbearing capacity criteria in fire resistance testing. *Materials and Structures*, 49(11), 4565-4581.
- EN 1363-1:2012, *Fire resistance tests - Part 1: General Requirements*. CEN, Brussels
- Franssen, J. M., Bruls, A., 1997. Design and tests of prestressed concrete beams. *Fire Saf. Sci*, 5, 1081-1092.
- Green et al., 2014. Performance in fire of fibre reinforced polymer strengthened concrete beams and columns: Recent research and implications for design. *J. Struct. Fire Eng.*, 5(4), 353-366.
- Hopkin et al., 2018. A structural fire strategy for an exposed weathering steel-framed building. *The Structural Engineer*, 96(1), 60-66.
- ISO 23932-1:2018, *Fire safety engineering - General principles - Part 1: General*. International Organisation for Standardisation, Geneva, CH.
- ISO/TR 24679-6:2017. *Fire safety engineering - Performance of structures in fire - Part 6: Example of an eight-storey office concrete building*. International Organisation for Standardisation, Geneva, CH.
- ISO/CD TR 24679-8:2020. *Fire safety engineering - Performance of structures in fire - Part 8: Example of a probabilistic fire design of structures*. International Organisation for Standardisation, Geneva, CH.
- Lange, D., Devaney, S., Usmani, A., 2014. An application of the PEER performance based earthquake engineering framework to structures in fire. *Engineering structures*, 66, 100-115.
- Law et al., 2011. The influence of travelling fires on a concrete frame. *Eng. Struct.*, 33(5), 1635-1642.
- Law et al., 2015. A risk based framework for time equivalence and fire resistance. *Fire Technol.*, 51, 771-84.
- Lelli, L., Loutan, J., 2018. Advanced analyses of the membrane action of composite slabs under natural fire scenarios. *Journal of Structural Fire Engineering*, 9(1), 77-90.
- Lilliu, G., Meda, A., 2013. Nonlinear phased analysis of reinforced concrete tunnels under fire exposure. *Journal of Structural Fire Engineering*, 4(3), 131-142.
- Naser, M., Hawileh, R., Rasheed, H., 2014. Performance of RC T-beams externally strengthened with CFRP laminates under elevated temperatures. *Journal of Structural Fire Engineering*, 5(1), 1-24.
- Ni, S., Gernay, T., 2021. A framework for probabilistic fire loss estimation in concrete building structures. *Structural Safety*, 88, 102029.
- Phan, L. T., McAllister, T. P., Gross, J. L., Hurley, M. J., 2010. *Best practice guidelines for structural fire resistance design of concrete and steel buildings*. NIST technical note, 1681, 199.
- RWS. (2017). *Richtlijnen Ontwerp Kunstwerken - ROK 1.4*. Rijkswaterstaat Grote Projecten en Onderhoud.
- The Stationery Office (2010). *Schedule 1, part 2 of building and buildings. The Building Regulations, England and Wales*. UK Statutory Instruments, 2010 No. 2214.
- Van Coile, R., Hopkin, D., Lange, D., Jomaas, G., Bisby, L., 2019. The need for hierarchies of acceptance criteria for probabilistic risk assessments in fire engineering. *Fire Technology*, 55(4), 1111-1146.

Proceedings of the International Conference in Ljubljana, 10-11 June 2021  
in edition of Applications of Structural Fire Engineering

**Session**

**Other topics I**

## DIATOMACEOUS EARTH FOR IMPROVING THE BUSHFIRE RESISTANCE OF CEMENT BLOCKS

Indunil E. Ariyaratne, Anthony D. Ariyanayagam

Queensland University of Technology (QUT), Faculty of Engineering, Brisbane, Australia

### Abstract

Buildings in bushfire prone areas should be designed and built so that they can withstand the effect of extreme heat exposures without any failures. Previous research studies have focused on developing lightweight concrete and masonry units for low energy consumption in buildings. However, limited studies have been conducted to investigate their bushfire resistance. The purpose of this study is to develop cement blocks using a lightweight aggregate called diatomaceous earth/diatomite and investigate their bushfire resistance. First, the physical properties of materials were determined. Then the cement-diatomite mix was developed by absolute volume method. Average density and compressive strength were obtained after 28 days of moist curing and the fire resistance of blocks was examined against the standard fire curve. Finally, the results are compared with the performance of a control cement-sand mix, which showed lightweight, loadbearing strength and improved fire resistance due to the use of diatomite aggregates.

**Keywords:** Bushfire, Diatomite, Lightweight masonry unit, Compressive strength, Fire resistance

### 1. INTRODUCTION

During bushfires, wall systems of buildings are generally exposed to embers, radiant heat and direct flames of bushfires. Buildings should be designed to transfer less amount of heat and withstand extreme fire conditions. Currently many studies have been conducted by developing lightweight construction materials with various natural aggregates, chemical admixtures and agricultural and industrial wastes to achieve improved energy efficiency compared to conventional construction materials (Hossain, 2004, Ramamurthy *et al.*, 2009, Sathiparan & Zoysa, 2018, Sengul *et al.*, 2011 and Xu *et al.*, 2012). However, even though these new materials show better thermal efficiency at ambient temperature, their bushfire/fire performance is not well understood. Hence the main aim of this study is to investigate the possibility of using one type of natural lightweight aggregates called “Diatomaceous earth/Diatomite” in the production of cement masonry blocks to enhance their bushfire resistance.

Diatomaceous earth: generally called as “Diatomite”, is a naturally occurring soft material. It can be easily crushed into a white powder. Because of its unique pore structure, it is mostly used as filtration material, fillers and insulation materials (Topcu and Uygunoglu, 2007, Posi *et al.*, 2013, and Pimraksa and Chindapasirt, 2009).

Several past studies have developed lightweight cement mixtures with diatomite (Topcu and Uygunoglu, 2007, Posi *et al.*, 2013, and Pimraksa and Chindapasirt, 2009). The most common tested properties in those studies were compressive strength, density, water absorption and thermal conductivity at ambient temperature. It is observed that higher the diatomite content, lower the unit weight, strength and thermal conductivity while increasing the water absorption. However, no experimental studies have been conducted to investigate the fire resistance of cement blocks made with diatomite aggregates. Thus, this research explores the possibility of using diatomite aggregates in cement masonry blocks for use as external walls of houses, shelters, and other buildings in bushfire prone areas. In this paper, the physical properties of materials are presented first, followed by the details of mix design and mixing. Then the details of tests and specimens are discussed. Finally, physical and mechanical properties and fire test results of cement mixes are presented and discussed.

## 2. EXPERIMENTAL PROGRAM

### 2.1 Materials

General purpose cement, locally available sand and diatomite fine aggregates sourced from Chalkmine, Australia and tap water were used as basic mix components. Specific gravity of cement, sand and diatomite aggregates are 3.06, 2.57 and 1.34, respectively. Also, the water absorption of saturated surface dry (SSD) sand and diatomite aggregates are 0.1% and 110.6%, respectively.

### 2.2 Mix design

In this study, two cement mixes; 1) Control Cement-Sand (C-S) and 2) Cement - Diatomite (C-D) were proposed and their mix proportions are given in Table 1. Both mixes were proportioned based on the absolute volume method. In the C-S mix, cement to sand ratio was 1:3 and effective water to cement ratio was 0.6:1. Then the sand volume in the C-S mix was fully replaced by equal diatomite aggregates volume to produce the C-D mix. Also, the entrapped air content in both mixes was assumed as 2% of the total mix volume.

Table 1 Mix proportions of cement mixes in SSD condition

Material Mix	Cement (kg/m <sup>3</sup> )	Sand (kg/m <sup>3</sup> )	Diatomite (kg/m <sup>3</sup> )	Effective water (kg/m <sup>3</sup> )
Cement-Sand (C-S)	478	1380	0	287
Cement-Diatomite (C-D)	471	0	729	283

(Note: The aggregates' moisture content variations were accounted in mix design calculations)

### 2.3 Details of mixing

Both cement mixes were prepared by following AS 1012.2-2014 (SA, 2014), AS 1012.8.1-2014 (SA, 2014) and ASTM C192/C192M-18 (ASTM, 2018). All the mix components were mixed in a pan mixer for 7 min. After completing mixing, test specimens (Fig. 1) were cast within the next 20 min. Later specimens were kept covered and undisturbed on a horizontal surface for a period of 18 – 36 hrs at the temperature of  $27 \pm 2^{\circ}\text{C}$ . After 24 hours of initial curing, the test specimens were demoulded and stored inside lime saturated water at the temperature of  $27 \pm 2^{\circ}\text{C}$  until 28 days.

### 2.4 Detail of tests

#### 2.4.1 Compressive strength

The compressive strength test of 100 mm diameter cylinders was conducted after 28 days of curing according to AS 1012.9-2014 (SA, 2014) and ASTM C39/C39M-18 (ASTM, 2018). The compressive strength was determined using a universal testing machine by applying the load at a rate of 0.3 (N/mm<sup>2</sup>)/s until failure. The unconfined compressive strength was calculated by multiplying the experimental compressive strength from the aspect ratio of 0.78 in AS/NZS 4456.4-2003 (SA, 2003).

#### 2.4.2 Density

Oven dry density of cement mixes was calculated using Eq. (1) in ASTM C567/C567M-14 (ASTM, 2014).

$$\text{Oven dry density } \left( \frac{\text{kg}}{\text{m}^3} \right) = \frac{1.2 \times \text{Cement mass (kg)} + \text{Dry mass of aggregates (kg)}}{\text{Volume of the batch (m}^3\text{)}} \quad (1)$$

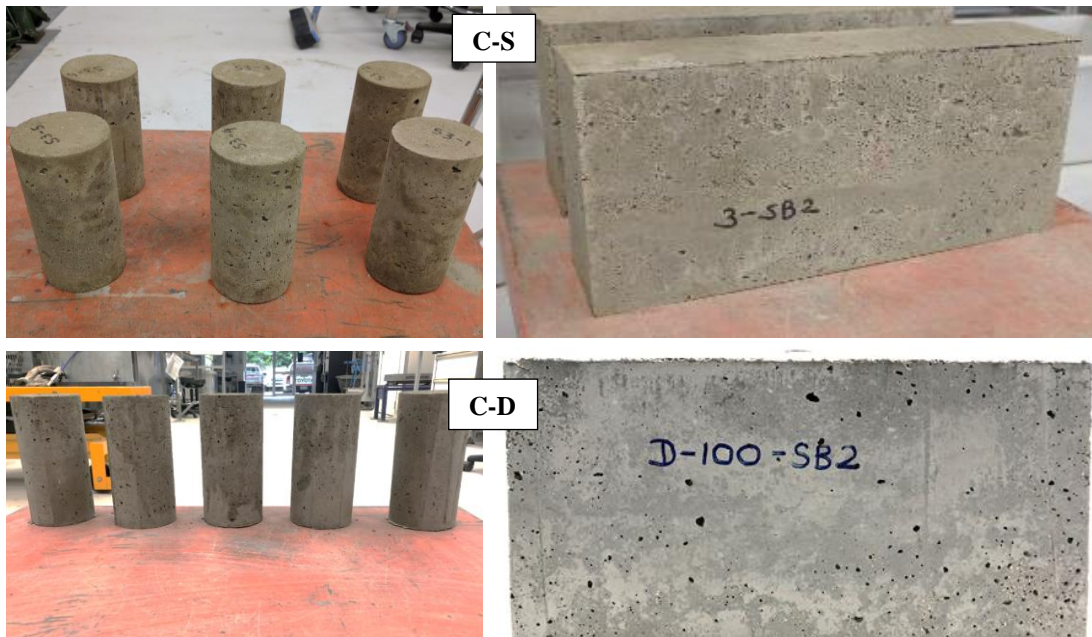


Fig. 1 Cylinder and block test specimens

Hardened densities of cement mixes were determined according to AS 1012.12.1-1998 (SA, 1998) using 100 mm diameter cylinders at their SSD condition.

### 2.4.3 Fire resistance of masonry blocks

After 28 days of curing, blocks were air dried for about two weeks before exposing them to fire. The block was subjected to standard fire in AS 1530.4-2014 (SA, 2014) for three hours simulating the bushfire flame zone condition in AS 1530.8.2-2018 (SA, 2018). Three ‘K’ type wired thermocouples were attached to the fire and ambient side surfaces of the block and a rod type thermocouple was kept inside the furnace to measure the surface and furnace temperatures, respectively.

## 3. RESULTS

The 28-day mean compressive strength (unconfined compressive strength) of C-S and C-D mixes are 33.6 (26.2) and 15.8 (12.3) N/mm<sup>2</sup>, respectively. Fig. 2 shows compression test failure patterns of each mix. Similar to compressive strength, C-S mix recorded the highest hardened and oven dry densities. Hardened and oven dry densities of C-D mix are 1494 and 911 kg/m<sup>3</sup>, respectively. Table 2 summarizes the properties of both cement mixes.

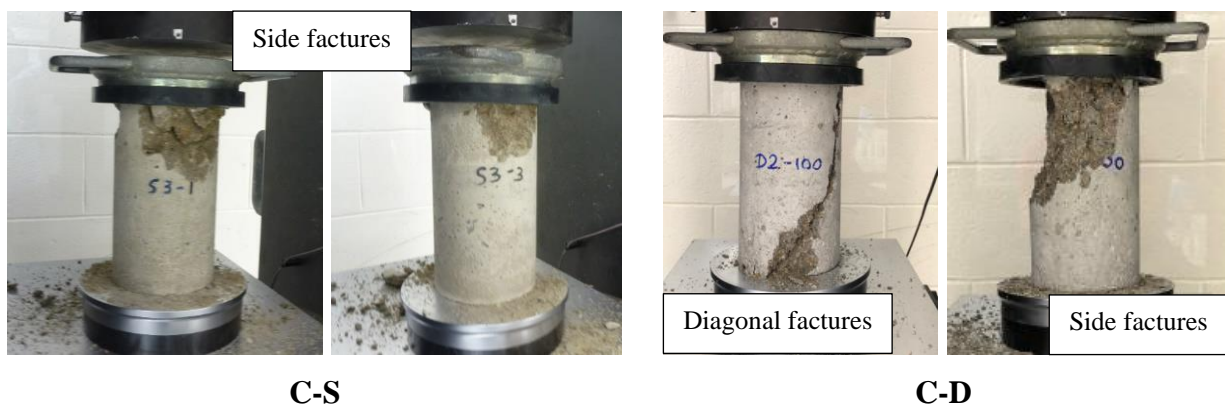


Fig. 2 Compression test failure patterns of C-S and C-D mixes

Table 2 Properties of C-S and C-D mixes

Mix	Mean compressive strength (N/mm <sup>2</sup> )	Mean hardened density (kg/m <sup>3</sup> )	Oven dry density (kg/m <sup>3</sup> )	Insulation failure (min)
C-S	33.6	2150	1952	115
C-D	15.8	1494	911	>180

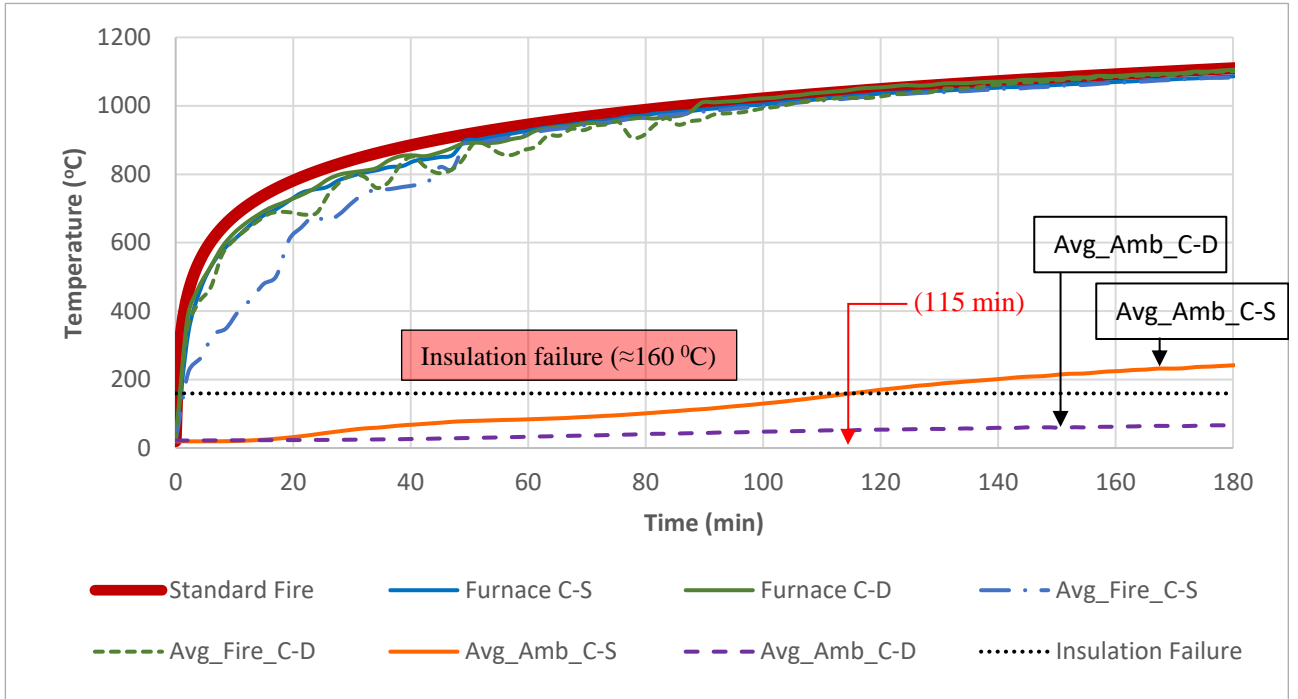


Fig. 3 Time - temperature curves – C-S and C-D blocks

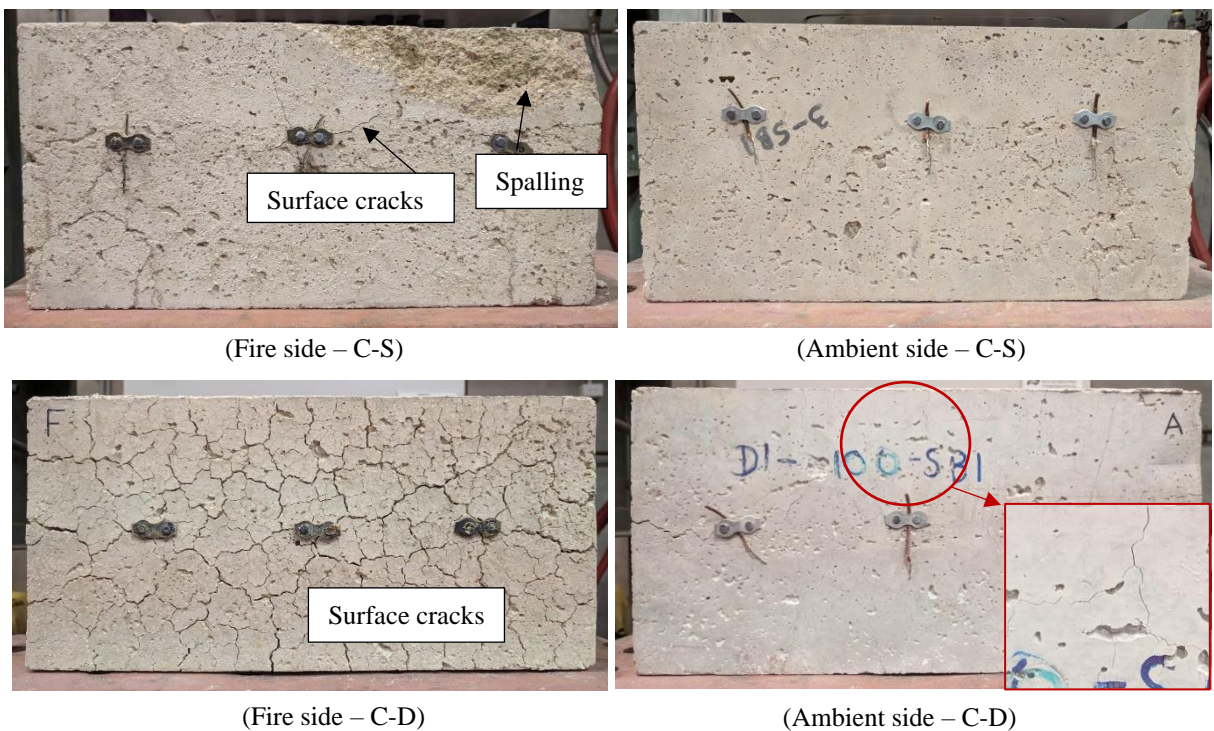


Fig. 4 Fire side and ambient side surfaces of the blocks after fire exposure

Fig. 3 shows the time – temperature curves of the fire tested blocks. The initial average temperature on the ambient side surface of the blocks was around 20 °C and hence the insulation failure is when the mean ambient surface temperature reached 160 °C (i.e. 140 + 20 °C). At the end of three hours of fire exposure, C-S and C-D blocks recorded average temperatures of 242 and 67 °C and 1094 and 1105 °C on the ambient and fire side surfaces, respectively. Hence as shown in Fig. 3, only the C-S block has failed under the insulation criterion at 115 min. Further, no integrity failure was observed in both blocks throughout the experiment. Also, as shown in Fig. 4, spalling on the fire side was only observed in the C-S block while C-D block recorded surface cracks on the fire side.

## 4. DISCUSSIONS

### 4.1 Density

The average SSD density recorded by the C-S and C-D mixes are 2150 and 1494 kg/m<sup>3</sup>, respectively. Therefore, there is a negative relationship between the density and the volume of lightweight aggregates in the mix as the density of control cement sand (C-S) mix can be reduced by 31% by replacing the sand fully with diatomite aggregates. Calculated oven dry density of C-D mix is 911 kg/m<sup>3</sup>. Therefore, based on the ASTM C90-16a (ASTM, 2016), developed C-D mix can be categorized under loadbearing lightweight concrete masonry units in terms of oven dry density.

### 4.2 Compressive strength

The highest compressive strength was recorded by the C-S mix and with the replacement of sand by lightweight aggregates compressive strength reduced by 53%. Hence there is a negative relationship between the volume of lightweight aggregates and the compressive strength of mixes. According AS 4773.2-2015 (SA, 2015), both mixes satisfy the strength requirement for loadbearing solid masonry units while C-D mix satisfies the loadbearing strength requirement for lightweight concrete masonry units (ASTM, 2016).

### 4.3 Fire resistance

Fire resistance level of C-S and C-D block is -/90/90 and -/180/180, respectively. The rate of temperature increment of C-S and C-D blocks can be calculated approximately as 1.30 and 0.3°C/min, respectively, by drawing the trend lines. Based on the final temperature recorded on the ambient surface (242 versus 67 °C), the temperature reduction on the ambient side is 72% when sand is replaced fully with diatomite. Therefore, considering the low temperatures recorded on the ambient side, lightweight density and loadbearing strength, C-D blocks can be utilized for external walls in bushfire prone areas over C-S. However, as shown in Fig. 4 the crack intensity level is considerably high on the fire side. Therefore, in order to be lightweight and perform well in strength, fire resistance and crack intensity, an optimum mix design should be further developed by using a combination of sand and diatomite aggregates.

## 5. CONCLUSION

This research explored the possibility of using diatomite lightweight cement blocks in the external walls of houses, shelters, and other buildings in bushfire prone areas over the normal weight masonry blocks. Physical and mechanical properties and fire resistance of cement-sand (C-S) and cement-diatomite (C-D) mixes and blocks under standard fire conditions were determined based on relevant Australian and American standards. Following conclusions are based on the experimental study reported in this paper.

- The control cement-sand (C-S) mix had the highest hardened density and compressive strength and the lowest fire resistance (FRL ≈ 90 min) than cement-diatomite (C-D) mix.
- There is a negative relationship of density, compressive strength and ambient side surface temperatures with the diatomite aggregate content.
- Cement-diatomite (C-D) mix satisfies the oven dry density and compressive strength requirement for loadbearing lightweight concrete masonry units.

- The lowest ambient surface temperatures and rate of temperature increment were recorded by the C-D mix and its fire resistance level was the highest at -/180/180.
- Considering lightweight, loadbearing compressive strength and low ambient surface temperatures, C-D mix shows the suitability for use in the external walls of houses, shelters and other buildings in bushfire prone areas. However, to avoid the high surface crack intensity on the fire side while satisfying the standard density and compressive strength requirements, development of an optimum mix design with a combination of sand and diatomite aggregates is needed.

## ACKNOWLEDGMENTS

The authors would like to thank Australian Research Council (ARC Grant DE180101598) and Queensland University of Technology for providing the necessary research facilities and support to conduct this research project.

## REFERENCES

- American Society for Testing and Materials, 2018. *ASTM C192/C192M-18: Standard Practice for Making and Curing Concrete Test Specimens in the Laboratory*<sup>1</sup>, ASTM International, Philadelphia.
- American Society for Testing and Materials, 2016. *ASTM C90-16a: Standard Specification for Loadbearing Concrete Masonry Units*<sup>1</sup>, ASTM International, Philadelphia.
- American Society for Testing and Materials, 2018. *ASTM C39/C39M-18: Standard Test Method for Compressive Strength of Cylindrical Concrete Specimens*<sup>1</sup>, ASTM International, Philadelphia.
- American Society for Testing and Materials, 2014. *ASTM C567/C567M-14: Standard Test Method for Determining Density of Structural Lightweight Concrete*<sup>1</sup>, ASTM International, Philadelphia.
- Anwar Hossain, K. M. 2004. *Properties of volcanic pumice-based cement and lightweight concrete. Cement and Concrete Research*, 34, p. 283-291.
- Pimraksa, K. & Chindaprasirt, P. 2009. *Lightweight bricks made of diatomaceous earth, lime and gypsum. Ceramics International*, 35, p. 471-478.
- Posi, P., Lertnimoolchai, S., Sata, V. & Chindaprasirt, P. 2013. *Pressed lightweight concrete containing calcined diatomite aggregate. Construction and Building Materials*, 47, p. 896-901.
- Ramamurthy, K., Kunhanandan Nambiar, E. K. & Indu Siva Ranjani, G. 2009. *A classification of studies on properties of foam concrete. Cement and Concrete Composites*, 31, p. 388-396.
- Sathiparan, N. & De Zoysa, H. T. S. M. 2018. *The effects of using agricultural waste as partial substitute for sand in cement blocks. Journal of Building Engineering*, 19, p. 216-227.
- Sengul, O., Azizi, S., Karaosmanoglu, F. & Tasdemir, M. A. 2011. *Effect of expanded perlite on the mechanical properties and thermal conductivity of lightweight concrete. Energy and Buildings*, 43, p. 671-676.
- Standards Australia, 2015. *AS 4773.2-2015: Masonry in small buildings – Construction*, Australia.
- Standards Australia/New Zealand, 2003. *AS 4456.4-2003: Masonry units, segmental pavers and flags-Methods of test-Determining compressive strength of masonry unit*, Australia.
- Standards Australia, 2014. *AS 1530.4-2014: Methods for fire tests on building materials, components and structures: Fire resistance tests for elements of construction*, Australia.
- Standards Australia, 2018. *AS 1530.8.2-2018: Methods for fire tests on building materials, components and structures: Tests on elements of construction for buildings exposed to simulated bushfire attack – Large flaming sources*, Australia.
- Standards Australia, 2014. *AS 1012.9-2014: Methods of testing concrete - Compressive strength tests - Concrete, mortar and grout specimens*, Australia.
- Standards Australia, 1998. *AS 1012.12.1-1998: Methods of testing concrete - Determination of mass per unit volume of hardened concrete - Rapid measuring method*, Australia.
- Standards Australia, 2014. *AS 1012.8.1-2014: Methods of testing concrete - Method for making and curing concrete - Compression and indirect tensile test specimens*, Australia.
- Standards Australia, 2014. *AS 1012.2-2014: Methods of testing concrete - Preparing concrete mixes in the laboratory*, Australia.
- Topçu, I. B. & Uygunoglu, T. 2007. *Properties of autoclaved lightweight aggregate concrete. Building and Environment*, 42, p. 4108-4116.
- Xu, Y., Jiang, L., Xu, J. & Li, Y. 2012. *Mechanical properties of expanded polystyrene lightweight aggregate concrete and brick. Construction and Building Materials*, 27, p.32-38.

## FULL-SCALE EXPERIMENT OF A BUSHFIRE SAFE ROOM

Sahani U. Hendawitharana, Anthony D. Ariyanayagam

Queensland University of Technology (QUT), Faculty of Engineering, Brisbane, Australia

### Abstract

Many countries witnessed record-breaking bushfire events in 2020 that resulted in the loss of many human lives and properties, leading to physiological and psychological impairment for humans. The loss of lives, valuables such as jewelry, certificates and memorabilia during devastating bushfires can lead to significant mental health problems. Due to practical difficulties, safe evacuation can become impossible if not undertaken early. The time associated with carrying valuables further reduces the success of safe evacuation and having a safe room is identified as a potential solution. In this study, a full-scale safe room using Light-gauge Steel Frame (LSF) wall systems was designed, constructed and tested under simulated realistic bushfire conditions. The temperature (internal and external) and heat flux values were recorded during the bushfire test. The results confirm excellent performance of the safe room with respect to heat transfer.

**Keywords:** Bushfire, Flame contact, Full-scale fire test, Radiant heat

### 1 INTRODUCTION

Many countries worldwide experience adverse effects of climate change through conditions such as frequent and extreme floods, droughts and bushfires and it is predicted to get worse in the future (Yu *et al.*, 2020, Zhang *et al.*, 2020). 2019/20 bushfire season caused record-breaking economic and environmental losses to many countries, such as Australia, Brazil and the USA, and can be identified as a recent example of bushfire disasters. Not only the damages to flora and fauna are irrecoverable in the long term, but also the physiological and psychological impairment for humans is significant (Duckett *et al.*, 2010, Filkov *et al.*, 2020). Studies have shown that people who experienced bushfires suffer from depression and severe distress and the loss of important documents, valuables, memorabilia, etc make this worse (Duckett *et al.*, 2010).

However, the population in the Bushland Urban Interfaces (BUI) is increasing significantly over time and thus more people will experience severe bushfire damages in the future (Eriksen and Gill, 2010). If warnings for evacuation are given at short notice, then evacuation may not be a valid option for these communities due to many reasons such as: blocked exit roads, unknown fire directions and speeds, psychological attachment to the house and valuables, etc. Studies have shown that people demonstrate unhelpful behaviour such as freezing (i.e., cannot think clearly) and engaging in unnecessary actions such as repeated egress and ingress from the house during unexpected disaster notices (Robinson, 2012). Having to prioritize the important tasks in a very short time puts them in a stressful situation, which can delay the evacuation process. Furthermore, contrary to early evacuation, late evacuation is considered dangerous and life-threatening and thus people are often advised to stay and defend rather than evacuating late. This argument is further confirmed by the bushfire fatality statistics in Australia, where the majority of the fatalities occurred due to direct flame contact and 30% of the bushfire fatalities during 1900-2008 were due to late evacuations (Haynes *et al.*, 2010). Therefore, the need for a safe room is considered important.

The availability of a well-engineered safe room solution that can withstand a catastrophic bushfire event can help to increase bushfire life safety and lessen the psychological impairment to some extent. The safe room can be built either as a separate building or as an attachment to an existing house and can be frequently used as a part of the house. Further, the valuables and important documents can be stored in the safe room, so that during a severe bushfire event, the safe room will be ready to function.

However, limited studies have investigated the bushfire performance of buildings, while full-scale experiments of rooms with respect to heat transfer and structural performance have not been undertaken. Also, the available studies have mostly focused on building fires and not on bushfires.

Availability of full-scale experimental studies for bushfire exposure conditions is important in decision making and to conduct further numerical studies for different bushfire conditions. In this study a full-scale experiment of bushfire safe room was conducted under simulated bushfire conditions and its results are presented in this paper.

## **2 BUSHFIRE ATTACK**

The main bushfire attack mechanisms include direct flame contact, radiant heat and ember attacks where the buildings located near vegetation such as forests will be subjected to all three of them (Leonard *et al.*, 2004). The buildings are subjected to increasing radiant heat when the bushfires approach. The rate of increment of the radiant heat depends on several factors such as the fuel load, wind conditions and Forest Fire Danger Index (FFDI), and the duration of the building exposure to the radiant heat varies based on them. The performance standard for private bushfire shelters assumes this duration as 7 min while in reality, it can be a longer duration (ABCB, 2014). The buildings are immersed in bushfire flame when the bushfires approach the building and the duration of flame immersion is considered to be around 1 to 2 min. Unlike structural fires, the bushfire flame temperatures can be significantly high as 1100 °C and this temperature increment is gained in a very short time duration, making the rate of temperature increment very high (Wotton *et al.*, 2012). The building performance can be highly affected by this sudden increment in temperatures. This study focuses on radiant heat and direct flame contact as the main bushfire attack mechanisms on the safe room.

## **3 EXPERIMENTAL PROGRAM**

The experimental program of this study consisted of the design and construction of a bushfire safe room and testing it under simulated bushfire exposure conditions. The dimensions of the safe room were 4m x 3m x 2.4m (W x L x H) where W, L and H refer to its width, length and height. The bushfire exposure was simulated using the heat flux versus time curve proposed by CSIRO, which was developed based on realistic bushfire characteristics (Leonard *et al.*, 2012).

### **3.1 Construction of Safe Room**

This full-scale safe room was constructed and tested in the Queensland Fire and Emergency Services (QFES) testing facility in Lytton, Port of Brisbane, Australia. The location of the safe room on the testing area was decided based on the wind direction and speed, available space and critical exposure sides of the safe room. The safe room was designed as a Light-gauge Steel Framed (LSF) structure mounted on concrete beams (Fig.1-A). Seven steel frames were built and transported to the site and assembled on site. Water and air barrier and class 2 vapour barrier sarking (1 mm thick) was used to limit any moisture leak into the safe room (Fig.1-B). The external cladding material used in the safe room was 75 mm thick 600 mm wide Autoclaved Aerated Concrete (AAC) panels, which were fixed to the studs using 25 mm battens (Fig.1-C). The external walls were cavity insulated using non-combustible, R 2.0, 90 mm thick Earthwool insulation (Fig.1-D). The internal surface consisted of two layers of 16 mm thick fire-rated gypsum plasterboards (1200 mm wide) (Fig.1-E). Two-hour fire-rated commercially available fire doors were used in the construction. The roof of the safe room consisted of two layers of 75 mm thick AAC panels on the external surface and 10 mm thick gypsum plasterboards on the internal surface.



Fig. 1 Construction sequence of the safe room

### 3.2 Experimental Setup and Testing

An LP gas-fired burner with two flame outlets (each outlet can be operated independently) was used to generate the bushfire exposure. The test duration was 47 min and had three identifiable phases of heat exposure to simulate approaching fire, fire immersion and post-fire situations. Fig.2 shows the safe room test during the fire immersion phase.



Fig. 2 Flame zone bushfire exposure on the safe room

The fire source was controlled manually by QFES staff, and the heat flux readings from the heat flux meter on the fire side wall were used in regulating the burner flame. One hundred and twenty-eight K-type thermocouples were located on each wall and roof of the safe room and more than 30 were located along and across the fire side wall. Even though the test duration was 47 min (2820 s), the temperature readings of the fire side wall were logged for more than 2 hours (more than 8000 s) to measure the heat transfer over time during the cooling phase.

## 4 RESULTS AND DISCUSSION

The visual observations on the exterior surfaces showed less than 2 mm wide horizontal cracks on the fire side surface of the safe room after the test. Furthermore, no damage to the internal wall surfaces nor a structural failure was observed during the test.

### 4.1 Heat Flux

The heat flux readings obtained during the experiment indicate a slow increase in the heat flux up to 40 kW/m<sup>2</sup> for 1800 s representing an approaching bushfire as indicated in Fig. 3. Next, the heat flux suddenly increased beyond 60 kW/m<sup>2</sup> for 110 s, which resembles a flame zone exposure. This duration can be considered as the most critical time period during the test. At the end of the flame zone exposure, the flame was reduced, and a constant radiant heat exposure was given until the end of the test duration (total test duration is 47 min). However, the heat flux reading was not recorded during the latter part of the curve as shown in Fig.3 due to malfunctioning of the heat flux sensor, but the exposure levels are reflected in the time-temperature curves (refer to Fig. 4).

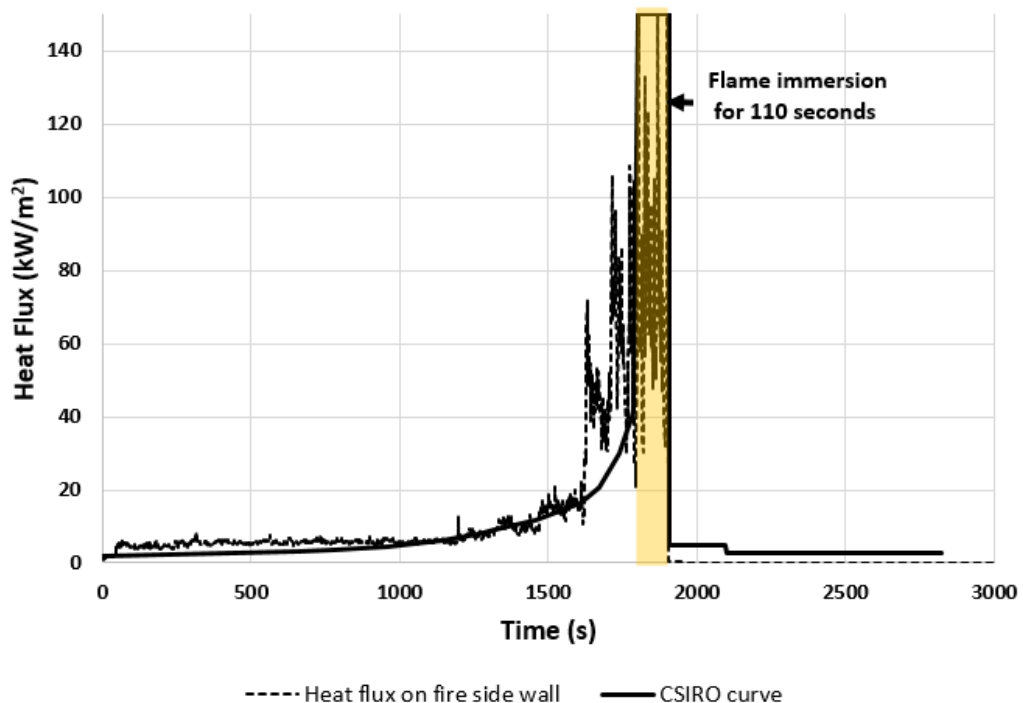


Fig. 3 Heat flux on the fire exposed wall versus time curve

### 4.2 Surface and Air Temperatures

Fig. 5 presents a summary of the maximum average external surface temperatures during the flame zone conditions, the maximum internal surface temperatures and the air temperatures. The results show that even though the fire side external temperature reached a maximum of 958 °C (average 869 °C during flame immersion), the internal surface temperatures remained at less than 29 °C and the rise in internal air temperatures was less than 1 °C. The average external and internal surface temperatures are shown in Fig. 4, where the gradual increment and decay phases of the bushfire exposure are clearly visible. When comparing the fire side and fire cavity temperatures, a 27.5 min lag is observed in reaching the peak temperatures. The maximum fire cavity temperature recorded was 73 °C and it is 13 times less than the maximum fire side temperatures while the maximum ambient wall temperatures are 33 times lower than the fire side maximum temperatures, which demonstrates excellent bushfire heat resistance. The temperature gradient over the wall thickness is 931 °C during the peak bushfire exposure time (i.e., at 30 min).

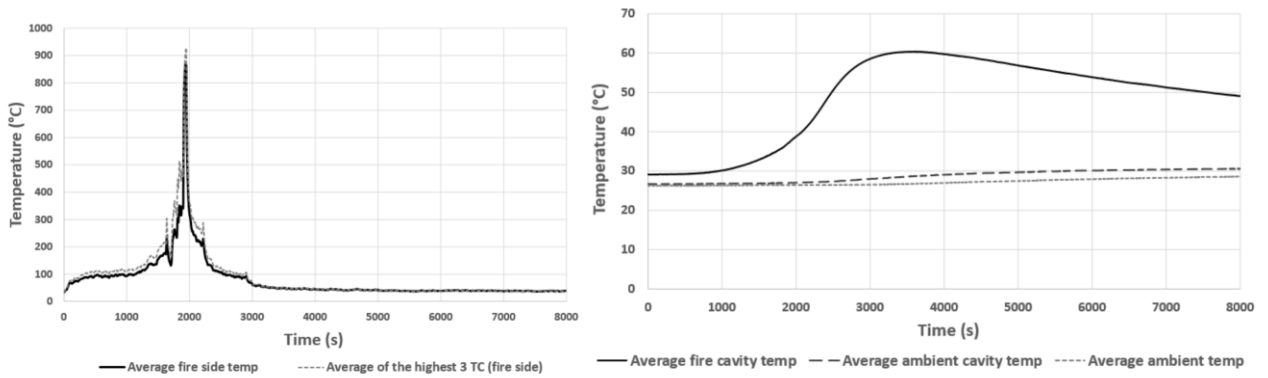


Fig. 4 Average temperatures on the fire side wall (left) and average temperatures on the fire cavity, ambient cavity and ambient side (right)

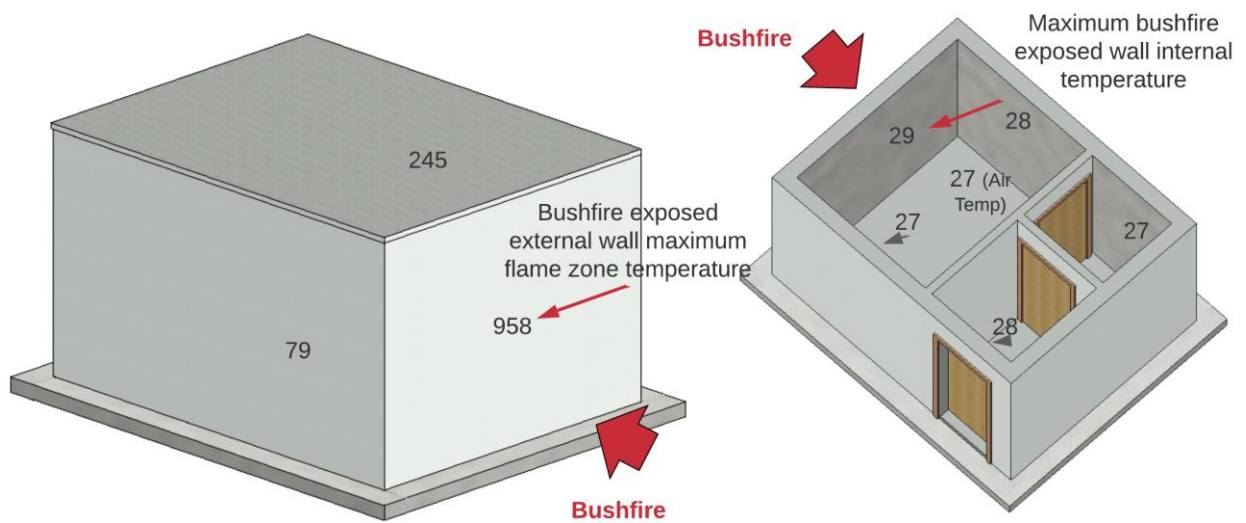


Fig. 5 Maximum surface and air temperatures

Therefore, the results of the full-scale bushfire simulation test have demonstrated excellent performance in terms of heat transfer. Further analysis of the obtained test data is in progress. This study confirms that bushfire-safe solutions of the safe room for the storage of valuables are possible under extreme bushfire conditions. However, other human tenability factors such as air quality, internal pressures and toxic emissions, human behaviour inside the safe room etc. need to be further investigated if this is to be used as a shelter for humans.

## 5 CONCLUSIONS

This study has presented the details of a full-scale bushfire experiment of a safe room exposed to simulated bushfire flame zone conditions. The results of the study showed that the internal air temperatures remained at 27°C throughout the safe room during the test. Furthermore, the maximum internal surface temperature recorded was 29°C, when the external average wall temperatures during flame immersion reached 869°C. The results of this study revealed that an engineered safe room solution is feasible and will survive extreme bushfire conditions. However, if this is to be used as a sheltering location for people, further studies are required on maintaining other tenability conditions such as air quality, internal pressures, toxic emissions and human behaviour.

## ACKNOWLEDGMENTS

The authors wish to thank Australian Research Council (ARC Grant DE180101598) for providing financial support, and Queensland University of Technology (QUT) and Queensland Fire and Emergency Services (QFES) for providing the testing facility and space, and for the immense support throughout the full-scale experiment.

## REFERENCES

- Yu, P., Xu, R., Abramson, M.J., Li, S. and Guo, Y., 2020. *Bushfires in Australia: a serious health emergency under climate change. The Lancet Planetary Health*, 4(1), pp.e7-e8.
- Zhang, Y., Beggs, P.J., McGushin, A., Bambrick, H., Trueck, S., Hanigan, I.C., Morgan, G.G., Berry, H.L., Linnenluecke, M.K., Johnston, F.H. and Capon, A.G., 2020. *The 2020 special report of the MJA–Lancet Countdown on health and climate change: lessons learnt from Australia’s “Black Summer”*. *Medical Journal of Australia*.
- Eriksen, C. and Gill, N., 2010. Bushfire and everyday life: examining the awareness-action ‘gap’ in changing rural landscapes. *Geoforum*, 41(5), pp.814-825.
- Robinson, S.J., 2012. *When disaster strikes: Human behaviour in emergency situations. Journal of the Institute of Civil Protection and Emergency Management*.
- Haynes, K., Handmer, J., McAneney, J., Tibbits, A. and Coates, L., 2010. *Australian bushfire fatalities 1900–2008: exploring trends in relation to the ‘Prepare, stay and defend or leave early’ policy. environmental science & policy*, 13(3), pp.185-194.
- Leonard, J.E., Blanchi, R. and Bowditch, P.A., 2004. Bushfire impact from a house's perspective. *In Earth Wind and Fire–Bushfire 2004 Conference*, Adelaide.
- Wotton, B.M., Gould, J.S., McCaw, W.L., Cheney, N.P. and Taylor, S.W., 2012. *Flame temperature and residence time of fires in dry eucalypt forest. International Journal of Wildland Fire*, 21(3), pp.270-281.
- Australian Building Codes Board (ABCB), 2014. *Performance standard for private bushfire shelters. The design and construction of private bushfire shelters*. Australian Government and States and Territories of Australia.
- Duckett, S., Mackey, W. and Stobart, A., 2020. The health effects of the 2019-20 bushfires. *Submission to the Royal Commission into National Natural Disaster Arrangements. Melbourne: Grattan Institute*. [Online][Accessed 31 October 2020]
- Filkov, A.I., Ngo, T., Matthews, S., Telfer, S. and Penman, T.D., 2020. *Impact of Australia's catastrophic 2019/20 bushfire season on communities and environment. Retrospective analysis and current trends. Journal of Safety Science and Resilience*, 1(1), pp.44-56.
- Leonard, J.E., Macindoe, L., Watson, K.B., Bennetts, I.D., Kelly, M.H., Clayton, T.G. and Baines, D., 2012. Testing of steel wall systems for use in bushfire flame zone areas. *In Australasian Structural Engineering Conference 2012: The past, present and future of Structural Engineering* (p. 1087). Engineers Australia.

## WUIFIRESAFE – STRUCTURAL FIRE RESISTANCE OF BUILDINGS IN WILDLAND-URBAN INTERFACE

Cesare Fiorini<sup>a</sup>, Hélder D. Craveiro<sup>a</sup>, Luís Simões da Silva<sup>a</sup>, Aldina Santiago<sup>a</sup>, Luís Laim<sup>a</sup>

<sup>a</sup> ISISE, Department of Civil Engineering, University of Coimbra, Coimbra, Portugal

### Abstract

Demographic pressure, high population density and unbalanced territorial planning options have led to the growth of urban areas in the vicinity of forest areas. Moreover, climate changes have increased wildfire potential and consequently, the risk to structures in the Wildland Urban Interface (WUI), causing major environmental destruction, severe property damage and loss of lives (i.e. catastrophic events such as the ones in 2017 in Portugal). This risk is not commonly considered in the field of structural fire design. The WUIFIRESAFE research project aims to investigate the risk of wildfires to the built environment assessing in detail the ignition potential in buildings and specific heat transfer phenomena, using a performance-based approach. The FDS software is used to simulate forest fires at the microscale level assessing its impacts on structures. This serves to define future strategies to consider wildfires in the WUI in the structural fire design.

**Keywords:** Wildland-Urban Interface, Fire Dynamics Simulator, Structure, Heat Transfer

### 1 INTRODUCTION

Wildfire events are more and more frequent worldwide (Bento-Gonçalves and Vieira, 2020) due to climate changes, lack of management and abandonment of forest and rural areas and activities. Simultaneously, demographic and urban pressure led to uncontrolled growth of urban settlements in the vicinity of wildland areas (for instance small towns and resorts). In the last decade, several megafires have occurred (Bento-Gonçalves and Vieira, 2020), such as the catastrophic fires in Pedrogão Grande in 2017 and Valparaíso (Chile) (Lourenço and Felix, 2019) with extreme spread rates of up to 1300 m<sup>2</sup>/min. In the Pedrogão Grande fire, 66 people were killed, and 253 injured. Moreover, the impacts in the built environment were also severe, with more than 458 houses destroyed and 49 companies directly affected by the fire. The direct and indirect impacts of wildfires were extreme and long-lasting in the built environment and civil society.

Several programs and projects focused on WUI-fire were launched in Europe (Boboulos, 2013), such as PROMETEUS, EUROFIRELAB and EFAISTOS. (Manzello *et al.*, 2018) summarizes the most severe events as well as a critical assessment in terms of research needs in the field of WUI fires. Wildfires are strictly related to the vegetation which must be converted to fuels to predict fire spread, intensity, flame size and finally the impact of fire. This is an incredibly difficult task and still requires extensive research to address WUI fires in the context of fire safety engineering principles.

To reduce the likelihood of starting wildland fires the fuel treatment aspect has to be assessed (Mell *et al.*, 2010). Vegetative and structural fuels can originate fire that can be provoked naturally or due to manmade cause. A prominent question regarding WUI fires is the structure ignition problem. Fires can start due to exposure to heat flux from flames or firebrands generated by a wildfire (Sandström, 2013). Vegetative fuels and fires in a wildland setting can be categorized into ground, surface or crown types (Mell *et al.*, 2009). Manzello *et al.* (2018) confirms that exists a lack of current understanding of how structures are ignited, mainly by firebrands showers. This approach is focused on the external origin of the fire source (from outdoor cause) that can spread to the buildings and finally behaving as a compartment fire. The main concern is to assess heat transfer from vegetation fires to structures. Manzello *et al.* (2018) suggests investigating the vulnerability of real structures as well as studying ignition vulnerabilities for the creation of scientific-based retrofitting methods to protect structures exposed to wildfire scenarios in the WUI.

The research project WUIFIRESAFE (Fig. 1) aims to contribute to the understanding of the heat transfer phenomena and fire propagation from forests to urban areas, promoting the development of tailored design specifications for buildings in the vicinity of forest areas, creating a more resilient built environment and society, to mitigate the catastrophic direct and indirect impacts arising from severe wildfires. Moreover, it intends to provide a global view on the problem of assessing the behaviour of wildfires at the macroscale level, conducting simulations considering multiple severe climate scenarios at different fire-prone locations (hence, considering topography) such as the central region of continental Portugal. This macroscale modelling using FlamMap (Finney, 2006) and Wildfire Analyst (Tecnosylva, 2020) will allow the identification of the urban areas as well most likely to be affected by severe wildfires. Finally, at the microscale level, CFD tools will be used to assess the impact of wildfires on structures.

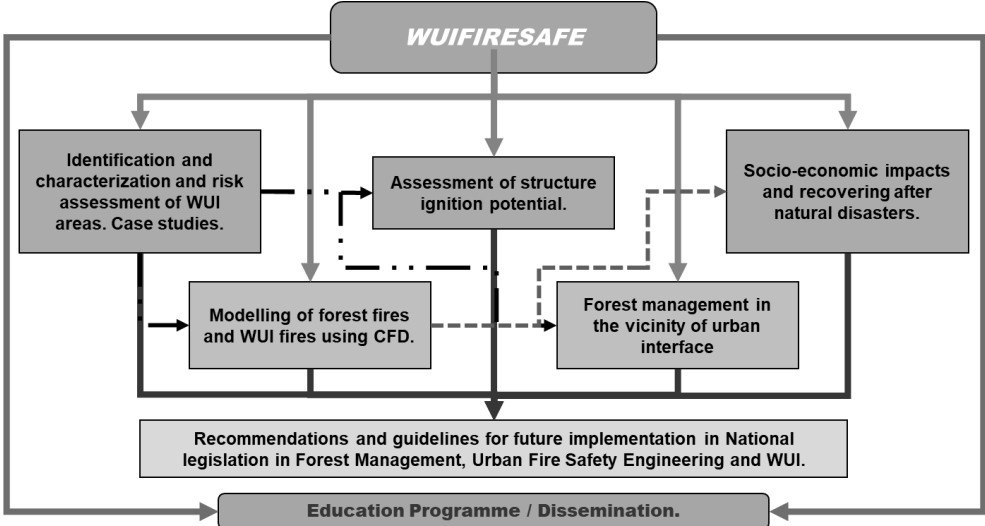


Fig. 1 Research project organogram.

In this paper a simple scenario is investigated, assessing the impact of vegetation in fire in a simple building. Data collected are thermal parameters such as wall temperatures and adiabatic surface temperatures. A parametric study is also presented by varying some characteristics of the vegetation in fire.

**2 METHODOLOGY**

CFD model is used to predict at the microscale level, the fire behaviour of the vegetation as a function of time and space as well as heat transfer phenomena to solid obstructions (building), whereas the finite element models are used to perform detailed heat transfer analysis and mechanical analysis considering the degradation of the mechanical properties of materials (Sandström , 2013). Governing equations that are used as reference in the CFD software are three and refer to the conservation of mass, momentum and energy as expressed by (Faiz Tharima *et al.*, 2017). The Fire Dynamics Simulator (FDS) (McGrattan *et al.*, 2013) is one of the most validated tools to model compartment fires, but it has also been used to model vegetation in fire (Mell *et al.*, 2009) successfully. Based on research conducted by (Mell *et al.*, 2009), this paper explains the numerical approach that was used to model the fire behaviour in the context of a WUI fire scenario solving with FDS the governing equations for fluid flow, combustion, thermal degradation of the vegetative fuel (pyrolysis and char oxidation). Convective and radiative heat transfer between the gas phase and the vegetation was investigated since the coefficient drag of the vegetation on the airflow was defined by (Falkenstein-Smith *et al.* 2019). Specifically, the combustion of trees was simulated with the description of moisture content, height and chemical composition of a real test conducted at NIST and reported by (Mell *et al.*, 2009). Also, the chemical part description referring to vegetation, charring and ash production have been maintained. In the CFD, trees were modelled with a conical shape. The conical volume was constituted by Lagrangian particles (this made by solid particles) that are stationary.

Lagrangian particles were used to model thermally fine elements such as: roundwoods (short, medium, long) and the foliage. Ignitors were located at the base of each tree (Mell *et al.*, 2009). The building was modelled as an obstruction (4m x 4m x 2m) and pyramid roof with 2 m height. The thickness of the concrete walls is 20 cm. A glass window with the following dimensions was considered, 0,5 m x 1,0 m and a thickness of 3cm, elevated 0,75 m from the ground level. In this study, several parameters were assessed, such as wind velocity and direction, and dimensions and density of the trees, providing detailed information on how these parameters could influence the heat transfer between the trees in fire and the building. For this purpose, several devices (Thermocouples, Wall temperature (WT), Adiabatic Surface Temperature (AST) were used to assess in detail the impact of the selected wildfire in the structure.

### 3 CASE STUDIES

Two situations were prepared considering a total duration for the simulation of 30 seconds. It was considered a dwelling in concrete with a group of 6 trees. All around grass is present and the wind was included as a parameter to be assessed and varied. The building is represented as a solid obstruction (4m x 4m x 2m) and pyramid roof with 2 m height. The thickness of the concrete walls is 20 cm. A glass window with the following dimensions was considered, 0,5 m x 1,0 m and a thickness of 3cm, elevated 0,75 m from the ground level. In this study, several parameters were assessed, such as wind velocity and direction, and dimensions and density of the trees, providing detailed information on how these parameters could influence the heat transfer between the trees in fire and the building. For this purpose, several devices (Thermocouples, Wall temperature (WT), Adiabatic Surface Temperature (AST) were used to assess in detail the impact of the selected wildfire in the structure.

Several points, located on the wall surface and on the glass, were monitored as well as a set of 6 thermocouples were used. In Fig. 2 the geometry, the position of the trees and building and the positioning of the devices used are depicted.

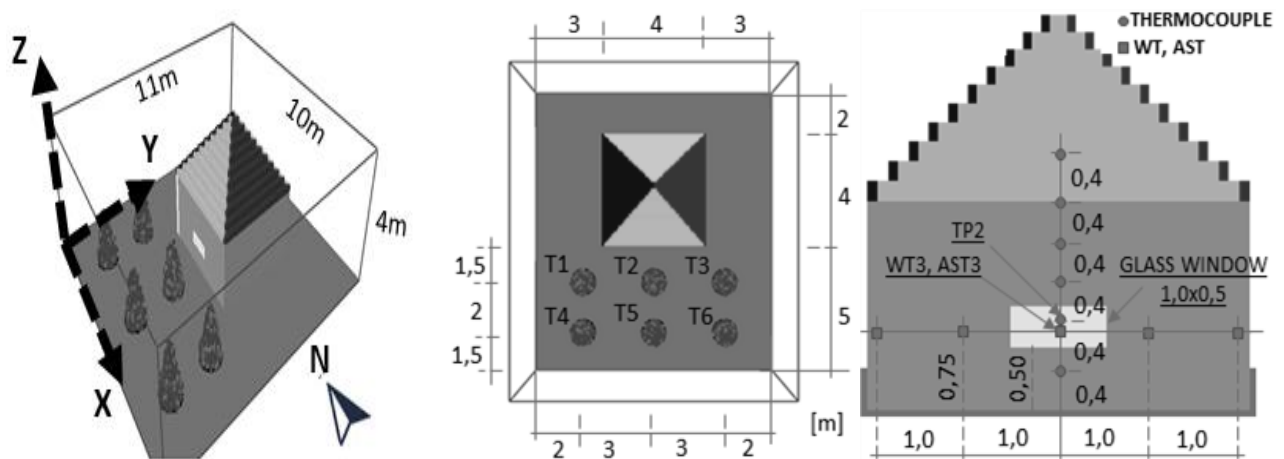


Fig. 2 a) 3D view. b) Plan view. c) Lateral (east) view.

Two lines of three trees distanced from 2 m are organized on the grass area. The shortest distance in the x-direction between the trees and the wall is 1,5m. The 6 trees have the same height in the domain. Simulations were launched modifying the height of the trees (1,9m; 2,7m; 3,5m). Therefore, the computational domain is fixed in plan ( $x=10$  m and  $y=11$  m) but with variable z dimension (4m; 5,5m; 7m). Mesh size was kept uniform with a dimension of 10 cm x 10 cm x 20 cm (in x, y and z-direction). The maximum number of cells was 385000. The external boundary domain was fixed as open for the following planes:  $X_{min}$ ,  $X_{max}$ ,  $Y_{min}$ ,  $Y_{max}$  and  $Z_{max}$ . Only the “floor” ( $Z_{min}$ ) was characterized as a grass plan. The number of particles per cell was set considering that exists an inverse proportion with the cell size, so compared with experiments described by Mell *et al.* (2009), the number of particles per cell was increased. In this case, 16 particles per cell were adopted. The ignition was set with a fire ramp in the first 10 seconds. The adopted HHRPUA for the ignitors was 250kW/m<sup>2</sup>. Additionally, cases with the wind blowing, separately in x-direction (wind N-S) and y-direction (wind E-W), both with 0,5m/s, were studied.

## 4 RESULTS AND DISCUSSION

### 4.1 Numerical simulations

The simulations were run on Intel Core 3.07 GHz processor. The simulations for the smaller domain took around 90 minutes whereas the ones for the larger domain took about 333,5 minutes. Time histories of the AST, WT, HRR are plotted in the next figures. The data obtained from the simulations and represented in Fig. 3 was extracted from the devices positioned in the middle of the glass window (see previous Fig. 2 c). Observing Fig. 3 a), the recorded behaviour can be separated into three time periods, namely [0s – 10s], [10s – 22s], [22s – 30s]. In the first period, the Adiabatic Surface Temperature increased slowly, and the value is essentially constant at around 75°C only due to the “Ignitor”. In the second period, the “flash-over” phase, AST has a significant increase of more than 400°C, reaching the peak value of 501°C in the AST3 device. Finally, in the last period, AST decreases rapidly since the available fuel was consumed and the fire self-extinguished. For this parameter, the most critical condition was reached with the direction of wind East-West (y-direction). This is reasonable since this is the direction where the wind blows directly against the façade with the glass window. For both Fig. 3 a), b) from 0s up to 20s, the two curves with wind N-S and E-W have quite the same values (reaching 450°C for AST and 55°C for WT). Just regarding Fig. 3b) the wall temperatures (WT) in the middle of the glass window show that the difference between peak values (at 24s) is 5°C for E-W and N-S wind. This discrepancy grows to 12°C when comparing E-W wind curve with the curve without wind.

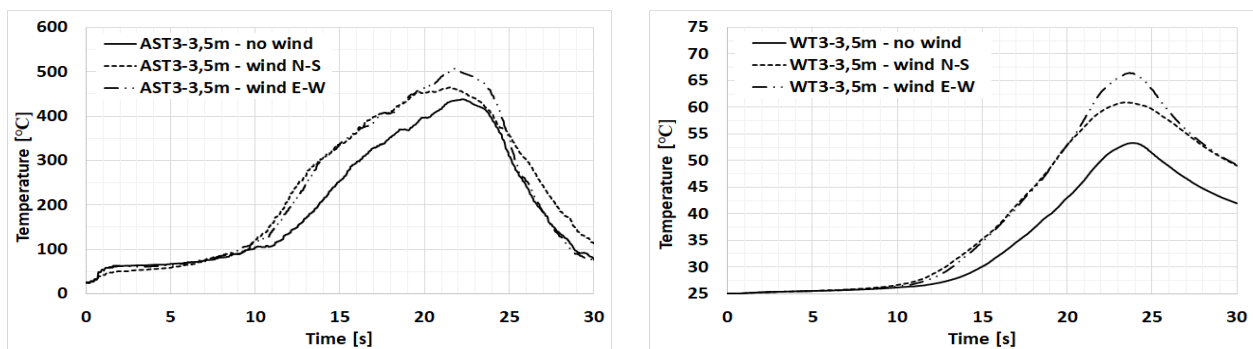


Fig. 3 a) Adiabatic surface temperature. b) Wall temperature

Concerning Fig. 4a) the maximum HRR was observed for the situation with no wind. When the wind was introduced the HRR peak value was reduced by about 19% (3MW), but it has presented almost identical results regardless of the adopted wind direction. A time delay of 5 seconds exists between HRR peak values of no wind case and N-S/E-W case. Regarding Fig. 4b) for thermocouple (TP2) (see Fig. 2c) the difference between top values of no wind case and wind E-W is 20°C, but the difference is reduced to 5°C when comparing no wind case with wind N-S.

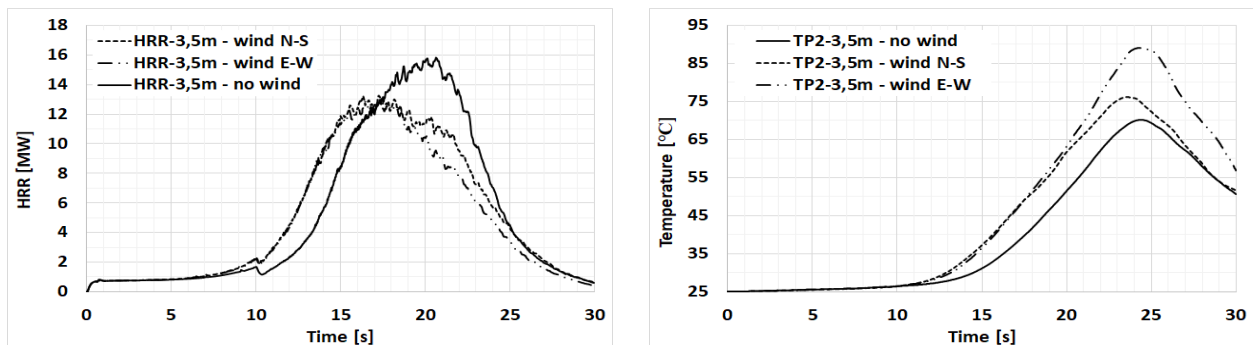


Fig. 4 a) HRR (Heat Release Rate). b) TP2 (thermocouple).

In Fig. 5 the Gas Temperature distribution is depicted as a function of time. The slice is parallel to the façade with the glass window and located at 1,5m from that façade (see Fig. 2 b). Three moments are represented considering 5 s intervals. The depicted images refer to the case with the wind blowing in North – South orientation with 0,5m/s. It is worth noting that due to the adopted wind speed the left tree in Fig. 5 did not combust despite the use of similar “Ignitors” for all trees, whereas the other two trees on the right side did combust completely reaching a temperature above 700°C.

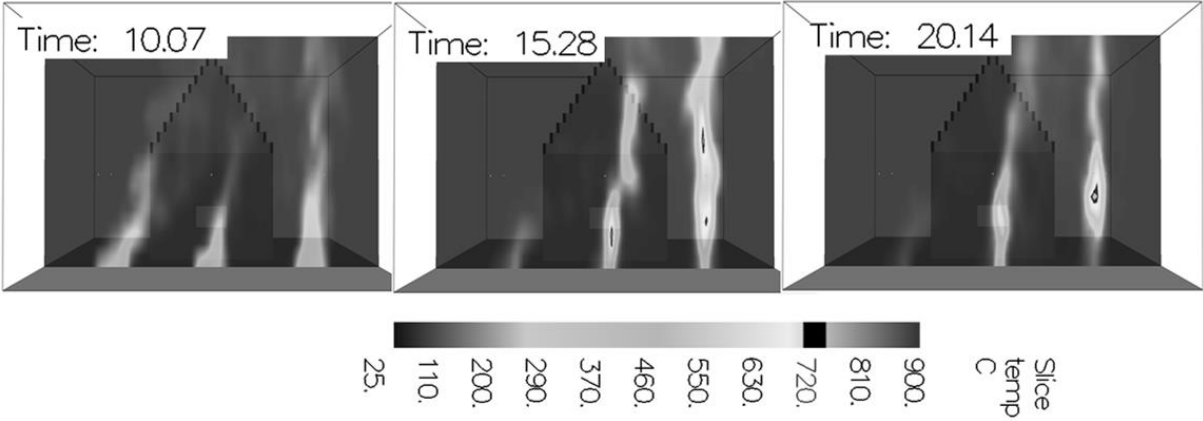


Fig. 5 Gas temperature distribution at the position of the trees (T1-T2-T3).

**4.2 Parametric study**

Considering the reference model developed taking into consideration the studies performed by (Mell *et al.*, 2009) a brief parametric study was undertaken to assess the influence of some parameters, such as the height of the trees, on the exposed surfaces of the building. Figure 6 a) and b) show respectively information about Adiabatic Surface Temperature and Wall Temperature in the middle of the glass window. It was observed that increasing the height of the trees also temperatures increased. Also, observing the time behavior, higher trees reached the maximum Adiabatic Surface Temperature (AST) after 22 s whereas with the shorter trees the maximum AST was reached after 14 s. For both thermal parameters AST3 and WT3, the difference between maximum and minimum values is identical (about 24%).

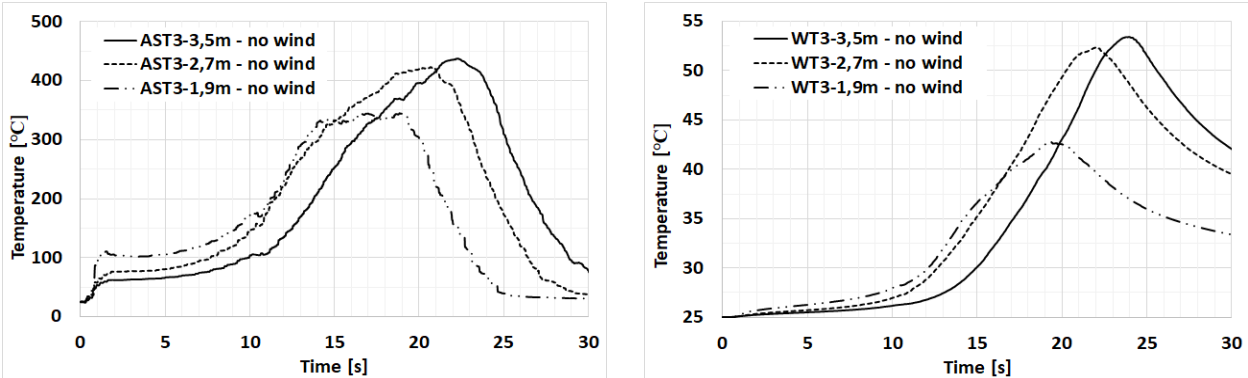


Fig. 6 a) Adiabatic Surface Temperature (AST). b) Wall Temperature.

**6 CONCLUSIONS**

Wildfires present severe risks to the built environment and communities. The paper intends to raise awareness on the subject showing future research paths based on the performance-based approach and considering a holistic approach. In this paper, a small theoretical wildfire scenario in the vicinity of a building was modelled and analysed. The Fire Dynamics Simulator software was used. Parameters such as adiabatic surface temperature, wall temperature, gas temperature and HRR were assessed, considering the variation of

physical elements like the presence of wind and its relative orientation as well as the height of trees. Results and trends curves were showed.

This is also the first step to consider the principles of fire safety engineering in the protection of the built environment against wildfires, with the final goal of creating specific legislation for buildings in the Wildland Urban Interface. Future research includes the definition of specific risk assessment methodologies for WUI areas, including simulation of wildfires at the macroscale and microscale level, understanding heat transfer and fire propagation phenomena between wildfires and urban fires, enabling the coupling between CFD and FEM tools to perform advanced numerical simulations to propose sounding and effective fire protection measures.

## ACKNOWLEDGMENTS

The authors gratefully acknowledge the Portuguese Foundation for Science and Technology (FCT) for its support under the framework of the research project PCIF/AGT/0062/2018 – INTERFACESEGURA – “Segurança e Resiliência ao Fogo das Zonas e Interface Urbana-Florestal”, financed by FCT through National funds. This work was partly financed by FCT / MCTES through national funds (PIDDAC) under the R&D Unit Institute for Sustainability and Innovation in Structural Engineering (ISISE), under reference UIDB / 04029/2020.

## REFERENCES

- Bento-Gonçalves A., Vieira. A. 2020. *Wildfires in the wildland-urban interface: Key concepts and evaluation methodologies*, Science of The Total Environment, Volume 707, 135592 - <https://doi.org/10.1016/j.scitotenv.2019.135592>.
- Boboulos Dr. M, 2013. *Biomass Properties and Fire Prediction Tools*, 1<sup>st</sup> edition. <http://thuvienso.bvu.edu.vn/bitstream/TVDHBRVT/15457/1/Biomass-Properties-and-Fire-Prediction-Tools.pdf>.
- Faiz Tharima A., Mujibur Rahman Md, Zamri Yusoff M. 2017. *Verification and Validation of Fire Dynamic Simulator for Enclosed Car Park*, International Journal of Modeling and Optimization, Vol. 7, No. 2, April 2017.
- Falkenstein-Smith R., McGrattan K., Toman B., Fernandez M., 2019. *Measurement of the Flow Resistance of Vegetation* - NIST Technical Note 2039 - <https://doi.org/10.6028/NIST.TN.2039>.
- Finney, Mark A., 2006, An Overview of FlamMap Fire Modeling Capabilities. In: Andrews, Patricia L.; Butler, Bret W., comps. 2006. *Fuels Management-How to Measure Success: Conference Proceedings*. 28-30 March 2006; Portland, OR. Proceedings RMRS-P-41. Fort Collins, CO: U.S. Department of Agriculture, Forest Service, Rocky Mountain Research Station. p. 213-220.
- Lourenço L.; Félix F.; 2019. *As vagas de incêndios florestais de 2017 em portugal continental, premissas de uma quarta ‘geração’?* territorium 26 (II), 2019, 35-48, journal homepage: <https://territorium.riscos.pt/numeros-publicados>. [https://doi.org/10.14195/1647-7723\\_26-2\\_3](https://doi.org/10.14195/1647-7723_26-2_3).
- Manzello S.L., Blanchi R., Gollner M.J., Gorham D., McAllister S., Pastor E., Planas E., Reszka P., Suzuki S., 2018. *Summary of workshop large outdoor fires and the built environment*, Fire Safety journal, Volume 100, pages 76-92. <https://doi.org/10.1016/j.firesaf.2018.07.002>.
- McGrattan K., McDermott R., Hostikka S., Weinschenk C., Overholt K.. 2013. *Fire Dynamics Simulator, Technical Reference Guide, Volume 1: Mathematical Model*. FDS Version 6.0.1 - SVN Repository Revision: 17529. Fire Research Division Engineering Laboratory Gaithersburg, Maryland, USA. Simo Hostikka VTT Technical Research Centre of Finland Espoo, Finland. Jason Floyd Hughes Associates, Inc. Baltimore, Maryland, USA.
- Mell W., Maranghides A., McDermott R, Manzello S.L., 2009. *Numerical simulation and experiments of burning douglas fire trees*, Combustion and Flame, Volume 156, Issue 10, pages 2023-2041. <https://doi.org/10.1016/j.combustflame.2009.06.015>.
- Mell W.E., Manzello S.L., Maranghides A., Butry D, Rehm R.G., 2010. The wildland–urban interface fire problem – current approaches and research need. International Journal of Wildland Fire 2010, 19, 238–251. <https://www.publish.csiro.au/wf/WF07131>.
- Sandström J., 2013. *Thermal Boundary Conditions Based on Field Modelling of Fires*. Lulea University of Technology, Sweden. <http://www.diva-portal.org/smash/get/diva2:990371/FULLTEXT01.pdf>.
- Tecnosylva (2020) Wildfire Analyst. Operational wildfire behavior system. <http://www.wildfireanalyst.com> (Verified August 2020).

## WIND DRIVEN (FORCED DRAUGHT) IMPACT ON ENCLOSURE FIRES

Jan Smolka<sup>a</sup>, Kamila Kempná<sup>a</sup>, Pavel Danihelka<sup>b</sup>, Eleni Asimakopoulou<sup>c</sup>,  
Tomaž Hozjan<sup>d</sup>, Petr Kučera<sup>a</sup>, Paul Grimwood<sup>e</sup>

<sup>a</sup> VSB-Technical University of Ostrava, Faculty of Safety Engineering, Czech Republic

<sup>b</sup> Occupational Safety Research Institute, Czech Republic

<sup>c</sup> University of Central Lancashire, School of Engineering, United Kingdom

<sup>d</sup> University of Ljubljana, Faculty of Civil and Geodetic Engineering, Ljubljana, Slovenia

<sup>e</sup> Kent Fire and Rescue Service, United Kingdom

### Abstract

Wind-driven, or forced draught, fires are usually caused by high velocity airflows entering the compartment of fire origin under numerous circumstances, e.g. external winds; failure of windows, façade components or erroneous PPV application. Their effects are more evident in modern energy efficient or high-rise building fires resulting in increased firefighter operational injuries and influencing tactical decision making of incident commanders, choice of equipment, and firefighting and evacuation procedures. In the current work, relevant data from wind driven fires encountered in various types of buildings including bio-based, historical and buildings of specific use are collected and analysed. It is revealed that wind-driven fires can inflict complex fire behaviour which can create difficulties in extinguishing, evacuation or have a negative impact on the structure. The hazards and risks associated with the health and wellbeing of occupants and firefighters are also highlighted and analysed.

**Keywords:** fire, wind, wind-driven, forced draught, high-rise buildings, fire dynamics.

### 1 INTRODUCTION

In the history, many big fires of cities were strongly influenced by wind, examples being a series of fires in USA, October 1871: Peshtigo Fire (ca. 1500 fatalities), Great Michigan Fire (482 fatalities), Great Chicago Fire (290 fatalities). Wind-driven fires in structures, especially in high-rise buildings, are due to external conditions (e.g. wind) or building features (e.g. orientation and geometry of vent or façade elements). Additional effects creating both positive or negative pressure differentials and forced air movements can also influence fire development due to stack-effects frequently encountered in high elevators, stair shafts or air conditioning systems. Another reason for the occurrence of forced draught conditions is the misuse of positive pressure ventilation (PPV) application during firefighting intervention (Grimwood, 2017; Fishlock, 1996; Kerber and Madrzykowski, 2009). Urban landscape constantly evolves globally, as high-rise residential and commercial buildings with new façade construction techniques continue to grow in height and number. Furthermore, due to stricter requirements for building energy performance, there is a growing trend of installing combustible thermal insulation materials, that are usually flammable such as polystyrene-based, on building façades. Although, wind-driven fires may affect all types of buildings, evidence highlight that modern energy efficient buildings with complex designs and increased sizes may have increased vulnerability. Recently, there has been an alarming occurrence of façade fires in high-rise buildings where the effect of external wind is significant, resulting in high numbers of casualties, structural damage and property loss. Currently, there is limited research on the understanding of the physical phenomena associated with wind-driven fires, design guidelines and firefighting procedures in modern combustible buildings. To fill this knowledge gap, in the current work relevant data from wind driven fires encountered in various types of buildings including bio-based, historical and buildings of specific use are collected and analysed. Data collected from a number of wind-driven fires occurred in the past two decades, indicate that

hazardous conditions and aftermath are particularly important in flammable structures as they can impact health and wellbeing of occupants, firefighters and compromise the building safety.

## 2 WIND DRIVEN FIRES

Wind driven fires are also referred to as Forced Draught (EN 1991-1-2, 2002), Force Draft, Blow Torch and Wind Fed fire. Wind-driven fire conditions can occur in specific conditions and can therefore rapidly change fire dynamics and fire development in building with a significant impact, leading in some cases to serious injuries or death of victims and firefighters. Wind driven fires can significantly change fire dynamics and flow path in a fire compartment. Main causes of wind-driven (forced draught) fires are identified and listed below (Fishlock, 1996):

- **External wind**, e.g. direction of vents, weather conditions or area
- **Mechanical ventilation**, e.g. appliance of PPV, air conditioning systems
- **Stack-effect**, e.g., elevators shafts, high buildings, geometry of the structure
- **Additional reasons**, e.g. inappropriate use of PPV or stack effect in structure.

A thorough investigation of wind-driven fire in non-flammable structures, conducted by National Institute of Standards and Technology (NIST), revealed its effect on prevailing conditions and firefighting approaches. In a series of large-scale experiments, structures were exposed to increased wind conditions, 9-11 m/s; experimental results indicate that increased temperatures can be observed in the flow-path of the bulkhead door exceeding 400°C. Just before window failure heat release rate (HRR) was 1 MW and after its failure during the post-flashover stage HRR suddenly increased from 15 MW to 20 MW. In case fire would involve part of the construction that would be combustible, the increase in HRR would be even higher (Kerber and Madrzykowski, 2009).

### 2.1 Repository of recent wind-driven fires

To investigate wind-driven fire development, its implication to intervention and impact on buildings and environment, a repository of recent high impact wind-driven fires is presented in Tab. 1. Cases are categorised as confined to a single structure (single-structure) and widely spreading into several adjacent structures (community-scale fire spread). They all have resulted in serious injuries or casualties of firefighters, limiting firefighting attacks and causing serious damages (in some cases even collapse) on structures and environment.

Tab. 1 –Repository of recent wind-driven fires.

Single-structure wind driven fires				
Location, year	Storeys	Consequences	Average/max wind speed [m/s]	Reference
Ottawa, Canada, 2007	4	Rapid (in a few minutes) fire development and spreading	-/ 16	(Ottawa Fire Services, 2007)
Houston, USA, 2009	1	Breaking large window changed flow-path of fire against firefighters	9/ 11	(Harlow and Hobbs, 2009)
Brownstone, USA, 2014	4	Changed of flow-path from basement, sudden fire development caused hose damage and trap of firefighters	20/ 31	(Cdc.gov, 2016)
Virginia, USA, 2008	2	Wind limited firefighting efficiency with combination of low pressure in hose line caused serious impact to firefighting intervention	11/ 21	(Bowyer, 2008)
Community-scale wind driven fires				
	Buildings			
Lærdal, Norway, 2014	40 (60 damaged)	Strong wind causes fast fire spreading between non-adjacent buildings	12/ 15	(Steen-Hansen et al., 2016)
Cohoe, USA, 2017	3 (29 damaged)	Strong wind caused fire spreading to adjacent buildings from external fire source. Intensive fire caused fast spreading in structure and premature collapse of building.	21/ 31	(Fahd, 2017)
Mati, Greece, 2018	2,500	In this WUI fire strong wind caused spread from vegetation to buildings and then to the whole community. Firebrands generated from vegetation and structure fuel were identified as the main mechanism of fire spread due to strong wind.	16/ 23	(Lagouvardos, 2019)

Tab. 1 provides evidence of the negative impact of rapid wind-driven fire spread in structures but also how it may evolve community-scale fires that affect numerous buildings or objects. It is worth indicating the two most significant fires on community scale, those are the Lærdal Fire in Norway or the most tragic fire in Europe in 21<sup>st</sup> century Mati Fire in Greece. These fires represent high risk of possible fire spread between buildings in windy conditions, caused mainly by lofted firebrands from vegetation or structure fuel. High speed wind can bend flames, affecting preheating of fuel influencing the rate of spread as happened in Mati Fire, according to victims’ testimonies and records. Under strong wind conditions and lofted firebrands, as demonstrated in Lærdal (Fig. 1), it is observed that fire spread can extend up to tens or hundreds of metres.

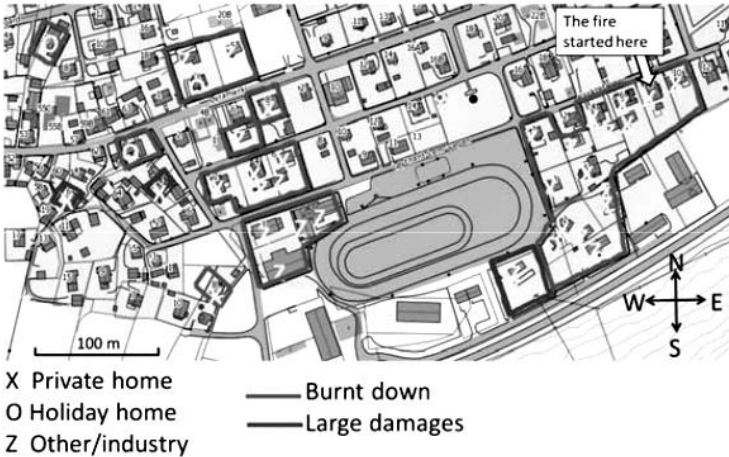


Fig. 1 – Map of area with damages and burnt buildings in Lærdal caused by strong wind (Steen-Hansen et al., 2016).

**2.2 Fire Hazard of Flammable Structures**

Additional findings from post-fire images in single-structure buildings are exhibited in the case of dormitories fire in Luleå (Björkman, 2013) and in Houston (Harlow, Sr. and Hobbs, 2009). During those cases, fire spreading in void spaces and negative impact of firefighting intervention to structures led to destruction of the buildings, Fig. 2.



Fig.2 – Buildings after Houston fire (left) and Luleå dormitories fire (right) (Björkman, 2013; Harlow, Sr. and Hobbs, 2009)

The above examples along with findings from research, interviews with firefighters and investigation reports provide further evidence on the extreme impacts that wind driven fires may have on structures with combustible components. Under such circumstances, it can be expected that forced draught conditions influence fire spread and may cause more intensive fire behaviour (Grimwood, 2017; Smolka et al., 2018). Also associated fire hazards include a more rapid growth of fire, the creation of natural flow-paths for fire, difficulty in observing hidden fire spread within the structure, premature collapse of buildings, building parts falling e.g., encapsulation as gypsum, repeated occurrence of flashover (in context with CLT (Karuse and Just, 2018)), repeated ignition of fire after extinguishing (hydrophobic materials), cracking of wood may pose hidden fire

spreading paths, unknown materials fire behaviour under real conditions and its reaction to extinguishing.

### 2.3 Wind Impact to Fire

Experimental investigation in wind-driven fires conducted by NIST (Kerber and Madrzykowski, 2009) highlight a fire that could not develop to its flashover stage due to excess of fuel pyrolysis and lack of ventilation in the room until windows fail, allowing a sudden delivery of fresh air into the compartment and increasing oxygen available to the fire. Under conditions without windows failing, the fire during the experiments did not spread outside the apartment of the fire origin. Circumstances however changed when a flow-path appeared despite absent external wind inducing increase of temperature and velocities profiles in corridors and fire spreading throughout the building. A forced draught therefore may support fire spreading within a building as well as between buildings. The wind driven fire spreading mechanism in a building can be divided into internal and external (including cladding, void spaces, combustible facades and floor to floor) fire spread. The serious impact of a forced draught to fire spreading in buildings and adjacent building is shown in Fig. 3, the Cohoe fire in New York (USA) (Fahd, 2017), where the wind that day approached to 31 m/s in gusts, fire damaged 29 buildings and 3 buildings were totally burned.



Fig. 3 – Development of Cohoe fire scene in 30 mins (OneShot, 2017).

The forced draught effect to fire conditions may result to dangerous conditions for firefighters and may further complicate firefighting attack. These conditions can change dramatically within a few seconds or minutes as described in investigation reports (Ottawa Fire Services, 2007; Harlow, Sr. and Hobbs, 2009; Bowyer, 2008; Cdc.gov, 2016; Madrzykowski and Kerber, 2009). Among them, the most common conditions occurred during wind driven fires are: initiation of extreme fire behaviour (flashover, backdraft, smoke-explosion, etc.), decrease / increase of fire intensity, flame deflection, change in flow-path, change in temperature profile in compartment and fire spread.

Parameters of a compartment relevant to vulnerabilities due to wind-driven fires can be based on the evidence summarised in Fig. 4 and in principle it follows and is complementary to Fire Behaviour Indicators (FBI) being used during Compartment Fire Behaviour Training (CFBT) of firefighters (Hartin, 2018). These parameters include construction, airflow, and oxygen access by openings and compartment fire load.

The significant effect of wind-driven fires is also observed in wildland urban interface (WUI) fires. During WUI, firebrands can ignite not only surrounding buildings but also buildings which are not adjacent. Example of dangerous if this kind of fire spread in community with flammable wood-based structures is Lærdal Fire (Norway) in 2014. The fire started in private home in the municipality and strong wind-driven fire caused 40 buildings burnt out and required evacuation of 681 people (Steen-Hansen et al., 2016).

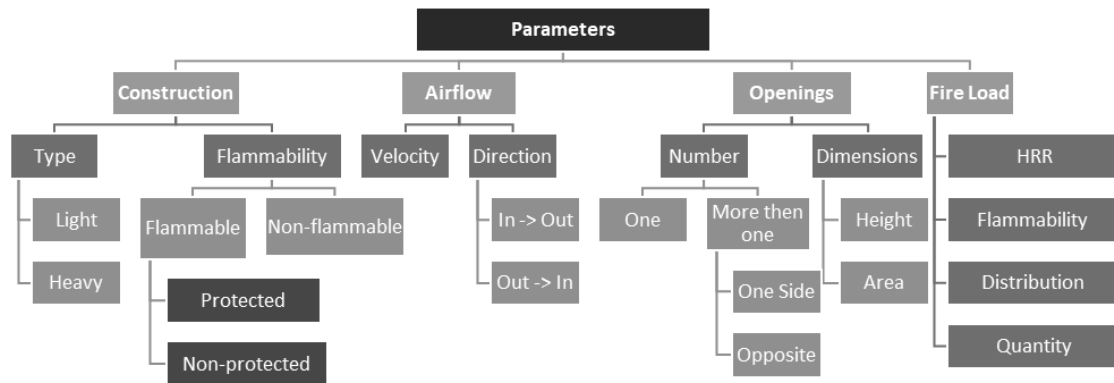


Fig. 4 Fire compartment parameters vulnerable to wind-drive fire conditions

### 3 EXTINGUISHING IMPACT TO STRUCTURE

Fire spreading under encapsulation or in void spaces are difficult for localization and may require disassembling construction for extinguishing of hidden fire. An important factor differentiating between required amounts of water for extinguishing of compartment fire is a non-combustible and combustible structure. This factor also influences structural fire resistance. Extinguishing a combustible structure may require increased amount of water due to the increased fire load of the structure and to prevent its smouldering and repeated ignition.

Evidence from Luleå fire (Björkman, 2013) demonstrate how damages to encapsulation of the structure can be caused by fire and water during intervention caused falling of gypsum board which may cause injury of firefighters present in building. Extinguishing of hidden spread fire may require forced opening up of the construction for extinguishing and exclusion of repeated fire ignition or fire development. This ‘cutting in’ procedure can decrease structural stability and may require calling out firefighters from inside and lead firefighting attack from outside for safety reasons (Björkman, 2013). Strong wind may prevent aerial platform fire truck from involvement in fire and rescue activities, too. Wind-driven conditions in compartment, where failure of windows cause flow-path from outside causing an increase of air velocity and fire intensity in compartment and its spreading inside the corridor of building, resulting in hazardous conditions for firefighters leading intervention (Madrzykowski and Kerber, 2009; Harlow, Sr. and Hobbs, 2009). In a wind-driven fire the water delivery by water mist and spray may be impacted and ineffective.. This may prevent fast and effective extinguishing. In this situation it is required to apply a solid stream or a combination of solid and spray stream which increases efficiency in approaching the fire (Fishlock, 1996). Based on described conditions, wind-driven fire may cause increased requirements on water used for extinguishing a fire and increasing damage to structure of buildings. The safety of firefighters during firefighting interventions needs to be considered, especially in high-rise buildings with combustible components.

### 4 FIRE SAFETY DESIGN CONCERNING FORCED DRAUGHT CONDITIONS

Building codes and regulations include methods and measures to ensure maximum safety against fire events. In the EU, the structural Eurocodes in combination with each member state’s regulations are applied in order to determine a wide range of analytical procedures and design rules concerning the construction of structures; in this context, a set of minimum requirements for the design and construction of buildings is proposed. There are two ways of demonstrating compliance with EN 1991-1-2 (EN1991-1-2, 2002), either following the prescriptive or the performance-based approach. The effects of wind, ventilation conditions and existence of balconies in the Externally Venting Flames (EVF)’s characteristics are also considered. According to EN 1991-1-2 if there are windows on opposite sides of the compartment or air flow from another source, then Forced Draught (FD) conditions apply. Otherwise, No Forced Draught (NoFD) conditions are used for the

calculations. Estimation of the EVF shape dimensions and its thermal characteristics is mainly based on the conservation laws of mass, momentum and energy of upwards flowing jets or, in the case of FD conditions, on temperature distribution patterns of jets without considering buoyancy and heat transfer effects (Asimakopoulou et al., 2017). Nevertheless, there is still lack of evidence on how EVF shape can be correlated in flammable façades.

## 5 DISCUSSION AND CONCLUSIONS

In the current work, relevant data from single-structure and community-scale wind driven fires in various types of buildings were collected and analysed. Relevant data indicate that wind-driven fires can inflict complex fire behaviour which can create difficulties in extinguishing, evacuation or have a negative impact on the structure. As demonstrated in this research work, it is imperative to update the scientific data regarding façade fires under external wind conditions, if one were to make direct suggestions for improving the existing fire safety design of buildings, regulations, evacuation strategies, firefighter operational decisions and strategies.

## ACKNOWLEDGMENT

This output was financially supported by institutional support for the long-term conceptual development of the research organization for the years 2018-2022 and is part of the "Occupational Safety in Volunteer Fire Brigades" project.

## REFERENCES

- Asimakopoulou E., Kolaitis D., Founti M. 2017, Assessment of Fire Engineering Design Correlations Used to Describe the Geometry and Thermal Characteristics of Externally Venting Flames. *Fire Technology* 53, pp 709-739.
- Björkman, C., 2013. Brand i flerbostadshus i Luleå Klintvägen. Fördjupad olycksundersökning. Luleå: Umeå kommun Brandförsvär & Säkerhet.
- Bowyer, M., 2008. Fire Fighter Fatality Investigation Report F2007-12 | NIOSH | CDC.
- Cdc.gov. 2021. Fire Fighter Fatality Investigation Report F2014-09 | NIOSH | CDC.
- EN 1991-1-2 (2002) (English): Eurocode 1: Actions on structures - Part 1-2: General actions - Actions on structures exposed to fire [Authority: The European Union Per Regulation 305/2011, Directive 98/34/EC, Directive 2004/18/EC
- Fahd, J., 2017. Fire Investigation Report of Findings. Cohoe: Homeland Security and Emergency Services.
- Fishlock, M, 2016. Can we Fight and Extinguish Full Height, Tall Building Fires? United Kingdom
- Grimwood, P., 2017. Eurofirefighter: 6,701 Building Fires. Huddersfield: D & M Heritage Press.
- Hanuska, Z., 1996. Metodický návod k vypracování dokumentace zdolávání požárů. Prague: Ministry of Interior - The General Directorate of Fire Rescue Service of CR.
- Harlow, Sr., J. and Hobbs, D., 2009. Investigation Number FY 09-01. Firefighter Fatality Investigation: Investigation Number FY 09-01. Houston, Texas, USA: TEXAS STATE FIRE MARSHAL'S OFFICE, TEXAS.
- Hartin, e., 2018. Extreme Fire Behavior: Understanding the Hazard. [online] Extreme Fire Behavior: Understanding the Hazard | CTIF - International Association of Fire Services for Safer Citizens through Skilled Firefighters.
- Karuse, M. and Just, A., 2018. LARGE SCALE FIRE TEST OF CLT – FIRE SPREAD THROUGH THE JOINTS AND PENETRATIONS.
- Kerber, S. and Madrzykowski, D., 2009. Fire Fighting Tactics Under Wind Driven Fire Conditions: 7-Story Building Experiments. NIST Technical Note 1629. Gaithersburg: U.S. Department of Commerce.
- Lagouvardos, K., Kotroni, V., Giannaros, T. and Dafis, S., 2019. Meteorological Conditions Conducive to the Rapid Spread of the Deadly Wildfire in Eastern Attica, Greece. *Bulletin of the American Meteorological Society*, 100(11), pp.2137-2145.
- Madrzykowski, D. and Kerber, S., 2009. Fire Fighting Tactics Under Wind Driven Conditions: Laboratory Experiments. NIST Technical Note 1618. U.S. Department of Commerce.
- OneShot, K., 2017. Fire Destroys Several Buildings. [video] Available at: <<https://www.youtube.com/watch?v=pLu8ivri9KY>: YouTube>
- Ottawa Fire Services, 2007. Incident #07 - 8038. Workers' Report - Critical Injured: Forward Avenue Fire. Ottawa: Ottawa Fire Services.
- Smolka, J, Kempna, K. et al., 2018. Guidance on Firefighting and Bio-Based Materials, COST Action FP1404, Zürich, Switzerland
- Steen-Hansen, A., Storesund, K., Fjellgaard Mikalsen, R., Paul Stensaas, J., Sæter Bøe, A. and Hox, K., 2016. The Large Fire in Lærdal, January 2014: How did the Fire Spread and what Restricted the Fire Damage?

## NUMERICAL VALIDATION OF FIREFOAM FOR NARROW FACADE CAVITY FIRE

Benjamin Khoo<sup>a</sup>, Wolfram Jahn<sup>b</sup>, Panagiotis Kotsovinos<sup>c</sup>, Guillermo Rein<sup>a</sup>

<sup>a</sup> Department of Mechanical Engineering, Imperial College London, United Kingdom

<sup>b</sup> Department of Mechanical and Metallurgical Engineering, Pontifical Catholic University of Chile, Chile

<sup>c</sup> Arup Manchester, United Kingdom

### Abstract

Facades with cavities can introduce additional fire risks in a building as the cavity may increase heat flux on structural components, causing the facade to fail. Therefore, it is essential to understand how different facade cavity configurations can affect heat transfer. Performing large-scale fire tests to study this, whilst desirable, can be very costly. This work assesses the capability of fireFOAM to model facade cavity fires to allow reliable use of the model to study the effect of different facade configurations. The results show that the model can accurately predict fluid flow, convective heat transfer, and air buoyancy. However, validation of the combustion physics shows the model underpredicts the flame height and upward exit velocity by up to 30%. The model was also incapable of simulating flame lift-off, which may affect heat flux prediction. However, provided caution is exercised to ensure the model's limitation is considered, the model suitable for extrapolation.

**Keywords:** Heat Flux, CFD, Cavity

### 1 INTRODUCTION

A facade is often one of the most complicated and largest construction cost of high rise building that can cost up to 20-25% of the total (Zemella and Faraguna, 2014). This is due to the multiple objectives that facade engineers must achieve to construct a safe and comfortable environment (Herzog, Krippner and Lang, 2017).

One typical typology in facade systems in modern building design is the presence of facade cavities in the building. These cavities may contribute to increased fire risk on the facade system due to the chimney effect and increased re-radiation heat transfer between the cavity walls. The increase in heat flux within the cavity could weaken the structural components of the facade, resulting in falling facade debris which could harm people around. Unfortunately, despite the considerable effect of the facade cavity, there are currently no well-established models or theories that allow engineers to quantify the impact of cavities on a facade fire (Bonner and Rein, 2018).

Investigations on heat transfer mechanism within the cavity were studied by several (TAMANINI and MOUSSA, 1980; Most *et al.*, 1989; Foley and Drysdale, 1995; Livkiss *et al.*, 2018). Their studies found that heat flux onto panels increases as cavity width reduces due to altered airflow that affects convective heat transfer and re-radiation from the opposite panel.

While these studies suggest that reducing cavity width would increase incident heat flux on the facade structural component, a narrow cavity does not always result in the highest heat transfer. A study by Jamison *et al.* found that a facade system with combustible insulation produces a more severe fire when the cavity is wider due to the increased air entrainment to support the combustion of the insulation in the cavity (Jamison and Boardman, 2016).

These studies suggest that the facade cavity fires are problem complex and that there may be a cavity width where the heat flux on the facade structural component is at the highest. Therefore, further experiments are needed to improve our understanding of how facade configuration affects heat flux within the cavity to help design facades in a more informed way. Studying the effect of facade configuration using numerical methods could be a complementary solution, as different parameters can be investigated without additional cost. Nevertheless, due to the complex physics involved in a facade cavity fire, all sub-models used by the simulation need to be validated for a narrow cavity scenario to ensure the model is robust and has a limited compensation effect.

In this work, FireFOAM, a fire specific CFD widely used model built on the OpenFOAM libraries, is validated against several experiments available in the literature to determine whether it could be used to study different facade configuration fires reliably

## 2 METHODOLOGY

The fundamental physics that are governing a facade cavity fire can be broken down into five different phenomena: fluid flow, heat transfer, buoyancy, pyrolysis and combustion. These physical processes interact with each other and can affect the overall fire dynamic within the cavity. Therefore it is essential to reduce the compensation effect from these physics to allow reliable extrapolation of the numerical model in order to study different facade configurations. This is achieved by splitting the validation into six different scenarios with increasing complexity, as shown in Fig. 1

Only scenarios 1 to 4 are presented in the present work, as the integration of pyrolysis chemistry into the CFD model corresponds to a major leap in terms of complexity. The experimental data used to validate these scenarios are found in the literature (Page *et al.*, 1952; Hussain and Reynolds, 1975; Miyamoto *et al.*, 1986; Livkiss *et al.*, 2018). Scenarios 5 and 6 are still in progress and are planned to be presented in future papers.

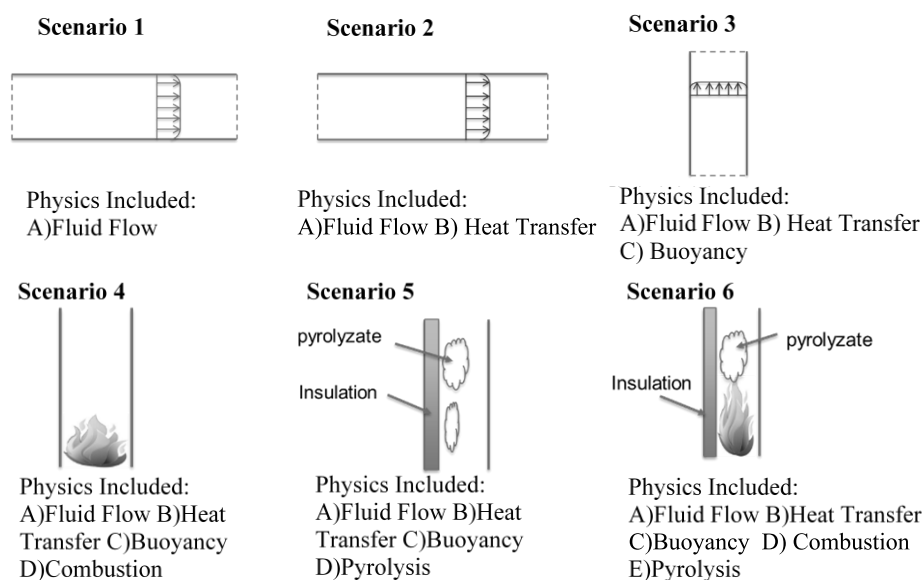


Fig. 1 The different physics involved in a cavity fire and the corresponding scenario to validate the model's physics

## 3 NUMERICAL MODELLING

The simulations were performed using fireFoam-dev (*FireFOAM, version dev, 2017*), a solver based on the open-source framework, OpenFOAM. developed specifically for fire related physics. OpenFOAM provides numerical routines for solving partial differential equations by discretising them using the Finite Volume technique on structured and unstructured meshes. (*OpenFOAM, CFD package, 2017*).

In this work, a maximum Courant number of 0.8 was used when solving the time term in order to ensure numerical stability, following a second-order backward scheme. The convective terms and diffusive terms are discretised using the central differencing scheme with the diffusive terms using an explicit non-orthogonal correction. As for species mass transport, the terms are discretised using a second-order Total Variation Diminishing (TVD) scheme with Sweby limiter to ensure a bounded solution.

FireFOAM provides several options for the subgrid-scale (SGS) turbulence model, combustion model, and thermal radiation modelling. In the section below, the model used in these scenarios are explained.

### 3.1 Wall Heat Transfer

In fireFOAM, the default settings assume the simulation is wall resolved and do not use a wall model to estimate the convective wall heat transfer. The convective heat transfer is calculated as shown

$$q_c'' = k \frac{dT}{dx} \quad (1)$$

Where  $q_c''$  is the convective heat flux,  $k$  is the fluid thermal conductivity and,  $\frac{dT}{dx}$  is the fluid thermal gradient at the wall.

For thermal radiation, the Finite Volume Discrete Ordinates Model (fvDOM) is used in the present work to solve the Radiative Transfer Equation in FireFOAM. The radiation emission is modelled via the radiative fraction approach. The radiative fraction approach assumes that a portion of the HRR of fuel combustion is converted into thermal radiation, as shown below

$$\nabla \cdot q_R'' = \chi q_{comb}''' \quad (2)$$

Where  $q_R''$  is the incident radiation heat flux,  $\chi$  is the radiative fraction constant and  $q_{comb}'''$  is the volumetric HRR due to combustion. The radiative fraction,  $\chi$ , used is 0.27 which is within the range found experimentally (Hamins *et al.*, 1996), and the number of solid angles used for the simulation is 112.

### 3.2 Turbulences

In the present study, the SGS turbulence was modelled mainly with wall adapting local eddy-viscosity (WALE) model, as it predicts the SGS kinetic energy,  $k_{sgs}$ , and SGS eddy viscosity,  $\nu_{sgs}$ , better at near-wall region compared to the default k-equation model used as default in FireFOAM that gives unrealistically high  $k_{sgs}$  (Nicoud and Ducros, 1999; Ren *et al.*, 2016). The WALE model computes the SGS eddy viscosity,  $\nu_{sgs}$  as follows:

$$\nu_{sgs} = (C_w \Delta^2) \frac{(S_{ij}^d S_{ij}^d)^{\frac{3}{2}}}{(\tilde{S}_{ij} \tilde{S}_{ij})^{\frac{5}{2}} + (S_{ij}^d S_{ij}^d)^{\frac{5}{4}}} \quad (3)$$

Where  $C_w$  is the model constant with a coefficient of  $C_w=0.55$  based on (Ren, Wang and Trouvé, 2013).  $\Delta$  is the LES filter size,  $S_{ij}^d$  is the special tensor defined by Nicoud (Nicoud and Ducros, 1999), and  $\tilde{S}_{ij}$  is the resolved scale strain rate tensor.

To ensure the WALE model implemented is suitable for cavity flow, Smagorinsky and k-equation eddy viscosity models are also used in Scenario 1 and 2 to compare the differences between the models.

### 3.3 Combustion

The modified eddy dissipation combustion model (EDM) proposed by Ren *et al.* is the most commonly used combustion model for FireFoam and was used in the present study (Ren, Wang and Trouvé, 2013). The modified EDM expressed the fuel mass reaction rate as:

$$\omega_F''' = \frac{\rho}{\min\left(\frac{k_{sgs}}{C_{EDC} \varepsilon_{sgs}}, \frac{\Delta^2}{C_{Diff} \alpha}\right)} \min\left(\tilde{Y}_F, \frac{\tilde{Y}_{O_2}}{r}\right) \quad (4)$$

Where  $\rho$  is the gas density,  $C_{EDC}$  is the turbulent mixing timescale the model coefficient  $C_{EDC} = 4$ ,  $C_{Diff}$  is the molecular diffusion timescale coefficient  $C_{Diff}=4$ ,  $\alpha$  is the thermal diffusivity,  $\tilde{Y}_F$  is the fuel mass fraction,  $\tilde{Y}_{O_2}$  is the oxygen mass fraction, and  $r$  is the stoichiometric oxygen-to-fuel mass ratio.

## 4 COMPUTATIONAL DOMAIN

In Scenario 1, the numerical domain was  $200 \times 100 \times 63.5 \text{ mm}^3$ . The boundary conditions of the simulation for both streamwise and spanwise were periodic boundaries. For both the top and bottom of the domain, a no-slip boundary was applied. The velocity in the domain is perturbed to generate the initial turbulent field, and the bulk velocity in the domain is  $5.77 \text{ m/s}$ .

For Scenario 2, the numerical domain was  $200 \times 100 \times 17.8 \text{ mm}^3$ . The spanwise and streamwise boundary condition were also periodic boundaries. The top and bottom boundaries were no slip and has a fixed temperature of  $46^\circ\text{C}$  and  $30^\circ\text{C}$ , respectively. The velocity in the domain was perturbed, and the bulk velocity is  $4.66 \text{ m/s}$ .

As for Scenario 3, the numerical domain and the domain boundaries was shown in Fig. 2a, with  $W = 50 \text{ mm}$  and  $100 \text{ mm}$ . For the heated wall boundary condition, a value of  $104 \text{ W m}^{-2}$  and  $208 \text{ W m}^{-2}$  was applied and investigated for each cavity width.

The numerical domain of Scenario 4 is as shown in Fig. 2b, where  $Y$  is 240, 250, 260, and 300 for cavity widths  $W = 40 \text{ mm}$ ,  $50 \text{ mm}$ ,  $60 \text{ mm}$ , and  $100 \text{ mm}$ , respectively. The simulated burner HRR were  $6.5 \text{ kW}$  and  $12.92 \text{ kW}$ . The wall is modelled as Calcium Silicate, and its temperature is predicted using a 1D heat transfer model.

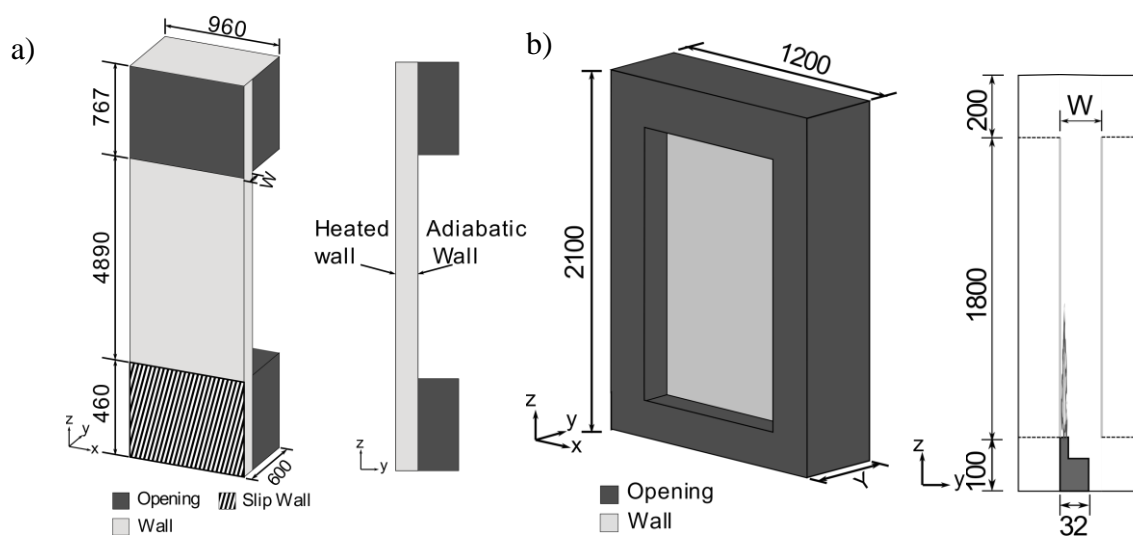


Fig 2 Computational domain of a) Scenario 3 and b) Scenario 4. All dimensions are in mm.

## 5 RESULTS

### 5.1 Scenario 1 – Fluid Flow Validation

The analysis shows that predictions of the mean velocity profile and the law of the wall of the three turbulence models fit the experimental data with reasonable accuracy, as presented in Fig 3a. The results show that all models can predict the fluid flow physics to a high degree of accuracy, although the k-equation and Smagorinsky model performs slightly better at predicting the law of the wall.

### 5.2 Scenario 2 – Heat Transfer Validation

For Scenario 2, all three turbulence models could accurately capture the velocity and temperature profile, as shown in Fig 3b. However, analysis indicates that the WALE model is slightly more capable of capturing both profiles. This is likely due to k-equation and Smagorinsky models taking a large incorrect value of  $v_{sgs}$  and  $k_{sgs}$  at the walls. In contrast, the WALE model can correctly predict the vanishing value of  $v_{sgs}$  and  $k_{sgs}$  near the wall, which is essential in predicting wall heat flux and near wall HRR for wall resolved simulations. Therefore, for Scenario 3 and Scenario 4, only the WALE model was used.

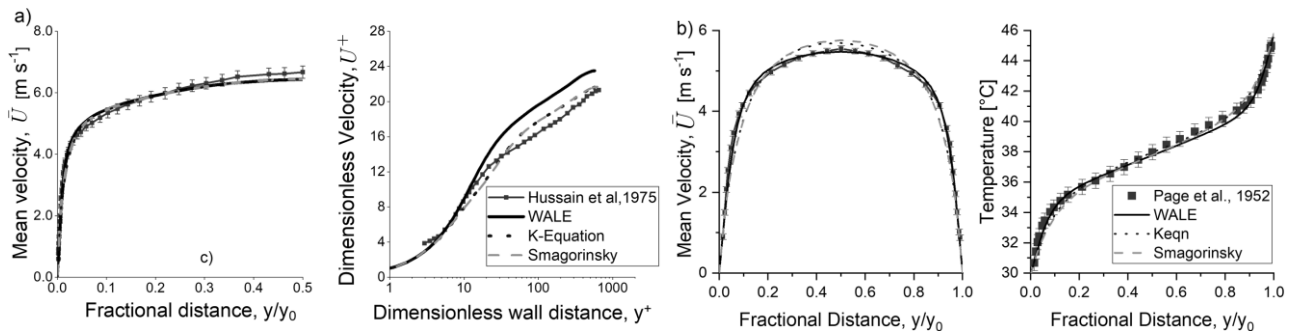


Fig 3 a) Mean velocity and law of the wall of Scenario 1 b) Mean velocity and temperature of Scenario 2

### 5.3 Scenario 3 – Buoyancy Validation

The results show that the model could capture the velocity profile due to buoyancy with reasonable accuracy for all cavity widths, albeit with slight overprediction, as shown in Fig 4a. This was likely due to the uncertainty of measured convection heat flux generated by the heated wall in the experiment. This may have resulted in an overestimation of the heat flux applied to the heated wall. Similarly, Fig b shows the heated wall temperature was predicted with reasonable accuracy.

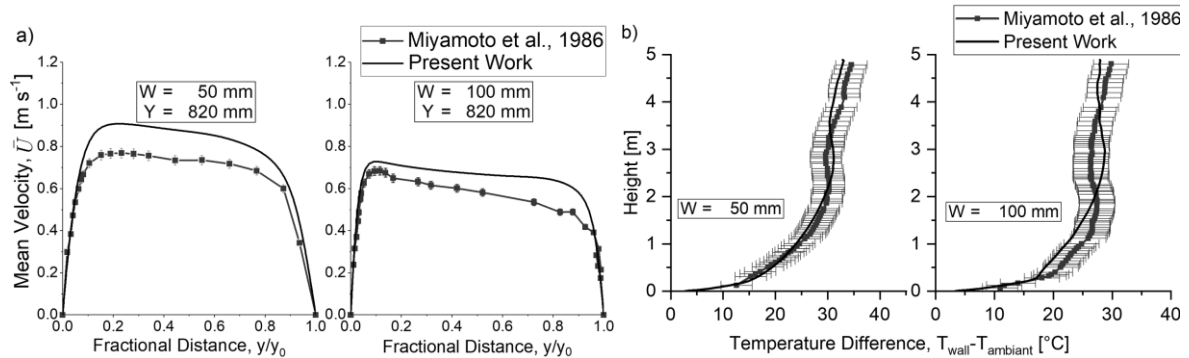


Fig 4 a) velocity profile for cavity widths of  $W = 50$  mm,  $100$  mm, at the height of  $820$  mm when  $q_w = 208$  W b) Temperature Difference along the heated wall when  $q_w = 104$  W

### 5.4 Scenario 4 – Combustion Validation

The simulation results show that for both burner HRR, the model tends to underpredict the flame height. Analysis shows that the flame heights were underpredicted by up to 30%. In both HRR, the underprediction seems to be worst when the cavity width is at  $40$  mm.

The upward exit velocity is measured  $1800$  mm above the burner. The predicted upward exit velocities for both burner HRR were averaged over  $10$  seconds. It was found that the predicted velocity was underpredicted at all locations by up to 30% too, as shown in Fig 7. The lack of physical bi-directional probes modelled in the simulation is likely to have caused these discrepancies.

The comparison of total heat flux along the centreline of the near wall of both  $6.5$  kW and  $12.92$  kW HRR at  $40$  mm cavity width is shown in Fig 7a and Fig 7b. The simulation results show a good prediction for HRR  $6.5$  kW HRR but were less accurate for the scenarios with HRR  $12.92$  kW. Plausible explanations for the errors are flame lift-off that was not simulated due to the combustion model used.

## 6 CONCLUSIONS

The ability of the fireFOAM model to predict the facade cavity fire with varying cavity width and configuration is investigated in this study. The model was validated against four scenarios in the present work to ensure that the fluid flow, heat transfer buoyancy, and combustion physics of the model is valid to study facade cavity fire. The current work does not consider the presence of any combustible insulation in the façade cavity that would introduce additional phenomena.

The results from the present work show that the current model is capable of simulating the four physics with reasonable accuracy. However, it is important to note that the model is only valid

if the model assumptions are true. Extrapolation of the model needs to be performed with caution to ensure the studies are within the model's capabilities and the effect of the model limitation is considered. Further experimental wall of façade cavity fires should be undertaken that would help to enhance current numerical models.

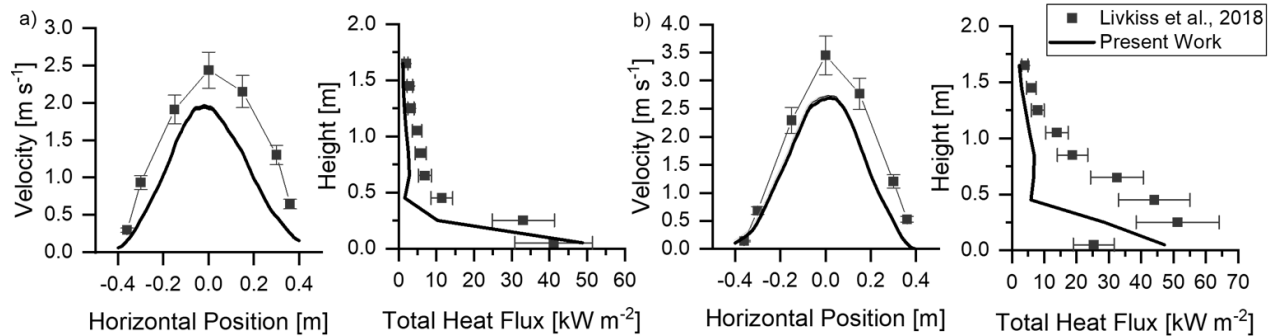


Figure 1 Upward exit velocity at the centre of the cavity and heat flux on the near wall with burner HRR of a) 6.5 kW and b) 12.92kW

## ACKNOWLEDGMENTS

This research has been funded by the Engineering and Physical Sciences Research Council (EPSRC, UK) and Arup (UK). Thank you to Matthew Bonner and Francesca Lugaresi for their support and suggestions.

## REFERENCES

- Bonner, M. and Rein, G. (2018) 'Flammability and Multi-objective Performance of Building Façades: Towards Optimum Design', *International Journal of High-Rise Building*, 7(4), pp. 363–374.
- FireFOAM, version dev (2017). Available at: <https://github.com/fireFoam-dev/fireFoam-dev>.
- Foley, M. and Drysdale, D. D. (1995) 'Heat transfer from flames between vertical parallel walls', *Fire Safety Journal*, 24(1), pp. 53–73. doi: 10.1016/0379-7112(94)00033-C.
- Hamins, A. *et al.* (1996) 'Global properties of gaseous pool fires', *Symposium (International) on Combustion*, 26(1), pp. 1429–1436. doi: 10.1016/S0082-0784(96)80363-8.
- Herzog, T., Krippner, R. and Lang, W. (2017) *Facade Construction Manual*. Second. Edited by S. Lenzen. Munich: DETAIL.
- Hussain, A. K. M. F. and Reynolds, W. C. (1975) 'Measurements in Fully Developed Turbulent Channel Flow', *Journal of Fluids Engineering*, 97(4), p. 568. doi: 10.1115/1.3448125.
- Jamison, K. L. T. and Boardman, D. A. (2016) 'A new fire performance test for cavity wall insulation', *MATEC Web of Conferences*, 46, pp. 1–12. doi: 10.1051/mateconf/20164602004.
- Livkiss, K. *et al.* (2018) 'Flame Heights and Heat Transfer in Façade System Ventilation Cavities', *Fire Technology*. Springer US, pp. 1–25. doi: 10.1007/s10694-018-0706-2.
- Miyamoto, M. *et al.* (1986) 'TURBULENT FREE CONVECTION HEAT TRANSFER FROM VERTICAL PARALLEL PLATES', in *Proceeding of International Heat Transfer Conference 8*. Connecticut: Begellhouse, pp. 1593–1598. doi: 10.1615/IHTC8.3200.
- Most, J. *et al.* (1989) 'Interaction Between Two Burning Vertical Walls', *Fire Safety Science*, 2, pp. 285–294. doi: 10.3801/IAFSS.FSS.2-285.
- Nicoud, F. and Ducros, F. (1999) 'Subgrid-scale stress modelling based on the square of the velocity', *Flow, Turbulence and Combustion*, 62, pp. 183–200. doi: 10.1023/A:1009995426001.
- OpenFOAM, CFD package (no date). Available at: <https://openfoam.org/>.
- Page, F. *et al.* (1952) 'TEMPERATURE GRADIENTS IN TURBULENT GAS STREAMS. POINT VALUES OF EDDY CONDUCTIVITY AND VISCOSITY. IN UNIFORM FLOW BETWEEN PARALLEL PLATES', *Industrial & Engineering Chemistry*, 44(2), pp. 424–430. doi: 10.1021/ie50506a059.
- Ren, N. *et al.* (2016) 'Large eddy simulation of turbulent vertical wall fires supplied with gaseous fuel through porous burners', *Combustion and Flame*, 169, pp. 194–208. doi: 10.1016/j.combustflame.2015.12.008.
- Ren, N., Wang, Y. and Trouvé, A. (2013) 'Large eddy simulation of vertical turbulent wall fires', *Procedia Engineering*, 62, pp. 443–452. doi: 10.1016/j.proeng.2013.08.086.
- TAMANINI, F. and MOUSSA, A. N. (1980) 'Experiments on the Turbulent Burning of Vertical Parallel Walls', *Combustion Science and Technology*, 23(3–4), pp. 143–151. doi: 10.1080/00102208008952405.
- Zemella, G. and Faraguna, A. (2014) *Evolutionary Optimisation of Façade Design*. London: Springer London. doi: 10.1007/978-1-4471-5652-9.

## BACKGROUND AND LIMITATIONS OF THE EUROCODE PARAMETRIC FIRE CURVES, INCLUDING THE FIRE DECAY PHASE

Andrea Lucherini<sup>a</sup>, Balša Jovanović<sup>a</sup>, Ruben Van Coile<sup>a</sup>, Bart Merci<sup>a</sup>

<sup>a</sup> Department of Structural Engineering and Building Materials, Ghent University, Belgium

### Abstract

The research study investigates the background and assumptions behind the definition of the Eurocode Parametric Fire Curves (EPFC), the most adopted methodology to replicate natural fire exposures on structural elements. The analysis explores the fire heating phase, as well as the fire decay phase. Particularly, a numerical analysis is carried out to explicitly quantify the maximum temperature, the cooling rate and the duration of the fire decay phase for a reference compartment. Results show that, for both ventilation- and fuel-controlled conditions, the fire decay phase can largely vary in function of the opening factor and fuel load density. Also, comparing empirical temperature-time curves from large-scale fire tests (BRE Cardington 1999-2000) and the calculated EPFC evidences that the EPFC constant cooling rates are not appropriate to correctly characterise the thermal exposure to structural elements during the fire decay phase.

**Keywords:** parametric fire curve, fire decay phase, cooling phase, natural fire, compartment fire dynamics

## 1 INTRODUCTION

Recent research (e.g. Gernay and Franssen, 2015, and Thienpont *et al.*, 2021) has highlighted the relevance of adopting holistic performance-based methodologies for the design of fire-safe structures that ensure structural integrity and stability until complete fuel burnout. These approaches do not only consider the growing and fully-developed phases of fires (e.g. standard fire curve), but also investigate the structural behaviour during the fire decay phase. Indeed, delayed failure may occur during or after the fire decay phase and a few cases have been reported (Gernay, 2019).

The most adopted methodology to replicate natural fire exposures on structures is represented by the Eurocode Parametric Fire Curves (EPFC) (EN 1991-1-2:2002). This method offers analytical equations to generate the temperature-time history of a natural fire as a function of a few input parameters related to the fuel load and compartment characteristics.

However, the background and assumptions behind the definition of the EPFC have not been comprehensively stated during its development, especially with respect to the fire decay phase. Furthermore, the goodness-of-fit of the EPFC relative to experimental data is not always clear to the new generation of structural fire engineers.

To help alleviate the limits to the readily available state-of-knowledge within the profession, the following review provides background to the EPFC, as well as a critical evaluation relative to experimental data, particularly focusing on the fire decay phase.

## 2 EUROCODE PARAMETRIC FIRE CURVES: BACKGROUND

### 2.1 Importance and interpretation of the Eurocode parametric fire curve

The EPFC have been the most popular parametrized approximation for one-zone compartment fires since its implementation in Annex A of EN 1991-1-2:2002. This methodology provides analytical (i.e. parametric) equations to estimate the temporal evolution of a uniform “gas temperature” in a post-flashover fire compartment. The EPFC are calculated as a function of the fuel load density, compartment geometry and characteristics (i.e. floor area, ventilation conditions and thermal effusivity of the lining materials) with specific limits of applicability: (i) compartments with a floor

area up to 500 m<sup>2</sup> and height up to 4 m; (ii) vertical openings only (walls, not ceiling); (iii) thermal effusivity of the compartment lining materials in the range 100-2200 J/m<sup>2</sup>s<sup>0.5</sup>K. The resulting temperature-time curves are adopted to quantify the thermal exposure to structural elements during all the typical phases of a natural fire in an enclosure (refer to Fig.2). The convective heat transfer is specified with respect to this “gas temperature”, considering a convection coefficient of 35 W/m<sup>2</sup>K. Also, the radiative heat transfer is specified with respect to this “gas temperature”, and EN 1991-1-2:2002 states that the configuration (view factor) can be taken as unity and the material emissivity as 0.8 (except where stated otherwise in the material-specific Eurocodes). In a real compartment fire, however, the convective heat transfer coefficient depends on the flow conditions of the hot gas near the structure, while the radiative heat transfer results from an interaction with the surroundings. In this regard, the “gas temperature” defined by the EPFC is more correctly described as an adiabatic surface temperature and it should be treated accordingly.

## 2.2 Background: origins of the heating phase formulation

The EPFC are commonly considered to have been derived from the “Swedish fire curves” (Magnusson and Thelandersson, 1970, and Petterson *et al.*, 1976) through energy balance considerations for ventilation-controlled compartment fires. However, Wickström (Wickström, 1981, and Wickström, 1985) derived the formulation of the EPFC heating phase from first principles, building on the concepts underlying the “Swedish fire curves”, and validated his approach against those curves. In his derivation, Wickström made the following assumptions: (i) uniform gas temperature in the fire compartment; (ii) total fuel burnout inside the compartment; (iii) ventilation-controlled fire; (iv) natural ventilation. The temperature-time curve is then obtained through energy-balance equations, additionally assuming that (i) the compartment linings can be approximated as semi-infinite solids with constant thermal properties, and (ii) the linings surface temperature equals the compartment gas temperature. This assumption results in an overestimation of heat losses and thus lower fire compartment temperatures, notably early in the fire. Considering the time-dependent temperature in the compartment, Wickström obtained a convolution equation for the heat losses to the walls. At this point, the concept of scaled time  $t^* = \Gamma \cdot t$  was introduced. This allowed to express post-flashover fires as a single time-temperature curve, for which time is scaled to account for the ventilation conditions and linings properties. The scaling factor  $\Gamma$  is defined by Eq. (1), where  $O_{ref}$  is the reference opening factor (0.04 m<sup>0.5</sup>) and  $b_{ref}$  the reference thermal effusivity (1160 J/m<sup>2</sup>s<sup>0.5</sup>K). This is explained in more detail by Hopkin *et al.* (2021), where also the heat balance equations themselves are outlined. The obtained curve was named the “general natural fire curve”. If the radiation contribution is fully neglected, a closed form solution is obtained (Wickström, 1984). Also, an analytical formulation for this general natural fire curve was obtained by curve fitting (Wickström, 1981). The curve is of the general format of Eq. (2), with coefficients as listed in Table 1. The obtained heating curve is close to the ISO 834:1975 standard heating regime for reasonable fire durations, e.g. up to  $t^* = 3$  hours (ISO 834:1975). Arguably considering this small discrepancy between the curve-fit and the ISO 834 heating regime, the coefficients applied by Wickström (1984) are those listed in the Swedish building code at that time as approximations for the ISO 834 standard heating regime. The general format of Eq. (2) applies to the EPFC as well, considering an ambient temperature of 20°C. It is clear from Table 1 that the listed coefficients proposed by Wickström (1984) have been adopted in EN 1991-1-2:2002. In this formulation, the duration of the heating phase is governed by the assumptions of ventilation-controlled fire and full combustion inside the compartment. This results in a heating phase duration proportional to the fire load density and inversely proportional to the ventilation factor. While the method is a major improvement over the consideration of a standard heating regime, Wickström (1984) highlights that the method is very approximate and should be used with care.

$$\Gamma = \left( \frac{O/O_{ref}}{b/b_{ref}} \right)^2 \quad (1)$$

$$\theta_f(t^*) = B_0 + \sum_{i=1}^3 B_i \exp(-\beta_i t^*) \quad (2)$$

Table 1. Coefficients for the “generalized natural fire curve” (heating regime).

	$B_0$ [°C]	$B_1$ [°C]	$\beta_1$ [h <sup>-1</sup> ]	$B_2$ [°C]	$\beta_2$ [h <sup>-1</sup> ]	$B_3$ [°C]	$\beta_3$ [h <sup>-1</sup> ]
<b>Wickström, 1981</b>	1110	-369.7	0.61	-200.4	4.94	-539.9	23.1
<b>Wickström, 1984</b>	1325	-430.0	0.20	-270.0	1.70	-625.0	19.0
<b>EN 1991-1-2:2002</b>	1325	-429.3	0.20	-270.3	1.70	-625.4	19.0

Comparing the above with the current heating phase formulation of EN 1991-1-2:2002 evidences that the generalized natural fire curve obtained by Wickström has been adopted in the Eurocode. Nevertheless, there are some important changes/specifications: (i) the time  $t_{max}$  of maximum temperature is defined both for ventilation-controlled fires and fuel-controlled fires (for the fuel-controlled fires a distinction is made based on occupancy type); (ii) equations are introduced for the thermal effusivity of multi-layered walls, following proposals by Franssen (2000). The final modifications to the EPFC proposal, however, resulted in a discontinuity in the calculation of the maximum temperature for ventilation-controlled and fuel-controlled fires. Reitgrüber *et al.* (2006) highlighted how the maximum compartment temperature discretely jumps over a hundred degrees at the transition. Furthermore, Reitgrüber *et al.* (2006) state that the EPFC calibration for  $t_{max}$  considers an effective heat of combustion of 18 MJ/kg (wood), which is at odds with the recommended value for the effective heat of combustion within Annex E of EN 1991-1-2:2002, where a value of 14 MJ/kg is recommended (taking into account a combustion factor of 0.8). This results in an underestimation of compartment fire temperatures within the EPFC. Additional background to the modifications made during the adoption can be found in Hopkin *et al.* (2021).

### 2.3 Background: origins of the fire decay phase formulation

The fire decay phase description of the EPFC is a direct remnant of a simplifying assumption made by Wickström (1981, 1985). In his seminal work, Wickström adopted the linear cooling rates specified in the at that time current ISO 834 standard (ISO 834:1975): 625°C per hour for a heating duration up to 0.5 hours, 250°C per hour for a heating duration of 2 hours or more, and an interpolated value for intermediate heating durations. The ISO standard specified these cooling rates “when an element of building construction has to fulfil certain functions during the heating period and during the subsequent cooling period” up to the point where the furnace temperature has decreased to 200°C. No further justification for the cooling rates in ISO 834:1975 could be determined. Wickström himself stated that the ISO 834 cooling rates “cannot be derived from the physical aspects of a compartment”.

EN 1991-1-2:2002 has adopted these linear cooling rates, while maintaining the ventilation-controlled time scaling factor  $\Gamma$  applied in the heating phase definition. This scaling results in EPFC cooling rates that can be much faster or slower than those originally listed in ISO 834:1975. In conclusion, the above implies that (i) the cooling rate of the EPFC is not based on clear physical considerations; (ii) application the heating phase time scaling to the decay phase definition results in EPFC cooling rates which differ strongly from the cooling rates listed in the original background.

## 3 EUROCODE PARAMETRIC FIRE CURVES: ANALYSIS ON THE DECAY PHASE

The previous section has evidenced the background behind the derivation of the heating and decay phases of the EPFC. Differently to the heating phase, the fire decay phase has been formulated including significant simplifications (i.e., linear cooling rates) and applying analogous concepts to the ones originally derived for the heating phase (e.g., time scaling factor). Consequently, the resulting representation of the fire decay phase is noticeably inaccurate and the EPFC cooling rates can be unrealistically high or low for certain combinations (Feasey and Buchanan, 2002).

According to the current formulation, the EPFC constant cooling rates are directly related to the scaled time of maximum temperature  $t_{max}^*$ , the product of the time of maximum temperature  $t_{max}$  and the (ventilation-controlled) scaling factor  $\Gamma$ . As a result, the cooling rate of the EPFC is directly influenced by the compartment opening factor, linings thermal effusivity, fuel load density and type (fire growth rate). However, due to its implicit formulation, it is difficult to understand how the different compartment and fuel characteristics affect the estimation of the EPFC cooling rate. To clarify these dependencies, a numerical analysis was carried out to explicitly quantify the maximum temperature, the cooling rate and the decay phase duration for a reasonable range of opening factors (0-0.4  $m^{1/2}$ ) and fuel load densities (0-2000  $MJ/m^2$ ). This evaluation was performed according to previous research outcomes, which highlighted that the EPFC has two real degrees of freedom and they can be studied using a reference compartment with a floor area of 10 x 10  $m^2$ , a height of 3 m, and linings thermal effusivity of 1450  $J/m^2s^{0.5}K$  (Thienpont *et al.* 2020). Note that the fuel load and opening factor limits of applicability when using the EPFC methodology do not apply to the reference compartment evaluation (see Thienpont *et al.* 2020).

As regards the heating phase, Fig. 1 shows how the compartment maximum temperature is affected by the fuel load density and opening factor. For ventilation-controlled conditions, the higher these values, the higher maximum compartment temperature. On the contrary, for fuel-controlled conditions, low temperatures are obtained for low fuel loads, but the maximum temperature is independent of the opening factor. Fig. 1 confirms the discrete shift in maximum temperature at the ventilation- and fuel-controlled transition, already underlined by Reitgrüber *et al.* (2006).

As regards the fire decay phase, the constant cooling rates and decay phase durations are closely related, but also influenced by the maximum compartment temperature. In the case of fuel-controlled conditions, the cooling rate is largely affected by the opening factor and the fuel load density, but the decay phase is typically short (below 30 min). On the other hand, for ventilation-controlled conditions, the opening factor strongly influences the decay phase, which can register a wide range of cooling rates and decay phase durations.

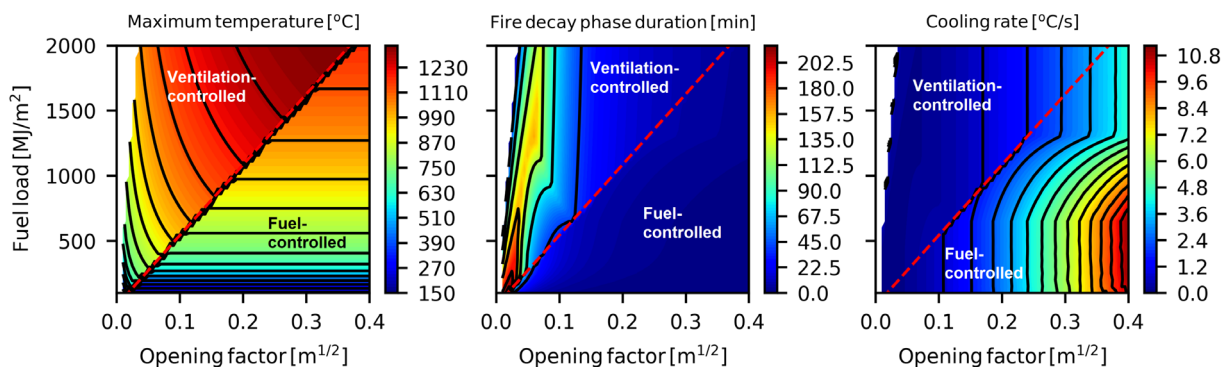


Fig. 1. Maximum temperature, cooling rate and decay phase duration estimated according to the EPFC as a function of opening factor and fuel load density, for ventilation- and fuel-controlled conditions.

In general, according to the EPFC methodology, an enclosure can experience a vast variety of thermal exposures during the fire decay phase based on its characteristics (e.g. ventilation- vs. fuel-controlled). In particular, the fire decay phase can last for less than 30 minutes in the case of well-ventilated compartments, but it can also register very low cooling rates (below 0.1  $^{\circ}C/s$ ) and last for more than 200 minutes in the case of under-ventilated compartments. As highlighted in the introduction, the thermal exposure during the fire decay phase can have significant consequences on the structural stability and integrity of load-bearing members. As a consequence, there is a need to comprehend if the EPFC methodology represents an appropriate design tool to predict the natural fire exposures to structural elements during the fire decay phase.

## 4 COMPARISON TO LARGE-SCALE FIRE EXPERIMENTS

To understand if the EPFC methodology is able to accurately predict the decay phase of natural fire exposures, the existing literature was reviewed to provide experimental evidence and a series of large-scale fire tests was chosen for comparison. The selected experimental programme was carried out in 1999-2000 at the BRE Cardington facilities within the scope of the “*Natural Fire Safety Concept 2 (NFSC2)*” series of fire tests. The experimental campaign investigated full-scale post-flashover fires performed in a large compartment measuring 12 x 12 m in plan, 3 m in height, and involved a total of eight scenarios, which differed for opening position, fuel load composition and the thermal insulation of the compartment boundaries. A detailed description of the experimental campaign has been provided by Lennon and Moore (2003). In accordance with the tested compartment and fuel characteristics, the corresponding EPFC were estimated for the eight tested scenarios by defining the following input parameters (Lennon and Moore 2003):

- Test 2 & Test 3:  $O = 0.10 \text{ m}^{0.5}$ ,  $q_f = 680 \text{ MJ/m}^2$ ,  $b = 720 \text{ J/m}^2\text{s}^{0.5}\text{K}$
- Test 1 & Test 8:  $O = 0.10 \text{ m}^{0.5}$ ,  $q_f = 680 \text{ MJ/m}^2$ ,  $b = 1600 \text{ J/m}^2\text{s}^{0.5}\text{K}$
- Test 4 & Test 5:  $O = 0.07 \text{ m}^{0.5}$ ,  $q_f = 680 \text{ MJ/m}^2$ ,  $b = 720 \text{ J/m}^2\text{s}^{0.5}\text{K}$
- Test 6 & Test 7:  $O = 0.07 \text{ m}^{0.5}$ ,  $q_f = 680 \text{ MJ/m}^2$ ,  $b = 160 \text{ J/m}^2\text{s}^{0.5}\text{K}$

The experimental temperature-time curves and the estimated EPFC are shown in Fig. 2. In their manuscript, Lennon and Moore (2003) highlighted a few shortcomings of the EPFC methodology as regards to the fire heating phase. On the contrary, this research study aims at understanding the limitations and potential improvements of EPFC related to the fire decay phase.

Fig. 2 underlines the different nature of the experimentally-measured temperature-time curves and the ones obtained according to the EPFC methodology. All the experimental curves follow a similar trend, which can be directly associated with the specific characteristics of the tested compartment and fuel. On the other hand, the linear EPFC cooling rates often under-estimate the thermal exposure during the fire decay phase. In addition, a linear relationship is certainly not a correct approximation, considering that the experimental temperature-time curves decrease following specific curved trends, much like power or exponential functions (with negative exponent). This aspect becomes more evident when the cooling rates are compared, as shown in Fig. 3. The EPFC methodology estimates constant cooling rates that are either largely overestimated or are not able to describe the typical temperature decay. The empirical curves are characterised by higher cooling rates at high temperatures, and they gradually decrease for lower temperatures. In this specific experimental campaign, the cooling rates vary roughly between 0.1 and 0.6 °C/s.

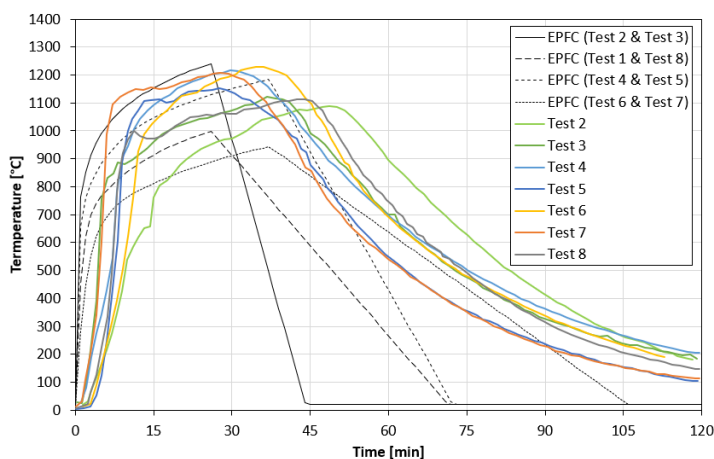


Fig. 2. Temperature-time curves comparison between the EPFC and the Cardington fire tests.

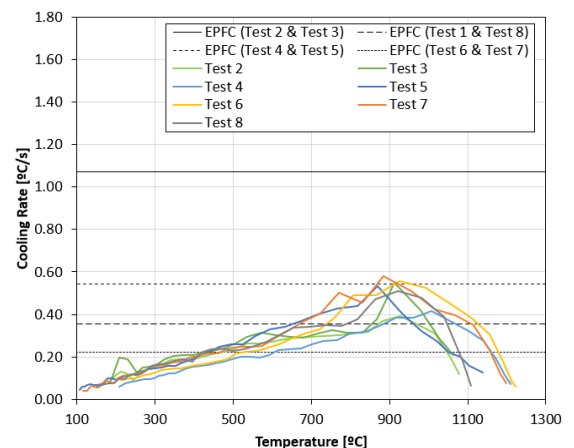


Fig. 3. Cooling rates comparison between the EPFC and the Cardington fire tests.

## 5 CONCLUDING REMARKS

The Eurocode Parametric Fire Curves (EPFC) currently represent the most adopted methodology to replicate natural fire exposures on structural elements. In the current research study, the background and assumptions of the present analytical formulation of the EPFC have been presented. Starting from the simplifications and assumptions made by Wickström to define the “general natural fire curve”, the literature review presents the background behind the formulation of both the heating and decay phase. Particular interest has been paid on the definition of the fire decay phase: in its current formulation, the fire decay phase is substantially simplified into a linear relationship, following constant cooling rates prescribed in the ISO 834:1975 standard. Furthermore, the time-scaling applied in the EPFC heating phase formulation has been applied to the decay phase without clear justification.

A numerical analysis aimed at explicitly quantifying the maximum temperature, the cooling rate and the duration of the fire decay phase according to the EPFC methodology has been presented. Results highlight how these values vary significantly as a function of the opening factor and fuel load density, for a given reference compartment. This investigation also shows that, for both ventilation- and fuel-controlled conditions, an enclosure can experience a vast variety of thermal exposures during the fire decay phase: this phase can last for less than 30 minutes and up to more than 200 minutes according to the EPFC, depending on the compartment and fuel characteristics. Comparing the temperature-time curves measured during large-scale fire tests (BRE Cardington 1999-2000) and the calculated EPFC evidences the incapacity of the methodology to correctly characterise the thermal exposure during the fire decay phase. To accurately predict the decay phase of natural fires, future research should focus on defining a better approximation and analytical expressions. This will allow to correctly study the behaviour of structural elements exposed to natural fires, considering all their typical phases, including the fire decay phase.

## REFERENCES

- European Committee for Standardization (CEN). 2002. *EN 1991-1-2 Eurocode 1: Actions on structures – Part 1.2: General actions – Actions on structures exposed to fire*. Brussels, Belgium.
- Feasey R., Buchanan B. 2002. *Post-flashover fires for structural design*. Fire Safety Journal, 37, 83-105.
- Franssen J.M. 2000. *Improvement of the parametric fire of Eurocode 1 based on experimental tests results*. Fire Safety Science, 6, 927-938.
- Gernay T., Franssen J.M. 2015. *A performance indicator for structures under natural fire*. Engineering Structures, 100, 94-103.
- Gernay T. 2019. *Fire resistance and burnout resistance of reinforced concrete columns*. Fire Safety Journal, 104, 67-78.
- Hopkin D., Van Coile R., Hopkin, C., LaMalva, K., Spearpoint, M., Wade, C. 2021. *The Constraint: Design Fires*. In: *Structural Fire Engineering Handbook*. D. Hopkin, K. LaMalva (Eds.), Springer.
- International Organization for Standardization (ISO). 1975. *ISO 834:1975: Fire-resistance tests – Elements of building construction*. Geneva, Switzerland.
- Lennon T., Moore D. 2003. *The natural fire safety concept - full-scale tests at Cardington*. Fire Safety Journal, 38, 623-643.
- Magnusson S.E., Thelandersson S. 1970. *Temperature - Time Curves of Complete Process of Fire Development*. Bulletin of Division of Structural Mechanics and Concrete Construction, 16, Lund Institute of Technology.
- Pettersson O., Magnusson S.E., Thor J. 1976. *Fire Engineering Design of Steel Structures*. Bulletin of Division of Structural Mechanics and Concrete Construction, 52, Lund Institute of Technology.
- Reitgrüber S., Di Blasi C., Franssen J.M. 2006. *Some comments on the parametric fire model of Eurocode 1*. Conference on Fire in Enclosures, University of Ulster, Jordanstown, UK.
- Thienpont T., Van Coile R., Caspee R., De Corte W. 2021. *Burnout resistance of concrete slabs: probabilistic assessment and global resistance factor calibration*. Fire Safety Journal, 119, 103242.
- Wickström U. 1981. *Temperature calculation of insulated steel columns exposed to natural fire*. Fire Safety Journal, 4(4), 219-225.
- Wickström U. 1985. *Application of the standard fire curve for expressing natural fires for design purposes*. Fire Safety: Science and Engineering, ASTM International.

## EFFECTS OF THE FIRE DECAY PHASE ON THE BENDING CAPACITY OF A FIRE-EXPOSED REINFORCED-CONCRETE SLAB

Balša Jovanović<sup>a,b\*</sup>, Andrea Lucherini<sup>a</sup>, Ruben Van Coile<sup>a</sup>, Bart Merci<sup>a</sup>, Robby Caspeele<sup>a</sup>, Edwin Reynders<sup>b</sup>, Geert Lombaert<sup>b</sup>

<sup>a</sup> Department of Structural Engineering and Building Materials, Ghent University, Belgium

<sup>b</sup> Department of Civil Engineering, KU Leuven, Belgium

### Abstract

The decay phase can have an important role in the behaviour and failure of the structure during and after a fire, and therefore, it should be properly defined. The most commonly used method to define natural fire exposure, the Eurocode parametric fire curve (EN 1991-1-2:2002), adopts a simplified linear approximation of the fire decay phase with a constant cooling rate defined in function of compartment characteristics. In this study an analysis of the influence of the decay phase cooling rate assumption on structural behaviour is made, considering the case of a simply supported reinforced-concrete slab exposed to fire from the bottom side. It is demonstrated that the cooling rate of the decay phase can have a significant effect on the reduction of the slab's bending capacity. It is also shown that the magnitude of this influence is affected by both the temperatures during the heating phase and the size of the concrete cover. The case study demonstrates that the difference between the cooling rates from the Eurocode parametric fire curve and available experimental test results are significant, and that this can have a significant effect on the assessment of the slab's structural performance.

**Keywords:** fire decay phase, parametric fire, natural fire, compartment fire dynamics, structural fire engineering

### 1 INTRODUCTION

Structural stability of a building in case of fire is of the utmost importance both for the safety of its occupants as well as for other fire safety objectives such as property protection. Current practice is mostly focused on prescriptive design approaches where the performance of the structure in case of fire is assessed based on its performance in standardized fire tests. Even though this practice can produce a robust design, it has its shortcomings, despite the fact that the standardized ISO 834 (ISO, 1999) fire exposure is often considered a “credible worst-case scenario” compared to most real fires. One of these shortcomings is the disregarding of the decay phase of the fire, i.e. the stage of the fire where both the heat release rate of the fire and the compartment temperatures decline.

Recent studies by (Gernay, 2019) and (Thienpont *et al.*, 2021) have demonstrated that the decay phase can have a crucial role in the stability and integrity of structural members exposed to fire. This is especially pronounced in concrete structures where, due to the combination of member dimensions and thermal properties, the element interior can reach its maximum temperature well after the fire has started to decay.

Adopting performance-based design approaches, it is possible to take into account the full fire exposure, both the heating and the decay phase. One of the most commonly used and straightforward methods is to model natural fire exposures by the Eurocode Parametric Fire Curve (EPFC) (CEN, 2002). This method presents a system of equations that produces a temperature-time curve of the hot gases inside the compartment in the case of a natural fire. The hot gases are assumed to be uniform in the compartment as well as opaque and they can thus be used as a boundary condition in the thermo-mechanical analysis of the structure. The inputs needed for this method are the characteristics of the compartment, more precisely its geometry, thermal properties of the walls, ventilation openings and combustible fuel load contained in the enclosure. The benefit of this method is that it instantly produces temperature-time curves for a wide range of situations based on a limited number of parameters.

However, due to its simplicity, the gas temperatures obtained with the EPFC generally do not match well with experimental test results. The gas temperature measurements from the large-scale Cardington tests show limited agreement with the EPFC, which is especially pronounced in the fire decay phase (Lennon and Moore, 2003). In the paper by Lucherini *et al.*, (2021) special emphasis has been put on those differences. It is shown that its duration is highly underestimated by the EPFC, also coupled with the fact that in experimental results the decay phase was highly non-linear. Furthermore, it was seen that even though the EPFC decay phases varied strongly in both their cooling rate and duration, experimental results show a similar decay of compartment temperature for all tests. This suggests that the EPFC formulation might not properly capture the most influential parameters governing the decay phase.

All of this demonstrates that the fire decay phase obtained from the commonly used EPFC differs from experimental results. This aspect can be important in the structural fire analysis. The aim of this paper is to explore the effects of the fire decay phase on the structural behaviour, by analyzing a case study represented by a simply supported reinforced concrete slab.

## 2 METHODOLOGY

### 2.1 Definition of fire scenarios

The EN 1991-1-2:2002 parametric fire curves are defined in two phases (CEN, 2002):. First, the heating phase where the hot gas temperature is monotonously growing according to an exponential law until it reaches a maximum temperature. Second, the decay phase where the hot gas temperature linearly decreases until it reaches ambient temperature (20 °C). Therefore, the decay phase can be fully characterized by any pair of these three parameters: cooling rate (slope of the temperature-time decay), fire decay phase duration and the maximum temperature.

In order to properly quantify the potential influence of the fire decay phase on the mechanical behaviour of the structure, the first step is to understand the limits that these three parameters can have. For that purpose, the “equivalent ’compartment” concept presented by (Thienpont *et al.*, 2021) will be used. They showed that the EPFC formulation has only two degrees of freedom and that the EPFC for any compartment can be obtained considering the EPFC formulation for an equivalent compartment with dimensions of 10 x 10 x 3 m<sup>3</sup>, thermal inertia  $b_{eq}$  of 1450 J/m<sup>2</sup>s<sup>1/2</sup>K, and opening factor  $O_{eq}$  and fuel load  $q_{f,eq}$  obtained with the following equations (Thienpont *et al.*, 2021):

$$O_{eq} = O \cdot \frac{b_{eq}}{b} \quad (1)$$

$$q_{f,eq} = q_f \cdot \frac{A_f}{A_t} \cdot \frac{A_{f,eq}}{A_{t,eq}} \cdot \frac{b_{eq}}{b} \quad (2)$$

where  $O$  and  $q_f$  are the opening factor and the fuel load,  $A_f$  and  $A_t$  the floor and total wall areas and  $b$  the thermal inertia of the walls for the “actual” compartment. Based on the limits of applicability of the parametric fire model ( $O = 0.02 - 0.20$  and  $b = 100 - 2200$ ), some unrealistic decay phases can be obtained (the decay phase duration can be as short as 5 s or as long as 18 h). In the following, the investigations are limited to equivalent opening factors smaller than 0.4 m<sup>1/2</sup> and equivalent fuel loads smaller than 2000 MJ/m<sup>2</sup>.

Figure 1 presents how three parameters defining the decay phase vary as a function of the opening factor and fuel load for the equivalent compartment. The cooling rate varies from really low values of 0.02 °C/s to high values of 11 °C/s, the fire decay phase duration from 8 s to 3.5 h and maximum temperatures from 150 °C to 1350 °C. Figure 1 also shows that the decay phase in the fuel-controlled fires is much shorter than in the ventilation-controlled ones.

To estimate the influence of the decay phase, three “types” of compartment fires are considered, all based on the equivalent compartment, considering a fixed fuel load of 1600 MJ/m<sup>2</sup> and varying opening factor. The first one has an opening factor  $O = 0.02 \text{ m}^{1/2}$  and it represents a fire with a slow and long heating phase that does not reach a high maximum temperature. The second one has an opening factor  $O = 0.05 \text{ m}^{1/2}$  which corresponds to the heating phase equal to ISO 834 standard fire curve. And the last one has an opening factor  $O = 0.20 \text{ m}^{1/2}$ , resulting in a fast-growing heating

phase with high maximum temperature. These three EPFCs were selected as fire design scenarios because they would produce different thermal gradients within concrete structural members and challenge the structural system in different ways, given their different natures: temperature ranges, heating rates and cooling rates, duration of the heating and decay phases. For each of them, the decay phase is defined by the maximum temperature achieved in the heating phase and a cooling rate. This cooling rate is varied from 0.02 to 11 °C/s, representing the extreme values shown in Figure 1. The selected fires and their cooling rate variations are presented in Figure 2. Using these fire curves, the influence of the cooling rate on the mechanical behaviour of a structural member is investigated.

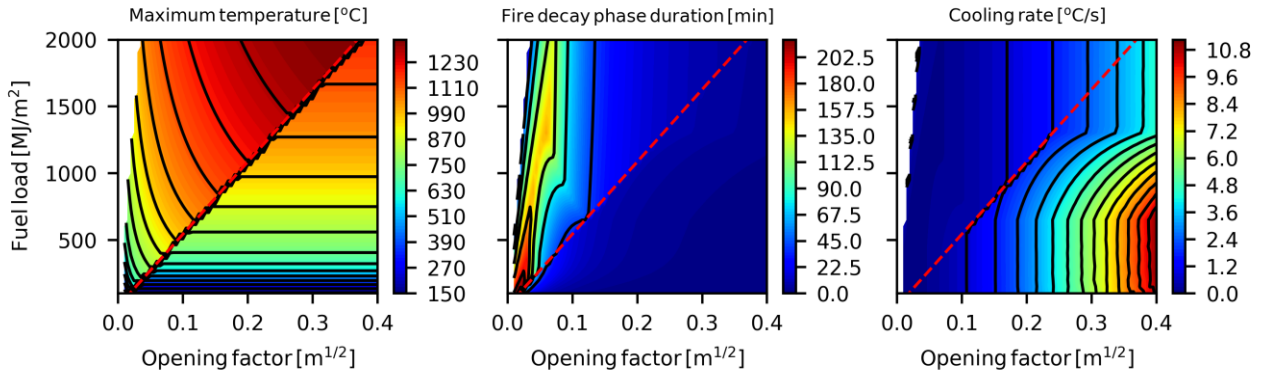


Figure 1 Maximum temperature, fire decay phase duration and cooling rate as a function of the opening factor and the fuel load for the equivalent compartment (above the red dashed line - ventilation controlled fires, below – fuel controlled)

## 2.2 Case study: reinforced-concrete slab

To understand the effect of the cooling rate on the capacity of structural members, a simply supported reinforced concrete slab is considered. The slab is exposed to the fire from the bottom side and the top side is in contact with the air at ambient conditions. The bending capacity of the slab is calculated using the following formula:

$$M_R = k_{fy}(T) \cdot f_y \cdot A_s \cdot z - \frac{(k_{fy}(T) \cdot f_y \cdot A_s)^2}{2 \cdot b \cdot f_c} \quad (3)$$

where  $k_{fy}(T_{max})$  represents the strength retention factor of steel at elevated temperatures according to EN 1992-1-2 (CEN, 2004), where  $T_{max}$  is the maximum temperature the reinforcement experiences,  $f_y = 500 \text{ MPa}$  is the yield strength of the steel reinforcement,  $A_s = 785 \text{ mm}^2/\text{m}$  is the steel reinforcement area of 10 Ø10 bars,  $f_c = 30 \text{ MPa}$  is the concrete strength,  $b = 1 \text{ m}$  is the slab width and  $z = 0.18 \text{ m}$  is the distance from the reinforcement from the top of the slab. This equation assumes that the temperatures at the top (compressed) part of the slab remains sufficiently low so as not to significantly influence the mechanical properties of concrete. This is usually the case for the slabs with these dimensions (thickness of approximately 0.2 m). The lever arm ( $z$ ) is kept constant in the further analysis in order to isolate the effects of the cooling regime and the size of the concrete cover on the bending capacity.

The heat transfer analysis is conducted using a 1D finite difference method. On the heated side convection coefficient  $h_{conv} = 0.35 \text{ W/m}^2\text{K}$  and surface emissivity of  $\varepsilon = 0.7$  are used and on the unheated side  $h_{conv} = 9 \text{ W/m}^2\text{K}$  with the assumption it contains the radiation effects. Thermal properties of concrete and reinforcing steel are considered according to EN 1992-1-2 (CEN, 2004) for a siliceous concrete with a moisture content of 3% of the concrete weight.

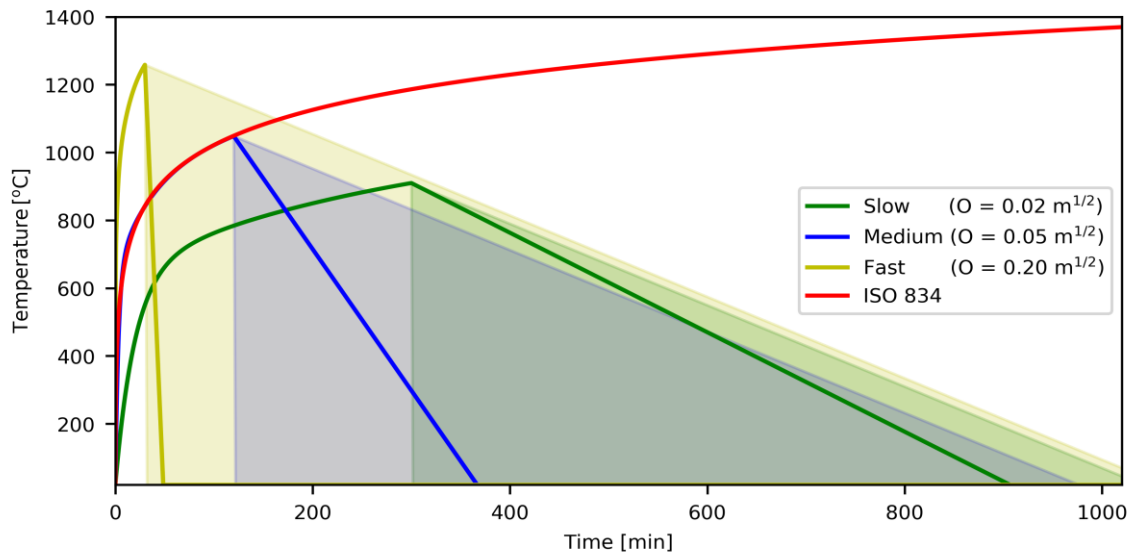


Figure 2 Fire curves used in the analysis with three distinct heating phases and a range of assumed cooling rates (0.02 to 11 °C/s).

### 3 RESULTS AND DISCUSSION

For each of the three presented heating phase types, the minimum bending capacity during the fire exposure is evaluated, considering both the variation in the cooling rate and the size of the concrete cover. In Figure 3 the ratio of the minimum bending capacity in case of fire relative to the initial bending capacity in ambient conditions is presented for all three heating regimes. The dashed horizontal lines represent the cooling rate according to the EPFC for these compartments and the black horizontal lines show the ranges of the cooling rates observed in the Cardington fire tests shown in (Lucherini *et al.*, 2021).

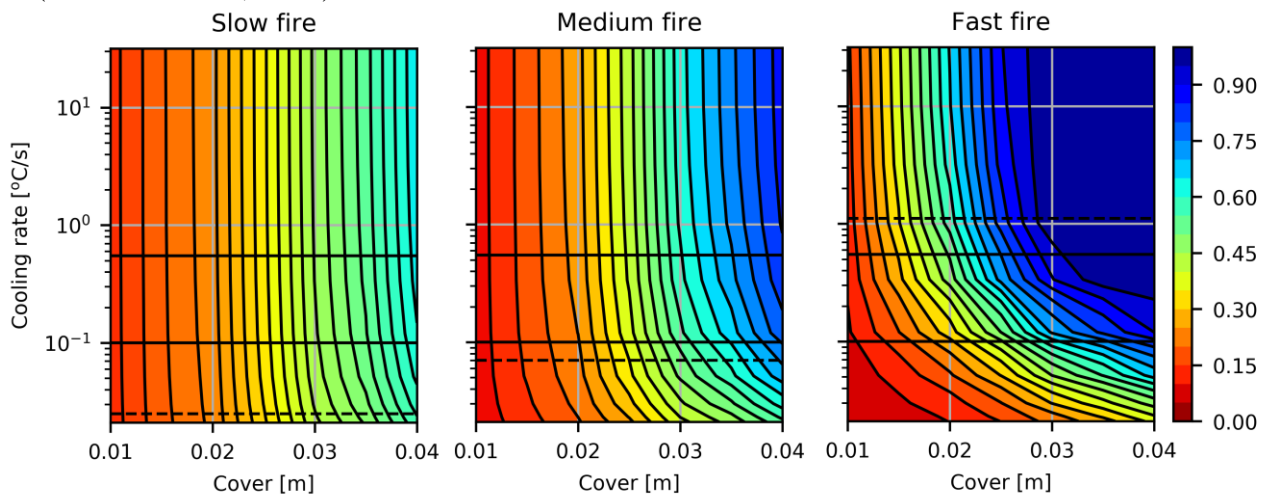


Figure 3 Ratio of the minimum bending capacity in case of fire relative to the bending capacity in ambient conditions in function of the cooling rate and concrete cover for three distinctive heating regimes (slow, medium and fast respectively).

When looking at the slow-growing fire, it is evident that the cooling rate has a negligible effect on the capacity. Only for cooling rates below 0.1 °C/s, there is a noticeable effect of the cooling rate assumption on the minimum capacity in case of fire. On the contrary, the fast-growing fire shows that the minimum capacity in case of fire is highly influenced by the cooling rate, especially for cooling rates below 1 °C/s. Lastly, the medium-growing fire shows that the cooling rate starts to significantly affect the capacity for cooling rates below 0.5 °C/s. Furthermore, it is evident for all three heating regimes that the variation of the cooling rate has a stronger influence on the capacity for higher values of the concrete cover.

In particular, Figure 4 compares the reduction in the slab bending capacity based on the cooling rates for all three heating regimes, considering a fixed concrete cover of 30 mm. This graph further highlights that the influence of the cooling rate on the slab capacity is strongly dependent on the type of heating phase, making the problem of isolating the effect of the decay phase challenging.

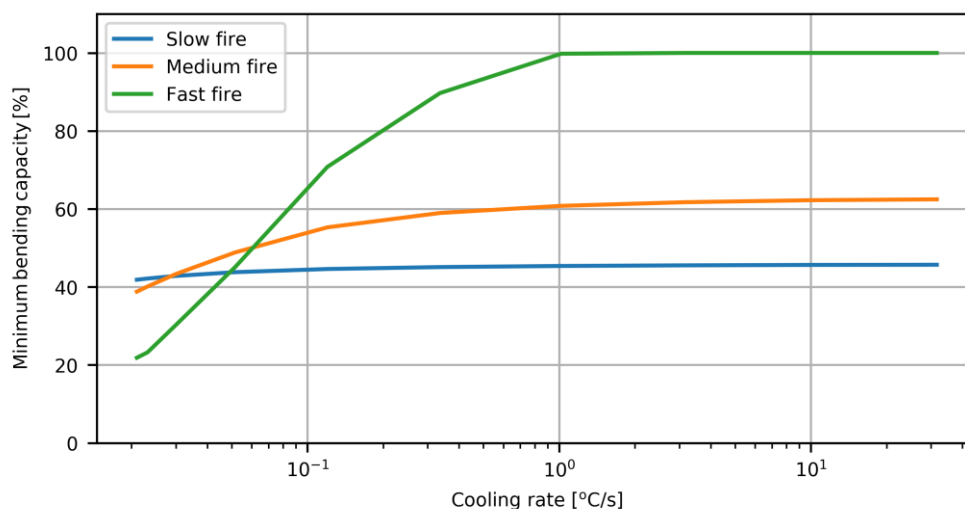


Figure 4 Reduction of the concrete slab bending capacity compared to the initial ambient capacity as a function of the cooling rate for three distinctive heating regimes (concrete cover of 30 mm)

The range of cooling rates inspected here is based on the range possible within the EPFC. In order to see its effect in a more realistic range, special focus is put on the fires recorded in the Cardington fire test (Lennon and Moore, 2003). Investigation of these tests indicates a cooling rate in the range 0.10-0.55 °C/s. Figure 5 (left) compares the Cardington experimental temperature curves with the EPFC where the compartment fuel load and opening factor have been adjusted to qualitatively match the heating phase. Doing this, a relatively good match for the maximum temperature and the heating duration is obtained. For the decay phase, however, a poor match is found, with the EPFC clearly overestimating the cooling rate. Application of the cooling rates 0.10-0.55 °C/s following the EPFC heating regime is visualized in Figure 6 (left) with the dashed lines.

In Figure 5 (right) the reduced capacity can be seen for the fast-growing fire as a function of the cooling rate for distinctive values of the concrete cover. The dashed vertical lines represent the 0.10-0.55 °C/s cooling rate range observed in the Cardington fire tests. It shows that, depending on the size of the concrete cover, the difference in minimum capacity during the fire can vary up to 30%. Furthermore, the reduced capacity is also calculated using each of the 7 decay phases from the Cardington tests. The ranges of the results for those cases are presented by the shaded area in Figure 5 (right), showing that even for the 7 quite similar decay phases the reduced capacity can vary by almost 10 %.

#### 4. CONCLUSIONS

For some structural materials, such as concrete, fire-related failure can occur during both the heating phase and the decay phase. Therefore, the effect of the cooling rate of the fire decay phase has been investigated comparing the constant cooling rates prescribed according to the Eurocode Parametric Fire Curve (EPFC) methodology and empirical ones from the large scale Cardington fire test series. A first comparison showed that the EPFC decay phase formulation does not agree well with reality. The impact of the cooling rate on structural fire performance was investigated considering the case of a simply supported reinforced concrete slab. The slab has been numerically subjected to three distinctive heating regimes with a varying cooling rate for the decay phase. It was demonstrated that the cooling rate does not have a big influence on the slab bending capacity for fires with a longer heating phase and lower maximum temperature. However, for the fires with a shorter heating phase and higher maximum temperature, the decay phase can have a significant influence, resulting in even

60% additional reduction of bending capacity for extreme cases. Furthermore, the size of the concrete cover plays an important role in the assessment of the decay phase influence, with a higher effect for bigger cover values. All of this leads to the conclusion that in order to properly analyse the structural behaviour during the fire, the decay phase must be properly defined. A relatively small variation in the fire decay phase can in some cases lead to a big difference in the members' capacity and result in unsafe post-fire assessments.

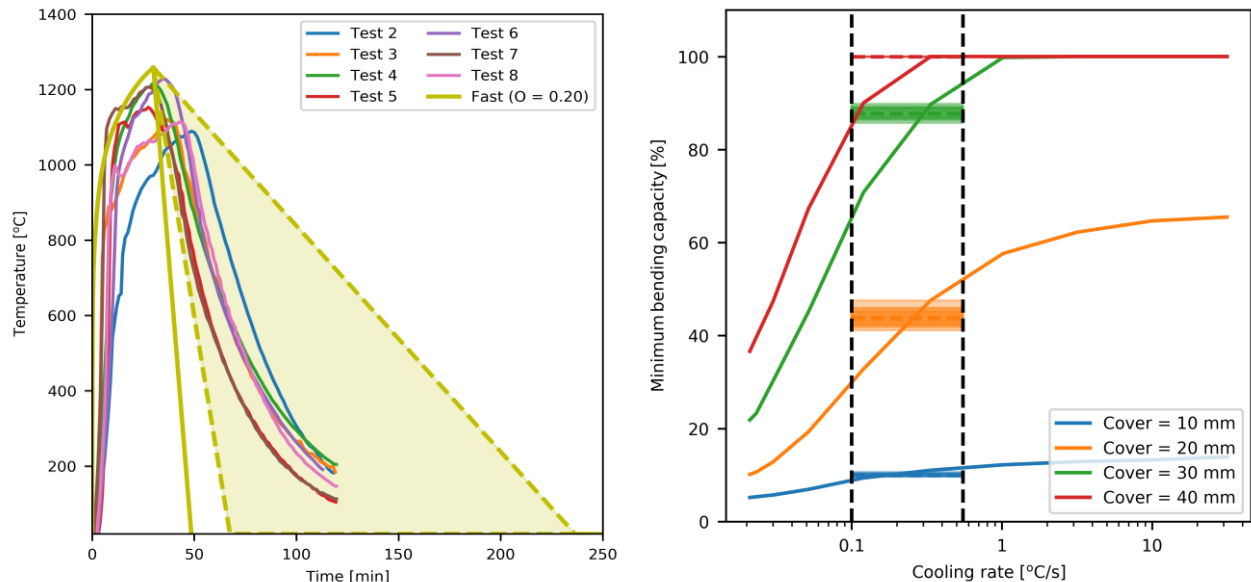


Figure 5 (left) Cardington test results compared with the fast-growing EPFC fire with varying cooling rate assumption; and (right) Reduction of the concrete slab bending capacity compared to the ambient conditions in function of the cooling rate compared to the reduction for the Cardington decay phases

## ACKNOWLEDGEMENTS

The authors wish to thank the Research Foundation of Flanders (FWO) for the financial support on the research project (Grant number 3G010220) “Vibration-based post-fire assessment of concrete structures using Bayesian updating techniques”

## REFERENCES

- CEN 2002. EN 1991-1-2:2002 Actions on structures - Part 1-2: General actions - Actions on structures exposed to fire, European Standard. European Standard.
- CEN 2004. EN 1992-1-2:2004: Eurocode 2: Design of concrete structures - Part 1-2: General rules. Structural fire design. European Standard.
- Gernay, T. 2019. Fire resistance and burnout resistance of reinforced concrete columns, *Fire Safety Journal*, 104, pp. 67–78. doi: 10.1016/j.firesaf.2019.01.007.
- International Organization for Standardization (ISO) 1999. ISO 834-1:1999 Fire-resistance tests - elements of building construction - part 1: general requirements. Geneva, Switzerland.
- Lennon, T. & Moore, D. 2003. The natural fire safety concept - Full-scale tests at Cardington, *Fire Safety Journal*, 38(7), pp. 623–643. doi: 10.1016/S0379-7112(03)00028-6.
- Lucherini, A. et al. 2021. Background and limitations of the eurocode parametric fire curves, including the fire decay phase, in *Applications of Structural Fire Engineering*. 10-11 June 2021, Ljubljana, Slovenia.
- Thienpont, T. et al. 2021. Burnout resistance of concrete slabs : probabilistic assessment and global resistance factor calibration, *Fire Safety Journal*, 119, p. 15.  
Available at: <http://dx.doi.org/10.1016/j.firesaf.2020.103242>.

Proceedings of the International Conference in Ljubljana, 10-11 June 2021  
in edition of Applications of Structural Fire Engineering

**Session**

**Composite and other structures II**

## SMALL-SCALE FIRE TESTS OF LSF FLOOR-CEILING SYSTEMS

Edward Steau<sup>a</sup> and Mahen Mahendran<sup>a</sup>

<sup>a</sup> Queensland University of Technology, Faculty of Engineering, Brisbane, Australia

### Abstract

Light gauge Steel Frame (LSF) floor-ceiling systems made of cold-formed steel (CFS) structural members deliver lightweight and cost effective building solutions for use in many floor assemblies. However, past studies of LSF floor-ceiling systems in fire are limited. Hence a series of fire tests was undertaken to investigate the fire performance of eight LSF floor-ceiling systems. Test results showed that the use of steel sheathing (0.55 mm) increased the fire resistance time by 21 to 32%. The steel sheathing located below the gypsum plasterboard enhanced the failure times by resisting gypsum plasterboard fall-off. Fire resistance improvement of 21% occurred when an additional gypsum plasterboard layer was included over plywood. A reduction of 40% occurred for a plywood joint above the joist. The use of cavity insulation resulted in increased plasterboard and joist hot flange temperatures and led to a reduction of 12% in insulation failure time.

**Keywords:** LSF floor-ceiling systems, Cold-formed steel section joists, Steel sheathing, Cavity insulation, Joint effects.

### 1 INTRODUCTION

Cold-formed Light gauge Steel Frame (LSF) floor-ceiling systems are widely adopted in contemporary buildings due to their higher strength-to-weight ratios, better durability, enhanced thermal retention, lightweight, aesthetic appearance and cost effectiveness in comparison with other types of floor systems. Cold-formed steel (CFS) Lipped Channel Beam sections are commonly used as floor joists in LSF floor-ceiling systems. Fire rated gypsum plasterboard is attached on the bottom (ceiling side) while structural plywood is used on the top to provide fire and structural resistance to the floor joists, respectively. Depending on specific building requirements, cavity insulation may be used to improve the thermal comfort and acoustic performance of floor-ceiling systems. Fig. 1 shows a typical fire resistant cold-formed LSF floor-ceiling system. Extensive research studies have been undertaken on the fire performance of LSF wall systems with many varying configurations (Feng et al., 2003; Sakumoto et al., 2003; Feng and Wang, 2005; Chen et al., 2012; Kwon and Jee, 2014; Ariyanayagam and Mahendran, 2019; Gnanachelvam et al., 2019). However, only limited research has been undertaken on the fire performance of LSF floor-ceiling systems (Sakumoto et al., 2003; Kwon and Jee, 2014). This paper presents the details of an experimental study into the thermal performance of eight LSF floor-ceiling systems (Fig. 2) including both the conventional gypsum plasterboard lined LCB joist systems and the new gypsum plasterboard and/or steel sheathed RHFCB joist systems under standard fire conditions.

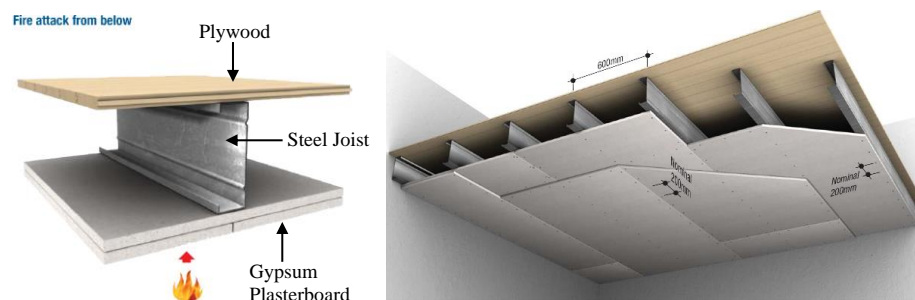


Fig. 1 Typical fire resistant cold-formed LSF floor-ceiling system

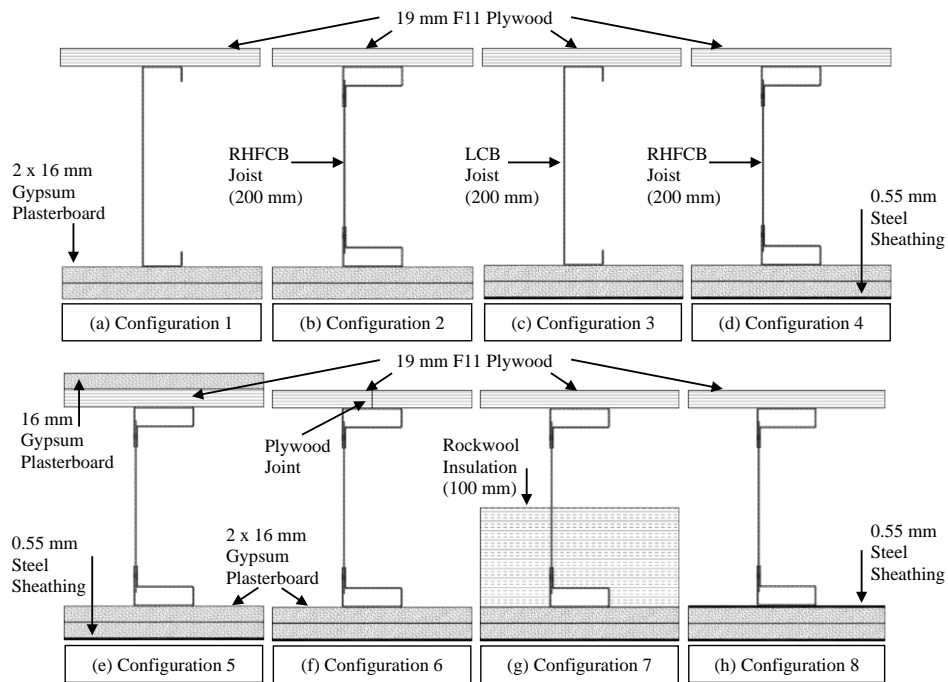


Fig. 2 LSF floor-ceiling configurations

## 2 SMALL-SCALE FIRE TESTS

### 2.1 Fire Test Details

Fire tests were conducted using a horizontally oriented radiant flame gas furnace at the QUT Wind and Fire Laboratory. The effective fire area of the furnace was 1.0 m x 1.0 m with an internal volume of 0.4 m<sup>3</sup>. All the fire tests were conducted based on the ISO 834 standard fire time-temperature curve using the EURO THERM 3504 high specification HYBIRD controller. Small-scale test floor specimens (1.2 m x 1.2 m) were placed on the furnace and rested on the outside perimeter (unrestrained on all four sides). Hence the bottom side of test floor specimen was exposed to fire. The fire exposure on one side (bottom side) of the specimen is considered critical. All four edges of the test specimen were insulated with 25 mm thick cerachem blankets (density 160 kg/m<sup>3</sup>) to minimise any heat loss during the fire tests.

### 2.2 LSF Floor-Ceiling Configurations

Eight different LSF floor-ceiling configurations were considered in this study (Fig. 2). They included combinations of two different floor joists made of 200x40x15x1.15 mm LCB section and 200x60x20x1.15x1.15 mm RHFCB section (100 mm rivet spacing) and 202x50x1.15mm unlippped channel beam (ULCB) tracks, and cavity insulation (rockwool insulation). All the steel floor joists and tracks were made of 1.15 mm thick Grade 500 steel (nominal yield stress of 500 MPa). The joists were spaced at 450 mm centres, and were protected with commercially available 16 mm thick fire rated gypsum plasterboards coupled with combinations of 0.55 mm thick steel sheathing. The thin steel sheathing was made of Grade 300 steel (nominal yield stress 300 MPa). Structural plywood (F11 Stress Grade) of 19 mm thickness was used as the subfloor that also provided lateral restraint to the floor joists. External dimensions of the test floor specimens were 1.2 m x 1.2 m. Overall, all the eight test floor specimens included two layers of 16 mm gypsum plasterboard on the fire side and one layer of 19 mm plywood on the ambient side and the differences in configurations were due to (i) joist section, LCB versus RHFCB (ii) thin steel sheathing on one or both sides of gypsum plasterboards (iii) cavity insulation (iv) additional gypsum plasterboard on the ambient side (v) plywood joint above the joist (Fig. 2).

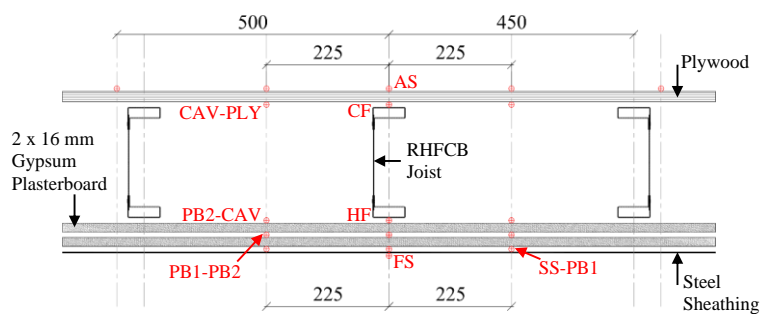


Fig. 3 Temperature measurement locations



Fig. 4 Fire test set-up of floor specimens

## 2.3 Temperature Measurements

Temperatures were obtained at various locations across the specimen thickness by using K-type cable thermocouples. Thermocouples were attached to the test specimens at equal spacing (250 mm) from the centre along the joist direction. They were also attached at 225 mm from centre in the perpendicular direction to the joist. Fig. 3 shows the thermocouple locations across the specimen height. In addition, an infrared gun was also used to measure the unexposed plywood surface temperatures. Fig. 4 shows the typical set-up of test floor specimen.

## 3 FIRE TEST RESULTS

This section presents the fire test results in terms of time-temperatures profiles for each LSF floor-ceiling system/configuration. Time-temperature measurements are shown across the specimen height and are identified as: FS – fire side (furnace temperature); SS-PB1 – steel sheathing to plasterboard one surface; PB1-PB2 – plasterboard one to plasterboard two surface; PB2-SS – plasterboard two to steel sheathing surface; PB2-CAV – plasterboard two to cavity surface; SS-CAV – steel sheathing to cavity surface; CAV-PLY – cavity to plywood surface; PLY-PB – plywood to plasterboard surface; AS – ambient side; HF – hot flange of the joist; CF – cold flange of the joist (see Fig. 3). Failure times from the small-scale fire tests are given in Table 1.

Table 1 Failure times for LSF floor-ceiling configurations

No.	Initial Temperature (°C)	Maximum Ambient Surface Temperature (°C)	Failure Time (min)	Incipient Spread of Fire (250°C)		Failure Criterion
				Temperature (°C)	Failure Time (min)	
1	25	205	103	250	72	Insulation
2	24	204	104	250	72	Insulation
3	27	207	125	250	78	Insulation
4	22	203	137	250	80	Insulation
5	25	205	126	250	77	Insulation
6	23	203	82	250	76	Insulation
7	25	-	120	250	70	Ceiling Collapse
8	22	-	90	250	77	Ceiling Collapse

Note: Insulation failure is determined as Maximum = 180K + Initial Temperature.

### 3.1 Configuration 1 (LCB Floor with two layers of 16 mm gypsum plasterboard)

Smoke and steam was observed after 3 min and its intensity increased until 6 min. After 35 min steam increased slightly for a period of 15 min. At 80 min the smoke increased again and was of white/grey colour. It continued to increase gradually, becoming severe from 95 min to the end. Configuration 1 failed by insulation criterion after 103 min when the maximum temperature on the ambient surface reached 205°C, ie. 180°C above the initial temperature of 25°C as shown in Table 1. Resistance to incipient spread of fire failure occurred when the average temperature on the unexposed surface of the plasterboard ceiling (PB2-CAV) exceeded 250°C at 72 min. This failure time is a measure of the floor configuration's resistance to fire spread. Fig. 5 shows the measured time-temperature profiles across the specimen height.

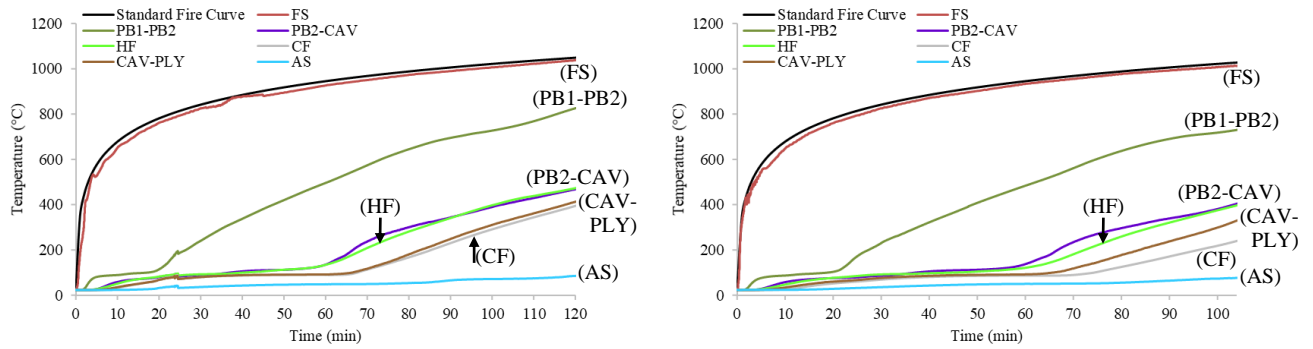


Fig. 5 Time-temperature profiles of Configuration 1 (left) and Configuration 2 (right)

### 3.2 Configuration 2 (RHFCB Floor with two layers of 16 mm gypsum plasterboard)

Test observations for Configuration 2 were similar to Configuration 1 in relation to smoke and steam propagation and temperature measurements. Insulation failure occurred after 104 min when the maximum temperature on the ambient surface reached 204°C. Resistance to incipient spread of fire failure occurred at 72 min when the average temperature on the unexposed surface of the plasterboard ceiling exceeded 250°C. Fig. 5 shows the measured time-temperature profiles across the specimen height.

### 3.3 Configuration 3 (Configuration 1 and steel sheathing)

Smoke and steam was observed after 4 min and its intensity increased during 7 to 11 min. Light steam was observed again at 75 min. At 100 min the smoke intensity increased considerably from the plywood on the ambient side and was of white/grey colour. Configuration 3 failed by insulation criterion after 125 min when the maximum temperature on the ambient surface reached 207°C. Resistance to incipient spread of fire failure occurred at 78 min when the average temperature on the unexposed side of the plasterboard ceiling exceeded 250°C. Fig. 6 shows the measured time-temperature profiles across the specimen height.

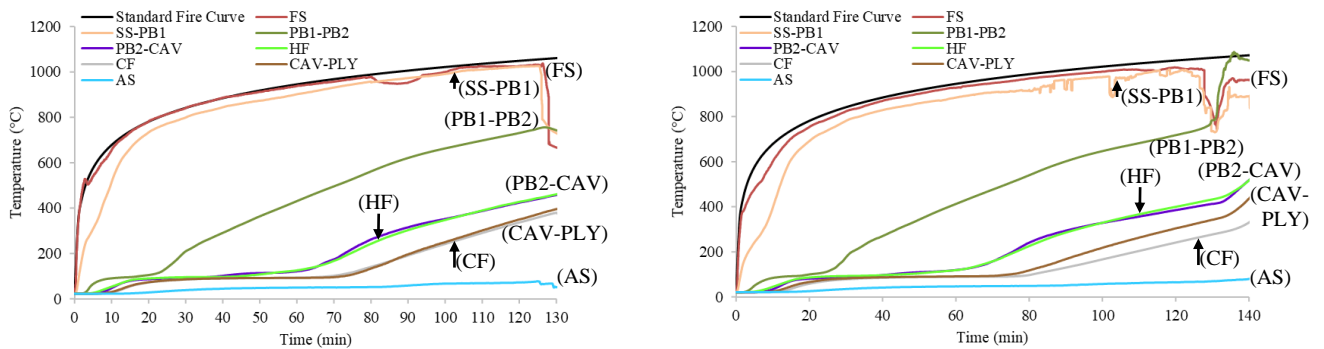


Fig. 6 Time-temperature profiles of Configuration 3 (left) and Configuration 4 (right)

### 3.4 Configuration 4 (Configuration 2 and steel sheathing)

Test observations for Configuration 4 were similar to those of Configuration 3 in regards to smoke and steam observations, burning of the plywood and fall-off of gypsum plasterboard and steel sheathing layers. Configuration 4 failed by insulation criterion after 137 min when the maximum temperature on the ambient surface reached 203°C. Resistance to incipient spread of fire failure occurred at 80 min. Fig. 6 shows the time-temperature profiles across the specimen height.

### 3.5 Configuration 5 (Configuration 4 and 16 mm gypsum plasterboard above plywood)

In order to improve the insulation failure time of Configuration 4, Configuration 5 included one additional 16 mm gypsum plasterboard above the plywood on the ambient side. Smoke and steam were observed after 4 min, its intensity increased at 11 min and continued until 20 min. Minor

levels of white/grey colour smoke were observed after 83 min, but it was clearly seen around the floor specimen after 90 min and increased until the end, becoming quite severe after 110 min. Configuration 5 failed by insulation criterion after 126 min when the maximum ambient surface temperature reached 205°C, that is, the insulation failure time was not higher than that of Configuration 4 (137 min) as expected. Resistance to incipient spread of fire failure occurred at 77 min. Fig. 7 shows the measured time-temperature profiles across the specimen height.

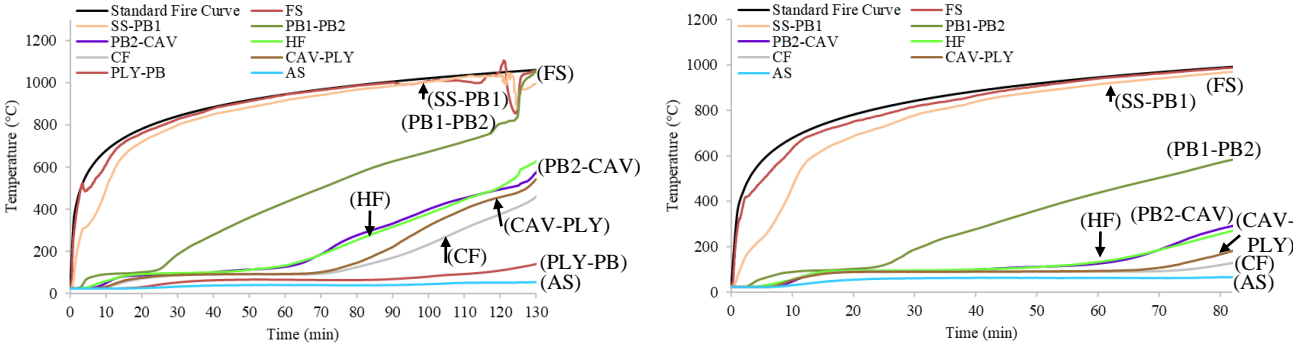


Fig. 7 Time-temperature profiles of Configuration 5 (left) and Configuration 6 (right)

**3.6 Configuration 6 (Configuration 4 modified with a plywood joint above the joint)**

Smoke and steam observations were similar to those of Configuration 5 until 25 min when it was clear that the smoke and steam was escaping from the joint in plywood. After 45 min, smoke increased slightly and was of white/grey colour by 60 min. Configuration 6 failed by insulation criterion after 82 min when the maximum ambient surface temperature reached 203°C. Resistance to incipient spread of fire failure occurred at 76 min. Fig. 7 shows the time-temperature profiles across the specimen height.

**3.7 Configuration 7 (Configuration 4 with cavity insulation)**

Configuration 7 failed after 120 min due to ceiling collapse. Resistance to incipient spread of fire failure occurred at 70 min. Fig. 8 shows the time-temperature profiles across the specimen height. Fig. 8 shows that the PB1-PB2 temperatures increased rapidly after 23 min when compared with Configuration 4 without cavity insulation. The collapse of the gypsum plasterboard layers is identified by the sudden temperature rise of over 200°C within a short period of time at the end as shown in Fig. 8.

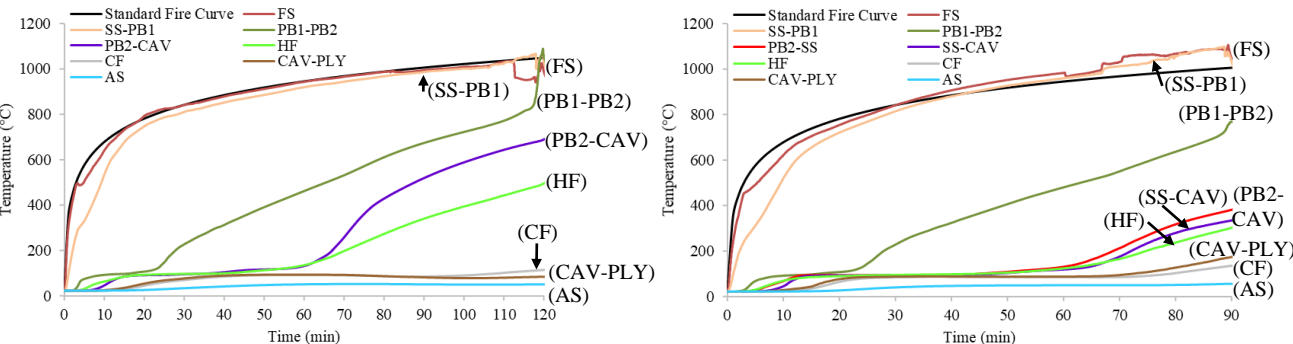


Fig. 8 Time-temperature profiles of Configuration 7 (left) and Configuration 8 (right)

**3.8 Configuration 8 (Configuration 4 modified with two steel sheathings)**

Configuration 8 failed by ceiling collapse at 90 min due to over-heating beyond the standard fire curve after about 30 min, and the test was stopped. Resistance to incipient spread of fire failure occurred at 77 min. Fig. 8 shows the time-temperature profiles across the specimen height.

## 4 COMPARISON OF THE BEHAVIOUR LSF FLOOR-CEILING CONFIGURATIONS

Table 2 compares the insulation failure times of LSF floor-ceiling configurations with respect to steel sheathing, joist section type, cavity insulation, additional plasterboard and plywood joint. The results presented in the last section are based on the fire tests of small-scale LSF floor-ceiling assemblies without a transverse load. It is likely that full scale LSF floor-ceiling assembly (4m x 3m) tests would have given reduced failure times due to earlier gypsum plasterboard-off caused by larger deflections. However, in this study aimed at investigating and comparing the effects of a range of floor-ceiling configuration parameters, small scale fire tests are most suitable and their results can be used to investigate and, in particular, to compare the effects of the selected range of parameters on the fire resistance behaviour of LSF floor-ceiling systems

Table 2 Comparisons between LSF floor-ceiling configurations

No.	Section Joist	Steel Sheathing Configuration	Failure Time (min)	Configuration Comparison	Improvement in Failure Time (min)	Increment
1	LCB	None	103	-	-	-
2	RHFCB	None	104	Config 1,2	1	1.01
3	LCB	Fire Side	125	Config 1,3	22	1.21
4	RHFCB	Fire Side	137	Config 2,4	33	1.32
				Config 3,4	12	1.10
5	RHFCB	Fire Side	126	Config 2,5	22	1.21
				Config 4,5	-11	0.92
6	RHFCB	Fire Side	82	Config 4,6	-55	0.60
7	RHFCB	Fire Side	120	Config 4,7	-17	0.88

## 5 CONCLUSIONS

This paper has presented the details of an experimental study on the fire resistance of LSF floor-ceiling configurations under standard fire conditions. This study included eight small-scale LSF floor-ceiling configurations and their fire resistance times. Results showed that insulation failure times are unlikely to be improved by using different types of joists if they are of the same depth and thickness. In all cases thin steel sheathing located on the ceiling side provided improved insulation failure times by increasing the resistance to plasterboard fall-off. It showed improvements of 21% for LCB floors while it showed improvements of 32% for RHFCB floors. The use of a gypsum plasterboard layer on the ambient side over the plywood increased the insulation failure time by 21%, but increased the rate of decomposition of plywood. The insulation failure time was reduced by 40% when a plywood joint was used above the joist. Cavity insulation caused a reduction of 12% in insulation failure time and led to higher plasterboard and joist hot flange temperatures.

## REFERENCES

- Feng M., Wang Y. C. and Davies J. M. 2003. Thermal performance of cold-formed thin-walled steel panel systems in fire. *Fire Safety Journal*. Vol. 38: pp. 365-394.
- Sakumoto, T., Hirakawa, T., Masuda, H. and Nakamura. K. 2003. Fire resistance of walls and floors using light-gauge steel shapes. *ASCE. Journal of Structural Engineering*. Vol. 129: pp. 1522-1530.
- Feng M., and Wang Y. C. 2005. An analysis of the structural behaviour of axially loaded full-scale cold-formed thin-walled steel structural panels tested under fire conditions. *Thin-Walled Structures*. Vol. 43: pp. 291-332.
- Chen, W., Ye, J., Yu Bai, Zhao, X. 2012. Full-scale fire experiments on load-bearing cold-formed steel walls lined with different panels. *Journal of Constructional Steel Research*. Vol. 79: pp. 242-254.
- Kwon, I. K. and Jee, N. Y. 2014. Experimental study of the fire resistance of walls and floors constructed with steel studs and steel joists. *Fire and Materials*. Vol. 38: pp. 77-91.
- Ariyanayagam, A. and Mahendran, M. 2019. Influence of cavity insulation on the fire resistance of light gauge steel framed walls. *Construction and Building Materials*. Vol. 203: pp. 687-710.
- Gnanachelvam, S., Ariyanayagam, A. and Mahendran, M. 2019. Fire resistance of light gauge steel framed wall systems lined with PCM-plasterboards. *Fire Safety Journal*. Vol. 108. pp. 102838.

## EXPERIMENTAL STUDY ON BOND BEHAVIOR BETWEEN STEEL AND CONCRETE AT ELEVATED TEMPERATURES

Ira Banoth<sup>a</sup>, Anil Agarwal<sup>b</sup>

<sup>a</sup> Research scholar, Department of Civil Engineering, Indian Institute of Technology Hyderabad (IITH), India

<sup>b</sup> Assistant Professor, Department of Civil Engineering, Indian Institute of Technology Hyderabad (IITH), India

### Abstract

Bond behaviour between steel and concrete is studied at the elevated temperature of 20,100,200,300,400 and 500°C. The parameters considered are different types of diameter (12, 20 mm) of rebar and two different types of heating rate (2°C/min and ISO 834). The compressive strength of concrete 22 MPa is used. Pull out tests were conducted on a cubical specimen of size 200x200x200 mm with eccentrically embedded rebar. Pull out load is applied after reaching the desired temperature at the interface.

The bond strength is reduced with the increase of temperature. The reduction of bond strength is more in the case of heating rate followed by ISO than the heating rate of 2°C/min, this may be due to large thermal gradients in the case of rapid heating rate ISO 834.

**Keywords:** Concrete, Rebar, Elevated temperature, Heating rate, Bond strength

### 1 INTRODUCTION

When structure is subjected to the external load, stresses occurred at the interface of steel and concrete. These stresses arise due to chemical adhesion at the interface between steel and concrete, mechanical interlocking of ribs, and friction resistance. This problem can be understood by conducting some tests namely pull-out test and beam tests, specifications of these test details are provided in [1]. Analytical bond stress slip model developed by conducting pull-out tests at ambient condition shown in Fig. 1.

Initial curved part represents rebar ribs penetrating in to the mortar mix, horizontal part occurred due to shearing off of the concrete only for confined concrete, decreasing branch represents the bond strength reduction due to occurrence of splitting cracks along the rebar. Understanding of bond mechanism becomes more complex, when structure is subjected to elevated temperature, it involves thermal stress, and material strength degradation. So, for understanding structural behaviour, it is necessary to understand the bond behaviour at the interface of steel and concrete.

In past years, many studies are available for the bond behaviour of steel-concrete in post fire conditions. But for during elevated temperature, the bond behaviour at the interface of steel and concrete are very less, hardly two literatures are available [2,3].

Diederichs et.al [2], studied bond behaviour of different types of rebar in different test conditions. Conclusions drawn from this study is bond behaviour depends not only on the temperature and but also depends on the testing methods. The bond strength of plain rebars is less than deformed rebars and pre-stressing steel rebars, this behaviour is due to ribs of rebar, it can resist the pull-out force for some extent. Bond stress-slip behaviour of prestressing steel rebars and deformed steel rebars are similar, because both the bars are having deformations. Royles et.al [3], studied bond behaviour in four testing conditions, namely: a) stressed during heating, b) unstressed during heating, c) stressed in residual condition and d) unstressed in residual condition. Up to the temperature of 250°C, bond strength is more in case of residual condition than hot condition. This is due to thermal stresses added to the external stresses up to the temperature 250°C, after that concrete cracks in residual condition is more significant than the thermal stresses. At ambient condition, bond strength is more in case of

unstressed condition than the stressed condition, due to there is some disturbance at the steel concrete interface while specimen is subjected to stresses. Stressed specimen gives slightly gives better performance than the unstressed specimen. This could be explained by, restrain provided by steady state bond stress can prevent the cracks at the steel concrete interface.

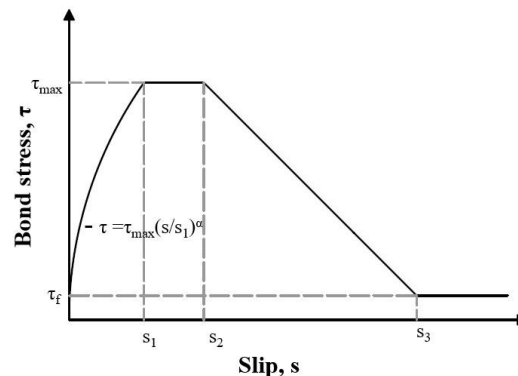


Fig. 1 Analytical bond stress slip model

Some of the researchers studied bond behaviour of steel and concrete in post fire conditions by considering different parameters, different types of concrete, bond length, different types of rebar, and effect of cooling conditions. Haddad et.al [4] used different types of fibres namely: hooked end steel bars, polypropylene and basalt coated fibres. Incorporation of fibres prevent cracks and increased ductility at the steel-concrete interface. The reduction of bond strength is more significant at 450°C due to decomposition of portlandite [5]. Varona et.al [6], studied bond behaviour of normal strength and high strength concrete with inclusion of fibres (steel, polypropylene) were studied. Conclusion from this study drawn are: polypropylene fibres used for preventing explosive spalling and inclusion of steel fibre with high aspect ratio improves peak bond strength. Deshpand et.al [7], studied bond behaviour with different types of concrete namely: conventional concrete of strength 35 and 60 MPa, strain hardening cementitious composite (SHCC) with Polyvinyl alcohol fibres and SHCC with the hybrid fibres. At room temperature bond strength is more in the case of Conventional concrete than the SHCC, due to interlock of rebar ribs and aggregate. At elevated temperature SHCC Hybrid fibre reinforced concrete gives more bond strength than the Mono fibre concrete. This is due to the presence of steel fibres prevents splitting crack along the rebar and increases the ductility at the concrete steel interface.

Ferhat et.al [8], were considered the effect of bond length and different cooling conditions. The bond strength is more in the case of air cooled specimens than the water cooled specimens. This is due to thermal shock occurs in the case of water cooled specimens. Lee et.al [9], studied bond behaviour with different types of rebar (epoxy coated and uncoated rebar), and types of heating rate. Bond strength increases at the temperature of 200°C in the case of uncoated rebar, this due to the expansion of concrete and steel increases at the bond region, but in the case of epoxy coated rebar, bond strength increases due to the melting of epoxy increase bond of concrete with the steel. And heating rate plays a very significant role in reduction of bond strength. Bond strength decreases with the increase of heating rate, this is due to large thermal gradients in the case of higher heating rate.

## 2 EXPERIMENTAL PROGRAMME

### 2.1 Materials

Ordinary portland cement of 53 grade, Fine aggregate (river sand), angular coarse aggregate, dhanalaxmi Fe550 grade locally available materials are used. Concrete mix is designed according to IS 10262 [10]. Cement, fine aggregate, coarse aggregate, water, superplasticizer: 370,828,1173,162,4.43 kg/m<sup>3</sup> is used. After 24 hours of casting, specimens demoulded and cured for 15 days and dried for 15 days before testing.

## 2.2 Specimen preparation

Type of specimen chosen by considering codal provisions [11] and practical scenario. Cubical specimen of size 200x200x200 mm with eccentrically (40 mm from the surface of the specimen) embedded rebar bonded in the middle portion (four times the diameter of rebar) is considered. Three thermocouples are placed in the interface, where the concrete is bonded with rebar to measure the interface temperature. Specimen details and preparation are shown in Fig. 2.

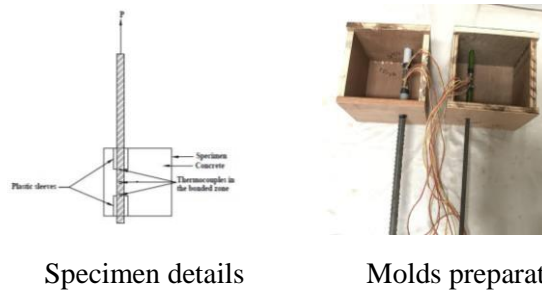


Fig. 2 Specimen details and preparation

## 3 TEST SETUP AND TEST PROCEDURE

Setup is designed to compress the concrete cube and pull out the rebar as shown in Fig. 3. Hollow rectangular beam (1) with a fixer resist the concrete cube. Specimen is heated in a rectangular heating chamber, arranged by four rectangular heating ceramic panels. Specimen is heated until the desired temperature reaches at the interface by following different heating rates. Temperature versus time data plots are shown as shown in Fig. 4. Once the desired temperature reaches at the interface pull-out load is applied through a fatigue testing machine of 500 kN capacity with a loading rate of 2.5 mm/min. The bond stress versus slip readings are measured.

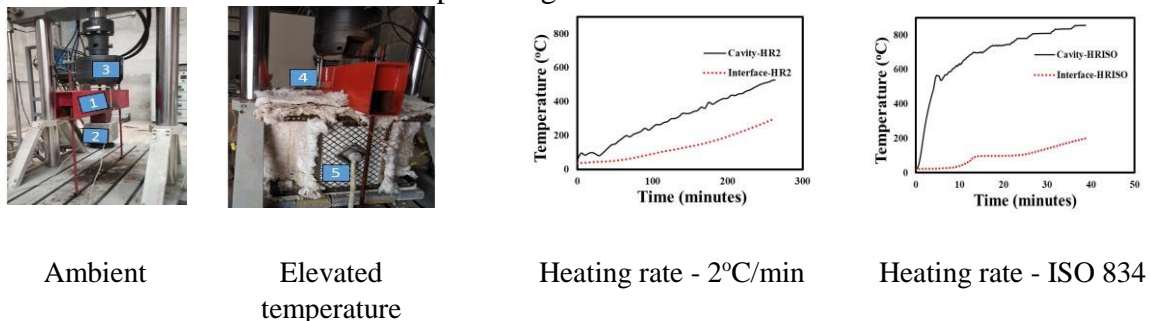


Fig. 3 Test setup

Fig. 4 Temperature versus time

## 4 TEST RESULTS AND DISCUSSION

### 4.1 Bond stress-slip behaviour

Bond stress versus slip results are plotted as shown in Fig.5. Bond strength of 12 mm diameter varying from 11.32 to 3.29 MPa, at elevated temperature of 25,100,200,300,400 °C by following heating rate of 2 °C/min and in the case of ISO heating rate; bond strength decreased rapidly from 11.32 to 0.14 MPa in the temperature range of 25-300°C. Bond stress-slip patterns are similar by both following heating rate, irrelevant of magnitude. All the specimens are failed by bond failure as shown in Fig. 6.

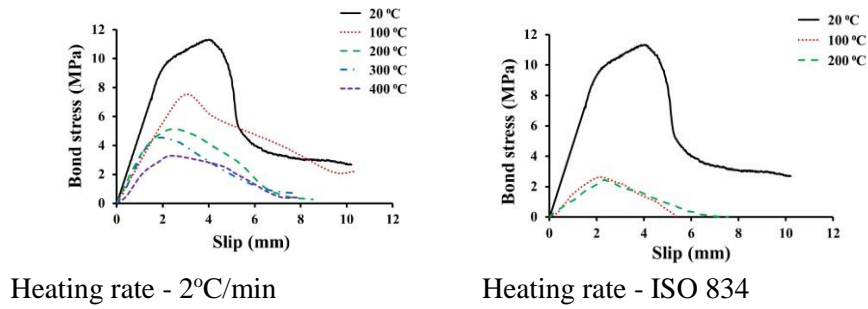


Fig.5 Bond stress versus slip

Table 1 Test results of 12 mm diameter rebar

Diameter of rebar (mm)	Heating rate (°C/min)	Temperature (°C)	Bond strength (MPa)	Slip (mm)	Residual bond strength (MPa)
12	ambient	25	11.32	4.02	100
12	2	100	7.26	3.03	64
12	2	200	5.09	2.25	45
12	2	300	4.38	2.48	39
12	2	400	3.29	2.46	29
12	ISO-834	100	2.61	2.03	23
12	ISO-834	200	2.43	2.31	21
12	ISO-834	300	0.14	3.09	1



Fig. 6 Failure patterns of 12mm diameter rebar by following different heating rate

Bond stress versus slip behaviour of 20 mm rebar is shown in Fig. 7. The curve is similar to the CEB model code bond stress-slip curve, except the horizontal part represented in model code. Bond strength varying from 12.19 to 3.19 MPa in the temperature range of 25-500°C in the case of heating rate followed by heating rate of 2°C/min in the case of ISO heating rate bond strength varying from 12.19 to 0.43 MPa. Test results are shown in Table 2. All the specimens are failed by pull out failure as shown in Fig. 8.

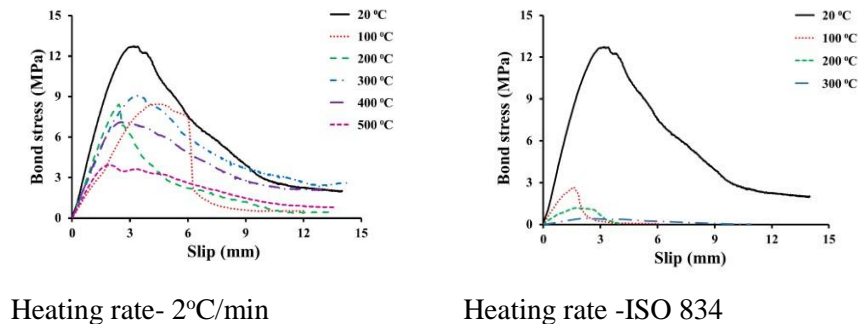


Fig. 7 Bond stress versus slip



Ambient

Heating rate- 2°C/min

Heating rate -ISO 834

Fig. 8 Failure patterns of 20 mm rebar by following different heating rates

Table 2 Test results of 20 mm rebar

Diameter of rebar (mm)	Heating rate (°C/min)	Temperature (°C)	Bond strength (MPa)	Slip (mm)	Residual bond strength (MPa)
20	ambient	25	12.19	2.79	100
20	2	100	8.42	4.34	69
20	2	200	8.40	2.43	69
20	2	300	9.06	3.31	74
20	2	400	7.13	2.59	59
20	2	500	3.92	1.89	32
20	ISO-834	100	2.64	1.63	22
20	ISO-834	200	1.19	1.86	10
20	ISO-834	300	0.43	2.12	4

#### 4.2 Residual bond stress

Normalized bond strength against temperature of all the cases as shown in Fig. 9. Reduction of bond strength of 12 mm rebar in the case of heating rate followed by 2°C/min, varying from 100 to 29 % in the temperature range of 100-400°C. In the case of ISO 834 heating rate bond strength at elevated temperature 100, 200,300°C are; 23%, 21 and 1%. In the case of 20 mm rebar RBS varies from 100-32% in the temperature range of 100-500 and in the case of ISO heating rate bond strength varies from 22 – 4% at temperature range of 100-300°C. in the case of slow heating rate, reduction of bond strength is more significant beyond the temperature of 300°C. But in the case of ISO heating rate the reduction of bond strength is almost 80 % in the case of both the diameter of rebar. The effect of heating rate is more significant on the reduction of bond strength, this may be due to the large thermal gradients in the case of ISO heating rate.

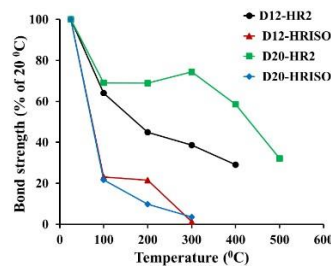


Fig. 9 Normalised bond strength against temperature

## 5 CONCLUSIONS

- Bond stress-slip behaviour of two different diameters 12 mm, 20 mm were studied by two different heating rate of 2°C/min and ISO 834 by conducting eccentric pull out test.
- Bond-stress slip behaviour is similar in all the cases irrelevant of magnitude.
- Reduction of bond strength is very significant in the case of heating rate followed by ISO Heating. Bond strength reduces at 100°C itself 80% and at the temperature of 300°C, bond strength is almost zero. Even though in the case of slow heating rate 2 °C/min, the reduction of bond strength at 300°C is 25% in the case of 20 mm rebar.

## REFERENCES

- CEB – FIP Model code 90, *first draft, committee euro-international du beton, bulletin d'information No.* 195,196.
- Diederichs U., Schneider U., 1981. *Bond strength at high Temperatures. Mag Concr Res*, 33(115), p. 75-84.
- Royles, R., Morley P.D. (1983), *Further responses of the bond in reinforced concrete to high temperatures. Mag Concr Res*, 35 (1983), P. 157–163.
- Haddad R.H., Al-Saleh R.J., Al-Akhras N.M., 2008. *Effect of elevated temperature on bond between steel reinforcement and fibre reinforced concrete, Fire Saf J*, 43, p. 334-343.
- Éva Lubl6y-Viktor, Hlavick6ka, 2017. *Bond after fire. Constr Bulid Mater*, 132, P. 210-218.
- Varona F.B., Baeza F.J., Bru D., Ivorra S., 2018. *Evolution of the bond strength between reinforcing steel and fibre reinforced concrete after high temperature exposure. Constr Bulid Mater*, 176, p. 359-370.
- Dhanendra Kumar, Ravi Ranade, Alok A. Deshpande, Negar Elhami Khorasani, 2018. Effects of elevated temperatures on residual bond strength of steel rebar with strain hardening cementitious composite, in *3<sup>rd</sup> RN Raikar Memorial Intl & Gettu-kodur Intl symposium on Advances in Science and technology of concrete*, 14- 15 December 2018, The St. Regis, Mumbai, India, p. 30-39.
- Bingol A.F., Gul R., (2009). *Residual bond strength between steel bars and concrete after elevated temperatures. Fire Saf J*, 44, p. 854–859.
- Jaesung Lee, Evan sheesley, yuxiang Jing, Yunping, Kaspar Willam, 2018. *The effect of heating and cooling on the bond strength between concrete and steel reinforcement bars with and without epoxy coating. Constr Bulid Mater*, 177, p. 230-236.
- IS: 10262-2009, *Concrete Mix Proportioning – Guidelines.*
- ENV 10080:1995, *Steel for the Reinforcement of Concrete – Weldable Reinforcing Steel – General.*

# CEMENT MORTAR AS PASSIVE FIRE PROTECTION IN STEEL COLUMNS

Hugo Caetano, Aldina Santiago, Luís Laím, Askan Shahbazian

<sup>a</sup>University of Coimbra, ISISE, Department of Civil Engineering, Coimbra, Portugal

## Abstract

During a fire event, the stability of steel members may be compromised, and the structural collapse may occur, due to the loss of its mechanical resistance as the temperature increase. In this sense, the main objective of this experimental work was to develop a cement mortar as a passive fire protection for steel members and to evaluate the structural behaviour of steel columns subject to axial compression and high temperatures when protected with: i) a developed mortar, ii) a commercial mortar and iii) without any kind of passive protection. When compared to the steel column without any type of fire protection, the results showed that a) the commercial mortar and the mortar developed in the laboratory contribute to the increased of fire resistance of the steel columns 4.5 and 5.0 times more, respectively and b) the developed mortar provided at least a fire protection of 10% more effective than the commercial solution.

**Keywords:** cement mortars, vermiculite, passive fire protection, steel structural elements.

## 1 INTRODUCTION

There is a growing interest in the development of alternative and sustainable construction materials with enhanced properties. As metals are infinitely recyclable, this type of construction is part of a future of “green construction”, thus contributing to a sector of the economy with low environmental impact (European Commission, 1997; Gervásio *et al.*, 2005; Gervásio *et al.*, 2008). However, steel structures also show some weaknesses, for example, their structural behaviour when subjected to fire (Devine, 2018; Mofizul Islam *et al.*, 2018; Outinen *et al.*, 2004; Ravindra *et al.*, 2017; Santiago *et al.*, 2008; Wald *et al.*, 2009). Due to the high thermal conductivity of the steel and the rapid degradation of the mechanical properties, with the increase of steel temperature, rapid change in the stiffness and mechanical resistance is noticed in the structure, and its stability may be compromised, leading to the collapse of some elements, or even of the entire structure (Franssen *et al.*, 1993; Lamont *et al.*, 2004; Usmani *et al.*, 2001; Wang *et al.*, 1995; Wang *et al.*, 2011; Vaz-Ramos *et al.*, 2019).

The thermal protection of these structural elements is of significant importance. One of the solutions to this protection is the coating with enhanced fire resistant mortars due to the introduction of thermally stable and porous aggregates (Caetano *et al.*, 2019). Vermiculite and/or perlite have been incorporated in cement mortars with the objective of improving their thermal performance when subjected to high temperatures (Laím *et al.*, 2021). Due to their highly porous structure and low thermal conductivity, these materials absorb moisture in varying degrees (depending on their type), extending their durability during the fire. As they are materials with good thermal properties, there is the potential to be used in the development of plaster or cement mortars as a passive fire protection solution in steel structures.

## 2 EXPERIMENTAL PROGRAM AND EXPERIMENTAL SET-UP

### 2.1 Experimental Program

This experimental investigation was carried out at the Laboratory of Testing Materials and Structures (LEMEC) of the University of Coimbra, in Portugal. In order to evaluate the thermal efficiency provided by the passive fire protection mortar developed in the laboratory, experimental tests were carried out on three short tubular steel columns at high temperatures: one without any

type of coating (SP1), the second one with a mortar commercial (SP2) and the third one with a mortar developed in the laboratory (SP3). The mortar developed in the laboratory consisted of cement, vermiculite and polypropylene fibres. The results obtained from the test carried out in column SP1 were used as a reference for comparison with those obtained in steel columns SP2 and SP3 and, thus, to evaluate the thermal insulation provided by the different mortars studied.

**2.2 Specimens**

The columns were defined by a hollow square section 150 x 150 x 8 mm, with a height of 1250 mm and the steel grade was S355. At the column ends, it was centered and welded a steel plate (section 300 x 300 x 20 mm). To evaluate the temperature evolution on the external surfaces of the steel columns during the test, 12 type K thermocouples were welded, equidistant from each other on all the specimen's surfaces, applied in 3 groups of 4 thermocouples at different heights. In order to guarantee a constant and uniform mortar thickness along the steel columns, a modular formwork was developed with the ability to assign the desired geometric shape, easy to assemble and disassemble while concreting the specimen. Figure 1 depict the location of the three groups of thermocouples and the different concreting steps of the steel columns.



Fig. 1 Distribution of thermocouples and the different steps of casting mortars on the steel columns.

**2.3 Test Set-Up**

The experimental layout (figure 2) consisted of a steel frame, used as reaction to the load applied to the specimen during the test.

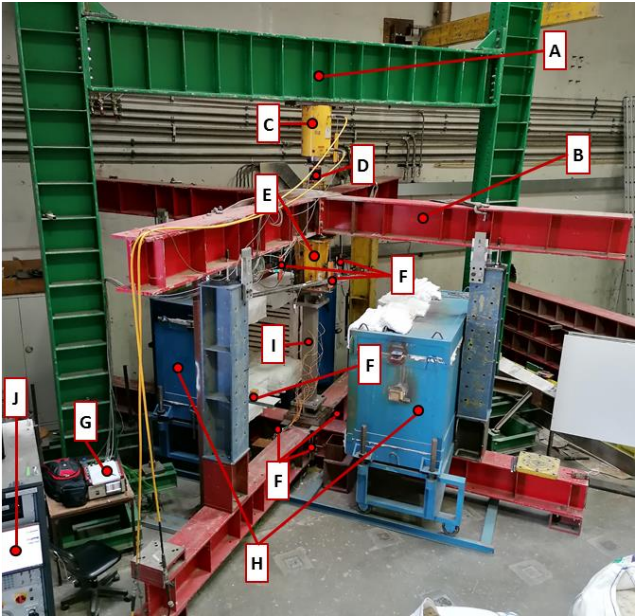


Fig. 2 Experimental system used in the laboratory in this research work.

This steel frame was defined by columns HEB 500 and a beam HEB 600 (A), with a stiffness capable of minimizing possible displacements of this steel structure during the tests; additionally, a second support structure consisting of two frames (B) with HEB 300 columns and HEB 400 beams, had the function of load transmission to the specimen. Regarding the test equipment, a 3 MN hydraulic jack (C) and its controller (J), a 3 MN load cell (D) and a 1 MN load cell (E) were used for measuring the compression forces, 10 linear variable displacement transducers were used for displacements measurements, (F), a Datalogger (G) for data acquisition and a furnace (H) to heat the steel columns (I).

## 2.4 Test Procedure

In order to simulate a service load on the specimen, the hydraulic jack controlled by a servo-controlled central was used and a preload of 50 % of the design value of the loadbearing capacity of the columns at room temperature (ULS) was applied (727.8 kN). After stabilized this loading in the specimen, the furnace was switched on and the specimen heated according to the temperature evolution established by the ISO 834 standard fire curve (EN 1993-1-2, 2005).

Due to the increase in temperature during the test, significant thermal elongation was generated in the specimen caused by the high temperatures. The test was stopped based on the axial contraction criterion defined by ISO 834-1: 1999 (ISO 834-1, 1999), which defines a limit shortening of the specimen according to its initial length, from which was considered the specimen could no longer support the initial applied load subjected to high temperatures. Thus, the final value of vertical deformation considered, was 12.5 mm. Finally, the degree of detachment of the protective mortar and the mode of instability that occurred in each specimen were observed.

## 3 RESULTS AND DISCUSSION

In the case of the SP1 specimen (steel column without passive fire protection), the temperature attributed to the column at its moment of instability, resulted from the arithmetic average of the temperatures obtained in the three groups of thermocouples. In the case of specimens SP2 and SP3 (coated with mortar for passive fire protection), the temperature attributed to the column at its moment of instability corresponds to the temperature of the group of thermocouples with the highest temperature, as there were areas of the column already unprotected and other areas of the spine that were still protected.

Until the specimens became unstable, graphs were generated with the evolution of the vertical deformation of the specimen as a function of time (figure 3) in order to identify the critical experimental temperature, as well as graphs of temperature evolution as a function of time (figure 4) to identify standard fire rating of steel columns.

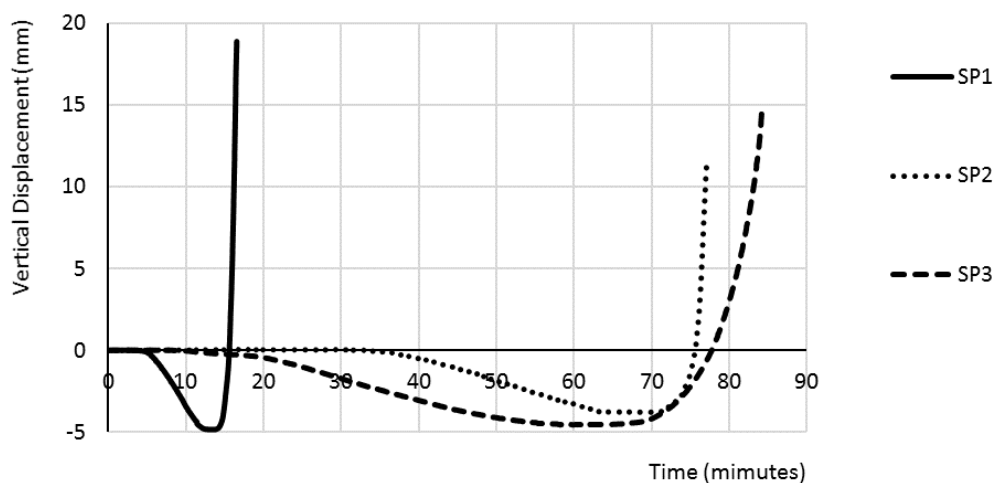


Fig. 3 Evolution of vertical deformation in the specimens as a function of time.

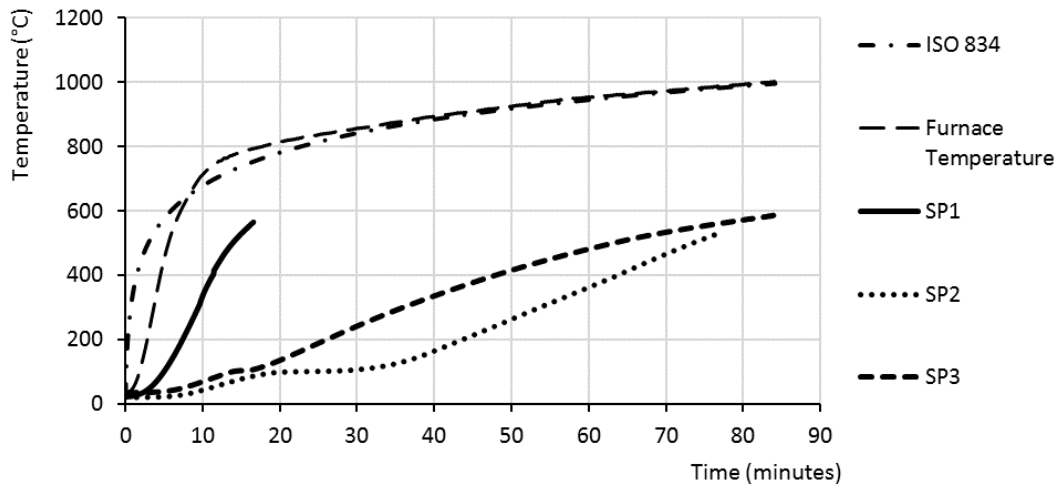


Fig. 4 Evolution of temperature in the specimens as a function of time.

In figure 3, it can be seen that the specimen SP1 failed at 17 minutes, SP2 at 76 and SP3 at 84 minutes, corresponding to temperature of 560, 531 and 587 °C, respectively. In addition, it appears that for lower temperatures the commercial mortar has a more effective thermal protection, but for higher temperatures, its thermal capacity tends to decrease due to the degradation of the mortar. This finding is justified by the development of the heating curve for the SP2 specimen.

Based on figure 4 it is possible to observe that the furnace temperatures had a small delay in the initial minutes in relation to the ISO 834 standard fire curve. This part of the curve is very difficult to reproduce in an electric furnace and this becomes worse for larger furnaces (high initial thermal inertia). However, 15 min after the beginning of the heating, the furnace temperatures followed the ISO 834 standard fire curve very well (ISO 834-1, 1999). Nevertheless, the evolution of temperatures inside the furnace over time was very uniform in all fire tests, meaning that the tests are comparable.

Figure 5 depicts specimen's images before and after being tested and the respective modes of column instability.



Fig. 5 Photos of the specimens before and after tested.

Table 1 shows the average temperature values acquired in the specimens after 15, 30, and 60 minutes, as well as the average temperature values for the instability instants of each specimens. The design critical temperature calculated according EN 1993-1-2: 2005 was 586.7 °C. (EN 1993-1-2, 2005).

Table 1 Average temperature value obtained on the specimens.

Specimens	Average temperature of specimens (°C)					
	15 minutes	17 minutes	30 minutes	60 minutes	76 minutes	84 minutes
SP1	525	560	-	-	-	-
SP2	77	86	108	362	531	-
SP3	103	106	242	481	561	587

Based on the evolution of deformation in the tested specimens (table 2) and the time corresponding to the beginning of accentuated deformations (parameter indicating the significant loss of mechanical resistance), it was possible to establish standard fire rating of the specimens (Regulamento, 2008).

Table 2 Assignment of the Standard Fire Rating of the specimens.

Specimens	Test time until the occurrence of significant deformations in the steel columns (minutes)	Standard Fire Rating
SP1	17	R 15
SP2	76	R 60
SP3	84	R 60

Table 2 shows that the specimen without passive fire protection (SP1) presented standard fire rating of R15, while the application of mortars as passive fire protection in the specimens SP2 and SP3 allowed standard fire rating of R60.

The tables of the commercial mortar tested, indicate that for a mass of 130 and for a covering thickness of only 17 mm (less than the 20 mm tested) the standard rating of fire resistance should be R90 minutes. However, the results obtained in the test of specimen SP2 (R60) clearly showed that they do not have the announced performance.

#### 4 CONCLUSIONS

The main objective of this experimental work was to show the performance of a new cement mortar that was developed as passive fire protection for steel members and to compare the mechanical behaviour of steel columns subject to axial compression and high temperatures when protected with the developed mortar, a commercial mortar and without any kind of thermal protection. The results showed that:

- The commercial mortar and the mortar developed in the laboratory increased the fire resistance of the steel columns: 4.5 and 5.0 times more, respectively and b) the developed mortar provided at least a thermal protection of 10% more effective than the commercial solution.
- The developed mortar and commercial mortar applied to the steel columns as passive fire protection proved to be an effective solution since the standard fire rating of a column without thermal protection went from R15 to R60.

Regarding the instability modes of the steel columns, local instability was observed despite the fact that the column was class 1 cross-section.

#### ACKNOWLEDGMENTS

The authors gratefully acknowledge to the Portuguese Foundation for Science and Technology (FCT) for its support under the framework of research project PTDC/ECI-EGC/31850/2017 (NANOFIRE - Thermal and

Mechanical behaviour of Nano Cements and their application in steel construction as fire protection) and also to the University of Coimbra (UC) for their support under the Scientific Employment Stimulus Programme given to the first author, as well as to the European Regional Development Fund, the European Social Fund, and European Structural and Investment Funds. This work was also financed by FEDER funds through the Competitiveness Operational Programme - COMPETE and by national funds through FCT within the scope of the project POCI-01-0145-FEDER-007633 and through the Regional Operational Programme CENTRO2020 within the scope of the project CENTRO-01-0145-FEDER-000006.

## REFERENCES

- Gervásio, H. e Simões da Silva, L., 2005. A sustentabilidade do aço, *Construção Metálica e Mista V, CMM*, Lisboa, Portugal, p. 719-730.
- European Commission, 1997. Communication from the European Commission: The competitiveness of the Construction Industry, COM (97) 539, Brussels.
- Gervásio, H., Simões da Silva, L., 2008. Comparative life-cycle analysis of steel-concrete composite bridges, *Structure and Infrastructure Engineering*, Vol 4, Issue 4, p. 251-269.
- Devine, J. W., 2018. Improving Ductility Fire Resistant Materials, Major Qualifying Project, Worcester Polytechnic Institute, Massachusetts.
- Ravindra, G, Puri., A. S. Khanna., 2017. Intumescent Coatings: A review on recent progress, *Journal of Coatings Technology and Research*, Vol. 14, Issue 1, p. 1-20.
- Mofizul Islam, Md., Rubieyat, Bin Ali., 2018. Fire Protection of Steel Structure: An Overall Review, *World Scientific News*, Vol. 102, p. 131-145.
- Outinen, J., & Mäkeläinen, P., 2004. Mechanical properties of structural steel at elevated temperatures and after cooling down, *Fire and Materials*, Vol. 28, p. 237-251.
- Santiago A., Simões da Silva L., Vaz G., Vila Real P. e Gameiro Lopes A., 2008, Experimental investigation of the behaviour of a steel sub-frame under a natural fire, *International Journal of Steel and Composite Structures* 8, p. 243-264.
- Wald, F., Chlouba, J., Uhlíř, A., Kallerova, P. and Štujberová, M., 2009. Temperatures during fire tests on structure and its prediction according to Eurocodes, *Fire safety journal*, Vol. 44, Issue 1, p. 135-146.
- Lamont, S., Usmani, A.S. and Gillie, M., 2004. Behaviour of a small composite steel frame structure in a “long-cool” and a “short-hot” fire, *Fire safety journal*, Vol. 39, Issue 5, p. 327-357.
- Vaz-Ramos J., Santiago A., Portugal A. e Durães L., 2019. Synthesis of Silica Nanoparticles to Enhance the Fire resistance of Cement mortars”. *Fire Research*, 3 (1), p. 44-48.
- Franssen, J.M., Cooke, G.M.E. and Latham, D.J., 1993. “Numerical simulation of a Full Scale Fire Test on a Loaded Steel Framework, *Journal of Constructional Steel Research*, Vol. 35, Issue 3, p. 377-408.
- Wang, Y.C., Dai, X.H. and Bailey, C.G., 2011. An experimental study of relative structural fire behaviour and robustness of different types of steel joint in restrained steel frames, *Journal of Constructional Steel Research*, Vol. 6, Issue 7, p. 1149-1163.
- Usmani, A.S., Rotter, J.M., Lamont, S., Sanad, A.M. and Gillie, M., 2001. Fundamental principles of structural behaviour under thermal effects, *Fire Safety Journal*, Vol. 36, Issue 8, p. 721-744.
- Wang, Y.C., Lennon, T. and Moore, D.B., 1995. The behaviour of steel frames subject to fire, *Journal of Constructional Steel Research*, Vol. 35, Issue 3, p. 291-322.
- Caetano, H., Vaz-Ramos, J., Santiago, A., Durães, L., Portugal, A., 2019. Desenvolvimento de argamassas cimentícias com nanosilica como protecção passiva para elementos metálicos, XII Congresso de Construção Metálica e Mista.
- Laím L., Caetano H. e Santiago A., 2021, A review on the role of nanoparticles in cement-based construction materials at ambient and fire conditions, *Journal of Building Engineering*, 102008
- EN 1993-1-2, 2005. Eurocódigo 3 – Projecto de estruturas de aço – Parte 1-2: Regras gerais, Verificação da resistência ao fogo, Comité Europeu de Normalização, Bruxelas.
- ISO 834-1, 1999. Ensaio de resistência ao fogo - Elementos de construção de edifícios - Parte 1: Requisitos gerais.
- Regulamento Técnico de Segurança contra Incêndio em Edifícios, 2008, Portaria n.º 1532/2008, de 29 de dezembro.

## EXPERIMENTAL AND NUMERICAL INVESTIGATION ON TEMPERATURE PROFILE IN TIMBER-CONCRETE COMPOSITE BEAM TYPE FLOOR SLAB IN FIRE

Cvetanka Chifliganec<sup>a</sup>, Meri Cvetkovska<sup>a</sup>, Robert Pečenko<sup>b</sup>, Tomaž Hozjan<sup>b</sup>,

<sup>a</sup> Ss. Cyril and Methodius University, Faculty of Civil Engineering, Skopje, North Macedonia

<sup>b</sup> University of Ljubljana, Faculty of Civil and Geodetic Engineering, Ljubljana, Slovenia

### Abstract

This paper presents the fire related experimental results that are part of an extensive research project on the behaviour of timber-concrete composite beam type floor slabs at ambient temperature and in fire conditions. The experimentally measured temperatures in the fire exposed cross-section of the composite beams are compared with the results from the thermal analysis conducted in FEM based software. The FE model simulates quite well the thermal behaviour of the beam, though fitting of the material thermal properties was necessary considering Eurocode prescribed material thermal properties produced faster temperature increase.

**Keywords:** timber-concrete composite (TCC) beam, fire, temperature profile, FE model

## 1 INTRODUCTION

Despite of the many advantages of timber as a building material, it's use is often limited by various safety requirements and regulations pertaining to its flammability, combustibility and spread of fire. Thus, fire safety of timber structures is one important aspects that needs to be considered during the design process. An efficient way of increasing the fire resistance of timber is by combining timber with concrete elements into timber-concrete composite (TCC) systems, such as TCC slabs.

The experimental research on TCC slabs in fire is not as extensive as the experimental research of TCC slabs at ambient temperature. A literature review on TCC slabs fire tests is given in Hozjan et al. (2019) and more on the related numerical modelling is presented in Chifliganec (2018). The fact that not even all fire tests are supported with appropriate numerical modelling brings forward the necessity of research in this area.

This paper presents the thermal results from the fire test of two TCC beam type floor slabs. The beams are designed for use in an office building in quasi-constant environmental conditions. In general, the design of the beam is governed by the design at ambient temperature but reaching a fire resistance of at least 60 minutes was set as a goal.

One of the aims of this research work is to obtain new data for further validation of numerical models which are used for analysis of TCC structures in fire. In addition, since there is no adequate regulatory framework (code rule) that deals with TCC structures at ambient temperature and especially in fire, this research strives towards data and knowledge base enrichment necessary for validation of future simplified design methods at fire conditions.

## 2 DESCRIPTON OF MATERIALS, TESTS SETUP AND TEST PROCEDURE

The TCC beams consist of normal strength concrete slab (class C20/25) and GL24 timber beam interconnected with a pair of parallel inclined screws (Würth Assy Plus VG,  $d=8$  mm,  $s_{eff} = 150$  mm,  $l_{eff} = 140$  mm). The self-tapping screws are installed without predrilling under inclination of  $45^\circ$  to the shear surface. Material property tests were conducted only for concrete and a characteristic compressive strength of  $f_{ck,cube} = 29.30$  MPa was obtained. The axial tensile strength

$f_{ctm} = 3.65$  MPa is derived from the flexural strength determined with three-point bending tests on three concrete prisms.

Prior to the fire test, the surface moisture content in the GL beams was measured with a digital surface resistant meter and it varied in the range of  $\omega = (11 \div 13)\%$ .

In each TCC beam twenty thermocouples were installed, ten in the timber (Fig. 1 a) and ten in the concrete (Fig. 1 b). Inside the chamber 8 plate thermocouples were installed to record the furnace temperature. The temperature on the exposed to fire beam surfaces was not measured and it was assumed that it would be equal to the furnace temperature.

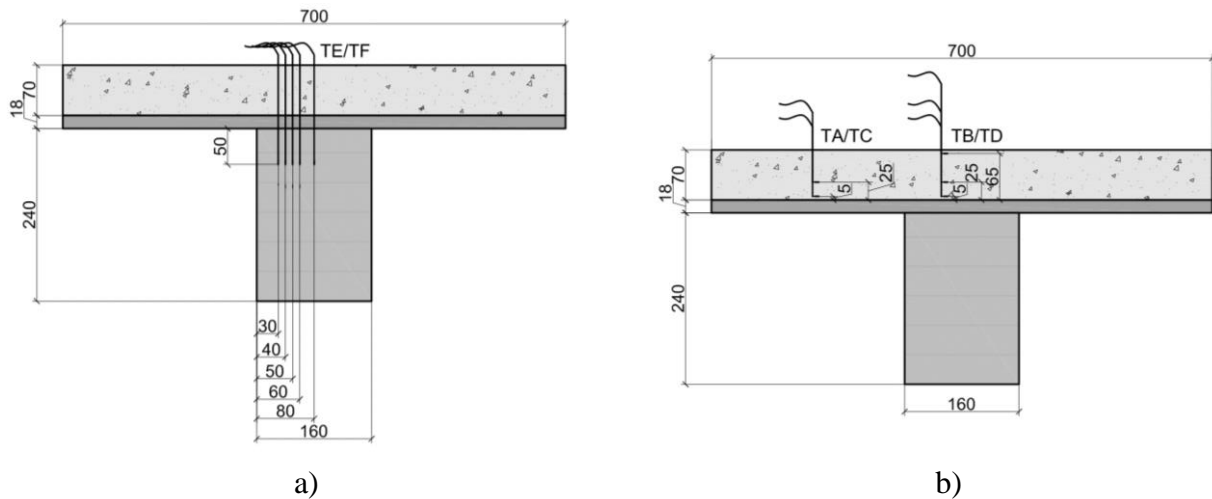


Fig. 1 TCC beam cross-section and position of installed thermocouples a) in timber b) in concrete



Fig. 2 Setup of the TCC beams over the horizontal furnace and loading equipment

The test set-up is presented in Fig. 2. The TCC beams were first mechanical loaded and the load was maintained constant though out the whole fire test. The beams were exposed to Standard fire ISO 834 and the temperatures within the burner and in the thermocouples were constantly monitored and recorded.

The ambient temperature inside the laboratory was also measured, being  $T_{ambient} = 23.9$  °C.

### 3 FIRE TEST RESULTS

After 90 minutes of fire, the burners were turned off and the fire test was stopped. By this time, the TCC beams did not collapse. When the disassembling process begun, due to air supply into the furnace and over the char, increased flaming combustion took place for a while and the pyrolysis of timber continued. Afterwards, due to decreased gasses temperature, the pyrolysis rate decreased and

burning of timber completely stopped. Twenty-five minutes after the end of the fire test the TCC beams collapsed into the furnace.

When the furnace was opened, the screws comprising the connection could not be seen (placed at in-between distance of 32 mm). Upon cooling of the completely burnt timber, it was observed that the screws had no plastic deformation.

During the test, some of the thermocouples did not work properly the entire time and some did not work at all. The thermocouples that did not work at all were probably damaged or broken during concreting of the slabs, transportation or storing of the beams.

The results in term of mean measured temperatures are presented in Fig. 6 and Fig.7, where comparison with the results from the FE based numerical thermal analysis are presented.

**4 FE MODELLING**

The FE modelling is done in the computer program Safir (Franssen (2005)). The software is based on the known Fourier partial differential equation that describes heat transfer through solids.

In the first attempt to model the TCC beam and conduct a thermal analysis, the thermal properties of the materials were taken from the appropriate Eurocode parts (EN 1992-1-2 (2004) and EN 1995-1-2 (2004)). This model did not deliver satisfactory results, mainly producing higher temperatures in both timber and concrete.

A test and try process was begun using available  $\rho - c - \lambda$  models for timber, OSB and concrete from the literature, but none fitted well. Because of that, calibration and fitting of thermal properties for all materials needed to be done.

Modelling the thermal behaviour of concrete was a bit complex since the concrete slab was fire protected at the beginning of the fire process by the OSB panel and few suggestions based on experimental data for numerical modelling of thermal properties of OSB are available in the literature. Additionally, none of the available suggestions in the literature for numerical modelling of the thermal behaviour of OSB delivered results that are in good agreement with the experimental ones.

In the FE model, the concrete is modelled as Silicon ETC (Gernay & Franssen (2012)) using: density  $\rho = 2395 \text{ kg/m}^3$ , moisture  $u = 3 \%$ , convective heat flux at exposed surfaces  $h_{hot} = 25$ , convective heat flux at unexposed surfaces  $h_{cold} = 4$  and parameter of thermal conductivity  $r = 1$ . The material emissivity factor is taken as 0.7. For concrete, the thermal model is done as suggested in Safir using the enthalpy formulation to consider the energy consumed for vaporization. The specific heat of the dry material and the specific mass of the material are taken according to EN 1992-1-2 (2004).

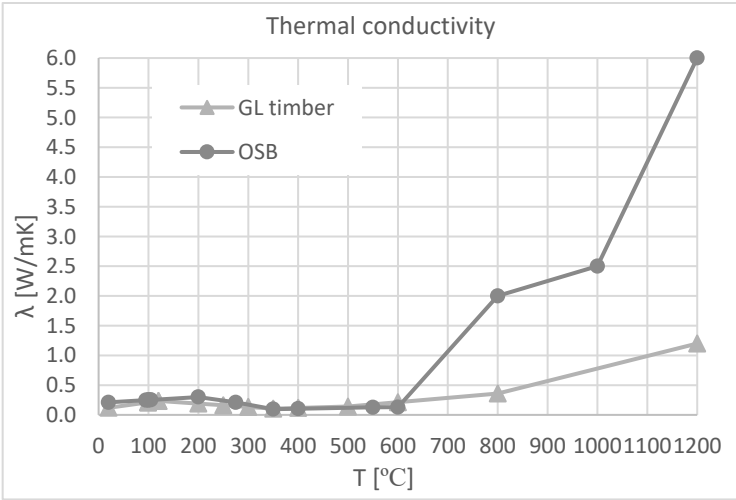


Fig. 3 Thermal conductivity of GL timber and OSB

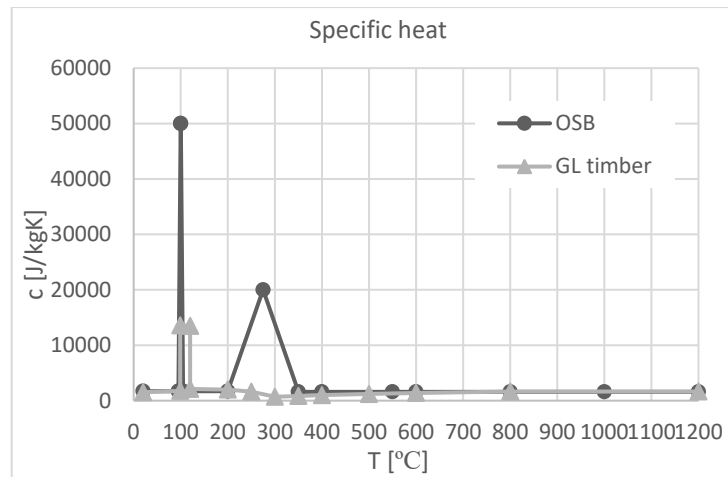


Fig. 4 Specific heat of GL timber and OSB

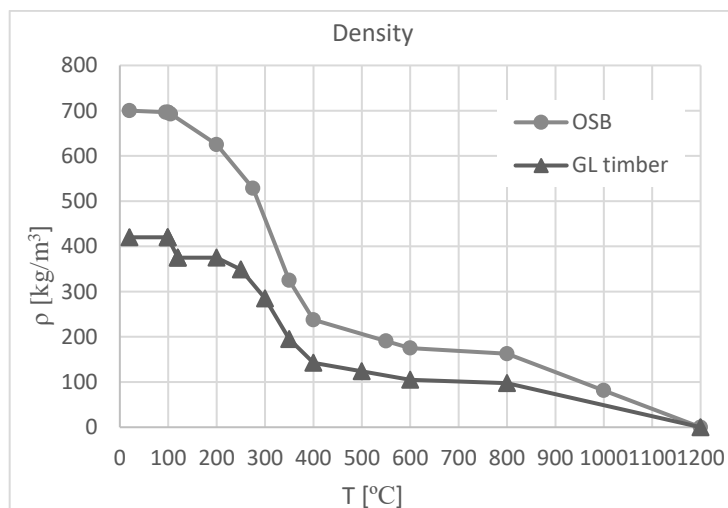


Fig. 5 Density of GL timber and OSB

The final best fitting thermal properties of OSB and GL timber, presented in Fig. 3, Fig. 4 and Fig. 5, are incorporated in the FE model as user defined material properties.

In order to simulate fall-off of the OSB panel at some point during the fire, increased thermal conductivity above temperature of 600 °C is introduced in the numerical model (Fig. 3). It has to be pointed out that in the thermal models considered for OSB and GL timber, the energy dissipation due to free water evaporation is considered with spikes in the specific heat capacity curve, instead as suggested in Safir with enthalpy formulation.

Upon the numerical calibration of the thermal properties, the thermal analysis is performed on an FE model of the TCC section consisting of 10023 solid elements. In the analysis, the initial temperature is taken as the ambient temperature corresponding to the real fire test environmental conditions. The time step is set to be constant and equal to  $\Delta t = 15 \text{ sec}$ .

Observed from Fig. 6 and Fig. 7 is the good correlation of the FE model to the experiment in terms of temperatures in the cross-section of the TCC beam. Although almost perfect match with the experimental results for timber is achieved with the numerical model, the temperatures in the concrete slab could not be matched that well. At position TA and TC at 5 mm from the bottom of the concrete flange, the FE model overestimates the temperatures until 60 minutes of fire exposure, after which the temperatures are almost identical with the mean experimental recordings. Similarly, at position

TA and TC at 25 mm from the bottom of the concrete flange, the FE model overestimates the temperatures after 40 minutes of fire exposure. It has to be pointed out that although the FE model produces higher temperatures compared to the mean experimental curve, the temperatures are still in the range between the upper and lower recorded limit temperature curves for the appropriate positions in the concrete.

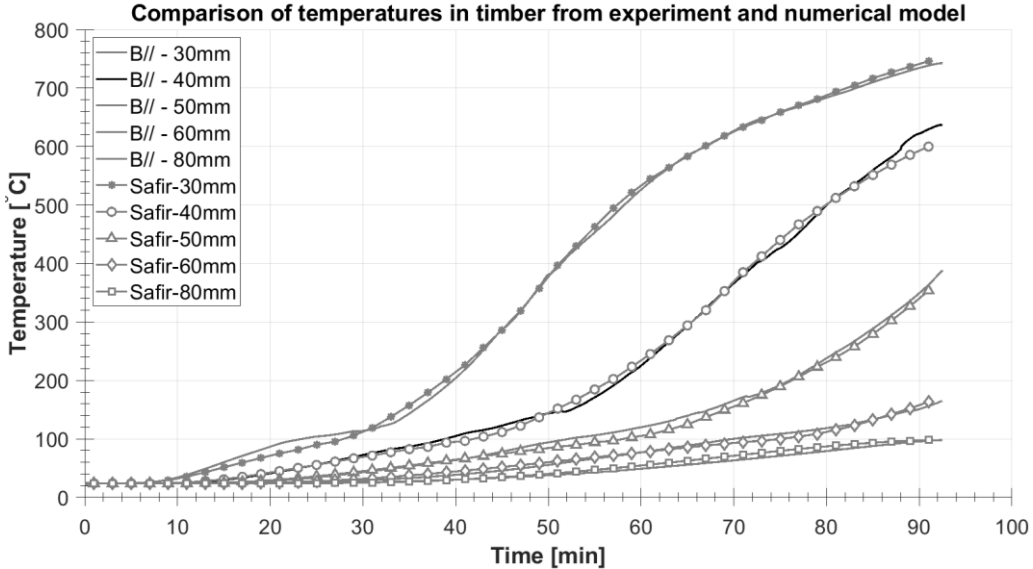


Fig. 6 Comparison of temperatures in GL timber from fire test and numerical analysis

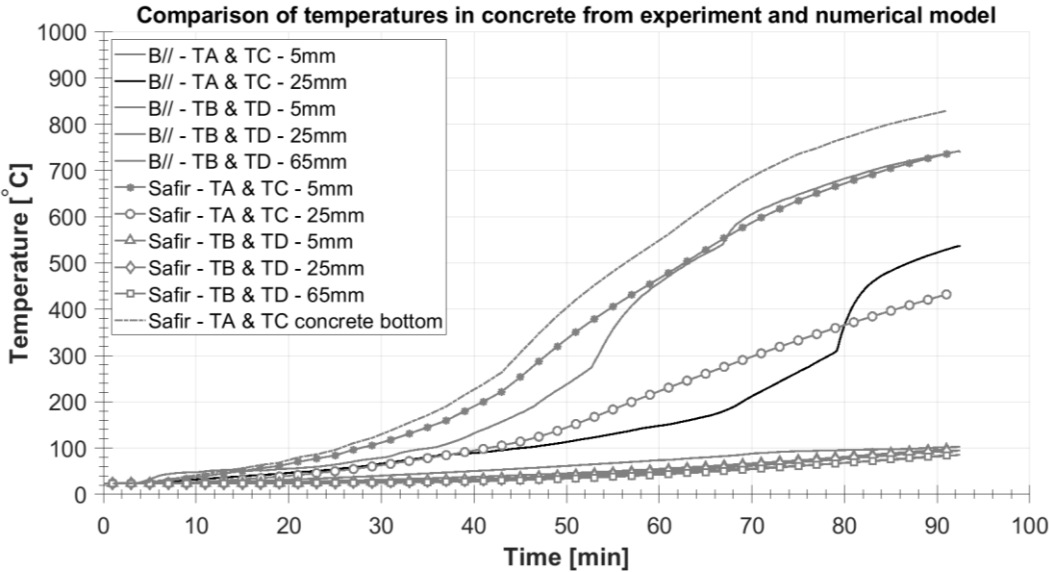


Fig. 7 Comparison of temperatures in concrete from fire test and numerical analysis

The temperature profiles at  $t = 60 \text{ min}$  and  $t = 90 \text{ min}$  are presented in Fig. 8 (up and down, respectively).

If the charring rate in the timber is considered as  $\beta = 0.7$  for GL timber and the simplified analytical reduced cross-section method given in EN 1995-1-2 (2004) is applied, the reduced cross-section is estimated to have dimensions of  $b_{eff}/h_{eff} = 60/191 \text{ mm}$  for 60 minutes of fire exposure and  $b_{eff}/h_{eff} = 20/170 \text{ mm}$  for 90 minutes of fire exposure. Using the  $300^\circ$  isotherm to define the char line, the residual cross section from the FE model is determined to have:  $b_{eff}/h_{eff} = 70/185 \text{ mm}$  for 60 minutes of fire exposure and  $b_{eff}/h_{eff} \approx 35/110 \text{ mm}$  for 90 minutes of fire exposure. Significant difference in the estimation of  $h_{eff}$  for 90 minutes of fire exposure can be observed.

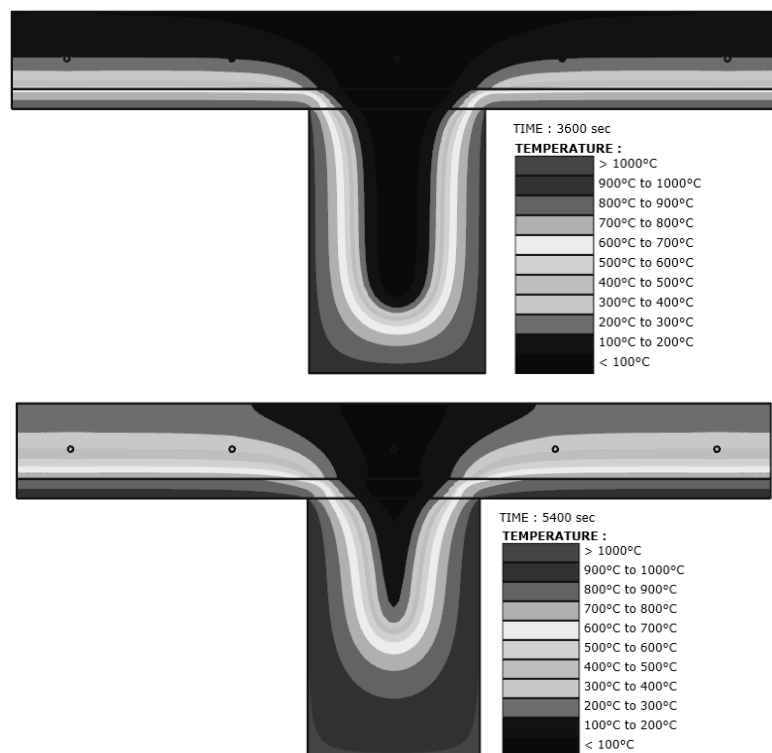


Fig. 8 Temperature profiles of the TCC beams at different times of fire exposure  $t = 60 \text{ min}$  (up) and  $t = 90 \text{ min}$  (down) from the numerical analysis

## 5 CONCLUSION

The TCC beam tested in fire according to the Standard fire time-temperature curve has fire resistance higher than 90 minutes. The collapse of the beam occurred 25 minutes later after additional ongoing pyrolysis in the timber.

The recorded temperatures in the concrete and in the timber could not be modelled with the thermal properties as suggested in the appropriate Eurocode parts. The FE model with numerically calibrated and fitted thermal properties of the timber and OSB successfully describes the thermal behaviour of the TCC beam in fire.

## ACKNOWLEDGMENTS

The first author gratefully acknowledges the financial support for the reported research from: Adora Engineering Skopje, BV Engineering LTD Bitola, Würth Slovenia, TD Rading Engineering Skopje, Faculty of Civil engineering Skopje and Faculty of Civil and Geodetic Engineering Ljubljana.

## REFERENCES

- Chifliganec, C. (2018). *Numerical modelling of timber-concrete composite slabs exposed to fire*. STSM report COST FP1404.
- EN 1992-1-2 (2004). *Eurocode 2: Design of concrete structures – Part 1-2: General rules – Structural fire design*. Brussels, Belgium: CEN.
- EN 1995-1-2 (2004). *Eurocode 5: Design of timber structures - Part 1-2: General – Structural fire design*. Brussels, Belgium: CEN.
- Franssen J. (2005). *SAFIR: A Thermal/Structural Program for Modeling Structures Under Fire*, *AISC Engineering Journal* 42 (2), p.143–158.
- Gernay, T., Franssen, J-M. (2012). *A formulation of the Eurocode 2 concrete model at elevated temperature that includes an explicit term for transient creep*. *Fire Safety Journal*, 51, pp. 1-9.
- Hozjan, T., Bedon, C., Ogrin, A., Cvetkovska, M., Klippel, M. (2019). *Literature Review on Timber–Concrete Composite Structures in Fire*. *J. Struct. Eng.*, 145(11): 04019142.

## MODELLING OF STEEL TO TIMBER JOINT EXPOSED TO FIRE

Kristýna Vopatová<sup>a</sup>, Jaroslav Zeman<sup>a</sup>, Kamila Cábová<sup>a</sup>

<sup>a</sup> Czech Technical University in Prague, Faculty of Civil Engineering, Prague, Czech Republic

### Abstract

The paper is focused on a timber joint with an inserted steel plate under fire exposure. According to EN 1995-1-2 (2004), the fire resistance of unprotected timber joints is limited to 30 minutes. However, in recent times, several studies have shown that these joints can achieve higher fire resistance comparing to values given in the standard. To verify that, fire tests of bolted timber joints with inserted steel plate were designed and carried out in the fire lab UCEEB, CTU in Prague. The results show a positive effect of inserted steel plate on timber burning rate caused by water accumulation in the timber element close to the steel plate and higher burning rate than predicted by the analytical model. The results and experience gained serve for numerical model development.

**Keywords:** timber joint, bolt, steel plate, fire, experiment

## 1 INTRODUCTION

Building fires were and are an integral part of everyday life. Thus, the fire resistance of structures is of the highest importance. With the right design of structures, it is possible to prevent loss of life and significant loss of property (Buchanan 2001).

The right design might include a variety of materials, technologies, and procedures. Based on the purpose, concrete, steel, timber, or a different material can be chosen. Timber is increasingly used for log cabins, administration buildings, large-span structures, and lookout towers. However, for these large-span structures and lookout towers, it is necessary to take into account elevated requirements on the joints under high load. Therefore, it is popular to design joints of timber structures with inserted steel plates, which are able to withstand high loads. These joints are called “steel-timber” joints according to the EN 1995-1-1 (2004).

This work is a part of research aiming to present an accurate approach for bolted steel-timber joints design under tensile stress at elevated temperatures. For this purpose, the experiments were performed, and the results were compared to the analytical model. Part of the work presented in this paper was published by Zeman (2021). Similar experiments, as well as a numerical model, are presented, for example, in work by Audebert et al. (2011).

## 2 JOINT CONFIGURATION

The following bolted steel-timber joint configuration with inserted steel plate regarding EN 1995-1-1 (2004) has been designed. The timber element has a square cross-section with dimensions 140 mm x 140 mm. The steel plate is placed in the middle of the timber elements, and it is 300 mm long, 6 mm thick, and 80 mm wide. Four M10 bolts are used on each side – in each timber element. A scheme of the designed steel-timber joint is presented in Fig. 1.

Timber elements are made of grown timber of strength class C24. Drilled holes are of the same dimension as bolts. The steel plate is made of S235 steel without surface treatment. The M10 bolts were made of threaded rods. The bolt is held by an 8 mm high nut on each end of a threaded rod. Between nuts and timber elements, construction washers with a diameter of 30 mm and a height of 2,5 mm are used. The threaded rods, nuts, and washers are also without surface treatment.

The connection is dimensioned for fire resistance R30 according to EN 1995-1-2 (2004). The fire resistance is achieved by increased thickness ( $a_{fi} = 18$  mm). The ends of bolts with nuts are left uncovered, protruding out of the timber element.

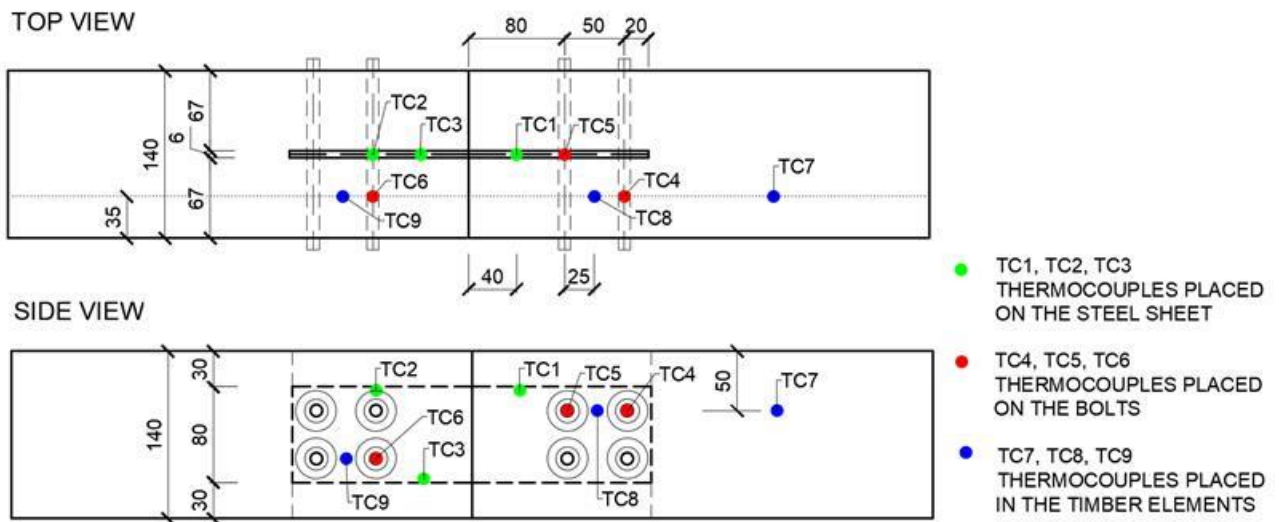


Fig. 1 The sample layout with thermocouple location

### 3 ANALYTICAL MODEL

The analytical model is based on the combination of load-bearing capacity at normal temperatures according to EN 1995-1-1 (2004) and load-bearing capacity at elevated temperatures according to EN 1991-1-2 (2004). It is developed for the steel-timber joint described in the previous chapter with corresponding dimensions and geometry.

At normal temperatures, according to EN 1995-1-1 (2004), the load-bearing capacity of the bolted joint is calculated from three possible modes of failure. The first mode of failure – the f-mode – is caused by pushing the bolt into the timber element (Fig. 2 a) f). In the case of the second failure mode – the g-mode, a failure occurs due to the pressure of the bolt on the timber element and the simultaneous formation of a plastic bolt deformation in place of the inserted steel plate (Fig. 2 a) g). In the third failure mode - the h-mode, plastic deformations form on the bolt in place of the inserted steel plate and also in the area of the timber element (Fig. 2 a) h).

At elevated temperatures, the resulting load-bearing capacity might also be affected by the load-bearing capacity of the weakened steel plate. To calculate the load-bearing capacity, the fire exposure following the standard temperature curve ISO834-1 (1999) according to EN 1991-1-2 (2004) is considered.

In each time step, the material characteristics such as the yield strength of the bolt and the yield strength of the connecting plate are reduced. At the same time, the cross-sectional geometries and material characteristics of the timber elements at elevated temperatures are also reduced. Based on reduced characteristics, the values of load-bearing capacity for that time step are calculated.

The assembled load-bearing capacity based on the failure modes as the function of the time of the fire is shown in Fig. 2 b) together with load-bearing capacities for f, g, and h failure modes. Moreover, the figure depicts the load-bearing capacity of the inserted steel plate. The resulting assembled load-bearing capacity is the minimum of the four individual load-bearing capacities.

### 4 EXPERIMENTAL STUDY

Two specimens of the steel-timber joint described in chapter 2 were assembled. Both specimens were tested under fire load in a furnace. The main focus of the test was to measure temperatures in various places of the joint that would serve for a better understanding of heat transfer and other ongoing processes inside the joint.

During the experiments, the joint specimens were exposed to gas temperature following the ISO834-1 (1999) curve. To investigate the temperature distribution and its transport into individual components of the joint during the fire, thermocouples were inserted into the specimens.

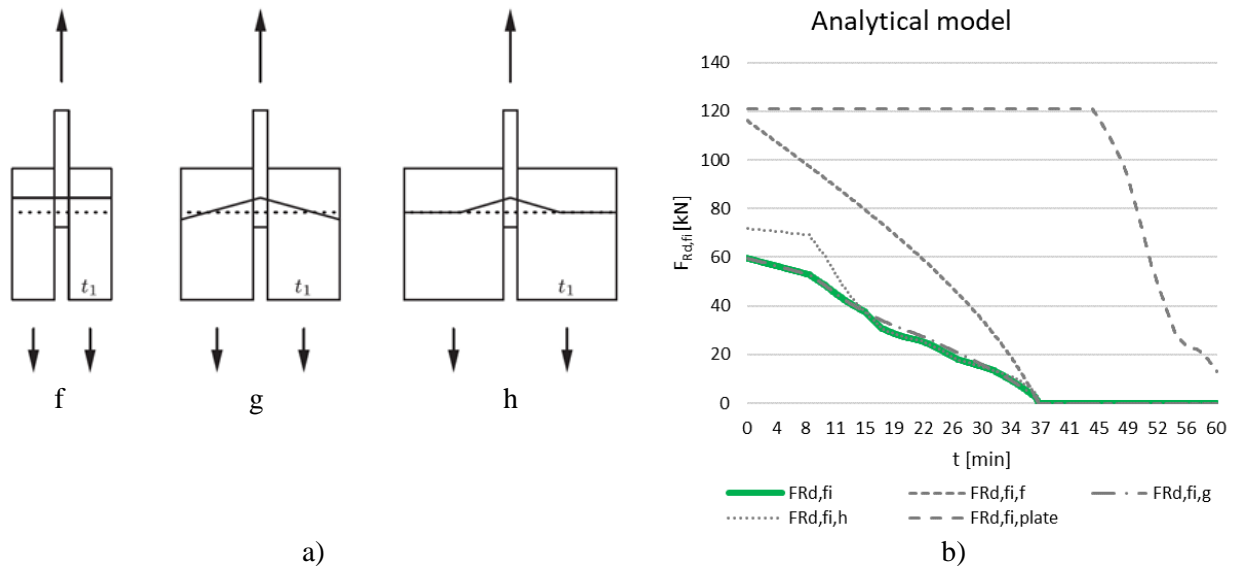


Fig. 2 a) Failure modes of steel-to-timer connections for a steel plate - the f-mode, the g-mode, and the h-mode; b) Load-bearing capacities for f, g, and h failure modes, the inserted steel plate, and the assembled load-bearing capacity as the functions of the time of the fire.

The K-type thermocouples were used. The locations of all nine thermocouples, as well as the main dimensions of the designed and tested steel-timber joint, are presented in Fig. 1. Three thermocouples (TC1-3) were placed on the steel sheet, three thermocouples (TC4-6) were placed on the bolts in the depths of 35 mm and 70 mm within the timber element, and three thermocouples (TC6-9) were placed in the timber elements in the depth of 35 mm.

The experiments were performed in a miniFUR furnace in the UCEEB laboratory. The miniFUR is used for indicative medium-sized tests. The geometry and dimensions of the furnace are shown in Fig. 3. Note that the tested samples were placed on the left side of the furnace. The side of the joint closer to the furnace centre is the “fireside”, and the side closer to the wall is the “cold side”.

A fuel used for the experiments is propane gas. The control system regulates the propane gas inflow and ventilation output to achieve the temperature following the ISO834-1 (1999) curve. However, during the experiments, the timber element combustion acts as an added heat source. Therefore, a reference experiment was conducted. The reference test consisted of an experiment following a basic ISO834-1 (1999) curve setup with one timber element inside the furnace. The reference timber element was of the same dimensions as the whole designed bolted steel-timber joint. During the reference test, it was found out that the timber element burning does not change the furnace environment much and does not change control system input values at all. The only temperatures that changed due to timber element burning were the temperatures close to the timber element. Therefore, there was no correction needed for the control system.

After the reference experiment, two regular experiments with the designed bolted steel-timber joint were performed. During the experiments, all the furnace constraints for specimen placement were respected to achieve optimal gas flow. At the beginning of each test, the exhaust ventilation output was set to 30 %, which increased to 50-60 % in the advanced phase of the experiment.

The time duration of each experiment was 30 minutes. After 30 minutes, the sample was taken out of the furnace and cooled down in the water. Sample number 1 before cooling down in the water is shown in Fig. 4 a). Afterward, the samples were cleaned (Fig. 4 b), measured, and all the results were compared with the analytical model.

## 5 RESULTS

One of the indicative values of a joint performance under a fire load is the residual thickness of the timber element. The values of the residual thickness  $t_1$  after 30 min of fire were calculated using the analytical model and measured after performed experiments. The experimentally

measured values were taken in place of bolts and between the bolts, which is approximately in place of thermocouples TC8 and TC9 in Fig 1.

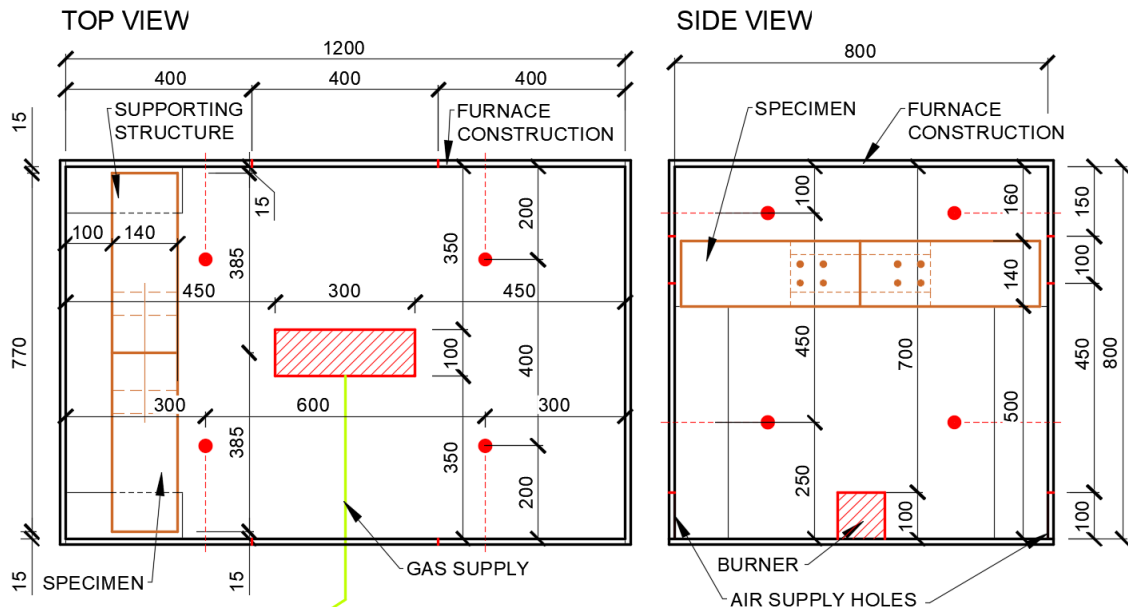


Fig. 3 The scheme of the miniFUR furnace with the location of a sample

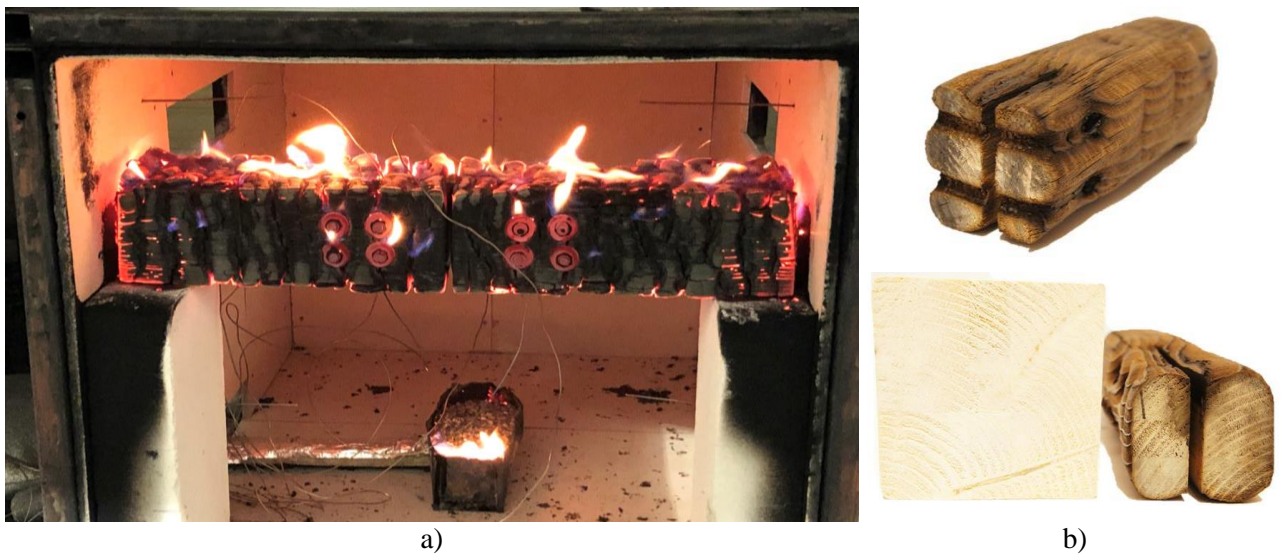


Fig. 4 Sample 1: a) before taking out of the furnace and cooling down in the water; b) after test

Table 1 compares these residual thicknesses  $t_1$  after 30 min of fire. According to the analytical model, the residual thickness  $t_1$  after 30 min of fire should be 43 mm. On the tested sample with the original cross-section of 140 mm x 140 mm, the measured thickness of the residual cross-section  $t_1$  depended on a site and on the side of measurement.

Table 1: Residual thickness  $t_1$  after 30 min fire

Source	Place	Fireside [mm]	Cold side [mm]	Average [mm]
Analytical model	-	-	-	43
Experiment	In place of bolts	32,5	42,3	37,4
Experiment	Between the bolts	38,5	47,0	42,8

The second set of parameters used to evaluate joint performance under a fire load are temperatures measured on steel members of a joint. Two temperature curves were calculated using the incremental method in the analytical model – the temperature of bolts and the temperature of the inserted steel plate. The maximum temperatures occur on the exposed surface of the bolt. During the experiments, temperatures of inserted steel sheet, bolts in the depth of 35 mm, and bolts at the steel sheet level were measured. These experimental values, as well as temperatures calculated using the analytical model, are shown in Fig. 5.

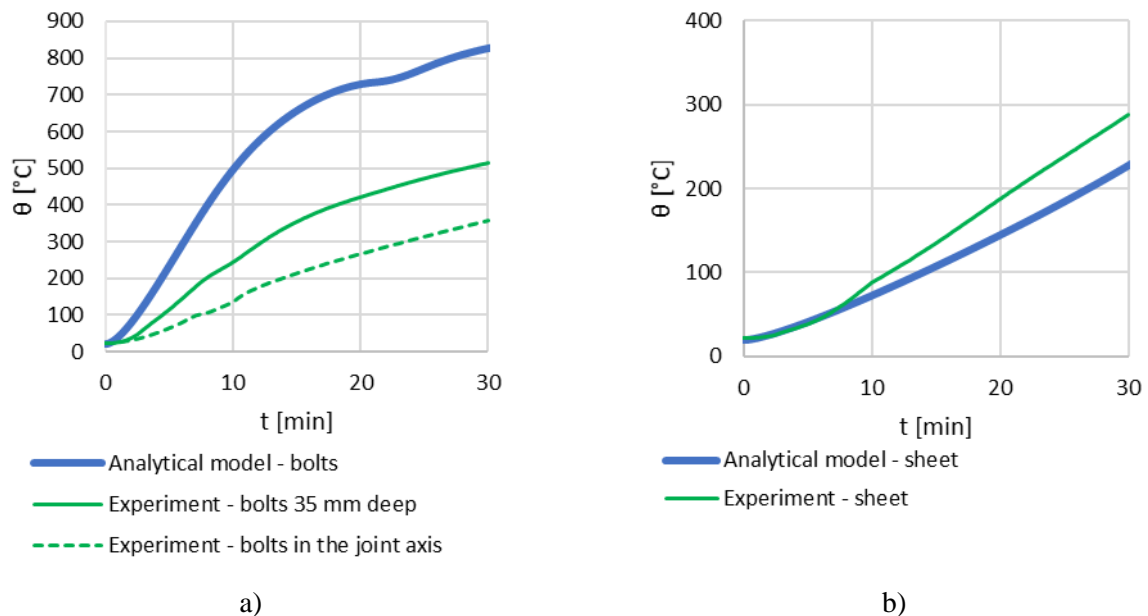


Fig. 5 The comparison of temperature courses on steel elements during the experiment and according to the analytical model: a) temperatures on the bolts; b) temperatures on steel plate

## 6 CONCLUSIONS

This paper describes a designed bolted steel-timber joint with inserted steel plate. Standards EN 1993 (2005) and EN 1995 (2004) consider fire resistance for a maximum of 30 min, but often in practice, the joints demonstrate higher fire resistance. The joint performance under a fire load was investigated using an analytical model and performing experiments.

The created analytical model is based on the principle of design at normal temperatures with reduced material properties of individual components. The properties of the steel element are reduced according to EN 1993-1-2 (2005) and wooden EN 1995-1-2 (2004).

The fire tests of steel-timber joints were performed in miniFUR furnace in the UCEEB, CTU in Prague fire laboratory. Two joints of the same geometry designed according to the EN 1995-1-1 (2004) were tested. The dimensions of these joints have been increased by the thickness  $a_{fi}$  for the fire-resistant 30 min. There were nine thermocouples in both joints. During the second test, results showed the temperatures higher than according to the ISO 834-1 (1999) curve, which was probably caused by increased exhaust ventilation.

Based on the values calculated using the analytical model and results obtained from experiments, the comparison was made. As two main characteristics used to evaluate the joint performance, the residual thickness of the timber element, temperatures measured of the bolts, and temperature of the inserted steel plate were used.

The analytical model does not take into account the effect of bolts. As it can be seen from Table 1, the residual thickness in place of bolts on the fireside is much lower than the value given by the analytical model. The residual thickness in the place of bolts on the cold side is close to the value given by the analytical model. The average for measures taken between bolts is also close to the analytical model. However, the individual values on the fireside and on the cold side differ by about 4-5 mm from the average.

As can be seen in Fig. 5 a), temperatures of bolts calculated using the analytical model are well above the measured values of the temperature of the bolts. This could be caused by the fact that the temperatures measured are in the depth of 35 mm and 70 mm. However, the temperatures calculated using the analytical model are the maximum temperatures that would occur on the surface of the bolt exposed to the thermal stress.

On the other hand, the temperatures of the bolts measured in the depth of 35 mm were taken from the fireside of the joint, that is, on the side where the fire source was placed. As can be seen from the results of the residual thickness in Table 1, the cold side burned slower than the fireside; therefore, it is expected that temperatures measured on the cold side were even lower than temperatures on the fireside.

From all the obtained results, it is also concluded that the inserted steel plate works as a vapor barrier in the timber element. In the experiments, it was found that the timber part close to the inserted steel sheet reaches temperatures around 100 °C for a long time. This might be caused by the accumulation of water vapor on the steel plate.

Based on the results presented and the discrepancies between the analytical model and experimental results, it was decided to develop a numerical model. The numerical model is being developed right now using ANSYS software and the Component-based Finite Element Method (Silva et al. 2001). It is focused on describing the effect of increased bolts thermal conductivity leading to a higher burning rate in place of bolts and the effect of water accumulation near the inserted steel plate. The effect of water accumulation is modelled by a modified timber layer with increased specific heat capacity. The sensitivity analysis of this layer will be performed.

A better understanding of these two effects and processes occurring in bolted steel-timber joints generally could lead to better design and changes in perceptions of these joints. Consequently, based on extended knowledge and verified numerical models, safer joints, structures, and buildings can be built, preventing loss of life and significant loss of property.

## ACKNOWLEDGMENT

The authors would like to thank for the financial support provided by the grant SGS19/150/OHK1/3T/11. The authors also wish to thank all the personnel of the UCEEB, CTU in Prague fire laboratory for the availability and technical support during the tests.

## REFERENCES

- Audebert M., Dhima D., Taazount M., Bouchair A., 2011. *Numerical investigations on the thermo-mechanical behavior of steel-to-timber joints exposed to fire*. *Engineering Structures*. 2011, 33(12), 3257-3268. ISSN 01410296.
- Buchanan A. H.: *Structural design for fire safety*. John Wiley & Sons, Chichester, UK 2001.
- EN 1991-1-2: 2003, Eurocode 1. *Actions on structures*. Part 1–2: General actions – actions on structures exposed to fire. 2003.
- EN 1993-1-2: 2005, Eurocode 3. *Design of steel structures*. Part 1–2: general rules – structural fire design. 2005.
- EN 1995-1-1: 2004, Eurocode 5. *Design of timber structures*. Part 1-1: General – Common rules and rules for buildings. CEN TC 250–SC5, 2004, Brussels.
- EN 1995-1-2: 2004, Eurocode 5. *Design of timber structures*. Part 1–2: General rules – Structural fire design. CEN TC 250–SC5, 2004, Brussels.
- Janssens M., 1994. *Thermo-physical properties for wood pyrolysis models*. *Pacific Timber Engineering Conference Gold Coast*, Australia, 1994.
- ISO 834-1: 1999, Fire-resistance tests – Elements of building construction. Part 1: General requirements. International Organization for Standardization, Genève, Switzerland, 1999.
- Simões da Silva L., Santiago A., Vila Real P., 2001. *A component model for the behaviour of steel joints at elevated temperatures*. *Journal of Constructional Steel Research*. 2001, 57(11), 1169-1195. ISSN 0143974X.
- Zeman J., 2021. *Modelling of steel to timber joint of timber structures exposed to fire*, Diploma Thesis, Czech technical university in Prague (in Czech).

Proceedings of the International Conference in Ljubljana, 10-11 June 2021  
in edition of Applications of Structural Fire Engineering

**Session**

**Modelling and application of structural fire engineering II**

## EARLY-WARNING METHODS FOR COLLAPSE OF STEEL PORTAL FRAMES UNDER FIRE

Wei Ji<sup>a</sup>, Guoqiang Li<sup>a,b</sup>, Chengyuan Feng<sup>a</sup>, Yao Wang<sup>a</sup>, Xinjie Li<sup>a</sup>

<sup>a</sup> College of Civil Engineering, Tongji University, Shanghai 200092, China

<sup>b</sup> State Key Laboratory for Disaster Reduction in Civil Engineering, Tongji University, Shanghai 200092, China

### Abstract

Steel portal frames are prone to collapse in fire, which seriously threatens the lives of firefighters and residents. Therefore, it is necessary to carry out the research on early-warning methods for fire induced collapse of steel portal frames. A three-dimensional finite element model is established in ABAQUS to simulate the collapse behavior of steel portal frames and four typical collapse modes are summarized. Under different collapse modes, the change law of the displacement of steel portal frames at key positions is studied, and then the early-warning indexes which can be used to predict the remaining collapse time are determined. The early-warning method applicable to different collapse modes as well as the method to predict possible collapse mode of the burning frame are put forward herein. The findings from this paper can help firefighters judge the collapse risk of the burning building and evacuate safely from the fire scene.

**Keywords:** steel portal frame, numerical simulation, collapse mode, early-warning methods

### 1 INTRODUCTION

When a building is on fire, firefighters usually rush to the fire scene to put out the fire and rescue the trapped people. In this case, accurately predicting the collapse time ahead can help firefighters foresee collapse danger and evacuate timely. Until now, firefighters rely mainly on their visual judgements to decide the possibility of the endangered building collapse. Since the artificial judgement is subjective and inaccurate, the building may collapse unexpectedly during the fire rescue, which is catastrophic for firefighters. Statistics have shown that the fire-induced collapse of buildings is a major killer of firefighters (Jiang *et al.*, 2012).

Steel portal frame is a common structural form used in industrial plants (Davison & Owens, 2008). However, steel portal frame is prone to collapse under fire due to its low level of redundancy and high level of fire loads. In fact, the collapse of steel portal frames under fire account for a large share of firefighter fatalities. Therefore, it is necessary to conduct research on the early-warning method of steel portal frames under fire.

Collapse mode is the summary of collapse laws and reflects the collapse mechanisms of structures. Finding out fire-induced collapse modes is the basis of early-warning method. Fire tests and numerical simulations have been done to explore the collapse modes of steel portal frames under fire (Wong, 2001; Ali *et al.*, 2004; Moss *et al.*, 2009; Lou *et al.*, 2018). However, these findings did not systematically cover all the possible collapse modes of steel portal frames under different fire scenarios. It is still unclear how many collapse modes the steel portal frames will have under fire.

To realize the early-warning of fire-induced collapse, it is also necessary to find out key parameters that are not only easy-measured, but also closely related to the collapse process. Jiang (2020) selected the temperature of heated components as key parameters and developed a safety monitoring system for steel truss structures. Jiang (2018) selected the displacements of heated columns and rafters as key parameters and proposed a simple approach to calculate the collapse time of steel portal frames. However, the approach needs further study since it covered only five typical portal frames and assumed the whole frame to be uniformly heated.

This paper presents early-warning methods for collapse prediction of steel portal frames under various fire scenarios with different geometric and physical parameters. Four typical collapse modes are summarized through parametric analysis. The key parameters for collapse prediction of steel portal frames are selected and the change laws of easy-measured key parameters of the frame under different collapse modes are investigated. Three-level early-warning methods applicable to different collapse modes of steel portal frames are proposed.

## 2 NUMERICAL MODELING

### 2.1 Establishment of FEM

Finite element models were created in the explicit dynamic analysis module of ABAQUS. The three-dimensional Timoshenko beam element B31 was used to simulate the steel members. The properties of steel materials referred to EC3. In order to save the computing cost of explicit analysis on the premise of calculation accuracy, the finite element model was set to run a 60-s explicit analysis instead of 1-h heating in a real fire.

### 2.2 Parameters for steel portal frames under fire

A basic numerical model established in ABAQUS is shown in Fig.1. The section and material information of steel components are shown in Table 1. A parameterized temperature-time curve was used to simulate the temperature history of steel components under fire (Usmani *et al.*, 2003). The temperature can be calculated as follows:

$$T(t) = T_0 + (T_{\max} - T_0)(1 - e^{-\alpha t}) \tag{1}$$

- where  $T_0$  ambient temperature, in this paper  $T_0 = 20^\circ\text{C}$ ,
- $T_{\max}$  maximum compartment temperature,
- $t$  duration of fire,
- $\alpha$  an arbitrary ‘rate of heating’ parameter, in this paper  $\alpha = 0.001$ .

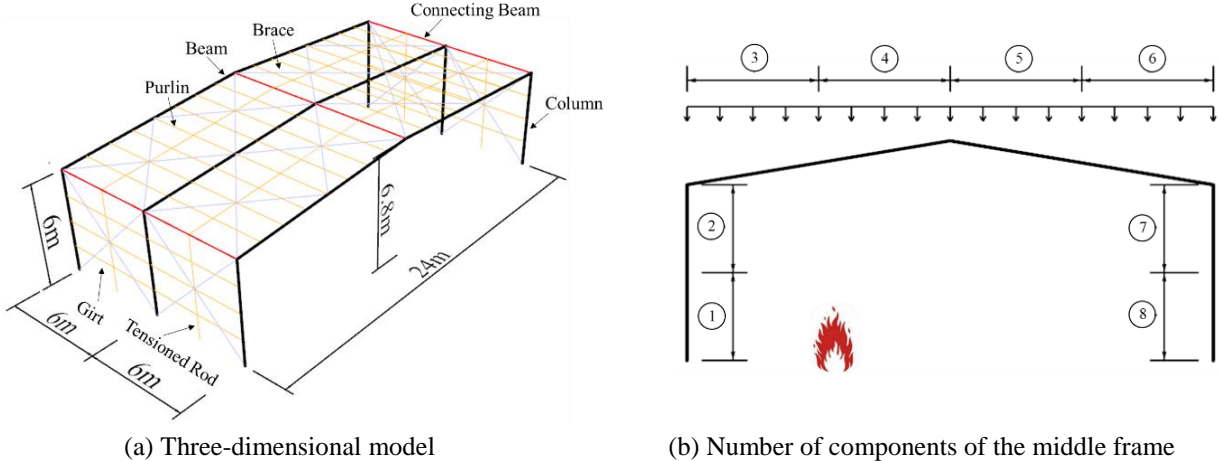


Fig. 1 Numerical model

Table 1 Material and section information of steel member

Member	Cross section(mm)	Yield strength(MPa)
Rafter, Column	H500mm × 200mm × 12mm × 15mm	345
Purlin, Girt	LH150mm × 100mm × 3.2mm × 4.5mm	235
Connecting Beam	Φ120mm × 5mm	
Tensioned Rod	Φ20mm	

To ensure the versatility of early-warning methods for collapse prediction of steel portal frame under fire, diverse possible fire scenarios and various geometric and physical parameters that may affect the collapse process of the frame were selected:

(1) Fire scenario: 12 heating conditions along span and 2 heating conditions along column spacing.

Table 2 shows the setting of heating conditions along the span direction. The number for each steel member of the middle frame can be found in Fig.1b. The maximum temperature for steel members belong to T2 was two thirds of that belong to T1. For steel members belong to T3, they were assumed to keep ambient temperature. Two heating conditions are set along the column spacing. Under 1st heating conditions, only the middle frame and adjacent purlins, girts and braces are exposed to fire. Under 2nd heating conditions, all three frames are affected by the fire.

Table 2 Heating conditions of the frame along the span direction

Heating conditions	T1	T2	T3	Heating conditions	T1	T2	T3
D1	1-2		3-8	D7	2-5	1,6,7	8
D2	1-2	3	4-8	D8	2-6	1,7,8	
D3	1-3	4	5-8	D9	1-6	7,8	
D4	1-4	5	6-8	D10	4-5	2,3,6,7	1,8
D5	3-4	2,5	1,6-8	D11	2-7	1,8	
D6	3-5	2,6,7	1,8	D12	1-8		

(2) Fire protection: 5 fire protection levels

Five levels of fire protection were considered according to GB50016. A linear temperature history was assumed for the protected members, vary from an ambient time (20°C) to a predefined critical temperature (600°C for beams and 550°C for columns) according to the fire rating of protected steel members.

(3) Cross-sectional temperature gradient: 0, 200°C/m, 400°C/m and 600°C/m.

(4) Spans of portal frames: 12m, 18m, 24m and 30m.

(5) Column spacing: 6m, 7.5m and 9m.

For portal frames with column spacing of 7.5m and 9m, braces were set at 1/3 and 2/3 span of purlins respectively.

(6) Stiffness of column base: fixed base and hinged base.

(7) Load ratio: 0.3, 0.4, 0.5 and 0.6;

Load ratio is defined as the imposed load over the capacity of the frames.

### 3 EARLY-WARNING METHODS FOR FIRE-INDUCED COLLAPSE

#### 3.1 Collapse modes

Through abundant parametric studies with the numerical models, totally four possible fire-induced collapse modes of single span steel portal frames were found as shown in Fig.2. Column lateral collapse mode (A) and column buckling collapse mode (B) occur when the fire is localized to the column, while overall inward collapse mode (C) and overall outward collapse mode (D) mainly occur in large-scale fire scenarios.

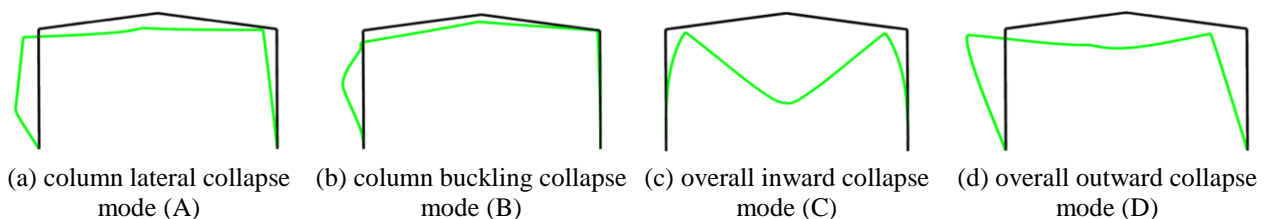


Fig. 2 Collapse modes of single span steel portal frames in fire

### 3.2 Key parameters for early warning

The eaves and apex are selected as the key positions (Fig.3). The horizontal and vertical deformation and deformation ratio at key positions are selected as key parameters for collapse prediction of steel portal frames under fire. Based on the results of parametric analysis, the variation of these parameters under four collapse modes will be investigated herein.

The left side of the frame in Fig.3 is defined as the side with higher temperature. Besides, the deformation rate of key positions are represented by  $V_p$  *et.al* for simplification herein.

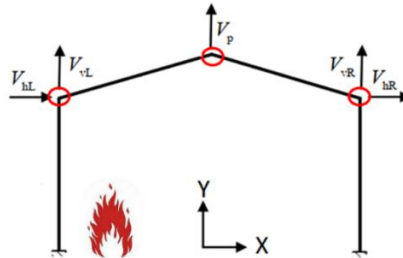


Fig. 3 Key easy-measured parameters of steel portal frames

### 3.3 Change laws of key parameters

Fig.4 shows typical displacement curves of key positions under different collapse modes, where the relative time is defined as the ratio of heating time over the total collapse time. The following change laws of key parameters can be obtained:

- (1) The vertical displacement  $V_{vL}$  and  $V_p$  increase firstly and then decrease with the increase of temperature.
- (2) Under column collapse modes, the horizontal displacement  $V_{hL}$  and  $V_{hR}$  increase in the same direction with the increase of temperature. Further analysis indicate that  $V_{hL}$  increases continuously for collapse mode A, while increases firstly then decrease and stabilize for collapse mode B.
- (3) Under overall collapse modes, the horizontal displacement  $V_{hL}$  and  $V_{hR}$  expand in opposite direction with the increase of temperature. Moreover,  $V_{hL}$  will increase continuously for collapse mode D, while decreases and moves inward for collapse mode C.

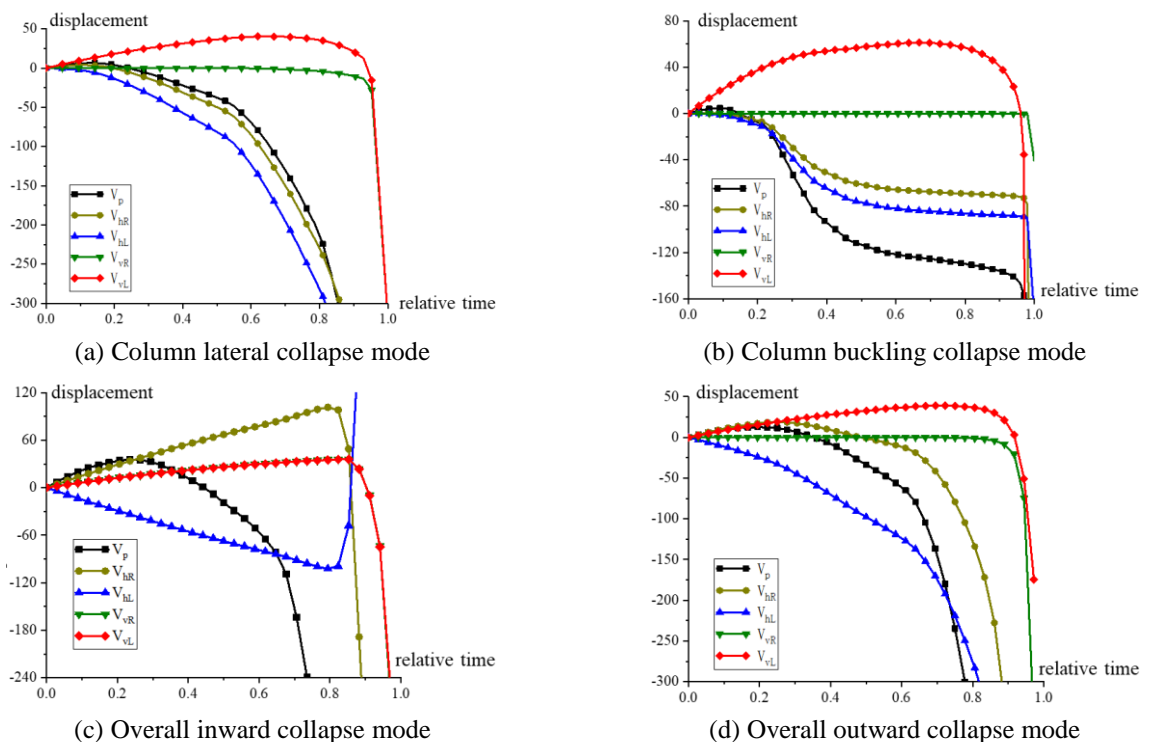


Fig. 4 Typical displacement curves (units in mm)

### 3.3 Early-warning indexes for different collapse modes

For column lateral collapse mode,  $V_p$ ,  $V_{vL}$ ,  $V_{hL}$  and corresponding deformation rate are chosen as the early-warning indexes for collapse prediction of column lateral collapse mode. The change laws of early-warning indexes are shown in Fig.5, where point A-D refer to the characteristic points of the curves of early-warning indexes and point E refers to the final collapse time. The definition of point A-E are shown in Table 6

- (1) Early-warning point A refers to the time when  $V_p$  reaches its peak value.
- (2) Early-warning point B refers to the time when  $V_{vL}$  reaches its peak value.
- (3) Early-warning point C refers to the time when  $V_{hL}$  has increased to twice of the average rate of  $V_{hL}$  from point A to point B.
- (4) Early-warning point D refers to the time when vertical displacement rate  $V_{vL}$  has decreased to opposite value of  $V_{vL}$  at point A.
- (4) Collapse point E refers to the time when the lateral displacement of the heated column reaches 1/5 of the eave height.

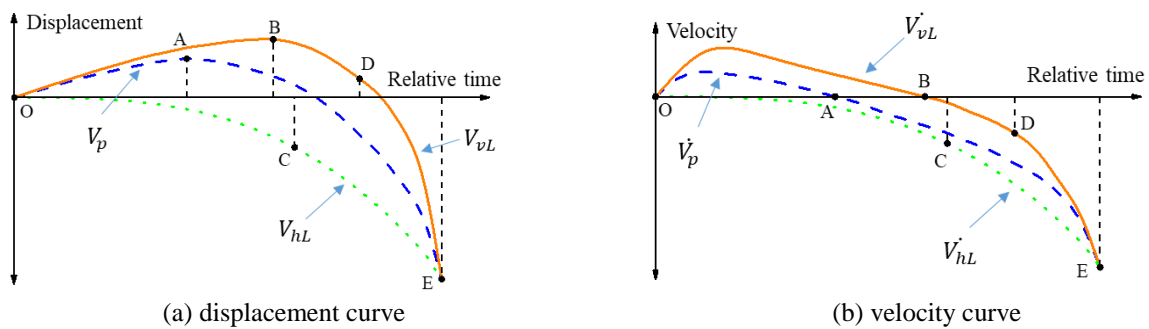


Fig. 5 Change laws of early-warning indexes of column lateral collapse mode

For column buckling collapse mode,  $V_{vL}$ ,  $V_{hL}$  and corresponding deformation rate are chosen as the early-warning indexes of column buckling collapse mode. The change laws of early-warning indexes are shown in Fig.6, where point A-C refer to the characteristic points of the curves of early-warning indexes and point D refers to the final collapse time.

The definition of point A-D are shown below:

- (1) Early-warning point A refers to the time when  $V_{hL}$  reaches its peak value.
- (2) Early-warning point B refers to the time when  $V_{hL}$  decreases to 3/5 of its peak value.
- (3) Early-warning point C refers to the time when vertical displacement rate  $V_{vL}$  has decreased to opposite value of  $V_{vL}$  at point A.
- (4) Collapse point E refers to the time when the lateral displacement of the heated column reaches 1/5 of the eave height.

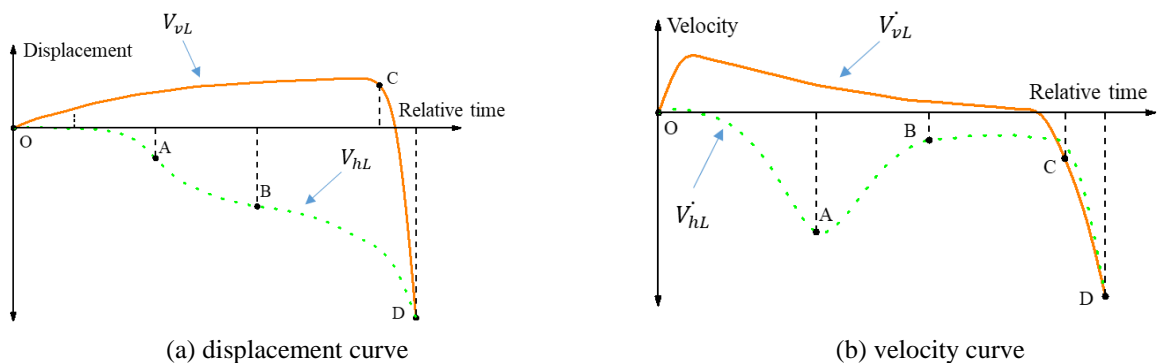


Fig. 6 Change laws of early-warning indexes of column buckling collapse mode

For overall inward collapse mode,  $V_p$ 、 $V_{vL}$ 、 $V_{hL}$  and corresponding deformation rate are chosen as the early-warning indexes of overall collapse mode. The change laws of early-warning indexes are shown in Fig.7, where point A-E refer to the characteristic points of the curves of early-warning indexes and point F refers to the final collapse time.

- (1) Early-warning point A refers to the time when  $V_p$  reaches its peak value.
- (2) Early-warning point B refers to the time when  $V_p$  decreases to zero.
- (3) Early-warning point C refers to the time when  $V_p'$  reaches 10 times of the average rate of  $V_p$  from point A to point B.
- (4) Early-warning point D refers to the time when  $V_{vL}'$  reaches its peak value.
- (5) For overall inward collapse mode, early-warning point E refers to the time when  $V_{hL}'$  reaches its peak value. For overall outward collapse mode, early-warning point E refers to the time when  $V_{hL}'$  reaches 10 times of the average rate of  $V_{hL}$  from point A to point B.
- (6) For overall inward collapse model, the collapse point F refers to the time when the vertical displacement of the heated rafters reaches 1/10 of the span. For overall outward collapse mode, the collapse point F refers to the time when the lateral displacement of the heated column reaches 1/5 of the eave height.

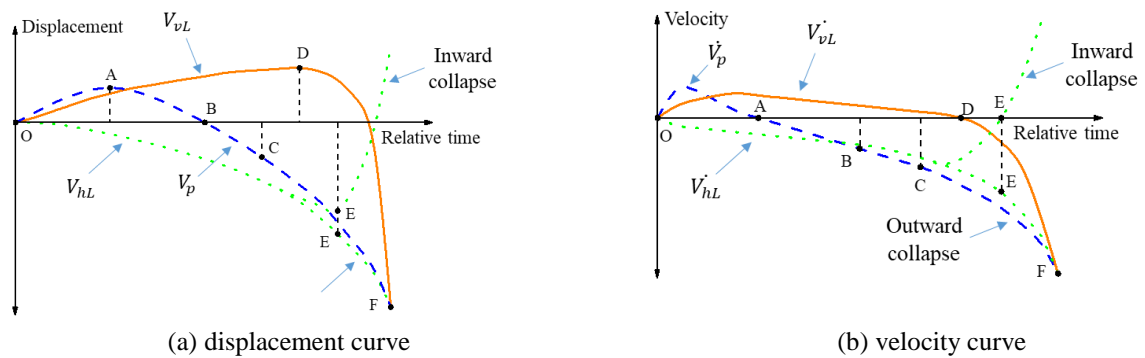


Fig. 7 Change laws of early-warning indexes of overall collapse mode

### 3.3 Early-warning methods for different collapse modes

Based on the findings mentioned above, the three-level early-warning methods for different collapse modes are proposed in Table 3.

Table 3 Early-warning methods for different collapse modes

Collapse mode	Early-warning level	Early-warning criteria	Time ratio
Column lateral collapse mode	1st level	Occurrence of point A	0.15
	2nd level	Occurrence of point B	0.55
	3rd level	Occurrence of one point C or D	0.8
Column buckling collapse mode	1st level	Occurrence of point A	0.4
	2nd level	Occurrence of point B	0.55
	3rd level	Occurrence of one point C	0.85
Overall collapse mode	1st level	Occurrence of point A	0.25
	2nd level	Occurrence of one point C, D or E	0.65
	3rd level	Occurrence of two points C, D or E	0.85

In order to quantitatively calculate the remaining collapse time of the burning frame under each early-warning level, the early-warning time ratios under different combinations of parameters in parametric studies for different collapse modes are shown in Fig.8.

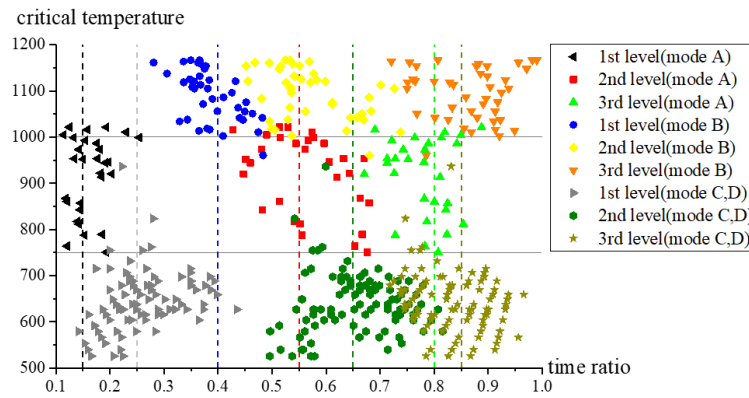


Fig. 8 Data distribution of early-warning time ratios in parametric studies

### 3.6 Judgement method

Based on the findings mentioned above, the judgement method of collapse modes is put forward in Fig.18. When the collapse mode is forecasted, the corresponding early-warning method can be chosen for collapse prediction.

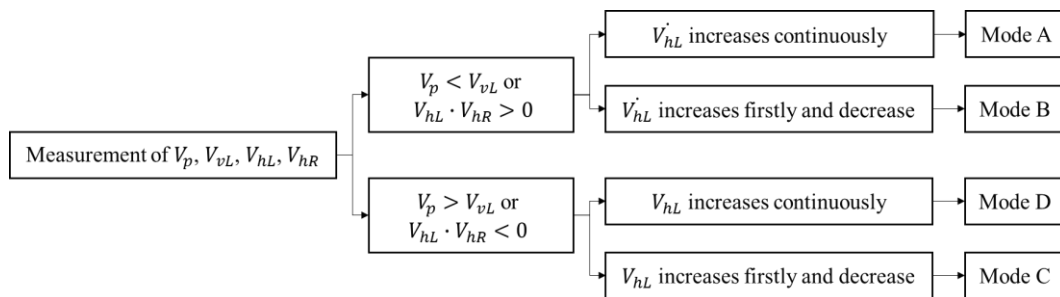


Fig. 9 Judgement method of collapse modes

## 4 CONCLUSION

(1) Single span steel portal frames subjected to fire may collapse either in column lateral collapse mode(A), column buckling collapse mode(B), overall inward collapse mode(C) or overall outward collapse mode(D).

(2) Apex and eaves are key positions of the early-warning methods of steel portal frames. The possible collapse mode of the burning frame can be predicted through analysing the displacements of apex and eaves.

(3)  $V_p$ ,  $V_{vL}$ ,  $V_{hL}$  and corresponding deformation rate are chosen as the early-warning indexes for collapse prediction. Early-warning points are the characteristic points of the early-warning indexes. The occurrence of early-warning points can help predicting the collapse time.

## REFERENCE

- Ali H. M., Senseny P. E., Alpert R. L., 2004. Lateral displacement and collapse of single-story steel frames in uncontrolled fires, *Engineering Structures*, 26, p. 593-607.
- Davison B., Owens G. W., 2008. *Steel Designers' Manual*, Steel Construction Institute (SCI), Blackwell Publishing.
- Jiang L. R., Zhang Q. L., Shi J. X., Li Y., 2012. Statistic study on sacrifices of firefighters in China, *Procedia Engineering*, 45, p. 700-704.
- Jiang S. C., Zhu S. J., Guo X. N., Chen C., Li Z. Y., 2020. Safety monitoring system of steel truss structures in fire, *Journal of Constructional Steel Research*, 172.
- Jiang J., Wang C. H., Lou G. B., Li G. Q., 2018. Quantitative evaluation of progressive collapse process of steel portal frames in fire, *Journal of Constructional Steel Research*, 150, p. 277-287.
- Lou G. B., Wang C. H., Jiang J., Jiang Y. Q., Wang L. W., Li G. Q., 2018. Experimental and numerical study on thermal-structural behaviour of steel portal frames in real fires, *Fire Safety Journal*, 98, p. 48-62.

Moss P. J., Dhakal R. P., Bong M. W., Buchanan A. H., Design of steel portal frame buildings for fire safety, 2009, *Journal of Constructional Steel Research*, 65. p. 1216-1224.

Wong S. Y., 2001. The structural response of industrial portal frame structures in fire (PhD Thesis) University of Sheffield, UK.

Usmani A. S., Chung Y. C., Torero J. L., How did the WTC towers collapse: a new theory, *Fire Safety Journal*, 38. p. 501-503.

GB50016, 2018. Code for fire protection design of buildings, China Architecture & Building Press.

# NUMERICAL SIMULATION OF A FIRE RESISTANCE TEST AND PREDICTION OF THE FLUE GAS LEAKAGE USING CFD/FEM COUPLING

Rene Prieler<sup>a</sup>, Simon Pletzer<sup>a</sup>, Stefan Thumser<sup>b</sup>, Günther Schwabegger<sup>b</sup>, Christoph Hochenauer<sup>a</sup>

<sup>a</sup> Graz University of Technology, Institute of Thermal Engineering, Inffeldgasse 25/B, 8010 Graz, Austria

<sup>b</sup> IBS-Institut für Brandschutztechnik und Sicherheitsforschung GmbH, Petzoldstraße 45, 4020 Linz, Austria

## Abstract

In fire resistance tests of building materials, a crucial criterion to pass the test procedure is the leakage of the hot flue gases caused by gaps and cracks occurring due to the thermal exposure. The present study's aim is to calculate the deformation of a steel door and the flue gas leakage in a fire resistance test. For this purpose, a CFD/FEM coupling was introduced representing an intermediate approach between one-way and a full two-way coupling. In contrast to a full two-way-coupling, the heat transfer through the steel door was simulated based on a one-way approach. The predicted temperature in the door from the one-way simulation was used in the following CFD/FEM simulation, where the fluid flow inside and outside the furnace as well as the deformation of the door were calculated simultaneously. The simulation showed large gaps and flue gas leakage above the door lock and at the upper edge of the door, which was in close accordance to the experiment.

**Keywords:** Fire resistance test, CFD/FEM coupling, Deformation, Flue gas leakage

## 1 INTRODUCTION

During fire resistance tests the thermal expansion (deformation) of a test specimen is a key issue for modern building materials exposed to a thermal load or fire, which is related to the combustion and heat transfer in the gas phase (fire) and the thermal heat transfer in the solid test specimen. Fire resistance tests, using natural gas or oil-fired furnaces, with its pre-defined thermal load (time-dependent temperature trend), are carried out to determine the fire response (thermal resistance, mechanical stability and flue gas leakage from the furnace) of fire safety equipment. Due to the increasing computational power the simulation of fire resistance tests has the potential to reduce extensive testing of test specimen before final certification for a certain fire resistance level.

A very popular approach applied in the past for modelling fire resistance tests was the consideration of the gas phase combustion and thermal heat transfer in the solid test specimen by coupled CFD/FEM (computational fluid dynamics/ finite element method) simulations (e.g. Cabova et al., 2017; Lazaro et al., 2016). The chemical reactions in the fire (flame) and the heat transfer in the gas phase are considered by CFD simulations based on the finite volume method. Heat fluxes to the solid are commonly determined using the concept of the “adiabatic surface temperature” (see Wickström, 2016). In the following FEM simulation, the thermal heat transfer in the solid was predicted. Enhanced CFD/FEM simulations also take the deformation process of the test specimen into account (e.g. Szymkuc et al., 2018; Alos-Moya, 2014), which can be denoted as one-way coupling (weak coupling) according to the definition in (Tondini et al., 2016). This means that the deformation process does not affect the heat transfer or the gas phase (fluid flow and heat transfer). Thus, no flue gas leakage can be predicted.

When using two-way coupling the deformation of the solid test specimen also affects the fluid flow and heat transfer in the gas phase, which increases the complexity of such simulations. Recently, first approaches were published (see Feenstra et al., 2018; de Boer et al., 2019), considering an office room fire and the failure of the façade elements, which reveals an additional exit for the flue gas to the ambient.

Since there is a lack of numerical studies applying two-way simulations for the analysis of fire scenarios, the present study investigates the application of an intermediate approach between the one-way and two-way approach for a fire resistance test of a fire safety steel door:

- A one-way coupled CFD/FEM simulation of the fire resistance test was carried out to predict the gas phase combustion as well as the temperature and deformation of the steel door.
- The predicted temperatures in the steel door from the simulation (one-way coupled) were further used as boundary condition for the two-way coupling approach. Thus, it was assumed that the heat transfer between the gas phase and the solid test specimen is the same in one-way and two-way coupling.
- A two-way coupled CFD/FEM simulation revealed the deformation, gap formation and flue gas leakage during the fire resistance test.

## 2 EXPERIMENTAL SETUP

For the validation of the predicted flue gas leakage, a fire resistance test, with the fire safety steel door as test specimen, was done according to the standard (EN 1363-1:2012-07). The tested steel door was embedded into a wall made of hollow-bricks, and placed at the front of the fire resistance testing furnace (furnace described in Prieler et al., 2019). Within the steel enclosure (thickness of the metal sheet of 1 mm) of the door a multi-layer construction made of mineral wool/gypsum board/mineral wool was arranged to increase the thermal resistance. The overall dimension of the door was 1.375 m (width), 2.5 m (height) and 64 mm (thickness). Since the highest deformation and flue gas leakage was already reached after several minutes, only 10 minutes of the testing time are considered in this study, also keeping the calculation time at a minimum (high calculation time for two-way coupling). In Fig. 1 the steel door is shown including the connections between the door and the frame/wall (hinges, bolts and door lock). Furthermore, the measurement positions for the deformation are displayed.

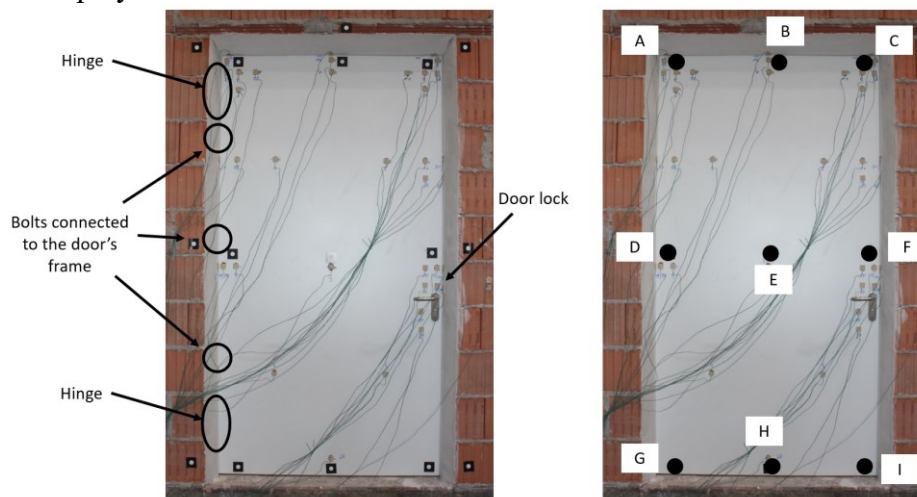


Fig. 1 Tested fire safety steel door with the connections between the door and the wall (left) as well as the deformation measurement positions (right)

## 3 NUMERICAL METHODOLOGY

Two approaches were used to numerically predict the fire response of the fire safety door: (i) one-way coupling and (ii) two-way-coupling of the CFD/FEM simulation.

### 3.1 One-way coupling

The approach of the one-way coupling in the present study was fully described in Prieler et al, 2019 and Prieler et al., 2020. In Fig. 2 the basic methodology is shown. It can be seen that the gas phase combustion and heat transfer in the solid test specimen is calculated by the CFD simulation (see Prieler et al, 2019). In the steel door the temperature at each position and for each time step during

the CFD simulation was stored and transported to the FEM code via an interface. A so-called “profile preserving” mapping method was further applied to map the temperatures on the numerical grid for the FEM simulation, where the structural analysis of the steel door was done. The contact treatment between the door and the wall/door frame as well as the material data are explained in detail in Prieler et al., 2020.

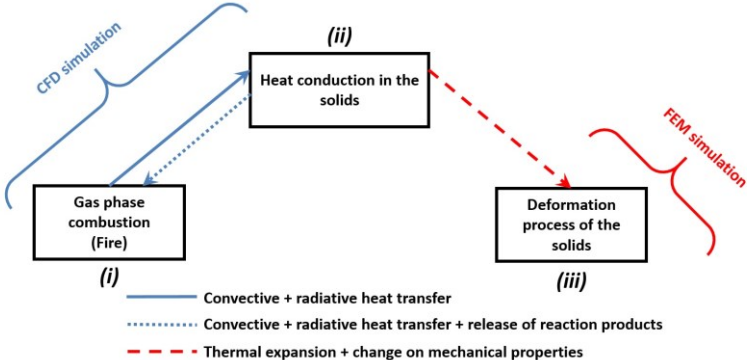


Fig. 2 Methodology of the one-way coupled approach

**3.2 Two-way coupling**

The numerical approach, denoted as two-way coupling, represents an intermediate method between the one-way and the full two-way coupling (consideration of all processes and interactions shown in Fig. 3 in the simulation). A full two-way coupling was not reasonable because of two issues regarding the heat transfer in the solid test specimen and the large dimension of the testing furnace:

- The heat transfer through the steel door and the deformation was not simulated simultaneously, caused by the missing knowledge about the contact between the mineral wool and gypsum board inside the door as well as the steel enclosure during the deformation. The deformation and contacts are very important for the heat transfer in the door.
- Since the dimension of the testing furnace is large (4.5 x 4 x 1.25 m), the calculation time would increase significantly for a full two-way approach. Therefore, the domain around the burners was neglected and the velocities, gas temperature, radiation intensity and pressure were extracted from the one-way simulation of the furnace for each time step. Thus, the transport equations for the reaction chemistry in the flame (fire) can be neglected in this two-way approach using the reduced domain, which saves calculation time.

Therefore, a simplified two-way methodology, shown in Fig. 3, was used in this study. First, a reduced domain of the gas phase in the was considered. The reduced domain of the gas phase in the furnace, and the furnace as well, can be seen in Fig. 4. In Fig. 4 the marked domain will be considered as gas phase in the simulation. At the boundaries of that domain temperature, velocity, radiation intensity and pressure are defined according to the one-way simulation of the furnace. Second, the temperatures in the steel door were the same as used for the one-way coupling in this study.

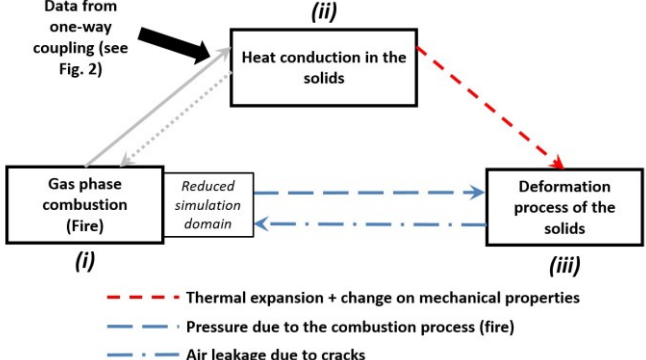


Fig. 3 Methodology of the two-way coupled approach

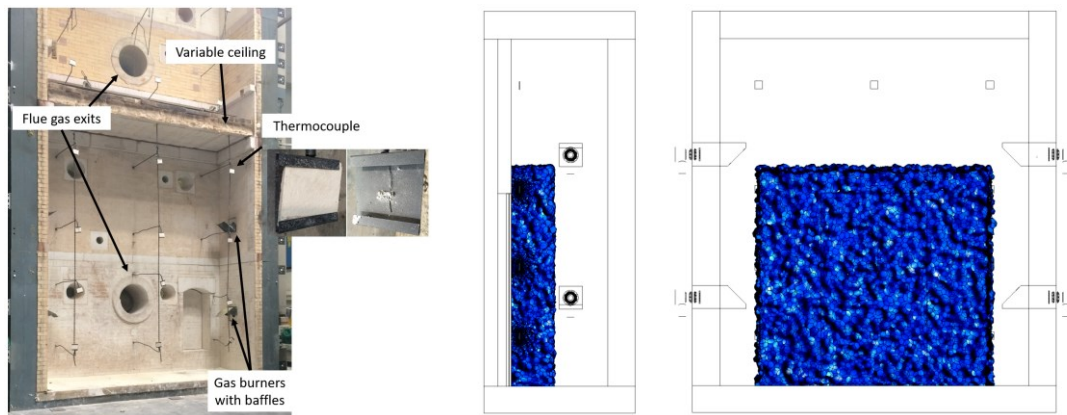


Fig. 4 Fire resistance testing furnace and the reduced domain of the gas phase in the furnace

The marked domain from Fig. 4 is also shown in Fig. 5 (left). Furthermore, the ambient gas phases outside of the furnace is highlighted, where flue gas leakage is simulated. This domain represents the entire simulation domain for the two-way approach. For example, the temperature boundary inside the furnace from the one-way simulation is shown. The hot zones represent the flames from the burner, deflected to the bottom by the baffles. Similar profiles were used for the velocity pressure and radiation intensity.

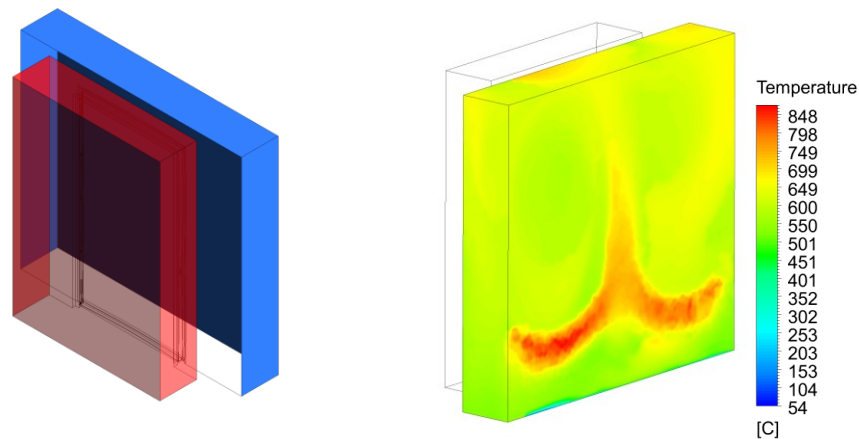


Fig. 5 Reduced domain (gas phase in the furnace and gas phase ambient) (left); Temperature boundary from the combustion (right)

It was found that for the simulation a time step size of 2 seconds and a maximum number of 2 iterations between the CFD simulation of the gas phase and the FEM simulation of the deformation of the door were sufficient. The numerical grid for the domain (CFD) consists of approx. 1,5 million cells (hexahedrons). Dynamic meshing was applied to adapt the numerical grid according to the predicted deformation from the FEM simulation. In the FEM simulation the door frame represents the adjacent brick wall, which was assumed to be rigid. The numerical grid of the solid door and the adjacent frame consisted of approx. 77,000 cells (mainly hexahedrons).

## 4 RESULTS AND DISCUSSION

### 4.1 Gap modelling

Both simulations, with the one-way and the two-way approach, showed that the maximum gap formation was above the door lock on the right edge of the door, as well as at the upper edge. In Fig. 6 the simulated deformation, using the two-way method, is shown after a testing time of 10 minutes, where a negative value means that the door is deforming to the fire exposed side. The calculated gap formation is marked by the black boxes at the upper edge (left) and above the door lock (right).

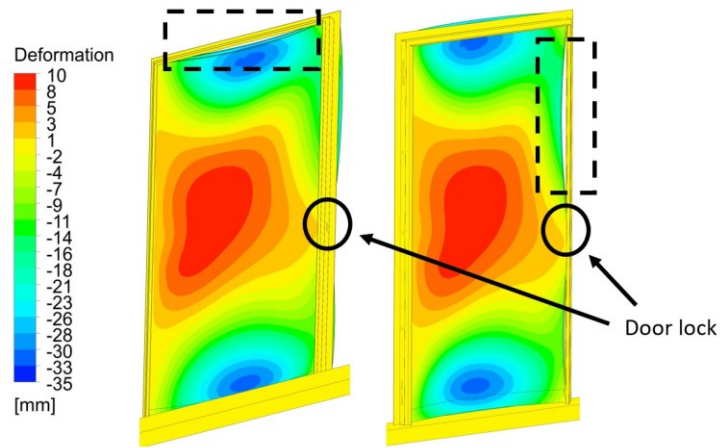


Fig. 6 Predicted gap formation between the door and the door frame by the two-way approach

#### 4.2 Deformation of the door

In Fig. 7 the deformation of the steel door at the upper edge (position “B”) and in the vicinity of the door lock (position “F”) is shown, where the highest gap formation occurs. At the upper edge both simulation approaches predicted a deformation of approx. -30 mm to the fire exposed side. However, the deformation observed in the experiment was much lower with a value of -10 mm. This deviation can be explained by the neglected deformation of the brick wall in the simulation. Thus, it might be possible that the flue gas leakage is over-predicted at the upper edge. A better agreement can be found in the vicinity of the door lock, where the deformation was between -1 and -2 mm to the fire exposed side. Also a close accordance between the simulations and the experiment was found in the centre of the door (position “E”), where the door is deforming to the fire unexposed side due to the increasing pressure inside the steel enclosure (release of water vapour from the gypsum board).

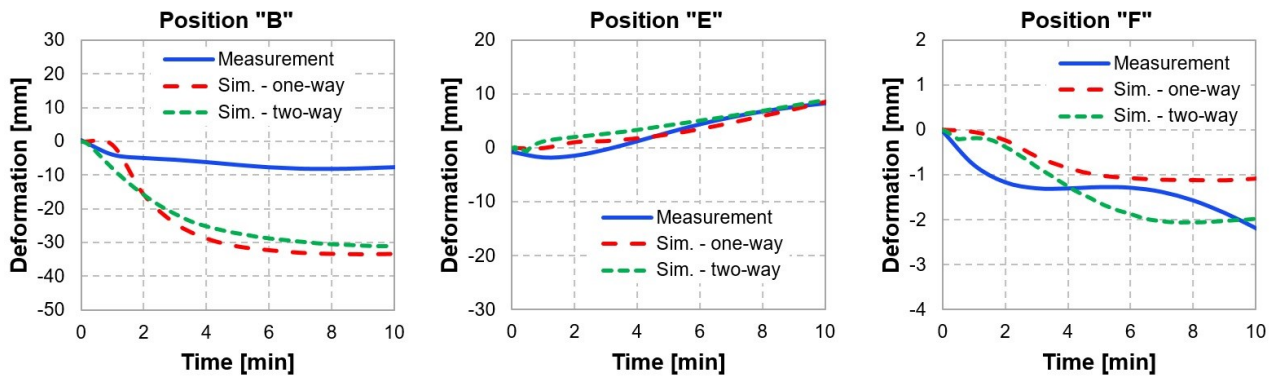


Fig. 7 Measured and simulated deformation of the steel door at position “B”, “E” and “F”

#### 4.3 Flue gas leakage

Using the two-way approach, it is possible to simulate the relative displacement of the steel door to the adjacent wall, and, subsequently, predict the flue gas leakage from the fire resistance testing furnace. In Fig. 8 (left) the side view of the upper edge of the door is shown with a volume rendering plot of the velocity of the flue gas exiting the furnace. It can be seen that the flue gas velocity is approx. 1.2 m/s. Above the door lock the flue gas velocity from the furnace is lower compared to the upper edge (see Fig. 8 right). This can be explained by the lower pressure in the furnace in the region above the door lock compared to the upper edge of the door. During the experiment the flue gas leakage was observed at the same position and the condensation of the water vapour was also detected at the upper edge of the door (at the lintel).

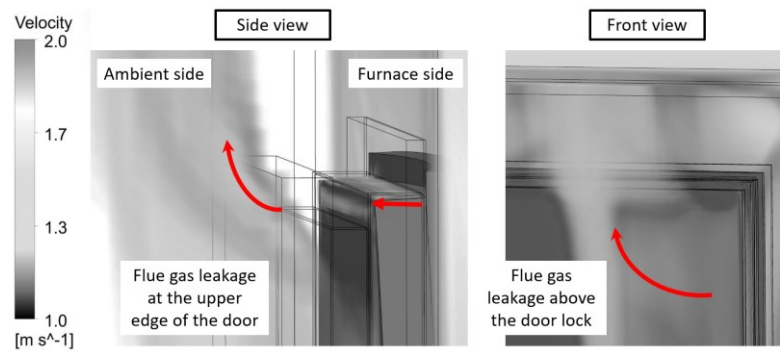


Fig. 8 Predicted flue gas leakage at the upper edge of the door (left) and above the door lock (right)

## 5 CONCLUSION

In this study a coupled CFD/FEM simulation of a fire resistance test of a steel door was carried out to predict the deformation, the gap formation (door/wall) as well as the flue gas leakage.

- The position of the predicted gap formation was in good agreement with the observations during the measurements.
- It was further determined that the flue gas leakage was higher at the upper edge of the door, caused by the higher pressure inside the furnace compared to the gap above the door lock.

## ACKNOWLEDGMENTS

This work was financially supported by the Austrian Research Promotion Agency (FFG), “Virtuelle Bauteilprüfung mittels gekoppelter CFD/FEM-Brandsimulation” (project 857075, eCall 6846234) and “Entwicklung von CFD/FEM Brandsimulationsmodellen mit Fokus auf Holz- und Gipsbauteile sowie komplexen Konstruktionen” (project 876469, eCall 28585806).

## REFERENCES

- Alos-Moya J., Paya-Zaforteza I., Garlock M.E.M., Loma-Ossorio E., Schiffner D., Hospitaler A. 2014. Analysis of a bridge failure due to fire using computational fluid dynamics and finite element models. *Engineering Structures*, 68, p. 96-110.
- Cabova K., Liskova N., Benysek M., Zeman F., Wald F., 2017. Numerical simulation of fire-resistance test of steel beam, in *EUROSTEEL*, 13-15 September 2017, Copenhagen, Denmark, p. 2518-2525.
- De Boer J.G.G.M., Hofmeyer H., Maljaars J., van Herpen R.A.P. 2018. Two-way coupled CFD fire and thermomechanical FE analyses of a self-supporting sandwich panel façade system. *Fire Safety Journal*, 105, p. 154-168.
- Feenstra J.A., Hofmeyer H., van Herpen R.A.P., Mahendran M. 2018. Automated two-way coupling of CFD fire simulations to thermomechanical FE analyses at the overall structural level. *Fire Safety Journal*, 96, p. 165-175.
- Lazaro D., Puente E., Lazaro M., Lazaro P.G., Pena J. 2016. Thermal modelling of gypsum plasterboard assemblies exposed to standard fire tests. *Fire and Materials*, 40, p. 568-585.
- Prieler R., Mayrhofer M., Eichhorn-Gruber M., Schwabegger G., Hochenauer C. 2019. *Development of a numerical approach based on coupled CFD/FEM analysis for virtual fire resistance tests—Part A: Thermal analysis of the gas phase combustion and different test specimens. Fire and Materials*, 43, p. 34-50.
- Prieler R., Gerhardter H., Landfahner M., Gaber C., Schluckner C., Eichhorn-Gruber M., Schwabegger G., Hochenauer C. 2019. *Development of a numerically efficient approach based on coupled CFD/FEM analysis for virtual fire resistance tests— Part B: Deformation process of a steel structure. Fire and Materials*, 44, p. 704-723.
- Szymkuc W., Glema A., Malendowski M., Mielcarek A., Smardz P., Poteralski A., 2018. Numerical investigation of fire and post-fire performance of CFT columns in an open car park fire, in *10th International Conference on Structures in Fire*, 6-8 June 2018, Belfast, UK, p. 407-414.
- Tondini N., Vassart O., Lechene S., Franssen J.-M. 2016. *An integrated modelling strategy between a CFD and an FE software. Journal Structural Fire Engineering*, 7(3), p. 217-233.
- Wickström U. 2016. *Methods for predicting temperatures in fire-exposed structures*, New York, NY, USA: Springer-Verlag.

## A TWO-SCALE FE MODEL TO ADDRESS CONNECTIONS IN COUPLED FIRE-STRUCTURE SIMULATIONS

Qingfeng Xu<sup>a</sup>, Herm Hofmeyer<sup>a</sup>, Johan Maljaars<sup>a,b</sup>

<sup>a</sup> Eindhoven University of Technology, Eindhoven, The Netherlands

<sup>b</sup> TNO, Delft, The Netherlands

### Abstract

A two-scale finite element model is proposed to improve two-way coupled fire-structure simulations. The model consists of (i) a global-scale model, which accounts for the structure, and (ii) a small-scale model for each connection. Structural parts on the global scale are connected by spring elements, which stiffness properties are updated by the small-scale models. A sandwich panel system, fixed with four screws, and exposed to fire, is simulated for demonstration purposes. The simulation shows that the two-scale model is able to transfer the mechanical response of the small-scale model, including failure, to the global-scale model. As soon as all screw connections fail, the panel is assumed to fail, and is removed in a subsequent part of the fire simulation. It is then demonstrated that the fire scenario changes from ventilation-controlled to fuel-controlled. Future research will incorporate more complex structures, and verification by experiments.

**Keywords:** two-scale model, fire-structure interaction, connections, sandwich panel system

### 1 INTRODUCTION

Structures under fire are difficult to research, for both the fluid dynamics behaviour of fire and the thermo-mechanical behaviour of structures are involved. The traditional way to assess the fire performance of a structure is by experiments, but these can be disproportionately expensive for large-scale structures. Therefore, coupled simulations may be useful, both in terms of costs and the potential to allow for parameter studies. In a coupled simulation, the results of the fire simulation, e.g. via Computational Fluid Dynamics (CFD), will be transferred to thermo-dynamical and thermo-mechanical simulations by e.g. the Finite Element Method (FEM). In literature also *two-way* coupled CFD-FEM simulations can be found, in which additionally the structural behaviour is coupled back to the CFD simulations: Luo (Luo *et al.* 2012) developed a Fire Interface Simulator Toolkit (AFIST) by integrating the CFD program FDS with a customized version of FEM program Abaqus, to investigate sandwich panels. Another two-way coupled method is FDS-2-Abaqus, in which sandwich panel failure is introduced as a compartment opening in the CFD simulation (Feenstra *et al.* 2018). Similarly, a more detailed sandwich panel model, yet with temperature *independent* properties, was presented in which the critical components (screws and bolts) were modelled by springs. When they failed, they led to an opening in the sandwich panel system, which changed the fire and consequently the façade temperature (De Boer *et al.* 2019). However, the mechanical behaviour of components is highly temperature-dependent, and connections need more accurate modelling than using simple springs. Therefore, this paper introduces a two-scale model to improve the above model (De Boer *et al.* 2019), so all the relevant structural details of the connections are modelled, including temperature dependent material behaviour.

### 2 TWO-SCALE MODEL

The two-scale model as proposed in this paper consists of (i) a global-scale model, which accounts for the behaviour of the structure, and (ii) a small-scale model for each connection. Structural parts in the global-scale model are connected by spring elements and the stiffness properties of the springs are updated by the results of the small-scale models. The material properties used in the small-scale model are temperature-dependent, and in this model the screw connection is modelled in detail, which results in accurate predictions of the connection's structural behaviour. Taking a screw that connects a plate and a column flange as an example, such a two-scale model is presented in Figure 1.

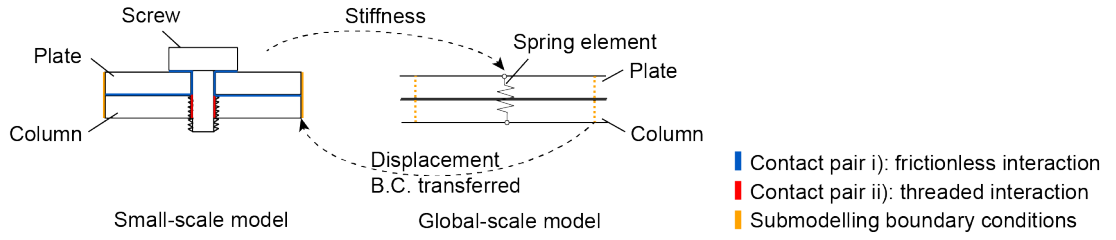


Fig. 1 Setup of the two-scale model.

The threads of screw and hole are simplified in the small-scale model by an Abaqus proprietary "threaded interaction" (show by red lines in Figure 1); while contact pairs of (a) the screw head and plate, (b) the plate and column, and (c) the plate and screw shank are using a frictionless "hard contact" interaction (show by blue lines). Boundary conditions for the small-scale model (positioned at the yellow lines) are provided by the global-scale model via the sub modelling approach (Abaqus, 2014). At the end of a load step of the small-scale model, its stiffness can be probed, which is then used to update the spring element's stiffness in the global-scale model. Details of the spring stiffness calculation are shown in Figure 2.

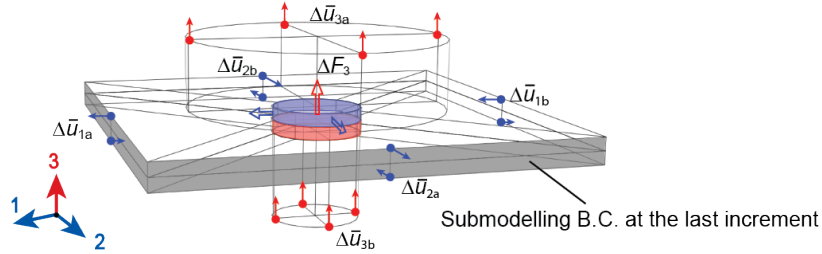


Fig. 2 Spring stiffness calculation.

The blue and red points in Figure 2 are the positions where displacements are measured within the small-scale model. At the end of a load step, displacements of the last increment are used to calculate the spring stiffness following Hooke's law:

$$\Delta F = k \cdot \Delta x \quad (1)$$

where  $\Delta F$  is the force increment, and  $\Delta x$  is the displacement increment. For example, the tension stiffness  $k_3$  (in 3-direction) can be found by the force increment in the threaded contact pair ii (see Figure 1)  $\Delta F_3$  and the displacement increment  $\Delta x_3$  in 3-direction. Where  $\Delta x_3$  is given by the averaged nodal displacements of the screw head  $\Delta \bar{u}_{3a}$  and the averaged displacements of the screw shank  $\Delta \bar{u}_{3b}$  by  $\Delta \bar{u}_{3a} - \Delta \bar{u}_{3b}$  (all shown by the red nodes). Hence, the tension stiffness can be calculated as:

$$k_3 = \frac{\Delta F_3}{\Delta x_3} \quad (2)$$

The shearing stiffness in the other two directions can be obtained in a similar fashion. More details can be found in Xu *et al.* (2021), including various demonstrated failure modes of the small-scale model, like shearing, bearing, tension, and pull-out failure.

### 3 TWO-WAY COUPLED CFD-FEM SIMULATION + TWO-SCALE MODEL

A two-way coupled CFD-FEM simulation is carried out to demonstrate the two-scale model. The fire is simulated by CFD program Fire Dynamics Simulator (FDS), which has been validated to simulate a fire accurately (McGrattan *et al.* 2013). The heat transfer and mechanical response are simulated by FEM program Abaqus. In this paper, a compartment is modelled with on the external side a (facade) sandwich panel, see Figure 3. The Adiabatic Surface Temperature (AST) on the panel is measured (Wickström *et al.* 2007) at the "AST points". Hereafter, the thermal data from the fire model are transferred to the finite element model as a flux, following the concept of the AST as given in Eq. (3):



(see also figure 4). Two materials were used, namely steel S355 for the sandwich inner and outer plates and the screw, and PIR for the insulation. Steel temperature dependent properties, including the thermal expansion coefficient, conductivity, and specific heat, are all defined according to Eurocode 3 part 1-2 (EN 1993-1-2 2005). The PIR material is modelled temperature independent, with a Young's modulus equal to 20000 N/mm<sup>2</sup>, a Poisson ratio of 0.2, a density equal to 45 kg/m<sup>3</sup>, and a thermal expansion coefficient equal to  $5.0 \times 10^{-5}$  1/K, all being ambient values. As for the interaction, a frictionless contact was applied for all contact pairs in the FE model, i.e. contact pairs of (a) the sandwich panel and C-column in the global-scale model and (b) the blue coloured contact pairs in the small-scale model in Figure 1.

## 4 RESULTS AND DISCUSSION

Although the simulation always starts with a load step in the CFD fire domain, here a discussion of the results will focus first on the two-scale model, so the FE domain.

### 4.1 FEM analyses

First, a thermo-dynamical analysis is carried out in the FE domain, using the global-scale model. Hereafter, the resulting time varying nodal temperatures are applied as boundary conditions in a thermo-mechanical model, again on the global scale. In Figure 4 on the left, the thermo-dynamical model shows the temperature distribution of the sandwich panel under fire at a time of 12s. Temperatures are relatively high near the ground, as there the burner is positioned in the FDS model. The temperatures shown lead to thermal expansion. As this expansion is restrained by the connections (the spring elements) at the corners, thermally induced strains occur as shown by the Von Mises in the middle surface of the plate at the fire side of the panel, see Figure 4 in the middle.

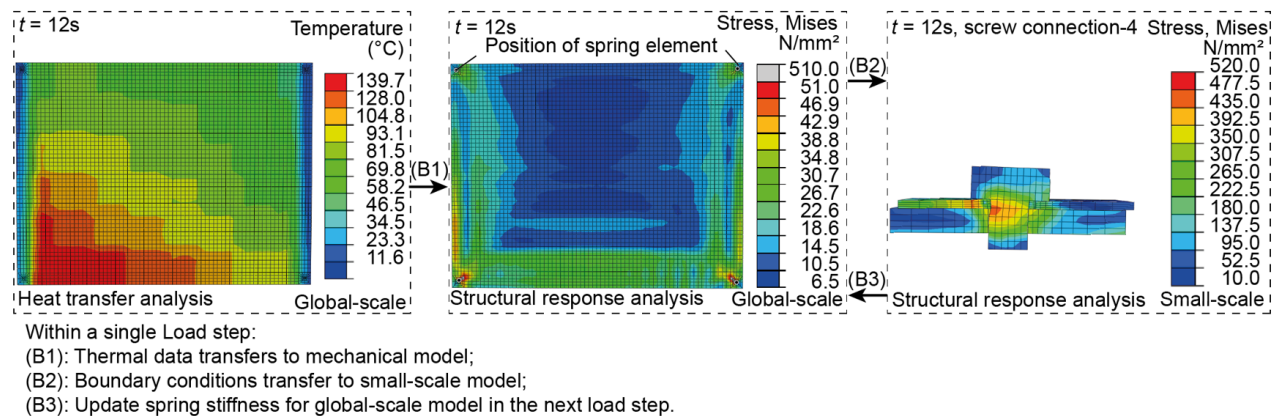


Fig. 4 Typical structural response. Middle figure contour is capped (grey coloured) to show plate compression, otherwise only plate bearing at the screws would be visible.

After each load step, the strains and stresses near the springs are used to formulate the boundary conditions (in time during the load step) for the small-scale model, on its edge surfaces of the plates, as shown in Figure 2. Note that for the temperature, the complete small-scale model inherits the temperature at the position of the spring in the global-scale model, of course as a function of time. As a result, Figure 4 on the right shows the mechanical response of Screw-4 (see Figure 3 for its position); clearly the screw is loaded in shear. Note that the small-scale model is able to simulate all relevant failure modes using either (Von Mises) normal plasticity or ductile damage material models (Xu *et al.* 2021); here the ductile failure model is used. This means that the element stiffness is reduced according to the amount of damage, as a function of the strains. As soon as finite elements within the small-scale model reach the ultimate stiffness, the screw is assumed to be failed. As soon as critical connections which support the complete structure, e.g. screw-1 and screw-2 fail, the panel is assumed to be failed, and will be removed in the CFD and FE models in the next load step. The bottom part of the sandwich panel expands more than the other parts due to the higher temperatures. This introduces a shear load on the screw connections (in the 3-direction in Figure 3).

As a consequence, it was found that all screwed connections (small-scale model) fail in plate bearing during the simulation. Figure 5 shows (a) the shear force for the small-scale models, also for a larger load step size of 5s for comparison, and (b) the shear force for the global and small-scale models, with a load step size of 2s.

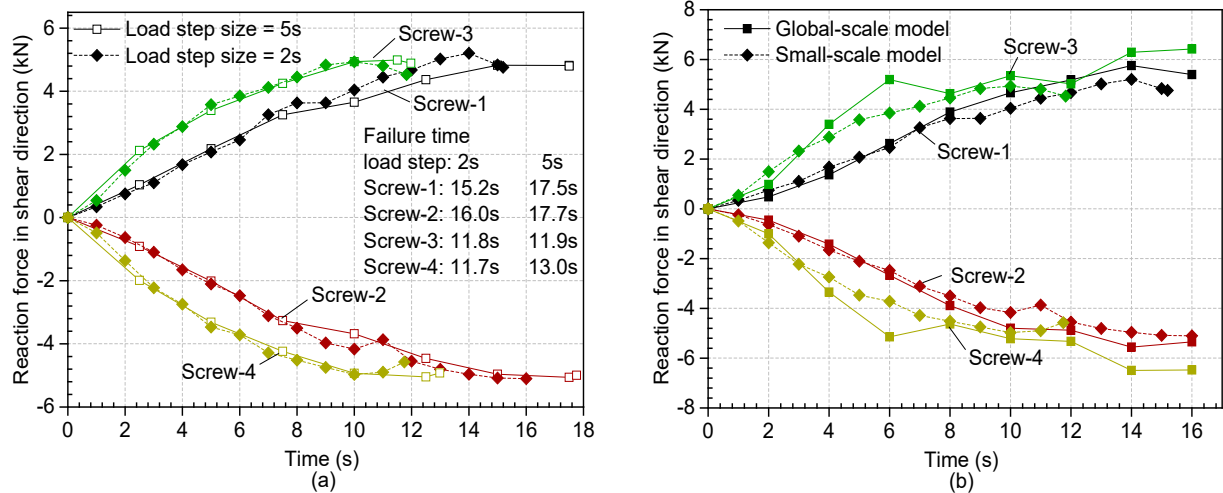


Fig. 5 Shear forces in the screw connection.

Figure 5a verifies the applied load step size by comparing it with a simulation using a larger load step of 5s. Note that each load step may contain several (converged) increments, and figure 5 uses data requested at certain time intervals (so may be interpolated from the increment-1 data). Results are comparable along the simulation path, however, screw failure times are determined more precisely for a smaller load step, as shown in the table in figure 5a. Also, Screw-3 and Screw-4, at the bottom of the panel, fail earlier than Screw-1 and Screw-2 at the top, caused by the higher temperatures at the bottom, see Figure 3. Figure 5b, on the right, shows that the global-scale and small-scale model show similar behaviour for shear in the screws/springs, which verifies that the detailed connection behaviour, as provided by the small-scale model, transfers correctly to the global-scale model. Some small differences can be seen though, because when the stiffness of the screw changes rapidly (e.g. from elastic to plastic), that information will only enter the global-scale model in a next load step. Note that when a screw fails, its last known stiffness in the global-scale model will be kept, to avoid singularities.

#### 4.2 Fire simulation in CFD

The overall duration for the fire simulation was 100 seconds, during which the fire simulation pauses and checks the status of the sandwich panel in the FE models after each load step. A failed sandwich panel is removed in the fire simulation in the next load steps, which in turn leads to the potential for on one hand more oxygen to flow into the compartment and, on the other hand, for exhaust gasses to leave the compartment. For the fuel, cellulose ( $C_6H_{10}O_5$ ) has been selected, with a formation enthalpy equal to -513 kJ/mol. If enough oxygen is available, the combustion is governed by the following fuel-controlled reaction:



However, the oxygen supply is the limiting factor in the considered compartment, given its limited designed openings. As a result, a ventilation-controlled fire occurs, producing carbon monoxide and releasing less heat as compared to a fuel controlled fire. The specified Heat Release Rate (HRR) is shown in Figure 6 in red, while the simulation result is shown in blue. It shows that the fire is governed by the oxygen supply at the beginning of the simulation, where the HRR is lower than the specified maximum value. The thermo-mechanical analysis from the FE model indicates that the sandwich panel fails at 16.0 s, due to the failure of the screw connections (see Figure 5a). Consequently, the fire simulation automatically removes the panel, oxygen enters the compartment, and the fire scenario

changes from ventilation-controlled to fuel-controlled, with an HRR now following the specified value. Thermal loads on the remaining parts of the structure subsequently increase, and a vicious circle of fire induced damage and damage reinforced fire may occur (for more complex structures).

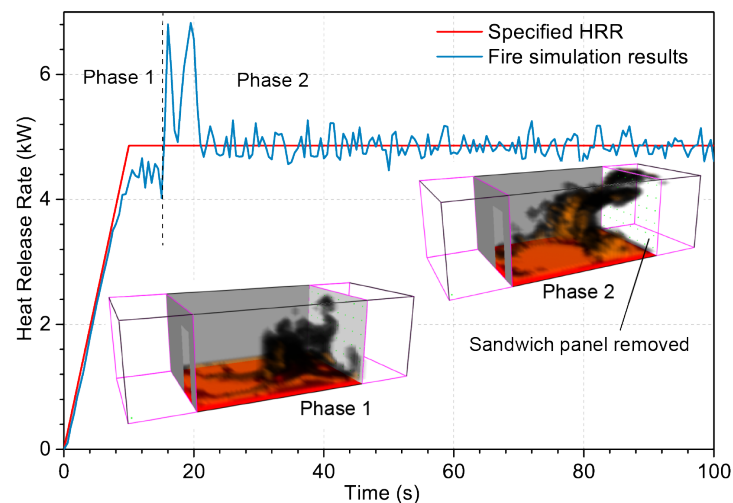


Fig. 6 HRR of the fire simulation.

## 5 CONCLUSIONS AND OUTLOOK

To model structural connections accurately, this paper presents a two-scale model as a part in two-way coupled simulations of structures in fire. Interactions are modelled (a) between the CFD and FEM domain; and (b) between a global-scale model (the entire structure) and a small-scale model (the connection). It can be concluded that:

- (1) When a structure with connections is subject to fire, connection failure may be a critical factor with respect to the fire resistance.
- (2) The two-scale model is able to transfer boundary conditions from the global-scale model to the small-scale model, whereafter the mechanical response of the small-scale model can be used to update the global-scale model.
- (3) For a compartment fire, the loss of a sandwich panel may change the fire scenario from ventilation-controlled to fuel-controlled, which stresses the need to incorporate two-way coupling.

In the future, structural systems with more components will be investigated (e.g. several panels), so more complex and progressively failing systems can be investigated. In addition, a number of fire experiments will be simulated to verify the simulation model further.

## REFERENCES

- Luo, C., Lua, J. and DesJardin, P.E., 2012. Thermo-mechanical damage modeling of polymer matrix sandwich composites in fire. *Composites Part A: Applied Science and Manufacturing*, 43(5), pp.814-821.
- Feenstra, J.A., Hofmeyer, H., Van Herpen, R.A.P. and Mahendran, M., 2018. Automated two-way coupling of CFD fire simulations to thermomechanical FE analyses at the overall structural level. In *Fire safety journal*, 96, pp.165-175.
- De Boer, J.G.G.M., Hofmeyer, H., Maljaars, J. and Van Herpen, R.A.P., 2019. Two-way coupled CFD fire and thermomechanical FE analyses of a self-supporting sandwich panel façade system. *Fire Safety Journal*, 105, pp.154-168.
- McGrattan, K., Hostikka, S., McDermott, R., Floyd, J., Weinschenk, C. and Overholt, K., 2013. Fire dynamics simulator user's guide. *NIST special publication*, 1019(6).
- Wickström, U., Duthinh, D. and McGrattan, K., 2007, September. Adiabatic surface temperature for calculating heat transfer to fire exposed structures. In *Proceedings of the Eleventh International Interflam Conference. Interscience Communications, London* (Vol. 167).
- EN 1993-1-2, Eurocode 3: Design of Steel Structures - Part 1-2: General Rules - Structural Fire Design, *European Committee for Standardisation*, Brussels, Belgium, 2005.
- Abaqus manuals, Version 6.14, Dassault Systèmes Simulia Corp, 2014.
- Xu, Q.; Hofmeyer, H.; Maljaars, J., 2021. A two-scale model for screw connections in a structural system under varying temperatures. to be submitted.

## BENCHMARK STUDY FOR FIRE DESIGN OF STEEL BEAM

Batuhan Der<sup>a</sup>, František Wald<sup>a</sup>, Martin Vild<sup>b</sup>

<sup>a</sup> Czech Technical University in Prague, Faculty of Civil Engineering, Prague, Czech Republic

<sup>b</sup> Brno University of Technology, Faculty of Civil Engineering, Veveří 95, Brno 602 00, Czech Republic

### Abstract

This paper presents a three-dimensional simple shell model for uniformly heated simply supported beam under point load considering geometrically/materially nonlinearity using the finite element analyses (FEA). The mechanical properties of steel at high temperatures were defined using the reduction factors presented by EN1993-1-2:2005. To simulate simple design rules, the thermal expansion, creep effect, and local imperfections are not considered in the proposed simple shell model. The numerical results are subjected to sensitivity studies changing different parameters including cross-section type, length of the span, loading type and boundary conditions. The results are presented in terms of bending moment resistance, critical elastic moment, and lateral torsional buckling moment at different temperature levels. The developed shell model is validated using analytical solutions.

**Keywords:** fire design, numerical simulation, shell element, beam, validation and verification

## 1 INTRODUCTION

In the fire, steel beams have significant reductions in their ambient temperature stiffness and strength, leading to a decrease in the ultimate load capacity. EN 1993-1-2:2005 suggests that the design of isolated steel members exposed to fire assuming a uniform temperature in the cross-section considering the mechanical properties of steel at elevated temperatures can be analysed using simplified analytical methods. When designing a steel beam, the influence of the fire action can be applied using the ambient temperature actions with reduction factors for the mechanical properties of structural steel at elevated temperature (Both, 2016). The benchmark solutions are highly important to check the correctness of the application of models (Kwasniewski, 2009). A good balance between simplicity and applicability are required in the representation of benchmark studies (Sawicki et al., 2013). Benchmarking in fire design is summarised in (Wald et al, 2014), and (Wald et al, 2014).

The study includes a beam from the IPE300 section with a span of  $L = 6$  m, which is loaded by concentrated force at the midspan at the top flange. The beam is assumed that it has a uniform temperature along the cross-section and length of the beam. Elastic modulus and yield strength of steel beam at room temperature are taken as  $210000 \text{ N/mm}^2$  and  $355 \text{ N/mm}^2$ , respectively. In all cases, Poisson's ratio is 0.3 and non-temperature dependent. Then, the three different moment resistance values, (bending, critical elastic, and lateral-torsional buckling) are calculated through the equations proposed in EN 1993-1-2:2005 to verify results from the proposed shell model. Finally, parametric studies are prepared changing the different parameters such as cross-section, length of the span, loading and boundary conditions. The objective of this study is to provide numerical and analytical results using the shell model generated in FEA software (Abaqus, 2000) and EN 1993-1-2:2005 equations to show the applicability of the simple shell model in structural fire engineering.

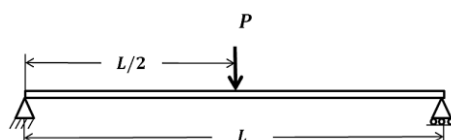


Fig. 1 Model description

## 2 PROCEDURES

In this study, the stress-strain response of grade S355 steel determined through equations given in EN 1993-1-2 as indicated in Fig. 2. The cross-sections studied in this paper belong to Class 1 based on the limits presented in EN 1993-1-1:2005.

### 2.1 Analytical Model

The moment resistance of the steel beams at elevated temperatures is calculated according to clause 4.2.3.3 in EN 1993-1-2: 2005. The design moment resistance  $M_{fi,\theta,Rd}$  of a Class 1, Class 2 or Class 3 cross-section with a uniform temperature  $\theta_a$  should be determined from:

$$M_{fi,\theta,Rd} = k_{y,\theta} [\gamma_{M0}/\gamma_{Mfi}] M_{Rd} \quad (1)$$

where  $k_{y,\theta}$  is the reduction factor for the yield strength of steel at a uniform temperature  $\theta_a$ , reached at time  $t$ ,  $\gamma_{M0}$  is a partial safety factor for the resistance of cross-sections,  $\gamma_{Mfi}$  is a partial safety factor for the relevant material property, for the fire situation,  $M_{Rd}$  is the design resistance for bending about one principal axis of a cross-section for normal temperature design. Clause 6.2.5 in EN 1993-1-1: 2005 gives the following expressions to calculate the design bending resistance of sections class 1 and 2 at ambient temperature:

$$M_{Rd} = M_{pl,Rd} = \frac{W_{pl} f_y}{\gamma_{M0}} \quad (2)$$

There is no formulation or guidance for the calculation of the elastic critical moment ( $M_{cr}$ ) in Clause 6.3.2.2(2) of EN 1993-1-1. A general expression proposed by NCCI SN003 (SCI, 2005) is used to calculate the elastic critical moment for lateral-torsional buckling considering the shape of the bending moment diagram, different end restraint conditions, warping restraints, in-plane curvature before buckling, and the level at which the load is applied.

$$M_{cr} = C_1 \frac{\pi^2 E I_z}{(kL)^2} \left( \sqrt{\left(\frac{k}{k_w}\right)^2 \frac{I_w}{I_z} + \frac{(kL)^2 G I_t}{\pi^2 E I_z} + (C_2 z_g)^2} - C_2 z_g \right) \quad (3)$$

in which  $I_t$  is the torsion constant,  $I_w$  is the warping constant,  $E$  is the modulus of elasticity,  $G$  is the shear modulus,  $I_z$  is the second moment of area about the minor axis,  $L$  is the length of the beam between points of lateral restraint,  $z_g$  is the distance between the level of application of the loading and the shear centre (and is positive for destabilising loads applied above the shear centre when the load is acting downwards),  $C_1$  and  $C_2$  are parameters, which can be taken from Table 1,  $k_w$  is a warping restraint parameter. Where no warping restraint is provided, and as a conservative assumption when the degree of warping restraint is uncertain,  $k_w$  should be taken equal to unity. According to clause 4.2.3.3 in EN 1993-1-2, the design lateral-torsional buckling resistance moment  $M_{b,fi,t,Rd}$  at time  $t$  of a laterally unrestrained member with a Class 1 or Class 2 cross-section should be determined from:

$$M_{b,fi,t,Rd} = \chi_{LT,fi} W_{pl,y} \frac{k_{y,\theta,com} f_y}{\gamma_{M1}} \quad (4)$$

where  $W_{pl,y}$  is the plastic section modulus of cross-section,  $k_{y,\theta,com}$  is the reduction factor for the yield strength of steel considering the maximum temperature in the compression flange  $\theta_{com}$  reached at time  $t$ , and  $\chi_{LT,fi}$  is the reduction factor for lateral-torsional buckling in the fire design situation, which is calculated using the following equation:

$$\chi_{LT,fi} = \frac{1}{\phi_{LT,\theta,com} + \sqrt{[\phi_{LT,\theta,com}]^2 - [\lambda_{LT,\theta,com}]^2}} \quad (5)$$

with

$$\phi_{LT,\theta,com} = \frac{1}{2} [1 + \alpha \bar{\lambda}_{LT,\theta,com} + (\bar{\lambda}_{LT,\theta,com})^2] \quad (6)$$

and the imperfection factor,  $\alpha$ , which was proposed by Vila Real et al (2003), is given by

$$\alpha = 0.65 \sqrt{\frac{235}{f_y}} \quad (7)$$

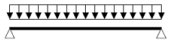
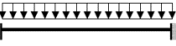
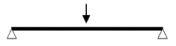
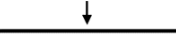
and, for Class 1, 2 and 3 the non-dimensional elevated temperature LTB slenderness of a steel beam  $\bar{\lambda}_{LT,\theta,com}$  is determined through the following expression:

$$\bar{\lambda}_{LT,\theta,com} = \bar{\lambda}_{LT} \sqrt{k_{y,\theta,com}/k_{E,\theta,com}} \quad (8)$$

in which  $k_{E,\theta,com}$  is the modulus of elasticity reduction factor at the maximum steel temperature in the compression flange,

$$\bar{\lambda}_{LT} = \sqrt{\frac{W_y f_y}{M_{cr}}} \quad (9)$$

Table 1  $C_1$  and  $C_2$  values for transverse loading (SCI, 2005)

Loading and support conditions	Bending moment diagram	$C_1$	$C_2$
		1.127	0.454
		2.578	1.554
		1.348	0.63
		1.683	1.645

## 2.2 Finite Element Model

The FEA code Abaqus was used to generate the finite element models. The model of the single-span beam presented here was meshed using a four-noded, reduced integration shell element S4R. To define mesh size in the shell model, 20 elements across the web height and 10 elements across the flange width were used. The shell model described above is indicated in *Fig. 2*.

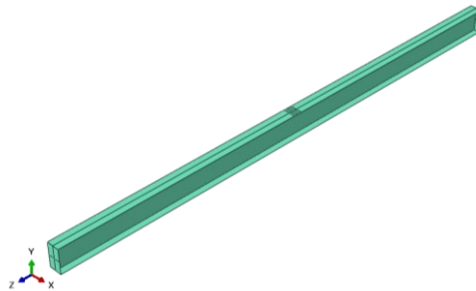


Fig. 2 Model description in the shell model

As shown in *Fig. 3*, the red point at the mass centre of the endplate is coupled to the red line along the width of the endplate using kinematic coupling constraints. At the left side of the model, the movements in all directions and the rotation in  $-z$  direction was constrained, whereas the movement in  $-z$  direction was allowed at the right side of the model to obtain simply supported beam. The concentrated load was equally applied to five nodes at the top flange with a 25 mm distance to each node. There was no defined constraint in the flanges because it was aimed to provide no warping constraint.

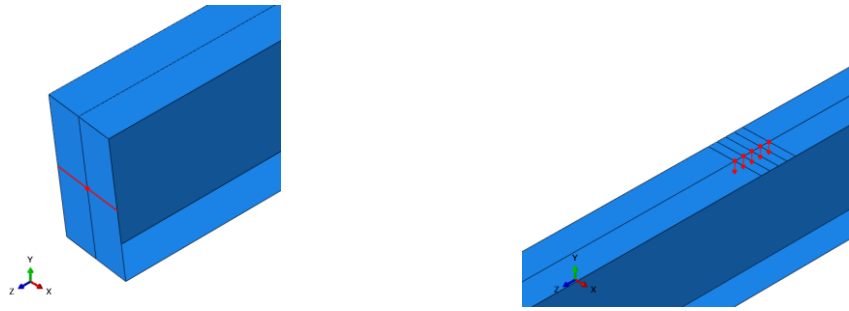


Fig. 3 Boundary conditions of the simply supported beam and loading conditions of point load

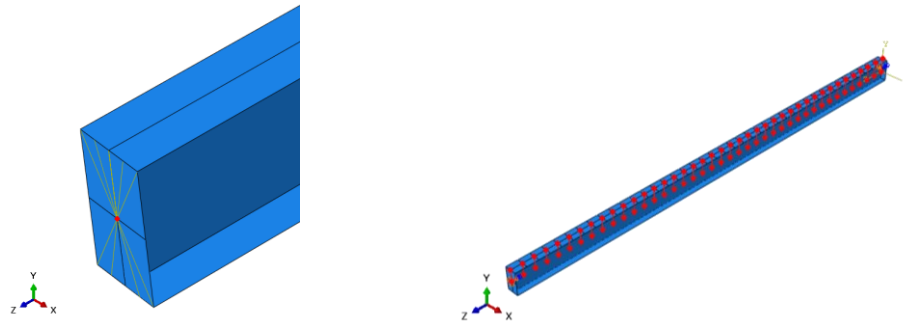


Fig. 4 Fix end support and distributed load

Furthermore, the distributed load and fixed end support were also investigated in this study. The distributed load was applied at the top flange overall span with a 150 mm distance. The total number of nodes used to apply load was 41. To provide fixed end support conditions, the reference node at the centre of mass was coupled to the beam section including flanges and web. The only degree of freedom that is not constrained was the movement in  $z$ -direction at the right side of beams. To find the bending resistance of beams, the static general analysis was used without imperfection. Then, a set of simulations was performed with geometric imperfection incorporated from the first mode eigenvalue buckling analysis considering the maximum amplitude of  $e_0/L$  (see table 5.1 in EN 1993-1-1:2005). Initial geometric imperfections were applied following the beams eigenmodes obtained by linear buckling analysis (LBA).

### 3 RESULTS AND DISCUSSIONS

The results were presented here in terms of bending resistance, critical elastic moment, and lateral-torsional buckling resistance. Even though the presence of endplates in the shell model creates some amount of warping restraint, it is assumed that  $k_w$  equals unity due to the uncertainty of warping restraint degree in the analytical model. This assumption may result in a difference between numerical and analytical results in the evaluation of critical elastic moment and lateral-torsional buckling resistance.

#### 3.1 Bending Resistance

The bending resistance of steel beams at high temperatures according to *Eq. (1)* is dependent on the steel grade and the cross-section type. In this study, only the cross-section type was changed in the shell model and the results are presented in Table 2.

Table 2 Bending resistance (kN.m)

$\theta$ (°C)	IPE 200		IPE 300		IPE 400	
	Analytical	Shell model	Analytical	Shell Model	Analytical	Shell Model
20	78.31	77.4	223.08	222.32	463.99	456.64
400	78.31	76.56	223.08	215.48	463.99	436.69
600	36.81	35.98	104.85	100.67	218.07	204.57
700	18.01	17.6	51.31	49.03	106.72	98.69

### 3.2 Critical Elastic Moment

This study consists of calculating the critical elastic moment, as shown in *Table 3*, using three different ways: analytical model (*Eq. 3*), LTBeam and shell model. The changing parameters were cross-section type, length of span, loading type and boundary conditions. The linear buckling analysis was performed to calculate the critical elastic moment in the shell model.

Table 3 Critical Elastic Moment (kN.m)

$\theta$ (°C)	IPE 200			IPE 300			IPE 400		
	Analytical	Shell Model	LTBeam	Analytical	Shell Model	LTBeam	Analytical	Shell Model	LTBeam
20	24.37	22.35	25.07	85.54	82.6	88.65	207.18	195.37	215.71
400	17.06	15.64	17.55	59.87	57.82	62.06	145.03	136.76	151
600	7.55	6.93	7.77	26.52	25.61	27.48	64.23	60.56	66.87
700	3.17	2.91	3.26	11.12	10.74	11.52	26.93	25.4	28.04
$\theta$ (°C)	5 m			6 m			7 m		
	Analytical	Shell Model	LTBeam	Analytical	Shell Model	LTBeam	Analytical	Shell Model	LTBeam
20	104.88	103.16	109.33	85.54	82.6	88.65	72.81	69.19	75.08
400	73.42	72.21	76.53	59.87	57.82	62.06	50.97	48.43	52.56
600	32.51	31.98	33.89	26.52	25.61	27.48	22.57	21.45	23.28
700	13.63	13.41	14.21	11.12	10.74	11.52	9.47	8.99	9.76
$\theta$ (°C)	Simply supported - point load			Simply supported - distributed load			Fix supported - point load		
	Analytical	Shell Model	LTBeam	Analytical	Shell Model	LTBeam	Analytical	Shell Model	LTBeam
20	85.54	82.6	88.65	78.78	75.11	78.36	138.68	124.37	134.71
400	59.87	57.82	62.06	55.14	52.58	54.85	97.08	87.06	94.3
600	26.52	25.61	27.48	24.42	23.29	24.29	42.99	38.55	41.76
700	11.12	10.74	11.52	10.24	9.76	10.19	18.03	16.17	17.51

### 3.3 Lateral Torsional Buckling Resistance

The lateral-torsional buckling resistance, as shown in *Table 4*, was predicted by the analytical and shell model presented in *Section 2*. The shell model obtained the results using geometrically and materially nonlinear analysis with imperfections (GMNIA). The global imperfection was considered taking the first eigenmode from linear buckling analysis. The changing parameters were the same as in the critical elastic moment.

## 4 CONCLUSIONS

The paper proposed a three-dimensional shell model to calculate the fire resistance of steel beam in terms of different moment values. The shell model was validated by analytical models. The main drawbacks of the shell model can be defined as the uncertainty in the degree of warping constraint and the differences between real section dimensions and the geometry used in the shell model leading to different torsion and warping constants. The lateral-torsional buckling resistance from the analytical model becomes higher than that from the shell model because the analytical model includes bending resistance depending on the reduction factor in the yield strength of steel. According to Eurocode, the yield strength of steel does not have reduction until 400°C. However, the results from the shell model were consistent with analytical results and they showed that using a simple shell model is possible to predict the moment resistance of beam at elevated temperature.

Table 4. Lateral torsional buckling resistance (kN.m)

$\theta$ (°C)	IPE 200 - 6 m		IPE 300 - 6 m		IPE 400 - 6 m		IPE300 - 5 m		IPE 300 - 7 m	
	Analytical	Shell Model	Analytical	Shell Model	Analytical	Shell Model	Analytical	Shell Model	Analytical	Shell Model
20	17.65	19.73	59.17	64.54	137.86	135.78	68.8	74.73	52.21	57.45
400	13.16	12.48	44.6	40.1	104.93	83.79	52.56	46.23	39.01	35.89
600	5.88	5.5	19.96	17.34	47.02	37.1	23.56	20.44	17.44	15.86
700	2.52	2.33	8.58	7.4	20.28	15.9	10.17	8.73	7.48	6.76
$\theta$ (°C)			Simply supported - point load		Simply supported - distributed load		Fix supported - point load			
			Analytical	Shell Model	Analytical	Shell Model	Analytical	Shell Model		
	0		59.17	64.54	55.54	52.02	83.27	81.7		
	400		44.6	40.1	41.67	32.4	65.04	52.98		
	600		19.96	17.34	18.64	14.29	29.25	23.16		
	700		8.58	7.4	8	6.06	12.72	10.24		

## ACKNOWLEDGMENTS

The work is supported by CVUT in Prague grant SGS19/150/OHK1/3T/11.

## REFERENCES

- Abaqus, 2000. Abaqus/Standard. Versison 6.14. USA: Hibbitt, Karlsson & Sorensen, Inc.
- Both, I; Wald, F.; Zaharia, R *Benchmark for numerical analysis of steel and composite floors exposed to fire using a general-purpose FEM code Journal of Applied Engineering Science*. 2016, 14(2), 275-284.
- CTICM, 2003. LTBeam software v. 1.0.11, CTICM, available at <https://www.cesdb.com/ltbeam.html>
- EN 1993-1-2:2005, *Eurocode 3: Design of steel structures - Part 1-2: General rules - Structural fire design*. European Committee for Standardization, Brussels, Belgium.
- EN-1993-1-1:2005, *Eurocode 3: Design of steel structures. Part 1-1: general rules and rules for buildings*, European Committee for Standardization, Brussels, Belgium.
- Gillie M., *Author's Analysis of heated structures: Nature and modelling benchmarks, Fire Safety Journal*. 2009, 44, p. 673–680.
- Kwasniewski L., *On practical problems with verification and validation of computational models, Archives of Civil Engineering*, 55 (3), 323-346, 2009.
- Sawicki B., Pełczyński J., Kwaśniewski l., 2013. *Benchmark examples problems for beams at elevated temperatures*. Application of Structural Fire Engineering, 19-20 April, Prague, Czech Republic.
- SCI, 2005. NCCI SN003: *Elastic critical moment for lateral torsional buckling*. <http://www.steelncci.co.uk>.
- Vila Real P. M. M., Piloto P. A. G., Franssen J. M., 2003, *A new proposal of a simple model for the lateral-torsional buckling of unrestrained steel I-beams in case of fire: experimental and numerical validation*. Journal of Constructional Steel Research, 59, p. 179-199.
- Wald F., Burges, I., Kwasniewski L., Horová K., Caldová E., Prachař M., Hricák J., Jandera M. *Benchmark studies, Experimental validation of numerical models in fire engineering*. . CTU Publishing House, 2014. ISBN 978-80-01-05443-7.
- Wald F., Burgess I., Kwasniewski L., Horová K., Caldová E., Prachař M., Hricák J.; Jandera M. *Benchmark studies, Verification of numerical models in fire engineering*. .CTU Publishing House, 2014.

# NUMERICAL MODELLING OF STEEL MEMBERS PROTECTED WITH INTUMESCENT COATING

Igor Džolev<sup>a</sup>, Sofija Kekez<sup>b</sup>, Andrija Rašeta<sup>a</sup>

<sup>a</sup> University of Novi Sad, Faculty of Technical Sciences, Novi Sad, Serbia

<sup>b</sup> Silesian University of Technology, Faculty of Civil Engineering, Gliwice, Poland

## Abstract

Load bearing fire resistance of steel members is commonly determined in relation to standard fire exposure. The most common and architecturally preferable passive fire protection measure is the application of intumescent coating (IC) in form of a thin film layer, which reacts chemically at elevated temperatures and expands, forming a low conductivity char, and insulating the member, thus, postponing the temperature rise in steel.

Finite element model (FEM) is developed in ANSYS, to determine fire resistance of simply supported steel IPE beams protected with water-based IC. Thermal properties of IC are modelled implicitly, to account for a complex chemical process in IC at elevated temperatures, with temperature-dependent thermal conductivity as a function of the coating thickness and the profile section factor. Thermal response is validated based on test results provided in the literature. Finally, failure criteria based on deflection and rate of deflection are used to determine fire resistance of the element.

**Keywords:** standard fire resistance, numerical modelling, intumescent coating

## 1 INTRODUCTION

Structural fire resistance needs to be provided for a specified period of time. Relatively high thermal conductivity of steel, compared to other structural materials, such as concrete or timber, ensures fast heat penetration and close-to-uniform temperature distribution through the member, eventually leading to progressive loss of load bearing function. To achieve the desired fire resistance, steel members are often protected using passive measures, aiming to shield and insulate members from direct fire exposure. The most common and architecturally preferable passive fire protection is the application of intumescent coating (IC), a chemically reactive thin film layer, expanding at elevated temperatures and forming an insulating char layer of low conductivity. The IC application is extensively studied in recent years (Lucherini and Maluk, 2019) and the key governing factors of its effectiveness are recognised to be the chemical formulation (solvent or water-based), heating conditions, coating thickness (Lucherini *et al.*, 2021) and substrate boundary conditions (Lucherini *et al.*, 2020). Although load bearing fire resistance is commonly determined using standard fire exposure, the behaviour of IC is also studied for different fire scenarios and heating rates, found to have significant effect on the type of coating used, solvent or water-based (Lucherini *et al.*, 2018). In a study by (Xu *et al.*, 2020), the effective thermal conductivity of IC obtained under standard ISO 834 furnace test conditions was found to be useful also for localized heating scenarios, providing reasonable agreement for the measured steel temperatures.

Complicated thermochemical phenomena of IC can be simplified in terms of numerical modelling, using an experimentally-based three-step numerical procedure to determine temperature-dependent thermal conductivity of a solvent-based IC (Kolšek and Češarek, 2015). The standard segmented multivariate linear regression analysis is applied to the data measured from the conducted tests, to develop the general thermal conductivity function, dependent on the initial coating thickness and the profile section factors ranging from 73 to 310 m<sup>-1</sup>. Similar approach is also used for a water-based IC for standard and smouldering fire exposure, for section factors of 67, 125, and 250 m<sup>-1</sup>, and dry film thicknesses ( $d_{IC}$ ) of 500, 1000, 1500, and 2000 μm (de Silva *et al.*, 2019). The equivalent conductivity function for the purpose of numerical modelling is then defined at specific

temperature points, identifying three distinct IC phases: inert, transient, and steady phase (de Silva *et al.*, 2020).

In the present study, the latter modelling procedure is used on a series of IPE simply supported steel beams protected with water-based IC, modelled in ANSYS. Thermal and structural models are developed, aiming to determine the fire resistance of beams exposed to standard ISO 834 fire.

## 2 MODELLING OF IC THERMAL PROPERTIES

Using standard multivariate linear regression analysis calibrated through fitting of the available data points, a simple formulation of the thermal conductivity function is proposed, dependent on the profile section factor and IC film thickness (de Silva *et al.*, 2020):

$$\lambda_{IC,j} \left( d_{IC}, \frac{A_m}{V} \right) = a_0^j + a_1^j d_{IC} + a_2^j \frac{V}{A_m} \quad (1)$$

where  $j$  refers to the three significant IC temperature values (120, 486, and 800°C), and  $a_0$ ,  $a_1$ , and  $a_2$  to the regression coefficients presented in Table 1. Thermal conductivity is defined for the whole range of IPE profiles (from IPE600 to IPE80, with section factors ranging from 130 to 430 m<sup>-1</sup>, respectively), although the proposed model was developed and validated in the section factor range of 67 to 250 m<sup>-1</sup>.

Table 1 Regression analysis coefficients of the thermal conductivity function (de Silva *et al.*, 2020)

Coeff.	$\theta_{IC}$ (°C)		
	120	486	800
$a_0$	0.0187	-0.0031	-0.0063
$a_1$	-0.9	6.32	14.5
$a_2$	1.39	0.80	2.02

### 2.1 Model validation

Thermal model is validated based on experimental data provided by (de Silva *et al.*, 2019), on a group of samples consisting of a steel plate with applied IC with a thickness of 1500 µm on one side of the plate, exposed to ISO 834 fire. Plate dimensions are 300 mm x 300 mm with a thickness of 4, 8, and 15 mm, corresponding to the section factors of 250, 125, and 67 m<sup>-1</sup>, respectively. Thermal properties of steel are modelled according to EN 1993-1-2 advanced modelling procedure, while properties of IC correspond to the study by (de Silva *et al.*, 2020). Comparison of the experiment temperatures measured in the plate and numerically obtained temperatures using ANSYS is presented in Figure 1.

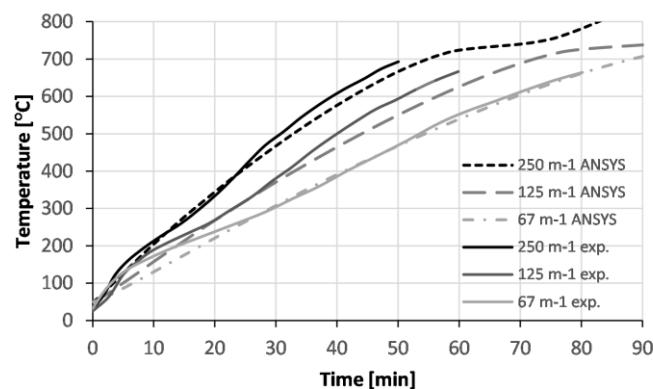


Fig. 1 Comparison of temperature-time curves in steel plates obtained by present model and experimentally (de Silva *et al.*, 2019)



Failure which determines the fire resistance is deemed to occur once the mid-span deflection of the beam exceeds  $L/20$ , or the rate of deflection exceeds  $L^2/9000d$ , where  $L$  is the span and  $d$  is the beam depth. The rate of deflection is only applicable once the mid-span deflection exceeds  $L/30$  (Alam *et al.*, 2021).

### 3.1 Parametric study

Beam is subjected to a uniformly distributed load corresponding to a certain degree of utilisation, representing the applied load during the fire limit state divided by the capacity of the section in normal design (Bailey, 1999). The initial utilisation is considered to be 0.5 and its influence on fire resistance is determined by varying its range from 0.5 to 0.7. The length of the beam is chosen in respect to the analysed profile, ranging from 12 to 20 of the profile depth. The influence of IC on fire resistance is determined by considering the IC dry film thickness as 400, 800, and 1200  $\mu\text{m}$ .

These variations are all considered for the whole range of IPE profiles (80, 100, 120, 140, 160, 180, 200, 220, 240, 270, 300, 330, 360, 400, 450, 500, 550, and 600), in attempt to analyse the effectiveness of the IC protection, leading to a total of 486 simulations conducted.

## 3 RESULTS AND DISCUSSION

Figure 4 presents mid-span deflection and rate of deflection evolution for IPE200 with a span of 2.5 m, utilisation 0.5, and for the previously described range of IC thicknesses.

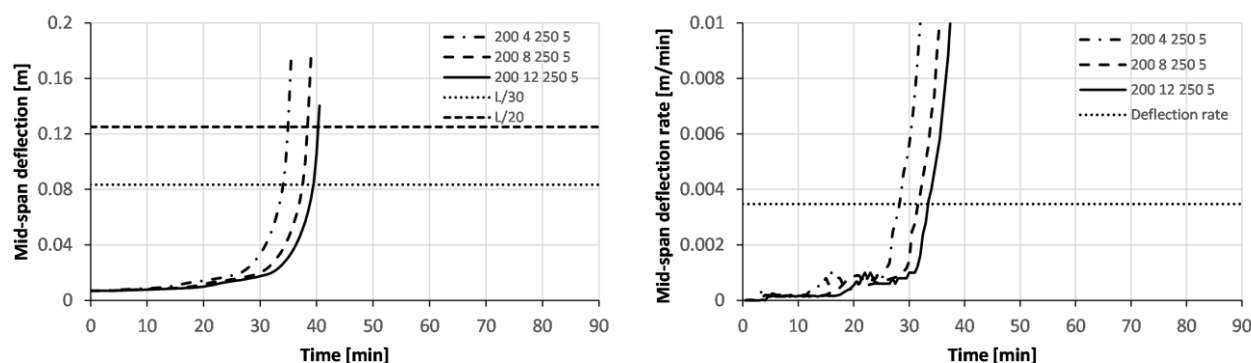
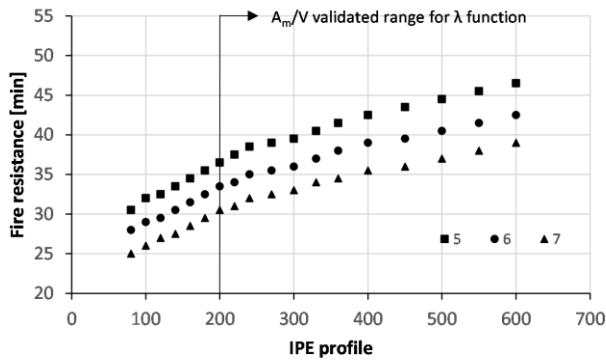


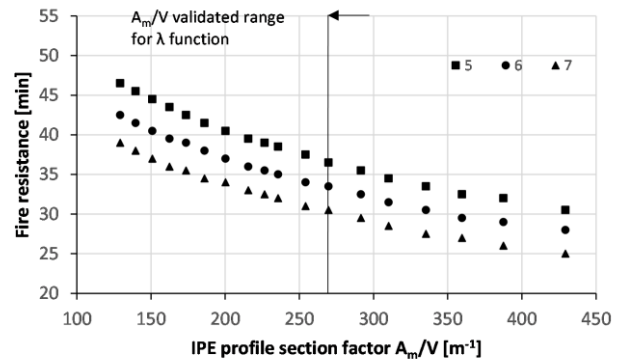
Fig. 4 Evolution of mid-span deflections and rate of deflections for the determination of fire resistance

Since the rate of deflection criterion is in all analysed cases met first, failure is determined once the mid-span deflection of the beam reaches the  $L/30$  threshold.

Fire resistance for the whole range of IPE profiles protected with IC with a thickness of 800  $\mu\text{m}$ , for length of beams corresponding to 16 of the beam depth, and for the utilisation of 0.5, 0.6, and 0.7 (5, 6, and 7, respectively) is presented in Figure 5. With the increase of beam utilisation, fire resistance decreases, as expected, by approximately 3 to 4 minutes for additional 10% of increase in utilisation. By fixing the utilisation to 0.5, Figure 6 shows the resistance of beams depending on the IC thickness of 400, 800, and 1200  $\mu\text{m}$  (4, 8, and 12, respectively). The efficiency of IC is much higher when the IC thickness is increased from 400 to 800  $\mu\text{m}$  than from 800 to 1200  $\mu\text{m}$ , given that the same amount of film is assumed to be added. Higher IC thicknesses contribute more to fire resistance of larger profiles with lower section factors. Clearly, the extrapolated thermal conductivity function beyond the investigated range of section factors (de Silva *et al.*, 2020) does not provide reasonable solutions for higher values of section factors, indicating non-physical solution of lower fire resistance for larger IC thicknesses. Fire resistance in respect to the beam length, which equals 12, 16, and 20 of the profile depth (0, 1, and 2, respectively), for the same utilisation, and for the IC thickness of 800  $\mu\text{m}$ , is shown on Figure 7, indicating that longer beams have slightly lower fire resistance than shorter beams, although the same thermal response, as well as the initial stress level is assumed at the time of fire.

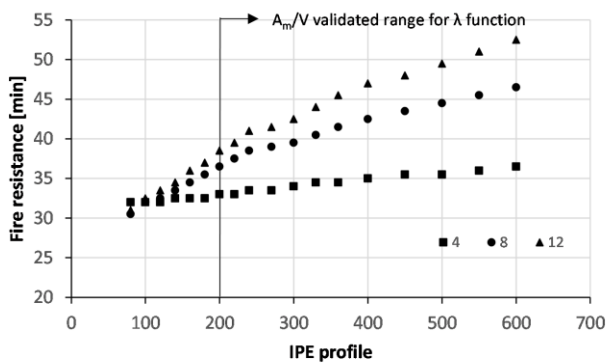


a) function of the IPE profile

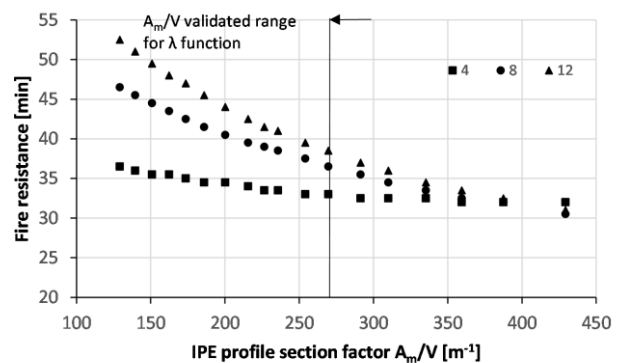


a) function of the IPE profile section factor

Fig. 5 Effect of the degree of utilisation on fire resistance of IPE beams

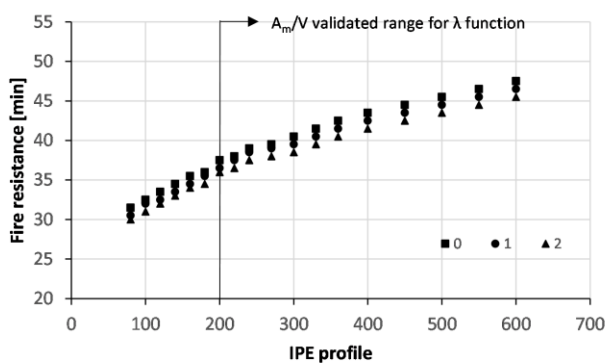


a) function of the IPE profile

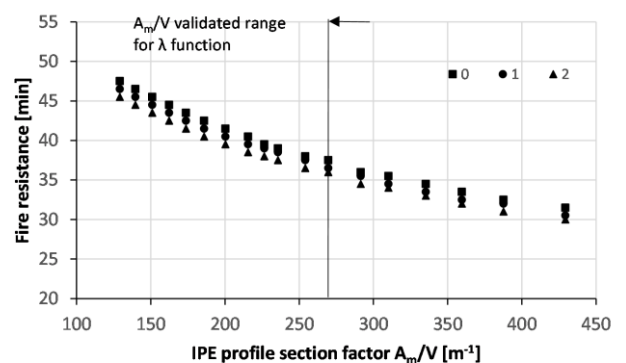


a) function of the IPE profile section factor

Fig. 6 Effect of the IC thickness on fire resistance of IPE beams



a) function of the IPE profile



a) function of the IPE profile section factor

Fig. 7 Effect of the beam length on fire resistance of IPE beams

## 4 CONCLUSIONS

Modelling IC for the purpose of numerical modelling of structural fire resistance is a challenging process. Complex phenomena occurring in the material can be implicitly accounted for through the implementation of the equivalent thermal conductivity function, dependent on the profile section geometry and the thickness of IC applied. Since behaviour of coatings currently present on the market could differ significantly, the development of the conductivity function should be preceded

by experimental testing of the specific type of coating to obtain relevant data based on which the regression analysis can be conducted. In the present study, water-based type of IC used in the study by (de Silva *et al.*, 2019) was considered in the thermal-structural analysis of IPE beams in fire. General procedure presented here could also be used for other types of ICs and steel profiles. Based on the results of the conducted analyses, it can be concluded that the efficiency of the applied IC protection is higher for larger profiles, i.e. for lower profile section factors. This is particularly observed for higher IC thicknesses, while in case of thin IC applied, the influence of profile size is less pronounced. The efficiency is not linearly proportional to the thickness of the coating applied and it becomes less efficient for higher IC thicknesses. As expected, fire resistance depends on the degree of utilisation of the member and is reduced as the utilisation increases. In terms of the beam length, practically, minor variations of the fire resistance are calculated, giving preference to beams with higher depth to length ratio.

## ACKNOWLEDGMENTS

This research (paper) has been supported by the Ministry of Education, Science and Technological Development through the project no. 451-03-9/2021-14/200156: “Innovative scientific and artistic research from the FTS (activity) domain”, and “SymIn”–Simulation in Engineering Interdisciplinary Ph.D. Studies, Silesian University of Technology [project number POWR.03.05.00-IP.08-00-PZ1/17].

## REFERENCES

- Alam N., Maraveas C., Tsavdaridis K.D., Nadjai A., 2021. *Performance of Ultra Shallow Floor Beams (USFB) exposed to standard and natural fires*, *Journal of Building Engineering*, 38, 102192.
- ANSYS® Academic Teaching Mechanical, 2016. *ANSYS Help Documentation, Release 16.0*. Canonsburg: ANSYS, Inc.
- Bailey C.G., 1999. *The behaviour of asymmetric slim floor steel beams in fire*, *Journal of Constructional Steel Research*, 50, p. 235–257.
- de Silva D., Bilotta A., Nigro E., 2020. *Approach for modelling thermal properties of intumescent coating applied on steel members*, *Fire Safety Journal*, 116, 103200.
- de Silva D., Bilotta A., Nigro E., 2019. *Experimental investigation on steel elements protected with intumescent coating*, *Construction and Building Materials*, 205, p. 232–244.
- Kolšek J., Češarek P., 2015. *Performance-based fire modelling of intumescent painted steel structures and comparison to EC3*, *Journal of Constructional Steel Research*, 104, p. 91–103.
- Lucherini A., Giuliani L., Jomaas G., 2018. *Experimental study of the performance of intumescent coatings exposed to standard and non-standard fire conditions*, *Fire Safety Journal*, 95, p. 42–50.
- Lucherini A., Hidalgo J.P., Torero J.L., Maluk C., 2021. *Influence of heating conditions and initial thickness on the effectiveness of thin intumescent coatings*, *Fire Safety Journal*, 120, 103078.
- Lucherini A., Maluk C., 2019. *Intumescent coatings used for the fire-safe design of steel structures: A review*, *Journal of Constructional Steel Research*, 162, 105712.
- Lucherini A., Torero J.L., Maluk C., 2020. *Effects of substrate thermal conditions on the swelling of thin intumescent coatings*, *Fire and Materials*, p. 1–14.
- Xu Q., Li G.-Q., Wang Y.C., Bisby L., 2020. *An experimental study of the behavior of intumescent coatings under localized fires*, *Fire Safety Journal*, 115, 103003.

Proceedings of the International Conference in Ljubljana, 10-11 June 2021  
in edition of Applications of Structural Fire Engineering

**Session**

**Other topics II**

## RELIABILITY EVALUATION OF CONCRETE BEAMS EXPOSED TO FIRE

Túlio A. P. Coelho<sup>a</sup>, Sofia M. C. Diniz<sup>a</sup>, Francisco C. Rodrigues<sup>a</sup>, Ruben Van Coile<sup>b</sup>

<sup>a</sup> Federal University of Minas Gerais, Department of Structural Engineering, Minas Gerais, Brazil

<sup>b</sup> Ghent University, Department of Structural Engineering and Building Materials, Ghent, Belgium

### Abstract

The state-of-the-art for the reliability evaluation of reinforced concrete beams in a fire situation is reviewed in this paper. Special emphasis is placed on addressing which parameters were considered probabilistically or deterministically, i.e. how the heat transfer in the concrete was treated, how the structural fire performance was quantified, and which probabilistic models were considered for the stochastic variables. Considering the state-of-the-art review, gaps in the literature are identified related to (i) the probabilistic evaluation of shear capacity for standard fires and parametric fires, and bending capacity for parametric fires, (ii) the absence of reference fragility curves for immediate design application / code calibration, and (iii) the specification of target safety levels for reliability-based design.

**Keywords:** reinforced concrete, reliability, fire, uncertainties, beams.

## 1 INTRODUCTION

Structural stability during fire is crucial for the overall safety of a building. The basic principle is that in a fire situation a building should not collapse, injuring occupants or firefighters. The structure should allow sufficient time for the occupants to evacuate the building and/or be rescued, and should, preferably, survive a complete burnout (Bailey and Houry, 2011).

In general, reinforced concrete (RC) structures perform well in fire situations (Bailey and Houry, 2011). This is because the concrete is a non-combustible material and has a relatively low thermal conductivity, which results in a slow heat transfer inside the concrete. The slow heat transfer implies that the interior of the concrete cross-section remains relatively cool also for longer fire durations, and that the reinforcing steel is not rapidly affected by temperature. This delay in the thermal response also explains why concrete structures may exhibit delayed (cooling phase) failure, as demonstrated by Gernay (2019).

During the high temperature exposure, concrete experiences a series of physical and chemical changes, such as water evaporation, disintegration of hydration products and aggregates, coarsening of microstructure and increase of porosity (Ma et al, 2015). These changes are considered to be responsible for the deterioration of mechanical properties of concrete at high temperature.

Designing structures in fire is one of the most difficult tasks faced by engineers (Fitzgerald, 2011). Mainly due to the complex and unpredictable nature of both (i) the behavior of fire itself and (ii) the response of structural elements when exposed to fire. Structural fire performance thus has to account for the uncertainties with respect to, for example, the fire exposure, the mechanical properties, the thermal response, loading conditions. Comprehensively taking into account the uncertainties in the performance evaluation allows to ensure safety, not through trial-and-error, but through explicit reliability-based design. The current paper investigates the state-of-the-art for reliability evaluations of concrete beams exposed to fire, with the intention to determine whether any gaps in knowledge should preferably be addressed in future research.

## 2 STATE-OF-THE-ART REVIEW

A brief state-of-the-art review of the reliability evaluation of RC beams exposed to fire is presented below. Some papers which at first sight appear relevant to the proposal were not included in this review, as their content was found to be beyond the scope of this research. These papers deal for example with the use of carbon fiber reinforced polymer (CFRP) sheets in beams, and analyzing

residual load-carrying capacity and reliability after fire (Li and Tang, 2005; Tang, 2006; Bai et al, 2007; Bai et al, 2009; Cai and Feng, 2019). The same goes for prestressed beams (Eamon and Jensen, 2012).

A probabilistic evaluation of RC beams in fire situation demands basically (i) a deterministic model of the phenomenon and (ii) statistics of stochastic variables and their distributions. A brief overview on both aspects is presented in the following for selected references.

### **2.1 Ellingwood and Shaver (1977)**

One of the first studies about the reliability of RC beams exposed to fire was developed by Ellingwood and Shaver in 1977. In this study, methods for analytically predicting the behavior of reinforced concrete beams subjected to fire are presented (Ellingwood and Shaver, 1977). The parameters that are important for predicting beam behavior are identified through a sensitivity study, considering the reliability of a T-beam. The loads were assumed deterministic and that resistance was given by a Weibull distribution (Ellingwood and Shaver, 1977). The application of reliability analysis techniques for developing fire-resistant design procedures is also examined in that paper.

### **2.2 Wang et al. (2010)**

In this study, a simple time-variant model of the resistance of RC beams under fire has been studied (Wang et al., 2010). The reliability index of different specifications of concrete beams at different time has been analyzed, considering standard fire exposure (Wang et al., 2010).

The influence of key parameters on the evolution of the reliability index with time has been presented, and the results have shown that increasing the reinforcement ratio and concrete cover thickness is an effective measure to improve the fire resistance of reinforced concrete beams (Wang et al., 2010). These authors considered random dead and live loads, but treated the beam resistance as deterministic (Wang et al., 2010).

### **2.3 Van Coile et al. (2011)**

In this paper, a simple computational tool is presented, which provides insight in the time and temperature dependent reliability of concrete beams during fire. The uncertainty of basic variables is taken into account through Monte Carlo simulations, resulting in a quantification of the uncertainty regarding the bending moment capacity during fire and the corresponding evolution of the safety level (Van Coile et al., 2011).

The results of these probabilistic simulations are compared with the design values specified in the Eurocodes, providing insight in the reliability level achieved by the current guidance documents. A specific finding was that the fire resistance of a beam can be increased by altering the beam configuration (e.g. increasing the nominal concrete cover), or by decreasing the uncertainty on the concrete cover, for example through improved quality control (Van Coile et al., 2011).

### **2.4 Eamon and Jensen (2013)**

In this paper a procedure for conducting reliability analysis of RC beams subjected to a fire is presented. This involved identifying relevant load combinations, specifying critical load and resistance random variables, and establishing a high-temperature performance model for beam capacity (Eamon and Jensen, 2013). Based on the procedure, an initial reliability analysis is conducted using currently available data based on a previous study by Jensen (2010). Significant load random variables are taken to be dead load, sustained live load, and fire temperature. Resistance was taken in terms of moment capacity, with random variables taken as steel yield strength, concrete compressive strength, placement of reinforcement, beam width, and thermal diffusivity (Eamon and Jensen, 2013). A semi-empirical model is used to estimate the beam moment capacity as a function of fire exposure time, considering the standard and parametrical fire. This model is calibrated to experimental data available in the literature. The effect of various beam parameters were considered, including cover, beam width, aggregate type, compressive strength, dead to live load ratio, reinforcement ratio, support conditions, mean fire temperature, and other parameters. Using the suggested procedure, the

reliability was evaluated from zero to four hours of fire exposure using Monte Carlo simulation (Eamon and Jensen, 2013). It was found that reliability decreased nonlinearly as a function of time, while the most significant parameters were concrete cover, span/depth ratio when axial restraints are present, mean fire temperature and support conditions (Eamon and Jensen, 2013).

## 2.5 Aneesha Balaji et al. (2016)

This paper examines a methodology for computing the probability of structural failure of RC beams subjected to fire. The significant load variables considered are dead load, sustained live load and fire temperature. Resistance is expressed in terms of moment capacity with random variables taken as yield strength of steel, concrete class (or grade of concrete), beam width and depth (Aneesha Balaji et al., 2016). The flexural capacity is determined based on the design equations recommended in Indian standards and the simplified method named “500°C isotherm method”, detailed in Eurocode, is incorporated for fire design. A transient thermal analysis is conducted using finite element software ANSYS (Aneesha Balaji et al., 2016).

Reliability is evaluated from the initial state to 4 hours of fire exposure based on the first order reliability method (FORM). A procedure is coded in MATLAB for finding the reliability index and the procedure is validated with available literature (Aneesha Balaji et al., 2016). The effect of various parameters such as effective cover, yield strength of steel, grade of concrete, distribution of reinforcement bars and aggregate type on reliability indices are studied. Effective cover of concrete and yield strength of steel are found to have a significant effect on reliability of beams. Both the limit states of flexure and shear are checked (Aneesha Balaji et al., 2016).

## 3 REFERENCES ANALYSIS

Analyzing the mentioned references, significant differences are found with respect to (i) the failure mode, (ii) fire specification and (iii) reliability calculation (i.e. the consideration of stochastic variables). This is explored in the following and summarized in Table 1.

Table 1 Analyzed parameters in the mentioned references

	DESIGN		FIRE		RELIABILITY		
	Bending Analysis	Shear Analysis	Standard Fire	Parametric Fire	Fire Resistance*	Fire Severity*	Target Safety Levels
Ellingwood and Shaver (1977)	X		X		SP	D	X
Wang et al. (2010)	X		X		D	P	
Van Coile et al. (2011)	X		X		P	D	X
Eamon and Jensen (2013)	X		X	X	P	P	
Aneesha Balaji et al. (2016)	X	X	X		P	P	

\* P – Probabilistic / D – Deterministic / SP – Semi-probabilistic (just few parameters considered as variables)

In terms of failure modes, there is a need to consider (i) bending moments and (ii) shear forces. Among the works available, it appears that only in one of them the shear limit state is evaluated, with the others being limited to the analysis of the bending limit state. Aneesha Balaji et al. (2016) point out the importance of reinforcement yield strength for the shear limit state, and highlight the importance of considering the possibility of shear failure.

In terms of fire, there is the possibility of using the (i) standard fire (ISO-834) and (ii) parametric fires curves. It is clear that the standard fire curve does not adequately represent the fire in a room, as it does not take into account extremely consequential factors, such as ventilation and the fire load present in it (Harmathy, 1970; Law, 1973). Parametric fire exposure is however only taken into

account in one of the studies, carried out by Eamon and Jensen (2013), demonstrating the great impact of this consideration on the reliability of reinforced concrete beams.

In the literature, especially the Eurocode (2002), adequate fire resistance can be demonstrated in three ways: (i) In terms of time ( $t_{fi,d} > t_{fi,req}$ ), (ii) in terms of load capacity ( $R_{fi,d,t} > E_{fi,d,t}$ ) and (iii) in terms of temperature ( $\theta_d < \theta_{cr,d}$ ). Only the first work on the theme, developed by Ellingwood and Shaver (1977), performs its analysis in terms of time, the other studies focus on the evaluation of the load capacity. Regarding the consideration of heat transfer inside the concrete (and the consequent reduction in strength), the following methods are used: (i) 500° C Isotherm Method, (ii) Zone Method and (iii) Finite Element Methods (FEM).

In the researched bibliographies, the main use of FEM methods was verified, more specifically with the help of the softwares DIANA, SAFIR and ANSYS. Other studies used empirical methods (e.g. 500° isotherm method). The authors Eamon and Jensen (2013) even mention that the 500° isotherm method shows results with little variability for the FEM methods when the standard fire is applied, which is not the case for parametric fires. A summary of the considerations used by the authors is summarized in Table 2.

Table 2 Fire resistance, mechanical response and concrete heat transfer considered by the authors

	Ellingwood and Shaver (1977)	Wang et al. (2010)	Van Coile et al. (2011)	Eamon and Jensen (2013)	Aneesha Balaji et al. (2016)
Fire resistance analysis	In term of time ( $t_{fi,d} > t_{fi,req}$ )	In terms of load capacity ( $R_{fi,d,t} > E_{fi,d,t}$ )	In terms of load capacity ( $R_{fi,d,t} > E_{fi,d,t}$ )	In terms of load capacity ( $R_{fi,d,t} > E_{fi,d,t}$ )	In terms of load capacity ( $R_{fi,d,t} > E_{fi,d,t}$ )
Mechanical response	Experimental testes	The profile of the beam has been divided into an elastic zone and a plastic zone based on the section temperature studied by the authors in another research.	Calculated by the finite element program DIANA.	Used the 500 °C isotherm method to determine the reduced cross-section;	Used the 500 °C isotherm method to determine the reduced cross-section;
Heat transfer	Experimental testes	Temperature distribution in the cross-section was according to temperature profiles studied by the authors in another research.	Temperature distribution in the cross-section was calculated by the finite element program DIANA.	Wickstrom equations to determine the reduced cross-section; (for Standard fire) Temperature distribution in the cross-section was calculated by the finite element program SAFIR. (for Parametric fires)	Temperature distribution in the cross-section was calculated by the finite element program ANSYS.

To interpret the reliability analysis, it is important to evaluate how the parameters of fire resistance and severity are treated, whether they are treated in a deterministic or probabilistic way. On one hand, it is clear that over the years studies tend to consider both parameters (fire resistance and severity) in a probabilistic way, bringing a more realistic assessment. About this, only the works developed by Eamon and Jensen (2013) and Aneesha Balaji et al. (2016) treated both of them in a probabilistic way and it is important to mention that the second study is based on the first, with regard to the

methodologies and probabilities involved. Furthermore, it is worth highlighting that all the presented studies can be considered as case study applications and that none presented reference fragility curves which can be used directly in follow up studies or design and assessment.

With respect to the probabilistic description of the stochastic variables, a great variability in the types of (i) distribution, (ii) mean values and (iii) COVs is noticeable. This highlights that the probabilistic models for concrete beams exposed to fire are not fully consolidated in the literature and require further investigation. For example, for the case of loads (dead and live) in fire situation, some recent studies point out a consolidated probabilistic load model, where the recommended distribution, mean and COV are listed in Table 3 (Jovanović et al, 2020). The study by Jovanović et al. indicates that relative differences of the probability of failure in the order of 10% can be observed in function of the load models used, because of the dispersion of statistics used in the models (Jovanović et al, 2020).

Table 3 Probabilistic characteristics of live and dead load

Load	Distribution	Mean	COV
Dead Loads	Normal	Equal to the nominal permanente load	0,10 (for a first assessment, if not evaluated on a project basis).
Live Loads	Gamma	0.2 times the nominal live load	0.60 for large load areas (> 200 m <sup>2</sup> ) and 0.95 for smaller load areas (<100 m <sup>2</sup> ).

Regarding the determination of target safety levels, only two of the authors address this issue (Ellingwood and Shaver (1977); Van Coile et al. (2011)) and the determination of reference fragility curves and a lifetime cost optimization analysis dedicated to RC beams was not verified in the available literature about the theme.

It appears that most papers are limited to case studies, assessing the influence of the parameters of (i) concrete, (ii) steel, (iii) beam, (iv) fire and (v) loads on the reliability assessment.

#### 4 CONCLUSIONS

The gaps in literature with respect to the reliability evaluation of concrete beams exposed to fire have been determined through a limited literature review. Three main gaps have been identified: (i) Probabilistic evaluation of bending and shear capacity for standard fires and parametric fires; (ii) Failure probability evaluation (development of reference fragility curves for immediate design application / code calibration); (iii) Evaluation of target safety levels for reliability-based design (e.g. through lifetime cost optimization).

Almost all existing studies considered the standard fire exposure, thereby neglecting uncertainty in the fire exposure. In this point, studies into the reliability of concrete beams considering parametric fire exposure will add to the topic a more realistic view of the reliability in the built environment.

Besides that, the reliability study of RC beams under fire subjected to pure bending was investigated by all the presented research, but with respect to shear capacity, only one study could be obtained as part of this review. Studies focussing on the shear performance are thus necessary to obtain a complete picture of the reliability in case of fire. Furthermore, the available studies focussed on specific case studies, and no fragility curves could be obtained which are applicable to a wide range of design cases. The absence of such published fragility curves is considered an obstacle for the application of reliability-based considerations in structural fire design.

Once this probabilistic assessment is made, target safety levels can be established, in order to be a reference for code calibration and design application, i.e. to allow a reliability-based design. Lifetime cost optimization can be applied in this regards to determine optimum safety levels. Studies dedicated to steel structures (Hopkin et al, 2020) and RC slabs (Van Coile et al, 2014) are available, but no published studies could be obtained which focused on RC beams in particular.

## REFERENCES

- Aneesha B., M., Aathira, T., Madhavan P., M., Nagarajan, P., 2016. *Reliability studies on RC beams exposed to fire based on IS456:2000 design methods*. Structural Engineering and Mechanics: An International Journal, 59(5), 853-866.
- Bai, L.; Wang, Z.; Han, Y., Zhu, D., 2007. *Analysis of residual load-carrying capacity and reliability of RC beams after exposure to fire*. Journal of Harbin Engineering University, 42(2), 126-138.
- Bai, L.; Wang, Z.; Su J.; Qiao M., 2009. *Bending reliability of RC beam after fire exposure*. Journal of Harbin Engineering University, 47(3), 226-238.
- Bailey, C.G., Khoury, G., 2011. *Performance of concrete structures in fire*. MPA The Concrete Centre, United Kingdom.
- Cai, B.; Feng, F., 2019. *A new reliability analysis approach for the flexural capacity of postfire reinforced concrete beams retrofitted with CFRPs*. ICE Proceedings Structures and Buildings.
- Eamon, C, Jensen, E, 2012. *Reliability analysis of prestressed concrete beams exposed to fire*. Journal of Structural Engineering, 43(1), 69-77.
- Eamon, C, Jensen, E, 2013. *Reliability analysis of reinforced concrete beams exposed to fire*. Journal of Structural Engineering, 139(2), 212-220.
- Ellingwood, B.R., Shaver, J.R., 1977. *Reliability of RC Beams Subjected to Fire*. ASCE Journal of the Structural Division. 103(ST5), 1047-1059.
- Gernay, T., 2019. *Fire resistance and burnout resistance of reinforced concrete columns*. Fire safety journal. 104, 67-78.
- Jensen, E, J. Van Horn, C. Eamon. 2010. *Variability of Fire and Concrete Temperatures and the Associated Uncertainty in Structural Behavior*. Proceedings, 6th Intl Conference on Structures in Fire, Lansing, MI, 959-966.
- Ma, Q., R. Guo, Z. Zhao, Z. Lin, K. He., 2015. *Mechanical properties of concrete at high temperature—A review*. Constr. Build. Mater. 93, 371–383
- Fitzgerald, R.W., 1996. *Structural Integrity During Fire*. Fire Protection Handbook. 18<sup>a</sup> Edition. National Fire Protection Association. Quincy, Massachusetts.
- Harmathy, T. Z., 1970. *Thermal Properties of Concrete at Elevated Temperatures*. J. of Materials 5, 47–74.
- Hopkin, D., Fu, I., Van Coile, R., 2020. *Adequate fire safety for structural steel elements based upon life-time cost optimization*. Fire Safety Journal, 120, 103095.
- Jovanović, B., Van Coile, R., Hopkin, D., Elhami Khorasani, N., Lange, D., Gernay, T., 2020. *Review of current practice in probabilistic structural fire engineering: permanent and live load modelling*. Fire Technology, 57(1), 1-30.
- Law, M., 1973. *Prediction of Fire Resistance*. Paper in Symposium No. 5, Fire Resistance Requirement of Buildings, A New Approach. Department of the Environment and Fire Offices Committee Joint Fire Research Organisation. HMSO. London, 1-16.
- Li, Y., Tang, Y., 2005. *Experiment Study and Function Reliability Analysis on RC Continuous Beam Subject to High Temperature and Strengthened with CFRP Sheets*. Journal of Harbin Engineering University.
- Tang, Y., 2006. *Experiment Study and Reliability Analysis on RC Continuous Beam under High Temperature Function Strengthened with CFRP Sheets*. Journal of Harbin Engineering University, 38(3), 05-20.
- Van Coile, R., Caspeelee, R., Taerwe, L., 2014 *Lifetime cost optimization for the structural fire resistance of concrete slabs*. Fire technology, 50(5), 1201-1227.
- Van Coile, R., Annerel, E., Caspeelee, R., Taerwe, L., 2011. *Full-Probabilistic Analysis of Concrete Beams During Fire*. Journal of Structural Fire Engineering, 4(3), 853-866.
- Wang, Z.; Qiao, M.; Zhu, D., Han, Y., 2010. *The Reliability Analysis of Reinforced Concrete Beams under High Temperature*. Proceedings, 2010 Third International Joint Conference on Computational Science and Optimization, 327-330.

## AN IMPROVED RELIABILITY-BASED APPROACH TO SPECIFYING FIRE RESISTANCE PERIODS FOR BUILDINGS IN ENGLAND

Ian Fu<sup>a</sup>, Ieuan Rickard<sup>b</sup>, Danny Hopkin<sup>a</sup>

<sup>a</sup> OFR Consultants, Oxford, United Kingdom

<sup>b</sup> OFR Consultants, Edinburgh, United Kingdom

### Abstract

For common building situations in England, the contemporary fire safety design guidance recommends structural fire resistance periods for elements based upon occupancy and building height. Deterministic and probabilistic time equivalence methods in guidance documents and the wider literature (Kirby *et al.*, 2004; BSI, 2019, 2007) provide an alternative approach to assess the required fire resistance rating for elements forming a specific building's structure. This study revisits the work of Kirby *et al.*, resolving some key limitations and incorporating advancements in the field to present a new approach to assessing the recommended fire resistance for structural elements. This results in revised fire resistance recommendations for office, retail and residential type buildings in England, linked to both the building Consequence Class and total floor area.

**Keywords:** Structural fire resistance, Probabilistic reliability assessment, Reliability index

### 1 INTRODUCTION

In the design of fire safety provisions for common building situations, the appropriate structural fire resistance for elements is selected from guidance based upon building height and occupancy characteristics (HM Government, 2020; BSI, 2017, 2015). This has been expanded upon in recent British Standards (BS 9991 and BS 9999), informed by work carried out by Kirby *et al.* (Kirby *et al.*, 2004), to include consideration of ventilation conditions and risk. Whilst novel, the ventilation dependant fire resistance tables developed by Kirby, *et al.*, have several limitations, as discussed in Hopkin (Hopkin, 2017). Recent advances in design approaches, including the introduction and widespread adoption of travelling fires (Stern-Gottfried & Rein, 2012) and the use of failure probability as a performance measure to assess the acceptability of fire resistance levels, provide an opportunity to revisit the work of Kirby, *et al.* to establish current relevance. In England, general structural performance expectations and those in the event of accidents excluding fire are covered by Part A of the Building Regulations. For the purpose of informing robustness provisions, the consequences of structural failure are differentiated through Consequence Classes (CC). Structural performance in the event of fire is covered by Part B of the Building Regulations, with the consequences of fire induced structural failure differentiated through trigger heights. For the purpose of harmonisation and consistency of performance, there are benefits in using a single means of differentiating failure consequences, irrespective of the cause / accident. It is proposed that this should be through Consequence Classes and the associated failure probabilities, as discussed in Hopkin, *et al.* (Hopkin *et al.*, 2017). To this end, probabilistically informed fire resistance recommendations (in function of Consequence Class) are developed herein, utilising current knowledge in respect of reliability indices (to define adequate performance) and fire models (capturing travelling fires for large enclosure fire dynamics).

The tool used, SFEPRAPY (Fu & Hopkin, 2020), is an open-source package that has been presented previously (Fu *et al.*, 2019). It is designed to streamflow Monte Carlo Simulations (MCS), particularly for the purpose of probabilistic applications of the time equivalence method. It has been adapted for the analysis presented herein to consider stochastic parameters associated with compartment geometry. This allows a generalised assessment to be carried out, like that by Kirby *et al.*, but utilising contemporary input parameters and design fire models. Through safety targets (failure probabilities) linked to a given building Consequence Class, SFEPRAPY is applied to conduc

t a scoping review and propose alternative fire resistance periods for residential, retail and office type buildings in England, as a function of their size (number of storeys, total floor area, etc).

## 2 DEFINING APPROPRIATE PERFORMANCE IN FIRE

The Building Regulations in England set out the minimum expectations under a life safety purview for structural performance in events of fire, with Regulation B3(1) stating: “*The building shall be designed and constructed so that, in the event of fire, its stability will be maintained for a reasonable period*”. Regulation B3(1) does not explicitly define the duration of structural stability required in the event of fire, with the structural fire safety performance objectives for a building varying in function of the consequences of fire-induced collapse (Hopkin *et al.*, 2020). This is elaborated through a bifurcation of objectives for different scales of building: a) provision of adequate time for means of escape, cognisant of building size; and b) adequate likelihood of surviving burnout. The former is most relevant to buildings that are small and do not have sleeping hazards. In such instances, structural fire performance is predominately dictated by the time required to facilitate typically quick escape and fire & rescue service intervention. This study addresses the latter, i.e., structural performance to provide an adequate likelihood of surviving burnout, where evacuation and fire & rescue service intervention is potentially protracted.

Following the above, adequate structural fire performance can be demonstrated through the balancing of the uncertain future costs and benefits of safety investments. Works by others (Joint Committee on Structural Safety, 2001; ISO, 2014; BSI, 2005; Van Coile *et al.*, 2017; Hopkin, Fu & Van Coile, 2020) quantify acceptable structural failure probabilities for buildings by optimising the cost/benefit ratio. For the purposes of this analysis, the cost-optimised failure probabilities (alternatively defined as reliability index  $\beta$ ) from the JCSS probabilistic model code (Joint Committee on Structural Safety, 2001) and ISO 2394:2014 are adopted. A tentative connection between Consequence Class (HM Government, 2013) and reliability index is proposed, as summarised in Table 1, considering a one-year reference period.

**Table 1. Consequence Class, building height (no. of storeys) and allowable failure probability considering residential, retail and office type buildings\***

	Consequence Class (or Building Class)		
	CC2A	CC2B	CC3
<b>No. of storeys</b>	$\leq 4$	$>4, \leq 15$	$\leq 15$
<b>Reliability index, <math>\beta</math> [-]</b>	3.7	4.2	4.4
<b>Allowable failure probability (<math>P_{f,a}</math>) [<math>year^{-1}</math>]</b>	$\approx 1 \times 10^{-4}$	$\approx 1 \times 10^{-5}$	$\approx 5 \times 10^{-6}$

\*Note the Consequence Class (or Building Class) also depends on building usage/characteristics. Specific to residential, retail and office building types, the only relevant parameter is the number of storeys.

## 3 DERIVATION OF STRUCTURAL FAILURE PROBABILITY FOR A GIVEN BUILDING

Once the maximum allowable failure probability has been defined, the probability of fire induced structural failure must be evaluated. A simplistic failure criterion has been adopted (Equation 1), whereby an element exposed to a fire of severity (defined through thermal time-equivalence) in exceedance of the element’s structural fire resistance is deemed to result in global structural failure. The (conditional) probability of fire-induced structural failure,  $P_{f,fi}$ , combined with the probability of a structurally significant fire occurring,  $p_{fi}$ , should remain lower than, or equal to the target probability of failure,  $P_{f,a}$  (Equation 1).

The probability of a structurally significant fire occurring can be evaluated based on a combination of the probability of ignition and subsequent interventions prior to the fire becoming fully developed (Equation 2). Through this approach, sprinklers are included in the evaluation of the probability of a structurally significant fire occurring (as a preventative measure mitigating structurally significant

fires). This is the approach of the natural fire safety concept valorisation project (NFSC) (Schleich & Cajot, 2001) underpinning EN 1991-1-2.

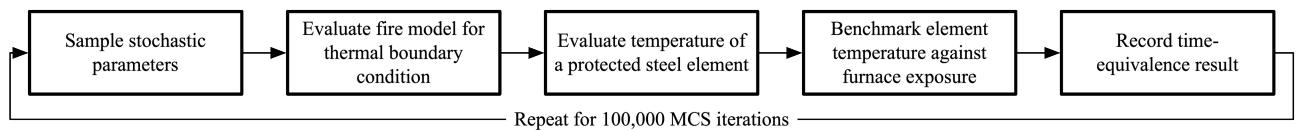
$$p_{fi} \cdot P_{f,fi} \leq P_{f,a} \quad (1)$$

$$p_{fi} = p_1 \cdot A \cdot p_2 \cdot p_3 \cdot p_4 \quad (2)$$

Where:

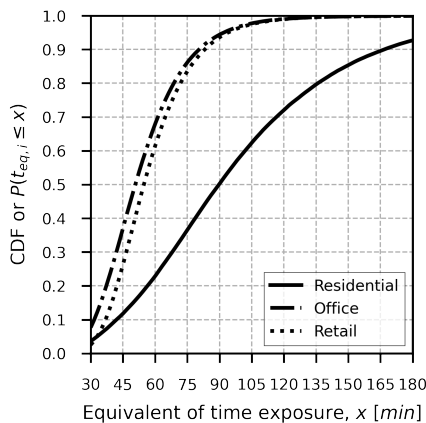
- $p_1$  is the probability of a severe fire occurring including the influence of occupants and standard fire service (per m<sup>2</sup> per year).
- $A$  is the area of compartment/occupancy (m<sup>2</sup>).
- $p_2$  is the probability of unsuccessful fire suppression by FRS intervention (considering improved professionalism/performance).
- $p_3$  is the probability of unsuccessful fire suppression associated with fire alarm and detection systems.
- $p_4$  is the probability of unsuccessful fire suppression by active fire protection systems (sprinkler).

Table 2 shows the adopted probability parameter values for the purposes of this study. The sprinkler system reliability (i.e.,  $1 - p_4$ ) adopted was based on PD 7974-7:2019 (BSI, 2019) and sprinkler statistics as garnered by the NFPA in 2017 (Ahrens, 2017). Sprinkler reliabilities of 91% and 93% were adopted for residential and office/retail areas, respectively.



**Figure 1. Simplified SFEPARPY streamflow**

The conditional failure probability due to a structurally significant fire,  $P_{f,fi}$ , is effectively the survival function (or complementary CDF) of a collection of time equivalence values,  $t_{eq,i}$ , and can be evaluated as  $1 - P(t_{eq,i} \leq x)$ . Figure 2 shows the solved cumulative density function (CDF) of time equivalence from a MCS study comprised of 100k iterations per occupancy based upon the parameters in Table 2, using SFEPARPY (Figure 1).



**Figure 2. CDF of time equivalence solved from an MCS study using SFEPARPY**

**Table 2. Probability parameters adopted in accordance with NFSC**

Occupancy	$p_1^*$ [m <sup>-2</sup> year <sup>-1</sup> ]	$p_2^\dagger$	$p_3^\ddagger$	$p_4^\S$
<b>Residential</b>	$6.5 \times 10^{-7}$	0.2	0.0625	1 (0.09)
<b>Office</b>	$3.0 \times 10^{-7}$	0.2	0.25	1 (0.07)
<b>Retail</b>	$4.0 \times 10^{-7}$	0.2	0.25	1 (0.07)

\* $6.5 \times 10^{-7}$ ,  $3.0 \times 10^{-7}$  and  $4.0 \times 10^{-7}$  are adopted based upon the NFSC report for residential, office and retail occupancy types, respectively.

†0.2 is adopted based upon the NFSC report assuming a professional fire service is provided to intervene, should a fire occur, in 20 to 30 minutes after the alarm activation.

‡0.0625 and 0.2 are adopted for residential and office/retail areas, respectively, based upon the NFSC report. This assumes that smoke and heat detectors are provided in the residential and office/retail areas, accordingly.

§Values in brackets consider situations where an appropriate sprinkler system is provided.

## 4 MODELS AND INPUTS

Enclosure fire dynamics are complex, and the development of fire is dependent upon compartment geometry, lining materials, ventilation, etc. These parameters will ultimately govern whether a fire is able to develop to an extent where all combustible material is near-simultaneously involved (i.e., flashover, parametric fire (BSI, 2002)) or whether the fire moves in search of both available un-burnt fuel and/or oxygen (i.e., a travelling fire (Stern-Gottfried & Rein, 2012)). This study is premised on both forms of fire development being credible scenarios. The choice of when to transition from one fire model to another is based upon the various parameters including fuel load density and compartment opening factors, etc. is specified within SFEPRAPY (Fu *et al.*, 2019), as originally adopted by Hopkin *et al.* (Hopkin *et al.*, 2017).

Table 3 summarises the key input parameters used in this study. The data for the fuel load and heat release rate, HRR, per unit area is obtained from PD 7974-1:2019 (BSI, 2019) and EN 1991-1-2 (BSI, 2002) and the data for the fuel load for retail areas is from EN 1991-1-2 (BSI, 2002). It is recognised that not all available fuel will generally be consumed in event of fire, therefore, a uniform distribution has been adopted between the combustion efficiency specified in BS EN 1991-1-2 (80%) and that of PD 6688-1-2 (100%) (BSI, 2007). Glazing failure in fire has been considered following the principle set out in the JCSS probabilistic model code (JCSS, 2001). The room and window geometry parameters used are as per the work carried out by Kirby (Kirby *et al.*, 2004).

**Table 3. Key parameters adopted for the time equivalence MCS**

Parameter	Distribution	Residential	Office	Retail
Fire load density [MJ/m <sup>2</sup> ]	Gumbel	Mean: 780 SD: 234	Mean: 420 SD: 126	Mean: 600 SD: 180
HRR per unit area‡ [MW/m <sup>2</sup> ]	Uniform	(0.32, 0.57)	(0.15, 0.65)	(0.27, 1.00)
Room height [m]	Uniform	2.4*	(2.8, 4.5)	(4.5, 7.0)
Floor area [m <sup>2</sup> ]	Uniform	(9, 30)	(50, 1000)	(50, 1000)
Window height to room height ratio [-]	Uniform	(0.3, 0.9)	(0.3, 0.9)	(0.5, 1.0)
Window area to floor area ratio [-]	Uniform	(0.05, 0.2)	(0.05, 0.4)	(0.05, 0.4)
Fuel combustion efficiency‡ [-]	Uniform	(0.8, 1.0)	(0.8, 1.0)	(0.8, 1.0)
Glazing breakage percentage‡ [-]	Complementary Lognormal†	Mean: 0.2 SD: 0.2	Mean: 0.2 SD: 0.2	Mean: 0.2 SD: 0.2
Model uncertainty factor§ [-]	Lognormal	Mean: 1 SD: 0.25	Mean: 1 SD: 0.25	Mean: 1 SD: 0.25

\*Constant is used in lieu of random values based upon a distribution. †Truncated between 0 and 1. ‡Parameters not considered in Kirby *et al.* §Truncated between 0 and 3.

## 5 THE REQUIRED STRUCTURAL FIRE PERFORMANCE

Based upon the established safety format defined previously (Equation 1). The minimum required fire resistance period,  $FR$ , can be evaluated as per Equation 3. Where  $Q$  is the quantile function of the solved time equivalence CDF, as shown in Figure 2.

$$FR = Q\left(1 - \frac{P_{f,a}}{p_1 \cdot A \cdot p_2 \cdot p_3 \cdot p_4}\right) \quad (3)$$

The solved fire resistance periods are presented in Figure 3 considering buildings that are not provided and provided with sprinklers, respectively. These figures may be used to interpret the fire resistance periods for a given building height (in terms of no. of storeys) and floor area.

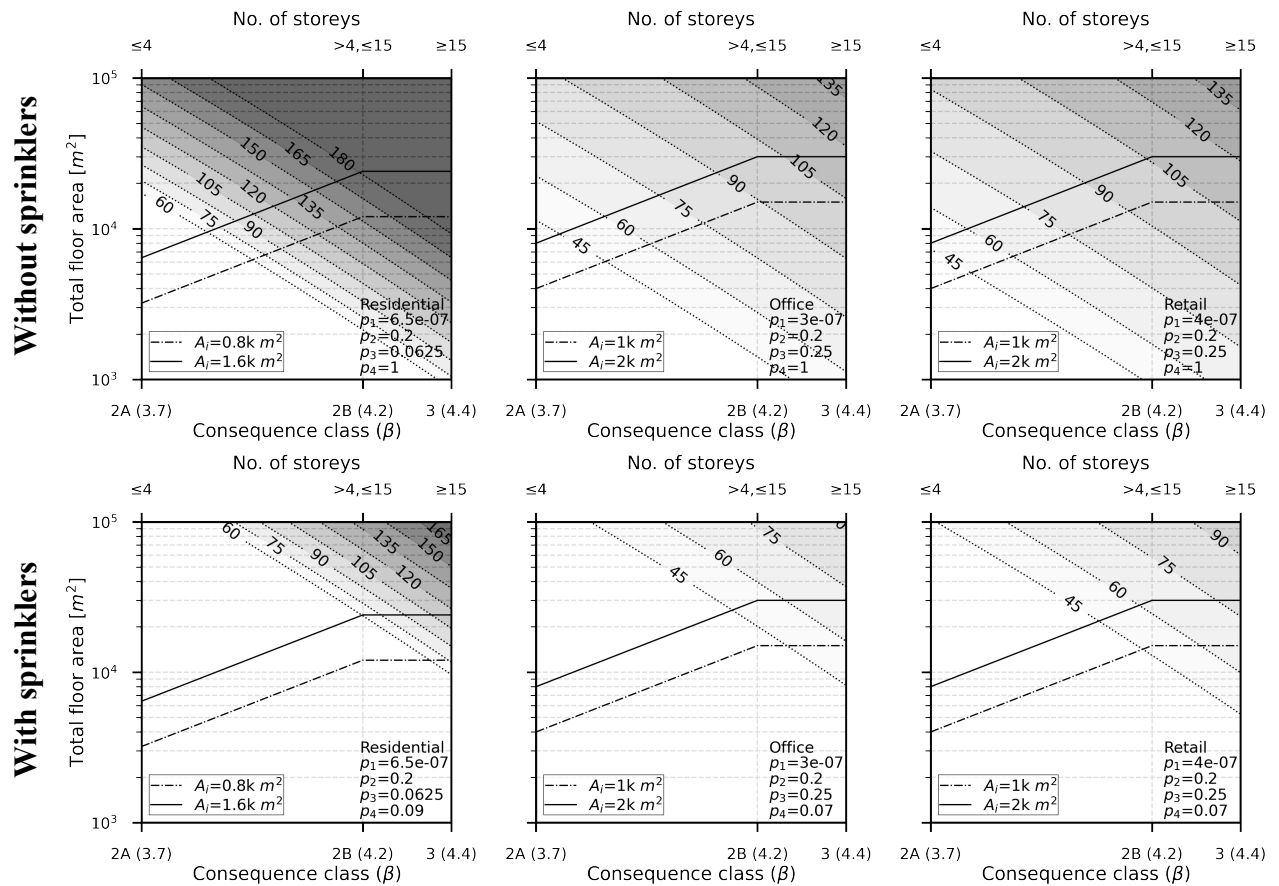


**Figure 3. Contour plots of the solved structural fire-resistance rating at various building heights and total floor area (without and with sprinklers);  $A_i$  denotes floor area per storey**

## 6 COMPARISON WITH GUIDANCE

For a fixed building footprint with floor area increasing with height, Table 4 shows the minimum fire resistance periods recommended in the contemporary guidance of BS 9999:2017 (as proposed in Kirby, et al.) and derived from the analysis presented in this study (“SFEPRAPY”). This study considers a building comprised of single occupancy based upon generalised compartment properties.

**Table 4. Minimum required fire resistance periods, a comparison between the derived and recommendation in contemporary guidance**

Occupancy	Method	Floor area per storey	Fire resistance periods based upon no. of storeys $S$ or building height $H$ (values in bracket include sprinklers) [min]		
			CC2A	CC2B	CC3
			$S \leq 4$ $5 < H \leq 18$ m	$4 < S \leq 15$ $18 < H \leq 30$ m	$S > 15$ $H \geq 30$ m
Residential	BS 9999†	-	60 (60)	90 (60)	120 (120)
	SFEPRAPY	800 m <sup>2</sup>	60 (60)	165 (60)	>180 (90)
		1600 m <sup>2</sup>	60 (60)	>180 (75)	>180 (120)
Office	BS 9999‡	-	60 (30)	90 (60)	120 (120)
	SFEPRAPY	1000 m <sup>2</sup>	45 (45)	90 (45)	105 (60)
		2000 m <sup>2</sup>	45 (45)	105 (60)	120 (75)
Retail	BS 9999§	-	60 (60)	90 (60)	120 (120)
	SFEPRAPY	1000 m <sup>2</sup>	45 (45)	105 (60)	120 (75)
		2000 m <sup>2</sup>	60 (45)	120 (75)	135 (90)

\*Assuming appropriate sprinkler system specification is provided. †Corresponds to risk profile C1/C2/C3 as defined in BS 9999:2017. ‡Corresponds to risk profile A1/A2, reduction to fire resistance when sprinkler is provided only applies to A1. §Corresponds to risk profile B1/B2, reduction to fire resistance with sprinklers only applies to B1. ◇ For comparison purposes, the recommendations in BS 9999 are included, however, the building heights defined in BS 9999 do not perfectly align with no. of storeys. For the purposes of this study, the building height bands in BS 9999 ( $>5, \leq 18$  m), ( $>18, \leq 30$  m) and ( $\geq 30$  m) are crudely mapped to  $\leq 4, \leq 15$  and  $>15$  storeys, respectively.

## 7 CONCLUSIONS

This paper presents a reliability-based approach to specifying fire resistance periods, using building area and Consequence Class to differentiate fire-induced failure consequences. Utilising the proposed reliability-based failure criteria for different building types, the potential importance of considering both floor area and the number of storeys in the specification of appropriate fire resistance ratings has been demonstrated. For a generalised storey area, the fire resistance ratings have been compared against the contemporary guidance in the UK and are broadly in agreement, with the proposed approach and methodology typically yielding a lower fire resistance when sprinklers are included. For a residential building, of the floorplate investigated, the study shows significantly higher fire resistance periods without sprinklers when compared to the guidance recommendations. In all cases, it is shown that the inclusion of sprinklers has a significant influence on the required passive fire protection to structural elements.

## 8 REFERENCES

- Ahrens, M. (2017) *U.S. Experience with Sprinklers*.
- BSI (2015) *BS 9991:2015 Fire safety in the design, management and use of residential buildings. Code of practice*.p.188.
- BSI (2017) *BS 9999:2017 Fire safety in the design, management and use of buildings. Code of practice*.p.418.
- BSI (2005) *BS EN 1990:2002+A1:2005 Eurocode. Basis of structural design*.
- BSI (2002) *BS EN 1991-1-2:2002 Eurocode 1. Actions on structures. General actions. Actions on structures exposed to fire*.
- BSI (2007) *PD 6688-1-2:2007 Background paper to the UK National Annex to BS EN 1991-1-2*.
- BSI (2019) *PD 7974-7:2019 Application of fire safety engineering principles to the design of buildings. Probabilistic risk assessment*.
- Fu, I. & Hopkin, D. (2020) *SFEPRAPY*. [Online]. 20 April 2020. Available from: <https://github.com/fsepy/SFEPRAPY> [Accessed: 12 May 2020].
- Fu, I., Rickard, I., Hopkin, D. & Spearpoint, M. (2019) *Application of python programming language in structural fire engineering - Monte Carlo simulation*. In: 2019 Royal Holloway, Interscience Communications Ltd. p.
- HM Government (2013) *The Building Regulations 2010, Approved Document A (Structure)*.
- HM Government (2020) *The Building Regulations 2010, Approved Document B (Fire Safety) Volume 2 (2019 edition, as amended May 2020)*.
- Hopkin, D. (2017) A Review of Fire Resistance Expectations for High-Rise UK Apartment Buildings. *Fire Technology*. [Online] 53 (1), 87–106. Available from: doi:10.1007/s10694-016-0571-9.
- Hopkin, D., Anastasov, S., Swinburne, K., Rush, D., et al. (2017) Applicability of ambient temperature reliability targets for appraising structures exposed to fire. In: *2nd International Conference on Structural Safety under Fire and Blast Loading*. 2017 p.
- Hopkin, D., Fu, I. & Van Coile, R. (2020) Adequate fire safety for structural steel elements based upon life-time cost optimization. *Fire Safety Journal*. [Online] 103095. Available from: doi:10.1016/j.firesaf.2020.103095.
- Hopkin, D., Spearpoint, M., Gorska, C., Krenn, H., et al. (2020) Compliance road-map for the structural fire safety design of mass timber buildings in England. *SFPE Europe*.Q4 (20).
- ISO (2014) *ISO/FDIS 2394:2014 - General principles on reliability for structures*.
- JCSS, J. (2001) Probabilistic model code. *Joint Committee on Structural Safety*.
- Joint Committee on Structural Safety (2001) *JCSS probabilistic model code - Part 2.20 Fire*.
- Kirby, B., Newman, G., Butterworth, N., Pagan, J., et al. (2004) A new approach to specifying fire resistance periods - The Institution of Structural Engineers. *The Structural Engineer: journal of the Institution of Structural Engineer*. (19), 34–37.
- Schleich, J. & Cajot, L.-G. (2001) *Valorisation Project - Natural Fire Safety Concept*.
- Stern-Gottfried, J. & Rein, G. (2012) Travelling fires for structural design—Part I: Literature review. *Fire Safety Journal*. [Online] 54, 74–85. Available from: doi:10.1016/j.firesaf.2012.06.003.
- Van Coile, R., Hopkin, D., Bisby, L. & Caspeele, R. (2017) The meaning of Beta: background and applicability of the target reliability index for normal conditions to structural fire engineering. *Procedia engineering*. 210, 528–536.

# A SIMPLIFIED MODEL FOR PREDICTING THE DEFORMED SHAPE OF NATURAL STONE MASONRY WALLS SUBJECTED TO FIRE LOADING

Elodie Donval<sup>a,b</sup>, Duc Toan Pham<sup>a</sup>, Ghazi Hassen<sup>b</sup>, Patrick de Buhan<sup>b</sup>, Didier Pallix<sup>c</sup>

<sup>a</sup> Centre Scientifique et Technique du Bâtiment (CSTB), 84 avenue Jean Jaurès, Champs-sur-Marne, 77447 Marne-la-Vallée Cedex 2, France

<sup>b</sup> Laboratoire Navier, Ecole des Ponts ParisTech, Université Gustave Eiffel, CNRS, 6-8 avenue Blaise Pascal, Cité Descartes, Champs-sur-Marne, 77455 Marne-la-Vallée Cedex 2, France

<sup>c</sup> Centre Technique de Matériaux Naturels de Construction, 17 rue Letellier, 75015 Paris, France

## Abstract

This contribution presents a simplified one-dimensional (1D) model able to predict the geometry change of a natural stone masonry wall during a fire exposure. Calculations are aimed at evaluating the final equilibrium configuration of the wall under the combined action of a thermal gradient and a vertical compressive load applied on its top. A linear thermo-elastic behaviour, taking into account the evolution of the material properties as a function of temperature increase, is assumed for the behaviour of natural stone. For illustrative purpose, the influence of boundary conditions and of the magnitude of the vertical load on the wall deflection are firstly studied. The risk of instability by buckling is then assessed. Finally, the theoretical predictions derived from this model are compared to available experimental results in order to assess their practical validity.

**Keywords:** Natural stone, masonry wall, fire loading, geometry change

## 1 INTRODUCTION

When exposed to fire, a natural-stone masonry wall is subjected to high thermal gradients through its thickness. These thermal gradients lead to a thermal bowing of the wall towards fire. In case of a bearing wall, this thermal bowing results in an eccentricity of the vertical load (applied on the top of the wall) with respect to its initial plane. This induces additional bending moments to the pre-existing compression which in turn may cause further mechanical curvature. Unreinforced masonries, generally designed to sustain mainly compressive loads, might not sustain these bending moments. Hence the thermal-induced geometry change, combined with the degradation of the material properties due to the increase of temperature, may possibly trigger the collapse of the structure.

In engineering practice, the reference text for the design of masonry structures in Europe is Eurocode 6 (EN 1996-1-2, 2005). However, recommendations for the analysis and design of natural stone masonry walls in fire conditions are still missing. In this context, a preliminary experimental campaign has been carried out by CSTB and CTMNC on two natural stone masonry walls, showing significant geometry changes of such structures in fire conditions. The present contribution deals with a simplified one-dimensional model in order to predict the geometry change of a natural stone masonry wall during a fire exposure.

## 2 STATEMENT OF THE PROBLEM AND GENERAL GOVERNING EQUATIONS

Prior to thermal loading, the wall is schematised by a vertical 1D-beam of height  $H$  along the  $Ox_1$ -axis, unit length along the  $Ox_2$ -axis and thickness  $h$  along the  $Ox_3$ -axis. It is assumed to be subject to plane strain conditions in the  $(Ox_1x_3)$  plane.

It should be noted that the following model allows for the determination of the deformed shape of the wall under various boundary conditions. However, as an illustrative example, two kinds of boundary conditions, which are common conditions encountered in full scale wall tests, are described. In both cases, the top of the wall is simply supported, allowing for vertical translation and rotation with respect to the  $Ox_2$ -axis. However, at the bottom of the wall, the real boundary condition is neither a

perfect hinge nor a perfectly clamped boundary condition. For that reason, a hinged wall (Figure 1(a)) and a clamped wall (Figure 1(b)), are considered.

The wall is subjected to fire loading on one side, which induces a pure thermal deflection  $u_{3,\theta}(x_1)$  oriented towards the fire, as shown in Fig. 1. A vertical load of magnitude  $P$  is also applied on top of the wall. Due to the thermal deflection of the wall, this applied surcharge induces an additional bending moment distribution to the pre-existing compression along the wall. Such a bending moment mechanically induces a curvature which, added to the pre-existing thermal deflection  $u_{3,\theta}(x_1)$ , gives a total deflection  $u_3(x_1)$ .

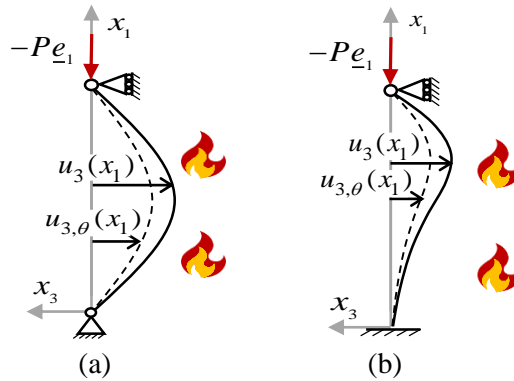


Figure 1 : Thermal-induced and total deflection of a wall modelled by (a) a hinged-simply supported and (b) a clamped-simply supported wall

## 2.1 Kinematics of the wall

The axial strain  $\varepsilon_{11}(x_1, x_3)$  at any point of the wall thickness can be written as:

$$\varepsilon_{11}(x_1, x_3) = e(x_1) - x_3 \chi_{11}(x_1) \quad (1)$$

where:

- $e(x_1)$  is the axial strain of the wall mid-plane ( $x_3=0$ );
- $u_3(x_1)$  is the deflection of this mid-plane and  $\chi_{11}(x_1) = \frac{\partial^2 u_3}{\partial x_1^2}(x_1)$  its curvature.

In order to evaluate the *P-delta* effect, a kinematics accounting for large deflections is used. In such a case, the axial strain at any point of the wall mid-plane is defined as:

$$e(x_1) = \frac{\partial u_1}{\partial x_1}(x_1) + \frac{1}{2} \left[ \frac{\partial u_3}{\partial x_1}(x_1) \right]^2 \quad (2)$$

where  $\partial u_1 / \partial x_1(x_1)$  is the linearized axial strain of the wall mid-plane and  $\partial u_3 / \partial x_1(x_1)$  its rotation with respect to the  $Ox_2$ -axis, the square of which being of the same order as  $\partial u_1 / \partial x_1(x_1)$ .

## 2.2 Thermo-elastic constitutive equations

Assuming that the thermo-mechanical characteristics of the mortar are close to those of the natural stone blocks (which may be accurate enough for a preliminary design of the wall), the influence of the joints may be neglected and the wall can be considered as being homogeneous. Furthermore, the evolution of material properties as a function of temperature is taken into account both for the thermal analysis (specific heat, thermal conductivity, bulk unit) and for the thermo-mechanical analysis (Young's modulus, coefficient of thermal expansion).

In the case of a simple structure as considered here, heat propagation across the wall can be considered as one-dimensional. Hence, the thermal distribution within the wall depends on the thickness coordinate  $x_3$  only. Consequently, thermal strains, which depend on the temperature  $T$ , on the

reference temperature  $T_0$  (20 °C here) and on the coefficient of thermal expansion of the material  $\alpha(T)$ , may be written as:

$$\varepsilon_{th}(T) = \int_{T_0}^T \alpha(\theta) d\theta \quad (3)$$

The thermo-elastic behaviour of the natural stone can be expressed by the following constitutive relationship corresponding to a plane state of strain in the  $Ox_1x_3$ -plane:

$$\sigma_{11}(x_1, x_3) = \frac{E(T(x_3))}{1-\nu^2} (\varepsilon_{11}(x_1, x_3) - (1+\nu)\varepsilon_{th}(x_3)) \quad (4)$$

where the elastic modulus  $E$  depends on the temperature, whereas the Poisson coefficient is assumed to remain unaffected by the temperature increase.

Such a stress distribution is in equilibrium with the resultant axial force  $N$  and bending moment  $M$ :

$$N(x_1) = \int_{-h/2}^{h/2} \sigma_{11}(x_1, x_3) dx_3 \quad \text{et} \quad M(x_1) = \int_{-h/2}^{h/2} -x_3 \sigma_{11}(x_1, x_3) dx_3 \quad (5)$$

Combining equations (4) and (5), it is possible to derive the global thermo-elastic behaviour of the wall as:

$$\begin{aligned} N(x_1) &= Ae(x_1) - B\chi_{11}(x_1) + N^T \\ M(x_1) &= -Be(x_1) + D\chi_{11}(x_1) + M^T \end{aligned} \quad (6)$$

where:

$$\begin{aligned} A &= \int_{-h/2}^{h/2} \frac{E(x_3)}{1-\nu^2} dx_3 \quad ; \quad B = \int_{-h/2}^{h/2} x_3 \frac{E(x_3)}{1-\nu^2} dx_3 \quad ; \quad D = \int_{-h/2}^{h/2} x_3^2 \frac{E(x_3)}{1-\nu^2} dx_3 \\ N^T &= \int_{-h/2}^{h/2} -\frac{E(x_3)}{1-\nu} \varepsilon_{th}(x_3) dx_3 \quad ; \quad M^T = \int_{-h/2}^{h/2} x_3 \frac{E(x_3)}{1-\nu} \varepsilon_{th}(x_3) dx_3 \end{aligned} \quad (7)$$

### 2.3 Equilibrium equations

Assuming that the self-weight of the wall is neglected, axial forces must satisfy the following equilibrium equation:

$$N'(x_1) = 0 \quad (8)$$

where ' denotes de derivative with respect to  $x_1$ , while the moment equilibrium equation taking into account the geometry change of the wall, writes:

$$M''(x_1) - N\chi_{11}(x_1) = 0 \quad (9)$$

When a downwards oriented vertical surcharge  $P$  is applied on top of the wall, this moment equilibrium equation can be combined with the thermo-elastic constitutive equations (6) to provide the following fourth order differential equation on the total deflection  $u_3(x_1)$ :

$$\frac{\partial^4 u_3}{\partial x_1^4}(x_1) + \frac{P}{D_e} \frac{\partial^2 u_3}{\partial x_1^2}(x_1) = 0 \quad (10)$$

where  $D_e = D - B^2 / A$  is the pure flexural stiffness of the wall.

### 2.4 Boundary conditions

As mentioned above, the boundary condition on the top of the wall can be modelled as a simple support but the boundary condition at the bottom of the wall cannot be modelled as a hinge or a full rotational restraint, and the actual boundary condition lies just in between these two conditions (Nadjai *et al.*, 2003). Consequently, the deflections calculated with these two boundary conditions may represent upper and lower estimates for the actual deflection of the wall. For that reason, both boundary conditions are dealt with in this section.

**Hinged-simply supported wall (figure 1(a))**

Boundary conditions for the hinged-simply supported wall are:

$$\begin{aligned} x_1 = 0: & \quad u_1 = u_3 = 0; M = 0 \\ x_1 = H: & \quad N_1 = -P; u_3 = 0; M = 0 \end{aligned} \quad (11)$$

Taking into account these boundary conditions, the solution to equation (10) is:

$$u_3(x_1) = \left( -\frac{B}{A} + l^2 \chi^T \right) \left( 1 - \cos\left(\frac{x_1}{l}\right) + \frac{\cos\left(\frac{H}{l}\right) - 1}{\sin\left(\frac{H}{l}\right)} \sin\left(\frac{x_1}{l}\right) \right) \quad (12)$$

where:

- $\chi^T = -\frac{AM^T + BN^T}{AD - B^2}$  is the thermal curvature in the absence of surcharge on top of the wall;
- $l = \sqrt{\frac{D_e}{P}}$  is a characteristic length of the system.

The classical critical buckling load can then be easily recovered from equation (12):

$$P^{cr} = D_e \frac{\pi^2}{H^2} \quad (13)$$

### **Clamped-simply supported wall (figure 1(b))**

In the same way, it is possible to derive the deflection of a clamped-simply supported wall for which the boundary conditions are given by equations (14).

$$\begin{aligned} x_1 = 0: & \quad u_1 = u_3 = 0; \frac{\partial u_3}{\partial x_1} = 0 \\ x_1 = H: & \quad N_1 = -P; u_3 = 0; M = 0 \end{aligned} \quad (14)$$

Deflection of the wall is then:

$$u_3(x_1) = \left( \frac{B}{A} - l^2 \chi^T \right) \frac{\left( \cos\left(\frac{x_1}{l}\right) - 1 \right) \left( \sin\left(\frac{H}{l}\right) - \frac{H}{l} \right) - \left( \sin\left(\frac{x_1}{l}\right) - \frac{x_1}{l} \right) \left( \cos\left(\frac{H}{l}\right) - 1 \right)}{\cos\left(\frac{H}{l}\right) \left( \sin\left(\frac{H}{l}\right) - \frac{H}{l} \right) - \sin\left(\frac{H}{l}\right) \left( \cos\left(\frac{H}{l}\right) - 1 \right)} \quad (15)$$

and the corresponding critical buckling load is:

$$P^{cr} = 2.05 D_e \frac{\pi^2}{H^2} \quad (16)$$

It can be noticed that the critical buckling load is then 2.05 times higher than the one of the hinged – simply supported wall.

## **3 ILLUSTRATIVE EXAMPLE**

As an illustrative application of the calculation procedure presented in the previous section, a 20 cm-thick wall of unit length, made of limestone blocks, is considered, with a parametric study conducted on its height. The thermo-mechanical properties of the blocks are those of Saint-Maximin limestone described in Vigroux *et al.* (2021).

The wall is exposed to an ISO 834 fire (EN 1991-1-2, 2003) on one of its face during 120 min. The distribution of temperature across the thickness of the wall due to fire exposure is determined by a preliminary heat transfer analysis. Then, the corresponding deflection of the wall is derived from the calculation procedure described in the previous section.

### **3.1 Thermal analysis**

The preliminary heat transfer is performed using the FE software Safir (Franssen, 2005). Figure 2 represents the temperature profiles for 30 min and 120 min of fire exposure.

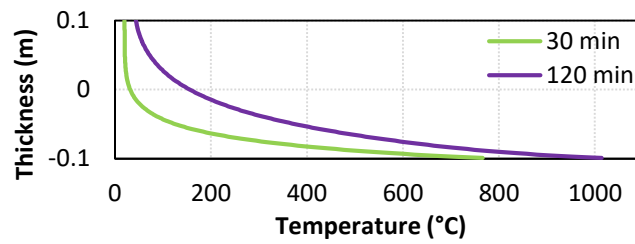


Figure 2 : Calculated temperature profiles across the wall thickness for 30 and 120 min of fire exposure

### 3.2 Deflection of the wall

From these temperature profiles, the corresponding thermal and final deflection are shown in figure 3 for a 3 m-high wall and a 5.4 m-high wall (corresponding to a slenderness ratio of 27, which is the maximal ratio recommended by Eurocode 6 (EN 1996-1-1, 2005)). In these examples, the surcharge is taken equal to  $P = 200$  kN/m on both walls.

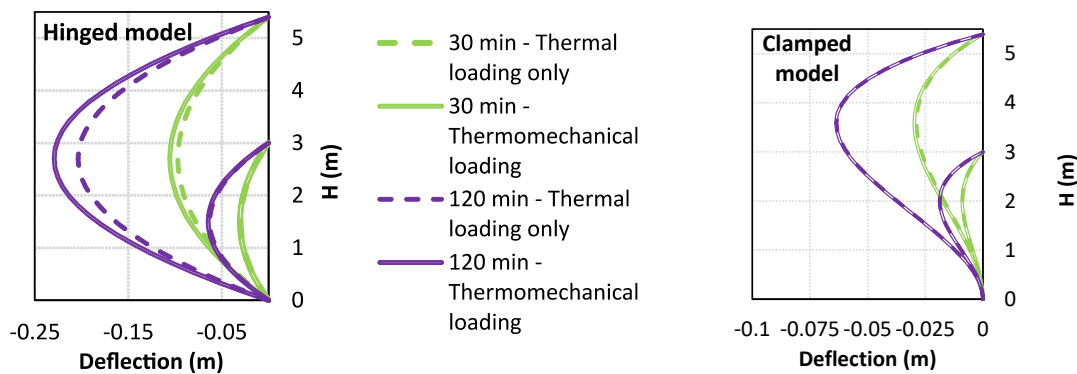


Figure 3 : Thermal-induced and total deflections of walls of different height under different boundary conditions and fire exposure

For the hinged 3 m-high wall, the  $P$ -delta effect is negligible while for the hinged 5.4 m-high wall, the  $P$ -delta effect represents 12 % of the total deflection. This application also shows the importance of the choice of the boundary condition at the bottom of the wall. Indeed, the maximal deflection of the clamped wall is around 3.6 times lower than the one of the hinged wall.

### 3.3 Assessment of the buckling risk

As shown in section 2.4, buckling occurs for a lower load in the hinged-simply supported model than for the clamped-simply supported one. For the simply-supported wall, after 120 min of fire exposure, the buckling load is 5.4 MN/m for a 3 m-high wall and 1.7 MN/m for a 5.4 m-high wall. In the latter case, which is the worst case considered in this study, the buckling load is still 7.6 times higher than the maximum characteristic load given by Eurocode 6, which is 220 kN/m. Such a high value of the ratio between the buckling and the applied load also explains why the  $P$ -delta effect remains negligible, especially for 3 m-high walls and for the clamped wall model.

### 3.4 Comparison with experimental results

Results of the proposed model are now compared to experiments performed by CSTB and CTMNC on two 3 m-high, 3 m-long, 20 cm-thick limestone walls. The thermomechanical properties of the Saint-Vaast limestone composing these walls are close to the ones of Saint-Maximin limestone described in Vigroux *et al* (2021). On both walls, blocks were bonded together by a natural hydraulic lime mortar (NHL 3.5).

Wall n°1 was not mechanically loaded while a 245 kN/m vertical load was applied on top of wall n°2. Both walls were exposed to an ISO 834 fire: wall n°1 during 120 min and wall n°2 during 30 min. Figure 4 shows the experimental and the numerical deflections of these two 3 m-high walls after being exposed to fire during 30 min.

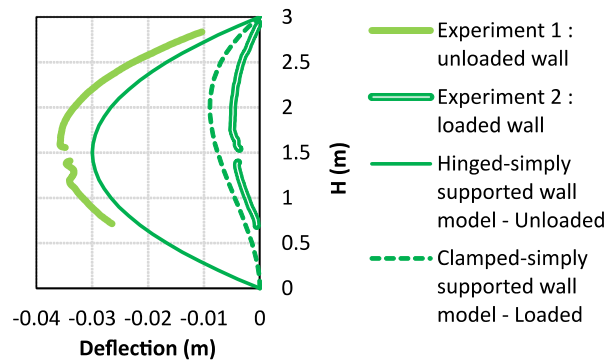


Figure 4 : Theoretical and experimental deflections of 3 m-high walls after 30 min of fire exposure

When the wall is unloaded, the deformed shape is rather close to the one predicted by the hinged wall model: the relative difference between the maximum deflection given by the model and the experiment is equal to 17%. For the loaded wall, its maximum deflection is four times lower than when it is unloaded. In this case, it seems that the deflection profile is closer to that predicted by the clamped wall model.

#### 4 CONCLUSION

Based on a simplified 1D modelling of the problem, this paper has developed a calculation procedure for evaluating the deformed configuration of masonry walls exposed to fire. It is notably shown that it is not necessary to take the *P-delta* effect into account for slenderness ratios lower than 15. However, this might become necessary for slenderness ratios between 15 and 27, which is the maximum slenderness ratio recommended by Eurocode 6.

Comparison between experimental results and theoretical predictions has shown that the maximum load applied on the wall is much lower than the buckling load, which means that failure of the wall by buckling may be discarded. Moreover, despite the fact that the joints are not accounted for in the analysis, the model is able to accurately predict the deformed shape of an unloaded wall. This conclusion seems to be valid for good quality mortars (the properties of which are similar to those of the block), but may be different for poorer quality mortars where the influence of the joints should be taken into account.

Finally, the analysis of the model has pointed out that boundary conditions have an important influence on the amplitude of the deformed shape of the wall. The comparison with experimental results suggests that the rotational restraint depends on the vertical load applied on the wall. However, further investigation is still needed to fully understand the impact of applied loads on the deformed shape of the wall.

#### ACKNOWLEDGMENTS

The authors wish to thank Mr. Denis Garnier, Mr. Martin Vigroux and Mr. Nicolas Pinoteau for their advice and discussions on the development of the model.

#### REFERENCES

- EN 1991-1-2, 2003. Eurocode 1: Action on structures-Part 1-2: General actions. Actions on structures exposed to fire.
- EN 1996-1-1, 2005. Eurocode 6: Design of masonry structures – Part 1–1: General Rules for Reinforced and Unreinforced Masonry Structures.
- EN 1996-1-2, 2005. Eurocode 6: Design of masonry structures – Part 1–2: General rules - Structural fire design
- Franssen, J.-M., 2005. SAFIR: A thermal/structural program for modeling structures under fire. *Eng. J.* 42, 143–158.
- Nadjai, A., O’Garra, M., Ali, F., 2003. Finite element modelling of compartment masonry walls in fire. *Comput. Struct.* 81, 1923–1930.
- Vigroux, M., Eslami, J., Beaucour, A.-L., Bourgès, A., Noumowé, A., 2021. High temperature behaviour of various natural building stones. *Constr. Build. Mater.* 272, 121629.

# TOWARDS A SAFETY CONCEPT FOR NATURAL FIRES – THE NEED OF CODE CALIBRATION

Marcus Achenbach<sup>a</sup>

<sup>a</sup> LGA KdöR, Department of Design Review, Nürnberg, Germany

## Abstract

The check of the fire resistance is part of the design process of buildings and regulated by building codes. These building codes specify a fire resistance class in dependence from the occupancy, the type of the building and the height above ground of the considered compartment. It is assumed by building authorities, that this procedure leads to commonly accepted levels of safety. The fire resistance of the considered members is normally checked using tabulated values, which are based on standardized tests under a nominal fire. There exists a big data base and long-lasting experience for standard fire tests. Hence, these tests are also considered to contain “stored” engineering knowledge.

On the other hand, performance-based methods have been developed and are more and more accepted by building authorities, because they allow a much more detailed analysis of the entire structure subjected to a natural fire. When it comes to design, the question of safety arises. First safety concepts have been developed using the specified target reliabilities given in Eurocode 0. But it is not known, which level of safety is achieved for natural fires, if members have been designed for a fire resistance according to the well accepted tabulated values. It is also expected that performance-based methods will lead to a design, which is at least as safe as a design by nominal fires. Hence there is a need for calibrating a safety concept for natural fires using the experience from tabulated values in combination with standard fires.

In this paper background information for code calibration of safety concepts for natural fires is presented. It is highlighted, which criteria must be met in order to fulfil the needs of the building codes. Finally, a draft for the code calibration procedure of concrete members is given.

**Keywords:** code calibration, safety, building authorities, natural fires

## 1 INTRODUCTION

Tests on the behaviour of structural members subjected to fire are performed since the beginning of the 20<sup>th</sup> century (Law and Bisby, 2020). The standard temperature-time curve (EN 1991-1-2, 2002) has prevailed as standard heating regime of laboratory tests in order to get comparable and repeatable results. The determined “fire resistance” has been adopted in building regulations in various countries (Law and Bisby, 2020) and is linked to the typical usage and height above ground of the considered compartment among other criteria. The so-called “prescriptive approach” is well accepted and reflects the experience with severe fires in the last century though the exact level of safety is not specified. Numerical methods have been developed, notably the Advanced Method (EN 1992-1-2, 2004), to simulate laboratory tests with the intention to replace testing by simulation. Hence the Advanced Method is validated by the recalculation of laboratory tests on members subjected to a standard fire (Haß, 1986). European standards, the Eurocodes, have been written with the objective to meet the requirements for structural performance and fire resistance specified in 89/106/EEC (1989), superseded by Regulation (EU) No 305/2011 (2011). It is assumed, that the load-bearing capacity of structural members is given for a specified time period. In case of a standard fire, this period is linked to a fire rating R30, R60 and so on. But in case of natural fires many questions arise, because:

1. failure can occur in the cooling phase,

2. the gas temperature is controlled by the physical properties of the compartment, ventilation conditions and fuel load.

The application of natural fires for design is accepted, if an adequate level of safety compared the prescriptive approach is given (MVV TB, 2020). But this safety level is not known and has not been quantified yet, which makes the proof of adequate safety challenging.

In Section 2 the state of technical knowledge given in Eurocodes is briefly described. Problems and possible pitfalls for determination of safety levels are given in Section 3. In Section 4 a procedure for the calibration of safety concepts, adapted to the needs of building authorities is proposed.

## 2 TREATMENT OF FIRE SAFETY IN EUROCODES

### 2.1 Prescriptive approach

A defined structural performance and fire resistance is a demand given in building codes. In these building codes, the required level of fire resistance can be specified in the transcriptions “fire resistant” or “fire retardant” and a translation into a fire resistance class is often specified in a separate document. This methodology allows to change a design code independent of a building code, because the exact technical term is not used in the building code. The required fire resistance is defined in the building code in dependence on the typical use of the building, the area of the compartment, the height above ground and the location of the considered member in the building. Table 1 contains an overview over the required fire resistance for residential and office buildings in Germany as example. It must be kept in mind, that building codes also specify the maximum length of corridors, the type and the location of staircases for evacuation among other parameters. Hence the “prescriptive approach” can be understood as a full “safety concept” with implicitly given safety levels.

Table 1 Required fire resistance of walls, columns and slabs for office and residential buildings in Germany (#: class of building according to building code,  $A$ : Area of compartment,  $h$ : height above ground,  $R$ : standard fire rating,  $R_b$ : standard fire rating of basement)

#	$A$ [m <sup>2</sup> ]	$h$ [m]	$R$ [min]	$R_b$ [min]
1 +2	≤ 400	≤ 7	30	30
3	no limit	≤ 7	30	90
4	≤ 400	≤ 13	60	90
5	no limit	≤ 22	90	90

In structural fire engineering, the required performance of the considered member is given in terms of a required fire resistance class (R30, R60,...) and is linked to well defined laboratory tests, which are performed using the standard temperature-time curve (EN 1991-1-2, 2002). It is assumed, that the standard temperature-time curve covers the peak temperatures of typical residential or office compartments (Zehfuß, 2004). But it must be remembered that the development of the standard temperature-time curve is also influenced by the discussion among the involved scientists and officials of building authorities (Law and Bisby, 2020), because there is a close relationship between a design codes and building regulations in structural fire engineering. Though an analytic relationship of the standard temperature-time curve to natural fires is not given, it must be recognised that there is a big test database for laboratory tests using standard fires which are the base for the tabulated values given in Eurocode 2 (EN 1992-1-2, 2004). Also, there is a big experience in designing members for fire resistance using tabulated values, e. g. keeping the 500 °C-limit for the maximum temperature of slack reinforcement for bending members, as described in Eurocode 2 (EN 1992-1-2, 2004).

## 2.2 Natural fires

The time-dependent evolution of the gas temperatures for natural fires is mainly characterised by the fuel load and the provided oxygen. In case of compartment fires a simple mathematical model is given by the parametric temperature-time curves of Eurocode 1 (EN 1991-1-2, 2002). This model consists of two parts: an ascending, nonlinear branch in the heating phase and a linear descending part in the cooling phase, as indicate in Figure 1. The gas temperature  $\theta_g$  [°C] in the heating phase is given by the empiric equation

$$\theta_g(t) = 20 + 1325 \left( 1 - 0.324e^{-0.2t^*} - 0.204e^{-1.7t^*} - 0.472e^{-19t^*} \right), \quad (1)$$

with the scaled time  $t^* = t \cdot \Gamma$ , the real time  $t$  [h] and the non-dimensional scaling factor  $\Gamma$ . The standard temperature-time curve is approximated by Eq. (1) for  $\Gamma = 1$ . The scaling factor is defined by

$$\Gamma = \left( \frac{O}{b} \right)^2 / \left( \frac{0.04}{1160} \right)^2 \quad (2)$$

with the opening factor  $O = 0.02 \dots 0.2$  [m<sup>1/2</sup>], describing the ventilation conditions, and the thermal properties of the compartment considered by  $b = \sqrt{\rho c \lambda}$  [J / m<sup>2</sup> s<sup>1/2</sup> K]. The maximum temperature is reached at  $t_{max}^* = t_{max} \cdot \Gamma$ , with

$$t_{max} = \max(0.2 \cdot 10^{-3} \cdot q_{t,d}/O ; t_{lim}). \quad (3)$$

The fire growth rate is taken into account by the tabulated parameter  $t_{lim}$  and the design fire load  $q_{f,d}$  is considered by  $q_{t,d} = q_{f,d} \cdot A_f/A_t$ , with the floor area  $A_f$  and total area  $A_t$  of the enclosure. The definition of the design fire load is given in Section 2.3. A fuel controlled fire is identified for  $t_{max} = t_{lim}$ : there is enough oxygen for combustion, but only limited fuel provided. In the other case, the fire is ventilation controlled. After the maximum temperature is reached, the linear ascending branch is given in dependence from  $t_{max}^{**} = (0.2 \cdot 10^{-3} \cdot q_{t,d}/O) \cdot \Gamma$ .

It must be pointed out that parametric temperature-time curves are empiric and based on fitting the results of experiments. Hence the given formulas are not based on physical equations and numbers are linked to the specified units. The accuracy of this approximation and the comparison to more sophisticated solutions are examined by Zehfuß (2004).

## 2.3 Design fire load

The design fire load is specified in Annex E to EN 1991-1-2 (2002) by

$$q_{f,d} = m \cdot q_{f,k} \cdot \delta_{q1} \cdot \delta_{q2} \cdot \delta_n, \quad (4)$$

with the combustion factor  $m$ , the characteristic fire load density  $q_{f,k}$  [MJ/m<sup>2</sup>], the factor  $\delta_{q1}$  to consider the size of the compartment and  $\delta_{q2}$  for the risk of activating a fire, the product  $\delta_n$  of the other factors  $\delta_i$  to take sprinklers or other firefighting measures into account. These factors can be summarized as  $\gamma_{q,f} = m \cdot \delta_{q1} \cdot \delta_{q2} \cdot \delta_n$  leading to  $q_{f,d} = \gamma_{q,f} \cdot q_{f,k}$ . The partial safety factor  $\gamma_{q,f}$  is derived using a semi-probabilistic concept, which assumes, that action (here: fire load) can be treated separately from the reaction (here: fire resistance) (Leonardo da Vinci Pilot Project CZ/02/B/F/PP-134007, 2005). It is also assumed that the probability of occurrence of a fire  $p_f$  is independent from the failure in case of fire  $p_{f,fi}$ . The values  $\delta$  of Annex E are calibrated to meet a target probability of failure  $p_t = 7,23 \cdot 10^{-5}$  for a return period of 55 years:

$$p_t = p_f \cdot p_{f,fi} \leq 7,23 \cdot 10^{-5}. \quad (5)$$

In terms of building regulations,  $p_f$  can be interpreted as a measure of the preventive fire protection, whereas  $p_{f,fi}$  can be regarded as structural fire safety.

Hosser *et al.* (2008) proposes a safety concept, which is also based on a target probability of failure. The level of safety is chosen in accordance with the specified levels in Eurocode 0 for a return period of one year (DIN EN 1990, 2010). The size of the compartment, occupancy, firefighting measures are considered by  $p_f = p_1 \cdot p_2 \cdot \dots$  and the conditional probability of structural failure  $p_{f,fi}$  can be calculated using Eq. (5) leading to a safety factor  $\gamma_{q,f}$  related to  $q_{f,k}$ . The proposed safety concept is

part of the German national Annex to Eurocode 1 (DIN EN 1991-1-2/NA, 2010). It is obvious, that both proposals are “related” to each other. The levels of safety of both methods are examined by Zehfuß *et al.* (2020) using semi-probabilistic methods.

### 3 COMMENTS ON THE CODIFIED SAFETY CONCEPTS OF EUROCODES

Though the safety of concept for natural fires is embedded in the design philosophy of Eurocode 0 (DIN EN 1990, 2010), questions arise when comparing it to the well-accepted prescriptive approach. Partial safety factors are introduced in order the meet a target probability of failure, while no clear failure probabilities are known for the prescriptive approach. The required fire resistance is increasing with the height of the building in the prescriptive approach – but there is no link to the point in time of failure for natural fires specified in the Eurocodes.

The dependency of the fire resistance on the height of a building can be understood from a historical point of view (Law and Bisby, 2020) and is justified by a long-lasting experience, only. From this viewpoint it appears to be justified to assume that structural members will not fail within the specified fire resistance up to a fire rating of 30 min. For longer fire ratings it can be supposed that structural members resist a fully developed fire including the cooling phase.

The standard temperature-time curve is regarded to cover the peak temperatures of fires in residential or office buildings (Zehfuß, 2004) and is accepted to simulate the effect of a severe fire on structural members (Law and Bisby, 2020). The gas temperatures of a compartment with a fire load density of 600 MJ/m<sup>2</sup> are displayed in Figure 1 for different ventilation in conditions in comparison to the standard temperature-time curve. It can be seen that the peak temperature of the standard fire is exceeded in the first 30 minutes by a natural fire. The standard temperature-fire curve does not capture the peak temperatures for the given set of parameters.

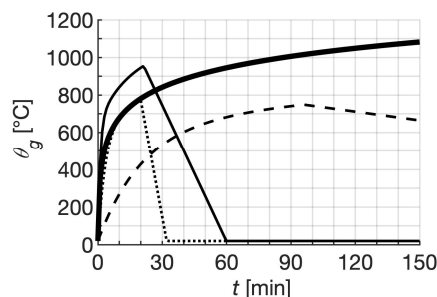


Fig. 1 Gas temperatures acc. to EN 1991-1-2 for  $q_{f,k} = 600$  [MJ/m<sup>2</sup>],  $m = 0.8$ ,  $A_t / A_f = 3$  [-]: standard temperature-time curve (—), parametric temperature-time cure with  $O = 0.09$  (—),  $O = 0.02$  (- - -) and  $O = 0.2$  (...) [m<sup>1/2</sup>]

The fire resistance of single span concrete slabs can be judged by the temperature evolution of the rebars. A temperature of 500 °C is assumed as the critical temperature leading to recommendations for the axis distance  $a$  to the surface (EN 1992-1-2, 2004). The rebar temperature for a concrete slab heated on one side is displayed in Figure 2 for  $a = 1$  cm given for the fire resistance class R30. A rebar temperature of approximately 500 °C is reached after 30 min of standard fire exposure but is exceeded for a natural fire within the first 20 minutes. Time of failure shifts for a ventilation controlled fire where the critical temperature is surpassed after 70 min. Hence it is necessary to specify if members should survive a fully developed fire or resist up to a specified time (here: 30 min).

The codified safety concept, described in Section 2.3, is derived separating action and resistance using semi-probabilistic methods, which allows the definition of partial safety factors. But this can be seen critical, because the resistance of a cross section subjected to fire is also determined by the gas temperatures, which is the action. It can be assumed, that the weighting factors of FORM (DIN EN 1990, 2010) may change, as the limit state function is highly nonlinear. It must be remembered also that it is recommended to use an accidental load combination in case of fire (EN 1991-1-2, 2002). In this combination rule, “fire” is treated as the main action and accompanying loads can be reduced because a certain level of damage is accepted.

For the design of a cross section subjected to fire, a partial safety factor of 1.0 is recommended for concrete and reinforcing steel (EN 1992-1-2, 2004). This safety factor has been scaled in order to use the Advanced Method to simulate laboratory tests (Anderberg *et al.*, 2004) with a standard fire. The procedure of Annex D to Eurocode 0 (DIN EN 1990, 2010) has been applied under the assumption that two tests are passed and the third test may fail. Lower probabilities of failure, leading to an increase of the partial safety factors for materials, are not considered here. It can be shown that Advanced Methods tend to underestimate the prediction of the time of failure for a standard fire (Achenbach *et al.*, 2019). There is a remarkable bias, which can be interpreted as “hidden safety”. But this fact is not considered in the safety factors for the Advanced Method of Eurocode 2 (Anderberg *et al.*, 2004).

The codified safety concept for natural fires is embedded in the specified target probabilities of failure, as described in Section 2.3. The values for  $p_t$  are given for the persistent or transient design situation. But for the accidental design situation a certain damage is accepted. Hence the necessary target probability of failure  $p_t$  can be discussed (Van Coile *et al.*, 2017,2019).

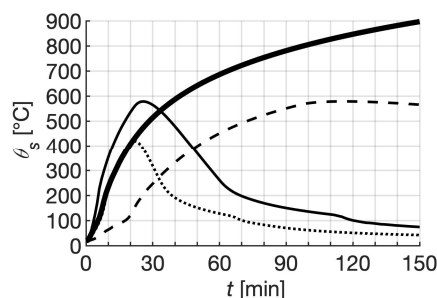


Fig. 2 Rebar temperatures for a concrete plate ( $a = 1$  [cm],  $h = 18$  [cm]) for the gas temperatures acc. to Fig. 1: standard temperature-time curve (—), parametric temperature-time curve with  $O = 0.09$  (—),  $O = 0.02$  (- - -) and  $O = 0.2$  (...) [ $m^{1/2}$ ]

#### 4 CALIBRATION PROCEDURE

The application of performance based structural fire engineering becomes more popular because the methods are much more flexible in comparison to the rigid system of prescriptive regulations. By the introduction of design methods applied for design, the question of safety and safety factors arises. These safety factors are included in the design fire load, as displayed in Section 2.3. It is also assumed, that the safety level, which is achieved by a performance-based design, will not be below the level of safety implicitly given in the prescriptive approach (MVV TB, 2020). Hence there is a need for calibration the safety factors for natural fires on the level of safety obtained by a prescriptive design. The principles of code calibration are described by Melchers (1999) and an adapted procedure is proposed here. The remarks given in Section 3 imply, that the probability of failure should be calculated using a full probabilistic approach to capture all effects of the highly non-linear limit states. It can be concluded also that model uncertainties on the action and the reaction side should be considered to capture the so called “hidden safety”. The following steps are proposed:

1. select a representative set of compartments covered by building regulations, e. g. given in Table 1,
2. perform a design at ambient temperatures for different members, e. g. beam, wall, column, slab,
3. determine the necessary fire rating and check concrete cover and dimensions according to tabulated values,
4. decide, if the considered time domain of failure is limited to the fire rating (30, 60,...min) or if fully developed fires including burn-out should be considered,
5. perform a full probabilistic analysis for each member and determine the conditional probability of failure in case of fire  $p_{f,fi}$  for the considered time domain,
6. select the corresponding probability of occurrence of a fire  $p_f$  for the selected compartment,

7. calculate the codified total probability of failure  $p_c = p_f \cdot p_{f,fi}$ ,
8. compare the results to the expected probability of failure  $p_t$ .

The question for the appropriate level of the target  $p_t$  can be challenging (Van Coile et al., 2019) and is still under discussion. It is also not known exactly, which level of safety  $p_c$  is obtained by a design for a standard fire. In the case of  $p_c = p_t$  a design for a natural fire or the standard fire leads to the same level of safety – but for  $p_c < p_t$  there is a lack of safety using a standard fire design. On the other hand, the prescriptive approach is well accepted, and it could be discussed to calibrate  $p_t$  using the results of step 7. It is possible to specify the structural fire safety  $p_{f,fi}$  in dependence from the fire rating. The derived target values  $p_{f,fi}$  can be interpreted as “deemed to satisfy approach”. This methodology is also accepted in other design situations (International Federation for Structural Concrete, 2012) and opens the possibility to link the safety of the prescriptive approach to performance based structural fire engineering.

## REFERENCES

- 89/106/EEC, 1989. *Council directive on the approximation of laws, regulations and administrative provisions of the Member States relating to construction products.*
- Achenbach, M., Gernay, T., Morgenthal, G., 2019. *Quantification of model uncertainties for reinforced concrete columns subjected to fire*, Fire Saf. J. 108, p. 1–10.
- Anderberg, Y., Forsén, N.E., Hietanen, T., Izquierdo, J.M., Le Duff, A., Richter, E., Whittle, R.T., 2004. *Background documents to EN 1992-1-2 – Eurocode 2: Design of concrete structures, Part 1-2: General rules – Structural fire design.*
- DIN EN 1990, 2010. *Eurocode: Grundlagen der Tragwerksplanung.*
- DIN EN 1991-1-2/NA, 2010. *Nationaler Anhang – National festgelegte Parameter – Eurocode 1: Einwirkungen auf Tragwerke – Teil 1-2: Allgemeine Einwirkungen – Brandeinwirkungen auf Tragwerke.*
- EN 1991-1-2, 2002. *Eurocode 1: Actions on structures – Part 1-2: General actions – Actions on structures exposed to fire.*
- EN 1992-1-2, 2004. *Eurocode 2: Design of concrete structures – Part 1-2: General rules - Structural fire design.*
- Haß, R., 1986. *Zur praxisgerechten brandschutztechnischen Beurteilung von Stützen aus Stahl und Beton*, PhD Thesis, Technische Universität Braunschweig.
- Hosser, D., Weilert, A., Klinzmann, C., Schnetgöke, R., Albrecht, C., 2008. *Sicherheitskonzept zur Brandschutzbemessung*, Abschlussbericht, Institut für Baustoffe, Massivbau und Brandschutz, Braunschweig.
- International Federation for Structural Concrete (Ed.), 2012. *Model Code 2010: final draft. Vol. 1, Bulletin / International Federation for Structural Concrete Draft model code*, International Federation for Structural Concrete, Lausanne.
- Law, A., Bisby, L., 2020. *The rise and rise of fire resistance*. Fire Saf. J. 116, p. 1–10.
- Leonardo da Vinci Pilot Project CZ/02/B/F/PP-134007, 2005. *Handbook 5, Design of buildings for the fire situation.*
- Melchers, R.E., 1999. *Structural Reliability Analysis and Prediction, 2nd edition*, ed. John Wiley & Sons, Chichester.
- MVV TB, 2020. *Muster-Verwaltungsvorschrift Technische Baubestimmungen.*
- Regulation (EU) No 305/2011, 2011. *Regulation (EU) No 305/2011 of the European Parliament and of the Council laying down harmonised conditions for the marketing of construction products and repealing Council Directive 89/106/EEC.*
- Van Coile, R., Hopkin, D., Bisby, L., Caspeele, R., 2017. *The meaning of Beta: background and applicability of the target reliability index for normal conditions to structural fire engineering*. Procedia Eng. 210, p. 528–536.
- Van Coile, R., Hopkin, D., Lange, D., Jomaas, G., Bisby, L., 2019. *The Need for Hierarchies of Acceptance Criteria for Probabilistic Risk Assessments in Fire Engineering*, Fire Technol. 55, p. 1111–1146.
- Zehfuß, J., 2004. *Bemessung von Tragsystemen mehrgeschossiger Gebäude in Stahlbauweise für realistische Brandbeanspruchung*, PhD Thesis, Technische Universität Braunschweig.
- Zehfuß, J., Schaumann, P., Gößwein, L., Meyer, P., Sander, L., 2020. *Bewertung von neuen Sicherheitsfaktoren zur Ermittlung der Brandlastdichte im Zuge der Novellierung von EN 1991-1-2 Anhang E.*

Proceedings of the International Conference in Ljubljana, 10-11 June 2021  
in edition of Applications of Structural Fire Engineering

**Session**

**Timber structures II**

## EXPERIMENTAL CHARACTERISATION OF THE FIRE BEHAVIOUR OF CLT CEILING ELEMENTS FROM DIFFERENT LEADING SUPPLIERS

Danny Hopkin<sup>a</sup>, Carmen Gorska<sup>b</sup>, Michael Spearpoint<sup>a</sup>, Ian Fu<sup>a</sup>, Harald Krenn<sup>c</sup>, Tim Sleik<sup>d</sup> & Gordian Stapf<sup>e</sup>

<sup>a</sup> OFR Consultants, Sevendale House, Lever Street, Manchester, M1 1JA

<sup>b</sup> Stora Enso Wood Products Oy Ltd, Kanavaranta 1, PO 309, Helsinki, FI-00101, Finland

<sup>c</sup> KLH, Gewerbestraße 4, 8842 Teufenbach-Katsch, Austria

<sup>d</sup> binderholz, Zillertal Straße 39 · A, 6263 Fügen, Austria

<sup>e</sup>Henkel & Cie. AG, Industriestrasse 17a, 6203 Sempach Station, Switzerland

### Abstract

This paper summarises a systematic experimental study to evaluate what, if any, differences in fire performance characteristics of cross-laminated timber (CLT) are apparent between samples manufactured by three different leading European suppliers. This element of the study focuses on samples in a ceiling orientation, subject to a constant incident heat flux of 50 kW/m<sup>2</sup> imposed via a radiant panel (from below) at the centre of the sample, for 60 minutes. Experiments are conducted on samples with varying lamella thickness (20 or 40 mm), adhesive type (heat resistant [HBX] vs. non-heat resistant polyurethane [HBS]) and edge-gluing procedure (edge vs. non-edge-glued). In-depth temperature, charring depth, mass loss rate (MLR) and heat release rate (HRR) form the basis of comparison. It is observed through a statistical assessment (ANOVA) that limited differences exist between suppliers when panels have the same characteristics, e.g., lamella thickness, adhesive type and edge-gluing procedure. Differences are marginally more pronounced for MLR vs. charring rate.

**Keywords:** cross-laminated timber, CLT, fire, heat release rate, charring rate, char depth, adhesive

## 1 INTRODUCTION

Mass timber in the form of cross-laminated timber (CLT) panels has become a popular design option for the construction of new office buildings across the UK, where CLT panels are to be used as part of the floor construction, often in hybrid construction (e.g., steel frame, with CLT floors). Currently, there is concern amongst approval authorities that the fire performance of CLT panels from different suppliers varies sufficiently such that existing experimental or testing evidence cannot be generalised and may not be transferable across projects. This often, for approval purposes, necessitates that ad-hoc, project-specific compartment testing be undertaken to evidence the design, using the specific supplier's CLT that is intended for use in/on the building. Such testing can have significant implications for the viability of mass timber schemes and ultimately does not advance knowledge as the data is rarely published or shared. To this end, as part of a larger Structural Timber Association (STA) project (2021) in the UK, and in support of demonstrating Building Regulations compliance, an experimental study was commissioned to study what, if any, differences exist in the fire performance characteristics of CLT manufactured by Europe's three leading suppliers (Stora Enso, KLH and binderholz).

## 2 THE EXPERIMENTAL CAMPAIGN

### 2.1 Objective

The primary objective of the study was to establish what, if any, difference in fire performance characteristics is to be expected between CLT panels manufactured and supplied by three organisations: Stora Enso, KLH and binderholz. In the context of fire performance, the difference between CLT suppliers has been evaluated through trends in mass loss rate (MLR), heat release rate (HRR) and in-depth temperature development, for upper and lower bound outer lamella thicknesses (20 to 40 mm) typically available from suppliers, in wall (vertical) and ceiling (horizontal)

orientations. This paper reports on the ceiling samples, with a separate study undertaken on wall samples.

## 2.2 Experimental configuration

The experimental configuration constitutes CLT samples (200 × 200 mm in plan and from 100 to 120 mm thick) subject to a constant incident heat flux of 50 kW/m<sup>2</sup> (at the centre of the sample) for 60 min, in a well-ventilated ambient environment. Experiments did not include a pilot as an ignition source and instead relied upon spontaneous ignition of the samples. Thermocouples were installed within the samples, oriented parallel to the isotherms. These thermocouples were located both within joints and away from joints (in lamella). Sample mass was measured via scales before, during and after the experiments, with total HRR also observed via oxygen depletion calorimetry. An indication of the experimental configuration is given in Figure 1 (left).

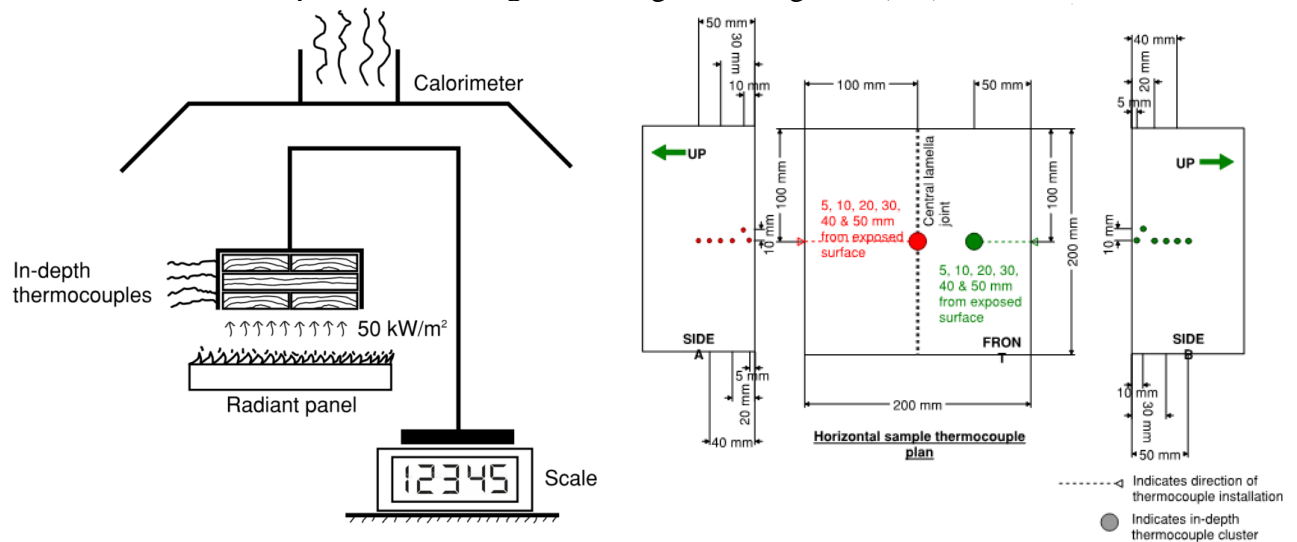


**Figure 1 – (left) Illustrative experimental configuration for ceiling samples; (right) thermocouple instrumentation.**

## 2.3 Samples for the experimental campaign

The overall experimental study comprised of a base campaign and two extensions. The base campaign used 18 samples from three suppliers, as summarised in Table 1. The extensions (extension 1 and extension 2) considered two further variables, resulting in a further 18 experiments (36 in total for the ceilings). For extension 1, the impact of not edge-gluing was considered for samples with thick lamella (40-40-40). This extension was considered as in dialogue with the manufacturers, it was made clear that differences exist in terms of both the edge-gluing procedure and the type of adhesive used to edge-glue. For extension 2, the impact of adopting a heat-resistant adhesive (HBX) was considered over the use of a non-heat-resistant adhesive (HBS), as utilised in the base campaign. In extension 2 the samples had thinner lamella (20-20-20-20-20) to exacerbate any potential glue line integrity failure. For objectivity moving forward, the data corresponding to specific suppliers is anonymised, with suppliers randomly assigned the designation A, B or C. In advance of each experiment, sample density and moisture content were measured. The former is shown in Figure 2, with the moisture content an average 9.4% across all samples (1 to 36).

## 2.4 Instrumentation

Instrumentation comprised in-depth thermocouples to measure solid-phase temperatures, as shown in Figure 1 (right). Temperatures were separately measured at the location of a joint in the first lamella and away from a joint. Thermocouples were sheathed Type K, with a 2 mm diameter. They were installed from the sample sides, i.e., parallel to the isotherms, at depths of 5, 10, 20, 30, 40 and 50 mm from the exposed face. To estimate the char depth in function of time, the 300°C isotherm was taken as the position of the char front (Bartlett et al., 2019). The position was linearly

interpolated between thermocouple locations. Alongside in-depth temperature, the total HRR of the sample and panel was measured via a calorimeter (in kW). The sample mass in function of time was measured via a scale (in kg).

**Table 1 – Samples for experimental campaign.**

Experiment number	Campaign	Adhesive	Edge-glued	Supplier	Lamella [mm]
1 – 3	Base (Base 20 mm or Base 40 mm)	HBS	Yes	A	40-40-40
4 – 6					20-20-20-20-20
7 – 9				B	40-40-40
10 – 12					20-20-20-20-20
13 – 15				C	40-40-40
16 – 18					20-20-20-20-20
19 – 21	Extension 1 (Ext 1)	HBS	No	A*	40-40-40
22 – 24				B	40-40-40
25 – 27				C	40-40-40
28 – 30	Extension 2 (Ext 2)	HBX	Yes	A*	20-20-20-20-20
31 – 33				B	20-20-20-20-20
34 – 36				C	20-20-20-20-20

\* Samples produced for R&D purposes and are not from the suppliers main production line / process.

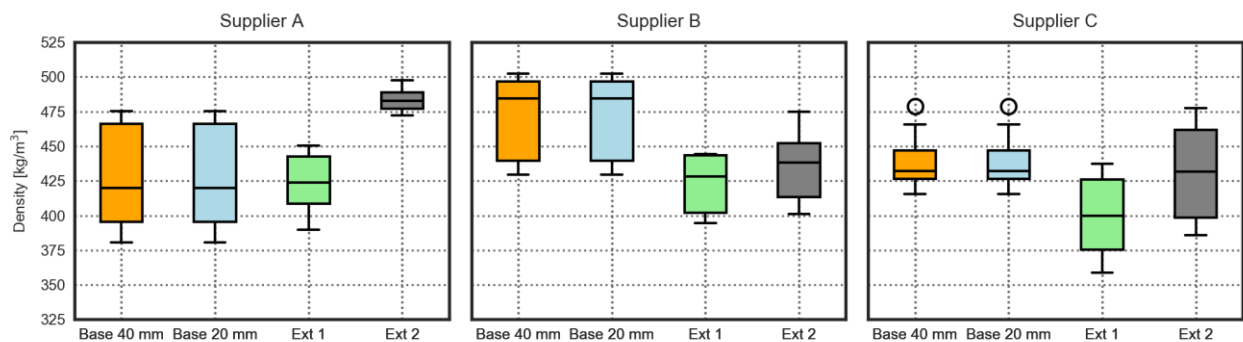


**Figure 2 – Sample density by supplier and campaign.**

### 3 RESULTS

Illustrative results are presented in terms of the two primary parameters of interest, charring depth and MLR in function of time, with a further comparison of results made in Section 4. Results are presented as mean values (dashed line) plus an uncertainty envelope corresponding to the standard error of the mean (shaded) (Guthrie, 2020).

#### 3.1 Charring depth

Figure 3 compares the charring depth with time for the three suppliers in the ‘base campaign’, as measured at the joint, within the lamella or the aggregated combination of the two locations. Figure 4 compares charring depth across campaigns for different thermocouple (TC) locations (for this purpose, manufacturer data is grouped together).

#### 3.2 Mass loss rate

To compare extensions, Figure 5 plots MLR for the extension 1 and extension 2 campaigns for all suppliers. The final plot provides a comparison across variables by grouping supplier samples together. For supplier B, joint results and the associated uncertainty envelope are influenced by a high degree of fluctuation and potential thermocouple failure in one of the three experiments.

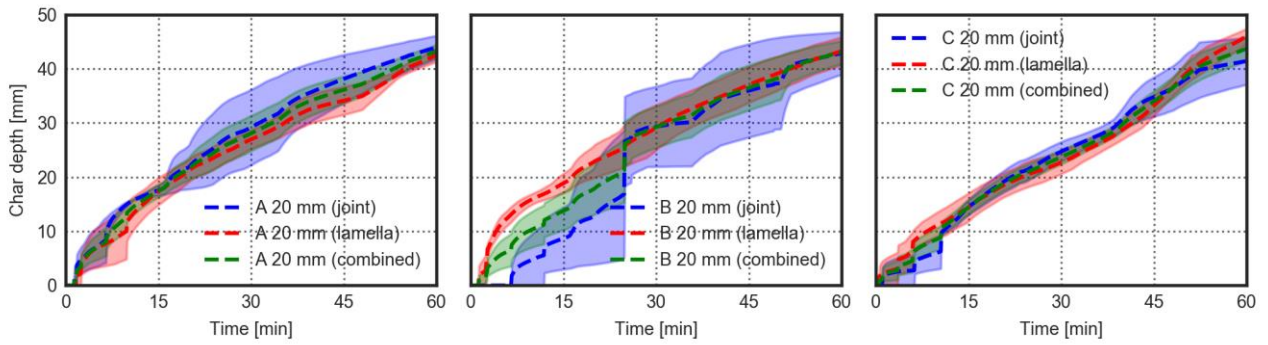


**Figure 3 - Mean sample charring depth and standard error of the mean in function of time, by supplier (20-20-20-20 samples) – Experiments 1 to 18.**

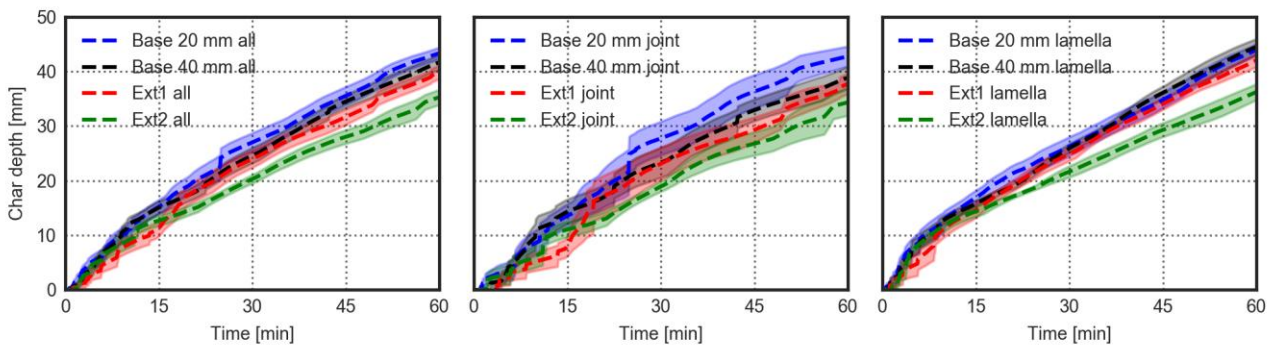


**Figure 4 – Charring depth with time, suppliers grouped: comparison across camp (left) comparison across campaigns for all TC locations; (centre) for TCs in central joint, and (right) for TCs in lamella.**

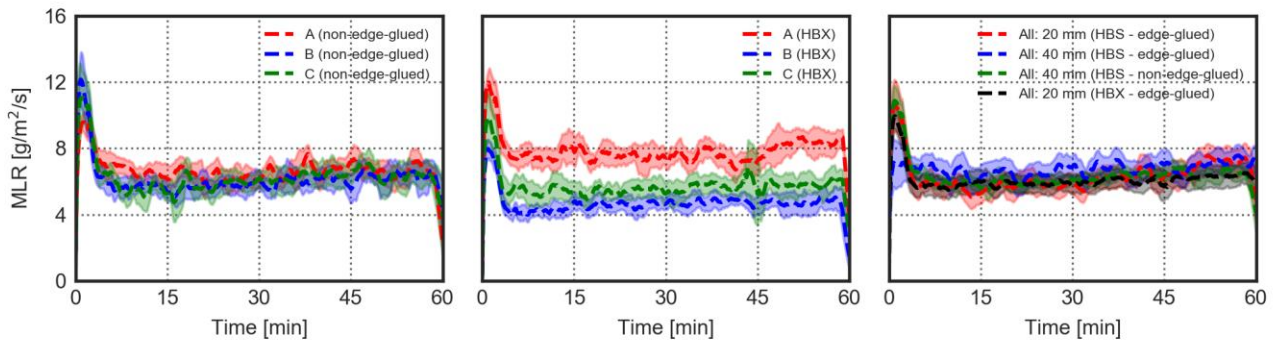


**Figure 5 - MLR with time – comparison across campaigns (left) by supplier comparison of non-edge-glued samples (experiments 19-27); (centre) by supplier comparison of HBX samples (experiments 18-36); (right) combined manufacturer data to compare base, extension 1 and extension 2 campaigns (all experiments).**

#### 4 ANALYSIS

The primary objective of the study was to establish if a notable difference exists in the fire performance characteristics of samples across suppliers, given the same lamella, adhesive and edge-gluing conditions. The secondary objective was to establish if varying parameters such as lamella thickness, edge-gluing or adhesive choice, impact the fire performance characteristics. These objectives are considered herein through a statistical assessment, i.e., analysis of variance (ANOVA). Comparisons are based on two parameters: (1) the final depth of char, taken as the position of the 300°C isotherm; and (2) the steady-phase MLR, taken as the mean MLR between 15 to 60 min from the onset of the experiment. The definition of the MLR in terms of a transient and steady-phase is in broad consistency with Emberley, et al. (2017).

## 4.1 Charring depth

Figure 6 provides a box plot of final charring depth after 60 min, where results at the joint and within the lamella are grouped. A plot is provided per supplier, with each bar corresponding with a campaign, i.e., base, extension 1 (edge-glued vs. not) and extension 2 (HBS vs. HBX). Two statistical tests have been undertaken on the final charring depth, Bartlett’s test, as detailed by Guthrie (2020), is adopted to check the homogeneity of variances, i.e., null hypothesis: samples from populations have equal variances. One way analysis of variance (ANOVA) (Guthrie, 2020) is adopted to test the consistency of the mean values of the population, i.e., null hypothesis: samples from populations have equal means. Both statistics return a p-value. Where the p-value is non-significant, there is no rejection of the null hypothesis and one concludes that data either has comparable means, variance, or both (depending upon the statistical test conducted). The threshold for significance of the p-value adopted is 0.05 in both cases, i.e., where the p-value is > 0.05, the null-hypothesis is accepted.

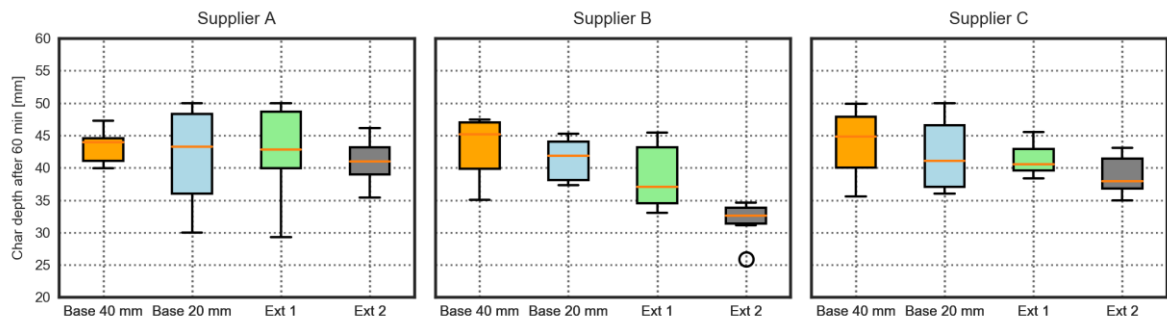


**Figure 6 - Charring depth after 60 min, by supplier and campaign.**

Table 2 gives the p-values from ANOVA (mean) and Bartlett (variance) for the base campaigns and extensions, considering the depth of char after 60 min of the experiment. Separate p-values are provided for the char depth at the joint, lamella or for the combination of both. The mean and variance in sample charring depth (position of the 300°C isotherm) after 60 min can be said to be dissimilar across suppliers where the p-value is less than 0.05. These instances are highlighted in **bold** and indicate that differences between suppliers (in terms of charring depth after 60 min) emerge: (i) at the joints of samples that are not-edge-glued; (ii) at the joints of samples that adopt a heat-resistant adhesive; and (iii) when considering the char formation across both char depth measurement locations in samples that adopt a heat-resistant adhesive.

**Table 2 - ANOVA (consistency of mean) and Bartlett (consistency of variance) tests for charring depth after 60 min, comparison across suppliers.**

Campaign	Measured at joint		Measured in lamella		Across both joint & lamella	
	ANOVA (mean) p-value	Bartlett (variance) p-value	ANOVA (mean) p-value	Bartlett (variance) p-value	ANOVA (mean) p-value	Bartlett (variance) p-value
Base – 20 mm	0.882	0.673	0.446	0.588	0.972	0.343
Base – 40 mm	0.391	0.636	0.103	0.408	0.979	0.217
Extension 1*	0.327 / <b>0.042</b>	0.167 / 0.281	0.296 / 0.059	0.503 / 0.183	0.495 / 0.287	0.108 / 0.154
Extension 2*	<b>0.027 / 0.029</b>	0.94 / 0.931	0.059 / 0.101	0.183 / 0.083	<b>0.001 / 0.004</b>	0.908 / 0.941

\* Including / excluding supplier A R&D samples

## 4.2 Mass loss rate

Figure 7 provides a box plot of steady-phase MLR. A plot is provided per supplier, with each bar corresponding with a campaign. Table 3 gives the p-values from ANOVA (mean) and Bartlett (variance) for the base campaigns and extensions, considering the steady-phase MLR. The results

would suggest that the mean values of MLR across suppliers are only comparable when comparing non-edge-glued samples (extension 1).

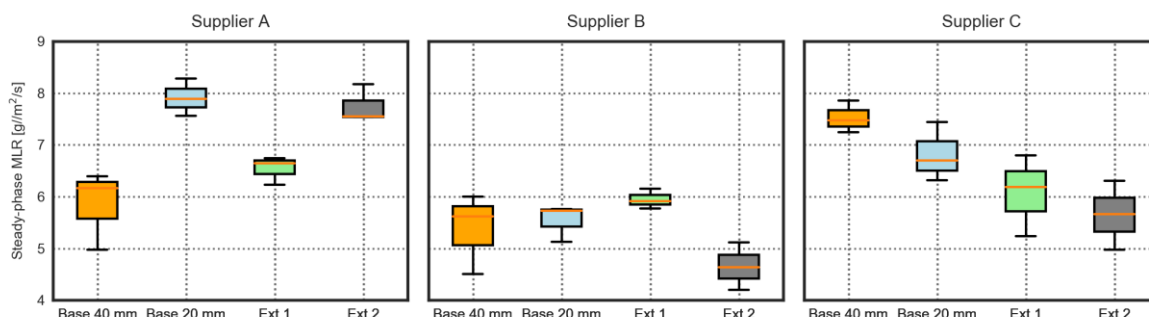


Figure 7 - Steady-phase MLR, by supplier and campaign.

Table 3 - ANOVA (consistency of mean) and Bartlett (consistency of variance) tests for steady-phase MLR, comparison across suppliers.

Campaign	Steady mass loss rate	
	ANOVA (mean) p-value	Bartlett (variance) p-value
Base – 20 mm	<b>0.015</b>	0.509
Base – 40 mm	<b>0.002</b>	0.777
Extension 1*	0.367 / 0.796	0.174 / 0.115
Extension 2*	<b>0.001 / 0.099</b>	0.738 / 0.647

\* Including / excluding supplier A R&D samples

## 5 CONCLUSIONS

Based upon the analyses conducted to date, the following can be concluded: (i) The final charring depth after 60 min is not statistically different between suppliers for the same panel configuration; (ii) Considering the charring depth after 60 min there is a statistically significant difference between samples adopting non-heat-resistant (HBS) vs. heat resistant (HBX) adhesives. No significant difference was observed across other variables, i.e., lamella thickness and edge-gluing procedure; (iii) Statistically significant differences exist between suppliers when considering the steady-phase MLR for all edge-glued samples, but regarding Figure 2, it is plausible that the difference is a function of the starting density and also variability in the type of adhesive used for edge-gluing; (iv) there is no statistical difference in steady-phase MLR between suppliers when considering non-edge-glued samples; and (v) Considering the steady-phase MLR, there are no significant statistical differences across the variables studied, i.e., lamella thickness, edge-gluing procedure or adhesive type. Given (i) to (v), it is suggested that there should be a high degree of transferability of findings from large-scale experiments across suppliers, with an emphasis on exposed ceilings, provided key parameters are consistent (e.g., lamella thickness, adhesive type and edge-glue condition). Further analysis of wall samples will establish if this conclusion might be further generalised.

## REFERENCES

- Bartlett, A.I., Hadden, R.M., Bisby, L.A., 2019. A review of factors affecting the burning behaviour of wood for application to tall timber construction. *Fire Technol.* 55, 1–49. <https://doi.org/10.1007/s10694-018-0787-y>
- CLT Special Interest Group Structural Timber Association [WWW Document], 2021. URL <http://www.structuraltimber.co.uk/sectors/clt-special-interest-group> (accessed 5.4.21).
- Emberley, R., Gorska, C., Bolanos, A., Lucherini, A., Solarte, A., Soriguer, D., Gonzalez, M.G., Humphreys, K., Hidalgo, J.P., Maluk, C., Law, A., Torero, J.L., 2017. Description of small and large-scale cross laminated timber fire tests. *Fire Saf. J.* 91, 327–335. <https://doi.org/10.1016/j.firesaf.2017.03.024>
- Guthrie, W.F., 2020. NIST/SEMATECH e-Handbook of Statistical Methods (NIST Handbook 151). <https://doi.org/10.18434/M32189>

## SENSITIVITY ANALYSIS OF A PYCiF MODEL

Robert Pečenko<sup>a</sup>, Tomaž Hozjan<sup>a</sup>

<sup>a</sup> University of Ljubljana, Faculty of Civil and Geodetic Engineering, Ljubljana, Slovenia

### Abstract

A sensitivity analysis of a recently developed model PyCiF is presented in the paper. The PyCiF model was derived to determine the charring of timber elements exposed to natural fire. It is based on a highly detailed physical description of the phenomenon and couples the process of heat and mass transfer in timber with the process of pyrolysis, where Broido-Shafizadeh pyrolysis model is embedded. The charring is determined based on a new more general criterion, which improves the existing, most commonly used charring criterion based on the 300°C isotherm. Since model contains many parameters, it is impossible to quickly estimate, the most and the least influential ones, that have the impact on the main model outcome, i.e. charring rate. For this purpose, an in-depth sensitivity analysis is performed to determine the impact of the kinetic parameters related to the process of pyrolysis which mainly governs the process of charring. The determination of the most/least influential parameters is needed for more specified experiments which are further needed to fully validate the model for wider application. In addition, discovering the non-influential model parameters can be a basis for model simplification

**Keywords:** PyCiF model, heat-mass-pyrolysis model, new charring criterion, sensitivity analysis

### 1 INTRODUCTION

In fire conditions, timber structures are subjected to charring, which leads to the reduction of fire resistance and increased deformability of the structure. Thus, charring is one of the most governing phenomena which determines the fire resistance of timber structures. There are different approaches of how to determine charring of timber. In the past, several experimental studies have been carried out, which yield empirical expressions for the determination of charring depth (Schaffer, 1967; Mikkola, 1990). However, due to the experimental background, these empirical expressions are usually limited to cases with simple geometry, standard fire exposure or precisely defined non-standard fires. This disadvantages were attempted to be overcome by the use of the heat and heat-mass transfer numerical models (Tsai *et al.*, 2013; Pečenko *et al.*, 2015), where the charring depth was determined based on the calculated temperature isotherm (char front temperature) 300 °C. However, the latest research studies showed that the char front temperature is valid in general only for standard fire exposure, while in case of non-standard fire exposure char front temperature varies and is dependent on the fire curve. For this reason, new, more advanced numerical model based on the detailed physical description of the charring phenomena, named PyCiF, was lately presented by the authors (Pečenko and Hozjan, 2021). The new model couples an advanced 2D heat-mass model with a pyrolysis model, where a new charring criterion based on a physical phenomenon is implemented in the PyCiF model to determine the charring of wood. This presents the main advantage of the new PyCiF model in comparison to common modelling approaches. However, to fully exploit the advantages of the new PyCiF model, an in-depth model validation and verification is required in order to be fully applicable for non-standard fires. Sensitivity analysis can represent a first step in achieving this, since it is a powerful tool to evaluate the influence of model input parameters on the model outcomes. Therefore, in this paper the sensitivity analysis of new PyCiF model (Pečenko and Hozjan, 2021) is presented. Since the derived model is highly complex, the main objective of this paper is to identify the most and the least influential parameters in order to have a better overview regarding the further model validation and verification.

## 2 PYCIF MODEL

The PyCiF model is divided in two sub-models, i.e. pyrolysis model and heat-mass transfer model, which are computationally coupled. Both sub-models are briefly presented in the following subsections.

### 2.1 Heat-mass model

The basic equations of the heat-mass model consist of three continuity equations describing the conservation of bound water, water vapour and residual gas-mixture, coupled by the energy conservation equation. The mass continuity equations are:

$$\frac{\partial c_b}{\partial t} = \nabla \cdot \left( \mathbf{D}_0 \exp\left(-\frac{E_b}{RT}\right) \nabla c_b + \mathbf{D}_0 \exp\left(-\frac{E_b}{RT}\right) \frac{c_b E_b}{RT^2} \nabla T \right) + \dot{c} \quad (1)$$

$$\frac{\partial(\varepsilon_g \tilde{\rho}_v)}{\partial t} = \nabla \cdot \left( -\varepsilon_g \tilde{\rho}_v \frac{\mathbf{K} K_g}{\mu_g} \nabla P_g + \varepsilon_g \tilde{\rho}_g \mathbf{D}_{vg} \nabla \left( -\frac{\tilde{\rho}_v}{\tilde{\rho}_g} \right) \right) \quad (2)$$

$$\frac{\partial(\varepsilon_g \tilde{\rho}_g^*)}{\partial t} = \nabla \cdot \left( -\varepsilon_g \tilde{\rho}_v \frac{\mathbf{K} K_g}{\mu_g} \nabla P_g + \varepsilon_g \tilde{\rho}_g \mathbf{D}_{gv} \nabla \left( -\frac{\tilde{\rho}_g^*}{\tilde{\rho}_g} \right) \right) \quad (3)$$

Above, denotations  $c_b$  and  $\tilde{\rho}_v$  represent the concentrations of bound water and water vapour. The concentration of residual gas mixture,  $\tilde{\rho}_g^*$ , consists of the concentration of the pyrolytic gases,  $\tilde{\rho}_{g,p}$  and air concentration  $\tilde{\rho}_a$ . Namely,  $\tilde{\rho}_g^* = \tilde{\rho}_{g,p} + \frac{M_{g,p}}{M_a} \tilde{\rho}_a$ , where  $M_{g,p}$  denotes the molar mass of pyrolytic gases and  $M_a$  is the molar mass of air. The concentration of the entire gas mixture  $\tilde{\rho}_g$  is determined as  $\tilde{\rho}_g = \tilde{\rho}_v + \tilde{\rho}_g^*$ .  $\varepsilon_g$  is porosity of timber,  $t$  is time,  $\nabla$  is nabla operator.  $\mathbf{D}_0$ ,  $\mathbf{K}$  and  $\mathbf{D}_{vg}$  ( $= \mathbf{D}_{gv}$ ) are matrices, that in the diagonal contain base values for bound water diffusion coefficients, specific permeability of dry wood and diffusion coefficients of residual gases into vapour for different material directions, i.e. longitudinal and transverse.  $E_b$  represent the activation energy  $R$  is universal gas constant,  $T$  is temperature,  $K_g$  is relative permeability,  $\mu_g$  is dynamic viscosity,  $P_g$  is pressure of the gas mixture and  $\dot{c}$  is sorption rate (Pečenko *et al.*, 2015; Pečenko and Hozjan, 2021)

Energy conservation equation is:

$$\rho C \frac{\partial T}{\partial t} = \nabla \cdot (\mathbf{k} \nabla T) - \left( \rho C \frac{\mathbf{K} K_g}{\mu_g} \nabla P_g \right) \nabla T - \Delta H_s \dot{c} - Q \quad (4)$$

where  $\rho C$  represent the heat capacity of the entire timber volume,  $\mathbf{k}$  is the matrix, containing in the diagonal the thermal conductivities for different material directions,  $\Delta H_s$  is latent heat of sorption and  $Q$  represent energy sink or release due to the endo- or exothermic pyrolysis reaction.

Boundary conditions, prescribing the bound water flux  $\mathbf{J}_b$ , water vapour flux  $\mathbf{J}_v$ , pressure and heat flux  $h_{cr}$  at the contact between timber volume and surroundings, are:

$$\mathbf{n} \cdot \mathbf{J}_b = 0, \mathbf{n} \cdot \mathbf{J}_v = \beta_v (\tilde{\rho}_{v,\infty} - \tilde{\rho}_v), h_{cr} = k \frac{\partial T}{\partial n}, P_g = P_{g,\infty} \quad (5)$$

where  $\mathbf{n}$  represents the unit vector normal to the outer surface of timber volume,  $\beta_v$  is mass transfer coefficient,  $\tilde{\rho}_{v,\infty}$  is the vapour concentration in the ambient,  $P_{g,\infty}$  is the pressure of the ambient.

The initial conditions are:  $c_b = c_{b,0}$ ,  $\tilde{\rho}_v = \tilde{\rho}_{v,0}$ ,  $P_g = P_{g,0}$  and  $T = T_0$ , where index 0 denotes the initial value of the variable.

### 2.2 Pyrolysis model

The pyrolysis of wood can be in a good approximation, described by the pyrolysis of the cellulose. For fire conditions the model of Broido-Shafizadeh (Bradbury *et al.*, 1979) describes the pyrolysis of cellulose with a sufficient accuracy. The cellulose pyrolysis is governed by the initiation reaction (active cellulose) followed by two competing reactions leading to volatiles, char and gases, as seen in Fig. 1.

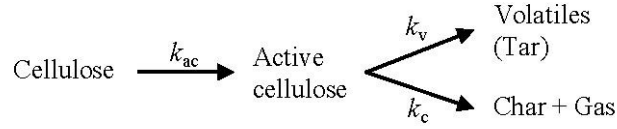


Fig. 1 Pyrolysis kinetic scheme (Broido-Shafizadeh)

The equations describing cellulose pyrolysis are as follow:

$$\frac{d\rho_c}{dt} = -k_{ac}\rho_c \quad (6)$$

$$\frac{d\rho_{ac}}{dt} = k_{ac}\rho_c - (k_v + k_c)\rho_{ac} \quad (7)$$

$$\frac{d\rho_t}{dt} = k_v \quad (8)$$

$$\frac{d\rho_{ch}}{dt} = 0.35 k_c\rho_{ac} \quad (9)$$

$$\frac{d\tilde{\rho}_{g,p}}{dt} = 0.65 k_c\rho_{ac} \quad (10)$$

where  $\rho_c$ ,  $\rho_{ac}$ ,  $\rho_t$  and  $\rho_{ac}$  denote the density of the cellulose, active cellulose, tar and char, respectively. Kinetic parameters  $k_i$  govern the rate of the  $i$ -th ( $i = ac, v, c$ ) pyrolysis reaction and follow the Arrhenius law:  $k_i = A_i \exp\left(\frac{-E_i}{RT}\right)$ , where  $R$  is the universal gas constant. Pre-exponential factors  $A_i$  ( $s^{-1}$ ) and activation energies  $E_i$  ( $\text{kJ mol}^{-1}$ ) are given as follow (Bradbury *et al.*, 1979):  $A_{ac} = 1.7 \cdot 10^{21}$ ,  $A_c = 7.9 \cdot 10^{11}$ ,  $A_v = 1.9 \cdot 10^{16}$  and  $E_{ac} = 242.6$ ,  $E_c = 153.1$ ,  $E_v = 197.9$ . As presented in Pečenko and Hozjan (2021), the charring is determined when the final char yield is reach, which can be determined from the equation  $\frac{d\rho_{ch}}{dt} = 0.35 k_c\rho_{ac}$ .

### 2.3 Solution procedure

The presented sub-models are computationally coupled, the solution of each sub-model is found numerically. The entire time domain is divided into times steps  $dt = t^i - t^{i-1}$ , within each time step the solution is obtained. The solution of pyrolysis model (Eqs. (6)-(7)) is obtained with Matlab embedded solver for solving ordinary partial differential equations ode23s. The results of this solution are then considered in the heat-mass sub-model, which is solved by the own developed software built in Matlab environment.

## 3 SENSITIVITY ANALYSIS

When using complex numerical models, the need of the sensitivity analysis is of utmost importance. The sensitivity analysis is a strong tool to evaluate the degree of the uncertainty in the model output when dealing with the uncertainties in the model input (Saltelli *et al.*, 2008). In addition, it also enables the identification of main input parameters on the model outcomes, which, in turn, provide better knowledge of the model and can be used for its verification. In general, two types of sensitivity analyses can be identified, i.e. local and global methods. In this paper, the local method is used, which determines the sensitivity measures for one variable at the time, meaning that one variable is being changed, while others being fixed.

The objective of the sensitivity analysis is to analyse the influence of pyrolysis model parameters on the charring rate. Therefore, the impact of kinetic parameters  $k_i$  is investigated. More precisely, the pre-exponential factors  $A_i$  and activation energies  $E_i$  are varied.

An index  $S_{y_j|x_i}$  is introduced to quantify the influence of the particular input variable  $x_i$  ( $E_i$  or  $A_i$ ) on the output variable  $y_j$  ( $\beta$ ), normalized by the reference value  $y_{ref}$ , which is calculated with the parameters of the pyrolysis reaction given in Table 1. Thus the index  $S_{y_j|x_i}$  is calculated as:

$$S_{\beta/x_i} = \frac{\beta_{x_i} - \beta_{\text{ref}}}{\beta_{\text{ref}}} \quad (11)$$

where  $\beta_{\text{ref}}$  represent the reference charring rate, determined based on the basic input parameters,  $\beta_{x_i}$  is the charring rate determined based on the varied input parameter  $x_i$ .

### 3.1 Model input and output parameters

Numerical setup for the sensitivity analysis, boundary conditions and initial conditions are shown in Fig.2. Fire exposure from one side is considered, where two different fire curves are accounted for in the analysis, i.e. “fast” and “slow” fire curve as presented. For the analysis, the timber specimen is discretized by 32 quadrilateral finite elements, giving the element size of  $2.5 \times 2.5$  mm. The thermal conductivity and specific heat are considered according to EN 1995-1-2 (2005), other material parameters can be found in Pečenko *et al.* (2015) and Pečenko and Hozjan (2021).

The variations of the pre-exponential factors  $A_i$  and activation energies  $E_i$  are given below:

$$E_{i,\Delta} = \{0.88 \ 0.9 \ 0.92 \ 0.94 \ 0.95 \ 0.96 \ 0.98 \ 1.02 \ 1.04 \ 1.06 \ 1.08 \ 1.1 \ 1.12\} E_i \quad (12)$$

$$A_{i,\Delta} = \{0.1 \ 0.2 \ 0.4 \ 0.5 \ 0.6 \ 0.8 \ 1.2 \ 1.4 \ 1.5 \ 1.6 \ 1.8\} A_i \quad (13)$$

where  $E_i$  and  $A_i$  ( $i = ac, c, v$ ) are base values given in section 2.1.

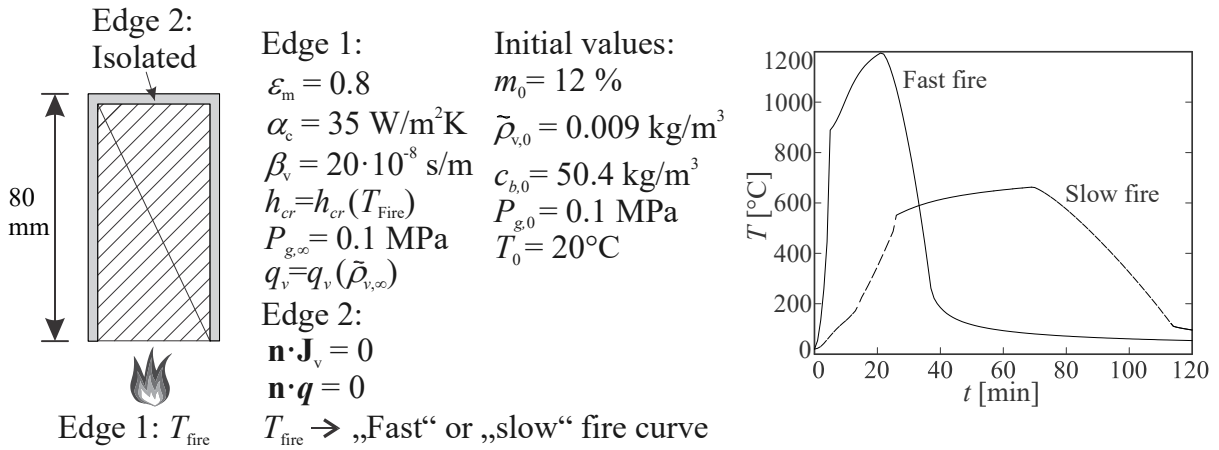


Fig. 2 Numerical setup, data for boundary and initial conditions, considered fire scenarios

### 2.3 Results and discussion

In Fig.3, the magnitude of the sensitivity index  $S_{\beta/x_i}$  for the case with fast fire is presented. The index indicates the impact of the input parameters on the charring rate, and takes values between 0.12 (Fig.3(b),  $E_{ac,\Delta} = 0.88 E_{ac}$ ) and  $-0.12$  (Fig.3(d),  $E_{c,\Delta} = 0.88 E_c$ ), meaning that this two parameters ( $E_{ac}$  and  $E_c$ ) have the most influence on the charring rate. When the parameter  $E_{ac,\Delta}$  is reduced to  $0.88 E_{ac}$ , the charring rate increases by 12 %. On the contrary, when parameter  $E_{c,\Delta}$  is reduced to  $0.88 E_c$ , the charring rate decreases by 12 %. The least influential are parameters that govern the rate of the volatile reaction ( $k_v$ ), namely,  $A_v$  and  $E_v$ , since the charring rate does not increase by more than 2 %. In general, it is also observed, that pre-exponential factors have less influence on the charring rate. Some trends are discovered as well. Namely, reducing  $E_{ac}$  and  $E_v$  (bigger  $k_{ac}$  and  $k_v$ ) leads to bigger charring rate, reducing  $E_c$  (bigger  $k_c$ ) leads to smaller charring rate, reducing  $A_{ac}$  and  $A_v$  (smaller  $k_{ac}$  and  $k_v$ ) leads to smaller charring rate, reducing  $A_c$  (smaller  $k_c$ ) leads to bigger charring rate.

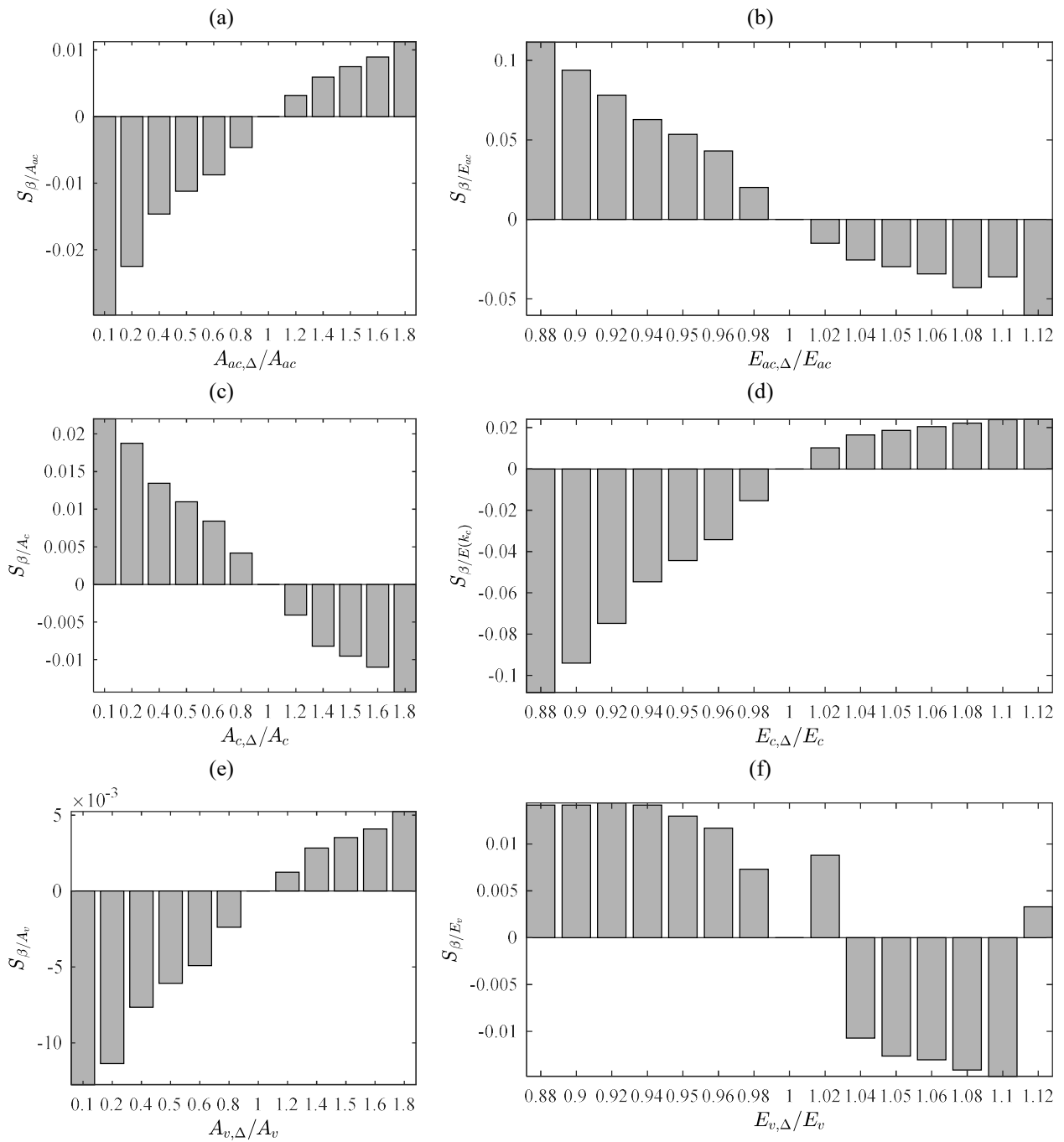


Fig. 3 The influence of parameters  $A_i$  and  $E_i$  on the sensitivity index  $S_{\beta/x_i}$  in case of fast fire regime

In Fig.4, the magnitude of the sensitivity index  $S_{\beta/x_i}$  for the case with slow fire is presented. It is evident that the parameters  $A_{ac}$  and  $A_v$  (Figs.4(a) and (e)) are almost non-influential, since the value of the sensitivity index  $S_{\beta/x_i}$  is very small, when this two parameters are varied. The most influential is parameter  $E_{ac}$ , since it increases the charring rate by around 75 % in case when  $E_{ac,\Delta} = 0.88 E_{ac}$  (Fig.4(b)). Parameters  $A_c$  and  $E_c$  have medium influence on the charring rate (around 2% increase), where the calculation with  $A_{c,\Delta} = 0.5 A_c$  could be a potential outlier. Parameter  $E_v$  has also medium influence on the charring rate (around 2%), where, similarly, the calculation with  $E_{v,\Delta} = 0.9 E_v$  could be a potential outlier. Compared to the case with fast fire, here, trends can be hardly discovered.

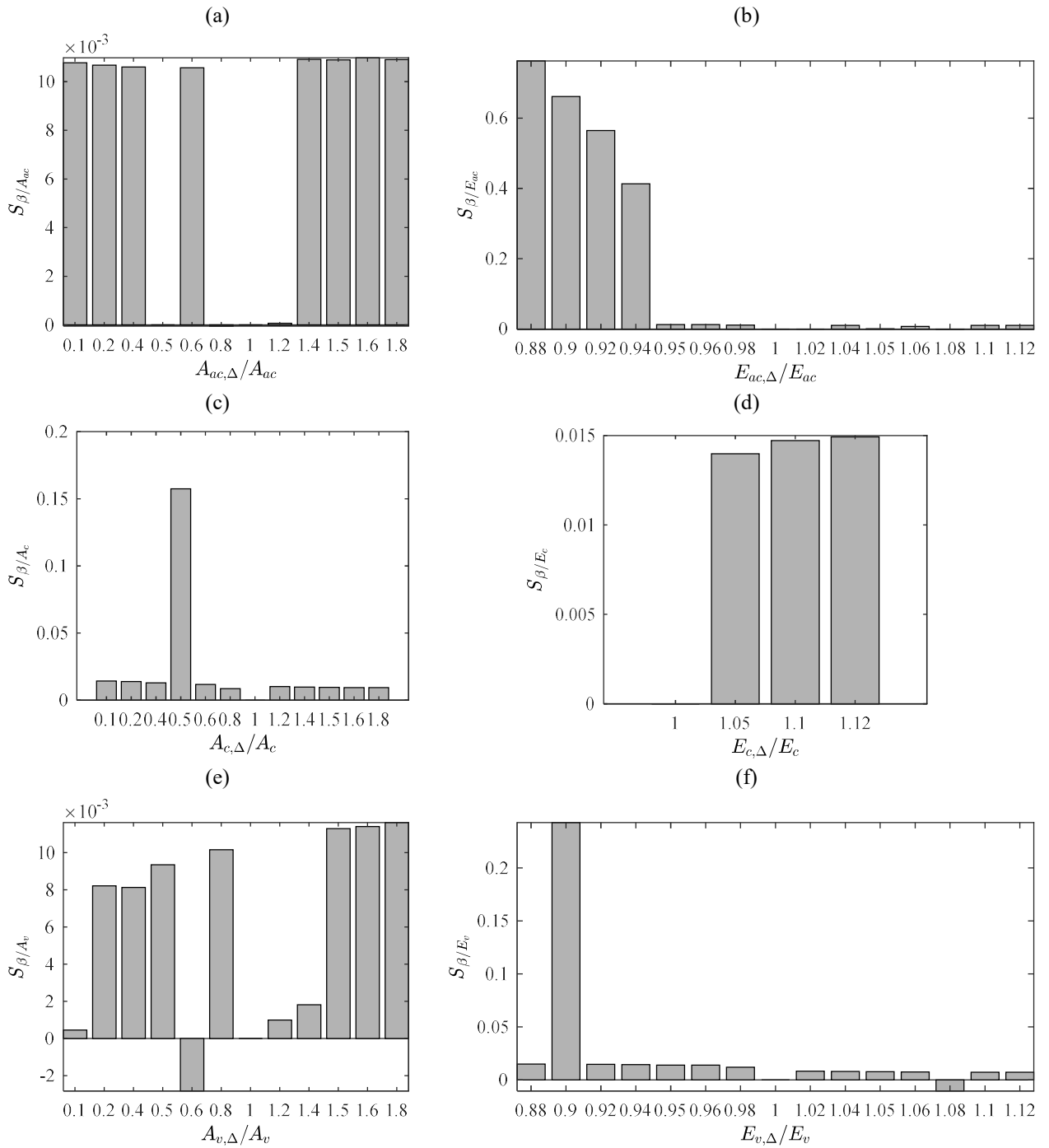


Fig. 4 The influence of parameters  $A_i$  and  $E_i$  on the sensitivity index  $S_{\beta/x_i}$  in case of slow fire regime

#### 4 CONCLUSIONS

The main objective of the paper was to perform a sensitivity study of a new PyCiF model (Pečenko and Hozjan, 2021) in order to discover the most and the least influential model parameters, which will allow a better further in-depth model validation and verification. Based on the sensitivity study, the following was discovered:

- In general, pre-exponential factors  $A_i$  have a smaller impact compared to the activation energies  $E_i$
- In case of the fast fire, the increase in  $k_{ac}$  and  $k_v$  leads to higher charring rate, while the increase in  $k_c$  leads to smaller charring rate.
- In case of the slow fire, the trend is not so obvious, however, it is evident that increasing  $k_{ac}$  leads to major increase of charring rate, compared to other input parameters.

- In case of the fast and the slow fire, the reaction rate  $k_v$  does not have significant influence on the charring rate.
- The sensitivity study shows, that for further model validation, the most influential parameters are reaction rate  $k_{ac}$  and  $k_c$ .

## ACKNOWLEDGMENTS

The author Robert Pečenko acknowledges the financial support from the Slovenian Research Agency for the project Z2-8160 “Modelling pyrolysis to determine the decomposition of wood in natural fire”.

The authors acknowledge the financial support from the Slovenian Research Agency (research core funding No. P2-0260).

## REFERENCES

- Bradbury A. G. W., Sakai Y., Shafizadeh F. 1979. *A Kinetic Model for Pyrolysis of Cellulose*. *Journal of Applied Polymer Science*, 23, p. 3271–3280.
- EN 1995-1-2. 2005. *Eurocode 5: Design of timber structures - Part 1-2: General - Structural fire design*.
- Mikkola, E. 1990. *Charring of wood*. Research reports 689, Espoo, VTT, Technical Research Centre of Finland
- Pečenko R., Hozjan T. 2021. *A novel approach to determine charring of wood in natural fire implemented in a coupled heat-mass-pyrolysis model*. *Holzforschung*, 75(2), p. 148–158.
- Pečenko R., Svensson S., Hozjan T. 2015. *Modelling heat and moisture transfer in timber exposed to fire*. *International journal of heat and mass transfer*, 78, p. 598–605.
- Saltelli A., Ratto M., Andres T., Campolongo, F., Cariboni J., Gatelli D., Saisana M., Tarantola S. 2008. *Global sensitivity analysis: the primer*, Wiley, Chichester, United Kingdom.
- Schaffer, E.L. 1967. *Charring rate of selected woods-transverse to grain*. Forest Service Research Paper FPL 69, Forest Products Laboratory, Madison, Wisconsin
- Tsai K., Carradine D., Moss P., Buchanan A. 2013. *Charring rates for double beams made from laminated veneer lumber (LVL)*. *Fire and Materials*, 37, p. 58-74.

## A SENSITIVITY ANALYSIS APPLIED TO THE REDUCED CROSS-SECTION METHOD OF A TIMBER BEAM UNDER PARAMETRIC FIRE

Sabina Huč<sup>a,b</sup>, Tomaž Hozjan<sup>a</sup>

<sup>a</sup> University of Ljubljana, Faculty of Civil and Geodetic Engineering, Ljubljana, Slovenia

<sup>b</sup> University of Ljubljana, Faculty of Chemistry and Chemical Technology, Ljubljana, Slovenia

### Abstract

The reduced cross-section method given in the standard EN 1995-1-2 is widely used in Europe to determine the mechanical resistance of timber structural members exposed to the standard fire. A current definition of the method's key parameters that are the charring depth and the thickness of zero-strength layer has to be further examined and possibly redefined to extent the method's use for the case of non-standard fires. In this regard, in the present paper a simple sensitivity analysis is applied to the reduced cross-section method of a timber beam subjected to a parametric fire. The influence of the bending resistance in fire conditions and the elastic section modulus of residual cross-section is investigated on the charring depth and the thickness of zero-strength layer. The results show that the latter should take higher value in the case of parametric fire than that currently prescribed for the standard fire if the charring depth remains unchanged.

**Keywords:** charring depth, parametric fire, reduced cross-section method, timber beam, zero-strength layer

### 1 INTRODUCTION

According to the European standard EN 1995-1-2 (2005) timber structures have to be designed to ensure an adequate fire resistance. The standard EN 1995-1-2 (2005) gives two methods to determine the fire resistance of timber elements, namely the reduced material properties method and the reduced cross-section method. Currently, the process of updating European standards is ongoing, and supposedly, in the future version of EN 1995-1-2 (2005), the reduced cross-section method will remain the only simplified method for a determination of fire resistance of timber elements.

The reduced cross-section method is based on the linear elastic theory where the bending resistance of timber beam in fire conditions  $M_{Rd,fi}$  is determined as a product of the characteristic bending strength and the elastic section modulus of an effective cross-section. The effective cross-section is a rectangular residual cross-section reduced by the thickness of zero-strength layer  $d_0$  as illustrated in Fig. 1, while the rectangular residual cross-section is an initial rectangular cross-section reduced for the charring depth  $d_{ch}$ . The elastic section modulus of residual cross-section  $W_{res}$  can either be determined by experiments or numerical models as a remaining part of the cross-section after being subjected to a fire. Commonly, the bending resistance in fire conditions  $M_{Rd,fi}$  is determined experimentally (Lange et al., 2015). Once the bending strength and the parameters  $W_{res}$  and  $M_{Rd,fi}$  are known, the thicknesses  $d_{ch}$  and  $d_0$  can be determined, respectively, using the reduced cross-section method. In the latter, the zero-strength layer is applied to account for the reductions of stiffness and strength of uncharred timber due to elevated temperatures. Standard EN 1995-1-2 (2005) gives a fixed value of the thickness of zero-strength layer  $d_0 = 7$  mm for the standard fire exposure and an expression to determine the charring depth  $d_{ch,EC}$  for parametric fire exposure. Whereas, no recommendations are given for the thickness  $d_0$  in case of parametric fire exposures, hence the value of 7 mm is commonly used in practice in those cases as well. Some scientific findings (Schmid et al., 2015; Lange et al., 2015; Huč et al., 2021) suggest that the thickness of zero-strength layer of 7 mm can be on an unsafe side for the parametric fire exposure. The present paper is an additional attempt

to find an adequate thickness of zero-strength layer in case of parametric fire exposure, which could contribute to an optimal update of the reduced cross-section method.

In the present paper, a simply supported timber beam under bending and subjected to a parametric fire is analysed by the use of advanced numerical models. A hygro-thermal model and a mechanical model are used to determine the elastic section modulus of residual cross-section  $W_{res}$  and the bending resistance in fire conditions  $M_{Rd,fi}$ , respectively. The charring depth  $d_{ch}$  and the thickness of zero-strength layer  $d_0$  are then determined for a reference case according to the reduced cross-section method. Furthermore, a sensitivity analysis is performed to study the influence of the bending resistance in fire conditions  $M_{Rd,fi}$  and the elastic section modulus of the residual cross-section  $W_{res}$  on the charring depth  $d_{ch}$  and the thickness of zero-strength layer  $d_0$ . The obtained results of thicknesses  $d_{ch}$  and  $d_0$  are compared to the charring depth  $d_{ch,EC}$  according to EN 1995-1-2 (2005) and commonly used value of  $d_0 = 7$  mm, respectively. Correspondingly, suggestions for a modification of the reduced cross-section method are proposed as well.

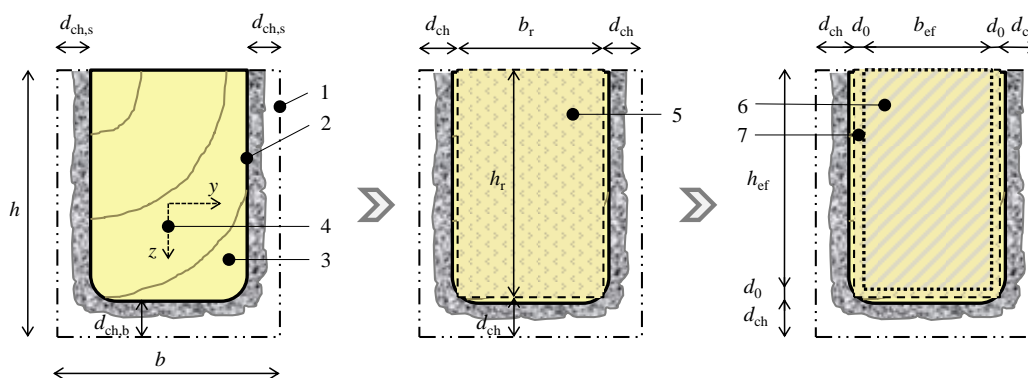


Fig. 1 Schematic of the reduced cross-section method: 1 Initial cross-section; 2 Charring line; 3 Residual cross-section with rounding; 4 Coordinate system; 5 Rectangular residual cross-section; 6 Effective cross-section; 7 Zero-strength layer

## 2 METHODS

The numerical analysis is divided into four consecutive phases. Firstly, a fire scenario is defined, secondly, a hygro-thermal analysis is performed to determine the charring depth  $d_{ch}$ , and thirdly, the mechanical analysis is carried out to determine the thickness of zero-strength layer  $d_0$ . Finally, a sensitivity analysis is performed to study the influence of the parameters  $W_{res}$  and  $M_{Rd,fi}$  on the thicknesses  $d_{ch}$  and  $d_0$ . In what follows, the first three phases are only briefly presented. For more information, please refer to Huč et al. (2021).

### 2.1 Fire scenario

Temperature of the gas surrounding the analysed timber structural member during fire exposure is determined according to the equations for a parametric fire given in EN 1991-1-2 (2002).

### 2.2 Hygro-thermal analysis

A hygro-thermal analysis is performed by an advanced coupled heat and moisture transfer model that was previously validated by Pečenko et al. (2015). The coupled heat and moisture transfer model constitutes of the energy conservation equation and three continuity equations, describing the conservation of bound water, water vapour and air. The model accounts for the sorption between bound water and water vapour, the energy released or required during sorption, the Soret effect and the convective heat transfer. A result of the hygro-thermal analysis is a temporal development of a two-dimensional (2D) temperature  $T$  field over the timber beam cross-section subjected to fire conditions. The isotherm  $T = 300^\circ\text{C}$  criterion is used to obtain the residual cross-section with rounding. The charring depth  $d_{ch}$  is determined by transforming the residual cross-section with

rounding to the rectangular residual cross-section, accounting for the equality of elastic section modulus  $W_{\text{res}}$

$$W_{\text{res}} = \frac{(b - 2 d_{\text{ch}}) (h - d_{\text{ch}})^2}{6} \quad (1)$$

where  $b$  and  $h$  are the width and the height of the initial rectangular timber cross-section, respectively. This way the charring depth  $d_{\text{ch}}$  is constant around the cross-section perimeter, which is in accordance to EN 1995-1-2 (2005).

### 2.3 Mechanical analysis

An advanced mechanical model previously developed and validated by Pečenko et al. (2019) is employed to determine the bending resistance in fire conditions  $M_{\text{Rd,fi,A}}$ . The planar beam model solves a system of equilibrium, kinematic and constitutive equations. A bi-linear stress-strain relationship for timber in tension and compression is considered in the model, as well as the 2D temperature field obtained by the hygro-thermal analysis. Reductions of strength and stiffness of timber at elevated temperatures are accounted for according to EN 1995-1-2 (2005). The thickness  $d_0$  is obtained by equating the bending resistance determined by the advanced mechanical model  $M_{\text{Rd,fi,A}}$  and the bending resistance determined simply by the reduced cross-section method  $M_{\text{Rd,fi,S}}$ , i.e.,

$$M_{\text{Rd,fi,S}} = f_{\text{m,k}} \frac{(b_r - 2 d_0) (h_r - d_0)^2}{6} = M_{\text{Rd,fi,A}} \quad (2)$$

where  $f_{\text{m,k}}$  is the characteristic bending strength of timber, and  $b_r$  and  $h_r$  are the width and the height of the rectangular residual cross-section, respectively. The mechanical resistances  $M_{\text{Rd,fi,S}}$  and  $M_{\text{Rd,fi,A}}$  are hereafter denoted as  $M_{\text{Rd,fi}}$ .

### 2.4 Sensitivity analysis

Once the thicknesses  $d_{\text{ch}}$  and  $d_0$  are determined for a reference case by the hygro-thermal and the mechanical analysis, respectively, a sensitivity analysis is applied to the reduced cross-section method to investigate the influence of the parameters  $W_{\text{res}}$  and  $M_{\text{Rd,fi}}$  on the thicknesses  $d_0$  and  $d_{\text{ch}}$ . The value of each numerically determined parameter for the reference case  $i = \{W_{\text{res}}, M_{\text{Rd,fi}}\}$  is multiplied by a set of numbers  $\Delta_i = \{0.7:0.025:1.3\}$ . When both parameters  $W_{\text{res}}$  and  $M_{\text{Rd,fi}}$  are simultaneously varied, it gives in total  $n = 625$  pairs of thickness  $d_0$  and  $d_{\text{ch}}$ .

### 2.4 Case study

A simply supported timber beam subjected to fire conditions from three sides and loaded with point loads on the thirds of a span  $L = 3.6$  m is considered. Dimensions of the rectangular cross-section are  $b/h = 20/24$  cm. The strength class of timber is C35, the density at ambient temperature  $T_{\text{g},0} = 20^\circ\text{C}$  is  $\rho_0 = 420$  kg/m<sup>3</sup>, and the initial moisture content is 12%. Fire scenario is designed by accounting for the following parameters: the opening factor,  $O = 0.04$  m<sup>0.5</sup>, the absorptivity for the total enclosure,  $b = 1000$  J/(m<sup>2</sup> K s<sup>0.5</sup>), the design value of the fire load density  $q_{\text{fd}} = 300$  MJ/m<sup>2</sup> and the fire compartment of dimensions 20 m  $\times$  15 m  $\times$  4 m. According to EN 1991-1-2 (2002), this gives a ventilation-controlled parametric fire curve that describes a development of gas temperature  $T_{\text{g}}$  surrounding the examined timber structural member over time of exposure to fire  $t$ . Material parameters used in the hygro-thermal model and the mechanical model can be found in Huč et al. (2021).

## 3 RESULTS AND DISCUSSION

The results of the hygro-thermal analysis are presented in Fig. 2 together with the charring depth  $d_{\text{ch,EC}}$  and the parametric fire curve  $T_{\text{g}}$ . The charring depth  $d_{\text{ch}}$  is expectedly greater than the charring depths from the bottom  $d_{\text{ch,b}}$  and from the sides  $d_{\text{ch,s}}$  of the rectangular cross-section, since it is determined in a way to eliminate the rounding effect of the residual cross-section as illustrated in Fig. 1. The numerical analysis of the reference case shows that charring of the timber cross-section ends, which means that the charring depths  $d_{\text{ch,b}}$ ,  $d_{\text{ch,s}}$  and  $d_{\text{ch}}$  become constant at approx.  $t = 62$  min, while

the stiffness and strength of uncharred timber continue reducing due to elevated temperatures, i.e.,  $20^{\circ}\text{C} < T < 300^{\circ}\text{C}$ , until time  $t = 86.2$  min at which the following results are obtained:  $M_{\text{Rd,fi}} = 13.8$  kNm,  $W_{\text{res}} = 801.32$  cm<sup>3</sup>,  $d_{\text{ch}} = 39.9$  mm and  $d_0 = 22.6$  mm. Nevertheless, an excellent match of  $d_{\text{ch}}$  and  $d_{\text{ch,EC}}$  is seen in Fig. 2 in particular towards the end of decay phase of the parametric fire curve, the obtained thickness  $d_0 = 22.6$  mm substantially exceeds the value of 7 mm that is prescribed in EN 1995-1-2 (2005) for the standard fire exposure.

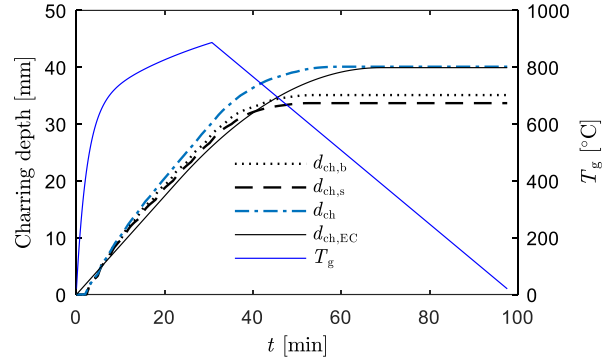


Fig. 2 Gas temperature-time curve ( $T_g - t$ ) of a considered parametric fire and the corresponding charring depths of a timber beam cross-section

Results of the applied sensitivity analysis are presented in Fig. 3 and Fig. 4. Fig. 3a shows that an increase of the parameter  $W_{\text{res}}$  applying the variation  $\Delta W_{\text{res}}$  at a constant parameter  $M_{\text{Rd,fi}}$ , i.e.,  $\Delta M_{\text{Rd,fi}} = 1$ , results in a decrease of the charring depth  $d_{\text{ch}}$  from 52.3 mm to 29.5 mm and in an increase of the thickness of zero-strength layer  $d_0$  from 10.2 mm to 33.0 mm. Despite a significant reduction of the parameter  $W_{\text{res}}$ , i.e., 30% ( $\Delta W_{\text{res}} = 0.7$ ), the minimum thickness  $d_0$  exceeds the prescribed value of 7 mm by 46%. Fig. 3b shows the influence of the variation  $\Delta M_{\text{Rd,fi}}$  at a constant parameter  $W_{\text{res}}$ , i.e.,  $\Delta W_{\text{res}} = 1$ , on the thicknesses  $d_{\text{ch}}$  and  $d_0$ . The thicknesses  $d_{\text{ch}}$  is obviously not affected by the variation  $\Delta M_{\text{Rd,fi}}$  at  $\Delta W_{\text{res}} = 1$ . It takes a constant value of  $d_{\text{ch}} = 39.9$  mm. On contrary, an increase of the parameter  $M_{\text{Rd,fi}}$  applying the variation  $\Delta M_{\text{Rd,fi}}$  at  $\Delta W_{\text{res}} = 1$  results in a decrease of the thickness  $d_0$  from 31.1 mm to 15.1 mm. The latter substantially exceeds the prescribed value of 7 mm.

The influence of applying all combinations of variations  $\Delta W_{\text{res}}$  and  $\Delta M_{\text{Rd,fi}}$  on the thicknesses  $d_{\text{ch}}$  and  $d_0$  is two-dimensionally presented in Fig. 3c and d in relation to the variations  $\Delta W_{\text{res}}$  and  $\Delta M_{\text{Rd,fi}}$ , respectively. For the sake of an easier visual interpretation of the results in Fig. 3c and d, a three-dimensional (3D) representation of the same results is shown in Fig. 4. The results in Fig. 3c, d and Fig. 4 show that only about 3% of all combinations ( $n = 625$ ) gives the thickness  $d_0$  smaller or equal to the prescribed value of 7 mm. The variations  $\Delta M_{\text{Rd,fi}}$  and  $\Delta W_{\text{res}}$  have to be greater or equal to 1.15 and smaller or equal to 0.775, respectively, for the thickness  $d_0$  to be smaller or equal to the value of 7 mm. Simultaneously, the thickness  $d_{\text{ch}}$  takes the values as high as 49.0 mm to 52.3 mm. The presented results imply that in case of parametric fire it is not safe to consider the thickness  $d_0 = 7$  mm as prescribed in EN 1995-1-2 (2005) for the standard fire. Should the reduced cross-section method (EN 1995-1-2, 2005) be on a safe side according to the presented results, either a substantial increase of the thickness  $d_0$  (up to 22.6 mm) at the charring depth of  $d_{\text{ch,EC}} = 39.9$  mm, or an increase of the charring depth  $d_{\text{ch,EC}}$  up to 49.0 mm leaving the thickness  $d_0$  at 7 mm, or finding a moderate increase of both values  $d_{\text{ch,EC}}$  and  $d_0$  are required.

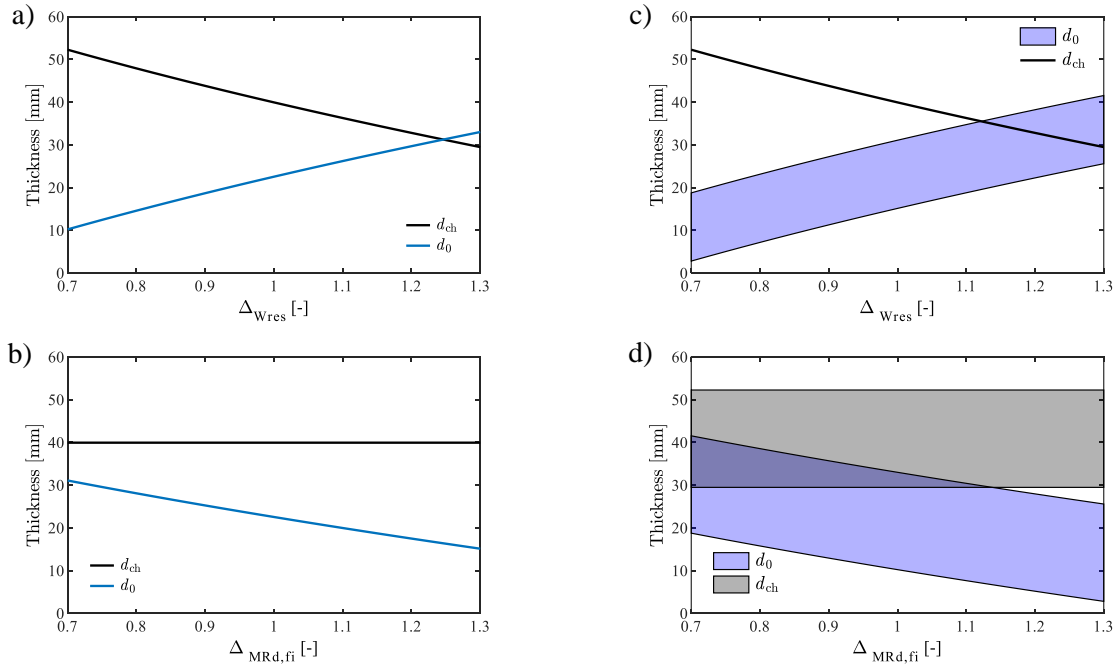


Fig. 3 Thicknesses  $d_{ch}$  and  $d_0$  determined by applying the following variations: a)  $\Delta_{W_{res}}$  at  $\Delta_{M_{Rd,fi}} = 1$  ( $M_{Rd,fi} = 13.8 \text{ kNm} = \text{const.}$ ), b)  $\Delta_{M_{Rd,fi}}$  at  $\Delta_{W_{res}} = 1$  ( $W_{res} = 801.32 \text{ cm}^3 = \text{const.}$ ), and c) and d)  $\Delta_{W_{res}}$  and  $\Delta_{M_{Rd,fi}}$

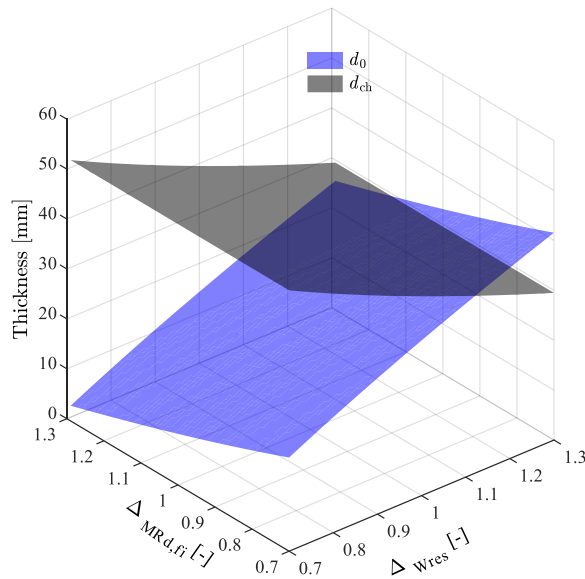


Fig. 4 A 3D representation of the thicknesses  $d_{ch}$  and  $d_0$  in relation to the variations  $\Delta_{W_{res}}$  and  $\Delta_{M_{Rd,fi}}$

#### 4 CONCLUSIONS

A simply supported timber beam subjected to parametric fire from three sides and loaded in bending is considered as a reference case. The advanced numerical models, i.e., the hygro-thermal model and the mechanical model are used to determine the elastic section modulus of residual cross-section  $W_{res}$  and the bending resistance of timber beam in fire conditions  $M_{Rd,fi}$ , respectively. Applying the reduced cross-section method given in EN 1995-1-2 (2005), the charring depth  $d_{ch}$  and the thickness of zero-strength layer  $d_0$  are determined for the reference case from the numerically obtained parameters  $W_{res}$  and  $M_{Rd,fi}$ . Then, a sensitivity analysis is performed to study the influence of the elastic section modulus of residual cross-section  $W_{res}$  and the bending resistance in fire conditions  $M_{Rd,fi}$  on the charring depth  $d_{ch}$  and the thickness of zero-strength layer  $d_0$ . The parameters  $W_{res}$  and  $M_{Rd,fi}$  are varied so that they are multiplied by a set of numbers  $\Delta_{M_{Rd,fi}} = \Delta_{W_{res}} = \{0.7; 0.025; 1.3\}$ .

The following can be concluded from the analysis of the reference case:

- the charring depth  $d_{ch} = 39.9$  mm obtained by the hygro-thermal model equals the charring depth  $d_{ch,EC}$  determined according to the expression in EN 1995-1-2 (2005);
- the obtained thickness of zero-strength layer  $d_0 = 22.6$  mm in case of parametric fire is substantially higher than the value of 7 mm prescribed in EN 1995-1-2 (2005) for the standard fire.

The results of the sensitivity analysis can be summarized as follows:

- the higher the charring depth  $d_{ch}$ , the lower the thickness of zero-strength layer  $d_0$ ;
- the thickness  $d_0$  is smaller or equal to the value of 7 mm only in about 3% of the analysed cases where the variations  $\Delta_{M_{Rd,fi}}$  and  $\Delta_{W_{res}}$  are greater or equal to 1.15 and smaller or equal to 0.775, respectively. Correspondingly, the charring depth  $d_{ch}$  takes the values between 49.0 mm and 52.3 mm.

Based on the results of the present paper, it is suggested to modify the reduced cross-section method in EN 1995-1-2 (2005) in one of the following ways to make it more conservative (and possibly safer) to use in case of parametric fire exposure:

- the charring depth  $d_{ch,EC}$  should be increased for approx. 23% if the value of 7 mm is prescribed for the thickness of zero-strength layer, or
- both thicknesses  $d_{ch,EC}$  and  $d_0$  should be moderately increased, which means that the expression for the charring depth  $d_{ch,EC}$  should be adapted and simultaneously a greater value of  $d_0$  than 7 mm should be prescribed, or
- a new parameter should be introduced, e.g.,  $d_{ch,0}$ , which would account for the charring depth and the thickness of zero-strength layer together, i.e.,  $d_{ch,0} = d_{ch,EC} + d_0$ . The new parameter would thus simply present the thickness of cross-section that has no contribution to the load-bearing capacity of timber beam subjected to fire. This would also simplify the use of the reduced cross-section method for structural engineers.

## ACKNOWLEDGMENTS

The financial support of the Slovenian Research Agency through the research core funding (grant number P2-0260) is gratefully acknowledged.

## REFERENCES

- EN 1991-1-2, Eurocode 1: *Actions on Structures - Part 1-2: General actions – Actions on structures exposed to fire*, European committee for standardization, Brussels, Belgium, 2002.
- EN 1995-1-2, Eurocode 5: *Design of timber structures, Part 1-2: Structural fire design*, European Committee for Standardization, Brussels, Belgium, 2005.
- Huč S., Pečenko R., Hozjan T. 2021. *Predicting the thickness of zero-strength layer in timber beam exposed to parametric fires*. *Engineering structures*, 229, p. 1-11.
- Lange D., Boström L., Schmid J., Albrektsson J. 2015. *The Reduced Cross Section Method Applied to Glulam Timber Exposed to Non-standard Fire Curves*. *Fire Technology* 51, p. 1311-1340.
- Pečenko R., Svensson S., Hozjan T. 2015. *Modelling heat and moisture transfer in timber exposed to fire*. *International Journal of Heat and Mass Transfer*, 87, p. 598-605.
- Pečenko R., Planinc I., Svensson S., Hozjan T. 2019. *Implementing coupled heat and moisture transfer model in the fire analysis of timber beams*. *Fire Safety Journal* 107, p. 170-178.
- Schmid J., Just A., Klippel M., Fragiaco M. 2015. *The Reduced Cross-Section Method for evaluation of the fire resistance of timber members: Discussion and determination of the zero-strength layer*. *Fire Technology*, 51, p. 1285-1309.

## **PREDICTION OF TEMPERATURE OF INDIVIDUAL PARTS OF CLADDING SYSTEMS DURING FIRE**

Nikola Lišková<sup>a</sup>, Kamila Cábová<sup>a</sup>, František Wald<sup>a</sup>, Kristo Mela<sup>b</sup> & Mikko Malaska<sup>b</sup>

<sup>a</sup>Czech Technical University in Prague, Prague, Czech Republic

<sup>b</sup>Tampere University of Technology, Tampere, Finland

### **Abstract**

Sandwich panels and trapezoidal sheets can be used to stabilize the main steel structure in fire. When using the cladding systems for stabilization, temperatures and behaviour of the individual parts of the cladding systems during the fire are the main information needed for their design. The paper describes a method how to determine the temperatures of screws in sandwich panel connections and an insulation capacity of the cladding systems during fire. The method was derived from results of fire tests of roof and wall sandwich panels with mineral wool core and polyisocyanurate foam (PIR) which were carried out in horizontal furnace. Based on the experiments, equations for the prediction of the temperature of individual parts of the structure and for the prediction of thermal degradation of the panel core by the mean of change of effective thermal conductivity were derived. These equations can be used for practical design of steel structures with cladding systems serving for stabilization of the structure during fire.

**Keywords:** stability; trapezoidal sheets; sandwich panels; fire tests; screw; temperature analysis.

### **1 INTRODUCTION**

The structural stability of steel building frames is ensured by frame action or bracing elements. Previous research has, however, demonstrated that considerable savings can be achieved in structural members, columns, beams and trusses by using elements forming the building envelope to provide stability. Already in 1995, the European recommendation was issued (ECCS Publication No. 88, 1995), which made it possible to take into account the effect of the cladding system with trapezoidal sheets on the stability of steel structures. Design recommendations for stabilizing steel structures using sandwich panels composed of thin metal faces with mineral wool and PIR cores have been developed and published more recently (Hedman-Petursson 2001) and (ECCS TC7 TWG 7.9, 2014). Unfortunately, these recommendations do not include the use of the cladding systems to stabilize steel structures in the fire.

When using the cladding systems for stabilizing steel structures in normal temperature then the most important part of the structure are the connectors between the cladding and structural members. The stiffness and resistance of the cladding itself can be omitted in the calculations.

The behaviour of steel structures exposed to elevated temperature is significantly different from the behaviour at normal temperatures. Due to high temperatures, the material is degraded and the load-bearing capacity of a structure is reduced. In order to determine the temperature of the connectors and the degradation of cladding systems material during a fire, a series of six full-scale fire tests of the roof cladding structures were performed. The tests have been carried out on the horizontal test furnace at fire laboratory PAVUS a.s. in the Czech Republic. The experiments were part of RFCS project STABFI.

### **2 EXPERIMENTAL STUDY**

The main target of the fire tests was to determine the temperature of screws fixing the cladding system to the supporting structure and to investigate behaviour of cladding systems exposed to fire.

## 2.1 Specimens and setup of tests

Test specimens consisted of a fire protected steel beam HEA 160 made of structural steel S355 installed across the longer span of the fire furnace and a load bearing cladding system mounted to the beam. The beam HEA 160 had 4.5 m span and was insulated with an intumescent coating of 1200  $\mu\text{m}$  thick for a fire resistant of 60 minutes. It was installed as a simply supported beam in the one third of the shorter span of the furnace to simulate of asymmetric loading condition of cladding. The furnace dimensions were 3 m  $\times$  4 m. The view and section of the setup of roof structure for fire test is presented in Fig. 1.

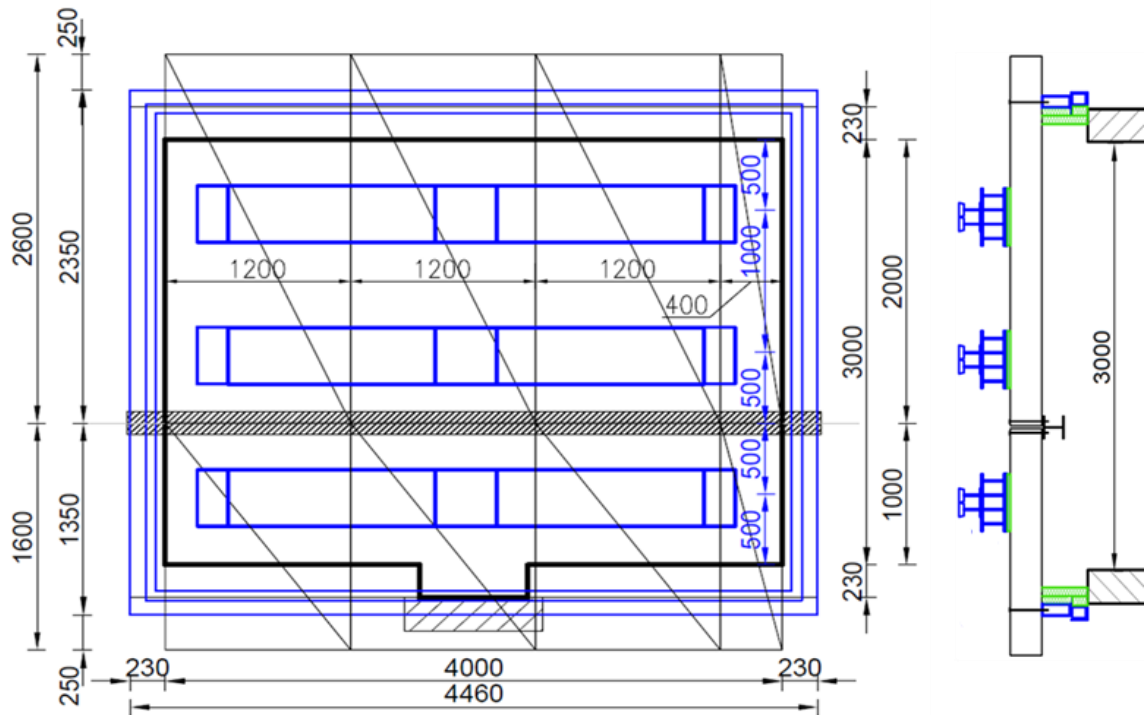


Fig. 1 Setup of roof structure for fire test

For tests cladding systems consisting of trapezoidal sheets made of steel of 0.9 mm thick; sandwich panels with mineral wool (MW) and Polyisocyanurate (PIR) insulation cores were chosen. Sandwich panel system with a PIR core is a through fixed insulated roofing element for use in normal applications. Sandwich panel system with a mineral wool (MW) lamella core is an external-wall panel typically used in facades. In Table 1 details on cladding systems and their fastening to the beam is shown.

Table 1: Cladding systems for the fire tests

Cladding reference	Insulation core	Thickness [mm]	Typical application	Screw connection with beam	Loading [ $\text{kN/m}^2$ ]	Dimensions width x length
SP_PIR 100	PIR	100	Roof/wall	SCX14-S19-5.5x190	1	1 x 1.6 m 1 x 2.6 m
SP_PIR 160	PIR	160	Roof/wall	SCX14-S19-5.5x240	1	
SP_MW 100	MW	100	Wall	SCX14-S19-5.5x190	0.5	
SP_MW 230	MW	230	Wall	SCX14-S19-5.5x275	0.5	
TR_100	-	100	Roof/wall	SD14 x T16-5.5x34	1	0.825 x 1.675 m 0.825 x 2.675 m
TR_153	-	153	Roof/wall		1	0.84 x 1.675 m 0.84 x 2.675 m

## 2.2 Test conditions

During the experiments, the temperature in the furnace was increased according to the standard fire curve described in (EN 1363-1 Fire resistance test, 2012). The furnace temperature was controlled using 8 plate thermometers, in accordance with (EN 1363-1 Fire resistance test, 2012).

Temperature distribution in steel beams, cladding elements and screw connectors was measured by K-type thermocouples (TC). The thermocouples were placed in the 1/2 and 1/4 span of the beam in the same places in each of the 6 experiments: along the height of the screw (at the end, in the middle and on the head of the screw), along the height of the beam and on the exposed and unexposed face of the cladding. A total of 33 thermocouples were installed in each specimen.

Deflections were measured at three points along the beam span: in the middle and in the 1/4 span and at the corresponding locations at the mid-span of the longer cladding elements.

## 3 RESULTS

The duration of the tests varied between 33 minutes and 88 minutes and the tests were terminated due to fast deflection rate of panels or temperatures exceeding 200 °C on unexposed face. Pictures of specimens after the tests are shown in Fig. 2.



a) SP\_MW\_100 after test



b) Mineral wool core SP\_MW\_100 after test



c) PIR foam core SP\_PIR\_160 after test

Fig. 2 Sandwich panels after the fire test: a) SP\_MW\_100 after test; b) Mineral wool core SP\_MW\_100 after test; c) PIR foam core SP\_PIR\_160 after test

### 3.1 Temperatures and deflections of beam and cladding

The temperature development of HEA sections was similar in all tests. In all tests up to 60 minutes the temperature difference between top and bottom flanges of beam sections were about 50 °C. In tests with trapezoidal sheets and PIR cores panels the temperatures of bottom sheet followed the furnace temperature. In tests with mineral wool core the bottom sheet temperatures were approximately 100 °C lower than the furnace temperature. The top sheet temperatures of the sandwich panels, including mineral wool and PIR cores, remained below 250 °C in all tests except near longitudinal joints between panels, where temperatures of 475 °C were measured. Higher temperatures were due to the opening of the panel edges between stitching screws. Maximum temperatures and deflections of the beams and cladding systems at 30 minutes and 60 minutes after ignition are reported in Table 2.

Table 2: Results of roof structure fire tests

Cladding reference	Max. temperature [°C] and deflection [mm]				End of the test [min]	Max. deflection of beam [mm]	Max. deflection of cladding [mm]
	30 min		60 min				
	Beam	Cladding	Beam	Cladding			
SP_PIR 100	354 °C 7.3 mm	95 °C 32 mm	573 °C 17.7 mm	169 °C 112.2 mm	77 min	41 mm	166 mm
SP_PIR 160	355 °C 3.4 mm	12 °C 10.4 mm	556 °C 6.3 mm	144 °C 60.3 mm	83 min	23 mm	120 mm
SP_MW 100	422 °C 13.7 mm	70 °C 135.8 mm	674 °C 28.5 mm	137 °C 152.1 mm	72 min	38 mm	156 mm
SP_MW 230	399 °C 11.7 mm	30.6 °C 32 mm	719 °C 26.6 mm	36.7 °C 93 mm	88 min	92 mm	172 mm
TR_100	457 °C -12.4 mm	760 °C 43.6 mm	-	-	41 min	-12,4 mm at 30 min	122 mm
TR_153	462 °C -10.3 mm	780 °C 45.8 mm	-	-	33 min	-10,3 mm at 30 min	82 mm

The results of the tests showed that sandwich panels with the PIR core had the most positive effect on the deflection of the supporting construction - HEA beam. In the case of 160 mm thick panels

with the rigid core made of the PIR foam, the measured beam deflection was almost half that of 100 mm thick panels. Similarly, in the case of trapezoidal sheets, the deflection of the beam was less in the case of sheets with of 153 mm height than in the case of sheets of 100 m height, however, the difference was very small. In the case of panels with the core made of mineral wool lamellas, the deflection for both samples was almost identical until 60 minutes, ie until the beam was sufficiently protected by the intumescent coating.

### 3.2 Screw temperatures

Temperatures measured on the end of screws in tests were very similar to those of the bottom sheet of the cladding systems. Temperatures of the end of the screw were higher than HEA beam top flange temperatures, because the beam was fire protected whereas the end of the screws were exposed to fire. In all tests with sandwich panels, the screw head temperatures were very low, below 150°C whereas in tests with trapezoidal sheets screw head temperatures were lower than sheet temperatures within 15 minutes after ignition and then were very similar. Temperature of screws in mid-depth of the panels with a thickness of 100mm was significantly higher in mineral wool core than in PIR core, see Table 3.

Table 3: Results of roof structure fire tests – screw temperatures

Cladding reference	Average temperature [°C]					
	30 min			60 min		
	head screw	screw in mid. of the panels	end of screw	head screw	screw in mid. of the panels	end of screw
SP_PIR 100	16	159	778	63	345	864
SP_PIR 160	20	96	775	41	200	878
SP_MW 100	64	210	805	141	395	826
SP_MW 230	37	88	742	41	225	799
TR_100	763	-	-	-	-	-
TR_153	798	-	-	-	-	-

### 3.2 Temperature analysis

Based on the test results, a thermal analysis of individual parts of the structure was performed. The analysis is based on the calculations described in (Wang Y. et al., 2013). Fourier's law of thermal conduction and a modified incremental heating method given in *Eq. (1)* were used to calculate temperatures in different parts of structure and level of degradation of panel core materials:

$$\Delta\theta = \frac{(\theta_{fi} - \theta_m) * \lambda_m}{d_m * \rho_m * c_m} * \Delta t \quad (1)$$

where  $\Delta\theta$  increase of temperature;  
 $\theta_{fi}$  ambient gas temperature;  
 $\theta_m$  temperature of the material;  
 $d_m$  thickness of the material;  
 $\rho_m$  material density;  
 $\lambda_m$  effective thermal conductivity of the material;  
 $c_m$  specific heat capacity of the material;  
 $\Delta t$  time increment.

From the tests, the temperatures of the screw connectors between the cladding and the beam at the location of the shear plane of the screw were obtained, which are crucial for the design of

stabilization of steel structures by cladding systems. This new knowledge has been generalized so that they can be used to predict the temperatures of these parts of the structures.

Temperature analysis show that for sandwich panels, the temperature in the shear plane of the screw is the same as the temperature of the beam. In the case of trapezoidal sheets temperature in the shear plane of the screw is close to the gas temperature, mainly 85% of the gas temperature within 15 minutes after ignition, when the gas temperature according to the standard fire curve reaches approximately 740 °C. In the following minutes, the temperature in the shear plane of the screw rises to 95% of the gas temperature.

Another result of the temperature analysis was to determine the temperature degradation of insulation core of sandwich panels. The degradation of the insulation core of panel is described by the effective thermal conductivity depending on the temperature. The thermal conductivity of PIR foam is  $\lambda_{20} = 0,018 \text{ W/m}^\circ\text{C}$  in ambient temperatures. The specimen SP\_PIR 100 mm showed no changes during first 20 minutes of the fire test, the gas temperature in furnace after 20 minutes reached 780 °C. The temperature on the unexposed side of the panel increased significantly from 20 minutes of the test and the effective thermal conductivity decreased depending on the temperature in the furnace according to equation  $\lambda_{\text{eff}} = 0,41 - \theta/1000 \text{ [W/m}^\circ\text{C]}$ , where  $\theta$  is the temperature of the specimen on the unexposed side. The specimen SP\_PIR 160 mm showed no changes during first 38 minutes of the fire test, the gas temperature in furnace after 38 minutes reached 880 °C. It means that the specimen with a core 60 mm thicker resist exposure to fire according to the standard temperature curve for 18 minutes longer. The effective thermal conductivity was degraded according to the equation  $\lambda_{\text{eff}} = 1,2 - \theta/1000 \text{ [W/m}^\circ\text{C]}$  from 38 minutes.

Mineral wool as a non-combustible material did not show almost any changes of thermal properties. The temperature increased linearly until the end of the test for both test specimens SP\_MW 100 mm and SP\_MW 230 mm.

#### 4 CONCLUSIONS

The results of the fire experiments confirmed the possibility of stabilization of the steel structure by the cladding systems exposed to fire. Although PIR foam is flammable material and its thermal degradation has been described by effective thermal conductivity, the sandwich panels with the rigid PIR foam had the most positive effect on the deflection of the supporting construction because of their bending stiffness. Screws in the mid-depth of the PIR core had a lower temperature than in the MW core. Panels with MW lamella core proved good insulation capacity and resistance against to thermal degradation but due to construction of the core from separate lamellas they had lower bending stiffness and minimal effect on deflection of the beam. Temperatures of the trapezoidal sheet parts were almost the same as the gas temperature in the fire and the height of the sheet wave had minimal effect on deflection of the beam.

#### ACKNOWLEDGMENTS

The authors would like to thank for the financial support provided by RFCS project STABFI.

#### REFERENCES

- ECCS Publication No. 88, 1995. *European recommendations for the application of metal sheeting acting as a diaphragm*. 263 p., ISBN 978-90-6363-081-2
- Hedman-Petursson, 2001. *Column Buckling with Restraint from Sandwich Wall Elements*. PhD Thesis. Luleå: Department of Civil and Mining Engineering, Division of Steel Structures, Luleå University of Technology. ISBN 13: 978-1-85942-226-7.
- ECCS TC7 TWG 7.9, 2014. *European recommendations on the stabilization of steel structures by sandwich panels*. s.l.: CIB – International Council for Research and Innovation in Building and Construction.
- EN 1363-1 Fire resistance test, 2012. Part 1: *General requirements*. Brussels: European Committee of Standardization.
- Wang Y. et al., 2013. *Performance-Based Fire Engineering of Structures*. New York, 394 p., ISBN 978-0-415-55733-7

### **STEERING COMMITTEE**

WALD Frantisek, *Czech Republic* (chairman)  
BURGESS Ian, *United Kingdom*  
KODUR, Venkatesh, *USA*  
TAN, Kang Hai, *Singapore*  
WANG, Yong, *United Kingdom*

### **SCIENTIFIC COMMITTEE**

BURGESS Ian, *United Kingdom* (chairman)  
ABU, Anthony, *New Zealand*  
ALI, Faris, *United Kingdom*  
BEDON, Chiara, *Italy*  
BISBY, Luke, *United Kingdom*  
BLOCK Florian, *Germany*  
BOSTRÖM, Lars, *Sweden*  
BOTH, Ioan, *Romania*  
BRATINA, Sebastjan, *Slovenia*  
CABOVA, Kamila, *Czech Republic*  
CHIFLIGANEC, Cvetanka, *N. Macedonia*  
ČEŠAREK, Peter, *Slovenia*  
FORTINO, Stefania, *Finland*  
FRAGIACOMO, Massimo, *Italy*  
FRANGI, Andrea, *Switzerland*  
FRANSSSEN, Jean-Marc, *Belgium*  
GAMBAROVA, Pietro, *Italy*  
GARDNER, Leroy, *United Kingdom*  
HOSTIKKA, Simo, *Finland*  
HOZJAN, Tomaž, *Slovenia*  
HUANG, Shan Shan, *United Kingdom*  
HUČ, Sabina, *Slovenia*  
KODUR, Venkatesh, *USA*  
LANGE, David, *Australia*  
LI, Guo Qiang, *China*  
MAHENDRAN, Mahen, *Australia*  
MALUK, Cristian, *Australia*  
NIGRO, Emidio, *Italy*  
OZAWA, Mitsuo, *Japan*  
PEČENKO, Robert, *Slovenia*  
PLANINC, Igor, *Slovenia*  
REIN, Guillermo, *United Kingdom*  
ROMERO, Manuel L., *Spain*  
RUKAVINA, Marija, *Croatia*  
SCHMID, Joachim, *Switzerland*  
SCHNABL, Simon, *Slovenia*  
SELAMET, Serdar, *Turkey*  
TAERWE, Luc, *Belgium*  
TAN, Kang Hai, *Singapore*  
TORIČ, Neno, *Croatia*  
TORERO, Jose, *United Kingdom*  
VILA REAL, Paulo, *Portugal*  
WALD, František, *Czech Republic*  
WANG, Yong, *United Kingdom*  
ZAHARIA, Raul, *Romania*

### **ORGANIZING COMMITTEE**

HOZJAN, Tomaž, *Slovenia* (chairman)  
CHIFLIGANEC, Cvetanka, *North Macedonia*  
FISTER, Iztok ml., *Slovenia*  
HUČ, Sabina, *Slovenia*  
OGRIN, Anita, *Slovenia*  
PEČENKO, Robert, *Slovenia*  
ZUPAN, Dejan, *Slovenia*